

# DIGITAL HUMAN MODELING AND MEDICINE

## THE DIGITAL TWIN



EDITED BY

GUNTHER E. PAUL  
MOHAMED H. DOWEIDAR



# Digital Human Modeling and Medicine

This page intentionally left blank

# Digital Human Modeling and Medicine

## The Digital Twin

Edited by

**Gunther Paul**

*Australian Institute of Tropical Health and Medicine,  
James Cook University, Townsville, QLD, Australia*

**Mohamed Hamdy Doweidar**

*Aragon Institute of Engineering Research (I3A),  
University of Zaragoza, Zaragoza, Spain;  
Mechanical Engineering Department,  
School of Engineering and Architecture (EINA),  
University of Zaragoza, Zaragoza, Spain;  
Centro de Investigación Biomédica en Red en Bioingeniería,  
Biomateriales y Nanomedicina (CIBER-BBN), Madrid, Spain*



**ACADEMIC PRESS**

An imprint of Elsevier

Academic Press is an imprint of Elsevier  
125 London Wall, London EC2Y 5AS, United Kingdom  
525 B Street, Suite 1650, San Diego, CA 92101, United States  
50 Hampshire Street, 5th Floor, Cambridge, MA 02139, United States  
The Boulevard, Langford Lane, Kidlington, Oxford OX5 1GB, United Kingdom

Copyright © 2023 Elsevier Inc. All rights reserved.

No part of this publication may be reproduced or transmitted in any form or by any means, electronic or mechanical, including photocopying, recording, or any information storage and retrieval system, without permission in writing from the publisher. Details on how to seek permission, further information about the Publisher's permissions policies and our arrangements with organizations such as the Copyright Clearance Center and the Copyright Licensing Agency, can be found at our website: [www.elsevier.com/permissions](http://www.elsevier.com/permissions).

This book and the individual contributions contained in it are protected under copyright by the Publisher (other than as may be noted herein).

### Notices

Knowledge and best practice in this field are constantly changing. As new research and experience broaden our understanding, changes in research methods, professional practices, or medical treatment may become necessary.

Practitioners and researchers must always rely on their own experience and knowledge in evaluating and using any information, methods, compounds, or experiments described herein. In using such information or methods they should be mindful of their own safety and the safety of others, including parties for whom they have a professional responsibility.

To the fullest extent of the law, neither the Publisher nor the authors, contributors, or editors, assume any liability for any injury and/or damage to persons or property as a matter of products liability, negligence or otherwise, or from any use or operation of any methods, products, instructions, or ideas contained in the material herein.

ISBN: 978-0-12-823913-1

For information on all Academic Press publications visit our website at  
<https://www.elsevier.com/books-and-journals>

*Publisher:* Mara E. Conner  
*Acquisitions Editor:* Carrie L. Bolger  
*Editorial Project Manager:* Tom Mearns  
*Production Project Manager:* Manju Paramasivam  
*Cover Designer:* Mark Rogers

Typeset by TNQ Technologies



Working together  
to grow libraries in  
developing countries

[www.elsevier.com](http://www.elsevier.com) • [www.bookaid.org](http://www.bookaid.org)

# Contents

Contributors.....	xxiii
-------------------	-------

## SECTION 1 Modeling methods

### CHAPTER 1 From the visible human project to the digital twin.... 3

*Gunther Paul*

Introduction.....	3
The visible human project.....	4
Anatomography.....	6
Virtual physiological human.....	6
The digital twin.....	8
References.....	16
Further reading.....	17

### CHAPTER 2 Massive data probabilistic framework for parameter estimation in biological problems.....19

*Marina Pérez-Aliacar, Jacobo Ayensa-Jiménez,  
Mohamed H. Doweidar and Manuel Doblaré*

Introduction.....	20
General framework .....	21
About modeling.....	21
About experiments: smart experiments .....	22
Model separability .....	26
Including model uncertainty .....	26
Mathematical tools and concepts.....	28
Managing data uncertainty .....	28
Estimation of probabilistic models.....	30
Design of experiments.....	31
Copulas.....	32
Methodology.....	36
Model adjustment.....	36
Model analysis and applications.....	37
A case study: GBM evolution.....	39
Mathematical model.....	40
Data generation .....	42
Results.....	43
Conclusions .....	57
Acknowledgments.....	58
References.....	58

<b>CHAPTER 3 Deep learning applied to detection of the vulnerable atherosclerotic plaque .....</b>	<b>63</b>
<i>M. Cilla, J. Martínez, M.A. Martínez and E. Peña</i>	
Introduction.....	63
The atheroma plaque problem.....	66
3D parametric study.....	66
Source data.....	68
Mathematical methods for regression .....	68
Artificial neural network .....	69
Support vector machine .....	71
Assuring the quality of the machine.....	71
Validation with a real geometry.....	74
Finite element models .....	75
Results.....	78
Discussion.....	80
Acknowledgments.....	80
References.....	80
<b>CHAPTER 4 Computational stability of human musculoskeletal systems .....</b>	<b>85</b>
<i>Farshid Ghezelbash, Abolfazl Shirazi-Adl, Masoud Sharifi, Navid Arjmand and Babak Bazrgari</i>	
Introduction.....	85
Methods.....	88
Criteria of structural stability .....	88
Stability of human MS systems.....	91
Stability of the human spine .....	94
Role of posture and passive ligamentous stiffness.....	94
Role of load orientation and elevation .....	94
Role of coactivity .....	95
Stability-based multicriteria simulations .....	96
Stability of human knee joint.....	97
Summary.....	99
Acknowledgments.....	100
References.....	100
<b>CHAPTER 5 Techniques for automatic landmark detection of human tissue .....</b>	<b>107</b>
<i>Juan-Roberto Jiménez-Pérez, José Negrillo-Cárdenas and Francisco R. Feito</i>	
Introduction.....	107

Machine learning techniques.....	108
Artificial neural networks.....	108
Decision trees .....	109
Support vector machines.....	110
Knowledge-based techniques.....	111
Shape analysis.....	111
Curvature analysis .....	112
Template-based approaches .....	114
Statistical shape modeling.....	115
Patient-specific templates.....	115
Conclusion .....	116
References.....	116
<b>CHAPTER 6 Multibody modeling of the musculoskeletal system.....</b>	<b>121</b>
<i>Michael Skipper Andersen and John Rasmussen</i>	
Introduction.....	121
Fundamentals of multibody modeling.....	123
Motion capture–based model.....	127
Cadaver-based lower extremity model .....	127
Linear geometric scaling law .....	130
Parameter identification .....	131
Mass and inertial properties.....	132
Mass-fat muscle strength scaling law .....	133
Over-determinate kinematic analysis.....	133
Inverse dynamic analysis.....	134
Analysis of gait modifications.....	136
Other applications.....	138
Concluding remarks.....	139
References.....	139
<b>CHAPTER 7 AnyBody modeling system .....</b>	<b>143</b>
<i>Michael Skipper Andersen and John Rasmussen</i>	
Background and context.....	143
Software design choices.....	144
AnyScript.....	145
Multibody system formulation .....	146
The model repository .....	146
Structuring principles .....	147
Applications .....	148
Fundamental science applications.....	148

Orthopedic applications .....	149
Industrial product design.....	150
Sports.....	151
Workplace ergonomics .....	153
Digital human models and the digital patient.....	155
References.....	156
<b>CHAPTER 8 The NEUROiD neuromusculoskeletal movement simulation platform.....</b>	<b>161</b>
<i>Raghuram Sesha Iyengar, Kapardi Mallampalli, Avinash Kumar Singh, Aditya Koppula, Kousik Sarathy Sridharan and Mohan Raghavan</i>	
Introduction.....	162
The NEUROiD movement simulation platform.....	163
Design philosophy and architecture.....	163
Model definition, simulation, and visualization .....	167
Integrative model development.....	171
Choosing a musculoskeletal model .....	172
Design and characterization of limbs in silico.....	172
Upper limb.....	172
Lower limb.....	177
Movement training of virtual limbs.....	179
Machine learning setup.....	180
NEUROiD in medicine .....	182
NEUROiD models .....	183
NEUROiD activities.....	183
Twinning in NEUROiD .....	183
Clinical trials and experimentation in silico with NEUROiD ..	184
Conclusion and future landscapes.....	192
References.....	193
<b>CHAPTER 9 HumMod: a modeling environment for the simulation of integrative human physiology.....</b>	<b>199</b>
<i>John S. Clemmer, W. Andrew Pruett and Robert L. Hester</i>	
Disclosures.....	199
History .....	199
Model content.....	201
HumMod for testing physiological concepts and hypotheses in pathophysiology .....	201
Example 1: salt sensitivity.....	203
Example 2: baroreceptor activation therapy .....	204

Example 3: arteriovenous fistula.....	206
The future of modeling: virtual populations.....	206
Conclusion, limitations, and future considerations .....	208
Acknowledgments.....	209
References.....	209

## SECTION 2 Organs

### CHAPTER 10 Computational biomechanics as a tool to improve surgical procedures for Uterine Prolapse..... 213

*Silva Elisabete, Bessa Nuno, Mascarenhas Teresa and António Augusto Fernandes*

Introduction .....	213
Mechanism of the development of POP .....	215
Biomechanical uterine prolapse simulation.....	218
Isotropic constitutive model—simulating the passive behavior.....	218
Computational model of the pelvic cavity .....	219
Computational model of the implant .....	219
Biomechanical properties of the soft tissues and mesh implant .....	220
Uterine prolapse simulation.....	221
Personalized models to repair the uterine prolapse.....	223
Conclusions .....	223
Acknowledgments.....	223
References.....	224

### CHAPTER 11 Computational modeling of aerosol particle transport and deposition in the healthy and stented human airways considering different breathing conditions and particle sizes ..... 227

*Rocío Fernández-Parra, Carmen Sánchez-Matás,  
José Luis López-Villalobos and Mauro Malvè*

Clinical background .....	228
Materials and methods.....	231
Geometries .....	231
Numerical model and boundary conditions.....	231
Results.....	235
Airflow patterns in healthy and stented airways .....	235
Airflow turbulent patterns in healthy and stented airways .....	239
Particle deposition and transport.....	240
Validation of the numerical findings.....	240

Regional deposition fractions.....	243
Conclusions and final remarks .....	246
Funding .....	246
Acknowledgments.....	246
References.....	247

## **CHAPTER 12 Ultrafine particle transport to the lower airways: airway diameter reduction effects ..... 253**

*Puchanee Larpruenrudee, Gunther Paul, Suvash C. Saha,  
Shahid Husain, HamidReza Mortazavy Beni, Christopher  
Lawrence, Xuzhen He, Yuantong Gu and Mohammad Saidul  
Islam*

Introduction.....	253
Geometrical development.....	256
Numerical methods.....	258
Result and discussion .....	260
Velocity functions.....	260
Pressure variations .....	261
Particle deposition fraction.....	263
Escaped particles.....	267
Conclusions.....	269
Limitations of the approach.....	269
References.....	270

## **CHAPTER 13 Aerosolized airborne bacteria and viruses inhalation: Micro-bioaerosols deposition effects through upper nasal airway inhalation ..... 275**

*Hamed Mortazavi, Hamidreza Mortazavy Beni,  
Mohammad Saidul Islam and Gunther Paul*

Nomenclature.....	276
Introduction.....	276
Materials and method.....	278
Computational model .....	278
Governing equations .....	279
Results.....	280
Discussion.....	283
Conclusion .....	285
Declaration of competing interest .....	286
Acknowledgments.....	286
References.....	286

<b>CHAPTER 14 Numerical simulation of the aortic arch behavior.....</b>	<b>289</b>
<i>Hamidreza Mortazavy Beni, Hamed Mortazavi, Gunther Paul, Mohammad Saidul Islam and Ali Asghar Zarei</i>	
Nomenclature.....	290
Introduction.....	290
Methods.....	291
Geometry reconstruction and grid generation.....	291
Governing equations .....	292
Boundary conditions and numerical solution .....	293
Results.....	294
Discussion.....	297
Conclusion .....	300
Disclosure of interest.....	300
Acknowledgments.....	300
References.....	301
<b>CHAPTER 15 Modern placental imaging methods .....</b>	<b>305</b>
<i>Christopher Edwards, Erika Cavanagh and Vicki L. Clifton</i>	
Introduction.....	305
Ultrasound.....	307
Doppler.....	308
Volume rendering .....	310
Sonoelastography.....	312
Placental elastography .....	315
Magnetic resonance imaging.....	316
Conclusion .....	319
References.....	320
<b>SECTION 3 Body parts</b>	
<b>CHAPTER 16 Foot digital twin and in silico clinical applications.....</b>	<b>331</b>
<i>Enrique Morales Orcajo and Andrea Stenti</i>	
Where a foot digital twin can help.....	331
Key aspects of foot biomechanics.....	331
Main foot pathologies by volume .....	332
Foot digital twin—scope of interest .....	334
The potential of foot CM&S.....	335
How to build a foot digital twin .....	336

Anatomy reconstruction.....	337
Loading and boundary conditions.....	338
Tissue properties.....	339
Verification and validation.....	341
Initiatives to improve model credibility in healthcare.....	341
Foot digital twin: a look into the future .....	342
In silico trials.....	342
What level of anatomical detail is required for clinical applications?.....	343
Foot CM&S for clinical applications.....	345
Foot CM&S for the footwear industry.....	348
Why foot and ankle CM&S is not yet in the clinic .....	350
References.....	353
<b>CHAPTER 17 Flow processes occurring within the body but still external to the body's epithelial layer (gastrointestinal and respiratory tracts).....</b>	<b>361</b>
<i>Paul W. Cleary, Simon M. Harrison and Matthew D. Sinnott</i>	
Introduction.....	362
Computational methods .....	363
SPH for fluids and foods.....	363
DEM for motion and collisions of particles.....	365
Collisions and rigid body dynamics in SPH.....	366
DEM-SPH coupling for slurry simulation .....	367
Flexible and deformable surfaces.....	367
Specialized intestinal models .....	368
Ingestion and oral digestion.....	371
Background .....	371
Example simulation scenario: melting of chocolate on the tongue .....	373
Stomach.....	381
Small intestine .....	387
Solute/nutrient diffusion and absorption.....	388
Spatially varying multiphase digesta rheology .....	390
Large intestine .....	392
Liquid transport and droplet formation in the respiratory tract.....	399
Conclusions .....	416
Acknowledgments.....	418
References.....	418

<b>CHAPTER 18 Digital modeling of the jaws for the evaluation of mandibular reconstruction techniques .....</b>	<b>425</b>
<i>Raymond Chung Wen Wong, Somasundaram Prasad, Timothy Jie Han Sng and Vaishnavi Ratheesh</i>	
Introduction.....	425
Anatomy and biomechanics of the mandible .....	427
The finite element method.....	429
Performing finite element analysis of the mandible.....	429
Alloplastic mandibular reconstruction methods: evaluating the implant design using finite element analysis .....	430
Computer-aided design of mandibular models .....	432
Design and plan of endoprostheses .....	432
Stress and magnitude of displacement of stem and wing design in unilateral loading conditions .....	433
Conclusion .....	437
References.....	438
<b>CHAPTER 19 Cornea digital twins for studying the critical role of mechanics in physiology, pathology and surgical repair.....</b>	<b>443</b>
<i>Ali Vahdati</i>	
Introduction.....	443
Corneal biomechanics .....	445
In silico biomechanical models of cornea.....	447
Toward accurate models of corneal collagen fibrils.....	449
Multiphasic and multiphysics computational models of cornea.....	452
Simulation-based subject-specific surgical planning .....	454
Concluding remarks .....	457
References.....	458
<b>CHAPTER 20 Influence of fluid–structure interaction on human corneal biomechanics under air puff non-contact tonometry .....</b>	<b>465</b>
<i>Osama M. Maklad</i>	
Introduction.....	465
Corneal biomechanics .....	467
Glaucoma.....	469
Aeroelasticity.....	470
Classification of fluid–structure interaction problems .....	471
Numerical methods .....	472

Three-dimensional eye model .....	473
Three-dimensional CFD turbulence model of the air puff .....	475
Air puff traverses and pressure on cornea.....	476
Parametric study statistics .....	476
Clinical dataset.....	479
Intraocular pressure algorithm (fIOP).....	481
Corneal material stress–strain index (fSSI).....	483
Conclusions.....	485
References.....	486

## SECTION 4 Biomedicine

### **CHAPTER 21 Digital twins for understanding the mechanical adaptation of bone in disease and postsurgery.... 493**

*Elizabeth Dimbath, Anup Pant and Ali Vahdati*

Introduction—the basics of bone remodeling.....	493
Computational models of bone remodeling in response to mechanical stimuli.....	496
Strain energy density as a mechanical stimulus for bone remodeling .....	496
Incorporation of stress, strain, and damage as remodeling stimuli .....	500
Fluid flow as a mechanical stimulus for bone remodeling .....	502
Effects of implants and pharmaceuticals on bone remodeling .....	503
Alternative or complementary numerical approaches to FE for in silico bone remodeling.....	505
Conclusion .....	506
References.....	507

### **CHAPTER 22 Bone strength, bone remodeling, and biomechanics of fracture..... 515**

*Vee San Cheong, Marco Palanca and Enrico Dall'Ara*

Bone physiology.....	516
Bone cells .....	517
Bone modeling and remodeling.....	520
Bone mechanical properties and fracture.....	521
Bone elasticity .....	523
Bone post-elastic behavior.....	523
Bone time-dependent properties .....	524
Predictions of bone strength with finite element models .....	525
DXA-based models.....	525

CT-based FE models .....	526
HR-pQCT-based FE models .....	527
MicroCT-based FE models.....	527
Model validation .....	528
Standard mechanical tests .....	528
Local deformation with strain gauges.....	528
Full field tests DIC and DVC.....	530
Examples of validation studies for FE models .....	531
Predictions of bone remodeling.....	531
Mechanoregulation.....	531
Bone adaptation algorithm and implementation in FE framework.....	532
Validation for murine studies .....	533
Morphometric and densitometric analysis .....	534
Spatial analysis and biomarkers for bone formation.....	536
References.....	537

## **CHAPTER 23 Single-cell based models for cell–cell and cell–extracellular matrix interactions .....** 547

*Pau Urdeix and Mohamed H. Doweidar*

Introduction.....	548
Methodology.....	550
Cell motility .....	552
Cell mechanotaxis.....	553
Cell electrotaxis .....	555
Drag force.....	556
Cell–cell interaction .....	557
Cell–cell contact.....	558
Cell–cell adhesion.....	558
Cell fate decision.....	559
Cell maturation .....	560
Cell differentiation.....	560
Cell proliferation .....	561
Model parameters and experiment setup .....	562
ECM discretization .....	562
Boundary conditions .....	562
Assumptions .....	562
Numerical implementation and applications .....	564
Cell–cell contact forces.....	565
Cell differentiation modulated by ECM stiffness.....	566
Cell adhesions modulated by ECM stiffness.....	569

Mechanically stimulated ECMs.....	570
Electrically stimulated ECM.....	574
Advanced materials for mechanoelectrical stimulation coupling.....	576
Conclusions.....	578
Acknowledgments.....	580
References.....	581
<b>CHAPTER 24 Flow and remodeling processes occurring within the body proper .....</b>	<b>591</b>
<i>Matthew D. Sinnott, Paul W. Cleary and Simon M. Harrison</i>	
Introduction.....	592
Computational methods .....	593
SPH method for fluids and solids .....	593
Continuity equation.....	593
Momentum equation for fluid (Navier–Stokes). ....	593
Momentum equation for solid deformation.....	594
Pressure solution .....	595
Solid boundary conditions.....	595
Soft bodies with flexible surfaces (such as cell membranes)....	596
Species concentration and diffusion .....	597
Integration of the SPH ordinary differential equations.....	597
Models for biological processes .....	598
Adhesion modeling for cells.....	598
Simple model for thrombin-controlled coagulation .....	602
SPH solid evolution for remodeling processes .....	603
Hemodynamics of vascular disease .....	603
Explicit modeling of cell mechanics at capillary scale.....	605
White blood cell rolling adhesion.....	611
Arterial scale flow.....	614
Blood coagulation and clot formation modeling.....	620
Background .....	620
Simple SPH coagulation model and predictions .....	622
Plaque rupture in an artery .....	630
Background .....	630
SPH model for plaque rupture.....	632
Bone remodeling .....	641
Conclusions.....	644
Acknowledgments.....	646
References.....	646

## SECTION 5 Medical devices

<b>CHAPTER 25 Digital co-creation: an early-stage product individualization framework to bridge the customer–designer void .....</b>	<b>659</b>
<i>Roatchanatam Anattasakul, Timothy James Slama and H. Onan Demirel</i>	
Introduction.....	659
Background .....	661
The transition from mass customization to mass individualization.....	661
The lack of customer participation in conventional product development .....	662
Methodology.....	663
Theoretical bases of the co-creation framework .....	663
Stages of the co-creation framework .....	665
Case study.....	668
Step 1: ideation and configure.....	668
Step 2: modeling and modify.....	669
Step 3: analysis and revise .....	672
Step 4: visualization and experience.....	673
Discussion and conclusions .....	674
References.....	675
<b>CHAPTER 26 Implant design on virtual digital human skull models for the creation of customized Patient-specific regenerative implants: biomechanical consideration.....</b>	<b>679</b>
<i>Jing Lim, Timothy Jie Han Sng and Raymond Chung Wen Wong</i>	
Introduction.....	679
Regenerative craniofacial surgery—current state of the art.....	681
Customized implant design—design considerations .....	683
Customized implant design—biomechanics.....	684
Commercialization considerations—a balancing act between design and regulation through in vivo tissue engineering .....	687
Future outlook.....	688
References.....	688

<b>CHAPTER 27 Virtual reality—assisted treatment planning, patient management, and educational approaches in dentistry.....</b>	<b>693</b>
<i>Poornima Ramamurthy and Dileep Sharma</i>	
Introduction.....	693
Implant treatment planning.....	695
Digital workflow in dental implantology.....	696
Software-guided implant surgery .....	696
Digital smile design .....	697
Virtual reality and dental anxiety.....	699
Virtual reality and dental education.....	700
Future directions.....	701
References.....	702
Further reading.....	706
<b>SECTION 6 Medical application</b>	
<b>CHAPTER 28 Whole-body movement modeling in realistic environments for understanding performance and injury.....</b>	<b>709</b>
<i>Simon M. Harrison, Raymond C.Z. Cohen and Paul W. Cleary</i>	
Introduction.....	710
Markerless motion capture for digital human model construction..	712
Background .....	712
Overview of MMC pipeline.....	714
Benefits and future applications.....	718
Computational methods .....	719
Biomechanical methods .....	719
SPH method for simulating the external environment.....	726
Using digital twins to understand performance and injury: sports examples.....	729
Swimming.....	729
Diving .....	736
Snow skiing.....	742
Realtime digital human applications: workplace injury example ...	749
Creating software products based on human digital twins .....	755
Conclusions.....	756
Acknowledgments.....	759
References.....	759

**CHAPTER 29 Digital human modeling in cleft care ..... 767***Hanyao Huang, Jingtao Li and Bing Shi*

Introduction.....	767
Presurgical infant orthopedics.....	769
Cleft lip and cleft lip nasal deformity repair.....	771
Cleft palate repair.....	773
Alveolar bone cleft reconstruction .....	775
Orthognathic surgery in cleft care.....	776
Conclusion .....	778
References.....	778

**CHAPTER 30 The virtual patient model for correction of facial deformity and accuracy of simulation and surgical guide construction..... 783***Raymond Chung Wen Wong, Chee Weng Yong,  
Matthias Wei Jin Chen, Timothy Jie Han Sng,  
Kian How Tan and Roland Lim*

Historical methods of planning.....	784
Overview .....	784
Orthognathic surgery.....	785
Postablative reconstructive jaw surgery.....	785
Craniofacial surgery .....	786
Limitations of traditional planning.....	787
3D imaging and biomechanical soft tissue simulation .....	787
Introduction.....	787
Multislice computed tomography.....	788
Applications .....	788
Cone beam computed tomography.....	788
Dental records.....	789
Stereophotogrammetry.....	789
Biosimulations .....	789
Virtual surgical planning, customized surgical guide, and fixation plates .....	790
Introduction.....	790
VSP in orthognathic surgery .....	791
Integration of digital information.....	791
Virtual operating theater .....	791
Designing and printing of surgical aids, guides, or implants...	792
VSP in reconstructive surgery of the jaw .....	794
VSP in craniofacial surgery .....	794
VSP in posttraumatic deformities .....	794

VSP in temporomandibular joint surgery .....	795
Comparison between traditional and modern planning.....	797
Traditional versus modern planning .....	797
Accuracy of surgical plan transfer .....	797
Cost and time.....	798
Surgical outcome/patient satisfaction.....	798
References.....	799

## **CHAPTER 31 Patient-specific modeling of pain progression: a use case on knee osteoarthritis patients using machine learning algorithms ..... 805**

*S. Moustakidis, C. Kokkotis and D. Tsaopoulos*

Introduction.....	805
Dataset description.....	808
Methods.....	810
Grouping/labeling.....	810
Data preprocessing.....	811
Feature selection.....	811
Machine learning.....	812
Validation.....	813
Results and discussion.....	813
Predictive capacity of the binary classifiers without pain-related variables .....	814
Predictive capacity of the binary classifiers with pain variables .....	814
Feature selection results.....	820
Data fusion results .....	823
Comparative analysis.....	823
Conclusions.....	826
References.....	826

## **CHAPTER 32 A design procedure for the development of VR platforms for the rehabilitation of patients after stroke..... 829**

*Daniel Lanzoni, Andrea Vitali, Daniele Regazzoni and  
Caterina Rizzi*

Introduction.....	829
Scientific background .....	831
Methods and tools.....	832
Definition of the rehabilitation exercise and related devices ...	833
Identification of ICT tools.....	833

Medical data management.....	834
Use cases .....	835
VR platform for the evaluation of the extra-personal neglect..	835
VR platform for the recovery of severe memory loss .....	838
Motor-skills tele-rehabilitation of hands.....	840
Evaluation .....	842
Conclusion .....	845
Acknowledgments.....	846
References.....	846
<b>CHAPTER 33 Personalization for surgical implants.....</b>	<b>849</b>
<i>Naomi C. Paxton, Kevin Tetsworth and     Maria A. Woodruff</i>	
Introduction to personalization of surgical implants.....	849
Personalized medical device definitions.....	851
Adoption of personalization in surgery .....	853
Orthopedic surgery .....	853
Craniomaxillofacial surgery.....	855
Spinal surgery.....	857
Vascular surgery .....	858
Urology surgery .....	860
Regulation.....	861
Summary and future perspectives .....	863
References.....	866
Index.....	875

This page intentionally left blank

# Contributors

**Roatchanatam Anattasakul**

Oregon State University, Corvallis, OR, United States

**Michael Skipper Andersen**

Department of Materials and Production, Aalborg University, Aalborg, Denmark

**W. Andrew Pruett**

Department of Physiology and Biophysics, University of Mississippi Medical Center, Jackson, MS, United States

**Navid Arjmand**

Department of Mechanical Engineering, Sharif University of Technology, Tehran, Iran

**Jacobo Ayensa-Jiménez**

Aragon Institute of Engineering Research (I3A), University of Zaragoza, Zaragoza, Spain; Mechanical Engineering Department, University of Zaragoza, Zaragoza, Spain; Aragon Institute of Health Research (IIS Aragón), University of Zaragoza, Zaragoza, Spain

**Babak Bazrgari**

F. Joseph Halcomb III, MD Department of Biomedical Engineering, University of Kentucky, Lexington, KY, United States

**Hamidreza Mortazavy Beni**

Department of Biomedical Engineering, Arsanjan Branch, Islamic Azad University, Arsanjan, Iran

**Erika Cavanagh**

School of Clinical Sciences, Faculty of Health, Queensland University of Technology, Brisbane, QLD, Australia; Centre for Biomedical Technologies, Queensland University of Technology, Brisbane, QLD, Australia; Mater Centre for Maternal-Fetal Medicine, Mater Mother's Hospital, South Brisbane, QLD, Australia

**Matthias Wei Jin Chen**

Discipline of Oral and Maxillofacial Surgery, Faculty of Dentistry, National University of Singapore, Singapore, Singapore

**M. Cilla**

Instituto de Investigación en Ingeniería de Aragón, Universidad de Zaragoza, Zaragoza, Spain; CIBER-BBN, Centro de Investigación en Red en Bioingeniería, Biomateriales y Nanomedicina, Madrid, Spain

**Paul W. Cleary**

CSIRO Data61, Clayton South, VIC, Australia

**John S. Clemmer**

Department of Physiology and Biophysics, University of Mississippi Medical Center, Jackson, MS, United States

**Vicki L. Clifton**

Mater Research Institute-University of Queensland, South Brisbane, QLD, Australia; Faculty of Medicine, The University of Queensland, Herston, QLD, Australia

**Raymond C.Z. Cohen**

CSIRO Data61, Clayton South, VIC, Australia

**Enrico Dall'Ara**

INSIGNEO Institute for In Silico Medicine, University of Sheffield, Sheffield, United Kingdom; Department of Oncology and Metabolism, University of Sheffield, Sheffield, United Kingdom

**H. Onan Demirel**

Oregon State University, Corvallis, OR, United States

**Elizabeth Dimbath**

Department of Biomedical Engineering, Pratt School of Engineering, Duke University, Durham, NC, United States

**Manuel Doblaré**

Aragon Institute of Engineering Research (I3A), University of Zaragoza, Zaragoza, Spain; Aragon Institute of Health Research (IIS Aragón), University of Zaragoza, Zaragoza, Spain; Centro de Investigación Biomédica en Red en Bioingeniería, Biomateriales y Nanomedicina (CIBER-BBN), Madrid, Spain

**Mohamed H. Doweidar**

Mechanical Engineering Department, School of Engineering and Architecture (EINA), University of Zaragoza, Zaragoza, Spain; Aragon Institute of Engineering Research (I3A), University of Zaragoza, Zaragoza, Spain; Centro de Investigación Biomédica en Red en Bioingeniería, Biomateriales y Nanomedicina (CIBER-BBN), Madrid, Spain

**Christopher Edwards**

School of Clinical Sciences, Faculty of Health, Queensland University of Technology, Brisbane, QLD, Australia; Mater Centre for Maternal-Fetal Medicine, Mater Mother's Hospital, South Brisbane, QLD, Australia

**Silva Elisabete**

LAETA, INEGI, Faculty of Engineering, University of Porto, Porto, Portugal

**Francisco R. Feito**

Graphics and Geomatics Group of Jaén, Center for Advanced Studies in Information and Communication Technologies, University of Jaén, Jaén, Spain

**António Augusto Fernandes**

LAETA, INEGI, Faculty of Engineering, University of Porto, Porto, Portugal

**Rocío Fernández-Parra**

Department of Small Animal Medicine and Surgery, Faculty of Veterinary Medicine, Catholic University of Valencia San Vicente Mártir, Valencia, Spain

**Farshid Ghezelbash**

Division of Applied Mechanics, Department of Mechanical Engineering, Polytechnique Montréal, Montreal, QC, Canada

**Yuantong Gu**

School of Mechanical, Medical and Process Engineering, Faculty of Engineering, Queensland University of Technology, Brisbane, QLD, Australia

**Simon M. Harrison**

CSIRO Data61, Clayton South, VIC, Australia

**Xuzhen He**

School of Civil and Environmental Engineering, University of Technology Sydney (UTS), Ultimo, NSW, Australia

**Robert L. Hester**

Department of Physiology and Biophysics, University of Mississippi Medical Center, Jackson, MS, United States

**Hanyao Huang**

State Key Laboratory of Oral Diseases and National Clinical Research Center for Oral Diseases and Department of Oral and Maxillofacial Surgery, West China Hospital of Stomatology, Sichuan University, Chengdu, Sichuan, China

**Shahid Husain**

Mechanical Engineering Department, AMU, Aligarh, India

**Mohammad Saidul Islam**

School of Mechanical and Mechatronic Engineering, University of Technology Sydney (UTS), Ultimo, NSW, Australia

**Raghu Sesha Iyengar**

Indian Institute of Technology, Department of Biomedical Engineering, Hyderabad, Telangana, India

**Juan-Roberto Jiménez-Pérez**

Graphics and Geomatics Group of Jaén, Center for Advanced Studies in Information and Communication Technologies, University of Jaén, Jaén, Spain

**C. Kokkotis**

Institute for Bio-Economy & Agri-Technology, Center for Research and Technology Hellas, Marousi, Greece; TEFAA, Department of Physical Education and Sport Science, University of Thessaly, Trikala, Greece

**Aditya Koppula**

Indian Institute of Technology, Department of Biomedical Engineering,  
Hyderabad, Telangana, India

**Daniel Lanzoni**

Department of Management, Information and Production Engineering, University  
of Bergamo, Bergamo, Italy

**Puchanee Larpruenrudee**

School of Mechanical and Mechatronic Engineering, University of Technology  
Sydney (UTS), Ultimo, NSW, Australia

**Christopher Lawrence**

School of Computer Science, University of Technology Sydney (UTS), Ultimo,  
NSW, Australia

**Jingtao Li**

State Key Laboratory of Oral Diseases and National Clinical Research Center for  
Oral Diseases and Department of Oral and Maxillofacial Surgery, West China  
Hospital of Stomatology, Sichuan University, Chengdu, Sichuan, China

**Jing Lim**

Osteopore International Pte Ltd, Singapore, Singapore

**Roland Lim**

Discipline of Oral and Maxillofacial Surgery, Faculty of Dentistry, National  
University of Singapore, Singapore, Singapore

**José Luis López-Villalobos**

Hospital Universitario Virgen del Rocío, Department of Thoracic Surgery, Sevilla,  
Spain

**Osama M. Maklad**

University of Liverpool, School of Engineering, Liverpool, United Kingdom;  
University of Greenwich, School of Engineering, Kent, United Kingdom

**Kapardi Mallampalli**

Indian Institute of Technology, Department of Biomedical Engineering,  
Hyderabad, Telangana, India

**Mauro Malvè**

CIBER-BBN, Centro de Investigación Biomédica en Red—Bioingeniería,  
Biomateriales y Nanomedicina, Zaragoza, Spain; Universidad Pública de  
Navarra (UPNA), Department of Engineering, Pamplona, Spain

**J. Martínez**

Universidad de Vigo, Vigo, Spain

**M.A. Martínez**

Instituto de Investigación en Ingeniería de Aragón, Universidad de Zaragoza, Zaragoza, Spain; CIBER-BBN, Centro de Investigación en Red en Bioingeniería, Biomateriales y Nanomedicina, Madrid, Spain

**Enrique Morales Orcajo**

Ambu Innovation GmbH, Augsburg, Germany

**Hamed Mortazavi**

Department of Biomedical Engineering, Arsanjan Branch, Islamic Azad University, Arsanjan, Iran

**S. Moustakidis**

AIDEAS OU, Tallinn, Estonia

**José Negrillo-Cárdenas**

Fundación I+D del Software Libre (FIDESOL), Granada, Spain

**Bessa Nuno**

LAETA, INEGI, Faculty of Engineering, University of Porto, Porto, Portugal

**Marco Palanca**

INSIGNEO Institute for In Silico Medicine, University of Sheffield, Sheffield, United Kingdom; Department of Oncology and Metabolism, University of Sheffield, Sheffield, United Kingdom

**Anup Pant**

Department of Engineering, College of Engineering and Technology, East Carolina University, Greenville, NC, United States

**Gunther Paul**

Australian Institute of Tropical Health and Medicine, James Cook University, Townsville, QLD, Australia

**Naomi C. Paxton**

Centre for Biomedical Technologies, Queensland University of Technology (QUT), Brisbane, QLD, Australia

**E. Peña**

Instituto de Investigación en Ingeniería de Aragón, Universidad de Zaragoza, Zaragoza, Spain; CIBER-BBN, Centro de Investigación en Red en Bioingeniería, Biomateriales y Nanomedicina, Madrid, Spain

**Somasundaram Prasad**

Discipline of Oral and Maxillofacial Surgery, Faculty of Dentistry, National University of Singapore, Queenstown, Singapore

**Marina Pérez-Aliacar**

Aragon Institute of Engineering Research (I3A), University of Zaragoza, Zaragoza, Spain; Mechanical Engineering Department, University of Zaragoza, Zaragoza, Spain

**Mohan Raghavan**

Indian Institute of Technology, Department of Biomedical Engineering, Hyderabad, Telangana, India

**Poornima Ramamurthy**

College of Medicine & Dentistry, James Cook University, Smithfield, QLD, Australia

**John Rasmussen**

Department of Materials and Production, Aalborg University, Aalborg, Denmark

**Vaishnavi Ratheesh**

Discipline of Oral and Maxillofacial Surgery, Faculty of Dentistry, National University of Singapore, Queenstown, Singapore; National University Centre for Oral Health, Singapore, Singapore; Faculty of Dentistry, Singapore, Singapore

**Daniele Regazzoni**

Department of Management, Information and Production Engineering, University of Bergamo, Bergamo, Italy

**Caterina Rizzi**

Department of Management, Information and Production Engineering, University of Bergamo, Bergamo, Italy

**Suvash C. Saha**

School of Mechanical and Mechatronic Engineering, University of Technology Sydney (UTS), Ultimo, NSW, Australia

**Vee San Cheong**

INSIGNEO Institute for In Silico Medicine, University of Sheffield, Sheffield, United Kingdom; Department of Automatic Control and Systems Engineering, University of Sheffield, Sheffield, United Kingdom

**Masoud Sharifi**

Division of Applied Mechanics, Department of Mechanical Engineering, Polytechnique Montréal, Montreal, QC, Canada

**Dileep Sharma**

School of Health Sciences, College of Health, Medicine and Wellbeing, The University of Newcastle, NSW, Australia

**Bing Shi**

State Key Laboratory of Oral Diseases and National Clinical Research Center for Oral Diseases and Department of Oral and Maxillofacial Surgery, West China Hospital of Stomatology, Sichuan University, Chengdu, Sichuan, China

**Aboulfazl Shirazi-Adl**

Division of Applied Mechanics, Department of Mechanical Engineering,  
Polytechnique Montréal, Montreal, QC, Canada

**Avinash Kumar Singh**

Indian Institute of Technology, Department of Biomedical Engineering,  
Hyderabad, Telangana, India

**Matthew D. Sinnott**

CSIRO Data61, Clayton South, VIC, Australia

**Timothy James Slama**

Oregon State University, Corvallis, OR, United States

**Timothy Jie Han Sng**

Discipline of Oral and Maxillofacial Surgery, Faculty of Dentistry, National  
University of Singapore, Singapore, Singapore

**Kousik Sarathy Sridharan**

Indian Institute of Technology, Department of Biomedical Engineering,  
Hyderabad, Telangana, India

**Andrea Stenti**

BEAMS Department, Université Libre de Bruxelles, Brussels, Belgium

**Carmen Sánchez-Matás**

Hospital Universitario Virgen del Rocío, Department of Thoracic Surgery, Sevilla,  
Spain

**Kian How Tan**

Discipline of Oral and Maxillofacial Surgery, Faculty of Dentistry, National  
University of Singapore, Singapore, Singapore

**Mascarenhas Teresa**

Department of Obstetrics and Gynecology, CHSJ-EPE/Faculty of Medicine,  
University of Porto Porto, Portugal

**Kevin Tetsworth**

Department of Orthopaedic Surgery, Royal Brisbane & Women's Hospital,  
Herston, QLD, Australia

**D. Tsaopoulos**

Institute for Bio-Economy & Agri-Technology, Center for Research and  
Technology Hellas, Marousi, Greece

**Pau Urdeix**

Mechanical Engineering Department, School of Engineering and Architecture (EINA), University of Zaragoza, Zaragoza, Spain; Aragon Institute of Engineering Research (I3A), University of Zaragoza, Zaragoza, Spain; Biomedical Research Networking Center in Bioengineering, Biomaterials and Nanomedicine (CIBER-BBN) Zaragoza, Spain

**Ali Vahdati**

Department of Engineering, College of Engineering and Technology, East Carolina University, Greenville, NC, United States

**Andrea Vitali**

Department of Management, Information and Production Engineering, University of Bergamo, Bergamo, Italy

**Raymond Chung Wen Wong**

Discipline of Oral and Maxillofacial Surgery, Faculty of Dentistry, National University of Singapore, Singapore, Singapore; Oral and Maxillofacial Surgery, Faculty of Dentistry, National University Centre for Oral Health, National University of Singapore, Singapore, Singapore

**Maria A. Woodruff**

Centre for Biomedical Technologies, Queensland University of Technology (QUT), Brisbane, QLD, Australia

**Chee Weng Yong**

Discipline of Oral and Maxillofacial Surgery, Faculty of Dentistry, National University of Singapore, Singapore, Singapore

**Ali Asghar Zarei**

Center for Neuroplasticity and Pain (CNAP), Department of Health Science and Technology, Aalborg University, Aalborg, Denmark

SECTION

# Modeling methods 1

This page intentionally left blank

# From the visible human project to the digital twin

# 1

**Gunther Paul**

*Australian Institute of Tropical Health and Medicine, James Cook University, Townsville, QLD, Australia*

## **Chapter outline**

---

<b>Introduction</b> .....	3
<b>The visible human project</b> .....	4
<b>Anatomography</b> .....	6
<b>Virtual physiological human</b> .....	6
<b>The digital twin</b> .....	8
<b>References</b> .....	16
<b>Further reading</b> .....	17

---

## **Introduction**

Arguably the US National Library of Medicine's (NLM) Visible Human Project (VHP) completed in 1995 was the first systematic attempt to develop complex and computerized models of a human body from high quality medical imaging. While the Visible Human Project data was originally based on only one male and one female donor, the data are still widely used nowadays in human modeling projects for the very reason that it is public domain, i.e., data are freely available and can be reproduced and shared with the only limitation of an NLM license agreement which permits NLM a full license to the resulting work. Many projects, applications, atlases, and movies are now based on the VHP data. A small number of similar projects, such as Anatomography, have later been launched in other countries, partially replicating the methodology however improving the modeling approach and advancing knowledge. The availability of powerful supercomputers, cloud computing with on-demand availability which allows to overcome the barrier to adoption of purchasing expensive hardware resources, as well as high-performance personal computer platforms has since opened new frontiers where data and models from these projects are merged and combined in very large frameworks that represent multiple body organs and systems, interacting on various levels of multimodality. One such framework is the European Virtual Physiological Human (VPH) initiative which employs *in silico* medicine methods to develop the Digital

Twin (DT), a single complex, holistic multiorgan human model which will inform medical practice of the future.

## The visible human project

In contrary to modern medical imaging which is mostly entirely based on magnetic resonance imaging (MRI) and computed tomography (CT) scan data, which is digitally sliced by the scanner device before it is remodeled into a coherent three-dimensional body, organ or object and digitally segmented, the VHP cadavers were additionally physically sliced, photographed, and digitized, producing 10 times higher quality data. The project initially completed in 1995 with the digitization of one male published in 1994 and one female body after 9 years of work.

The VHP project is based on three donors, two healthy donors (a 39-year-old male Texas murderer executed in 1993; an anonymous 59-year-old obese female; and an 87-year-old female multimorbid cancer patient who passed in 2015). In order to produce the 1871 slices of the male model, the cadaver was frozen and stabilized in a gelatine and water mixture. After each removal of a 1 mm thick “slice” from the body, photos were taken and digitized. This data was complemented by axial section CT, and coronal section MRI data. Head and neck were also scanned in the axial plane using MRI. The same process was used for processing the female bodies, however at 0.33 mm intervals in the axial and vertical planes, thus creating 5189 anatomical images and cubic voxels which allow for three-dimensional reconstruction.

While the male body was spaced horizontally into 1 mm slices, the female body data has a higher density with 0.33 mm slicing. For the male donor, MRI data was obtained horizontally at 4 mm intervals ( $256 \times 256p$ , 12 bits gray) and horizontal CT scans were taken at 1 mm intervals ( $512 \times 512p$ , 12 bits gray). Axial anatomical images were produced with  $2048 \times 1216p$  in 24 bits color, resulting in 7.5 MB of data (Fig. 1.1).

Anatomical and CT images coincide at 1871 cross sections, which leads to 15 GB of data for the male dataset compared to 40 GB of data for the female body (Waldby, 2004). In the year 2000 higher resolution photographs which had been taken previously were digitized at  $4096 \times 2700p$  for all cross sections, expanding the male dataset to 32 MB. Eventually a third female body was digitized from 2015. All VHP digitization was performed at the University of Colorado under NLM contract, and the work is ongoing.

The 59-year-old female specimen was eventually recreated digitally at the Worcester Polytechnic Institute. It was said that “their phantom is the most detailed digital reconstruction of a whole human body ever to be pieced together. She has 231 tissue parts ranging from windpipe to eyeballs but is missing nose cartilage and 14 other bits of the body” (Hamzelou, 2015).

Problems with the data originate in the donors’ health status, pathologies, process, and cadaver preparation. None of the specimen provided a “perfect” representation of the human body.

**FIGURE 1.1**

Section through visible human male—upper thigh below femoral head, including prominent musculature, part of male reproductive system (from Pelvis subset) [749 × 450 24-bit color JPG, 64159 bytes].

Source: <https://www.nlm.nih.gov/research/visible/photos.html>.

Today the data is integrated in the most commonly used computerized medical education and training packages such as Primal Pictures (<https://www.primalpictures.com/>), Anatomage (<https://www.anatomage.com/table/>), the Voxel-Man interactive 3D anatomy atlas, surgery simulator (<https://www.voxel-man.com/>) and virtual body models (<https://www.voxel-man.com/3d-navigators/downloads/>), or Body Voyage (Tsiaras, 1997), a three-dimensional educational voyage through the body. Data could previously be viewed, extracted, and animated from a data server (the Visible Human Server) at the École Polytechnique Fédérale de Lausanne's Peripheral Systems Lab, which had added complex data extraction features such as curved surfaces and a library of animations to the data pool. Due to the retirement of the head of department Prof. R.D. Hersch, however, this service is no longer available.

NLM currently lists 16 projects based on the VHP dataset, with several projects hosted at the University of Michigan's VHP (<http://vhp.med.umich.edu/>) which appears as the central VHP instance for data and software retrieval outside NLM. Information on the website however is mostly 20 years old as of 2022. The University of Michigan lab notably announces a future aim of their project to develop “an integrated physiological representation of the human body, from molecular, biochemical, genetic, cellular, to system levels.” Such an approach will resemble what we will further on call the **“Digital Twin”** (DT).

NLM remains the only notable and up-to-date source of information for the VHP, maintains its homepage ([https://www.nlm.nih.gov/research/visible/visible\\_human.html](https://www.nlm.nih.gov/research/visible/visible_human.html)), and provides a list of VHP projects (<https://www.nlm.nih.gov/research/visible/applications.html>).

---

## Anatomography

Anatomography (<http://lifesciencedb.jp/bp3d/?lng=en>) was launched in 2009 by the DNA Data Bank of Japan at the National Institute of Genetics (Mitsuhashi et al., 2009) and is now hosted by the Database Center for Life Science institute at the University of Tokyo. Anatomography uses human body polygon data called “BodyParts3D” which are extracted from “TARO” full-body MRI images which is the 8 mm<sup>3</sup> voxel dataset of a human male created by the Japanese National Institute of Information and Communications Technology and published freely in 2004. BodyParts3D uses the Foundational Model of Anatomy (FMA) open-source ontology from the University of Washington to register each body part with a unique identifier FMAxxxxx.

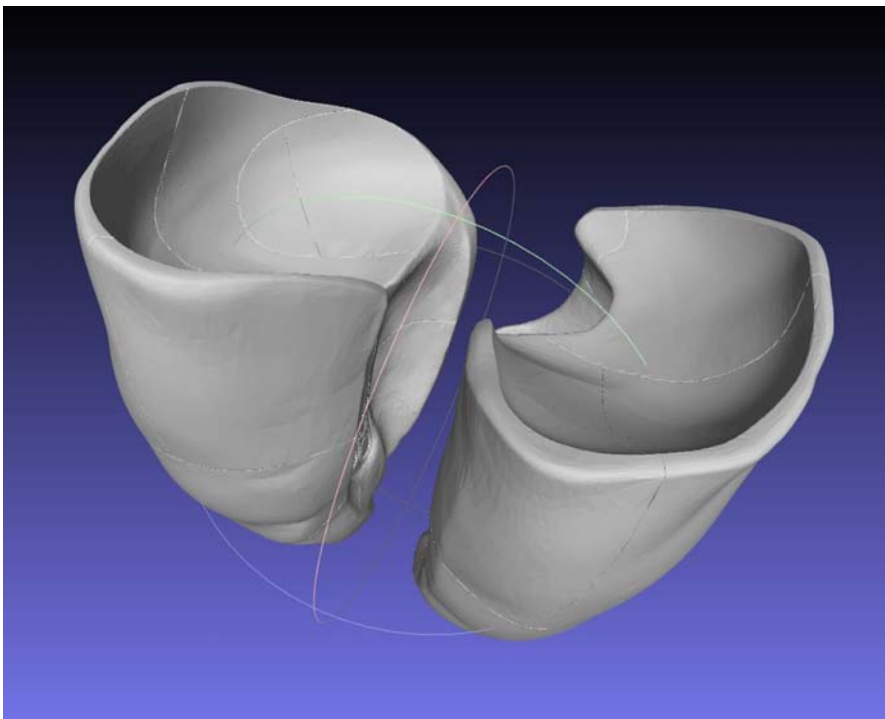
Anatomography anatomical diagrams and BodyParts3D are now openly available under a Creative Commons license where BodyParts3D polygon data are distributed in the OBJ file format (Fig. 1.2).

The dataset size was 136 MB for a 99% reduced polygon mesh as of version 4.0. The number of body parts (organs) registered in the most recent version of BodyParts3D is 2573 as of version 4.3i.

---

## Virtual physiological human

The Virtual Physiological Human (VPH) (<https://www.vph-institute.org/>) originated in a 1997 European initiative named the Physiome Project (Hunter & Borg, 2003). This predecessor project aimed to develop databases and models to define the human physiome based on an improved bottom-up understanding of organisms. In 2005, the VPH emerged from the Physiome Project as a joint framework to develop multilevel modeling and simulation of human anatomy and physiology, enabling study of the human body as a holistic complex system. Since 2006 the STEP: Structuring the EuroPhysiome consortium has received significant funding through the European Commission research framework (FP6 and FP7) and has since evolved into a roadmap toward the Virtual Physiological Human including patient-specific computer models and their application in personalized and predictive healthcare (Kohl & Noble, 2009). The VPH framework includes creation of integrated computer models representing biomechanical, physiological, and biochemical functions of the living human body. The VPH is the first such framework that is not only descriptive in its nature but also integrative and predictive.

**FIGURE 1.2**

Parenchyma of bronchopulmonary segment in BodyParts3D.

*Source: BodyParts3D, The Database Center for Life Science licensed under CC Attribution-Share Alike 2.1 Japan.*

While previous projects were clearly focused on creating “knowledge,” “generalization,” and “understanding,” the VPH framework can be described as focused on “solutions” and “personalization.” New modeling environments are created for predictive, individualized healthcare solutions to result in better individual patient health outcomes, patient safety, and drug efficacy. Such a “strategy for the realisation and wide scale adoption of results emerging from the Virtual Physiological Human Initiative ...” ([VPH-Institute, 2022](#)) was created through the DISCIPULUS support action, a European Commission project that ran from 2011 to 2013, and successfully delivered the Digital Patient roadmap ([The DISCIPULUS Project, 2022](#)). While aiming to improve individual health service provision and outcomes, the VPH continues to explore healthcare system improvement through greater understanding of pathophysiological processes. In a systemic approach, the framework makes it possible to combine patient-specific data with a population-based perspective. For example, the use of a biomedical model of a patient may simulate potential treatments and outcomes that could prevent the patient from being subjected to avoidable (redundant) or useless treatments. The same models can be used in the modeling and

testing of medical devices and drugs at population level which could reduce, refine, and replace the need for experiments on animals with their associated cost and ethical demands. This has also been called “**in silico medicine**” (medicine by computer simulation).

The VPH Institute has recorded a significant number of European projects in support of in silico medicine (see examples listed in [Table 1.1](#)).

As a central resource for the in silico medicine community, the VPH also offers introductory information about noteworthy external resources which are mostly in the public domain ([Table 1.2](#)).

The overarching future goal of the VPH is a holistic approach to medicine where the body is treated as one single, however complex multiorgan system rather than as a collection of individual organs. This framework aims to overcome the segregated organ-based organization of current western medicine practice (e.g., specializations and specialist referral system) with its obvious shortfalls. If fully implemented, this framework will revolutionize the way we understand, and practice medicine and it will form the basis for the Digital Twin.

---

## The digital twin

Much has been written about the Digital Twin in recent years, and the term has been used across various industries in widely different ways and meanings, as was found by [Kritzinger et al. \(2018, p. 1016\)](#) in their systematic review: “The Digital Twin (DT) is commonly known as a key enabler for the digital transformation, however, in literature is no common understanding concerning this term. It is used slightly different over the disparate disciplines.” [Wakefield \(2022\)](#), for example, uses the term for a digital doppelganger with a purpose, or as she says: “A digital twin is an exact replica of something in the physical world, but with a unique mission - to help improve, or in some other way provide feedback to, the real-life version. Initially such twins were just sophisticated 3D computer models, but artificial intelligence (AI) combined with the internet of things—which uses sensors to connect physical things to the network—have meant that you can now build something digitally that is constantly learning from and helping improve the real counterpart.” She then finds that the real value of Digital Twins lies in healthcare—surprisingly though, the term has only recently entered the domain of in silico medicine. In contrary to the medical domain, the term Digital Twin has been used extensively over the last 10 years in publications exploring the framework of Industry 4.0 ([Havard et al., 2019; Kritzinger et al., 2018; Paul et al., 2021](#)), where DT commonly refers to a construct that Human Factors and Ergonomics (HFE) as well as Biomechanics scientists have called Digital Human Modeling (DHM) since the 1980s, see [Scataglini and Paul \(2019\)](#). Because DHM originally focused on a whole-body representation of generalized populations in avatars that could be used in engineering design work, these models were typically based on anthropometry and population based percentiled body size data. The DHM concept was later expanded and now

**Table 1.1** Selected in silico medicine research projects under guidance or participation of the VPH.

Name	Field	Date	URL	Funding body, project number
AVICENNA (roadmap)	Digital patient strategy	10/2013 –9/ 2015	<a href="http://www.cordis.europa.eu/project/id/611819">www.cordis.europa.eu/ project/id/611819</a>	EC FP7 611819
Airway disease predicting outcomes through patient specific computational modeling—AIRPROM	Respiratory diseases	3/2011 –6/ 2016	<a href="http://www.europeanlung.org/en/projects-and-research/projects/airprom/home">www.europeanlung.org/en/ projects-and-research/ projects/airprom/home</a>	EC FP7 270194
Modeling and simulation environment for systems medicine—SYNERGY COPD	Respiratory diseases	2/2011 –4/ 2014	<a href="http://www.Synergy-COPD.eu">www.Synergy-COPD.eu</a>	EC FP7 70086
Integrated cardiac care using patient-specific cardiovascular modeling—euHEART	Cardio-vascular	6/2008 –5/ 2012	<a href="http://www.euheart.org">www.euheart.org</a>	EC FP7 224495
Mathematical modeling of the cardiovascular system—HAEMODEL	Cardio-vascular	10/2002 –9/ 2006	<a href="http://cordis.europa.eu/project/rcn/67790_en.html">cordis.europa.eu/project/rcn/ 67790_en.html</a>	EC FP5
Real-time simulation for safer vascular stenting—RT3S	Cardio-vascular	1/2011 –3/ 2014	<a href="http://www.rt3s.eu">www.rt3s.eu</a>	EC FP7 248801
Computer model—derived indices for optimal patient-specific treatment selection and planning in heart failure—VP2HF	Cardio-vascular	10/2013 –9/ 2016	<a href="http://www.kcl.ac.uk/medicine/research/divisions/imaging/centres/vp2hf/index.aspx">www.kcl.ac.uk/medicine/ research/divisions/imaging/ centres/vp2hf/index.aspx</a>	EC FP7 611823
Virtual pathological heart of the virtual physiological human—VPH2	Cardio-vascular	7/2008 –10/ 2011	<a href="http://cordis.europa.eu/project/rcn/87317_en.html">cordis.europa.eu/project/rcn/ 87317_en.html</a>	EC FP7 224635

*Continued*

**Table 1.1** Selected in silico medicine research projects under guidance or participation of the VPH.—*cont'd*

Name	Field	Date	URL	Funding body, project number
Multiscale immune system simulator for the onset of type 2 diabetes integrating genetic, metabolic, and nutritional data—MISSION-T2D	Endocrinology	3/2013 –4/ 2016	<a href="http://www.mission-t2d.eu/MISSION-T2D/Welcome.html">www.mission-t2d.eu/ MISSION-T2D/Welcome.html</a>	EC FP7 600803
Models and simulation techniques for discovering diabetes influence factors—MOSAIC	Endocrinology	1/2013 –4/ 2016	<a href="http://www.mosaicproject.eu">www.mosaicproject.eu</a>	EC FP7 600914
A generic open-end simulation environment for minimally invasive cancer treatment—GO-SMART	Oncology	4/2013 –6/ 2016	<a href="http://www.gosmart-project.eu">www.gosmart-project.eu</a>	EC FP7 600641
From data sharing and integration via VPH models to personalized medicine—P-MEDICINE	Oncology	27/2011 –7/ 2015	<a href="http://p-medicine.eu">p-medicine.eu</a>	EC FP7 270089
Virtual physiological Human: Personalized predictive breast cancer therapy through integrated tissue microstructure modeling—VPH-PRISM	Oncology	3/2013 –2/ 2016	<a href="http://www.vph-prism.eu/home">www.vph-prism.eu/home</a>	EC FP7 601040
Digital radiation therapy patient—DR THERAPAT	Oncology	2/2013 –1/ 2016	<a href="http://drtherapat.eu">drtherapat.eu</a>	EC FP7 600852
The osteoporotic virtual physiological human—VPHOP	Musculoskeletal	8/2008 –10/ 2012	<a href="http://www.vphop.eu">www.vphop.eu</a>	EC FP7 223865
Patient-specific spinal treatment simulation—MYSPINE	Musculoskeletal	3/2011 –8/ 2014	<a href="http://www.myspineproject.eu">www.myspineproject.eu</a>	EC FP7 269909

Decision support software for orthopedic surgery—DESSOS	Musculoskeletal	1/2006 –9/ 2008	<a href="http://cordis.europa.eu/project/rcn/79488_en.html">cordis.europa.eu/project/rcn/79488_en.html</a>	EC FP6 27252
Improving safety and predictability of complex musculoskeletal surgery using a patient-specific navigation system—TLEMSAFE	Musculoskeletal	3/2010 –8/ 2014	<a href="http://www.tlemsafe.eu">www.tlemsafe.eu</a>	EC FP7 247860
Virtual, physiological, and computational neuromuscular models for the predictive treatment of Parkinson's disease—NOTREMOR	Neurology	1/2014 –12/ 2016	<a href="http://notremor.eu/notremor">notremor.eu/notremor</a>	EC FP7 610391
From patient data to personalized healthcare in Alzheimer's disease—PREDICTAD	Neurology	6/2008 –11/ 2011	<a href="http://www.predictad.eu">www.predictad.eu</a>	EC FP7 224328
Evidence-based treatment planning solution for traumatic brain injuries—TBICARE	Neurology	2/2011 –7/ 2014	<a href="http://www.tbicare.eu">www.tbicare.eu</a>	EC FP7 270259
In silico world	Medicines and Medical Devices, in silico trials	1/2021 –	<a href="http://www.insilico.world">www.insilico.world</a>	EC Horizon2020
SIMCOR	Medicines and Medical Devices, in silico trials	1/2021 –12/ 2023	<a href="http://www.cordis.europa.eu/project/id/101017578">www.cordis.europa.eu/project/id/101017578</a>	EC Horizon2020 101017578
SimCardioTest	Medicines and Medical Devices, in silico trials	1/2021 –12/ 2024	<a href="http://www.cordis.europa.eu/project/id/101016496">www.cordis.europa.eu/project/id/101016496</a>	EC Horizon2020 101016496
AVICENNA (alliance)	Medicines and Medical Devices, in silico trials	2016–	<a href="http://www.cordis.europa.eu/programme/id/H2020_SC1-PM-16-2017">www.cordis.europa.eu/programme/id/H2020_SC1-PM-16-2017</a>	EC Horizon2020

**Table 1.2** Up-to-date in silico relevant resources listed by the VPH.

Resource	URL
Biomodels database (>3000 models)	<a href="http://ebi.ac.uk/biomodels-main">ebi.ac.uk/biomodels-main</a>
Cardiac Atlas (>2500 3 FEM patient models)	<a href="http://cardiacatlas.org">cardiacatlas.org</a>
Cardiovascular and pulmonary model repository	<a href="http://vascularmodel.com">vascularmodel.com</a>
SimVascular (simulation software)	<a href="http://simvascular.github.io">simvascular.github.io</a>
CellDesigner.org (v. 4.4.2)	<a href="http://celldesigner.org">celldesigner.org</a>
CellML (XML markup language)	<a href="http://cellml.org">cellml.org</a>
Color Atlas of medical diseases (v. 2004)	<a href="http://ecureme.com/atlas/version2001/atlas.asp">ecureme.com/atlas/version2001/atlas.asp</a>
Swiss bioinformatics resource portal (Expasy)	<a href="http://www.expasy.org">www.expasy.org</a>
MedPix (>12,000 patient case scenarios and nearly 59,000 images)	<a href="http://medpix.nlm.nih.gov/home">medpix.nlm.nih.gov/home</a>
Open science repository (research papers)	<a href="http://www.open-science-repository.com">www.open-science-repository.com</a>
OpenSim (musculoskeletal modeling)	<a href="http://opensim.stanford.edu">opensim.stanford.edu</a>
Patient contributed image repository (PCIR)	<a href="http://www.pcir.org">www.pcir.org</a>
Virtual metabolic human	<a href="http://www.vmh.life">www.vmh.life</a>

comprises two distinct areas, “artistic human avatars” and “scientific DHM,” which are used in analysis, design, and information systems ([Scataglini & Paul, 2019](#), p. 5). Interestingly, such DHM systems which when integrated in HFE engineering, industrial engineering, or systems engineering applications have recently been dubbed Digital Twins or Cyber-Physical-Systems (CPS) by many non-HFE disciplines, while [Paul et al. \(2021\)](#) have pointed out the necessary reorientation from a population-based approach toward an individual based modeling attempt when aiming to progress from a DHM based framework in the direction of the Digital Twin.

Based on semantic analysis of a large number of publications, [Paul et al. \(2021\)](#), p. 9) have also described the context in which the term DT is currently used, which is “cloud (computing), robot (simulation), AR, bionic, interconnectivity, IoT, digital factory, automation, DHM, personalization, Industry 4.0., (plant) simulation, cyberphysical, system, (human-robot) collaboration, evaluate work (performance), client-server, technologies, operator, (assembly) process, data (model), games, HF, production, integration, VR, virtual (engineering), (digital) information, scalable, machine interface, HFE analysis, intelligent manufacturing, co-simulation, computer-aided ergonomics, CPS, (digital) process, integrated (manufacturing), enhance, data acquisition, maintenance, sustainable manufacturing, (system, IT, communication, simulation) architecture, immerse real worker, motion/movement, CPPS, human model, interacting/interaction, real-time, analysis, prediction, digital mock-up, biomechanics, musculoskeletal, CAD, cognitive, (virtual) prototyping, HMD, Artificial Intelligence, (additive, flexible) manufacturing, assembly,

(conceptual, experimental, product) design, (virtual) environment, ergonomic assessment, factory prototype, cybersecurity, training, immersion, virtual ergonomics, posture, connectivity, visualization, surrogate model, planning, fully artificial, decision making, workplace, work station, communication, continuous learning, agile HMI, managerial, knowledge, smart, transition, transformation, strategy, skills, robot control, digital human, manikins, factory.”

This however *is not* the way we understand or wish to define the Digital Twin.

[Wikipedia \(2022\)](#) defines the Digital Twin as: “A digital twin is a virtual representation that serves as the real-time digital counterpart of a physical object or process. Though the concept originated earlier (attributed to Michael Grieves, then of the University of Michigan, in 2002) the first practical definition of a digital twin originated from NASA in an attempt to improve physical-model simulation of spacecraft in 2010. Digital twins are the result of continual improvement in the creation of product design and engineering activities. Product drawings and engineering specifications have progressed from handmade drafting to computer-aided drafting/computer-aided design to model-based systems engineering.”

This ingoing definition is highly disputable, as it clearly refers to constructs which we would rather understand as computer-aided design (CAD), computer-aided engineering (CAE), and DHM. More relevant though, the article then refers to the Digital Twin in the healthcare industry and states: “Healthcare is recognized as an industry being disrupted by the digital twin technology. The concept of digital twin in the healthcare industry was originally proposed and first used in product or equipment prognostics. With a digital twin, lives can be improved in terms of medical health, sports and education by taking a more data-driven approach to healthcare. The availability of technologies makes it possible to build personalized models for patients, continuously adjustable based on tracked health and lifestyle parameters. This can ultimately lead to a virtual patient, with detailed description of the healthy state of an individual patient and not only on previous records. Furthermore, the digital twin enables individual’s records to be compared to the population in order to easier find patterns with great detail. The biggest benefit of the digital twin on the healthcare industry is the fact that healthcare can be tailored to anticipate on the responses of individual patients. ....”

While still ingrained in Industry 4.0 thinking and incomplete in the sense of an authoritative definition, this foundation of the Digital Twin provides a fair introduction into the powerful implications which the concept may have in the health sector.

The [digital twin consortium \(2022\)](#) in 2020 defined the Digital Twin more appropriately for our purposes:

- “A digital twin is a virtual representation of real-world entities and processes, synchronized at a specified frequency and fidelity.
- Digital twin systems transform business by accelerating holistic understanding, optimal decision-making, and effective action.
- Digital twins use real-time and historical data to represent the past and present and simulate predicted futures.

- Digital twins are motivated by outcomes, tailored to use cases, powered by integration, built on data, guided by domain knowledge, and implemented in IT/OT systems.”

[Siemens Healthcare GmbH \(2019\)](#) summarize the importance of the DT in a healthcare environment by saying that “A digital twin can help healthcare enterprises identify ways to enhance and streamline processes, improve patient experience, lower operating costs, and increase higher value of care. The digital twin creates models of physical spaces and processes. Then, cost and quality optimization parameters are examined and ultimately selected based on the insights gained from simulations leveraging the digital twin. Digital twin insights can be further enhanced with complimentary technologies like Real-Time Locating Systems (RTLS), which provides a robust data source and a means to test changes in layout, process, etc.”

Similarly, Henk van Houten as the Philips CTO stresses the “importance of getting the whole picture,” because “different data may point to different conclusions when viewed in isolation. Medical practitioners should ideally have an integrated understanding of a person’s health.” He then asks, “Could the ‘digital patient’—a digital twin of the human body—be the means to this end?” and finds that “digital twins are proving to be a powerful paradigm for personalizing healthcare and making it more effective and efficient” and provides the examples of medical device testing and organ models that may support diagnosis and management. However, the digital patient concept goes beyond having “isolated models of different organs, a digital patient or ‘health avatar’ integrates every relevant piece of medical knowledge about you. A digital patient is a lifelong, integrated, personalized model of a patient that is updated with each measurement, scan or exam, and that includes behavioral and genetic data as well” ([Philips, 2022](#)).

Digital Twins in Medicine are virtual patients which are interconnected with their environment, as modular, smart, and shared instances; they have an observer, they are time and location independent, data driven, and they inform an artificial intelligence (AI) enabled inference stage at both personal and population level based on a standardized information model and interface (see also [Discipulus Project, 2022](#)). This goes beyond the more generic DT description by [Guzina et al. \(2022, p. 449\)](#) who find that “digital twin goes beyond traditional computer-aided applications and represents a two-way communication bridge between the physical and the digital worlds. The concept model of DT consists of three parts being the physical object in the real world, the virtual object in the digital world, and the connections between these two objects that provide data flow.”

The Digital Twin in Medicine in the first place requires an extended modeling approach where biological and physical/biomechanical models are coupled and interact, as presented in [Ceresa et al. \(2018\)](#) for the study of emphysema progression. Such a modeling approach goes significantly beyond what has been presented in previous strictly biomechanical or mechanobiological models (see, for example, [Doweidar, 2019](#)). Any interaction between models requires standardization ([Lidell et al., 2022; Paul & Wischniewski, 2012](#)).

Saxby et al. (2020) effectively describe an inference stage in the domain of personalized neuromusculoskeletal modeling (which in fact is a specific type of DT) where data and physical models are merged using big data and machine learning to generate a new model and process.

The European EDITH project (<https://www.edith-csa.eu/>), which stands for “Ecosystem for DIgital Twins in Healthcare” is a strategic approach to develop a taxonomy of Digital Twins in healthcare and plan for their development and implementation in medical practice. EDITH mentions *in silico* medicine, health data, and High-Performance Computing (HPC) as Digital Twin elements, however given its early days, does not yet provide the complete definition or visionary framework. It aims to develop a roadmap and cloud-based repository of resources and best practice, controlled by a governance context of standards, regulations, and metadata. The project eventually includes an infrastructure component in the form of a simulation platform to “realize the vision of the integrated digital twin for personalized healthcare.”

“Personalized healthcare” is a term that epitomizes what the Digital Twin in Medicine should be about, which effectively entails providing the best possible health service to the patient based on their very personal condition. While modern digital health data wallets, such as the MyHealth record in Australia (<https://www.myhealthrecord.gov.au>), have attempted to join a multitude of disconnected health data records from the many medical providers into one single resource, the reality is that this approach has not changed or improved medical practice and the outcome for the patient. The Guardian in 2020 found that “... A decade since it was first announced, the federal government [AUS] has spent close to \$2bn on its troubled My Health Record system, and half of the 23m records created lie empty almost a year after the government made the system opt-out.” (Guardian, 2020).

A reason for this failure may be that the system has proven time-consuming and impractical for the practitioners, and inaccessible for the patient. Neither side will see much benefit in engaging with such a record, which has been developed without consideration of human factors principles. Obviously, we can draw conclusions from this malfunction for the Digital Twin. DT must not simply output lengthy timeline records of multimodal specialist medical and healthcare data. Instead, DT must be based on models which can read such multimodal data, merge data, infer data, and serve any resulting recommendations or warnings to both the medical practitioner and patient.

Beyond the patient focus, it is obvious that the DT can and will help us develop a much more time and cost-efficient medical practice framework, where duplication, redundancy, and any trial and error-based methods will be mostly eliminated.

The Digital Twin in Medicine in this sense is the ultimate attempt to unite health system, practitioner, and patient interests in a holistic future healthcare apparatus.

## References

- Ceresa, M., Olivares, A. L., Noailly, J., & González Ballester, M. A. (2018). Coupled immunological and biomechanical model of emphysema progression. *Frontiers in Physiology*, 9. <https://doi.org/10.3389/fphys.2018.00388>
- digital twin CONSORTIUM. (2020). *Digital twin definition*. <https://www.digitaltwinconsortium.org/initiatives/the-definition-of-a-digital-twin/>. (Accessed 21 July 2022).
- DISCIPULUS Project. (2012). *The digital patient: Roadmap*. <https://cordis.europa.eu/docs/projects/cnect/3/288143/080/deliverables/001-discipulusleafletextendedversion1.pdf>. (Accessed 21 July 2022).
- Doweidar, M. H. (Ed.). (2019). *Advances in biomechanics and tissue regeneration*. London: Academic Press, ISBN 978-0-12-816390-0.
- Guardian. (2020). *My health record: Almost \$2bn spent but half the 23 m records created are empty*. <https://www.theguardian.com/australia-news/2020/jan/23/my-health-record-almost-2bn-spent-but-half-the-23m-records-created-are-empty>. (Accessed 10 July 2022).
- Guzina, L., Ferko, E., & Bucaioni, A. (2022). Investigating digital twin: A systematic mapping study. *Advances in Transdisciplinary Engineering*, 21, 449–460. <https://doi.org/10.3233/ATDE220164>
- Hamzelou, J. (September 23, 2015). Virtual human built from more than 5000 slices of a real woman. An American woman's body has been reconstructed digitally from very thin slices, creating a model for experiments too risky to try on the living. <https://www.newscientist.com/article/mg22730404-000-virtual-human-built-from-more-than-5000-slices-of-a-real-woman/#bx304040B1>.
- Havard, V., Benoit, J., Lacomblez, M., & Baudry, D. (2019). Digital twin and virtual reality: A co-simulation environment for design and assessment of industrial workstations. *Production & Manufacturing Research*, 7(1), 472–489. <https://doi.org/10.1080/21693277.2019.1660283>
- Hunter, P. J., & Borg, T. K. (2003). Integration from proteins to organs: The physiome project. *Nature Reviews Molecular Cell Biology*, 4(3), 237–243. <https://doi.org/10.1038/nrm1054>.
- Kohl, P., & Noble, D. (2009). Systems biology and the virtual physiological human. *Molecular Systems Biology*, 5(1), 292. <https://doi.org/10.1038/msb.2009.51>
- Kritzinger, W., Karner, M., Traar, G., Henjes, J., & Sihn, W. (2018). Digital twin in manufacturing: A categorical literature review and classification. *IFAC-Paper*, 51(11), 1016–1022. <https://doi.org/10.1016/j.ifacol.2018.08.474>
- Lidell, A., Ericson, S., & Ng, A. H. C. (2022). The current and future challenges for virtual commissioning and digital twins of production lines. *Advances in Transdisciplinary Engineering*, 21, 508–519. <https://doi.org/10.3233/ATDE220169>
- Mitsuhashi, N., Fujieda, K., Tamura, T., Kawamoto, S., Takagi, T., & Okubo, K. (2009). BodyParts3D: 3D structure database for anatomical concepts. *Nucleic Acids Research*, 37(Database issue), D782–D785.
- Paul, G., Abele, N. D., & Kluth, K. (2021). A review and qualitative meta-analysis of digital human modelling and cyber-physical-systems in ergonomics 4.0. *TOEHF*, 9(3–4), 111–123. <https://doi.org/10.1080/24725838.2021.1966130>
- Paul, G., & Wischniewski, S. (2012). Standardization of digital human models. *Ergonomics*, 55(9), 1115–1118. <https://doi.org/10.1080/00140139.2012.690454>
- Philips. (2018). *The digital patient: Will we one day have our own health avatars?*. <https://www.philips.com/a-w/about/news/archive/blogs/innovation-matters/20181211-the-digital-patient-will-we-one-day-have-our-own-health-avatars.html>. (Accessed 21 July 2022).

- Saxby, D. J., Killen, B. A., Pizzolato, C., Carty, C. P., Diamond, L. E., Modenese, L., Fernandez, J., Davico, G., Barzan, M., Lenton, G., Brito da Luz, S., Suwarganda, E., Devaprakash, D., Korhonen, R. K., Alderson, J. A., Besier, T. F., Barrett, R. S., & Lloyd, D. G. (2020). Machine learning methods to support personalized neuromusculoskeletal modelling. *Biomechanics and Modeling in Mechanobiology*, 19, 1169–1185. <https://doi.org/10.1007/s10237-020-01367-8>
- Scataglini, S., & Paul, G. (Eds.). (2019). *DHM and posturography*. London: Academic Press. <https://doi.org/10.1016/C2018-0-00529-0>
- Siemens Healthcare GmbH. (2019). White Paper: The value of digital twin technology—transforming care delivery in a single department or an entire healthcare enterprise. <https://www.siemens-healthineers.com/services/value-partnerships>. (Accessed 5 July 2022).
- Tsiaras, A. (1997). *Body voyage: A three-dimensional tour of a real human body*. New York: Warner Books, ISBN 0-446-52009-8.
- VPI-Institute. (2013). DISCIPULUS. <https://www.vph-institute.org/discipulus.html>. (Accessed 21 July 2022).
- Wakefield, J. (June 13, 2022). Why you may have a thinking digital twin within a decade. *BBC News*. <https://www.bbc.com/news/business-61742884>.
- Waldby, C. (2004). *The visible human project: Informatic bodies and posthuman medicine*. Routledge, ISBN 978-0-203-36063-7.
- Wikipedia. (July 3, 2022). *Digital twin*. [https://en.wikipedia.org/wiki/Digital\\_twin](https://en.wikipedia.org/wiki/Digital_twin).

---

## Further reading

- ISO/TC 184/SC 4 Industrial data Committee. (2021). ISO 23247-1:2021 Automation systems and integration—digital twin framework for manufacturing—Part 1: Overview and general principles. <https://www.iso.org/standard/75066.html>.

This page intentionally left blank

# Massive data probabilistic framework for parameter estimation in biological problems

# 2

Marina Pérez-Aliacar<sup>1,2</sup>, Jacobo Ayensa-Jiménez<sup>1,2,3</sup>, Mohamed H. Doweidar<sup>1,2,4</sup>,  
Manuel Doblaré<sup>1,3,4</sup>

<sup>1</sup>Aragon Institute of Engineering Research (I3A), University of Zaragoza, Zaragoza, Spain;

<sup>2</sup>Mechanical Engineering Department, University of Zaragoza, Zaragoza, Spain; <sup>3</sup>Aragon Institute of Health Research (IIS Aragón), University of Zaragoza, Zaragoza, Spain; <sup>4</sup>Centro de Investigación Biomédica en Red en Bioingeniería, Biomateriales y Nanomedicina (CIBER-BBN), Madrid, Spain

## Chapter outline

<b>Introduction.....</b>	20
<b>General framework.....</b>	21
About modeling .....	21
About experiments: smart experiments .....	22
<i>Strategy 1: in one stroke .....</i>	23
<i>Strategy 2: divide and conquer .....</i>	25
<i>Strategy 3: the general situation .....</i>	25
Model separability .....	26
Including model uncertainty .....	26
<b>Mathematical tools and concepts.....</b>	28
Managing data uncertainty .....	28
Estimation of probabilistic models .....	30
<i>Parametric methods .....</i>	30
<i>Nonparametric methods .....</i>	31
Design of experiments.....	31
Copulas .....	32
<i>Mathematical definition.....</i>	33
<i>Theorem 1: Sklar's theorem.....</i>	34
<i>Parametric copulas .....</i>	34
<i>Nonparametric copulas.....</i>	35
<b>Methodology.....</b>	36
Model adjustment.....	36
Model analysis and applications .....	37

Parameter estimation.....	38
<b>A case study: GBM evolution .....</b>	<b>39</b>
Mathematical model.....	40
Data generation.....	42
Results.....	43
<i>Model adjustment</i> .....	43
<i>Model validation</i> .....	45
<i>Parameter estimation</i> .....	48
<i>Experimental design</i> .....	52
<b>Conclusions.....</b>	<b>57</b>
<b>Acknowledgments .....</b>	<b>58</b>
<b>References .....</b>	<b>58</b>

---

## Introduction

Modeling and simulation are essential tools for better understanding biological processes such as cancer evolution (Byrne et al., 2006; Kitano, 2002). However, the interaction between several coupled mechanisms, usually observed in these processes, makes the associated mathematical models highly nonlinear and multiparametric, with many and varied experiments required to calibrate the model parameters. The associated parameter fitting is typically complicated as well as inaccurate due to the high number of parameters involved, their dependency on the particular state conditions, the hidden correlations among them, and, finally, the difficulty in getting reliable values in similar experimental conditions. All this gives rise to wide ranges of variation in the parameter values, sometimes of orders of magnitude in scientific literature. Consequently, a proper parametric analysis is mandatory. This requires an extensive and detailed study of the values reported in the existing bibliography, a careful sensitivity analysis, and a sufficient number of different experiments, not only for calibration but also for validation, to avoid parameter overfitting. The recent development of in vitro experimental techniques, such as microfluidics, not only allows a more accurate and three-dimensional reproduction of the cell microenvironment but also enables the generation of great amounts of data (Bhatia & Ingber, 2014). This fact can be used to fit more complex and richer models and opens the possibility of considering them as random correlated variables subjected to uncertainty. This allows to more accurately reproduce the biological reality, where there exists an inherent variability among the organisms and, therefore, among the parameters of each population.

The objective of this chapter is to introduce a general framework to analyze parameter uncertainty and correlation in complex multiparametric and multiphysics mathematical models, such as those appearing in biological problems (Ayensa-Jiménez et al., 2021). We explain the theoretical foundations and explore the possibilities of a methodology, based on copulas, able to identify and to separate, in a certain sense, the correlated effects of the model. As a consequence, it is possible

to get a more accurate and reliable representation of the experimental results in the parametric space. Copulas have been used in risk theory and reliability analysis to deal with models where uncertainty is dominant and correlation between phenomena plays a major role. Indeed, the independence assumption, very usual in many statistical procedures related to parameter fitting, is a common conservative approach that results in an unnecessary waste of time and material resources, which increased copula popularity in fields like asset and portfolio management (Kole et al., 2007), insurance (Eling & Toplek, 2009), and extreme events and catastrophe modeling (Chao & Zou, 2018). It seems natural, then, to progressively establish such probabilistic frameworks in fields where resources availability is also a critical aspect, such as biotechnology and biomedical engineering, in order to accelerate model developments, for the sake of the biomedicine's holy Grail: the human digital patient.

This chapter is structured in different sections. In a section **General framework**, the general framework is presented. The general structure of models and their features is described, the fitting strategies are presented, and the adoption of a stochastic approach is justified. In a section **Mathematical tools and concepts**, the main mathematical tools and concepts needed are briefly presented. This section includes notions on random variables, distribution characterization, design of experiments and copulas, with the aim of making the text self-contained. Next, in the section **Methodology**, previously presented tools are combined to define the methodology used to obtain a probabilistic model and to analyze the results. In the final section **A case study: GBM evolution**, the methodology is applied to the study of GBM evolution, a paradigmatic case of application of the framework presented in **Methodology** section. The work is completed with the main conclusions in the section.

---

## General framework

In this section, we present the main theoretical concepts that are used in the following paragraphs. The discussion is not pretended to be exhaustive, but to introduce the notation of the probabilistic tools in such a way that the text is self-contained.

### About modeling

Modeling is one of the fundamental tasks of the scientist. A model representing any general (physical, biological, engineering ...) problem may be described in terms of the following mathematical equation:

$$\mathbf{u} = \mathcal{F}(\lambda), \quad (2.1)$$

whose terms mean the following:

- $\mathbf{u}$  is the measurable variable, that is, the (in general tensorial) variable that may be measured in a certain experiment. For example,  $\mathbf{u}$  may be a scalar variable,

such as temperature ( $u = T$ ); a vector quantity, such as an electric vector at a given point ( $u = E$ ); or a tensor, like the strain tensor ( $u = \epsilon$ ). When working with field theories, the notation can be extended to tensorial fields, via a suitable discretization. If  $\mathbf{T}(x, t)$  is a tensorial field dependent on point  $x$  and time  $t$ , we may write  $\mathbf{u} = (\mathbf{T}(x_i, t_j))_{i \in \mathcal{I}, j \in \mathcal{J}}$ , where  $\mathcal{I}, \mathcal{J} \subset \mathbb{N}$  are subsets of integers indexing different spatiotemporal points.

- $\lambda$  is a controlled variable, that is, a parametric representation of a given experiment. It can refer to environmental variables, control variables, geometric parameters, and/or boundary conditions that may be controlled by the experimentalist or scientist.
- $\mathcal{F}$  is a mathematical model, that relates the control with the observable variable. It is common to work with parametric models, that is, the model  $\mathcal{F} = \mathcal{F}_\theta$  is given in terms of a set of parameters  $\theta \in \Theta$ , called the model parameters, where  $\Theta$  is the parametric space.

The relationship (2.1) is ubiquitous in any area of physics and engineering. The model  $\mathcal{F}_\theta$  may be formulated as an explicit parametrized function, the solution of a system of Ordinary, Algebraic, or Partial Differential Equations (ODEs, DAEs, PDEs), or, in general, *black box* relationships on some model parameters  $\theta$ . If the parameters are not known, Eq. (2.1) becomes

$$\mathbf{u} = \mathbf{F}(\lambda, \theta). \quad (2.2)$$

In general, predictive sciences seek to solve the problem of computing the value of  $\mathbf{u}$  for a given value of  $\lambda$ . When  $\theta \in \emptyset$  or  $\theta$  are known, the problem is a straightforward evaluation of the model  $\mathbf{F}$ . However, when the parameters are unknown, they have to be previously adjusted. This is usually done by combining experiments with mathematical optimization. In a first step, a dataset of experiments is generated. That is, we look for the (preferably *smart*) generation of points  $(\lambda, \mathbf{u}) \in \mathcal{M} \times \mathcal{U}$ , with  $\mathcal{M}$  the whole space of parametrized experiments,  $\lambda \in \mathcal{M}$  and  $\mathcal{U} \subset \mathbb{R}^m$  the functional space of the variable  $\mathbf{u}$ . Here, the word *smart* is crucial and will be explained later. Let us suppose that we have a finite sample of  $N$  experiments, that is  $\mathcal{E} = \{(\lambda^i, \mathbf{u}^i)\}_{i=1,\dots,N}$ , obtained by measuring the value of  $\mathbf{u} = \mathbf{u}^i$  when we control the value of  $\lambda = \lambda^i$ . Of course, this measurement is subject to an error related to experimental configurations. Then, the parameters may be obtained by minimizing the residual function  $R : \Theta \rightarrow \mathbb{R}^+$ , defined as

$$R(\theta) = \sum_{i=1}^N \left\| \mathbf{u}^i - \mathbf{F}(\lambda^i, \theta) \right\|^2, \quad (2.3)$$

using, for instance, the Levenberg–Marquardt algorithm (Marquardt, 1963).

### About experiments: smart experiments

The difficulty of the parameter fitting depends on both the characteristics of the function  $\mathbf{F}$  and the sampling strategy. In general, this step of the process is complex and

critical in any experimental campaign. Here we summarize, however, some possibilities when the model  $\mathbf{F}$  has some specific characteristics.

### Strategy 1: in one stroke

Let us suppose, for the moment, that we have only  $N = 1$  measurement of  $\mathbf{u}$  that we consider noise-free. The idea is to establish criteria to sample  $\mathbf{u}$  by selecting the experiments that will be used for the parameter fitting. This sampling strategy will depend on the characteristics of  $\mathbf{F}$ .

If the function  $\mathbf{F}(\lambda, \cdot) : \Theta \rightarrow \mathcal{U}$  is linear in  $\Theta$  for some  $\lambda \in \mathcal{M}$ , that is,  $\mathbf{F}(\lambda) = \mathbf{A}(\lambda)\boldsymbol{\theta}$  being  $\mathbf{A}(\lambda)$  any matrix, the solution is directly obtained by Linear Least Squares (LLS), that solves the problem of minimizing the residual  $R$ . Writing Eq. (2.2) in matrix form, the orthogonal projection can be obtained by solving the linear system of normal equations:

$$\mathbf{A}(\lambda)^T \mathbf{A}(\lambda) \boldsymbol{\theta} = \mathbf{A}(\lambda)^T \mathbf{u}. \quad (2.4)$$

In particular, if the linear operator is invertible, the system becomes  $\mathbf{A}(\lambda)\boldsymbol{\theta} = \mathbf{u}$ . Therefore, a smart experiment would be any such that  $\mathbf{F}(\lambda, \boldsymbol{\theta})$  is linear in  $\boldsymbol{\theta}$ . In other words, we assume that  $\exists \lambda^* \in \mathcal{M}$ , such that

$$\mathbf{F}(\lambda^*, \boldsymbol{\theta}) = \mathbf{A}(\lambda^*)\boldsymbol{\theta}, \quad (2.5)$$

or, if  $\mathbf{F}$  is sufficiently smooth:

$$\left. \frac{\partial^2 \mathbf{F}}{\partial \boldsymbol{\theta} \partial \boldsymbol{\theta}^T} \right|_{\lambda=\lambda^*} = 0. \quad (2.6)$$

Unfortunately, solving Eq. (2.6) for  $\lambda$ , when possible, is usually difficult or computationally demanding, especially if  $\mathbf{F}$  is not an explicit expression of  $\boldsymbol{\theta}$  and  $\lambda$ . It is also possible that the equation has no solution or that the solution comes outside the physically or experimentally possible range of control values. As an example, consider a function of type  $\mathbf{F}(\lambda, \boldsymbol{\theta}) = \mathbf{k} \|\lambda\| \boldsymbol{\theta} \|\lambda\|^2$  with  $\mathbf{k} \in \mathbb{R}^k$ . If we select  $\lambda$  at the unit sphere,  $\|\lambda\| = 1$ , and then,  $\mathbf{F}(\lambda, \boldsymbol{\theta}) = \mathbf{k}\boldsymbol{\theta}$ , it yields  $\boldsymbol{\theta} = (\mathbf{k}^T \mathbf{k})^{-1} \mathbf{k}^T \mathbf{u}$ .

Let us now derive the normal equations using one fundamental argument, which will serve us below as inspiration. The residual function  $R$  can be expressed as

$$R(\boldsymbol{\theta}) = \left\| \mathbf{A}(\lambda)\boldsymbol{\theta} - \mathbf{u} \right\|^2, \quad (2.7)$$

so, taking derivatives:

$$\frac{\partial R}{\partial \boldsymbol{\theta}} = 2(\mathbf{A}(\lambda)\boldsymbol{\theta} - \mathbf{u})^T \mathbf{A}(\lambda), \quad (2.8)$$

and

$$\frac{\partial^2 R}{\partial \boldsymbol{\theta} \partial \boldsymbol{\theta}^T} = 2\mathbf{A}(\lambda)^T \mathbf{A}(\lambda), \quad (2.9)$$

where  $\mathbf{A}(\lambda)^T \mathbf{A}(\lambda)$  is a positive-definite matrix and, therefore,  $R$  is a convex function. Solving for  $\frac{\partial R}{\partial \theta} = 0$ , using Eq. (2.8), the LLS solution is recovered.

Now, let us move to the nonlinear case. We look for the function  $\mathbf{F}(\lambda, \cdot) : \Theta \rightarrow \mathcal{U}$  to have the desirable properties for certain values of  $\lambda$ . This implies that, expressing  $\mathbf{F}(\lambda, \theta) = \mathbf{G}_\lambda(\theta)$ , the equation  $\mathbf{u} = \mathbf{G}_\lambda(\theta)$  is more easily solved for such values of  $\lambda$ , which brings us back to the concept of *smart* experiments, but now in a more general context. For example, if  $\mathbf{G}_\lambda$  is invertible, we may write  $\theta = \mathbf{G}_\lambda^{-1}(\mathbf{u})$ .

In the general case, inspired by the linear case, the residual function  $R$  may be expressed as

$$R(\theta) = \| \mathbf{F}(\lambda, \theta) - \mathbf{u} \|^2. \quad (2.10)$$

Taking the derivative with respect to  $\theta$ , we have

$$\frac{\partial R}{\partial \theta} = 2(\mathbf{F}(\lambda, \theta) - \mathbf{u})^T \frac{\partial \mathbf{F}}{\partial \theta}. \quad (2.11)$$

Solving for  $\frac{\partial R}{\partial \theta} = 0$ , Eq. (2.11) becomes

$$\frac{\partial \mathbf{F}^T}{\partial \theta} \mathbf{F}(\lambda, \theta) = \frac{\partial \mathbf{F}^T}{\partial \theta} \mathbf{u}. \quad (2.12)$$

This expression is nonlinear in  $\theta$ , unlike Eq. (2.4). Nevertheless, depending on the form of the function  $\mathbf{F}$ , this equation might be easier to solve. As an illustrative example, if we look for  $\lambda^* \in \mathcal{M}$  such that

$$\left. \frac{\partial \mathbf{F}^T}{\partial \theta} \right|_{\lambda=\lambda^*} \mathbf{F}(\lambda^*, \theta) = \mathbf{B}(\theta) \theta, \quad (2.13)$$

with invertible  $\mathbf{B}(\theta)$  and verifying that  $\mathbf{B}(\theta)^{-1} \frac{\partial \mathbf{F}^T}{\partial \theta}$  is independent of  $\theta$ , the solution is given by

$$\theta = \mathbf{B}(\theta)^{-1} \frac{\partial \mathbf{F}^T}{\partial \theta} \mathbf{u}. \quad (2.14)$$

Of course, when  $\mathbf{F}(\lambda^*, \theta) = \mathbf{A}(\lambda^*) \theta$  for a certain  $\lambda^*$ , the LLS solution is recovered, with  $\mathbf{B}(\theta) = \mathbf{A}(\theta)^T \mathbf{A}(\theta)$ .

Evaluating higher derivatives, we have

$$\frac{\partial^2 R}{\partial \theta \partial \theta^T} = 2 \frac{\partial \mathbf{F}^T}{\partial \theta} \frac{\partial \mathbf{F}}{\partial \theta} + 2(\mathbf{F}(\lambda, \theta) - \mathbf{u})^T \frac{\partial^2 \mathbf{F}}{\partial \theta \partial \theta^T}. \quad (2.15)$$

Therefore, it would be desirable to choose  $\lambda^* \in \mathcal{M}$  so that the quadratic form in Eq. (2.15) was positive-definite, in order to guarantee the minimality condition when minimizing  $R(\theta)$ , hence improving the performance of the minimization algorithm.

In summary, even in the nonlinear case, we can seek for experiments  $\lambda \in \mathcal{M}$  so that  $R$  has good properties, either for direct solvers or numerical schemes.

### Strategy 2: divide and conquer

Another possibility is when we are not interested in fitting the whole dataset of parameters  $\boldsymbol{\theta}$ , but only a particular parameter, let us say  $\theta_j$ . It may be then interesting to find a function  $g : \mathcal{U} \rightarrow \mathbb{R}$ , such that  $g \circ \mathbf{F}$  only depends on  $\theta_j$ . That is:

$$g(\mathbf{F}(\boldsymbol{\lambda}, \boldsymbol{\theta})) = f(\theta_j). \quad (2.16)$$

As this function depends on the chosen experiment  $\lambda$ , in what follows it will be denoted as  $g_\lambda$ . Therefore, a new interpretation of a *smart* experiment arises: an experiment  $\lambda^*$  which allows to define a function  $g_\lambda$ , verifying Eq. (2.16). The problem is, therefore, completely solved if we look for  $n = \dim(\Theta)$  experiments  $\{\lambda^i\}_{i=1,\dots,n}$ , and  $n$  functions  $g_i = g_{\lambda^i}$  such that

$$g_i(\mathbf{F}(\lambda^i, \boldsymbol{\theta})) = f_i(\theta_i), i = 1, \dots, n. \quad (2.17)$$

Thus, the problem of finding  $n$  parameters has been separated into  $n$  one-parameter problems, given by the equations:

$$f_i(\theta_i) = g_i(\mathbf{u}^i), i = 1, \dots, n, \quad (2.18)$$

where  $\mathbf{u}^i$  are the data associated with the experiment  $\lambda^i$ . Here, although the equation to be solved may be nonlinear, it is much simpler from both the computational and the theoretical points of view.

A particular and desirable case of the previous situation is when the function  $g$  is a projection, that is,  $g(\mathbf{u}) = u_i$ .

### Strategy 3: the general situation

In general, this case is neither like the first nor the second one. However, the selection of the experiments  $\lambda^i$  can be performed as to reach one of the previous situations. Let us suppose that  $i = 1, \dots, N$  experiments have been chosen so that the residual function to minimize is given by

$$R(\boldsymbol{\theta}) = \sum_{i=1}^N \|\mathbf{u}^i - \mathbf{F}(\lambda^i, \boldsymbol{\theta})\|^2 = \sum_{i=1}^N \|\mathbf{u}^i - \mathbf{F}_i(\boldsymbol{\theta})\|^2 = \sum_{i=1}^N E_i^2 \quad (2.19)$$

It is clear that if a single  $\boldsymbol{\theta}^*$  that minimizes each of the terms  $E_i^2$  is found, then it minimizes the total residual  $R$ , so it is the sought solution. However, the reciprocal is not true. In fact, each of the terms has its own minimal value, found for a given  $\boldsymbol{\theta}^i$ . Now the strategy is how to find suitable experiments in the sense that, for each of them, we can find a function  $g_i : \mathcal{U} \rightarrow \mathbb{R}^k$  that satisfies

- $g_i(\mathbf{u}^i)$  is only a function of a subset of the parameters, say  $\boldsymbol{\theta}_{(i)} = (\theta_{i_1}, \theta_{i_2}, \dots, \theta_{i_{n_i}})$ , following the *divide and conquer* strategy. The subsets form a partition of the whole set of parameters.
- $g_i$  has suitable functional properties, e.g.,  $g_i(\mathbf{u}^i)$  is linear in  $\boldsymbol{\theta}_{(i)}$ , following the *in one stroke* strategy.

In this case, Eq. (2.19) writes

$$R(\boldsymbol{\theta}) = \sum_{i=1}^N E_i^2(\boldsymbol{\theta}_{(i)}), \quad (2.20)$$

and minimizing each of the terms in  $E_i^2$  is equivalent to minimizing the whole residual  $R$ . It may seem that, instead of solving a single minimization problem, we now have to solve several, but each of them is easier than the original one.

## Model separability

Separability of the model  $\mathbf{F}$  has a direct impact on the feasibility of finding *smart* experiments. A model  $\mathbf{F}$  is separable if it is possible to approximate it as

$$\mathbf{F}(\lambda, \boldsymbol{\theta}) \simeq \mathbf{F}^M(\lambda, \boldsymbol{\theta}) = \sum_{i=1}^M \prod_{j=1}^n F_{i,j}(\lambda, \theta_j), \quad (2.21)$$

where the product has to be interpreted as a point-wise multiplication. Let us assume that the model is totally separable in terms of the model parameters. Therefore, a set of  $n$  *smart* experiments  $\{\lambda^k\}_{k=1,\dots,n}$  is obtained looking for experiments satisfying that  $F_{i,j}(\lambda^k, \theta_j)$  do not depend on  $\theta_j$  for  $j \neq k$ . Under these conditions, we have

$$\mathbf{F}(\lambda^k, \boldsymbol{\theta}) \simeq \sum_{i=1}^M \prod_{j=1}^n F_{i,j}(\lambda, \theta_j) = \sum_{i=1}^M \left( \prod_{j=1}^n F_{i,j}(\lambda) \right) (\theta_j) = \mathbf{G}(\theta_j). \quad (2.22)$$

Thus, the problem is reduced to a one-parameter fitting. For this purpose, we may try to find  $\lambda^k$  satisfying the equations:

$$\left. \frac{\partial F_{i,j}}{\partial \theta_j} \right|_{\lambda=\lambda^k} = 0, j = 1, \dots, n, j \neq k. \quad (2.23)$$

Eq. (2.23) forms a set of  $n - 1$  equations with  $n$  unknowns,  $\lambda_1^k, \dots, \lambda_n^k$ . The analysis of this system may be complex in the general case and can be done from a systematic perspective only in the linear case, thanks to the Rouché–Fröbenius–Capelli theorem. Anyway, if this set of  $n$  values is found, the problem is solved. Partial separability of the model may be used analogously for finding a subset of the parameters. In that sense, there is a direct link between model separability and the existence of appropriate (*smart*) experiments for the parameter-fitting step.

## Including model uncertainty

Let us now analyze the minimization of Eq. (2.3) in general terms, even if it can be expressed in a simplified form as in Eq. (2.20). In relation to the accuracy and precision of the model it is possible to define three levels of analysis: (1) the model is perfect and the experimental measures are noise-free; (2) the model is perfect and

the experimental measures are noisy, and (3) the model is not perfect and the measurements are noisy. Only the third case is, in general, realistic for complex problems.

From a mathematical point of view, the first case gives us overdetermined problems if, for smart and independent experiments,  $\mathcal{N} = N \times m > n$ . However, depending on the model complexity, it might be difficult, or even impossible, to design these so-called smart experiments and, consequently, the problem would be ill-posed and undetermined, that is, two different sets of parameters may result in an identical set of measurements. The problem worsens when considering noise in the experimental measurements and, therefore, a minimization strategy should be considered. The existence of coupled phenomena and nonseparable models is fatal for minimization procedures, both from the theoretical and numerical points of view. This is even more dramatic when the model is not perfect and, therefore, the error is of a more complex nature or, even worse, when there exist hidden parameters, not considered in the model, which may warp the minimization procedure.

A problem of a different nature is faced when minimizing Eq. (2.3) and there exists high variability in the underlying parameters between samples. This is very common in biological problems, as the one presented next, where, even for very accurate models, it is difficult to define universal values of the parameters for a large enough set of samples.

As a consequence of these two observations, it is, therefore, more appropriate to state:

$$\mathbf{u} = \mathbf{F}(\boldsymbol{\lambda}, \boldsymbol{\theta}) + \boldsymbol{\epsilon}_{u|F} + \boldsymbol{\epsilon}_e, \quad (2.24)$$

where  $\boldsymbol{\epsilon}_{u|F}$  is the error associated with the model and  $\boldsymbol{\epsilon}_e$  is the measurement or experimental error. Using this notation,  $R$  may be rewritten as

$$R(\boldsymbol{\theta}) = \sum_{i=1}^N \left( \boldsymbol{\epsilon}_{u|F}^i + \boldsymbol{\epsilon}_e^i \right)^2 = \sum_{i=1}^N \left\| \mathbf{u}^i - \mathbf{F}(\boldsymbol{\lambda}^i, \boldsymbol{\theta}) \right\|^2. \quad (2.25)$$

As the error  $\boldsymbol{\epsilon} = \boldsymbol{\epsilon}_{u|F} + \boldsymbol{\epsilon}_e$  is unknown, it is then more appropriate to take a stochastic approach and reformulate Eq. (2.24) as

$$\mathbf{U} = \mathbf{F}(\boldsymbol{\lambda}, \boldsymbol{\Theta}), \quad (2.26)$$

where, now,  $\mathbf{U}$  and  $\boldsymbol{\Theta}$  are random variables.

Under this framework, the different measurements  $\mathbf{u}^i$  are in fact realizations of the random variable  $\mathbf{U}$ , that is,  $\mathbf{u}^i = \mathbf{F}(\boldsymbol{\mu}^i, \boldsymbol{\theta}^i)$ , where  $\boldsymbol{\theta}^i$  are realizations of the random variable  $\boldsymbol{\Theta}$ . Instead of minimizing the whole residual function  $R$  in Eq. (2.3), it is now more convenient to minimize the error for each experiment and to analyze the statistical distribution of  $\boldsymbol{\theta}^i$ . Of course, this approach may be followed if the output measurement space,  $\mathcal{U}$ , is large enough, so that each of the  $N$  minimization problems, for the  $N$  experiments chosen, is well-posed or overdetermined, and if the experiments are sufficient in number and varied enough in order to adequately characterize the model parameters from a statistical point of view.

In the end, the approach that is presented next is suitable for parametric models when the following conditions are satisfied:

- Many coupled phenomena are present, and it is difficult to design experiments to isolate each of them (complexity).
- The measurement space is large, and it is possible to obtain a high number of experiments in a simple way (data availability).

From a mathematical point of view, these two statements may be reformulated as

- The model  $F$  presents many parameters ( $n \gg 1$ ) and/or is nonseparable ( $M \gg 1$ ).
- The dimension of the measurement space is high ( $m \gg 1$ ) and/or the sample size is large enough ( $N \gg 1$ ). Without loss of generality, we consider that  $m$  is, actually, the reduced dimensionality of the space or, in other words, that all variables of the ambient space are independent.

## Mathematical tools and concepts

### Managing data uncertainty

A random phenomenon is described as a situation in which we know what outcomes can occur, but whose precise outcome is not certainly known. Classical examples are the throwing of dice or coin-flipping. The outcomes of such phenomena are treated as random variables. A random variable may be seen as a variable whose value is uncertain or unpredictable, but whose distribution is known. Formally, a random variable is a measurable function defined on a probability space, which gives a probability value to each possible outcome of the considered phenomenon (Kottegoda & Rosso, 2008). Random variables are statistically specified by their probability distribution, called mass function (pmf) when referred to discrete random variables and density function (pdf) when referred to continuous ones; or by their cumulative distribution function (CDF).

Random variables can be characterized in terms of descriptors, which summarize important distribution features. For instance, a location descriptor of the random variable  $X$  is given by

$$\hat{x} = \mathbb{P}(X), \quad (2.27)$$

where  $\mathbb{P}$  is a central tendency operator (that is, a functional acting on the pmf or pdf), aiming to locate a representative value of the random variable. On the other hand, a spread descriptor is

$$\Delta\hat{x} = \mathbb{S}(X) \quad (2.28)$$

where  $\mathbb{S}$  is a spread operator (a functional acting again on the pmf or pdf) which gives information about the dispersion of the random variable, that is, the inability to locate it. In particular,  $\mathbb{P}$  may be the expectation operator  $\mathbb{E}$ , minimizing the  $L^2$  squared norm dispersion, being its minimum the variance; or the geometric median

operator  $\mathbb{M}$ , minimizing the  $L^2$  norm dispersion, and being its minimum the mean absolute deviation. That is:

$$\begin{aligned}\sigma^2 &= \text{Var}(X) = \mathbb{E}[(X - \mathbb{E}[X])^2], \\ D_m &= \text{MAD}(X) = \mathbb{E}[|X - \mathbb{M}[X]|].\end{aligned}\quad (2.29)$$

The square root of the variance  $\sigma$  is called the standard deviation. It is common to characterize a random variable  $X$  using both its expected value  $\mu_X = \mathbb{E}[X]$  and its standard deviation  $\sigma_X = \sqrt{\text{Var}(X)}$ .

These concepts can be generalized to include more than one random variable, as it is the aim of this work, in which we consider models with many parameters, each treated as a different random variable. In this case, we talk about random vectors  $X = (X_1, \dots, X_n)$  and probability laws are described as joint probability functions defined in  $\mathbb{R}^n$ . The expectation operator  $\mathbb{E}$  can be extended to the multivariable case. As it is a linear operator, we can write, for two random variables  $X_1, X_2$ , and two arbitrary constants  $a, b$ :

$$\mathbb{E}[aX_1 + bX_2] = a\mathbb{E}[X_1] + b\mathbb{E}[X_2]. \quad (2.30)$$

However, the variance of the sum of variables yields

$$\text{Var}(aX_1 + bX_2) = a^2\text{Var}(X_1) + b^2\text{Var}(X_2) + 2ab\text{Cov}(X_1, X_2), \quad (2.31)$$

where a third term appears, representing the covariance between  $X_1, X_2$ . The covariance is a measure of the linear correlation between two variables defined as

$$\text{Cov}(X_1, X_2) = \mathbb{E}[(X_1 - \mathbb{E}[X_1])(X_2 - \mathbb{E}[X_2])]. \quad (2.32)$$

Normalizing the covariance, we obtain the Pearson's linear correlation coefficient  $\rho_p$ , the most extended parameter to characterize the correlation between variables:

$$\rho_p = \frac{\text{Cov}(X_1, X_2)}{\sigma_{X_1}\sigma_{X_2}}. \quad (2.33)$$

Let us now try to generalize the definition of the correlation coefficient. Suppose we have a sample of  $N$  pairs  $(x_i, y_i)$ ,  $i = 1, \dots, N$ . To any pair, we assign an  $x$ -score  $a_{ij}$  and a  $y$ -score  $b_{ij}$ , so that  $a_{ij} = -a_{ji}$  and  $b_{ij} = -b_{ji}$ . Thus, a general correlation coefficient may be defined as

$$\Gamma = \frac{\sum_{i,j=1}^N a_{ij}b_{ij}}{\sqrt{\sum_{i,j=1}^N a_{ij}^2 \sum_{i,j=1}^N b_{ij}^2}}. \quad (2.34)$$

Note that, if  $\bar{x}$  and  $\bar{y}$  are the mean values of  $x_i$  and  $y_i$ , respectively, taking  $a_{ij} = (x_i - \bar{x})$  and  $b_{ij} = (y_i - \bar{y})$ , we obtain  $\Gamma = \rho_p$ , the Pearson's correlation coefficient. Although the bilinear nature of this coefficient is very useful in many contexts (linear models, quadratic optimization, linear regression ...), the use of this

coefficient has an inconvenient. Denoting by  $f$  a monotonic and measurable function, in general it is not true that  $\rho_p(X_i, X_j) = \rho_p(f(X_i), f(X_j))$ , so the Pearson's correlation coefficient is not conserved under measurable bijections. Because of this, it is common to use correlation coefficients that are maintained when applying this type of functions. As the functions  $f$  are monotonic, one way is using the so-called rank correlation coefficients, which are used to characterize an ordinal association between variables. The most common rank correlation coefficients are the so-called Kendall's  $\tau$  and Spearman's  $\rho_s$ . The first one is defined by taking in Eq. (2.34):

$$a_{ij} = \text{sgn}(r_j - r_i), b_{ij} = \text{sgn}(s_j - s_i), \quad (2.35)$$

with  $r_i$  and  $s_i$  the ranks of the  $i$ th-member  $(x_i, y_i)$  regarding  $x$  or  $y$ , respectively. On the other hand, Spearman's  $\rho_s$  is defined by taking:

$$a_{ij} = r_j - r_i, b_{ij} = s_j - s_i. \quad (2.36)$$

## Estimation of probabilistic models

In this section, we deal with parameter estimation. The aim is, given a sample of data that follows a known distribution, to obtain the distribution parameters. Some of the most common methods used for this purpose are presented next. Finally, a method is presented to characterize distributions from a nonparametric point of view.

### Parametric methods

#### Method of moments

The moments of a distribution (or, in general, of a mathematical function) are measures related to the shape of the function's graph. The moment of order  $n$  of a real-valued continuous function about a value  $k$  can be expressed as

$$\mu_n = \mathbb{E}[(X - k)^n]. \quad (2.37)$$

The basic idea underlying the method is to extend the known facts about the population to the sample. The population moments are expressed as a function of the parameters that are going to be estimated and equated to the sample moments (Bowman & Shenton, 1998). This is a widely used method as it is simple and provides consistent estimations. However, the estimates may be biased (Kottekoda & Rosso, 2008).

#### Maximum likelihood method

This method is an alternative to the method of moments. The parameters  $\theta$  are estimated by maximizing a likelihood function  $L(\theta)$ . The intuitive idea is that this method gives the parameter values which make the sample data the most probable (Rossi, 2018). Given a random variable  $X$ , with a known pdf  $f(x)$  and a sample  $x_i$ ,  $i = 1, \dots, N$ , the likelihood function is

$$L(\theta) = \prod_{i=1}^N f(x_i|\theta). \quad (2.38)$$

The maximum likelihood method is preferred by statisticians, although large samples are required to obtain unbiased estimates.

### Nonparametric methods

Kernel estimation is a nonparametric statistical technique that allows transforming discrete data into probabilistic distributions (Bowman & Azzalini, 1997; Silverman, 1986). This kind of estimation is commonly used when a parametric distribution does not describe the data properly, or to avoid any assumption about the distribution of the data. A kernel distribution is a representation of the probability density function (pdf) or cumulative distribution function (CDF) of a random variable derived from a kernel estimation. A kernel distribution is defined by a smoothing function and a bandwidth value,  $h$ , which controls the smoothness of the resulting density or distribution function. Despite being a general and nonparametric approach to any data distribution, kernel estimation only works properly when enough data are available. Thus, it is ideal for problems where no suitable parametric distributional family can be clearly postulated, there are enough data to infer the marginal distributions and the sampling space is large enough to capture the multidimensional structural dependence.

Given a set of random samples  $x_i$ ,  $i = 1, \dots, N$ , the kernel density estimator with bandwidth  $h$  is defined by the expression:

$$\hat{f}_h(x) = \frac{1}{Nh} \sum_{i=1}^N K\left(\frac{x - x_i}{h}\right), \quad (2.39)$$

where  $K : \mathbb{R} \rightarrow \mathbb{R}^+$  is the kernel function satisfying  $\int_{-\infty}^{+\infty} K(u)du = 1$  (usually symmetric about  $u = 0$ ,  $K(u) = K(-u)$ ). Common kernel functions are the triangular kernel,  $K(u) = (1 - |u|)1_{|u| \leq 1}(u)$ , the Epanechnikov kernel,  $K(u) = \frac{3}{4}(1 - u^2)1_{|u| \leq 1}(u)$ , the cosine kernel,  $K(u) = \frac{\pi}{4}\cos\left(\frac{\pi}{2}u\right)1_{|u| \leq 1}(u)$ , and the Gaussian kernel,  $K(u) = \phi(u) = \frac{1}{\sqrt{2\pi}}e^{-\frac{1}{2}u^2}$  (Silverman, 1986).

### Design of experiments

In the case of complex phenomena, the number of experiments required to accurately characterize the multivariate distribution of the results may be extremely large. In these situations, statistical tools can help to maximize the information obtained from each experiment. These techniques are often referred to as design of experiments (DOE) (Ronald & Fisher, 1937). One of the most powerful techniques within DOE is based on the Bayesian interpretation of probability.

Probability can be defined either as the relative frequency of an event as the number of trials approaches infinity (*frequentist or classical approach*) or as the degree

of confidence in an event, that is, a measure of the likelihood of an event given incomplete knowledge (*Bayesian approach*) (Gelman et al., 2013). According to the Bayesian interpretation, probabilities can change as additional knowledge is obtained. Bayes' theorem links the degree of confidence in a proposition before and after accounting for evidence. Bayesian design of experiments aims to maximize the expected utility of the experiment outcome. The utility function expresses how accurate is the information provided by an experiment. The optimal experiment design depends on the particular utility criterion chosen (Kathryn & Isabella, 1995). In this work, the definition of the utility function is based on the Shannon entropy or Information entropy, which is one of the main concepts of the Theory of Information, introduced by Shannon (1948). Entropy quantifies the amount of uncertainty involved in the value of a random variable. The more unlikely a value is, the more information it provides and, therefore, the more entropy it has (Fazlollah & Reza, 1994).

Given a discrete random variable  $X$ , its entropy is defined as

$$H(X) = \mathbb{E}[I(x_i)] = \sum_{i=1}^N p(x_i)I(x_i) = -\sum_{i=1}^N p(x_i)\log(p(x_i)), \quad (2.40)$$

where  $I(x_i) = -\log p(x_i)$  is the amount of information generated by the occurrence of  $x_i$ . The utility function is then defined as the prior-posterior gain in Shannon Entropy or Information. That is, the difference between the Entropy of the posterior and prior distributions, respectively. Given the discrete random variable  $X$ , its prior distribution  $p$ , and the posterior distribution provided that the experiment  $\beta \in B$  is selected  $p(x|\beta)$ , the utility function of  $\beta$  is expressed as

$$U(\beta) = \sum_{i=1}^N p(x_i|\beta)\log p(x_i|\beta) - \sum_{i=1}^N p(x_i)\log p(x_i). \quad (2.41)$$

In order to determine the best experimental configuration, we should search for the experiment  $\beta$  that maximizes the utility:

$$\beta^* = \arg \max_{\beta \in B} U(\beta). \quad (2.42)$$

It is also possible to proceed recursively to design an experimental campaign. Given a sample of size  $N$ , different experiments already performed  $\beta_1, \dots, \beta_N$ , and a fitted model with utility  $U_N$ , we search for the value of the following experimental configuration  $\beta_{N+1}$  as

$$\beta_{N+1} = \arg \max_{\beta \in B} U_N(\beta). \quad (2.43)$$

Subsequently, new data can be obtained, and the process is repeated.

## Copulas

In Probability and Statistics, a copula is an  $n$ -multivariate probability distribution function  $\mathbf{U}$  whose marginals,  $U_i$ , are uniform distributions (Jaworski et al., 2010). They were introduced by Sklar (1959). As the distribution of marginals is known, a copula describes the structure of the dependence between random variables, so

it is defined on the unit hypercube  $[0; 1]^n$  linking multivariate with one-dimensional distributions.

Copulas have been applied in different fields. The most relevant and extended application field is Quantitative Finance and Risk Theory (McNeil et al., 2015), where copulas have been used in Risk Management (Kole et al., 2007), Portfolio Management and optimisation (Boubaker & Sghaier, 2013), and derivatives pricing (Cherubini et al., 2004). Copulas allow to separately model marginal distributions and dependence between variables, in such a way that we can model assets with general models. The dependence model may be different in downside/crisis/panic regimes, where it presents higher correlations than in expansion periods (Ang & Chen, 2002; Longin & Solnik, 2001). Despite the fact that the first copula models remained symmetric and predictions were inaccurate (MacKenzie & Spears, 2014), certain families of copulas have been defined in order to model this asymmetry from an integral point of view (Aas et al., 2009; Joe & Kurowicka, 2011). Most recent models have been successfully applied in portfolio optimization and risk management applications, improving statistical and economic performance. Other approaches include the use of different copulas for different scenarios (Meucci, 2011). For derivatives pricing, dependence modeling with copulas is widely used in applications of financial risk assessment and actuarial analysis. In fact, it is believed that the methodology of applying the Gaussian copula to credit derivatives was one of the reasons behind the global financial crisis of 2008–09 (Jones, 2009). Copulas are also used in Risk Theory for warranty analysis (Shaomin, 2014).

Recently, copula functions have been successfully applied to the database formulation for the reliability analysis of highway bridges, and to various multivariate simulation studies in civil (Kilgore & Thompson, 2011), mechanical and structural (Bartoli et al., 2011), and offshore engineering (Zhang et al., 2015). A particularly hot topic in these disciplines is the study of climate-agent time series (Joakim & Joakim, 2017; Solari & Losada, 2011), hydrology (Arya & Zhang, 2017; Laux et al., 2009), and weather and climate research (Laux et al., 2011; Schölzel & Friederichs, 2008). Some efforts have been made in the field of transportation research to understand the interaction of individual drivers behavior of an entire traffic flow (Wan & Kornhauser, 2010). Another field of application is reliability engineering (Pham, 2003). For example, in complex systems of machine components with competing failure modes (Wang & Pham, 2012), in Reliability-Based Design Optimization (RBDO) (Noh et al., 2009) and in coherent reliability systems (Eryilmaz, 2011). Besides, copulas are used for complexity reduction in some simulation problems such as turbulent combustion (Darbyshire & Swaminathan, 2012; Ruan et al., 2014). In the field of biology, copulas have been applied to model gene dependencies (Kim et al., 2008).

### **Mathematical definition**

Mathematically, a copula is a function  $C : I^d \rightarrow I$ , where  $I = [0; 1]$ , such that

- For  $u_1, \dots, u_d \in I$ ,  $C(u_1, \dots, u_d) = 0$ , if  $u_i = 0$  for some  $1 \leq i \leq d$ .

- For  $u_1, \dots, u_d \in I$ ,  $C(u_1, \dots, u_d) = u$ , if  $u_i = u$  for some  $1 \leq i \leq d$  and  $u_j = 1$  for  $j \neq i$ .
- $C$  is  $d$ -non decreasing, i.e., for each  $B = \prod_{i=1}^d [x_i; y_i] \subset I^d$ , the  $C$ -volume of  $B$  is non-negative:

$$\int_B dC(u) = \sum_{z \in \times_{i=1}^d \{x_i; y_i\}} (-1)^{\#\{k z_k = x_k\}} \geq 0. \quad (2.44)$$

From the point of view of probability theory,  $C$  may be seen as the  $d$ -dimensional multivariate distribution function of the random vector  $(U_1, \dots, U_d)$ , whose marginals are distributed uniformly in  $[0; 1]$ , that is,

$$C(u_1, \dots, u_d) = \Pr[U_1 \leq u_1, \dots, U_d \leq u_d]. \quad (2.45)$$

Consider now a random vector  $X = (X_1, \dots, X_d)$ . Supposing that its marginals  $F_i(x) = \Pr[X_i \leq x]$  are continuous, we can define the random vector  $(U_1, \dots, U_d) = (F_1(X_1), \dots, F_d(X_d))$ . By applying the probability integral transform theorem, each variable  $U_i$  is now uniform in  $[0; 1]$ . Hence, it is possible to assign a copula to the random vector  $X$  by Eq. (2.45). Thanks to this definition, for a given copula  $C$ , we can recall the random vector as the one defined in terms of  $d$  uniform distributions:

$$(X_1, \dots, X_d) = (F_1^{-1}(U_1), \dots, F_d^{-1}(U_d)). \quad (2.46)$$

As the CDFs  $F_i$  are continuous and monotonous, their inversion is possible, so Eq. (2.45) may be rewritten as

$$C(u_1, \dots, u_d) = \Pr[X_1 \leq F_1^{-1}(u_1), \dots, X_d \leq F_d^{-1}(u_d)]. \quad (2.47)$$

It is therefore clear that, with this formulation, marginal distributions are totally characterized by the functions  $F_i$ , whereas all the dependence structure is encapsulated in the selection of an appropriate functional for  $C$ . This formulation is, actually, universal, as was proven by Sklar in his foundational paper (Sklar, 1959):

### **Theorem 1: Sklar's theorem**

Every multivariate cumulative distribution function,

$$H(x_1, \dots, x_d) = \Pr[X_1 \leq x_1, \dots, X_d \leq x_d], \quad (2.48)$$

of a random vector  $(X_1, \dots, X_d)$  can be expressed in terms of its marginals  $F_i(x_i) = \Pr[X_i \leq x_i]$  and a copula  $C$ , such that

$$H(x_1, \dots, x_d) = C(F_1(x_1), \dots, F_d(x_d)). \quad (2.49)$$

Moreover, if the marginals  $F_i$  are continuous, the copula is unique.

Copulas can be classified into parametric and nonparametric copulas.

### **Parametric copulas**

Most copula applications are based on parametric models for copulas (Nadarajah et al., 2017). It is common to assume the copula  $C$  as belonging to a parametric

family  $C = C_{\alpha_0}$  and to adjust the parameters  $\alpha_0$  so that the copula fits some known data. Besides, the marginals are also usually considered to belong to parametric families  $F_i = F_{\alpha_i}$ . Thereby, our model parameters are  $\alpha = (\alpha_0, \alpha_1, \dots, \alpha_d)$  and the multivariate cumulative distribution function is

$$H(x_1, \dots, x_d; \alpha) = C(F_1(x_1; \alpha_1), \dots, F_d(x_d; \alpha_d); \alpha_0). \quad (2.50)$$

If the parameters are not known but estimated from data using any of the methods explained before, Eq. (2.50) is replaced by

$$H(x_1, \dots, x_d; \hat{\alpha}) = C(F_1(x_1; \hat{\alpha}_1), \dots, F_d(x_d; \hat{\alpha}_d); \hat{\alpha}_0), \quad (2.51)$$

where  $\hat{\alpha}_i$  are estimates for  $\alpha_i, i = 0, \dots, d$ .

Among the parametric families of copulas, one of the most used due to its simplicity is the Gaussian family (Cherubini et al., 2004), where the copula is modeled using a parametric matrix representing the correlations. This model has proven to be useful in financial assets analysis (Malevergne & Sornette, 2003), credit analysis (Frey et al., 2001), and extreme value analysis (Renard & Lang, 2007), among other applications. Also, the *t*-Student family (Demarta & McNeil, 2005) is very frequent, including one more parameter  $\nu$  (when  $\nu \rightarrow \infty$ , we recover the Gaussian copula) that allows further tail dependencies (Daul et al., 2003; Schloegl & O’Kane, 2005). Another important parametric family is the Archimedean family of copulas, able to capture asymmetric tail dependencies, unlike *t*-Student copulas (Naifar, 2011). Archimedean copulas are an associative class of copulas that admit an explicit formula. They are popular because they allow modeling the multivariate dependence in arbitrarily high dimensions with only one parameter  $\alpha$ , governing the level of dependence in an *isotropic* way. There exist several Archimedean copulas, being those described in Ali et al. (1978); Clayton (1978); Nelsen (2007) the most popular. Each of them is more appropriate for a given framework, although there are some general guidelines for their selection (Durrelman et al., 2000; Kole et al., 2007).

### Nonparametric copulas

Another possibility is to establish nonparametric models. In this case, empirical marginal distributions and empirical copulas are used, so that

$$C^N(u_1, \dots, u_d) = \frac{1}{N} \sum_{j=1}^N 1(\bar{U}_1^j \leq u_1, \dots, \bar{U}_d^j \leq u_d), \quad (2.52)$$

where 1 is the multidimensional step function and  $\bar{U}_i^j = (F_i^N)^{-1}(X_i^j), j = 1, \dots, N, i = 1, \dots, d$ . Besides, the empirical marginal distribution is defined by

$$F_i^N(x) = \frac{1}{N} \sum_{j=1}^N 1(X_i^j \leq x). \quad (2.53)$$

Empirical copulas are used when the dataset size is large enough to get accurate statistical inferences. This is not usually the case when working in highly multidimensional spaces ( $d \gg 1$ ), because the dataset size grows as  $\mathcal{O}(2^d)$ .

In general, parametric copulas are a trade-off between statistical power and efficiency. An intermediate approach is using smoothing techniques for the copula estimation, such as kernel estimation (Charpentier et al., 2007). We can also use hybrid solutions. For example, in portfolio analysis, it is common to fit the marginal distributions by means of kernel estimators of the cumulative distribution functions (Bouyé et al., 2000) and use a parametric copula. With this approach, the required dataset size grows as  $\mathcal{O}(d)$ . This latter approach will be the one followed in this work.

To finish this introduction to copulas, it is worth mentioning back correlation coefficients. As explained in the [Managing data uncertainty](#) section, Kendall's  $\tau$  and Spearman's  $\rho_s$  are not affected by increasing transformations, and therefore they are not altered under CDF transformations. An obvious consequence is that if we have a multidimensional random vector  $X$ , the value of  $\Gamma_{ij} = \Gamma(X_i, X_j) = \Gamma(U_i, U_j)$  is valid to explore the copula dependence, provided one of those rank correlation coefficients is used. Actually, for a parametric copula, it is possible to find a relationship between all correlation coefficients  $\Gamma_{ij}$  and the copula parameters, and to estimate them by the method of moments (MME) (Kottogoda & Rosso, 2008). In this work, however, the rank correlation coefficients will be used as an intuitive parameter characterizing the strength of the dependence between variables while the copula parameters will be estimated by Maximum Likelihood Estimation (MLE).

## Methodology

### Model adjustment

In this section, we will present the development of the proposed methodology for this work. The aim is to obtain, from a dataset, a probabilistic model which is able to describe both the marginals and the structural dependence between variables in terms of copulas.

Let us suppose we have a dataset of  $N$  values for different experiments,  $\lambda^i$ ,  $i = 1, \dots, N$ , characterized in terms of a resultant mean value  $\mu^i$  and a covariance matrix  $\Sigma^i$ , obtained from different experimental realizations of configuration  $i$ . As the assumed model  $\mathbf{F}$  is known, it is possible, for each data  $i$ , to minimize the (weighted) residual function:

$$R^i(\boldsymbol{\theta}) = (\mathbf{F}(\lambda^i, \boldsymbol{\theta}) - \mu^i)^T (\Sigma^i)^{-1} (\mathbf{F}(\lambda^i, \boldsymbol{\theta}) - \mu^i), \quad (2.54)$$

where we have used the Mahalanobis distance to consider samples variability. If we assume uncorrelation between sensor measurements, that is,  $\Sigma^i = (\sigma^i)^2 \mathbf{I}$ , the previous equation becomes

$$R^i(\boldsymbol{\theta}) = \frac{1}{(\sigma^i)^2} \left\| \mathbf{F}(\lambda^i, \boldsymbol{\theta}) - \boldsymbol{\mu}^i \right\|^2. \quad (2.55)$$

As a result of the minimization process, the set of parameters  $\boldsymbol{\theta}^i$  which best fits each result for the experimental configuration  $i$  is obtained:

Once  $\boldsymbol{\theta}^i, i = 1, \dots, N$  are obtained, the next step is the adjustment of the marginal distributions. A nonparametric approach is followed in this step, estimating the marginal distributions via kernel estimation. The values  $\theta_j^i, j = 1, \dots, n$ , where  $n$  has been previously defined as the number of parameters, are used for fitting the marginal random variable  $\Theta_j$  whose cumulative distribution is assumed to be  $G_j$  (estimated by means of kernel density estimation). The values  $\theta_j^i$  are therefore transformed into uniform distributed data via the transformation  $y_j^i = G_j(\theta_j^i)$ . As  $\mathbf{y}^i$  are considered uniformly distributed with a joint dependence, it is possible to fit this structural dependence using parametric copulas. To summarize, the steps of the training process are

1. Minimization problem to obtain  $\boldsymbol{\theta}^i$ .
2. Fitting of the marginal distributions from data  $(\theta_j^i)$  by means of kernel density estimation.
3. Transformation to uniform data  $y_j^i$ .
4. Copula fitting of  $\mathbf{y}$  data in order to capture the joint dependence.

With the purpose of avoiding overfitting, we follow a typical train-test approach. That is, we divide the dataset  $\lambda^i, \mathbf{u}^i$  in two separate subsets, one used for training and the other used for testing. For the testing procedure, we only perform the minimization step and then we test the probabilistic model. Thus, the procedure is

1. Minimization problem to obtain  $\boldsymbol{\theta}^i$ .
2. Statistical tests to evaluate the model adjustment. Marginal distributions fitting are tested, thanks to Q-Q plots, histograms, boxplots, and empirical cumulative distribution functions (ecdf) among other tests ([Kotegoda & Rosso, 2008](#)). Moreover, the joint 2 versus 2 correlations and the whole structural dependence can be tested ([Fan, 1997](#)).

## Model analysis and applications

In this section, we deal with some applications of the proposed methodology, once the model is already characterized from a probabilistic point of view. That is, we know the distribution of the random variable  $\Theta$ , including both marginal distributions (kernel pdf estimation) and dependence between variables (copula model).

### Parameter estimation

The first straightforward application is parameter estimation. It is important to emphasize that with “parameter estimation” we refer to the parameters of the mathematical model, not to the parameters of the distributions used in the statistical characterization, that may be estimated via common statistical inference techniques, like the ones presented in the [Managing data uncertainty](#) section. As was proposed in that Section, [Eq. \(2.27\)](#), we can use point estimates  $\hat{\theta}$  to estimate parameters. However, it is more interesting to estimate the model parameters using confidence regions, as they are associated with a probability. Confidence regions are the multidimensional generalization of confidence intervals. Nonetheless, in the multidimensional case, when estimating a confidence region for a given parameter, it is not always clear which region should be used, even if the confidence level of the region is fixed. There are many solutions reported in the bibliography, such as selecting a symmetric hypercube or ellipsoid about the mean or about the median. An alternative is the Highest Density Regions (HDR) method in which regions fulfill the following conditions ([Hyndman, 1996](#)):

- For a given probability, the region covering the sample space should have the smallest volume possible.
- For every point in the region, its probability density should be as large as the probability density of every point outside the region.

The use of such Highest Density Regions is recommended because of their easy interpretation, straightforward generalization to multidimensional spaces, and direct computation. Recall that, under some distributional assumptions (e.g., normality assumption), HDR computation is reduced to other standard confidence region computation techniques (e.g.,  $\chi^2$  quantile tolerance ellipsoids). HDR computation enables reliable parameter estimation since given a significant level threshold  $\alpha$ , it is possible to define an HDR region in which the parameters are located with a probability  $p = 1 - \alpha$ . This may be performed for single parameters, or, in general, for  $k$ -tuples of parameters.

Given an observation  $\mathbf{u}$ , a vector of parameters to be determined  $\boldsymbol{\theta}$ , a prior probability distribution function over those parameters  $f(\boldsymbol{\theta})$  (determined by means of copula analysis) and the probability distribution function of  $\mathbf{u}$  given parameter values  $\boldsymbol{\theta}$  and an experimental design  $\boldsymbol{\mu}$ ,  $f(\mathbf{u}|\boldsymbol{\mu}, \boldsymbol{\theta})$  (obtained from the experimental configuration), the marginal probability in the observation space is

$$f(\mathbf{u}|\lambda) = \int f(\boldsymbol{\theta})f(\mathbf{u}|\lambda, \boldsymbol{\theta})d\boldsymbol{\theta}, \quad (2.56)$$

and the posterior probability distribution function is calculated as

$$f(\boldsymbol{\theta}|\lambda, \mathbf{u}) = \frac{f(\mathbf{u}|\lambda, \boldsymbol{\theta})f(\boldsymbol{\theta})}{f(\mathbf{u}|\lambda)}. \quad (2.57)$$

We can then define the expected utility of an experiment  $\lambda$  as

$$U(\lambda) = \int f(\mathbf{u}|\lambda) U(\mathbf{u}, \lambda) d\mathbf{u}, \quad (2.58)$$

where  $U(\mathbf{u}, \lambda)$  is some functional of the posterior probability distribution function  $f(\boldsymbol{\theta}|\lambda, \mathbf{u})$ . As previously detailed in the [Design of experiments](#) section, we chose  $U(\mathbf{u}, \lambda)$  to be the prior-posterior gain in the Shannon Information, so that

$$U(\lambda) = \iint f(\boldsymbol{\theta}, \mathbf{u}|\lambda) \log f(\mathbf{u}|\boldsymbol{\theta}, \lambda) d\boldsymbol{\theta} d\mathbf{u} - \int f(\mathbf{u}|\lambda) \log f(\mathbf{u}|\lambda) d\mathbf{u}, \quad (2.59)$$

and, consequently, the utility  $U(\lambda)$  can be expressed as

$$U(\lambda) = \int f(\boldsymbol{\theta}) \left( \iint f(\mathbf{u}|\boldsymbol{\theta}, \lambda) \log f(\mathbf{u}|\boldsymbol{\theta}, \lambda) d\mathbf{u} \right) d\boldsymbol{\theta} - \int f(\mathbf{u}|\lambda) \log f(\mathbf{u}|\lambda) d\mathbf{u}. \quad (2.60)$$

This information gain can also be expressed as the mutual information between the observation  $\mathbf{u}$  and the parameter vector ([Liepe et al., 2013](#)), which is a magnitude that describes the dependence between those two variables. It is defined as follows:

$$U(\lambda) = I(\mathbf{u}; \boldsymbol{\theta}) = \iint f(\boldsymbol{\theta}) f(\mathbf{u}|\boldsymbol{\theta}, \lambda) \log \left( \frac{f(\mathbf{u}|\boldsymbol{\theta}, \lambda)}{f(\mathbf{u}|\lambda)} \right) d\boldsymbol{\theta} d\mathbf{u}. \quad (2.61)$$

## A case study: GBM evolution

Modeling the Tumor MicroEnvironment (TME) is not only a challenging problem due to its complexity and heterogeneity but it is also greatly complements in vitro experiments, since computer simulation allows to separate effects and to test hypothesis in a quick and efficient way. Many new concepts in cancer have been proposed coming from mathematical approaches ranging from evolutionary dynamics to adaptative therapies, or quantifying the effect into tumor evolution of oxygen, biochemical molecules, ECM stiffness, cell proliferation rate, among many others ([Altrock et al., 2015](#); [Byrne et al., 2006](#); [Hatzikirou et al., 2005](#); [Mousavi & Doweidar, 2016](#); [Mousavi et al., 2013](#)). In particular, this work is focused on the in vitro evolution of glioblastoma (GBM), the most common and lethal among primary brain tumors. Its evolution is complex, and there have been many attempts to develop models able to describe it, both from the experimental (in vitro) and computational (in silico) points of view ([Alfonso et al., 2017](#); [Stanković et al., 2021](#)). Microfluidics has also arisen as a powerful tool to recreate the complex and three-dimensional environment in which the tumors are developed. In particular, the main histopathological features of GBM have been reproduced in microfluidic devices: the formation of a necrotic core ([Ayuso et al., 2016](#)) and of a pseudopalisade ([Ayuso et al., 2017](#)). Besides, a mathematical model has recently been proposed for GBM evolution in microfluidic devices under hypoxic conditions ([Ayensa-Jiménez et al., 2020](#)), together with an extensive parametric discussion, in which correlation between parameters was identified. Previous research in the field of computational biology has been focused on the value of the parameters and, in the same cases, on their

individual uncertainty, overlooking the correlations that might exist. In fact, in many cases, model parameters are highly correlated due to two main facts:

- **Samples variability:** Physical phenomena might have an inherent correlation originated by physical considerations. These correlations exist regardless of the experiments performed or the model used, being inherent to the problem in hands. Taking as an example cell culture, cells do not behave in a deterministic way, so two identical experimental configurations may lead to different outcomes. In GBM evolution, we distinguish between random cell movement (pedesis) and movement toward oxygen (chemotaxis). A cell that has faster motility will move faster in all the cases, so the parameters governing both phenomena are correlated. It is also possible to talk about *prior* correlation.
- **Model complexity:** In this case, it is the nonseparability of the model or the experiments what does not allow the separation between effects of different mechanisms. These correlations are inherent to the model or the experimental setup used, whereas they may have no physical meaning. Taking again the example of GBM evolution, without measurements of oxygen concentration or flux, it is not possible to determine if lack of oxygen in a region is due to high cell consumption or low oxygen diffusion. Therefore, the mathematical parameters related to these phenomena will also be correlated, but this correlation is the result of a lack of information. We refer to this correlation also as *posterior* correlation as it is experiment-dependent.

The problem of GBM evolution in microfluidic devices, from a mathematical approach, is defined in terms of a nonseparable model with many parameters and coupled phenomena. Also, thanks to the flexibility, portability, and automation of microfluidic devices, this type of experiments allow the generation of great amounts of data. Consequently, this problem lays within the domain of application of the framework here presented (the conditions were detailed in the [Including model uncertainty](#) section), and the methodology will be illustrated with the analysis of the mathematical model presented in [Ayensa-Jiménez et al., \(2020\)](#).

The example of application here presented was introduced in a recent work ([Ayensa-Jiménez et al., 2021](#)) to study the correlation between oxygen diffusion and consumption parameters. Here, we extend the work analyzing the pair of parameters related to cell motility: the diffusion and chemotaxis coefficients; and presenting a new application of experimental design: the design of experimental campaigns.

## Mathematical model

In this section, the main equations of the model are summarized, referring to [Ayensa-Jiménez et al. \(2020\)](#) for further details. The model is based on a system of three advection–reaction–diffusion equations describing alive cells ( $C_a$ ), dead cells ( $C_d$ ), and oxygen ( $O_2$ ) concentration evolution:

$$\frac{\partial C_a}{\partial t} = \frac{\partial}{\partial x} \left( D_a \frac{\partial C_a}{\partial x} - K_a \chi_a(O_2) F_a(C_a) C_a \frac{\partial O_2}{\partial x} \right) + \frac{1}{\tau_a} \beta_a(O_2) G_a(C_a, C_d) C_a - \frac{1}{\tau_{ad}} S_{ad}(O_2) C_a, \quad (2.62)$$

$$\frac{\partial C_d}{\partial t} = \frac{1}{\tau_{ad}} S_{ad}(O_2) C_a, \quad (2.63)$$

$$\frac{\partial O_2}{\partial t} = D_{O_2} \frac{\partial^2 O_2}{\partial x^2} - \alpha_a H_a(O_2) C_a. \quad (2.64)$$

The model includes several nonlinear correction and activation functions accounting for cell behavior. First,  $\chi_a$  and  $\beta_a$  are, respectively, migration and proliferation ReLU activation functions modeling the *go or grow* behavior of GBM cells (Hatzikirou et al., 2012), in terms of a certain hypoxia threshold  $O_2^H$ :

$$\chi_a(O_2) = \begin{cases} 1 - O_2/O_2^H & \text{if } 0 \leq O_2 \leq O_2^H \\ 0 & \text{if } O_2 > O_2^H \end{cases}, \quad (2.65)$$

$$\beta_a(O_2) = \begin{cases} O_2/O_2^H & \text{if } 0 \leq O_2 \leq O_2^H \\ 1 & \text{if } O_2 > O_2^H \end{cases}. \quad (2.66)$$

Besides, proliferation and migration are also limited by the availability of space and nutrients, which is limited by the saturation concentration  $C^M$ . In this line,  $F_a$  defines a ReLU correction for chemotaxis, while  $G_a$  is a logistic correction for proliferation.

$$F_a(C_a) = \begin{cases} 1 - C_a/C^M & \text{if } 0 \leq C_a \leq C^M \\ 0 & \text{if } C_a > C^M \end{cases}, \quad (2.67)$$

$$G_a(C_a, C_d) = \left( 1 - \frac{C_a + C_d}{C^M} \right). \quad (2.68)$$

Cells die both due to apoptosis and necrosis. A death activation function  $S_{ad}$  is selected to take into account both phenomena, in terms of an anoxia threshold  $O_2^A$  and a spread parameter  $\Delta O_2^A$ :

$$S_{ad}(O_2) = \frac{1}{2} \left( 1 - \tanh \left( \frac{O_2 - O_2^A}{\Delta O_2^A} \right) \right). \quad (2.69)$$

Finally, cells consume oxygen following a Michaelis–Menten model (Chance & Williams, 1956) with constant  $O_2^M$ :

$$H_a(O_2) = \frac{O_2}{O_2^M + O_2}. \quad (2.70)$$

The model equations are completed with suitable boundary and initial conditions. For cell populations, total impermeability is assumed (Neumann boundary conditions with no flux), and the oxygen level is fixed at both the right  $O_2^r$  and

left  $O_2^l$  lateral channels (Dirichlet boundary conditions). The initial concentration of alive cells  $C_0$  is assumed to be homogeneous throughout the chip, and there are no dead cells at the initial time. The oxygen initial concentration, also homogeneous, is selected as  $O_2(x, t = 0) = \max(O_2^l, O_2^r)$ .

Some model parameters have a clear meaning in cell metabolism and are assumed to be known and constant, at least for our illustrative purpose. These parameters are the ones regulating the activation functions:  $O_2^M, O_2^A, \Delta O_2^A, O_2^H$ . Besides,  $C^M$  is dependent on the particular experimental setup and therefore also assumed to be known and constant. Therefore, the analysis is going to be focused on the following parameters:

- The normoxic cell diffusion coefficient  $D_a$ .
- The normoxic cell chemotaxis coefficient  $K_a$ .
- The oxygen diffusion coefficient  $D_{O_2}$ .
- The oxygen consumption coefficient  $\alpha_a$ .
- The growth characteristic time  $\tau_a$ .
- The death characteristic time  $\tau_{ad}$ .

The reason for selecting these parameters is that they illustrate both types of correlations exposed before. For instance, it is not strange to think of the correlation of the parameters  $D_a$  and  $K_a$ , as they both refer to the ability of the cell to migrate, regardless of whether they migrate or not in response to different stimuli. On the other hand, parameters like  $\tau_a$ ,  $\tau_{ad}$ ,  $D_{O_2}$ , and  $\alpha_a$  have a direct impact on the oxygen level. Of course, we have here ventured some correlations, but there may exist many more.

## Data generation

The proposed methodology is based on the availability of sufficient data. However, the dataset used for this illustrative example was generated synthetically using the proposed mathematical model, which was validated with experimental results in [Ayensa-Jiménez et al. \(2020\)](#). Experimental measures, consisting of both alive and dead cells concentration profiles, were generated via simulation using randomly generated boundary and initial conditions, which are the control parameters  $\lambda$  described in the [About modeling](#) section. More precisely,  $\lambda = [O_2^l, O_2^r, C_0]$ , where the oxygen boundary conditions were randomly set using two uniform distributions varying from 0 to 7 mmHg; and the initial cell concentration was randomly sampled from a reciprocal distribution, between  $4 \times 10^6$  and  $5 \times 10^7$  cell/mL. The virtual experiment lasted 8 days, was performed in a chip of  $L = 0.1$  cm, and the numerical discretization parameters were selected as  $\Delta x = 0.0025$  cm and  $\Delta t = 1000$  s. The parameter values used for generating the data can be found in [Ayensa-Jiménez et al. \(2021\)](#). The numerical solutions  $\mathbf{u}^i$  were obtained for  $i = 1, \dots, 400$  and perturbed at each mesh point  $j$  with a uniform noise  $\varepsilon_j = 0.2 \times u_j \times V$ , with  $V$  representing a random uniform distribution  $V \sim \mathcal{U}[-1, 1]$ .

## Results

### Model adjustment

Following the methodology proposed in the [Methodology](#) section, the first step is to obtain the fitting of the univariate marginal distributions. They were obtained by means of kernel estimation, choosing a Gaussian kernel for all the estimations, with a variable bandwidth ( $w_1 = 7.46 \times 10^{-11} \text{ cm}^2/\text{s}$ ,  $w_2 = 9.52 \times 10^{-10} \text{ cm}^2/(\text{mmHg} \cdot \text{s})$ ,  $w_3 = 1.66 \times 10^{-6} \text{ cm}^2/\text{s}$ ,  $w_4 = 2.17 \times 10^{-10} \text{ mmHg} \cdot \text{cm}^3/(\text{cell} \cdot \text{s})$ ,  $w_5 = 9.57 \times 10^4 \text{ s}$ ,  $w_6 = 2.74 \times 10^4 \text{ s}$ ). In order to avoid pathological numerical convergence, we only took into account those sets of parameters that lie inside the bibliography ranges considered in [Ayensa-Jiménez et al. \(2020\)](#), amplified by 50% to avoid considering the parameter bounds as deterministic values ([Ayensa-Jiménez et al., 2021](#)). The bounds are detailed in [Table 2.1](#). As a result of this process, we have a dataset with  $n = 6$  parameters of size  $N = 111$ , and a measurement space dimension of  $m = 41$ , compliant with the framework:  $N \times m \gg n > 1$ .

Next, the uniform distributions were obtained using the CDF associated with the estimation kernel and a *t*-Student copula fitted by ML estimation. We chose this family of copulas because it allows establishing different degrees of correlation between each pair of variables ([Kole et al., 2007](#)), which is natural when working with parametric models, where the parameters have utterly different meanings while they are related to each other. Also, when compared with a Gaussian copula (which is also nonisotropic), the *t*-Student copula outperforms it when estimating the co-occurrence of extreme events ([Demarta & McNeil, 2005](#)).

The obtained copula has  $\nu = 1.8$  degrees of freedom, a value far enough from the Gaussian limit ( $\nu \rightarrow \infty$ ), which justifies the presence of this extra parameter. The matrix of Kendall's tau correlation coefficients for each pair of parameters is displayed in [Fig. 2.1](#).

To gain insight into the model, we represent in [Fig. 2.2](#) the bivariate joint distribution of the diffusion and chemotaxis coefficients ( $D_a, K_a$ ). Recall that these two parameters are responsible for the cell movement and are correlated, so this analysis

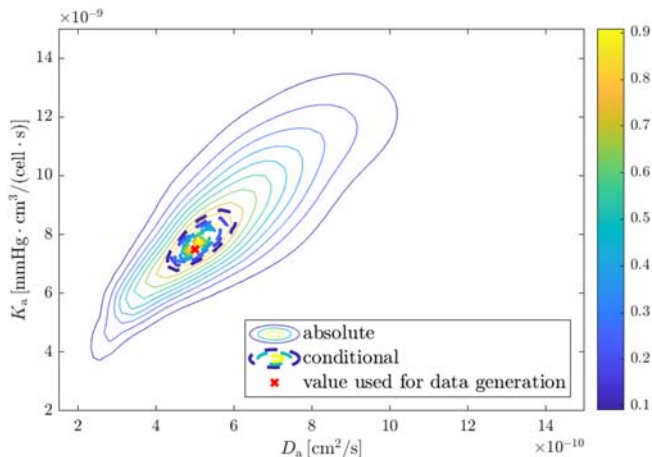
**Table 2.1 Parameter ranges considered.** Minimum and maximum value of each parameter used for the dataset generation.

Parameter	Lower bound	Upper bound	Units
$D_a$	$3.3 \cdot 10^{-12}$	$7.5 \cdot 10^{-5}$	$\text{cm}^2/\text{s}$
$K_a$	$1 \cdot 10^{-10}$	$1.1 \cdot 10^{-3}$	$\text{cm}^2/\text{mmHg} \cdot \text{s}$
$D_{O_2}$	$5 \cdot 10^{-6}$	$3 \cdot 10^{-5}$	$\text{cm}^2/\text{s}$
$\alpha_a$	$5 \cdot 10^{-10}$	$1.1 \cdot 10^{-6}$	$\text{mmHg} \cdot \text{cm}^3/\text{cell} \cdot \text{s}$
$\tau_a$	8	3000	h
$\tau_{ad}$	24	917	h

$D_a$	1.00	0.77	0.51	0.56	0.50	0.26
$K_a$	0.77	1.00	0.53	0.53	0.56	0.25
$D_{O_2}$	0.51	0.53	1.00	0.73	0.41	0.13
$\alpha_a$	0.53	0.53	0.73	1.00	0.36	0.17
$\tau_a$	0.50	0.56	0.41	0.36	1.00	0.16
$\tau_{ad}$	0.26	0.25	0.13	0.17	0.16	1.00
	$D_a$	$K_a$	$D_{O_2}$	$\alpha_a$	$\tau_a$	$\tau_{ad}$

**FIGURE 2.1 Correlation matrix**

Kendall's tau correlation matrix for each pair of parameters in the fitted model.

**FIGURE 2.2 Joint distributions of the diffusion and chemotaxis coefficients.**

Comparison between the absolute distribution of the diffusion and chemotaxis coefficients, and the conditional distribution of those parameters, when we assume that the value of the rest of the parameters is known.

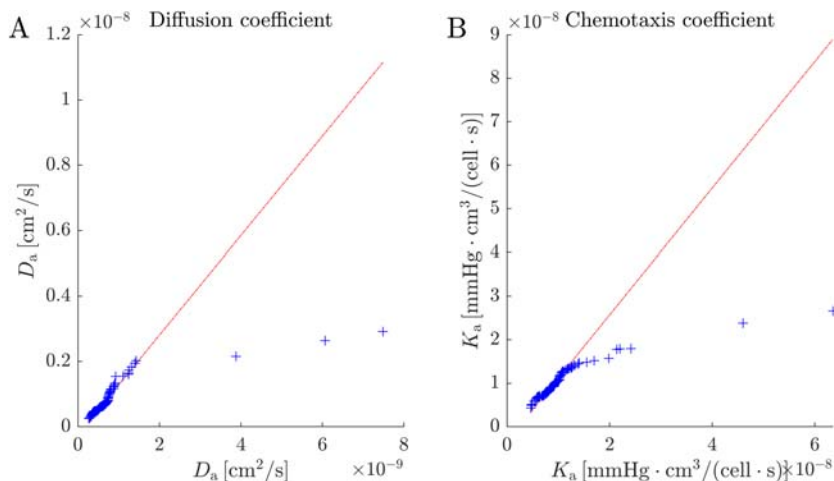
is focused on them. As the whole distribution function is known (although not represented because it has six dimensions), it is possible to calculate the conditional joint distribution of  $(D_a, K_a)$  assuming that the values of the rest of the parameters

are known. This a posteriori correction can be done using Bayesian theory and conditional probability, and the resulting conditional distribution is also shown in Fig. 2.2, together with the value of  $(D_a, K_a)$  used for synthetic data generation. Both contour plots are normalized between 0 and 1 to compare them more easily. It can be seen that conditioning significantly reduces the uncertainty in the parameter values.

### Model validation

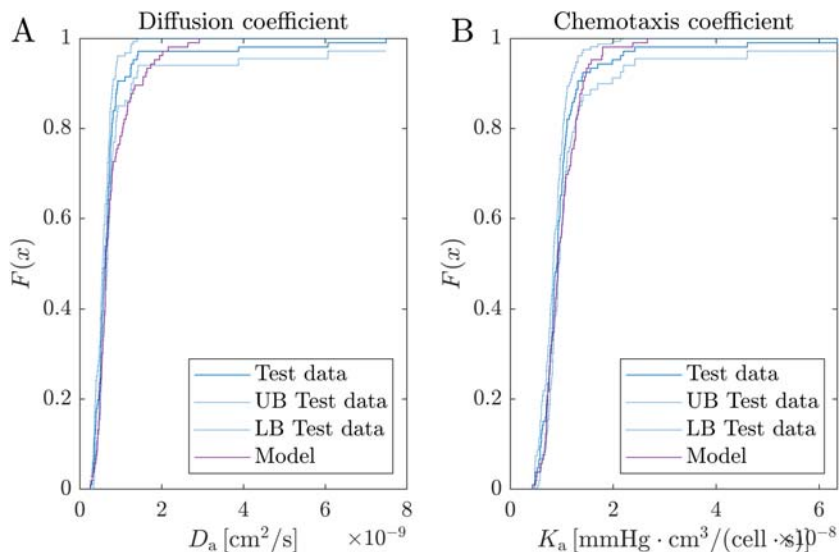
Overfitting is a common problem in any statistical or numerical parametric fitting. To avoid it, in the proposed methodology a train-test approach is followed, as detailed in [Model adjustment](#) section. A new test dataset is generated for validation, using the same procedure described in [Data generation](#) section, and a copula is fitted using these data. First, to test the marginals fitting, the Q-Q plot of the data, when compared to the model, is shown in Fig. 2.3 for  $D_a$  and  $K_a$ . Besides, the ecdf of the test data (with a confidence interval of 95%) compared to the model is shown in Fig. 2.4. The validation of the whole set of marginals has been performed. Good agreement has been found between the model and test data except for the extreme values (at the tail values of the distributions). Finally, violin plots for the two parameters considered are depicted in Fig. 2.5, showing again good agreement between test data and the fitted model.

It is more difficult to test the structural dependencies between the variables. As an exploratory approach, we illustrate in Fig. 2.6 both the scatterplots and the linear

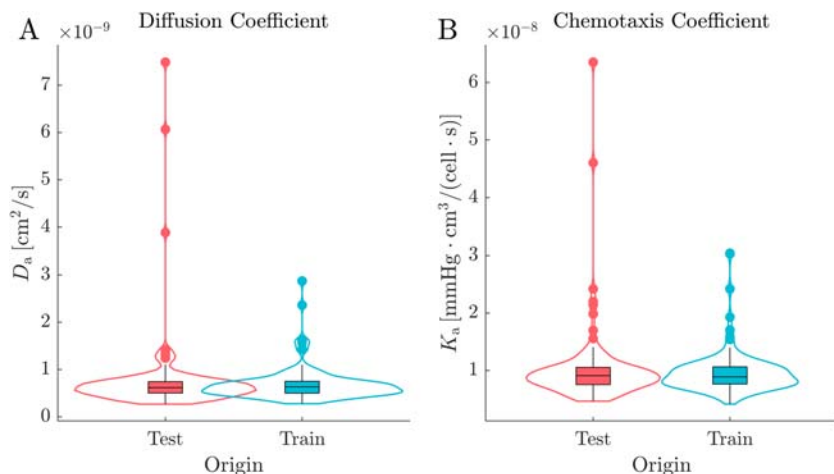


**FIGURE 2.3 Validation Q-Q plots.**

Q-Q plot comparing the marginal distributions of the fitted model to the ones obtained with the test data for both the diffusion (A) and the chemotaxis (B) coefficients.

**FIGURE 2.4 Validation of ecdf plots.**

Empirical cumulative distribution functions (ecdf) for the diffusion (A) and chemotaxis (B) coefficients, comparing the model marginal distribution to the test data.

**FIGURE 2.5 Validation of violin plots.**

Violin plots comparing model and test data for both the diffusion (A) and the chemotaxis (B) coefficients.

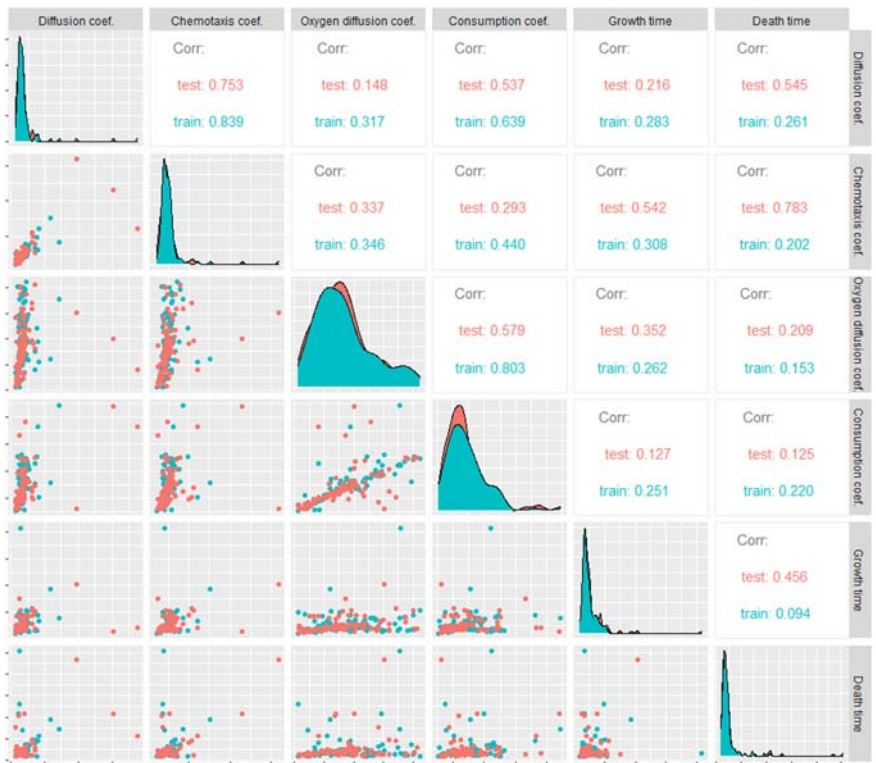


**FIGURE 2.6 Scatterplot and linear correlation coefficients.**

Scatterplot and linear correlation coefficients for model and test data.

correlation coefficients between variables. Good agreement is observed between the model values of the correlation coefficients and those obtained from the sample of the test data, even though the train and test sample are finite, which can cause differences between the model parametric descriptors and their statistical values.

If we are interested in the particular dependence between any two variables, a deeper analysis may be done by using multivariate goodness of fit tests. For instance, suppose we are interested in the (nonlinear) structural dependence  $(D_a, K_a)$ . We analyze the dependence between the variables  $U_1 = F_1(D_a)$  and  $U_2 = F_2(K_a)$ , where  $F_1$  and  $F_2$  are the marginal CDF associated to parameters  $D_a$  and  $K_a$ , using the  $\chi^2$  goodness of fit test. Given a partition of the unit square in  $k^2$  regions, we define:

$$D = \sum_{i,j=1}^k \frac{(O_{ij} - E_{ij} - 0.5)^2}{E_{ij}}, \quad (2.71)$$

where  $O_{ij}$  and  $E_{ij}$  are the observed and expected value at the region  $i - j$  and the term  $-0.5$  accounts for Yates correction (Adler, 1951). The null hypothesis in this test is that the test data follows our fitted statistical model. If we choose a significance level  $\alpha$ , we may reject the null hypothesis if  $D \geq \chi^2_{\nu,1-\alpha}$ , with  $\chi^2_{\nu,1-\alpha}$  the critical value of the chi-squared distribution of  $\nu$  degrees of freedom corresponding to the  $\alpha$  significance level. Fig. 2.7 and Table 2.2 show the intermediate computations for the goodness of fit evaluation for a 3 by 3 grid. Selecting  $\alpha = 0.05$ , the statistic yields a value  $\chi^2_{9,0.95} = 15.5$ , so we may not reject the null hypothesis. This allows us to conclude, therefore, that both model and test data follow the same distribution.

### Parameter estimation

The next figures show  $p$ -confident HDR regions for  $p = 0.9$  (Fig. 2.8)  $p = 0.95$  (Fig. 2.9), and  $p = 0.99$  (Fig. 2.10), for the studied pair of parameters ( $D_a, K_a$ ). The results are presented for both the absolute and conditional distributions, showing again that adding information (the value of the rest of the parameters is assumed as known) decreases the size of the region and, consequently, the uncertainty in the estimation. Due to the complex dependence between variables, the HDR regions have complex shapes, different from the commonly assumed ellipsoids.

In addition to the parameters, the proposed methodology can be applied to estimate the model output variables, i.e., the concentration profiles for both alive and

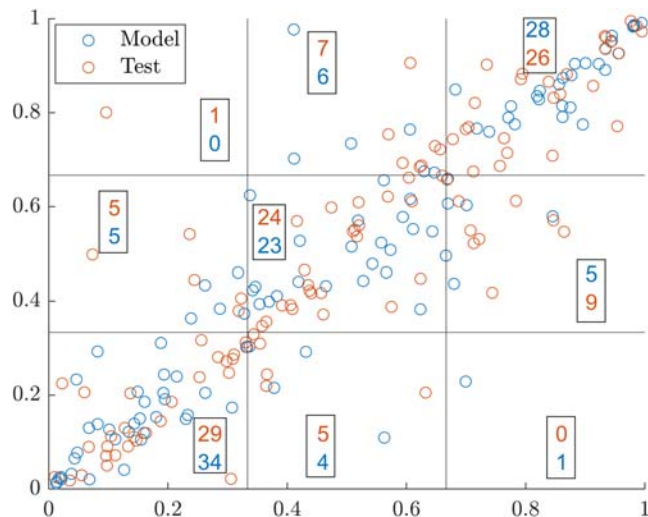
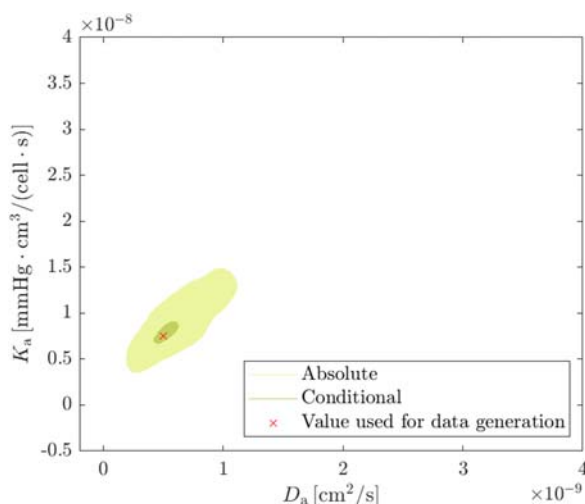


**FIGURE 2.7 Scatterplot of model and test data.**

The unit square is divided into nine regions to perform the chi-squared test. Observed and expected data are marked in orange and blue, respectively.

**Table 2.2 Chi-squared evaluation.** Observed and expected values for the 2D chi-squared goodness of fit test, and value of the D statistic.

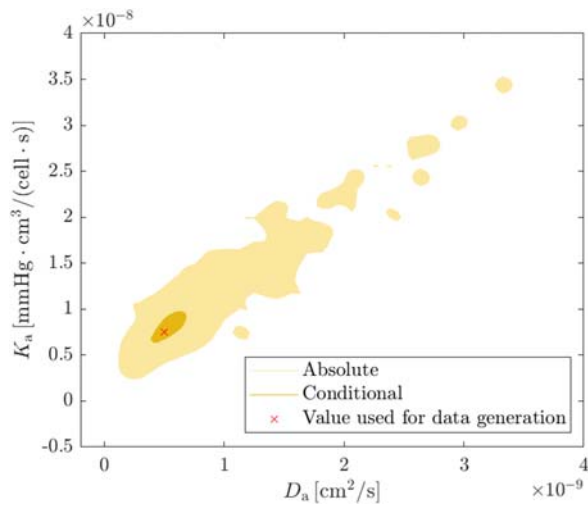
Observed	Expected	D = (observed - expected - 0.5) <sup>2</sup> /expected
29	34	0.89
5	5	0.05
5	4	0.06
24	23	0.01
7	6	0.04
0	1	2.25
9	5	2.45
26	28	0.22
		5.98



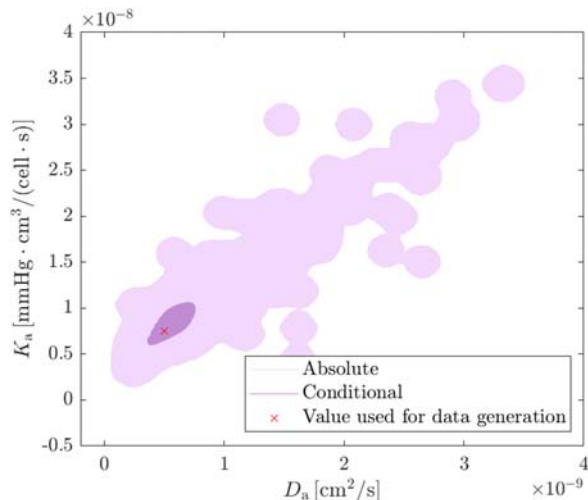
**FIGURE 2.8 HDR for a confidence level of 90%.**

Highest Density Regions (HDRs) for the estimation of the diffusion and chemotaxis coefficients with a level of confidence of 90%, using both the absolute and the conditional distributions.

dead cells. That is, once the distribution of the model parameters  $\Theta$  is characterized, the output variables can be obtained as  $\mathbf{U} = \mathbf{F}(\lambda, \Theta)$  for each particular experiment  $\lambda$ . We have reproduced three different experiments corresponding to the main histopathological features of GBM. In Fig. 2.11, a low concentration of cells was subjected to an oxygen gradient ( $O_2^l = 2$  mmHg,  $O_2^r = 0$  mmHg,  $C_0 = 4 \cdot 10^6$  cell/mL), resulting in a migrating wave toward the oxygenated area,

**FIGURE 2.9** HDR for a confidence level of 95%.

Highest Density Regions (HDRs) for the estimation of the diffusion and chemotaxis coefficients with a level of confidence of 95%, using both the absolute and the conditional distributions. Note that the irregular shape is due to kernel estimation of extreme events.

**FIGURE 2.10** HDR for a confidence level of 99%.

Highest Density Regions (HDRs) for the estimation of the diffusion and chemotaxis coefficients with a level of confidence of 99%, using both the absolute and the conditional distributions. Note that the irregular shape is due to kernel estimation of extreme events.

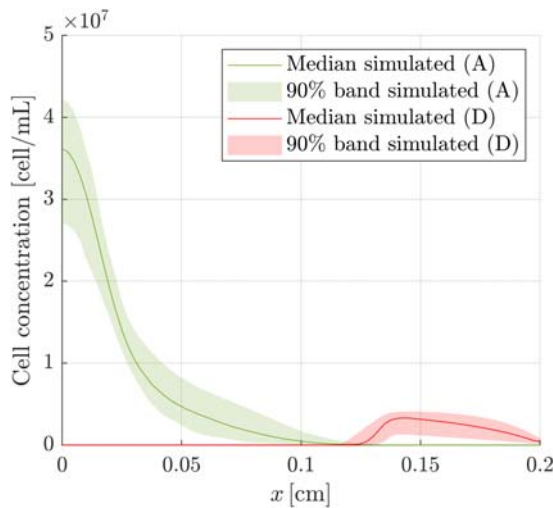


**FIGURE 2.11 Pseudopalisade experiment.**

Distribution of alive and dead cell concentrations for the formation of a pseudopalisade.

forming a pseudopalisade (Ayuso et al., 2017). In Fig. 2.12, the same low concentration of cells was put through normoxic conditions ( $O_2^l = 7 \text{ mmHg}$ ,  $O_2^r = 7 \text{ mmHg}$ ,  $C_0 = 4 \cdot 10^6 \text{ cell/mL}$ ), forming a double pseudopalisade

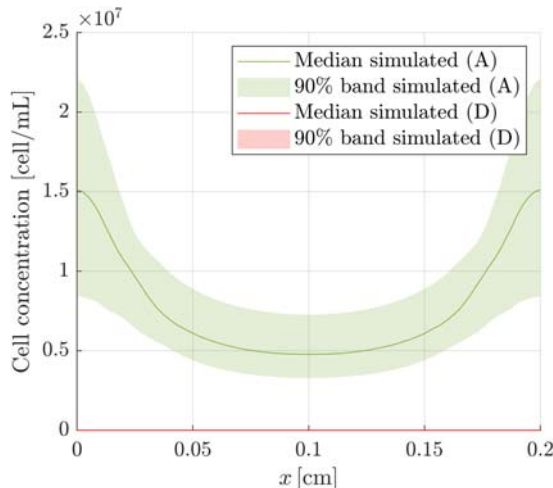


**FIGURE 2.12 Double pseudopalisade experiment.**

Distribution of alive and dead cell concentrations for the formation of a double pseudopalisade.

(Ayensa-Jiménez et al., 2020). Finally, in Fig. 2.13, the formation of a necrotic core is reproduced, in which cells at a high concentration are seeded in normoxic conditions ( $O_2^l = 7 \text{ mmHg}$ ,  $O_2^r = 7 \text{ mmHg}$ ,  $C_0 = 4 \cdot 10^7 \text{ cell/mL}$ ), creating a hypoxic region in the center of the chamber where cells die and form the necrotic core.

### Experimental design

In this section, we follow the methodology described in the [Model analysis and applications](#) section to determine the experimental configuration  $\lambda$  with the highest utility, i.e., the experiment which would give the maximum information to determine the value of a parameter or a subset of them. To illustrate the methodology, we search for the experiment with the highest utility to determine both the diffusion and the chemotaxis parameters ( $D_a, K_a$ ), with the rest of the parameters fixed at the value set for data generation. In Fig. 2.14, the isutility curves for estimating this pair of parameters, fixing the cell initial concentration at  $C_0 = 1 \cdot 10^7 \text{ cell/mL}$ , and varying the oxygen level at both channels from 0 to 9 mmHg. In this figure, we can see the most useful experiment for learning ( $D_a, K_a$ ), when we assume that we know the rest of the parameters; and also those experiments which provide little information for this task. The configurations with the highest utility are those in which an oxygen gradient is generated. This is logical, as without it, cells would not move due to chemotaxis. Moreover, as the initial concentration of cells is constant, if cells do not move due to chemotaxis, there would be no significant cell gradients to make cells move due to diffusion. However, if the

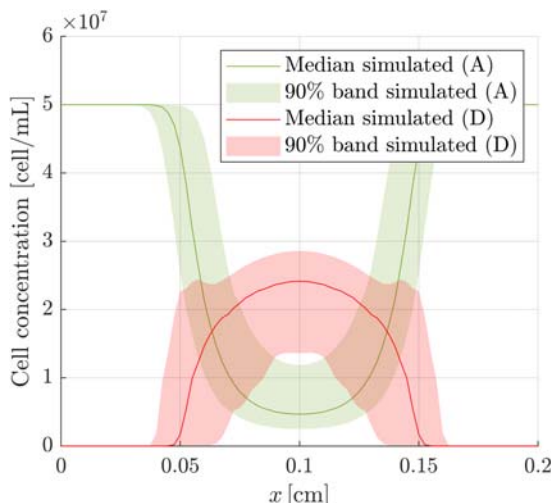


**FIGURE 2.13 Necrotic core experiment.**

Distribution of alive and dead cell concentrations for the formation of a necrotic core.

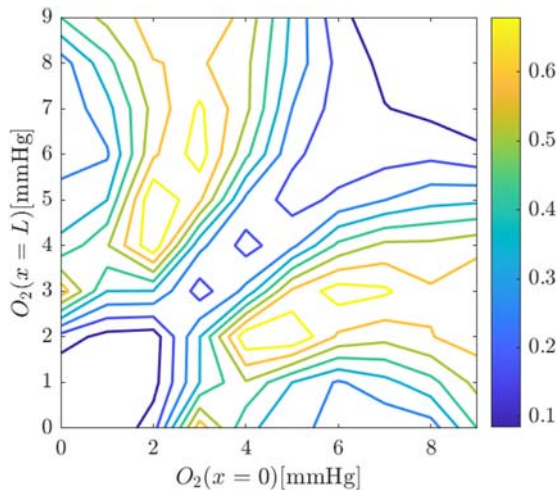


**FIGURE 2.14 Isouility curves for the diffusion and chemotaxis coefficients.**

Isouility curves for the diffusion and the chemotaxis coefficient for different levels of oxygen and an initial concentration of 10 million cells/mL.

oxygen levels are close to 0 or 9 mmHg, there are regions where the effect on chemotaxis is imperceptible (cells are dead or in a normoxic ambient) which explains the low utility of experiments close to the borders of the considered domain. It is worth remarking that the isouility curves are symmetric with respect to the line  $O_2^l = O_2^r$ , which is coherent with the symmetric geometry of the microfluidic device. Also, the fact that this is a six-dimensional model makes it difficult to provide a precise interpretation of these curves. To get more information, in Fig. 2.15, we represent the variation of the utility with the initial cell concentration (ranging from  $C_0 = 1 \cdot 10^6$  cell/mL to  $C_0 = 5 \cdot 10^7$  cell/mL, which is the device saturation capacity). The utility is computed for three different situations: hypoxic ( $O_2^l = O_2^r = 2$  mmHg), normoxic ( $O_2^l = O_2^r = 9$  mmHg), and with an oxygen gradient ( $O_2^l = 2$  mmHg,  $O_2^r = 9$  mmHg). It can be seen that the highest utility values are obtained for the gradient configuration, as expected, and reach a maximum value for concentrations of around  $C_0 = 1 \cdot 10^7$  cell/mL.

Another application of the Bayesian Design of Experiments is the design of experimental campaigns. To illustrate it, a simple case has been here developed as follows. As we lack sufficient experimental data, we have supposed an underlying correlation structure and marginal distributions (which are not known by the experimental campaign designers, of course). These correlations are due to samples variability and exist between the parameters related to cell motility ( $D_a, K_a$ ), and the parameters related to cell metabolism ( $\tau_a, \tau_{ad}$ ). Supposing that each of the

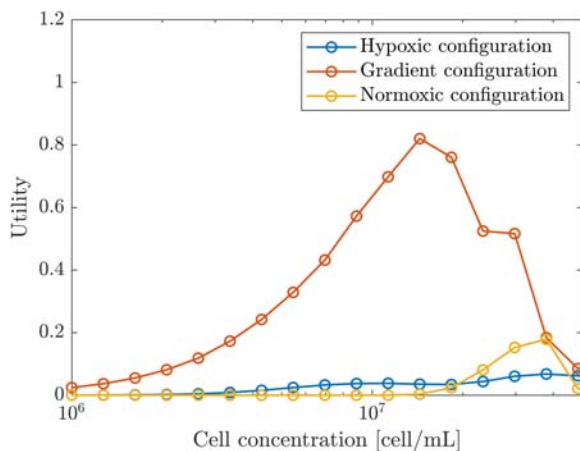


**FIGURE 2.15 Variation of the utility with the initial concentration.**

Variation of the utility of an experiment to estimate the diffusion and chemotaxis parameters when the initial cell concentration varies. The utility is depicted for three oxygen configurations: hypoxic (both channels with 2 mmHg), gradient (channels with 2 and 9 mmHg), and normoxic (both channels with 9 mmHg).

parameters follows a normal distribution whose mean and standard deviation are detailed in Table 2.3, a Gaussian copula is fitted and its Kendall's  $\tau$  matrix is shown in Fig. 2.16.

Initially, we assume that we have the three experiments detailed in Parameter estimation section (formation of a pseudopalisade, formation of a double pseudopalisade, and formation of a necrotic core), each with  $N = 10$  repetitions. The process followed in the experimental campaign design is

1. Synthetic data generation corresponding to the experiments that we have, using a value of the model parameters obtained from their normal distribution. The data

**Table 2.3 Parameters of the normal distributions.** Mean and standard deviation for the assumed normal distribution for each parameter for the design of the experimental campaign.

Parameter	Mean	Standard deviation	Units
$D_a$	$5 \cdot 10^{-10}$	$5 \cdot 10^{-11}$	$\text{cm}^2/\text{s}$
$K_a$	$7.5 \cdot 10^{-9}$	$1.5 \cdot 10^{-9}$	$\text{cm}^2/\text{mmHg} \cdot \text{s}$
$D_{O_2}$	$11 \cdot 10^{-7}$	$5 \cdot 10^{-7}$	$\text{cm}^2/\text{s}$
$\alpha_a$	$1 \cdot 10^{-9}$	$1 \cdot 10^{-10}$	$\text{mmHg} \cdot \text{cm}^3/\text{cell} \cdot \text{s}$
$\tau_a$	200	20	h
$\tau_{ad}$	48	4.8	h

$D_a$	1.00	0.59	0.00	0.00	0.00	0.00
$K_a$	0.59	1.00	0.00	0.00	0.00	0.00
$D_{O_2}$	0.00	0.00	1.00	0.00	0.00	0.00
$\alpha_a$	0.00	0.00	0.00	1.00	0.00	0.00
$\tau_a$	0.00	0.00	0.00	0.00	1.00	-0.26
$\tau_{ad}$	0.00	0.00	0.00	0.00	-0.26	1.00
	$D_a$	$K_a$	$D_{O_2}$	$\alpha_a$	$\tau_a$	$\tau_{ad}$

**FIGURE 2.16 Tau matrix of the underlying copula.**

Kendall's tau coefficients for the underlying copula used in the design of the experimental campaign. Recall that this copula is not known, it is used only for data generation.

are perturbed with a uniform noise  $\epsilon_j = 0.2 \times u_j \times V$ , where  $V$  is a random uniform distribution  $V \sim \mathcal{U}[-1, 1]$ . These data are supposed to be obtained in the laboratory but are generated here synthetically for illustration purposes.

2. Minimization problem to obtain  $\theta_i$ .
3. Marginal distribution fitting for each parameter.
4. Transformation from marginal to uniform distributions.
5. Copula fit.
6. Calculation of the utility of the experiments for different values of  $\lambda$  (in particular, oxygen levels range from 0 to 9 mmHg and initial cell concentration can be either  $4 \cdot 10^6$  or  $4 \cdot 10^7$  cell/mL).
7. Obtention of the configuration with the highest utility value. Once this is done, the selected experiment would be conducted  $N$  times (in our case, simulated) and added to the available experiments in step 1, restarting the process.

Three iterations of the process are carried out, considering in the first one the three experiments detailed above. The experiments are detailed in [Table 2.4](#).

In [Fig. 2.17](#), the evolution of the marginal distribution for both  $D_a$  and  $K_a$  are represented, together with the real normal distribution. It can be seen that in each iteration, the marginal distribution (calculated by means of kernel estimation) approaches more the normal distribution, as expected when we add extra information. Also, the parameters characterizing the copula evolve toward their real value in each iteration, as can be seen in [Table 2.5](#). Finally, Kendall's tau matrix of correlation coefficient obtained after the three iterations performed is displayed in [Fig. 2.18](#), where

**Table 2.4 Experiments performed.** Experimental configurations carried out in the experimental campaign.

Iteration	Experiment	$O'_2$ [mmHg]	$O''_2$ [mmHg]	$C_0$ [cell /mL]
1	1	2	0	$4 \cdot 10^6$
	2	7	7	$4 \cdot 10^6$
	3	7	7	$4 \cdot 10^7$
2	4	9	0	$4 \cdot 10^7$
3	5	9	0	$4 \cdot 10^7$

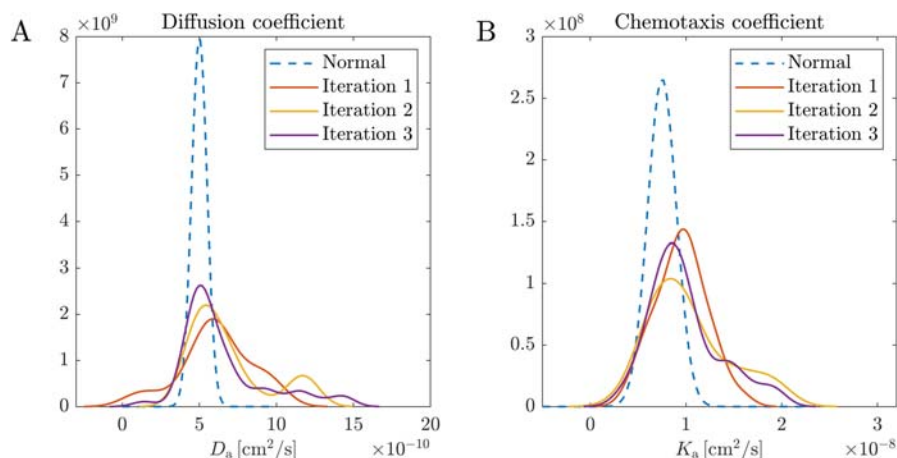


**FIGURE 2.17 Evolution of the parameter distributions in an experimental campaign.**

Evolution of the marginal distributions of the diffusion (A) and chemotaxis (B) coefficients at successive iterations.

**Table 2.5 Evolution of copula parameters.** Evolution of the copula parameters defining the correlation between the diffusion and chemotaxis coefficients at each iteration.

	$\rho$	$\nu$
Real	0.8	$\infty$
Iteration 1	0.5719	2.6863
Iteration 2	0.9248	4.0282
Iteration 3	0.8296	5.7404

$D_a$	1.00	0.62	0.32	0.31	0.05	0.45
$K_a$	0.62	1.00	0.35	0.31	0.01	0.50
$D_{O_2}$	0.32	0.35	1.00	0.53	-0.00	0.31
$\alpha_a$	0.31	0.31	0.53	1.00	0.09	0.23
$\tau_a$	0.05	0.01	-0.00	0.09	1.00	-0.13
$\tau_{ad}$	0.45	0.50	0.31	0.23	-0.13	1.00
	$D_a$	$K_a$	$D_{O_2}$	$\alpha_a$	$\tau_a$	$\tau_{ad}$

**FIGURE 2.18 Tau matrix of the resulting copula after three iterations.**

Kendall's tau coefficients for the resulting copula after three iterations of the experimental campaign.

it can be observed that spurious correlations, induced by the model, have appeared, which were not present in Fig. 2.16. These correlations are due to the model complexity and nonseparability.

## Conclusions

Mathematical modeling of complex biological problems is often very challenging due to their intrinsic nonlinearity, highly coupled multiphysic interactions, and the many correlated parameters which are difficult to identify, estimate, or simply unknown. The design of smart experiments is crucial to fit the parameters, but often difficult due to the model features, namely nonseparability. Hence, the parameters are traditionally fitted for a particular problem and treated as deterministic values. This fact may lead to conclusions that are difficult to generalize, and which overlook the correlation that exists in most cases between the different parameters and phenomena, both due to physical reasons and induced by the model limitations.

To overcome this limitation, we propose in this chapter a new stochastic approach, treating the parameters as random variables and studying their structural dependence by means of copulas. Copulas have proven to be a simple and powerful tool to describe biological multiparametric mathematical models, as long as there are enough data available to adjust the probabilistic models. Once fitted, this model can be used to estimate the model parameters, using the highest density regions, or to estimate the output variables taking into account the uncertainty.

In addition, the proposed methodology provides key information for the optimal design of new experiments, with the aim of getting the maximum gain of

information, resulting in time and resources saving both in vitro and in vivo experiments. This approach has been adapted to carry out experimental campaigns, using the ideas from the Bayesian Design of Experiments, which allows us to identify the optimal experiment to be carried out next.

In summary, the presented methodology based on copulas has demonstrated to be a good approach for dealing with multiparametric biological models in contexts of data availability, both for estimating parameters, predicting new outcomes, and design future directions and experimental tasks. As a consequence, the framework presented moves toward a better understanding of biological phenomena in digital human modeling.

---

## Acknowledgments

The authors gratefully acknowledge the financial support from the Spanish Ministry of Science and Innovation (MICINN), the State Research Agency (AEI), and FEDER, UE through the projects PGC 2018-097257-B-C31 and PID 2019-106099RB-C44/AEI/10.13039/501100011033, the Government of Aragon (DGA) and the Centro de Investigacion Biomedica en Red en Bioingenieria, Biomateriales y Nanomedicina (CIBER-BBN). CIBER-BBN is financed by the Instituto de Salud Carlos III with assistance from the European Regional Development Fund.

---

## References

- Aas, K., Czado, C., Frigessi, A., & Bakken, H. (2009). Pair-copula constructions of multiple dependence. *Insurance: Mathematics and Economics*, 44(2), 182–198. <https://doi.org/10.1016/j.insmatheco.2007.02.001>
- Adler, F. (1951). Yates' correction and the statisticians. *Journal of the American Statistical Association*, 46(256), 490–501. <https://doi.org/10.1080/01621459.1951.10500804>
- Alfonso, J. C. L., Talkenberger, K., Seifert, M., Klink, B., Hawkins-Daarud, A., Swanson, K. R., Hatzikirou, H., & Deutsch, A. (2017). The biology and mathematical modelling of glioma invasion: A review. *Journal of The Royal Society Interface*, 14(136), 20170490. <https://doi.org/10.1098/rsif.2017.0490>
- Ali, M. M., Mikhail, N. N., & Haq, M. S. (1978). A class of bivariate distributions including the bivariate logistic. *Journal of Multivariate Analysis*, 8(3), 405–412. [https://doi.org/10.1016/0047-259X\(78\)90063-5](https://doi.org/10.1016/0047-259X(78)90063-5)
- Altrock, P. M., Liu, L. L., & Michor, F. (2015). The mathematics of cancer: Integrating quantitative models. *Nature Reviews Cancer*, 15(12), 730–745. <https://doi.org/10.1038/nrc4029>
- Ang, A., & Chen, J. (2002). Asymmetric correlations of equity portfolios. *Journal of Financial Economics*, 63(3), 443–494. [https://doi.org/10.1016/S0304-405X\(02\)00068-5](https://doi.org/10.1016/S0304-405X(02)00068-5)
- Arya, F. K., & Zhang, L. (2017). Copula-based Markov process for forecasting and analyzing risk of water quality time series. *Journal of Hydrologic Engineering*, 22(6). [https://doi.org/10.1061/\(ASCE\)HE.1943-5584.0001494](https://doi.org/10.1061/(ASCE)HE.1943-5584.0001494)

- Ayensa-Jiménez, J., Pérez-Aliacar, M., Randelovic, T., Oliván, S., Fernández, L., Sanz-Herrera, J. A., Ochoa, I., Doweidar, M. H., & Doblaré, M. (2020). Mathematical formulation and parametric analysis of in vitro cell models in microfluidic devices: Application to different stages of glioblastoma evolution. *Scientific Reports*, 10(1). <https://doi.org/10.1038/s41598-020-78215-3>
- Ayensa-Jiménez, J., Pérez-Aliacar, M., Randelovic, T., Sanz-Herrera, J. A., Doweidar, M. H., & Doblaré, M. (2021). Analysis of the parametric correlation in mathematical modeling of in vitro glioblastoma evolution using copulas. *Mathematics*, 9(1), 1–22. <https://doi.org/10.3390/math9010027>
- Ayuso, J. M., Monge, R., Martínez-González, A., Virumbrales-Muñoz, M., Llamazares, G. A., Berganzo, J., Hernández-Laín, A., Santolaria, J., Doblaré, M., Hubert, C., Rich, J. N., Sánchez-Gómez, P., Pérez-García, V. M., Ochoa, I., & Fernández, L. J. (2017). Glioblastoma on a microfluidic chip: Generating pseudopalisades and enhancing aggressiveness through blood vessel obstruction events. *Neuro-Oncology*, 19(4), 503–513. <https://doi.org/10.1093/neuonc/now230>
- Ayuso, J. M., Virumbrales-Muñoz, M., Lacueva, A., Lanuza, P. M., Checa-Chavarria, E., Botella, P., Fernández, E., Doblaré, M., Allison, S. J., Phillips, R. M., Pardo, J., Fernandez, L. J., & Ochoa, I. (2016). Development and characterization of a microfluidic model of the tumour microenvironment. *Scientific Reports*, 6. <https://doi.org/10.1038/srep36086>
- Bartoli, G., Mannini, C., & Massai, T. (2011). Quasi-static combination of wind loads: A copula-based approach. *Journal of Wind Engineering and Industrial Aerodynamics*, 99(6–7), 672–681. <https://doi.org/10.1016/j.jweia.2011.01.022>
- Bhatia, S. N., & Ingber, D. E. (2014). Microfluidic organs-on-chips. *Nature Biotechnology*, 32(8), 760–772. <https://doi.org/10.1038/nbt.2989>
- Boubaker, H., & Sghaier, N. (2013). Portfolio optimization in the presence of dependent financial returns with long memory: A copula based approach. *Journal of Banking and Finance*, 37(2), 361–377. <https://doi.org/10.1016/j.jbankfin.2012.09.006>
- Bouyé, E., Durrleman, V., Nikeghbali, A., Riboulet, G., & Roncalli, T. (2000). *Copulas for finance-a reading guide and some applications*.
- Bowman, A. W., & Azzalini, A. (1997). *Applied smoothing techniques for data analysis: The kernel approach with S-plus illustrations*, 18.
- Bowman, K. O., & Shenton, R. (1998). Estimator: Method of moments. In *Encyclopedia of statistical sciences* (pp. 2092–2098). Wiley.
- Byrne, H. M., Alarcon, T., Owen, M. R., Webb, S. D., & Maini, P. K. (2006). Modelling aspects of cancer dynamics: A review. *Philosophical Transactions of the Royal Society A: Mathematical, Physical and Engineering Sciences*, 364(1843), 1563–1578. <https://doi.org/10.1098/rsta.2006.1786>. Royal Society.
- Chance, B., & Williams, G. R. (1956). The respiratory chain and oxidative phosphorylation. *Advances in Enzymology and Related Areas of Molecular Biology*, 17, 65–134.
- Chao, W., & Zou, H. (2018). Multiple-event catastrophe bond pricing based on CIR-copula-POT model. *Discrete Dynamics in Nature and Society*. <https://doi.org/10.1155/2018/5068480>
- Charpentier, A., Fermanian, J. D., & Scalliet, O. (2007). *The estimation of copulas: Theory and practice*.
- Cherubini, U., Luciano, E., & Vecchiato, W. (2004). *Copula methods in finance*. John Wiley & Sons.

- Clayton, D. G. (1978). A model for association in bivariate life tables and its application in epidemiological studies of familial tendency in chronic disease incidence. *Biometrika*, 65(1), 141–151. <https://doi.org/10.1093/biomet/65.1.141>
- Darbyshire, O. R., & Swaminathan, N. (2012). A presumed joint pdf model for turbulent combustion with varying equivalence ratio. *Combustion Science and Technology*, 184(12), 2036–2067. <https://doi.org/10.1080/00102202.2012.696566>
- Daul, S., Giorgi, Lindskog, F., & McNeil, A. (2003). *The grouped t-copula with an application to credit risk*.
- Demarta, S., & McNeil, A. J. (2005). The t copula and related copulas. *International Statistical Review*, 73(1), 111–129. <https://doi.org/10.1111/j.1751-5823.2005.tb00254.x>
- Durrleman, V., Nikeghbali, A., & Roncalli, T. (2000). *Which copula is the right one*. Available at: SSRN 1032545.
- Eling, M., & Toplek, D. (2009). Risk and return of reinsurance contracts under copula models. *European Journal of Finance*, 15(7–8), 751–775. <https://doi.org/10.1080/13518470902864092>
- Eryilmaz, S. (2011). Estimation in coherent reliability systems through copulas. *Reliability Engineering and System Safety*, 96(5), 564–568. <https://doi.org/10.1016/j.ress.2010.12.024>
- Fan, Y. (1997). Goodness-of-fit tests for a multivariate distribution by the empirical characteristic function. *Journal of Multivariate Analysis*, 62(1), 36–63. <https://doi.org/10.1006/jmva.1997.1672>
- Fazlollah, M., & Reza. (1994). *An introduction to information theory*.
- Frey, R., McNeil, A. J., & Nyfeler, M. (2001). Copulas and credit models. *Risk*, 10.
- Gelman, A., Stern, J. B., Carlin, D. B., Dunson, A., Vehtari, D. B., & Rubin. (2013). *Bayesian data analysis*. Chapman and Hall/CRC.
- Hatzikirou, H., Basanta, D., Simon, M., Schaller, K., & Deutsch, A. (2012). “Go or grow”: The key to the emergence of invasion in tumour progression? *Mathematical Medicine and Biology*, 29(1), 49–65. <https://doi.org/10.1093/imammb/dqq011>
- Hatzikirou, H., Deutsch, A., Schaller, C., Simon, M., & Swanson, K. (2005). Mathematical modelling of glioblastoma tumour development: A review. *Mathematical Models and Methods in Applied Sciences*, 15(11), 1779–1794. <https://doi.org/10.1142/S0218202505000960>
- Hyndman, R. J. (1996). Computing and graphing highest density regions. *American Statistician*, 50(2), 120–126. <https://doi.org/10.1080/00031305.1996.10474359>
- Jaworski, P., Durante, F., Härdle, W. K., & Rychlik, T. (2010). In *Copula theory and its applications: Proceedings of the workshop held in warsaw, 25-26 september 2009*, 198. Springer Science & Business Media.
- Joakim, M., & Joakim, W. (2017). An autocorrelation-based copula model for generating realistic clear-sky index time-series. *Solar Energy*, 9–19. <https://doi.org/10.1016/j.solener.2017.09.028>
- Joe, H., & Kurowicka, D. (2011). *Dependence modeling: Vine copula handbook*. World Scientific.
- Jones, S. (2009). The formula that felled wall street. *The Financial Times*, 22(04).
- Kathryn, C., & Isabella, V. (1995). Bayesian experimental design: A review. *Statistical Science*, 10(3). <https://doi.org/10.1214/ss/1177009939>
- Kilgore, R. T., & Thompson, D. B. (2011). Estimating joint flow probabilities at stream confluences by using copulas. *Transportation Research Record*, 2262, 200–206. <https://doi.org/10.3141/2262-20>

- Kim, J. M., Jung, Y. S., Sungur, E. A., Han, K. H., Park, C., & Sohn, I. (2008). A copula method for modeling directional dependence of genes. *BMC Bioinformatics*, 9, 225.
- Kitano, H. (2002). Computational systems biology. *Nature*, 420(6912), 206–210. <https://doi.org/10.1038/nature01254>
- Kole, E., Koedijk, K., & Verbeek, M. (2007). Selecting copulas for risk management. *Journal of Banking and Finance*, 31(8), 2405–2423. <https://doi.org/10.1016/j.jbankfin.2006.09.010>
- Kottek, N. T., & Rosso, R. (2008). *Applied statistics for civil and environmental engineers*. Malden, MA: Blackwell.
- Laux, P., Vogl, S., Qiu, W., Knoche, H. R., & Kunstmann, H. (2011). Copula-based statistical refinement of precipitation in RCM simulations over complex terrain. *Hydrology and Earth System Sciences*, 15(7), 2401–2419. <https://doi.org/10.5194/hess-15-2401-2011>
- Laux, P., Wagner, S., Wagner, A., Jacobbeit, J., Bárdossy, A., & Kunstmann, H. (2009). Modeling daily precipitation features in the volta basin of west africa. *International Journal of Climatology*, 29(7), 937–954. <https://doi.org/10.1002/joc.1852>
- Liepe, J., Filippi, S., Komorowski, M., & Stumpf, M. P. H. (2013). Maximizing the information content of experiments in systems biology. *PLoS Computational Biology*, 9(1). <https://doi.org/10.1371/journal.pcbi.1002888>
- Longin, F., & Solnik, B. (2001). Extreme correlation of international equity markets. *Journal of Finance*, 56(2), 649–676. <https://doi.org/10.1111/0022-1082.00340>
- MacKenzie, D., & Spears, T. (2014). “The formula that killed wall street”: The Gaussian copula and modelling practices in investment banking. *Social Studies of Science*, 44(3), 393–417.
- Malevergne, Y., & Sornette, D. (2003). Testing the Gaussian copula hypothesis for financial assets dependences. *Quantitative Finance*, 3(4), 231–250. <https://doi.org/10.1088/1469-7688/3/4/301>
- Marquardt, D. W. (1963). An algorithm for least-squares estimation of nonlinear parameters. *Journal of the Society for Industrial and Applied Mathematics*, 431–441. <https://doi.org/10.1137/0111030>
- McNeil, A., Frey, R., & Embrechts, P. (2015). *Quantitative risk management: Concepts, techniques, and tools*.
- Meucci, A. (2011). *A new breed of copulas for risk and portfolio management*.
- Mousavi, S. J., & Doweidar, M. H. (2016). Numerical modeling of cell differentiation and proliferation in force-induced substrates via encapsulated magnetic nanoparticles. *Computer Methods and Programs in Biomedicine*, 130, 106–117. <https://doi.org/10.1016/j.cmpb.2016.03.019>
- Mousavi, S. J., Doweidar, M. H., & Doblaré, M. (2013). Cell migration and cell-cell interaction in the presence of mechano-chemo-thermotaxis. *Molecular & Cellular Biomechanics: MCB*, 10(1), 1–25.
- Nadarajah, S., Afuecheta, E., & Chan, S. (2017). A compendium of copulas. *Statistica*, 77(4), 279–328.
- Naifar, N. (2011). Modelling dependence structure with Archimedean copulas and applications to the iTraxx CDS index. *Journal of Computational and Applied Mathematics*, 235(8), 2459–2466. <https://doi.org/10.1016/j.cam.2010.10.047>
- Nelsen, R. B. (2007). *An introduction to copulas*.
- Noh, Y., Choi, K. K., & Du, L. (2009). Reliability-based design optimization of problems with correlated input variables using a Gaussian Copula. *Structural and Multidisciplinary Optimization*, 38(1), 1–16. <https://doi.org/10.1007/s00158-008-0277-9>

- Pham, H. (2003). Recent studies in software reliability engineering. In *Handbook of reliability engineering* (pp. 285–302). Springer.
- Renard, B., & Lang, M. (2007). Use of a Gaussian copula for multivariate extreme value analysis: Some case studies in hydrology. *Advances in Water Resources*, 30(4), 897–912. <https://doi.org/10.1016/j.advwatres.2006.08.001>
- Ronald, A., & Fisher. (1937). *The design of experiments*. Edinburgh; London: Oliver And Boyd.
- Rossi, R. J. (2018). *Mathematical statistics: An introduction to likelihood based inference*. John Wiley & Sons.
- Ruan, S., Swaminathan, N., & Darbyshire, O. (2014). Modelling of turbulent lifted jet flames using flamelets: A priori assessment and a posteriori validation. *Combustion Theory and Modelling*, 18(2), 295–329.
- Schloegl, L., & O’Kane, D. (2005). A note on the large homogeneous portfolio approximation with the Student-t copula. *Finance and Stochastics*, 9(4), 577–584. <https://doi.org/10.1007/s00780-004-0142-7>
- Schölzel, C., & Friederichs, P. (2008). Multivariate non-normally distributed random variables in climate research – introduction to the copula approach. *Nonlinear Processes in Geophysics*, 15(5), 761–772. <https://doi.org/10.5194/npg-15-761-2008>
- Shannon, C. E. (1948). A mathematical theory of communication. *Bell System Technical Journal*, 379–423. <https://doi.org/10.1002/j.1538-7305.1948.tb01338.x>
- Shaomin, W. (2014). Construction of asymmetric copulas and its application in two-dimensional reliability modelling. *European Journal of Operational Research*, 476–485. <https://doi.org/10.1016/j.ejor.2014.03.016>
- Silverman, B. W. (1986). *Density estimation for statistics and data analysis*, 26.
- Sklar, M. (1959). Fonctions de répartition à n dimensions et leurs marges. *Publ. Inst. Statist. Univ.*, 8, 229–231.
- Solari, S., & Losada, M. (2011). Non-stationary wave height climate modeling and simulation. *Journal of Geophysical Research: Oceans*, 116.
- Stanković, T., Randelović, T., Dragoj, M., Stojković Burić, S., Fernández, L., Ochoa, I., Pérez-García, V. M., & Pešić, M. (2021). In vitro biomimetic models for glioblastoma – a promising tool for drug response studies. *Drug Resistance Updates*, 55. <https://doi.org/10.1016/j.drup.2021.100753>
- Wang, Y., & Pham, H. (2012). Modeling the dependent competing risks with multiple degradation processes and random shock using time-varying copulas. *IEEE Transactions on Reliability*, 61(1), 13–22.
- Wan, K., & Kornhauser, A. L. (2010). *Turn-by-turn routing decision based on copula travel time estimation with observable floating-car data* (pp. 10–2723).
- Zhang, Y., Beer, M., & Quek, S. T. (2015). Long-term performance assessment and design of offshore structures. *Computers & Structures*, 154, 101–115.

# Deep learning applied to detection of the vulnerable atherosclerotic plaque

# 3

M. Cilla<sup>1,2</sup>, J. Martínez<sup>3</sup>, M.A. Martínez<sup>1,2</sup>, E. Peña<sup>1,2</sup>

<sup>1</sup>*Instituto de Investigación en Ingeniería de Aragón, Universidad de Zaragoza, Zaragoza, Spain;*

<sup>2</sup>*CIBER-BBN, Centro de Investigación en Red en Bioingeniería, Biomateriales y Nanomedicina, Madrid, Spain; <sup>3</sup>*Universidad de Vigo, Vigo, Spain**

## Chapter outline

<b>Introduction.....</b>	63
<b>The atheroma plaque problem.....</b>	66
3D parametric study .....	66
Source data .....	68
<b>Mathematical methods for regression.....</b>	68
Artificial neural network .....	69
Support vector machine .....	71
Assuring the quality of the machine .....	71
Validation with a real geometry .....	74
<i>How the decision support system works.....</i>	74
Finite element models .....	75
<b>Results.....</b>	78
<b>Discussion.....</b>	80
<b>Acknowledgments .....</b>	80
<b>References .....</b>	80

## Introduction

Computer science is being increasingly used in modern medicine and technological innovation and computers have made possible to become a vital tool in the medical field. Computer facilities have now tremendous applications in medical field. Major uses of computers science in medicine include hospital information system, medical imaging laboratory computing, data analysis in medicine, computer-assisted medical decision-making, computer-assisted therapy, or care of critically ill patients (Mehta et al., 1994). In addition, the clinical data and information in hospitals become larger and larger, which causes a load of difficulties in extracting useful data and knowledge for decision support, especially when traditional not automatic data analysis has become obsolete or inefficient and the use of computer methods

analysis are indispensable (Itchhaporia et al., n.d.). Therefore, there is an urgent need to introduce more effective and efficient computational methods in medical analysis for decision support to assist medical professionals. The concept is to build decision support tools based upon numerical methods that is able to use and store the knowledge from different sources such as experienced clinicians, computer simulations, or statistical analysis, and then, these automatic tools gather knowledge and use mathematical and optimization methods to return proper answers to queries or accurate predictions on unknown data (Lavrac et al., 2000; Mitchell, 1997). There are many methods to achieve this goal, however, Machine Learning Techniques (MLT) have shown to be quite useful for this automation process (Langley & Simon, 1995). These techniques are based on the ability to learn from examples which is an important facet of intelligence that has been an especially fertile area of study in the last decade (Alpaydin, 2001). Nevertheless, it can be assumed that there are many methods to achieve this target. However, MLT have been shown to play an important role in this automatic process (Mehta et al., 1994).

Nevertheless, since there is no intelligence without learning, MLT are considered one of major branches of artificial intelligence, which is the part of computer science that tries to make computers more intelligent. For that reason, they have been applied successfully to a wide variety of problems and data for prediction tasks and real problems of practical interest (Mitchell, 1997; Widrow et al., 1994). Thanks to computer science, mathematics, statistics, and engineering, the multidisciplinary nature of MLTs are underscored by its applicability to different disciplines, such as electronic, industry (Evans & Fisher, 1992), space science (Fayyad et al., 1993), language (Liu et al., 2005), or geology (López et al., 2010a; Taboada et al., 2007) among many others. Within the clinical context, these techniques have been also successfully applied to different medical purposes, for instance; diagnosis of melanomas or breast cancer, diagnosing dementia, interpreting electrocardiograms or predicting prognosis and survival rates (Gniadecka et al., 2004; Handels et al., 1999; Huang & Kecman, 2005). And, of course, they have been used for treating cardiovascular diseases (Itchhaporia et al., 1995, n.d.; Poli et al., 1991). Additionally, it has been proven some benefits of introducing this kind of tools into medical analysis such as a reduction of costs, increase of diagnostic accuracy and decrease human resources (Cheung, 2001; Kononenko, 2001).

Within the atherosclerosis framework, cardiovascular complications related to atherosclerosis disease are the first cause of death in the developed countries (Hanke et al., 2001). The best way to prevent the consequences of the atherosclerosis disease is to detect it in the early stages, before a cardiovascular accident occurs. When the atheroma plaque grows and expands causing severe stenosis of the arterial lumen, the problem could be irreversible, resulting in fatal events such as heart attacks or strokes. It should be noted that the clinical procedures for detection of vulnerable atheroma plaques can be arranged into two different areas: (i) image diagnosis and (ii) data analysis. Image diagnosis is the use of available screening medical tests to acquire an image of the lesion for the purpose of analyzing the injury status. On the other hand, data analysis brings the patient's condition analysis from measured

test results or observed symptoms into focus. Nevertheless, despite current advances in the treatment and diagnosis of symptomatic atherosclerotic events, available methods for early detection and treatment of asymptomatic coronary artery disease are insufficient to identify most of the victims prior to a fatal event occurs.

Within the different kinds of MLTs, Artificial Neural Networks (ANN) are mathematical models based on biological neural networks. They consist of an interconnected group of artificial neurons, where it processes information using an approach to computation (Gurney, 1997; McCulloch & Pitts, 1943). In addition, a multilayer perceptron (MLP) is a feed-forward network characterized by its layered structure where each layer consists of a set of perceptron neurons and utilizes a supervised learning technique called backpropagation for training (Bishop, 1995). Support Vector Machine (SVM) constructs a hyperplane or set of hyperplanes in a high or infinite dimensional space (Vapnik, 1982). A good separation is achieved by the hyperplane that has the largest distance to the nearest training data point of any class (so-called functional margin), since in general the larger the margin the lower the generalization error of the classifier or regressor (Cortes & Vapnik, 1995; Meyer et al., 2003). Whereas the original problem may be stated in a finite dimensional space, it often happens that the sets to discriminate are not linearly separable in that space. For this reason, it was proposed that the original finite dimensional space be mapped into a much higher dimensional space, presumably making the separation easier in that space. To keep the computational load reasonable, the mappings used by SVM schemes are designed to ensure that dot products may be computed easily in terms of the variables in the original space, by defining them in terms of a kernel function selected to suit the problem (Burges, 1998; Scholkopf & Smola, 2002).

The development of numerical models for arterial behavior in order to understand cardiovascular pathologies, mostly based on Finite Element (FE) methods have been motivated by these relevant facts. Nonetheless, the use of numerical FE methods for the design and analysis of bioengineering processes often requires long computational time cost (hours or even days) and a large memory consumption, which presents an important disadvantage for fast diagnosis in real time. However, the simulation time can be meaningfully decreased combining MLT with FE methods.

In a previous work of the same authors (Cilla, Martinez, et al., 2012), a quantitative study using MLT for cumulative risk assessment of atheroma plaque vulnerability based on its morphology was performed. In this study, different MLTs, such as ANN and SVM, were tested to study the role of stress in plaque vulnerability as a function of the main geometrical features. It has been proved that these techniques are very powerful tools for classification or regression (López et al., 2010a, 2010b; Taboada et al., 2007). It was demonstrated that both SVM and ANN techniques have the capacity to produce accuracy, obtaining relative errors of 4.14% and 6.76% for the SVM and ANN techniques, respectively. In addition, this study showed that the developed tool could replace the time-consuming FE simulations used to predict atheroma plaque vulnerability. These MLTs were trained with an FE parametric coronary vessel model, which was performed in a different

previous study of the same authors (Cilla, Peña, & Martínez, 2012). This parametric model is comprised of a series of idealized atheroma plaque morphology models, mimicking different variations and stages in atherosclerotic lesion growth (Cilla, Peña, & Martínez, 2012). Consequently, the MLT tool predicts the atheroma plaque vulnerability and rupture in terms of four of the most influential geometrical factors in the plaque rupture (Cheng et al., 1993; Finet et al., 2004; Ohayon et al., 2008; Williamson et al., 2003) which are the input of the MLT: (i) fibrous cap thickness; (ii) stenosis ratio; (iii) lipid core width; and (iv) lipid core length. The maximum Maximal Principal Stress (MPS) occurred in an atherosclerotic coronary vessel with the input dimensions was the output predicted by the MLT.

In this chapter, we go one step further and we prove the effectiveness of the tool with real patient-specific geometries. Therefore, the four parameters studied have been measured at different patient-specific intravascular ultrasound (IVUS) and the atheroma plaque tool was used to predict the maximum MPS of these geometries. These value of maximum MPS predicted by the MLT, which was based on ANN and SVM, has been compared to the maximum MPS of an FE model of the patient-specific intravascular ultrasound in order to check the accuracy of the tool.

---

## The atheroma plaque problem

### 3D parametric study

A 3D parametric study of the geometric factors used to check the vulnerability of atherosclerotic plaque was performed (Cilla, Peña, & Martínez, 2012). A 3D idealized geometry corresponding to a coronary vessel with atherosclerosis was modeled. Such plaques are characterized by a large lipid pool with a thin fibrous cap (Davies, 1996; Finet et al., 2004; Ohayon et al., 2001). Atherosclerotic vessel morphology and average dimensions were obtained from Versluis et al. (Versluis et al., 2006) and Bluestein et al. (Bluestein et al., 2008). A vessel length of 20 mm, external radius of 2 mm and vessel wall thickness of 0.5 mm were considered as base geometry. A 3D FE model was developed using the commercial FE code ABAQUS 6.9, taking into account both the composition and dimensions of the different layers of the tissue (media and adventitia), the fibrous plaque and the lipid core.

The arterial wall was approximated as a hollow cylinder with a circular lumen. The atherosclerotic plaque was modeled as a symmetric volume with respect to the central cross section (longitudinal axis), located inside the vessel. Finally, the lipid core was approximated as a blunt volume (see Fig. 3.1). In areas with atherosclerosis, the whole media layer was considered as fibrotic, whereas only the adventitia was considered as a healthy layer. All tissues were considered to be nonlinear, hyperelastic, and incompressible materials (Holzapfel et al., 2005). The behavior of the tissue was modeled by the Gasser, Ogden, and Holzapfel (GOH) strain energy function (SEF) (Gasser et al., 2006). In order to obtain the material parameters for

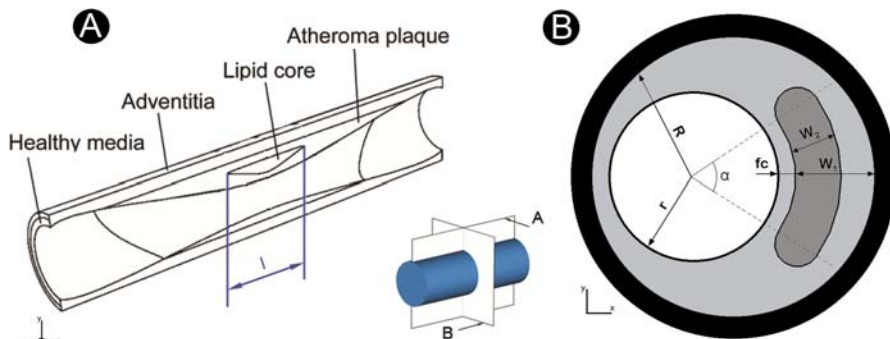


**FIGURE 3.1** Idealized geometry of the artery.

(A) Idealized geometry of an atherosclerotic arterial model. Transversal section. (B) Geometrical parameters shown on the central cross section of the atherosclerotic vessel.

Modified from (N.d.-a). <https://doi.org/10.1007/s10237-011-0369-0>.

the constitutive law of the tissue, experimental data presented in previous works (adventitia and media properties from Holzapfel et al. (2005) and plaque and lipid core properties from Versluis et al. (2006) were fitted using the Levenberg–Marquardt minimization algorithm (Marquardt, 1963).

Regarding the boundary conditions, the longitudinal displacements were constrained at the end of the vessel, whereas the radial displacement was allowed. Symmetry conditions were imposed in the corresponding symmetry planes. In order to introduce the longitudinal residual stress, the model was stretched a 4.4% of the vessel length (longitudinal direction), representing in vivo conditions (Holzapfel et al., 2005). Then, a constant internal pressure of 140 mmHg (18.7 kPa) was imposed on the inner surface of the lumen, simulating the blood flow pressure (Ohayon et al., 2008).

The parametric model consists of a series of idealized plaque morphology models, mimicking different stages and variations in atherosclerotic lesion growth. According to previous works (Cheng et al., 1993; Cilla, Peña, & Martínez, 2012; Finet et al., 2004; Ohayon et al., 2008; Williamson et al., 2003), the most influential geometric parameters considered were fibrous cap thickness ( $fc$ ), stenosis ratio ( $Sr$ ), which is obtained by dividing the lumen radius by the lumen radius of a normal artery ( $R = 1.5$  mm),  $Sr (\%) = r (\text{mm}) / 100$ , lipid core length ( $l$ ) and lipid core width ( $w$ ). Lipid core width ( $w$ ) was defined as the ratio between the percentage of the atheroma plaque width ( $w_1$ ) and the distance from the inner point of the lipid core to the outer point of the fibrotic plaque ( $w_2$ ),  $w (\%) = w_1 (\text{mm}) / 100$ . The central section of the 3D model is shown in Fig. 3.1 where the lipid core length was measured in the perpendicular direction (Fig. 3.1).

Five variations or levels for each parameter were considered with a total of  $54 = 625$  idealized eccentric vessel models with atherosclerotic lesions. Realistic

morphological data was investigated by varying lipid core length ( $1 \text{ mm} \leq l \leq 8 \text{ mm}$ ), stenosis ratio ( $46.7\% \leq Sr \leq 66.7\%$ ), fibrous cap thickness ( $0.025 \text{ mm} \leq fc \leq 0.25 \text{ mm}$ ), and lipid core width ( $30\% \leq w \leq 90\%$ ) (Fujii et al., 2005). The different level values of the geometrical parameters used to define the idealized coronary plaque models are included in Table 3.1.

### Source data

MPS was considered as the mechanical factor for the purpose of comparison in the parametric study in order to define vulnerability risk.

Regarding the vulnerability of the plaque, different threshold stress values have been proposed by several authors (Cheng et al., 1993; Loree et al., 1994). In this study, a threshold value of 247 kPa has been used according to the set of experimental data obtained by Loree et al. supposing a normal distribution of the data. This threshold value indicates that the probability of having plaque rupture is 0.95 for the cases whose combination of parameters have maximum MPS equal to or higher than 247 kPa.

Maximum MPS for each combination of parameters is shown in Fig. 3.2. The two most influential parameters; fibrous cap thickness and lipid core width,  $fc$  and  $w$ , were chosen as the variables represented by the surfaces approximation. In each subfigure, five surfaces are presented, one for each  $l$  variation, where the safety threshold plane at 247 kPa is presented (Loree et al., 1994). The geometrical parameters and MPS represented in Fig. 3.2 were selected as inputs and output, respectively, to predict the atheroma vulnerability risk using ANNs and SVM methods.

---

### Mathematical methods for regression

The different mathematical models (or black box models) built to estimate the maximum MPS are presented in this section. In this case, the two machine learning algorithms studied were ANN and SVM.

**Table 3.1** Variations of analyzed geometrical parameters.

Level	<i>l</i> (mm)	<i>sr</i> (%)	<i>fc</i> (mm)	<i>w</i> (%)
1	1	46.7	0.025	30
2	2	53.3	0.05	45
3	4	56.7	0.1	60
4	6	60	0.15	75
5	8	66.7	0.25	90

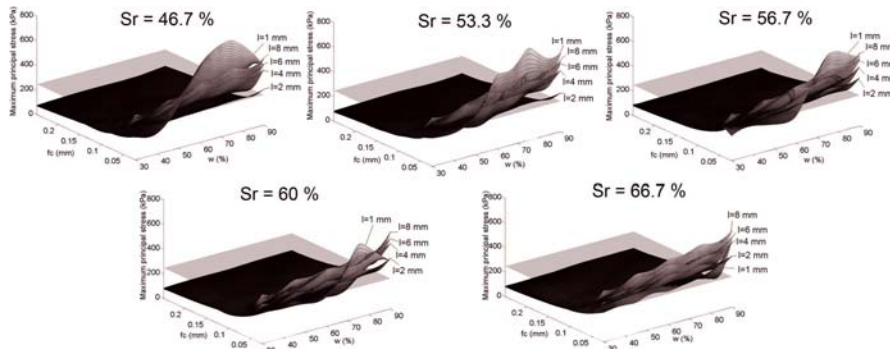


**FIGURE 3.2 Source data.**

Maximum MPS surfaces for a given stenosis ratio.

Modified from (N.d.-b). <https://pubmed.ncbi.nlm.nih.gov/22227796/>.

## Artificial neural network

ANNs are mathematical models that are inspired by the structure and functional aspects of biological neural networks. It is a useful and robust computational tool for prediction which can acquire, store, and utilize experimental knowledge (McCulloch & Pitts, 1943).

This model consists of two basic elements:

1. A structure consisting of a set of basic units, called neurons, organized in layers. The network consists of three layers: input, hidden, and output. Each unit consists of the following neuronal components,
  1. A set of input connections, along with a set of weights that regulate the input signals intensity.
  2. The activation threshold, which is subtracted from the aggregation of the transmitted input signals.
  3. An activation function which focuses on the input signals.
  4. The output of the neuron as a function of the input signals, called transfer function.

This structure is often called the network architecture, being able to make a classification of the networks as a function of the number of networks layers, the interconnection degree of the structure or according to the character of the connections.

2. A training algorithm for calibrating the network weights and other parameters as a function of deviations of the outputs provided by the network and the actual values.

When considering the network functional model, we focus on the feed-forward network (network architecture in which each layer is connected with the following forward direction only, so that can be represented by an acyclic graph), with specific activation functions and weights. So, the network

implements a function  $f : X \subset R^d \rightarrow Y \subset R^c$  where  $d$  is the input space dimension and  $c$  is the output space dimension. The functions implemented by a network feed-forward can be formulated by the following general model:

$$\begin{aligned} f(x) &= \phi(\psi(x)) = (\phi \circ \psi)(x) \\ \psi: X \subset R^d &\rightarrow U \subset R^m \\ \phi: U \subset R^m &\rightarrow Y \subset R^c \end{aligned} \quad (3.1)$$

where  $U$  is the hidden variables space with dimension  $m$  (number of neurons of this layer), and it is called feature space. A particular case of neural networks is the multilayer perceptron (MLP) with a layered structure where each neuron is a perceptron. Thus, based on the architecture defined above for the case of MLP (Bishop, 1995), see Fig. 3.3:

1.  $\psi_j(x) = \psi(wTx + wj_0)$  being  $\psi$  the hidden layer activation function,  $w_j \in R^d$  the parameter vector of the hidden layer and  $wj_0 \in R$  its threshold value. The function  $\psi$  can be a sigmoid, a logistic or a hyperbolic tangent.
2.  $\phi_j(u) = \phi(cTu + cj_0)$  being  $\phi$  the output layer activation function,  $c_j \in R^m$  the weights and  $cj_0 \in R$  its threshold value. The activation function  $\phi$  can be the identity function, Heaviside function or any dichotomous function.

The sigmoid-type and the linear functions have been selected for the hidden layer and the output layer, respectively, among all the possible transfer functions (Bishop, 1995).

A typical feature of MLP is the training algorithm of back-propagation (Bishop, 1995) which minimizes a combination of squared errors and weights starting from randomly distributed weights, and then determines the correct combination. Once an MLP is trained, it has input data fed into it, and from that, generates an appropriate output. The structure of the MLP, combined with the nonlinearity and its weights, adjusted by the training algorithm, creates general function approximations that allow for the generation of practically any nonlinear function.

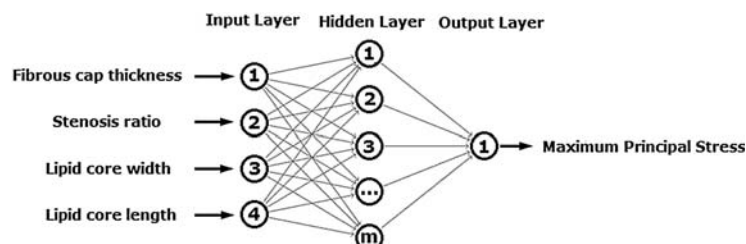


**FIGURE 3.3 ANN.**

Artificial neural network structure.

A cross-validation process was implemented in order to minimize the selection of the test set. The original set of training data is split into three groups: the first group consists of a training data set with the 80% of the data patterns; the remaining groups are the validation data set with the 10% of the patterns and, the remaining 10% of the data patterns are used to evaluate the performance of the MLP. The weight configuration for the best performance reached is stored and only replaced if a better performance has occurred. In this way, the best weight configuration can be determined. This process is repeated 10 times (fold cross-validation) (Stone, 1974).

## Support vector machine

Vapnik (1982) is considered the pioneer in introducing the concept of optimum separating hyperplane of a sample of data in a classification problem, which is the core of the SVM method.

Different historical facts can be highlighted in the development of SVMs,

1. The feature space generation from input space by the transformation  $\psi : X \subset R^d \rightarrow Z \subset R^s$  with  $s \geq d$  (can be  $\infty$ ). By the reverse transformation, the linear boundaries of the separating hyperplanes in the feature space result in nonlinear boundaries in the input space. This transformation is called the Kernel Trick.
2. The appearance of Soft-Margin algorithm for problems where perfect separability is not reachable (problems with noise in the sample data).
3. The SVM generalization to regression problems by way of Vapnik's  $\epsilon$ -insensitive loss function (Drucker et al., 1997).

It is possible to introduce a parameter in the SVM regression model (Nu-SVR) in order to control the number of support vectors determined.

A 10-fold cross-validation has been also implemented in order to determine the optimal SVM parameters according to the best fit criterion.

## Assuring the quality of the machine

In a perfect world, we would always have all the data we need to represent a given classification or regression problem. However, the world is far from perfect in this respect. Consequently, some previous considerations should be taken to improve the performance of these techniques on the medical field. Many patterns will be banal and uninteresting. Others will be spurious, contingent on accidental coincidences in the particular data set used. In addition, real data, specially in the medical field, are imperfect; some parts will be garbled, and some will be missing. Anything discovered will be inexact; there will be exceptions to every rule and cases not covered by any rule. Thus, algorithms need to be robust enough to cope with imperfect data and to extract regularities that are inexact but useful. An MLT useful to

solve medical diagnostic tasks should include the following desirable features ([Cheung, 2001](#); [Itchhaporia et al., 1995](#); [Kononenko, 2001](#)):

1. Good performance: The algorithm has to be able to extract significant information from the available data. The diagnostic accuracy on new cases has to be as high as possible. Furthermore, if there is a possibility to measure an accurate in prediction of clinicians in the given problem, their performance can be used as the lower bound on the required accuracy of the MLT. In the majority of learning problems, various approaches typically achieve similar performance in terms of the classification or regression accuracy, although in some cases some algorithms may perform significantly better than others ([Fulkerson et al., 1995](#)). Therefore, *a priori*, almost none of the algorithms can be excluded with respect to the performance criterion. Rather, several learning approaches should be tested on the available data and the one or few with best estimated performance should be considered for the development of the application.
2. Dealing with missing data: In medical diagnosis very often the description of patients in records lacks certain data. The algorithms have to be able to appropriately deal with such incomplete descriptions of patients.
3. Dealing with noisy data: Medical data typically suffer from uncertainty and errors. Therefore, MLT appropriate for medical applications have to have effective means for handling noisy data.
4. Transparency of diagnostic knowledge: The generated knowledge and the explanation of decisions should be transparent to the clinicians. Furthermore, they should be able to analyze and understand the generated knowledge.
5. Explanation ability: The system must be able to explain decisions when diagnosing new patients. When faced with an unexpected solution to a new problem, the clinicians shall require further explanation, otherwise they will not seriously consider the suggestions of the system.
6. Reduction of the number of tests: In medical practice, the collection of patient data is often expensive, time consuming, and harmful for the patients. Therefore, it is desirable to have a classifier/regressor that is able to reliably diagnose with a small amount of data about the patients.

Moreover, we have to be very careful not to overfit our models. Overfitting essentially occurs when a model begins to adapt too well to the specific training set. This will lead to an increase of the error when measured on an independent data set not previously seen by the model. As mentioned above, the data set is split such that 80% of the instances are randomly selected for training and the remainder are used for testing (10% for validation tasks and 10% for test tasks), and in principle they are used for different stages during the construction of a prediction model. An example of overfitting is presented in [Fig. 3.4](#) where the error of the model, during training and testing, is plotted against its complexity.

This means that when developing models and later adapting them to data, we need to have an independent data set to validate the performance. Otherwise, we would never know if our model just memorized the data or if it actually has learned

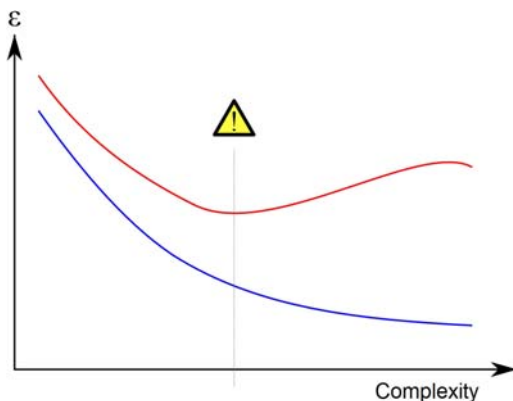


**FIGURE 3.4 Overfitting.**

Plot of the training and validation error against the complexity of the model. The *blue* and *red line* represents the error from the training and validation data, respectively. The *dashed line* marks the point indicates where overfitting starts to occur.

something. You will most likely get different results depending on the way you divide the data. Thus, you would have to do this splitting several times and use the average of all the validation results as the performance measurement. Several methods have been proposed to generate these repeated training and validation sets such as the hold out method which cuts the data in half, using the first half for training and the other one for testing or the bootstrap approach which samples from the original data with replacement meaning that some data points will be present more than once in the created data sets, but there will also be some data points left out which are used as the validation set (Efron & Tibshirani, 1997; Wehrens et al., 2000). Nevertheless, probably the currently most used method of randomly split in order to quantify generalization performance of a classifier or regressor is k-fold cross validation (Efron & Tibshirani, 1997; Kohavi, 1995; Stone, 1974).

k-fold cross-validation: This method basically randomly splits the data set into  $k$  equally sized parts. Of the  $k$  subsamples, two single subsamples are retained as the validation and test data, respectively, and the remaining  $k-2$  subsamples are used as training data. The cross-validation process is then repeated  $k$  times (the folds), with each of the  $k$  subsamples used exactly once as the validation and test data. The  $k$  results from the folds then can be averaged to produce a single estimation. The advantage of this method over repeated random subsampling is that all observations are used for both training, validation and test, and each observation is used for validation and test exactly once. 10-fold cross-validation is commonly used, but in general  $k$  remains an unfixed parameter (Seymour, 1993). An example of this sample division strategy can be found in Fig. 3.5, where  $k$  equals to 10 has been chosen.

The original set of training data is split into three groups: the first group consists of a training data set with the 80% of the data patterns; the remaining groups are the validation data set with the 10% of the patterns and, the remaining 10% of the data

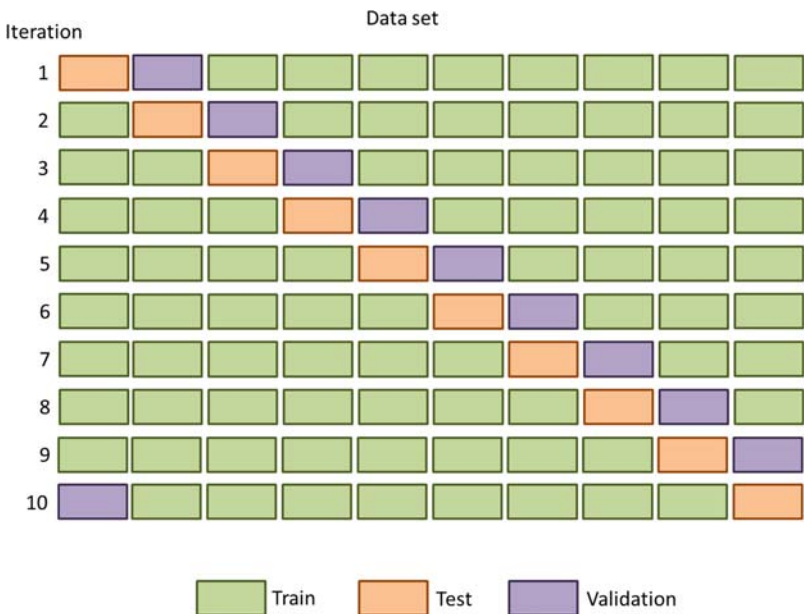


**FIGURE 3.5 k-fold cross-validation.**

Illustration of a k-fold cross-validation with  $k = 10$ . The green boxes correspond to the training data, the *orange ones* to the data that will be used for testing and the *purple ones* to the validation set.

patterns are used to evaluate the performance of the MLP. The weight configuration for the best performance reached is stored and only replaced if a better performance has occurred. In this way, the best weight configuration can be determined. This process is repeated 10 times (10-fold cross-validation) (Efron & Tibshirani, 1997; Kohavi, 1995; Stone, 1974).

## Validation with a real geometry

### How the decision support system works

The decision support system is the knowledge source, and the optimization method is the mechanism for problem solving, which returns a customized recommendation based on the query's individual information. The MLT tool should provide an appropriate recommendation which would be used by the expert clinical professionals to assess the vulnerability of the atheroma plaque. Therefore, once the ANN and SVM have been trained, these are the three steps to assist the clinicians on decisions of the stability of the atheroma plaque;

1. For a specific patient, clinicians should measure in standard coronary artery IVUS or similar clinical images the four dimensions defined as the most

influential parameters in the risk of plaque vulnerability (Cilla, Peña, & Martínez, 2012). These parameters which have been used in the algorithms as input are (i) fibrous cap thickness, (ii) stenosis ratio, (iii) lipid core length, and (iv) lipid core width.

2. The value of these four geometrical measurements will be introduced in the MLT tool developed (using either the ANN or the SVM algorithms as input).
3. Then, the medical staff would have an immediate assessment on the atheroma plaque vulnerability risk. They will get as the output of the decision support system the maximum MPS value occurred in an idealized coronary artery model with the same dimensions as those measured in the specific patient. The obtained response will be used by the experienced clinician in conjunction with other clinical variables to decide the therapies and treatments required.

### Finite element models

In order to validate the tool, two different tests have been proposed: (i) a complete patient-specific 3D geometry and (ii) three slices (2D geometry) from patient-specific IVUS images. All these geometries have been segmented and modeled using the same material parameters and boundary conditions. The 3D geometry has been selected due to the 3D parametric models is based on a 3D geometry. However, the clinicians usually measure the parameters on IVUS slices. Therefore, both kinds of geometries have been explored and tested.

Regarding the 3D geometry, the real geometry of a left coronary artery with atherosclerosis disease was obtained by IVUS images (obtained with an automatic pullback with a speed of 0.5 mm/s) from an adult male patient, Fig. 3.6. The Mimics 10.0 commercial code was used to reconstruct the 20 cross sections of the human coronary vulnerable plaque.

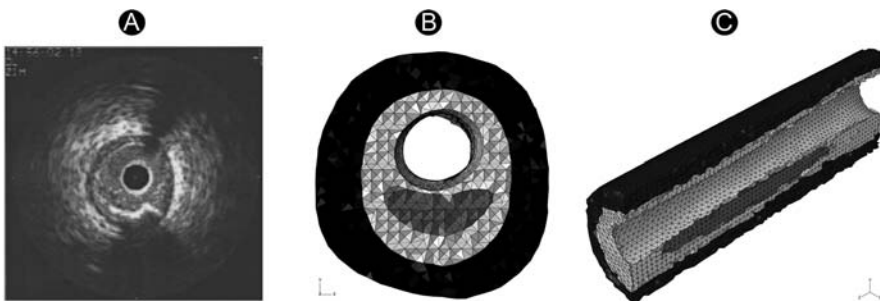


**FIGURE 3.6 3D reconstruction of a vessel with an atherosclerotic lesion.**

3D reconstruction of a vessel with an atherosclerotic lesion obtained by IVUS. (A) One of the 20 cross sections of the human coronary obtained by IVUS. (B) Cross section reconstructed from a real geometry. (C) Transversal section reconstructed from a 3D real geometry.

Dimensions of lipid core and fibrous cap thickness were measured in the geometrical reconstruction from the IVUS for the purpose of comparison with a case with similar dimensions and properties in the 3D parametric study. The 3D model was meshed with 252,216 linear tetrahedral C3D4H elements of type with similar size to those of the 3D parametric mesh, and 52,312 nodes.

Among all the 3D parametric models, the geometry with more similar parameters to the real geometry segmented from IVUS has been chosen, see [Table 3.2](#). The lipid core length is 2 mm shorter in the idealized geometry than in the specific-patient model because 8 mm is the largest value studied for the lipid core length in the parametric study. However, the influence of lipid core length on the maximum MPS is not relevant for long lipid core lengths ([Cilla, Peña, & Martínez, 2012](#)), therefore this can be considered as a good approximation.

On the other hand, three slices from 3D patient-specific geometries of coronary vessels were reconstructed and measured ([Floc'H & Vasculaire, 2009](#)). These geometries correspond to vulnerable plaque morphologies from a group of patients who underwent an IVUS examination at the Lyon cardiological hospital in the department of hemodynamics and interventional cardiology by Prof. G'erard Finet ([Floc'H & Vasculaire, 2009](#)). For each vulnerable lesion selected, the section used is the one with the most the thinnest fibrous screed. IVUS scanning was performed using the iLab platform (Boston Scientific, Watertown, MA) equipped with a 40 MHz catheter (Atlantis SR Pro 3.6F, Boston Scientific). The Mimics 10.0 commercial code was used to reconstruct the cross-sections of the three human coronary vulnerable plaque geometries, [Fig. 3.7](#).

Dimensions of lipid core and fibrous cap thickness were measured in the three slices for the purposes of comparison with a case with similar dimensions and properties in the 3D parametric study. The models were meshed with 438,120, 474,803, and 474,160 linear tetrahedral C3D4H elements, respectively, and 631,120, 672,689, and 671,923 nodes. Plane strain conditions were assumed as the plaque length is large with regard to the radial dimension and neighboring cross-sectional morphologies remain similar.

Among all the 3D parametric models, the geometries with more similar parameters to the real geometries segmented from IVUS have been chosen, see [Table 3.3](#). The lipid core length was taken as 8 mm is the largest value studied for the lipid core length in the parametric study and we have assumed plane strain. However, as

**Table 3.2** Parameters measured in the 3D reconstruction of a vessel with atherosclerotic lesion obtained by IVUS patient-specific geometry and parameters selected for the closest case from the parametric analysis.

	<i>I</i> (mm)	<i>sr</i> (%)	<i>fc</i> (mm)	<i>w</i> (%)
Real geometry	10	46.6	0.04	55
Idealized geometry	8	46.6	0.05	60

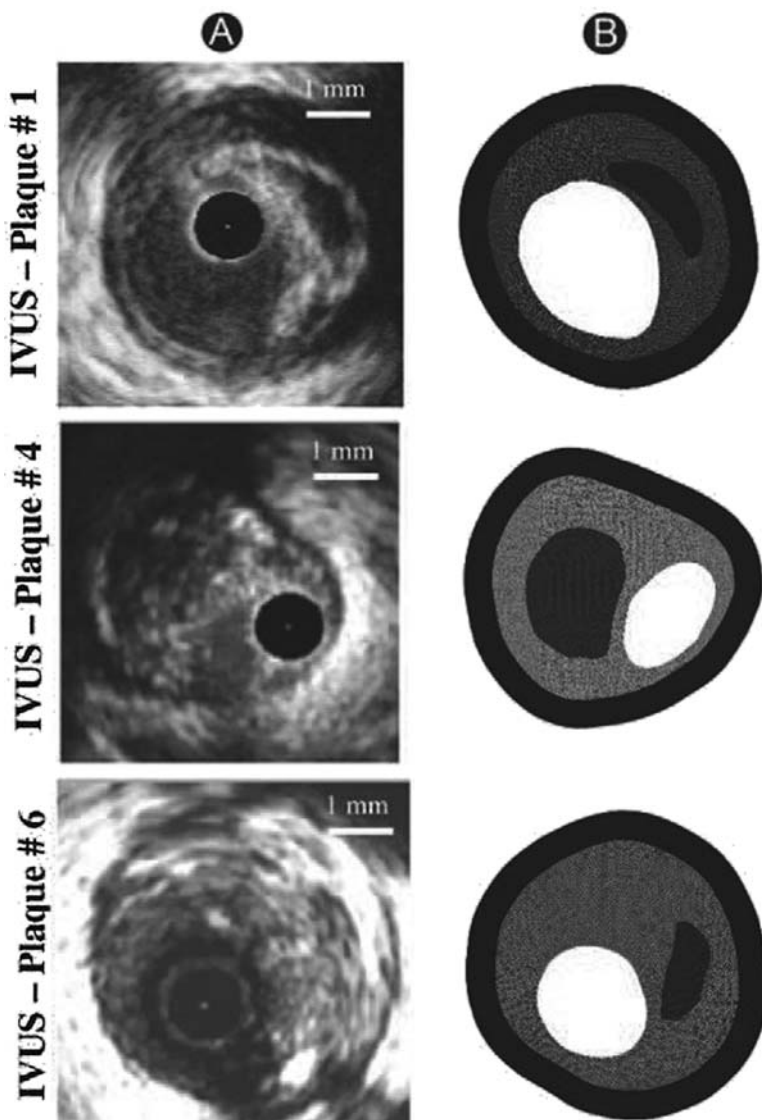


**FIGURE 3.7** 2D reconstruction of vessels with an atherosclerotic lesion.

2D reconstruction of vessels with an atherosclerotic lesion obtained by IVUS. (A) Cross sections of the human coronary obtained by IVUS. (B) Cross section reconstructed from a real geometry.

mentioned before, the influence of lipid core length variation on the maximum MPS is not relevant for long lipid core lengths (Cilla, Peña, & Martínez, 2012), so this can be considered as a good approximation. The dimensions measured on both the three real geometries obtained by IVUS images and the idealized geometries are shown in Table 3.3.

**Table 3.3** Parameters measured in the 2D reconstruction of a vessel with atherosclerotic lesion obtained by IVUS and parameters selected to compare the idealized 3D with the real geometry.

	<i>I</i> (mm)	<i>sr</i> (%)	<i>fc</i> (mm)	<i>w</i> (%)
Real geometry IVUS plaque 1	—	57.01	0.062	54.63
Idealized geometry IVUS plaque 1	8	56.7	0.05	60
Real geometry IVUS plaque 4	—	43.1	0.11	74.25
Idealized geometry IVUS plaque 4	8	46.7	0.1	75
Real geometry IVUS plaque 6	—	50.66	0.16	47.73
Idealized geometry IVUS plaque 6	8	53.3	0.15	45

## Results

Regarding the 3D IVUS geometry, the spatial distribution of the MPS is quite similar and the maximum are both located in the fibrous cap in the real reconstructed vessel and in the idealized model. The maximum MPS of the real and idealized geometries are 322 and 305 kPa (Fig. 3.8), respectively, showing a difference of 5%, and the MPS maps are similar in both cases, showing the validity of the idealized geometry, see Fig. 3.8. In both models, the maximum MPS is greater than 247 kPa, so according to the defined threshold of 247 kPa (Cilla, Peña, & Martínez, 2012), both cases could be considered as vulnerable plaque.

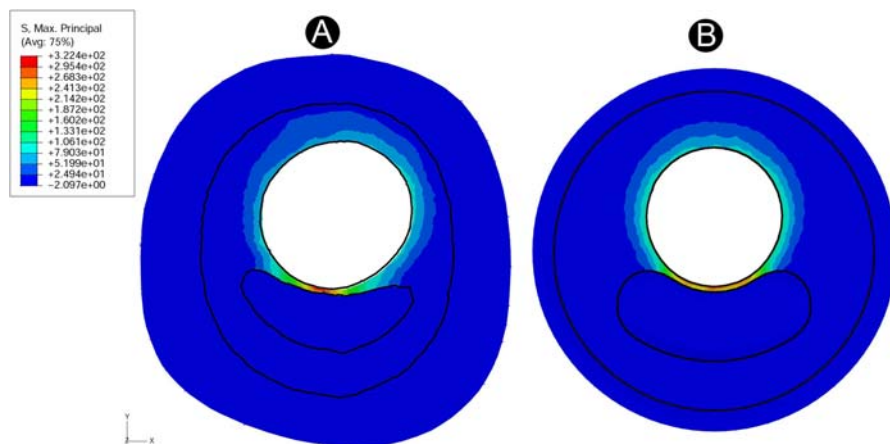


**FIGURE 3.8 Distribution 3D.**

MPS distribution (kPa). Comparison between the real geometry reconstructed from the IVUS and the idealized geometry of the 3D parametric study. (A) Real geometry reconstructed from the IVUS. (B) Idealized geometry.

The dimensions measured for the 3D real geometry obtained from IVUS images (lipid core length of 10 mm, stenosis ratio of 46.6%, fibrous cap thickness of 0.04 mm, and lipid core width of 55%) were introduced in the MLT tool, obtaining an approximation for the MPS of 315 and 308 kPa, for the SVM and ANN, respectively. This supposes an underestimated difference with respect to the reconstructed geometry of 3.2% and 4.3%, for the SVM and ANN, respectively. On the other hand, the maximum MPS for the IVUS reconstructed models for the plaques number 1, 4, and 6 are 151, 191, and 106 kPa, respectively, while for the idealized geometries 154.7 (overestimation of 2.45%), 188 (underestimation 1.59%), and 89 (underestimation of 19.1%), are obtained, respectively (Fig. 3.9).

Finally, on one hand, the MLT tool based on SVM gives a prediction of 147.7, 176.2, and 111 kPa for the plaques number 1, 4, and 6, respectively, showing differences with respect to the reconstructed geometries of 2.23% (underestimation), 8.39% (underestimation), and 4.71% (overestimation). And, on the other hand, the MLT tool based on ANN gives a prediction of 155.4, 201, and 110.7 kPa for the plaques number 1, 4, and 6, respectively. This supposes a difference with respect to the reconstructed geometry of 2.25% (overestimation), 5.23% (overestimation), and 4.43% (overestimation), for the plaques number 1, 4, and 6, respectively. It should be noted that once the parameters were measured in the IVUS, the time response to obtain the MPS value from the MLT tool was immediate for both the 2D and 3D models (less than seconds).

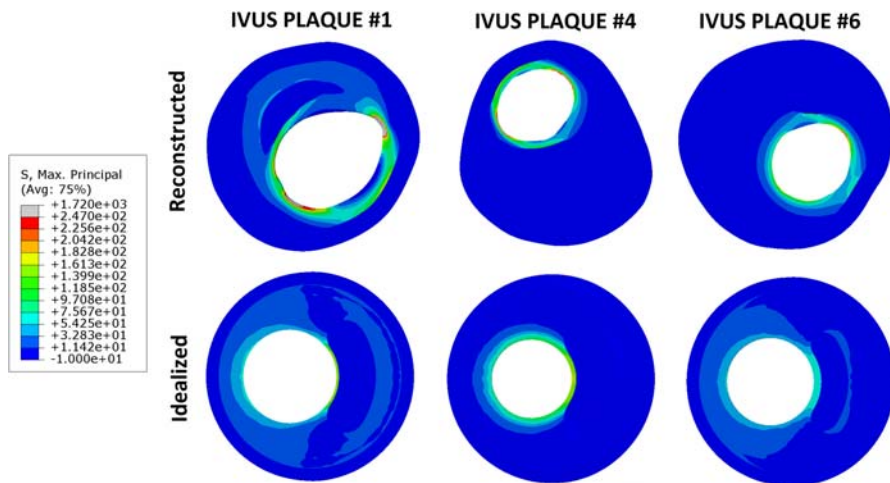


**FIGURE 3.9 Distribution 2D.**

MPS distribution (kPa). Comparison of distributions between the real geometry reconstructed from the IVUS and the idealized geometry from the 3D parametric study for plaques numbers 1, 4, and 6.

---

## Discussion

Quantifying the mechanical stresses in the wall of a vessel with atheroma plaque and, more specifically, in the area of the fibrous cap, is a very important step to predict the risk of atheroma plaque rupture based on biomechanical features. Computational models, based on FE techniques, are playing an increasing role in clinical practice, being used in cases of preoperative surgical planning with enough time to wait for the prediction and response from the computational FE model and analyze the results. However, computational models usually have the drawback of very high computational cost (time and memory consumption). However, both ANN and SVM techniques are powerful tools to replace computational simulations used in cardiovascular mechanics to quantify the vulnerable atheroma plaque risk since they provide an immediate response and, if a correct training is performed, with low relative errors (Cilla, Martínez, et al., 2012).

The idealized straight geometry used to perform the FE parametric analysis of the study (Cilla, Peña, & Martínez, 2012) has been validated comparing with the reconstructed and idealized contour maps. Therefore, according to the results obtained, the following conclusion could be drawn; the ANN and SVM techniques are able to replace FE simulations to predict the maximum MPS on both patient-specific geometries and idealized coronary models with a good error tolerance and avoiding the time-consuming 3D FE analysis.

Finally, the MLT tool was validated, obtaining a prediction error of less than 10% for all the geometries tested. In addition, it should be noted that the tool could be more precise if the number of training cases increases.

---

## Acknowledgments

The authors gratefully acknowledge research support from the Spanish Ministry of Science and Technology through research project PID2019-107517RB-I00 and the regional Government of Aragón support for the funding of the research project T24-20R. The authors thank the research support from the CIBER initiative. CIBER Actions are financed by the Instituto de Salud Carlos III with assistance from the European Regional Development Fund.

---

## References

- Alpaydin, E. (2001). *Introduction to machine learning*.
- Bishop, C. M. (1995). *Neural networks and pattern recognition*.
- Bluestein, D., Alemu, Y., Avrahami, I., Gharib, M., Dumont, K., Ricotta, J. J., & Einav, S. (2008). Influence of microcalcifications on vulnerable plaque mechanics using FSI modeling. *Journal of Biomechanics*, 41(5), 1111–1118. <https://doi.org/10.1016/j.jbiomech.2007.11.029>
- Burges, C. J. C. (1998). *Data mining and knowledge discovery* (Vols. 121–167). <https://doi.org/10.1023/A:1009715923555>

- Cheng, G. C., Loree, H. M., Kamm, R. D., Fishbein, M. C., & Lee, R. T. (1993). Distribution of circumferential stress in ruptured and stable atherosclerotic lesions: A structural analysis with histopathological correlation. *Circulation*, 87(4), 1179–1187. <https://doi.org/10.1161/01.CIR.87.4.1179>
- Cheung, N. (2001). *Machine learning techniques for medical analysis*. School of Information Technology and Electrical Engineering.
- Cilla, M., Martinez, J., Peña, E., & Martinez, M. A. (2012). Machine learning techniques as a helpful tool toward determination of plaque vulnerability. *IEEE Transactions on Biomedical Engineering*, 59(4), 1155–1161. <https://doi.org/10.1109/TBME.2012.2185495>
- Cilla, M., Peña, E., & Martínez, M. A. (2012). 3D computational parametric analysis of eccentric atheroma plaque: Influence of axial and circumferential residual stresses. *Biomechanics and Modeling in Mechanobiology*, 11(7), 1001–1013. <https://doi.org/10.1007/s10237-011-0369-0>
- Cortes, C., & Vapnik, V. (1995). Support-vector networks. *Machine Learning*, 273–297. <https://doi.org/10.1007/bf00994018>
- Davies, M. J. (1996). Stability and instability: Two faces of coronary atherosclerosis: The Paul Dudley White lecture 1995. *Circulation*, 94(8), 2013–2020. <https://doi.org/10.1161/01.CIR.94.8.2013>
- Drucker, H., Burges, C., Kaufman, L., Smola, A., & Vapnik, V. (1997). *Support vector regression machines*.
- Efron, B., & Tibshirani, R. (1997). Improvements on cross-validation: The .632+ bootstrap method. *Journal of the American Statistical Association*, 92(438), 548–560. <https://doi.org/10.1080/01621459.1997.10474007>
- Evans, B., & Fisher, D. (1992). *Process delay analyses using decision-tree induction*. Technical report CS92-06. Nashville, Tennessee: Department of Computer Science, Vanderbilt University.
- Fayyad, U. M., Weir, N., & Djorgovski, S. (1993). A machine learning system for automated cataloging of large scale sky surveys. In , Vol. 1. *Proceedings of the tenth international conference on machine learning and applications*.
- Finet, G., Ohayon, J., & Rioufol, G. (2004). Biomechanical interaction between cap thickness, lipid core composition and blood pressure in vulnerable coronary plaque: Impact on stability or instability. *Coronary Artery Disease*, 15(1), 13–20. <https://doi.org/10.1097/00019501-200402000-00003>
- Floc'H, L., & Vasculaire, M. (2009). *Application a l'identification in-vivo du module de Young local des plaques d'athérosclérose. Mécanique*.
- Fujii, K., Carlier, S. G., Mintz, G. S., Wijns, W., Colombo, A., Bose, D., Erbel, R., dde Ribamar Costa, J., Kimura, M., Sano, K., Costa, R. A., Lui, J., Stone, G. W., Moses, J. W., & Leon, M. B. (2005). Association of plaque characterization by intravascular ultrasound virtual histology and arterial remodeling. *American Journal of Cardiology*, 96, 1476–1483.
- Fulkerson, B., Michie, D., Spiegelhalter, D. J., & Taylor, C. C. (1995). Machine learning, neural and statistical classification. *Technometrics*, 37(4). <https://doi.org/10.2307/1269742>
- Gasser, T. C., Ogden, R. W., & Holzapfel, G. A. (2006). Hyperelastic modelling of arterial layers with distributed collagen fibre orientations. *Journal of The Royal Society Interface*, 3, 15–35.
- Gniadecka, M., Philipsen, P. A., Sigurdsson, S., Wessel, S., Nielsen, O. F., Christensen, D. H., Hercogova, J., Rossen, K., Thomsen, H. K., Gniadecki, R., Hansen, L. K., & Wulf, H. C. (2004). Melanoma diagnosis by Raman spectroscopy and neural networks: Structure

- alterations in proteins and lipids in intact cancer tissue. *Journal of Investigative Dermatology*, 122(2), 443–449. <https://doi.org/10.1046/j.0022-202X.2004.22208.x>
- Gurney, K. (1997). *An introduction to neural networks*.
- Handels, H., Roß, T., Kreusch, J., Wolff, H. H., & Pöppl, S. J. (1999). Feature selection for optimized skin tumor recognition using genetic algorithms. *Artificial Intelligence in Medicine*, 16(3), 283–297. [https://doi.org/10.1016/S0933-3657\(99\)00005-6](https://doi.org/10.1016/S0933-3657(99)00005-6)
- Hanke, H., Lenz, C., & Finking, G. (2001). The discovery of the pathophysiological aspects of atherosclerosis—a review. *Acta Chirurgica Belgica*, 4, 162–169.
- Holzapfel, G. A., Sommer, G., Gasser, C. T., & Regitnig, P. (2005). Determination of layer-specific mechanical properties of human coronary arteries with nonatherosclerotic intimal thickening and related constitutive modeling. *American Journal of Physiology—Heart and Circulatory Physiology*, 289(5), H2048–H2058. <https://doi.org/10.1152/ajpheart.00934.2004>
- Huang, T. M., & Kecman, V. (2005). Gene extraction for cancer diagnosis by support vector machines—an improvement. *Artificial Intelligence in Medicine*, 35(1–2), 185–194. <https://doi.org/10.1016/j.artmed.2005.01.006>
- Itchhaporia, D., Almassy, R., Kaufman, L., Snow, P., & Oetgen, W. (1995). Artificial neural networks can predict significant coronary disease. *Journal of the American College of Cardiology*, 25.
- Itchhaporia, D., Snow, P. B., Almassy, R. J., & Oetgen, W. J. (n.d.). Artificial neural networks: Current status in cardiovascular medicine. *Journal of the American College of Cardiology*, 28(2), 515–521. [https://doi.org/10.1016/0735-1097\(96\)00174-X](https://doi.org/10.1016/0735-1097(96)00174-X)
- Kohavi, R. (1995). A study of cross-validation and bootstrap for accuracy estimation and model selection. In , Vol. 1. *Proceedings of the fourteenth international joint conference on artificial intelligence* (pp. 1137–1145).
- Kononenko, I. (2001). Machine learning for medical diagnosis: History, state of the art and perspective. *Artificial Intelligence in Medicine*, 23(1), 89–109. [https://doi.org/10.1016/S0933-3657\(01\)00077-X](https://doi.org/10.1016/S0933-3657(01)00077-X)
- Langley, P., & Simon, H. A. (1995). Applications of machine learning and rule induction. *Communications of the ACM*, 38(11), 54–64. <https://doi.org/10.1145/219717.219768>
- Lavrac, N., Keravnou, E., & Zupan, B. (2000). *Intelligent data analysis in medicine*. Encyclopedia of Computer Science and Technology.
- Liu, Y. H., Lin, C. C., & Chang, F. (2005). Language identification of character images using machine learning techniques. In , Vol 2005. *Proceedings of the international conference on document analysis and recognition* (pp. 630–634). ICDAR. <https://doi.org/10.1109/ICDAR.2005.149>
- López, M., Martínez, J., Matías, J. M., Taboada, J., & Vilán, J. A. (2010a). Functional classification of ornamental stone using machine learning techniques. *Journal of Computational and Applied Mathematics*, 234(4), 1338–1345. <https://doi.org/10.1016/j.cam.2010.01.054>
- López, M., Martínez, J., Matías, J. M., Taboada, J., & Vilán, J. A. (2010b). Shape functional optimization with restrictions boosted with machine learning techniques. *Journal of Computational and Applied Mathematics*, 234, 2609–2615.
- Loree, H. M., Grodzinsky, A. J., Park, S. Y., Gibson, L. J., & Lee, R. T. (1994). Static circumferential tangential modulus of human atherosclerotic tissue. *Journal of Biomechanics*, 27(2), 195–204. [https://doi.org/10.1016/0021-9290\(94\)90209-7](https://doi.org/10.1016/0021-9290(94)90209-7)
- Marquardt, D. W (1963). An algorithm for least-squares estimation of nonlinear parameters. *SIAM Journal on Applied Mathematics*, 11, 431–441.

- McCulloch, W. S., & Pitts, W. (1943). A logical calculus of the ideas immanent in nervous activity. *The Bulletin of Mathematical Biophysics*, 5(4), 115–133. <https://doi.org/10.1007/BF02478259>
- Mehta, V. K., Deb, P. S., & Rao, D. S. (1994). Application of computer techniques in medicine. *Medical Journal, Armed Forces India*, 50(3), 215–218. [https://doi.org/10.1016/S0377-1237\(17\)31065-1](https://doi.org/10.1016/S0377-1237(17)31065-1)
- Meyer, D., Leisch, F., & Hornik, K. (2003). The support vector machine under test. *Neurocomputing*, 55(1–2), 169–186. [https://doi.org/10.1016/S0925-2312\(03\)00431-4](https://doi.org/10.1016/S0925-2312(03)00431-4)
- Mitchell, T. (1997). *Machine learning* (Vol. 1). McGraw Hil.
- Ohayon, J., Finet, G., Gharib, A. M., Herzka, D. A., Tracqui, P., Heroux, J., Rioufol, G., Kotys, M. S., Elagha, A., & Pettigrew, R. I. (2008). Necrotic core thickness and positive arterial remodeling index: Emergent biomechanical factors for evaluating the risk of plaque rupture. *American Journal of Physiology—Heart and Circulatory Physiology*, 295(2), H717–H727. <https://doi.org/10.1152/ajpheart.00005.2008>
- Ohayon, J., Teppaz, P., Finet, G., & Rioufol, G. (2001). In-vivo prediction of human coronary plaque rupture location using intravascular ultrasound and the finite element method. *Coronary Artery Disease*, 12(8), 655–663. <https://doi.org/10.1097/00019501-200112000-00009>
- Poli, R., Cagnoni, S., Livi, R., Coppini, G., & Valli, G. (1991). A neural network expert system for diagnosing and treating hypertension. *Computer*, 24(3), 64–71. <https://doi.org/10.1109/2.73514>
- Predictive interference*. (1993). Chapman and Hall.
- Scholkopf, B., & Smola, A. J. (2002). *Learning with kernels: Support vector machines, regularization, optimization, and beyond*.
- Stone, M. (1974). Cross-validatory choice and assessment of statistical predictions. *Journal of the Royal Statistical Society: Series B (Methodological)*, 111–133. <https://doi.org/10.1111/j.2517-6161.1974.tb00994.x>
- Taboada, J., Matías, J. M., Ordóñez, C., & García, P. J. (2007). Creating a quality map of a slate deposit using support vector machines. *Journal of Computational and Applied Mathematics*, 204(1), 84–94. <https://doi.org/10.1016/j.cam.2006.04.030>
- Vapnik. (1982). *Estimation of dependences based on empirical data*.
- Versluis, A., Bank, A. J., & Douglas, W. H. (2006). Fatigue and plaque rupture in myocardial infarction. *Journal of Biomechanics*, 39(2), 339–347. <https://doi.org/10.1016/j.jbiomech.2004.10.041>
- Wehrens, R., Putter, H., & Buydens, L. M. C. (2000). The bootstrap: A tutorial. *Chemometrics and Intelligent Laboratory Systems*, 54(1), 35–52. [https://doi.org/10.1016/S0169-7439\(00\)00102-7](https://doi.org/10.1016/S0169-7439(00)00102-7)
- Widrow, B., Rumelhart, D. E., & Lehr, M. A. (1994). Neural networks: Applications in industry, Business and science. *Communications of the ACM*, 37(3), 93–105. <https://doi.org/10.1145/175247.175257>
- Williamson, S. D., Lam, Y., Younis, H. F., Huang, H., Patel, S., Kaazempur-Mofrad, M. R., & Kamm, R. D. (2003). On the sensitivity of wall stresses in diseased arteries to variable material properties. *Journal of Biomechanical Engineering*, 125(1), 147–155. <https://doi.org/10.1115/1.1537736>

This page intentionally left blank

# Computational stability of human musculoskeletal systems

# 4

**Farshid Ghezelbash<sup>1</sup>, Abolfazl Shirazi-Adl<sup>1</sup>, Masoud Sharifi<sup>1</sup>, Navid Arjmand<sup>2</sup>, Babak Bazrgari<sup>3</sup>**

<sup>1</sup>*Division of Applied Mechanics, Department of Mechanical Engineering, Polytechnique Montréal, Montreal, QC, Canada;* <sup>2</sup>*Department of Mechanical Engineering, Sharif University of Technology, Tehran, Iran;* <sup>3</sup>*F. Joseph Halcomb III, MD Department of Biomedical Engineering, University of Kentucky, Lexington, KY, United States*

## Chapter outline

<b>Introduction .....</b>	85
<b>Methods .....</b>	88
Criteria of structural stability .....	88
Stability of human MS systems .....	91
<b>Stability of the human spine .....</b>	94
Role of posture and passive ligamentous stiffness .....	94
Role of load orientation and elevation .....	94
Role of coactivity .....	95
Stability-based multicriteria simulations .....	96
<b>Stability of human knee joint .....</b>	97
<b>Summary .....</b>	99
<b>Acknowledgments .....</b>	100
<b>References .....</b>	100

## Introduction

Subject to large gravity, external, inertial, and muscle loads as well as finite motions during various occupational, recreational, and regular daily living activities, human joints experience internal loads and deformations of substantial magnitudes that may approach or exceed their failure tolerance limits (Kutzner et al., 2010). This demanding mechanical environment constantly exposes the human musculoskeletal (MS) systems (e.g., spine, hip, knee) to a high risk of injuries and degenerations that are often debilitating and painful. With the epidemics of low back and osteoarthritis (OA) diseases and the aging working population of many industrial societies, the suffering, disability, health care needs, and economic burden likely continue to rise (Guilak, 2011; Katz et al., 2010; Kim, 2008; Losina et al., 2012;

Murphy et al., 2008; Ryder et al., 1997; Vos et al., 2012). With the pathoanatomy of many related diseases still unknown, there is hence a call for more effective preventive and treatment programs. The dramatic increase in the treatment interventions, especially in younger and more active age groups that expect to remain active even after surgery, as well as the ever-growing obesity and aging in the population, further highlight the gravity of the current situation.

Clinical instability is a common pathology associated with the disc degeneration, joint excessive laxity (following a ligament rupture or surgical interventions, for example), back pain, joint OA, muscle dysfunction, and implant malfunction (Ahuja et al., 2020; Cottino et al., 2016; Hurd & Snyder-Mackler, 2007; van Tunen et al., 2018). Stability is a fundamental concept in many branches of science in particular continuum mechanics, dynamics, and control. It aims to examine and improve the system performance under regular design inputs (e.g., loads) and sudden small external–internal perturbations to mitigate excessive outputs (e.g., motions), dysfunction, and failure. In engineering, sufficient stability margin is critical to safeguard the normal function and operation of a system and to avoid sudden and catastrophic failures. Depending on the system parameters and existing external interventions, instability manifests itself, locally and/or globally, as either a monotonically growing output (divergence type) or an oscillation with increasing amplitude (flutter type). In human MS systems, however, there is hardly any standard strategy to gauge clinical instability, nor a single concrete definition to apply universally. In accordance with its pivotal textbook definition of “bounded output under bounded input,” the stability appears as the ability to maintain and control, within safe limits, joint positions and motions in submaximal activities under voluntary tasks and suddenly applied internal–external disturbances. Despite foregoing definitions, there remain numerous interpretations when considering the general notion of stability (Hasan, 2005). Description of stability, however, calls for special considerations depending on the phenomenon investigated; for example, when treating disturbances in the economy, politics, weather, public health, and finally in the electromechanical, aerodynamic, or biological systems. Here to get a better grasp, the textbook definition of small and bounded deviations (within some defined norms) under small perturbations may need to be challenged and generalized. The definition of smallness in the observed deviations (outputs) should be interpreted based on the particular system under consideration and its normal (i.e., safe and painless) range of operation. Here, due considerations of the conditions of stable in the small but unstable in the large (Fig. 4.1) and unstable in the small but stable in the large (Fig. 4.1) (Leipholz, 2013) are useful when attempting to extend the notion of stability to various applications and systems. As another example, a very shallow pin–pin arc ( $h/L \ll 1$ , Fig. 4.2) under a point load at its summit does not exhibit any instability in its load–displacement response. As the ratio  $h/L$  grows (Fig. 4.2), instabilities appear initially in the small and then in the large. While all conditions associated with a temporal loss of stiffness can mathematically and rigorously be identified as an instability, a more meaningful condition and a practical marker in general in biomedical systems also need to include the risk of

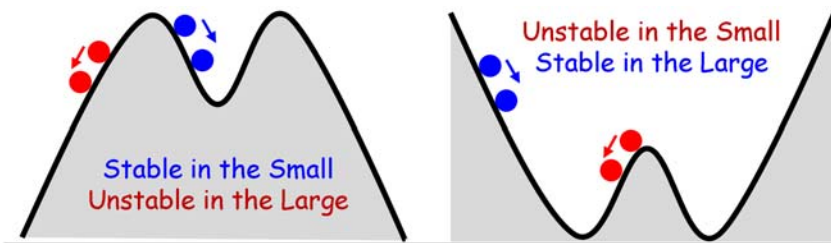


FIGURE 4.1

Schematics of two systems exhibiting opposite states of stability in the small and in the large (Leipholz, 2013).

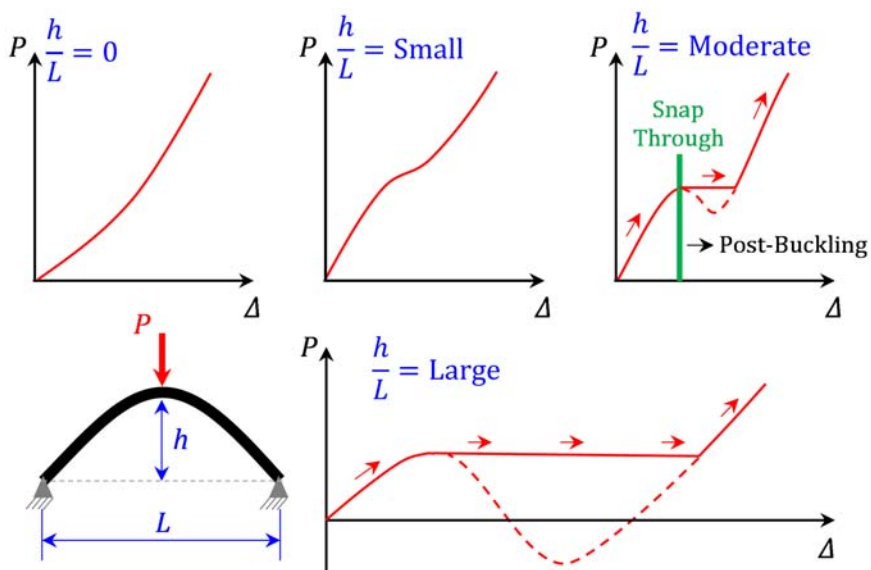


FIGURE 4.2

Schematics of an arc with variable depth ( $h$ ) under a point load at its summit showing the appearance of small and large instabilities (snap through) as the ratio  $h/L$  increases.

failure of tissues involved and perturbation of the joint normal function. In biomedical applications, this could encompass the risk of fracture—rupture, deformity, and pain. In other words, and short of a joint full dislocation or a global instability as that in a fall, events with small uncontrolled displacements that can potentially increase the risk of further injury and pain should be included.

In too many instances, researchers with structural engineering or clinical background interchange “instability” and “hypermobility” when describing the stability of MS systems. This latter term encompasses conditions as “giving way” after knee anterior cruciate ligament (ACL) rupture or excessive laxity expected after spinal decompression surgery (that requires fusion and instrumentations) and joint

arthroplasty (that could lead to failure and revision surgery). The stability in human MS systems is provided by a complex interplay between three connected subsystems: passive joint–musculature tissues with nonlinear and time-dependent properties and contributions, feed-forward voluntary and anticipatory muscle exertions, and neuromuscular subsystem with coordination and reflex feed-back contractions (Panjabi, 1992). Injuries and impairments in these subsystems (due, for example, to pain, degeneration, muscle atrophy, fatigue, altered proprioception, creep, subluxation, increased reflex delay, contamination) would deteriorate the system performance (via laxity, muscle activity–coordination–cocontraction, and latency) and stability which in turn could subsequently lead to further injuries and pain. As an example, one may recall the response of a slender column under a conservative compressive point load that is often presented in structural stability textbooks. When the column is perfectly straight, a well-known Euler buckling with a symmetric bifurcation instability mode occurs. A slight geometric imperfection or a small transverse preload, however, vanishes the bifurcation instability resulting in a nonlinear load–displacement response with positive, though initially very small, slope. In such conditions with no limit-point instability or with a continuously positive-definite second variation of the system potential energy, the strict mathematical notions of instability fail. Hypermobility and system normal operation should instead be considered when investigating the structural failure and instability.

Here in this chapter and based on years of research, we intend to introduce a single definition that unifies clinical and engineering instabilities, robust techniques to compute the stability margin, and concrete examples on the role of various parameters in enhancing or deteriorating the stability of human trunk and knee joints in static–dynamic activities.

---

## Methods

### Criteria of structural stability

Stability of a mechanical or biological structure during regular operations may be defined as its ability to withstand small (internal and/or external) disturbances without hypermobility or excessive motions that could potentially cause malfunction, damage, or pain. The gold standard in the analysis of stability of a system is to perform a nonlinear response investigation under the external loads-motions and (internal–external) perturbations. A nonlinear analysis predicts the short- and long-term effects of imperfections and disturbances on the response at all equilibrium points. In many practical applications and due to the substantial decay in or a negative slope of the system stiffness (see, for example, the complex nonlinear path in the example of Fig. 4.2), computational and experimental estimations of the entire postbuckling response however can only be handled with displacement-control protocols or temporary pseudo loads (Croll & Walker, 1972). Short of a nonlinear solution procedure, one is left with the option to exploit the nature of

linearized responses at the close neighborhoods of equilibrium states of interest. It is evident that the prediction of the limit load (reserve margin or buckling load) in this case improves as this equilibrium configuration further approaches the system instability (limit point). For example, in the arc of Fig. 4.2, the estimation of the snap-through load by linearized stability analyses continues to improve as the selected equilibrium state approaches this point. The same rule applies to imperfect structures (made of columns and plates).

To examine the stability of a mechanical system at an equilibrium state, few equivalent approaches are possible (Croll & Walker, 1972). The equilibrium state may be perturbed by a small admissible displacement field and the linear response be evaluated. If the net resultant of external and internal loads act in a direction to restore the initial position, then the system is called stable in that neighborhood. This approach is a static criterion of stability. Equivalently, an energy criterion of stability can be used in which the sign of the second variation of the system potential energy in that small perturbation is verified; a positive value assures a stable system in that neighborhood. Finally, the dynamic criterion of stability can be employed where the eigenvalues of the linearized system are examined to identify the nature of the equilibrium state in that neighborhood (expansion or decay). It is helpful here to further demonstrate these criteria in two idealized systems. First, we consider a massless inverse pendulum with a length  $L$  that holds a lumped mass  $M$  while constrained at the bottom by a spring with a linear angular stiffness  $C$  (Fig. 4.3). A similar model, with

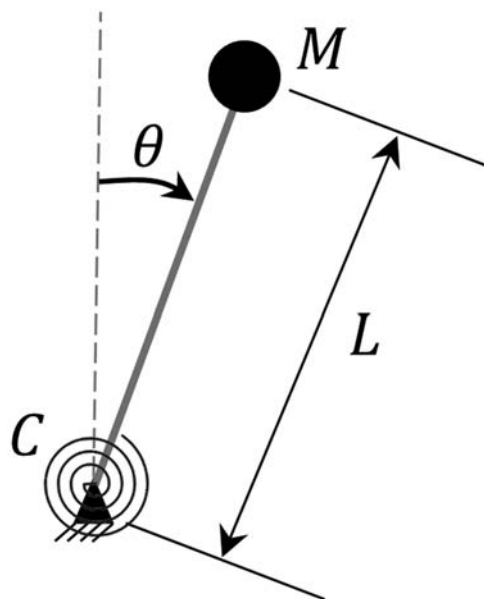


FIGURE 4.3

Schematics of a simple inverse pendulum with length  $L$ , a lumped mass  $M$  at the top, and a spring with a linear angular stiffness  $C$  at the base. The perturbed position by a small angle  $\theta$  is shown.

the ground reaction force acting instead of the angular spring at the base, has been used elsewhere to study the global stability (fall) of the human body during locomotion (Hof et al., 2005). The dynamic equation of motion at a deformed configuration (perturbed by a small angle  $\theta$ ) reads as follows:

$$ML^2\ddot{\theta} + C\theta - MgL \sin\theta = 0 \quad 4.1$$

With linearization:  $\ddot{\theta} + \left(\frac{C}{ML^2} - \frac{g}{L}\right)\theta = 0$

$$\text{Taking } \theta = Ae^{\pm\lambda t} \text{ results in } \lambda = \pm\sqrt{\left(\frac{g}{L} - \frac{C}{ML^2}\right)} \quad 4.2$$

This suggests a stable state when  $C > MgL$  and  $\lambda$  becomes complex. This condition can also be directly established via the static criterion where the internal spring resistant moment grows larger than the external moment of the weight that as a result tends to restore the perturbed system to its prior vertical position.

Another example is an idealized equilibrium model of the spine in the upright state in the sagittal plane supported passively by an angular spring  $C$  at the base (sacrum) with an initial angle  $\theta_0$  and two vertical extensor and flexor muscle groups with forces  $F_e$  and  $F_f$  at lever arms  $r_e$  and  $r_f$  and stiffnesses  $K_e$  and  $K_f$ , respectively (Fig. 4.4). Upon the perturbation of  $\theta$ , one may compute the potential energy of the

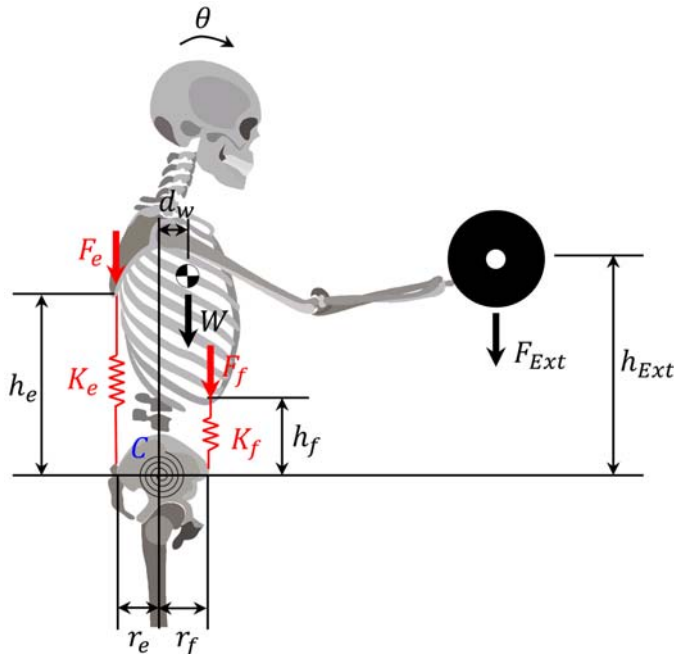


**FIGURE 4.4**

Schematics of a simplified sagittal-plane model of the trunk in the upright posture. The perturbed position is not shown (after a small angle  $\theta$ ).

system at the deformed configuration and evaluate its first variation for the static equilibrium and its second variation to examine the stability of this equilibrium state.

To maintain the equilibrium:

$$F_f r_f + F_{Ext} d_{Ext} + W d_W = F_e r_e + C \theta_0 \quad 4.3$$

and its stability

$$\left( K_e r_e^2 + K_f r_f^2 + C \right) - \left( F_f h_f + F_e h_e + W h_W + F_{Ext} h_{Ext} \right) > 0 \quad 4.4$$

where  $d_{Ext}$  and  $F_{Ext}$  as well as  $dW$  and  $W$  are the lever arm and weight of the external load in hands and the upper body, respectively. The energy criterion of stability here underlines the terms that improve the stability (first parenthesis, Eq. 4.4) and those detrimental to the stability (second parenthesis) in an upright spinal column with a weight in hands. Two interesting observations can be made here in Eq. (4.4). Activity in muscles (agonists  $F_e$  and antagonists  $F_f$ ) has opposing effects, on the one hand, it reduces the system stability through the additional compression it generates (second parenthesis); while on the other hand, it improves the stability indirectly by increasing muscle stiffnesses  $K_e$  and  $K_f$  (first parenthesis). The second observation is that while the stability increases at greater muscle lever arms (first parenthesis), it reduces at higher elevations of body weight and load in hands (second parenthesis) which is found in agreement with others (El Ouaid et al., 2016; Granata & Orishimo, 2001).

## Stability of human MS systems

As a prerequisite in the stability investigations of human MS systems, the resolution of kinetic redundancy to estimate muscle forces remains a formidable challenge. In the forward dynamics approach, forces in muscles can be calculated based on the measured activation via limited surface electromyography (EMG) and constraints on some kinematics trajectories, measured feet contact forces, joint moments, and/or objective functions (Thelen et al., 2003). In the inverse dynamics, however, joint moments are initially evaluated by equations of motion using measured joint kinematics, external loads, and body anthropometric characteristics. The redundant muscle forces are subsequently estimated, either using an optimization (DeMers et al., 2014; Kim et al., 2009; Knarr & Higginson, 2015; Lerner et al., 2014, 2015, Miller et al., 2015; Steele et al., 2012), an EMG-driven (Besier et al., 2009; Gerus et al., 2013; Kumar et al., 2012; Lloyd & Besier, 2003; Manal & Buchanan, 2013; Van Dieen & Kingma, 2005), or a combination (hybrid EMG-assisted optimization) algorithm (Gagnon et al., 2011; Jacek Cholewicki & McGill, 1994; Shamsi et al., 2017). In the optimization-based methods, muscle forces are estimated by minimizing single or multiple objective functions, such as the sum of muscle forces to different powers, system margin of stability, or muscle activations (Adouni et al., 2012;

Adouni & Shirazi-Adl, 2013a, 2013b; Arjmand & Shirazi-Adl, 2006b; Jacek Cholewicki & McGill, 1994; Gagnon et al., 2011; Lerner et al., 2014; Mokhtarzadeh et al., 2014). While EMG-driven approaches are biological in using recorded individual's muscle activity with inter- and intrasubject volitional variations, they remain susceptible to assumptions and shortcomings associated with the limited available surface EMG, location in large and deep muscles, cross-talk considerations, complexity in force–EMG relation, as well as signal processing and normalization (Arjmand et al., 2010; Gerus et al., 2013).

Using MS models of the lower extremity and human trunk with nonlinear validated finite element models of the knee joint and ligamentous thoracolumbar spine, in the first phase, we resolve the redundancy and estimate muscle forces at equilibrium states using a kinematics-driven optimization approach (Adouni et al., 2012; Adouni & Shirazi-Adl, 2013a, 2013b; Bazrgari, Shirazi-Adl, & Parnianpour, 2009; Ghezelbash, El Ouaaid, et al., 2018; Ghezelbash, Eskandari, et al., 2018; Ghezelbash et al., 2020; Marouane et al., 2016, 2014; Sharifi et al., 2020). In this way, not only joint passive properties are accurately represented but also joint moments and kinematics (from measurements) are used to compute muscle forces resulting in a synergistic passive–active protocol. By considering the measured kinematics, these kinematics-driven MS models also fall into the category of biological approaches as joint kinematics and human posture are controlled, voluntarily in feed-forward or reflexively in feed-back, in static and transient movements by the central nervous system (CNS). Through the prescribed kinematics, the MS model hence accounts for subject-specific neural responses affected by fatigue, disorders, and pain.

With complete characterization of the joint equilibrium states, particularly calculation of muscle forces using an iterative procedure in the first phase as described above, the stability of the system can subsequently be quantified. To do so, earlier constraints on the joint angles (i.e., vertebrae in the spine model, ankle–knee–hip joints in the lower extremity model) are released (i.e., unconstrained joints) and each muscle is replaced with a uniaxial spring element between its insertion (or wrapping) points while carrying the already estimated muscle force. Stiffness of each spring ( $K = q F/L$ ) is assumed proportional to its estimated muscle force ( $F$ ) and inversely proportional to its current length ( $L$ ) (Bergmark, 1989; Crisco 3rd & Panjabi, 1991) with  $q$  as a constant dimensionless muscle stiffness coefficient taken the same for all muscles. Despite the complex relation between the muscle stiffness, muscle activation, and rate of change in muscle length, this model is acceptable given the small perturbations around the linearized equilibrium states (Cholewicki & McGill, 1995; Gardner-Morse & Stokes, 1998). Linear buckling, linear perturbation, and free vibration analyses at the deformed configurations are then carried out with different values of  $q$  in order to identify the critical (minimum)  $q$  at which the system ceases to be stable (Bazrgari, Shirazi-Adl, & Parnianpour, 2009; Bazrgari, Shirazi-Adl, & Lariviere, 2009; El Ouaaid et al., 2018; El-Rich et al., 2004;

Sharifi et al., 2017). This manifests itself (while reducing the coefficient  $q$ ) either when the estimated displacement under the unit load in the perturbation approach blows up, when the system margin (reserved load) disappears in the buckling analysis, or finally when the lowest eigenvalue approaches nil in the free vibration analysis. At each equilibrium point under constant muscle forces, a larger critical  $q$  indicates a less stable system requiring greater contribution from muscles while at the extreme a critical  $q = 0$  signifies that no muscle stiffness is required to maintain stability (though activation is still needed for equilibrium) (Arjmand & Shirazi-Adl, 2006a; Bazrgari et al., 2007; Farshid Ghezelbash et al., 2017; Gardner-Morse & Stokes, 1998).

Buckling analysis at a given  $q$  predicts the reserve additional load (buckling load) that the system can support before exhibiting instability. At the neutral stable condition (critical  $q$ ), however, this buckling load approaches zero. The perturbation analysis, on the other hand, quantifies the displacement response under a small load that tends to infinity as the system approaches instability. Therefore, as demonstrated in Fig. 4.5, in the perturbation and buckling analyses, a unit force (along the ground reaction force on the foot in the lower extremity model and along loads in hands in the trunk model) is applied and the response is estimated under varying muscle stiffness coefficient values,  $q$ .

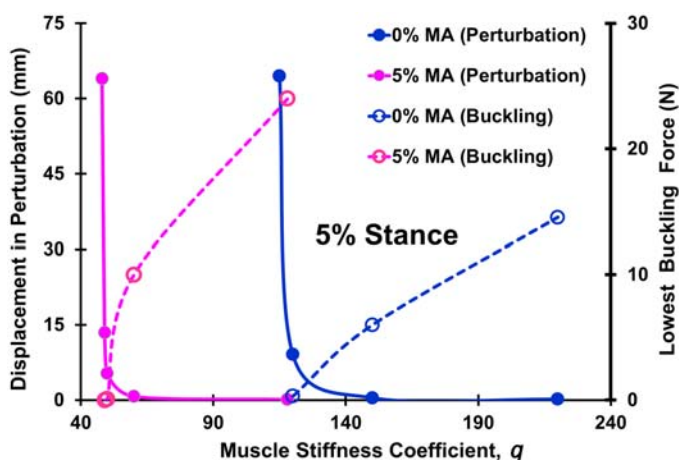


**FIGURE 4.5**

Displacement at unit perturbation load along the ground reaction force (on the left side) and lowest buckling force (on the right side) at different values of  $q$  (muscle stiffness coefficient) in linear perturbation and buckling analyses performed at the deformed loaded configurations of the intact knee joint at the 5% stance of gait. Results are also given for the case assuming minimal activity (preactivation) of 5% of the maximum force in all muscles.

## Stability of the human spine

Analogous to an imperfect column under a conservative compression force, the human ligamentous thoracolumbar and lumbar spines devoid of muscles exhibit hypermobility under compression loads as low as ~20 and 90 N, respectively (Crisco 3rd & Panjabi, 1991; Morris et al., 1961; Shirazi-Adl & Parnianpour, 2000). It is hence evident that other mechanisms involving the trunk musculature, with preactive as well as voluntary-reflex exertions, should intervene to control and stabilize human motions in various daily activities and sudden loading conditions. In fact, model and experimental studies have long exploited an idealized wrapping compression loading that follows the deformed curvature of multimotion segment spines in an attempt to circumvent the instability while applying meaningful compression forces (Patwardhan et al., 1999; Rohlmann et al., 2006; Shirazi-Adl, 2006; Shirazi-Adl & Parnianpour, 2000). Here, few examples are presented to demonstrate the crucial stabilizing mechanisms.

### Role of posture and passive ligamentous stiffness

The moment-rotation stiffness of the passive spinal motion segments substantially increases at larger moments and angles (Shirazi-Adl, 2006). In parallel, the passive ligamentous resistance in various directions also markedly augments in presence of greater axial compression preload that is always physiologically present and often applied as a follower load (Shirazi-Adl, 2006; Stokes & Gardner-Morse, 2003; Zhang et al., 2020). The forgoing effects considerably influence the spinal stability in static and dynamic loading conditions. Our earlier works have demonstrated the stabilizing effect of initially flexed postures under vertical seat vibrations (Bazrgari, Shirazi-Adl, & Lariviere, 2009; Bazrgari, Shirazi-Adl, & Kasra, 2008; Bazrgari, Shirazi-Adl, Trottier, & Mathieu, 2008) and sudden perturbations (Shahvarpour et al., 2015). In a study on the stability of spine (critical  $q$ ) in unconstrained forward flexion-backward extension tasks of healthy subjects at three speeds of low (~6s), intermediate (~3s), and fast (<2s), the estimated critical  $q$  dropped to as low as nil at larger trunk flexion angles (Fig. 4.6). This observation is due primarily to the greater stiffness of the passive ligamentous spine at larger flexion and compression. Due also to the associated higher activity in muscles, the fastest flexion-extension yields a more stable response.

In agreement with forgoing observations, the trunk stability also increases in larger flexion with loads in hands but deteriorates in the lighter tasks and at the upright relaxed standing (beginning and end of movements in Fig. 4.6) and in presence of injuries (Arjmand & Shirazi-Adl, 2006a; El-Rich et al., 2004).

### Role of load orientation and elevation

In addition to the posture, the load orientation and elevation also influence the spinal stability response. Earlier works (Arjmand et al., 2008; El Ouaaid et al., 2013;

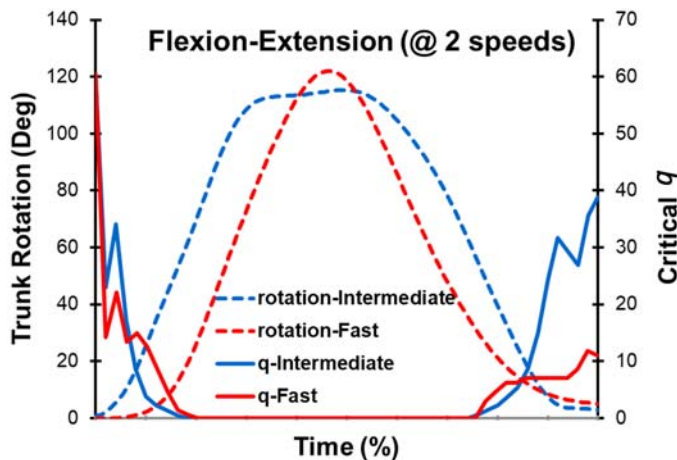


**FIGURE 4.6**

Computed temporal variation of minimum (critical) muscle stiffness coefficient,  $q$ , (right axis) required for the trunk stability of one subject who performed trunk flexion–extension movement at two speeds (fast and intermediate lasting, respectively, <2 and ~3 s). Lower  $q$  values indicate higher trunk stability and  $q = 0$  suggests that no muscle stiffness is needed to stabilize the trunk. The measured (prescribed) trunk rotations are also shown (left axis).

Granata & Orishimo, 2001 have shown that the trunk stability margin decreases with load elevation. Besides, the load orientation also affects the trunk stability. Vertical gravity loads most deteriorate the trunk stability while in contrast upward pull forces followed by horizontal pull forces enhance the trunk stability (El Ouaaid et al., 2016). The deteriorating effect of a 9 kg weight at higher elevations at a constant 30 cm lever arm to the S1 on the trunk stability is evident in Fig. 4.7 (Arjmand et al., 2008) where the critical  $q$  monotonically increases with the weight elevation.

### Role of coactivity

As in any other human joint, the trunk stability depends on the preactivation or coactivation in trunk muscles. Such preactivities stiffen the spine and increase the post-perturbation trunk stability (Bazrgari, Shirazi-Adl, & Lariviere, 2009; Shahvarpour et al., 2015). Coactivation in abdominal muscles are effective means to stiffen and stabilize the spine especially in the upright neutral posture where the spine is found least stable (Arjmand et al., 2008). Moderate coactivation in abdominals are shown in Fig. 4.7 to stabilize the spine especially when the weight in hands is held at higher elevations. This stabilizing effect, however, disappears and even reverses to deteriorate the trunk stability when the coactivation in abdominal muscles further

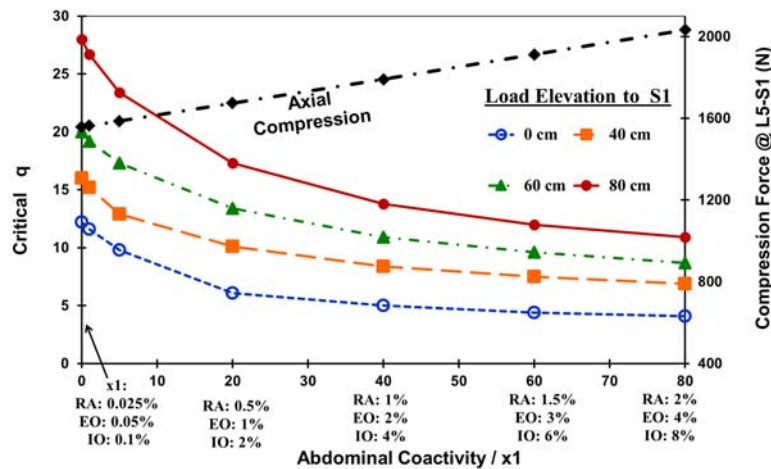


**FIGURE 4.7**

Computed variation of the critical muscle stiffness coefficient (left axis) and spinal compression (right axis) for different prescribed coactivation levels in abdominal muscles as external load elevation in hands rises from 0 (at the S1 level) to 40, 60, and 80 cm, while the lever arm in the sagittal plane remains constant at 30 cm. The relative activity of the internal oblique (IO) to that of the external oblique (EO) and of the EO to the rectus abdominus (RA) remains constant at 2 in all cases. For an identical level of abdominal coactivities, compression on spine does not vary with load elevation but the critical  $q$  does (i.e., stability margin decreases).

increases (El Ouaaid et al., 2013). In this respect, it is important to note that increases in activity, preactivation, and antagonistic coactivation in muscles on the one hand increase the spine stiffness and stability by enhancing the stiffness in the passive ligamentous spine (via added compression) and muscles (via added antagonist and agonist activation) while on the other hand deteriorate the spinal stability due to the added compression on the spine. The constant increase in the compression on spine with the coactivity level in abdominal muscles is also evident in Fig. 4.7.

### Stability-based multicriteria simulations

During daily activities, the CNS maintains both equilibrium and stability by assigning appropriate forces to agonistic and antagonistic muscles. EMG activities of abdominal (antagonistic) and extensor (agonistic) muscles have been measured to concurrently increase in response to the deterioration in the spinal stability when a given hands-held load, while at a constant horizontal lever arm, is lifted at higher elevations (Granata & Orishimo, 2001). Concurrent activations of antagonistic and

agonistic muscles at the presence of constant external moments cannot be predicted by traditional optimization-driven models that are developed based only on equilibrium requirements. Therefore, stability-driven MS models of the spine have emerged to resolve the joint redundancy problem by taking into account both equilibrium and stability demands. As indicated earlier, for a stable MS spine model at a given activity, the Hessian matrix of the model potential energy should remain positive definite (i.e., with eigenvalues  $>0$ ) (Cholewicki & McGill, 1996; Howarth et al., 2004).

Granata and Wilson (Granata & Wilson, 2001) developed a simplified, two-joint, six degrees of freedom biomechanical model of the spine in which forces in 12 trunk muscles were estimated while satisfying both the equilibrium and stability conditions. They showed that muscle activity patterns are predicted more accurately (compared to *in vivo* EMG activities) once the stability criterion is also incorporated into the optimization algorithm. Hajihosseinali et al. (Hajihosseinali et al., 2015) developed a more anatomically detailed (18 rotational-degrees-of-freedom) stability-driven model of the human spine that used a multicriteria optimization algorithm considering both equilibrium and stability demands. They simulated several symmetric tasks in upright and flexed standing postures. Unlike the pure optimization-driven model, this stability-driven model could predict abdominal (antagonistic) cocontractions that, in agreement with EMG data, increased as load elevation rose at a constant horizontal moment arm.

Traditional EMG-assisted models also calculate muscle forces based solely on moment equilibrium requirements with no consideration for the stability. For example, an EMG-assisted MS trunk model predicted results that were verified to be associated with an unstable spine during some static tasks that were otherwise stable, i.e., when carried out by a subject (Mohammadi et al., 2015). This is an indication of an improper prediction of muscle forces by the traditional equilibrium-based EMG-assisted models. To resolve this shortcoming, Samadi and Arjmand (Samadi & Arjmand, 2018) developed a novel stability-based EMG-assisted optimization algorithm in which trunk muscle forces were estimated while satisfying both equilibrium and stability conditions. They predicted different, generally larger, muscle forces and spinal loads compared to the conventional equilibrium-based EMG-assisted models.

---

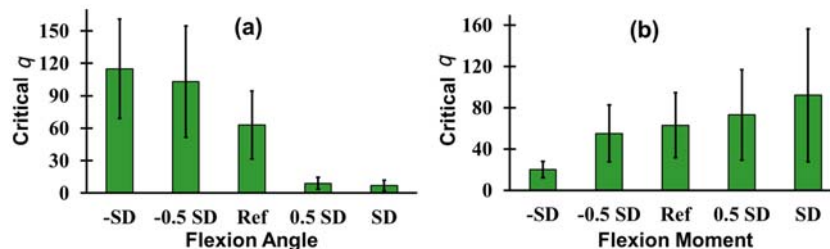
## Stability of human knee joint

Stability of the human knee joints, similar to other human articulations, is maintained by an intricate interplay between active musculature and passive tissues. Knee instability usually manifests itself in giving way, excessive laxity and pain. In a clinical environment, the knee joint stability is commonly examined by its laxity

under external loads and disturbances; for example, when Lachman and pivot shift tests are performed to detect ACL injuries (Galway & MacIntosh, 1980; Torg et al., 1976).

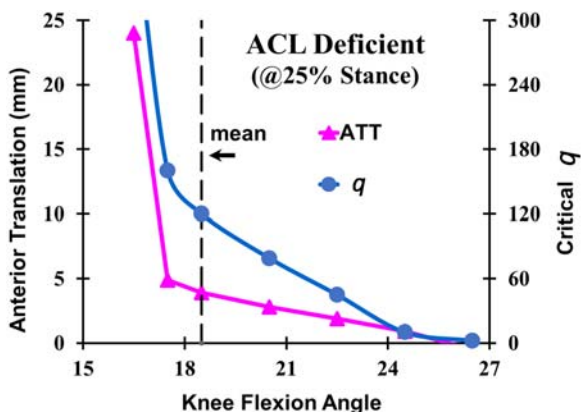
Our earlier MS model studies of the lower extremity in gait have demonstrated the crucial roles of the knee flexion angle and activation in muscles on the stability of the human knee joint in intact and ACL deficient conditions (Sharifi et al., 2017, 2018, 2020; Sharifi & Shirazi-Adl, 2021). As the angles and moments at the knee joint are varied within their reported mean  $\pm$  one standard deviation (SD) of the recorded values in gait of healthy subjects (Sharifi et al., 2020), the knee stability and critical  $q$  are substantially influenced by changes in the knee flexion angle, sagittal moment, and hence muscle activation. For example, at 25% instance of gait stance, the critical  $q$  drops (i.e., more stable knee joint) as the flexion angle increases and flexion moment decreases (Fig. 4.8).

Following an ACL rupture, the anterior tibial translation and critical  $q$  substantially increase to levels indicating an unstable joint in which case a convergent solution is no more possible (Sharifi & Shirazi-Adl, 2021). Under constant input gait kinematics–kinetics at hip–knee–ankle joints, the knee stability, however, improves as the knee flexion angle alone is increased by only few degrees beyond its mean of reported data but conversely deteriorates as the flexion angle decreases (Fig. 4.9 at 25% stance). Under an increased knee flexion angle, an ACL deficient joint can regain its near-normal function and become as or more stable than its pre-injury intact level. ACL-deficient joint stability is also markedly dependent on the activity index (ratio of muscle forces in ACL antagonists (gastrocnemii and quadriceps) to ACL agonists (hamstrings)); it increases as this index drops (Sharifi & Shirazi-Adl, 2021). At the first-half of gait stance, this could happen at a smaller knee sagittal moment resulting in lower forces in quadriceps (ACL antagonists) and in the presence of coactivity in hamstrings (ACL agonists). At the second-half of stance under extension moments with activated flexors, on the other hand, this occurs as forces in gastrocnemii (ACL antagonists) diminish compared to those



**FIGURE 4.8**

Predictions ( $\text{mean} \pm \text{SD}$ ) at 25% stance of gait of the critical muscle stiffness coefficient  $q$  for different knee moments and angles as knee angles and moments (in three directions) alter within one SD of their mean.

**FIGURE 4.9**

Computed anterior tibial translation (ATT, left axis) and critical muscle stiffness coefficient  $q$  (right axis) with variations in the knee flexion angle from its mean of reported data at 25% gait stance in the ACL-deficient joint.

in hamstrings. These results help improve our understanding of the biomechanics and stability of ACL-deficient joints toward improved prevention, treatment, and rehabilitation strategies.

## Summary

Quantification of the stability margin (reserve load) of the intact/injured/reconstructed human MS systems is crucial in performance evaluation, injury prevention, implant design, and treatment managements. Despite apparently diverse interpretations of stability that are commonly used in various applications, a unified definition based on hypermobility can be considered in both engineering and clinical disciplines. This definition encompasses the anticipated system or joint operation and normal function with minimal risk of damage, injury, and pain. Joint hypermobility (instability) is however associated with pain, implant failure, injury, and OA (Mulvey et al., 2013). Dynamic stability of human articulations in daily activities and sudden loading conditions is maintained by a delicate interplay between passive tissues and active musculature (voluntary and reflex). The contribution of these subsystems varies with alterations in posture, alignment, muscle preactivation/coactivation, muscle reflex response, external loading, and therapeutic devices (e.g., braces, exoskeletons, wedged insoles, footwears). Understanding the mechanisms affecting the stability response of human MS systems can hence be beneficial in the prevention, rehabilitation, and treatment of associated disorders.

---

## Acknowledgments

The current work was supported by a grant from the Natural Sciences and Engineering Research Council of Canada (RGPIN5596).

---

## References

- Adouni, M., & Shirazi-Adl, A. (2013a). Evaluation of knee joint muscle forces and tissue stresses-strains during gait in severe OA versus normal subjects. *Journal of Orthopaedic Research*, 32(1), 69–78.
- Adouni, M., & Shirazi-Adl, A. (2013b). Consideration of equilibrium equations at the hip joint alongside those at the knee and ankle joints has mixed effects on knee joint response during gait. *Journal of Biomechanics*, 46(3), 619–624.
- Adouni, M., Shirazi-Adl, A., & Shirazi, R. (2012). Computational biodynamics of human knee joint in gait: From muscle forces to cartilage stresses. *Journal of Biomechanics*, 45(12), 2149–2156. <https://doi.org/10.1016/j.jbiomech.2012.05.040>
- Ahuja, S., Moideen, A. N., Dudhniwala, A. G., Karatsis, E., Papadakis, L., & Varitis, E. (2020). Lumbar stability following graded unilateral and bilateral facetectomy: A finite element model study. *Clin Biomech (Bristol, Avon)*, 75, 105011. <https://doi.org/10.1016/j.clinbiomech.2020.105011>
- Arjmand, N., Gagnon, D., Plamondon, A., Shirazi-Adl, A., & Lariviere, C. (2010). A comparative study of two trunk biomechanical models under symmetric and asymmetric loadings. *Journal of Biomechanics*, 43(3), 485–491.
- Arjmand, N., & Shirazi-Adl, A. (2006a). Model and in vivo studies on human trunk load partitioning and stability in isometric forward flexions. *Journal of Biomechanics*, 39(3), 510–521.
- Arjmand, N., & Shirazi-Adl, A. (2006b). Sensitivity of kinematics-based model predictions to optimization criteria in static lifting tasks. *J Medical Engineering Physics*, 28(6), 504–514.
- Arjmand, N., Shirazi-Adl, A., & Parnianpour, M. (2008). Relative efficiency of abdominal muscles in spine stability. *Computer Methods in Biomechanics and Biomedical Engineering*, 11(3), 291–299. <https://doi.org/10.1080/10255840802020404>
- Bazrgari, B., Shirazi-Adl, A., & Arjmand, N. (2007). Analysis of squat and stoop dynamic liftings: Muscle forces and internal spinal loads. *J European Spine Journal*, 16(5), 687–699.
- Bazrgari, B., Shirazi-Adl, A., & Kasra, M. (2008). Computation of trunk muscle forces, spinal loads and stability in whole-body vibration. *Journal of Sound Vibration*, 318(4–5), 1334–1347.
- Bazrgari, B., Shirazi-Adl, A., & Lariviere, C. (2009). Trunk response analysis under sudden forward perturbations using a kinematics-driven model. *J Journal of Biomechanics*, 42(9), 1193–1200.
- Bazrgari, B., Shirazi-Adl, A., & Parnianpour, M. (2009). Transient analysis of trunk response in sudden release loading using kinematics-driven finite element model. *J Clinical Biomechanics*, 24(4), 341–347.

- Bazrgari, B., Shirazi-Adl, A., Trottier, M., & Mathieu, P. (2008). Computation of trunk equilibrium and stability in free flexion–extension movements at different velocities. *Journal of Biomechanics*, 41(2), 412–421.
- Bergmark, A. (1989). Stability of the lumbar spine: A study in mechanical engineering. *Acta Orthopaedica Scandinavica*, 60(Suppl. 230), 1–54.
- Besier, T. F., Fredericson, M., Gold, G. E., Beaupré, G. S., & Delp, S. L. (2009). Knee muscle forces during walking and running in patellofemoral pain patients and pain-free controls. *Journal of Biomechanics*, 42(7), 898–905.
- Cholewicki, Jacek, & McGill, S. M. (1994). EMG assisted optimization: A hybrid approach for estimating muscle forces in an indeterminate biomechanical model. *Journal of Biomechanics*, 27(10), 1287–1289.
- Cholewicki, J., & McGill, S. M. (1995). Relationship between muscle force and stiffness in the whole mammalian muscle: A simulation study. *J Biomech Eng*, 117(3), 339–342. <https://doi.org/10.1115/1.2794189>
- Cholewicki, J., & McGill, S. M. (1996). Mechanical stability of the in vivo lumbar spine: Implications for injury and chronic low back pain. *Clinical Biomechanics*, 11(1), 1–15. [https://doi.org/10.1016/0268-0033\(95\)00035-6](https://doi.org/10.1016/0268-0033(95)00035-6)
- Cottino, U., Sculco, P. K., Sierra, R. J., & Abdel, M. P. (2016). Instability after total knee arthroplasty. *Orthop Clin North Am*, 47(2), 311–316. <https://doi.org/10.1016/j.ocl.2015.09.007>
- Crisco, J., 3rd, & Panjabi, M. M. (1991). The intersegmental and multisegmental muscles of the lumbar spine. A biomechanical model comparing lateral stabilizing potential. *Spine*, 16(7), 793–799.
- Croll, J. G. A., & Walker, A. C. (1972). *Elements of structural stability*. John Wiley & Sons.
- DeMers, M. S., Pal, S., & Delp, S. L. (2014). Changes in tibiofemoral forces due to variations in muscle activity during walking. *Journal of Orthopaedic Research*, 32(6), 769–776.
- El Ouaaid, Z., Shirazi-Adl, A., & Plamondon, A. (2016). Effects of variation in external pulling force magnitude, elevation, and orientation on trunk muscle forces, spinal loads and stability. *Journal of Biomechanics*, 49(6), 946–952.
- El Ouaaid, Z., Shirazi-Adl, A., & Plamondon, A. (2018). Trunk response and stability in standing under sagittal-symmetric pull–push forces at different orientations, elevations and magnitudes. *Journal of Biomechanics*, 70, 166–174.
- El Ouaaid, Z., Shirazi-Adl, A., Plamondon, A., & Larivière, C. (2013). Trunk strength, muscle activity and spinal loads in maximum isometric flexion and extension exertions: A combined in vivo-computational study. *Journal of Biomechanics*, 46(13), 2228–2235.
- El-Rich, M., Shirazi-Adl, A., & Arjmand, N. (2004). Muscle activity, internal loads, and stability of the human spine in standing postures: Combined model and in vivo studies. *Spine*, 29(23), 2633–2642.
- Gagnon, D., Arjmand, N., Plamondon, A., Shirazi-Adl, A., & Larivière, C. (2011). An improved multi-joint EMG-assisted optimization approach to estimate joint and muscle forces in a musculoskeletal model of the lumbar spine. *Journal of Biomechanics*, 44(8), 1521–1529.
- Galway, H. R., & MacIntosh, D. L. (1980). The lateral pivot shift: A symptom and sign of anterior cruciate ligament insufficiency. *Clin Orthop Relat Res*, 147, 45–50.
- Gardner-Morse, M. G., & Stokes, I. A. (1998). The effects of abdominal muscle coactivation on lumbar spine stability. *Spine*, 23(1), 86–91.
- Gerus, P., Sartori, M., Besier, T. F., Fregly, B. J., Delp, S. L., Banks, S. A., Pandy, M. G., D'Lima, D. D., & Lloyd, D. G. (2013). Subject-specific knee joint geometry improves

- predictions of medial tibiofemoral contact forces. *Journal of Biomechanics*, 46(16), 2778–2786.
- Ghezelbash, F., El Ouaaid, Z., Shirazi-Adl, A., Plamondon, A., & Arjmand, N. (2018). Trunk musculoskeletal response in maximum voluntary exertions: A combined measurement-modeling investigation. *Journal of Biomechanics*, 70, 124–133.
- Ghezelbash, F., Eskandari, A., Shirazi-Adl, A., Arjmand, N., El-Ouaaid, Z., & Plamondon, A. (2018). Effects of motion segment simulation and joint positioning on spinal loads in trunk musculoskeletal models. *Journal of Biomechanics*, 70, 149–156.
- Ghezelbash, F., Shirazi-Adl, A., El Ouaaid, Z., Plamondon, A., & Arjmand, N. (2020). Subject-specific regression equations to estimate lower spinal loads during symmetric and asymmetric static lifting. *Journal of Biomechanics*, 102, 109550.
- Ghezelbash, Farshid, Shirazi-Adl, A., Plamondon, A., Arjmand, N., & Parnianpour, M. (2017). Obesity and obesity shape markedly influence spine biomechanics: A subject-specific risk assessment model. *Annals of Biomedical Engineering*, 45(10), 2373–2382.
- Granata, K. P., & Orishimo, K. F. (2001). Response of trunk muscle coactivation to changes in spinal stability. *Journal of Biomechanics*, 34(9), 1117–1123.
- Granata, K. P., & Wilson, S. E. (2001). Trunk posture and spinal stability. *Clinical Biomechanics*, 16(8), 650–659. [https://doi.org/10.1016/S0268-0033\(01\)00064-X](https://doi.org/10.1016/S0268-0033(01)00064-X)
- Guilak, F. (2011). Biomechanical factors in osteoarthritis. *Best Practice & Research Clinical Rheumatology*, 25(6), 815–823.
- Hajhosseinali, M., Arjmand, N., & Shirazi-Adl, A. (2015). Effect of body weight on spinal loads in various activities: A personalized biomechanical modeling approach. *Journal of Biomechanics*, 48(2), 276–282. <https://doi.org/10.1016/j.jbiomech.2014.11.033>
- Hasan, Z. (2005). The human motor control system's response to mechanical perturbation: Should it, can it and does it ensure stability? *Journal of Motor Behavior*, 37(6), 484–493.
- Hof, A., Gazendam, M., & Sinke, W. (2005). The condition for dynamic stability. *Journal of Biomechanics*, 38(1), 1–8.
- Howarth, S. J., Allison, A. E., Grenier, S. G., Cholewicki, J., & McGill, S. M. (2004). On the implications of interpreting the stability index: A spine example. *Journal of Biomechanics*, 37(8), 1147–1154. <https://doi.org/10.1016/j.jbiomech.2003.12.038>
- Hurd, W. J., & Snyder-Mackler, L. (2007). Knee instability after acute ACL rupture affects movement patterns during the mid-stance phase of gait. *J Orthop Res*, 25(10), 1369–1377. <https://doi.org/10.1002/jor.20440>
- Katz, J. N., Earp, B. E., & Gomoll, A. H. (2010). Surgical management of osteoarthritis. *Arthritis Care & Research*, 62(9), 1220.
- Kim, S. (2008). Changes in surgical loads and economic burden of hip and knee replacements in the US: 1997–2004. *Arthritis Care & Research*, 59(4), 481–488.
- Kim, H. J., Fernandez, J. W., Akbarshahi, M., Walter, J. P., Fregly, B. J., & Pandy, M. G. (2009). Evaluation of predicted knee-joint muscle forces during gait using an instrumented knee implant. *Journal of Orthopaedic Research*, 27(10), 1326–1331.
- Knarr, B. A., & Higginson, J. S. (2015). Practical approach to subject-specific estimation of knee joint contact force. *Journal of Biomechanics*, 48(11), 2897–2902.
- Kumar, D., Rudolph, K. S., & Manal, K. T. (2012). EMG-driven modeling approach to muscle force and joint load estimations: Case study in knee osteoarthritis. *Journal of Orthopaedic Research*, 30(3), 377–383.
- Kutzner, I., Heinlein, B., Graichen, F., Bender, A., Rohlmann, A., Halder, A., Beier, A., & Bergmann, G. (2010). Loading of the knee joint during activities of daily living measured in vivo in five subjects. *Journal of Biomechanics*, 43(11), 2164–2173.

- Leipholz, H. (2013). *Stability theory: An introduction to the stability of dynamic systems and rigid bodies*. Springer-Verlag.
- Lerner, Z. F., DeMers, M. S., Delp, S. L., & Browning, R. C. (2015). How tibiofemoral alignment and contact locations affect predictions of medial and lateral tibiofemoral contact forces. *Journal of Biomechanics*, 48(4), 644–650.
- Lerner, Z. F., Haight, D. J., DeMers, M. S., Board, W. J., & Browning, R. C. (2014). The effects of walking speed on tibiofemoral loading estimated via musculoskeletal modeling. *Journal of Applied Biomechanics*, 30(2), 197.
- Lloyd, D. G., & Besier, T. F. (2003). An EMG-driven musculoskeletal model to estimate muscle forces and knee joint moments in vivo. *Journal of Biomechanics*, 36(6), 765–776.
- Losina, E., Thornhill, T. S., Rome, B. N., Wright, J., & Katz, J. N. (2012). The dramatic increase in total knee replacement utilization rates in the United States cannot be fully explained by growth in population size and the obesity epidemic. *The Journal of Bone Joint Surgery. American Volume*, 94(3), 201.
- Manal, K., & Buchanan, T. S. (2013). An electromyogram-driven musculoskeletal model of the knee to predict in vivo joint contact forces during normal and novel gait patterns. *Journal of Biomechanical Engineering*, 135(2), 021014.
- Marouane, H., Shirazi-Adl, A., & Adouni, M. (2016). Alterations in knee contact forces and centers in stance phase of gait: A detailed lower extremity musculoskeletal model. *Journal of Biomechanics*, 49(2), 185–192.
- Marouane, H., Shirazi-Adl, A., Adouni, M., & Hashemi, J. (2014). Steeper posterior tibial slope markedly increases ACL force in both active gait and passive knee joint under compression. *Journal of Biomechanics*, 47(6), 1353–1359.
- Miller, R. H., Esterson, A. Y., & Shim, J. K. (2015). Joint contact forces when minimizing the external knee adduction moment by gait modification: A computer simulation study. *The Knee*, 22(6), 481–489.
- Mohammadi, Y., Arjmand, N., & Shirazi-Adl, A. (2015). Comparison of trunk muscle forces, spinal loads and stability estimated by one stability- and three EMG-assisted optimization approaches. *Medical Engineering & Physics*, 37(8), 792–800. <https://doi.org/10.1016/j.medengphy.2015.05.018>
- Mokhtarzadeh, H., Perraton, L., Fok, L., Muñoz, M. A., Clark, R., Pivonka, P., & Bryant, A. L. (2014). A comparison of optimisation methods and knee joint degrees of freedom on muscle force predictions during single-leg hop landings. *Journal of Biomechanics*, 47(12), 2863–2868.
- Morris, J. M., Lucas, D. B., & Bresler, B. (1961). Role of the trunk in stability of the spine. *JBJS*, 43(3), 327–351.
- Mulvey, M. R., Macfarlane, G. J., Beasley, M., Symmons, D. P., Lovell, K., Keeley, P., Woby, S., & McBeth, J. (2013). Modest association of joint hypermobility with disabling and limiting musculoskeletal pain: Results from a large-scale general population-based survey. *Arthritis Care Res*, 65(8), 1325–1333. <https://doi.org/10.1002/acr.21979>
- Murphy, L., Schwartz, T. A., Helmick, C. G., Renner, J. B., Tudor, G., Koch, G., Dragomir, A., Kalsbeek, W. D., Luta, G., & Jordan, J. M. (2008). Lifetime risk of symptomatic knee osteoarthritis. *Arthritis Care & Research: Official Journal of the American College of Rheumatology*, 59(9), 1207–1213.
- Panjabi, M. M. (1992). The stabilizing system of the spine. Part I. Function, dysfunction, adaptation, and enhancement. *Journal of Spinal Disorders*, 5, 383–383.

- Patwardhan, A. G., Havey, R. M., Meade, K. P., Lee, B., & Dunlap, B. (1999). A follower load increases the load-carrying capacity of the lumbar spine in compression. *Spine*, 24(10), 1003–1009.
- Rohlmann, A., Zander, T., Schmidt, H., Wilke, H.-J., & Bergmann, G. (2006). Analysis of the influence of disc degeneration on the mechanical behaviour of a lumbar motion segment using the finite element method. *Journal of Biomechanics*, 39(13), 2484–2490.
- Ryder, S. H., Johnson, R. J., Beynnon, B. D., & Ettlinger, C. F. (1997). Prevention of ACL injuries. *Journal of Sport Rehabilitation*, 6(2), 80–96.
- Samadi, S., & Arjmand, N. (2018). A novel stability-based EMG-assisted optimization method for the spine. *Medical Engineering & Physics*, 58, 13–22. <https://doi.org/10.1016/j.medengphy.2018.04.019>
- Shahvarpour, A., Shirazi-Adl, A., Larivière, C., & Bazrgari, B. (2015). Trunk active response and spinal forces in sudden forward loading—analysis of the role of perturbation load and pre-perturbation conditions by a kinematics-driven model. *Journal of Sport Rehabilitation*, 48(1), 44–52.
- Shamsi, M., Sarrafzadeh, J., Jamshidi, A., Arjmand, N., & Ghezelbash, F. (2017). Comparison of spinal stability following motor control and general exercises in nonspecific chronic low back pain patients. *Clinical Biomechanics*, 48, 42–48.
- Sharifi, M., & Shirazi-Adl, A. (2021). Knee flexion angle and muscle activations control the stability of an anterior cruciate ligament deficient joint in gait. *Journal of Biomechanics*, 117, 110258. <https://doi.org/10.1016/j.jbiomech.2021.110258>
- Sharifi, M., Shirazi-Adl, A., & Marouane, H. (2017). Computational stability of human knee joint at early stance in Gait: Effects of muscle coactivity and anterior cruciate ligament deficiency. *Journal of Biomechanics*, 63, 110–116.
- Sharifi, M., Shirazi-Adl, A., & Marouane, H. (2018). Computation of the role of kinetics, kinematics, posterior tibial slope and muscle cocontraction on the stability of ACL-deficient knee joint at heel strike – towards identification of copers from non-copers. *Journal of Biomechanics*, 77, 171–182. <https://doi.org/10.1016/j.jbiomech.2018.07.003>
- Sharifi, M., Shirazi-Adl, A., & Marouane, H. (2020). Sensitivity of the knee joint response, muscle forces and stability to variations in gait kinematics-kinetics. *Journal of Biomechanics*, 99, 109472.
- Shirazi-Adl, A. (2006). Analysis of large compression loads on lumbar spine in flexion and in torsion using a novel wrapping element. *Journal of Biomechanics*, 39(2), 267–275.
- Shirazi-Adl, A., & Parnianpour, M. (2000). Load-bearing and stress analysis of the human spine under a novel wrapping compression loading. *Clinical Biomechanics*, 15(10), 718–725.
- Steele, K. M., DeMers, M. S., Schwartz, M. H., & Delp, S. L. (2012). Compressive tibiofemoral force during crouch gait. *Gait & Posture*, 35(4), 556–560.
- Stokes, I. A., & Gardner-Morse, M. (2003). Spinal stiffness increases with axial load: Another stabilizing consequence of muscle action. *Journal of Electromyography Kinesiology*, 13(4), 397–402.
- Thelen, D. G., Anderson, F. C., & Delp, S. L. (2003). Generating dynamic simulations of movement using computed muscle control. *Journal of Biomechanics*, 36(3), 321–328.
- Torg, J. S., Conrad, W., & Kalen, V. (1976). Clinical diagnosis of anterior cruciate ligament instability in the athlete. *Am J Sports Med*, 4(2), 84–93. <https://doi.org/10.1177/036354657600400206>
- van Tunen, J. A. C., Dell'Isola, A., Juhl, C., Dekker, J., Steultjens, M., Thorlund, J. B., & Lund, H. (2018). Association of malalignment, muscular dysfunction, proprioception,

- laxity and abnormal joint loading with tibiofemoral knee osteoarthritis - a systematic review and meta-analysis. *BMC Musculoskelet Disord*, 19(1), 273. <https://doi.org/10.1186/s12891-018-2202-8>
- Van Dieen, J., & Kingma, I. (2005). Effects of antagonistic co-contraction on differences between electromyography based and optimization based estimates of spinal forces. *Ergonomics*, 48(4), 411–426.
- Vos, T., Flaxman, A. D., Naghavi, M., Lozano, R., Michaud, C., Ezzati, M., Shibuya, K., Salomon, J. A., Abdalla, S., & Aboyans, V. (2012). Years lived with disability (YLDs) for 1160 sequelae of 289 diseases and injuries 1990–2010: A systematic analysis for the global burden of disease study 2010. *The Lancet*, 380(9859), 2163–2196.
- Zhang, C., Mannen, E. M., Sis, H. L., Cadel, E. S., Wong, B. M., Wang, W., Cheng, B., Friis, E. A., & Anderson, D. E. (2020). Moment-rotation behavior of intervertebral joints in flexion-extension, lateral bending, and axial rotation at all levels of the human spine: A structured review and meta-regression analysis. *Journal of Biomechanics*, 100, 109579.

This page intentionally left blank

# Techniques for automatic landmark detection of human tissue

5

**Juan-Roberto Jiménez-Pérez<sup>1</sup>, José Negrillo-Cárdenas<sup>2</sup>, Francisco R. Feito<sup>1</sup>**

<sup>1</sup>*Graphics and Geomatics Group of Jaén, Center for Advanced Studies in Information and Communication Technologies, University of Jaén, Jaén, Spain;* <sup>2</sup>*Fundación I+D del Software Libre (FIDESOL), Granada, Spain*

## Chapter outline

<b>Introduction</b> .....	107
<b>Machine learning techniques</b> .....	108
Artificial neural networks.....	108
Decision trees .....	109
Support vector machines.....	110
<b>Knowledge-based techniques</b> .....	111
Shape analysis .....	111
<i>Approximation to simple shapes</i> .....	111
Curvature analysis .....	112
Template-based approaches .....	114
<i>Atlas-based templates</i> .....	114
Statistical shape modeling .....	115
Patient-specific templates .....	115
<i>Spatial coherence</i> .....	115
<b>Conclusion</b> .....	116
<b>References</b> .....	116

## Introduction

The automatic identification of tissues is a challenging line of research of modern medicine. In the 1970s, the applications dealing with patient-specific images were focused on 3D visualization (Brooks & Chiro, 1976). However, the identification of the existing elements was manually performed by an expert. This fact causes its exclusion for high-demanding scenarios due to its tediousness and inaccuracy. Latest advances allow us to create new computer-assisted tools for diagnosis, taking advantage of the detection of features, organs, and landmarks (Stefan et al., 2019).

The heterogeneity of the organs and tissues increases the complexity of the detection, requiring specific approaches for each type of tissue or feature. In this

chapter, we give the reader a brief introduction of different approaches to detect anatomical landmarks in human tissues. We classify them into two categories depending on the nature of the solution: machine learning-based and knowledge-based techniques.

---

## Machine learning techniques

Machine learning is a technology which is nowadays employed in almost every aspect of our lives, including medicine. It tends to mathematically conceptualize the relationships between variables in order to predict values or classify new data. Machine learning follows a simple schema: the algorithm receives input information, makes an abstraction of them, and finally, creates a generalization of the data provided. A labeled dataset is commonly employed to train the system.

This section provides a brief explanation of the most used techniques for detecting landmarks and tissues in medical imaging. Based on their popularity in the field of medical image analysis, we propose a classification according to the type of algorithm: artificial neural networks, decision trees, and support vector machines (SVMs).

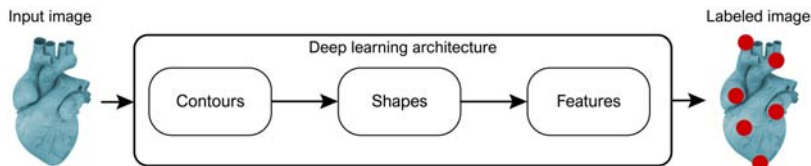
### Artificial neural networks

An artificial neural network is a computational system inspired by the connection of biological neurons of animal brains. It consists of a set of many simple processors producing a sequence of activations, serving as input for other connected neurons. The data introduced into the network passes through the neurons where is processed and finally, combined by some nonlinear functions. By modifying weights, layers, and functions, we can adapt a neural network for diverse problems (Schmidhuber, 2015).

The modeling of a neural network is similar to fitting a line or plane through a set of points to define the relationships between them or simplify the representation of the data on a smaller scale. A neural network is trained by analyzing the difference from the predicted to the real value (the error). The weights are iteratively adjusted according to a learning rule to modify this error (Shanmuganathan, 2016).

Artificial neural networks are widely employed for image recognition being medicine directly benefited from them. They can be applied for multiple types of medical images: magnetic resonances (Yang et al., 2015), fluoroscopy (Grupp et al., 2020) or X-rays (Bier et al., 2019), among others.

Recently, deep learning techniques have emerged being a current trend for every imagined task. Deep learning represents a step forward for artificial neural networks. They try to decompose a problem from different levels of abstraction (Fig. 5.1). Most authors explain this concept using image recognition as a didactic example: Initial layers consider an image as a matrix of pixels, retrieving some contours. Successive steps compose the detected contours as shapes. Then, they evolve to features, and finally, the desired object is recognized (Bengio, 2009; Schmidhuber, 2015). The term *deep* is employed as there are multiple layers in the network.

**FIGURE 5.1**

Schematic simplification of a deep learning layer architecture.

As can be inferred, deep learning techniques are widely employed in medical image analysis. Multiple tasks can be carried out in organs: segmentation, detection, registration, classification, landmark placement, and many others. Current trends of deep learning techniques are focused on automatizing manual procedures, such as segmentation or medical imaging optimization (Ghesu et al., 2019). There are many examples for detecting features with many purposes for brain (Liu et al., 2018; Yang et al., 2019) or the heart (Alansary et al., 2019). We refer the reader to Litjens et al. (2017) for an exhaustive review of these techniques for medical image analysis.

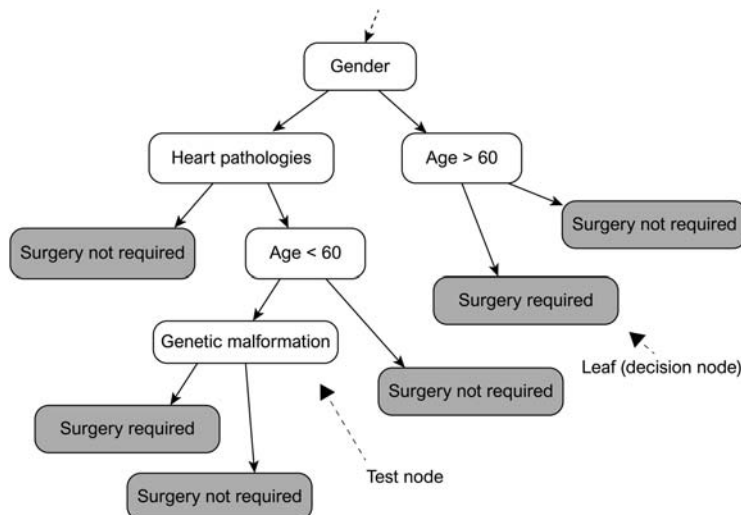
## Decision trees

We name decision trees as the machine learning techniques which consist of a hierarchical structure based on a divide-and-conquer strategy. They try to classify observations into classes by a sequence of recursive splits. Each split node consists of a test to decide which branch is selected. When an item reaches a leaf during this iterative process, a decision is encountered and the item is labeled. Depending on we deal with discrete or numeric variables, the tree can be used for classification or regression.

Decision trees are nonparametric models because the structure is flexible and when they grow during learning, new branches and leaves are added. As other machine learning techniques, a decision tree can be replicated many times to create forests, thus improving the results (Alpaydin & Bach, 2014).

In the beginning, decision trees were used in medicine to create protocol for decision-making processes, being primarily carried out by hand (see Fig. 5.2). Currently, their applications go further:

- Distinguish between benign or malignant tumors by employing a hybrid approach (KNN, decision trees, and random forests) (Garg & Garg, 2021).
- Analyze the size of several landmarks or regions of organs, such as the volume of the hippocampus of the brain (useful for Alzheimer's disease diagnosis) (Zhang et al., 2016).
- Assess the myocardial perfusion MR data, including the most relevant landmarks, to analyze blood flow through the heart (Kim et al., 2017).
- Others.

**FIGURE 5.2**

Example of part of a decision tree for medical diagnosis.

## Support vector machines

SVMs are learning models which separate or classify two high-dimensional classes by a hyperplane. This plane is located in a position which maximizes its distance with the instances of the problem. Therefore, the basic idea is to obtain a value ( $w$ ) to solve the following inequations:

$$\begin{aligned} w^T x^T + w_0 &\geq +1 \text{ if } y_i = 1 \\ w^T x^T + w_0 &\leq -1 \text{ if } y_i = -1 \end{aligned} \quad (5.1)$$

This means that a value is labeled as 1 when the value is above the hyperplane and  $-1$  when it is below. However, there are situations in where we cannot linearly divide the points. In these cases, a kernel can be applied to the examples to transform the features (kernel trick method). The vectors will be moved to another dimension in where a linear separation can be performed. We refer the reader to [Hastie et al. \(2009\)](#); [Steinwart & Christmann \(2008\)](#) for more details regarding SVM.

SVM is a classical tool for supporting medical algorithms. It can be applied for feature detection by discriminating boundaries between landmarks and background ([Chakrabarty et al., 2003](#)). Additionally, they can be part of more complex hybrid algorithms and can be used to support diagnosis. In brain diseases such as Alzheimer's, it can be employed after the landmark detection to prematurely detect it ([Zhang et al., 2016](#)).

## Knowledge-based techniques

In contrast to machine learning which employs a training set to label or measure the organs for diagnosis, we encounter knowledge-based approaches, which employ the human knowledge to detect the landmarks. In other words, a set of rules, relationships, or spatial coherence are defined to locate a feature. A prior training is rarely required when using this kind of techniques.

Knowledge-based techniques can be classified according to their approach: shape analysis, template-based approaches, and spatial coherence.

### Shape analysis

When detecting a landmark by using shape analysis, we address the physical aspect of a tissue. Shape analysis-based approaches apply anatomical knowledge to model a landmark as a mathematical concept. Depending on the type of the technique, we can define a classification: approximation to simple shapes or curvature analysis.

#### Approximation to simple shapes

The simplest technique consists of approximating the geometry to basic shapes like circles, spheres or cylinders, among others. In this case, one of the mentioned figures is fitted on the surface of the studied tissue.

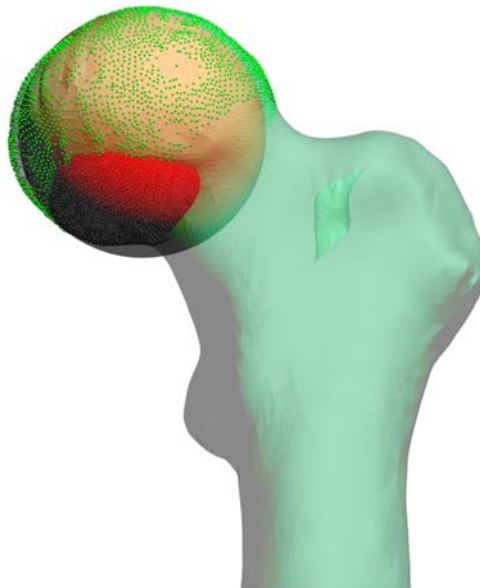
A typical statistical approach is the least squares fitting of points. This method consists of selecting a parametrized equation that represents the initial points in a continuous manner. The quality of the adjustment is measured by the residuals ( $r_i$ ), described as the difference between the observed ( $y_i$ ) and the predicted ( $f(x_i, \beta)$ ). To guarantee an accurate fitting, the method tries to obtain a set of parameters which minimize the squared residuals ( $S$ ):

$$\begin{aligned} r_i &= y_i - f(x_i, \beta) \\ S &= \sum_{i=1}^n r_i^2 \end{aligned} \tag{5.2}$$

We can adapt the input data to points by selecting a representative part of the analyzed tissue, e.g., vertices of a triangle mesh or centers of the voxels of a region of a volumetric model. There are multiple numerical algorithms to estimate a model function, depending on the purpose. The reader is referred to [Eberly \(2000\)](#) and [Scheider & Eberly \(2003\)](#) for more details. See also [Fig. 5.3](#).

This method is very common, especially in orthopedics due to the rigidity of bone tissue. Some authors simplify the representation of bones by exclusively using quadrics and simple shapes ([Sholukha et al., 2011](#)). In addition, least squares fitting are commonly used as part of more sophisticated algorithms ([Memiş et al., 2019](#)).

Other similar approaches are based on fitting some parametric intensity values, especially useful for raster images (2D or 3D). They describe a set of

**FIGURE 5.3**

An example of a sphere fitting performed on the points belonging to the head of a femur.

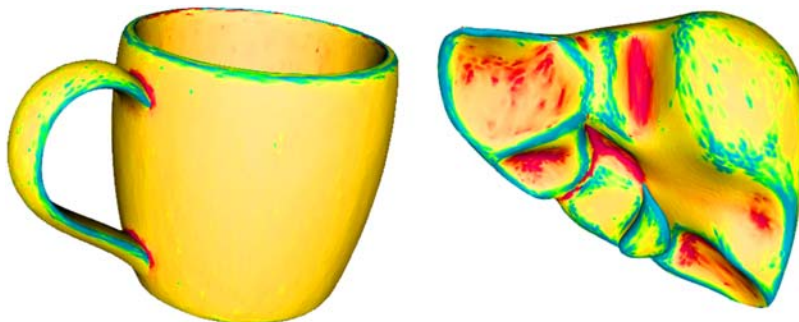
intensities of an anatomical region as a function. By modifying a template, the algorithm is able to detect different types of shapes, e.g., spherical or tip-like, among others (Wörz & Rohr, 2006).

### Curvature analysis

There is another mathematical technique to detect some features of human tissue depending on how a surface is *deformed*. Curvature is a value to measure the deviation of a curve from being a straight line or a surface from being a plane.

The curvature of a surface in a given point is mathematically defined as the curvature of its normal section. This section corresponds with the intersection of a plane containing the point normal and the surface. By rotating that plane around the normal, different curvature values are obtained. There are two values, maximum ( $k_{\max}$ ) and minimum ( $k_{\min}$ ) for two perpendicular planes, denoted as principal curvatures. Depending on the method, the mean and Gaussian curvatures can be obtained. On the one hand, as the name suggests, the mean curvature ( $H$ ) is computed as the average of both values per point. On the other hand, the Gaussian curvature ( $K$ ) is obtained by multiplying them. For more details about the mathematical basis of curvature, the reader is referred to Bærentzen et al. (2012) and Mari et al. (2019).

The combination of the described approaches allows to discover some geometrical properties of the model, based on differential properties of the mesh (Mari

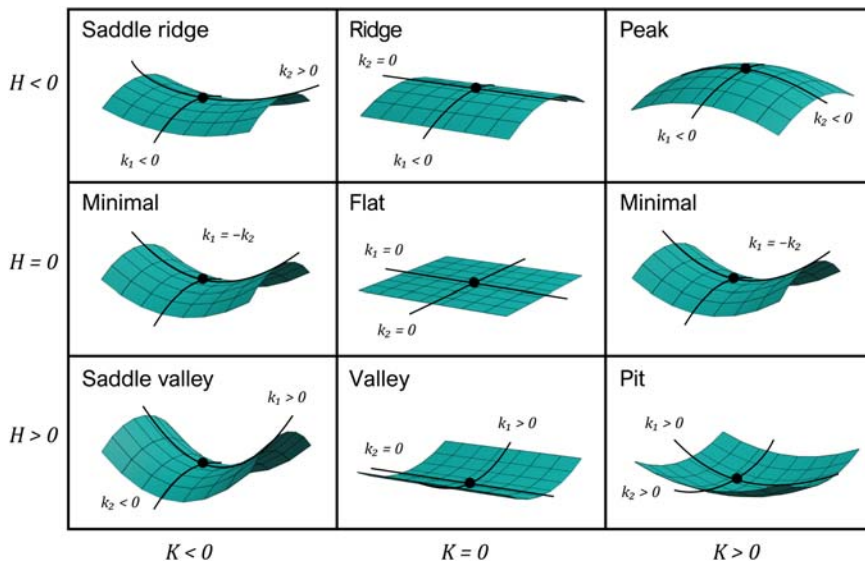
**FIGURE 5.4**

Two examples of the values of curvature for a mug (left) and the rear part of a human liver (right).

et al., 2019), as Fig. 5.4 depicts. The analysis of the obtained values allows to determine the local shape of the surface at a given point:

- $K > 0$  Principal curvatures have the same sign, meaning a convex or concave local feature.
- $K < 0$  Principal curvatures have different sign, meaning a saddle-like shape.

Nevertheless, by using  $K$  values, the type of a singular point cannot be defined. Then, the mean curvature provides the remaining information. The remaining cases  $K = 0$  or/and  $H = 0$  define ridges, valleys, minimal or flat surfaces (see Fig. 5.5).

**FIGURE 5.5**

Different types of regions of interest according to the values of mean ( $H$ ) and Gaussian ( $K$ ) curvatures.

This analysis can be applied to human organs and tissues. As can be inferred, most relevant landmarks can be classified as mentioned. In most cases, the curvature method is used as a first approximation to specific landmarks, discarding irrelevant data. It is a very common approach for computer-assisted orthopedic trauma surgery (Cerveri et al., 2012; Fischer et al., 2019; Subburaj et al., 2009).

## Template-based approaches

When detecting landmarks or measuring a human tissue, the studied case can be compared with a template. In most cases, an algorithm needs a preannotated image serving as a template for new introduced cases. In other words, the landmarks are detected by extrapolating the manually labeled ones.

Depending on the type of the employed templates, we classify them into three categories: atlas-based, statistical shape models, and patient-specific.

### *Atlas-based templates*

As their name suggests, this type of approaches employs atlases as a template for measuring and registering the images. An atlas is a mapping of  $n$ -dimensional spatial coordinates to label of a set of classes. It can be considered as a special type of image (label image). Therefore, in order to segment or label a new image using the atlas, we need to implement a coordinate mapping between both images, i.e., registering one image to the other. The reader is referred to Rohlfing et al. (2005) for more mathematical details of atlas-image segmentation.

Commonly, in medicine, an expert annotates one or multiple images to use as a template for registering specific cases, see Fig. 5.6.

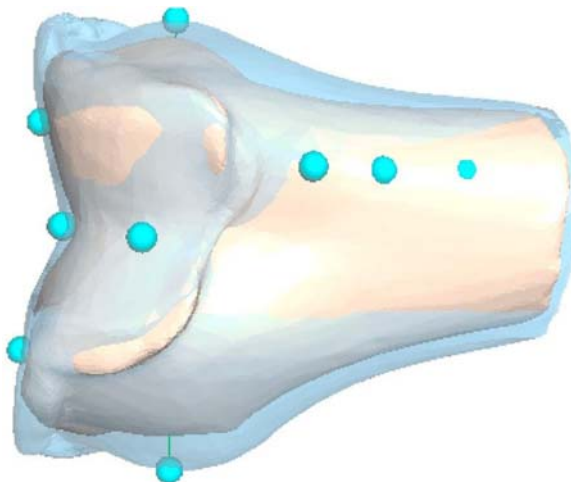


**FIGURE 5.6**

Example of the extrapolation of an atlas to a patient-specific image. In blue, the annotated atlas. In beige, the studied case.

Extracted from Jacinto, H., Valette, S., & Prost, R. (2018). Multi-atlas automatic positioning of anatomical landmarks. Journal of Visual Communication and Image Representation, 50, 167–177. <https://doi.org/10.1016/j.jvcir.2017.11.015>.

The atlas-based registration of tissues is broadly used in medicine for assisting in the landmark detection and segmentation (Brehler et al., 2019; Ehrhardt et al., 2004; Iglesias & Karssemeijer, 2009; Jacinto et al., 2018).

### Statistical shape modeling

Statistical shape models (SSMs) describe a set of semantically similar objects based on their geometry. SSMs try to replicate human intuitive perception of appearance and similarity as input for algorithms. Statistical shape models store the average shape of multiple objects and some variants of their structure. In other words, these types of models tend to represent an abstract item used as a reference to model other objects. Statistical shape analysis requires a discretization of the data, e.g., convert to a finite tridimensional mesh. The reader is referred to Ambellan et al. (2019) for more details of this technique and its applications in medicine.

Among others, SSMs can be used to provide a healthy template of a damaged/injured organ or tissue to measure or obtain certain landmarks, with reconstruction purposes in fractures or deformations (Baek et al., 2013; Poltaretskyi et al., 2017). In addition, they can be employed for automating tasks, such as obtaining the optimal scout image in the planning of magnetic resonances (Bystrov et al., 2007).

### Patient-specific templates

Apart from the information collected from knowledge or atlases, there are some data that can be implicitly obtained from their surroundings or context, being specific for each patient. The most typical scenario is the use of contralateral properties. Due to the bilateral symmetry of the human body, there are certain organs having a symmetrical copy in the other side, e.g., bones of the extremities, kidneys or lungs, among others (Bakhshayesh et al., 2020; DeLude et al., 2007).

It is reasonable to think that we can employ a mirrored copy of the healthy side as a template for identify landmarks or measures or even compare the goodness of the result of a surgical procedure (McDonald et al., 2009; Negrillo-Cárdenas et al., 2020; Vlachopoulos et al., 2018).

### Spatial coherence

There are other approaches in where the detection of landmarks is determined by the spatial localization of others. For example, we know that a human heart has two ventricles, right and left. This means that when one will be properly determined, the localization of the other will be centered on the other side. By discarding nonrelevant data, the detection is performed faster and more reliable.

The techniques based on spatial coherence allows to study certain geometrical properties of tissues. Different from the bilateral symmetry mentioned above, we are referring to a local symmetry, in where the organ has symmetrical properties. The skull (Neelapu et al., 2018), mandible (Voss et al., 2016), or vertebrae (Kim & Lee, 2017) have these properties.

The employment of these techniques for detecting landmarks allows to establish correspondences between regions of a tissue and can serve as a reference for diagnostic processes.

---

## Conclusion

In this chapter, we have detailed many types of techniques for detecting landmarks in human tissue. We have proposed a classification according to the nature of the solution, being learning-based or knowledge-based. A subclassification has been also defined for each group, according to specific aspects of the algorithms.

On the one hand, machine learning techniques are promising and currently obtain satisfactory results. A machine learning algorithm can be applied to almost every problem. However, most of them require large preannotated datasets, becoming challenging for rare diseases (too few specimens to analyze). On the other hand, knowledge-based are often more efficient in terms of performance, but, in general, the methods are case-dependent. In addition, knowledge-based techniques do not require training the algorithm in most cases, becoming a simple but efficient solution.

As a final remark, we invite novel researchers to develop hybrid techniques and explore the advantages of each type of algorithm.

---

## References

- Alansary, A., Oktay, O., Li, Y., Folgoc, L. L., Hou, B., Vaillant, G., Kamnitsas, K., Vlontzos, A., Glocker, B., Kainz, B., & Rueckert, D. (2019). Evaluating reinforcement learning agents for anatomical landmark detection. *Medical Image Analysis*, 53, 156–164. <https://doi.org/10.1016/j.media.2019.02.007>
- Alpaydin, E., & Bach, F. (2014). Introduction to machine learning. In *Introduction to machine learning*. MIT Press.
- Ambellan, F., Lamecker, H., von Tycowicz, C., & Zachow, S. (2019). Statistical shape models: Understanding and mastering variation in anatomy. In *Advances in experimental medicine and biology* (Vol 1156, pp. 67–84). Springer New York LLC. [https://doi.org/10.1007/978-3-030-19385-0\\_5](https://doi.org/10.1007/978-3-030-19385-0_5)
- Baek, S. Y., Wang, J. H., Song, I., Lee, K., Lee, J., & Koo, S. (2013). Automated bone landmarks prediction on the femur using anatomical deformation technique. *CAD Computer Aided Design*, 45(Issue 2), 505–510. <https://doi.org/10.1016/j.cad.2012.10.033>
- Bakhshayesh, P., Sandberg, O., Kumar, V., Ali, A., & Enocson, A. (2020). Volume fusion of CT images to measure femoral symmetricity. *Surgical and Radiologic Anatomy*, 42(6), 635–639. <https://doi.org/10.1007/s00276-019-02389-3>
- Bærentzen, J. A., Gravesen, J., Anton, F., & Aanæs, H. (2012). Curvature in triangle meshes. In *Guide to computational geometry processing* (pp. 143–158).
- Bengio, Y. (2009). Learning deep architectures for AI. *Foundations and Trends® in Machine Learning*, 1–127. <https://doi.org/10.1561/2200000006>

- Bier, B., Goldmann, F., Zaech, J. N., Fotouhi, J., Hegeman, R., Grupp, R., Armand, M., Osgood, G., Navab, N., Maier, A., & Unberath, M. (2019). Learning to detect anatomical landmarks of the pelvis in X-rays from arbitrary views. *International Journal of Computer Assisted Radiology and Surgery*, 14(9), 1463–1473. <https://doi.org/10.1007/s11548-019-01975-5>
- Brehler, M., Thawait, G., Kaplan, J., Ramsay, J., Tanaka, M. J., Demehri, S., Siewerdsen, J. H., & Zbijewski, W. (2019). Atlas-based algorithm for automatic anatomical measurements in the knee. *Journal of Medical Imaging*, 6(2). <https://doi.org/10.1117/1.JMI.6.2.026002>
- Brooks, R. A., & Chiro, D. G. (1976). Principles of computer assisted tomography (CAT) in radiographic and radioisotopic imaging. *Physics in Medicine and Biology*, 21(5), 689–732. <https://doi.org/10.1088/0031-9155/21/5/001>
- Bystrov, D., Pekar, V., Young, S., Dries, S. P. M., Heese, H. S., & Van Muiswinkel, A. M. (2007). Automated planning of MRI scans of knee joints. *Progress in biomedical optics and imaging - proceedings of SPIE*, 6509(Issue 2). <https://doi.org/10.1117/12.709255>
- Cerveri, P., Manzotti, A., Marchente, M., Confalonieri, N., & Baroni, G. (2012). Mean-shifted surface curvature algorithm for automatic bone shape segmentation in orthopedic surgery planning: A sensitivity analysis. *Computer Aided Surgery*, 17(3), 128–141. <https://doi.org/10.3109/10929088.2012.670667>
- Chakrabarty, S., Yagi, M., Shibata, T., & Cauwenberghs, G. (2003). Robust cephalometric landmark identification using support vector machines. In *ICASSP, IEEE international conference on acoustics, speech and signal processing - proceedings* (Vol. 2, pp. 825–828).
- DeLude, J. A., Bicknell, R. T., MacKenzie, G. A., Ferreira, L. M., Dunning, C. E., King, G. J. W., Johnson, J. A., & Drosdowech, D. S. (2007). An anthropometric study of the bilateral anatomy of the humerus. *Journal of Shoulder and Elbow Surgery*, 16(4), 477–483. <https://doi.org/10.1016/j.jse.2006.09.016>
- Eberly, D. H. (2000). *3D game engine design: A practical approach to real-time computer graphics*.
- Ehrhardt, J., Handels, H., Plötz, W., & Pöppel, S. J. (2004). Atlas-based recognition of anatomical structures and landmarks and the automatic computation of orthopedic parameters. *Methods of information in medicine*, 43(4), 391–397. <https://doi.org/10.1055/s-0038-1633882>
- Fischer, M. C. M., Krooß, F., Habor, J., & Radermacher, K. (2019). A robust method for automatic identification of landmarks on surface models of the pelvis. *Scientific Reports*, 9, 1–10.
- Garg, G., & Garg, R. (2021). *Brain tumor detection and classification based on hybrid ensemble classifier* (pp. 1–18).
- Ghesu, F. C., Georgescu, B., Zheng, Y., Grbic, S., Maier, A., Hornegger, J., & Comaniciu, D. (2019). Multi-scale deep reinforcement learning for real-time 3D-landmark detection in CT scans. *IEEE Transactions on Pattern Analysis and Machine Intelligence*, 41(1), 176–189. <https://doi.org/10.1109/TPAMI.2017.2782687>
- Grupp, R. B., Unberath, M., Gao, C., Hegeman, R. A., Murphy, R. J., Alexander, C. P., Otake, Y., McArthur, B. A., Armand, M., & Taylor, R. H. (2020). Automatic annotation of hip anatomy in fluoroscopy for robust and efficient 2D/3D registration. *International Journal of Computer Assisted Radiology and Surgery*, 15(5), 759–769. <https://doi.org/10.1007/s11548-020-02162-7>
- Hastie, T., Tibshirani, R., & Friedman, J. (2009). *The elements of statistical learning*.

- Iglesias, J. E., & Karssemeijer, N. (2009). Robust initial detection of landmarks in film-screen mammograms using multiple ffdm atlases. *IEEE Transactions on Medical Imaging*, 28(11), 1815–1824. <https://doi.org/10.1109/TMI.2009.2025036>
- Jacinto, H., Valette, S., & Prost, R. (2018). Multi-atlas automatic positioning of anatomical landmarks. *Journal of Visual Communication and Image Representation*, 50, 167–177. <https://doi.org/10.1016/j.jvcir.2017.11.015>
- Kim, Y. C., Chung, Y., & Choe, Y. H. (2017). Automatic localization of anatomical landmarks in cardiac MR perfusion using random forests. *Biomedical Signal Processing and Control*, 38, 370–378. <https://doi.org/10.1016/j.bspc.2017.07.001>
- Kim, K., & Lee, S. (2017). Vertebrae localization in CT using both local and global symmetry features. *Computerized Medical Imaging and Graphics*, 58, 45–55. <https://doi.org/10.1016/j.compmedimag.2017.02.002>
- Litjens, G., Kooi, T., Bejnordi, B. E., Setio, A. A. A., Ciompi, F., Ghafoorian, M., van der Laak, J. A. W. M., van Ginneken, B., & Sánchez, C. I. (2017). *A survey on deep learning in medical image analysis*. arXiv <https://arxiv.org/>
- Liu, M., Zhang, J., Adeli, E., & Shen, D. (2018). Landmark-based deep multi-instance learning for brain disease diagnosis. *Medical Image Analysis*, 43, 157–168. <https://doi.org/10.1016/j.media.2017.10.005>
- Mari, J., Hétroy-Wheeler, F., & Subsol, G. (2019). Geometric features based on curvatures. In *Geometric and topological mesh feature extraction for 3D shape analysis* (pp. 1–98).
- McDonald, C. P., Peters, T. M., King, G. J. W., & Johnson, J. A. (2009). Computer assisted surgery of the distal humerus can employ contralateral images for pre-operative planning, registration, and surgical intervention. *Journal of Shoulder and Elbow Surgery*, 18(3), 469–477. <https://doi.org/10.1016/j.jse.2009.01.028>
- Memiş, A., Albayrak, S., & Bilgili, F. (2019). A new scheme for automatic 2D detection of spheric and aspheric femoral heads: A case study on coronal MR images of bilateral hip joints of patients with Legg-Calve-Perthes disease. *Computer Methods and Programs in Biomedicine*, 175, 83–93. <https://doi.org/10.1016/j.cmpb.2019.04.001>
- Neelapu, B. C., Kharbanda, O. P., Sardana, V., Gupta, A., Vasamsetti, S., Balachandran, R., & Sardana, H. K. (2018). Automatic localization of three-dimensional cephalometric landmarks on CBCT images by extracting symmetry features of the skull. *Dentomaxillofacial Radiology*, 47(2). <https://doi.org/10.1259/dmfr.20170054>
- Negrillo-Cárdenas, J., Jiménez-Pérez, J. R., Cañada-Oya, H., Feito, F. R., & Delgado-Martínez, A. D. (2020). Automatic detection of landmarks for the analysis of a reduction of supracondylar fractures of the humerus. *Medical Image Analysis*, 64. <https://doi.org/10.1016/j.media.2020.101729>
- Poltaretskyi, S., Chaoui, J., Mayya, M., Hamitouche, C., Bercik, M. J., Boileau, P., & Walch, G. (2017). Prediction of the pre-morbid 3D anatomy of the proximal humerus based on statistical shape modelling. *Bone and Joint Journal*, 99B(7), 927–933. <https://doi.org/10.1302/0301-620X.99B7.BJJ-2017-0014>
- Rohlfing, T., Brandt, R., Menzel, R., Russakoff, D. B., & Maurer, C. R. (2005). Quo vadis, atlas-based segmentation?. In *Handbook of biomedical image analysis* (pp. 435–486). Springer US. [https://doi.org/10.1007/0-306-48608-3\\_11](https://doi.org/10.1007/0-306-48608-3_11)
- Schmidhuber, J. (2015). Deep learning in neural networks: An overview. *Neural Networks*, 61, 85–117. <https://doi.org/10.1016/j.neunet.2014.09.003>
- Schneider, P. J., & Eberly, D. H. (2003). *Geometric tools for computer graphics*.
- Shanmuganathan, S. (2016). Artificial neural network modelling: An introduction. *Studies in Computational Intelligence*, 628, 1–14. [https://doi.org/10.1007/978-3-319-28495-8\\_1](https://doi.org/10.1007/978-3-319-28495-8_1)

- Sholukha, V., Chapman, T., Salvia, P., Moiseev, F., Euran, F., Rooze, M., & Van Sint Jan, S. (2011). Femur shape prediction by multiple regression based on quadric surface fitting. *Journal of Biomechanics*, 44(4), 712–718. <https://doi.org/10.1016/j.jbiomech.2010.10.039>
- Stefan, P., Traub, J., Hennersperger, C., Esposito, M., & Navab, N. (2019). Challenges in computer assisted interventions. In *Handbook of medical image computing and computer assisted intervention* (pp. 979–1012). Elsevier. <https://doi.org/10.1016/B978-0-12-816176-0.00045-4>
- Steinwart, I., & Christmann, A. (2008). *Support vector machines*.
- Subburaj, K., Ravi, B., & Agarwal, M. (2009). Automated identification of anatomical landmarks on 3D bone models reconstructed from CT scan images. *Computerized Medical Imaging and Graphics*, 33(5), 359–368. <https://doi.org/10.1016/j.compmedimag.2009.03.001>
- Vlachopoulos, L., Carrillo, F., Dünner, C., Gerber, C., Székely, G., & Fürnstahl, P. (2018). A novel method for the approximation of humeral head retroversion based on three-dimensional registration of the bicipital groove. *Journal of Bone and Joint Surgery*, 100.
- Voss, J. O., Varjas, V., Raguse, J. D., Thieme, N., Richards, R. G., & Kamer, L. (2016). Computed tomography-based virtual fracture reduction techniques in bimandibular fractures. *Journal of Cranio-Maxillofacial Surgery*, 44(2), 177–185. <https://doi.org/10.1016/j.jcms.2015.11.010>
- Wörz, S., & Rohr, K. (2006). Localization of anatomical point landmarks in 3D medical images by fitting 3D parametric intensity models. *Medical Image Analysis*, 10(1), 41–58. <https://doi.org/10.1016/j.media.2005.02.003>
- Yang, X., Tang, W. T., Tjio, G., Yeo, S. Y., & Su, Y. (2019). Automatic detection of anatomical landmarks in brain MR scanning using multi-task deep neural networks. *Neurocomputing*. <https://doi.org/10.1016/J.NEUROCOMPUTING.2018.10.105>
- Yang, D., Zhang, S., Yan, Z., Tan, C., Li, K., & Metaxas, D. (2015). Automated anatomical landmark detection on distal femur surface using convolutional neural network. In *Proceedings - international symposium on biomedical imaging* (Vol 2015, pp. 17–21). IEEE Computer Society. <https://doi.org/10.1109/ISBI.2015.7163806>
- Zhang, J., Gao, Y., Gao, Y., Munsell, B. C., & Shen, D. (2016). Detecting anatomical landmarks for fast Alzheimer's disease diagnosis. *IEEE Transactions on Medical Imaging*, 35(12), 2524–2533. <https://doi.org/10.1109/TMI.2016.2582386>

This page intentionally left blank

# Multibody modeling of the musculoskeletal system

# 6

**Michael Skipper Andersen, John Rasmussen**

*Department of Materials and Production, Aalborg University, Aalborg, Denmark*

## Chapter outline

<b>Introduction.....</b>	121
<b>Fundamentals of multibody modeling.....</b>	123
<b>Motion capture-based model .....</b>	127
Cadaver-based lower extremity model .....	127
<i>Scaling of the template model to subject-specific data .....</i>	129
Linear geometric scaling law .....	130
Parameter identification .....	131
Mass and inertial properties .....	132
Mass-fat muscle strength scaling law .....	133
Over-determinate kinematic analysis .....	133
Inverse dynamic analysis.....	134
<b>Analysis of gait modifications .....</b>	136
<b>Other applications.....</b>	138
<b>Concluding remarks .....</b>	139
<b>References .....</b>	139

## Introduction

Obtaining a fundamental understanding of why a biomechanical system moves and/or deforms in a certain manner requires insight into the forces and moments that cause these movements and/or deformations. Unlike pure mechanical systems, directly measuring these forces, i.e., forces in the muscles, cartilage, bones, and ligaments, is often invasive and not ethically justifiable for a large array of applications. To overcome this, computational models are being developed to provide estimates of these quantities based on model inputs that can be obtained under normal circumstances.

Besides providing estimates of the internal quantities that we, in general, cannot measure, models of the musculoskeletal system also open an array of other possibilities, such as allowing us to investigate the causal relationship between model inputs and outputs, and understanding how alterations to the system affects the performance and, hereby, enable optimization of the system's performance.

Within a musculoskeletal model, the bones are typically assumed to be rigid bodies (and we will, for the rest of chapter, denote them as segments to avoid confusion with the human body). The mechanical properties of the muscles are typically modeled with the phenomenological Hill-type muscle model (Zajac, 1989), accounting for the elastic properties of the tissues as well as the contractile element to account for the force-generating capacity's dependency on muscle length and contraction velocity. The joints are either modeled through kinematic constraint equations to capture the gross joint movements (Begon et al., 2018) or through more advanced joint models with elastic descriptions of both ligaments and cartilage (Dejtiar et al., 2019; Skipper Andersen et al., 2017).

As the human body contains multiple bones that are connected by joints, we have a so-called multibody system and, for this reason, musculoskeletal models are based on the theories of multibody modeling. Therefore, we will introduce briefly the fundamental concepts within multibody modeling before we look more in detail at musculoskeletal modeling. A few examples of musculoskeletal models are shown in Fig. 6.1.

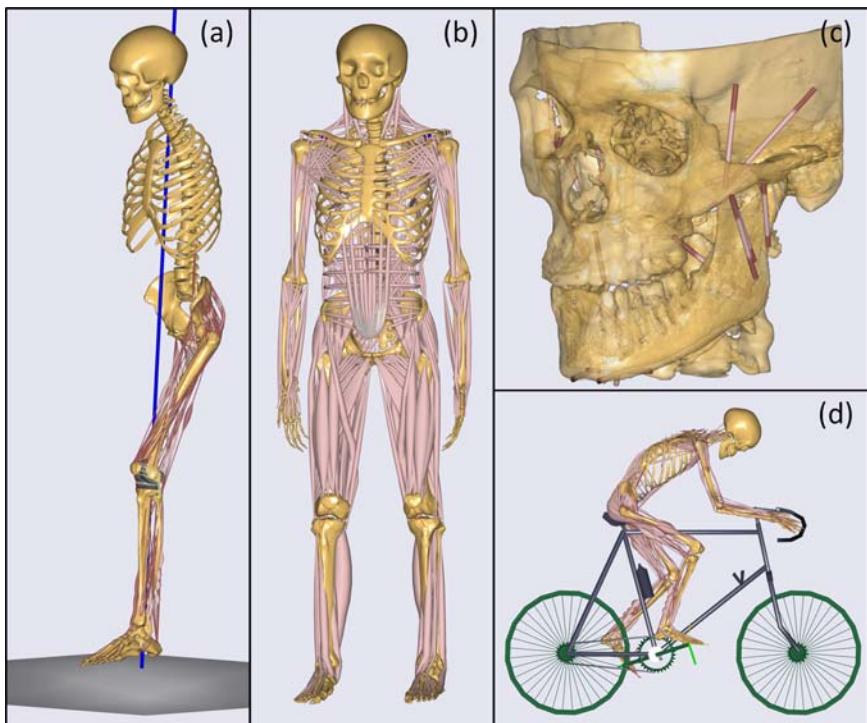


**FIGURE 6.1** Illustrations of musculoskeletal models.

(A) A musculoskeletal model of a total knee arthroplasty patient during gait. (B) A full body model standing. (C) A mandible model. (D) A model of human on a bicycle.

---

## Fundamentals of multibody modeling

Multibody modeling is fundamentally based on Newton's laws. These were originally derived for a single particle and, thereafter, extended to rigid segments and, hereafter, to a collection of rigid segments that are connected by joints. The latter is what we call a multibody system. But, before we dive into multibody systems, we will briefly recapitulate Newton's laws as they are the foundation for all we will discuss in this chapter.

Newton's laws describe the relationships between forces acting on a particle and how they affect its movement, and how forces are transferred between particles. Qualitatively, we can describe a force as:

1. a quantity that can cause to accelerate (e.g., a free fall).
2. an action of one system that affects another system.
3. a quantity that can deform an object (e.g., a spring).

Observations (1) and (2) are expressed by Newton's laws, whereas the third is described by Hook's law in case of linear elastic materials.

From experience, we all know that the magnitude and direction of the force also seem to matter. Therefore, we formally define a force as a 2D or 3D vector, so that we can capture both its magnitude and direction.

*Newton's first law of motion* states that, unless acted upon by a net external force, a particle at rest will remain at rest and a particle in constant motion will remain at constant motion. This law actually follows as a natural consequence of Newton's second law of motion.

*Newton's second law of motion* relates the resultant force acting on the particle, the mass of the particle, and the acceleration of the particle:

$$\sum_{i=1}^{N_F} \mathbf{F}_i = m\mathbf{a} \quad (6.1)$$

where  $m$  is the particle's mass,  $\mathbf{a}$  is the linear acceleration vector of the particle, and  $N_F$  is the number of applied forces. This equation holds for both 2D and 3D.

Finally, *Newton's third law* explains how forces are transferred between adjacent particles as it states that all forces between two particles are equal in magnitude but opposite in direction. This is also referred to as the *law of action and reaction*.

While particle dynamics has many applications in its own right, this is not sufficient to analyze the human musculoskeletal systems. Here, we instead have to analyze segments, which we can describe as collections of infinitely small particles. This extension to segments can be accomplished for both rigid as well as deformable segments, but in this chapter, we focus solely on rigid segments, as the bones are frequently modeled as rigid segments when analyzing the musculoskeletal system.

While a particle can only translate, a segment can translate and rotate. In 2D, the segment can rotate about one axis and, in 3D, about three axes. For a segment, a force vector can still cause linear acceleration of the segment's center of mass but

it can also cause a rotation of the segment. This is caused by the moment that the force vector creates about the segment's center of mass:

$$\mathbf{M}^O = \mathbf{r} \times \mathbf{F} \quad (6.2)$$

where  $\mathbf{M}^O$  is the moment vector around the point  $O$ , the center of mass, and  $\mathbf{r}$  is a vector from the point  $O$  to the line-of-action of the force vector,  $\mathbf{F}$ . The cross product is only defined for 3D vectors but can be applied to 2D problems by setting the coordinate that points out of the plane to zero.

In terms of the relationship between the resultant moment vector and the rotation of the segment, then it depends on whether the system is modeled in 2D or 3D. In 2D, the equation is

$$\sum_{i=1}^{N_M} M_i^O = J\alpha \quad (6.3)$$

where  $M_i^O$  is the  $i$ th moment around the center of mass,  $J$  is the mass moment of inertia referring to the center of mass, and  $\alpha$  is the angular acceleration of the segment around the axis pointing out of the 2D plane.  $N_M$  is the number of applied moments. In 3D, the equation, referred to as Euler's equation, is

$$\sum_{i=1}^{N_M} \mathbf{M}_i^O = \mathbf{J}' \dot{\omega}' + \boldsymbol{\omega}' \times \mathbf{J}' \boldsymbol{\omega}' \quad (6.4)$$

where  $\mathbf{M}_i^O$  is the  $i$ th moment vector applied to the segment,  $\mathbf{J}'$  is the inertial tensor in segment-fixed coordinates, denoted by the apostrophe, and given with respect to the segment's center of mass, and  $\boldsymbol{\omega}'$  is the angular velocity vector of the segment measured relative to its segment-fixed coordinate system.  $\dot{\boldsymbol{\omega}}$  is the angular acceleration vector of the segment computed as the time derivative of the angular velocity vector. The dot denotes the derivative with respect to time.

These equations are called the Newton–Euler equations. In case of a system of multiple bodies, then their interactions are modeled by introducing reaction forces and moments between the bodies as described by Newton's third law. These can both be reaction forces and moments within the human segment but also between the human and external objects. The remaining forces acting on the bodies come from gravity, muscles, ligaments, intraabdominal pressure, and external forces.

To allow modeling of a system of segments, we need to decide on a terminology to refer to them and, for the rest of this chapter, we focus solely on 3D analysis. Here, we will apply the so-called full Cartesian formulation, where the position and orientation of the  $i$ th segment in 3D is described by  $\mathbf{q}_i = [\mathbf{r}_i^T \quad \mathbf{p}_i^T]^T$ , where  $\mathbf{r}_i$  is the position vector of the segment's center of mass relative to the global coordinate system and  $\mathbf{p}_i = [e_{i0} \quad e_{i1} \quad e_{i2} \quad e_{i3}]^T$  are four Euler parameters used to describe the orientation of the segment relative to the global coordinate system. While it may seem more intuitive to use other rotational coordinates, such as Cardan angles, all choices of rotational coordinates in 3D that only include three parameters will

also introduce singularities somewhere in the solution space. This issue is avoided with Euler parameters and is, therefore, a computationally attractive approach.

However, as a rigid segment in 3D only has three rotational degrees-of-freedom, but four Euler parameters are introduced, a constraint equation must be introduced to ensure that the vector  $\mathbf{p}_i$  has unity length, i.e.,  $\mathbf{p}_i^T \mathbf{p}_i - 1 = 0$  for each segment. A thorough description of Euler parameters can be found in other textbooks, for instance (Nikravesh, 1987).

The velocity of the  $i$ th segment is described by  $\mathbf{v}_i = [\dot{\mathbf{r}}_i^T \quad \boldsymbol{\omega}_i^T]^T$ . To keep the equations concise, the time-dependency of these variables is not explicitly written, e.g., when we write  $\mathbf{q}$ , it is to be understood as  $\mathbf{q}(t)$  and similar for  $\mathbf{v}$  etc. Finally, we assemble the position and velocity vectors of all bodies in vectors  $\mathbf{q} = [\mathbf{q}_1^T \quad \mathbf{q}_2^T \quad \dots \quad \mathbf{q}_n^T]^T$  and  $\mathbf{v} = [\mathbf{v}_1^T \quad \mathbf{v}_2^T \quad \dots \quad \mathbf{v}_n^T]^T$ , respectively.

The joints between the bodies of a mechanical systems, we will describe through a set of kinematic constraint equations:

$$\Phi(\mathbf{q}) = 0 \quad (6.5)$$

The constraint equations can be used to describe a large array of joint types, such as the most common types: revolute, spherical, and universal joints but more advanced joints, e.g., points-on-contacts, etc., can also be modeled. How these constraint equations are formulated depends on the type of joint connecting the bodies and details of this can be found in other textbooks (Andersen, 2021; Nikravesh, 1987).

When we introduce kinematic constraint equations, associated reaction forces and moments must also be introduced in accordance with Newton's third law. In general, the reaction forces and moments imposed on the whole system by the constraints can be computed as  $\Phi_q^T \boldsymbol{\lambda}$ , where the subscript denotes the partial derivative with respect to  $\mathbf{q}$  and  $\boldsymbol{\lambda}$  are the generalized reaction forces (Damsgaard et al., 2006; Nikravesh, 1987) and this is also the most common approach to implement Newton's third law systematically when analyzing multibody systems.

The set of kinematic constraint equations must be solved together with the Newton–Euler equations, but exactly how this is accomplished depends on whether a forward or inverse dynamic approach is taken. In the section “Inverse dynamic analysis” later in this chapter, we will expand on how it can be handled in the case of inverse dynamic analysis.

To have the equations in a condensed form, the Newton–Euler equations for the  $i$ th segment can be written as follows, which comes directly from Eqs. (8.1) and (8.4):

$$\begin{bmatrix} m_i \mathbf{I} & 0 \\ 0 & \mathbf{J}'_i \end{bmatrix} \dot{\mathbf{v}}_i + \begin{bmatrix} 0 \\ \tilde{\boldsymbol{\omega}}'_i \mathbf{J}'_i \boldsymbol{\omega}'_i \end{bmatrix} = \mathbf{g}_i^{(\text{ext})} \quad (6.6)$$

where  $m_i$  is the mass of the  $i$ th segment,  $\mathbf{I}$  is the identity matrix,  $\mathbf{J}'_i$  is the inertial tensor for the  $i$ th segment, and  $\mathbf{g}_i^{(\text{ext})}$  is the vector of all forces (top three components) and moments (bottom three components) acting to the segment. The  $\sim$  denotes the skew-symmetric matrix.

We denote the mass matrix  $\mathbf{M}_i$  and the second term, containing the gyroscopic terms,  $\mathbf{b}_i$ , to get

$$\mathbf{M}_i \dot{\mathbf{v}}_i + \mathbf{b}_i = \mathbf{g}_i^{(\text{ext})} \quad (6.7)$$

This can be written up for all  $n$  bodies in the mechanical system as

$$\begin{aligned} \mathbf{M}_1 \dot{\mathbf{v}}_1 + \mathbf{b}_1 &= \mathbf{g}_1^{(\text{ext})} \\ \mathbf{M}_2 \dot{\mathbf{v}}_2 + \mathbf{b}_2 &= \mathbf{g}_2^{(\text{ext})} \\ &\vdots \\ \mathbf{M}_n \dot{\mathbf{v}}_n + \mathbf{b}_n &= \mathbf{g}_n^{(\text{ext})} \end{aligned} \quad (6.8)$$

which on condensed form can be written as

$$\mathbf{M} \dot{\mathbf{v}} + \mathbf{b} = \mathbf{g}^{(\text{ext})} \quad (6.9)$$

where

$$\mathbf{M} = \begin{bmatrix} \mathbf{M}_1 & & 0 \\ & \mathbf{M}_2 & \\ & & \ddots \\ & & & \mathbf{M}_n \end{bmatrix}, \quad \mathbf{b} = \begin{bmatrix} \mathbf{b}_1 \\ \mathbf{b}_2 \\ \vdots \\ \mathbf{b}_n \end{bmatrix}, \quad \mathbf{g}^{(\text{ext})} = \begin{bmatrix} \mathbf{g}_1^{(\text{ext})} \\ \mathbf{g}_2^{(\text{ext})} \\ \vdots \\ \mathbf{g}_n^{(\text{ext})} \end{bmatrix} \quad (6.10)$$

Depending on whether we know the forces and moments acting on the system, or the movements, it follows from the Newton–Euler equations that we can compute the other. If we know the forces and moments, we can compute the movements of the segments and, if we know the movements, we can compute the forces and moments that cause this movement. These two approaches are called forward and inverse dynamics, respectively. If we do not know the forces, moments and movement, predictive methods can be applied to compute these simultaneously. However, this type of analysis is beyond the scope of this chapter and we refer to the relevant literature (Anderson & Pandy, 1999; Falisse et al., 2019; Farahani et al., 2015, 2016).

The pure form of forward dynamic analysis, where only forces and moments are used as inputs, is rarely seen when analyzing the human musculoskeletal system. On the contrary, measured kinematics and external forces and moments and, in some cases, electromyography (EMG) are typically used as inputs and the internal forces computed. So-called forward dynamics-based tracking methods (Seth & Pandy, 2007; Thelen et al., 2003) or inverse dynamics-based methods (Crowninshield & Brand, 1981; Damsgaard et al., 2006; Rasmussen et al., 2001) can be applied to accomplish this. In the remainder of this chapter, we will look into an inverse dynamics-based method.

## Motion capture–based model

To clarify the ideas behind how a musculoskeletal model is created, we will focus the descriptions around an example. The example we will look into investigates so-called gait modification strategies aimed at reducing the loading in the medial compartment of the knee which is one of the early intervention strategies for knee osteoarthritis patients (Dziale et al., 2019). The data we will use for modeling comes from one healthy male subject (age: 53, height: 1.91 m, weight: 88 kg) who was part of a larger study cohort (Karatsidis et al., 2016, 2019). These subjects underwent, among others, marker-based movement analysis for an array of different walking trials such as normal walking at a self-selected pace and gait modifications including toe-in and toe-out modifications, which are the three walking conditions we will investigate in this chapter. The full experimental procedures for the data collections are described in (Karatsidis et al., 2016, 2019) and we will briefly describe the essential procedures relevant for the descriptions in this chapter.

The movements of the subject were collected with an eight infrared camera marker-based motion capture system (Oqus 300, Qualysis AB, Gothenburg, Sweden) and the software Qualisys Track Manager v. 2.12 (QTM) sampling at 240 Hz. A full-body marker set was applied that included a total of 52 markers. For our study, however, we will exclude the markers on the arms as we are only interested in the loads in the knee and, therefore, only need to create a model that includes the lower extremities, spine and thorax, where the latter is necessary for inclusion of the origins of all muscles crossing the hip. A full description of the marker protocol can be found in the appendix of (Karatsidis et al., 2016). Synchronously with the measurements of the marker trajectories, the ground reaction forces and moments were also measured at 2400 Hz with three force plates (AMTI, Advanced Mechanical technology, Inc, Watertown, MA, USA) embedded in the floor.

The analysis of these data will be based on the AnyMocap model from the AnyBody Managed Model Repository (AMMR) v. 2.3.2 (Lund et al., 2021) and the analysis is performed with the AnyBody Modeling System v. 7.3.3 (AMS, AnyBody Technology A/S, Aalborg Denmark). More details about the modeling system itself can be found in the chapter on AMS in this book.

The model is illustrated in Fig. 6.2 for the three different walking conditions and the details of how this model is created is explained in the following sections.

## Cadaver-based lower extremity model

The first step to analyze the data is to create a template musculoskeletal model that we can scale and adjust to model a specific subject of interest. This is the most elaborate step in the creation of the models. An anatomically accurate musculoskeletal model, even if it is just the lower extremity, requires thousands of parameters of which many cannot easily be obtained on living subjects. The cadaver studies and data processing necessary to procure these parameters are an endeavor that can

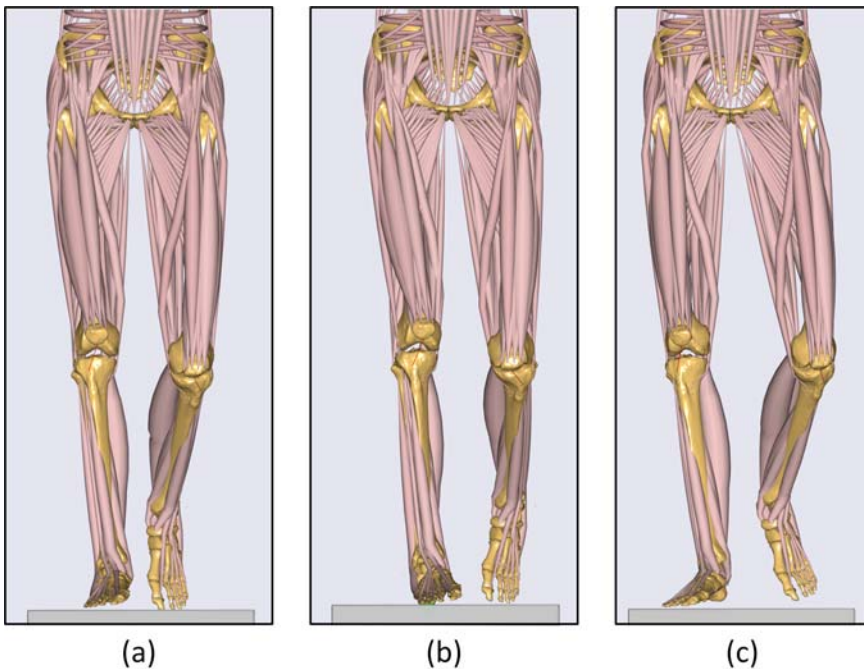


**FIGURE 6.2** Frontal view of the subject during the stance phase of gait during the three different walking trials.

(A) Normal walking. (B) Toe-in walking. (C) Toe-out walking.

easily take man-years to complete. Therefore, most modeling systems come with precreated musculoskeletal model templates that the common users subsequently adjust to their specific needs.

Therefore, the typical approach is to create a template model comprising all required parameters. Subsequently, the cadaver template is adjusted and tuned to match the parameters available for a specific subject. The nature of the adjustment depends on the available subject-specific data, which can range from movement data and basic information about body height and body mass to detailed medical images and strength tests. Within this chapter, we limit the workflow description to the simple case of overall body mass and height plus marker-based motion data. This is also the common situation for most modeling studies.

So, how is such a cadaver-based template created? Obviously, it starts with cadaver dissections, where the following overall data are obtained:

1. Bone geometries typically in the form of medical images.
2. Mass and inertial properties of each segment.
3. Identification of joint centers and axes. This can either be accomplished by functional measurements, bony landmarks, or through geometrical fits to the specific parts of the anatomy.

4. Identification of the parameters needed to model muscles, including origin and insertion points, via points or wrapping surfaces and mechanical parameters required for the specific muscle model used. This is typically the Hill-type muscle model (Zajac, 1989) that requires parameters such as the physiological cross-sectional area (PCSA), tendon slack lengths, pennation angles, optimal fiber lengths, and so on.

For a full description of experimental procedures and parameters, please refer to papers on the creation of such datasets (Carbone et al., 2015; Klein Horsman et al., 2007).

For our investigation, the template model is based on two datasets. The lower extremity model is based on the Twente Lower Extremity v. 2.0 dataset (Carbone et al., 2015) and the lumber spine model is based on (de Zee et al., 2007). In the lower extremity model, pelvis, thigh, shank, talus, and foot segments are included. These are connected by two spherical hip joints, two revolute knee joints, two revolute ankle joints, and two subtalar revolute joints. Additionally, the spine model includes thorax as one rigid segments and the five lumber vertebra. The connection between each vertebra is modeled as a spherical joint. A linear spinal rhythm is introduced to control the rotation of the lumber vertebra relative to each other based on the three relative angles between thorax and pelvis (de Zee et al., 2007). In total this leads to a model with 21 degrees of freedom (DoFs).

### ***Scaling of the template model to subject-specific data***

With the template model in place, we now need to adjust it to match our available data for our subject and hereby create a so-called subject-specific model. However, the term subject-specific model is not accurately defined in the literature and does not say to what degree the model is subject-specific. Sometimes, only the overall height and weight of the subject is used to scale the model while sometimes, medical images (Marra et al., 2015; Carbone, 2016), and strength tests (Heinen et al., 2016; Van Campen et al., 2014; Carbone, 2016) are used as well.

In general, we can split the properties in a musculoskeletal model into

- *Geometrical properties* such as joint centers and axis, center-of-mass location, and muscle and ligament origin/insertion points and via points and or wrapping surfaces.
- *Mass and inertial properties* for each segment of the model.
- *Muscle mechanical properties* such as maximum isometric force, pennation angles, optimal fiber length, tendon slack length, etc.
- *Ligament mechanical properties* such as the stiffness and slack length. Ligaments are frequently not included in models as their effects are captured by the reaction forces and moments associated with the kinematic constraint equations used to model idealized joint models. The interested reader is referred to other literature about detailed joint models for information about how ligaments can be included in these models (Dejtiar et al., 2019; Marra et al., 2015; Skipper Andersen et al., 2017).

Therefore, for a fully subject-specific model, we must obtain all these parameters on the subject, which for most applications is not possible. In our case, we have the subject's mass and height and marker trajectories of the subject during a standing reference trial available, and we will only cover how to create the model based on such data. The reader interested in more elaborate workflows, including geometry from medical images and/or muscle strength scaling based on isometric and isokinetic measurements, is referred to several papers covering this (Dejtar et al., 2019; Heinen et al., 2016; Marra et al., 2015; Van Campen et al., 2014).

To accomplish our scaling task, we must apply so-called scaling laws (Rasmussen et al., 2005). In our case, this will include scaling of the geometry and scaling of the maximum isometric muscle strengths.

### Linear geometric scaling law

To scale the geometry of the model, we have to beware that an array of geometric quantities must be scaled:

- *Points*: e.g., joint centers, muscle origin, via points, insertions, etc.
- *Vectors*: e.g., joint axis, vectors specifying initial guesses for wrapping algorithms, etc.
- *Surfaces*: e.g., parametric or surface representations of muscle or ligament wrapping surfaces.

To accomplish this, we will create scaling laws for points. These are defined by a 3D mapping, taking the initial (source) point to its target location, i.e., a function  $s : \mathbb{R}^3 \rightarrow \mathbb{R}^3$ . To scale points, this approach will work directly, but it does not directly enable scaling of vectors and surfaces. Therefore, vectors and surfaces are implemented to be scaled using point-based scaling laws. To this end, joint axes are defined by two points instead of a vector. Parametric surfaces, e.g., cylinders and spheres, are also defined by points, e.g., for a sphere, we define it by a point at its center and one on its surface.

A linear scaling law is defined as (John Rasmussen et al., 2005)

$$\mathbf{s}'_{\text{scaled}} = \mathbf{S}\mathbf{s}'_{\text{unscaled}} + \mathbf{t} \quad (6.11)$$

where  $\mathbf{s}'_{\text{unscaled}}$  is the unscaled point in local segment-fixed coordinates,  $\mathbf{s}'_{\text{scaled}}$  is the scaled point,  $\mathbf{S}$  is a  $3 \times 3$  scaling matrix, and  $\mathbf{t}$  is a translation vector. The translation  $\mathbf{t}$  can in general be used to translate the point in the local coordinate system, but it is rarely used and, therefore, the linear scaling functions to be used here include only the matrix  $\mathbf{S}$ . Depending on how  $\mathbf{S}$  is defined, different scaling laws are obtained. A uniform scaling law is obtained if we define  $\mathbf{S}$  as a diagonal matrix with the same factor on all diagonal places:

$$\mathbf{S} = k\mathbf{I} \quad (6.12)$$

where  $k$  is the scale ratio. With this approach, all points scale uniformly in all directions. A nonuniform scaling law is obtained if we introduce a different scaling factor for each diagonal element:

$$\mathbf{S} = \begin{bmatrix} k_x & & \\ & k_y & \\ & & k_z \end{bmatrix} \quad (6.13)$$

where  $k_x$ ,  $k_y$ , and  $k_z$  are the scaling ratios along the local  $x$ ,  $y$ , and  $z$  axis and can be used to stretch/compress the segment. These ratios are typically computed as the ratio between the given parameter in the cadaver model and the corresponding parameter from the subject it is desired to scale to.

Depending on how the local coordinate systems are defined for each segment, it can happen that the natural length/width directions do not align with the local segment coordinate system. In this case, the scaling matrix can be defined as

$$\mathbf{S} = \mathbf{A}\mathbf{S}'\mathbf{A}^T \quad (6.14)$$

where  $\mathbf{A}$  is an orthogonal rotation matrix that rotates from the natural coordinate system to the segment coordinate system.  $\mathbf{S}'$  is the nonuniform scaling matrix (see eq. 8.13) in the rotated coordinate system.

With this general approach to linear scaling, multiple scaling approaches can be defined. It is beyond scope of this chapter to describe them in detail. Within the AMMR, there are an array of different scaling laws implemented and the one we will apply is the so-called “XYZ” scaling law. The overall idea behind this scaling law is that it is possible for the user to provide as input information about all three scaling ratios for all segments, but implemented such that it as minimum requires the length of the segments in the longitudinal directions, i.e., thigh length, shank length, pelvis width, and the off-diagonal elements are computed based on an overall scaling factor of the whole body. More details can be found in the AMMR ([Lund et al., 2021](#)). This approach we will apply when scaling based on the marker trajectories in the standing reference trial, where we will “only” provide as input the longitudinal dimensions of the segments.

## Parameter identification

The question is now how to obtain the segment dimensions that we need as inputs to scale the model? There are an array of approaches for this ranging from manual measurements with a tape measure to automatic processing of 3-D surface scans. However, when we have measured marker trajectories, we have the opportunity to identify the segment lengths from the data. This can be accomplished using either a standing or a dynamic trial to optimize the model to match as well as possible the experimental data ([Andersen et al., 2010](#); [Lund et al., 2015](#); [Reinbold et al., 2005](#)). To do this, we will apply the method by ([Andersen et al., 2010](#)). The idea behind this method is to minimize the difference between measured marker

trajectories and the corresponding points on the model by varying simultaneously the movement of the model, the segment dimensions and the local coordinates of markers not located on bony landmarks. This is formulated as the following optimization problem:

$$\begin{aligned} \min \quad & \sum_{i=1}^N G(\Psi(\mathbf{q}(t_i), \mathbf{d}, t_i)) \\ \text{s.t.} \quad & \Phi(\mathbf{q}(t_i), \mathbf{d}, t_i) = 0, \quad i = 1, \dots, N \\ & T(\mathbf{d}) = 0 \end{aligned} \quad (6.15)$$

where  $\Psi(\mathbf{q}(t_i), \mathbf{d}, t_i)$  are so-called soft constraint equations that compute the residual between the experimental and modeled markers.  $\mathbf{q}(t_i)$  is the vector of system coordinates at the  $i$ th time step,  $\mathbf{d}$  is a vector of the model constants to be optimized, i.e., segment lengths and local marker coordinates,  $t_i$  is the time at the  $i$ th time step, and  $N$  is the number of time steps.  $G$  is the objective function on the soft constraint equations, typically implemented as a weighted least-square function.  $\Phi(\mathbf{q}(t_i), \mathbf{d}, t_i) = 0$  are the kinematic joint constraints that must be fulfilled at all-time steps and  $T(\mathbf{d}) = 0$  are constraints only on the constant parameters and can be used to include relationships between the constants, e.g., to enforce left and right symmetry in the model.

In general, this leads to a large-scale optimization problem because the system coordinates at all-time steps and the model constants are unknowns. However, due to a special structure in the linearized optimality conditions of the problem, it can be solved efficiently as shown by (Andersen et al., 2010).

This method can be applied in multiple ways depending on how it is desired to scale the model to the movement data. (Lund et al., 2015) showed different approaches of how this can be accomplished, i.e., the so-called *Linearly scaled model* and *Kinematically scaled model*. The AnyMocap model from AMMR is based on the *Linearly scaled model* approach, where the segment lengths are optimized together with the local marker coordinates and a linear scaling law, as described previously, is applied. In the study of our subject, we optimize these parameters for the standing reference trial using the *Linearly scaled model* approach as implemented in the AnyMocap model.

## Mass and inertial properties

In general, bone, muscle, fat, and other tissues are nonuniformly distributed over the human body and vary between subjects. Although this is widely accepted, musculoskeletal models typically only require the total body mass as input and distribute the mass to all the segments based on regression equations from average data (Winter, 2009). This can, of course, be improved upon, if subject-specific mass distributions are known. The location of each segment's center-of-mass is based on the cadaver data and scaled together with all other points in the model.

The inertial properties are estimated by assuming an idealized shape of the segment, typically a cylinder that is aligned with the long axis of the segment, and the inertial parameters estimated from the segment's mass and length.

### Mass-fat muscle strength scaling law

Besides scaling the geometry and estimating the mass and inertial properties, it is also important to estimate the mechanical properties of the muscles. Here, the most common approach is that the isometric muscle strength is scaled based on the segment lengths and mass and to this end we will describe the so-called *Mass-fat* law implemented in AMMR. The idea behind this method is to include the mass and fat percentage in the estimation of the strength. In general, we can write (Rasmussen et al., 2005)

$$R_{\text{muscle}} = 1 - R_{\text{fat}} - R_{\text{other}} \quad (6.16)$$

where  $R_{\text{muscle}}$  and  $R_{\text{fat}}$  are the ratios of muscle and fat tissues, respectively.  $R_{\text{other}}$  is the ratio of other tissues, i.e., organs, blood, skeleton, etc. With this, it is possible to derive an expression for the isometric strength of a muscle as (John Rasmussen et al., 2005)

$$F = F_0 \frac{k_m}{k_l} \frac{R_{\text{muscle},1}}{R_{\text{muscle},0}} = F_0 \frac{k_m}{k_l} \frac{1 - R_{\text{fat},1} - R_{\text{other},1}}{1 - R_{\text{fat},0} - R_{\text{other},0}} \quad (6.17)$$

where  $F_0$  is the isometric strength of the unscaled, template model,  $k_m$  is the ratio of the scaled model segment mass to the unscaled, template segment mass, and  $k_l$  is the ratio of the scaled model segment length to the unscaled, template segment length. The subscripts “1” and “0” of the muscle, fat, and other ratios refer to the scaled (“1”) and unscaled (“0”) configurations. If the fat percentage of the person is known, then it can be applied in the model directly or, alternatively, it can be estimated with regression equations based on the Body Mass Index (BMI) for instance using the equations described by (Frankenfield et al., 2001).

### Over-determinate kinematic analysis

Having scaled the model, we can start performing the kinematic analysis for the dynamic trials that we wish to analyze. For our subject, this is the normal gait trial at self-selected pace and the two gait modifications, i.e., toe-in and toe-out walking patterns.

The motion capture data comprise the trajectories of the skin markers from which we wish to compute the movements of all segments in the model. However, as we have 23 marker trajectories (i.e., 69 measured spatial coordinates) but the model only has 21 DOFs, creating a so-called *kinematically overdeterminate system* (Andersen et al., 2009). This means that we have more measured information than we strictly need and, therefore, have to allow some of our constraint equations related to the measured marker trajectories to be violated.

To overcome this, (Andersen et al., 2009) introduced the concept of soft and hard constraints, where violations of the soft constraints, denoted  $\Psi(\mathbf{q}, \mathbf{d}, t)$ , are allowed while the hard constraints,  $\Phi(\mathbf{q}, \mathbf{d}, t)$ , always have to be fulfilled. This is set up as an optimization problem where an objective function, defined based on the soft constraints, is minimized while the hard constraints must be satisfied for all time steps of the analysis:

$$\begin{aligned} \min \quad & G(\Psi(\mathbf{q}, \hat{\mathbf{d}}, t)) \\ \text{s.t.} \quad & \Phi(\mathbf{q}, \hat{\mathbf{d}}, t) = 0 \end{aligned} \quad (6.18)$$

where  $G(\Psi(\mathbf{q}, \hat{\mathbf{d}}, t))$  is a scalar objective function and is the same as the one applied during the parameter identification. Vector  $\hat{\mathbf{d}}$  denotes the model constants and the hat indicates that they are fixed for this analysis. These model constant are those identified from the parameter identification for the standing trial.

The result from this analysis is the vector of system coordinates  $\mathbf{q}$  at all-time steps. However, the subsequent inverse dynamic analysis also requires velocities and accelerations. Within AMS, this is accomplished by first computing the joint angles from the segment positions and orientations. These subsequently drive a second identical kinematic model. The segment velocities and accelerations are then computed using standard kinematic approaches for multibody dynamics (Damsgaard et al., 2006). This is accomplished by fitting B-splines through the joint angles trajectories and estimating the joint velocities and accelerations by differentiating the B-spline curves. The resulting set of kinematic constraint equations, stemming from the joint constraints and the joint angle drivers, are finally solved and the segment positions and orientations and the associated velocities and accelerations are obtained.

## Inverse dynamic analysis

Knowing all segments' positions, velocities, and accelerations, we are left with determining the muscle and joint reaction forces that cause these movements. In the form given in Eq. (8.9), these forces are included with all other external forces on the right-hand side. Therefore, we must reorganize the equations such that we have them expressed in terms of our unknown muscle and joint reaction forces. If we expand the right-hand side, we get

$$\mathbf{M}\dot{\mathbf{v}} + \mathbf{b} = \mathbf{C}^{(M)}\mathbf{f}^{(M)} + \mathbf{C}^{(R)}\mathbf{f}^{(R)} + \mathbf{g}^{(app)} \quad (6.19)$$

where  $\mathbf{g}^{(app)}$  includes all applied loads. The applied forces and moments are moved to the other side:

$$\mathbf{C}^{(M)}\mathbf{f}^{(M)} + \mathbf{C}^{(R)}\mathbf{f}^{(R)} = \mathbf{M}\dot{\mathbf{v}} + \mathbf{b} - \mathbf{g}^{(app)} \quad (6.20)$$

We will denote  $\mathbf{d} = \mathbf{M}\dot{\mathbf{v}} + \mathbf{b} - \mathbf{g}^{(app)}$  and assemble the coefficient matrices for the muscles and joint reaction forces in one matrix:

$$\begin{bmatrix} \mathbf{C}^{(M)} & \mathbf{C}^{(R)} \end{bmatrix} \begin{bmatrix} \mathbf{f}^{(M)} \\ \mathbf{f}^{(R)} \end{bmatrix} = \mathbf{d} \quad (6.21)$$

We define  $\mathbf{C} = [\mathbf{C}^{(M)} \quad \mathbf{C}^{(R)}]$  and  $\mathbf{f} = [\mathbf{f}^{(M)} \quad \mathbf{f}^{(R)}]^T$  to get the dynamic equilibrium equations on the desired form:

$$\mathbf{C}\mathbf{f} = \mathbf{d} \quad (6.22)$$

Generally, the coefficient matrix for the reaction forces,  $\mathbf{C}^{(R)}$ , can be computed as the partial derivative of the constraint equations with respect to a set of coordinates that correspond to  $\mathbf{v}$  but with all constraint equations specifying movements that should be controlled by the muscles removed. The coefficient matrix for the muscles,  $\mathbf{C}^{(M)}$ , is computed as the partial derivative of the origin-to-insertion-length of the muscle with respect to the system coordinates (Damsgaard et al., 2006).

One of the challenges with inverse dynamic approaches for musculoskeletal models is that there are typically many more muscles included in the model than the model has DOFs. This is also the case for our lower extremity model. Hereby, we end up with having fewer dynamic equilibrium equations than we have unknown muscle and joint reaction forces, meaning that there are infinitely many combinations of these forces that satisfy the dynamics equilibrium equations. To handle this, it is frequently assumed that the muscles are recruited in an optimal way and the forces are determined as the solution to the following optimization problem:

$$\begin{aligned} \min \quad & H(\mathbf{f}^{(M)}) \\ \text{s.t.} \quad & \mathbf{C}\mathbf{f} = \mathbf{d} \\ & 0 \leq \mathbf{f}^{(M)} \leq \mathbf{s}^{(M)} \end{aligned} \quad (6.23)$$

where  $H$  is a scalar objective function formulated as a function of the muscle forces that is minimized while ensuring that the dynamic equilibrium equations are fulfilled. Inequalities are also introduced to ensure that the muscles can only pull and that the maximum muscle force remains below the instantaneous strength of the muscle,  $\mathbf{s}^{(M)}$ . It is still an open research question which specific objective function best represents the central nervous system and multiple criteria have been proposed. The most common criterion applied is a polynomial criterion with a second- or third-order exponent (Rasmussen et al., 2001):

$$H(\mathbf{f}^{(M)}) = \sum_{i=1}^{n^{(M)}} \left( \frac{\mathbf{f}_i^{(M)}}{\mathbf{s}_i^{(M)}} \right)^p \quad (6.24)$$

where  $p$  is the polynomial exponent and  $\mathbf{s}_i^{(M)}$  is the instantaneous muscle strength for the  $i$ th muscle. We will apply the third-order polynomial when analyzing the gait data of our subject in the following.

## Analysis of gait modifications

After the muscle recruitment analysis is complete, we can start looking at the results for our gait modification gait trials for our subject. As we have modeled the knee as a revolute joint, the direct outputs from the knee model are three forces and two moments. However, the aim of the gait modifications is to alter the load balance between the medial and lateral compartments. Therefore, to analyze this, we need to estimate the compressive forces on each condyle and here we follow the same procedure as reported by (Stoltze et al., 2018). The idea here is to set up a moment equilibrium in the frontal plane and compute the medial and lateral compressive forces by assuming that they act in the middle of each contact area and that they are in equilibrium with the total compressive force and the abduction/adduction moment. The moment arms are estimated based on the distance between the medial and lateral condyles in the scaled model and the knee dimensions reported by (Seedhom et al., 1972).

The estimated compressive on the medial and lateral condyles during the stance phase of the normal, toe-in and toe-out gait trials are shown in Fig. 6.3. Additionally, the first and second peak of the medial compressive force as well as the medial and lateral compressive force impulse are shown in Table 6.1.

These results are interesting and clearly show that the relationship between the gait modification and the resulting change in joint loading is not straightforward. Both the toe-in and toe-out gait modifications show a reduction in the first peak compressive force for the medial compartment and a more or less unchanged second peak. However, for both the toe-in and toe-out gait, the impulse of the medial compressive force is slightly increased whereas the impulse of the lateral compressive force is increased for the toe-in modification and decreased for the toe-out modification. These results are in line with those obtained by (Dziale et al., 2019), who found that the best patient-specific intervention, capturing both gait modifications and insoles, depended on which output parameter was investigated.

At this point, it is not known which mechanical parameters are the drivers of cartilage degeneration in knee osteoarthritis, so it is not currently possible to conclude which of the two gait modifications (if any) are beneficial for our subject. However, now that we are able to estimate these quantities with musculoskeletal models, this is something that can be investigated further and, in the future, we may be able to use the models to tailor the intervention specifically to the given patient.

The outputs from the musculoskeletal model can also be applied as boundary conditions to more detailed joint models to estimate the cartilage stress and strain as, for instance, done by (Halonen et al., 2017). Such a workflow enables a more detailed understanding of how gait modifications alter the stresses in each individual structure in the knee and may play a key role in the future to identify optimal interventions for the individual patient.

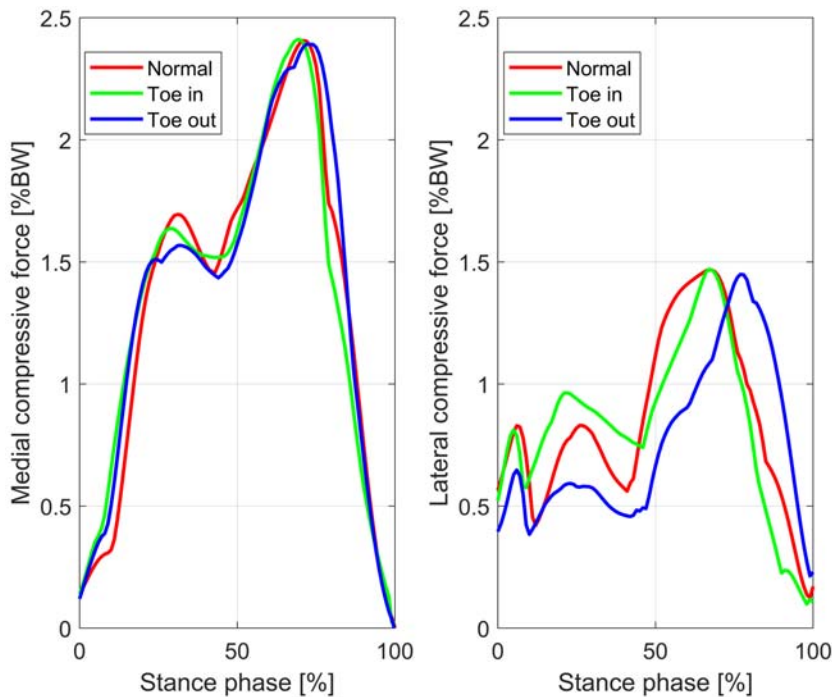


**FIGURE 6.3** Medial and lateral knee compressive forces during the stance phase of gait for normal, toe-in and toe-out gait.

Left: medial knee compressive force. Right: Lateral knee compressive force during the stance phase of the gait cycle for the normal, toe-in and toe-out gait trials for the right knee of the subject.

**Table 6.1** Knee compressive force peaks and impulse. First and second peak medial compressive force and the medial and lateral knee compressive force impulse during the stance phase of the gait cycle for normal, toe-in and toe-out gait.

Variable	Normal gait	Toe-in gait	Toe-out gait
Medial compressive force 1st peak (%BW)	1.68	1.64	1.57
Medial compressive force 2nd peak (%BW)	2.40	2.41	2.39
Medial compressive force impulse (%BW)	0.99	1.06	1.04
Lateral compressive force impulse (%BW s)	0.62	0.65	0.57

---

## Other applications

In this chapter, we specifically created a model to investigate gait and particularly the effect of gait modifications on the knee compressive forces. However, there are many other possibilities with musculoskeletal models and in the following, we will take a look at a few other examples.

Along the same line as our gait model, the model can be used to gain insight into quantities that cannot be measured directly. ([Mellon et al., 2013](#)) exploited this potential to investigate the direction of the hip reaction force for metal-on-metal hip resurfacing patients and showed how this relates to the observed metal ion levels. They found that, among patients with mal-aligned cups, those with high metal ion levels were also those where the hip joint reaction force was closest to the edge of the cup and that the explanation for the hip metal ion levels may, therefore, be edge-loading.

Musculoskeletal models can be used to investigate relationships that may not be accessible experimentally. For example, ([Smith et al., 2019](#)) investigated whether neuromuscular coordination changes exist that can compensate for the altered knee biomechanics in Anterior Cruciate Ligament (ACL)-deficient knees. They ran 10,000 different perturbations to the neuromuscular coordination and found that none of them were able to restore normal knee biomechanics when the ACL was torn. Such a study would be experimentally intractable as it would require an unfeasibly large amount of retraining of the neuromuscular coordination.

Along the same lines, ([Simonsen et al., 2019](#)) studied the effect of tibialis posterior muscle pain on the muscle recruitment of other muscles in the lower limb. They found that flexor digitorum longus and flexor hallucis longus compensate for the tibialis posterior when it is recruited less due to pain. This compensation strategy was also found to increase the ankle joint reaction forces and that it could potentially be contributing to the forefoot deformities frequently seen for rheumatoid arthritis patients.

Although there are many other application areas, the last example that I will mention is to use the model to design equipment that interacts with living organisms, e.g., the human body. This could be artificial limbs, joint replacements, and exoskeletons. To accomplish this, a model of the human together with the equipment is created so that the mutual dynamics can be co-simulated to estimate both the movements and forces and moments within the human and the equipment and also the forces and moments exchanged between the two. Hereby, the effects of altering the design of the equipment on these parameters can be investigated and the most suited design for the task identified and optimized. An example of this can be found in ([Zhou et al., 2015](#)), who optimized springs in a passive shoulder and arm orthosis to compensate simulated lesions to the brachial plexus nerves.

As it enables optimization of the equipment, cosimulation of the human body and interacting equipment has become a hot research topic and I expect to see large progress in this area in the coming years.

---

## Concluding remarks

To conclude, in this chapter, we introduced multibody modeling of the musculoskeletal system and applied the model to evaluate the effect of gait modifications on the estimate the knee compressive forces for one subject. Along the way, we covered the fundamentals of multibody modeling after which we introduced the steps of creating a motion capture-based musculoskeletal modeling, including definition of a cadaver-based template model, scaling of the model, kinematic analysis, and finally estimations of the muscle, joint, and ligament forces with a muscle recruitment algorithm.

Finally, we discussed briefly other applications of musculoskeletal models to show the endless possibilities these models offer.

---

## References

- Andersen, Michael Skipper (2021). Introduction to musculoskeletal modelling. In Z. Jin, J. Li, & Z. Chen (Eds.), *Computational modelling of biomechanics and biotribology in the musculoskeletal system* (2nd ed., pp. 88–103). Woodhead Publishing.
- Andersen, M. S., Damsgaard, M., MacWilliams, B., & Rasmussen, J. (2010). A computationally efficient optimisation-based method for parameter identification of kinematically determinate and over-determinate biomechanical systems. *Computer Methods in Biomechanics and Biomedical Engineering*, 13(2), 171–183. <https://doi.org/10.1080/10255840903067080>
- Andersen, M. S., Damsgaard, M., & Rasmussen, J. (2009). Kinematic analysis of over-determinate biomechanical systems. *Computer Methods in Biomechanics and Biomedical Engineering*, 12(4), 371–384. <https://doi.org/10.1080/10255840802459412>
- Anderson, F. C., & Pandy, M. G. (1999). A dynamic optimization solution for vertical jumping in three dimensions. *Computer Methods in Biomechanics and Biomedical Engineering*, 2(3), 201–231.
- Begon, M., Andersen, M. S., & Dumas, R. (2018). Multibody kinematics optimization for the estimation of upper and lower limb human joint kinematics: A systematized methodological review. *Journal of Biomechanical Engineering*, 140(3). <https://doi.org/10.1115/1.4038741>
- Carbone, Vincenzo (2016). *Subject-Specific lower extremity modeling Personalization of musculoskeletal models using medical imaging and functional measurements*. PhD thesis. University of Twente.
- Carbone, V., Fluit, R., Pellikaan, P., van der Krogt, M. M., Janssen, D., Damsgaard, M., Vigneron, L., Feilkas, T., Koopman, H. F. J. M., & Verdonschot, N. (2015). TLEM 2.0 - a comprehensive musculoskeletal geometry dataset for subject-specific modeling of lower extremity. *Journal of Biomechanics*, 48(5), 734–741. <https://doi.org/10.1016/j.jbiomech.2014.12.034>
- Crowninshield, R. D., & Brand, R. A. (1981). A physiologically based criterion of muscle force prediction in locomotion. *Journal of Biomechanics*, 14(11), 793–801.
- Damsgaard, M., Rasmussen, J., Christensen, S. T., Surma, E., & de Zee, M. (2006). Analysis of musculoskeletal systems in the AnyBody modeling system. *Simulation Modelling Practice and Theory*, 14(8), 1100–1111.

- Dejtiar, D. L., Dzialo, C. M., Pedersen, P. H., Jensen, K. K., Fleron, M., & Andersen, M. S. (2019). Development and evaluation of a subject-specific lower limb model with an 11 DOF natural knee model using MRI and EOS during a quasi-static lunge. *Journal of Biomechanical Engineering*. <https://doi.org/10.1115/1.4044245>
- Dzialo, C. M., Mannisi, M., Halonen, K. S., de Zee, M., Woodburn, J., & Andersen, M. S. (2019). Gait alteration strategies for knee osteoarthritis: A comparison of joint loading via generic and patient-specific musculoskeletal model scaling techniques. *Null*, 6(1), 54–65. <https://doi.org/10.1080/23335432.2019.1629839>
- Falisse, A., Serrancolí, G., Dembia, C. L., Gillis, J., Jonkers, I., & De Groot, F. (2019). Rapid predictive simulations with complex musculoskeletal models suggest that diverse healthy and pathological human gaits can emerge from similar control strategies. *Journal of the Royal Society, Interface*, 16(157), 20190402. <https://doi.org/10.1098/rsif.2019.0402>
- Farahani, S., Andersen, M. S., de Zee, M., & Rasmussen, J. (2016). Optimization-based dynamic prediction of kinematic and kinetic patterns for a human vertical jump from a squatting position. *Multibody System Dynamics*, 36(1), 37–65.
- Farahani, S., Bertucci, W., Andersen, M. S., de Zee, M., & Rasmussen, J. (2015). Prediction of crank torque and pedal angle profiles during pedaling movements by biomechanical optimization. *Structural and Multidisciplinary Optimization*, 51(1), 251–266.
- Frankenfield, D. C., Rowe, W. A., Cooney, R. N., Smith, J. S., & Becker, D. (2001). Limits of body mass index to detect obesity and predict body composition. *Nutrition (Burbank, Los Angeles County, Calif.)*, 17(1), 26–30.
- Halonen, K., Dzialo, C. M., Mannisi, M., Venäläinen, M., de Zee, M., & Andersen, M. S. (2017). Workflow assessing the effect of gait alterations on stresses in the medial tibial cartilage: combined musculoskeletal modelling and finite element analysis. *Scientific Reports*, 7(14), Article 17396.
- Heinen, F., Lund, M. E., Rasmussen, J., & de Zee, M. (2016). Muscle-tendon unit scaling methods of Hill-type musculoskeletal models: An overview. *Proceedings of the Institution of Mechanical Engineers, H, Journal of Engineering in Medicine*, 230(10), 976–984. <https://doi.org/10.1177/0954411916659894>
- Karatsidis, A., Bellusci, G., Schepers, H. M., de Zee, M., Andersen, M. S., & Veltink, P. H. (2016). Estimation of ground reaction forces and moments during gait using only inertial motion capture. *Sensors (Basel, Switzerland)*, 17(1). <https://doi.org/10.3390/s17010075>
- Karatsidis, A., Jung, M., Schepers, H. M., Bellusci, G., de Zee, M., Veltink, P. H., & Andersen, M. S. (2019). Musculoskeletal model-based inverse dynamic analysis under ambulatory conditions using inertial motion capture. *Medical Engineering & Physics*, 65, 68–77. <https://doi.org/10.1016/j.medengphy.2018.12.021>
- Klein Horsman, M. D., Koopman, H. F. J. M., van der Helm, F. C. T., Prosé, L. P., & Veeger, H. E. J. (2007). Morphological muscle and joint parameters for musculoskeletal modelling of the lower extremity. *Clinical Biomechanics (Bristol, Avon)*, 22(2), 239–247.
- Lund, M. E., Andersen, M. S., de Zee, M., & Rasmussen, J. (2015). Scaling of musculoskeletal models from static and dynamic trials. *International Biomechanics*, 2(1), 1–11.
- Lund, M. E., Christensen, S. T., De Pieri, E., Simonsen, S. T., Iversen, K., & Engellund, B. K. (2021). AnyBody managed model repository. <https://doi.org/10.5281/zenodo.4305559>. version 2.3.2.
- Marra, M. A., Vanheule, V., Fluit, R., Koopman, B. H. F. J. M., Rasmussen, J., Verdonschot, N., & Andersen, M. S. (2015). A subject-specific musculoskeletal modeling framework to predict in vivo mechanics of total knee arthroplasty. *Journal of Biomechanical Engineering*, 137(2), 020904. <https://doi.org/10.1115/1.4029258>

- Mellan, S. J., Grammatopoulos, G., Andersen, M. S., Pegg, E. C., Pandit, H. G., Murray, D. W., & Gill, H. S. (2013). Individual motion patterns during gait and sit-to-stand contribute to edge-loading risk in metal-on-metal hip resurfacing. *Proceedings of the Institution of Mechanical Engineers. Part H, Journal of Engineering in Medicine*, 227(7), 799–810. <https://doi.org/10.1177/0954411913483639>
- Nikravesh, P. (1987). *Computer-aided analysis of mechanical systems*. Englewood Cliffs, New Jersey: Prentice Hall.
- Rasmussen, J., Damsgaard, M., & Voigt, M. (2001). Muscle recruitment by the min/max criterion – a comparative numerical study. *Journal of Biomechanics*, 34(3), 409–415.
- Rasmussen, John, de Zee, M., Damsgaard, M., Christensen, S. T., Marek, C., & Siebertz, K. (2005). A general method for scaling musculo-skeletal models. In *International symposium on computer simulation in biomechanics*.
- Reinboldt, J. A., Schutte, J. F., Fregly, B. J., Koh, B. I., Haftka, R. T., George, A. D., & Mitchell, K. H. (2005). Determination of patient-specific multi-joint kinematic models through two-level optimization. *Journal of Biomechanics*, 38(3), 621–626.
- Seedhom, B. B., Longton, E. B., Wright, V., & Dowson, D. (1972). Dimensions of the knee. Radiographic and autopsy study of sizes required by a knee prosthesis. *Annals of the Rheumatic Diseases*, 31(1), 54–58.
- Seth, A., & Pandy, M. G. (2007). A neuromusculoskeletal tracking method for estimating individual muscle forces in human movement. *Journal of Biomechanics*, 40(2), 356–366.
- Simonsen, M. B., Yurtsever, A., Næsborg-Andersen, K., Leutscher, P. D. C., Hørslev-Petersen, K., Hirata, R. P., & Andersen, M. S. (2019). A parametric study of effect of experimental tibialis posterior muscle pain on joint loading and muscle forces—Implications for patients with rheumatoid arthritis? *Gait & Posture*, 72, 102–108. <https://doi.org/10.1016/j.gaitpost.2019.06.001>
- Skipper Andersen, M., de Zee, M., Damsgaard, M., Nolte, D., & Rasmussen, J. (2017). Introduction to force-dependent kinematics: Theory and application to mandible modeling. *Journal of Biomechanical Engineering*, 139(9). <https://doi.org/10.1115/1.4037100>
- Smith, C. R., Brandon, S. C. E., & Thelen, D. G. (2019). Can altered neuromuscular coordination restore soft tissue loading patterns in anterior cruciate ligament and menisci deficient knees during walking? *Journal of Biomechanics*, 82, 124–133. <https://doi.org/10.1016/j.jbiomech.2018.10.008>
- Stoltze, J. S., Rasmussen, J., & Andersen, M. S. (2018). On the biomechanical relationship between applied hip, knee and ankle joint moments and the internal knee compressive forces. *International Biomechanics*, 5(1), 63–74.
- Thelen, D. G., Anderson, F. C., & Delp, S. L. (2003). Generating dynamic simulations of movement using computed muscle control. *Journal of Biomechanics*, 36(3), 321–328.
- Van Campen, A., Pipeleers, G., De Groote, F., Jonkers, I., & De Schutter, J. (2014). A new method for estimating subject-specific muscle-tendon parameters of the knee joint actuators: A simulation study. *International Journal for Numerical Methods in Biomedical Engineering*, 30(10), 969–987. <https://doi.org/10.1002/cnm.2639>
- Winter, D. (2009). *Biomechanics and motor control of human movement* (4th ed.). John Wiley & Sons, Inc.
- Zajac, F. E. (1989). Muscle and tendon: Properties, models, scaling, and application to biomechanics and motor control. *Critical Reviews in Biomedical Engineering*, 17(4), 359–411.
- de Zee, M., Hansen, L., Wong, C., Rasmussen, J., & Simonsen, E. B. (2007). A generic detailed rigid-body lumbar spine model. *Journal of Biomechanics*, 40(6), 1219–1227.
- Zhou, L., Bai, S., Andersen, M. S., & Rasmussen, J. (2015). Modeling and design of a spring-loaded, cable-driven, wearable exoskeleton for the upper extremity. *Modeling, Identification and Control (Online Edition)*, 36(3), 167–177.

This page intentionally left blank

# AnyBody modeling system

7

**Michael Skipper Andersen, John Rasmussen**

*Department of Materials and Production, Aalborg University, Aalborg, Denmark*

## Chapter outline

<b>Background and context .....</b>	143
<b>Software design choices .....</b>	144
AnyScript .....	145
Multibody system formulation .....	146
<b>The model repository .....</b>	146
Structuring principles .....	147
<b>Applications .....</b>	148
Fundamental science applications .....	148
Orthopedic applications .....	149
Industrial product design .....	150
Sports .....	151
Workplace ergonomics .....	153
<b>Digital human models and the digital patient .....</b>	155
<b>References .....</b>	156

## Background and context

The AnyBody Modeling System (AMS) originated as a research project at Aalborg University in the early 1990s. It quickly became apparent that the technology has applications beyond fundamental research and, to secure its continuous development and distribution, a software company, AnyBody Technology, was founded.

The evolution of microprocessors and computational technology has enabled a range of software for simulation of physical systems governed by differential equations. Field problems are governed by partial differential equations and are typically solved by the finite element method. Typical applications are mechanics of materials (Belytschko et al., 2009), heat transfer (Huang & Usmani, 2012), electromagnetics (Chen & Konrad, 1997), acoustics (Thompson, 2006), and fluid dynamics. Some mechanical problems are naturally discrete and can be formulated in terms of ordinary differential equations. This is the case in the field of machines and mechanisms, and the resulting, so-called multibody dynamics systems (Schiehlen, 1997), are, for instance, used for analysis of vehicle dynamics. AMS is of the latter category; its

models are based on rigid segments connected by joints, muscles, and ligaments. As the name indicates, AMS is a modeling system, and it allows users to construct models of organisms from scratch. However, most users draw upon an existing library of anatomical models of humans that will be described later.

This field of computer simulation of physical phenomena is known as Computer-Aided Engineering, CAE. In addition to simulation of products, the methods are also used extensively in the analysis of biological problems, for instance, in bone mechanics, soft tissue deformation, blood flow simulation, or modeling of accidents such as automobile crashes. However, living creatures performing voluntary movements cannot be formulated solely as physical problems and cannot immediately be described by differential equations, because muscle actions, and the movements they create, are reactions to prior learning processes, sensory input, thought processes, and independent choices. The desire to extend CAE technology to analysis of voluntary movements by musculoskeletal systems was the background and motivation for development of the AMS.

The idea to develop AMS was sparked by a bicycle design project. Mechanical engineering students at Aalborg University were experimenting with optimization of bicycle frames for weight and stiffness. Traditional CAE tools were useful to create designs with a better stiffness/weight ratio, but stiffness and light weight are often conflicting criteria, and the work ultimately required a decision of how much material mass should be invested to increase the stiffness, i.e., is low mass and, therefore, less weight to carry up the hills more important than high stiffness, and, therefore, less muscle work lost to elastic deformation of the frame? The answer to this question required models comprising the bicycle and rider in concert, and the rider's voluntary muscle actions could not be modeled by the CAE technology available at the time.

This chapter will cover an introduction to the fundamentals of the system followed by examples of applications and a discussion of the system's relevance as a biomechanical digital twin. The mathematical and technical details of the system are mostly beyond the scope of this chapter, and the interested reader is referred to Chapter 6 and published papers ([Andersen et al., 2009, 2010](#); [Damsgaard et al., 2006](#); [Rasmussen et al., 2001](#)).

---

## Software design choices

Most modern application software follows a design paradigm known as Model-View-Controller ([Krasner, 1988](#)). For technical software, this paradigm addresses the problem that the internal Model is usually a mathematical abstraction of the laws of physics, which in its raw form would not make sense to users. The View provides a comprehensible interpretation of the model and its analysis results, and the Controller allows the user to make modifications to the model via a—hopefully—friendly interface. In terms of the View, AMS, like most technical software, provides a 3-D graphical rendition and a logical tree structure organization of the elements of

the model and allows the user to interact with both through different Controllers. This type of Graphical User Interface (GUI) usually suffices for application software with a limited scope of use, for instance, word processors or spreadsheets. However, when the Model is complex and a result of a user design process, it becomes difficult for the software designer to encapsulate View and Controller interfaces that are user-friendly and can cope with any form of the model. This is the case for AMS, whose users have been known to model living organisms of many different forms, for instance, insects, fish, humans, and large mammals in addition to the environments they occupy, for instance, the aforementioned bicycles.

## AnyScript

In response to this problem, the primary modeling tool in AMS is a computer language, AnyScript, in which the user describes the model elements and their relationships. AnyScript is an object-oriented language with predefined classes representing biomechanical elements such as bones (segments), joints, and muscles. The system compiles the AnyScript code into the Model and subsequently presents the model to the user as graphical renditions and tree structures. The difference between this software design and a purely GUI-based system is akin to the difference between office type word processors, such as Microsoft Word, and a typesetting system like LaTeX. Fig. 7.1 shows typical elements of the AMS user interface with component tree, AnyScript editor window, graphical representation of the model, and analysis results output.

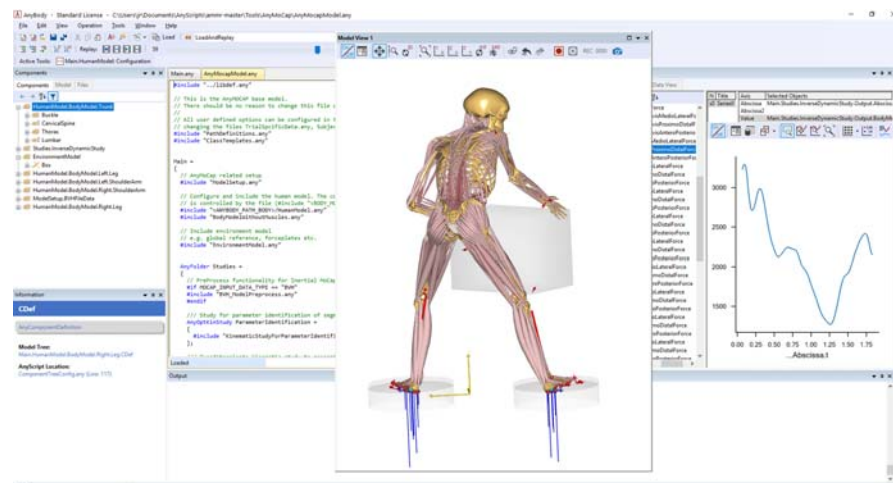


**FIGURE 7.1** The AnyBody modeling system user interface.

A typical screen shot of the AnyBody modeling system while analyzing a lifting situation.

## Multibody system formulation

At the core of AMS is a multibody simulation system, i.e., a collection of algorithms to compile and simulate the equations of motion for a system of linked bodies. To avoid confusion in terminology with the anatomical body, the mass-bearing bodies of biomechanical systems are often referred to as segments. AMS is a three-dimensional modeling system, so each rigid segment has six degrees-of-freedom, i.e., three translations and three rotations. The segments are connected by joints and other constraints, each of which reduces the total number of degrees-of-freedom, resulting in a mechanism with some remaining movement options. For instance, the hip joint is usually defined as a spherical joint, which eliminates the mutual translations between the acetabulum and the femoral head but leaves all three rotations free.

Despite the many constraints from anatomical joints, a model of a living organism has many movement options remaining; a typical full-body model in AnyBody has more than 100 degrees-of-freedom, and the combinations of these determine posture and movement. To specify the actual movement performed by the body, the joint constraints are supplemented with kinematic drivers. Driver information is typically derived from experimental data, i.e., motion capture data, and a large range of modalities can be used to collect such information, for instance, camera and marker-based motion capture systems, inertial measurement units, electrogoniometers, depth cameras, and stretch sensors. Accepting input from such different sources requires a rather general multibody formulation allowing for combinations of forward and inverse kinematics.

Multibody formulations have traditionally been classified into methods for open and closed chains referring to the topology of the mechanism at hand. Open chains are much easier to formulate in terms of kinematics as well as kinetics, and they lead to numerically efficient analysis methods. However, to retain maximum generality of the formulation, AMS relies on the so-called full cartesian method (Nikravesh, 1988), which handles any combination of open and closed chains. Please refer to the chapter on Multibody Modeling of the Musculoskeletal System for a comprehensive description of the mathematical formulation.

---

## The model repository

One of the early realizations of musculoskeletal modeling is that the modeling task is overwhelmingly complicated when comparing with other CAE technologies, due to the complexity of the human anatomy. This means that the task of modeling the human body—or even single body parts—cannot be left to the individual user; some sort of template model of the human anatomy must be made available, and procuring it is a monumental task in its own right.

In the case of AMS, the answer to this problem has been the creation of a repository of human models, the AnyScript Managed Model Repository (AMMR), which has been developed in an international cooperation between scientists, is managed by AnyBody Technology, and resides physically on the Internet site [www.anyscript.org](http://www.anyscript.org). The organization of this effort tries to strike a balance between the need for openness and the need for quality assurance.

On the one hand, the repository requires input from experts in general physiology, biomechanics, and functional anatomy of the individual body parts. For instance, to create a knee model for investigation of cruciate ligament injuries, the model developer must understand knee anatomy, injury mechanisms, and biomechanics in general and make sure that all of these fields are duly considered in the modeling choices. Furthermore, for users of such a model to have faith in its correctness, they must be able to scrutinize it, confirm that the necessary considerations are made, and understand the limitations of the model. This requires models that are open for contributions, modifications, investigations, and scrutiny in general; the models must be open. Finally, models must be validated independently (Lund et al., 2012).

On the other hand, models risk disruption of their functionality if everybody can change them without some sort of revision control; thus the term “Managed” in the name of the library. The solution has been to place the library in a publicly accessible home on the Internet and encourage contributions, error reports, and the like, while placing the responsibility for maintaining an official release of the models with a single organization, AnyBody Technology A/S from Aalborg in Denmark.

## Structuring principles

In the typical use situation for AMMR, the user analyzes a model comprising the human body—or parts thereof—and some sort of environment in which the body is working. For a gait model, the environment may be as simple as a floor. In other cases, the environment may be a mechanical system in its own right, such as a box (Fig. 7.1), a fitness machine (Fig. 7.2), a bicycle, a space suit, an exoskeleton, or a

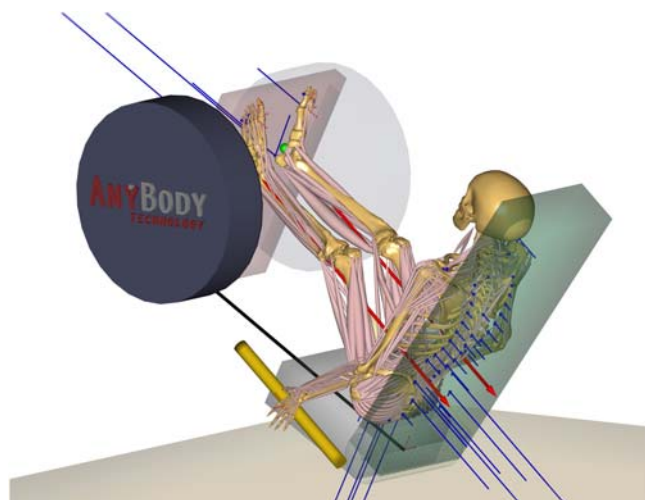


**FIGURE 7.2** Analysis of leg press exercise.

A musculoskeletal model comprising a body and a leg press machine environment.

collaborative robot. The body parts are needed by almost any user and are relatively static parts of musculoskeletal models, although they are often scaled or otherwise modified to fit an individual. The environment, on the other hand, is different for almost every new investigation.

For this reason, AMMR is divided into two main sections: Body and Application. The Body part contains the anatomical models that have been approved and are building blocks for general use. This means that the models of different body parts plug into each other to allow analysis of subsets of the body, for instance, upper or lower extremities attached to the thorax. The body models also contain a common geometrical scaling strategy that allows the models to scale according to overall dimensions, individual segment dimensions, geometrical morphing functions, and even to user-defined scaling functions. For details on the scaling strategy, please refer to the chapter on Multibody Modeling of the Musculoskeletal System. The body models contain all the morphological information for the detailed anatomy, but they lack information about motion drivers, mechanical supports, and connections with the environment, because this information is not generic. Therefore, body models cannot be analyzed in isolation.

The Application part of AMMR contains examples of loadable models, which we refer to as applications. The applications are specific instances of musculoskeletal models of particular situations as shown in [Figs. 7.1 and 7.2](#). Each application imports a body model and connects it to an environment, to subject-specific scaling information, and to motion specifications, thus creating an analyzable biomechanical model. In the interest of model structure, the part of the model that connects the body to the environment is often placed in a separate branch of the structure called the model–environment connection. This is convenient when analyzing several versions of the same situation, for instance, several gait trials for the same subject, or different subjects in the same environment.

---

## Applications

The applications of musculoskeletal modeling are diverse as it would be expected from a CAE technology, and they range from fundamental research to product design and across living species such as insects, fish, small and large quadrupeds, and humans. The majority of published studies are concerned with human biomechanics, where the best repository models also are available.

### Fundamental science applications

Musculoskeletal modeling has a potential to answer fundamental research questions, because the models provide information of what is impossible or very difficult to measure, i.e., internal forces in living or even extinct organisms, and because models can add causality to empirical observations. Some of the fundamental questions in human biomechanics relate to the interplay between the genetic evolution of the

human species in response to its environment. For instance, it has been speculated whether the ability to move at low metabolic cost and perform persistence hunting has been important for the survival of early hominids (Pontzer et al., 2009; Raichlen et al., 2011). With a musculoskeletal model, it is possible to investigate the economy of gait (Hedegaard et al., 2020) and other movements and understand how it relates to anthropometry (Xu et al., 2020), gender (Obrebska et al., 2020), muscle configuration (Ogrodnik & Piszczatowski, 2017), and motion patterns (Guan et al., 2019).

The same principles apply to animal evolution, where AMS has been used to investigate a number of species, for instance, the evolution of mastication in dragonflies and other insects (David et al., 2016a, 2016b).

### Orthopedic applications

Orthopedics is a major application field for musculoskeletal simulation. External loads on the human body typically have much larger moment arms than the internal muscle forces balancing them, and this creates surprisingly large internal biomechanical forces in the body. Surgically modified tissues and implants must withstand these loads, and the dependency of the loads on external conditions such as movement patterns, sports activities, and supportive devices, such as crutches and orthotics, are important knowledge for injury prevention and rehabilitation. Forces also depend on the design and implantation of trauma devices and joint replacements, as depicted in Fig. 7.3. This particular model allows for changes of implantation parameters, such as joint center coordinates and anteversion angle, and simulation of the effects of these parameters on the implant forces, and therefore on its longevity. Multiple similar studies are available on the mandible

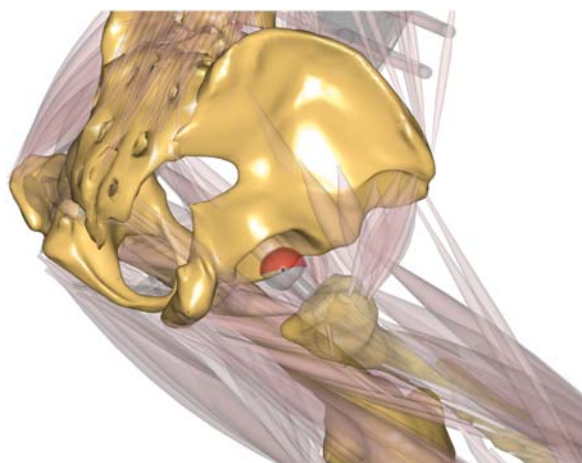


**FIGURE 7.3 Total hip arthroplasty model.**

Musculoskeletal model of a total hip arthroplasty. Parts of the musculature has been removed, and remaining muscles made transparent to display the implant.

(de Zee et al., 2009), shoulders (Sins et al., 2016), wrists (Eschweiler et al., 2016a, 2016b), the spine (Ignasiak, 2020), knees (Askari & Andersen, 2021), ankles (Zhang et al., 2020), and feet (Kim et al., 2019).

### Industrial product design

Many industrial products derive their value from the ability to interact with humans and from enabling humans to perform in ways that are otherwise impossible. Hand tools allow us to perform work processes that the bare hands cannot accomplish, bicycles (Fig. 7.4) give us the superpower of movement over distances and at speeds much beyond walking and running, and furniture provide relaxation or working postures that can be sustained for hours on end.

From the biomechanical point-of-view, the human body and the products we connect it with form a single mechanical system in which the constraints and support forces of the product influences the working conditions for the human body. Therefore, the design of the product influences its quality, as can be attested by anyone seated too long in an uncomfortable chair or riding a bicycle with a too low saddle.

The musculoskeletal model of the human and the product provides an opportunity for product optimization, because changes in the product parameters will result in different simulation results for the human part of the model, for instance, different levels of muscle activation. In the model of Fig. 7.4, a reduction of the saddle height will result in higher muscle activity in the quadriceps muscles, indicating more effort to cycle at a given power output.



**FIGURE 7.4** Cycling model.

Musculoskeletal model of a human on a bicycle.

## Sports

Musculoskeletal models are used in a variety of sports to optimize performance and minimize injury risk. In some branches of sports, such as golf, tennis (Fig. 7.5), baseball, cricket, weightlifting, and athletics, all or parts of the performance is conducted without intrusion from opponents, and much emphasis is devoted to refinement of technique. Musculoskeletal modeling can be used to study the transfer of mechanical energy between segments in kinetic chain movements, and it can reveal which parts of the musculature might be bottlenecks for better performance as illustrated by the magenta-colored muscles in Fig. 7.5. The technology can subsequently identify fitness exercises (Fig. 7.2), which target the muscles of interest.

Participants in endurance sports, such as distance running, are susceptible to repetitive injuries. Distance running has become popular as a fitness activity, and recreational distance runners have been reported susceptible to repetitive load injuries such as jumper's knee and Achilles tendinopathy (Mulvad et al., 2018). These injuries are results of many submaximal loads and happen when the rate of damage

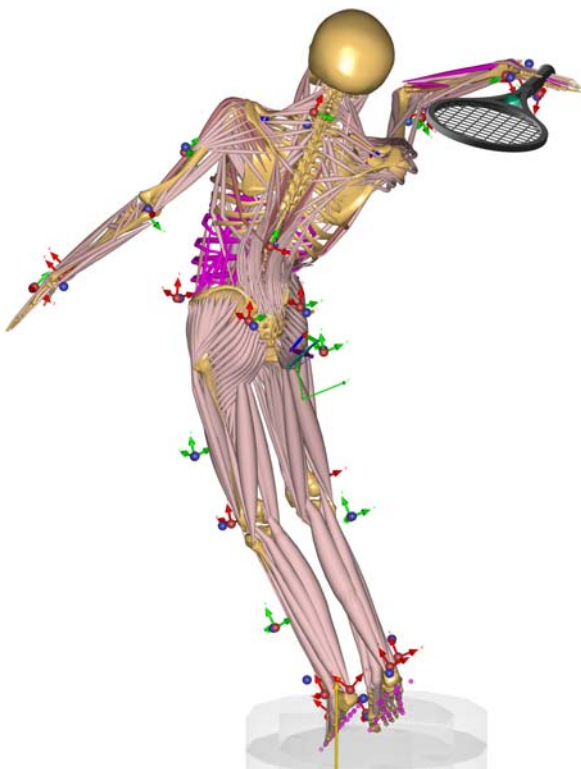


**FIGURE 7.5** Tennis serve.

Musculoskeletal model of a tennis serve near the point of maximum vertical acceleration.

exceeds tissue repair for a sufficiently extended period, i.e., the homeostasis of the tissues is disrupted. The nature of this problem is such that small changes of loads caused by running technique can tip the balance either way.

Musculoskeletal models of running ([Rasmussen & Lund, 2020](#)), as depicted in [Fig. 7.6](#), can predict the loads on isolated structures, such as the Achilles tendon or the patella ligament, in response to proposed changes of running style compared with the individual runner's current style. This predictive ability requires generation of running patterns from machine learning techniques that will be briefly described in the section on Digital Human Models and The Digital Patient below.



**FIGURE 7.6 AnyBody running model.**

A musculoskeletal model of an individual with a given running pattern.

## Workplace ergonomics

Manual work remains important in the labor market despite predictions of replacement by automation. Childcare, elderly care, and health care, for any foreseeable future, will contain manual work with relatively high physical loads. While traditional manual work in farming has been much reduced in the industrialized countries, other types of manual working processes, especially in logistics, seem to be accelerating. Also the building industry sees no decline in the demand for skilled workers, who continue to perform mounting, painting, plumbing, wiring, and other construction processes manually. These conditions coincide with the aging society in many countries postponing the retirement age and therefore increasing the average workforce age.

These developments highlight the need to create physical workplaces that are safe and have physical requirements compatible with a large part of the population. Occupational injuries share many traits with the sports injuries described in the preceding section; they can be acute or result from repetitive loads, sometimes over decades, and their cause–effect structures, progression, and management can be elusive.

Musculoskeletal models have much to offer in this context because they can be made specific to the individual and simulate the human biomechanics to a detailed level as illustrated by the figures in this chapter. Until now, the process of collecting motion data and subject-specific parameters has been too laborious for most cases in this field, but new types of motion capture equipment—especially based on inertial measurement units—have facilitated the process of collecting motion data in the workplace. Manual handling situations can typically be recorded in an hour *in situ*.

As an example, please consider the box lifting task depicted in Fig. 7.7. The motion data and subject-specific dimensions for this example are recorded *in situ* with an Xsens Awinda system (Xsens, Enschede, The Netherlands) and imported into AMS for analysis. The point-of-interest of this case is whether a change of the workplace to require lifting to a smaller height would relieve loads on the lumbar spine and the shoulders respectively.

To this end, a second trial was recorded with a smaller lifting height as depicted in Fig. 7.8.

Analysis of the output data reveals that the lower shelf height reduces the maximum load on the shoulder musculature and compression forces in the gleno-humeral joint, but it does not reduce the maximum loads in the lumbar spine, because these occur just when the box is lifted from the floor, and this condition is similar in the two cases. The analysis, therefore, points out that another type of intervention, for instance, an exoskeleton might be necessary, and this intervention could then also be analyzed for its effect.

Along the same lines (Skals et al., 2021), recently analyzed lifts in the Danish supermarket sector using a combination of on-site measurements and musculoskeletal modeling.

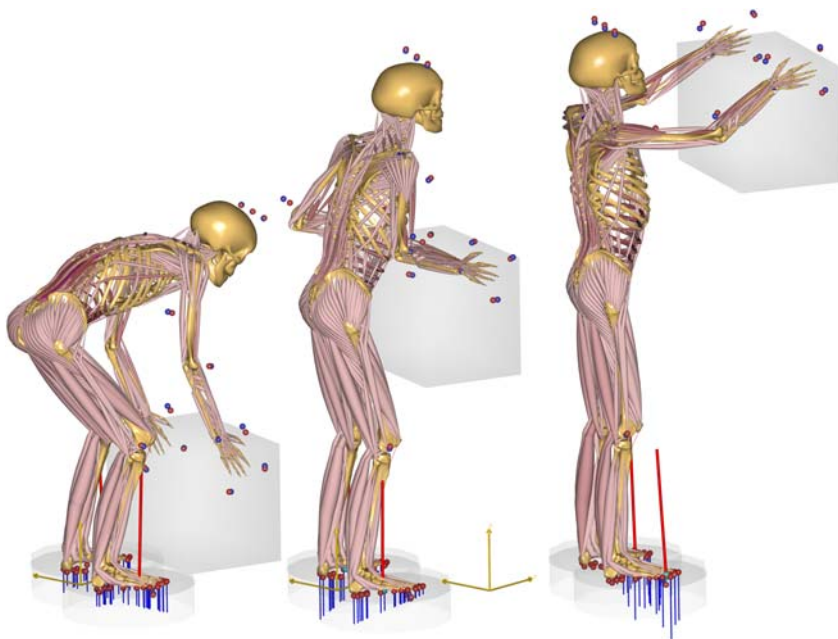


**FIGURE 7.7 High box lifting.**

Subject-specific musculoskeletal model lifting a 10 kg box to a shelf placed 1580 mm above floor height.

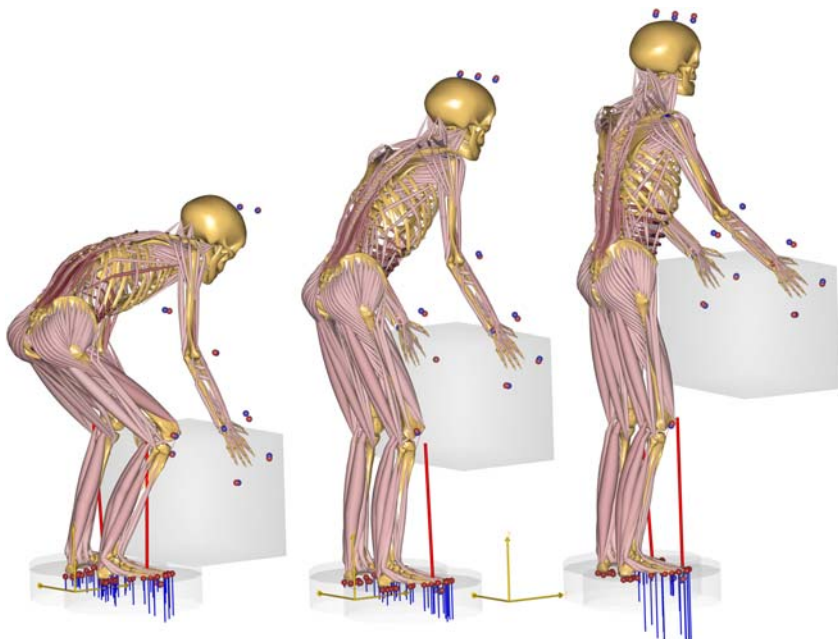


**FIGURE 7.8 Box lifting model to low height.**

Musculoskeletal model of box lifting to a height of 590 mm.

## Digital human models and the digital patient

While the design choices described in the preceding sections have certain drawbacks for the casual user—such as having to learn a scripting language with a formalized syntax and having to understand kinematics and kinetics—it carries significant advantages with respect to the technology’s evolution toward a digital description of the biomechanics of individuals and populations. To understand this, let us briefly introduce an informatics-inspired interpretation of The Digital Patient.

Patient information has traditionally been recorded in personal medical records. These records were originally stored on paper in hospitals or with each patient’s general physician. With digitalization of society, most countries have centralized these records to database servers to allow for remote access and update by the variety of GPs and hospitals responsible for different forms of treatment. However, the potential of digital medical records goes much beyond this. With enough information compiled about each patient, a digital twin model of the patient forms and can be constantly updated and work as an advanced basis for medical decisions. This arguably requires models that go beyond data and are able to simulate the function of the body and disease progression in a variety of physiology fields. This vision has been recognized since the change of the millennium (Bassingthwaite, 2000; Hunter et al., 2010). Its general realization appears to be very complicated, but implementation in particular fields such as musculoskeletal modeling is approaching with the assistance of machine learning algorithms.

To understand the concept, we start by noting that a full-body musculoskeletal model, as depicted in Fig. 7.1, contains thousands of parameters describing bone geometries, joint axes, muscle parameters, movements, and such, and this set extends with the evolution of more detailed body models resulting from continuous development of the technology, i.e., the data are dynamic. At any given time, the parameter set describes a particular individual performing a particular task, and the full set of parameters is necessary to perform the analysis. Whenever the model is refined, existing data become incomplete, and incomplete data from medical investigations would be useless. In other words, to be useful as a digital patient model, we need a system running on any combination of incomplete data. This can be obtained by modern data science methods. In the field of biomechanics, this type of simulation also requires reliable simulation of ground reaction forces, which has been shown possible with AMS for a range of different daily activities (Fluit et al., 2014) and sports movements (Skals et al., 2021), provided the movement of the whole body is included.

To illustrate the implementation of the flow depicted in Fig. 7.9, please consider the example of running as a small subset of what a digital patient might comprise. Many runners get injuries, either acute, such as ankle sprains, or repetitive loading injuries such as shin splints. Furthermore, the injury influences the running pattern, causing limping or other asymmetries, or perhaps decreased performance compared with normal, so complete data for a patient would contain dependencies between the disease and the motion data. Similarly, tall individuals would predominantly have

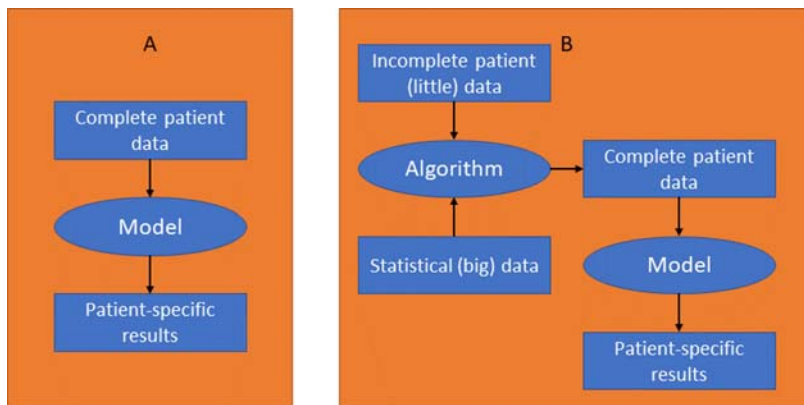


**FIGURE 7.9 Data flow for the biomechanical models and the digital patient.**

Traditional (A) and enhanced (B) data flows for parameters related to digital patient models.

long legs, and long legs tend to take longer steps than shorter legs, so the data contain dependencies between anthropometrical parameters and between anthropometry and functional parameters.

Machine learning can draw on these dependencies to infer on the nature of missing data. This produces the big data/little data relationship depicted in Fig. 7.9. Incomplete data for a single patient are termed “little data” and they are insufficient for a workable model. However, they are supplemented by statistical data termed “big data” which represent variations of parameters over a population. The inference of the missing parameters in little data from big data has already been demonstrated for running (Rasmussen & Lund, 2020; Skejø et al., 2021). The result is adaptive models that will work from any subset of the necessary subject-specific parameters and grow in accuracy as more information is added to the digital medical records.

In conclusion, musculoskeletal simulation, as implemented in the AMS, is a CAE technology for modeling of living organisms. It has similarities with—but also some differences from the CAE technologies that grew out of industrial applications. Among the notable differences is that model development is an integral part of the research, and that models of individuals can be extended to populations and will play an important role for the digital patient of the future.

## References

- Andersen, M. S., Damsgaard, M., MacWilliams, B., & Rasmussen, J. (2010). A computationally efficient optimisation-based method for parameter identification of kinematically determinate and over-determinate biomechanical systems. *Computer Methods in Biomechanics and Biomedical Engineering*, 13(2), 171–183.

- Andersen, M. S., Damsgaard, M., & Rasmussen, J. (2009). Kinematic analysis of over-determinate biomechanical systems. *Computer Methods in Biomechanics and Biomedical Engineering*, 12(4), 371–384.
- Askari, E., & Andersen, M. S. (2021). Effect of ligament properties on nonlinear dynamics and wear prediction of knee prostheses. *Journal of Biomechanical Engineering*, 143(2).
- Bassingthwaite, J. B. (2000). Strategies for the physiome project. *Annals of Biomedical Engineering*, 28(8), 1043–1058.
- Belytschko, T., Gracie, R., & Ventura, G. (2009). A review of extended/generalized finite element methods for material modeling. *Modelling and Simulation in Materials Science and Engineering*, 17(4), 043001. <https://doi.org/10.1088/0965-0393/17/4/043001>
- Chen, Q., & Konrad, A. (1997). A review of finite element open boundary techniques for static and quasi-static electromagnetic field problems. *IEEE Transactions on Magnetics*, 33(1), 663–676.
- Damsgaard, M., Rasmussen, J., Christensen, S. T., Surma, E., & De Zee, M. (2006). Analysis of musculoskeletal systems in the AnyBody modeling system. *Simulation Modelling Practice and Theory*, 14(8), 1100–1111.
- David, S., Funken, J., Potthast, W., & Blanke, A. (2016a). Musculoskeletal modelling of the dragonfly mandible system as an aid to understanding the role of single muscles in an evolutionary context. *Journal of Experimental Biology*, 219(7), 1041–1049.
- David, S., Funken, J., Potthast, W., & Blanke, A. (2016b). Musculoskeletal modelling under an evolutionary perspective: Deciphering the role of single muscle regions in closely related insects. *Journal of The Royal Society Interface*, 13(123), 20160675.
- Eschweiler, J., Stromps, J.-P., Fischer, M., Schick, F., Rath, B., Pallua, N., & Radermacher, K. (2016a). A biomechanical model of the wrist joint for patient-specific model guided surgical therapy: Part 2. *Proceedings of the Institution of Mechanical Engineers, H: Journal of Engineering in Medicine*, 230(4), 326–334.
- Eschweiler, J., Stromps, J.-P., Fischer, M., Schick, F., Rath, B., Pallua, N., & Radermacher, K. (2016b). Development of a biomechanical model of the wrist joint for patient-specific model guided surgical therapy planning: Part 1. *Proceedings of the Institution of Mechanical Engineers, Part H: Journal of Engineering in Medicine*, 230(4), 310–325.
- Fluit, R., Andersen, M. S., Kolk, S., Verdonschot, N., & Koopman, H. F. J. M. (2014). Prediction of ground reaction forces and moments during various activities of daily living. *Journal of Biomechanics*, 47(10), 2321–2329. <https://doi.org/10.1016/j.biomech.2014.04.030>
- Guan, X., Kuai, S., Song, L., Liu, W., Liu, Y., Ji, L., & Wang, R. (2019). Effects of ankle joint motion on pelvis-hip biomechanics and muscle activity patterns of healthy individuals in knee immobilization gait. *Journal of Healthcare Engineering*, 38, Article 3812407. <https://doi.org/10.1155/2019/3812407>
- Hedegaard, M., Anvari-Moghaddam, A., Jensen, B. K., Jensen, C. B., Pedersen, M. K., & Samani, A. (2020). Prediction of energy expenditure during activities of daily living by a wearable set of inertial sensors. *Medical Engineering & Physics*, 75, 13–22. <https://doi.org/10.1016/j.medengphy.2019.10.006>
- Huang, H.-C., & Usmani, A. S. (2012). *Finite element analysis for heat transfer: Theory and software*. Springer Science & Business Media.
- Hunter, P., Coveney, P. V., De Bono, B., Diaz, V., Fenner, J., Frangi, A. F., Harris, P., Hose, R., Kohl, P., & Lawford, P. (2010). A vision and strategy for the virtual physiological human in 2010 and beyond. *Philosophical Transactions of the Royal Society A: Mathematical, Physical and Engineering Sciences*, 368(1920), 2595–2614.

- Ignasiak, D. (2020). A novel method for prediction of postoperative global sagittal alignment based on full-body musculoskeletal modeling and posture optimization. *Journal of Biomechanics*, 102, 109324.
- Kim, Y., Kim, J., Lee, K. M., & Koo, S. (2019). The increase of joint contact forces in foot joints with simulated subtalar fusion in healthy subjects. *Gait & Posture*, 74, 27–32.
- Krasner, G. E. (1988). A cookbook for using model-view-controller user interface paradigm in smalltalk-80. *Journal of Object Oriented Programming*, 1(3), 26–49.
- Lund, M. E., de Zee, M., Andersen, M. S., & Rasmussen, J. (2012). On validation of multi-body musculoskeletal models. *Proceedings of the Institution of Mechanical Engineers, Part H: Journal of Engineering in Medicine*, 226(2), 82–94.
- Mulvad, B., Nielsen, R. O., Lind, M., & Ramskov, D. (2018). Diagnoses and time to recovery among injured recreational runners in the RUN CLEVER trial. *PloS One*, 13(10), e0204742.
- Nikravesh, P. E. (1988). *Computer-aided analysis of mechanical systems*. Prentice-Hall International, Inc.
- Obrebska, P., Skubich, J., & Piszczałkowski, S. (2020). Gender differences in the knee joint loadings during gait. *Gait & Posture*, 79, 195–202. <https://doi.org/10.1016/j.gaitpost.2020.05.017>
- Ogrodnik, J., & Piszczałkowski, S. (2017). Influence of modified muscle morphology and activity pattern on the results of musculoskeletal system modelling in cerebral palsy patient. *Acta of Bioengineering and Biomechanics*, 19(3), 63–75. <https://doi.org/10.5277/ABB-00809-2017-02>
- Pontzer, H., Raichlen, D. A., & Sockol, M. D. (2009). The metabolic cost of walking in humans, chimpanzees, and early hominins. *Journal of Human Evolution*, 56(1), 43–54. <https://doi.org/10.1016/j.jhevol.2008.09.001>
- Raichlen, D. A., Armstrong, H., & Lieberman, D. E. (2011). Calcaneus length determines running economy: Implications for endurance running performance in modern humans and Neandertals. *Journal of Human Evolution*, 60(3), 299–308. <https://doi.org/10.1016/j.jhevol.2010.11.002>
- Rasmussen, J., Damsgaard, M., & Voigt, M. (2001). Muscle recruitment by the min/max criterion—a comparative numerical study. *Journal of Biomechanics*, 34(3), 409–415.
- Rasmussen, J., & Lund, M. E. (2020). Data-based parametric biomechanical models for cyclic motions. In *DHM2020: Proceedings of the 6th international digital human modeling symposium* (Vol. 11, p. 372). IOS Press.
- Schiehlen, W. (1997). Multibody system dynamics: Roots and perspectives. *Multibody System Dynamics*, 1(2), 149–188. <https://doi.org/10.1023/A:1009745432698>
- Sins, L., Tétreault, P., Nuño, N., & Hagemeister, N. (2016). Effects of prosthetic mismatch and subscapularis tear on glenohumeral contact patterns in total shoulder arthroplasty: A numerical musculoskeletal analysis. *Journal of Biomechanical Engineering*, 138(12).
- Skals, S., Bláfoss, R., Andersen, L. L., Andersen, M. S., & de Zee, M. (2021). Manual material handling in the supermarket sector. Part 2: Knee, spine and shoulder joint reaction forces. *Applied Ergonomics*, 92, 103345. <https://doi.org/10.1016/j.apergo.2020.103345>
- Skejø, S. D., Lund, M. E., Stensvig, M., Kaae, N. M., & Rasmussen, J. (2021). Running in circles: Describing running kinematics using Fourier series. *Journal of Biomechanics*, 115, 110187.
- Thompson, L. L. (2006). A review of finite-element methods for time-harmonic acoustics. *The Journal of the Acoustical Society of America*, 119(3), 1315–1330.

- de Zee, M., Cattaneo, P. M., Svensson, P., Pedersen, T. K., Melsen, B., Rasmussen, J., & Dalstra, M. (2009). Prediction of the articular eminence shape in a patient with unilateral hypoplasia of the right mandibular ramus before and after distraction osteogenesis—a simulation study. *Journal of Biomechanics*, 42(8), 1049–1053.
- Xu, C., Reifman, J., Baggaley, M., Edwards, W. B., & Unnikrishnan, G. (2020). Individual differences in women during walking affect tibial response to load carriage: The importance of individualized musculoskeletal finite-element model. *IEEE Transactions on Biomedical Engineering*, 67(2), 545–555. <https://doi.org/10.1109/TBME.2019.2917415>
- Zhang, Y., Chen, Z., Peng, Y., Zhao, H., Liang, X., & Jin, Z. (2020). Predicting ground reaction and tibiotalar contact forces after total ankle arthroplasty during walking. *Proceedings of the Institution of Mechanical Engineers, Part H: Journal of Engineering in Medicine*, 234(12), 1432–1444.

This page intentionally left blank

# The NEUROiD neuromusculoskeletal movement simulation platform

# 8

Raghu Sesha Iyengar, Kapardi Mallampalli, Avinash Kumar Singh, Aditya Koppula,  
Kousik Sarathy Sridharan, Mohan Raghavan

Indian Institute of Technology, Department of Biomedical Engineering, Hyderabad, Telangana,  
India

## Chapter outline

<b>Introduction.....</b>	162
<b>The NEUROiD movement simulation platform.....</b>	163
Design philosophy and architecture.....	163
<i>Multiscale, multidiscipline, and multifunction platform</i> .....	163
Workflow in NEUROiD .....	166
Model definition, simulation, and visualization.....	167
<i>Curation and definition</i> .....	167
<i>Experiment and simulation</i> .....	169
<i>Visualization</i> .....	169
Integrative model development .....	171
Choosing a musculoskeletal model.....	172
<b>Design and characterization of limbs in silico .....</b>	172
Upper limb .....	172
Lower limb.....	177
<b>Movement training of virtual limbs.....</b>	179
Machine learning setup.....	180
<b>NEUROiD in medicine .....</b>	182
NEUROiD models .....	183
NEUROiD activities .....	183
Twinning in NEUROiD .....	183
Clinical trials and experimentation in silico with NEUROiD .....	184
<i>Clinical triage for spasticity</i> .....	184
<i>Design and test of prostheses</i> .....	185
<i>Diabetic neuropathy—induced diabetic foot</i> .....	186
<i>Stroke: cross-sectional modeling of stroke severity and corticospinal residuum</i>	186

<i>Stroke: longitudinal modeling of recovery and computational neurorehabilitation .....</i>	188
<i>Spinal cord stimulation .....</i>	190
<i>Motor neuron disease (amyotrophic lateral Sclerosis, spinal muscular atrophy, familial spastic paraplegia).....</i>	190
<i>Peripheral neuropathies .....</i>	191
<i>Mechanisms and consequences of aging-induced changes in motor unit structure.....</i>	191
<i>Limitations .....</i>	192
<i>Medical education and training .....</i>	192
<b>Conclusion and future landscapes.....</b>	192
<b>References .....</b>	193

---

## Introduction

Movement, even of the simplest type, needs coordinated activity from the neuronal, muscular, and skeletal systems. The quest to understand such movements has been partially satisfied by building models that simulate various aspects of these subsystems. Many of the subsystems involved in movement generation and control have been modeled. These include models of individual motoneurons (McIntyre et al., 2002; Safronov & Vogel, 1995), models of spinal circuitry (Moraud et al., 2016; Pierrot-Deseilligny & Burke, 2012), pattern generators (Danner et al., 2019; McCrea & Rybak, 2008), cerebello-thalamocortical models (Izhikevich & Edelman, 2008; Zhang & Santaniello, 2019), and models of basal ganglia for movement selection (Gurney et al., 2001a, 2001b). Models of musculoskeletal subsystems include models of muscle cells (Kim, 2017; Wang et al., 2008), models of single and multi-joint musculoskeletal subsystems (Delp et al., 1990; Holzbaur et al., 2005), and physics-based musculoskeletal models (Song & Geyer, 2015a, 2015b). Such subsystem models have been developed at the micro (cellular), meso (network), and macro (system) scales.

Musculoskeletal modeling is rooted in mechanics while neural signaling is electrical in nature. Research and modeling in each of these disciplines have evolved over the decades. Tools used in these disciplines are naturally different, e.g., OpenSim (Seth et al., 2018) and NEURON (Hines & Carnevale, 1997) are popular simulators for modeling the musculoskeletal and nervous systems, respectively. Models built and simulated on these platforms span the disciplines of neuroscience and musculoskeletal mechanics. However, modeling virtual movement physiology needs integration of these subsystem models based on biologically plausible communication. Constraining the model parameters, inputs, or outputs in order to match one or more physiological traits or measurements such as electrophysiology, imaging or kinematics makes virtual physiology a digital twin of the real subject. Such a digital twin of the neuromusculoskeletal system which is capable of generating movement as an emergent phenomenon across multiple scales and disciplines has immense potential. It can aid in In-Silico Clinical Trials of medical devices and drugs, the study of movement disorders, or the design of biomimetic systems and prosthetics.

---

## The NEUROiD movement simulation platform

The NEUROiD (NEUROmotor integration and Design) platform (Iyengar et al., 2019) is a neuromusculoskeletal model design, curation, and integration platform. Its architecture inherently embraces the multidisciplinary nature of movement simulation by enabling cosimulation of neural components on NEURON and musculoskeletal components on OpenSim. NEUROiD models are inherently multiscale and can be built from scratch or integrated in a bottom-up fashion starting from the cellular level and going up to the systems level. The models can accommodate anatomical, physiological, and biomechanical realism at all levels. The model building experience is made intuitive and simple by using a spreadsheet for most of the model definition, followed by automatic model code generation. Apart from acting as a model builder and cosimulator, NEUROiD also includes a web-based user interface for visualization of models, inputs, and outputs across scales and disciplines (neural activity and musculoskeletal movement).

### Design philosophy and architecture

#### *Multiscale, multidiscipline, and multifunction platform*

The principles that govern the design of NEUROiD are best summarized on a  $3 \times 3$  cube shown in Fig. 8.1.

We briefly describe the salient features of NEUROiD here. Detailed information can be found in (Iyengar et al., 2019):

- Multiscale and multidisciplinary simulation: NEUROiD inherently incorporates the multiscale and multidisciplinary nature of movement. These form the first two axes of the representative cube (Fig. 8.1). As of this writing, spinal cord and musculoskeletal models involved in movement control, form the core focus of NEUROiD. Along the scale axis, models of cellular morphologies and sub-cellular physiology form the microscale model definition. Models of various cell groups, laminae boundaries, and spinal circuits form the mesoscale model definitions. Models of spinal segments and the entire spinal cord form the system-level model definition. Along the discipline axis, the model definition encompasses neuroanatomy, physiology, and musculoskeletal mechanics. The ability to build models with biological realism across various scales and disciplines is crucial for building an effective digital twin platform for movement simulation.
- Multifunction: The function axis of the representative cube shows aspects of NEUROiD functionality which are essential for building a system-level movement simulation.
  1. Model definition: Defining a model on NEUROiD involves specifying various parameters of the model at the scales and disciplines identified in Fig. 8.1. Anatomical details of neuronal cell models (for example, dendritic tree structure, length and diameter of soma, axon, and dendrite) form the

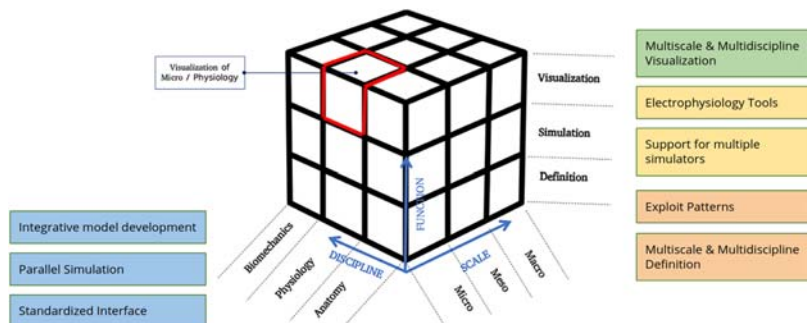


**FIGURE 8.1 NEUROiD design philosophy**

The architecture of NEUROiD is represented on a  $3 \times 3 \times 3$  cube with function, scale, and discipline being the three axes. The function axis represents major operations performed on a neuromotor system, namely model definition, simulation/virtual experimentation (on the defined model), and visualization (of model and results). The scale axis represents micro, meso, and macroscales of a neuromotor model. The discipline axis represents different disciplines that come together in a virtual neuromotor system, namely anatomy, physiology, and biomechanics. The cubelet corresponding to visualization of microphysiology is highlighted.

From <https://doi.org/10.3389/fninf.2019.00056>

microlevel anatomical definitions. Various channel mechanisms, ion channel parameters are examples of microlevel physiology definitions. The 3-dimensional spatial boundaries of various laminae in spinal segments are an example of the macroscale anatomical definition. NEUROiD also generates the spinal circuit connections based on muscle synergy. These are defined in spreadsheets or plain text files. The model definition is parsed to create an intermediate model representation by NEUROiD. Position of electrodes for current stimulation, magnitude and duration of stimulation, position of electrodes to measure the response are examples of definition for the experimental setup on the model. These are specified in json format in plain text file by the user. NEUROiD generates the code for simulation from the definition of model and experimental setup.

## 2. Simulation:

(a) Intermediate model representation: Currently, we use NEURON (Hines & Carnevale, 1997) to simulate neuronal cells and circuits. We also allow simulation of some very simple musculoskeletal models using simplistic rigid body models on NEURON along with the rest of the neuronal model. However, the preferred mode is cosimulation with OpenSim (Seth et al., 2018) for most practical scenarios. Our architecture separates the model definition (in spreadsheets) from the intermediate model representation (Fig. 8.2). This representation is used to generate the code for model simulation and hence makes the model

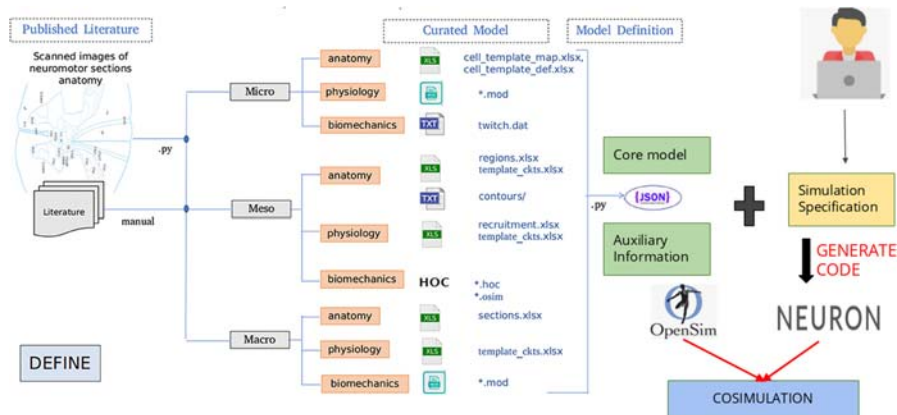


**FIGURE 8.2 NEUROiD workflow**

Workflow for model curation and definition (read from left to right). Published literature is scoured manually for the parameters required for the model of interest. The parameters pertaining to different scales and disciplines are separated and entered in the relevant tables in xlsx. Python scripts are used to parse the structured curated xlsx sheets to create a composite model definition in the form of JSON files. Simulation-specific information from the user is then used to perform the simulation with the NEURON backend.

From Iyengar RS, Pithapuram MV, Singh AK and Raghavan M (2019) Curated Model Development Using NEUROiD: A Web-Based NEUROmotor Integration and Design Platform. *Front. Neuroinform.* 13:56. doi: <https://doi.org/10.3389/fninf.2019.00056>

definition simulator agnostic. A plugin layer could implement conversion of this model definition to any target simulator.

- (b) Virtual electrophysiology tools: Electrophysiological tools form the virtual hands of the researcher while probing a neuronal system. NEUROiD provides virtual electrophysiological tools to probe the models and perform design interventions. Standard tools to inject current at desired sections of the model, measure membrane potential, and slice the model to view cross sections are a part of NEUROiD.
- 3 Visualization: There is no better alternative to gain insights into a model than to visualize it. Visible Human Project (Ackerman, 1998), which is an effort toward visualizing the anatomical cross sections in humans, underscores the importance of visualization. NEUROiD allows researchers to visualize the model at multiple scales, starting from the cellular scale to the system scale. To list a few, the researcher can visualize detailed cell morphology, 3D boundaries of laminae, and 3D structures of spinal segments thus, providing greater insights into the model.
- Integrative model development: The ability to integrate multiple models and obtain a new integrated model that displays the properties of all constituent models is an indispensable feature to build larger and biologically realistic

models. NEUROiD provides tools to facilitate this type of model integration to build larger system-level models.

- Virtual physiology as a bio-digital twin: In order to build virtual physiologies or bio-digital twins, it is imperative that the real and biological entities should have compatible formats for interfaces, inputs, and outputs. By constraining the model to match one or more inputs, outputs, or internal variables with the corresponding values measured in real physiology, the virtual physiology becomes a digital twin of the biological entity. NEUROiD defines such biologically plausible software interfaces between and across its modules. It further enables machine learning–based methods for identifying the model constraints or their inputs that reproduce real biological behavior within the virtual physiology (Iyengar et al., 2021)
- Exploit parallelism: Large-scale simulations require efficient parallelized execution. The simulation of neuronal systems has been successfully parallelized (Iyengar & Raghavan, 2020) in NEUROiD. NEURON supports parallelization on a cluster of CPUs using ParallelContext.<sup>1</sup> Dockerizing software applications have helped in quick and consistent deployment across different hardware platforms. Dockerized NEUROiD supporting parallel execution across CPUs over MPI proves to be an extremely important step toward creating a portable and parallelized simulation environment.

### ***Workflow in NEUROiD***

The high-level workflow in NEUROiD is shown in Fig. 8.2. Along with the introduction of NEUROiD as a platform, (Iyengar et al., 2019) also demonstrated building exemplar models on NEUROiD. Below is a brief summary of the process involved in building and simulating an exemplar model on NEUROiD.

Musculoskeletal joint(s) of interest (e.g., ankle joint) for simulation and study is (are) identified. The muscle groups (e.g., tibialis anterior, gastrocnemius, soleus) and corresponding motor neurons controlling the joint(s) are then identified. A literature study is performed to identify relevant models of motor neurons, interneurons and circuits. First a motoneuron model is defined in NEUROiD based on parameters from a published model (Moraud et al., 2016). The parameters of the model are defined in spreadsheets using a well-defined schema. The cell model is then validated by measuring its single cell neurophysiological properties such as frequency–current curve and spike-rate adaptation. A system level neuronal model of relevant spinal cord segments (L4 and L5 in this case) is then built. Instances of the interneuron, motoneuron, and relevant cell models are placed in relevant laminae of the spinal segments. Based on muscle synergies, the spinal circuits which are known to influence movement (e.g., monosynaptic Ia pathways, Ia and II reciprocal inhibition pathways, recurrent inhibition) are also modeled. This system level model is validated by comparing the system level properties such as the spinal reflex recruitment curve with that of a

---

<sup>1</sup> [https://www.neuron.yale.edu/neuron/static/py\\_doc/modelspec/programmatic/network/parcon.html](https://www.neuron.yale.edu/neuron/static/py_doc/modelspec/programmatic/network/parcon.html)

standard model. The neuronal model can then be interfaced to a musculoskeletal model to observe changes in joint angles as a result of simulation.

## Model definition, simulation, and visualization

### Curation and definition

#### Model specification to the definition

Objectives of the experiment decide the kind of component models to be used or the scales at which to model. For example, the objective of the experiment could be to model the rheobase of a particular type of motoneuron model and to observe the effect of change in a particular ion channel conductance or distribution density on rheobase. For such experiments, the model specifications should cover the cellular (e.g., soma diameter, the diameter of the dendrite, number of dendritic segments, membrane resistance, capacitance) and subcellular (e.g., types of ion channels, conductance, activation, and inactivation variables) properties. If the objective of the experiment is to observe a phenomenon such as H-reflex, the model specification would also need to cover motor neuron morphology and the interplay of sensory and afferent fibers. Orderly recruitment of groups of motor units requires models of multiple motoneuron groups—slow, fast-fatigable, and fatigue-resistant. If the goal is to model the triphasic pattern of muscle activation during ballistic movement, then the need is to model spinal circuits along with muscle models.

Relevant literature is studied to find reusable models and determine the parameters of the models based on the specifications. Cellular models and models of ion channels could be obtained from standard repositories such as ModelDB (Peterson et al., 1996) or Channelpedia (Ranjan et al., 2011). Essential properties from these models are then loaded into xlsx files for automatic model generation. NEUROiD has exemplar models that are available when installed. These models could be used directly if it serves the objectives of the experiment. These could also be modified or completely new models could be created. Morphological and physiological properties at various scales (cellular, network, system) are loaded into different files as per the scale-discipline matrix as described below.

### Definition across scale and discipline

**Micro/Anatomy:** Properties such as the diameter of soma, diameter of the dendrite, number of dendritic sections, axon diameter, position, and diameter of nodes are some examples that form the microlevel anatomical definitions. These properties for the model of interest could be either obtained from existing models (Capogrosso et al., 2013; Pietro et al., 2014, 2015) or defined by the user.

**Meso/Anatomy:** Laminae boundaries (Bror, 1954), rostro-caudal maps of the laminae regions (Sharrard, 1964), type and densities of cell types in various laminae are some examples of the mesolevel anatomical definitions. The laminae boundaries are stored as a set of x–y coordinates in a clockwise direction (as seen from the rostrocaudal direction). For the exemplar models available with installation, these boundaries were obtained from high-resolution images of the spinal cord at various sections in the transverse plane scanned from (Sengul, 2012).

**Macro/Anatomy:** Lengths of various spinal cord segments, their alignment along the neuraxis, and the position of various tracts are some examples of mesoscale anatomical definitions. For the exemplar model, these were derived from (Ko et al., 2004).

**Micro/Physiology:** Models of various types of ion channels, density of channels present, and models of synaptic transmission are some examples of microscale physiological aspects which are modeled. The channel models available with the exemplar models were ported from open-source repositories such as ModelDB (Peterson et al., 1996) and Channelpedia (Ranjan et al., 2011).

**Meso/Physiology:** Models of spinal reflex pathways, such as the recurrent inhibition, Ia and II reciprocal inhibition, and disinhibition pathways (Pierrot-Deseilligny & Burke, 2005, 2012), spinal circuitry involving motoneurons and interneurons, models of pattern formation, and rhythm generator circuits are some examples of mesoscale physiological aspects. NEUROiD uses a unique muscle synergy-based circuit generation technique that exploits the patterns in spinal circuits to store these mesoscale connection descriptions in a concise rule-based manner.

**Macro/Physiology:** System-level physiology models that can evaluate the Local Field Potential (LFP) or the electromyogram response for a given stimulation, effects of stimulation electrode geometry, and orientation are some examples for macroscale physiology aspects of modeling. NEUROiD has integrated LFPSim (Harilal et al., 2016) which is a library to evaluate the LFP at a given 3D point using point source, line source, or RC filter approximation.

**Micro/Biomechanics:** Models of twitch responses of individual types of muscle fibers (Freeman & Durfee, 2006; Fuglevand et al., 1993) form a very important component of the microscale biomechanical property. However, based on the specifications of the experiment, cellular and subcellular properties such as excitation–contraction coupling could very well form the microlevel biomechanical component.

**Meso/Biomechanics:** The relation between the force generated in a muscle to the firing frequency of motoneurons, the cross-sectional area of the muscle, or the pennation angle are some examples of the mesoscale biomechanical property of the system model.

**Macro/Biomechanics:** At the macroscale, size principle-based orderly recruitment, amount of force generated based on recruitment, or the actual angles of the joints that are being simulated form some key biomechanical properties.

### Neuromusculoskeletal interface design

NEURON and OpenSim are popular neuronal and musculoskeletal simulators. Each of these has been widely adopted in the respective communities and a large body of models has been built and used on these platforms. The NEUROiD interface layer implements the efferent and afferent connections between NEURON and OpenSim. On the efferent side, a function of the time-ensemble average of spike rates represent the muscle activation (Fuglevand et al., 1993). While on the afferent side, we use proprioceptive models (Prochazka, 1999) to arrive at the afferent firing frequency based on the muscle length, change in length, and force generated. Musculoskeletal response times are typically in the range of tens of milliseconds (Freeman & Durfee,

2006), much larger than neuronal response times. NEUROiD allows the NEURON and OpenSim step interval to be independently configured to exploit this fact. NEURON and OpenSim cosimulation with the proprioceptive loop closed provides a biologically plausible regime to experiment with neuromusculoskeletal models.

### **Experiment and simulation**

#### **Experiment specification to the definition**

NEUROiD generates a model definition from the curated model using automated scripts. This model definition is then used to generate NEURON code that can be simulated. At this point, the researcher needs to specify the various specifications that define the experiment (Fig. 8.2). These specifications can be categorized into input, response, and plots. The specifications related to input can include the type of input stimulation (e.g., epidural electrical stimulation, implemented as Netstim or a current clamp, implemented as iclamp, in NEURON), spatial location or the cell group where the input stimulation should be provided, the amplitude, duration, or pattern of input stimulation. The specifications related to response include the spatial location or the cell group a measurement has to be made and recorded, the parameter that needs to be recorded and stored. The specification on plots includes the variables that need to be plotted, the type of plot, and the specifications for any preprocessing that needs to be applied before plotting. The generated model and these experiment specifications are used by NEUROiD to run a NEURON-OpenSim cosimulation.

### **Parallelization**

NEURON supports MPI parallelization on a cluster of CPUs using the ParallelContext method. NEUROiD is parallelized and dockerized (Iyengar & Raghavan, 2020) to enable quick and scalable deployment. NEUROiD uses a docker swarm to parallelize model simulation on a cluster. NEURON parallelization does not work out-of-the-box on models that are containerized and run on a docker swarm. Please refer to Iyengar & Raghavan (2020) for further details on parallel execution of NEUROiD models inside containers on a cluster of CPUs using docker swarm.

### **Visualization**

Models are built bottom-up on NEUROiD with anatomical and physiological details across scales. It is important to visualize the model and its response at all scales and disciplines. Fig. 8.3 shows the various visualizations available on NEUROiD, laid across the scale-discipline matrix. For example, we could visualize the morphologies of individual cell models built on NEUROiD. Similarly, the experiment specification from the user could specify to record and visualize various ionic channel currents in the cell model, which would form a microscale physiological visualization. This simultaneous visualization across the scale and discipline matrix for a given model and experiment allows researchers to probe the model at various levels and gain an in-depth understanding.

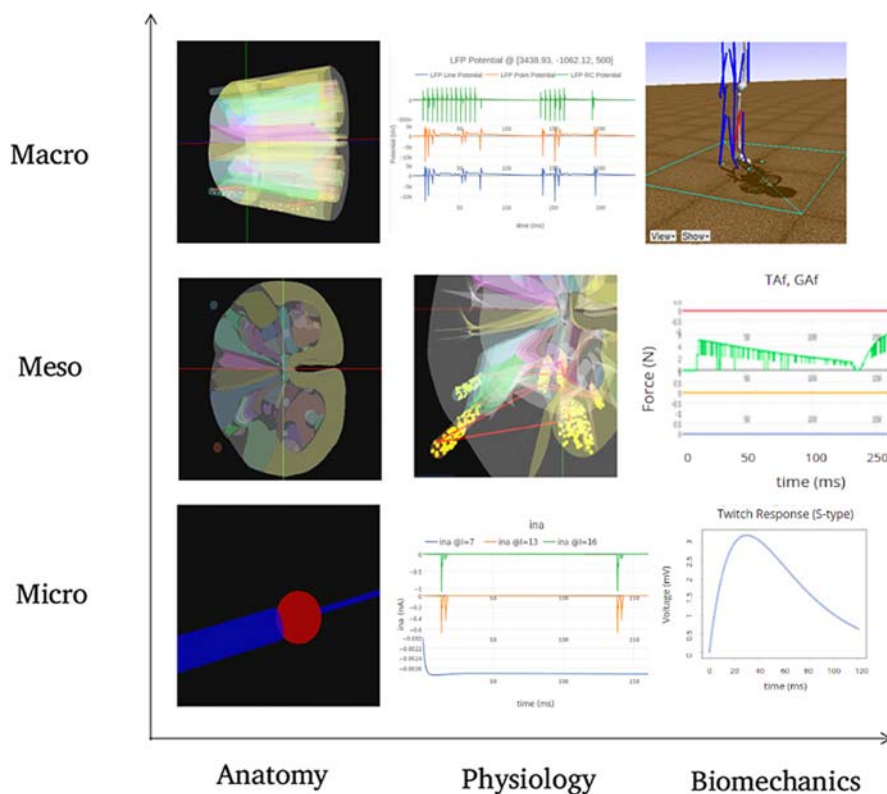


**FIGURE 8.3 NEUROiD visualization**

The figure shows snapshots from various simulations in NEUROiD representing the 9 cubelets of the visualization plane. In the Macro/Anatomy cubelet, we see the 3D model of L4 and L5 segments of the spinal cord. Contours in the sliced L4 segment are seen in the Meso/Anatomy cubelet. The cell morphology that forms the Micro/Anatomy component, can be seen in the corresponding cubelet. In the Macro/Physiology cubelet, we see the local field potential evaluated at a user-specified point in 3D space. The Meso/Physiology cubelet shows the synaptic connections and neural circuits that we have defined in the L4 and L5 segments. Ionic currents due to channel mechanisms forming the Micro/Physiology component are seen in the corresponding cubelet. Along with the biomechanics discipline, the ankle model and angle made at the ankle joint are seen in the Macro/Biomechanics cubelet. Force generated in muscles as a response to the motoneuron activation is seen in the Meso/Biomechanics cubelet. The Micro/Biomechanics component seen is the twitch response of a muscle fiber.

*From Iyengar RS, Pithapuram MV, Singh AK and Raghavan M (2019) Curated Model Development Using NEUROiD: A Web-Based NEUROmotor Integration and Design Platform. Front. Neuroinform. 13:56. doi: <https://doi.org/10.3389/fninf.2019.00056>*

## Integrative model development

Computational models are typically built to demonstrate specific features of interest. However, to build large virtual physiological models that can be used as virtual patients or digital twins, it is imperative to have a single model of a specific component that could demonstrate all the properties of interest seen in various constituent models. To achieve this, NEUROiD provides a framework to integrate multiple models. We briefly outline the steps to achieve this goal:

- Curating constituent models: The first step is to identify the constituent models that display specific features that are of interest to the researcher. For example, in neuromusculoskeletal models built with an aim to demonstrate movement, the model of a motoneuron should demonstrate well-known and accepted properties of motoneurons. Some of these are the rheobase of known types of motoneurons, generation of plateau potential in motoneurons, characteristic F-I curve, etc. Constituent models that demonstrate these properties are identified and ported to NEUROiD.
- Selecting parameters of interest: NEUROiD stores the constituent cellular model parameters in a structured form in xlsx files. This enables a clear and concise comparison of various cell models to gain insight into the parameters of the constituent model. The researcher now selects the list of parameters from the constituent models that are known to be reasonably responsible for the properties of interest. This step is key to reducing the dimensionality of the parameter space for the search.
- Desired system response: In order to automatically perform a parameter search and obtain optimal parameters that could demonstrate the properties of constituent models, we define the desired system response that encapsulates all the desired features of interest. The goal of the parameter search algorithm is then to look for optimal parameters that result in a system response that is as close as possible to the desired system response.
- Parameter search: Once the parameters of interest and the desired system response are defined, the parameter search algorithm searches the parameter space to obtain the optimal set of parameters. Biological systems are known to achieve homeostasis at the level of behaviors that are physiologically relevant rather than at the level of synapses or other cellular parameters (Marder & Goaillard, 2006). In our exemplar model, we use well-known system-level properties (e.g., H-reflex) and cellular physiological responses as the optimization target to search for parameters of the model. It is also obvious that there could be many sets of parameters that could result in similar higher-level activity in a biological system (Prinz et al., 2004). Thus, the parameters to which our search algorithm converges are one such possible solution. NEUROiD implements a coordinate ascent search for parameter search on its exemplar integrated model. However, it is evident that any other suitable parameter optimization technique could be used at this point.

## Choosing a musculoskeletal model

The nervous system drives the musculoskeletal system and an observed movement is the outcome of the physical interaction between the muscles, the skeletal system, and the world/environment. For modeling and simulating these physical components and their interaction, we use OpenSim musculoskeletal models. These OpenSim models are files with .osim extension, which contain a description of neuromuscular and musculoskeletal dynamics pertaining to the musculoskeletal system of interest organized as model components (as hierarchical XML tags). These components are an encapsulation of system dynamics governing the model or element of the model, e.g., bodies (3d representation of bones or objects); joints describing the type of physical relationship between bodies; forces (acting on bodies or between bodies, e.g., force due to actuation of muscles, contact forces); constraints describing kinematic constraints on bodies/objects, etc.

In biologically realistic musculoskeletal models, the parameters are obtained by performing experiments such as cadavers studies or MRI scans (Handsfield et al., 2014; Ward et al., 2009) to accurately represent bone geometry and musculotendon parameters (e.g., muscle insertion points, pennation angle, physiological cross-sectional area (PSCA), tendon-slack). But as all models come with certain assumptions, the parameters used might not be in biological range or not suitable for purpose of the intended study. For example, a modeler might have taken measurements of PSCA from elderly cadavers with significant muscle atrophy, so the model may not accurately represent the force distribution in young healthy individuals. It is always best practice to check the description under the <credits> and <publications> tag of a supplied .osim file, for assumptions, parameters, and data sources before using them.

All OpenSim models that have muscles modeled as Hill-type muscle (Hill & Vivian, 1938) actuators are suitable for muscle-driven simulations and can be used with NEUROiD. It may be desirable to ensure that the model of interest is well optimized and does away with some complexities that might lead to slower simulation. E.g., to represent musculoskeletal geometry accurately, the modelers make extensive use of ellipsoidal wrapping surfaces which is computationally expensive, this can make the model infeasible for many muscle-driven forward simulations, such as gait. However, this comes at the cost of some accuracy but an optimal decision should be made based on the goal of investigation.

---

## Design and characterization of limbs in silico

We describe below a walk of the design and characterization of an upper limb and a lower limb using the NEUROiD platform.

### Upper limb

We describe three exemplar composite upper limb models ranging from a simple one joint model to a multijoint model (all obtained from the OpenSim website). The Arms26 model (Fig. 8.4, right) consists of three muscles and one active elbow joint.

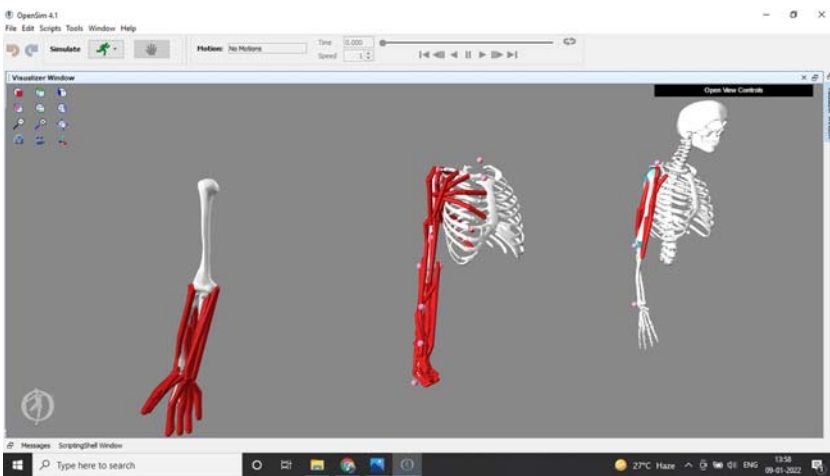


**FIGURE 8.4 Upper limb model**

Screenshot of upper limb models deployed in NEUROiD. Wrist, Arms26, and MOBL-Arm (from left to right).

The MOBL-Arms (Fig. 8.4, center) consists of 50 muscles, and 3 major joints namely the shoulder, elbow, and wrist accounting for a total of 7 degrees of freedom. The wrist model (Fig. 8.4, left) contains 23 muscles and accounts for 2 degrees of freedom for every digit. There are a few constraints in each of these models. But on a whole, they help us in understanding the influence of spinal circuitry on the dynamics of movements.

Below, we describe some details on how the neuromusculoskeletal model was created and simulated on NEUROiD. Please refer to [Mallampalli et al. \(2022\)](#) for further details. Most inputs to NEUROiD are given in the form of spreadsheets having well-defined templates. Cellular level details encompassing the geometry of the cell, its biophysical properties, the kind of synapses it is susceptible to, and the location of current injection are entered in `cell_template_def.xlsx`. Data from exemplar models are available with NEUROiD installation. A user can either use them or modify as per the needs of experiment.

In the next step, we assign the template to a particular cell type, map it to a particular location within the spinal cord segment, mention its population size, and finally conjunct it to a particular muscle. The above tasks are completed by filling the details in `cell_template.xlsx` and `spinal_neurons.xlsx`, wherein the template of a particular cell is assigned in `cell_template.xlsx` and the rest in `spinal_neurons.xlsx`. The `spinal_neurons.xlsx` contains three subsheets each of them devoted to motor neurons, interneurons, and afferent cells in Dorsal Root Ganglion (DRG). In addition, we can also mention the side in which the cells are going to be populated. We then mention the rules set for the connection of various cell types. For example, [Table 8.1](#) below replicates `spinal_neurons.xlsx` where we specify the motor neurons

**Table 8.1** Recruitment of motor neurons.

The table showcases an example of spinal\_neurons.xlsx sheet, where 35 motor neurons associated to biceps long muscle are populated in Bi9 lamina within C5 and C6 segments. Every motor neuron is assigned an M\_cell template.

Neuron_type	Segment	Lamina	Target muscle_name	Num of cells	Side (L/R/Both)	Target osim muscle name	Hoc_template
aMot	C5,C6	Bi9	Biceps long	35	R	BiClong	M_Cell

associated with the biceps long muscle head to be placed in the lamina Bi9 of segments C5, C6. We specify the population size to be 35. The corresponding target muscle in OpenSim for Biceps long is BIClong. The cell template assigned for alpha motor neurons (aMot) is M\_Cell.

The rules are filled in connection\_rules.xlsx. In this sheet we mention the source, target, and type of connection, that is, either inhibitory or excitatory. Apart from these, we can also feed the strength of the connection, convergence, and delay through which they are operating. The above-mentioned details are the same for all three upper models employed, only in spinal\_neurons.xlsx, the user has to add or remove the muscles based on the model that is being currently used. The network-level connections can only be completed after it assigns the bridge between the cellular details to the system level. The muscles.xlsx sheet helps to form the bridge. In this sheet, we mention the muscle and its relevant primary and secondary/assisted movements. Based on this, NEUROiD forms an agonist–antagonist muscle pair and a synergy pair. For instance, in Table 8.2 we specify a set of connections from inhibitory interneurons to motor neurons with synaptic properties as  $\tau = 1.5$  ms, and  $e = -80$  mV. These connections are formed from any Ia inhibitory interneuron that receives inputs from the afferents of the triceps muscle to the antagonistic motor neurons.

The details of the OpenSim model are entered in osim\_muscles.xlsx. The muscle names in the OpenSim model are numbered and encoded in short form, for example, biceps long is mentioned as BIClong. Hence, it is appropriate and necessary to map the actual muscle names with their encoded names and indices. The same applies to joints as well, apart from this we should also mention the degree of freedom/number of coordinates that the joint supports. In addition, we can also lock or unlock a particular joint in the OpenSim model.

From the model parameters provided by the user, NEUROiD then generates NEURON hoc code that can be used for simulation of the neural components. This is done using the helper script run.py, with two arguments stating the beginning and end of the required spinal cord segments, for example, run.py -s Human\_C2, Human\_T1. The generated model, along with specifications for the experiment (also provided as json) is used to perform cosimulation of the neural and musculoskeletal models. We launch the NEUROiD server by executing a server.js file and launching a Firefox browser. In the browser, we enter the address as localhost:3000. This enables us to see the rendered model and selects a particular experiment to be performed, the red electrodes denote the input cells and blue electrodes denote the cells that are selected for recording during the experiment. Concurrently execute the neuroid\_osim\_glue.py file which forms a stable socket enabling information transfer between the curated model and the OpenSim model. Fig. 8.5 demonstrates the working of NEUROiD coupled with the Arms26 model. The two graphs represent the cellular activity of the biceps motor neuron and the corresponding muscle activation profile of the brachialis (i.e., synergist muscle for the biceps).

**Table 8.2** Connection rules.

The table depicts the connection between *Ia* inhibitory interneurons of Triceps muscle is connected to Biceps motor neurons with convergence of 0.5. The strength of the connection is 0.18 and delay for the effect to take place is 2 ms.

Connection_type	Source	Target	Target_Muscle_group	Side	Reference	Properties
Inter-Moto	Ialn	aMot	Antagonist	Ipsilateral	Jankowska, Burke	{"weight": 0.18, "delay": 2, "fan_in": 0.5, "name": "IHB"}

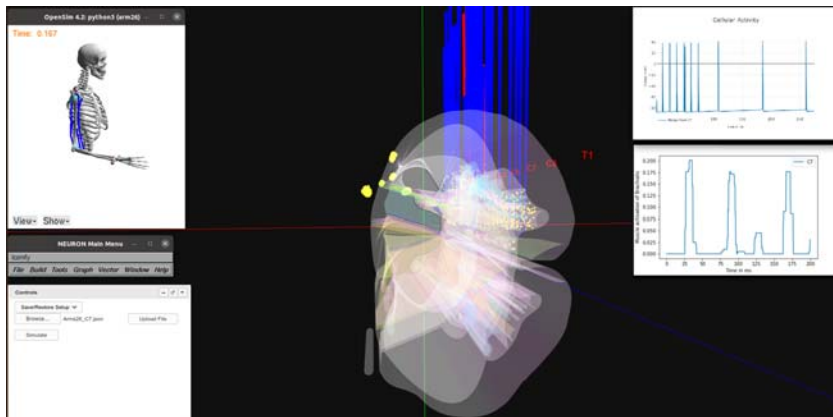


**FIGURE 8.5 Simulating Arms26 in NEUROiD**

A screenshot was captured from the NEUROiD postsimulation.

### Lower limb

Similar to the previous section a suitable model for a lower limb is defined to produce the model shown in Fig. 8.6, gait14dof22musc (obtained from the Osim-rl<sup>2</sup> repository), which has 14 degrees of freedom (DOF) and contains 22 Hill-type muscles (11 in

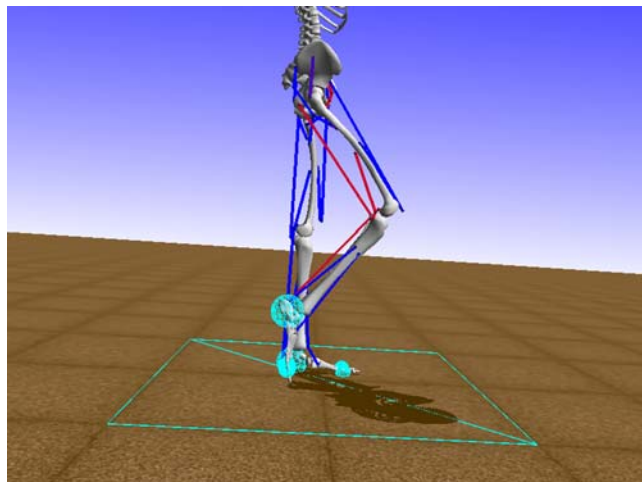


**FIGURE 8.6 Simulating movement in NEUROiD**

A frame captured from NEUROiD OpenSim cosimulation, the lower musculoskeletal model is being driven by spinal circuits defined by connection rules shown in Fig. 8.7.

<sup>2</sup> <https://github.com/stanfordnml/osim-rl>

each leg). The musculoskeletal model also has an implementation for contact forces between the ground and feet, and although some default parameters such as the muscle's maximum isometric force are not biologically plausible in this model, this simplified model is suitable for our demonstration purpose as it is very fast and has appropriate abstractions of bodies, forces, and major muscles involved in normal human gait.

Now we can start populating relevant spreadsheets for NEUROiD, to form the model definition in our simulation platform, proceeding from the micro- to the macrolevel of model definition. The building blocks of neural circuits are neurons, hence we start with the appropriate cell type template definition in `cell_template_def.xlsx`, which will be used by NEUROiD to generate neurons of spinal circuits. By default a few cell type definitions are already present in this file, and one can use the same or specify their own by populating columns in the same format as existing entries. The format is intuitive and self-explanatory, and a completely new definition of a cell template can be created by just changing a few entries.

Next, we need to specify where to populate these cell templates in the spinal cord. These entries are made in `cell_template_map.xlsx` and `spinal_neurons.xlsx`; `cell_template_map.xlsx` holds information regarding the `cell_type`, the template file to use for that cell type and muscle type for that particular cell type; `spinal_neurons.xlsx` on the other hand has a description of `cell_type` with their location in rexed laminae, target muscle, number, whether present on the right/left/both sides of the spinal cord and connection properties. There are 3 sheets in `spinal_neurons.xlsx` that need to be populated, each for motor neurons, interneurons, and DRGs, respectively. Once having defined cell properties we specify how these cells are connected to form circuits. This we define in another separate excel sheet named `connection_rules.xlsx` as shown in Fig. 8.7; here connection properties such as the strength of connection, delay in the circuit, and target muscle group (antagonists/agonists/self), and nature of connection (ipsilateral/contralateral) for the source and target cells are specified.

Another spreadsheet that NEUROiD uses while generating a connection is `muscle.xlsx`. Here details about the muscle and its associated movement type are

connection_type	source	target	target_muscle_group	side	reference	props
Ia_excitation	Ia	aMotS	self	ipsilateral	jankowska,burke	{"weight": 0.5, "delay": 2, "fan_in":1, "name": "IAlex"}
Ia_excitation	Ia	aMotS	agonist	ipsilateral	jankowska,burke	{"weight": 0.5, "delay": 2, "fan_in":1, "name": "IAlex"}
Ia_excitation	Ia	aMotFF	self	ipsilateral	jankowska,burke	{"weight": 0.5, "delay": 2, "fan_in":1, "name": "IAlex"}
Ia_excitation	Ia	aMotFF	agonist	ipsilateral	jankowska,burke	{"weight": 0.5, "delay": 2, "fan_in":1, "name": "IAlex"}
Ia_excitation	Ia	aMotFR	self	ipsilateral	jankowska,burke	{"weight": 0.5, "delay": 2, "fan_in":1, "name": "IAlex"}
Ia_excitation	Ia	aMotFR	agonist	ipsilateral	jankowska,burke	{"weight": 0.5, "delay": 2, "fan_in":1, "name": "IAlex"}
Ia_inhibition	IaIn	aMotS	antagonist	ipsilateral	jankowska,burke	{"weight": 0.1, "delay": 2, "fan_in":1, "name": "IAInNex"}
Ia_inhibition	IaIn	aMotS	self	ipsilateral	jankowska,burke	{"weight": 0.01, "delay": 2, "fan_in":1, "name": "IAInIn"}
Ia_inhibition	IaIn	aMotFF	self	ipsilateral	jankowska,burke	{"weight": 0.01, "delay": 2, "fan_in":1, "name": "IAInIn"}
Ia_inhibition	IaIn	aMotFR	self	ipsilateral	jankowska,burke	{"weight": 0.01, "delay": 2, "fan_in":1, "name": "IAInIn"}
Ib_inhibition	IbIn	aMotS	self	ipsilateral	jankowska,burke	{"weight": 0.1, "delay": 2, "fan_in":1, "name": "IAInNex"}
Ib_inhibition	IbIn	aMotFF	self	ipsilateral	jankowska,burke	{"weight": 0.1, "delay": 2, "fan_in":1, "name": "IAInNex"}
Ib_inhibition	IbIn	aMotFR	self	ipsilateral	jankowska,burke	{"weight": 0.1, "delay": 2, "fan_in":1, "name": "IAInNex"}
Ib_inhibition	IbIn	aMotS	agonist	ipsilateral	jankowska,burke	{"weight": 0.1, "delay": 2, "fan_in":1, "name": "IAInNex"}
Ib_excitation	IbEx	aMotS	self	ipsilateral	jankowska,burke	{"weight": 0.1, "delay": 2, "fan_in":1, "name": "IAlex"}
Ib_excitation	IbEx	aMotFF	self	ipsilateral	jankowska,burke	{"weight": 0.1, "delay": 2, "fan_in":1, "name": "IAlex"}
Ib_excitation	IbEx	aMotFR	self	ipsilateral	jankowska,burke	{"weight": 0.1, "delay": 2, "fan_in":1, "name": "IAlex"}
Ib_excitation	IbEx	aMotFF	agonist	ipsilateral	jankowska,burke	{"weight": 0.1, "delay": 2, "fan_in":1, "name": "IAlex"}
Ib_excitation	IbEx	aMotFR	agonist	ipsilateral	jankowska,burke	{"weight": 0.1, "delay": 2, "fan_in":1, "name": "IAlex"}
Recurrent Inhibition	aMotS	Ren	self	ipsilateral	jankowska,burke	{"weight": 0.1, "delay": 2, "fan_in":1, "name": "IAlex"}
Recurrent Inhibition	aMotFF	Ren	self	ipsilateral	jankowska,burke	{"weight": 0.1, "delay": 2, "fan_in":1, "name": "IAlex"}
Recurrent Inhibition	aMotFR	Ren	self	ipsilateral	jankowska,burke	{"weight": 0.1, "delay": 2, "fan_in":1, "name": "IAlex"}
Recurrent Inhibition	Ren	aMotS	self,agonist	ipsilateral	jankowska,burke	{"weight": 0.01, "delay": 2, "fan_in":1, "name": "IAInIn"}
Recurrent Inhibition	Ren	aMotFF	self,agonist	ipsilateral	jankowska,burke	{"weight": 0.01, "delay": 2, "fan_in":1, "name": "IAInIn"}
Recurrent Inhibition	Ren	aMotFR	self,agonist	ipsilateral	jankowska,burke	{"weight": 0.01, "delay": 2, "fan_in":1, "name": "IAInIn"}

FIGURE 8.7 Connection rules

Connection rules are specified for an example circuit.

specified, and based on this information agonist and antagonist groups are decided which in turn influences the overall connections to be made based on muscle synergies. Another spreadsheet that needs to be filled to complete the model definition is osim\_muscle.xlsx, where relevant information about the muscle, joints, and parameters, e.g., max\_isometric force, optimal\_fiber\_length (extracted from the musculoskeletal model being used) are populated. The second sheet in the same file specifies whether to lock certain joints (joint\_lock\_state).

Once all spreadsheets for model definitions are duly populated, we can move to generation of code for the model. In this step, NEUROiD parses all the information from the spreadsheets and generates spine.json, which has all the relevant details of the model in a compact organized form. This is handled by the run.py script which takes two arguments, the start and an end section, e.g., run.py -s Human\_L2, Human\_S3. Next, we run the NEUROiD web server by running server.js script and an OpenSim instance that can handle to and fro communications between spinal circuits and musculoskeletal model by running neuroid\_osim\_glue.py. Now typing the address localhost:3000 into a Firefox web browser loads the rendered spinal cord shown in Fig. 8.8 which is ready for a simulation experiment.

## Movement training of virtual limbs

NEUROiD allows the creation of neuromusculoskeletal models with relevant spinal cord sections, circuitry, and OpenSim models for musculoskeletal components. Stereotypical reflex patterns such as the H reflex could be observed with this setup by

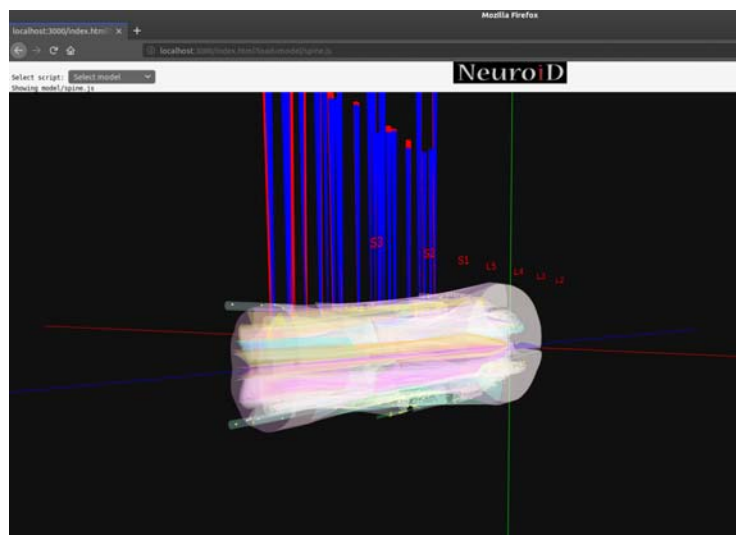


**FIGURE 8.8 Lumbo-sacral spinal cord**

3D rendering of lumbo-sacral spinal cord segment (L2 to S3) in NEUROiD, with stimulation (red) and recording electrodes (blue).

providing appropriate stimulations to the model. However, the exact nature of movement control and movement selection (Georgopoulos et al., 1982) by the motor cortex is still unclear, especially in the control of the upper limb in vertebrates, with multiple proposed models (Omraní et al., 2017). While it is generally agreed that cortical motor activity reflects more than just muscle activity, there is no consensus on what else is encoded and the subset of neurons responsible for the same. Cortical output from a subset of neurons, residing in caudal M1 that presents cortical output to the alpha motor neurons, commonly called as the corticomotoneurons (CM) has been found to correlate with various kinetic and kinematic movement parameters.

A possible solution to study this cortical influence on movement is to use a suitable machine learning algorithm to learn the possible patterns of activation necessary to effect a specific volitional movement. However, it is crucial to ensure the biological plausibility of the various interfaces used in this setup to debate the biological plausibility of the learned signals. It is known that for a given cortical stimulation, the observed muscle activations vary depending on the state of the joint (Graziano et al., 2004). Such state-dependent response implies our model of cortical regions should have access to the afferents and generate (a time series of) patterned input to the spinal networks. It is also apparent that the (functionally equivalent) model should interact with the musculoskeletal model continuously in a closed loop. Hence, reinforcement learning is well suited to obtain a model of the cortical regions. For an exemplar learning system following this paradigm (Iyengar et al., 2021), reinforcement learning was used. This paradigm may also be viewed as a method to induce an output in the virtual limb that matches a real limb trajectory, thereby performing a twinning operation with a real biological limb. These methods may be extended in order to perform a twinning based on any set of output observable data points or internal states based on the objectives of the bio-digital twin.

### Machine learning setup

We used the upper limb model built on NEUROiD. The model includes the relevant sections of spinal cord, neuronal cell types, and spinal networks. A musculoskeletal model of the upper limb is interfaced to the neuronal model. Both neuronal and musculoskeletal model are cosimulated (Fig. 8.9). By using NEURON and OpenSim for simulation in the backend, we gain from advances in both these widely supported simulators in the two domains. We then wrap the neuromusculoskeletal model in a Reinforcement Learning (Sutton & Barto, 2018) framework.

We used the OpenAI Gym toolkit to create a custom environment with a unified interface to encapsulate the NEUROiD model. OpenAI Gym offers many inbuilt environments to perform research on various reinforcement learning algorithms. It also allows creating custom environments so that researchers can use the framework to apply reinforcement learning on problems in various domains. We extended the OpenAI Gym class and encapsulated the NEUROiD environment in that. The observation space of this environment was the Ia, II, and Ib afferent firing rates from the muscles. The action space was set to be a vector of two normalized values that were used to activate the flexor and extensor spinal networks.

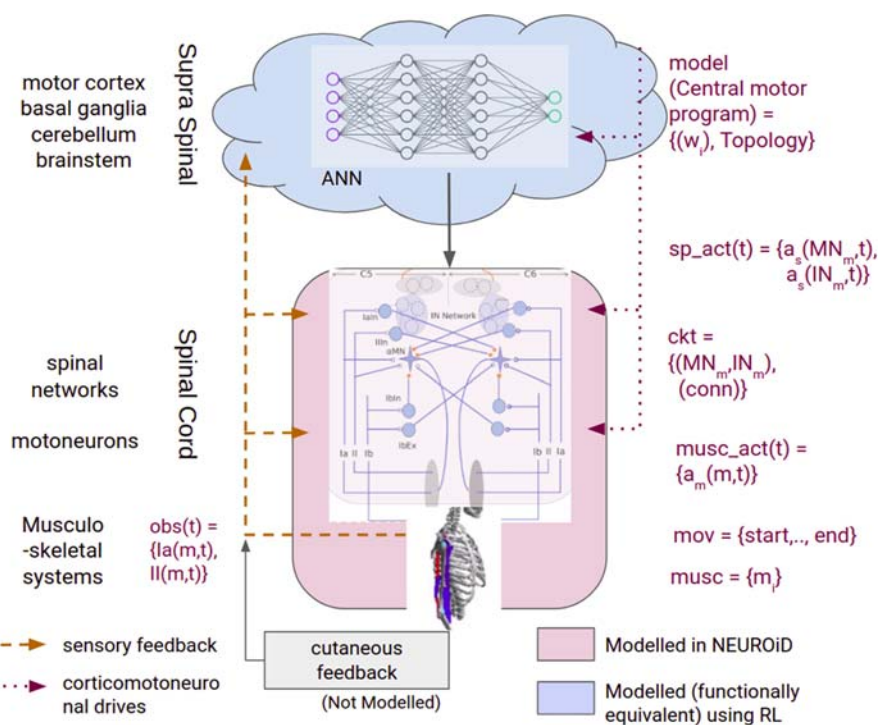


**FIGURE 8.9 Components of the setup used for Reinforcement Learning**

Components of nervous system involved in movement control. The components modeled in NEUROiD and those learnt using Reinforcement Learning are highlighted. Please refer to the paper (Iyengar et al., 2021) for detailed description of various components of the model.

With the setup shown in Fig. 8.10, a neural network was trained using deep reinforcement learning. We were then able to reach different target positions controlled by a descending drive in the reward designed to encourage the movement of a limb from a fixed initial position to a fixed final position. It was observed that the activation learned by the algorithm elicited a response very similar to the biologically known triphasic response (Hallett et al., 1975) for such goal-directed movements. In an effort to reach the goal as early as possible (defined as part of the reward), the algorithm also learned to change the amplitude and timing of activation in a manner that matched known results (Berardelli et al., 1996; Mustard & Lee, 1987). The solution that the RL agent converged to is one of the many possible solutions for the given problem. It has been shown (Marder & Goaillard, 2006; Prinz et al., 2004) that such degeneracy is an inherent property of biological systems across scales. Further, it was observed that changing the target angle was equivalent to providing an offset to the afferent firing. Such a constant inhibitory or excitatory

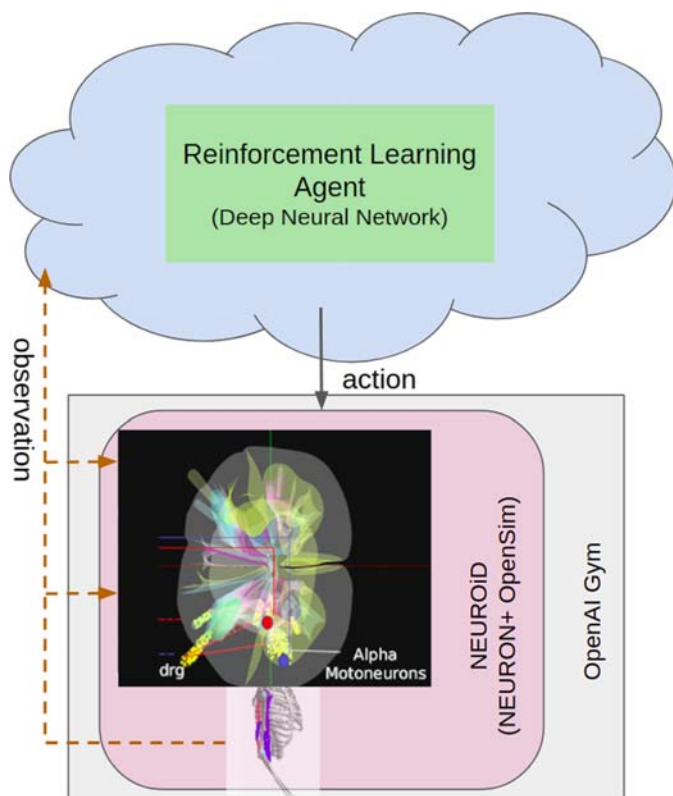


**FIGURE 8.10 NEUROiD Reinforcement Learning environment**

Spinal and musculoskeletal models were built on NEUROiD. Spinal networks were simulated on NEURON and musculoskeletal models were simulated on OpenSim. The NEUROiD (NEURON+OpenSim) model was encapsulated as an OpenAI Gym environment. Reinforcement Learning was used to learn an optimal policy to approximate the Central Motor Program for a specific movement task.

signal could be thought of as the signals from the supraspinal areas that modulate the target encoding. Probing the weights of trained artificial neural network revealed that specific neurons in the ANN behaved similar to corticomotorneurons, providing activations necessary to generate specific movements.

### NEUROiD in medicine

Clinical practice and research may be viewed as an experiment on a subject, a phenotype, or a cohort. The subjects individually or collectively may be healthy or pathological. They may be endowed with physiological add-ons in the form of

prostheses as well. Clinicians perform a variety of actions on the subjects. Diagnosis and measurements, physical examination, triage, a surgical procedure, or prescription of a drug are examples of such activities. An experiment may also involve a set of activities in sequence or parallel or both. For instance, a gait test involves concurrent measurement and regulated locomotion (triage) of the subject. NEUROiD is built to be a clinical laboratory in silico, based on a paradigm of models, activities, and a third dimension called twinning, which will be explained further on. We describe below the design framework and steps therein for hypothetical use cases when NEUROiD is used as an in silico platform in medicine.

## NEUROiD models

The models of upper and lower limbs described in the previous sections are examples of NEUROiD models. Specific disease pathologies may be created in these models by suitably modifying neural model parameters. Orthopedic prostheses and implants may be modeled in OpenSim.

## NEUROiD activities

Electrical stimulation therapies are modeled by means of focused cellular or extracellular current injections in NEUROiD. Clinical triaging is performed by designing specific movement trajectories along with a set of external forces mimicking the assistive or resistive forces exerted by the clinician. A plethora of visual, electrophysiological, and mechanical measurements exist. Some examples are intracellular and extracellular field potential measurements on the nervous system and movement trajectories and kinematics on the musculoskeletal side. Anatomical probing and slicing too are possible activities in NEUROiD. Further, NEUROiD offers a structured platform for building more activities as required.

## Twinning in NEUROiD

Twinning implies a constraint or conditioning of the model so as to match the outputs or some other attribute of the virtual physiology to that of the real physiology. While virtual physiology is a testbed in itself, a bio-digital twin of real physiology is a testbed where experimental results can be used to draw insights of importance to the real biological subject. NEUROiD is compatible with the AI environment Open AI gym, which allows a generic framework for constraining the NEUROiD models and thereby achieving twinning with a real biological entity. Musculoskeletal twinning must precede pathophysiological twinning if the motor output of the digital twin is to match that of the real person whose virtual replica it is. Musculoskeletal twinning is implemented by matching the OpenSim model to the anthropometric measurements of an individual person. In all the clinical examples of twinning that follow, it is to be presumed that musculoskeletal twinning is an indispensable component.

## Clinical trials and experimentation *in silico* with NEUROiD

Constructing experimental setups or testbeds within NEUROiD can be thought of as a sounding board for drug or device designers to explore and bounce ideas. It allows relatively quick testing of hypothesis, uncovering emergent phenomena that pose potential risks at later stages in clinical trials. It also allows designers to optimize designs, doses, intersubject variabilities, pathological complications, and a host of such effects.

The ability to create a digital twin with interindividual and intraindividual trial-to-trial variability offers a real possibility of performing clinical trials of therapies affecting the spinal-neuromusculoskeletal system, completely *in silico*, either as a bridge to the Randomized Controlled Trials (RCT) or as an acceptable substitute where RCT is not possible. Even when RCT can be done, the number of factors/variables that can be explicitly explored by a conventional RCT is limited. *In silico* clinical trials using NEUROiD allow the testing of any number of relevant variables overcoming the limitations imposed by RCT in terms of the number of variables that can be studied and is also unconstrained by the availability of participants. We see below a few examples of how clinical trials or experiments may be constructed using this Model-Activity-Twinning (MAT) paradigm. The following may only be treated as indicative of the design methodology in a neuromusculoskeletal cosimulation framework such as NEUROiD. However, the authors wish to state that the actual development of the same within the NEUROiD would still require significant development and modifications—within and outside NEUROiD based on the specific experiments to be simulated.

### ***Clinical triage for spasticity***

Imagine a case where we want to simulate a clinical test for checking spasticity in the patient (clasp knife phenomena). We describe below how this may be achieved in NEUROiD using the MAT paradigm.

**Model:** Here the model used is a lower limb musculoskeletal model. The neural models will need to come in two variants, a healthy control model and a pathological variant where the excitability of reflex loops are modified.

**Activity:** The activity required here is a clinical triage to check for the presence of the clasp knife phenomena. The patient is made to lie in supine condition and from the initial position of the leg slightly flexed, is asked to resist the force applied around the ankle to extend the legs. So here we need to train the neural control circuits to perform a sequence of three steps on the model. (i) Make it lie in supine position; (ii) Knee needs to be semiflexed; (iii) A force needs to be applied at tibia on the distal end. In OpenSim, one can set the joint coordinates, to initialize the musculoskeletal model in a supine pose (see Fig. 8.11). To make the model's knee half flexed we set relevant coordinate values, using the setQ function while initializing the model at the OpenSim side. We also discover the set of neural activations required to maintain this posture. To apply external force at a particular site of the musculoskeletal model, a point actuator is created with a set amount of force musculoskeletal, direction and location to be applied on.

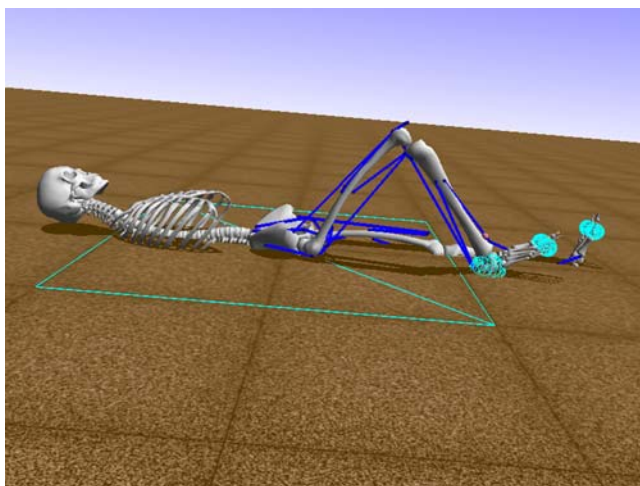


**FIGURE 8.11 Setting up clinical test scenarios in silico**

Setting pose of a musculoskeletal model in the supine position, the pink dot is the site of external force application using a point actuator.

Twinning is performed with an average response both in control and spastic subjects. One can gain powerful insights which were not possible earlier about mechanisms underlying the test.

### ***Design and test of prostheses***

NEUROiD can serve as the testing bed for a range of devices like spinal cord stimulators and prosthetic devices. A critical issue in the development of these devices is the optimization of stimulation parameters with respect to the disease in question. As the motor and network consequences of stimulation paradigms can be directly read off from the musculoskeletal model built into NEUROiD, device development can potentially be accelerated by a good measure.

In consonance with the MAT paradigm described above, Models of prostheses used in orthopaedic surgery can be tested in NEUROiD. The development of personalized prostheses has taken a major leap after the introduction of additive manufacturing technologies, enabling the creation of highly customized prosthetic devices.

Once the CAD model of a prosthesis is designed, the Activity component of the same can be assessed by evaluating the kinematic parameters and performance of Activities of Daily Living (ADL) of the limb in which the prosthesis is to be implanted. The advantage of NEUROiD over purely musculoskeletal modeling platforms comes from the fact that spinal neural network level adaptations to the altered biomechanical load imposed, and the influence of various physical properties of the prosthesis can be systematically investigated enabling a better design of the prosthetic device.

The Twinning component of the MAT is fulfilled as the CAD model of an individual patient's prosthetic is used for the testing on NEUROiD as described above, which allows the assessment of movement performance of the individualized prosthetic even before the functional prototype is built. This has the effect of adding another layer of refinement to personalized prosthetic design.

### ***Diabetic neuropathy—induced diabetic foot***

Diabetic foot is a serious public health concern, with a lifetime incidence up to 34% among diabetics (Armstrong et al., 2017). Diabetic foot and ulcers develop as a result of cumulative damage due to increased pressure and shear stress on the sole of the foot in the background of altered properties of the skin over the sole. This increased pressure/shear stress is engendered by abnormal ankle joint biomechanics resulting from a confluence of factors viz., proprioceptive and motor nerve conduction velocity slowing and consequent abnormal timing of muscle contraction, limited joint mobility, muscle weakness, muscle/soft tissue stiffening, etc. These factors predispose an individual with diabetic peripheral neuropathy to arthropathy (Charcot's joints) and diabetic foot ulcers (Wrobel & Najafi, 2010).

A mechanistic model of a diabetic foot can be built in NEUROiD by simulating the known pathophysiological mechanisms viz., nerve conduction velocity decrement profile in the sensory and/or motor axons and the above-mentioned musculoskeletal alterations.

The activity component of the MAT paradigm can be evaluated by simulating gait in the virtual diabetic foot model and estimating the resulting joint reaction forces and pressure profile on the sole of the foot, abnormalities of which are known to eventually accelerate the complications of diabetic foot.

Twinning would entail adjusting stimulation parameters to reproduce in the virtual diabetic foot model, the kinematic parameters recorded in an individual patient, or by the representative values of the same from a patient cohort. Digital twinning can help evaluate the relative contributions of the above-mentioned factors, both neural and musculoskeletal, on the joint reaction forces and ground reaction forces on the sole in an individual patient. This disambiguation between neural and non-neural factors in diabetic foot pathology can be of potential clinical value as the pathological muscle/soft tissue alterations can be easily treated by techniques from physical medicine. It has been pointed in a review (Wrobel & Najafi, 2010), that exercise training and stretching can be fruitfully used in the treatment of diabetic foot, in addition to conventional management. In addition to the hypothesized utility as a tool to gain a mechanistic understanding of this pathology, NEUROiD simulation has the potential to aid clinical decision-making in an individual patient with respect to the choice of treatment in this context.

### ***Stroke: cross-sectional modeling of stroke severity and corticospinal residuum***

Stroke is a macrovascular disorder of the nervous system characterized by sudden occlusion or hemorrhage of blood vessels supplying the brain with consequences

spanning multiple domains of neural function viz., sensorimotor, cognitive, language, etc. The motor deficit seen in stroke has a variegated impairment pattern with greater disruption of skilled movements of distal upper extremities. The eventual motor phenotype in stroke depends on the corticospinal residuum, i.e., the number of surviving CorticoSpinal Tract (CST) neurons. This residuum of CST is assessed by Diffusion Tensor Imaging (DTI) and Transcranial Magnetic Stimulation (TMS), and it is a good prognostic marker of motor recovery.

Modeling the severity of the stroke, the residuum of CST and prognostication of resultant movement is a distinct possibility in a neuromusculoskeletal simulation platform like NEUROiD. It is possible to account for and include the patterned innervation of corticospinal inputs onto the spinal circuitry. Based on the well-known anatomy of the CST and its innervation pattern on spinal interneurons and alpha motor neurons, a virtual replica of the tract can be created. This CST can be virtually lesioned and the stroke severity associated with CST residuum is modeled by exercising control over the amount and pattern of corticospinal tract innervation in the spinal cord to create a cross-sectional model of stroke/stroke severity. Controlled lesioning is an experimental strategy used to interrogate the neural function since the inception of neuroscience and has been extensively used in animal models, but it is not a viable approach in humans due to ethical concerns. Simulation platforms like NEUROiD provide an anatomically realistic and physiologically plausible closest human model to deploy a controlled lesioning strategy obviating ethical issues.

The consequences of the controlled virtual lesioning of the corticospinal tract can then be assessed by simulating a variety of simple motor activities, like the performance of pincer grasp, during which kinematic and force-related metrics are estimated by the model. This can offer exquisite insights into the mechanistic basis of fine motor deficits seen in stroke patients. Similarly, other motor deficits of stroke can be modeled.

The generic virtual stroke model can be subjected to two types of digital twinning viz., forward and inverse.

In forward twinning, the CST lesion features in an individual patient, like lesion location and spatial extent revealed by imaging methods like diffusion tensor MRI, may be used to constrain the CST of a virtual stroke model by replicating measured lesion attributes, and the resulting motor phenotype is characterized while different movements are simulated. Forward twinning has the following potential applications: (1) Comparison of the motor phenotype in the patient and their forward digital twin can help assess the validity of the virtual stroke model. Some discrepancy is definitely expected as the eventual motor phenotype of any stroke patient is the result of a combination of two effects viz., the primary effect of the lesion and the secondary effect of the physiological recovery process, although the cross-sectional virtual stroke model captures the primary effect of lesion. (2) This discrepancy between the motor phenotype of a patient and the digital twin can be used to infer the influence of the postlesional recovery processes. By creating a cohort of such digital twins from the diffusion tensor MRI of a patient cohort, the mechanistic basis of the postlesional recovery process can be better explored.

In the inverse twinning, the motor phenotype of the patient, in terms of clinical scoring systems like ARAT/FMA scores or more elaborate kinematic metrics extracted with wearable sensors/3D-motion capture systems, can be used to constrain the parameters of the stroke model. A search in high-dimensional hyperspaces with an objective function that minimizes the error between simulated and measured movement can help identify potential system states that result in observed movement phenotypes. These measures can also be used to derive the supraspinal stimulation required to evoke the measured movement trajectories using machine learning–based approaches. In a recent work (Iyengar et al., 2021) using NEUROiD, deep reinforcement learning algorithms were used to derive central motor programs/supraspinal inputs required for motor action. Central motor programs derived from the activity of the affected limb can be compared with those of paralyzed limb to yield an estimate of functional CST residuum, which is a known prognostic marker of the recovery potential in a stroke patient. To implement such a comparison, one can start with the derived central motor program of the unaffected limb as the seed motor program for reinforcement learning of the same for the affected limb. Derivation of supraspinal inputs for a motor action can also be used to explore the mechanistic basis of handedness with respect to the differences in the dexterity of both hands in health at the level of central motor programs that impinge on the spinal motor neurons. By using a factorial experimental design in a cohort of stroke patients, including left/right-sided strokes in left/right-handed patients, the effects of handedness of patient and sidedness of stroke can be disambiguated and their interaction explored with regards to the effect on motor phenotype.

### ***Stroke: longitudinal modeling of recovery and computational neurorehabilitation***

Over weeks and months following stroke, there is a gradual recovery of the affected motor function. The motor deficit has a variegated recovery pattern with the skilled movements of the distal extremities the least and the last to recover. This recovery occurs by two major mechanisms viz., spontaneous biological recovery in the lesioned areas (restitution) and compensatory motor learning within the nonlesioned areas (compensation), both of which are accelerated by the sensorimotor activity provided in the rehabilitation training.

An excellent review outlined the possibilities and opportunities offered by computational models of stroke recovery and neurorehabilitation (Reinkensmeyer et al., 2016). A three-component framework was proposed to create a computational neurorehabilitation model of stroke, including (1) Quantitative measures of sensorimotor activity of the patient undergoing rehabilitation as the input, (2) A recovery model based on activity-dependent plasticity, and (3) Quantitative measures of patient's clinical and kinematic variables as the output. Unsupervised, supervised, and reinforcement learning paradigms were proposed to be included in the models of activity-dependent plasticity to account for the effect of ADL/rehabilitation training on the recovery of motor function.

It is possible to design and implement the recovery and rehabilitation model as outlined above including activity-dependent plasticity. The components of a possible model on recovery are the following: (1) Virtual replica of bilateral corticospinal tracts up to the motor cortex with horizontal connectivity between the corticospinal neurons within the same and opposite motor cortex, (2) Two sources of supraspinal inputs to match the pyramidal (corticospinal) and extrapyramidal systems with an appropriate pattern of connectivity to the spinal circuitry, and (3) Unsupervised, supervised, and reinforcement learning paradigms to model activity-mediated plasticity at the cortical and spinal level. Virtual stroke is then modeled by removing a small set of neurons from the motor cortex. The strength of a model based on NEUROiD would be the inclusion of spinal circuitry integrated with the entire gamut of musculoskeletal apparatus and the ability to characterize movements during recovery and rehabilitation in unprecedented kinematic and kinetic detail in contrast to what could be done with some of the previous models on stroke recovery (Han et al., 2008; Reinkensmeyer et al., 2012).

Activity patterns resembling ADL and/or movements during rehabilitation can be simulated in the motor cortex-spinal cord-musculoskeletal model in NEUROiD before the cortical lesioning. Following the virtual cortical lesion, induced by removal of corticospinal neurons, the model is trained to relearn and perform the disrupted movements/actions, by supervised or reinforcement learning, using errors in trajectory or the endpoint of movement in targeted reach as the feedback. By subjecting this longitudinal stroke model to training over longer periods of time, and assessing the movement recovery in terms of ARAT/FMA scores or kinematic/kinetic variables, a number of interesting questions can be explored, with predictions grounded in multiscale anatomical/physiological realism, few of which are (1) Relative contributions of restitution (lesioned network) and compensation (nonlesioned network) in recovery, (2) Time course of restitution and compensation which has been shown to have a prognostic value, (3) Effect of frequency, intensity, and type of rehabilitation therapy, (4) Prognostication of recovery potential as a function of various predictors viz., initial severity of lesion/corticospinal residuum, the timing of initiation of rehabilitation, initial motor deficit, and (5) Interhemispheric interactions in recovery or its lack, etc.

Forward twinning may be done by matching the virtual stroke lesion to that from diffusion-weighted MRI and/or DTI of the patient following which the model is trained as above. Forward twinning in this context has the potential to yield the following outcomes in an individual patient who has been twinned: (1) Prognosis of motor recovery, and (2) Titration of the type and dosage of rehabilitation treatment. Inverse twinning can be done either independently of forward twinning or in addition to forward twinning by coupling clinical measures, like ARAT/FMA scores, or kinematic/kinetic metrics, from wearable sensors/3D-motion capture/robotic rehabilitation devices to that of the virtual stroke model. Inverse twinning either alone or in combination can help fine-tune the rehabilitation regimen to the progress of motor recovery in each patient and hence could inform and facilitate the iterative adjustment of therapy in contrast to hitherto used stereotyped

conventional therapy. Another approach to twinning is to create a database of virtual stroke models with varying sites and properties of lesions, with the statistical distribution based on a cohort of stroke patients. Each model is subjected to a factorial combination of different types and dosages of treatments creating a set of recovery trajectory models. An individual patient may then be mapped to the closest virtual model (Greiner et al., 2021) to get a snapshot of possible recovery trajectory with different types of treatments, given the deficit, which can help plan an individualized treatment regimen.

The feasibility to simulate motor recovery following has a number of potential benefits as outlined by (Reinkensmeyer et al., 2016): (1) Gaining insights into the mechanisms of recovery, (2) Characterizing the optimal method and dosage of rehabilitation therapy, and 3) With a digital twin, personalization of rehabilitation regimen to individual patients.

### ***Spinal cord stimulation***

Spinal cord stimulation in the epidural space has been evaluated as a treatment modality for abnormalities of gait and balance (Moraud et al., 2016) or upper limb mobility after spinal cord injury (Greiner et al., 2021), dystonia, tremors (Thiriez et al., 2014), spasticity in cerebral palsy (Dekopov et al., 2015), etc.

The first step in the computational exploration of the above movement disorders is to create disease models of the same in a simulation platform like NEUROiD. For example, spinal cord injury can be modeled by tweaking ion channel conductances to reproduce depressed spinal circuitry following disrupted supraspinal influence (Moraud et al., 2016).

The motor activities could then be induced or modulated by a simulation of spinal cord stimulation with an objective to optimize the stimulation parameters like pulse width, amplitude, frequency, duration, and the site of stimulation that will alleviate pathological motor phenotype. Stimulation pattern that is appropriate for the severity of spinal injury (complete/partial transection) and motor task (gait control vs. balance vs. upper limb mobility) can be independently investigated. Virtual stimulation experiments have the potential to guide the design of an optimal stimulation regimen for any movement disorder that can be treated by spinal cord stimulation.

Forward twinning can be done by using the spinal MRI of the patient to reproduce a virtual spinal transection and the optimal stimulation pattern is devised for the individual patient. Inverse twinning may be used to further fine-tune the optimization process by constraining the motor output of the model to the kinematic/kinetic movement profile of the patient.

### ***Motor neuron disease (amyotrophic lateral Sclerosis, spinal muscular atrophy, familial spastic paraplegia)***

Amyotrophic lateral sclerosis is a common clinical label for a set of distinct but overlapping pathophysiological mechanisms culminating in progressive degeneration of upper (corticospinal neurons) and lower motor neurons (alpha motor neurons) resulting in a clinical phenotype characterized by a variable combination of

upper motor neuron (UMN) and lower motor neuron (LMN) lesion signs and symptoms. While the lost corticospinal tracts are replaced by glial scar (lateral sclerosis), denervation of skeletal muscles caused by degeneration of lower motor neurons is accompanied by reinnervation of those muscles by surviving motor neurons resulting in an expansion of motor unit size eventually progressing to muscular atrophy (amyotrophy) after a substantial loss of motor neurons.

NEUROiD can be used to model the pathophysiology of ALS in two ways: (1) Construct a sequence of models with a progressively lesser number of motor neurons, both UMN and LMN, to represent motor neuron degeneration, and (2) Computational model of motor neuron degeneration (Le Masson et al., 2014; Morrice et al., 2018) to induce a spontaneous loss of neurons to represent the pathology instead of manual removal of neurons as in the first approach. The two crucial issues which must be addressed in ALS modeling are (1) Depleting variable combinations of UMN and LMN to represent various subtypes of ALS, and (2) Modeling muscular denervation induced motor unit reorganization and amyotrophy.

The consequences of virtual degeneration induced as above can be investigated during various activities like gait, posture and balance, movements of extremities. The motor performance is quantitatively assessed by measurement of kinematics/kinetics and qualitatively clinical tests like tone/spasticity, reflexes, power of muscles, fatigability, etc.

The model that best predicts the motor phenotype of a patient is refined by inverse twinning done by coupling the kinematic measurements in an individual patient to that of the model. Recalibration of the model by successive kinematic profile serves to fine-tune the model. Inverse twinning can be used to (1) Assess the progress of motor deterioration, the rate of which can be explored for prognostic utility, and (2) Early stratification of ALS subtype in the patient by motor phenotypic markers, as some variants have a better prognosis.

### ***Peripheral neuropathies***

Peripheral neuropathies are demyelinating and/or axonal loss disorders affecting the peripheral nervous system involving sensory, motor, sensorimotor, and autonomic nerve fibers. Isolated sensory or motor fiber defects or both can cause impairments in motor function.

One can create a model with pure sensory (Ia/II/Ib fibers) or motor (alpha motor axons) or mixed fiber defects by simulating demyelination and/or axonal loss in the fiber population. NEUROiD simulation of fine and gross motor activity can help disambiguate them and characterize the differences in subtle patterns of movements and their abnormalities in different types of peripheral neuropathies. Inverse twinning using individual patient kinematic data can help distinguish between reversible demyelinating from irreversible axonal loss pathophysiology in the patient.

### ***Mechanisms and consequences of aging-induced changes in motor unit structure***

It is well established that with aging the motor neurons innervating the Fast Fatigable (FF) muscle fibers of IIb motor units degenerate leaving the muscle fibers in a denervated state. These “orphaned” muscle fibers are reinnervated by

neighboring axons of I and IIa motor units. This expansion of smaller motor units results in impairment of fine movements, and loss of IIb neurons results in a reduction in the maximum force produced by a muscle (Enoka & Fuglevand, 2001).

A sequence of models can be devised to replicate an age-related longitudinal decrease in motor neuron number and the resulting motor unit reorganization. The motor consequences of these changes can be explored in NEUROiD by the assessment of various activities including skilled movements, gait, joint biomechanics, and balance. The refinement of the model by inverse twinning based on a variety of metrics including kinematics, force platforms for posture and gait analysis, dynamic posturography, etc., from an individual person can be an invaluable aid to personalized geriatric medicine with respect to motor abnormalities.

### ***Limitations***

It must be emphasized that the above set of steps for constructing clinical use-cases using NEUROiD are only indicative of the possible range of activities using the NEUROiD framework. The actual task of creating the right models, activities, and twinning for a given use-case still involves a significant amount of model, activity, and stimulus design and is not readily available for end-use at this moment. The NEUROiD framework makes it possible to design and simulate such clinical scenarios in a multiscale manner, which is a small yet significant step forward over the current state of art.

### ***Medical education and training***

NEUROiD has an undeniable utility as a pedagogical tool in medical schools to teach and train medical students in the physiology and pathology of the spinal neuromusculoskeletal system. It can be productively used to teach fundamental concepts in neuromuscular physiology for students in medical and allied health sciences courses. Concepts like Hanneman's principle in motor unit recruitment, reciprocal innervation of spinal circuits, physiology of muscle spindle and Golgi tendon organs, and multilevel effects of ion channel pathophysiology and pharmacology can be taught to good effect with interactive live demonstrations. Such interactive demos of all the clinical conditions/diseases discussed above with NEUROiD help a student acquire the mechanistic understanding of the chain events that transpire between cellular/subcellular events and final motor behavior in health and disease. This seamless transition between different layers of abstraction, between cellular/subcellular and system-level features, which can be explored by NEUROiD, forms the bedrock of clinical reasoning.

---

## **Conclusion and future landscapes**

In this chapter, we have described the NEUROiD platform, which can be used to build multiscale and multidisciplinary neuromusculoskeletal models. Some of the salient features of the platform include its ability to facilitate integration of multiple

constituent models, anatomical and physiological realism in the models, a rich set of electrophysiological tools, visualization across scales and disciplines. We have also briefly described how NEUROiD exploits parallel hardware to accelerate simulation. We have also used NEUROiD in a reinforcement learning environment to identify corticospinal signals necessary to generate specific controlled movements, an instance of biomimetic movement on a cosimulated neuromusculoskeletal limb. Further, the client–server architecture of NEUROiD allows the compute-intensive operations to be performed on a high-performance server and let the users work on a potentially resource-constrained laptop.

We also describe a Model-Activity-Twinning paradigm for the design of virtual biological systems as twins of a real entity. We further describe a number of potential clinical scenarios in which this paradigm can be used to create *in silico* simulations of a virtual patient. We believe that the development of the NEUROiD framework is a small step toward creating a clinically relevant, neuromusculoskeletal bio-digital twin by integrating multiple well-accepted tools like NEURON, OpenSim, and Open AIGym.

---

## References

- Ackerman, M. J. (1998). The visible human project: A resource for anatomical visualization. *Studies in Health Technology and Informatics*, 52(Pt 2), 1030–1032.
- Armstrong, D. G., Boulton, A. J. M., & Bus, S. A. (2017). Diabetic foot ulcers and their recurrence. *New England Journal of Medicine*, 376(24), 2367–2375. <https://doi.org/10.1056/NEJMra1615439>
- Berardelli, A., Hallett, M., Rothwell, J. C., Agostino, R., Manfredi, M., Thompson, P. D., & Marsden, C. D. (1996). Single-joint rapid arm movements in normal subjects and in patients with motor disorders. *Brain*, 119(2), 661–674. <https://doi.org/10.1093/brain/119.2.661>
- Bror, R. (1954). A cytoarchitectonic atlas of the spinal cord in the cat. *The Journal of Comparative Neurology*, 297–379. <https://doi.org/10.1002/cne.901000205>
- Capogrosso, M., Wenger, N., Raspopovic, S., Musienko, P., Beauparlant, J., Bassi Luciani, L., Courtine, G., & Micera, S. (2013). A computational model for epidural electrical stimulation of spinal sensorimotor circuits. *The Journal of Neuroscience : The Official Journal of the Society for Neuroscience*, 33(49), 19326–19340. <https://doi.org/10.1523/JNEUROSCI.1688-13.2013>
- Danner, S. M., Zhang, H., Shevtsova, N. A., Borowska-Fielding, J., Deska-Gauthier, D., Rybak, I. A., & Zhang, Y. (2019). Spinal V3 interneurons and left–right coordination in mammalian locomotion. *Frontiers in Cellular Neuroscience*, 13. <https://doi.org/10.3389/fncel.2019.00516>
- Dekopov, A. V., Shabalov, V. A., Tomsky, A. A., Hit, M. V., & Salova, E. M. (2015). Chronic spinal cord stimulation in the treatment of cerebral and spinal spasticity. *Stereotactic and Functional Neurosurgery*, 93(2), 133–139. <https://doi.org/10.1159/000368905>
- Delp, S. L., Loan, J. P., Hoy, M. G., Zajac, F. E., Topp, E. L., & Rosen, J. M. (1990). An interactive graphics-based model of the lower extremity to study orthopaedic surgical procedures. *IEEE Transactions on Biomedical Engineering*, 37(8), 757–767. <https://doi.org/10.1109/10.102791>

- Enoka, R. M., & Fuglevand, A. J. (2001). Motor unit physiology: Some unresolved issues. *Muscle & Nerve*, 24(1), 4–17. [https://doi.org/10.1002/1097-4598\(200101\)24:1<4::AID-MUS13>3.0.CO;2-F](https://doi.org/10.1002/1097-4598(200101)24:1<4::AID-MUS13>3.0.CO;2-F)
- Freeman, S. R., & Durfee, W. K. (2006). Twitch response of intact human tibialis anterior muscle to doublet stimulation at graded strengths. In *Annual International Conference of the IEEE Engineering in Medicine and Biology - Proceedings* (pp. 6757–6760). <https://doi.org/10.1109/IEMBS.2006.260940>
- Fuglevand, A. J., Winter, D. A., & Patla, A. E. (1993). Models of recruitment and rate coding organization in motor-unit pools. *Journal of Neurophysiology*, 70(6), 2470–2488. <https://doi.org/10.1152/jn.1993.70.6.2470>
- Georgopoulos, A. P., Kalaska, J. F., Caminiti, R., & Massey, J. T. (1982). On the relations between the direction of two-dimensional arm movements and cell discharge in primate motor cortex. *The Journal of Neuroscience: The Official Journal of the Society for Neuroscience*, 2(11), 1527–1537.
- Graziano, M. S. A., Patel, K. T., & Taylor, C. S. R. (2004). Mapping from motor cortex to biceps and triceps altered by elbow angle. *Journal of Neurophysiology*, 92(1), 395–407.
- Greiner, N., Barra, B., Schiavone, G., Lorach, H., James, N., Conti, S., Kaeser, M., Fallegger, F., Borgognon, S., Lacour, S., Bloch, J., Courtine, G., & Capogrosso, M. (2021). Recruitment of upper-limb motoneurons with epidural electrical stimulation of the cervical spinal cord. *Nature Communications*, 12(1), 435. <https://doi.org/10.1038/s41467-020-20703-1>
- Gurney, K., Prescott, T. J., & Redgrave, P. (2001a). A computational model of action selection in the basal ganglia. I. A new functional anatomy. *Biological Cybernetics*, 84, 401–410. <https://doi.org/10.1007/PL00007984>
- Gurney, K., Prescott, T. J., & Redgrave, P. (2001b). A computational model of action selection in the basal ganglia. II. Analysis and simulation of behaviour. *Biological Cybernetics*, 84, 411–423. <https://doi.org/10.1007/PL00007985>
- Hallett, M., Shahani, B. T., & Young, R. R. (1975). EMG analysis of stereotyped voluntary movements in man. *Journal of Neurology, Neurosurgery and Psychiatry*, 38(12), 1154–1162. <https://doi.org/10.1136/jnnp.38.12.1154>
- Han, C. E., Arbib, M. A., & Schweighofer, N. (2008). Stroke rehabilitation reaches a threshold. *PLoS Computational Biology*, 4(8), e1000133. <https://doi.org/10.1371/journal.pcbi.1000133>
- Handsfield, G. G., Meyer, C. H., Hart, J. M., Abel, M. F., & Blemker, S. S. (2014). Relationships of 35 lower limb muscles to height and body mass quantified using MRI. *Journal of Biomechanics*, 47(3), 631–638. <https://doi.org/10.1016/j.jbiomech.2013.12.002>
- Harilal, P., Bipin, N., Egidio, D., Michael, H., Giovanni, N., & Shyam, D. (2016). Computational modeling of single neuron extracellular electric potentials and network local field potentials using LFPsim. *Frontiers in Computational Neuroscience*. <https://doi.org/10.3389/fncom.2016.00065>
- Hill, A., & Vivian. (1938). *The heat of shortening and the dynamic constants of muscleProc.*
- Hines, M. L., & Carnevale, N. T. (1997). The NEURON simulation environment. *Neural Computation*, 9(6), 1179–1209. <https://doi.org/10.1162/neco.1997.9.6.1179>
- Holzbaur, K. R. S., Murray, W. M., & Delp, S. L. (2005). A model of the upper extremity for simulating musculoskeletal surgery and analyzing neuromuscular control. *Annals of Biomedical Engineering*, 33(6), 829–840. <https://doi.org/10.1007/s10439-005-3320-7>
- Iyengar, R. S., Mallampalli, K., & Raghavan, M. (2021). A novel paradigm for deep reinforcement learning of biomimetic systems. *BioRxiv*. <https://doi.org/10.1101/2021.03.28.437396>

- Iyengar, R. S., Pithapuram, M. V., Singh, A. K., & Raghavan, M. (2019). Curated model development using NEUROiD: A web-based NEUROmotor integration and design platform. *Frontiers in Neuroinformatics*, 13. <https://doi.org/10.3389/fninf.2019.00056>
- Iyengar, R. S., & Raghavan, M. (2020). MPI parallelization of NEUROiD models using docker swarm. In , Vols 2020. *Proceedings of the International Conference on Parallel and Distributed Systems - ICPADS* (pp. 655–660). IEEE Computer Society. <https://doi.org/10.1109/ICPADS51040.2020.00092>
- Izhikevich, E. M., & Edelman, G. M. (2008). Large-scale model of mammalian thalamocortical systems. *Proceedings of the National Academy of Sciences of the United States of America*, 105(9), 3593–3598. <https://doi.org/10.1073/pnas.0712231105>
- Kim, H. (2017). Muscle length-dependent contribution of motoneuron Cav1.3 channels to force production in model slow motor unit. *Journal of Applied Physiology*, 123(1), 88–105. <https://doi.org/10.1152/japplphysiol.00491.2016>
- Ko, H.-Y., Park, J. H., Shin, Y. B., & Baek, S. Y. (2004). Gross quantitative measurements of spinal cord segments in human. *Spinal Cord*, 42(1), 35–40.
- Le Masson, G., Przedborski, S., & Abbott, L. F. (2014). A computational model of motor neuron degeneration. *Neuron*, 83(4), 975–988. <https://doi.org/10.1016/j.neuron.2014.07.001>
- Mallampalli, K., Pithapuram, M. V., Rangayyan, Y. M., Iyengar, R. S., Singh, A. K., Sripada, S., & Raghavan, M. (2022). In-silico neuro musculoskeletal model reproduces the movement types obtained by spinal micro stimulation. *Computer Methods and Programs in Biomedicine*, 220. <https://doi.org/10.1016/j.cmpb.2022.106804>
- Marder, E., & Goaillard, J. (2006). Variability, compensation and homeostasis in neuron and network function. *Nature Reviews Neuroscience*, 7(7), 563–574. <https://doi.org/10.1038/nrn1949>
- McCrea, D. A., & Rybak, I. A. (2008). Organization of mammalian locomotor rhythm and pattern generation. *Brain Research Reviews*, 57(1), 134–146. <https://doi.org/10.1016/j.brainresrev.2007.08.006>
- McIntyre, C. C., Richardson, A. G., & Grill, W. M. (2002). Modeling the excitability of mammalian nerve fibers: Influence of afterpotentials on the recovery cycle. *Journal of Neurophysiology*, 87(2), 995–1006. <https://doi.org/10.1152/jn.00353.2001>
- Moraud, E. M., Capogrosso, M., Formento, E., Wenger, N., DiGiovanna, J., Courtine, G., & Micera, S. (2016). Mechanisms underlying the neuromodulation of spinal circuits for correcting gait and balance deficits after spinal cord injury. *Neuron*, 89(4), 814–828. <https://doi.org/10.1016/j.neuron.2016.01.009>
- Morrice, J. R., Gregory-Evans, C. Y., & Shaw, C. A. (2018). Animal models of amyotrophic lateral sclerosis: A comparison of model validity. *Neural Regeneration Research*, 13(12), 2050–2054. <https://doi.org/10.4103/1673-5374.241445>
- Mustard, B. E., & Lee, R. G. (1987). Relationship between EMG patterns and kinematic properties for flexion movements at the human wrist. *Experimental Brain Research*, 66(2), 247–256. <https://doi.org/10.1007/BF00243302>
- Omrani, M., Kaufman, M. T., Hatsopoulos, N. G., & Cheney, P. D. (2017). Perspectives on classical controversies about the motor cortex. *Journal of Neurophysiology*, 118(3), 1828–1848. <https://doi.org/10.1152/jn.00795.2016>
- Peterson, B. E., Healy, M. D., Nadkarni, P. M., Miller, P. L., & Shepherd, G. M. (1996). ModelDB: An environment for running and storing computational models and their results applied to neuroscience. *Emerging Infectious Diseases*, 3(6), 389–398. <https://doi.org/10.1136/jamia.1996.97084512>

- Pierrot-Deseilligny, E., & Burke, D. (2005). The circuitry of the human spinal cord: Its role in motor control and movement disorders. In *The circuitry of the human spinal cord: Its role in motor control and movement disorders* (pp. 1–642). Cambridge University Press. <https://doi.org/10.1017/CBO9780511545047>
- Pierrot-Deseilligny, E., & Burke, D. (2012). The circuitry of the human spinal cord: Spinal and corticospinal mechanisms of movement. In *The circuitry of the human spinal cord: Spinal and corticospinal mechanisms of movement* (pp. 1–606). Cambridge University Press. <https://doi.org/10.1017/CBO9781139026727>
- Pietro, B., Sergio, M., & Paolo, M. (2015). Axon-somatic back-propagation in detailed models of spinal alpha motoneurons. *Frontiers in Computational Neuroscience*. <https://doi.org/10.3389/fncom.2015.00015>
- Pietro, B., Sergio, M., Roberto, C., & Paolo, M. (2014). Modelling recurrent discharge in the spinal  $\alpha$ -motoneuron: Reappraisal of the F wave. *Clinical Neurophysiology*, 427–429. <https://doi.org/10.1016/j.clinph.2013.09.025>
- Prinz, A. A., Bucher, D., & Marder, E. (2004). Similar network activity from disparate circuit parameters. *Nature Neuroscience*, 7(12), 1345–1352.
- Prochazka, A. (1999). Quantifying proprioception. *Progress in Brain Research*, 123, 133–142. [https://doi.org/10.1016/s0079-6123\(08\)62850-2](https://doi.org/10.1016/s0079-6123(08)62850-2)
- Ranjan, R., Khazen, G., Gambazzi, L., Ramaswamy, S., Hill, S. L., Schürmann, F., & Markram, H. (2011). Channelpedia: An integrative and interactive database for ion channels. *Frontiers in Neuroinformatics*. <https://doi.org/10.3389/fninf.2011.00036>
- Reinkensmeyer, D. J., Burdet, E., Casadio, M., Krakauer, J. W., Kwakkel, G., Lang, C. E., Swinnen, S. P., Ward, N. S., & Schweighofer, N. (2016). Computational neurorehabilitation: Modeling plasticity and learning to predict recovery. *Journal of NeuroEngineering and Rehabilitation*, 13(1), 42. <https://doi.org/10.1186/s12984-016-0148-3>
- Reinkensmeyer, D. J., Guigou, E., & Maier, M. A. (2012). A computational model of use-dependent motor recovery following a stroke: Optimizing corticospinal activations via reinforcement learning can explain residual capacity and other strength recovery dynamics. *Neural Networks*, 29–30, 60–69. <https://doi.org/10.1016/j.neunet.2012.02.002>
- Safronov, B. V., & Vogel, W. (1995). Single voltage-activated Na<sup>+</sup> and K<sup>+</sup> channels in the somata of rat motoneurones. *The Journal of Physiology*, 487(1), 91–106. <https://doi.org/10.1113/jphysiol.1995.sp020863>
- Sengul, G. (2012). *Atlas of the spinal cord: Mouse, rat, rhesus, marmoset, and human*.
- Seth, A., Hicks, J. L., Uchida, T. K., Habib, A., Dembia, C. L., Dunne, J. J., Ong, C. F., DeMers, M. S., Rajagopal, A., Millard, M., Hamner, S. R., Arnold, E. M., Yong, J. R., Lakshmikanth, S. K., Sherman, M. A., Ku, J. P., & Delp, S. L. (2018). OpenSim: Simulating musculoskeletal dynamics and neuromuscular control to study human and animal movement. *PLoS Computational Biology*, 14(7). <https://doi.org/10.1371/journal.pcbi.1006223>
- Sharrard, W. J. (1964). The segmental innervation of the lower limb muscles in man. *Annals of the Royal College of Surgeons of England*, 35, 106.
- Song, S., & Geyer, H. (2015a). A neural circuitry that emphasizes spinal feedback generates diverse behaviours of human locomotion. *Journal of Physiology*, 593(16), 3493–3511. <https://doi.org/10.1113/JP270228>
- Song, S., & Geyer, H. (2015b). Regulating speed in a neuromuscular human running model. In *Vols 2015. IEEE-RAS International Conference on Humanoid Robots* (pp. 217–222). IEEE Computer Society. <https://doi.org/10.1109/HUMANOIDS.2015.7363554>

- Sutton, R. S., & Barto, A. G. (2018). *Reinforcement learning: An introduction*. A Bradford Book.
- Thiriez, C., Gurruchaga, J.-M., Goujon, C., Fénelon, G., & Palfi, S. (2014). Spinal stimulation for movement disorders. *Neurotherapeutics*, 11(3), 543–552. <https://doi.org/10.1007/s13311-014-0291-0>
- Wang, Y. J., Lin, M. W., Lin, A. A., & Wu, S. N. (2008). Riluzole-induced block of voltage-gated Na<sup>+</sup> current and activation of BKCa channels in cultured differentiated human skeletal muscle cells. *Life Sciences*, 82(1–2), 11–20. <https://doi.org/10.1016/j.lfs.2007.10.015>
- Ward, S. R., Eng, C. M., Smallwood, L. H., & Lieber, R. L. (2009). Are current measurements of lower extremity muscle architecture accurate? *Clinical Orthopaedics and Related Research*, 467(4), 1074–1082. <https://doi.org/10.1007/s11999-008-0594-8>
- Wrobel, J. S., & Najafi, B. (2010). Diabetic foot biomechanics and gait dysfunction. *Journal of Diabetes Science and Technology*, 4(4), 833–845. <https://doi.org/10.1177/193229681000400411>
- Zhang, X., & Santaniello, S. (2019). Role of cerebellar GABAergic dysfunctions in the origins of essential tremor. *Proceedings of the National Academy of Sciences of the United States of America*, 116(27), 13592–13601. <https://doi.org/10.1073/pnas.1817689116>

This page intentionally left blank

# HumMod: a modeling environment for the simulation of integrative human physiology

9

**John S. Clemmer, W. Andrew Pruett, Robert L. Hester***Department of Physiology and Biophysics, University of Mississippi Medical Center, Jackson, MS,  
United States*

## Chapter outline

<b>Disclosures .....</b>	199
<b>History .....</b>	199
Model content .....	201
<b>HumMod for testing physiological concepts and hypotheses in pathophysiology .....</b>	201
Example 1: salt sensitivity.....	203
Example 2: baroreceptor activation therapy .....	204
Example 3: arteriovenous fistula .....	206
The future of modeling: virtual populations.....	206
<b>Conclusion, limitations, and future considerations .....</b>	208
<b>Acknowledgments .....</b>	209
<b>References .....</b>	209

## Disclosures

HC Simulation, LLC <http://hesimulation.com> has the exclusive license from University of Mississippi Medical Center for the commercial use of HumMod.

Robert L. Hester, Ph.D. is CEO of HC Simulation, LLC.

William A. Pruett, Ph.D. is Chief Science Officer of HC Simulation, LLC.

## History

Mathematical models have been used to understand biological systems since William Harvey's cardiac output model in 1628 (Schultz, 2002). Krogh et al. demonstrated the utility of modeling the oxygen flux in skeletal muscle (Krogh, 1919). Hodgkin and Huxley used computational modeling to understand the electrical potential across a cellular membrane (Hodgkin & Huxley, 1952). These early

physiological models provided much groundwork for later experimental and clinical studies. However, integration across multiple biological systems was only first attempted in the early 1960s, when Dr. Arthur Guyton began developing a mathematical model of human physiology. In 1972, Coleman, Guyton, and Granger published an article in Annual Review of Physiology describing an integrative model of the cardiovascular system (Guyton et al., 1972). This simulation was comprised of 354 mathematical equations and was implemented using an analog computer. Over the next 10 years, this was expanded into the model HUMAN (Coleman & Randall, 1983), a DOS-based simulation. HUMAN is available from Skidmore College, where it is used as a web-based teaching tool (<http://placid.skidmore.edu/human/index.php>). A Windows version, QCP (Quantitative Circulatory Physiology), was later developed in the early 2000s and is available at <http://hummod.org>. With HUMAN and QCP, the major limitation is that the underlying physiological relationships were not accessible or easily editable by the user because of the compiled programming.

In 2005 Coleman transitioned to developing a simulation of human physiology that would be easier to add and edit physiological responses with full transparency of the relationships in the model. This project, now known as HumMod, is in continued development in the Department of Physiology and Biophysics at the University of Mississippi Medical Center. This chapter describes HumMod as an integrative model of human physiology and its use in understanding human physiology, pathological conditions, and how medical devices are used to treat pathophysiological states.

HumMod is a deterministic model comprised of ~9000 distinct variables and ~2000 model parameters. HumMod has 14 organ systems, including left/right heart, lungs, left/right kidney, skin, skeletal and respiratory muscles, gastrointestinal tract, liver, pancreas, bone, adipose, and brain. The endocrine system includes the renin–angiotensin–aldosterone system, vasopressin, atrial natriuretic peptide, insulin/glucagon, cortisol, thyroid hormones, sex hormones, parathyroid hormone, and norepinephrine/epinephrine. The nervous system includes afferent nerves such as the carotid and atrial baroreceptors and heart mechanoreceptors as well as pre- and post-ganglionic efferent nerves to the heart, vasculature, kidneys, adrenal glands, and other peripheral organs.

HumMod is comprised of a series of files describing physiology, display characteristics of the simulations, and several executable files: HumMod.exe, Interactive Controller.exe, and Scripted Controller.exe. The executable files are written in C++ using standard libraries. The compiled executable code contains a fast XML parser that is a numerical solver for algebraic and differential equations. HumMod.exe and Interactive Controller.exe run in Windows and allow the XML representation of the model to be solved and displayed to the user. While programming language is beyond the scope of this chapter, a user guide providing details of the XML programming has been developed by researchers at Penn State University and is available at <http://hummod.org>.

## Model content

HumMod can simulate a patient's normal physiology with time-dependent responses ranging from seconds to years. Panels listed in the different menus allow users to investigate and adjust physiological parameters in more detail. Panel features include graphical data displays, information buttons, and adjustable parameters. Pressures and flows through the left and right heart, lung vasculature, and veins as well as cardiac wall stresses are found in the *Circulation* menu. Respiratory physiology including breathing, gas exchange, lung gas percentages, and peripheral oxygen levels can be seen in the *Respiration* menu. The *Metabolism* menu lets the user view changes in fuel usage, energy stores, and circulating nutrients such as amino acids, glucose, ketoacids, free fatty acids, and triglycerides. The *Organs* menu breaks down each organ into panels that allow the user to view or manipulate organ metabolism, blood flow, and other physiology included under other menus such as acid–base, oxygen, and sympathetic nerve activity within each organ. These organs include adipose tissue, adrenal gland, bladder, bone, brain, gastrointestinal system, kidney, right and left heart, liver, pancreas, respiratory and skeletal muscles, skin, and “other tissue” that represents small organs and tissue mass not accounted for by these main organ systems. Other menus include *Body Fluids*, *Electrolytes*, *Hormones*, *Nervous System*, *Acid–Base*, and *Heat*.

Users may also change environmental parameters such as altitude, temperature, humidity, and barometric pressure. Further, users can manipulate partial pressures of individual gases in inspired air, nutritional composition of food, and amount of ingested food and fluids. Users can adjust a patient's hour-to-hour basic functions (i.e., sleeping, working, and feeding) by controlling the daily routine. Further, the *Exercise* panels facilitate studying the effects of treadmill or cycle exercises.

Pathophysiological states (e.g., myocardial infarction, hemorrhage, renal artery stenosis, or type 1 diabetes) are created by switches and slider bars that allow values to be changed or fixed. HumMod allows users to administer pharmacological agents to treat a patient. Some treatment options include placing the patient on a ventilator, administering fluids via an IV drip with the ability to change tonicity or colloid of the solution, or performing a blood transfusion. A summary of pathophysiological conditions, pharmacological treatments, and device-based therapies that can be simulated in HumMod are listed in [Table 9.1](#).

---

## HumMod for testing physiological concepts and hypotheses in pathophysiology

Modeling human physiology should always have the end goal of clinical translation to improve future experiments or clinical trials by better understanding physiology/pathophysiology. Most systems biology models do not integrate multiple levels, i.e., from cellular to organ systems. Integration, rather than reductionism, can add

**Table 9.1** Multiple pathophysiologies and treatments can be simulated in HumMod

Pathophysiologies in HumMod	
Hypertension	Other
-sympathetic overactivation	-MI
-high/non-responding RAS	-adrenal insufficiency (Addisons disease)
-increased tubular Na <sup>+</sup> reabsorption (hyperaldosteronism)	-orthostatic hypotension
(Liddle's syndrome)	-hemorrhage
-low renal mass/function	-diabetes insipidus (central or nephrogenic)
-renal artery stenosis	-SIADH
-high salt intake	-CKD or ESRD
Diabetes	-anemia
-Type 1 or Type 2	-carbon monoxide poisoning
-obesity	-starvation
	-decreased tubular Na <sup>+</sup> reabsorption (Gitelman Syndrome)
	(Bartter Syndrome)
Treatments in HumMod	
Hypertension	Other
-thiazide diuretic	-digoxin
-loop diuretic	-midodrine
-alpha or beta blocker	-acetazolamide
-ACE inhibitor/ANGII receptor blocker	-atropine
-mineralocorticoid antagonist	-alpha or beta agonist
-calcium channel blocker	-dialysis
Devices	-volume resuscitation
-renal denervation	-insulin
-baroreceptor stimulation	-leptin
-arteriovenous fistula	

RAS indicates renin-angiotensin system; Na<sup>+</sup>, sodium; MI, myocardial infarction; SIADH, syndrome of inappropriate antidiuretic hormone secretion; CKD, chronic kidney disease; ESRD, end stage renal disease; ACE, angiotensin converting enzyme; and ANG, angiotensin.

credibility to model predictions for clinical outcomes by allowing more points of comparison. However, with the integration of complex multilevel systems comes greater room for error, and more validation of each of the model's components is needed. This is further complicated by the variability of the data and model either (cell, animal, or human) used to generate the data.

Pathophysiology is modeled within physiological models by altering the coefficients of the equations. For example, the primary symptom of type 2 diabetes mellitus is an insensitivity to insulin. This can be realized as a derangement of a function that connects insulin concentration in the plasma to glucose availability in cells. In complex pathophysiological states, many relationships may be altered, but in some cases, even a single change is sufficient to generate pathophysiology. For instance, decreasing the conductance of both renal arteries in humans causes a particular hypertension, clinically known as bilateral renal artery stenosis or experimentally designated as Goldblatt hypertension. Alteration of sodium absorption in the distal tubule of the nephrons gives a model that replicates the conditions of Liddle's syndrome. Following this logic, we can asset a parameter basis of pathophysiology: pathophysiology can be expressed by the derangement of one or more existing relationships in an appropriately designed model. Most research work with HumMod has been conducted from this perspective rather than adding specific functions for simulating pathophysiology.

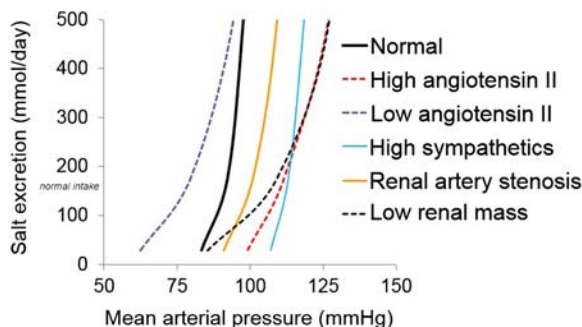
Performing simulations with HumMod under different conditions provides a way to identify research hypotheses and may provide novel insight into pathophysiological mechanisms. The following sections will discuss studies published in peer-reviewed journals using HumMod to test concepts and potential mechanisms to support research hypotheses.

### Example 1: salt sensitivity

Increased salt intake has been shown to increase blood pressure and increase the risk for cardiovascular disease. However, the level of increase in blood pressure varies considerably across individuals, and some individuals have no change in pressure or any detrimental effect on the cardiovascular system with increased salt intake. The mechanisms responsible for salt's impact on blood pressure and the reason for interpatient variability has been debated for many years.

Much evidence exists for the important role of the kidney in controlling blood volume and arterial pressure (Hall, 2016). However, other groups have suggested the importance of peripheral vasculature in the blood pressure response to chronic salt intake. The relationship between blood pressure (BP), cardiac output (CO), and total peripheral resistance (TPR) is  $BP = CO \times TPR$ . The vascular hypothesis of salt sensitivity proposes that, in salt-sensitive patients, an increased salt intake does not decrease TPR sufficiently to lower blood pressure. Some of the experimental limitations to directly test this hypothesis include accurately measuring BP, CO, and TPR.

HumMod was used to simulate several pathophysiological conditions during changes in chronic salt intake (Clemmer et al., 2017). These conditions included high angiotensin II and low renal mass (two conditions with well-known empirical evidence of salt-sensitivity) as well as conditions with unclear effects on salt-sensitivity: high renal sympathetic nerve activity and renal artery stenosis (Fig. 9.1). The simulations revealed that salt sensitivity was not associated with

**FIGURE 9.1**

The blood pressure response to chronic changes in salt intake under normal conditions or in pathophysiological conditions with varying salt sensitivity (the slope of the renal–function curve).

*Simulations adapted from Clemmer, J. S., Pruett, W. A., Coleman, T. G., Hall, J. E., & Hester, R. L. (2017). Mechanisms of blood pressure salt sensitivity: new insights from mathematical modeling. The American Journal of Physiology-Regulatory, Integrative and Comparative Physiology, 312, R451–R466. [10.1152/ajpregu.00353.2016](https://doi.org/10.1152/ajpregu.00353.2016).*

the changes in peripheral vasculature nor in volume retention, but in the change in glomerular filtration rate and tubular sodium reabsorption. These effects were driven by the ability of the renin–angiotensin system to respond to the salt challenge (Clemmer et al., 2017). To our knowledge, no other mathematical model contains detailed neural, hormonal, renal, and cardiovascular physiology that can realistically simulate much of the phenotype in a wide range of pathophysiological conditions and predict the responses to changes in chronic salt intake.

### Example 2: baroreceptor activation therapy

Over the past 15 years, medical devices have been developed for the treatment of hypertension, particularly for patients who are not responsive to current antihypertensive medications (Lohmeier & Hall, 2019). One of these devices is called baroreceptor activation therapy (BAT). The baroreceptor nerves normally respond to changes in blood pressure and send signals to the medulla, resulting in inverse changes in sympathetic nerve activity which can buffer acute changes in blood pressure. BAT is an implantable pulse generator that stimulates the baroreceptor nerves in the carotid artery and decreases sympathetic outflow from the brain. In the first animal experiments, BAT significantly decreased blood pressure. Interestingly, this occurred in animals that were either normal, obese, with angiotensin II hypertension, or in animals without renal sympathetic nerves (Lohmeier & Hall, 2019); the latter suggesting that the decrease in blood pressure following BAT was not due to a decrease in renal sympathetic nerve activity.

HumMod was used to hypothesize that BAT worked through more than just the renal nerves (Clemmer et al., 2018). HumMod demonstrated similar responses to BAT as those observed in animal studies (Lohmeier et al., 2010). Simulation of BAT showed alterations in both sympathetic and parasympathetic activity leading to a depression of cardiac sympathetic activity and heart rate. A decrease in cardiac sympathetic nerve activity and heart rate resulted in an increase in atrial pressure and plasma ANP (Fig. 9.2). Elevations of ANP resulted in an increase in renal excretory

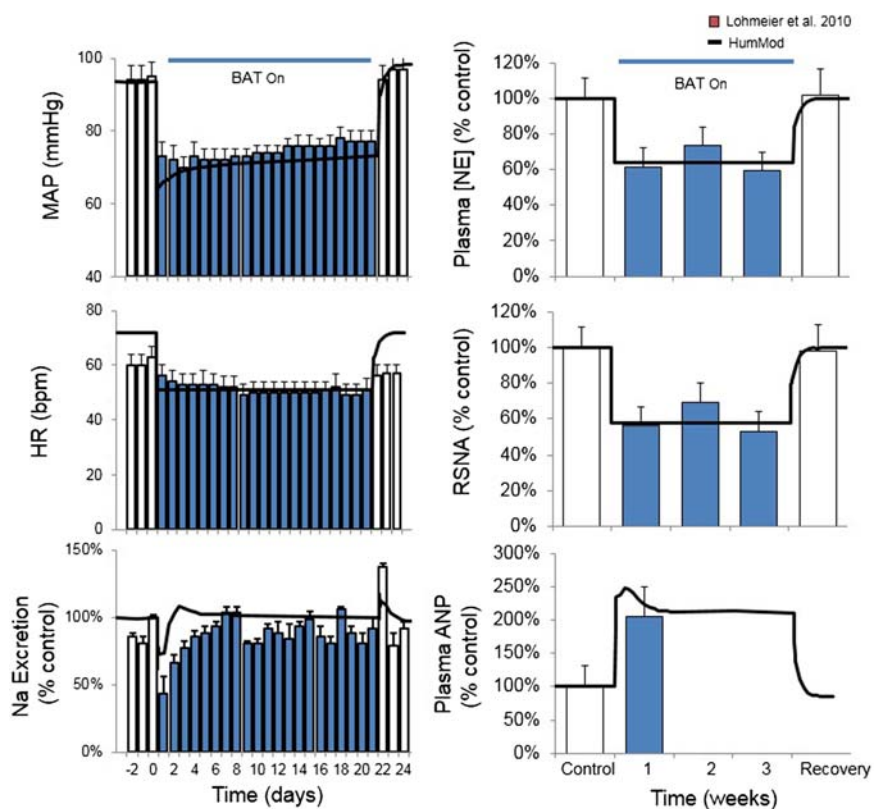


**FIGURE 9.2**

Changes in mean arterial pressure (MAP), heart rate (HR),  $\text{Na}^+$  excretion, plasma norepinephrine (NE), renal sympathetic nerve activity (RSNA), and plasma atrial natriuretic peptide (ANP) during 3 weeks of baroreflex activation. Experimental data is resembled by the bars. White bars indicate control periods and blue bars indicate BAT periods. Values are means  $\pm$  SE for  $n = 6$  dogs from Lohmeier et al. (2010). Black lines show the results from the simulation.

Graphs are adapted from Clemmer, J. S., Prueett, W. A., Hester, R. L., Iliescu, R., & Lohmeier, T. E. (2018). Role of the heart in blood pressure lowering during chronic baroreflex activation: Insight from an *in silico* analysis.

American Journal of Physiology-Heart and Circulatory Physiology. [10.1152/ajpheart.00302.2018](https://doi.org/10.1152/ajpheart.00302.2018).

function and lowered blood pressure. HumMod was also used to test multiple scenarios, including BAT without changes in cardiac sympathetic nerve activity or without changes in renal sympathetic nerve activity, or both, and revealed that ANP, through the suppression of cardiac sympathetic nerve activity, was a key mechanism for the blood pressure lowering effects of this device. This level of testing would be virtually impossible to perform in an experimental or clinical setting, thus demonstrating one of the strengths of HumMod in testing physiological hypotheses.

### Example 3: arteriovenous fistula

Another medical device under development is the arteriovenous (AV) fistula in which a connection between an artery and a vein is created. AV fistulas are used routinely in dialysis patients. This device creates a high flow shunt with a high conductance, operating in parallel with the current circulatory system resulting in an overall decrease in resistance and blood pressure. In a clinical study, an AV fistula between the iliac artery and vein was created in patients with hypertension ([Lobo et al., 2017](#)). After 6 months, there was a substantial but variable decrease in systolic blood pressure ( $-27 \pm 24$  mmHg). The authors suggested that the improvement in blood pressure may have been due to improvements in circulation rather than through any impact on the sympathetic nervous system. However, the actual mechanisms responsible for the decrease in blood pressure following AV fistula are unknown.

HumMod was used to simulate an AV fistula during hypertension caused by elevated sympathetic nerve activity and impaired renal function, similar to the patients treated with this device ([Lobo et al., 2017](#)). The AV fistula simulation resulted in a significantly decreased mean blood pressure ( $-14$  mmHg), a  $\sim 25\%$  increase in cardiac output, an increase in cardiac pressures, and resultant increase in ANP (approximately threefold). When we clamped ANP so that there was no increase in ANP, despite the similar fall in peripheral resistance, there was very little fall in blood pressure at the end of the 8-week AV fistula simulation ([Fig. 9.3](#)). These results suggest that a primary mechanism of this device works through the ANP system. Further analysis also demonstrated a possible role of low-pressure baroreceptors in the sustained hypotensive effects of this device ([Clemmer et al., 2019](#)).

### The future of modeling: virtual populations

Until recently, all of our research studies using HumMod have focused on a single deterministic simulation. However, these simulations describe only a few different models and do not represent the response or variability seen in the entire population. With most treatments, there are responders and nonresponders. Rather than

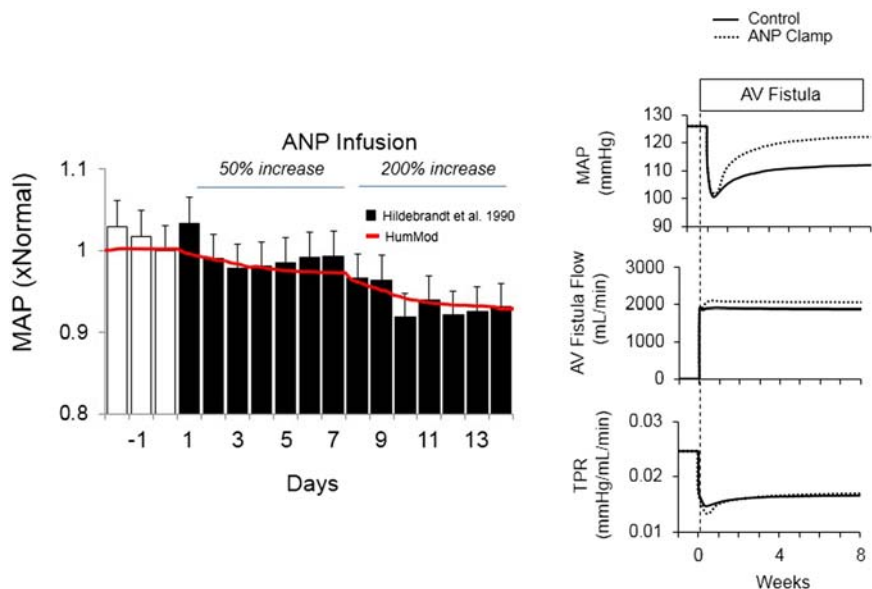


**FIGURE 9.3**

Blood pressure in response to infusing atrial natriuretic peptide in the model and in normal dogs from Hildebrandt et al. (1990). Right panel demonstrates the response to chronic arteriovenous (AV) fistula in a hypertensive model (Control) and in the hypertensive model but without the increase in endogenous atrial natriuretic peptide (ANP Clamp).

Graphs adapted from Clemmer, J. S., Pruitt, W. A., Hester, R. L., & Lohmeier, T. E. (2019). Preeminent role of the cardiorenal Axis in the antihypertensive response to an arteriovenous fistula: An *in silico* analysis. American Journal of Physiology-Heart and Circulatory Physiology. [10.1152/ajpheart.00354.2019](https://doi.org/10.1152/ajpheart.00354.2019).

matching the mean response to an intervention, a more credible validation might be obtained by matching the entire distribution of responses. Formalizing this intuitive concept requires a change in perspective.

When we consider the nature of variability in human or animal models, some intraindividual differences can be laid at the feet of clear genetic differences. For example, differences in metabolism rates of certain pharmaceuticals have been well described in the literature (Bijl et al., 2009). In this chapter, we have already discussed multiple examples where changing a single model parameter can yield a credible model of a pathophysiological state. Physiological systems are time-varying feedback systems and are therefore examples of dynamical systems. In dynamical systems, small changes in coefficients can yield very different system behavior. This would appear to analogize small differences in multitudes of genes

and epigenetic factors giving rise to unique individuals with differences in phenotype impossible to ascribe to a single factor. What might occur in our physiological model if multiple parameters were allowed to vary?

To create a virtual population in HumMod, we identify the model as a set of equations  $M(t)$  with coefficients  $\theta$ , so that  $M(t; \theta)$  is a time-dependent system. Letting time advance, the system progresses toward a steady-state or repeating loop of states. Interacting with the model by changing a parameter at a specific time  $\tau$  yields a new model:

$$M(t, (\theta_1, \tau), (\theta_2, \infty)) = \begin{cases} M(t; \theta_1) & t \leq \tau \\ M(t; \theta_2) & t > \tau \end{cases}. \quad (9.1)$$

Assessing model validity involves addressing the question of whether the relationships  $M$  are sufficient to find a distribution of parameters  $\Theta$  so that for  $\theta \in \Theta$ ,  $M(t, (\theta, \tau_i), \dots)$  are statistically equivalent to a set of comparator data. A population is obtained by sampling from  $\Theta$  and executing a sequence of interventions.

One of the challenges with developing a virtual population is having high quality human data as a comparator for creating of the population. For proof-of-concept, HumMod was used to simulate BAT responses in a virtual population statistically similar to obese, hypertensive dog responses (Lohmeier et al., 2012). Within HumMod, 335 parameters were varied randomly and simultaneously (up to 5%) from their baseline value and resulted  $\sim 6000$  virtual patients. These initial models were used for calibration, in which experimental data (blood pressure, glomerular filtration rate, and renin levels before and after BAT) were used to select the most similar models, creating coefficient sets that yielded a virtual population with statistically similar to experimental BAT responses (Clemmer et al., 2021). This calibrated population was further used to simulate BAT with ANP, RSNA, or both fixed at baseline levels. The simulations suggested that, in hypertension caused by obesity and sympathetic nerve activation, renal sympathetic and ANP responses play important roles in lowering blood pressure during BAT.

---

## Conclusion, limitations, and future considerations

HumMod executes complex and stable integrative physiological simulations with realistic outputs in many scenarios. It has been used over the last several decades to test hypotheses not easily done in experimental or clinical settings. In this chapter, we have shown several areas that HumMod replicated empirical findings and predicted possible mechanisms in the areas of hypertension. All models should have as one of its immediate goals to be validated by benchmark testing. When a simulation produces an output that is within a physiological and statistical bounds of comparative data, it is considered validated in that particular context. However, one difficulty in model validation is the data used to validate. The outputs from a particular experimental or clinical study are highly dependent on the chosen

methods and protocol, study population, and environment. The outputs of the model should be stable with limited physiological errors. Model validation can be qualitative, quantitative at steady-state, or dynamically quantitative (Summers et al., 2009). Quantitative validation of a model in dynamic transitions is more difficult and there are no current standard methods. General trend matching allows a model to fit data loosely enough to provide valid, stable results. HumMod has yet to be fully validated against each submodel and physiological concept currently included in the model, which is one of our group's primary goals.

---

## Acknowledgments

This work was supported by grants from the National Institute on Minority Health and Health Disparities (K99 MD014738), the Joe and Dorothy Dorsett Brown Foundation, and the National Heart, Lung, and Blood Institute (P01 HL051971). Free downloads of HumMod for academic work are available at <http://hummod.org>.

---

## References

- Bijl, M. J., Visser, L. E., van Schaik, R. H., Kors, J. A., Witteman, J. C., Hofman, A., et al. (2009). Genetic variation in the CYP2D6 gene is associated with a lower heart rate and blood pressure in beta-blocker users. *Clinical Pharmacology & Therapeutics*, 85, 45–50. <https://doi.org/10.1038/clpt.2008.172>
- Clemmer, J. S., Pruett, W. A., Coleman, T. G., Hall, J. E., & Hester, R. L. (2017). Mechanisms of blood pressure salt sensitivity: New insights from mathematical modeling. *American Journal of Physiology-Regulatory, Integrative and Comparative Physiology*, 312, R451–R466. <https://doi.org/10.1152/ajpregu.00353.2016>
- Clemmer, J. S., Pruett, W. A., & Hester, R. L. (2021). In silico trial of baroreflex activation therapy for the treatment of obesity-induced hypertension. *PLoS One*, 16, e0259917. <https://doi.org/10.1371/journal.pone.0259917>
- Clemmer, J. S., Pruett, W. A., Hester, R. L., Iliescu, R., & Lohmeier, T. E. (2018). Role of the heart in blood pressure lowering during chronic baroreflex activation: Insight from an in silico analysis. *American Journal of Physiology-Heart and Circulatory Physiology*. <https://doi.org/10.1152/ajpheart.00302.2018>
- Clemmer, J. S., Pruett, W. A., Hester, R. L., & Lohmeier, T. E. (2019). Preeminent role of the cardiorenal Axis in the antihypertensive response to an arteriovenous fistula: An in silico analysis. *American Journal of Physiology-Heart and Circulatory Physiology*. <https://doi.org/10.1152/ajpheart.00354.2019>
- Coleman, T. G., & Randall, J. E. (1983). HUMAN. A comprehensive physiological model. *Physiologist*, 26, 15–21.
- Guyton, A. C., Coleman, T. G., & Granger, H. J. (1972). Circulation: Overall regulation. *Annual Review of Physiology*, 34, 13–46. <https://doi.org/10.1146/annurev.ph.34.030172.000305>
- Hall, J. E. (2016). Renal dysfunction, rather than nonrenal vascular dysfunction, mediates salt-induced hypertension. *Circulation*, 133, 894–906. <https://doi.org/10.1161/CIRCULATIONAHA.115.018526>

- Hildebrandt, D. A., Mizelle, H. L., Brands, M. W., Gaillard, C. A., Smith, M. J., Jr., & Hall, J. E. (1990). Intrarenal atrial natriuretic peptide infusion lowers arterial pressure chronically. *American Journal of Physiology*, 259, R585–R592. <https://doi.org/10.1152/ajpregu.1990.259.3.R585>
- Hodgkin, A. L., & Huxley, A. F. (1952). A quantitative description of membrane current and its application to conduction and excitation in nerve. *The Journal of Physiology*, 117, 500–544. <https://doi.org/10.1113/jphysiol.1952.sp004764>
- Krogh, A. (1919). The number and distribution of capillaries in muscles with calculations of the oxygen pressure head necessary for supplying the tissue. *The Journal of Physiology*, 52, 409–415. <https://doi.org/10.1113/jphysiol.1919.sp001839>
- Lobo, M. D., Ott, C., Sobotka, P. A., Saxena, M., Stanton, A., Cockcroft, J. R., et al. (2017). Central iliac arteriovenous anastomosis for uncontrolled hypertension: One-year results from the ROX CONTROL HTN trial. *Hypertension*, 70, 1099–1105. <https://doi.org/10.1161/HYPERTENSIONAHA.117.10142>
- Lohmeier, T. E., & Hall, J. E. (2019). Device-based neuromodulation for resistant hypertension therapy. *Circulation Research*, 124, 1071–1093. <https://doi.org/10.1161/CIRCRESAHA.118.313221>
- Lohmeier, T. E., Iliescu, R., Dwyer, T. M., Irwin, E. D., Cates, A. W., & Rossing, M. A. (2010). Sustained suppression of sympathetic activity and arterial pressure during chronic activation of the carotid baroreflex. *American Journal of Physiology-Heart and Circulatory Physiology*, 299, H402–H409. <https://doi.org/10.1152/ajpheart.00372.2010>
- Lohmeier, T. E., Iliescu, R., Liu, B., Henegar, J. R., Maric-Bilkan, C., & Irwin, E. D. (2012). Systemic and renal-specific sympathoinhibition in obesity hypertension. *Hypertension*, 59, 331–338. <https://doi.org/10.1161/HYPERTENSIONAHA.111.185074>
- Schultz, S. G. (2002). William Harvey and the circulation of the blood: The birth of a scientific revolution and modern physiology. *News Physiol Sci*, 17, 175–180.
- Summers, R. L., Ward, K. R., Witten, T., Convertino, V. A., Ryan, K. L., Coleman, T. G., et al. (2009). Validation of a computational platform for the analysis of the physiologic mechanisms of a human experimental model of hemorrhage. *Resuscitation*, 80, 1405–1410. <https://doi.org/10.1016/j.resuscitation.2009.09.001>

**SECTION**

Organs

2

This page intentionally left blank

# Computational biomechanics as a tool to improve surgical procedures for Uterine Prolapse

# 10

Silva Elisabete<sup>1</sup>, Bessa Nuno<sup>1</sup>, Mascarenhas Teresa<sup>2</sup>,  
António Augusto Fernandes<sup>1</sup>

<sup>1</sup>LAETA, INEGI, Faculty of Engineering, University of Porto Porto, Portugal; <sup>2</sup>Department of Obstetrics and Gynecology, CHSJ-EPE/Faculty of Medicine, University of Porto Porto, Portugal

## Chapter outline

Introduction.....	213
Mechanism of the development of POP .....	215
Biomechanical uterine prolapse simulation .....	218
Isotropic constitutive model—simulating the passive behavior .....	218
Computational model of the pelvic cavity .....	219
Computational model of the implant .....	219
Biomechanical properties of the soft tissues and mesh implant .....	220
Uterine prolapse simulation.....	221
Personalized models to repair the uterine prolapse.....	223
Conclusions.....	223
Acknowledgments .....	223
References .....	224

## Introduction

Pelvic floor dysfunction (PFD) defines a wide range of clinical conditions that could have significantly negatively impacted a woman's daily activities and life quality. Pelvic Organ Prolapse (POP) is one of those, and often occurs when the support structures, such as ligaments and pelvic floor muscles (PFMs), no longer support the pelvic organs adequately, resulting in the protrusion (prolapse) from their normal position (MacCraith et al., 2021). Due to its relation with soft tissue support, it is most common after vaginal childbirth and often gets more evident with the intraabdominal pressure in daily activities such as defecating or physical activity. The

prevalence of POP, which is now up to 41.1%, is likely to increase due to improvements in overall health care and increase in life expectancy (Rada et al., 2020).

The treatments for POP are complex due to the intricate nature of the disorder. Overall, one can start with lifestyle recommendations/noninvasive treatments (weight loss, avoiding heavy lifting and physiotherapy); however, this approach is not helpful for women with severe POP. In this sense, surgery remains the mainstay of therapy for POP.

There is a multitude of surgeries for POP repair. They can be primarily divided based on the approach, i.e., vaginal or abdominal (either by open abdomen or by laparoscopy) repair. Procedures can also be divided in how the defects are repaired, using either native tissue or synthetic meshes. Unfortunately, native tissue repairs have a relatively high failure rate (29%), and surgeons began to augment native tissue repairs with synthetic mesh (Houman et al., 2017). It is estimated that from 2010 to 2050, the total number of women undergoing surgery for POP will increase by 48.2% (Kiyosaki et al., 2012), with a reoperation rate of 30% (Wu et al., 2011). In Germany, France, and England, in 2005, the number (rate) of admissions for POP surgery was 102,492 (1.05 per 1000 women) and the involved costs were 308.335,289€ (Subramanian et al., 2009). In Portugal, 46,819 diagnoses of genital prolapse were registered from 2000 to 2012, with a 105% increase during the study period, associated with an increase in synthetic meshes using (Mascarenhas et al., 2015). Recently, the safety and effectiveness rates of the meshes used for POP surgery has been queried, due to the high rates of complications such as mesh erosion, chronic pain, and voiding symptoms, as reported by Continence Society and Urogynecology Association (Haylen et al., 2010). In 2019, the Food and Drug Administration (FDA) ordered the manufacturers to discontinue their products immediately, although the use of sacrocolpopexy meshes is still allowed (FDA, 2019). Despite intensive clinical research efforts, the progress in reducing complications after surgeries has been slow. Consequently, the development of innovative tools to increase the biomechanical knowledge associated with this condition may be crucial to carry out effective and viable therapeutic procedures. Previous studies showed that the POP recurrence is common after vaginal mesh implantation that may be associated with a strong attachment point for mesh fixation (Wu et al., 2020). Recently, Silva et al. simulated the absence/presence of the synthetic implant when total rupture of the cardinal ligaments and uterosacral ligaments occurs that caused a variation of the vaginal displacement (9% for the cardinal ligaments and 27% for the uterosacral ligaments). Additionally, these authors showed that there was a variation of the supero-inferior displacement of the vaginal wall between different anchoring techniques (simple stich and continuous stitch) being approximately of 10% for the simulation with implant to mimic the uterosacral ligaments and cardinal ligaments (Silva et al., 2021).

Imaging techniques, including magnetic resonance imaging (MRI), provide useful anatomical information, rapid, complete evaluation of the entire pelvis, including support structures and organs at rest position and during pelvic maneuvers (Valsalva maneuver and muscle contraction) (Boyadzhyan et al., 2008). Therefore, elucidating

the impact of the pelvic surgery to repair the POP in the women's quality of life using pelvic floor biomechanics can lead to the development of preventive and therapeutic strategies which can be helped to improve the outcomes of the prolapse surgery, reducing the rates of recurrence of the surgery.

### Mechanism of the development of POP

The main objective of this chapter is to study the POP, so the main subjects regarding the POP need to be presented, with the purpose of gathering the essential knowledge about this PFD. Thus, it is important to distinguish the different POP classification systems (see Table 10.1) (Persu et al., 2011), since there are several types with different effects and treatments to them. The pathophysiological conditions to understand the several damage levels associated and the support levels.

**Table 10.1 Prolapse classification.**

Type of POP	Characterization of the POP
<b>Urethrocele</b>	POP of the lower anterior vaginal wall involving the urethra only.
<b>Cystocele</b>	POP of the upper anterior vaginal wall involving the bladder.
<b>Uterovaginal prolapse</b>	This term is used to describe POP of the uterus, cervix, and upper vagina.
<b>Enterocèle</b>	POP of the upper posterior wall of the vagina usually containing loops of small bowel.
<b>Rectocele</b>	POP of the lower posterior wall of the vagina involving the rectum bulging forwards into the vagina.

Adapted from (Persu, C., Chapple, C. R., Cauni, V., Gutue, S., & Geavlete, P. (2011). Pelvic organ prolapse quantification system (POP-Q) - a new era in pelvic prolapse staging. Journal of Medicine and Life, 4(1), 75–81.

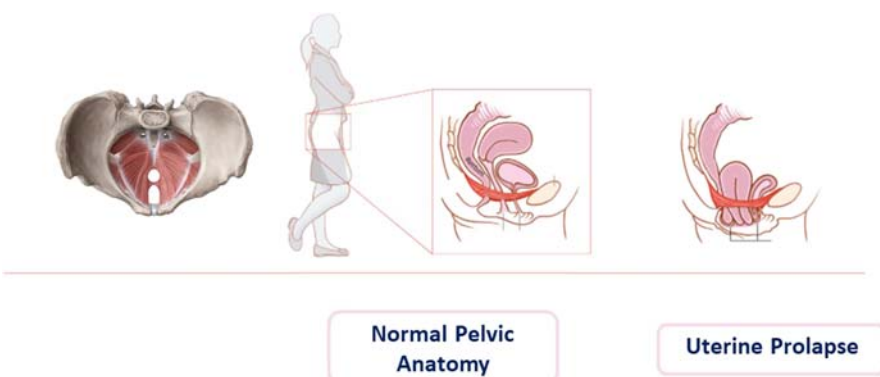


**FIGURE 10.1**

Normal pelvic anatomy and uterine prolapse.

For the uterine prolapse, the uterosacral–cardinal ligaments are the ones that provide the most support to the uterus (Fig. 10.1). The uterosacral and cardinal ligaments form a complex of connective tissue, comprising the level I support of the vagina. Its function is to suspend the upper vagina and uterus, to maintain vaginal length and keep the axis of the vagina in its normal orientation, that is, almost horizontal. Thus, the rupture or damage of this structure is a predisposition to the prolapse of the uterus and/or vaginal wall.

The study of pelvic biomechanics is still a relatively new field of research that benefits from advances in medical imaging, segmentation techniques, multiscale computational mechanics analysis methods, improved tissue modeling, the development of noninvasive biomechanical measurement methods, and increased computational power, which make *in silico* analysis very relevant in this field. Patient-specific modeling is a potential tool to improve diagnosis or optimize clinical procedures, attracting the attention of many research groups (Eggermont et al., 2018). Also, studies on the safety and efficacy of medical devices are based on clinical trials, and in fact meshes may not be effective to a specific patient (Neal & Kerckhoffs, 2009).

There is an increased interest in the computational mechanics study of synthetic meshes. Researchers have recently studied the biomechanical performance of laparoscopic surgery after partial hysterectomy, by correcting an apical prolapse using previous computational model of the pelvic structures, based on cadaveric dimensions (Bhattarai & Staat, 2020).

Our research group has taken essential steps to understand the biomechanics of the pelvic cavity. Namely, by using MRI-based (Brandão et al., 2013) computational models (Roza et al., 2015; Silva et al., 2016, 2017a); implementation of viscohy-perelastic constitutive models (Vila Pouca et al., 2018); studying the deformation of the pelvic structures during pelvic maneuvers (contraction and Valsalva maneuver) (Silva et al., 2017b, 2018); studying vaginal delivery—which is the main risk factor responsible for the development of PFD (Silva et al., 2015)—through a biomechanical perspective; or by retrieving muscle internal arrangement noninvasively from MR Diffusion Tensor Imaging, which provides an *in vivo* representation of the orientation of muscle fibers (Brandão, Parente, Silva, et al., 2017b). Our computational mechanics models were also used to evaluate midurethral displacement when these supportive structures are impaired, and how the use of synthetic slings reduces bladder and bladder neck mobility during stressful maneuvers. We observed that a synthetic mesh's stiffness to correct stress urinary incontinence (SUI) might be relevant when considering personalized options (Brandão, Parente, Da Roza, et al., 2017). Taking another approach, an inverse finite element analysis (FEA) was implemented to obtain *in vivo* biomechanical properties of the PFM for a specific subject, comparing their displacement with dynamic MRI obtained during Valsalva maneuver and contraction (Silva et al., 2018, 2019). This methodology was also used to estimate the *in vivo* biomechanical properties of different pathological conditions, including patients with SUI and those with POP (Silva et al., 2017b, 2018). With the inverse FEA, it was observed that PFM of patients with POP are stiffer than that of incontinent patients, which is in agreement with published literature (Silva et al., 2018).

Biomechanical analysis of the pelvic floor tissues is important to understand different PFD. Decreased tissue elasticity often causes inability to preserve the normal anatomical position of the pelvic organs, so such analysis will also improve clinical outcomes by better understanding the effect of changes in tissue elasticity.

Previous studies showed that POP influences the biomechanical properties of the PFM (Fig. 10.2) suggested that the PFM of patients with POP presented an increase of stiffness when compared with asymptomatic patients (Silva et al., 2017b, 2018). Additionally, in patients with prolapse, the force produced was 47% and 82% higher when compared to women without pathology and with SUI, respectively (Silva et al., 2018).

Therefore, PFD may result from changes in the biomechanical properties of the supportive structures that occur from weakness of PFM or ligaments, or alterations

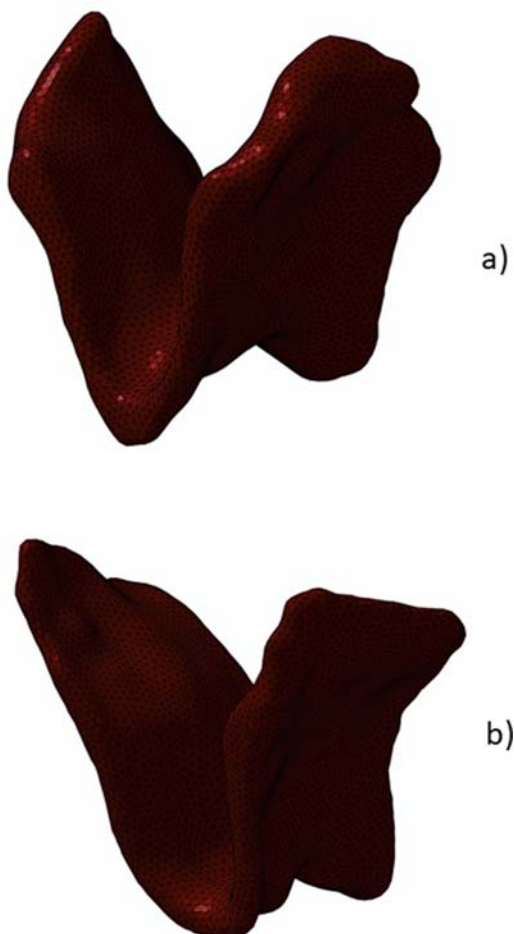


**FIGURE 10.2**

Computational model of the PFM for a patient without prolapse (A) and with prolapse (B).

in the stiffness of the pelvic fascia related to the risk factors—age, hormonal changes, childbirth, among others (Abramowitch et al., 2009).

Another item to take into consideration is the fact that the pelvic floor (muscles) are under a downward loading pressure of the abdomino-pelvic organs, both at rest and during Valsalva maneuver. These values have been achieved for subjects lying supine, the average is approximately 0.5 kPa at rest and 4.5 kPa during Valsalva maneuver (Noakes et al., 2008). Accordingly, to simulate the Valsalva maneuver in our computational models, we apply a pressure of 4 kPa in the inner surface of the muscle, since they already incorporate resting tone.

---

### Biomechanical uterine prolapse simulation

Important steps and studies have been undertaken, in the past, toward the understanding of the biomechanics of the pelvic floor cavity, namely the ability to use MRI (Boyadzhyan et al., 2008; Brandão et al., 2013; Brandão, Parente, Silva, et al., 2017b), to build computational models (Mayer et al., 2016; Roza et al., 2015; Silva et al., 2016, 2017a); the study of the displacements and deformations of the pelvic structures during pelvic maneuvers (contraction and Valsalva maneuver) (Noakes et al., 2008; Silva et al., 2017a, 2018); the study of vaginal delivery, which is the main risk factor responsible for the development of POP (Parente et al., 2009; Silva et al., 2015). Computational models have also been used to evaluate midurethral displacements when its supportive structures are impaired and assess how the use of synthetic slings reduce the displacement of the bladder and bladder neck. It was observed that the stiffness of a synthetic mesh to correct SUI may be relevant when considering personalized options (Brandão, Parente, Da Roza, et al., 2017). Other approaches used include inverse FEA, which were implemented to obtain *in vivo* biomechanical properties of the PFM for specific subjects, comparing the results from the dynamic MRI during Valsalva maneuver and contraction (Silva et al., 2018, 2019) and also to estimate the *in vivo* biomechanical properties of different pathological groups, including patients with SUI and with POP (Silva et al., 2017a; 2017b). Other authors used computer modeling for surgical planning of sacrocolpopexy (Albanesi et al., 2019). Sacrocolpopexy is minimally invasive and is the gold standard procedure for stage III–IV apical prolapse, a downward displacement of the vaginal apex (Albanesi et al., 2019).

---

### Isotropic constitutive model—simulating the passive behavior

Constitutive laws are applied to mimic the biomechanical behavior of the pelvic structures, taking into account the details of their inner structure. Most of the pelvic structures are assumed to be hyperelastic (describing nonlinear material behavior

and large shape changes) and often incompressible materials (maintaining volume constant under pressure). Also, as some structures, the pelvic striated skeletal muscles, are embedded in a connective tissue matrix, their features have to be set, as for instance, their anisotropic and isotropic behavior, respectively. Isotropy is the property of being directionally independent, as opposed to anisotropy, which means heterogeneity in all directions.

To simulate the mechanical behavior of the pelvic cavity tissues, Yeoh and Ogden constitutive models are frequently used. These are simple models that employ a nonlinear relationship between stress and strain to describe incompressible hyperelastic materials and they have proved to properly describe the biomechanical behavior of the PFM during simulation of Valsalva maneuver (Silva et al., 2017a; 2017b) and impairment of the pelvic ligaments (Brandão et al., 2015; Brandão, Parente, Da Roza, et al., 2017).

Neglecting viscous, temperature and time-dependent effects, Ogden, Yeoh models are the most widely used strain energy function to characterize the pelvic tissues in the context of nonlinear hyperelasticity (Bhattarai, 2018).

The Yeoh constitutive model (Eq. 10.1) is described by elsewhere (Martins et al., 2006):

$$W = c_1(I_1 - 3) + c_2(I_1 - 3)^2 + c_3(I_1 - 3)^3 \quad (\text{Eq. 10.1})$$

where  $W$  is the strain energy function and  $c_1$ ,  $c_2$ , and  $c_3$  are the material parameters to be determined and have dimensions of stress,  $I_1$  is the principal strain invariant (Eq. 10.2) of the right Cauchy–Green tensor (Noakes et al., 2008). For the case of uniaxial stretching, the principal strain invariants are represented as follows:

$$I_1 = \lambda^2 + \frac{2}{\lambda} \quad (\text{Eq. 10.2})$$

where is  $\lambda$  the maximum principal stretch.

The Ogden constitutive model (Eq. 10.3) is characterized by (Martins et al., 2006)

$$W = \sum_{i=1}^n \mu_n \frac{(\lambda_1^{\alpha_n} + \lambda_2^{\alpha_n} + \lambda_3^{\alpha_n} - 3)}{\alpha_n} \quad (\text{Eq. 10.3})$$

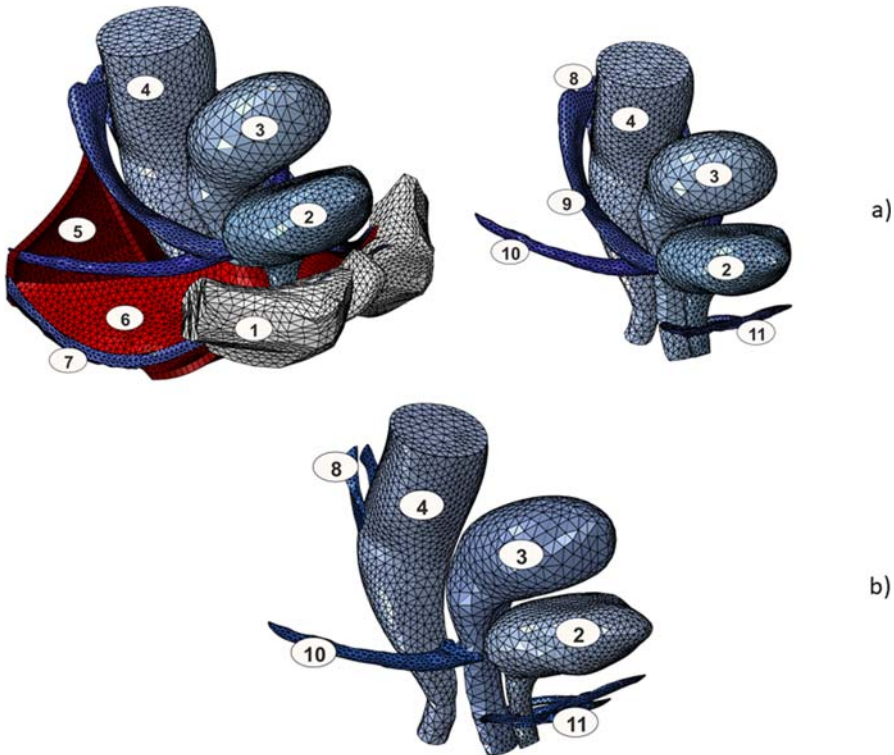
where  $\mu_n$  and  $\alpha_n$  are material parameters and  $n$  is the number of material parameters.

## Computational model of the pelvic cavity

The 3D computational model of the pelvic cavity, illustrated in Fig. 10.2, was adapted from Brandão et al. and corresponds to a nulliparous 24-year-old healthy female (Fig. 10.3) (Brandão, Parente, Da Roza, et al., 2017).

## Computational model of the implant

In order to mimic the USLs, computational model of the synthetic implant is represented in Fig. 10.4A.

**FIGURE 10.3**

Healthy 3D computational model (A); 3D computational model after rupture of the USLs (B). (1) symphysis pubis, (2) bladder, (3) uterus, (4) rectum, (5) levator ani muscle, (6) pelvic fascia, (7) arcus tendineous fasciae pelvis, (8) lateral ligaments of the rectum, (9) uterosacral ligaments, (10) cardinal ligaments, (11) pubourethral ligaments.

The implant synthetic is a monofilament polypropylene mesh and its process of fabrication consists of knitting continuous fibers around each other with the desired pattern (Rynkevic, 2019).

The red point visualized on the anterior vaginal wall point (Fig. 10.4B) is used to measure the supero-inferior displacement of the vagina.

### Biomechanical properties of the soft tissues and mesh implant

PFD affects the quality of life of many women and can be related to changes in the biomechanical properties of muscles, ligaments, and fascia (Abramowitch et al., 2009). In this sense, the biomechanical analysis of the pelvic floor tissues is important to understand different PFD. Table 10.2 represents the biomechanical properties used by Brandão et al. (2015).

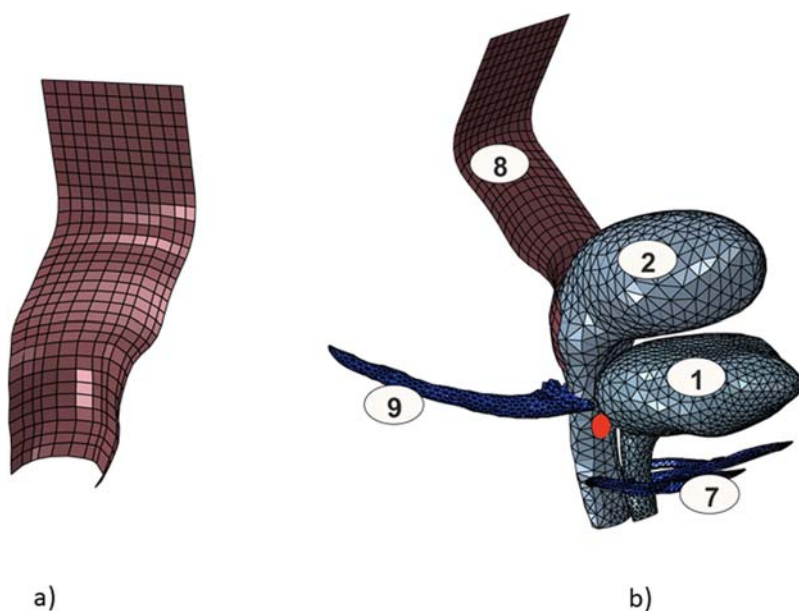


**FIGURE 10.4**

Development and incorporation of the surgical implant to mimic the USLs, after their rupture (100% impairment) on the pelvic cavity, (A) mesh implant; (B) Implantation of the USLs implant; (1) bladder, (2) uterus, (3) rectum, cardinal ligaments, (4) lateral ligaments of the rectum, (5) uterosacral ligaments, (6) CLs implant, (7) pubourethral ligaments, (8) USLs implant, (9) cardinal ligaments.

## Uterine prolapse simulation

Total rupture of the USLs cause variation in the supero-inferior displacement and in the magnitude of the displacement of the vagina and uterus. Table 10.3 shows the supero-inferior displacement and maximum magnitude of displacement of the vagina, during Valsalva maneuver, when rupture of the USLs occurs. The displacement was measured on the anterior vaginal wall (Fig. 10.4B, red point).

The numerical simulations showed that there is an increase of the supero-inferior displacement and magnitude of the displacement of the vagina after rupture of the USLs. The application of the synthetic mesh caused an inverse effect to rupture, decreasing the displacements of the vagina. When a total rupture of the USLs occurs, the absence/presence of the synthetic implant caused a variation in the supero-inferior displacement and maximum magnitude of displacements of the vagina, being 26.99% and 24.88%, respectively.

When a mesh is used to replace the USLs (when applicable), the support function appears to be partially established. The numerical simulations showed a reduction of the supero-inferior displacement and magnitude of displacements of the anterior vaginal wall, after implantation of the surgical mesh to values similar to the asymptomatic case.

**Table 10.2** Material parameters of the hyperelastic constitutive models (Ogden and Yeoh) applied to pelvic structures and synthetic mesh implants.

Structures					Model
		$\alpha_1$	$\mu_1$	$\alpha_2$	
<b>Bladder and urethra</b>		$\alpha_1 = 0.19$	$\mu_1 = 5.14$		Ogden ( $n = 1$ )
<b>Rectum</b>		$\alpha_1 = 4.25$	$\alpha_1 = 4.25$		Ogden ( $n = 2$ )
		$\alpha_2 = -3.83$	$\mu_2 = 13.24$		
<b>Vagina and uterus</b>		$\alpha_1 = -3.41$	$\mu_1 = -92.24$		Ogden ( $n = 3$ )
		$\alpha_2 = -0.66$	$\mu_2 = 39.29$		
		$\alpha_3 = -6.48$	$\mu_3 = 54.68$		
<b>PUL</b>		$\alpha_1 = 10.95$	$\mu_1 = 1.58$		Ogden ( $n = 1$ )
	<b>c<sub>1</sub> [MPa]</b>		<b>c<sub>2</sub> [MPa]</b>	<b>c<sub>3</sub> [MPa]</b>	<b>Model</b>
<b>Pubocervical fascia</b>		0.93	-0.62	0.47	Yeoh
<b>ATFP, CL, LLR, USLs</b>		1.74	6.60	4.79	Yeoh
<b>PFM</b>		0.003	0.002	0.001	Yeoh
<b>Mesh implant</b>		4.15	-9.10	48.38	Yeoh

Note: AFTP, Arcus tendineae fasciae pelvis; CL, Cardinal ligaments; LLR, Lateral ligaments of the rectum; PUL, Pubourethral ligaments; USLs, Uterosacral ligaments.

Adapted from Brandão, S., Parente, M., Mascarenhas, T., da Silva, A. R. G., Ramos, I., & Jorge, R. N. (2015). Biomechanical study on the bladder neck and urethral positions: Simulation of impairment of the pelvic ligaments. Journal of Biomechanics, 48(2), 217–223. <https://doi.org/10.1016/j.jbiomech.2014.11.045>

**Table 10.3** Supero-inferior displacement and maximum magnitude of displacement for the vagina, during Valsalva maneuver, when total rupture of the uterosacral ligament occurs.

Variable		Supero-inferior disp. of the vagina (mm)	Max mag. of disp. of the vagina (mm)
<b>Healthy</b>	<b>Rest</b>	....	....
	<b>Valsalva</b>	7.69	9.38
<b>Total rupture of the USLs</b>		12.67	16.00
		<b>Synthetic implant</b>	
		<b>Supero-inferior disp. of the vagina (mm)</b>	<b>Max mag. of disp. of the vagina (mm)</b>
<b>Total rupture of the USLs</b>		9.25	12.02
<b>Total rupture of the USLs</b>		26.99%	24.88%
<b>Variation (%)</b>			

Note: Max mag. of disp. of the vagina, Maximum magnitude of displacement of the vagina; Supero-inferior disp. of the vagina, Supero-inferior displacement of the vagina; USLs, Uterosacral ligaments.

---

## Personalized models to repair the uterine prolapse

In recent years, Personalized Medicine (PM) is shifting health care toward the selection and monitorization of the best treatment for each patient based on patient characteristics and diagnostic information ([International Consortium for Personalised Medicine, 2017](#)). Personalized clinical processes involve multiple diagnostic tests and treatments over time. The sequences of tests and treatments may differ between individual patients. The use of randomized controlled trials (RCTs) for collecting evidence, and to inform health economic evaluations, is increasingly being questioned in a PM context. RCTs are designed to draw conclusions on a population-level, while PM focusses on patient-level outcomes ([Degeling et al., 2017](#)).

The development of the personalized patient model, which can be used to predict the outcome of the pelvic surgery with native tissues and/or synthetic meshes, has a potential to change the way the health care industry and hospitals deal with PFD, namely the POP. Preventing patient complications after surgery, reducing health care costs by reducing both the number of reoperations and size of RCTs. This virtual model could also contribute to help the manufacturers to validate the surgical meshes for regulatory purposes, as recommended by the FDA ([FDA, 2019](#)).

---

## Conclusions

In conclusion, it was possible to demonstrate that the computer modeling and simulation of the pelvic cavity can be an important tool in the design and development of new meshes, shortening the lead time of launching novel, safer and more effective meshes. Further work in progress in our group covers different topics, namely: (1) production of biodegradable surgical meshes using new fabrication processes such as melt electrowriting; the development of new computational tools; (2) virtual patient model that can be used to predict the outcome of the pelvic surgery with native tissues and/or synthetic and biodegradable meshes, which has a potential to change the way the health care industry and hospitals deal with POP. The computational simulation studies of the pelvic cavity can contribute to help the manufacturers to validate the surgical meshes for regulatory purposes (Premarket Approval), as recommended by the FDA ([FDA, 2019](#)).

---

## Acknowledgments

The authors gratefully acknowledge the funding by Ministério da Ciência Tecnologia, e Ensino Superior, FCT, Portugal and Programa Operacional Competitividade e Internacionalização—POCI the project SPINMESH—Melt electrospinning of polymeric bio-absorbable meshes for pelvic organ prolapse repair—POCI-01-0145-FEDER-029232, and LAETA—UIDB/50022/2020.

---

## References

- Abramowitch, S. D., Feola, A., Jallah, Z., & Moalli, P. A. (2009). Tissue mechanics, animal models, and pelvic organ prolapse: A review. *European Journal of Obstetrics and Gynecology and Reproductive Biology*, 144(1), S146–S158. <https://doi.org/10.1016/j.ejogrb.2009.02.022>
- Albanesi, G., Giannini, A., Carbone, M., Russo, E., Mannella, P., Ferrari, V., & Simoncini, T. (2019). Computed-tomography image segmentation and 3D-reconstruction of the female pelvis for the preoperative planning of sacrocolpopexy: Preliminary data. *International Urogynecology Journal*, 30(5), 725–731. <https://doi.org/10.1007/s00192-018-3706-3>
- Bhattarai, A. (2018). *Constitutive modeling of female pelvic floor dysfunctions and reconstructive surgeries using prosthetic mesh implants*.
- Bhattarai, A., & Staat, M. (2020). A computational study of organ relocation after laparoscopic pectopexy to repair posthysterectomy vaginal vault prolapse. *Computer Methods in Biomechanics and Biomedical Engineering: Imaging and Visualization*, 8(3), 277–286. <https://doi.org/10.1080/21681163.2019.1670095>
- Boyadzhyan, L., Raman, S. S., & Raz, S. (2008). Role of static and dynamic MR imaging in surgical pelvic floor dysfunction. *Radiographics*, 28(4), 949–967. <https://doi.org/10.1148/rug.284075139>
- Brandão, S., Da Roza, T., Mascarenhas, T., Duarte, S., Ramos, I., Parente, M., & Jorge, R. N. (2013). Moment of inertia as a means to evaluate the biomechanical impact of pelvic organ prolapse. *International Journal of Urology*, 20(1), 86–92. <https://doi.org/10.1111/j.1442-2042.2012.03219.x>
- Brandão, S., Parente, M., Da Roza, T. H., Silva, E., Ramos, I. M., Mascarenhas, T., & Jorge, R. M. N. (2017). On the stiffness of the mesh and urethral mobility: A finite element analysis. *Journal of Biomechanical Engineering*, 139(8). <https://doi.org/10.1115/1.4036606>
- Brandão, S., Parente, M., Mascarenhas, T., da Silva, A. R. G., Ramos, I., & Jorge, R. N. (2015). Biomechanical study on the bladder neck and urethral positions: Simulation of impairment of the pelvic ligaments. *Journal of Biomechanics*, 48(2), 217–223. <https://doi.org/10.1016/j.jbiomech.2014.11.045>
- Brandão, S., Parente, M., Silva, E., Da Roza, T., Mascarenhas, T., Leitão, J., Cunha, J., Natal Jorge, R., & Nunes, R. G. (2017b). Pubovisceralis muscle fiber architecture determination: Comparison between biomechanical modeling and diffusion tensor imaging. *Annals of Biomedical Engineering*, 45(5), 1255–1265. <https://doi.org/10.1007/s10439-016-1788-y>
- Degeling, K., Koffijberg, H., & IJzerman, M. J. (2017). A systematic review and checklist presenting the main challenges for health economic modeling in personalized medicine: Towards implementing patient-level models. *Expert Review of Pharmacoeconomics and Outcomes Research*, 17(1), 17–25. <https://doi.org/10.1080/14737167.2017.1273110>
- Eggermont, F., Derikx, L. C., Verdonschot, N., Van Der Geest, I. C. M., De Jong, M. A. A., Snyers, A., Van Der Linden, Y. M., & Tanck, E. (2018). Can patient-specific finite element models better predict fractures in metastatic bone disease than experienced clinicians? *Bone and Joint Research*, 7(6), 430–439. <https://doi.org/10.1302/2046-3758.76.BJR-2017-0325.R2>
- FDA. (2019). <https://www.fda.gov/news-events/press-announcements/fda-takes-action-protect-womens-health-orders-manufacturers-surgical-mesh-intended-transvaginal>.
- Haylen, B. T., De Ridder, D., Freeman, R. M., Swift, S. E., Berghmans, B., Lee, J., Monga, A., Petri, E., Rizk, D. E., Sand, P. K., & Schaer, G. N. (2010). An international urogynecological association (IUGA)/international continence society (ICS) joint report on the

- terminology for female pelvic floor dysfunction. *Neurourology and Urodynamics*, 29(1), 4–20. <https://doi.org/10.1002/nau.20798>
- Houman, J., Weinberger, J. M., & Eilber, K. S. (2017). Native tissue repairs for pelvic organ prolapse. *Current Urology Reports*, 18(1). <https://doi.org/10.1007/s11934-017-0648-0>
- International Consortium for Personalised Medicine. (2017). [https://www.ipermed.eu/media/content/ICPerMed\\_Actionplan\\_2017\\_web.pdf](https://www.ipermed.eu/media/content/ICPerMed_Actionplan_2017_web.pdf). Accessed 8 Agust 2022.
- Kiyosaki, K., Ackerman, A. L., Histed, S., Sevilla, C., Eilber, K., Maliski, S., Rogers, R. G., & Anger, J. (2012). Patients' understanding of pelvic floor disorders: What women want to know. *Female Pelvic Medicine and Reconstructive Surgery*, 18(3), 137–142. <https://doi.org/10.1097/SPV.0b013e318254f09c>
- MacCraith, E., Cunnane, E. M., Joyce, M., Forde, J. C., O'Brien, F. J., & Davis, N. F. (2021). Comparison of synthetic mesh erosion and chronic pain rates after surgery for pelvic organ prolapse and stress urinary incontinence: A systematic review. *International Urogynecology Journal*, 32(3), 573–580. <https://doi.org/10.1007/s00192-020-04612-x>
- Martins, P. A. L. S., Jorge, R. M. N., & Ferreira, A. J. M. (2006). A comparative study of several material models for prediction of hyperelastic properties: Application to silicone-rubber and soft tissues. *Strain*, 42(3), 135–147. <https://doi.org/10.1111/j.1475-1305.2006.00257.x>
- Mascarenhas, T., Mascarenhas-Saraiva, M., Ricon-Ferraz, A., Nogueira, P., Lopes, F., & Freitas, A. (2015). Pelvic organ prolapse surgical management in Portugal and FDA safety communication have an impact on vaginal mesh. *International Urogynecology Journal*, 26(1), 113–122. <https://doi.org/10.1007/s00192-014-2480-0>
- Mayeur, O., Witz, J. F., Lecomte, P., Brieu, M., Cosson, M., & Miller, K. (2016). Influence of geometry and mechanical properties on the accuracy of patient-specific simulation of women pelvic floor. *Annals of Biomedical Engineering*, 44(1), 202–212. <https://doi.org/10.1007/s10439-015-1401-9>
- Neal, M. L., & Kerckhoffs, R. (2009). Current progress in patient-specific modeling. *Briefings in Bioinformatics*, 11(1), 111–126. <https://doi.org/10.1093/bib/bbp049>
- Noakes, K. F., Pullan, A. J., Bissett, I. P., & Cheng, L. K. (2008). Subject specific finite elasticity simulations of the pelvic floor. *Journal of Biomechanics*, 41(14), 3060–3065. <https://doi.org/10.1016/j.jbiomech.2008.06.037>
- Parente, M. P., Jorge, R. M. N., Mascarenhas, T., Fernandes, A. A., & Martins, J. A. C. (2009). The influence of an occipito-posterior malposition on the biomechanical behavior of the pelvic floor. *European Journal of Obstetrics & Gynecology and Reproductive Biology*, 144, S166–S169.
- Persu, C., Chapple, C. R., Cauni, V., Gutue, S., & Geavlete, P. (2011). Pelvic Organ Prolapse Quantification System (POP-Q) - a new era in pelvic prolapse staging. *Journal of Medicine and Life*, 4(1), 75–81.
- Rada, M. P., Jones, S., Falconi, G., Milhem Haddad, J., Betschart, C., Pergialiotis, V., & Doumouchtsis, S. K. (2020). A systematic review and meta-synthesis of qualitative studies on pelvic organ prolapse for the development of core outcome sets. *Neurourology and Urodynamics*, 39(3), 880–889. <https://doi.org/10.1002/nau.24297>
- Roza, T. D., Brandão, S., Oliveira, D., Mascarenhas, T., Parente, M., Duarte, J. A., & Jorge, R. N. (2015). Football practice and urinary incontinence: Relation between morphology, function and biomechanics. *Journal of Biomechanics*, 48(9), 1587–1592. <https://doi.org/10.1016/j.jbiomech.2015.03.013>
- Rynkevici, R. (2019). In vivo models and in silico simulations of mesh augmented prolapse. PhD Thesis, Faculty of Engineering, University of Porto. <https://lirias.kuleuven.be/2805178>

- Silva, M. E. T., Bessa, J. N. M., Parente, M. P. L., Mascarenhas, T., Natal Jorge, R. M., & Fernandes, A. A. (2021). Effect of mesh anchoring technique in uterine prolapse repair surgery: A finite element analysis. *Journal of Biomechanics*, 127, 110649. <https://doi.org/10.1016/j.jbiomech.2021.110649>
- Silva, M. E. T., Brandão, S., Parente, M. P. L., Mascarenhas, T., & Natal Jorge, R. M. (2016). Establishing the biomechanical properties of the pelvic soft tissues through an inverse finite element analysis using magnetic resonance imaging. *Proceedings of the Institution of Mechanical Engineers, Part H: Journal of Engineering in Medicine*, 230(4), 298–309. <https://doi.org/10.1177/0954411916630571>
- Silva, M. E. T., Brandão, S., Parente, M. P. L., Mascarenhas, T., & Natal Jorge, R. M. (2017a). Biomechanical properties of the pelvic floor muscles of continent and incontinent women using an inverse finite element analysis. *Computer Methods in Biomechanics and Biomedical Engineering*, 20(8), 842–852. <https://doi.org/10.1080/10255842.2017.1304542>
- Silva, M. E. T., Brandão, S., Parente, M. P. L., Mascarenhas, T., & Natal Jorge, R. M. (2017b). The influence of pelvic organ prolapse on the passive biomechanical properties of pelvic floor muscles. *Journal of Mechanics in Medicine and Biology*, 17(6). <https://doi.org/10.1142/S0219519417500907>
- Silva, M. E. T., Oliveira, D. A., Roza, T. H., Brandão, S., Parente, M. P. L., Mascarenhas, T., & Natal Jorge, R. M. (2015). Study on the influence of the fetus head molding on the biomechanical behavior of the pelvic floor muscles, during vaginal delivery. *Journal of Biomechanics*, 48(9), 1600–1605. <https://doi.org/10.1016/j.jbiomech.2015.02.032>
- Silva, M. E. T., Parente, M. P. L., Brandão, S., Mascarenhas, T., & Natal Jorge, R. M. (2018). Characterization of the passive and active material parameters of the pubovisceralis muscle using an inverse numerical method. *Journal of Biomechanics*, 71, 100–110. <https://doi.org/10.1016/j.jbiomech.2018.01.033>
- Silva, E., Parente, M., Brandão, S., Mascarenhas, T., & Natal Jorge, R. (2019). Characterizing the biomechanical properties of the pubovisceralis muscle using a genetic algorithm and the finite element method. *Journal of Biomechanical Engineering*, 141(1). <https://doi.org/10.1115/1.4041524>
- Subramanian, D., Szwarcensztein, K., Mauskopf, J. A., & Slack, M. C. (2009). Rate, type, and cost of pelvic organ prolapse surgery in Germany, France, and England. *European Journal of Obstetrics and Gynecology and Reproductive Biology*, 144(2), 177–181. <https://doi.org/10.1016/j.ejogrb.2009.03.004>
- Vila Pouca, M. C. P., Ferreira, J. P. S., Oliveira, D. A., Parente, M. P. L., & Natal Jorge, R. M. (2018). Viscous effects in pelvic floor muscles during childbirth: A numerical study. *International Journal for Numerical Methods in Biomedical Engineering*, 34(3), e2927. <https://doi.org/10.1002/cnm.2927>
- Wu, C.-J., Chang, W.-C., Huang, K.-J., Hsieh, Y.-C., Wei, L.-H., & Sheu, B.-C. (2020). Long-term follow-up of 453 patients with pelvic organ prolapse who underwent transvaginal sacrospinous colpopexy with Veronikis ligature carrier. *Science Reports*, 10, 4997. <https://doi.org/10.1038/s41598-020-61995-z>
- Wu, J. M., Kawasaki, A., Hundley, A. F., Dieter, A. A., Myers, E. R., & Sung, V. W. (2011). Predicting the number of women who will undergo incontinence and prolapse surgery, 2010 to 2050. *American Journal of Obstetrics and Gynecology*, 230.e1–230.e5. <https://doi.org/10.1016/j.ajog.2011.03.046>

# Computational modeling of aerosol particle transport and deposition in the healthy and stented human airways considering different breathing conditions and particle sizes

# 11

Rocío Fernández-Parra<sup>1</sup>, Carmen Sánchez-Matás<sup>2</sup>, José Luis López-Villalobos<sup>2</sup>,  
Mauro Malvè<sup>3,4</sup>

<sup>1</sup>Department of Small Animal Medicine and Surgery, Faculty of Veterinary Medicine, Catholic University of Valencia San Vicente Mártir, Valencia, Spain; <sup>2</sup>Hospital Universitario Virgen del Rocío, Department of Thoracic Surgery, Sevilla, Spain; <sup>3</sup>CIBER-BBN, Centro de Investigación Biomédica en Red—Bioingeniería, Biomateriales y Nanomedicina, Zaragoza, Spain; <sup>4</sup>Universidad Pública de Navarra (UPNA), Department of Engineering, Pamplona, Spain

## Chapter outline

Clinical background .....	228
Materials and methods .....	231
Geometries .....	231
Numerical model and boundary conditions .....	231
Continuous phase: airflow .....	231
Discrete phase: particle transport and deposition modeling.....	234
Results .....	235
Airflow patterns in healthy and stented airways .....	235
Airflow turbulent patterns in healthy and stented airways .....	239
Particle deposition and transport .....	240
Validation of the numerical findings .....	240
Comparison between healthy and stented human upper airways.....	242
Regional deposition fractions.....	243

Conclusions and final remarks .....	246
Funding .....	246
Acknowledgments .....	246
References .....	247

---

## Clinical background

The drug aerosol therapy is a clinical technique aimed to treat respiratory diseases. The administration of aerosolized drugs is carried out using a variable type of devices which deliver the drug to the respiratory system. The results of the treatment depend on the efficiency of the delivery. The inhaled drug must normally target specific airways regions located in the lower respiratory tract. However, the delivery consists of the inspiration of aerosol through the mouth and/or the nose. As a consequence, the drug distribution is not uniform within the whole airways but tends to concentrate in the upper tract of the respiratory and/or digestive system. Additionally, often the inhaled drug does not reach specific regions to be targeted. For these reasons, an uncontrolled local overdoses or hotspots takes place in the upper airways or targeted regions remains untreated or less treated than necessary. The nonoptimal distribution makes the treatment not effective as it highlights a nonuseful depositions, dangerous and unknown side effects for the patient, a part of a drug waste. With this aim, in the last decades, several inhalers devices have been designed for improving the aerosol delivery within the respiratory system with aim of maximizing the absorption. Especially the use of spacers has been demonstrated to help the inhalation in human (Kleinstreuer, Shi, & Zhe, 2007). The use of a spacer has improved the inhalation and reduced the deposition in the oral tract.

For the analysis of the drug deposition and absorption, different methods are available. Traditionally, experimental and computational models can be adopted. The experimental observation is challenging, due to the inherent difficulties of setting up a sufficiently trustable device capable of providing the necessary information. Nevertheless, some studies attempted the observation and evaluation of drug transport and deposition in human cast model and/or experimental setups (Alhamad et al., 2015; Cheng et al., 1999; Verbanck et al., 2011; Zhang & Finlay, 2005; Zhou & Cheng, 2005).

With all the recent advances of computer technology, *in silico* models can be used for several biomechanical applications including the fluid–particle dynamics simulation. The computational fluid dynamics (CFD) is in fact an attractive noninvasive tool that has been used for computing the flow patterns in the airways with different applications, from the pure respiration physiology to the particle transport and distribution in the human pulmonary tract.

Different virtual models have been used for evaluating a detailed information of the nano- and microparticle transport within the human airways. Idealized and realistic models have been recently used by several research groups (Chen et al., 2018; Chen, Zhong, Zhou, et al., 2012; Huang & Zhang, 2011; Huang et al., 2011;

Kolanjiyil & Kleinstreuer, 2017; Koullapis et al., 2016, 2018, 2019), among others. Patient-specific human airways models have been used by different authors (Ahoo-khosh et al., 2020; Calmet, Houzeaux, et al., 2018; Farkhadnia et al., 2016 ; Islam et al., 2020a, 2021a, 2021b, 2021c; Kadota et al., 2018; Pourmehran et al., 2015, 2016; Rahimi-Gorji et al., 2015, 2016; Xu et al., 2017; Zhang et al., 2018), among others. These studies have provided relevant clinical results reconstructing geometrical models from computed tomography scans, magnetic resonance imaging, and/or considering comprehensive models incorporating the oral cavity and several generations of the bronchi or even the entire human airways. Specific works on the human nasal cavities have been proposed by Inthavong and coworkers (Calmet, Kleinstreuer, et al., 2018; Inthavong, Choi, et al., 2010; Inthavong et al., 2006, 2011; Inthavong, Tu, et al., 2010; Shang et al., 2015). Patient-specific nasal airways have been analyzed also for assessing pre- and postvirtual surgery (Bahmanzadeh et al., 2015; Ghahramani et al., 2017).

These exhaustive works in the literature allowed revealing important differences of the particle kinetics in patient-specific or based and simplified geometries. Recent studies concluded that for an accurate estimation of the drug transport and deposition the use of medical image-based geometries is necessary (Islam et al., 2020b; Rahimi-Gorji et al., 2015, 2016). However, idealized Weibel models (Weibel, 1963) have been also extensively used for giving regional particle transport and deposition reports. Kleinstreuer and coworkers (Feng et al., 2015; Feng & Kleinstreuer, 2014; Kleinstreuer, Zhang, & Kim, 2007; Kleinstreuer & Zhang, 2010; Li et al., 2007; Zhang & Kleinstreuer, 2004), Longest and coworkers (Longest et al., 2006, 2008, 2019; Longest & Vinchurkar, 2007; Longest & Xi, 2007, 2012), and Snitzman and coworkers (Heller-Algazi et al., 2020; Koullapis et al., 2019; Koullapis et al., 2018; Stylianou et al., 2016) provided an extensive research in this sense. Other groups (Deng et al., 2018, 2019) analyzed the impact on the health of the physical activity in polluted air using a complete Weibel model till the alveolar region. These studies have demonstrated that Weibel-based models are capable of getting the most important features of the airways fluid dynamics and of the associated deposition (Kleinstreuer & Zhang, 2010).

Although all these studies have contributed to provide a substantial knowledge on the drug delivery and absorption within healthy subjects, surprisingly less interest has been given to the case of respiratory pathologies. Only few studies have been centered on obstructed geometries (Chen, Zhong, Sun, et al., 2012; Farkas & Balásházy, 2007; Farkhadnia et al., 2016; Inthavong, Tu, et al., 2010; Luo et al., 2007; Singh et al., 2020b; Yan et al., 2019). Nevertheless, the lung injury promoted by a nonuseful particles inhalation and deposition and local overdoses is still unclear. However, this information is crucial for assessing health risks and for improving the clinical therapy, especially for patients with pulmonary diseases and patients undergoing airways surgery. The incidence of chronic obstructive pulmonary disease (COPD) is estimated around 10% in adult patients (Atsou et al., 2011). Chronic bronchitis and emphysema are the main pathologies among others that lead to obstructive diseases such as increased airflow resistance due to airway inflammation, edema, and mucus retention.

Airways stenting technique is the treatment of choice for solving many acute obstructions. The stents modify the inner airway lumen restoring the airflow passage or preventing lumen collapse after surgery. The main indications for stenting treatment are tracheal and bronchial stenoses caused by benign or malignant pathologies as well as invasive procedures on the airway. The common feature in all cases is high-grade stenosis. Normally all the affected patients have a previous history of pulmonary diseases since both COPD and lung neoplasia development, one of the main indications for stenting, have a close relationship with the use of tobacco (Chen, Zhong, Sun, et al., 2012; Farkas & Balásházy, 2007; Farkhadnia et al., 2016; Longest & Xi, 2008). Many types of stents are commercially available for the respiratory tract. The most commonly used, in the case of malign tumors, are silicone prosthesis and silicone-covered metallic stent as they are capable of prevent restenosis (Sun et al., 2008). The most used silicone prosthesis is called Dumon stent (Dumon, 1990). The decision to place a stent is always made during therapeutic endoscopy if resection of an obstructing lesion or dilatation of a stenosis fails to achieve an adequate airway (Dumon et al., 1996). However, stent placement is the last option, when no other possibilities are available. In fact, stenting technique is related with frequent adverse events. Migration (9.5%), granuloma (7.9%), and obstruction by secretions (3.6%) are the main complications and for tracheal stenosis are more frequent than cases of tumor. Rare complications include ulceration of the tracheal or bronchial wall, secondary tumor obstruction, infection, septic shock, and aphonia (Dumon et al., 1996). In this context, it is clear that for patients that undergo surgical treatment and stent implantation, and additionally need the aerosol inhalation therapy, an inadequate drug transport may enhance the aforementioned secondary effects and promote new ones. The presence of the stent in the airways is a foreign body in the tube in which is placed. Drug concentrations have been highlighted near obstructed airways and, with a similar mechanism, the prosthesis may tend to concentrate drug and cause unphysiological depositions. Even inhalation therapy has been studied in details for healthy and obstructed airways, the case of patients with airway stents has been not considered. In a previous study, we have compared the particle deposition in healthy and stented patients using both Weibel-based and patient-specific geometries (Malvè et al., 2020). However, the latter included only the trachea and the first two generations. For this reason, additional knowledge is necessary and a comprehensive model is required. The present study uses a well-known idealized baseline healthy geometry (Yeh & Schum, 1980) which includes the oral tract, the nasopharynx, larynx, and trachea and the main bifurcations after the carina. Furthermore, the commercial silicone Dumon prosthesis is virtually inserted in the trachea. A systematic computational analysis has been carried out providing a detailed regional information of the particle transport and deposition in healthy and stented airways. The final goal of this chapter is to illustrate the influence of the presence of a prosthesis in the particle transport and distribution with aim of help improving the drug inhalation therapy.

## Materials and methods

### Geometries

The airways geometries have been created using the commercial package Rhinoceros (Robert McNeil and Associates, Seattle, WA, USA) using the dimensions of the asymmetric human airway of “the typical path lung model” (Yeh & Schum, 1980) in the same way as performed by Huang and Zhang (Huang et al., 2011; Huang & Zhang, 2011). The baseline model, in which we have inserted the prostheses, consists of the oropharyngeal region, which includes the oral cavity, the pharynx and the larynx, the tracheal tracts, and a series of bifurcating straight tubes that represent the airways inside the two main bronchi. The model includes the airways down to the fourth generation and it is represented in Fig. 11.1. Furthermore, the model is asymmetric and planar. Table 11.1 describes the main geometry data.

The considered Dumon stents are tracheal and two bronchial silicone prostheses that have been inserted in the middle of trachea and in the middle of the left and right bronchus. These stents have a cylindrical shape and they are available in various thicknesses and lengths that can be inserted using bronchoscopy. In Table 11.2 the main geometrical features of the stents are summarized.

### Numerical model and boundary conditions

#### Continuous phase: airflow

The geometrical models were discretized using unstructured tetrahedral elements by means of the commercial software Ansys ICEM CFD, Version 20.R2 (ANSYS Inc., Canonsburg, PA, USA). To ensure independent results from the mesh element size, a

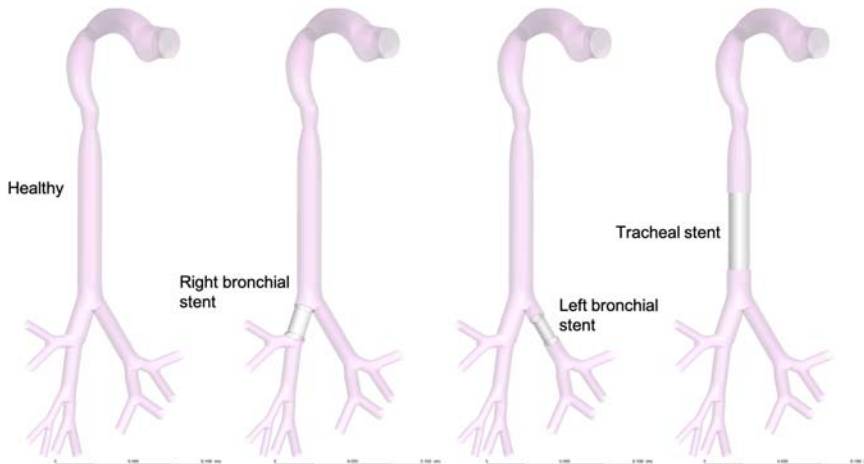


FIGURE 11.1

Geometries of the healthy and stented upper human respiratory model.

**Table 11.1** Main dimensions of the baseline model.

*Geometrical features of the baseline airways geometry: airway segment length, airway segment diameter, and main angles.*

Part	Diameter (mm)	Length (mm)	Angle (°)
Oral cavity	20	8	
Trachea	15.8	100	
G1	G1 to G2.1	13.8	22
	G1 to G2.2	10.9	41
G2.1	G2.1 to G3.1	8	7.8
	G2.1 to G3.2	10.5	22
G2.2	G2.2 to G3.3	9	15.5
	G2.2 to G3.4	8.1	7.8
G3.1	G3.1 to G3.1.1	6	21.5
	G3.1 to G3.1.2	6	21.5
G3.2	G3.2 a G4.1	5.7	12.5
	G3.2 a G4.2	8	7.8
G3.3	G3.3.1	7.1	21.5
	G3.3.2	7.1	21.5
G3.4	G3.4.1	6.6	21.5
	G3.4.2	6.6	21.5
G4.1	G4.1.1	4.9	16.8
	G4.1.2	4.9	16.8
G4.2	G4.2.1	6.3	16.8
	G4.2.2	6.3	16.8

**Table 11.2** Dimensions of the Dumon prosthesis used in this chapter.

*Main dimensions of the considered silicone Dumon endoprostheses (Dumon, 1996).*

	Thickness (mm)	Length (mm)	Inner diameter (mm)
Tracheal stent	1	40	16
Left bronchial stent	1	20	10
Right bronchial stent	1	20	12

mesh independence study was carried out. In particular, it was considered as converged a mesh providing velocity profiles within 5% from the finest tested mesh (Chen et al., 2018). We tested four different grids of about  $1 \times 10^6$ ,  $2.5 \times 10^6$ ,  $5 \times 10^6$ , and  $10 \times 10^6$  elements. Convergence was reached with a grid size of about  $5 \times 10^6$  elements. The computational grid of the healthy model is depicted in Fig. 11.2 along with the mesh refinement at selected locations. To fully

capture the turbulent boundary layer profile at the near wall regions, the mesh structure includes five prismatic layers at each geometry surface (see details in Fig. 11.2).

CFD simulations were carried out using the commercial software Ansys CFX, Version 20.R2 (Ansys Inc., Canonsburg, PA, USA). This software is well known in the scientific community for solving such problems and details of the software methodology, algorithms, and other information are given in the Ansys documentation. The solution of the flow field was assumed as converged when the scaled residuals decreased to less than  $10^{-6}$ . Typical computational time for the fluid flow simulations run in eight parallel algorithms of an Intel 9 HP Workstation was approximately 6 h. Air was assumed to be an incompressible and Newtonian fluid with a density of  $1.225 \text{ kg/m}^3$  and a viscosity of  $1.83 \times 10^{-5} \text{ kg/(m s)}$ . The airways walls were assumed to be rigid with a no-slip boundary condition. Constant flow rates of 15, 30, and 60 L/min that corresponds to light, normal, and heavy breathing conditions, respectively (Huang et al., 2011; Huang & Zhang, 2011; Rahimi-Gorji et al., 2015; Zhang & Kleinstreuer, 2004) were imposed at the inlet of the models (see Fig. 11.2). Moreover, a zero pressure gradient was imposed at each outlet of the models (Rahimi-Gorji et al., 2015). The human airflow was considered turbulent

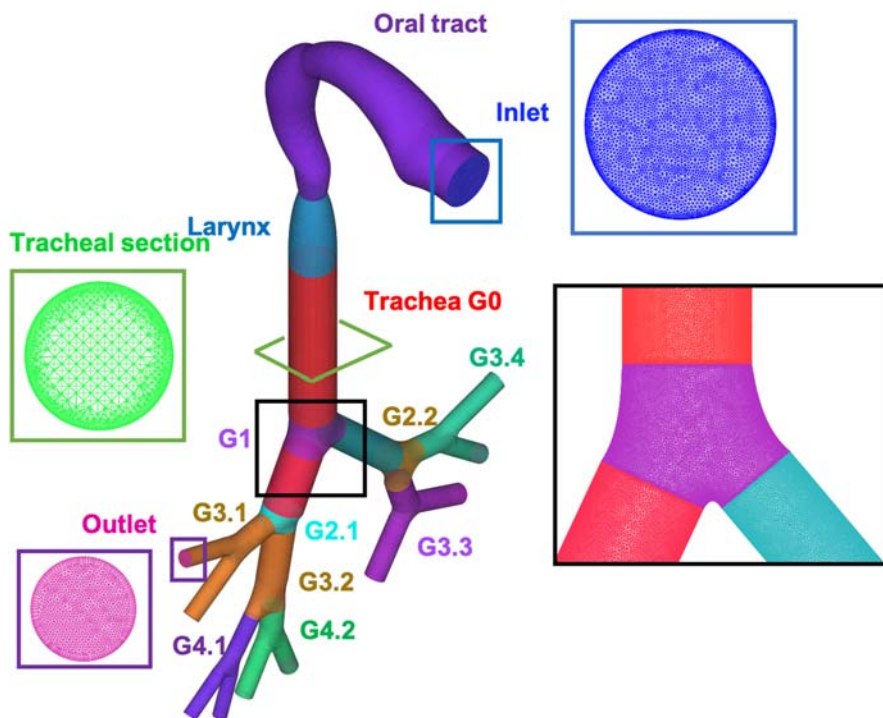


**FIGURE 11.2**

Volume mesh of the healthy human upper airways with regional subdivision. At the inlet, outlet, and tracheal sections, the prism layers of the grid surface refinement are shown.

(with a turbulence intensity value of 5% for the turbulence kinetic energy) under steady conditions.

The governing equations for the airflow in the respiratory tract are the Reynolds averaged Navier–Stokes (RANS) equations that under steady inhalation employing the eddy viscosity hypothesis and eddy diffusivity hypothesis can be written in the following form:

$$\nabla \cdot \bar{\mathbf{v}} = 0, \\ \frac{\partial \mathbf{v}}{\partial t} + \nabla \cdot (\bar{\mathbf{v}} \otimes \bar{\mathbf{v}}) = -\frac{1}{\rho} \nabla p' + \nabla \cdot (\nu_{\text{eff}} (\nabla \bar{\mathbf{v}} + \nabla \bar{\mathbf{v}}^T))$$

where  $\bar{\mathbf{v}}$

$$\frac{\partial \omega}{\partial t} + \nabla \cdot (\mathbf{v} \omega) = \nabla \cdot \left[ \left( \nu + \frac{\nu_t}{\sigma_\omega} \nabla \omega \right) \right] + \alpha \frac{\omega}{k} P_k - \beta \omega^2$$

where  $P_k = \nu_t \nabla \mathbf{v} \cdot (\nabla \mathbf{v} + (\nabla \mathbf{v})^T)$ .

### **Discrete phase: particle transport and deposition modeling**

The transport and deposition of the aerosol particles is modeled and computed in the commercial package Ansys CFX. Particles are tracked in a Lagrangian reference frame that is applicable for a low volume fraction of the dispersed particle phase. Each particle is individually followed defining its initial position, velocity, size, and temperature. Since the particles move through the flow, the trajectories are computed applying the force balance, using the local continuous phase conditions. The latter is performed integrating the force balance that can be expressed as follows:  $\sum F = m_p \frac{dv_p}{dt}$

$$m_p \frac{\partial v_p}{\partial t} = \frac{1}{8} \rho \pi d_p^2 c_{Dp} |v_p - v| (v_p - v)$$

where  $m_p$ ,  $v_p$ ,  $d_p$  are the spherical particle mass, velocity vector, and diameter, respectively,  $v$  is the flow velocity,  $c_{Dp}$  is the drag force coefficient given by

$$c_{Dp} = \frac{c_D}{C_{\text{slip}}}$$

where  $C_{\text{slip}}$  is the Cunningham correction slip factor (Clift et al., 1978) and

$$c_D = \max \left( \frac{24}{(Re_p)(1 + 0.15Re_p^{0.687})}, 0.44 \right)$$

In this equation,  $Re_p$  represents the particle Reynolds number that can be obtained as

$$Re_p = |v - v_p| d_p / \nu$$

where  $\nu$  is the cinematic viscosity.

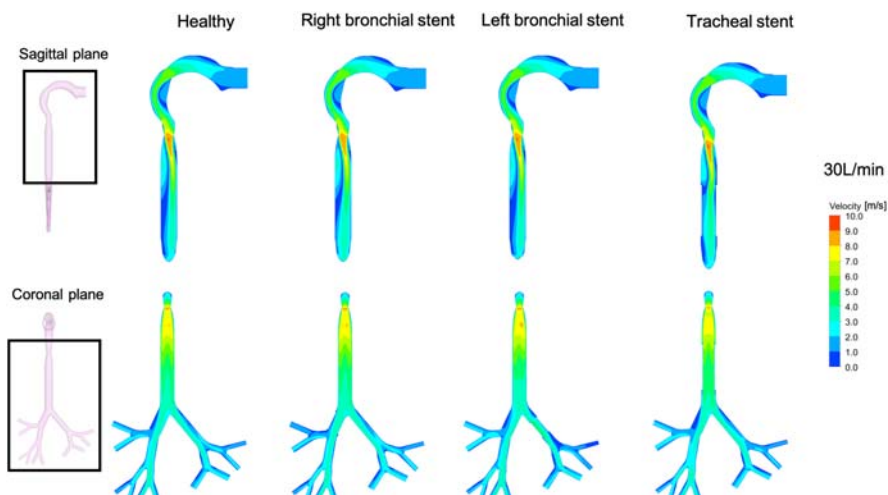
Particles of specific sizes were uniformly injected through the mouth at the inlet face of the computation domain, and tracked through the airways geometry until

they meet one of the three specific conditions: they collide (and are trapped on the airways walls), they escape from the domain through one of the outlet (and they are considered as traveling to the lungs), or they continue in suspension in the flow. The present work considers one-way coupling between airflow and particle motion (the continuous phase is not affected by the discrete phase). In fact, since the particles size is sufficiently small and the suspension is dilute, the effect of the particles on the airflow is actually negligible (Huang et al., 2011; Huang & Zhang, 2011; Rahimi-Gorji et al., 2015; Zhang et al., 2002). Particles were modeled as rigid spheres mono-dilute and in suspension with diameters of 1, 5, and 10  $\mu\text{m}$ . The initial particle velocities were set equal to that of the fluid. 20,000 particles with a uniform distribution were released at the mouth inlet after a particle sensitivity study. The latter was performed for ensuring the independence of the results from the number of injected particles and the statistical relevance of the selected number of particles.

## Results

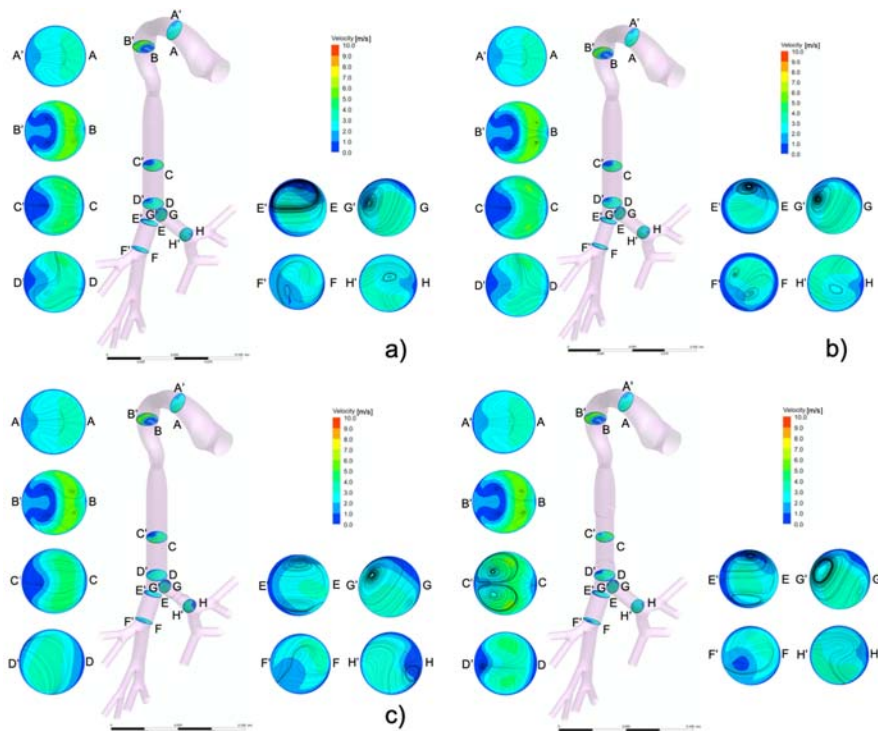
### Airflow patterns in healthy and stented airways

Fig. 11.3 shows the mean-velocity field by means of velocity contours in the healthy and stented airways models under normal breathing conditions ( $Q = 30 \text{ L/min}$ ). Additionally, in Fig. 11.4, the flow structure developing in the healthy and stented airways for normal breathing is represented by means of velocity contours and projected streamlines on transversal cross sections at selected locations. The displayed



**FIGURE 11.3**

Airflow velocity contours for normal breathing at sagittal and coronal cross section for the oral tract and airways G0-4, respectively.

**FIGURE 11.4**

Velocity contours and projected streamlines for normal breathing rate (30 L/min) at selected transversal sections within the healthy (A), the right bronchial stented (B), the left bronchial stented (C), and the tracheal stented (D) human upper airways.

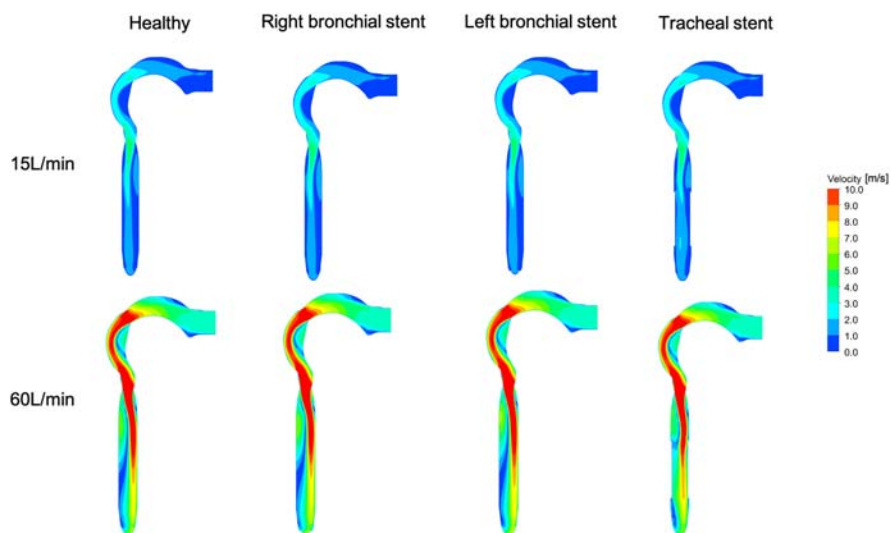
cross sections depict the axial velocity and the airflow structure at different locations of the healthy and stented airways. As visible, both figures show the main features of the respiration physiology found in the literature and the airflow structure and intensity match well the characteristics pattern found in other studies (Huang et al., 2011; Huang & Zhang, 2011; Zhang et al., 2005).

After section A-A', the flow becomes skewed in the curved portion of the oral cavity and the pharynx/larynx due to centrifugal force effects (region between sections A-A' and the glottis). The latter promotes a secondary flow due to the centrifugally induced pressure gradient at the bent tract between the mouth and the pharynx. The intensity of secondary flows tends to decrease after the glottis, especially when the flow reaches the trachea. Additionally, a flow separation occurs due to the physiological geometrical changes provided by the glottis (region before and after section B-B'). Later on, the well-known asymmetric laryngeal jet is generated after the glottis (region between the glottis and the trachea). The asymmetry of the bronchia promotes a deflection of the velocity profile after section C-C' also

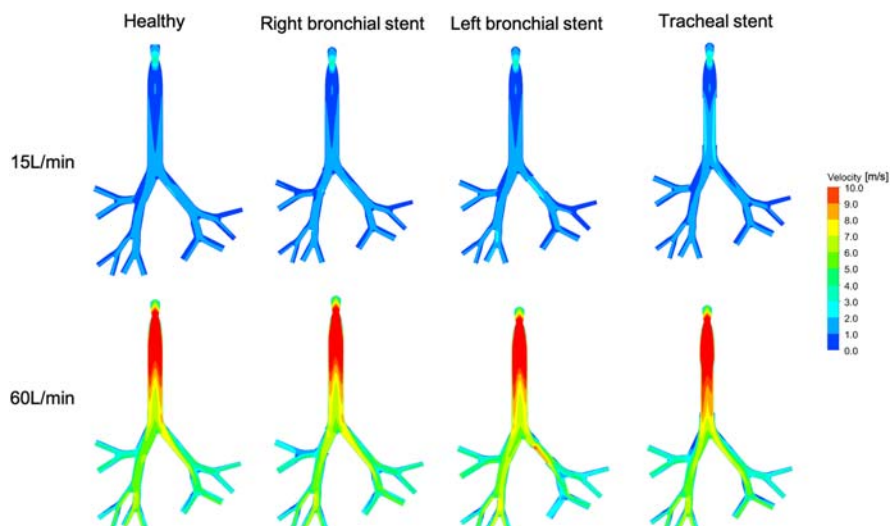
visible at section D-D'. Secondary flows develop within the first (E-E' and F-F') and second bifurcations (G-G' and H'-H') and skewed axial velocity profile are visible in the downstream generations.

Comparing the healthy with the stented airways at normal inspiration, different patterns can be highlighted, especially looking to the secondary flow at the lower branching. As documented in the literature (Malvè et al., 2020), the flow structures result locally affected by the presence of the endoprostheses, even when the main features are similar. The upstream patterns are similar within healthy and stented models (from the oral tract till the larynx), in all the cases. However, the stent promotes a localized change of the flow velocity and structure due to the reduction of the cross section at the trachea and at the main bronchia (i.e., in the stented regions). Changes can be seen in the downstream flow structures. The airways in the presence of the bronchial devices show a local change of the velocity patterns in the lower generations (see Fig. 11.3) and differences in the secondary flow structure (see Fig. 11.4). The presence of the device causes in fact a local increase of the airflow velocity within the stents and enhanced secondary structures even the flow enters unaltered from the oral and tracheal tract as in the healthy case (sections A-A', B-B', C-C' and D-D'). This aspect is especially evident for the tracheal and for the left bronchial stent. The secondary flow structures of the downstream generations are altered in comparison with the healthy geometry. The tracheal stent seems to increase the local flow intensity at the trachea only, due to the reduced tracheal sections imposed by the device, while the airflow at the downstream generations looks similar to that of the healthy airways. As the left bronchus has a smaller diameter and emerges from the carina with a different angulation than the right, the local flow intensity is more asymmetric in the lower left generations in comparison with the other cases. Other changes in the secondary flow in the lower generations can be seen at section F-F' and H-H' within the bronchial stented models.

For light and heavy inhalations, similar conclusions can be extracted. In Fig. 11.5, the velocity contours at sagittal sections of the oral tract for healthy and stented human upper airways at light and heavy breathing conditions are represented. The flow structure is similar to that of the normal breathing. Only a reduction and an enhancement of the intensity can be observed at light and heavy breathing rates, respectively. Comparing the contours, at light inspiratory flow can be observed that the laryngeal jet intensity is considerably reduced. The flow enters the trachea skewed and it is located at the rear wall. A local recirculation region is visible at the anterior side of the trachea. This situation reverts at normal and heavy flow rates, as the laryngeal jet moves to the anterior wall and a local recirculation appears at the rear wall. These patterns are independent of the model, as they could be observed in the healthy and in the stented models. From Fig. 11.5, it can be also seen that the laryngeal jet is more pronounced for the tracheal stented model than the rest of the models. This aspect can be seen as well in Fig. 11.6. The airways contours are depicted for the generation G0-4 by means of coronal sections. In this figure, an increased intensity of the laryngeal jet in the tracheal stented airways can be seen respect to the remaining cases. Regarding the bronchial stented airways it can be observed that while the effect of the right bronchial stent is limited with

**FIGURE 11.5**

Velocity contours at sagittal sections of the oral tract for healthy and stented human upper airways at light and heavy breathing conditions.

**FIGURE 11.6**

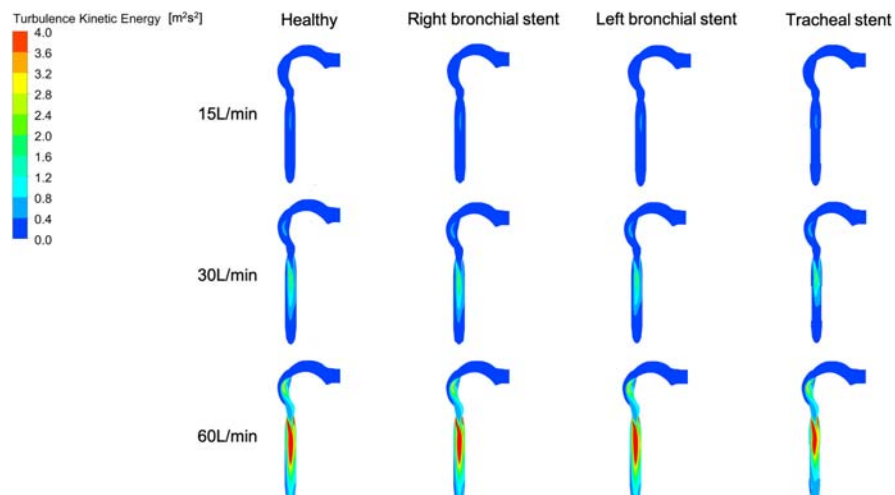
Velocity contours at coronal sections of the airways G0-4 for healthy and stented human upper airways at light and heavy breathing conditions.

respect to the healthy case, the left bronchial stent seems to promote a local increase of the velocity patterns at this bronchus. The reason can be found in the dimensions and the geometrical disposition of the bronchi. The right bronchi is in fact larger respect to the left bronchi so that the section reduction promoted by the device, that in both cases has the same thickness, has a higher impact in the smaller tube.

### Airflow turbulent patterns in healthy and stented airways

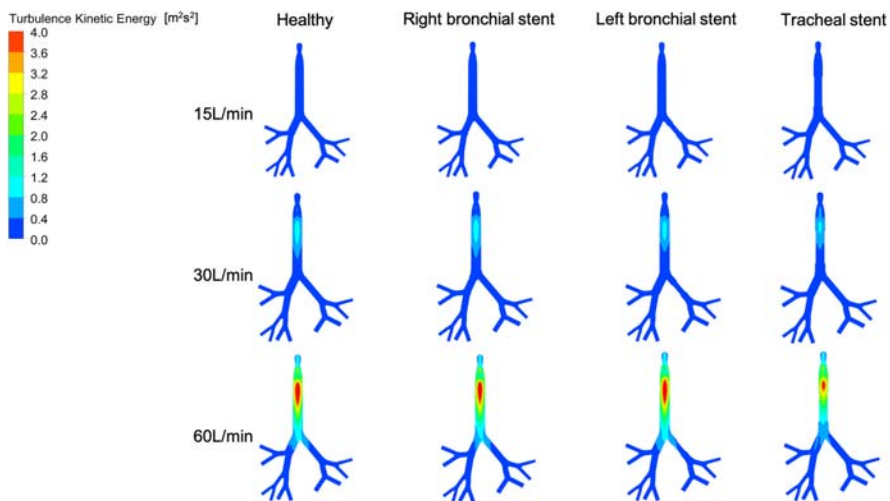
The distribution of the turbulent kinetic energy within the healthy airways has been widely computed and commented using computational models in the literature. Turbulence occurs in the respiratory tract for high Reynolds numbers ( $Re > 2000$ ) because of the sudden changes of the airways geometries that expand and contract at different locations. As found by other researchers, the turbulence fluctuations are weak in the oral cavity and start rising after the soft palate (Zhang et al., 2002; Zhang & Kleinstreuer, 2004). Then, a rapid increase is visible at the glottis due to the physiological constriction (Fig. 11.7). Finally, fluctuations decay within the trachea some diameters after the larynx. In the lower airways (see Fig. 11.8), the turbulent kinetic energy is lower than in the upper tract. However, locally, it is higher at the carina and decreases at the lower tubes and further bifurcations. For increasing flow rates (i.e., Reynolds numbers) the turbulent energy tends to increase and its features become more enhanced. This is especially visible observing the turbulent laryngeal jet that becomes stronger in all the considered cases.

The turbulence flow features in the stented airways are moderately more pronounced. The presence of the device, as observed before by means of the velocity



**FIGURE 11.7**

Turbulent Kinetic Energy contours at sagittal cross section of the healthy and stented models at light, normal, and heavy breathing.

**FIGURE 11.8**

Turbulent Kinetic Energy contours at coronal cross section of the healthy and stented models at light, normal, and heavy breathing.

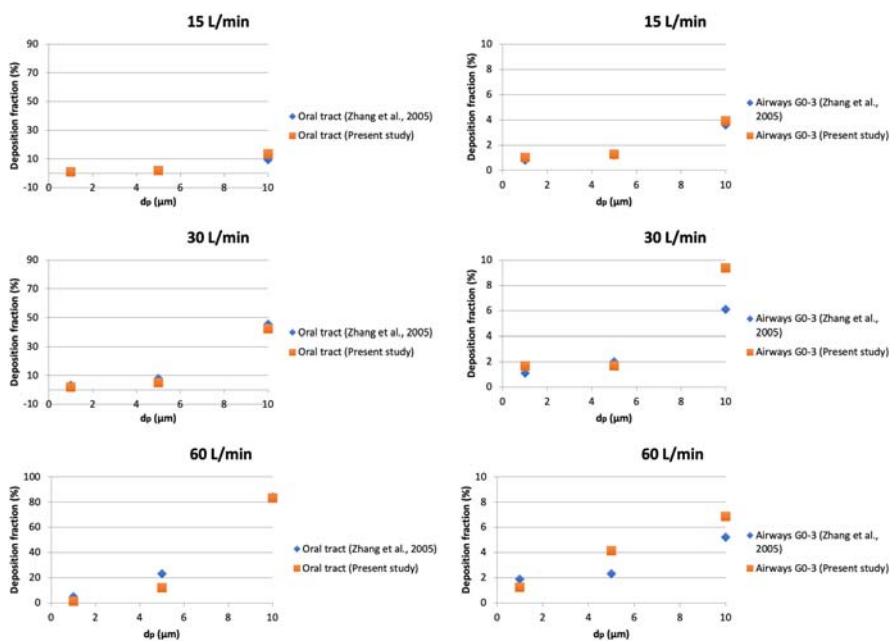
contours, promotes local increase of the flow velocity in comparison with the healthy case. However, the turbulent kinetic energy results almost unaffected, even near the stented regions. While the laryngeal jet and the main turbulent features before the trachea are similar within healthy and stented model, at the trachea some changes can be highlighted. The turbulent kinetic energy is visibly attenuated by the presence of the prosthesis, in comparison with the other cases. This is especially marked at normal and heavy breathing conditions (compare the tracheal stented with the healthy model at 30 and 60 L/min in Figs. 11.7 and 11.8). At light breathing conditions, as expected, similar patterns can be found within all the models, even in the region between the glottis and the larynx. Finally, similar values can be found at the main bronchia and downstream generations. The turbulent energy is reduced in these regions and the stents are not capable of promoting changes.

### Particle deposition and transport

The deposition fraction accordingly to Zhang et al. (2018) among other authors is computed as  $DF(\%) = \frac{n_{dp}}{n_{ip}} \times 100$ .

### Validation of the numerical findings

The accuracy of the computational results must be proved by validation of the proposed method/model. With this aim, the obtained particle deposition fraction has been compared with previous works in order to assess the degree of confidence

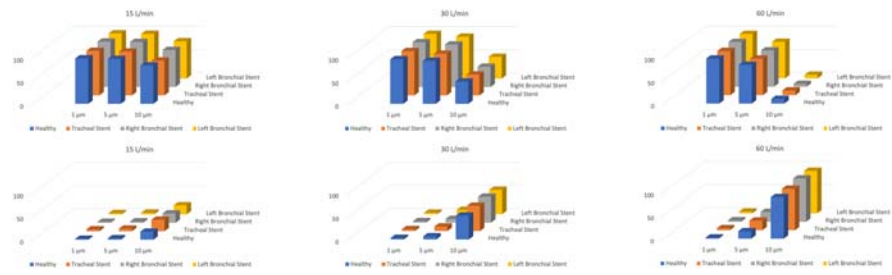


**FIGURE 11.9**

Comparison of particle deposition fractions of the present study with literature data (Zhang et al., 2005) at different flow rates and for different particle sizes in the oral tract and airways tubes.

and applicability of the simulation results. A summary plot of regional particle deposition fraction in the upper airways is shown in Fig. 11.9 for different breathing conditions and particle sizes.

The deposition fractions obtained in the simulation with an inspiratory flow of 30 L/min are compared with the numerical findings of Zhang et al. (2005). Their study provides a comprehensive regional deposition fraction of nano- and microparticles in the oral tract and in the airways from the carina till the third generation at different flow rates, i.e., 15, 30, and 60 L/min. The main findings of the present computational simulations are in line with the deposition reported in the oral tract. Only slight differences can be seen, especially related to the deposition fraction for 10  $\mu\text{m}$ . In the airways (region from G0 to G3) the presented depositions seem to slightly overestimate the deposition fraction obtained in the literature. However, these differences may be due to the different configurations of the lower airways in the present work compared to that of Zhang et al. In fact, our model is not symmetric as that of Zhang et al. and additionally includes more branches. As the geometries are different, of course, the deposition is also consequently different. However, the order of magnitude of the depositions found in this study demonstrates that the model is capable of performing the intended analysis.

**FIGURE 11.10**

Particle deposition fractions at light (15 L/min), normal (30 L/min), and heavy (60 L/min) breathing rates for different microparticle sizes (upper panel) and percentage of inhaled particles traveling to the lung (lower panel).

### **Comparison between healthy and stented human upper airways**

#### Total deposition fractions

In Fig. 11.10, upper and lower panels, the particle leaving the domain and the total depositions in the upper airways are represented by means of histograms. In the upper panel of Fig. 11.10, nondeposited particles traveling to the lung are depicted for the considered models as a function of the particle size and breathing conditions. It can be seen that at heavy and normal conditions, the nondeposited particles that reach the lung are around 10% or less for a flow rate of 60 L/min and less than 50% for a flow rate of 30 L/min. On the contrary, over 95% of the inhaled particles of 1 μm reach the lung independently of the inhalation flow rates, while around 80% and 90% of the inhaled particles of 5 μm reach the lung for light and normal breathing rates, respectively. According to the lower panel, the particles that reach the lung are systematically higher in the healthy upper airways. Overall, particles of 1 μm travel in a larger amount independently of the breathing conditions and on the considered geometry.

In the lower panel, for increasing breathing rates, it is visible that the particle deposition tends to increase for increasing particle size. However, comparing healthy and stented configurations, the histograms show that the stents promote slightly higher total depositions within the upper airways independently of the breathing conditions and of the particle sizes. At light breathing conditions, the highest deposition corresponds systematically to the tracheal stented model, independently of the particle size (3.95%, 5.55%, and 24.9% for 1, 5, and 10 μm, respectively). At normal breathing inspiration, again the tracheal stent shows the maximal deposition except for a particle diameter of 10 μm in which it is shown by the right bronchial stent. Deposition fractions are 3.95, 9.7, 54.7% for the tracheal stented configuration and 3.1, 7.9, 56.1% for the right bronchial stented geometry. At heavy inhalation, this bronchus promotes the highest deposition fractions for particle diameters of 5 and 10 μm (21.3% and 93.88%, respectively), while for particle diameter of 1 μm this is promoted by the tracheal stent (4.3%).

## Regional deposition fractions

In Figs. 11.11 and 11.12, a comparison of the regional deposition fraction between healthy and stented models is shown at light, normal, and heavy flow rates for different particle sizes. The comparison is shown separately for the oral tract and larynx (Fig. 11.11) and for the generations G0 to 4 (Fig. 11.12) for sake of clarity. As visible, for higher breathing rates, the most of the deposition takes place in the oral tract and larynx and the deposited particles fractions are considerably different in the two mentioned parts. These results are consistent with the findings of other authors

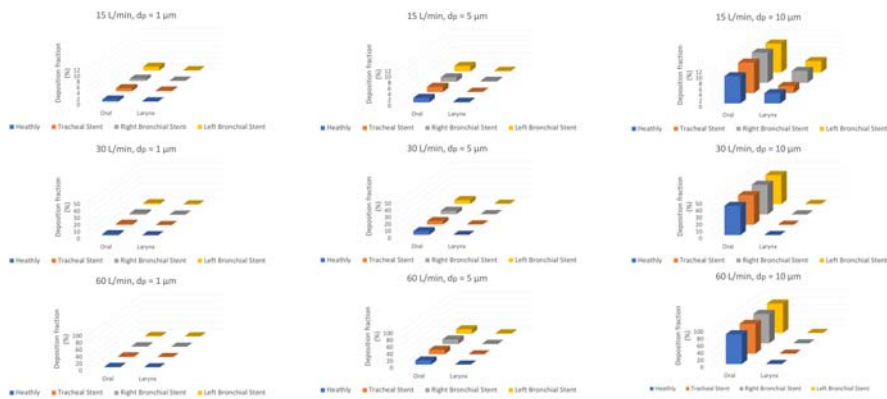


**FIGURE 11.11**

Regional deposition fractions are represented by means of 3D histograms for particle diameters of 1, 5, and 10  $\mu\text{m}$  and inhalation flow rates of 15, 30, and 60 L/min in the oral tract.

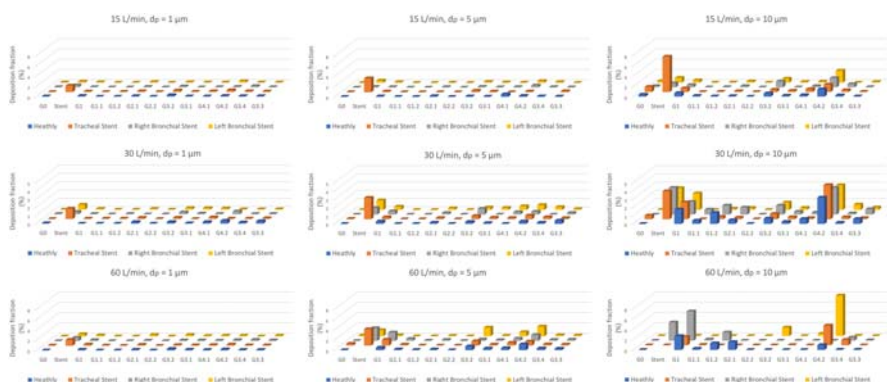


**FIGURE 11.12**

Regional deposition fractions are represented by means of 3D histograms for particle diameters of 1, 5, and 10  $\mu\text{m}$  and inhalation flow rates of 15, 30, and 60 L/min in the airways G0-4.

in the healthy airways (Huang et al., 2011; Huang & Zhang, 2011; Zhang et al., 2005). The deposition in the oral tract is systematically higher for particle of 10 µm independently of flow rates and especially enhanced in the oropharynx duct in comparison with the larynx due to the impact deposition that occurs because of its curved geometry.

The deposition in the airways G0-4 depicted in Fig. 11.12 is considerably lower than those depicted in Fig. 11.11. However, several considerations can be made. Firstly, the increase of deposition due to the stents can be clearly seen at every breathing rates and for every particle sizes. Additionally, it is visible an increase of the deposition fractions for the generations G1 and G4.2 for increasing breathing rates and particles size (60 L/min and 10 µm). On the contrary, only moderate increases involve generations 2 and 3 for increasing flow rates.

Fig. 11.13 represents an overview of the depositions at the stents surfaces. The presence of a stent can be considered as a light airways constriction so that important depositions are expected. At 15 and 30 L/min, the deposition of the stents increases for increasing particle sizes due to the inertial impaction. The highest deposition is promoted at the tracheal stent at 15 L/min (6.9%). At 60 L/min, this decreases drastically. The histograms related to the left and right bronchial stents suggest that higher depositions are also promoted on these two devices, especially at higher flow rates. In particular, the right bronchial stent shows the maximum depositions fraction at 60 L/min (3.55%).

In Fig. 11.14, deposition patterns for the simulations with inspiratory flows of 15 and 60 L/min is depicted within the four models for particle size of 10 µm. In the figure, the two extreme breathing conditions and the largest particle dimensions are considered because they allow a better visualization of the qualitative deposition. Particles mainly deposit near abrupt geometric changes, such as at the oropharynx

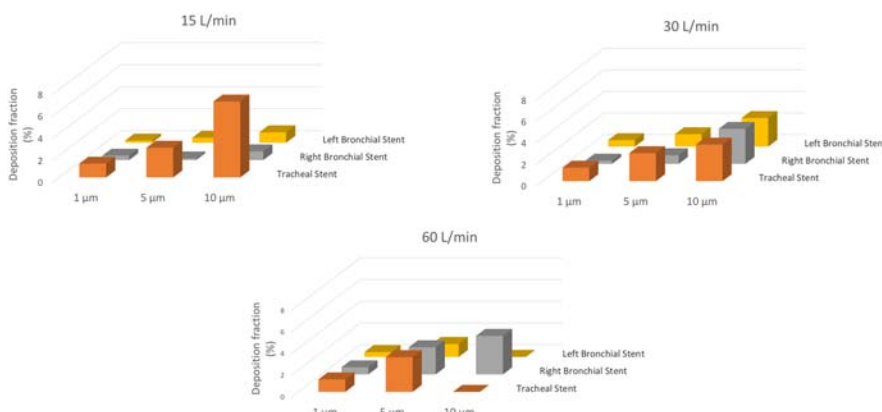


**FIGURE 11.13**

Summary of the deposition fractions on the stent represented by means of 3D histograms for particle diameters of 1, 5, and 10 µm and inhalation flow rates of 15, 30, and 60 L/min.

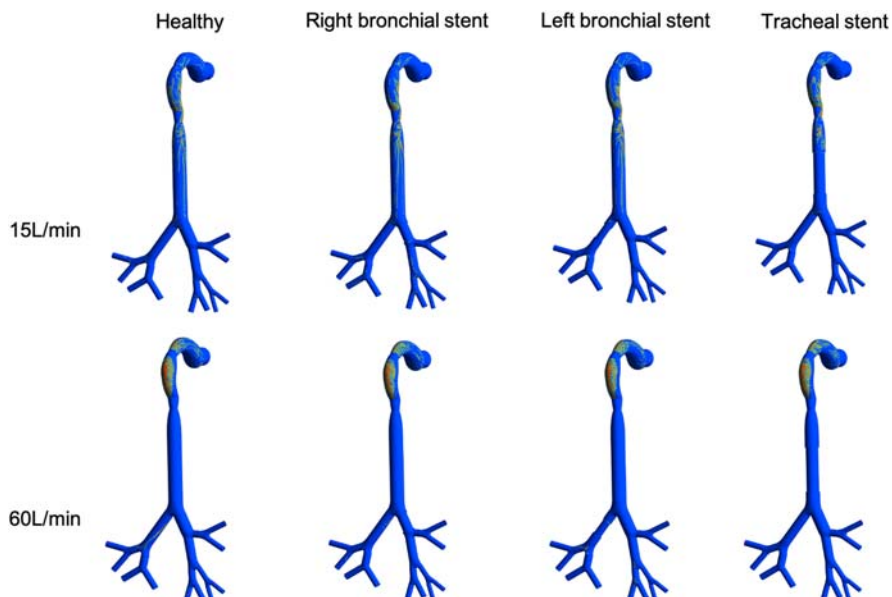


**FIGURE 11.14**

Particle deposition patterns in the human healthy and stented upper airways for light and heavy breathing conditions and particle size of  $10 \mu\text{m}$ .

region and at the soft palate, upstream of the laryngeal constriction, and at the carina of bronchial bifurcations. According with the flow structures depicted in Figs. 11.3, 11.5, and 11.6, the velocity profiles are skewed near regions with important changes of geometry due to the centrifugal force in the curved or bifurcating locations and the airflow velocity increases near the outer bend, as found by previous authors (Huang et al., 2011; Huang & Zhang, 2011). The most important mechanism of microparticle deposition is in fact the inertial impact. In the healthy case, only few particles deposit near the trachea and main bronchi tubes as shown in Fig. 11.14, due to the turbulent dispersion. As the flow structures are similar within models, the main features of the particle patterns of course are similar.

A large quantity of particles tends to deposit in the oral cavity. Due to the blockage effect discussed in the previous sections and to the recirculation flow, particles also tend to deposit near the stented regions, as visible particularly for the left bronchial stent. Additional hotspots appear also near the bifurcations after the prosthesis for light and heavy conditions in all the stented models in comparison with the healthy case. On the contrary, at heavy inspiratory flow, in all the models the deposition in straight tubes becomes almost zero while it tends to concentrate only in curved regions and at the bifurcations, where the effect of the geometrical changes becomes more important than turbulence or the recirculation.

---

## Conclusions and final remarks

In this chapter, the particle transport and deposition of microparticles of 1, 5, and 10  $\mu\text{m}$  has been presented for three different inspiratory breathing conditions (15, 30, and 60 L/min) that correspond to light, normal, and heavy flow rates within four different configurations. In particular, this work is oriented toward human upper airways in the presence of tracheo-bronchial prostheses. We have compared healthy and stented geometries considering commercial tracheal and bronchial silicone Dumon stents. At 15 L/min, the deposition is low and a considerable part of inhaled particles travel to the lung. The deposition tends to increase for increasing particle size at this flow rate. By increasing inspiratory flow rate, the deposition tends to increase and the highest deposition takes place at the oral cavity. In the stented geometries, the computed depositions are systematically higher than the healthy case. The tracheal stent promotes higher depositions for 15 and 30 L/min, while at 60 L/min the highest deposition corresponds to the right bronchial stent. More important, the regions with higher deposition in the healthy case are affected by the presence of the devices and their depositions further increase. The oral cavity is still the preferable location for particles to deposit due to its curved shape and due to the inertial impact and eventually secondary flows. Turbulence dispersion causes lower particle depositions in the regions near the prostheses and in the straight tubes for low inspiratory flows.

Considering that the tracheo-bronchial endoprostheses promotes inflammations, tissue reactions, and other side effects, local aerosol overdoses or hotspots near their locations may contribute to additional undesired effects. Based on the present results, patients undergoing airways surgery are prone to increased drug depositions in the stented regions as the device acts as a local airway constriction similar to an obstruction. Even an additional increase of depositions has been found also in different regions in comparison with the stented tubes, the location where the stent is placed is that more sensible to tissue pathologies, and thus is the one that should be especially considered. In this sense, targeting specific airways regions in the aerosol therapies is of special importance for patients with tracheobronchial prosthesis. The knowledge of the particle deposition kinematics for these patients may help to improve their conditions of life.

---

## Funding

The study is financially supported by the Spanish Ministry of Education, Industry and Competitiveness via the research project DPI2017-83259-R (AEI/FEDER, UE)

---

## Acknowledgments

The support of the Instituto de Salud Carlos III (ISCIII) through the CIBER-BBN initiative is highly appreciated.

## References

- Ahookhosh, K., Saidi, M., Aminfar, H., Mohammadpourfard, M., Hamishehkar, H., & Yaqoubi, S. (2020). Dry powder inhaler aerosol deposition in a model of tracheobronchial airways: Validating CFD predictions with in vitro data. *International Journal of Pharmaceutics*, 587, 119599. <https://doi.org/10.1016/j.ijpharm.2020.119599>
- Alhamad, B. R., Fink, J. B., Harwood, R. J., Sheard, M. M., & Ari, A. (2015). Effect of aerosol devices and administration techniques on drug delivery in a simulated spontaneously breathing pediatric tracheostomy model. *Respiratory Care*, 60(7), 1026–1032. <https://doi.org/10.4187/respcare.03592>
- Atsou, K., Chouaid, C., & Hejblum, G. (2011). Variability of the chronic obstructive pulmonary disease key epidemiological data in Europe: Systematic review. *BMC Medicine*, 9(7), 1–16. <https://doi.org/10.1186/1741-7015-9-7>
- Bahmanzadeh, H., Abouali, O., Faramarzi, M., & Ahmadi, G. (2015). Numerical simulation of airflow and micro-particle deposition in human nasal airway pre- and post-virtual spheno-oidotomy surgery. *Computers in Biology and Medicine*, 61, 8–18. <https://doi.org/10.1016/j.combiomed.2015.03.015>
- Calmet, H., Houzeaux, G., Vázquez, M., Eguzkitza, B., Gambaruto, A. M., Bates, A. J., & Doorly, D. J. (2018). Flow features and micro-particle deposition in a human respiratory system during sniffing. *Journal of Aerosol Science*, 123, 171–184. <https://doi.org/10.1016/j.jaerosci.2018.05.008>
- Calmet, H., Kleinstreuer, C., Houzeaux, G., Kolanjiyil, A. V., Lehmkuhl, O., Olivares, E., & Vázquez, M. (2018). Subject-variability effects on micron particle deposition in human nasal cavities. *Journal of Aerosol Science*, 115, 12–28. <https://doi.org/10.1016/j.jaerosci.2017.10.008>
- Chen, X., Feng, Y., Zhong, W., Sun, B., & Tao, F. (2018). Numerical investigation of particle deposition in a triple bifurcation airway due to gravitational sedimentation and inertial impaction. *Powder Technology*, 323, 284–293. <https://doi.org/10.1016/j.powtec.2017.09.050>
- Cheng, Y. S., Zhou, Y., & Chen, B. T. (1999). Particle deposition in a cast of human oral airways. *Aerosol Science and Technology*, 31(4), 286–300. <https://doi.org/10.1080/027868299304165>
- Chen, X., Zhong, W., Sun, B., Jin, B., & Zhou, X. (2012). Study on gas/solid flow in an obstructed pulmonary airway with transient flow based on CFD-DPM approach. *Powder Technology*, 217, 252–260. <https://doi.org/10.1016/j.powtec.2011.10.034>
- Chen, X., Zhong, W., Zhou, X., Jin, B., & Sun, B. (2012). CFD-DEM simulation of particle transport and deposition in pulmonary airway. *Powder Technology*, 228, 309–318. <https://doi.org/10.1016/j.powtec.2012.05.041>
- Clift, R., Grace, J., & Weber, M. E. (1978). *Bubbles, drops and particles*. New York: Academic Press.
- Deng, Q., Ou, C., Chen, J., & Xiang, Y. (2018). Particle deposition in tracheobronchial airways of an infant, child and adult. *Science of the Total Environment*, 612, 339–346. <https://doi.org/10.1016/j.scitotenv.2017.08.240>
- Deng, Q., Ou, C., Shen, Y. M., Xiang, Y., Miao, Y., & Li, Y. (2019). Health effects of physical activity as predicted by particle deposition in the human respiratory tract. *Science of the Total Environment*, 657, 819–826. <https://doi.org/10.1016/j.scitotenv.2018.12.067>
- Dumon, J. F. (1990). A dedicated tracheobronchial stent. *Chest*, 97(2), 328–332. <https://doi.org/10.1378/chest.97.2.328>

- Dumon, J. F., Cavaliere, S., Diaz-Jimenez, J. P., Vergnon, J. M., Venuta, F., Dumon, M. C., & Kovitz, K. L. (1996). Seven-year experience with the dumon prosthesis. *Journal of Bronchology*, 3(1), 6–10. <https://doi.org/10.1097/00128594-199601000-00003>
- Farkas, A., & Balásházy, I. (2007). Simulation of the effect of local obstructions and blockage on airflow and aerosol deposition in central human airways. *Journal of Aerosol Science*, 38(8), 865–884. <https://doi.org/10.1016/j.jaerosci.2007.06.004>
- Farkhadnia, F., Gorji, T. B., & Gorji-Bandpy, M. (2016). Airflow, transport and regional deposition of aerosol particles during chronic bronchitis of human central airways. *Australian Physical and Engineering Sciences in Medicine*, 39(1), 43–58. <https://doi.org/10.1007/s13246-015-0394-x>
- Feng, Y., & Kleinstreuer, C. (2014). Micron-particle transport, interactions and deposition in triple lung-airway bifurcations using a novel modeling approach. *Journal of Aerosol Science*, 71, 1–15. <https://doi.org/10.1016/j.jaerosci.2014.01.003>
- Feng, Y., Kleinstreuer, C., & Rostami, A. (2015). Evaporation and condensation of multicomponent electronic cigarette droplets and conventional cigarette smoke particles in an idealized G3-G6 triple bifurcating unit. *Journal of Aerosol Science*, 80, 58–74. <https://doi.org/10.1016/j.jaerosci.2014.11.002>
- Ghahramani, E., Abouali, O., Emdad, H., & Ahmadi, G. (2017). Numerical investigation of turbulent airflow and microparticle deposition in a realistic model of human upper airway using LES. *Computers and Fluids*, 157, 43–54. <https://doi.org/10.1016/j.compfluid.2017.08.003>
- Heller-Algazi, M., Nof, E., Das, P., Bhardwaj, S., Kassinos, S. C., & Sznitman, J. (2020). In silico optimization of targeted aerosol delivery in upper airways via Inhaled Volume Tracking. *Clinical Biomechanics*, 80, 105138. <https://doi.org/10.1016/j.clinbiomech.2020.105138>
- Huang, J., & Zhang, L. (2011). Numerical simulation of micro-particle deposition in a realistic human upper respiratory tract model during transient breathing cycle. *Particuology*, 9, 424–431. <https://doi.org/10.1016/j.partic.2011.02.004>
- Huang, J., Zhang, L., & Yu, S. (2011). Modeling micro-particle deposition in human upper respiratory tract under steady inhalation. *Particuology*, 9, 39–43. <https://doi.org/10.1016/j.partic.2010.04.003>
- Inthavong, K., Choi, L. T., Tu, J., Ding, S., & Thien, F. (2010). Micron particle deposition in a tracheobronchial airway model under different breathing conditions. *Medical Engineering & Physics*, 32, 1198–1212. <https://doi.org/10.1016/j.medengphy.2010.08.012>
- Inthavong, K., Ge, Q., Se, C. M. K., Yang, W., & Tu, J. Y. (2011). Simulation of sprayed particle deposition in a human nasal cavity including a nasal spray device. *Journal of Aerosol Science*, 42(2), 100–113. <https://doi.org/10.1016/j.jaerosci.2010.11.008>
- Inthavong, K., Tian, Z. F., Li, H. F., Tu, J., Yang, W., Xue, C. L., & Li, C. G. (2006). A numerical study of spray particle deposition in a human nasal cavity. *Aerosol Science and Technology*, 40(11), 1034–1045. <https://doi.org/10.1080/02786820600924978>
- Inthavong, K., Tu, J., Ye, Y., Ding, S., Subic, A., & Thien, F. (2010). Effects of airway obstruction induced by asthma attack on particle deposition. *Journal of Aerosol Science*, 41, 587–601. <https://doi.org/10.1016/j.jaerosci.2010.03.001>
- Islam, M. S., Gu, Y. T., Farkas, A., Paul, G., & Saha, S. C. (2020a). Helium-oxygen mixture model for particle transport in CT-based human lung. *International Journal of Environmental Research and Public Health (IJERPH)*, 17(10), 3574. <https://doi.org/10.3390/ijerph17103574>

- Islam, M. S., Paul, G., Ong, H. X., Young, P. M., Gu, Y. T., & Saha, S. C. (2020b). A review of respiratory anatomical development, air flow characterisation and particle deposition. *International Journal of Environmental Research and Public Health (IJERPH)*, 17(2), 380.
- Islam, M. S., Larpruenrudee, P., Saha, S., Pourmehran, O., Paul, A. R., Gemci, T., Collins, R., Paul, G., & Gu, Y. (2021a). How severe acute respiratory syndrome coronavirus-2 aerosol propagate through the age-specific upper airways. *Physics of Fluids*, 33(8), 081911. <https://doi.org/10.1063/5.0061627>
- Islam, M. S., Larpruenrudee, P., Hossain, S. I., Gorji, M. R., Gu, Y. T., Saha, S. C., & Paul, G. (2021b). Polydisperse aerosol transport and deposition in upper airways of age-specific lung. *Journal of Environmental Research and Public Health (IJERPH)*, 18(12), 6239. <https://doi.org/10.3390/ijerph18126239>
- Islam, M. S., Larpruenrudee, P., Paul, A. R., Paul, G., Gemci, T., Gu, Y. T., & Saha, S. C. (2021c). SARS CoV-2 aerosol: How far it can travel to the lower airways? *Physics of Fluids*, 33(6), 061903. <https://doi.org/10.1063/5.0053351>
- Kadota, K., Imanaka, A., Shimazaki, M., Takemiy, T., Kubo, K., Uchiyama, H., & Tozuka, Y. (2018). Effects of inhalation procedure on particle behavior and deposition in the airways analyzed by numerical simulation. *Journal of the Taiwan Institute of Chemical Engineers*, 90, 44–50. <https://doi.org/10.1016/j.jtice.2017.11.008>
- Kleinstreuer, C., Shi, H., & Zhe, Z. (2007). Computational analyses of a pressurized metered dose inhaler and a new drug-aerosol targeting methodology. *Journal of Aerosol Medicine: Deposition, Clearance, and Effects in the Lung*, 20(3), 294–309. <https://doi.org/10.1089/jam.2006.0617>
- Kleinstreuer, C., & Zhang, Z. (2010). Airflow and particle transport in the human respiratory system. *Annual Review of Fluid Mechanics*, 42, 301–334. <https://doi.org/10.1146/annurev-fluid-121108-145453>
- Kleinstreuer, C., Zhang, Z., & Kim, C. S. (2007). Combined inertial and gravitational deposition of microparticles in small model airways of a human respiratory system. *Journal of Aerosol Science*, 38(10), 1047–1061. <https://doi.org/10.1016/j.jaerosci.2007.08.010>
- Kolanjiyil, A. V., & Kleinstreuer, C. (2017). Computational analysis of aerosol-dynamics in a human whole-lung airway model. *Journal of Aerosol Science*, 114, 301–316. <https://doi.org/10.1016/j.jaerosci.2017.10.001>
- Koullapis, P. G., Hofemeier, P., Sznitman, J., & Kassinos, S. C. (2018). An efficient computational fluid-particle dynamics method to predict deposition in a simplified approximation of the deep lung. *European Journal of Pharmaceutical Sciences*, 113, 132–144. <https://doi.org/10.1016/j.ejps.2017.09.016>
- Koullapis, P. G., Kassinos, S. C., Bivolarova, M. P., & Melikov, A. K. (2016). Particle deposition in a realistic geometry of the human conducting airways: Effects of inlet velocity profile, inhalation flowrate and electrostatic charge. *Journal of Biomechanics*, 49(11), 2201–2212. <https://doi.org/10.1016/j.jbiomech.2015.11.029>
- Koullapis, P., Ollson, B., Kassinos, S. C., & Sznitman, J. (2019). Multiscale in silico lung modeling strategies for aerosol inhalation therapy and drug delivery. *Current Opinion in Biomedical Engineering*, 1, 130–136. <https://doi.org/10.1016/j.cobme.2019.11.003>
- Li, Z., Kleinstreuer, C., & Zhang, Z. (2007). Simulation of airflow fields and microparticle deposition in realistic human lung airway models. Part II: Particle transport and deposition. *European Journal of Mechanics, B/Fluids*, 26(5), 650–668. <https://doi.org/10.1016/j.euromechflu.2007.02.004>
- Longest, P. W., Bass, K., Dutta, R., Rani, V., Thomas, M. L., El-Achwah, A., & Hindle, M. (2019). Use of computational fluid dynamics deposition modeling in respiratory drug delivery. *Expert Opinion on Drug Delivery*, 16(1), 7–26. <https://doi.org/10.1080/17425247.2019.1551875>

- Longest, P. W., Hindle, M., Das Choudhuri, S., & Xi, J. (2008). Comparison of ambient and spray aerosol deposition in a standard induction port and more realistic mouth-throat geometry. *Journal of Aerosol Science*, 39(7), 572–591. <https://doi.org/10.1016/j.jaerosci.2008.03.008>
- Longest, P. W., & Holbrook, L. T. (2012). In silico models of aerosol delivery to the respiratory tract—development and applications. *Advanced Drug Delivery Reviews*, 64, 296–311. <https://doi.org/10.1016/j.addr.2011.05.009>
- Longest, P. W., & Vinchurkar, S. (2007). Effects of mesh style and grid convergence on particle deposition in bifurcating airway models with comparisons to experimental data. *Medical Engineering and Physics*, 29(3), 350–366. <https://doi.org/10.1016/j.medengphy.2006.05.012>
- Longest, P. W., Vinchurkar, S., & Martonen, T. (2006). Transport and deposition of respiratory aerosols in models of childhood asthma. *Journal of Aerosol Science*, 37(10), 1234–1257. <https://doi.org/10.1016/j.jaerosci.2006.01.011>
- Longest, P. W., & Xi, J. (2007). Computational investigation of particle inertia effects on sub-micron aerosol deposition in the respiratory tract. *Journal of Aerosol Science*, 38(1), 111–130. <https://doi.org/10.1016/j.jaerosci.2006.09.007>
- Longest, P. W., & Xi, J. X. (2008). Condensational growth may contribute to the enhanced deposition of cigarette smoke particles in the upper respiratory tract. *Aerosol Science and Technology*, 42(8), 579–602. <https://doi.org/10.1080/02786820802232964>
- Luo, H. Y., Liu, Y., & Yang, X. L. (2007). Particle deposition in obstructed airways. *Journal of Biomechanics*, 40(14), 3096–3104. <https://doi.org/10.1016/j.jbiomech.2007.03.027>
- Malvè, M., Sánchez-Matás, C., & López-Villalobos, J. L. (2020). Modelling particle transport and deposition in the human healthy and stented tracheobronchial airways. *Annals of Biomedical Engineering*, 48(6), 1805–1820. <https://doi.org/10.1007/s10439-020-02493-1>
- Pourmehran, O., Gorji, T. B., & Gorji-Bandpy, M. (2016). Magnetic drug targeting through a realistic model of human tracheobronchial airways using computational fluid and particle dynamics. *Biomechanics and Modeling in Mechanobiology*, 15(5), 1355–1374. <https://doi.org/10.1007/s10237-016-0768-3>
- Pourmehran, O., Rahimi-Gorji, M., Gorji-Bandpy, M., & Gorji, T. B. (2015). Simulation of magnetic drug targeting through tracheobronchial airways in the presence of an external non-uniform magnetic field using Lagrangian magnetic particle tracking. *Journal of Magnetism and Magnetic Materials*, 393, 380–393. <https://doi.org/10.1016/j.jmmm.2015.05.086>
- Rahimi-Gorji, M., Gorji, T. B., & Gorji-Bandpy, M. (2016). Details of regional particle deposition and airflow structures in a realistic model of human tracheobronchial airways: Two-phase flow simulation. *Computers in Biology and Medicine*, 74, 1–17. <https://doi.org/10.1016/j.combiom.2016.04.017>
- Rahimi-Gorji, M., Pourmehran, O., Gorji-Bandpy, M., & Gorji, T. B. (2015). CFD simulation of airflow behavior and particle transport and deposition in different breathing conditions through the realistic model of human airways. *Journal of Molecular Liquids*, 209, 121–133. <https://doi.org/10.1016/j.molliq.2015.05.031>
- Shang, Y. D., Inthavong, K., & Tu, J. Y. (2015). Detailed micro-particle deposition patterns in the human nasal cavity influenced by the breathing zone. *Computers and Fluids*, 114, 141–150. <https://doi.org/10.1016/j.compfluid.2015.02.020>
- Singh, P., Raghav, V., Padhmashali, V., Paul, G., Islam, M. S., & Saha, S. C. (2020). Airflow and particle transport prediction through Stenosis Airway. *International Journal of*

- Environmental Research and Public Health (IJERPH)*, 17(3), 1119. <https://doi.org/10.3390/ijerph17031119>
- Stylianou, F. S., Sznitman, J., & Kassinos, S. C. (2016). Direct numerical simulation of particle laden flow in a human airway bifurcation model. *International Journal of Heat and Fluid Flow*, 61, 677–710. <https://doi.org/10.1016/j.ijheatfluidflow.2016.07.013>
- Sun, F., Usón, J., Ezquerra, J., Crisóstomo, V., Luis, L., & Maynar, M. (2008). Endotracheal stenting therapy in dogs with tracheal collapse. *Veterinary Journal*, 175(2), 186–193. <https://doi.org/10.1016/j.tvjl.2007.01.011>
- Verbancz, S., Kalsi, H. S., Biddiscombe, M. F., Agnihotri, V., Belkassem, B., Lacor, C., & Usmani, O. S. (2011). Inspiratory and expiratory aerosol deposition in the upper airway. *Inhalation Toxicology*, 23(2), 104–111. <https://doi.org/10.3109/08958378.2010.547535>
- Weibel, E. (1963). Morphometry of the human lungs. In *Morphometry of the human lung*. Springer. <https://doi.org/10.1016/C2013-0-08161-3>
- Xu, X. Y., Ni, S. J., Fu, M., Zheng, X., Luo, N., & Weng, W. G. (2017). Numerical investigation of airflow, heat transfer and particle deposition for oral breathing in a realistic human upper airway model. *Journal of Thermal Biology*, 70, 53–63. <https://doi.org/10.1016/j.jtherbio.2017.05.003>
- Yan, W., Tang, C., Liu, Y., & Li, G. (2019). Numerical study on abnormal airflow patterns and particle deposition characteristics in the realistic HUA model with pharyngeal obstruction. *Powder Technology*, 356, 148–161. <https://doi.org/10.1016/j.powtec.2019.08.007>
- Yeh, H. C., & Schum, G. M. (1980). Models of human lung airways and their application to inhaled particle deposition. *Bulletin of Mathematical Biology*, 42, 461–480. [https://doi.org/10.1016/0034-5687\(84\)90068-9](https://doi.org/10.1016/0034-5687(84)90068-9)
- Zhang, Y., & Finlay, W. H. (2005). Measurement of the effect of cartilaginous rings on particle deposition in a proximal lung bifurcation model. *Aerosol Science and Technology*, 39(5), 394–399. <https://doi.org/10.1080/027868290945785>
- Zhang, Z., & Kleinstreuer, C. (2004). Airflow structures and nano-particle deposition in a human upper airway model. *Journal of Computational Physics*, 198(1), 178–210. <https://doi.org/10.1016/j.jcp.2003.11.034>
- Zhang, Z., Kleinstreuer, C., Donohue, J. F., & Kim, C. S. (2005). Comparison of micro- and nano-size particle depositions in a human upper airway model. *Journal of Aerosol Science*, 36(2), 211–233. <https://doi.org/10.1016/j.jaerosci.2004.08.006>
- Zhang, Z., Kleinstreuer, C., & Kim, C. S. (2002). Micro-particle transport and deposition in a human oral airway model. *Journal of Aerosol Science*, 33(12), 1635–1652. [https://doi.org/10.1016/S0021-8502\(02\)00122-2](https://doi.org/10.1016/S0021-8502(02)00122-2)
- Zhang, B., Qi, S., Yue, Y., Shen, J., Li, C., Qian, W., & Wu, J. (2018). Particle disposition in the realistic airway tree models of subjects with tracheal bronchus and COPD. *BioMed Research International*, 2018, 1–18. <https://doi.org/10.1155/2018/7428609>
- Zhou, Y., & Cheng, Y. S. (2005). Particle deposition in a cast of human tracheobronchial airways. *Aerosol Science and Technology*, 39(6), 492–500. <https://doi.org/10.1080/027868291001385>

This page intentionally left blank

# Ultrafine particle transport to the lower airways: airway diameter reduction effects

# 12

Puchanee Larpruenrudee<sup>1</sup>, Gunther Paul<sup>2</sup>, Suvash C. Saha<sup>1</sup>, Shahid Husain<sup>3</sup>,  
HamidReza Mortazavy Beni<sup>4</sup>, Christopher Lawrence<sup>5</sup>, Xuzhen He<sup>6</sup>, Yuantong Gu<sup>7</sup>,  
Mohammad Saidul Islam<sup>1</sup>

<sup>1</sup>School of Mechanical and Mechatronic Engineering, University of Technology Sydney (UTS), Ultimo, NSW, Australia; <sup>2</sup>Australian Institute of Tropical Health and Medicine, James Cook University, Townsville, QLD, Australia; <sup>3</sup>Mechanical Engineering Department, AMU, Aligarh, India; <sup>4</sup>Department of Biomedical Engineering, Arsanjan Branch, Islamic Azad University, Arsanjan, Iran; <sup>5</sup>School of Computer Science, University of Technology Sydney (UTS), Ultimo, NSW, Australia; <sup>6</sup>School of Civil and Environmental Engineering, University of Technology Sydney (UTS), Ultimo, NSW, Australia; <sup>7</sup>School of Mechanical, Medical and Process Engineering, Faculty of Engineering, Queensland University of Technology, Brisbane, QLD, Australia

## Chapter outline

Introduction .....	253
Geometrical development .....	256
Numerical methods .....	258
Result and discussion .....	260
Velocity functions .....	260
Pressure variations .....	261
Particle deposition fraction .....	263
Escaped particles .....	267
Conclusions .....	269
Limitations of the approach .....	269
References .....	270

## Introduction

Both human activities and natural phenomena are the main creators of ultrafine particles ( $\text{PM}_{0.1}$ ; particles of size  $\leq 0.1 \mu\text{m}$  in diameter) in the atmosphere, contributing to air pollution. Such sources include bushfires, oceanic activity, volcanic eruptions, combustion processes used to power vehicles or plant or produce heating, or even home cooking (Hendryx et al., 2020; Islam et al., 2017; Schraufnagel,

2020). Nanoparticles, which are also called ultrafine particles is a term that mostly refers to such particles sized 100 nm in aerodynamic diameter or less when produced by controlled engineering processes. Nanoparticles are considered to be one of the leading causes of human respiratory diseases because their small size allows particles to travel to the lower generations of the lungs and even escape to the alveolar region of the airways during inhalation and translocate to other organs (Dong et al., 2019). There is agreement among researchers that toxic nanoparticles result in a greater negative impact on the respiratory system compared to toxic microparticles (Frampton, 2001; Hsiao & Huang, 2013; Oberdörster, 2000). Exposure to ultrafine particles increases the risk of inflammation and infection, potentially causing respiratory diseases as well as cardiovascular and neurological disorders (Bai et al., 2001; Baulig et al., 2003; Garshick et al., 2008; Holder et al., 2008; Kagawa, 2002; Lewtas, 2007; McClellan, 1987; Moller et al., 2008; Oberdorster, 2005). Children and the elderly have been reported to suffer the greatest risk from this exposure (Dockery et al., 2005; Frampton, 2007; Frampton et al., 2004; Nogueira, 2009; Oberdorster et al., 1995, 2005; Park et al., 2005; Pedata et al., 2010). Research into this issue so far has mainly focused on nanoparticle transport and deposition in the upper airways of the human respiratory tract and was conducted as computational studies or in vivo and in vitro experiment studies. Examples of in vivo studies measuring ultrafine particle deposition within the nasal and oral airways under different conditions are Cheng, Yeh, et al. (1996) who measured monodisperse silver particles and polystyrene latex particles within the nasal airways of four healthy, adult male subjects, and Cheng, Cheng, et al. (1996), who measured ultrafine aerosol deposition efficiency within the nasal and oral airways of 10 male adults. Swift and Strong (1996) studied respiratory radiation dose from ultrafine  $^{218}\text{Po}$  aerosol exposure in the nasal passage of three adults for constant flow rates of 5.9–17.5 L/min and particle diameters from 0.53 to 0.62 nm. These studies found similar high deposition rates based on the surface area of the nasal cavity, minimum cross-sectional area, and shape complexity. Jakobsson et al. (2018) measured deposition of inhaled nanoparticles in the lungs of 67 elderly subjects who were either healthy or suffered from chronic obstructive pulmonary disease (COPD). The deposition fraction was found to be lower with emphysema when compared to healthy subjects. Smaller particle sizes had higher deposition fraction rates. Other studies have employed in vitro methods to analyze particle deposition in more specific regions as well as reduce the risk to human subjects. Cheng et al. (1993) investigated radon progeny deposition in adults' nasal and oral airways for particles ranging from 1.2 to 1.7 nm at constant flow rates of 4–20 L/min. Gradon and Yu (1989) studied ultrafine particle diffusion in both nasal and oral airways of a 30-year-old male subject compared ultrafine particle deposition within the nasal airway, Kelly et al. (2004), which were replicated in different stereolithography models. The results of both studies claimed that a higher deposition efficiency was found in the nasal airways rather than the oral airway. Furthermore, smaller ultrafine particle sizes generate higher deposition rates. Cheng et al. (1988, 1996, 2007) have produced a track of papers

about nanoparticle deposition in both nasal and oral airways, comparing breathing conditions for inhalation and exhalation of adult oral and nasal airways. They found the particle deposition rate in exhalation to be slightly higher than in inhalation. However, their method was found to have limitations for investigating the deposition characteristics at specific surface locations (Schraufnagel, 2020).

To enhance health-risk assessment for the respiratory system, computational fluid dynamics (CFD) has been applied to investigate airflow characteristic as well as particle transport and deposition, complementing and refining experimental in vivo or in vitro methods. Particle transport and deposition within the nasal cavity and through the tracheobronchial airway has been analyzed under various conditions such as microparticle or nanoparticle size, different CFD analysis methods, different aerosol types (Fan et al., 2021; Farhadi Ghalati et al., 2012; Ghosh et al., 2020; Inthavong et al., 2011; Islam et al., 2018, 2019b, 2020a, 2020b; Kimbell et al., 2001; Liu et al., 2007; Moghadas et al., 2011; Rahman et al., 2021; Wang et al., 2009; Xi et al., 2008, 2009, 2012; Zamankhan et al., 2006), and based on lung diseases such as cancer, stenosis areas, or even the effect of sinus on the lung airways (Gu et al., 2019; Larpruenrudee et al., 2021; Pourmehran et al., 2016, 2020a, 2020b, 2021; Singh et al., 2020). A model of the reconstructed upper airways of a 24-year-old female subject was used for the comparison of micro- and nanoparticle deposition using Lagrangian and Eulerian model approaches with 5–15 L/min flow rates and various particle sizes (Farhadi Ghalati et al., 2012). Their study showed that micro- and nanoparticles are mostly trapped in the nasal cavity. Larynx deposition fraction however was the lowest for nanoparticles, compared to being the second highest deposition fraction for microparticles. The second highest deposition fraction for nanoparticles was found in the pharynx. Inthavong et al. (2010) studied nanoparticle deposition in the nasal and tracheobronchial airways using a Lagrangian Brownian model. Again, a higher deposition rate was found in the nasal airways for smaller nanoparticle sizes of 1–10 nm. Moghadas et al. (2011) investigated nano- and microparticle deposition in the nasal passages under a septal deviation condition, where a CT-scan based CFD model of a 25-year-old male subject with septal deviation was used. They found that total particle deposition of microparticles depended significantly on the flow field and nasal passage geometry. Wang et al. (2009) compared micro- and nanoparticle deposition in the nasal cavity and determined that the deposition patterns for the left and right cavities were significantly different, however only for microparticles. Zamankhan et al. (2006) evaluated the airflow and nanoparticle deposition in the nasal cavity using an MRI-based model of a human subject and reported that smaller nanoparticle sizes caused higher deposition rates. Zhang and Kleinstreuer (2011) analyzed the airflow and nanoparticle deposition in both the nasal and oral tracheobronchial airways using an MRI-based model of a healthy 53-year-old male subject for numerical simulation. They reported that the nanoparticle deposition rates in the pharynx, larynx, and trachea significantly depended on flow rate.

This chapter focuses on expanding these studies with an investigation of airflow characteristics, nanoparticle transport, and nanoparticle deposition in the nasal and upper airways of different age which relates to different lung proportions. Few studies have compared the airflow pattern, nanoparticle transport, and nanoparticle deposition for different age lungs. [Xi et al. \(2012\)](#) studied ultrafine particle deposition in the nasal–laryngeal airways, comparing a newborn, an infant, a child, and a 53-year-old adult in models developed from CT. They studied nanoparticle sizes of 1–200 nm and flow rates between 3 and 45 L/min and found only little difference in the total deposition fractions for all cases despite differences in morphology and dimension. [Olvera et al. \(2012\)](#) compared ultrafine particle deposition between children and adults. Particle sizes of 10–200 nm were studied under asthmatic and nonasthmatic conditions. At 28%, the deposition fraction in children was found to be higher than in adults. Moreover, at 21% the deposition fraction was higher in asthmatic than in nonasthmatic. [Rissler et al. \(2017\)](#) investigated deposition efficiency in healthy children and adults' lungs using experimental methods. Particle sizes of 15–5000 nm were studied in 67 subjects aged 7–70 years. High deposition rates were found throughout the respiratory tract for all particle sizes ranging from 15 to 3500 nm. In recent model-based studies of aerosol transport in three different age adult upper airway sections, [Islam, Larpruenrudee, Hossain, et al. \(2021\)](#) studied particle sizes of 1–10  $\mu\text{m}$  at 7.5, 15, 30, and 60 L/min flow rates. This study predicted higher deposition efficiencies with flow rate and age. [Islam, Larpruenrudee, Saha, et al. \(2021\)](#) also studied SARS COV-2 aerosol propagation in the same age-related models and predicted higher SARS COV-2 aerosol concentrations in the airways of older compared to younger adults. Beyond these studies, there is no numerical investigation focusing on ultrafine particle transport and deposition in the oral and upper airways for different lung sizes as a function of aging. Previous studies have focused mainly on the comparison of deposition patterns in children and adults.

This chapter expands previous work ([Islam, Larpruenrudee, Hossain, et al., 2021](#)) to ultrafine particle transport and deposition in the elderly upper airways from the mouth–throat area to generation 5 of the lungs. A comparison of airflow patterns and ultrafine particle transport and deposition is provided for three different lung sizes representing a 50-, 60-, and 70-year-old at various flow rates.

---

## Geometrical development

A combination of a CT-based upper airway model and a scalable bronchial airway model was reconstructed to generate models of 50-, 60-, and 70-year-old lungs. While these three models contained the same dimensions for the CT-based upper airway, the large bronchial airway model from the trachea to generation 5 was adjusted. Weibel's-based model from the trachea to generation 5 was used to represent a 50-year-old lung ([Zhu et al., 1963](#)). The model was created with

uneven surfaces in order to improve its realism. For the 60- and 70-year-old lungs, the dimensions from the trachea to generation 5 were reduced by 10% and 20%, respectively. The lung dimensions of the 60-year-old were designed based on the lung morphology case presented by [bib\\_Niewoehner\\_and\\_Eleinerman\\_1974](#)[Niewoehner and Eleinerman \(1974\)](#), and the airway size was reduced by 10%. Later, [Xu and Yu \(1986\)](#) developed an analytical equation to represent ageing effects on the lungs resulting in a 10% lung size reduction. For the CFD airflow simulation, an age-specific model was used to analyze airflow in cases older than 50 years ([Kim et al., 2017](#)). In reality, differences in age, sex, physiological conditions, and interpersonal variation will affect airway dimensions. [Fig. 12.1](#) presents the reconstructed lung model with different dimensions for the three different ages, [Fig. 12.1A](#) for a 50-, [Fig. 12.1B](#) for a 60-, and [Fig. 12.1C](#) for a 70-year-old, respectively.

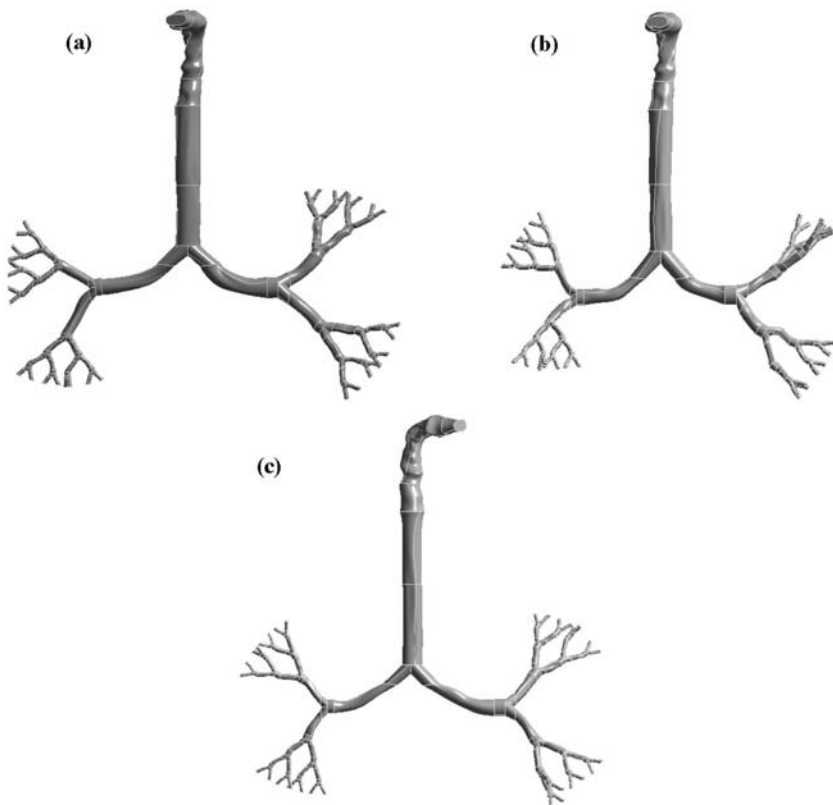


**FIGURE 12.1**

Reconstructed models from a CT-based mouth–throat model and Weibel's model of a large bronchial airway: (A) 50-year-old lung, (B) 60-year-old lung, and (C) 70-year-old lung.

## Numerical methods

The Lagrangian scheme and finite volume–based discretization techniques were used in ANSYS 19.2 (FLUENT). The governing equations are solved as follows (Islam, Larpruenrudee, Paul, et al., 2021):

$$\nabla \cdot (\rho \vec{v}) = 0 \quad (12.1)$$

$$\nabla \cdot (\rho \vec{v} \vec{v}) = -\nabla p + \nabla \cdot \left( \mu \left( \nabla \vec{v} + \nabla \vec{v}^T \right) \right) + \rho \vec{g}, \quad (12.2)$$

where  $p$  is the static pressure,  $\rho \vec{g}$  is the gravitational body force, and  $\mu$  is the molecular viscosity.

The internal energy equation is as follows:

$$\nabla \cdot (\rho \vec{v} e) = -\nabla \cdot \vec{j} \quad (12.3)$$

where  $e$  is the specific internal energy, and  $\vec{j}$  is the heat flux vector which is the sum of all contributions from the heat condition and enthalpy diffusion effects.

Nanoparticle transport was modeled based on Inthavong and Ahmadi (2009),

$$\begin{aligned} \frac{dv_i^p}{dt} &= F_D + F_{\text{Brownian}} + F_{\text{Lift}} + \frac{\rho_p - \rho_g}{\rho_p} g_i, \\ F_D &= \frac{1}{C_c} C_D A_p \frac{\rho_g |v_i^g - v_i^p| (v_i^g - v_i^p)}{2m_p} = \frac{18\mu_g}{\rho_p d_p^2 C_c} (v_i^g - v_i^p), \\ C_c &= 1 + \frac{2\lambda}{d_p} \left( 1.257 + 0.4e^{-\frac{1.1d_p}{2\lambda}} \right), \end{aligned} \quad (12.4)$$

where  $F_D$  is the drag force per unit particle mass  $m_p$ ,  $C_D$  denotes the drag coefficient,  $A_p$  is the cross-sectional area of the particle,  $C_c$  is the Cunningham correction factor, and  $\lambda$  is the mean free path of the gas molecules.  $v_i^p$  and  $v_i^g$  are the  $i$ -th component of the time-averaged particle velocity and gas (air) velocity, respectively.  $\rho_p$  and  $\rho_g$  are the density of particle material and gas (air), respectively.  $g_i$  is defined as the gravitational component,  $\mu_g$  is the gas (air) viscosity, and  $d_p$  denotes a particle diameter. For the low particle Reynolds number ( $Re_p$ ) which is less than 0.5, the drag coefficient can be expressed by Haider and Levenspiel (1989)

$$C_D = \frac{24}{Re_p}, \quad Re_p < 0.5. \quad (12.5)$$

The particle Reynolds number is then calculated as

$$Re_p = \rho_g \frac{d_p |v_r|}{\mu_g} \quad (12.6)$$

where  $v_r$  is the relative velocity.

The amplitude for the Brownian force (Li & Ahmadi, 1992; Worth Longest & Xi, 2007) is determined as

$$F_{\text{Brownian}} = \zeta \sqrt{\frac{\pi S_o}{\Delta t}}, \quad (12.7)$$

where  $\zeta$  is the zero-mean unit variance for an independent Gaussian random number, at time step  $\Delta t$ .  $S_o$  denotes the spectral intensity which can be expressed by

$$S_o = \frac{216 \rho k_B T}{\pi^2 \rho_p d_p^5 \left( \frac{\rho_p}{\rho_g} \right)^2 C_c}, \quad (12.8)$$

where  $T$  is the fluid absolute temperature,  $k_B$  denotes the Boltzmann constant, and  $\rho_g$  is the gas density.

This study employs the SIMPLE coupling scheme and second-order pressure discretization technique (Kumar et al., 2019). The energy and momentum are solved based on the second-order upwind technique (Kumar et al., 2019). In the Lagrangian discrete phase model, nanoparticles were released from the inlet surface at the mouth area using steady injection. The inlet velocity in the mouth area and the terminal outlet pressure were used as boundary conditions. The numerical analysis was conducted for three flow rate conditions of 7.5, 15, and 20 L/min at the inlet and a zero-gauge pressure as outlet condition. Air was set to be the primary component which is considered as a continuous phase, while nanoparticles were the secondary component considered as a discrete phase. Table 12.1 presents the summary properties of these two components.

A uniform nanoparticle distribution was assumed at the inlet surface. Nanoparticles of sizes 1 nm, 10 nm, and 50 nm were deployed with a total of 1346 injected particles for each size. A “trap” boundary condition was applied to the walls as particles could become trapped when they touched the wall (Islam, Saha, Gemci, et al., 2019). Thus, trajectory calculations were terminated and recorded as trapped when particles touched the wall. The deposition fraction (DF) was calculated as

$$DF = \frac{\text{Number of deposited particles on the wall}}{\text{Total number of particles entering the inlet}}$$

DF is defined here as the ratio of deposited particles with a given size and in a given region to the total number of particles entering the respiratory tract.

**Table 12.1** Properties of air and nanoparticle.

Properties	Air	Nanoparticle
Density (kg/m <sup>3</sup> )	1.225	1100
Viscosity (kg/m <sup>-s</sup> )	$1.7893 \times 10^{-5}$	—

Deposition efficiency on the other hand is defined for the ratio of deposited particles to the total number of particles entering a given region (Cheng & Swift, 1995).

## Result and discussion

The simulation was conducted under breathing conditions reflecting normal daily physical activities with flow rates of 7.5, 15, and 20 L/min.

## Velocity functions

Velocity contours present a fluid flow field across a sectional area. Velocity contours were converted into a line graph and values are presented as the average airflow velocity at a selected cross section. The maximum velocities in Fig. 12.3 were calculated at the selected planes as shown in Fig. 12.2, consisting of the oral areas, upper airways, and bronchial airways. The comparison of airflow characteristics for the three lung models is presented for the three different flow rates. Fig. 12.3A shows the lung velocities of a 50-year-old, while Fig. 12.3B represents a 60-year-old, and Fig. 12.3C a 70-year-old.

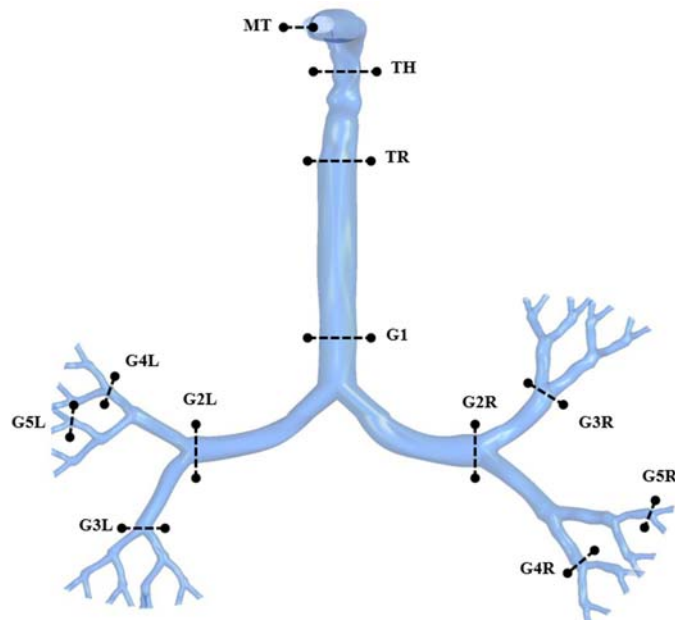
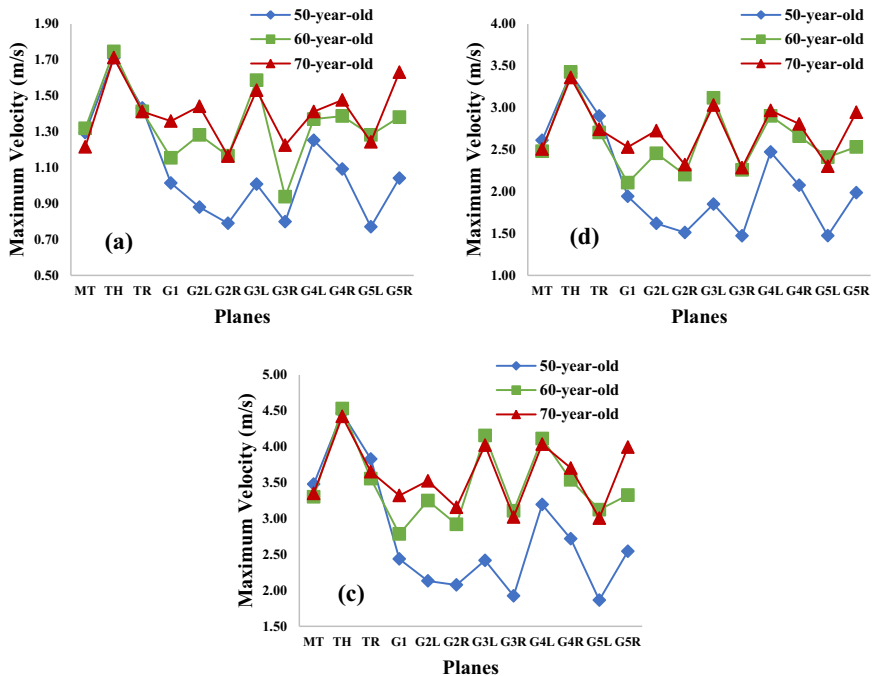


FIGURE 12.2

Selected planes for velocities at selected positions of the upper airways.

**FIGURE 12.3**

Maximum velocities at selected positions of the upper airways for a 50-year-old, 60-year-old, and 70-year-old at (A) 7.5 L/min, (B) 15 L/min, (C) 20 L/min.

From Fig. 12.3, the highest velocity magnitudes were found in the throat region (Plane TH) for all lung sizes at all flow rates. The lowest velocity magnitudes were generally located in the left lung at generation 5 (Plane G5L) for the 50- and 70-year-old cases at all flow rates, while the lowest velocity magnitude of the 60-year-old was located in the right lung at generation 3 (Plane G3R) for 7.5 L/min flow rate and in generation 1 (Plane G1) for 15 L/min and 20 L/min. When comparing the velocity magnitudes between the left and right lungs in all lung sizes and for all flow rates, the velocities in the left lung were generally higher than in the right lung, however only from generation 2 to generation 4. For generation 5, the right lung had higher velocity magnitudes than the left lung. The highest velocities occurred in the throat of all lung sizes.

## Pressure variations

Pressure variations play a significant role in airway resistance. The flow types, the viscosity of the gas, as well as the dimensions of the airways highly affect the degree of resistance to flow within the airways (Islam et al., 2015). Pressure at the eight

selected locations is presented in Fig. 12.4. Again calculations were made from the mouth through to generation 5 of the lungs. Fig. 12.4A presents the combined right and left side pressures in the 50-year-old lung, while Fig. 12.4B and C show the pressures in the 60- and 70-year-old lungs, respectively. Throughout this section, MT refers to the mouth area, while TH and TR refer to the throat and trachea areas, respectively. G1–G5 refer to generations 1–5. As seen in Fig. 12.4, the pressure was highest in the mouth area and then continually decreased toward the lower generations in all three lung sizes and for all flow rates. The highest flow rate of 20 L/min caused the highest pressure in all lung sizes. The 50- and 70-year-old cases (Fig. 12.4A and C) had similar pressure patterns with the most significant pressure drops between generation 3 and generation 4, while the a much more pronounced pressure drop in the 60-year-old case (Fig. 12.4B) was found between generation 1 and generation 2 instead. It is also noted that the pressure drops were by far the greatest at the highest flow rate of 20 L/min in all lung sizes, however particularly in the 60-year-old case.

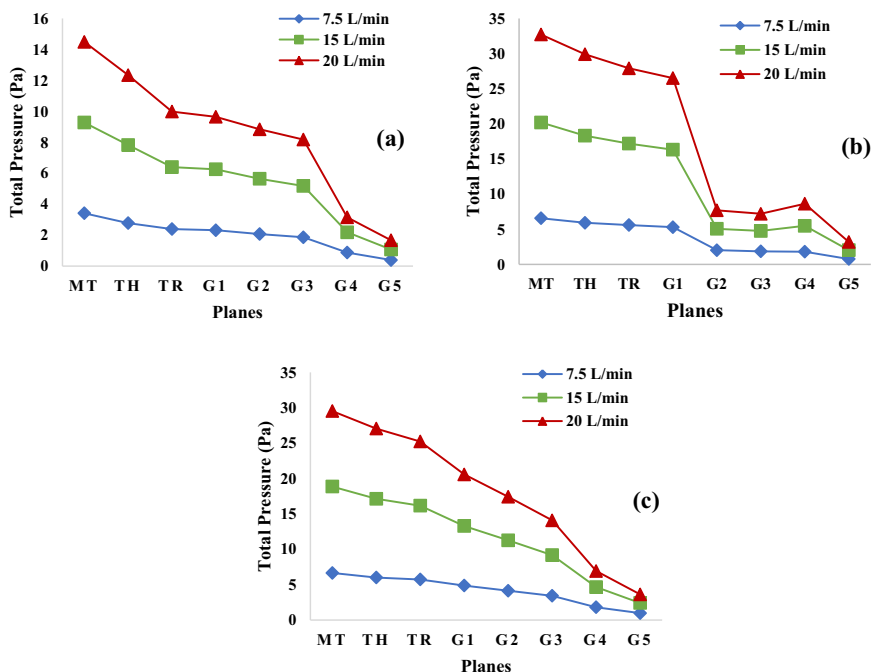


FIGURE 12.4

Combined right and left side pressures represented as “total pressure” at different selected positions of the mouth–throat and upper airways for three different flow rates, (A) 50-year-old lung, (B) 60-year-old lung, and (C) 70-year-old lung.

## Particle deposition fraction

The estimation of particle deposition in the human respiratory tract is important in predicting potential health outcomes from inhaled aerosols. While particle deposition estimation contributes to the aerosol toxicology assessment, it is also used in the optimization of drug delivery to the lungs through inhalation (Kleinsteuer et al., 2008; Moskal et al., 2010). Many factors affect regional and total deposition of particles, causing a high variability in the prediction. Main factors include lung geometry, which is highly variable with age, body size, and health conditions, and the breathing pattern, which mainly depends on age, health, and momentary physical activity. Other factors are particle properties such as size, shape, and density (Sosnowski, 2011). Particle deposition fraction (DF) when inhaling assumes a defined total number of particles injected into the mouth and through the airways, where the percentage of DF corresponds to the percentage of particles trapped along the lung walls in a certain area while traveling through the airways. Fig. 12.5 presents DF in the mouth–throat area for three nanoparticle sizes. From Figs. 12.5 and 12.6, the largest proportion of nanoparticles were trapped in the mouth–throat area at between 11% and 15% DF in all three lung sizes, and that this maximum was particularly elevated for a particle size of 1 nm. For other nanoparticle sizes of 10 and 50 nm, DF rates in the mouth–throat area were similar and ranged at around 3%–4%.

Fig. 12.6 shows DF throughout the airways in the three lung size models and for three flow rates. Fig. 12.6A shows a 7.5 L/min flow rate, Fig. 12.6B a 15 L/min, and Fig. 12.6C a 20 L/min flow rate. The mouth–throat (MT) area had the highest DF for all three lung sizes and all flow rates. DF in the right lung (RL) was higher than the left lung (LL) in all three lung sizes at 7.5 L/min and 15 L/min flow rates (Fig. 12.6A).

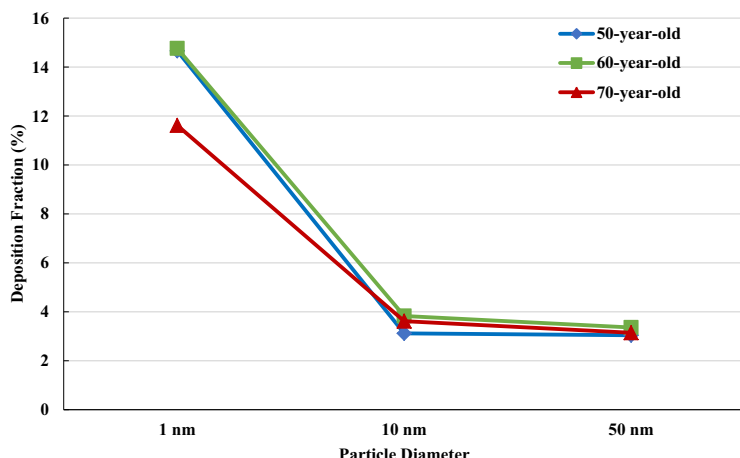
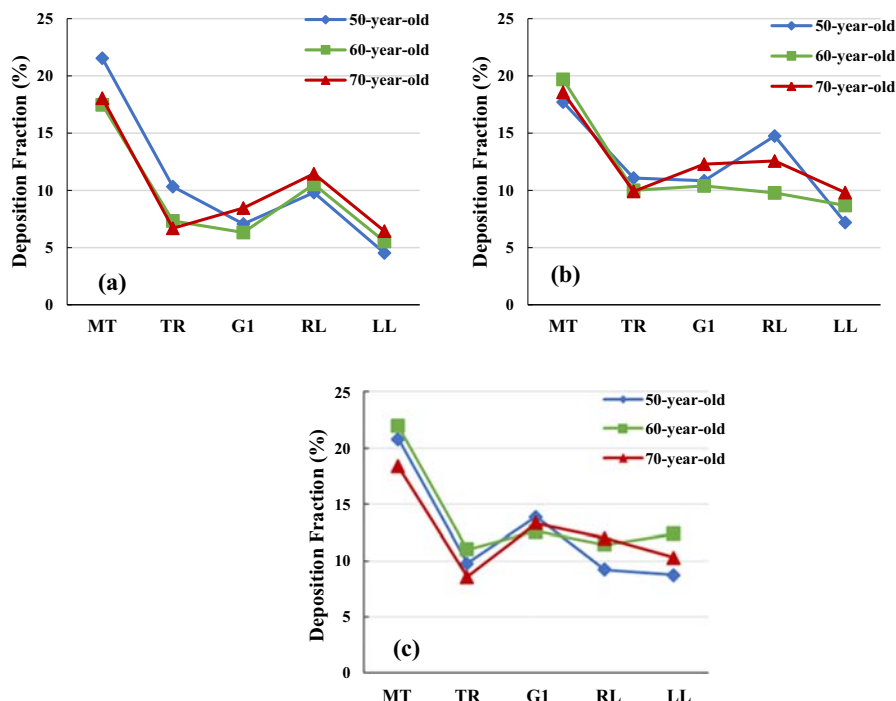


FIGURE 12.5

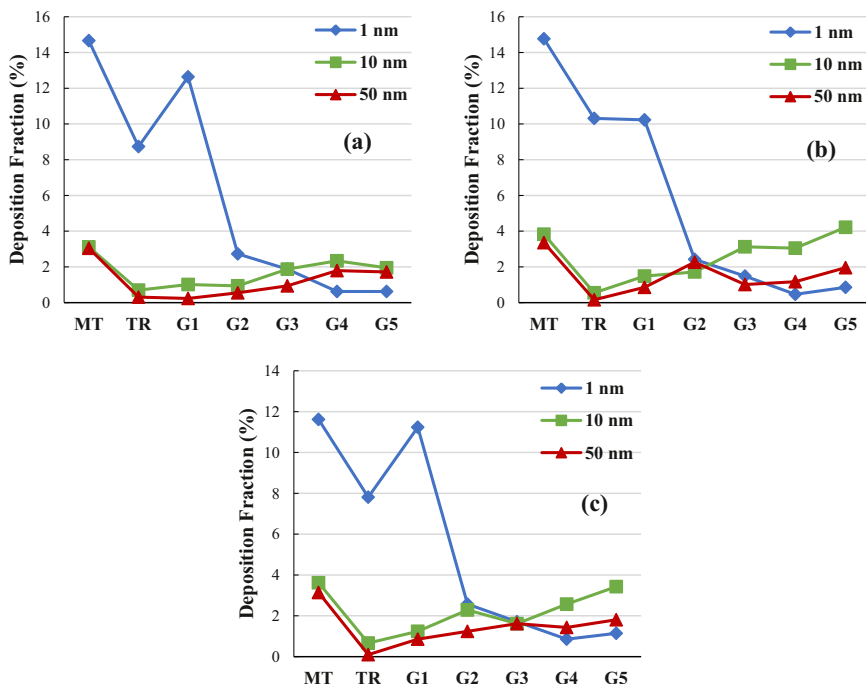
Nanoparticle deposition fraction (DF) in the mouth–throat area at 20 L/min for three lung size models.

**FIGURE 12.6**

Nanoparticle deposition fraction (DF) at various airway positions, (A) for 7.5 L/min, (B) for 15 L/min, and (C) for 20 L/min flow rate. MT: mouth–throat; TR: trachea; G1: generation 1; RL: right lung; LL: left lung.

and B). At the highest flow rate of 20 L/min however, DF of the right lung (RL) was higher than the left lung (LL) only in the 50- and 70-year-old cases (Fig. 12.6C). In summary, nanoparticles were primarily trapped in the mouth–throat area for all lung sizes. The right lungs had a higher DF rate than the left lungs.

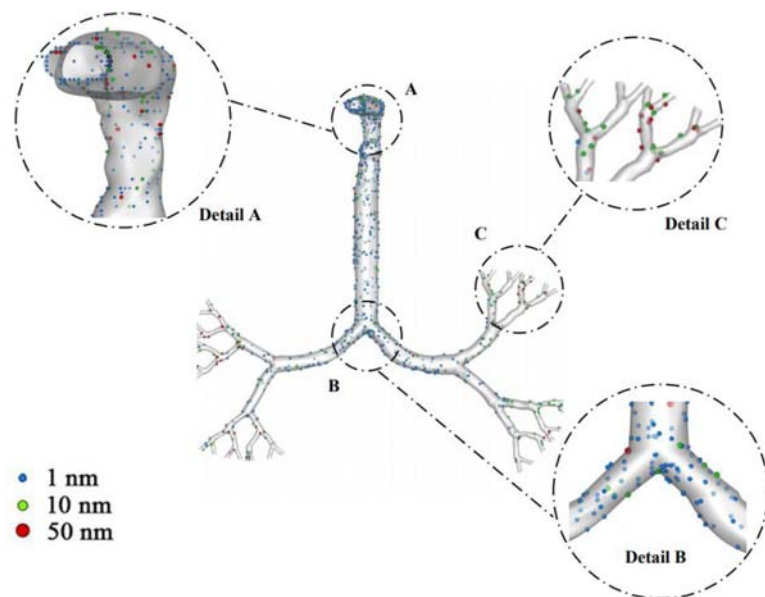
Fig. 12.7 provides deposition fractions for different nanoparticle sizes in the three lung cases. Fig. 12.7A is for the 50-year-old lung, and Fig. 12.7B and C for the 60- and 70-year-old lungs, respectively. Respiratory tract DF follows a U-shaped curve, with minimal DF in the particle size range of 0.1–1.0 µm and increasing diffusive deposition below for nanoparticles and increasing aerodynamic deposition above this range for microparticles (PM<sub>1</sub>–PM<sub>10</sub>). Both larger microparticles and smaller nanoparticles are mostly trapped in the nasopharyngeal upper airways. This assumption was confirmed as seen in Fig. 12.7 with the highest DF rate found for the smallest nanoparticle size of 1 nm in all lung sizes. The maximum DF was found in 50- and 60-year-old lungs at 14% DF for a nanoparticle size of 1 nm. In the mouth–throat (MT) area, trachea (TR), and up to generation 1 (G1) a significantly higher DF was found for the 1 nm particle size in all lung size

**FIGURE 12.7**

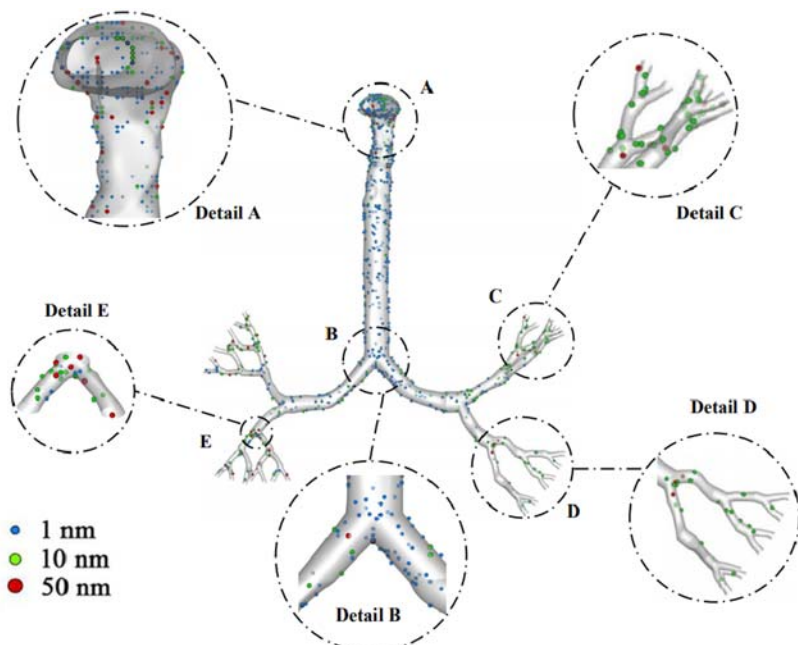
Deposition fraction (DF) hot spots for different nanoparticle diameters at 20 L/min flow rate, (A) 50-year-old lung, (B) 60-year-old lung, and (C) 70-year-old lung. MT: mouth–throat; TR: trachea; G1: generation 1; G2: generation 2; G3: generation 3; G4: generation 4; G5: generation 5.

cases. For nanoparticle sizes of 10 and 50 nm, DF ranged between 1% and 4% in all lung sizes. Furthermore, these nanoparticle sizes also had a higher DF at generation 4 (G4) and generation 5 (G5).

A nanoparticle deposition scenario for the three lung cases is presented in Figs. 12.8, 12.9 and 12.10. The three nanoparticle sizes were injected at a 20 L/min flow rate. Fig. 12.8 presents the deposition scenario of the 50-year-old case, while Figs. 12.9 and 12.10 are the deposition scenarios of the 60- and 70-year-old cases, respectively. In the 50-year-old case (Fig. 12.8), most particles sized 1 nm were trapped in the mouth–throat area (detail A), trachea, and at the bifurcation of generation 1 (detail B). Only a few particles of this size were trapped at the right upper lobe (detail C). A similar deposition pattern was found in the 70-year-old case (Fig. 12.10), however, deposition clusters for this particle size were also found at the bifurcation of generation 2 (detail C). In the 60-year-old case (Fig. 12.9), the mouth–throat area (detail A), trachea, and generation 1 (detail B) again showed the highest deposition rates for the 1 nm particles, however another cluster was found at the bifurcation generation 3 (detail E). Moreover, in this case, only particles

**FIGURE 12.8**

Nanoparticle deposition scenario with deposition hot spots at 20 L/min flow rate for the 50-year-old case.

**FIGURE 12.9**

Nanoparticle deposition scenario with deposition hot spots at 20 L/min flow rate for the 60-year-old case.

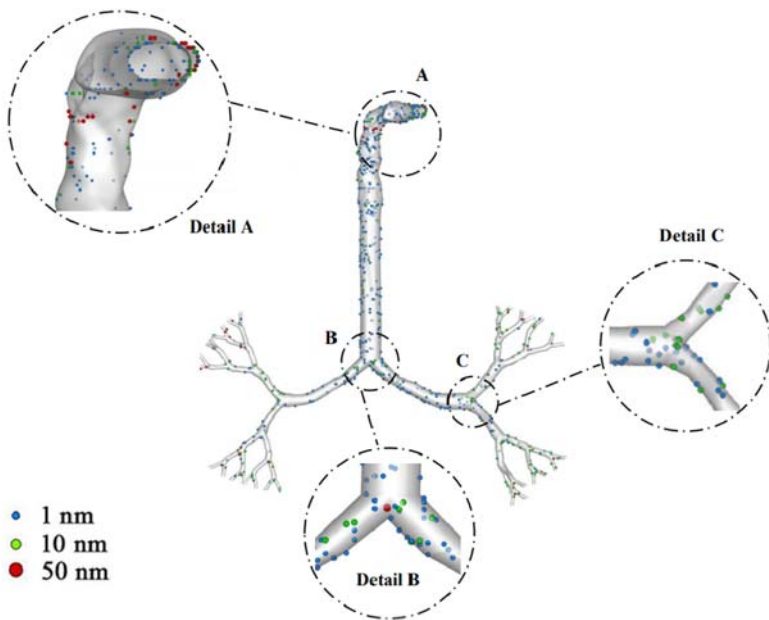


**FIGURE 12.10**

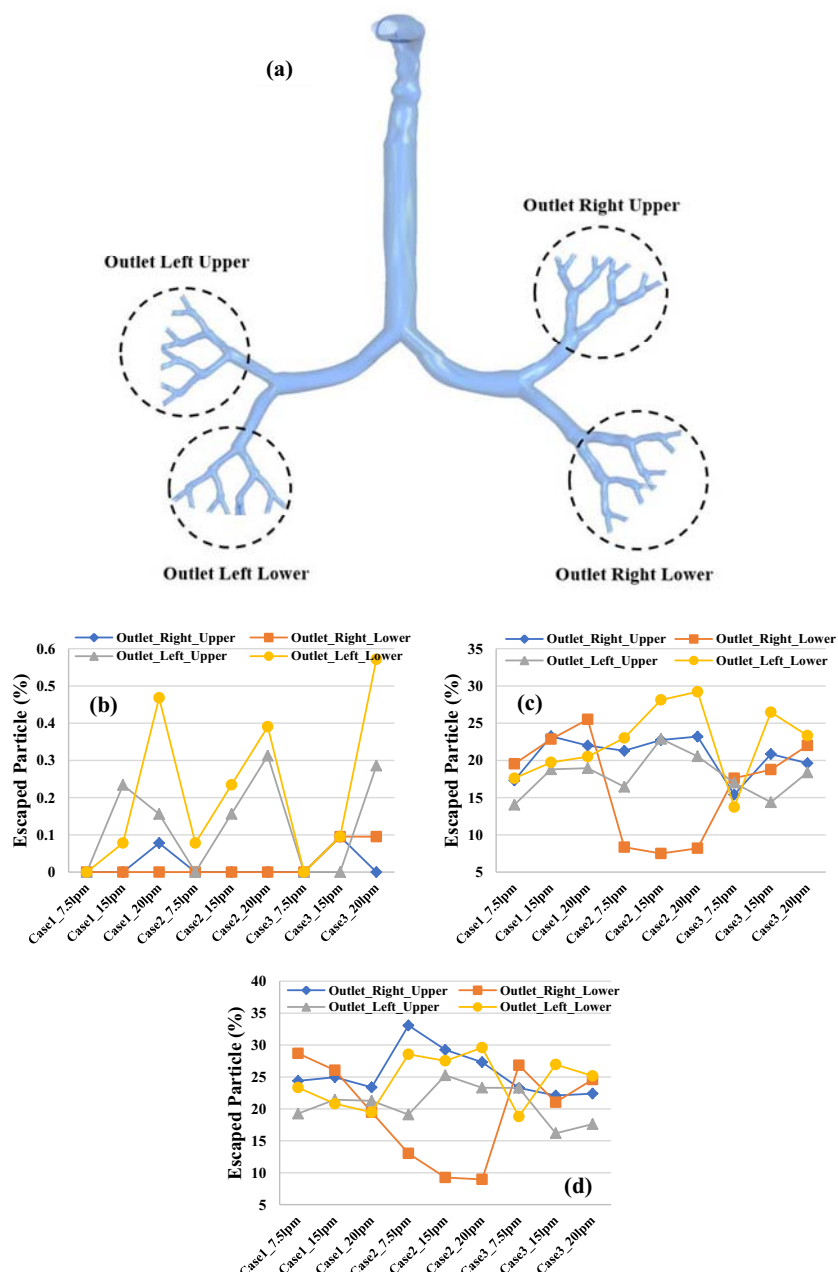
Nanoparticle deposition scenario with deposition hot spots at 20 L/min flow rate for the 70-year-old case.

of size 10 and 50 nm were trapped in the right upper lobes (detail C) and right lower lobes (detail D). These three scenarios support previous findings.

## Escaped particles

While most small nanoparticles of 1 nm diameter were trapped in the oral and upper airways, a residue of particles will pass through generation 5 and travel to the lower generations of the lungs. These particles are shown as escaped particles in Fig. 12.11 at the outlet of generation 5. The outlets of this fifth generation were separated into four areas, the right upper, right lower, left upper, and left lower areas. Fig. 12.11A shows the location of these four outlet areas. Fig. 12.11B presents a graph for the escaped particles of 1 nm size, Fig. 12.11C for 10 nm size, and Fig. 12.11D for 50 nm size.

As seen in Fig. 12.11, typically nanoparticles of 1 and 10 nm size escaped through the left lower lung area outlet in all three lung sizes (Fig. 12.11B and C). The larger 50 nm particles (Fig. 12.11D), escaped mostly through the right upper region outlet. Overall, most nanoparticles escaped through the left lower outlet, while the fewest particles escaped through the right lower outlet. A higher DF was found in the right lung, corresponding to fewer escaped particles through the right lung

**FIGURE 12.11**

Percentage of particles escaped through the fifth generations of lungs for the three lung size cases and three particle sizes, (A) outlet definition, (B) for particle size 1 nm, (C) for particle size 10 nm, and (D) for particle size 50 nm. Case 1: 50-year-old; Case 2: 60-year-old; Case 3: 70-year-old.

outlets. Similarly, a lower DF rate in the left lung resulted in more escaped particles through the left lung outlets.

---

## Conclusions

The simulation of airflow, nanoparticle transport, and particle deposition in the human lung airways provided insights into the understanding of age-related and interpersonal variability-related effects of lung size on particle exposure, which will have an impact on lung pathology:

- Velocity patterns depend on flow rates and lung geometries. Due to its geometry, the left lung generally has higher velocities than the right lung up to the fifth generation.
- The highest pressures were found at the inlet of the mouth area in all three lung sizes, and pressures continually decreased through the generations. The pressure patterns for the 50- and 70-year-old lungs were similar and pressure significantly dropped from generation 4 to 5. In the 60-year-old lung however a significant pressure drop occurred from generation 1–2.
- Deposition fraction is influenced by flow rate and lung size. A higher flow rate results in higher deposition fraction. Smaller particles of 1 nm are mostly trapped in the upper airways in the mouth–throat area, trachea, and generation 1, while larger nanoparticle sizes mostly escape to the lower regions in all three lung sizes. The 50- and 60-year-old lungs have similar deposition rates for 1 nm, which are higher than the deposition rate in the 70-year-old lung.
- Nanoparticles mostly escape to the lower airways and through the left lower outlet of generation 5 for the 50- and 70-year-olds for all particle sizes, and throughout the right upper outlet in the 60-year-old with 50 nm particles.

The improved understanding of pressure variation in the lungs will inform clinical treatment, such as the application of mechanical ventilation in some patient groups for the treatment of asthma and COPD. The prediction of nanoparticle deposition patterns in the lungs will also improve risk assessment for respiratory health in occupational and environmental exposures. Future studies should expand the simulation toward more lung sizes, more lobes, and more particle sizes. The comparison of airflow, nanoparticle transport, and particle deposition in three age groups, children, adults, and the elderly, would be of particular interest in environmental health risk assessment.

---

## Limitations of the approach

- This chapter focused on the airflow and nanoparticle transport in only three different size human lung models, representing a 50-, 60-, and 70-year-old when inhaling only.

- We employed only a small number of lung generations where the end of generation 5 was set to be the outlet for the outflow.
- The same upper airway model was used in all models, and similar geometries for all three cases were reconstructed from the same model.
- Dynamic wall motion was not considered, nor was any airway deformation.
- The effect of mucus was not considered.
- Electromagnetic effects, which can be considerable in nanoparticles, were not considered.
- We applied open outlets and a constant pressure condition at the outlets as boundary conditions.

---

## References

- Bai, Y., Suzuki, A. K., & Sagai, M. (2001). The cytotoxic effects of diesel exhaust particles on human pulmonary artery endothelial cells in vitro: Role of active oxygen species. *Free Radical Biology and Medicine*, 30(5), 555–562.
- Baulig, A., Garlatti, M., Bonvallot, V., Marchand, A., Barouki, R., Marano, F., & Baeza-Squiban, A. (2003). Involvement of reactive oxygen species in the metabolic pathways triggered by diesel exhaust particles in human airway epithelial cells. *American Journal of Physiology-Lung Cellular and Molecular Physiology*, 285(3), L671–L679.
- Cheng, K.-H., Cheng, Y.-S., Yeh, H.-C., Guilmette, R. A., Simpson, S. Q., Yang, Y.-H., & Swift, D. L. (1996). In vivo measurements of nasal airway dimensions and ultrafine aerosol deposition in the human nasal and oral airways. *Journal of Aerosol Science*, 27(5), 785–801.
- Cheng, K.-H., Cheng, Y.-S., Yeh, H.-C., & Swift, D. L. (2007). Deposition of ultrafine aerosols in the head airways during natural breathing and during simulated breath holding using replicate human upper airway casts. *Aerosol Science and Technology*, 41(3), 465–474.
- Cheng, Y.-S., Su, Y.-F., Yeh, H.-C., & Swift, D. L. (1993). Deposition of thoron progeny in human head airways. *Aerosol Science and Technology*, 18(4), 359–375.
- Cheng, K.-H., & Swift, D. L. (1995). Calculation of total deposition fraction of ultrafine aerosol in human extrathoracic and intrathoracic regions. *Aerosol Science and Technology*, 22(2), 194–201.
- Cheng, Y.-S., Yamada, Y., Yeh, H.-C., & Swift, D. L. (1988). Diffusional deposition of ultrafine aerosols in a human nasal cast. *Journal of Aerosol Science*, 19(6), 741–751.
- Cheng, Y. S., Yeh, H. C., Guilmette, R. A., Simpson, S. Q., Cheng, K. H., & Swift, D. L. (1996). Nasal deposition of ultrafine particles in human volunteers and its relationship to airway geometry. *Aerosol Science and Technology*, 25(3), 274–291.
- Dockery, D. W., Luttmann-Gibson, H., Rich, D. Q., Link, M. S., Mittleman, M. A., Gold, D. R., Koutrakis, P., Schwartz, J. D., & Verrier, R. L. (2005). Association of air pollution with increased incidence of ventricular tachyarrhythmias recorded by implanted cardioverter defibrillators. *Environmental Health Perspectives*, 113(6), 670–674.
- Dong, J., Shang, Y., Tian, L., Inthavong, K., Qiu, D., & Tu, J. (2019). Ultrafine particle deposition in a realistic human airway at multiple inhalation scenarios. *International Journal for Numerical Methods in Biomedical Engineering*, 35(7), e3215.

- Fan, Z., Holmes, D., Sauret, E., Islam, M. S., Saha, S. C., Ristovski, Z., & Gu, Y. T. (2021). A multiscale modelling method incorporating spatial coupling and temporal coupling into transient simulations of the human airways. *International Journal for Numerical Fluids*, 93(3), 2905–2920.
- Farhadi Ghalati, P., Keshavarzian, E., Abouali, O., Faramarzi, A., Tu, J., & Shakibafard, A. (2012). Numerical analysis of micro- and nano-particle deposition in a realistic human upper airway. *Computers in Biology and Medicine*, 42(1), 39–49.
- Frampton, M. W. (2001). Systemic and cardiovascular effects of airway injury and inflammation: Ultrafine particle exposure in humans. *Environmental Health Perspectives*, 109(Suppl. 4), 529–532.
- Frampton, M. W. (2007). Does inhalation of ultrafine particles cause pulmonary vascular effects in humans? *Inhalation Toxicology*, 19(Suppl. 1), 75–79.
- Frampton, M. W., Utell, M. J., Zareba, W., Oberdorster, G., Cox, C., Huang, L. S., Morrow, P. E., Lee, F. E., Chalupa, D., Frasier, L. M., Speers, D. M., & Stewart, J. (2004). Effects of exposure to ultrafine carbon particles in healthy subjects and subjects with asthma. *Research Report (Health Effects Institute)*, 126(126), 1–47. discussion 9-63.
- Garshick, E., Laden, F., Hart, J. E., Rosner, B., Davis, M. E., Eisen, E. A., & Smith, T. J. (2008). Lung cancer and vehicle exhaust in trucking industry workers. *Environmental Health Perspectives*, 116(10), 1327–1332.
- Ghosh, A., Islam, M. S., & Saha, S. C. (2020). Targeted drug delivery of magnetic nanoparticle in the specific lung region. *Computation*, 8(1), 10.
- Gradon, L., & Yu, C. P. (1989). Diffusional particle deposition in the human nose and mouth. *Aerosol Science and Technology*, 11(3), 213–220.
- Gu, Q., Qi, S., Yue, Y., Shen, J., Zhang, B., Sun, W., Qian, W., Islam, M. S., Saha, S. C., & Wu, J. (2019). Structural and functional alterations of the tracheobronchial tree after left upper pulmonary lobectomy for lung cancer. *BioMedical Engineering OnLine*, 18, 1–18.
- Haider, A., & Levenspiel, O. (1989). Drag coefficient and terminal velocity of spherical and nonspherical particles. *Powder Technology*, 58(1), 63–70.
- Hendryx, M., Islam, M. S., Dong, G.-H., & Paul, G. (2020). Air pollution emissions 2008–2018 from australian coal mining: Implications for public and occupational health. *International Journal of Environmental Research and Public Health*, 17, 1570.
- Holder, A. L., Lucas, D., Goth-Goldstein, R., & Koshland, C. P. (2008). Cellular response to diesel exhaust particles strongly depends on the exposure method. *Toxicological Sciences*, 103(1), 108–115.
- Hsiao, I. L., & Huang, Y. J. (2013). Effects of serum on cytotoxicity of nano- and micro-sized ZnO particles. *Journal of Nanoparticle Research*, 15, 1829.
- Inthavong, K., Choi, L.-T., Tu, J., Ding, S., & Thien, F. (2010). Micron particle deposition in a tracheobronchial airway model under different breathing conditions. *Journal of Medical Engineering*, 32(10), 1198–1212.
- Inthavong, K., Tu, J., & Ahmadi, G. (2009). Computational modelling of gas-particle flows with different particle morphology in the human nasal cavity. *The Journal of Computational Multiphase Flows*, 1(1), 57–82.
- Inthavong, K., Zhang, K., & Tu, J. (2011). Numerical modelling of nanoparticle deposition in the nasal cavity and the tracheobronchial airway. *Computer Methods in Biomechanics and Biomedical Engineering*, 14(7), 633–643.
- Islam, M. S., Gu, T., Farkas, A., Paul, G., & Saha, S. C. (2020). Helium-Oxygen mixture model for particle transport in CT-based upper airways. *International Journal of Environmental Research and Public Health*, 17, 3574.

- Islam, M. S., Larpruenrudee, P., Hossain, S. I., Rahimi-Gorji, M., Gu, Y., Saha, S. C., & Paul, G. (2021). Polydisperse aerosol transport and deposition in upper airways of age-specific lung. *International Journal of Environmental Research and Public Health*, 18(12).
- Islam, M. S., Larpruenrudee, P., Paul, A. R., Paul, G., Gemci, T., Gu, Y., & Saha, S. C. (2021). SARS CoV-2 aerosol: How far it can travel to the lower airways? *Physics of Fluids*, 33(6).
- Islam, M. S., Larpruenrudee, P., Saha, S., Pourmehran, O., Paul, A. R., Gemci, T., Collins, R., Paul, G., & Gu, Y. (2021c). How SARS coronavirus-2 aerosol propagate through the age-specific upper airways. *Physics of Fluids*, 33(8), 081911.
- Islam, M. S., Paul, G., Ong, H. X., Young, P. M., Gu, Y. T., & Saha, S. C. (2020). A review of respiratory anatomical development, air flow characterization and particle deposition. *International Journal of Environmental Research and Public Health*, 17, 380.
- Islam, M. S., Saha, S. C., Gemci, T., Yang, I. A., Sauret, E., & Gu, Y. T. (2018). Polydisperse microparticle transport and deposition to the terminal bronchioles in a heterogeneous vasculature tree. *Scientific Reports*, 8(1), 1–9.
- Islam, M. S., Saha, S. C., Gemci, T., Yang, I. A., Sauret, E., Ristovski, Z., & Gu, Y. T. (2019). Euler-Lagrange prediction of diesel-exhaust polydisperse particle transport and deposition in lung: Anatomy and turbulence effects. *Scientific Reports*, 9(1), 12423.
- Islam, M. S., Saha, S. C., Sauret, E., Gemci, T., Yang, I. A., & Gu, Y. T. (2017). Ultrafine particle transport and deposition in a large scale 17-generation lung model. *Journal of Biomechanics*, 64, 16–25.
- Islam, M. S., Saha, S. C., Sauret, E., Gu, Y. T., & Ristovski, Z. (2015). Numerical investigation of aerosol particle transport and deposition in realistic lung airway. *Proceeding of the 6th International Conference on Computational Methods*, 2, 1–9.
- Islam, M. S., Saha, S. C., Sauret, E., Ong, H., Young, P., & Gu, Y. (2019). Euler-Lagrange approach to investigate respiratory anatomical shape effects on aerosol particle transport and deposition. *Toxicology Research and Application*, 3, 1–15.
- Jakobsson, J. K. F., Aaltonen, H. L., Nicklasson, H., Gudmundsson, A., Rissler, J., Wollmer, P., & Londahl, J. (2018). Altered deposition of inhaled nanoparticles in subjects with chronic obstructive pulmonary disease. *BMC Pulmonary Medicine*, 18(1), 129.
- Kagawa, J. (2002). Health effects of diesel exhaust emissions—a mixture of air pollutants of worldwide concern. *Toxicology*, 181–182, 349–353.
- Kelly, J. T., Asgharian, B., Kimbell, J. S., & Wong, B. A. (2004). Particle deposition in human nasal airway replicas manufactured by different methods. Part II: Ultrafine particles. *Aerosol Science and Technology*, 38(11), 1072–1079.
- Kimbell, J. S., Overton, J. H., Subramaniam, R. P., Schlosser, P. M., Morgan, K. T., Conolly, R. B., & Miller, F. J. (2001). Dosimetry modeling of inhaled formaldehyde: Binning nasal flux predictions for quantitative risk assessment. *Toxicological Sciences*, 64(1), 111–121.
- Kim, J., Heise, R. L., Reynoldsm, A. M., & Pidaparti, R. M. (2017). Aging effects on airflow dynamics and lung function in human bronchioles. *PLoS One*, 12(8).
- Kleinstreuer, C., Zhang, Z., & Donohue, J. F. (2008). Targeted drug-aerosol delivery in the human respiratory system. *Annual Review of Biomedical Engineering*, 10, 195–220.
- Kumar, B., Srivastav, V. K., Jain, A., & Paul, A. R. (2019). Study of numerical schemes for the CFD simulation of human airways. *International Journal of Integrated Engineering*, 11(8), 32–40.
- Larpruenrudee, P., Islam, M. S., Paul, G., Paul, A. R., Gu, Y. T., & Saha, S. C. (2021). Model for Pharmaceutical aerosol transport through stenosis airway. *Handbook of Lung Targeted Drug Delivery*, 91–128 (CRC Press).

- Lewtas, J. (2007). Air pollution combustion emissions: Characterization of causative agents and mechanisms associated with cancer, reproductive, and cardiovascular effects. *Mutation Research*, 636(1–3), 95–133.
- Li, A., & Ahmadi, G. (1992). Dispersion and deposition of spherical particles from point sources in a turbulent channel flow. *Aerosol Science and Technology*, 16, 209–226.
- Liu, Y., Matida, E. A., Gu, J., & Johnson, M. R. (2007). Numerical simulation of aerosol deposition in a 3-D human nasal cavity using RANS, RANS/EIM, and LES. *Journal of Aerosol Science*, 38(7), 683–700.
- McClellan, R. O. (1987). Health effects of exposure to diesel exhaust particles. *Annual Review of Pharmacology and Toxicology*, 27, 279–300.
- Moghadas, H., Abouali, O., Faramarzi, A., & Ahmadi, G. (2011). Numerical investigation of septal deviation effect on deposition of nano/microparticles in human nasal passage. *Respiratory Physiology & Neurobiology*, 177(1), 9–18.
- Moller, P., Folkmann, J. K., Forchhammer, L., Brauner, E. V., Danielsen, P. H., Risom, L., & Loft, S. (2008). Air pollution, oxidative damage to DNA, and carcinogenesis. *Cancer Letters*, 266(1), 84–97.
- Moskal, A., Sosnowski, T. R., & Grdon, L. (2010). Inhalation and deposition of nanoparticles: Fundamentals, phenomenology and particle aspects. *Inhalation and Health Effects*, 113–144 (Dordrecht: Springer).
- Niewoehner, D. E., & Eleinerman, J. (1974). Morphologic basis of pulmonary resistance in the human lung and effects of aging. *Journal of Applied Physiology*, 36, 412–418.
- Nogueira, J. B. (2009). Air pollution and cardiovascular disease. *Revista Portuguesa de Cardiologia*, 28(6), 715–733.
- Oberdörster, G. (2000). Pulmonary effects of inhaled ultrafine particles. *International Archives of Occupational and Environmental Health*, 74, 1–8.
- Oberdorster, G., Gelein, R. M., Ferin, J., & Weiss, B. (1995). Association of particulate air pollution and acute mortality: Involvement of ultrafine particles? *Inhalation Toxicology*, 7(1), 111–124.
- Oberdorster, G., Maynard, A., Donaldson, K., Castranova, V., Fitzpatrick, J., Ausman, K., Carter, J., Karn, B., Kreyling, W., Lai, D., Olin, S., Monteiro-Riviere, N., Warheit, D., Yang, H., & Group, I. R. F. R. S. I. N. T. S. W. (2005). Principles for characterizing the potential human health effects from exposure to nanomaterials: Elements of a screening strategy. *Particle and Fibre Toxicology*, 2, 8.
- Oberdorster, G., Oberdorster, E., & Oberdorster, J. (2005). Nanotoxicology: An emerging discipline evolving from studies of ultrafine particles. *Environmental Health Perspectives*, 113(7), 823–839.
- Olvera, H. A., Perez, D., Clague, J. W., Cheng, Y. S., Li, W. W., Amaya, M. A., Burchiel, S. W., Berwick, M., & Pingitore, N. E. (2012). The effect of ventilation, age, and asthmatic condition on ultrafine particle deposition in children. *Pulmonary Medicine*, 2012, 736290.
- Park, S. K., O'Neill, M. S., Vokonas, P. S., Sparrow, D., & Schwartz, J. (2005). Effects of air pollution on heart rate variability: The VA normative aging study. *Environmental Health Perspectives*, 113(3), 304–309.
- Pedata, P., Garzillo, E. M., & Sannolo, N. (2010). [Ultrafine particles and effects on the body: Review of the literature]. *G Ital Med Lav Ergon*, 32(1), 23–31.
- Pourmehran, O., Arjomandi, M., Cazzolato, B., Ghanadi, F., & Tian, Z. (2020). The impact of geometrical parameters on acoustically driven drug delivery to maxillary sinuses. *Biomechanics and Modeling in Mechanobiology*, 19, 557–575.

- Pourmehran, O., Arjomandi, M., Cazzolato, B., Tian, Z., Vreugde, S., Javadiyan, S., Psaltis, A. J., & Wormald, P. J. (2021). Acoustic drug delivery to the maxillary sinus. *International Journal of Pharmaceutics*, 606, 120927.
- Pourmehran, O., Cazzolato, B., Tian, Z., & Arjomandi, M. (2020). Acoustically-driven drug delivery to maxillary sinuses: Aero-acoustic analysis. *European Journal of Pharmaceutical Sciences*, 151, 105398.
- Pourmehran, O., Gorji, T. B., & Gorji-Bandpy, M. (2016). Magnetic drug targeting through a realistic model of human tracheobronchial airways using computational fluid and particle dynamics. *Biomechanics and Modeling in Mechanobiology*, 15, 1355–1374.
- Rahman, MdM., Zhao, M., Islam, M. S., Dong, K., & Saha, S. C. (2021). Aging effects on airflow distribution and micron-particle transport and deposition in a human lung using CFD-DPM approach. *Advanced Powder Technology*.
- Rissler, J., Gudmundsson, A., Nicklasson, H., Swietlicki, E., Wollmer, P., & Londahl, J. (2017). Deposition efficiency of inhaled particles (15–5000 nm) related to breathing pattern and lung function: An experimental study in healthy children and adults. *Particle and Fibre Toxicology*, 14(1), 10.
- Schraufnagel, D. E. (2020). The health effects of ultrafine particles. *Experimental & Molecular Medicine*, 52(3), 311–317.
- Singh, P., Raghav, V., Padhmashali, V., Paul, G., Islam, M. S., & Saha, S. C. (2020). Airflow and particle transport prediction through stenosis airways. *International Journal of Environmental Research and Public Health*, 17(3), 1119.
- Sosnowski, T. R. (2011). Importance of airway geometry and respiratory parameters variability for particle deposition in the human respiratory tract. *Journal of Thoracic Disease*, 3, 153–155.
- Swift, D. L., & Strong, J. C. (1996). Nasal deposition of ultrafine  $^{218}\text{Po}$  aerosols in human subjects. *Journal of Aerosol Science*, 27(7), 1125–1132.
- Wang, S. M., Inthavong, K., Wen, J., Tu, J. Y., & Xue, C. L. (2009). Comparison of micron- and nanoparticle deposition patterns in a realistic human nasal cavity. *Respiratory Physiology & Neurobiology*, 166(3), 142–151.
- Worth Longest, P., & Xi, Jinxiang (2007). Effectiveness of direct Lagrangian tracking models for simulating nanoparticle deposition in the upper airways. *Aerosol Science and Technology*, 41(4), 380–397.
- Xi, J., Berlinski, A., Zhou, Y., Greenberg, B., & Ou, X. (2012). Breathing resistance and ultrafine particle deposition in nasal-laryngeal airways of a newborn, an infant, a child, and an adult. *Annals of Biomedical Engineering*, 40(12), 2579–2595.
- Xi, J., & Longest, P. W. (2008). Numerical predictions of submicrometer aerosol deposition in the nasal cavity using a novel drift flux approach. *International Journal of Heat and Mass Transfer*, 51(23–24), 5562–5577.
- Xi, J., & Longest, P. W. (2009). Characterization of submicrometer aerosol deposition in extra-thoracic airways during nasal exhalation. *Aerosol Science and Technology*, 43(8), 808–827.
- Xu, G., & Yu, C. (1986). Effects of age on deposition of inhaled aerosols in the human lung. *Aerosol Science and Technology*, 5(3), 349–357.
- Zamankhan, P., Ahmadi, G., Wang, Z., Hopke, P. K., Cheng, Y.-S., Su, W. C., & Leonard, D. (2006). Airflow and deposition of nano-particles in a human nasal cavity. *Aerosol Science and Technology*, 40(6), 463–476.
- Zhang, Z., & Kleinstreuer, C. (2011). Computational analysis of airflow and nanoparticle deposition in a combined nasal–oral–tracheobronchial airway model. *Journal of Aerosol Science*, 42(3), 174–194.
- Zhu, N., Zhang, D., Wang, W., Li, X., Yang, B., Song, J., Zhao, X., Huang, B., Shi, W., Lu, R., Niu, P., Zhan, F., Ma Weibel, E. R., Cournand, A. F., & Richards, D. W. (1963). *Morphometry of the human lung*, 1. Berlin: Springer.

# Aerosolized airborne bacteria and viruses inhalation: Micro-bioaerosols deposition effects through upper nasal airway inhalation\*

# 13

Hamed Mortazavi<sup>1</sup>, Hamidreza Mortazavy Beni<sup>1</sup>, Mohammad Saidul Islam<sup>2</sup>,  
Gunther Paul<sup>3</sup>

<sup>1</sup>Department of Biomedical Engineering, Arsanjan Branch, Islamic Azad University, Arsanjan, Iran; <sup>2</sup>School of Mechanical and Mechatronic Engineering, University of Technology Sydney (UTS), Ultimo, NSW, Australia; <sup>3</sup>Australian Institute of Tropical Health and Medicine, James Cook University, Townsville, QLD, Australia

## Chapter outline

Nomenclature .....	276
Introduction .....	276
Materials and method .....	278
Computational model .....	278
Governing equations .....	279
Results .....	280
Discussion .....	283
Conclusion .....	285
Declaration of competing interest .....	286
Acknowledgments .....	286
References .....	286

\* All procedures performed in studies involving human participants were in accordance with the ethical standards of the institutional and/or national research committee and with the 1964 Helsinki declaration and its later amendments or comparable ethical standards.

---

## Nomenclature

Body forces (N)	$F_i$
Brownian force (N)	$F_x$
Cunningham correction factor	$C_c$
Fluid passage path hydraulic diameter	$d_c$
Fluid velocity (m/s)	$u_f$
Gravitational constant (m/s <sup>2</sup> )	$g$
Microaerosol velocity (m/s)	$u_i^P$
Normal vector	$n$
Particle diameter (m)	$d$
Pressure (Pa)	$P$
Reynolds number	$Re$
Stokes number	$St^P$
Structural displacement (m)	$D_i$
Time (s)	$t$
Velocity (m/s)	$U$
X Cartesian coordinate	$x_i$
Y Cartesian coordinate	$x_j$
Young's modulus (kpa)	$E$

## Greek symbols

Average molecular distance for air ( $\mu\text{m}$ )	$\lambda$
Characteristic time (s)	$\tau$
Density (kg/m <sup>3</sup> )	$\rho$
Dynamic viscosity (N.s/m <sup>2</sup> )	$\mu$
Fluid stress tensor	$\sigma_{ij}^f$
Kinematic viscosity (m <sup>2</sup> /s)	$\nu$
Kronecker delta	$\delta_{ij}$
Particle density (kg/m <sup>3</sup> )	$\rho^P$
Poisson's ratio	$\vartheta$
Solid stress tensor	$\sigma_{ij}^s$
Strain tensor	$\epsilon_{ij}$

---

## Introduction

Respiration may introduce aerosolized airborne bacteria, viruses, or bioaerosol pollutants into the respiratory airways. While spirometry studies have been conducted for a long time, the enormous development in computational methods has permitted analytic studies of respiratory processes, including the effects of breathing through the nasal passage, and the transmission and deposition of inhaled fine bio-aerosols, such as airborne bacteria and virus particles in both the upper and lower airways. The respiratory tract has a complicated geometry which is difficult to reconstruct even when using computerized modeling. More recently, however, using

sophisticated advanced imaging techniques, more realistic and intricate geometric models of human airways could be developed to support predictive analytic studies.

Bioaerosols affect human health when inhaled due to the presence of pathogens. Even in regular conversations, bacterial and viral aerosols with diameters of less or equal than 10  $\mu\text{m}$  can float in the air (Burgstaller et al., 2017; Shiu et al., 2019). When such aerosols are inhaled, an analysis of Shanley et al. (2008) under a steady flow condition illustrated that the deposition in the nasal cavity increased with larger particle size and flow velocity. In another study by Kleinstreuer and Zhang (2010), turbulent respiratory system flow was modeled. Islam et al. (2020) depicted that neither Euler–Lagrange (E-L) nor Euler–Euler (E-E) methods influenced the deposition patterns of nanoparticles with a diameter of 50 nm at a flow rate of 25 L/min. Ma et al. (2019) exploited a standard Discrete Phase Model (DPM) method to model particle deposition, and the results showed how particle deposition was affected by a narrow throat path. The reduction of the cross-sectional area of the pharynx in the epiglottis had a significant impact on the flow field in the airways, and oral inhalation affected the regional deposition. Keyhani et al. (1995) found that the highest velocity of inhaled air alongside the nasal floor occurred under the lower turbinate in the main nasal route. Moreover, weak airflow occurred in the central airway, between the lower and central turbinate and the septum. About 30% of an inhaled nasal volume flow rate passes under the lower turbinate, and about 10% passes through the olfactory airway. Hörschler et al. (2003) used a numerical simulation of airflow in a human nasal cavity multiblock structural grid model and compared their simulation results with experimental data. In the nostrils, inhalation and exhalation at rest were simulated under laminar conditions. Grgic et al. (Grgic et al., 2004a, b) illustrated that aerosol deposition, caused by morphological limitations of the pharynx, glottal, and flow jets, was more common in the larynx and trachea. Also, they found that the deposition efficiency of particles was related to their inertia parameters (Grgic et al., 2004a, b; Jin. et al., 2007; Xi & Longest, 2007; Jayaraju et al., 2007; Li et al., 2014). Heenan et al. (Heenan et al., 2004) showed a strong relationship between local deposition and the local fluid velocity field. The level of local deposition was strongly related to both velocity and curvature of the flow. Shi et al. (2006) found that tiny particles  $\leq 5$  nm in diameter were absorbed more rapidly, while larger particles had higher toxicity and therapeutic effects. Xi and Longest (2008) examined particles with 1 nm up to 1  $\mu\text{m}$  in size at inhalation flow rates of 4–30 L/min. Under these circumstances, turbulence was visible only in the nasal valve area and the nasopharynx posterior region. Chen et al. (2012) found that secondary flow contributed to particle deposition in inhalation. Secondary flow along the respiratory stream direction is the result of the generation, vanishing, and movement of vortex lines. Nicolaou and Zaki (2013) provided insight into how geometry changes affect aerosol deposition and the related dispersion of the deposition data. The assessment of flow fields in different nasal, mouth, and throat geometries helped in investigating the cause of deposition

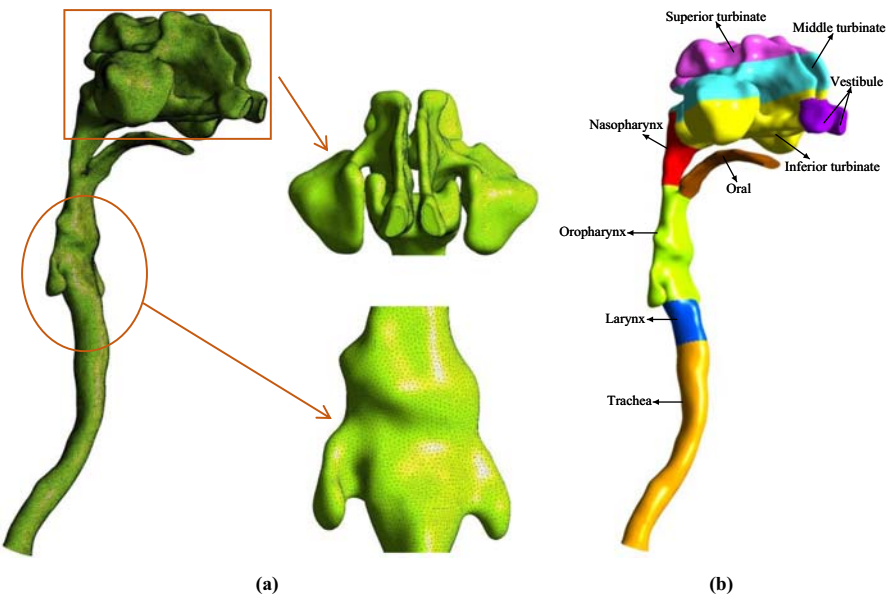
patterns. Shinneeb and Pollard (2012) showed that the nature of flow in the respiratory system is three-dimensional and that it is associated with recirculation, jet-like and sink-like forms of flow. Yet little information is available on aerosol deposition patterns in the nasal part of the respiratory system. The Fluid–Structure Interaction (FSI) method (Mortazavy Beni et al., 2019a, b) will be forth on used to model the complex geometry of the respiratory system to simulate aerosol deposition. This chapter describes the investigation of bacterial and viral effects from bioaerosols of  $\leq 10 \mu\text{m}$  diameter on the nasal upper human respiratory system. Small microaerosols can pass through ordinary respirator masks and contaminate the environment or the mask wearer (Shiu et al., 2019), while such masks are more useful for filtering aerosols of  $>10 \mu\text{m}$  diameter (Leung et al., 2020). Realistic geometry is necessary in respiratory system modeling, and viscoelastic behavior of the respiratory system affects the results based on the FSI method.

---

## Materials and method

### Computational model

The model used in this study is derived from a 30-year-old healthy man without respiratory indications and was presented in a previous study, in which the validity of the model was demonstrated in terms of its turbulence characteristics and the behavior of the elastic wall boundary condition (Mortazavy Beni et al., 2019a, b) of the respiratory system. This model could accurately predict the deposition of bacterial and viral aerosols in the human upper respiratory system by injecting droplets through upper airway inhalation (Mortazavi et al., 2020; Mortazavy Beni et al., 2021a, b). To construct the airway model, CT scans were obtained while the person was in a supine posture. Under professional radiographer supervision, the boundary between the airway mucosa and air in the upper respiratory tract was defined in each slice of the CT scans. The three-dimensional (3D) model of the upper airway was then generated from the CT images. The 3D model includes the nasal cavity, pharynx, larynx, and trachea. The slice boundaries were imported to ANSYS 2021 R1, a Computational Fluid Dynamics preprocessor software, where the boundaries were connected and smoothed to produce a coherent volume. Eventually, an unstructured triangular hybrid volume mesh was generated inside the airway passage. Details of the reconstruction of geometry and meshing of this model have been presented in Mortazavy et al. (Mortazavy Beni et al., 2019a, b) and are not repeated here. Fig. 13.1 shows the meshed geometry and segmentation of the computational model. Due to the importance of the nasal area and its complex geometry, this area is subdivided into three essential segments: superior turbinate, the middle turbinate, and the inferior turbinate. The model applies air inhaled through the nose. The DPM method is used to inject aerosols into the model. The FSI model includes variations in bacterial and viral aerosol size and density at a low airflow velocity.

**FIGURE 13.1**

Segmentation and meshing of the computational model. (A) Mesh generation. (B) Anatomical segmentation of the 3D model.

### Governing equations

Air is considered as a viscous and incompressible fluid. The governing equations for the quasi-steady turbulent flow in the human respiratory system are the Navier–Stokes and continuity equations:

$$\frac{\partial U_i}{\partial x_i} = 0 \quad (13.1)$$

$$U_i \frac{\partial U_j}{\partial x_i} = -\frac{1}{\rho} \frac{\partial P}{\partial x_i} + \frac{\partial}{\partial x_i} \left[ \nu \left( \frac{\partial U_i}{\partial x_j} + \frac{\partial U_j}{\partial x_i} \right) - \bar{U}_i' \bar{U}_j' \right] + G_i \quad (13.2)$$

In these equations, the parameters  $U$ ,  $\rho$ ,  $P$ ,  $v$ , and  $G_i$  of the air-fluid represent speed, density, pressure, kinematic viscosity, and a gravity term, respectively. Also,  $\mathbf{i}$  and  $\mathbf{j}$  represent the Cartesian coordinates. Based on Kleinstreuer and Zhang (2010), the E-L method is selected to investigate the microaerosol particle movement along with the fluid. The equation of motion for the microaerosol is

$$\frac{du_i^P}{dt} = \left( \frac{18\mu}{\rho^P d^2 C_c} \right) (U_i - u_i^P) + g_i + F_x \quad (13.3)$$

where  $\mu$ ,  $\rho^P$ ,  $d$ ,  $g_i$ , and  $F_x$  are viscosity, particle density, particle diameter, a gravity term, and the Brownian Force, respectively. Furthermore, in this equation,  $\frac{dx_i}{dt} = u_i^P$ .  $C_c$  is the Cunningham correction factor, which is equal to (ANSYS-Fluent, 2006)

$$C_c = 1 + \frac{2\lambda}{d} \left( 1.257 + 0.4e^{-\frac{1.1d}{2\lambda}} \right) \quad (13.4)$$

In this equation,  $\lambda$  is the average molecular distance for air and is assumed to be 0.065  $\mu\text{m}$ . The Stokes number is used to calculate the ratio characteristic time of the aerosol per the characteristic time scale of the flow, which is defined as

$$St^P = \frac{\tau u_f}{d_c} \quad (13.5)$$

Here  $\tau$  is the characteristic time,  $u_f$  is the velocity of the fluid, and  $d_c$  is the hydraulic diameter of the tract through which the fluid passes. By inserting the residence time for the characteristic time, the following equation is obtained:

$$St^P = \frac{\rho^P d^2 u_f}{18\mu d_c} \quad (13.6)$$

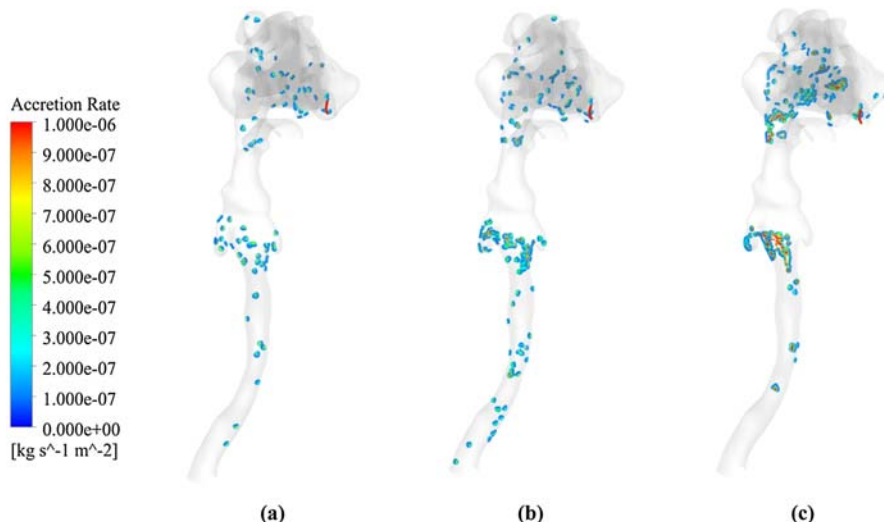
The walls of the airway are considered elastic walls. Also, it is assumed that the aerosols are absorbed in the first encounter with the wall. More details on the governing equations of FSI are mentioned in Mortazavy et al. (Mortazavy Beni et al., 2019a, b). In the present model, based on Shanley et al. (2008), fixed boundary conditions are applied to the nostrils and the end of the trachea (carina zone) where the flow enters and exits, respectively, and a wall boundary condition is applied to the mouth entrance. The geometry is analyzed in Ansys 2021 R1. ANSYS Fluent converts and solves the governing equations into algebraic equations using the finite volume method. Here, the second-order upwind scheme is used for the momentum equation discretization, and the SIMPLE algorithm is used to couple the pressure and velocity equations. The k-epsilon turbulence model used is a subcategory of the RANS group, which has been shown to produce viable results in the use of DPM in the study of deposition mapping in the human respiratory system (Ma et al., 2019). In this simulation, 25 °C warm air enters the model through the nostrils. The average infectious aerosol density is assumed to be  $\rho_p = 1119 \text{ kg/m}^3$  (Decaro, 2011), and the size range of aerosol diameters in a normal conversation is considered to lie between 1 and 10  $\mu\text{m}$  (Zhang et al., 2015). For the respiratory wall, the expansion of the Young's modulus and Poisson's ratio are considered in the range of  $0.51 \text{ kpa} \leq E \leq 100.64 \text{ kpa}$  and  $\vartheta = 0.3 - 0.45$ , respectively (Birch & Srodon, 2009).

## Results

In this study, airflow enters from the nostrils with the mouth closed through the respiratory tract; the study then investigates airflow and aerosol parameters and

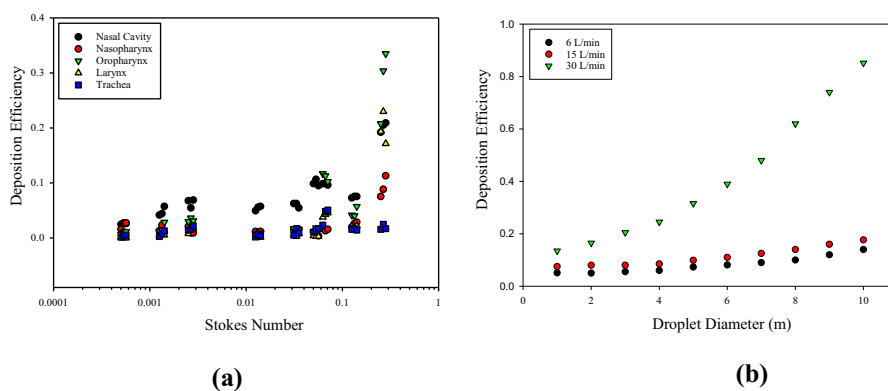
analyzes wall deformation. Three flow rates of 6, 15, and 30 L/min are considered in the study along with aerosol diameters of 1–10  $\mu\text{m}$ . During normal breathing in a state of rest, a man breathes about  $500 \text{ cm}^3$  or half a liter of air per inhalation, which is also called the tidal volume (TV) (Cameron et al., 1992). TV was confirmed through spirometry testing of patients (Mortazavy Beni et al., 2019a, b). The average minute ventilation is then 6 L/min. In Fig. 13.2, the aerosol deposition pattern contours are presented for 1, 5, and 10  $\mu\text{m}$  aerosol diameter and a 30 L/min flow rate. After entry through the nostrils, the bacterial and viral contamination zones are in sequence the vestibule, inferior turbinate, nasopharynx, oropharynx, larynx, and trachea arch. Aerosol deposition increases in these zones with aerosol diameter; as a result, less bacterial and viral aerosol matter reaches the lungs for larger aerosols.

To further analyze the relationship between the fluid, aerosol diameter, and airflow rate, deposition efficiency is plotted against the Stokes number and aerosol diameter in Fig. 13.3. In Fig. 13.3A at higher Stokes numbers beyond 0.2 deposition efficiency increases exponentially only in some parts of the respiratory system, however deposition efficiency does not exceed 40%. The highest and the lowest deposition rates are found in the oropharynx and the trachea, respectively. Fig. 13.3B shows the effect of flow rate and aerosol diameter on deposition efficiency in the respiratory system. In general, deposition efficiency increases with flow rate. Aerosol diameter has a significantly higher impact on deposition efficiency at a flow rate of 30 L/min compared to 6 or 15 L/min. While aerosol diameter has a negligible impact on deposition efficiency at lower flow rates, aerosol deposition efficiency increases from 15% (1  $\mu\text{m}$ ) to 85% (10  $\mu\text{m}$ ) at the higher flow rate of 30 L/min.



**FIGURE 13.2**

Aerosol deposition for 1, 5, and 10  $\mu\text{m}$  aerosol diameter at 30 L/min airflow. (A) Nose inlet 1  $\mu\text{m}$  aerosol. (B) Nose inlet 5  $\mu\text{m}$  aerosol. (C) Nose inlet 10  $\mu\text{m}$  aerosol.

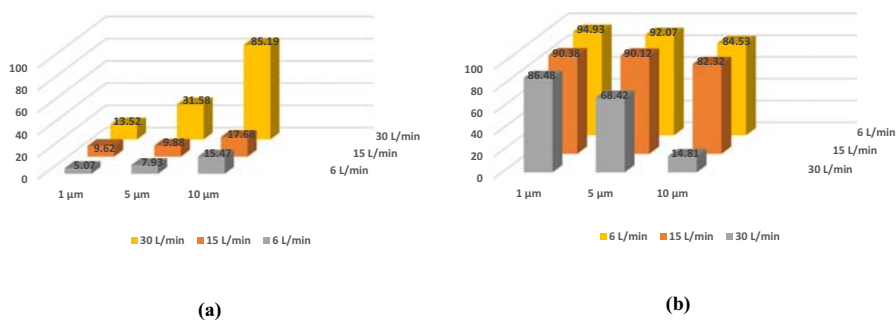
**FIGURE 13.3**

Deposition efficiency in the nasopharyngeal and upper respiratory system. (A) As a function of the Stokes number. (B) As a function of aerosol diameter.

**Table 13.1** summarizes the upper respiratory tract deposition efficiency of aerosols and their throughput to the lungs dependent on flow rate and aerosol diameter. The last two columns of this table present the average bioaerosol deposition percentage in the upper respiratory airway, and the average escaped bacterial and viral aerosol throughput to the lungs when averaged across particle sizes. For all studied conditions, the average aerosol deposition which coincides with bacterial and viral contamination is less than 50% for the upper respiratory tract and more than 50% for the lungs. At 6 L/min and 15 L/min flow rates, the average lung contamination is above 87%. Due to the activation of bacterial and viral receptors

**Table 13.1** Deposition efficiency of aerosols at different flow rates and for different aerosol sizes and throughput to the lung.

Flow rate [L/min]	Particle size [ $\mu\text{m}$ ]	Aerosol deposition in the upper airways [%]	Aerosol throughput to the lungs [%]	Average aerosol deposition in the upper airways [%]	Average aerosol throughput to the lungs [%]
6	1	5.07	94.93	9.49	90.51
	5	7.93	92.07		
	10	15.47	84.53		
15	1	9.62	90.38	12.39	87.61
	5	9.88	90.12		
	10	17.68	82.32		
30	1	13.52	86.48	43.43	56.57
	5	31.58	68.42		
	10	85.19	14.81		

**FIGURE 13.4**

Aerosol contamination probability in percent for nasal inhalation and aerosol diameters 1, 5, and 10  $\mu\text{m}$  at 6, 15, and 30 L/min airflow. (A) Upper airways contamination probability. (B) Lung contamination probability.

in the lungs (Baig et al., 2020), the lung immune response then increases significantly.

Aerosol deposition efficiency in the airways and lungs contributes to the likelihood of lung contamination. This effect is shown in Fig. 13.4A as a function of flow rate and aerosol diameter, where the upper airway contamination likelihood increases significantly for a 10  $\mu\text{m}$  aerosol and 30 L/min airflow rate. Vice versa, the probability of lung contamination decreases with higher flow rate and aerosol diameter (Fig. 13.4B). Overall, the possibility of lung contamination in nasal inhalation is high.

## Discussion

At inhalation, we injected a constant number of bioaerosols into the respiratory system from the nose entrance. Such an airflow entering only through the nostrils with a shut mouth poses a limitation of the study. Undoubtedly though, this model for tracking the deposition of bacterial and viral aerosol loads in the upper respiratory tract can inform medical diagnosis and treatment. The model could be further expanded to study transmission effects when exhaling, to better understand the spread of bacterial and viral aerosols, their suspension in the air and airborne transmission over longer distances. Indoors the risk of virus transmission through aerosols increases with improper ventilation (Mortazavi et al., 2020; Mortazavy Beni et al., 2021a, b). When a person conducts moderate physical indoors activity, depending on the type of activity, the respiratory airflow rate will be likely at the 15 L/min to 30 L/min mark (Fig. 13.2). With an increasing Stokes number (Fig. 13.3A), the deposition efficiency generally increased under all study conditions. A particle with a low Stokes number has a tendency to follow airflow streamlines, while a particle with a high Stokes number is dominated by its inertia and

continues along its initial trajectory. Aerosol diameter thus plays a decisive role in bacterial and viral aerosol deposition in the respiratory system. As the aerosol diameter or the flow rate increases, the deposition efficiency in the upper respiratory tract increases. Furthermore, dead space must be considered when modeling contamination. Dead space is the volume of air that is inhaled that does not take part in the gas exchange. This volume may remain in the conducting upper airways, including the trachea, bronchi, and terminal bronchioles or reach alveoli that do not contribute to gas exchange. Not all the air in each breath is available for gas exchange. Some dead space air volume is returned to the lungs after exhalation during the next inhalation (Quinn & Rizzo, 2018; Intagliata et al., 2019). For this reason, aerosol contamination will increase if dead space retains deposited bacterial and viral aerosols.

Respiratory diseases are a leading cause of death and disability in the world. Many respiratory diseases go along with physical changes in the airways and lungs. At rest, only a small fraction of our lung aerobic capacity is used. Thus, a lung disease that reduces the aerobic capacity often does not produce noticeable symptoms in its early stages. However, lung function tests force the breathing mechanism to its limits and thus detect changes in aerobic capacity that are not ordinarily apparent. In emphysema, the divisions between lung alveoli break down. This destruction of lung tissue reduces their springiness. The lungs become compliant—a slight change in pressure produces a more significant than usual change in their volume. While this appears to make it easier to breathe at a first glance, the opposite is true. Much of the work of breathing is done in overcoming the resistance of the airways. The resulting expansion of the chest wall and narrowing of the significant airways causes an increase in airway resistance. To further explain this relationship, Fig. 13.5 shows a normal lung (Fig. 13.5A) and a Standard Linear Solid (SLS)

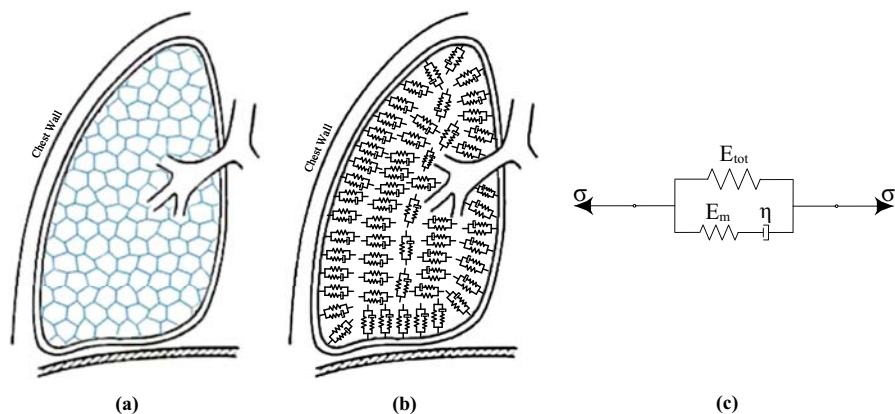


**FIGURE 13.5**

The relationship between ECM properties and biomechanical characteristics of the lung tissue strip. (A) The extracellular matrix in a healthy condition. (B) Spring–dashpot network model (infinite SLS) in a healthy condition. (C) SLS model for one ECM unit.

network model representation of a lung (Fig. 13.5B). Fig. 13.5C shows the analytic representation of the SLS model, which helps understand the physics of lung tissue health impacting on respiratory processes. We can think of the elasticity of the tissues in the normal lungs as millions of interconnected SLS models. These SLS models allow us to determine the forces which collapse the lungs and pull on the chest wall. The forces also pull on the walls of the airways; this keeps the airways open and helps reduce airway resistance during expiration. The number of working SLS models is significantly reduced in bacterial and viral diseases of the lungs, and those present are much weaker than normal. This produces two essential changes: (1) The lung becomes flabby and expands as the reduced tension allows the chest wall to expand; and (2) The tissues do not have much pull on the airways, permitting the narrowed airways to collapse easily during expiration. This increased airway resistance is a major symptom of severe lung diseases.

Fig. 13.5 describes this relationship between the lung extracellular matrix (ECM) properties and the biomechanical characteristics of the lung tissue strip. In the SLS model, a spring is in parallel with a spring–dashpot to represent the biomechanical properties of the alveolar wall composed of elastin, collagen, phosphatidylglycerols (PGs), and the surrounding matrix inside the parenchymal cell (Fig. 13.5C). Elastin, collagen, and PGs act as a linear spring, while the surrounding matrix is represented by a Maxwell element with viscoelastic behavior (Sopakayang & De Vita, 2011). The SLS model is representative of the ECM unit performance (Mortazavy Beni et al., 2021a, b).

The SLS network model permits the dynamic study of lung and airway tissue strip behavior and can be adjusted to specific disease conditions by modifying the volume ratio of ECM ingredients as related to the type of respiratory disease. Bacterial and viral respiratory diseases are associated with changes in the ECM composition. The variation in ECM volume fraction composition results in modified lung tissue strength, elastic modulus (storage modulus), and viscous modulus (loss modulus). Therefore, a transient airflow biomedical computational model of the airways should consider the airway and lung walls as flexible tissue, with their viscoelastic properties. Future studies could use the computational model utilized in this chapter. Also, adopting the models with pathological consideration can provide more data for physicians to choose better treatment methods (Alaodolehei et al., 2020; Beni & Mortazavi, 2022; Mortazavy Beni et al., 2022).

## Conclusion

This chapter provides an example for modeling the deposition of bacterial and viral aerosols inhaled through the nose into the human respiratory system. Consideration of the viscoelastic behavior of the alveolar lung ECM is important when modeling the respiratory system. When increasing the flow rate and bioaerosol diameter, upper airway contamination was maximum for the largest studied 10  $\mu\text{m}$  diameter aerosol and the maximum 30 L/min airflow considered. Vice versa, with the increasing flow

rate and aerosol diameter lung contamination decreased, although secondary contamination from dead space increased. These findings have implications for occupational and environmental health management and the prevention of respiratory diseases from bacterial and viral aerosols. This chapter shows how an analytic modeling study of respiratory contamination can explain and confirm public health advice and epidemiologic evidence of increased respiratory safety in outdoors and well-ventilated areas indoors.

### Declaration of competing interest

The authors of the manuscript hereby declare that they have no conflict of interest. The research was not funded by any organization or University.

---

### Acknowledgments

The authors thank the Taba-Parto Shiraz radiology center for assistance with providing 3D CT scans for the study. All procedures performed in the study involving human participants were in accordance with the institutional and/or national research committee's ethical standards and with the 1964 Helsinki declaration and its later amendments or comparable ethical standards.

---

### References

- Alaodolehei, B., Jafarian, K., Sheikhani, A., & Mortazavy Beni, H. (2020). Performance enhancement of an achalasia automatic detection system using ensemble empirical mode decomposition denoising method. *Journal of Medical and Biological Engineering*, 40, 179–188.
- ANSYS-Fluent. (2006). *Fluent 6.3 users guide*. Lebanon, USA.
- Baig, A. M., Khaleeq, A., Ali, U., & Syeda, H. (2020). Evidence of the COVID-19 virus targeting the CNS: Tissue distribution, host-virus interaction, and proposed neurotropic mechanisms. *ACS Chemical Neuroscience*, 11(7), 995–998.
- Beni, H. M., & Mortazavi, H. (2022). Mathematical modeling of the solar regenerative heat exchanger under turbulent oscillating flow: Applications of renewable and sustainable energy and artificial heart. *Results in Engineering*, 13, 100321.
- Birch, M. J., & Srodon, P. D. (2009). Biomechanical properties of the human soft palate. *The Cleft Palate-Craniofacial Journal*, 46(3), 268–274.
- Burgstaller, G., Oehrle, B., Gerckens, M., White, E. S., Schiller, H. B., & Eickelberg, O. (2017). The instructive extracellular matrix of the lung: Basic composition and alterations in chronic lung disease. *European Respiratory Journal*, 50, 1601805.
- Cameron, J. R., Skofronick, J. G., & Grant, R. M. (1992). *Medical physics: Physics of the body*. Medical Physics Publishing Corporation.
- Chen, X., Zhong, w., Sun, B., Sheng, B., & Zhou, X. (2012). Study on gas/solid flow in an obstructed pulmonary airway with transient flow based on CFD–DPM approach. *Powder Technology*, 217, 252–260.

- Decaro, N. (2011). Betacoronavirus<sup>‡</sup>. In C. Tidona, & G. Darai (Eds.), *The Springer index of viruses* (pp. 385–401). New York, NY: Springer New York.
- Grgic, B., Finlay, W. H., Burnell, P. K. P., & Heenan, A. F. (2004a). In vitro intersubject and intrasubject deposition measurements in realistic mouth–throat geometries. *Journal of Aerosol Science*, 35(8), 1025–1040.
- Grgic, B., Finlay, W. H., & Heenan, A. F. (2004b). Regional aerosol deposition and flow measurements in an idealized mouth and throat. *Journal of Aerosol Science*, 35(1), 21–32.
- Heenan, A. F., Finlay, W. H., Grgic, B., Pollard, A., & Burnell, P. K. (2004). An investigation of the relationship between the flow field and regional deposition in realistic extra-thoracic airways. *Journal of Aerosol Science*, 35(8), 1013–1023.
- Hörschler, I., Meinke, M., & Schröder, W. (2003). Numerical simulation of the flow field in a model of the nasal cavity. *Computers and Fluids*, 32, 39–45.
- Intagliata, S., Rizzo, A., & Gossman, W. G. (May 15, 2019). *StatPearls [Internet]*. Treasure Island (FL): StatPearls Publishing. Physiology, Lung Dead Space.
- Islam, M. S., Paul, G., Ong, H. X., Young, P. M., Gu, Y. T., & Saha, S. C. (2020). A review of respiratory anatomical development, air flow characterization and particle deposition. *International Journal of Environmental Research and Public Health*, 17(2), 380.
- Jayaraju, S. T., Brouns, M., Verbanck, S., & Lacor, C. (2007). Fluid flow and particle deposition analysis in a realistic extrathoracic airway model using unstructured grids. *Journal of Aerosol Science*, 38(5), 494–508.
- Jin, H. H., Fan, J. R., Zeng, M. J., & Cen, K. F. (2007). Large eddy simulation of inhaled particle deposition within the human upper respiratory tract. *Journal of Aerosol Science*, 38(3), 257–268.
- Keyhani, K., Scherer, P. W., & Mozell, M. M. (November 1995). Numerical simulation of airflow in the human nasal cavity. *Journal of Biomechanical Engineering*, 117(4), 429–441.
- Kleinstreuer, C., & Zhang, Z. (2010). Airflow and particle transport in the human respiratory system. *Annual Review of Fluid Mechanics*, 42(1), 301–334.
- Leung, N. H. L., Chu, D. K. W., Shiu, E. Y. C., et al. (2020). Respiratory virus shedding in exhaled breath and efficacy of face masks. *Nat Medicine*, 26(5), 676–680.
- Li, D., Xu, Q., Liu, Y., Libao, Y., & Jun, J. (January 2014). Numerical simulation of particles deposition in a human upper airway. *Advances in Mechanical Engineering*.
- Ma, B., Kourmatzis, A., Zhao, B., Yang, R., Chan, H., Salehi, F., & Cheng, S. H. (2019). Potential effects of lingual fats on airway flow dynamics and particle deposition. *Aerosol Science of Technology*, 54(3), 321–331.
- Mortazavi, H., Mortazavy Beni, H., Aghaei, F., & Sajadian, H. (2020). SARS-CoV-2 droplet deposition path and its effects on the human upperairway in the oral inhalation. *Computer Methods and Programs in Biomedicine*. <https://doi.org/10.1016/j.cmpb.2020.105843>
- Mortazavy Beni, H., Hassani, K., & Khorramymehr, S. (2019a). Study of the sneezing effects on the real human upper airway using fluid–structure interaction method. *Journal of the Brazilian Society of Mechanical Sciences and Engineering*, 41, 1–13.
- Mortazavy Beni, H., Hassani, K., & Khorramymehr, S. (2019b). In silico investigation of sneezing in a full real human upper airway using computational fluid dynamics method. *Computer Methods and Programs in Biomedicine*, 177, 203–209.
- Mortazavy Beni, H., Mortazavi, H., Aghaei, F., & Kamalipour, S. (June 2021a). Experimental tracking and numerical mapping of novel coronavirus micro-droplet deposition through nasal inhalation in the human respiratory system. *Biomechanics and Modeling in Mechanobiology*, 20(3), 1087–1100.

- Mortazavy Beni, H., Mortazavi, H., & Islam, M. S. (October 2021b). Biomedical and biophysical limits to mathematical modeling of pulmonary system mechanics: A scoping review on aerosol and drug delivery. *Biomechanics and Modeling in Mechanobiology*. <https://doi.org/10.1007/s10237-021-01531-8>
- Mortazavy Beni, H., Mortazavi, H., Tashvighi, E., & Islam, M. S. (2022). Investigation of the upper respiratory tract of a male smoker with laryngeal cancer by inhaling air associated with various physical activity levels. *Atmosphere*, 13(5), 717.
- Nicolaou, L., & Zaki, T. A. (2013). Direct numerical simulations of flow in realistic mouth–throat geometries. *Journal of Aerosol Science*, 57, 71–87.
- Quinn, M., & Rizzo, A. (December 6, 2018). *StatPearls [Internet]*. Treasure Island (FL): StatPearls Publishing. Anatomy, Anatomic Dead Space.
- Shanley, K. T., Zamankhan, P., Ahmadi, G., Hopke, P. K., & Cheng, Y. S. (2008). Numerical simulations investigating the regional and overall deposition efficiency of the human nasal cavity. *Inhalation Toxicology*, 20(12), 1093–1100.
- Shi, H., Kleinstreuer, C., & Zhang, Z. (2006). Laminar airflow and nanoparticle or vapor deposition in a human nasal cavity model. *Journal of Biomechanical Engineering*, 128(5), 697–706.
- Shinneeb, A. M., & Pollard, A. (2012). Investigation of the flow physics in the human pharynx/larynx region. *Experiments in Fluids*, 53(4), 989–1003.
- Shiu, E. Y. C., Leung, N. H. L., & Cowling, B. J. (2019). Controversy around airborne versus droplet transmission of respiratory viruses: Implication for infection prevention. *Current Opinion in Infectious Diseases*, 32(4), 372–379.
- Sopakayang, R., & De Vita, R. (2011). A mathematical model for creep, relaxation and strain stiffening in parallel-fibered collagenous tissues. *Medical Engineering & Physics*, 33, 1056–1063.
- Xi, J., & Longest, P. W. (2007). Transport and deposition of micro-aerosols in realistic and simplified models of the oral airway. *Annals of Biomedical Engineering*, 35(4), 560–581.
- Xi, J., & Longest, P. W. (2008). Numerical predictions of submicrometer aerosol deposition in the nasal cavity using a novel drift flux approach. *International Journal of Heat and Mass Transfer*, 51(23–24), 5562–5577.
- Zhang, H., Li, D., Xie, L., & Xiao, Y. (2015). *Documentary research of human respiratory droplet characteristics* (Vol 121, pp. 1365–1374). Procedia Engineering.

# Numerical simulation of the aortic arch behavior\*

# 14

Hamidreza Mortazavy Beni<sup>1</sup>, Hamed Mortazavi<sup>1</sup>, Gunther Paul<sup>2</sup>,  
Mohammad Saidul Islam<sup>3</sup>, Ali Asghar Zarei<sup>4</sup>

<sup>1</sup>Department of Biomedical Engineering, Arsanjan Branch, Islamic Azad University, Arsanjan, Iran; <sup>2</sup>Australian Institute of Tropical Health and Medicine, James Cook University, Townsville, QLD, Australia; <sup>3</sup>School of Mechanical and Mechatronic Engineering, University of Technology Sydney (UTS), Ultimo, NSW, Australia; <sup>4</sup>Center for Neuroplasticity and Pain (CNAP), Department of Health Science and Technology, Aalborg University, Aalborg, Denmark

## Chapter outline

<b>Nomenclature .....</b>	290
<b>Introduction .....</b>	290
<b>Methods .....</b>	291
Geometry reconstruction and grid generation .....	291
Governing equations .....	292
Boundary conditions and numerical solution .....	293
<b>Results .....</b>	294
<b>Discussion .....</b>	297
<b>Conclusion .....</b>	300
<b>Disclosure of interest .....</b>	300
<b>Acknowledgments .....</b>	300
<b>References .....</b>	301

\* All procedures performed in studies involving human participants were in accordance with the ethical standards of the institutional and/or national research committee and with the 1964 Helsinki declaration and its later amendments or comparable ethical standards.

## Nomenclature

$a$	Acceleration	$\text{m}^2/\text{s}$	$\mu$	Dynamic viscosity	$\text{kg}/\text{m.s}$
$c_f$	Local skin friction coefficient	—	$\mu_t$	Turbulent viscosity	$\text{kg}/\text{m.s}$
$d$	Deformation	$\text{m}$	$\mu_t/\mu$	Eddy viscosity ratio	—
$F$	Force	$\text{N}$	$\rho$	Density	$\text{kg}/\text{m}^3$
$k$	Turbulent kinetic energy	$\text{J/kg}$	$\sigma$	Stress tensor	$\text{Pa}$
$P$	Static pressure	$\text{Pa}$	$\tau$	Wall shear stress	$\text{Pa}$
$Q$	Flow rate	$\text{m}^3/\text{s}$	$\omega$	Vorticity	$1/\text{s}$
$R_e$	Reynolds number	—	<b>Subscripts</b>		
$T_u$	Turbulence intensity	%	ave	Average	
$t$	Time	$\text{s}$	$b$	Body force	
$V$	Velocity	$\text{m/s}$	$d$	Deformation	
<b>Greek symbols</b>					
$\epsilon$	Strain	—	$f$	Fluid	
$\dot{\epsilon}$	Strain rate	$1/\text{s}$	$g$	Grid	
			$s$	Solid	
			$x, y, z$	Cartesian coordinates	

## Introduction

Pressoreceptors or baroreceptors are sensors located in the cardiovascular system, such as the aortic arch. They sense the blood pressure and relay the information to the brain to maintain proper blood pressure. Baroreceptors monitor hemodynamic force variations exerted to the vascular wall and control the appropriate response to return stresses and strains to the normal range and maintain homeostasis (Carlson et al., 2008; Hall, 2015; Rizzo, 2015). Knowledge of the aortic arch pressoreceptor has been pioneered by Seto (1935). They demonstrated that large myelinated fibers enter the wall of the human aorta and end in its adventitia in the form of neurofibrillary endplates. Additionally, the arterial wall's viscoelastic properties (i.e., dynamic storage and loss modulus) have also been mentioned to play an essential role in determining the location of the aortic arch pressoreceptors. Pressoreceptors or baroreceptors are sensors located in the aortic arch. They sense the blood pressure and relay the information to the brain to maintain proper blood pressure. Several studies have investigated the frequency dependency of stress-strain behavior in both animal and human arteries (Bergel, 1961; Goedhard & Knoop, 1973; Learoyd & Taylor, 1966). Stress relaxation and creep tests have also been assessed in dog arteries (Tanaka & Fung, 1974), where the arterial wall showed a nonlinear stress-strain relationship with physiological hemodynamic forces (Gow & Taylor, 1968). Viscoelastic properties of the human aortic vessel wall, including the aortic elastic modulus, were investigated *in vivo* (Imura et al., 1990). Wall shear stress (WSS) and normal stress, however, that could not be determined with current *in vivo* techniques could be obtained by computational fluid dynamics (CFD) and fluid-structure interaction (FSI) methods from measuring the blood pressure domain gradient.

CFD and FSI methods are verified powerful modeling tools to simulate the cardiovascular system. Image-based models can accurately reconstruct the flow domain by numerically solving the momentum and continuity equations. The stress and strain

magnitudes inside the vascular wall imposed by hemodynamic forces can be simulated using the FSI technique. Wall deformation, however, does affect the boundaries of the fluid domain in FSI analysis. In silico investigations of the aorta have been reported in several studies. Tokuda et al. suggested an aortic arch CFD model to simulate blood flow during cardiopulmonary bypass surgery (Tokuda et al., 2008), modeling pressure flow fields to reduce the risk of stroke during the operation. Tse et al. presented a CFD model of intricate geometrical aorta features and investigated their effect on hemodynamics (Tse et al., 2012). The aortic arch's flow field and WSS distribution have also been modeled using the CFD technique (Numata et al., 2016). Several studies have used the FSI method for human aorta modeling (Crossetto et al., 2011; Lantz et al., 2011; Suito et al., 2014) by extracting aorta geometry from CT or MRI images and analyzing the deformation and WSS distribution. However, simplifying assumptions in previous computational studies have caused deviations from in vivo results, with the specific importance of the aortic arch wall viscoelastic effect in living tissue being pointed out. This chapter shows an analytical approach to locate the aortic arch baroreceptors in the human aorta under normal hemodynamic conditions, considering the frequency-dependent viscoelastic nonlinear arterial behavior. In this chapter, first a realistic 3D image-based model of the aortic arch is presented. We then perform numerical analysis, using the FSI method and a dynamic mesh approach. In the next step, we analyze the hemodynamic field in the fluid domain, including velocity and pressure distributions. In the final step, the stress and strain fields are discussed in the solid domain.

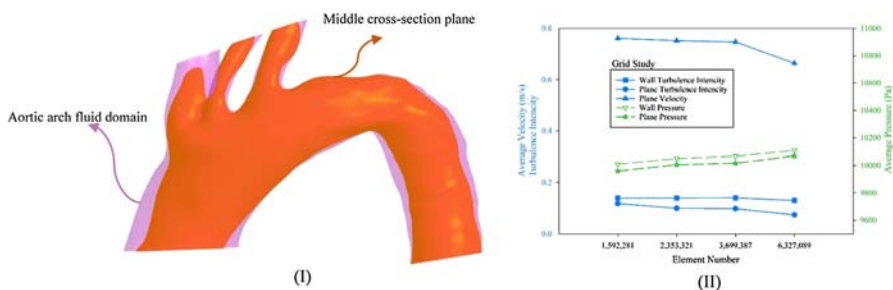
---

## Methods

### Geometry reconstruction and grid generation

Geometry of an aortic arch was provided by the Taba Parto Shiraz radiology center. The donor subject was a 49-year-old healthy man. First, CT-derived DICOM (Digital Imaging and Communications in Medicine) images were imported to Mimics software, developed by Materialise NV, using thresholding to reconstruct the human aortic arch as a point cloud. From literature, aortic arch wall thickness was considered to be 2.68 mm (Liu et al., 2015). Eventually, the aortic arch fluid domain consisted of 3,252,778 nodes for 2,353,321 tetrahedral elements. The aortic arch solid domain was discretized to 50,250 tetrahedral elements and 43,551 nodes. Discretization solver runs were repeated until aortic arch grid independency was achieved as shown in Fig. 14.1 for the middle cross-section plane. Grid independency analysis was performed in the fluid domain based on velocity, pressure, and turbulence intensity in the middle cross section. Grid parameters and mesh metric quality for the different mesh element sizes are reported in Table 14.1.

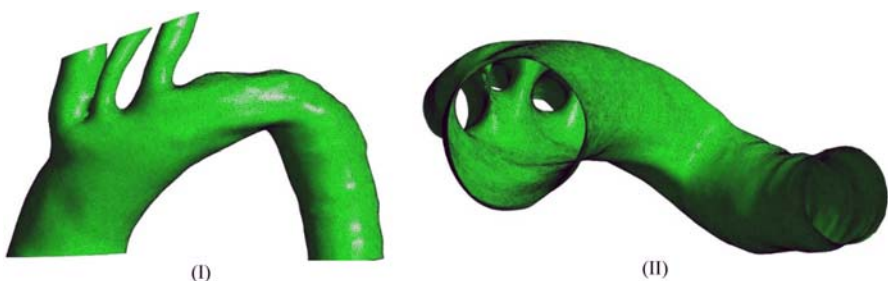
We utilized unstructured mesh cells of the fluid and solid geometries because the aortic wall is complex and nonuniform so that we cannot produce a mesh structure. Fig. 14.2 shows that the mesh was refined near the aortic walls for the cover boundary layer to achieve a more precise computation of hemodynamic parameters, so that the thickness of the first sublayer of the boundary layer in the internal areas of the respiratory system was 0.021 mm and the total number of layers was 20 layers at a growth rate of 1.1.

**FIGURE 14.1**

The aortic arch grid independence analysis for the middle cross-section plane. (I) The aorta middle cross-section plane. (II) The aortic arch grid independence analysis.

**Table 14.1** Summary of grid parameters and mesh metric quality for different mesh element sizes.

Grid parameters			Mesh metric quality		
Element size (m)	Nodes	Elements	Aspect ratio	Orthogonal quality	Skewness
<b>0.0008</b>	2,214,476	1,592,281	1.8054	0.78309	0.2157
<b>0.0007</b>	3,252,778	2,353,321	1.7934	0.78761	0.21121
<b>0.0006</b>	5,082,141	3,699,387	1.7797	0.79289	0.20593
<b>0.0005</b>	8,639,930	6,327,089	1.7692	0.79709	0.20175

**FIGURE 14.2**

Unstructured mesh cells of the fluid and solid geometries. (I) Fluid domain mesh cells in the coronal plane. (II) Solid domain mesh cells in the transverse plane.

### Governing equations

The flow was assumed to be turbulent, transient with pulse wave inlet velocity, and an incompressible Newtonian fluid. The continuity and momentum equations using

the Arbitrary Lagrangian–Eulerian (ALE) formulation for the fluid model are as follows.

$$\nabla \cdot V_f = 0 \quad (14.1)$$

$$\rho_f \frac{\partial V_f}{\partial t} + \rho_f ((V_f - V_g) \cdot \nabla) V_f = \nabla \cdot \sigma_f + F_b \quad (14.2)$$

The ALE formulation accounts for deformability in the fluid domain via the grid velocity  $V_g$ , and the time derivative of the fluid velocity. The term  $\sigma_f = \mu_f (\nabla V_f + \nabla V_f^T) - P_f$  for a Newtonian fluid denotes the Cauchy stress tensor. Also,  $V_f$ ,  $P_f$ ,  $\rho_f$ ,  $\mu_f$ , and  $F_b$  denote the fluid velocity, fluid pressure, fluid density, dynamic viscosity of the fluid, and body force, respectively. Fluid density and dynamic viscosity are chosen as  $\rho_f = 1060 \text{ kg/m}^3$  (Cutnell & Johnson, 1998, p. 308) and  $\mu_f = 3.5 \times 10^{-3} \text{ Pa.s}$  (Cameron et al., 1992). Within this turbulent flow chaotic variations in pressure and flow velocity occur. The governing equation in the solid domain is based on the momentum conservation principle and is given as

$$\nabla \cdot \sigma_s + F_b = \sigma_s a \quad (14.3)$$

Here  $\sigma_s$  and  $a$  are the solid stress tensor and local acceleration vector, respectively. At the fundamental frequency of 1.2 Hz, the aortic elastic modulus amplitude was found to be  $0.88 \times 10^6 \text{ Pa}$  and the phase lag was  $-6.7$  degrees under in vivo experimental conditions (Imura et al., 1990 May). Moreover, Liu et al. determined that pulse wave velocity existed in the aortic arch and that hypertension was related to increased aortic stiffness (Liu et al., 2015 May).

## Boundary conditions and numerical solution

Physiological flow rate pressure waveforms at the inflow and outflow surfaces are illustrated in Fig. 14.3 (Alimohammadi et al., 2014). Boundary conditions for the fluid include a no-slip condition at the arterial wall, zero displacement of the inlet

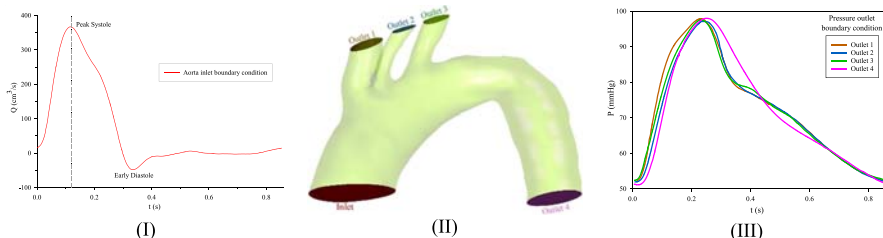


**FIGURE 14.3**

Physiological flow rate pressure waveforms at the inflow and outflow surfaces. (I) Flow rate waveform at the aortic arch inlet surface. (II) The geometry of the aortic arch with various boundary planes: Inlet—ascending aorta, Outlet 1—brachiocephalic trunk, Outlet 2—left common carotid artery, Outlet 3—left subclavian artery, Outlet 4—descending aorta. (III) Pressure waveforms at the aortic arch outlet surfaces.

and outlet faces, and equal displacements of the solid-fluid domains so that tractions from the fluid–solid domains are at equilibrium. A detailed description of the governing FSI equations can be found in Mortazavy et al. (2021).

Fluid and solid coupling domains were carried out using the Ansys 2021 R1 software. Ansys Fluent was used for creating the fluid and solid domains, and Ansys Static Structural discretized results. The finite volume method and the finite element method were used for the fluid domain and solid domain, respectively. The fluid forces with FSI technique are imported to the solid domain, and the consequent deformation shifts in the boundaries of the fluid domain using the dynamic mesh approach. The SIMPLE algorithm was used in solid–fluid models, with the assistance of the least-square cell-based gradient, in which both momentum and pressure are assumed to be second order. Also, the k-epsilon turbulence model with standard wall function treatment was used in this study. At the final stage, the unsteady solution was achieved with a time step of 0.01 s in both domains.

## Results

Initially a 3D model of the aortic arch was generated from CT images. Fluid and solid domains were then coupled, and an unsteady mathematical solution was computed for the simulation. The results describe the dynamic behavior of hemodynamic variables, including fluid velocity, aortic WSS, and aortic pressure distributions. Furthermore, the stress and deformation distributions in the arterial wall are shown. Similar to previous pulsatile studies in the literature, the transient turbulent aortic flow is reported at two critical times of the flow rate extrema in Fig. 14.3 (PS: Peak Systole, ED: Early Diastole) (Cavalcanti, 2000; Ursino, 1998). Fig. 14.4 shows

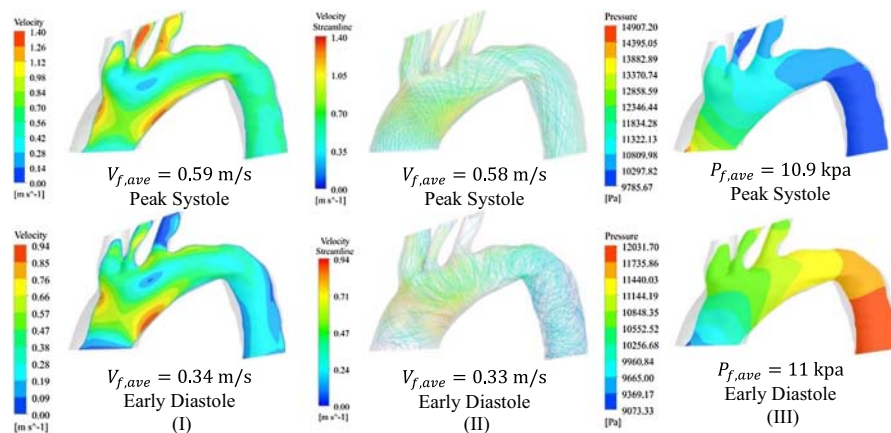


**FIGURE 14.4**

The blood flow velocity and pressure contours in the aortic arch at PS and ED time instants. (I) Velocity contours in the middle cross-section plane. (II) Stream lines of the fluid flow domain. (III) Pressure contours in the middle cross-section plane.

the blood flow velocity and pressure contours in the aortic arch at PS and ED times. The ventricular outflow hastens to its maximum systolic peak flow when the aortic valve opens. The supraaortic branches achieve their maximum velocity flow due to the aortic arch functioning as a convergent nozzle. The maximum flow velocity occurs in the smallest diameter carotid artery branch (left common carotid artery) (Fig. 14.4I). When the ventricular outflow begins to decelerate, creating a vortical disturbed fluid flow during ED, the aortic valve closes. A recirculation zone and reversal fluid flow can now be considered in the curvature of the ascending aorta. Helical spiral streamlines become visible in the fluid flow field as the luminal diameter of the aorta arch reduces, that is, in some zones along with secondary flows. Finally, at the early diastole, a great recirculation region is visible at the aortic arch (Fig. 14.4II). Fig. 14.4III shows that during PS, the fluid flow moves forward to the descending aorta, and blood has a negative pressure gradient. As mentioned before, the aortic valve closes during ED, producing a positive pressure gradient. In addition to the overall pressure drop due to viscous forces, lower pressure magnitudes can be observed in supraaortic branches in the ED.

The  $Y^+$  value is a nondimensional distance from the wall to the first mesh node based on local cell fluid velocity. In line with this, according to Mortazavy et al. (2019) the local skin friction coefficient  $c_f$  and WSS were calculated. According to Fig. 14.5,  $c_f$ , WSS, and  $Y^+$  reach their maximum in the ascending aorta region, where the  $Y^+$  parameter maximum varies from 9.2 to 7.5 at PS and ED, respectively.  $Y^+$  average values vary from 4.3 to 3.1 for the overall wall domain at PS and ED, respectively. Also, WSS is one of the most important hemodynamic criteria that

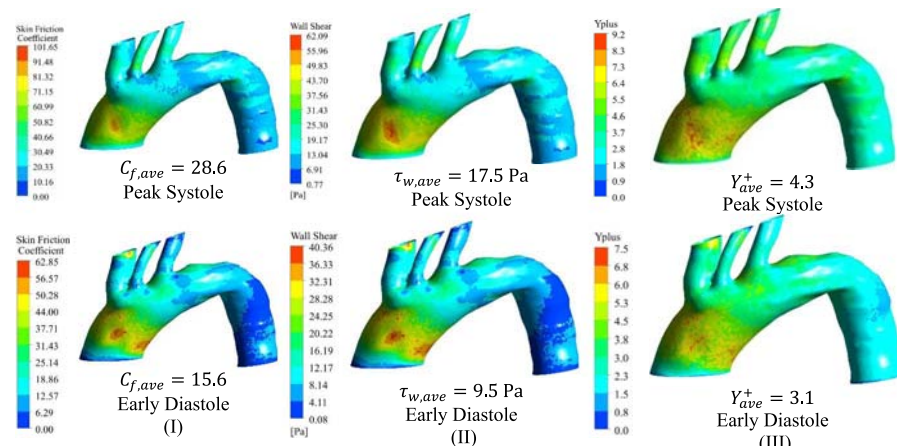


FIGURE 14.5

The blood flow local skin friction coefficient and wall shear stress and wall  $Y^+$  contours in the aortic arch at PS and ED time instants. (I) Local skin friction coefficient in the fluid flow domain. (II) Wall shear stress contours in the fluid flow domain. (III)  $Y^+$  contours in the fluid flow domain.

is typically predicted in numerical simulation. WSS has a standard range in healthy individuals and values outside this range can lead to cardiovascular diseases (Cavalcanti, 2000). Endothelial cells located in the arterial lumen's internal lining are shear receptors that sense abnormal tensions and transit these biological signals to the brain to keep vascular homeostasis (Teng et al., 2010). WSS distribution in the aortic arch is shown in Fig. 14.5II at PS and ED. Higher WSS was found at the ascending aorta wall concave reaching 62 Pa, which is consistent with Tse et al. (2012). This high value stems from significant speed gradients entering the ascending aorta zone. Average WSS values are 17.5 and 9.5 Pa in the aortic arch at PS and ED, respectively. In the supraaortic branches root, WSS is about 20 Pa. Lower WSS zones occurred in the descending aortic zone, coinciding with the extreme pressure variation region at PS and ED. In the descending aortic arch, WSS values are lower due to lower blood flow velocity.

Effective stress, equivalent strain, and the strain rate imposed on the aortic arch wall by the blood flow at PS and LD are illustrated in Fig. 14.6. The viscoelastic ascending aorta region acts as an energy reservoir that holds the blood exited from the aortic valve and softly releases it to the vascular system. A higher stress magnitude occurs in the supraaortic branches root zone because of the stress concentration in the branching zone where the supraaortic branches leave the arch. Fig. 14.6I shows that the von Mises stress changes from 150 kPa at the ascending aorta to 50 kPa in the descending aorta at PS, while the average effective stress is 50.3 and 50.1 kPa in the aortic arch at PS and ED, respectively. The effective stress reaches 188 kPa at the supraaortic branch roots at PS. As seen in Fig. 14.6II, the equivalent strain changes in the aortic arch are similar to the effective stress variation; so that a higher equivalent strain can be anticipated in the supraaortic branches root zone. Equivalent strain changes from 0.3 in the ascending aorta to 0.03 in the

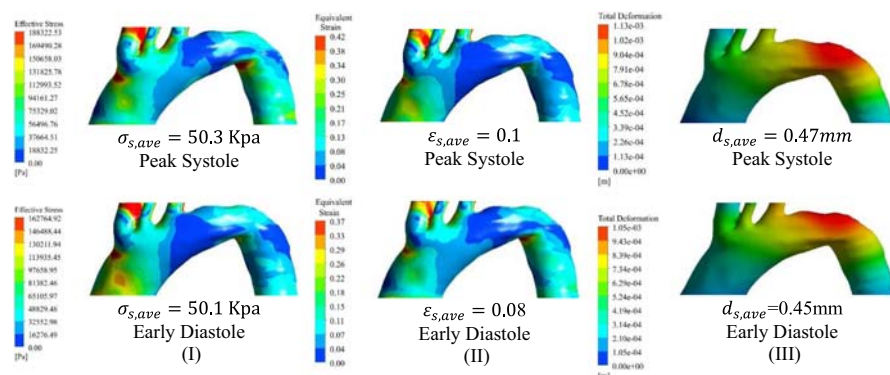


FIGURE 14.6

The blood flow effective stress, equivalent strain, and deformation contours in the aortic arch at PS and ED time instants. (I) Effective stress in the artery. (II) Equivalent strain contours in the artery. (III) Deformation contours in the artery.

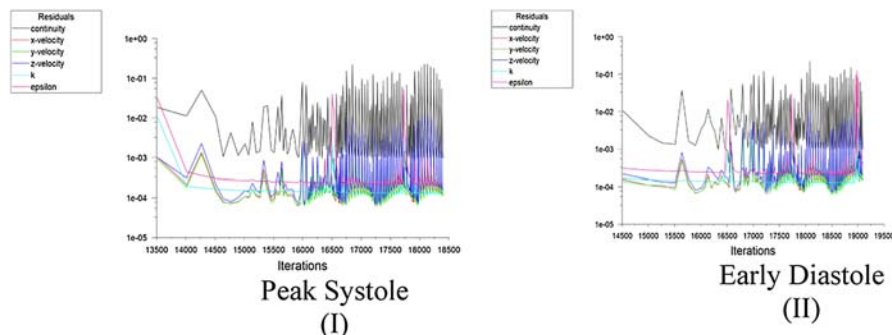
descending aorta at PS. The average equivalent strain in the aortic arch is 0.1 and 0.08 at PS and ED, respectively. Fig. 14.6III shows the influence of the blood impact on the aortic bending part with maximum wall displacements higher than 1 mm.

In contrast to the stress distribution, the supraaortic branch root zone doesn't show much deformation, which remains below 0.07 mm because of movement restrictions. Medium level displacement at the junctures of the supraaortic branches, however, coincides with maximum effective stress in the region. A unique characteristic of the roots of juncture branches is the highly compliant behavior of its artery wall due to finite collagen content, leading to soft deformation in each pulse wave (Kass & Mizrahi, 2016). Moreover, vessel deformation will affect the fluid domain boundaries in the FSI analysis. Hemodynamic forces are considered in the solid domain by two-way coupling of the dynamic mesh which interfaces the blood and artery intima layer. The deformation from the solid domain then modifies the fluid domain boundaries, producing a higher fidelity of the simulation.

---

## Discussion

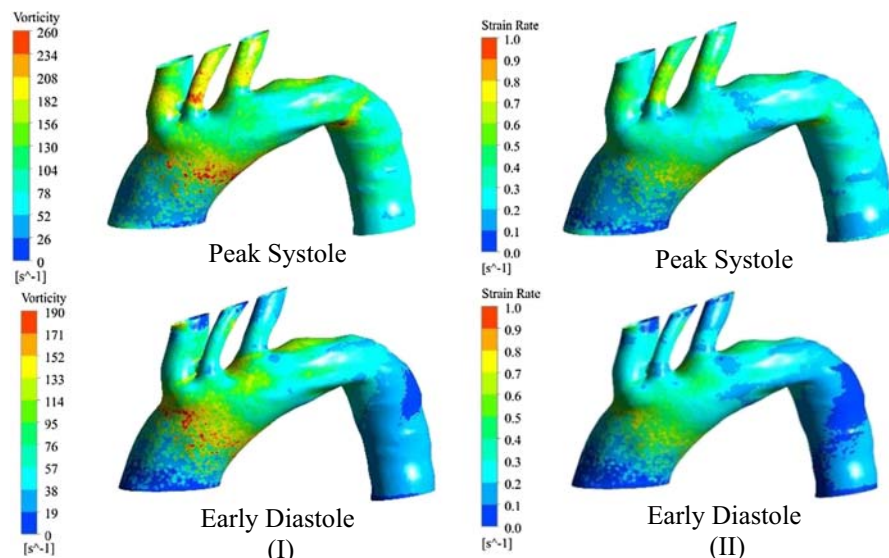
Pressoreceptors are mechanosensitive afferent nerve fibers that are generally located in the aortic arch arterial wall. These mechanoreceptors are controlled by a stretch of the arterial wall which results from blood pressure. It has been reported that aging is associated with arterial wall stiffening (Klabunde, 2011, p. 8; Kougias et al., 2010), and arterial compliance is usually reduced following atherosclerosis plaques (Levy & Pappano, 2007). Therefore, the viscoelastic properties of the aortic wall play an essential role in finding the exact location of the baroreceptors. With the aim of further developing and improving the current procedure for treating pressure regulating mechanism malfunction, we need a detailed comprehension of the pathology and physiology of pressoreceptors and the entire baroreceptor reflex. According to the aforementioned clinical research, which studied aging effects and vascular diseases, inappropriate systemic pressure regulation may worsen from the local malfunction of aortic arch pressure sensors. All the above cases lead to a variation of the vascular wall mechanical properties, such as vessel wall stiffening at the location of the pressoreceptor. Therefore, inappropriate stretching of the artery wall may lead to false signals being sent to the central nervous system, causing baroreflex malfunction. This chapter presented a 3D blood flow field model of the aortic arch based on CT images, as the baroreceptors locations considering interaction with the artery wall. All the boundary conditions of the simulation (i.e., the pressure and flow waveforms) were adopted from previously published studies. Uniform vessel wall thickness was considered in the aortic model as this assumption is valid in healthy cases and was thus used in previous FSI studies (Suito et al., 2014). The cyclic variation of the pressure (Fig. 14.3), velocity, WSS, and turbulence property distributions in the fluid domain and also stress, strain, and deformation contours in the solid domain were analyzed. In order to reach hemodynamic stability of the model, a large number of model iterations were needed and repeated for the consecutive cardiac cycles

**FIGURE 14.7**

The convergence history for residuals. (I) Peak Systole iteration history. (II) Early Diastole iteration history.

(Fig. 14.7), requiring significant computing time in a High Performance Computing Research Centre to achieve final results.

The range of vorticity changes (see recirculation stream lines in Fig. 14.4II in results) is shown in Fig. 14.8I. Vorticity results are consistent with results presented by Von Spiczak et al. (2015) for the *in vivo* aortic blood vorticity. The variation of the strain rate is illustrated in Fig. 14.8II. The strain rate is relatively large due to the short creep time at systole and diastole time steps. These results are confirmed by

**FIGURE 14.8**

Blood flow vorticity and artery strain rate contours in the aortic arch at PS and ED time instants. (I) Blood flow vorticity. (II) Aorta strain rate.

in vivo electrocardiography (ECG) presented by Hoit et al. (2011). In general, the amount of vorticity and strain rate in the ascending aorta is the highest. Based on our comparison with experimental study results reported in the literature, this model-based simulation can be considered to be validated.

The numerical simulation replicates turbulent blood flow in the aortic arch. To better understand the conditions of this turbulent flow, variations of the dimensionless turbulent parameters such as the eddy viscosity ratio and turbulence intensity are shown in Fig. 14.9. In general, the eddy viscosity ratio and turbulence intensity is highest in the ascending aorta. As shown in Fig. 14.9I, the average eddy viscosity ratio is beyond 300; hence, the turbulent viscosity has a stronger influence than the molecular viscosity. The turbulence intensity is defined as follows:

$$Tu = \frac{\sqrt{\frac{2k}{3}}}{\bar{V}} \quad (14.4)$$

where  $Tu$ ,  $k$ , and  $\bar{V}$  are turbulence intensity, turbulent kinetic energy, and mean velocity at the same location over the same time period, respectively. Large fluctuations in speed or direction in the unsteady flow can lead to more turbulence in the flow, leading to the turbulence intensity increasing to more than 1. In the aortic arch geometry, the turbulence intensity in the ascending aorta region is more than 1 (Fig. 14.9II).

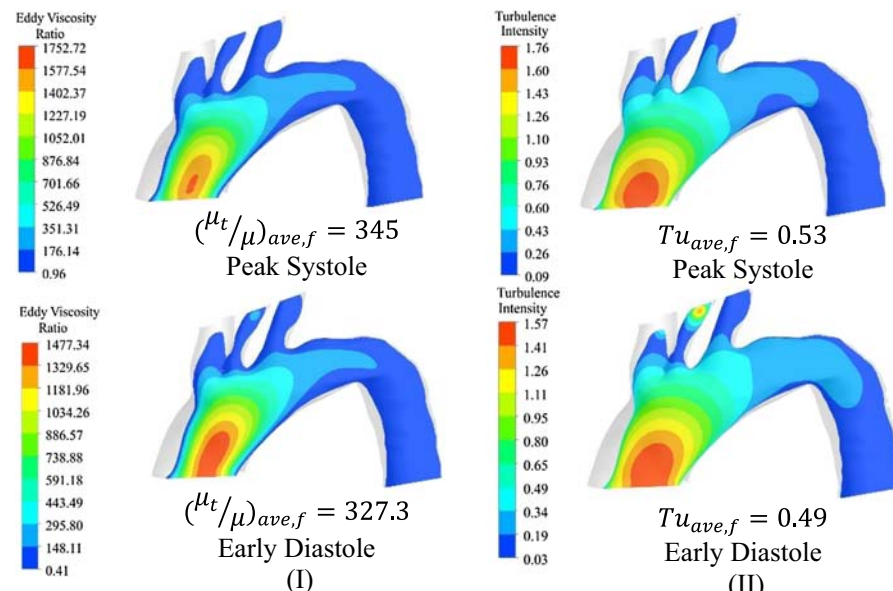


**FIGURE 14.9**

Eddy viscosity ratio and turbulence intensity contours in the aortic arch at PS and ED time instants. (I) Blood flow eddy viscosity ratio. (II) Blood flow turbulence intensity.

Abraham (1969) determined through microscopic studies that the sensory nerve baroreceptor terminals in dog were distributed within the aortic arch and the roots of its juncture branches. Moreover, Abraham found the form of endplates to be flat and to attach to the vessel wall with their flat surfaces. The normal stress applied to the aortic arterial wall is the determinative index to determine baroreceptor locations. Generally, shear forces are monitored by the endothelial cells in the intima layer (Meng et al., 2014), and perpendicular forces are sensed by the smooth muscle cells in the media layer (Lacolley et al., 2012), respectively. Our study shows that at the junctures of the supraaortic branches, the normal stress is the highest with 188 kPa, in a region which is a known zone for baroreceptors. Also, adopting the models with pathological consideration can provide more data for physicians to choose better treatment methods (Alaodolehei et al., 2020; Beni et al., 2021; Beni & Mortazavi, 2022; Mortazavi, 2020; Mortazavy Beni et al., 2022). Future studies could use the computational model utilized in this chapter to investigate the relationship between baroreceptor function and the central nervous system control of blood pressure.

---

## Conclusion

Since regulation of blood pressure is one of the most critical control mechanisms in the cardiovascular system, blood pressure control malfunction can lead to very harmful consequences. Developing models with a capacity to simulate and analytically study blood pressure control is therefore of great importance. In this chapter, a model of the human aortic arch, which is where the baroreceptors are located, was presented. The model couples the pulsatile blood flow domain with the artery wall domain while considering their viscoelastic properties. The average WSS was 17.5 Pa in the aortic arch at PS, while it was about 20 Pa at the junctures of the branching arteries where baroreceptors are located. The effective stress reached 188 kPa at the location of baroreceptors where the wall deformation was no more than 1 mm.

---

## Disclosure of interest

The authors of the manuscript hereby declare that they have no conflict of interest.

---

## Acknowledgments

We thank the Taba-Parto Shiraz radiology center for assistance with the 3D CT scan. All procedures performed in studies involving human participants were in accordance with the institutional and/or national research committee's ethical standards and with the 1964 Helsinki declaration and its later amendments or comparable ethical standards.

## References

- Abraham, A. (1969). *Microscopic innervation of the heart and blood vessels in vertebrates including man*. Oxford: Pergamon.
- Alaodolehei, B., Jafarian, K., Sheikhani, A., & Mortazavy Beni, H. (2020). Performance enhancement of an achalasia automatic detection system using ensemble empirical mode decomposition denoising method. *Journal of Medical and Biological Engineering*, 40, 179–188.
- Alimohammadi, M., Agu, O., Balabani, S., & Díaz-Zuccarini, V. (2014). Development of a patient-specific simulation tool to analyse aortic dissections: Assessment of mixed patient-specific flow and pressure boundary conditions. *Medical Engineering and Physics*, 36(3), 275–284.
- Beni, H. M., & Mortazavi, H. (2022). Mathematical modeling of the solar regenerative heat exchanger under turbulent oscillating flow: Applications of renewable and sustainable energy and artificial heart. *Results in Engineering*, 13, 100321.
- Beni, H. M., Mortazavi, H., & Islam, M. S. (2021). Biomedical and biophysical limits to mathematical modeling of pulmonary system mechanics: A scoping review on aerosol and drug delivery. *Biomechanics and Modeling in Mechanobiology*. <https://doi.org/10.1007/s10237-021-01531-8>
- Bergel, D. H. (1961). The dynamic elastic properties of the arterial wall. *The Journal of Physiology*, 156, 458–469.
- Cameron, J. R., Skofronick, J. G., & Grant, R. M. (1992). *Medical physics: Physics of the body*. Medical Physics Publishing Corporation.
- Carlson, B. E., Arciero, J. C., & Secomb, T. W. (2008). Theoretical model of blood flow autoregulation: Roles of myogenic, shear-dependent, and metabolic responses. *The American Journal of Physiology-Heart and Circulatory Physiology*, 295(4), H1572–H1579.
- Cavalcanti, S. (2000). Arterial baroreflex influence on heart rate variability: A mathematicalmodel-based analysis. *Medical & Biological Engineering & Computing*, 38(2), 189–197.
- Crosetto, P., Reymond, P., Deparis, S., Kontaxakis, D., Stergiopoulos, N., & Quarteroni, A. (2011). Fluid–structure interaction simulation of aortic blood flow. *Computers and Fluids*, 43(1), 46–57.
- Cutnell, J., & Johnson, K. (1998). *Physics* (4th ed.). Wiley.
- Goedhard, W. J. A., & Knoop, A. A. (1973). A model of the arterial wall. *The Journal of Biomechanics*, 6, 281–288.
- Gow, B. S., & Taylor, M. G. (1968). Measurement of viscoelastic properties of arteries in the living dog. *Circulation Research*, 23, 111–122.
- Hall, J. E. (2015). *Guyton and hall textbook of medical physiology e-Book*. Elsevier Health Sciences.
- Mortazavi, H., Beni, H. M., Aghaei, F., & Sajadian, S. H. (2020). SARS-CoV-2 droplet deposition path and its effects on the human upperairway in the oral inhalation. *Comput Methods and Programs in Biomedicine*. <https://doi.org/10.1016/j.cmpb.2020.105843>
- Hoit, B. D. (March 2011). Strain and strain rate echocardiography and coronary artery disease. *Circulation: Cardiovascular Imaging*, 4(2), 179–190.
- Imura, T., Yamamoto, K., Satoh, T., Kanamori, K., Mikami, T., & Yasuda, H. (May 1990). In vivo viscoelastic behavior in the human aorta. *Circulation Research*, 66(5), 1413–1419. <https://doi.org/10.1161/01.res.66.5.1413>. PMID: 2185904.

- Kass, J. S., & Mizrahi, E. M. (2016). *Neurology secrets E-Book*. Elsevier Health Sciences.
- Klabunde, R. (2011). *Cardiovascular physiology concepts* (p. RA1). Lippincott Williams & Wilkins.
- Kougias, P., Weakley, S. M., Yao, Q., Lin, P. H., & Chen, C. (2010). Arterial baroreceptors in the management of systemic hypertension. *Medical Science Monitor: International Medical Journal of Experimental and Clinical Research*, 16(1), RA1.
- Lacolley, P., Regnault, V., Nicoletti, A., Li, Z., & Michel, J.-B. (2012). The vascular smooth muscle cell in arterial pathology: A cell that can take on multiple roles. *Cardiovascular Research*, 95(2), 194–204.
- Lantz, J., Renner, J., & Karlsson, M. (2011). Wall shear stress in a subject specific humanaorta—fluence of fluid-structure interaction. *International Journal of Applied Mechanics*, 3(04), 759–778.
- Leary, B. M., & Taylor, M. G. (1966). Alterations with age in the viscoelastic properties of human arterial walls. *Circulation Research*, 18, 278–292.
- Levy, M. N., & Pappano, A. J. (2007). Regulation of the heart beat. In W. Schmitt (Ed.), *Cardiovasc. physiol* (pp. 104–105). Mosby Elsevier.
- Liu, C. Y., Chen, D., Bluemke, D. A., Wu, C. O., Teixido-Tura, G., Chugh, A., Vasu, S., Lima, J. A., & Hundley, W. G. (May 2015). Evolution of aortic wall thickness and stiffness with atherosclerosis: Long-term follow up from the multi-ethnic study of atherosclerosis. *Hypertension*, 65(5), 1015–1019.
- Meng, H., Tutino, V. M., Xiang, J., & Siddiqui, A. (2014). High WSS or low WSS? Complex interactions of hemodynamics with intracranial aneurysm initiation, growth, and rupture: Toward a unifying hypothesis. *American Journal of Neuroradiology*, 35(7), 1254–1262.
- Mortazavy Beni, H., Hassani, K., & Khorramymehr, S. (2019). Study of the sneezing effects on the real human upper airway using fluid–structure interaction method. *The Journal of the Brazilian Society of Mechanical Sciences and Engineering*, 41, 1–13.
- Mortazavy Beni, H., Mortazavi, H., Aghaei, F., & Kamalipour, S. (March 2021). Experimental tracking and numerical mapping of novel coronavirus micro-droplet deposition through nasal inhalation in the human respiratory system. *Biomechanics and Modeling in Mechanobiology*, 1, 1–14.
- Mortazavy Beni, H., Mortazavi, H., Tashvighi, E., & Islam, M. S. (2022). Investigation of the upper respiratory tract of a male smoker with laryngeal cancer by inhaling air associated with various physical activity levels. *Atmosphere*, 13(5), 717.
- Numata, S., Itatani, K., Kanda, K., Doi, K., Yamazaki, S., Morimoto, K., Manabe, K., Ikemoto, K., & Yaku, H. (2016). Blood flow analysis of the aortic arch using computational fluid dynamics. *European Journal of Cardio-Thoracic Surgery*, 49(6), 1578–1585.
- Rizzo, D. C. (2015). *Fundamentals of anatomy and physiology*. Cengage Learning.
- Seto, H. (1935). Ueber zwischen Aorta und Arteria pulmonalis gelegene Herzparaganglien. *Zschr. Zellforsch.*, 22, 213–231.
- Suito, H., Takizawa, K., Huynh, V. Q. H., Sze, D., & Ueda, T. (2014). FSI analysis of the blood flow and geometrical characteristics in the thoracic aorta. *Computational Mechanics*, 54(4), 1035–1045.
- Tanaka, T., & Fung, Y. C. (1974). Elastic and inelastic properties of the canine aorta and their variation along the aortic tree. *Journal of Biomechanics*, 7, 357–370.
- Teng, Z., Canton, G., Yuan, C., Ferguson, M., Yang, C., Huang, X., Zheng, J., Woodard, P. K., & Tang, D. (2010). 3D critical plaque wall stress is a better predictor of carotid plaque-rupture sites than flow shear stress: An in vivo MRI-based 3D FSI study. *Journal of Biomechanical Engineering*, 132(3), 31007.

- Tokuda, Y., Min-Ho, S., Yuichi, U., Akihiko, U., Toshiaki, A., Shigeru, Y., & Shigeru, M. (2008). Three-dimensional numerical simulation of blood flow in the aorticarch during cardiopulmonary bypass. *European Journal of Cardio-Thoracic Surgery*, 33(2), 164–167.
- Tse, K. M., Chang, R., Lee, H. P., Lim, S. P., Venkatesh, S. K., & Ho, P. (2012). A computational fluid dynamics study on geometrical influence of the aorta on haemodynamics. *European Journal of Cardio-Thoracic Surgery*, 43(4), 829–838.
- Ursino, M. (1998). Interaction between carotid baroregulation and the pulsating heart: A mathematical model. *American Journal of Physiology-Heart and Circulatory Physiology*, 275(5), H1733–H1747.
- Von Spiczak, J., Crelier, G., Giese, D., Kozerke, S., Maintz, D., & Bunck, A. C. (2015). Quantitative analysis of vortical blood flow in the thoracic aorta using 4D phase contrast MRI. *PLoS One*, 10(9), e0139025. Published 2015 Sep. 29.

This page intentionally left blank

# Modern placental imaging methods

# 15

Christopher Edwards<sup>1,3</sup>, Erika Cavanagh<sup>1,2,3</sup>, Vicki L. Clifton<sup>4,5</sup>

<sup>1</sup>School of Clinical Sciences, Faculty of Health, Queensland University of Technology, Brisbane, QLD, Australia; <sup>2</sup>Centre for Biomedical Technologies, Queensland University of Technology, Brisbane, QLD, Australia; <sup>3</sup>Mater Centre for Maternal-Fetal Medicine, Mater Mother's Hospital, South Brisbane, QLD, Australia; <sup>4</sup>Mater Research Institute-University of Queensland, South Brisbane, QLD, Australia; <sup>5</sup>Faculty of Medicine, The University of Queensland, Herston, QLD, Australia

## Chapter outline

Introduction .....	305
Ultrasound .....	307
Doppler .....	308
Volume rendering .....	310
Sonoelastography .....	312
Placental elastography .....	315
Magnetic resonance imaging .....	316
Conclusion .....	319
References .....	320

## Introduction

The primary function of the human placenta is to provide a sophisticated mechanism for gas and nutrient exchange between the mother and the fetus (Regnault et al., 2002). Successful placental development is pivotal for the fetus's immediate and long-term growth and development. The placenta is the body's only temporary organ but simultaneously performs the actions of several permanent organs during fetal development, including the lungs, gut, liver, and kidneys. The hormonal impacts of the placenta on the body are also significant (Saw et al., 2021). For example, developing metabolic and cardiovascular reserves (Sanghavi & Rutherford, 2014) to keep pace with fetal growth late in pregnancy and optimizing maternal physiology and the timing of lactation postdelivery (Brunton & Russell, 2010). Surprisingly, even with such importance, it is one of the most poorly understood organs. Accurately diagnosing impaired placental function that results in poorer pregnancy outcomes and potential long-term effects is an ongoing challenge in obstetric care (Zhang et al., 2010).

Physiologically maternal blood is supplied to the placenta by the spiral arteries of the myometrium. Arterial remodeling during early pregnancy ensures a high volume of oxygenated maternal blood is delivered at an appropriate rate and pressure to the intervillous space (Burton et al., 2009). Within the intervillous space, the placenta comprises placental villous trees that provide an extensive surface area to facilitate maternal–fetal exchange. Materno–fetal exchange, including the diffusion of oxygen and nutrients to the fetal circulation, occurs as the blood passes over the surface of the placental villi (Lim, 2017). The successful development of this complex maternal–fetal network early in pregnancy ultimately determines the placenta’s ability to sustain fetal growth throughout the pregnancy (Dellschaft et al., 2020). A primary research goal is to understand how inherent maternal physiological drivers influence the structural properties of the placenta’s microarchitecture and how pathophysiological conditions may alter this structure (Guttmacher et al., 2014).

A biomechanical analysis involves studying the physical properties of biological tissues and modeling a relationship with organ structure and function. Analyzing human organs and diseases from a biomechanics perspective can lead to a better understanding of the pathophysiology and pathogenesis of various diseases (Lee & Lim, 2007). This relates to the fact that changes occurring at the cellular level can be correlated to changes at the macroscopic level. For example, the biomechanical properties of cancer cells are unique compared to normal cells. Research into the elastic properties of breast, lung, and cervical cancer cells demonstrates a significant reduction in elasticity (Kwon et al., 2020). Such an approach provides an alternative to assessing disease onset or progression by identifying immediate structural variations that could be used to improve diagnostic accuracy and tailor therapeutic intervention. Biomechanical placental studies, however, are not commonly adopted, with research primarily focusing on biological and anatomical features.

Histological evidence suggests that biomechanical changes in the placental microstructure occur in the presence of disease. These include vascular thrombosis and necrosis (Roberts & Post, 2008) and changes in elastin and collagen (Macara et al., 1996; Wilhelm et al., 2002), potentially impacting the placental tissue’s broader biomechanics. Indeed direct mechanical testing of the delivered placenta demonstrates increased placental stiffness in pregnancies affected by intrauterine growth restriction compared to normal (Saw et al., 2018). However, research involving the delivered placenta has limitations; it is often only available at the end of its lifespan, so the biomechanical properties ex vivo may not be reflective of those in situ. It is well established that many failures in adequate placenta remodeling occur earlier in pregnancy (Cartwright et al., 2010). With the ongoing development of novel non–invasive imaging, such as ultrasound and MRI (Magnetic Resonance Imaging), these biomechanical changes can be detected in living tissue during disease states. Understanding these changes is essential for developing accurate placental physiological and pathophysiological models. Developing digital placenta models from noninvasive imaging could then predict adverse outcomes during pregnancy and their impact on individual long-term effects (Barker, 2006).

Anatomical digital models of the human placenta also provide a direct tool to assist surgical planning. 3D (three-dimensional) placenta models developed from MRI images of living placenta tissue provide accurate preoperative guidance in cases of placental invasion disorders such as placenta accreta (Mulligan et al., 2022).

Further, such human placenta models can also overcome some difficulties associated with using animal models of placental function. The placenta of great apes (orangutans, gorillas, and chimpanzees) is the most comparable to humans. However, sustainability and the need to protect these species require using alternative animal species with functionally and physiologically different pregnancies and placentas, thus limiting the interpretation of the findings and their relevance to human pregnancy. Research involving primates with similar models of placental function (such as baboons) has allowed a greater understanding of the underlying vascular mechanisms of human placental disease (Sunderland et al., 2011). Several detailed reviews outline critical differences between animal and human placenta models (Carter, 2007; Grigsby, 2016) and describe the choice of an animal model depending on the research aims and essential questions. The following sections introduce contemporary imaging modalities used to examine living placental tissue as a prerequisite for modeling the digital placenta. We discuss advantages and limitations, focusing on novel adaptations of standard imaging tools that assist in developing digital biomechanical models of the placenta.

---

## Ultrasound

Ultrasound provides excellent direct macroscopic imaging of the placenta, it is safe, cost-effective, and easily accessible and remains the primary tool for diagnosing and monitoring placental dysfunction's effects on the fetus. Even though it remains the primary tool used in obstetric care, the ability of traditional ultrasound technology to provide necessary structural and functional information specific to the placenta remains challenging. The placenta appears relatively homogeneous on B-mode (brightness mode) ultrasound (Fig. 15.1) during the 1<sup>st</sup> and 2<sup>nd</sup> trimester but can demonstrate some structural variability, particularly in the 3<sup>rd</sup> trimester, even in normal pregnancy (Abramowicz & Sheiner, 2008). This variability includes the presence of macroscopic placental calcifications and areas of sonographic lucencies, called placental lakes. Attempts have been made to grade the visible acoustic features of the placenta (Grannum classification); however, the utility of this system has not been found to correlate well with the degree of disease or perinatal outcomes (Fadl et al., 2017).

Placental development and disease are therefore modeled via indirect ultrasound measurements, such as fetal growth assessment, amniotic fluid volumes, biophysical profile, and fetal and maternal Doppler velocimetry measurements (Breeze & Lees, 2007). The current application of Doppler indices only indirectly estimates placental resistance and the possibility of microvasculature changes. In the case of Fetal Growth Restriction (FGR), it can be clinically suspected on serial ultrasound

**FIGURE 15.1**

Third trimester ultrasound image of the placental parenchyma displayed in B-mode (Brightness mode), demonstrating a typical third trimester appearance. (GE Healthcare Voluson).

examinations when the estimated fetal weight falls below the 10th percentile or there is a sustained reduction in growth velocity, usually most evident on serial measurements of the fetal abdominal circumference (Sovio et al., 2015). Doppler indices from the utero-placental circulation and within the fetus provide further clues on the degree of placental dysfunction. Surveillance in this manner aims to balance the risk of antepartum stillbirth with the risk of early invention (prematurity), which may result in significant neonatal morbidity or death (Unterscheider et al., 2014).

To date, there is limited evidence to support a benefit to the mother or baby from routine ultrasound surveillance using conventional Doppler to detect placental disease in low-risk women (Bricker et al., 2015; Johanson et al., 2002). However, recent ultrasound technological advancements now allow detailed microvascular mapping and the ability to reconstruct 3D placenta volumes in real-time (Leung & Wan, 2022). Further, the application of noninvasive shear wave elastography techniques to placental tissue provides an opportunity to assess biomechanical properties.

## Doppler

The vital role of the placental vascular network is evidenced by corrosion casting studies using MicroCT techniques that associate alterations in the structure of the vascular tree with placental disease (Junaid et al., 2017; Langheinrich et al., 2008). MicroCT is a 3D imaging technique using X-rays, similar to a clinical CT (computed tomography) machine but works on specimens and produces images of significantly increased resolution. These studies showed changes in vascular

volume, vessel size, and length in the presence of placental disease (Junaid et al., 2017). Unfortunately, the ability to display the intricate vascular network of the placenta via traditional Color Doppler Ultrasound (CDU) and Power Doppler Ultrasound (PDU) is limited despite improvements in transducer design and image processing capabilities. CDU has limited sensitivity to slow-flow vessels and is angle-dependent. PDU, which measures, and records flow amplitude affords better visualization of low flow but is still susceptible to blooming artifacts. Blooming artifacts result when the color signal on the image extends beyond the true boundaries of the vessel wall. To address these, High-Definition Flow (HDF) techniques are now available on commercial systems (Fig. 15.2). Compared to conventional CDU and PDU, HDF techniques place a lower priority on velocity and direction and can assign color to the measured Doppler shift. This technique allows the use of shorter pulses resulting in improved axial resolution and sensitivity to flow in smaller vessels. Attempts have been made to combine HDF techniques and 3D ultrasound data to visualize the placental microcirculation. Studies have developed novel placental vascular indexes using 3D data and have shown a reduction in placental vascular flow in women with preeclampsia in the first trimester (Abdallah et al., 2021). Reduced placental flow indexes have also been demonstrated in placentas of growth-restricted twin pregnancies (Sun et al., 2018).

More recently, Microvascular Flow Imaging (MFI) has been introduced and likely holds the most promise in detailing the vasculature network of the placenta (Fig. 15.3). Using digitally encoded ultrasound signals MFI can boost low-velocity flow and enhance spatial resolution. The combination of an enhanced wall filtering system separates low-velocity flow from overlapping background artifacts (Leung & Wan, 2022). The result is a significant improvement in resolution and

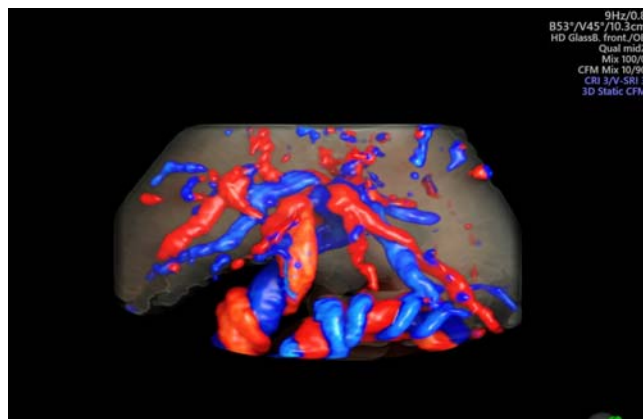


**FIGURE 15.2**

Glass body imaging (GE Healthcare Voluson) combines high-definition color Doppler imaging and 3D/4D technology to demonstrate the placental vessels and umbilical cord insertion.

**FIGURE 15.3**

Microvascular flow imaging (GE Healthcare Voluson) of the placental microvascular network. The technique boosts low-velocity flow and uses enhanced wall filtering to avoid the interruption of background artifacts.

the ability to image the placental microvasculature without adding contrast. Early work has detailed the feasibility of using MFI to visualize the placental villous tree, including vascular branching at different gestational time points. In a study by Sainz et al. (2020), imaging a normal cohort, they tracked villous branch development and demonstrated secondary and tertiary branches were visible with MFI from 20 weeks gestation. By modeling the standard placental villous branching patterns, researchers hope to extrapolate this to detect placental disease. One observational study using this technology observed fewer secondary and tertiary placental villi in intra-uterine growth restriction compared to normal (García-Jiménez et al., 2021). The cohort was a small group of 16 pregnancies, imaged in the 3<sup>rd</sup> trimester, but provides the basis for future work to investigate the clinical significance.

## Volume rendering

The construction of 3D volumes using ultrasound imaging is possible by directing the beam through three spatial dimensions of tissue and combining them via image processing. Reconstructing a 3D volume during live scanning provides a fourth “time” dimension allowing images that display fetal movements and anatomical relationships in real time. Several techniques are available to generate a 3D volume of ultrasound data; traditional methods either use the steady movement of the sonographers’ hand or motors in the transducer to sweep the beam mechanically (Osipov et al., 2018). More sophisticated techniques now utilize electronic sweeping of

the beam in a matrix design. Matrix transducers contain many thousands of elements allowing the agility to steer and focus the beam in multiple directions electronically. Improvements in graphics processing and data transfer rates now allow rapid reconstruction of 3D data (GE Healthcare). Such techniques also allow the simultaneous visualization of two orthogonal planes on a single screen. Another technique is known as VOCAL (Virtual Organ Computer-aided AnaLysis), which enables the reconstruction of the placental volume using multiplanar images acquired at various angles (Sainz et al., 2020) (Fig. 15.4). VOCAL and other 3D methods provide a quantitative measure of placental volume and link to fetal outcomes. In particular, small placental volumes in the first trimester is associated with fetal growth restriction (Collins et al., 2013; Plasencia et al., 2011) and preeclampsia (Hafner et al., 2006).

More recently, the application of artificial intelligence in obstetric ultrasound may provide further opportunities (Edwards, Cavanagh, et al., 2022). Placental volume estimates are still operator-dependent and result in additional postprocessing time. To acquire an individualized digital model of the placenta in real time, investigators use machine learning techniques to segment the placental volume. One novel application developed by Looney et al. (Looney et al., 2018) and trained on a large three-dimensional US dataset, OxNNNet, segments the placenta in the first trimester. This system demonstrates excellent volume accuracy compared to a growth-truth data set, and the results were correlated with the prediction of small

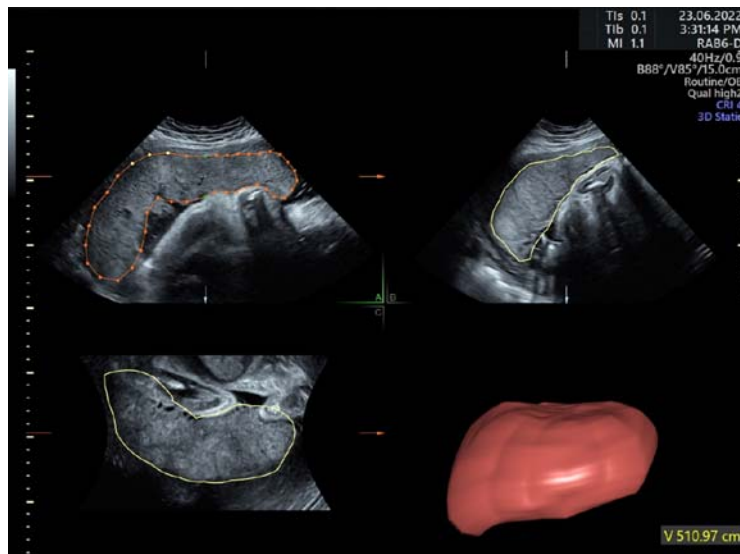


**FIGURE 15.4**

Three-dimensional reconstruction of the placenta at 34 weeks' gestation, using the VOCAL (GE Healthcare Voluson) method with a 30-degree rotation angle. VOCAL Virtual Organ Computer-aided AnaLysis.

for gestational age babies at term. In machine learning techniques, a ground-truth dataset has known properties and is used to check the accuracy of newly developed algorithms (Chartrand et al., 2017). Borrowed from meteorology, the “ground truth” refers to direct weather observations on-site and can be used to check remote sensors such as a Doppler radar system. Other deep learning methods to automate placental segmentation and volume calculation are also under development (Barr et al., 2015).

Developing clinically relevant ultrasound-based deep learning algorithms is not without problems. The size and availability of high-quality ultrasound datasets are limited compared to other imaging modalities (MRI and CT) (Edwards, Cavanagh, et al., 2022). The broader practical applicability of trained algorithms may also present issues, for example, one set of parameters may fail when using different equipment manufacturers or methods. Regardless, the field is rapidly expanding, and new tools with specific functions, such as automating measurement calculations to reduce operator dependency, are in development (Edwards, Cavanagh, et al., 2022).

---

## Sonoelastography

Sonoelastography measures changes in tissue deformation, reflective of its elastic properties when an internal or external force is applied (Edwards, Cavanagh, et al., 2022), indicative of underlying pathology (Barr et al., 2015; Berzigotti, 2017; Monpeyssen et al., 2013; Nakashima et al., 2013). For example, ultrasound elastography can reliably estimate the severity of hepatic fibrosis (Cosgrove et al., 2013; Dietrich & Bamber, 2018; Shiina et al., 2015). Indeed, sonoelastography is routinely used in patients with chronic liver disease (Ferraioli et al., 2014) and for characterizing breast and thyroid masses (Cimsit et al., 2015; Kılıç et al., 2015). More recently, research has shown utility in estimating cervical incompetence (O’Hara, Zelesco, & Sun, 2019) and vascular and cardiac function (Song et al., 2016). Using sonoelastography to assess the placenta is a relatively new field of study (Edwards et al., 2020).

Depending on the method used to apply the distortion force to soft tissue, ultrasound systems use two different techniques—quasi-static and dynamic elastography (Fig. 15.5) (Bamber et al., 2013). Quasi-static refers to Strain Elastography (SE) or Strain Rate Imaging (SRI), in which the relative deformation of the given target tissue is estimated by applying pressure with the ultrasound transducer (Bamber et al., 2013; Li & Cao, 2017; Sigrist et al., 2017). The relative deformation of the imaged tissue becomes a measure of strain, and used to estimate its relative stiffness (Shiina et al., 2015). The force applied at the surface is unknown, so accurate elasticity quantification at varying depths is challenging to achieve (Bamber et al., 2013). In contrast, dynamic elastography modifies the ultrasound pulse to produce an acoustic radiation impulse (Fig. 15.5B) or force applied via an externally controlled vibration (Nightingale, 2011) (Fig. 15.5C). Tissue displacement can then be displayed directly as an image property, as is demonstrated in Acoustic Radiation Force Impulse (ARFI) imaging (Nightingale et al., 2002), or via the calculation of a

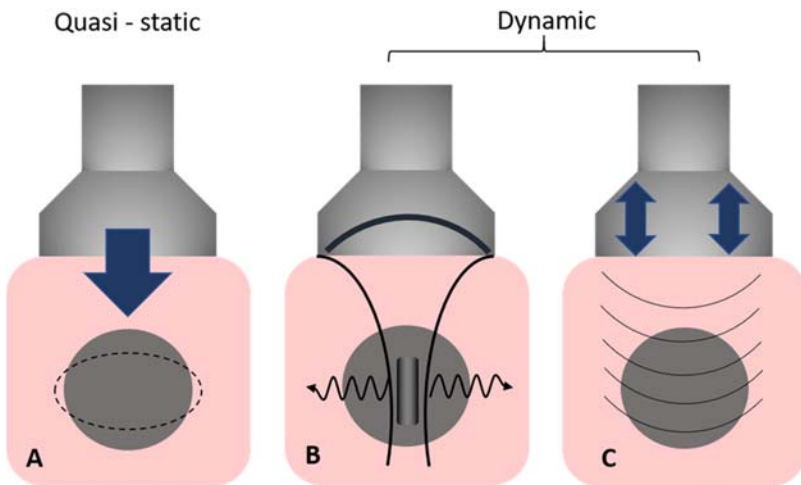


**FIGURE 15.5**

Main methods used in sonoelastography. (A) Manual compression with the transducer (strain elastography). (B) Radiation force impulse generating local shear waves (shear wave elastography). (C) External controlled vibration generating surface shear waves (transient elastography).

generated shear wave velocity, known as Shear Wave Elastography (SWE) ([Sigrist et al., 2017](#)).

Transient Elastography (TE) is the term used to describe a technique in which the force is applied via an externally controlled vibration, for example, the commercially available FibroScan (Echosens, France) designed to assess liver disease ([Garra et al., 1997; Kudo et al., 2013; Pang et al., 2014](#)). Both types of systems, TE and SWE calculate Shear Wave Velocity (SWV) in tissue. TE systems measure the velocity of the shear wave generated at the surface, while SWE systems measure the SWV at a specific depth after applying a focused acoustic radiation pulse ([Shiina et al., 2015](#)). Compared to the primary ultrasound beam, shear waves travel more slowly and perpendicularly ([Shiina, 2013](#)). In the case of SWE, the shear wave is tracked using Doppler technology, typically utilizing a time-of-flight method ([O'Hara, Zelesco, & Sun, 2019](#)). Therefore, SWE is a quantitative measure of tissue elasticity, with higher velocities correlating with stiffer tissue and lower velocities to softer, more elastic structures ([Shiina, 2013](#)).

Ultrasound system manufacturers have designed systems to apply the acoustic radiation force pulse to a fixed region of interest, as for point Shear Wave Elastography (pSWE) ([Akbas et al., 2019; Dietrich et al., 2017](#)). Alternatively, multiple acoustic force pulses produce a two-dimensional parametric color map of tissue stiffness, referred to as two-dimensional Shear Wave Elastography (2D-SWE) ([Berzigotti & Bosch, 2018; Sigrist et al., 2017](#)). 2D-SWE then allows the operator to “sample” areas within this color map to obtain quantitative measurements of

tissue elasticity by either measuring the SWV or converting this to an elasticity value. 2D-SWE systems also provide the operator with a range of tools to assess the reliability of the elastography measurements via quality and propagation maps (O'Hara, Zelesco, Rocke et al., 2019) (Fig. 15.6).

Many equipment manufacturers provide the option to convert SWV to a unit of pressure, using a simplified Young's modulus equation:  $E$  [kPa] =  $3 \times (\text{SWV})^2$  (Shiina et al., 2015). It is essential to understand the relationship between SWV, Young's modulus  $E$ , and the shear modulus  $G$ . Both elastic moduli  $E$  and  $G$  indicate the difficulty to deform tissue via either compression ( $E$ ) or shear stress ( $G$ ). The relationship between the Young's modulus and the shear modulus can be expressed as

$$G = \frac{E}{2(1 + \vartheta)} \quad (15.1)$$

In this equation,  $\vartheta$  represents the Poisson's ratio, a ratio of a material's transverse to axial strain. Given the high-water content of soft tissue, the Poisson's ratio is assumed to be 0.5 and equal to that of incompressible material. Therefore, for practical purposes, the following approximation can be made:

$$G \approx \frac{E}{3} \quad (15.2)$$

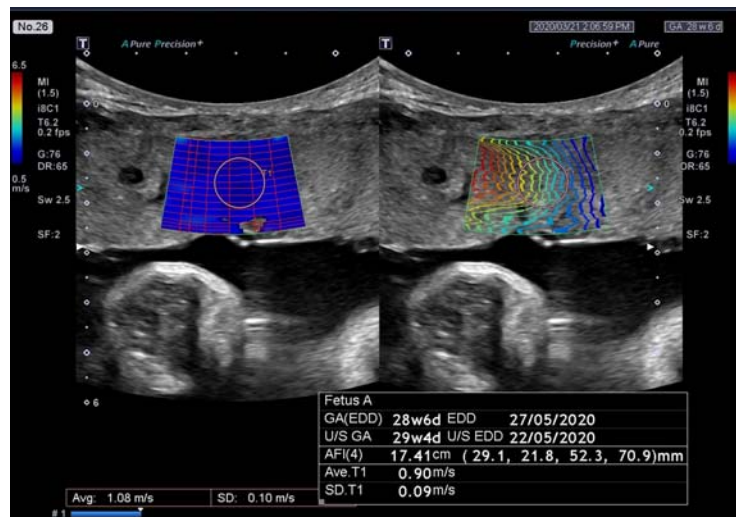


**FIGURE 15.6**

Placental 2D-SWE display from Aplio 600, i-series (Canon Medical Systems Japan), left side 2D color coded shear wave speed map with 1 cm<sup>2</sup> Region Of Interest (ROI), right side reliability propagation map, parallel lines represent areas of high reliability. Box display provides user with SWV [m/s] and the ROI standard deviation (SD).

Since there is a direct relationship between the shear modulus  $G$  and SWV via the following equation:

$$\text{SWV} = \sqrt{\frac{G}{\rho}} \quad (15.3)$$

An estimate of  $E$  can then be made via the simplified Young's modulus equation.

$$E \equiv 3\rho\text{SWV}^2 \quad (15.4)$$

In this equation,  $\rho$  is the material density, typically assumed to be 1 g/cm<sup>3</sup> for soft tissue. Therefore, commercial ultrasound systems using SWV as the physical quantity calculate the Young's modulus assuming that the interrogated tissue is homogeneous, isotropic, and incompressible with a constant density.

$$E \equiv 3\text{SWV}^2 \quad (15.5)$$

Magnetic Resonance Elastography (MRE) systems combine MRI imaging with low-frequency vibrations to create a visual map (elastogram) which reflects the stiffness of body tissues. Due to the different technologies, values reported on an ultrasound system are not directly interchangeable with those reported on an MRE system. Further, it is essential to understand that different techniques and technology used to measure tissue elasticity in different commercially available ultrasound systems often result in output variations, making direct comparison problematic (Ferraioli et al., 2018; Hall et al., 2013).

---

## Placental elastography

A range of research has evaluated the typical elastic properties of placental tissue in vivo and ex vivo using sonoelastography (Abeysekera et al., 2017; Altunkeser et al., 2019; Edwards et al., 2021; Li et al., 2012; McAleavy et al., 2016; Ohmaru et al., 2015; Saw et al., 2018; Simon et al., 2017; Sugitani et al., 2013; Wu et al., 2016). Reports measure elasticity as SWV in [m/s] or [kPa], and some variation reflects the different technologies and systems used. However, initial reports of the reliability of in vivo placental elastography measurements on a single system appear promising. Akbas et al. (Akbas et al., 2019), using a pSWE system, reported high intra- and inter-observer reliability (ICC 0.89 and 0.87, respectively). This is further supported by studies of placental elastography in different cohorts of women where utilizing similar ultrasound platforms often resulted in comparable mean SWV (Fujita et al., 2019; Wu et al., 2016). Longitudinal studies designed to assess placental stiffness at varying stages of pregnancy also suggest relative stability. (Edwards et al. 2021), modeled a range of regular fetal and maternal physiology changes with ultrasound elasticity values and reported relative stability of placental stiffness at various gestational ages. These findings provide confidence that significant changes in SWV during pregnancy represent changes in the placenta's physical

elastic properties and are likely reflective of placental disease rather than the normal growth and development of the placenta.

Several studies have used sonoelastography to investigate the placentae of hypertensive and preeclamptic women in both ex vivo (Sugitani et al., 2013) and in vivo (Alan et al., 2016; Fujita et al., 2019; Karaman et al., 2016; Ohmaru et al., 2015) conditions. The histological and morphological changes in these placentae appear to result in much higher SWV than normal controls. Further, studies in vivo (Altunkeser et al., 2019; Roberts & Post, 2008; Song et al., 2016) and ex vivo (Kwon et al., 2020; Langheinrich et al., 2008; Li et al., 2012; McAleavy et al., 2016) suggest that parenchymal SWV is higher in placentae from pregnancies complicated by FGR. Research has also linked stiffness changes in the placenta to maternal conditions such as obesity (Edwards et al., 2022). Modeling these adaptations is essential to understanding the placenta's role in chronic metabolic diseases later in life (Catalano & Ehrenberg, 2006; Curhan et al., 1996; Voerman et al., 2019).

Safety consideration of in vivo placental elastography has centered on the possible consequences of tissue/cell displacement due to the radiation force pulse resulting in damage to the developing fetus (Society P by the SG of the BMU, 2010). However, no placental histological changes resulting from sonoelastography have been reported. Although radiation force-based elastography operates with a higher thermal index (TI), it remains within recommended safety limits. TI is an on-screen indicator that indicates the potential for tissue temperature rise and is dependent on tissue types (Society P by the SG of the BMU, 2010). Some studies have reported mean TI values comparable to that generated by conventional Doppler ultrasound (Kılıç et al., 2015). Nevertheless, the British Medical Ultrasound Society recommends that SWE exposure be limited to less than 15 min (Society P by the SG of the BMU, 2010).

Modeling changes in placental biomechanical properties via ultrasound also has implications beyond the immediate diagnosis of placental dysfunction and disease. A range of research activities have investigated the impact of interventions on developing pregnancies; for example, exercise regimes used to promote positive pregnancy outcomes (Kubler et al., 2022). Structural placental health is a measure of its volume and the growth and distribution of chorionic villi within the placenta (Biswas et al., 2008). Therefore, there is interest in whether specific interventions provide positive placental adaptations that may reduce the risk of placental disease. Research suggests an increase in placental volume with exercise (Clapp et al., 2000), although whether tailored training also results in structural adaptations remains unknown.

## Magnetic resonance imaging

Magnetic Resonance Imaging (MRI) is a noninvasive cross-sectional imaging tool that provides excellent anatomical detail by exploiting differences in water and fat content of the tissue. In the absence of a strong magnetic field, protons of hydrogen atoms bound in water or fat spin randomly. When placed into the electric

field of an MRI machine, these protons align to the strong magnetic field. The protons spin out of equilibrium after applying a radiofrequency (RF) pulse, rotating their axes away from the magnetic field. When the RF field is switched off, the MRI sensors detect and record the energy released by the realigning protons. The different relaxation properties of these tissue types can be separated, resulting in images with high soft tissue contrast and resolution. MRI during pregnancy is most commonly used to assess suspected fetal structural anomalies or diseases of abnormal placental adherence (Saleem, 2014). MRI has the advantage that image quality is less dependent on operator skill, maternal obesity, and lack of contrast due to pregnancy complications such as low amniotic fluid level (oligohydramnios), which can severely impair ultrasound image quality.

The application of MRI for imaging the placenta is becoming more common due to its increasing availability and ongoing improvements in image quality. MRI, like ultrasound, can reconstruct images without ionizing radiation and therefore has a favorable safety profile. However, studies investigating MR's safety during pregnancy have examined the potential for teratogenic effects due to magnetic field strength and the potential for tissue heating due to pulsing RF fields (Lum & Tsioris, 2020). Another consideration is the potential for hearing loss in the developing fetus (Strizek et al., 2015). MR machines can produce audible noise approaching 100 dB at higher field strengths (Price et al.). MRI studies during pregnancy include prospective animal studies and extensive retrospective cohort studies in humans (Lum & Tsioris, 2020). In vivo studies in which mammalian animals were exposed to MR for long periods showed reduced fetal size in early pregnancy, reduced birth weights and increased fetal loss (Heinrichs et al., 1988; Magin et al., 2000). Importantly, retrospective human studies have not confirmed these effects, which use much shorter exposure times of approximately 30 min or less. A large Canadian study that included 1.4 million pregnancies between 2003 and 2015 (Ray et al., 2016) retrospectively investigated the effect of MRI exposure during the first trimester and the risk of stillbirth or neonatal death as well as congenital anomaly, hearing and vision loss and cancer from birth to 4 years of age. The study included 5654 pregnancies that had an MRI scan and found MRI use was not associated with detrimental fetal outcomes. This study excluded pregnancies that ended before 21 weeks, so it failed to determine the risk of spontaneous abortion before this time. A field strength of 1.5T (Victoria et al., 2014) is commonly used in clinical studies, and to date, the safety of higher field strengths, such as 3T, is yet to be determined using longitudinal follow-up studies. The current guidance from the American College of Obstetricians and Gynecologists is "MRI is not associated with risk but should be used prudently and only when use is expected to answer a relevant clinical question or otherwise provide medical benefit to the patient" (American College of Obstetricians and Gynecologists' Committee on Obstetric Practice, 2016).

The safety of gadolinium-based contrast agents is less specific. There is evidence of transplacental pharmacokinetics of these agents (Mühler et al., 2011) and, therefore, the potential to expose the fetus. The possibility of fetal teratogenic effects from gadolinium is unclear; however, studies have confirmed signal changes in adult

brains following multiple administrations (Kanda et al., 2013). Furthermore, the rapid development of the fetal brain and the potential for repeated exposure in later life is of particular concern (Lum & Tsioris, 2020). Studies have not directly associated any risk in utero; however, a single cohort study was linked to a slight increase in neonatal death and increased rates of rheumatological, inflammatory, or infiltrative skin conditions in the early pediatric period (Ray et al., 2016). As a result, guidelines stress balancing the fetal and maternal benefits and risks before using gadolinium-based agents during pregnancy (Lum & Tsioris, 2020).

MRI can visualize the placenta's size and shape and offers a diagnostic role in cases of abnormal placental attachment (Lax et al., 2007). A significant advantage is the entire placenta can be imaged at any gestational age. In a normally developing placenta, the organ appears homogeneous with low signal intensity on T1-weighted sequences and high signal intensity on T2-weighted sequences (Fig. 15.7) (Gowland, 2005). In cases of placental dysfunction, such as FGR and PE, the T2-signal has been shown to be depressed, resulting in a darker appearance that may result from fibrosis, necrosis, and infarction (Aughwane et al., 2020). Various other placental MR sequences have been proposed in the research literature but have not been widely applied in clinical practice (Aughwane et al., 2020). One such method is diffusion-weighted sequences, which are sensitive to water molecules in the extracellular and intracellular environment (Gowland, 2005). Water molecules in the extracellular spaces experience free random diffusion, whereas intracellular water is restricted. Pathological processes such as tissue infarction and malignancy demonstrate an increase in the intracellular portion resulting in diffusion of water that is relatively more restricted. Studies of placental dysfunction using diffusion-

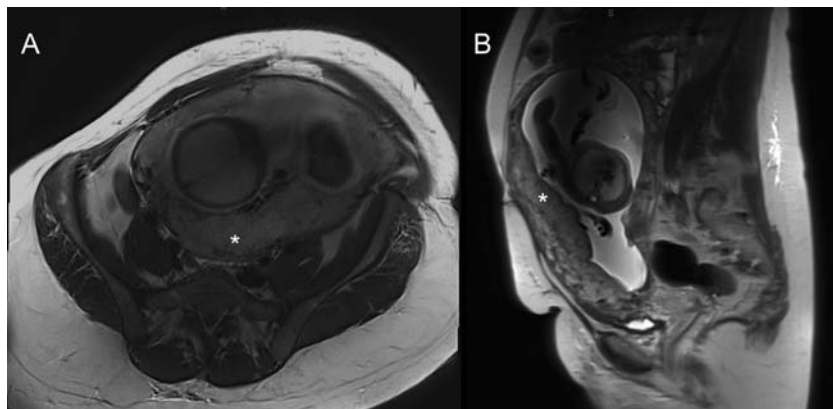


**FIGURE 15.7**

MRI can visualize the entire placental size and shape, at any gestational age. (A) Parenchyma and placental/myometrial interface in the axial plane; (B) Demonstrates a T2-weighted sagittal plane. (\* Indicates the placenta).

weighted sequences have shown restricted diffusion as a potential early marker for fetal growth restriction ([Gowland, 2005](#)).

Functional studies of the placenta using MRI are less common, some of which require administering a contrast agent. The recommendation mentioned above to restrict the use of gadolinium-based contrast agents in pregnancy limits some MR sequences. However, newer sequences in which hemoglobin is used as an “endogenous contrast agent” could offer new ways to assess the microvascular and functional properties of the placenta ([Siauve et al., 2015](#)). One such approach is adapting imaging sequences used for functional brain imaging. Blood Oxygen Level-Dependent (BOLD) maps the oxygenation levels within the tissue, potentially allowing the detection of clinically significant placental hypoxia ([Luo et al., 2017](#)). However, several physiological and technical difficulties must be overcome, such as random fetal movements, before these are more widely instigated. With further development, MRI will likely increase our understanding of abnormal placental function, improve diagnostic accuracy, and help guide intervention and monitor response.

Several international collaborative studies have been initiated to gain further insight into the role of MRI imaging in the placenta and overcome some of the challenges. These include the Human Placenta Project (HPP) and the Placenta Imaging Project (PIP), funded by the United States National Institute of Child Health and Development (NICHD) ([Human Placenta Project, n.d.](#); [Placenta Imaging Project, n.d.](#)). These studies aim to develop new tools to study the organ during pregnancy to learn how it develops and functions. As part of this research, investigators are developing novel ways to account for the motion of the uterus and fetus to make it easier to study ([Turk et al., 2017](#); [Using MRI to Visualize the Placenta n.d.](#)). Other techniques such as microstructure assessment based on diffusion imaging and optimized placental imaging using conventional T1 and T2 sequences are being developed. This work will also examine the safety of MRE in assessing the human placenta in normal and abnormal pregnancies ([Placenta Imaging Project, n.d.](#)) and is expected to support a biomechanical modeling perspective.

MRI has also been used to evaluate the stillborn fetus, and some investigators have demonstrated a correlation between lung parenchyma and pleural changes and the postmortem interval ([Barber et al., 2016](#); [Paternoster et al., 2019](#)). Evaluating the placenta in cases of stillbirth by MRI may also provide additional evidence to model and explain the events leading to stillbirth. However, the role of imaging in this field is yet to be defined, and more studies are required ([Paternoster et al., 2019](#)).

---

## Conclusion

Technological advancements in imaging methods are leading to a greater understanding of the placental/feto—maternal system; however, more work is needed to develop comprehensive models. The aim is to create a complete digital twin of the entire microvascular structure of the placenta to better understand the impact

of disease on this unique environment. Such models could then be individualized using patient-specific imaging and clinical data to improve pregnancy outcomes. MRI and ultrasound offer promising avenues to develop sophisticated digital twin models, and new techniques are evolving. However, both modalities will require improved precision and accuracy and overcome substantial technical hurdles for greater clinical transferability. In terms of ultrasound elastography, the ability to noninvasively quantify the biomechanical properties of the placenta is promising. Developing more sophisticated elastic models and technological standardizations across platforms will improve clinical utility. Faster and more sophisticated MRI sequences are also needed to quantify the intricate developmental changes within the placenta during pregnancy. The large amount of data acquired during imaging studies also provide new opportunities for researchers to develop deep learning-based computerized models. Once validated, these models will likely present new insights and improve our knowledge of the placenta's critical role in human health and development.

---

## References

- Abdallah, A., Khairy, M., Tawfik, M., Mohamed, S., Abdel-Rasheed, M., Salem, S., et al. (2021). Role of first-trimester three-dimensional (3D) power Doppler of placental blood flow and 3D placental volume in early prediction of pre-eclampsia. *International Journal of Gynecology & Obstetrics*, 154, 466–473. <https://doi.org/10.1002/IJGO.13572>
- Abeysekera, J. M., Ma, M., Pesteie, M., Terry, J., Pugash, D., Hutcheon, J. A., et al. (2017). SWAVE imaging of placental elasticity and viscosity: Proof of concept. *Ultrasound in Medicine and Biology*, 43, 1112–1124. <https://doi.org/10.1016/j.ultrasmedbio.2017.01.014>
- Abramowicz, J. S., & Sheiner, E. (2008). Ultrasound of the placenta: A systematic approach. Part I: Imaging. *Placenta*, 29, 225–240. <https://doi.org/10.1016/j.placenta.2007.12.006>
- Akbas, M., Koyuncu, F. M., & Artunç-Ulkumen, B. (2019). Placental elasticity assessment by point shear wave elastography in pregnancies with intrauterine growth restriction. *Journal of Perinatal Medicine*, 47, 841–846. <https://doi.org/10.1515/jpm-2019-0238>
- Alan, B., Tunç, S., Agacayak, E., & Bilici, A. (2016). Diagnosis of pre-eclampsia and assessment of severity through examination of the placenta with acoustic radiation force impulse elastography. *International Journal of Gynecology & Obstetrics*, 135, 43–46. <https://doi.org/10.1016/j.ijgo.2016.03.037>
- Altunkeser, A., Alkan, E., Günenç, O., Tolu, İ., & Körez, M. K. (2019). Evaluation of a healthy pregnant placenta with ShearWave elastography. *Iranian Journal of Radiology*, 16. <https://doi.org/10.5812/iranjradiol.68280>
- American College of Obstetricians and Gynecologists' Committee on Obstetric Practice. (2016). Committee opinion No. 656 summary. *Obstetrics & Gynecology*, 127, 418. <https://doi.org/10.1097/AOG.0000000000001309>
- Aughwane, R., Ingram, E., Johnstone, E. D., Salomon, L. J., David, A. L., & Melbourne, A. (2020). Placental MRI and its application to fetal intervention. *Prenatal Diagnosis*, 40, 38–48. <https://doi.org/10.1002/pd.5526>

- Bamber, J., Cosgrove, D., Dietrich, C. F., Fromageau, J., Bojunga, J., Calliada, F., et al. (2013). EFSUMB guidelines and recommendations on the clinical use of ultrasound elastography. Part 1. Basic principles and technology. *Ultraschall in der Medizin*, 34, 169. <https://doi.org/10.1055/s-0033-1335205>
- Barber, J. L., Hutchinson, J. C., Sebire, N. J., & Arthurs, O. J. (2016). Pleural fluid accumulation detectable on paediatric post-mortem imaging: A possible marker of interval since death? *International Journal of Legal Medicine*, 130, 1003–1010. <https://doi.org/10.1007/S00414-016-1320-9/FIGURES/5>
- Barker, D. J. P. (2006). Adult consequences of fetal growth restriction. *Clinical Obstetrics and Gynecology*, 49, 270–283. <https://doi.org/10.1097/00003081-200606000-00009>
- Barr, R. G., Nakashima, K., Amy, D., Cosgrove, D., Farrokhi, A., Schafer, F., et al. (2015). WFUMB guidelines and recommendations for clinical use of ultrasound elastography: Part 2: Breast. *Ultrasound in Medicine and Biology*, 41, 1148–1160. <https://doi.org/10.1016/j.ultrasmedbio.2015.03.008>
- Berzigotti, A. (2017). Non-invasive evaluation of portal hypertension using ultrasound elastography. *Journal of Hepatology*, 67. <https://doi.org/10.1016/j.jhep.2017.02.003>
- Berzigotti, A., & Bosch, J. (2018). Diagnostic methods for cirrhosis and portal hypertension. <https://doi.org/10.1007/978-3-319-72628-1>.
- Biswas, S., Ghosh, S. K., & Chhabra, S. (2008). Surface area of chorionic villi of placentas: An index of intrauterine growth restriction of fetuses. *Journal of Obstetrics and Gynaecology Research*, 34, 487–493. <https://doi.org/10.1111/j.1447-0756.2008.00719.x>
- Breeze, A. C., & Lees, C. C. (2007). Prediction and perinatal outcomes of fetal growth restriction. *Seminars in Fetal and Neonatal Medicine*, 12, 383–397. <https://doi.org/10.1016/j.siny.2007.07.002>
- Bricker, L., Medley, N., & Pratt, J. J. (2015). Routine ultrasound in late pregnancy (after 24 weeks' gestation). *Cochrane Database Systematic Reviews*, 2015, Cd001451. <https://doi.org/10.1002/14651858.CD001451.pub4>
- Brunton, P. J., & Russell, J. A. (2010). Endocrine induced changes in brain function during pregnancy. *Brain Research*, 1364, 198–215. <https://doi.org/10.1016/J.BRAINRES.2010.09.062>
- Burton, G. J., Woods, A. W., Jauniaux, E., & Kingdom, J. C. P. (2009). Rheological and physiological consequences of conversion of the maternal spiral arteries for uteroplacental blood flow during human pregnancy. *Placenta*, 30, 473–482. <https://doi.org/10.1016/j.placenta.2009.02.009>
- Carter, A. M. (2007). Animal models of human placentation – a review. *Placenta*, 28, S41–S47. <https://doi.org/10.1016/J.PLACENTA.2006.11.002>
- Cartwright, J. E., Fraser, R., Leslie, K., Wallace, A. E., & James, J. L. (2010). Remodelling at the maternal–fetal interface: Relevance to human pregnancy disorders. *Reproduction*, 140, 803–813. <https://doi.org/10.1530/REP-10-0294>
- Catalano, P., & Ehrenberg, H. (2006). Review article: The short- and long-term implications of maternal obesity on the mother and her offspring. *BJOG: An International Journal of Obstetrics & Gynaecology*, 113, 1126–1133. <https://doi.org/10.1111/j.1471-0528.2006.00989.x>
- Chartrand, G., Cheng, P. M., Vorontsov, E., Drozdal, M., Turcotte, S., Pal, C. J., et al. (2017). Deep learning: A primer for radiologists. *Radiographics*, 37, 2113–2131. <https://doi.org/10.1148/rg.2017170077>
- Cimsit, C., Yoldemir, T., & Akpinar, I. N. (2015). Shear wave elastography in placental dysfunction: Comparison of elasticity values in normal and preeclamptic pregnancies in

- the second trimester. *Journal of Ultrasound in Medicine*, 34, 151–159. <https://doi.org/10.7863/ultra.34.1.151>
- Clapp, J. F., Kim, H., Burciu, B., & Lopez, B. (2000). Beginning regular exercise in early pregnancy: Effect on fetoplacental growth. *American Journal of Obstetrics and Gynecology*, 183, 1484–1488. <https://doi.org/10.1067/MOB.2000.107096>
- Collins, S. L., Stevenson, G. N., Noble, J. A., & Impey, L. (2013). Rapid calculation of standardized placental volume at 11 to 13 Weeks and the prediction of small for gestational age babies. *Ultrasound in Medicine and Biology*, 39, 253–260. <https://doi.org/10.1016/J.UCLASMEDBIO.2012.09.003>
- Cosgrove, D., Piscaglia, F., Bamber, J., Bojunga, J., Correas, J.-M., Gilja, O., et al. (2013). EFSUMB guidelines and recommendations on the clinical use of ultrasound elastography. Part 2: Clinical applications. *Ultraschall Der Medizin - European Journal of Ultrasound*, 34, 238–253. <https://doi.org/10.1055/s-0033-1335375>
- Curhan, G. C., Chertow, G. M., Willett, W. C., Spiegelman, D., Colditz, G. A., Manson, J. E., et al. (1996). Birth weight and adult hypertension and obesity in women. *Circulation*, 94, 1310–1315. <https://doi.org/10.1161/01.CIR.94.6.1310>
- Dellschaft, N. S., Hutchinson, G., Shah, S., Jones, N. W., Bradley, C., Leach, L., et al. (2020). The haemodynamics of the human placenta in utero. *PLoS Biology*, 18, e3000676. <https://doi.org/10.1371/journal.pbio.3000676>
- Dietrich, C., & Bamber, J. (2018). Editorial on the special issue of applied sciences on the topic of elastography. *Applied Sciences*, 8, 1232. <https://doi.org/10.3390/app8081232>
- Dietrich, C. F., Bamber, J., Berzigotti, A., Bota, S., Cantisani, V., Castera, L., et al. (2017). EFSUMB guidelines and recommendations on the clinical use of liver ultrasound elastography, update 2017 (long version). *Ultraschall Der Medizin - European Journal of Ultrasound*, 38. <https://doi.org/10.1055/s-0043-103952>. e16–47.
- Edwards, C., Cavanagh, E., Kumar, S., Clifton, V. L., Borg, D. J., Priddle, J., et al. (2021). Changes in placental elastography in the third trimester - analysis using a linear mixed effect model. *Placenta*, 114, 83–89. <https://doi.org/10.1016/j.placenta.2021.09.001>
- Edwards, C., Cavanagh, E., Kumar, S., Clifton, V. L., Borg, D. J., Priddle, J., et al. (2022). Relationship between placental elastography, maternal pre-pregnancy body mass index and gestational weight gain. *Placenta*, 121, 1–6. <https://doi.org/10.1016/j.placenta.2022.02.015>
- Edwards, C., Cavanagh, E., Kumar, S., Clifton, V., & Fontanarosa, D. (2020). The use of elastography in placental research – a literature review. *Placenta*, 99, 78–88. <https://doi.org/10.1016/j.placenta.2020.07.014>
- Edwards, C., Chamunyonga, C., Searle, B., & Reddan, T. (2022). The application of artificial intelligence in the sonography profession: Professional and educational considerations. *Ultrasound*. <https://doi.org/10.1177/1742271X211072473>, 1742271X2110724.
- Fadl, S., Moshiri, M., Fligner, C. L., Katz, D. S., & Dighe, M. (2017). Placental imaging: Normal appearance with review of pathologic findings. *Radiographics*, 37, 979–998. <https://doi.org/10.1148/rg.2017160155>
- Ferraioli, G., De Silvestri, A., Lissandrini, R., Maiocchi, L., Tinelli, C., Filice, C., et al. (2018). Evaluation of inter-system variability in liver stiffness measurements. *Ultraschall Der Medizin*, 40, 64–75. <https://doi.org/10.1055/s-0043-124184>
- Ferraioli, G., Parekh, P., Leviton, A. B., & Filice, C. (2014). Shear wave elastography for evaluation of liver fibrosis. *Journal of Ultrasound in Medicine*, 33, 197–203. <https://doi.org/10.7863/ultra.33.2.197>

- Fujita, Y., Nakanishi, T. O., Sugitani, M., & Kato, K. (2019). Placental elasticity as a new non-invasive predictive marker of pre-eclampsia. *Ultrasound in Medicine and Biology*, 45, 93–97. <https://doi.org/10.1016/j.ultrasmedbio.2018.09.007>
- García-Jiménez, R., Arroyo, E., Borrero, C., García-Mejido, J. A., Sosa, F., Fernández-Palacín, A., et al. (2021). Evaluation of placental micro-vascularization by superb micro-vascular imaging Doppler in cases of intra-uterine growth restriction: A first step. *Ultrasound in Medicine and Biology*, 47, 1631–1636. <https://doi.org/10.1016/j.ultrasmedbio.2021.01.029>
- Garra, B., Cespedes, E., Ophir, J., Spratt, S., Zurbier, R., Magnant, C., et al. (1997). Elastography of breast lesions. *Radiology*, 202, 79–86.
- GE Healthcare. (n.d.). VolusonTM E10 | Women's Health Ultrasound | GE Healthcare (United States) . <https://www.gehealthcare.com/products/ultrasound/voluson/voluson-e10>. Accessed July 14, 2022.
- Gowland, P. (2005). Placental MRI. *Seminars in Fetal and Neonatal Medicine*, 10, 485–490. <https://doi.org/10.1016/j.siny.2005.05.001>
- Grigsby, P. L. (2016). Animal models to study placental development and function throughout normal and dysfunctional human. *Pregnancy*, 34, 11–16.
- Guttmacher, A. E., Maddox, Y. T., & Spong, C. Y. (2014). The Human Placenta Project: Placental structure, development, and function in real time. *Placenta*, 35, 303–304. <https://doi.org/10.1016/J.PLACENTA.2014.02.012>
- Hafner, E., Metzenbauer, M., Hofinger, D., Stonek, F., Schuchter, K., Waldhor, T., et al. (2006). Comparison between three-dimensional placental volume at 12 weeks and uterine artery impedance/notching at 22 weeks in screening for pregnancy-induced hypertension, pre-eclampsia and fetal growth restriction in a low-risk population. *Ultrasound in Obstetrics & Gynecology*, 27, 652–657. <https://doi.org/10.1002/UOG.2641>
- Hall, T. J., Milkowski, A., Garra, B., Carson, P., Palmeri, M., Nightingale, K., et al. (2013). RSNA/QIBA: Shear wave speed as a biomarker for liver fibrosis staging. *IEEE International Ultrasonics Symposium IUS*, 397–400. <https://doi.org/10.1109/ULTSYM.2013.0103>
- Heinrichs, W. L. R., Fong, P., Flannery, M., Heinrichs, S. C., Crooks, L. E., Spindle, A., et al. (1988). Midgestational exposure of pregnant BALBc mice to magnetic resonance imaging conditions. *Magnetic Resonance Imaging*, 6, 305–313. [https://doi.org/10.1016/0730-725X\(88\)90407-9](https://doi.org/10.1016/0730-725X(88)90407-9)
- Human Placenta Project. (n.d.) Human Placenta Project | NICHD - Eunice Kennedy Shriver National Institute of Child Health and Human Development. <https://www.nichd.nih.gov/research/supported/HPP/default>. Accessed June 26, 2022.
- Johanson, R., Newburn, M., & Macfarlane, A. (2002). Has the medicalisation of childbirth gone too far? *BMJ*, 324, 892–895.
- Junaid, T. O., Bradley, R. S., Lewis, R. M., Aplin, J. D., & Johnstone, E. D. (2017). Whole organ vascular casting and microCT examination of the human placental vascular tree reveals novel alterations associated with pregnancy disease. *Scientific Reports*, 7, 1–10. <https://doi.org/10.1038/s41598-017-04379-0>
- Kanda, T., Ishii, K., Kawaguchi, H., Kitajima, K., & Takenaka, D. (2013). High Signal Intensity in the Dentate Nucleus and Globus Pallidus on Unenhanced T1-weighted MR Images: Relationship with Increasing Cumulative Dose of a Gadolinium-based Contrast Material. *Radiology*, 270, 834–841. <https://doi.org/10.1148/RADIOL.13131669>
- Karaman, E., Arslan, H., Çetin, O., Şahin, H. G., Bora, A., Yavuz, A., et al. (2016). Comparison of placental elasticity in normal and pre-eclamptic pregnant women by acoustic

- radiation force impulse elastosonography. *Journal of Obstetrics and Gynaecology Research*, 42, 1464–1470. <https://doi.org/10.1111/jog.13078>
- Kılıç, F., Kayadibi, Y., Yüksel, M. A., Adaletli, İ., Ustabasoğlu, F. E., Öncül, M., et al. (2015). Shear wave elastography of placenta: In vivo quantitation of placental elasticity in preeclampsia. *Diagnostic and Interventional Radiology*, 21, 202–207. <https://doi.org/10.5152/dir.2014.14338>
- Kubler, J. M., Clifton, V. L., Moholdt, T., & Beetham, K. S. (2022). The effects of exercise during pregnancy on placental composition: A systematic review and meta-analysis. *Placenta*, 117, 39–46. <https://doi.org/10.1016/J.PLACENTA.2021.10.008>
- Kudo, M., Shiina, T., Moriyasu, F., Iijima, H., Tateishi, R., Yada, N., et al. (2013). JSUM ultrasound elastography practice guidelines: Liver. *Journal of Medical Ultrasonics*, 40. <https://doi.org/10.1007/s10396-013-0460-5>
- Kwon, S., Yang, W., Moon, D., & Kim, K. S. (2020). Comparison of cancer cell elasticity by cell type. *Journal of Cancer*, 11, 5403. <https://doi.org/10.7150/JCA.45897>
- Langheinrich, A. C. C., Vorman, S., Seidenstücker, J., Kampschulte, M., Bohle, R. M. M., Wienhard, J., et al. (2008). Quantitative 3D micro-CT imaging of the human fetoplacental vasculature in intrauterine growth restriction. *Placenta*, 29, 937–941.
- Lax, A., Prince, M. R., Mennitt, K. W., Schwebach, J. R., & Budorick, N. E. (2007). The value of specific MRI features in the evaluation of suspected placental invasion. *Magnetic Resonance Imaging*, 25, 87–93. <https://doi.org/10.1016/J.MRI.2006.10.007>
- Lee, G. Y. H., & Lim, C. T. (2007). Biomechanics approaches to studying human diseases. *Trends in Biotechnology*, 25, 111–118. <https://doi.org/10.1016/j.tibtech.2007.01.005>
- Leung, K. Y., & Wan, Y. L. (2022). Update on color flow imaging in obstetrics. *Life*, 12, 1–21. <https://doi.org/10.3390/life12020226>
- Li, G. Y., & Cao, Y. (2017). Mechanics of ultrasound elastography. *Proceedings of the Royal Society A: Mathematical, Physical and Engineering Sciences*, 473. <https://doi.org/10.1098/rspa.2016.0841>
- Lim, R. (2017). Concise review: Fetal membranes in regenerative medicine: New tricks from an old dog? *Stem Cells Translational Medicine*, 6. <https://doi.org/10.1002/sctm.16-0447>
- Li, W. J., Wei, Z. T., Yan, R. L., & Zhang, Y. L. (2012). Detection of placental elasticity modulus by quantitative real-time shear wave imaging. *Clinical and Experimental Obstetrics and Gynecology*, 39, 470–473.
- Looney, P., Stevenson, G. N., Nicolaides, K. H., Plasencia, W., Molloholli, M., Natsis, S., et al. (2018). Fully automated, real-time 3D ultrasound segmentation to estimate first trimester placental volume using deep learning. *JCI Insight*, 3. <https://doi.org/10.1172/jci.insight.120178>
- Lum, M., & Tsioris, A. J. (2020). MRI safety considerations during pregnancy. *Clinical Imaging*, 62, 69–75. <https://doi.org/10.1016/J.CLINIMAG.2020.02.007>
- Luo, J., Abaci Turk, E., Bibbo, C., Gagoski, B., Roberts, D. J., Vangel, M., et al. (2017). In vivo quantification of placental insufficiency by BOLD MRI: A human study. *Scientific Reports*, 7, 1–10. <https://doi.org/10.1038/s41598-017-03450-0>
- Macara, L., Kingdom, J. C. P., Kaufmann, P., Kohnnen, G., Hair, J., More, I. A. R., et al. (1996). Structural analysis of placental terminal villi from growth-restricted pregnancies with abnormal umbilical artery Doppler waveforms. *Placenta*, 17, 37–48. [https://doi.org/10.1016/S0143-4004\(05\)80642-3](https://doi.org/10.1016/S0143-4004(05)80642-3)
- Magin, R. L., Lee, J. K., Klintsova, A., Carnes, K. I., & Dunn, F. (2000). Biological effects of long-duration, high-field (4 T) MRI on growth and development in the mouse. *Journal of Magnetic Resonance Imaging*, 12, 140–149. <https://doi.org/10.1002/1522-2586>

- McAleavey, S. A., Parker, K. J., Ormachea, J., Wood, R. W., Stodgell, C. J., Katzman, P. J., et al. (2016). Shear wave elastography in the living, perfused, post-delivery placenta. *Ultrasound in Medicine and Biology*, 42, 1282–1288. <https://doi.org/10.1016/j.ultrasmedbio.2016.01.009>
- Monpeyssen, H., Tramalloni, J., Poirée, S., Hélon, O., & Correas, J. M. (2013). Elastography of the thyroid. *Diagnostic and Interventional Imaging*, 94, 535–544. <https://doi.org/10.1016/j.diii.2013.01.023>
- Mühler, M. R., Clément, O., Salomon, L. J., Balvay, D., Autret, G., Vayssettes, C., et al. (2011). Maternofetal pharmacokinetics of a gadolinium chelate contrast agent in mice. *Radiology*, 258, 455–460. <https://doi.org/10.1148/RADIOL.10100652>
- Mulligan, K. M., Bartels, H. C., Armstrong, F., Immel, E., Corcoran, S., Walsh, J. M., et al. (2022). Comparing three-dimensional models of placenta accreta spectrum with surgical findings. *International Journal of Gynecology & Obstetrics*, 157, 188–197. <https://doi.org/10.1002/IJGO.13743>
- Nakashima, K., Shiina, T., Sakurai, M., Enokido, K., Endo, T., Tsunoda, H., et al. (2013). JSUM ultrasound elastography practice guidelines: Breast. *Journal of Medical Ultrasonics*, 40, 359–391. <https://doi.org/10.1007/s10396-013-0457-0>
- Nightingale, K. (2011). Acoustic radiation force impulse (ARFI) imaging: A review. *Current Medical Imaging Reviews*, 7, 328–339. <https://doi.org/10.2174/157340511798038657>
- Nightingale, K. R., Soo, M. S., Nightingale, R., & Trahey, G. (2002). Acoustic radiation force impulse imaging: In vivo demonstration of clinical feasibility. *Ultrasound in Medicine and Biology*, 28, 227–235. [https://doi.org/10.1016/S0301-5629\(01\)00499-9](https://doi.org/10.1016/S0301-5629(01)00499-9)
- O’Hara, S., Zelesco, M., Rocke, K., Stevenson, G., & Sun, Z. (2019). Reliability indicators for 2-dimensional shear wave elastography. *Journal of Ultrasound in Medicine*, 38, 3065–3071. <https://doi.org/10.1002/jum.14984>
- O’Hara, S., Zelesco, M., & Sun, Z. (2019). Shear wave elastography of the maternal cervix: A transabdominal technique. *Australasian Journal of Ultrasound in Medicine*, 22, 96–103. <https://doi.org/10.1002/ajum.12116>
- Ohmaru, T., Fujita, Y., Sugitani, M., Shimokawa, M., Fukushima, K., & Kato, K. (2015). Placental elasticity evaluation using virtual touch tissue quantification during pregnancy. *Placenta*, 36, 915–920. <https://doi.org/10.1016/j.placenta.2015.06.008>
- Osipov, L. V., Kulberg, N. S., Leonov, D. V., & Morozov, S. P. (2018). 3D ultrasound: Current state, emerging trends and technologies. *Biomedical Engineering (NY)*, 52, 199–203. <https://doi.org/10.1007/s10527-018-9813-0>
- Pang, J. X. Q., Zimmer, S., Niu, S., Crotty, P., Tracey, J., Pradhan, F., et al. (2014). Liver stiffness by transient elastography predicts liver-related complications and mortality in patients with chronic liver disease. *PLoS One*, 9, 1–9. <https://doi.org/10.1371/journal.pone.0095776>
- Paterno, M., Perrino, M., Travaglino, A., Raffone, A., Saccone, G., Zullo, F., et al. (2019). Parameters for estimating the time of death at perinatal autopsy of stillborn fetuses: A systematic review. *International Journal of Legal Medicine*, 133, 483–489. <https://doi.org/10.1007/S00414-019-01999-1/TABLES/3>
- Placenta Imaging Project. (n.d.). About | Placenta Imaging Project. <https://placentaimagingproject.org/project/>. Accessed June 26, 2022.
- Plasencia, W., Akolekar, R., Dagklis, T., Veduta, A., & Nicolaides, K. H. (2011). Placental volume at 11–13 weeks’ gestation in the prediction of birth weight percentile. *Fetal Diagnosis and Therapy*, 30, 23–28. <https://doi.org/10.1159/000324318>

- Price DL, De Wilde JP, Papadaki AM, Curran JS, Kitney RI. Investigation of Acoustic Noise on 15 MRI Scanners from 0.2 T to 3 T 2001. <https://doi.org/10.1002/1522-2586>.
- Ray, J. G., Vermeulen, M. J., Bharatha, A., Montanera, W. J., & Park, A. L. (2016). Association between MRI exposure during pregnancy and fetal and childhood outcomes. *JAMA*, 316, 952–961. <https://doi.org/10.1001/JAMA.2016.12126>
- Regnault, T. R. H., Galan, H. L., Parker, T. A., & Anthony, R. V. (2002). Placental development in normal and compromised pregnancies - a review. *Placenta*. <https://doi.org/10.1053/plac.2002.0792>
- Roberts, D. J., & Post, M. D. (2008). The placenta in pre-eclampsia and intrauterine growth restriction. *Journal of Clinical Pathology*, 61, 1254–1260. <https://doi.org/10.1136/JCP.2008.055236>
- Sainz, J. A., Carrera, J., Borrero, C., García-Mejido, J. A., Fernández-Palacín, A., Robles, A., et al. (2020). Study of the development of placental microvascularity by Doppler SMI (superb microvascular imaging): A reality today. *Ultrasound in Medicine and Biology*, 46, 3257–3267. <https://doi.org/10.1016/j.ultrasmedbio.2020.08.017>
- Saleem, S. N. (2014). Fetal MRI: An approach to practice: A review. *Journal of Advanced Research*, 5, 507–523. <https://doi.org/10.1016/J.JARE.2013.06.001>
- Sanghavi, M., & Rutherford, J. D. (2014). Cardiovascular physiology of pregnancy. *Circulation*, 130, 1003–1008. <https://doi.org/10.1161/CIRCULATIONAHA.114.009029>
- Saw, S. N., Dai, Y., & Yap, C. H. (2021). A review of biomechanics analysis of the umbilical–placenta system with regards to diseases. *Frontiers in Physiology*, 12, 1–17. <https://doi.org/10.3389/fphys.2021.587635>
- Saw, S. N., Low, J. Y. R., Ong, M. H. H., Poh, Y. W., Mattar, C. N. Z., Biswas, A., et al. (2018). Hyperelastic mechanical properties of ex vivo normal and intrauterine growth restricted placenta. *Annals of Biomedical Engineering*, 46, 1066–1077. <https://doi.org/10.1007/s10439-018-2019-5>
- Shiina, T. (2013). JSUM ultrasound elastography practice guidelines: Basics and terminology. *Journal of Medical Ultrasonics*, 40, 309–323. <https://doi.org/10.1007/s10396-013-0490-z>
- Shiina, T., Nightingale, K. R., Palmeri, M. L., Hall, T. J., Bamber, J. C., Barr, R. G., et al. (2015). WFUMB guidelines and recommendations for clinical use of ultrasound elastography: Part 1: Basic principles and terminology. *Ultrasound in Medicine and Biology*, 41, 1126–1147. <https://doi.org/10.1016/j.ultrasmedbio.2015.03.009>
- Siauve, N., Chalouhi, G. E., Deloison, B., Alison, M., Clement, O., Ville, Y., et al. (2015). Functional imaging of the human placenta with magnetic resonance. *American Journal of Obstetrics and Gynecology*, 213, S103–S114. <https://doi.org/10.1016/J.AJOG.2015.06.045>
- Sigrist, R. M. S., Liau, J., El Kaffas, A., Chammas, M. C., & Willmann, J. K. (2017). Ultrasound elastography: Review of techniques and clinical applications. *Theranostics*, 7, 1303–1329. <https://doi.org/10.7150/thno.18650>
- Simon, E., Remenieras, J. P., Marcheteau, G., Patat, F., Perrotin, F., & Calle, S. (2017). 2D transient elastography system adapted to shear wave speed dispersion measurement in placenta: Ex vivo comparison between normal pregnancies and placental insufficiencies. <https://doi.org/10.1109/ULTSYM.2017.8092313>.
- Society P by the SG of the BMU. (2010). Guidelines for the safe use of diagnostic ultrasound equipment. *Ultrasound*, 18, 52–59. <https://doi.org/10.1258/ult.2010.100003>
- Song, P., Bi, X., Mellemma, D. C., Manduca, A., Urban, M. W., Greenleaf, J. F., et al. (2016). Quantitative assessment of left ventricular diastolic stiffness using cardiac shear wave

- elastography. *Journal of Ultrasound in Medicine*, 35, 1419–1427. <https://doi.org/10.7863/ultra.15.08053>
- Sovio, U., White, I. R., Dacey, A., Pasupathy, D., & Smith, G. C. S. S. (2015). Screening for fetal growth restriction with universal third trimester ultrasonography in nulliparous women in the pregnancy outcome prediction (POP) study: A prospective cohort study. *Lancet*, 386, 2089–2097. [https://doi.org/10.1016/S0140-6736\(15\)00131-2](https://doi.org/10.1016/S0140-6736(15)00131-2)
- Strizek, B., Jani, J. C., Mucyo, E., De Keyzer, F., Pauwels, I., Ziane, S., et al. (2015). Safety of MR imaging at 1.5 T in fetuses: A retrospective case-control study of birth weights and the effects of acoustic noise. *Radiology*, 275, 530–537. <https://doi.org/10.1148/radiol.14141382>
- Sugitani, M., Fujita, Y., Yumoto, Y., Fukushima, K., Takeuchi, T., Shimokawa, M., et al. (2013). A new method for measurement of placental elasticity: Acoustic radiation force impulse imaging. *Placenta*, 34, 1009–1013. <https://doi.org/10.1016/j.placenta.2013.08.014>
- Sunderland, N., Hennessy, A., & Makris, A. (2011). Animal models of pre-eclampsia. *American Journal of Reproductive Immunology*, 65, 533–541. <https://doi.org/10.1111/J.1600-0897.2010.00929.X>
- Sun, W., Liu, J., Zhang, Y., Cai, A., Yang, Z., Zhao, Y., et al. (2018). Quantitative assessment of placental perfusion by three-dimensional power Doppler ultrasound for twins with selective intrauterine growth restriction in one twin. *European Journal of Obstetrics & Gynecology and Reproductive Biology*, 226, 15–20. <https://doi.org/10.1016/J.EJOGRB.2018.05.021>
- Turk, E. A., Luo, J., Gagoski, B., Pascau, J., Bibbo, C., Robinson, J. N., et al. (2017). Spatio-temporal alignment of in utero BOLD-MRI series. *Journal of Magnetic Resonance Imaging*, 46, 403–412. <https://doi.org/10.1002/jmri.25585>
- Unterscheider, J., O'Donoghue, K., Daly, S., Geary, M. P., Kennelly, M. M., McAuliffe, F. M., et al. (2014). Fetal growth restriction and the risk of perinatal mortality-case studies from the multicentre PORTO study. *BMC Pregnancy Childbirth*, 14, 1–6. <https://doi.org/10.1186/1471-2393-14-63/FIGURES/2>
- Using MRI to Visualize the Placenta - YouTube. (n.d.). <https://www.youtube.com/watch?v=EMoMqJJ2g34&t=9s>. Accessed June 26, 2022.
- Victoria, T., Jaramillo, D., Roberts, T. P. L., Zarnow, D., Johnson, A. M., Delgado, J., et al. (2014). Fetal magnetic resonance imaging: Jumping from 1.5 to 3 tesla (preliminary experience). *Pediatric Radiology*, 44, 376–386. <https://doi.org/10.1007/S00247-013-2857-0/FIGURES/9>
- Voerman, E., Santos, S., Golab, B. P., Amiano, P., Ballester, F., Barros, H., et al. (2019). Maternal body mass index, gestational weight gain, and the risk of overweight and obesity across childhood: An individual participant data meta-analysis. *PLoS Med*, 16, 1–22. <https://doi.org/10.1371/journal.pmed.1002744>
- Wilhelm, D., Mansmann, U., Neudeck, H., Matejevic, D., Vetter, K., & Graf, R. (2002). Decrease of elastic tissue fibres in stem villus blood vessels of the human placenta during IUGR and IUAGR with concomitant pre-eclampsia. *Anatomy and Embryology*, 205, 393–400. <https://doi.org/10.1007/S00429-002-0252-Y>
- Wu, S., Nan, R., Li, Y., Cui, X., Liang, X., & Zhao, Y. (2016). Measurement of elasticity of normal placenta using the Virtual Touch quantification technique. *Ultrasonography*, 35, 253–257. <https://doi.org/10.14366/usg.16002>
- Zhang, J., Merialdi, M., Platt, L. D., & Kramer, M. S. (2010). Defining normal and abnormal fetal growth: Promises and challenges. *American Journal of Obstetrics and Gynecology*, 202, 522–528. <https://doi.org/10.1016/j.ajog.2009.10.889>

This page intentionally left blank

**SECTION**

Body parts

**3**

This page intentionally left blank

# Foot digital twin and in silico clinical applications

# 16

**Enrique Morales Orcajo<sup>1</sup>, Andrea Stenti<sup>2</sup>**

<sup>1</sup>*Ambu Innovation GmbH, Augsburg, Germany;* <sup>2</sup>*BEAMS Department, Université Libre de Bruxelles, Brussels, Belgium*

## **Chapter outline**

<b>Where a foot digital twin can help .....</b>	331
Key aspects of foot biomechanics .....	331
Main foot pathologies by volume .....	332
Foot digital twin—scope of interest .....	334
The potential of foot CM&S .....	335
<b>How to build a foot digital twin .....</b>	336
Anatomy reconstruction .....	337
Loading and boundary conditions .....	338
Tissue properties .....	339
Verification and validation .....	341
Initiatives to improve model credibility in healthcare .....	341
<b>Foot digital twin: a look into the future .....</b>	342
In silico trials .....	342
What level of anatomical detail is required for clinical applications? .....	343
Foot CM&S for clinical applications .....	345
Foot CM&S for the footwear industry .....	348
Why foot and ankle CM&S is not yet in the clinic .....	350
<b>References .....</b>	353

---

## **Where a foot digital twin can help**

### **Key aspects of foot biomechanics**

Despite not receiving as much attention as other joints of the human body like the knee, the hip, or the shoulder, the foot and ankle complex plays a very important role in our well-being. The foot is the only point of contact of our body with the ground. It has evolved into an elaborate structure that allows us to walk upright. To fulfill this task, the foot is at the same time pliant to adjust to the uneven ground,

semirigid to help during the push-off phase, and rigid to withstand weightbearing (Sidak et al., 2018).

Such adaptability is achieved by its unique anatomy. The foot consists of 26 bones that together with the long bones of the lower limb form a total of 33 joints. These bones are kept together, thanks to a complex network of over a 100 ligaments that provide high stability, despite bearing enormous compressive and shear forces during foot movement (Brockett & Chapman, 2016).

Twelve extrinsic muscles control the position of the foot during gait by either absorbing or generating power at different stages. Meanwhile, the intrinsic musculature adjusts the stiffness of the structure by stretching or relaxing the foot arch. This capacity of the foot to change its structural stiffness as a function of the activity gives the foot great responsiveness.

The foot and ankle complex reaches forces up to several times the body weight under high demanding conditions. For example, when walking, it supports forces of approximately five times the body weight, and when running or jumping can reach values over 12 times the body weight (Komi, 1990).

Furthermore, ankle joint movements are complex in nature. This is because the foot motion is not only driven by its own musculature but also by the reaction and adaptation to the surface in contact. During gait, the most prominent movement happens in the sagittal plane, i.e., plantarflexion/dorsiflexion, but small movements in the coronal and transverse planes also take place (Brockett & Chapman, 2016). These movements together with the rotation of the knee and the hip provide stability during gait.

Such intricate anatomy together with variability factors like gender, age, and lifestyle results in a complex biomechanical equilibrium that is difficult for surgeons to predict when performing an orthopedic treatment. Especially considering that changes in the biomechanical response of the foot influence the entire lower limb movement. All this makes it difficult, in practice, to find clear and standardized procedures among practitioners to treat foot pathologies, resulting in a sort of “each to his own.”

Within this context, computational modeling and simulation (CM&S) can help to shed light on the cause–effect relationship between treatment and patient outcome, for example, by simulating the biomechanical response of the patient before and after surgery. Furthermore, CM&S can not only allow educated guess on the after-treatment patient state but also can estimate parameters that cannot be measured *in vivo* with the current technology, like internal stress distribution and joint contact pressures. Such techniques embedded into a foot digital twin and lower limb gait models will be used for surgery risk evaluation and treatment optimization.

### Main foot pathologies by volume

From a 50 million insured—patients database in the United States, six of the most common foot and ankle operations performed by orthopedic surgeons and podiatrists (hallux valgus correction, calcaneus fracture, pilon fracture, triple arthrodesis,

and total ankle replacement) amounted to a total of 285,162 in a 10-year period (between 2005 and 2014) (Burton et al., 2021). This represents 57 procedures per 100,000 persons/year on average on this period, from which 59.2% were hallux valgus (33.8 per 100,000 persons/year), 31.6% ankle fracture (18 per 100,000 persons/year), 4.1% pilon fracture (2.3 per 100,000 persons/year), 1.3% calcaneus fracture (1.3 per 100,000 persons/year), 1.6% triple arthrodesis (0.9 per 100,000 person/year), and 1.1% ankle replacement (0.6 per 100,000 persons/year). Still in the United States, another study based on fee-for-service Medicare beneficiaries reported 1.9 total ankle replacement and 3.3 ankle arthrodesis per 100,000 patients in 2010 (Pugely et al., 2014). The US trends in foot- and ankle-related arthrodesis accounted for up to 20.2 per 100,000 persons in 2006 (Best et al., 2015). By anatomic location: 5.31 metatarsophalangeal, 5.1 ankle, 3.64 triple, 2.72 subtalar, 1.17 midtarsal, 2.41 tarsometatarsal per 100,000 persons.

In Australia, a descriptive analysis of foot and ankle surgical procedures extracted from the Australian Medicare Benefits Schedule database reported a total of 996,477 surgical procedures between 1997 and 2006, being toenail surgery (64%), trauma (16%), lesser toe (6%), and ankle (6%) surgery the most frequent surgeries (Menz et al., 2008). Per capita, they represent 124 foot and ankle surgical procedures per 100,000 persons in the database in 2006. In that year, the total cost of subsidizing surgeons' fees was over 14 million Australian dollars. Another clinical audit of foot surgeries in Australia revealed that the most commonly performed procedures are for lesser toe deformities (46.1%), followed by hallux valgus (20.8%), intermetatarsal neuroma (7.8%), hallux rigidus (6.6%), and onychocryptosis (6.7%) (Bennett, 2007). The same prevalence of foot pathologies has been documented in the United Kingdom and the United States.

Similar numbers are found in European studies. A study of hallux valgus and forefoot deformities in Sweden reported 51.3 forefoot surgeries per 100,000 inhabitants in 2000 (Saro et al., 2008). In particular, osteotomies 27.3, excisions 16.8, arthroplasties 3.1, tendon surgeries 2.4, and fusions 1.6 per 100,000 inhabitants. The main diagnoses were hallux valgus accounted for 55.1% of the cases, followed by hammer toes 22.3%, and hallux rigidus 15.9%. Finally, an analysis of trends in foot and ankle surgery in Germany reported 10.1 first metatarsophalangeal arthrodesis, 4.6 ankle arthrodesis, 1 total ankle replacement, and 0.4 total metatarsophalangeal replacement per 100,000 persons in 2017 (Milstrey et al., 2021).

Regarding the incidence of revision surgeries, total ankle replacement exchange or removal reach 0.58, and first metatarsophalangeal exchange or removal 0.16 per 100,000 persons in 2017 in Germany (Milstrey et al., 2021). Total ankle replacement has an average failure rate of 10% at 5 years (Gouglias et al., 2010). Publications from 1990 to 2005 found implant survivorship of 78% at 5 years (Haddad et al., 2007). A systematic review available in the literature for the STAR Ankle, consisting of 16 studies with 2088 implants, showed an average survivorship of 85.9% at 5 years and 71.1% at 10 years (Zhao et al., 2011). These results are much lower than the reported greater than 90% over 10-year hip survivorship and 15-year knee survivorship (Extremities, 2018; Victor et al., 2014). Similar percentages can be found in international joint registries.

Although the number of foot and ankle surgeries is steadily increasing, when compared with knee, hip, and spine interventions is still very low. When we look at the US market, for example, the foot and ankle surgical interventions per year are on average 30,000 (Burton et al., 2021), with hallux valgus correction surgeries covering 60% of the interventions. According to the Agency for Healthcare Research and Quality, in 2017, more than 754,000 knee replacements were performed in the United States. These numbers explain the slow pace at which CM&S is addressing foot and ankle pathologies and surgical interventions when compared to the other orthopedic joints.

### Foot digital twin—scope of interest

CM&S of the foot has been widely used in the scientific literature since the early 1990s to gain insight into a broad range of applications like biomechanics, pathomechanics, surgery, orthosis, and footwear (Morales-Orcajo et al., 2016). However, its real applications in clinical practice have been very limited. During the last decade, the field has evolved enough to reach a level of maturity that now can provide insights into daily clinical applications such as clinical decision-making and personalized medicine.

Here, we briefly summarize the evolution of the foot CM&S in the last 3 decades and its uses until now. In section [Foot digital twin: a look into the future](#) we focus on state-of-the-art applications, discussing limitations, and suggesting future directions for development.

The earliest simulations were focused on a better understanding of the basic foot physiology and gait biomechanics, defining healthy and pathological ranges. These were also the first attempts to capture the biomechanical response of the foot in a computational model. Soon, foot models evolved to assess injury risk on ankle sprains and ligaments failures due to high impact activities, or car crashes as well as posture impact on bone healing after fracture.

Since then, virtual foot models have been used extensively in pathomechanics, particularly in the diabetic foot, plantar ulceration, flatfoot and toe deformities, to understand the causes of the pathologies. Similarly, simulation studies on arthrodesis, arthroplasties, osteotomies, bone fixations, orthopedics implants, ligament reconstructions, tendon transfers, and plantar fasciotomies are common in the literature to evaluate the quality of surgery output or compare the effectiveness among different surgical protocols.

Other common applications of foot models are orthoses and footwear design to reduce peak plantar pressure or improve overall biomechanical response. Usually, these studies are focused on insole shape and material properties to redistribute the plantar pressure for specific pathologies and activities.

Foot CM&S has been also explored in sports biomechanics. For example, barefoot versus cushioned running, foot injury during high-demand physical activities, or football shooting.

These early foot CM&S approaches present several limitations such as anatomy simplifications, quasi-static simulations, linear material models, narrow validations, and labor-intensive and time-consuming model-building strategies, which makes their applicability outside of the research space very difficult.

### The potential of foot CM&S

It should be noted that most studies in the literature are based on generic feet, although there is clinical evidence of wide variation of foot kinematics and patient-specific response to orthoses (Nester, 2009). The first patient-specific foot model did not appear until 2012. However, since then, tremendous progress has been made in generating faster and more reliable patient-specific models. The accessibility to patient-specific models, aka patient digital twins (Fig. 16.1), will create new markets, transforming CM&S from being a research tool, as it is now, to a surgical enhancing tool, where surgeons can gain insights that help them in the clinical decision-making process.

Developing personalized models is key to allow CM&S to be used for clinical applications. When looking at personalized medicine, CM&S can impact the



**FIGURE 16.1 Virtual foot cohort.**

Virtual cohort of five right feet (patient-specific foot and ankle models) generated semiautomatically via custom script + segmentation + CAD + FE software at Digital Orthopaedics.

cost-effectiveness of surgical and nonsurgical treatments for foot and ankle pathologies. Cost-effectiveness analyses consider how clinically useful interventions are, in the context of how much they cost and are used to redistribute healthcare resources and to evaluate the adoption of new healthcare technologies. With focus on foot and ankle pathologies, today cost-effectiveness analysis has been done only for ankle osteoarthritis treatments (Walsh et al., 2022). In general, the willingness-to-pay (cost) by consumers, including governments, for an additional quality-adjusted life-year gain (QALY) due to a healthcare intervention, is expressed via the incremental cost-effectiveness ratio (ICER): cost/QALY. This value represents a threshold above which governments do not consider the intervention cost-effective. This ICER threshold varies between countries. In the United States, it is around US\$ 50,000/QALY (Shiroiwa et al., 2010). The challenge for healthcare providers is to marry the effectiveness of an intervention with an acceptable cost that benefits both the patient and society. Foot and ankle CM&S should focus on reducing the ICER per intervention, in order to be considered as a viable healthcare technology.

## How to build a foot digital twin

The process to create a virtual replica, aka digital twin, of the foot and ankle complex is common to all orthopedic models. It consists of four steps: reconstruction of the anatomy, imposition of the loads and boundary conditions, assignment of tissue properties, verification and validation of the model (Fig. 16.2). Although the process is straightforward, there are many modeling and simulation decisions still open to the judge of the modeler, which is demonstrated in the great variability of foot models that are found in the literature. All these little decisions of the modeler are considered in the field as the “art of modeling” and have a large impact on the results of the model (Erdemir et al., 2019).

First and foremost, when creating a model, it is to define its context of use. The V&V 40 recommends that the context of use should include a detailed statement of

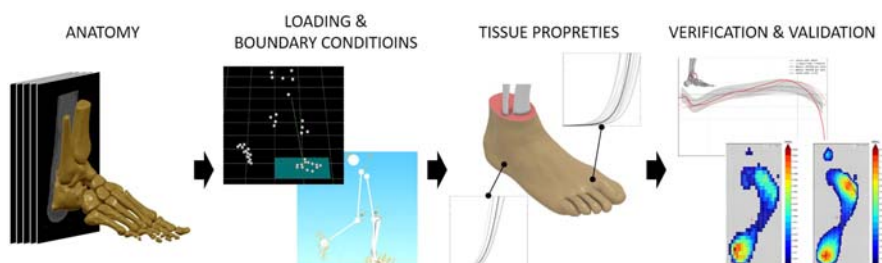


**FIGURE 16.2** Foot digital twin workflow.

Example of a workflow to generate a foot digital twin.

what will be modeled and how the outputs from the computational model will be used to answer or inform the question of interest (V&V40, 2018—Assessing Credibility of Computational Modeling through Verification and Validation: Application to Medical Devices, 2018). A well-defined context of use will guide the modeler to tackle most of the questions during the development process.

In the rest of this section, we will go through the entire process of generating a foot digital twin making emphasis on the most relevant factors in the foot and ankle CM&S.

## Anatomy reconstruction

It all starts with the DICOM of the patient. The Digital Imaging and Communications in Medicine (DICOM) is a standard which specifies a non-proprietary data interchange protocol, digital image format, and file structure for biomedical images and image-related information (Bidgood et al., 1997). For the purpose of the discussion, we refer here to a DICOM file as simply the stack of 2D images that goes from the distal part of the tibia to the tip of the toes. These files can be generated from a CT scan or an MRI. The main difference is that the CT scan has a sharper definition of the bones outlines, while the MRI has better contrast of soft tissues.

From the technical point of view, the slice distance is one of the most important parameters in a DICOM. This is the distance between one image and the next one. The reconstruction software compares the images on two consecutive slices and fills the gap with a voxel (3D pixel) whenever consider that the pixels belong to the same entity. Therefore, the bigger the slice distance, the coarser the volumes generated. Generally, in foot and ankle segmentation a slice distance of 0.6 mm or smaller is recommended. This is due to the small bones of the forefoot. For large bones like the femur and the tibia, it is common to use a 3 mm slice distance, but such a gap in a foot scan makes it impossible to distinguish when a bone finish and starts the next one.

From the practical point of view, the scanning position of the foot has a direct impact on the simulation results. The goal of the anatomy reconstruction step is to capture the foot anatomy in the free-stress state. In other words, the foot should be scanned in a neutral position under no load. Besides, the foot should not be in contact with any surface that could deform the plantar soft tissue like a flat surface or a grid. A deformation in the plantar sole will create artifacts that distort the plantar pressure results. We can only simulate how the foot deforms under specific loading conditions but not the other way around.

From the modeling point of view, the model can be population-based or patient-specific. A population-based model would be intended to gain insight into foot biomechanics or pathomechanics. However, a patient-specific model will be focused on answering a specific clinical question for the patient. That is the goal of a patient digital twin, tests the treatment in the virtual replica before trying it in the patient. Patient-specific models are very costly because require the generation of a new geometry for every patient which is the most user-demanding step.

In this regard, the efforts of the startup Digital Orthopaedic in generating digital foot twins on a mass scale are noteworthy (Fig. 16.1). They were able to generate a high detailed anatomical foot CAD model from the patient's DICOM in less than two working days, i.e., 16h. Initially, they reconstructed the 3D surface of the bones and the skin and imported it in a CAD software. Then, using bone landmarks, they added the cartilages, ligaments, fascia, retinaculum, tendons, and fat pads quasi-automatically via scripting (Morales-Orcajo et al., 2020).

It is also common, editing the model geometry to add nonanatomical parts, like prosthesis, plates, and insoles, or to simulate surgeries like an osteotomy, a surgical operation in which a bone is cut to change its alignment.

### Loading and boundary conditions

The loading and boundary conditions are probably the most subjective part of the model and where the modeler has to tackle more questions. In the ideal case, the less biased simulation will be a forward dynamic simulation of the complete gait cycle. This is a challenging simulation case in which all forces acting on the model in each instance must keep the model in upright balance. Such a simulation, taking into account a detailed anatomy of the foot, has not been achieved yet. However, several workarounds and simplifications have been proposed to address this challenge.

It should be noticed that direct measurement of the tendon forces during gait is not feasible with the current technology. One approach to guess this force is via EMG. But EMG does not measure force if not the level of muscle activation, i.e., electrical signals that cause muscles to contract and relax, and it is not well understood the relationship between EMG signal and the magnitude of force generation within the muscles (Erdemir et al., 2007). Besides, EMG has many sources of errors during measurement. Electrical noise, motion artifacts, cross-talk contamination, clipping, and physiological noise are some of the factors that affect EMG signal quality.

For that reason, the trend in orthopedics is to estimate tendon forces by musculoskeletal modeling (Trinler et al., 2018). First, a motion capture system is used in a gait lab to capture 3D marker positions and ground reaction forces. In some cases, EMG data is also recorded for validation purposes. Second, joint kinematics (i.e., joint angles, velocities, and accelerations) are estimated using an inverse kinematics procedure. The error between the physical marker positions and the virtual marker positions is minimized by varying the segment positions following the segment's DOFs (i.e., rotations or translations) and imposed constraints. Third, muscle forces and joint torques are estimated via inverse dynamics using the joint kinematics previously computed combined with the ground reaction forces measured in the gait lab. Finally, in the ideal case, these musculoskeletal forces (i.e., muscle forces, and joint torques) are used as an initial guess for a forward dynamic simulation, where a force-driven musculoskeletal simulation estimates the resulting kinematics and dynamics. These simulations allow establishing a cause–effect relationship between the forces acting on the human body and the resulting movement, predictive simulations, and “what-if scenarios” (Killen et al., 2020).

Cosimulation is the procedure to couple a musculoskeletal model, i.e., rigid bodies that compute the forces in the system, with a finite element model, i.e., deformable bodies that compute the internal stresses and contact pressures. This approach is computationally costly and no study has been published to successfully couple a forward dynamic musculoskeletal model with a foot finite element model yet.

In foot CM&S, the closest approach using state-of-the-art models is to drive the finite element model imposing prescribed kinematics, i.e., inverse kinematic musculoskeletal model coupled with a finite element model (Morales-Orcajo et al., 2020). That means the patient's foot finite element model rolls on the ground following the patient marker's movement recorded in the gait lab. The limitation of this approach is that only prerecorded movements can be simulated. Therefore, not allowing the prediction of the after-surgery patient outcome before performing the surgery. For that, a force-driven simulation will be necessary.

However, the most common approach in the literature is the quasi-static simulation. It consists of simulating only the time instant of interest. In other words, freeze the movement of the patient at a specific time frame and compute the forces in that instant, which makes it easier to achieve model convergence. The limitation of this approach is that the results depend strongly on the loading and boundary conditions defined at that particular instant. To understand the complexity of this estimation, at any particular instant of the gait cycle, the forces acting on the foot are the ground reaction force (depends on body weight, inertia, ground location, and foot position), the nine extrinsic tendons (most of them working antagonist to each other), and the internal musculature (which is very complex to include in the model but plays an important role in the flexibility of the foot arch). Furthermore, the force estimation rarely comes from the same patient, since this is an entire challenge on its own. Most of the studies extrapolate the loads and boundary conditions from literature gait musculoskeletal simulations, mathematical models, cadaveric robotic actuator models, or clinical cadaveric studies and then impose those forces on the patient finite element model. That is why it is difficult to extrapolate the simulation result into real clinical advice.

But there is hope for the future. The capacity of musculoskeletal models and finite element models to work together advances quickly. In recent years, new techniques for combining multibody and finite element models are appearing (Lloyd et al., 2019). Also, experimental methods are getting better and are able to capture more data (Wang et al., 2020). In the knee, where the loading conditions are less demanding than in the foot, there are already good examples of accurate predictions which are promising to address real clinical cases (Kinney et al., 2013). Recently, an inverse dynamic musculoskeletal model was coupled with a knee finite element model to compute stresses in the tibial cartilage (Halonen et al., 2017).

## Tissue properties

The computational cost of a simulation depends on the complexity of three factors: geometry (anatomy), boundary conditions, and material models (tissue properties).

As the demand for these three factors increases, the computational cost increases. Therefore, the modeler should trade-off some simplifications to reduce the computational cost.

By nature, the foot anatomy is intricate. Although it is possible to make some simplifications like the fusion of the phalanx's joints, there is not much room to simplify the geometry without compromising the results, as is the case of partial models or 2D models which have limited applications. Similarly, the loading and boundary conditions of the foot are demanding and have a direct impact on the results, which makes simplification tricky. Therefore, in the foot CM&S literature, it is common to sacrifice the tissue properties to keep the computational cost in practical times (below 24h). Other factors that tilt the balance to make concessions on the tissue properties are the limited experimental data, the perception of reduced impact on the results, and the few material models implemented in commercial software.

For these reasons, in foot CM&S linear elastic material models are generally used for all the tissues except for the plantar soft tissue. The plantar soft tissue plays an important role in the simulation because it is the part of the model in contact with the ground and determines the plantar pressure, the most straightforward result to validate. Two approaches are found in the literature to simulate the mechanical response of the plantar soft tissue. The simplest one is to generate a bulk soft tissue where the foot skeleton is embedded. Another approach, a bit more elaborate, adds a thin outer layer on top of this bulk soft tissue as a skin. The former uses an equivalent material model that matches the impact attenuation properties of the plantar pads. The latter uses softer material properties for the inner bulk soft tissue behaving like fat for impact absorption and a stiffer outer layer holding the soft tissue together, which is closer to the way the heel pad works. Nonlinear hyperelastic models namely Neo-Hookean, Ogden, Mooney–Rivlin, or Yeoh are common in the foot simulation literature for skin, fat, and equivalent soft tissue components.

As explained, despite the nonlinear nature of all biological tissues, the rest of the tissues of the foot, i.e., bones, ligaments, tendons, fascia, cartilage, are generally simulated with linear material models. Due to the high stiffness of bones compared to the other tissues, some models use rigid elements (no stress computed) which save a considerable amount of computing power. When the stress in the bones is important, a Young modulus of 7300 MPa is often used. Ligaments are commonly simulated as springs with K values ranging from 40 to 240 N/mm or linear elastic properties with a Young modulus of 260 MPa. Tendons' Young modulus varies between 200 and 2000 MPa and fascia Young modulus is 350 MPa. Finally, cartilage is simulated with a Young modulus between 1 and 10 MPa. In all cases, the Poisson's ratio is 0.3 or 0.4, and for cartilage up to 0.49. For more details on foot tissue properties, the interested reader is referred to [Morales-Orcajo et al. \(2016\)](#), and [Phan et al. \(2021\)](#).

## Verification and validation

In summary, the workflow to build a virtual replica of the patient foot biomechanics is to import the patient's anatomy, assign tissue properties, define constraints between components, determine boundary conditions, apply loads and calibrate the model. Model calibration is the step where input parameters are optimized, i.e., fine-tuned, to reduce the differences between the experimental measurements and the model predictions.

Then, to establish confidence in the model results—trust in the predictive capability of the model within the context of use—verification and validation activities are performed. Following the V&V 40 standard terminology ([V&V40, 2018](#)—Assessing Credibility of Computational Modeling through Verification and Validation: Application to Medical Devices, 2018), the context of use defines the specific role and scope of the computational model used to address the question of interest. Verification and validation aim to assess the degree to which the computational model is an accurate representation of the reality of interest through the comparison of simulation results with theory, and experiments, or other sources of relevant information. It is important to distinguish between model calibration, where model results are tuned to a specific set of data, versus validation, where model predictions are assessed relative to unseen data.

Some credibility factors evaluated during verification and validation are quantification of the uncertainty, model sensitivity, mesh quality, and energy balance among others. Uncertainty quantification examines the degree to which known or assumed uncertainties in the model inputs are propagated to uncertainties in the simulation results. Sensitivity analysis examines the degree to which the computational model outputs are sensitive to the model inputs. Mesh quality assesses the suitability—fidelity to the underlying physics, accuracy, and efficiency—of a discrete computational domain for simulations. Energy balance ensures the numerical results of the model follow the basic rule of physics—the conservation of energy. All these activities help to understand the performance of the model within the context of its intended use.

We recommend modelers follow the V&V40 ([V&V40, 2018](#)—Assessing Credibility of Computational Modeling through Verification and Validation: Application to Medical Devices, 2018) to gain credibility on foot CM&S. This Standard provides a risk-informed credibility assessment framework to determine and justify the appropriate level of credibility for using a computational model to inform a decision. Specific metrics on finite element validation methods can be found on [Burkhart et al. \(2013\)](#).

## Initiatives to improve model credibility in healthcare

Foot CM&S is opening many possibilities in the healthcare sector from clinical decision support systems to fast-to-market medical devices. However, such applications require a great level of credibility, reproducibility, and standardization to

reach the market. In this matter, it is worth follow three ongoing initiatives that are addressing these challenges to pave the road for the mass adoption of CM&S in the healthcare sector.

To address the credibility challenge, the committee on credible practice of modeling and simulation in healthcare has recently provided 10 rules for credible practice of CM&S in healthcare. In brief, the rules are (1) Define context clearly. (2) Use contextually appropriate data. (3) Evaluate within context. (4) List limitations explicitly. (5) Use version control. (6) Document appropriately. (7) Disseminate broadly. (8) Get independent reviews. (9) Test competing implementations. (10) Conform to standards (Erdemir et al., 2020). To help in the dissemination and adoption of these rules, the committee has created an open repository of models and simulations, updated yearly, that epitomize the application of each of the Ten Rules.<sup>1</sup>

To address the reproducibility challenge, the Kneehub<sup>2</sup> project aims for understanding the influence of modelers' approaches and decisions throughout the life-cycle of modeling and simulation. Their reasoning is that detailed documentation of implementation details, motivation, and justification behind the preferences of modelers will eventually lead to standardization and best practices of knee modeling, facilitating exchange, and repurposing (Erdemir et al., 2019). Although focused on the knee, the reasoning behind the modeler's decisions can be extrapolated to other orthopedic models like the foot.

Finally, to address the standardization challenge, the community challenge toward consensus on characterization of biological tissue, c4bio<sup>3</sup> in short, has recently launched a test campaign aiming to achieve community consensus regarding the testing protocols for material characterization of biological tissue. The first test campaign is focused on uniaxial tensile testing of the aorta, but the project is intended to be extended to other testing methods, tissues, and physical properties.

## Foot digital twin: a look into the future

### In silico trials

The FDA is pushing toward the definition of a solid regulatory framework to promote the use of CM&S as an additional source of evidence.<sup>4</sup> Although at a slower pace, The European Union is also following the same direction, toward the adoption of the so-called in silico evidence (Viceconti et al., 2021). The recent activities of the Avicenna Alliance<sup>5</sup> (a nonprofit organization reuniting academics and

---

<sup>1</sup> <https://simtk.org/plugins/moinmoin/crms/10%20Simple%20Rules%20Examples>.

<sup>2</sup> <https://simtk.org/projects/kneehub>.

<sup>3</sup> <https://c4bio.eu>.

<sup>4</sup> FDA Medical Device Development Tools.

<sup>5</sup> <https://avicenna-alliance.com>.

pharmaceutical and medical device industrial stakeholders) and its interaction with the European Commission are boosting up the adoption of in silico medicine as a standard in healthcare. Whether the benefits of CM&S in the product life-cycle development phase (from the design phase to virtual testing and the identification of worst-case scenarios) is unquestionable, the regulatory uncertainty in using CM&S for product certification is still hindering its full deployment. This is true for all pharma and medical device applications using CM&S; in addition, orthopedics of the foot and ankle is advancing at a slower pace as they suffer the lower volume numbers of surgical interventions with respect to other orthopedic joints.

Whether for personalized medicine or in silico clinical trials, high-level foot and ankle CM&S is necessary. To understand, diagnose, and perform surgical preplanning of foot and ankle pathologies, the knowledge of the preoperative internal stress levels and the possibility to predict the outcome of surgical operations on internal stresses is mandatory. Since there are currently no protocols to measure in vivo stress levels, modeling is the only option (Fig. 16.3). Foot models exist for at least 2 decades; however, their clinical impact is still relatively low with respect to other orthopedics joints: easy access, accuracy and relevance of the information that foot models can provide to the clinicians in their daily practice is still an open issue (Behforootan et al., 2017).

### What level of anatomical detail is required for clinical applications?

A stand-alone foot model in open configuration is of little use for clinical applications. A “walking” foot model, as part of a lower limb gait model, capable of representing the different foot pathologies and retroactively influencing the gait pattern (i.e., impact on the knee and the hip) must be the goal to enhance clinical applications. A holistic approach is mandatory, although state of the art is not there yet.

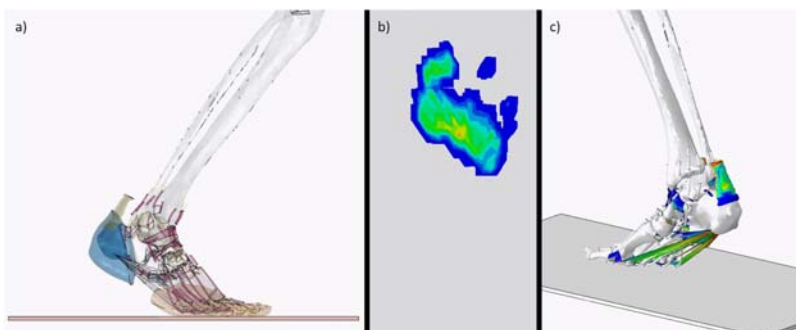


**FIGURE 16.3** Highly detailed patient-specific finite element model.

- a) Model coupled with a rigid body musculoskeletal model developed at Digital Orthopedics.
- b) Plantar pressure.
- c) Stresses on the ligaments, fascia, and Achilles tendon.

Lower limb walking models do exist. Independently from foot models, walking simulation is modeled today via predesigned finite state machines, motion capture data, optimization-based controls, or more recently deep reinforcement learning (Park et al., 2019). Open sources for musculoskeletal gait models do exist (e.g., OpenSim<sup>6</sup>, Anybody<sup>7</sup>) (Falisson et al., 2018), however, these models often solve an inverse dynamic problem, where typically 3D markers gait motion data is combined with contact force measurement data to derive patient-specific gait kinetics and kinematics. Further optimization methods are often used to reconstruct, from patient-specific muscle moment arms, patient-specific muscle activation schemes (Trinler et al., 2019). Inverse dynamic problems—reconstructing the internal forces and/or torques from measured movements and external forces—are much easier to solve than forward dynamic problems—calculating motion from known internal forces and/or torques and resulting reaction forces (Otten, 2003). Also, inverse dynamics allows mainly for descriptive approaches, e.g., diagnosis of pathology, rather than predictive approaches—predicting the risk of surgery A versus surgery B. A mixed approach is also possible, where at some critical point in time one reverses the process into forward dynamics and takes the calculated moments and force from the latest time step as a guideline (Otten, 2003). For clinical applications where the goal is to design patient-specific optimal treatments, it is apparent the need to develop physics-based predictive “walking” foot models. However, large computational costs, difficulties in model control strategies and manual generation of personalized models, time- and cost-intensive workflows have limited their use for clinical applications up to today (De Groote & Falisse, 2021; Falisse et al., 2019).

Modeling the foot, modeling the gait, and developing an interacting foot-lower limb “walking” model are different things. Foot models used in conjunction with lower limb “walking” models are often oversimplified multisegment models (van Hoeve & Poeze, 2019) or 2D FE models (Halloran et al., 2009; Qian et al., 2013). In addition, “walking” models are used mainly for walking pathologies (Febrero-Nafría et al., 2021) and not specifically for foot pathologies. Although an obvious interaction with the hip and the knee biomechanics exists, inverse dynamic models are overall less sensitive on the knee and the hip with respect to foot details than forward dynamic models (De Groote & Falisse, 2021).

In general, very simple foot models have been developed so far for clinical applications, using different CM&S techniques: multisegment, multibody, mixed multibody/FEM, and FEM. These models generally lack sufficient degrees of freedom, are not in conjunction with “walking” models, do not consider all the anatomical foot parts, nor the soft tissues (gait analysis theory was developed before foot soft-tissues behavior was considered). These models are rarely personalized, and the model-building process is mostly manual. The clinical relevance of these models is yet to be validated. Industrialization of these models for clinical applications is far

---

<sup>6</sup> <https://simtk.org>.

<sup>7</sup> <http://www.anybodytech.com>.

away as the impact of CM&S on the cost-effectiveness analysis of foot interventions has not been investigated yet.

## Foot CM&S for clinical applications

During the last 3 decades, various foot models have been developed and proven useful in increasing the biomechanical knowledge of the foot and ankle complex. Several review articles have been published documenting the advancement in foot and ankle CM&S and their clinical applications (Leardini et al., 2019; Mondal & Ghosh, 2020; Morales-Orcajo et al., 2016; Perrier et al., 2017; Phan et al., 2021; van Hoeve & Poeze, 2019). However, up to today, none of these models has proven ready for clinical applications. Particularly interesting is the critical review from Mondal and Ghosh (2020) as it is the only review that focuses entirely on the current status and limitations of using CM&S for the design and evaluation of total ankle replacement.

Measured marker-based multibody models, although proven useful in the diagnosis of foot and ankle trauma and pathologies, have nevertheless shown several limitations including skin-markers artifacts and rigid body assumptions, which up to today, did not allow them to be included in daily clinical practice (Leardini et al., 2019; van Hoeve & Poeze, 2019). Furthermore, they present a description of the foot functions in terms of external variables ignoring internal variables such as internal stresses in soft tissues and contact pressure between cartilages, which are key for comprehending specific foot injuries and pathologies as in the case of the diabetic foot. In many applications, these foot and ankle models have been coupled to neuromusculoskeletal lower limb gait models via open-source platforms. However, these applications (Peng et al., 2020; Zhang, Chen, et al., 2020; Zhang, Lv, et al., 2020) were mostly research investigations rather than protocols to be included in daily clinical practice.

Via the ArthiSynth platform<sup>8</sup>, the group from the University of Grenoble Alpes and the innovative pressure-sensor developers from TexiSense<sup>9</sup> focused mainly on personalized medicine strategies for diabetic foot. A hybrid multisegmented and finite element model is developed to investigate foot internal variables to characterize the influence of orthosis design on foot functions, to characterize the diabetic foot (Perrier et al., 2016), and to predict the associated risk of foot ulcers (Bucki et al., 2016; Luboz et al., 2014; Niroomandi et al., 2019). The foot and ankle models developed within these studies present high anatomical details including soft tissues as skin, fat tissue, heel pad and muscle tissue, intrinsic and extrinsic tendons, and ligaments, whose insertion points are evaluated from both patient-specific MRIs and from literature. The geometry of the soft tissues is also evaluated from

<sup>8</sup> <https://www.artisynth.org>.

<sup>9</sup> <https://www.texisense.com>.

patient-specific MRIs, however material properties, although considered nonlinear, are homogeneous and non-patient-specific. Cartilage is not modeled.

Finite element models have been developed mainly with focus on the foot and ankle complex, without involving the musculoskeletal lower limb gait. The foot and ankle complex is generally fixed at the tibia-fibula level and simulations are performed in balance-standing or via a quasi-static gait approach by imposing forces, torques, and movement on the ground support. These models are generally highly anatomically detailed, including soft tissues as skin, heel pad, plantar pad, muscles, tendons, ligaments, and cartilages, represented often via nonlinear material models. Intrinsic muscle representation is, however, not present.

The group from the Polytechnic University of Hong-Kong has been working the most with this approach and various potential clinical applications were investigated, from insole design evaluations (Cheung, 2007); footwear applications (Yu et al., 2013), and orthopedics applications comparing ankle arthrodesis and total ankle replacement surgical techniques (Wang et al., 2019). The model was further adapted to investigate the effect of ligaments laxity on the risks of deterioration of hallux valgus deformity (Wong et al., 2020).

A similar approach was followed by the group from the University of Zaragoza, where a model was first developed (García-Aznar et al., 2009), and then used for clinical applications focusing on claw toe deformity (García-González et al., 2009) and on hallux valgus (Morales-Orcajo et al., 2015). The model was further used for research-oriented topics to investigate the relation between foot internal stress distribution and tendon forces (Morales-Orcajo et al., 2017), and to investigate the foot internal stress distribution during barefoot running (Morales-Orcajo et al., 2018).

The group from the University of Washington, still presenting similar modeling approaches concerning boundary conditions and load cases, focused firstly on specific orthopedic topics such as studying the effect of muscle overpull on the formation of the clawed hallux deformity and the simulation of different surgical treatments (modified Jones procedure and FHL tendon transfer) (Isvilanonda et al., 2012). Secondly, they focused on developing a patient-specific diabetic foot model (Isvilanonda, 2015), where an inverse FE analysis protocol is proposed to obtain *in vivo* subject-specific plantar soft tissue material properties.

In the same direction, the group from the University of Beihang focused on foot and ankle physiological studies (Guo, Liu, et al., 2018) and surgical evaluations on the hallux valgus pathology (Guo, Wang, et al., 2018).

Recently, the start-up Digital Orthopaedics investigated total ankle replacement (TAR) applications by using a digital foot twin generator previously developed (Morales-Orcajo et al., 2020). In a first study, they compared the wearing performance of a TAR prosthesis by virtually reproducing the ISO 22622:2019 standard, with the same prosthesis then inserted in a digital twin simulating the complete stance phase (Stenti et al., 2020b). In a second study, the prosthesis performance in terms of range of motion, ligament loadings, and contact pressure distribution on the polyethylene insert was investigated on two different subjects (Stenti et al., 2020a). Although their models still suffer the limitations of the inverse dynamic

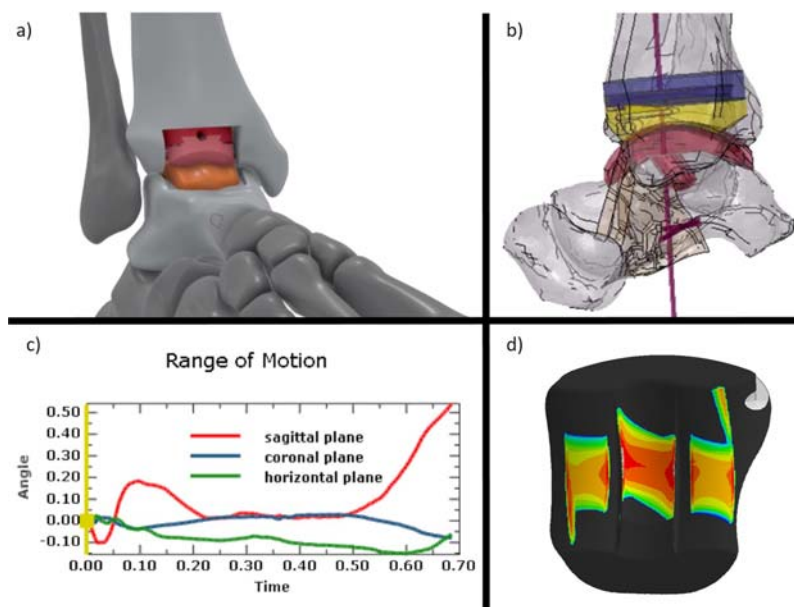


**FIGURE 16.4 Analysis of a TAR prosthesis performance under patient-specific biomechanical conditions.**

a) Virtual surgery of the TAR prosthesis in the CAD model of the patient. b) Detail of the prosthesis position during finite element simulation. c) Range of motion of the TAR prosthesis in the three planes. d) Wear map estimation of the prosthesis. Simulation performed at Digital Orthopaedics.

approach when simulating predictive gait, and it is still in the clinical validation process, to the authors' knowledge, these studies represent the first effort of using foot and ankle CM&S for in silico clinical trials at commercial scale (Fig. 16.4).

The list presented here is not exhaustive. The focus has been on complete three-dimensional models, anatomically highly detailed, which presented or were potentially considered ready for clinical applications. For a complete review on CM&S on the foot and ankle complex, the reader is referred to the following references (Leardini et al., 2019; Mondal & Ghosh, 2020; Morales-Orcajo et al., 2016; Perrier et al., 2017; Phan et al., 2021; van Hoeve & Poeze, 2019).

In summary, although finite elements modeling allows the most reliable representation of the anatomical and functional behavior of the foot and ankle complex, several drawbacks still question their advantages in daily clinical practice. Creating patient-specific detailed foot models is a long and tedious manual process, which results in models which are too computationally heavy to comply with clinical requirements. In addition, to include patient-specific soft tissue properties, *in vivo* measurement strategies are needed; and nonhomogeneous nonlinear material models need to be considered.

## Foot CM&S for the footwear industry

With respect to barefoot walking, shod walking influences the foot pattern, especially imposing specific foot motion patterns during the push-off phase (Morio et al., 2009). Besides years of development in the field of orthopedics and sports biomechanics, there are no standardized guidelines for designing therapeutic and functional footwear, i.e., orthotics, shoe soles, and shoes. Existing treatments and products are based on limited experimental evaluations or empirical knowledge of clinicians and engineers (Cheung & Man, 2009).

Athletic footwear functions include traction, motion control, and the attenuation of impact forces during motion. Tuning the stiffness of running shoes in an optimal range can be beneficial for performance-related variables. Softer midsoles can reduce impact forces and loading rates. Thicker midsoles can provide better cushioning and attenuate shock during impact at the cost of losing foot plantar sensation. Minimalist shoes improve running economy at the cost of increasing the metatarsophalangeal and ankle joint loading compared to conventional shoes. While running shoes can effectively influence running biomechanics, optimize performance-related variables, and prevent running-related injuries, additional research is needed before viable scientific guidelines can be made and standard testing protocols are developed (Sun et al., 2020). Therefore, reducing injuries and improving performances by using running shoes have become a focus in both the sports industry and academia.

The development of 3D geometrically accurate foot models became popular in the field of biomechanics starting in early 2000. A complete historical review on the use of CM&S for footwear applications can be found in Azariadis (2012, pp. 321–340), Cheung & Man (2009), Zhang et al. (2014). Aiming to optimize the performance of sports shoes, research has focused on understanding the foot–shoe–ground interaction during motion: evaluation of the foot soles impacts characteristics on the plantar pressure distribution during the different walking phases and on heel strike insole stability and cushioning ability during running.

The group from the Polytechnic University of Hong-Kong extended their highly developed foot and ankle model to study the impact of insole design on plantar pressure in balance standing (Cheung & Zhang, 2008) and simulating the foot–shoe interaction during walking (Cheung, 2007) by using a quasi-static approach. A similar modeling approach was followed in Yu et al. (2013) with focus on high-heel shoes.

Several other geometrically accurate FE foot models have been developed recently for the design and evaluation of footwear. It is apparent the importance of correctly modeling the foot–shoe–ground interaction for the foot movements characteristic of the sport of interest (Ishii et al., 2014), to the extent of considering the player specific style when shoe personalization is the goal (Cho et al., 2009).

Overall, apart from a few impact analysis studies, most literature follows a quasi-static approach that hinders important dynamic or inertia effects of the ankle–foot, especially during heel strike and push-off phases. Besides, the validation of existing FE foot and footwear models relies mainly on plantar pressure distributions and

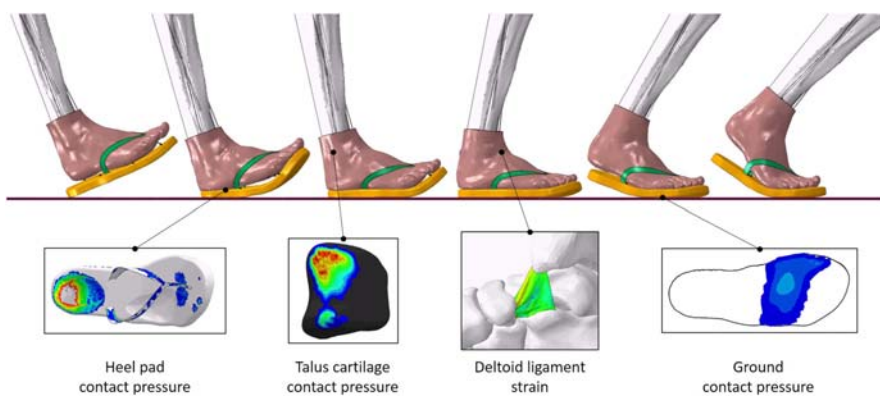


**FIGURE 16.5**

One step dynamic simulation of a foot wearing a flip-flop. Contact pressures and strains are plotted at different time steps. Simulation developed at Digital Orthopedics.

gross tissue and foot deformations, ignoring, for example, ligament loading, which is responsible for most of the foot and ankle injuries. Above all, to improve the foot–shoe–ground interaction analysis and study the coupling mechanism among the lower limb joints, a musculoskeletal computational model of the hip–knee–ankle–foot needs to be developed. An attempt in this direction is presented in Fig. 16.5. The foot finite model developed at Digital Orthopaedics is coupled with a flip-flop during a walking step simulation to compute the contact pressure of the foot with the insole and the insole with the ground as well as the contact pressure of the tibiotalar joint and the strain of the deltoid ligament.

There is an increasing customer demand for functional footwear guaranteeing higher performances and health benefits. Computer-aided design (CAD) alone, which focuses mainly on design for manufacturing, will no longer be able to fulfill the needs of the modern footwear industry. Considering the physics governing the foot–shoe–ground interaction via CM&S is the key technological step forward expected in the evaluation and design for footwear and footwear components. Combining virtual testing approaches (Azariadis et al., 2007; Fraser, 2015) with highly detailed foot and ankle CM&S is the direction to take.

In spite the use of CM&S for product development in the footwear industry is increasing, e.g., ASICS,<sup>10</sup> ADIDAS,<sup>11</sup> PUMA,<sup>12</sup> and the recent publication from SALOMON (Sissler & Giandolini, 2019) correlating cushioning and tibia vibration during impact, there is no evidence yet on the use of foot and ankle highly detailed anatomical models within the footwear industry product development standards. It

<sup>10</sup> <https://blogs.3ds.com/simulia/better-running-shoes-simulation/>.

<sup>11</sup> [https://www.ssanalysis.co.uk/hubfs/KB\\_NEW\\_DOCS/Case\\_Studies/adidas-achieved-design-cycle-reduction-Abaqus-FEA-10-07.pdf](https://www.ssanalysis.co.uk/hubfs/KB_NEW_DOCS/Case_Studies/adidas-achieved-design-cycle-reduction-Abaqus-FEA-10-07.pdf).

<sup>12</sup> <https://mitdesignlab.herokuapp.com/projects/puma-auxetic-recurve-midsole>.

should be considered that highly detailed anatomical foot and ankle CM&S models already require an enormous effort to build and to compute. Adding the foot–shoe–ground interaction in the equation raises the challenge to the next level. Nevertheless, a coupled 3D foot–shoe model is a prerequisite to secure both the effectiveness and reliability of the numerical evaluation of landing impact characteristics (Cho et al., 2009).

### Why foot and ankle CM&S is not yet in the clinic

Besides the enormous development efforts and advancements in foot and ankle CM&S in the last 3 decades, today it remains an academic research subject rather than a well-established daily clinical practice.

International consensus on foot and ankle clinical measures and assessments, within musculoskeletal disease management, is building up. Consensus statements by the American College of Foot and Ankle Surgeons on specific surgical treatments have been published recently (Shibuya et al., 2020). Within this continuously evolving context, foot and ankle CM&S has found itself considered more as a tool to understand foot and ankle biomechanics than a tool to improve clinical practice.

Nevertheless, improving patients care via personalized medicine is a general challenge that foot and ankle clinical practice will have to face. There is no question that CM&S will play a crucial role in improving patient care by developing digital twins and performing risk-analyses of surgical interventions: never first time on the patient!

However, foot and ankle CM&S is still not a viable healthcare technology. Technological, economical, and regulatory barriers are still hindering its full deployment.

A holistic approach is mandatory. The majority of the foot models existing today in literature are either highly anatomically detailed and used in balance standing simulations, or heavily simplified and coupled with musculoskeletal models. A musculoskeletal model coupled to a highly detailed anatomical foot and ankle model, capable to represent the hip–knee–ankle–foot coupled behavior, is still not state of the art. A forward dynamic approach, which can be used for predicting the risk of injuries during sports activities or to evaluate the risk and the efficacy of proposed treatments is still the subject of academic research.

Generating a foot CM&S is too expensive: automatization of the digital twin generation workflow is mandatory. The number of inputs required to build up a highly anatomically detailed foot digital twin—CTs, MRIs, Gait Lab measurements, EMGs, etc.—requires economical evaluations and ethical considerations. In addition, these inputs are not generally available in hospitals, and acquisition protocols are yet to be accepted. Digital twin generation is a time-consuming and manual operation that still requires highly technical expertise, the “art of modeling,” having an impact on the modeling results. A digital twin should be generated automatically via a quality-controlled workflow, starting from subject-specific measurements following accepted protocols. Alternative techniques have been developed. A

proposed solution is to start from a predefined high-resolution model (so-called atlas or generic model) and adjust the geometric distribution of its components to fit the morphology of each new patient (Bucki et al., 2016). Although mathematically possible, the clinical relevance of the generated models is still to be demonstrated.

Solving foot CM&S is too expensive. The computational resources needed to simulate and perform robustness analyses of such models, represent an additional technological and economical challenge. Models to be used for daily clinical practice should be able to provide results in a timescale of minutes, rather than in several hours as is the case today. Drastic reduction in computational cost is needed, but it can only be achieved through radical simplifications in tissue modeling and foot functions. The real risk of the resulting loss in accuracy and range of applicability is decreasing credibility and confidence by the community of clinicians in the predictive power of foot CM&S. Alternative solutions are in development, including surrogate models or reduced-order models (Chinesta et al., 2020).

Although the level of anatomical detail is progressively increasing, there is not sufficient attention and clinical validation on the foot biomechanics. The complex joints behavior during gait, the talocrural, the subtalar, the Chopart, the Lisfranc, and the metatarsophalangeal behavior during the protonation at first heel contact, through loading response and midstance, till supination during push-off are rarely investigated in detail by the models. These typical unique foot movements impact the longitudinal and transversal foot arches and thus the redistribution of pressure within the foot during gait. This redistribution of internal pressure allows the foot to become flexible and adaptative to any surface during landing and single-limb walking, to then become a rigid lever for the Triceps Surae during the push-off phase. This unique characteristic of the human foot, together with the high variability in joints topology, is of fundamental importance for personalized foot and ankle CM&S.

Models existing in the literature are not personalized in the soft tissues. Although methodologies for in vivo measurements have been the object of research, e.g., ultrasounds elastography (Sigrist et al., 2017), protocols for daily clinical practice do not exist yet. Studies show that using a population average value for plantar soft tissues and not a patient-specific value can change up to 7% on peak plantar pressure (Erdemir et al., 2006). Realistic simulation of the mechanical behavior of soft tissues, especially ligaments and tendons, is of paramount importance in studies that focus on ligament or tendon biomechanics, on the effect of pathological conditions, or the efficiency of relevant treatments (Behforootan, Chatzistergos, Naemi, & Chockalingam, 2017). In vivo measurements such as plantar surface indentation are limited to superficial tissue properties estimation (Petre et al., 2013). In addition, nonhomogeneous, nonlinear, and orthotropic material models, typically required for soft tissue modeling, do not exist in commercial software. Development of ad-hoc user subroutines is required, for which standardization is difficult, and acceptance by clinicians as daily clinical practice protocols is far from reality.

For foot CM&S to be accepted and considered credible by the community of clinicians, validation and verification are mandatory. Today, in vivo validation of foot and ankle CM&S is possible on external measurable quantities (plantar pressures,

### Foot & Ankle CM&S readiness for clinical applications

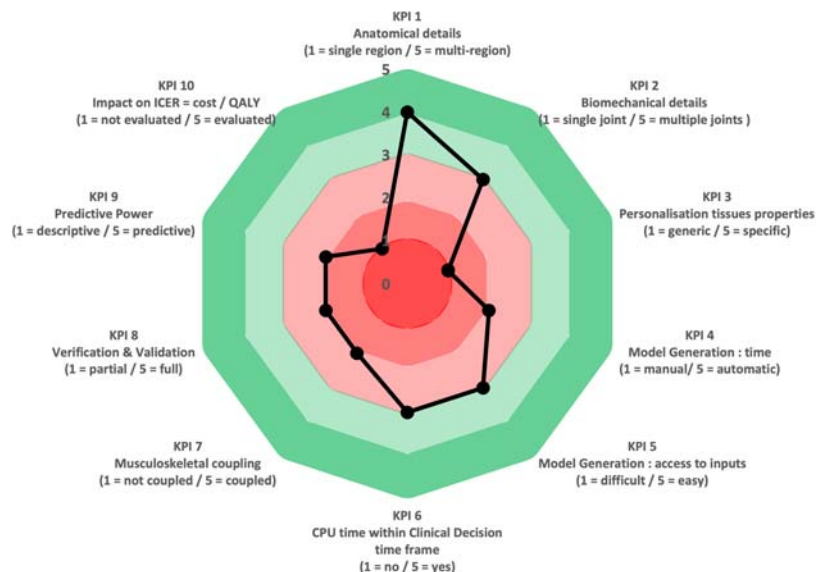


**FIGURE 16.6 Foot and ankle CM&S readiness for clinical applications.**

Spider plot of 10 key performance indicators (KPIs) quantifying the maturity level and readiness of the foot and ankle CM&S for clinical applications. An average level of three is chosen as the minimum requirement to consider foot and ankle CM&S as available health care technology. The values given reflect authors' opinions and are based on their experience in building foot digital twins for clinical applications.

marker movements, ground forces) (Abdul Razak et al., 2012), and via bones relative displacement and arch deformation on radiographic images (Cheng et al., 2008). However, validation on internal quantities, such as ligament stresses and strains and joint cartilages contact pressure, which are not feasible to measure in vivo although extremely important in clinical assessment, is not performed. Protocols are needed to validate model reliability, accuracy, and specificity for the target populations of interest (healthy, pathological, walking, running, etc.).

Finally, building a digital twin to solve a specific clinical problem should have a direct and quantifiable impact in reducing the incremental cost-effectiveness ratio (ICER) for the proposed treatment. This is the only way for foot and ankle CM&S to be accepted and considered as a viable healthcare technology.

Fig. 16.6 summarizes the discussion by identifying 10 key performance indicators (KPIs), which quantify the maturity level and readiness of the foot and ankle CM&S for clinical applications. The values given here are based on the experience of the authors and reflect solely their opinion. An average level of three is chosen as

the minimum requirement to consider foot and ankle CM&S as a viable healthcare technology.

The first two KPIs deal with the level of modeling realism. A model with the anatomical KPI rated 5 is a model including skin, fat pads, muscles, tendons, ligaments, cartilages, and bones. The biomechanical KPI rating 5 indicates a model capable to represents the behavior of the main foot joints during balance standing or gait: the talocrural, the subtalar, the Chopart, the Lisfranc, and the metatarsophalangeal. KPI 3 relates to how much the soft tissues are patient-specific. KPIs 4 and 5 deal with the model generation workflow in terms of automatization of the model build-up and easiness to obtain the necessary inputs, respectively. The 6th KPI focuses on the computational burden of solving the model. A model with the 6th KPI rated 5 is considered ready to be used within the clinical decision time frame of interest. KPI 7 measures the degree of coupling with a musculoskeletal model. KPIs 8 and 9 relate to the level of verification and validation activities performed and the power of the model to predict postsurgical scenarios. Finally, KPI 10 indicates the CM&S impact on the cost-effectiveness ratio of the treatment of interest.

---

## References

- Abdul Razak, A. H., Zayegh, A., Begg, R. K., & Wahab, Y. (2012). Foot plantar pressure measurement system: A review. *Sensors (Switzerland)*, 12(7), 9884–9912. <https://doi.org/10.3390/s120709884>
- Azariadis. (2012). *Finite element analysis in footwear design*. <https://doi.org/10.1201/b13021-19/design-custom-shoe-lasts-challenging-feet-ravindra-goonetilleke>
- Azariadis, P., Moulianitis, V., Alemany, S., González, J. C., Jong, P. D., Zande, M. V. D., & Brands, D. (2007). Virtual shoe test bed: A computer-aided engineering tool for supporting shoe design. *Computer-Aided Design and Applications*, 4(6), 741–750. <https://doi.org/10.1080/16864360.2007.10738507>
- Behforootan, S., Chatzistergos, P. E., Chockalingam, N., & Naemi, R. (2017). A simulation of the viscoelastic behaviour of heel pad during weight-bearing activities of daily living. *Annals of Biomedical Engineering*, 45(12), 2750–2761. <https://doi.org/10.1007/s10439-017-1918-1>
- Behforootan, S., Chatzistergos, P., Naemi, R., & Chockalingam, N. (2017). Finite element modelling of the foot for clinical application: A systematic review. *Medical Engineering and Physics*, 39, 1–11. <https://doi.org/10.1016/j.medengphy.2016.10.011>
- Bennett, P. J. (2007). Prevalence and type of foot surgery performed in Australia: A clinical review. *Foot*, 17(4), 197–204. <https://doi.org/10.1016/j.foot.2007.05.001>
- Best, M. J., Buller, L. T., & Miranda, A. (2015). National trends in foot and ankle arthrodesis: 17-year analysis of the national survey of ambulatory surgery and national hospital discharge survey. *Journal of Foot and Ankle Surgery*, 54(6), 1037–1041. <https://doi.org/10.1053/j.jfas.2015.04.023>
- Bidgood, et al. (1997). *Journal of the American Medical Informatics Association*, 4. <https://doi.org/10.1136/jamia.1997.0040199>
- Brockett, C. L., & Chapman, G. J. (2016). Biomechanics of the ankle. *Orthopaedics and Trauma*, 30(3), 232–238. <https://doi.org/10.1016/j.mporth.2016.04.015>

- Bucki, M., Luboz, V., Perrier, A., Champion, E., Diot, B., Vuillerme, N., & Payan, Y. (2016). Clinical workflow for personalized foot pressure ulcer prevention. *Medical Engineering and Physics*, 38(9), 845–853. <https://doi.org/10.1016/j.medengphy.2016.04.017>
- Burkhart, T. A., Andrews, D. M., & Dunning, C. E. (2013). Finite element modeling mesh quality, energy balance and validation methods: A review with recommendations associated with the modeling of bone tissue. *Journal of Biomechanics*, 46(9), 1477–1488. <https://doi.org/10.1016/j.jbiomech.2013.03.022>
- Burton, A., Aynardi, M. C., & Aydogan, U. (2021). Demographic distribution of foot and ankle surgeries among orthopaedic surgeons and podiatrists: a 10-year database retrospective study. *Foot and Ankle Specialist*, 14(3), 206–212. <https://doi.org/10.1177/1938640020910951>
- Cheng, H. Y. K., Lin, C. L., Chou, S. W., & Wang, H. W. (2008). Nonlinear finite element analysis of the plantar fascia due to the windlass mechanism. *Foot and Ankle International*, 29(8), 845–851. <https://doi.org/10.3113/FAI.2008.0845>
- Cheung, J. T. M. (2007). A 3D finite element simulation of foot-shoe interface. In *Proceedings of the 8th Symposium on footwear biomechanics* (pp. 45–46).
- Cheung, J., & Man, T. (2009). Review of computational models for footwear design and evaluation. *Korean Journal of Sport Biomechanics*, 19(1), 13–25.
- Cheung, J. T. M., & Zhang, M. (2008). Parametric design of pressure-relieving foot orthosis using statistics-based finite element method. *Medical Engineering and Physics*, 30(3), 269–277. <https://doi.org/10.1016/j.medengphy.2007.05.002>
- Chinesta, F., Cueto, E., Abisset-Chavanne, E., Duval, J. L., & Khaldi, F. E. (2020). Virtual, digital and hybrid twins: A new paradigm in data-based engineering and engineered data. *Archives of Computational Methods in Engineering*, 27(1), 105–134. <https://doi.org/10.1007/s11831-018-9301-4>
- Cho, J. R., Park, S. B., Ryu, S. H., Kim, S. H., & Lee, S. B. (2009). Landing impact analysis of sports shoes using 3-D coupled foot-shoe finite element model. *Journal of Mechanical Science and Technology*, 23(10), 2583–2591. <https://doi.org/10.1007/s12206-009-0801-x>
- De Groote, F., & Falisse, A. (2021). Perspective on musculoskeletal modelling and predictive simulations of human movement to assess the neuromechanics of gait. *Proceedings. Biological Sciences*, 288, 20202432. <https://doi.org/10.1098/rspb.2020.2432>
- Erdemir, A., Besier, T. F., Halloran, J. P., Imhäuser, C. W., Laz, P. J., Morrison, T. M., & Shelburne, K. B. (2019). Deciphering the art in modeling and simulation of the knee joint: Overall strategy. *Journal of Biomechanical Engineering*, 141(7). <https://doi.org/10.1115/1.4043346>
- Erdemir, A., McLean, S., Herzog, W., & van den Bogert, A. J. (2007). Model-based estimation of muscle forces exerted during movements. *Clinical Biomechanics*, 22(2), 131–154. <https://doi.org/10.1016/j.clinbiomech.2006.09.005>
- Erdemir, A., Mulugeta, L., Ku, J. P., Drach, A., Horner, M., Morrison, T. M., Peng, G. C. Y., Vadigepalli, R., Lytton, W. W., & Myers, J. G. (2020). Credible practice of modeling and simulation in healthcare: Ten rules from a multidisciplinary perspective. *Journal of Translational Medicine*, 18(1). <https://doi.org/10.1186/s12967-020-02540-4>
- Erdemir, A., Viveiros, M. L., Ulbrecht, J. S., & Cavanagh, P. R. (2006). An inverse finite-element model of heel-pad indentation. *Journal of Biomechanics*, 39(7), 1279–1286. <https://doi.org/10.1016/j.jbiomech.2005.03.007>
- Extremities, E. (2018). VANTAGE TAR design Rationale.
- Falisse, A., Serrancolí, G., Dembia, C. L., Gillis, J., Jonkers, I., & De Groote, F. (2019). Rapid predictive simulations with complex musculoskeletal models suggest that diverse healthy

- and pathological human gaits can emerge from similar control strategies. *Journal of the Royal Society Interface*, 16(157). <https://doi.org/10.1098/rsif.2019.0402>
- Falisse, A., Van Rossum, S., Gijsbers, J., Steenbrink, F., Van Basten, B. J. H., Jonkers, I., Van Den Bogert, A. J., & De Groot, F. (2018). OpenSim versus human body model: A comparison study for the lower limbs during gait. *Journal of Applied Biomechanics*, 34(6), 496–502. <https://doi.org/10.1123/jab.2017-0156>
- Febrero-Nafría, M., Pallarès-López, R., Fregly, B. J., & Font-Llagunes, J. M. (2021). Prediction of three-dimensional crutch walking patterns using a torque-driven model. *Multibody System Dynamics*, 51(1). <https://doi.org/10.1007/s11044-020-09751-z>
- Fraser, S. (2015). *A Method of Using Computer Simulation to Assess the Functional Performance of Football Boots* (Vol 209).
- García-Aznar, J. M., Bayod, J., Rosas, A., Larraínzar, R., García-Bogalo, R., Doblaré, M., & Llanos, L. F. (2009). Load transfer mechanism for different metatarsal geometries: A finite element study. *Journal of Biomechanical Engineering*, 131(2). <https://doi.org/10.1115/1.3005174>
- García-González, A., Bayod, J., Prados-Frutos, J. C., Losa-Iglesias, M., Jules, K. T., de Bengoa-Vallejo, R. B., & Doblaré, M. (2009). Finite-element simulation of flexor digitorum longus or flexor digitorum brevis tendon transfer for the treatment of claw toe deformity. *Journal of Biomechanics*, 42(11), 1697–1704. <https://doi.org/10.1016/j.jbiomech.2009.04.031>
- Gougloulias, N., Khanna, A., & Maffulli, N. (2010). How successful are current ankle replacements?: A systematic review of the literature. *Clinical Orthopaedics and Related Research*, 468(1), 199–208. <https://doi.org/10.1007/s11999-009-0987-3>
- Guo, J., Liu, X., Ding, X., Wang, L., & Fan, Y. (2018). Biomechanical and mechanical behavior of the plantar fascia in macro and micro structures. *Journal of Biomechanics*, 76, 160–166. <https://doi.org/10.1016/j.jbiomech.2018.05.032>
- Guo, J., Wang, L., Mao, R., Chang, C., Wen, J., & Fan, Y. (2018). Biomechanical evaluation of the first ray in pre-/post-operative hallux valgus: A comparative study. *Clinical Biomechanics*, 60, 1–8. <https://doi.org/10.1016/j.clinbiomech.2018.06.002>
- Haddad, S. L., Coetze, J. C., Estok, R., Fahrbach, K., Banel, D., & Nalysnyk, L. (2007). Intermediate and long-term outcomes of total ankle arthroplasty and ankle arthrodesis: A systematic review of the literature. *Journal of Bone and Joint Surgery - Series A*, 89(9), 1899–1905. <https://doi.org/10.2106/JBJS.F.01149>
- Halloran, J. P., Erdemir, A., & Van Den Bogert, A. J. (2009). Adaptive surrogate modeling for efficient coupling of musculoskeletal control and tissue deformation models. *Journal of Biomechanical Engineering*, 131(1). <https://doi.org/10.1115/1.3005333>
- Halonen, K. S., Dzialo, C. M., Mannisi, M., Venäläinen, M. S., De Zee, M., & Andersen, M. S. (2017). Workflow assessing the effect of gait alterations on stresses in the medial tibial cartilage—combined musculoskeletal modelling and finite element analysis. *Scientific Reports*, 7(1). <https://doi.org/10.1038/s41598-017-17228-x>
- van Hoeve, S., & Poeze, M. (2019). Multisegment foot models and clinical application after foot and ankle trauma: A review. *Journal of Foot and Ankle Surgery*, 58(4), 748–754. <https://doi.org/10.1053/j.jfas.2018.11.013>
- Ishii, H., Sakurai, Y., & Maruyama, T. (2014). Effect of soccer shoe upper on ball behaviour in curve kicks. *Scientific Reports*, 4. <https://doi.org/10.1038/srep06067>
- Isvalanonda, V. (2015). *Finite element modeling of the foot*.
- Isvalanonda, V., Dengler, E., Iaquinto, J. M., Sangeorzan, B. J., & Ledoux, W. R. (2012). Finite element analysis of the foot: Model validation and comparison between two common

- treatments of the clawed hallux deformity. *Clinical Biomechanics*, 27(8), 837–844. <https://doi.org/10.1016/j.clinbiomech.2012.05.005>
- Killen, B. A., Falisse, A., De Groote, F., & Jonkers, I. (2020). In silico-enhanced treatment and rehabilitation planning for patients with musculoskeletal disorders: Can musculoskeletal modelling and dynamic simulations really impact current clinical practice? *Applied Sciences (Switzerland)*, 10(20), 1–22. <https://doi.org/10.3390/app10207255>
- Kinney, A. L., Besier, T. F., D'Lima, D. D., & Fregly, B. J. (2013). Update on grand challenge competition to predict in vivo knee loads. *Journal of Biomechanical Engineering*, 135(2). <https://doi.org/10.1115/1.4023255>
- Komi, P. V. (1990). Relevance of in vivo force measurements to human biomechanics. *Journal of Biomechanics*, 23(1), 23–34. [https://doi.org/10.1016/0021-9290\(90\)90038-5](https://doi.org/10.1016/0021-9290(90)90038-5)
- Leardini, A., Caravaggi, P., Theologis, T., & Stebbins, J. (2019). Multi-segment foot models and their use in clinical populations. *Gait and Posture*, 69, 50–59. <https://doi.org/10.1016/j.gaitpost.2019.01.022>
- Lloyd, J. E., Sánchez, A., Widing, E., Stavness, I., Fels, S., Niroomandi, S., Perrier, A., Payan, Y., & Perrier, P. (2019). New techniques for combined FEM-Multibody anatomical simulation. In , Vol 999. *Lecture notes in computational vision and biomechanics* (pp. 75–92). Springer Netherlands. [https://doi.org/10.1007/978-3-030-23073-9\\_6](https://doi.org/10.1007/978-3-030-23073-9_6)
- Luboz, V., Perrier, A., Stavness, I., Lloyd, J. E., Bucki, M., Cannard, F., Diot, B., Vuillerme, N., & Payan, Y. (2014). Foot ulcer prevention using biomechanical modelling. *Computer Methods in Biomechanics and Biomedical Engineering: Imaging and Visualization*, 2(4), 189–196. <https://doi.org/10.1080/21681163.2013.837410>
- Menz, H. B., Gilheany, M. F., & Landorf, K. B. (2008). Foot and ankle surgery in Australia: A descriptive analysis of the medicare benefits Schedule database, 1997–2006. *Journal of Foot and Ankle Research*, 1(1). <https://doi.org/10.1186/1757-1146-1-10>
- Milstrey, A., Domnick, C., Garcia, P., Raschke, M. J., Evers, J., & Ochman, S. (2021). Trends in arthrodeses and total joint replacements in Foot and Ankle surgery in Germany during the past decade—Back to the fusion? *Foot and Ankle Surgery*, 27(3), 301–304. <https://doi.org/10.1016/j.fas.2020.05.008>
- Mondal, S., & Ghosh, R. (2020). Experimental and finite element investigation of total ankle replacement: A review of literature and recommendations. *Journal of Orthopaedics*, 18, 41–49. <https://doi.org/10.1016/j.jor.2019.09.019>
- Morales-Orcajo, E., Bayod, J., & Barbosa de Las Casas, E. (2016). Computational foot modeling: Scope and applications. *Archives of Computational Methods in Engineering*, 23(3), 389–416. <https://doi.org/10.1007/s11831-015-9146-z>
- Morales-Orcajo, E., Bayod, J., Becerro-de-Bengoa-Vallejo, R., Losa-Iglesias, M., & Doblaré, M. (2015). Influence of first proximal phalanx geometry on hallux valgus deformity: A finite element analysis. *Medical and Biological Engineering and Computing*, 53(7), 645–653. <https://doi.org/10.1007/s11517-015-1260-4>
- Morales-Orcajo, E., Becerro de Bengoa Vallejo, R., Losa Iglesias, M., Bayod, J., & Barbosa de Las Casas, E. (2018). Foot internal stress distribution during impact in barefoot running as function of the strike pattern. *Computer Methods in Biomechanics and Biomedical Engineering*, 21(7), 471–478. <https://doi.org/10.1080/10255842.2018.1480760>
- Morales-Orcajo, E., Souza, T. R., Bayod, J., & Barbosa de Las Casas, E. (2017). Non-linear finite element model to assess the effect of tendon forces on the foot-ankle complex. *Medical Engineering and Physics*, 49, 71–78. <https://doi.org/10.1016/j.medengphy.2017.07.010>

- Morales-Orcajo, E., Stenti, A., Fan, A., Balabanis, A., Ye, S., Leemrijse, T., & Lété, E. (2020). *3DOrthoTwin: Highly automatic generation of subject-specific foot finite element models.*
- Morio, C., Lake, M. J., Gueguen, N., Rao, G., & Baly, L. (2009). The influence of footwear on foot motion during walking and running. *Journal of Biomechanics*, 42(13), 2081–2088. <https://doi.org/10.1016/j.jbiomech.2009.06.015>
- Nester, C. J. (2009). Lessons from dynamic cadaver and invasive bone pin studies: Do we know how the foot really moves during gait? *Journal of Foot and Ankle Research*, 2(1). <https://doi.org/10.1186/1757-1146-2-18>
- Niroomandi, S., Perrier, A., Bucki, M., & Payan, Y. (2019). Real-time computer modeling in prevention of foot pressure ulcer using patient-specific finite element model and model order reduction techniques. In *Innovations and Emerging Technologies in Wound Care* (pp. 87–102). Elsevier. <https://doi.org/10.1016/B978-0-12-815028-3.00005-5>
- Otten, E. (2003). Inverse and forward dynamics: Models of multi-body systems. In , 358. *Philosophical Transactions of the Royal Society B: Biological Sciences* (pp. 1493–1500). Royal Society. <https://doi.org/10.1098/rstb.2003.1354>
- Park, H., Yu, R., & Lee, J. (2019). Multi-segment foot for human modelling and simulation. *Computer Graphics Forum*. <https://doi.org/10.1111/cgf.13896>
- Peng, Y., Wong, D. W. C., Wang, Y., Chen, T. L. W., Tan, Q., Chen, Z., Jin, Z., & Zhang, M. (2020). Immediate effects of medially posted insoles on lower limb joint contact forces in adult acquired flatfoot: A pilot study. *International Journal of Environmental Research and Public Health*, 17(7). <https://doi.org/10.3390/ijerph17072226>
- Perrier, A., Dumas, R., Parratte, B., Rochette, M., Payan, Y., Vuillerme, N., Bucki, M., & Carlier, R. (2016). *Conception et évaluation d'un modèle biomécanique, éléments finis, patient-spécifique, du pied humain. Applications en podologie, orthopédie et diabétologie : Applications en podologie.*
- Perrier, A., Luboz, V., Bucki, M., Cannard, F., Vuillerme, N., & Payan, Y. (2017). Biomechanical modeling of the foot. In *Biomechanics of Living Organs: Hyperelastic Constitutive Laws for Finite Element Modeling* (pp. 545–563). Elsevier Inc. <https://doi.org/10.1016/B978-0-12-804009-6.00025-0>
- Petre, M., Erdemir, A., Panoskaltsis, V. P., Spirka, T. A., & Cavanagh, P. R. (2013). Optimization of nonlinear hyperelastic coefficients for foot tissues using a magnetic resonance imaging deformation experiment. *Journal of Biomechanical Engineering*, 135(6). <https://doi.org/10.1115/1.4023695>
- Phan, P. K., Vo, A. T. N., Bakhtiyaridavijani, A., Burch, R., Smith, B., Ball, J. E., Chander, H., Knight, A., & Prabhu, R. K. (2021). In silico finite element analysis of the foot ankle complex biomechanics: A literature review. *ASME Journal of Biomechanical Engineering*, 143(9), 090802. <https://doi.org/10.1115/1.4050667>
- Pugely, A. J., Lu, X., Amendola, A., Callaghan, J. J., Martin, C. T., & Cram, P. (2014). Trends in the use of total ankle replacement and ankle arthrodesis in the United States medicare population. *Foot and Ankle International*, 35(3), 207–215. <https://doi.org/10.1177/1071100713511606>
- Qian, Z., Ren, L., Ding, Y., Hutchinson, J. R., & Ren, L. (2013). A dynamic finite element analysis of human foot complex in the sagittal plane during level walking. *PLoS One*, 8(11). <https://doi.org/10.1371/journal.pone.0079424>
- Reiber, G. E. (2010). *Epidemiology of Foot Ulcerations and Amputations in Diabetes.*
- Saro, C., Bengtsson, A. S., Lindgren, U., Adami, J., Blomqvist, P., & Felländer-Tsai, L. (2008). Surgical treatment of hallux valgus and forefoot deformities in Sweden: A

- population-based study. *Foot and Ankle International*, 29(3), 298–304. <https://doi.org/10.3113/FAI.2008.0298>
- Shibuya, N., McAlister, J. E., Prissel, M. A., Piraino, J. A., Joseph, R. M., Theodoulou, M. H., & Jupiter, D. C. (2020). Consensus statement of the American College of foot and ankle surgeons: Diagnosis and treatment of ankle arthritis. *Journal of Foot and Ankle Surgery*, 59(5), 1019–1031. <https://doi.org/10.1053/j.jfas.2019.10.007>
- Shiroiwa, T., Sung, Y. K., Fukuda, T., Lang, H. C., Bae, S. C., & Tsutani, K. (2010). International survey on willingness-to-pay (WTP) for one additional qaly gained: What is the threshold of cost effectiveness? *Health Economics*, 19(4), 422–437. <https://doi.org/10.1002/hec.1481>
- Sidak, D., Prasoon, K., Sivaraman, A., K, G. P., & Monica, C. (2018). Foot biomechanics and relation to the gait cycle. *Journal of Foot and Ankle Surgery (Asia Pacific)*, 5(2), 68–72. <https://doi.org/10.5005/jp-journals-10040-1093>
- Sigrist, R. M. S., Liau, J., Kaffas, A. E., Chammas, M. C., & Willmann, J. K. (2017). Ultrasound elastography: Review of techniques and clinical applications. *Theranostics*, 7(5), 1303–1329. <https://doi.org/10.7150/thno.18650>
- Sissler, L., & Giandolini, M. (2019). Finite element modelling of tibial vibrations during running. *Footwear Science*, 11(1), S75–S77. <https://doi.org/10.1080/19424280.2019.1606086>
- Stenti, Andrea, Morales-Orcajo, E., Giuliani, F., & Desmet, R. (2020). *Foot & Ankle orthopaedics: Towards In Silico Clinical Trials in Prosthesis Wear Estimation*. VPH 2020 <https://vph2020.sciencesconf.org/>.
- Stenti, A., Morales-Orcajo, E., Leemrijse, T., Deleu, P.-A., & Ferré, B. (2020). Foot & ankle orthopaedics: Towards the use of in silico clinical trials in prosthesis placement criteria. *NAFEMS France*, 20.
- Sun, X., Lam, W. K., Zhang, X., Wang, J., & Fu, W. (2020). Systematic review of the role of footwear constructions in running biomechanics: Implications for running-related injury and performance. *Journal of Sports Science and Medicine*, 19(1), 20–37. [www.jssm.org/hfpdf.php?volume=19&issue=1&page=20](http://www.jssm.org/hfpdf.php?volume=19&issue=1&page=20).
- Trinler, U., Hollands, K., Jones, R., & Baker, R. (2018). A systematic review of approaches to modelling lower limb muscle forces during gait: Applicability to clinical gait analyses. *Gait and Posture*, 61, 353–361. <https://doi.org/10.1016/j.gaitpost.2018.02.005>
- Trinler, U., Schwameder, H., Baker, R., & Alexander, N. (2019). Muscle force estimation in clinical gait analysis using AnyBody and OpenSim. *Journal of Biomechanics*, 86, 55–63. <https://doi.org/10.1016/j.jbiomech.2019.01.045>
- V&V40. (2018). *Assessing credibility of computational modeling through verification and validation: Application to medical devices*, 2018.
- Viceconti, M., Pappalardo, F., Rodriguez, B., Horner, M., Bischoff, J., & Musuamba Tshinanu, F. (2021). In silico trials: Verification, validation and uncertainty quantification of predictive models used in the regulatory evaluation of biomedical products. *Methods*, 185, 120–127. <https://doi.org/10.1016/j.ymeth.2020.01.011>
- Victor, J., Ghijssels, S., Tajdar, F., Van Damme, G., Deprez, P., Arnout, N., & Van Der Straeten, C. (2014). Total knee arthroplasty at 15–17 years: Does implant design affect outcome? *International Orthopaedics*, 38(2), 235–241. <https://doi.org/10.1007/s00264-013-2231-8>
- Walsh, T. P., Merlo, G. B., Rutter, C., Abell, B., Platt, S. R., & Arnold, J. B. (2022). Cost-effectiveness of interventions for musculoskeletal foot and ankle conditions: a systematic review. *Arthritis Care and Research*, 74(4), 626–637. <https://doi.org/10.1002/acr.24514>

- Wang, D., Wang, W., Guo, Q., Shi, G., Zhu, G., Wang, X., & Liu, A. (2020). Design and validation of a foot–ankle dynamic simulator with a 6-degree-of-freedom parallel mechanism. *Proceedings of the Institution of Mechanical Engineers, H: Journal of Engineering in Medicine*, 234(10), 1070–1082. <https://doi.org/10.1177/0954411920938902>
- Wang, Y., Wong, D. W.c., Tan, Q., Li, Z., & Zhang, M. (2019). Total ankle arthroplasty and ankle arthrodesis affect the biomechanics of the inner foot differently. *Scientific Reports*, 9(1). <https://doi.org/10.1038/s41598-019-50091-6>
- Wong, D. W. C., Wang, Y., Chen, T. L. W., Yan, F., Peng, Y., Tan, Q., Ni, M., Leung, A. K. L., & Zhang, M. (2020). Finite element analysis of generalized ligament laxity on the deterioration of hallux valgus deformity (aunion). *Frontiers in Bioengineering and Biotechnology*, 8. <https://doi.org/10.3389/fbioe.2020.571192>
- Yu, J., Cheung, J. T. M., Wong, D. W. C., Cong, Y., & Zhang, M. (2013). Biomechanical simulation of high-heeled shoe donning and walking. *Journal of Biomechanics*, 46(12), 2067–2074. <https://doi.org/10.1016/j.jbiomech.2013.05.009>
- Zhang, Y., Chen, Z., Zhao, H., Liang, X., Sun, C., & Jin, Z. (2020). Musculoskeletal modeling of total ankle arthroplasty using force-dependent kinematics for predicting in vivo joint mechanics. *Proceedings of the Institution of Mechanical Engineers, Part H: Journal of Engineering in Medicine*, 234(2), 210–222. <https://doi.org/10.1177/0954411919890724>
- Zhang, H., Lv, M. L., Yang, J., Niu, W., Cheung, J. C. W., Sun, W., Wong, D. W. C., & Ni, M. (2020). Computational modelling of foot orthosis for midfoot arthritis: A aaguchi approach for design optimization. *Acta of Bioengineering and Biomechanics*, 22(4), 1–17. <https://doi.org/10.37190/ABB-01694-2020-03>
- Zhang, M., Yu, J., Cong, Y., Wang, Y., & Cheung, J. T. M. (2014). Foot model for investigating foot biomechanics and footwear design. In *Computational biomechanics of the musculoskeletal system* (pp. 3–18). CRC Press. <https://doi.org/10.1201/b17439>
- Zhao, H., Yang, Y., Yu, G., & Zhou, J. (2011). A systematic review of outcome and failure rate of uncemented Scandinavian total ankle replacement. *International Orthopaedics*, 35(12), 1751–1758. <https://doi.org/10.1007/s00264-011-1339-y>

This page intentionally left blank

# Flow processes occurring within the body but still external to the body's epithelial layer (gastrointestinal and respiratory tracts)

# 17

**Paul W. Cleary, Simon M. Harrison, Matthew D. Sinnott**

*CSIRO Data 61, Clayton South, VIC, Australia*

## Chapter outline

<b>Introduction.....</b>	362
<b>Computational methods.....</b>	363
SPH for fluids and foods .....	363
DEM for motion and collisions of particles.....	365
Collisions and rigid body dynamics in SPH .....	366
DEM-SPH coupling for slurry simulation.....	367
Flexible and deformable surfaces.....	367
Specialized intestinal models .....	368
<i>Genome-scale metabolic models.....</i>	368
<i>0D model of microbial fermentation.....</i>	369
<i>Reduced 1D models.....</i>	370
<i>A potentially powerful multiscale approach: hierarchical 3D-1D-0D model.....</i>	370
<b>Ingestion and oral digestion .....</b>	371
Background .....	371
Example simulation scenario: melting of chocolate on the tongue .....	373
<b>Stomach .....</b>	381
<b>Small intestine .....</b>	387
Solute/nutrient diffusion and absorption .....	388
Spatially varying multiphase digesta rheology.....	390
<b>Large intestine.....</b>	392
<b>Liquid transport and droplet formation in the respiratory tract.....</b>	399
<b>Conclusions.....</b>	416
<b>Acknowledgments .....</b>	418
<b>References .....</b>	418

## Introduction

This chapter focuses on processes that occur within the enclosed volume of the human body but not within its cellular structure. That is, within the overall volume enclosed by the body but outside the epithelial layers that surround the body's cells. There are two principal systems to which this applies, specifically the gastrointestinal (GI) tract and the respiratory tract.

Human health is strongly linked to nutrition, nutritional uptake, and the generation of beneficial chemicals by the gut microbiome. Many health problems relate to dysfunction in different parts of the human GI tract, starting with oral and dental problems through to irritable bowel and constipation in the large intestine. Digestion (physical, chemical, and enzymic breakdown of ingested foods), nutrient absorption, and microbiological processing are critical but poorly understood drivers for health and well-being. Data are very difficult to obtain for these internal processes both because of instrumentation limitations and ethical considerations. Modeling can provide critical insight into these digestion processes. Such modeling needs to be able to include a wide range of material types (liquids, soft solids, brittle solids, and multiphase combinations of these) and many physical processes (fluid flow, solid deformation, fracture of and into particles, dissolution, both chemical and enzymic). Material changes from complex structured and larger scale in the mouth to intermediate size fragments in a low pH slurry in the stomach to fine grained slurry in the small intestine to bacterial loaded slurry in the large intestine. In all stages of the GI tract, large-scale deformation of the enclosing surfaces (teeth, tongue, and cheeks in the mouth) to large-scale deformation create combinations of haustral pouches and propagating waves of muscular compression and relaxation in the large intestines. In the respiratory tract, issues can relate to transport into, blockage of, and/or absorption by the lungs such as dysphagic ingestions of solids and liquids, to drug delivery. They can also relate to transport from the lungs and bronchi of mucus and fluids which can relate strongly to respiratory disease emission via virus/bacteria laden droplets and aerosols.

Smoothed Particle Hydrodynamics (SPH) coupled to rigid body dynamics (Discrete Element Method) and biomechanics models have proven to be a powerful tool for modeling all stages of the digestion process. This will be demonstrated here in a series of advanced case studies

1. Eating—melting of chocolate in the mouth and transport of the resulting liquid around the tongue.
2. Multiphase flow in the stomach.
3. Mixing, absorption, and transport of fine multiphase slurry in the small intestine.
4. Transport and microbiological digestion (fermentation) that occur on longer timescales in the large intestine. This will also present multiscale ideas that allow the microbiome (with its very long intrinsic timescales) to be coupled to transport processes.

These methods are also suitable for modeling of challenging problems in the respiratory system. Here an example of viscous liquid transport and droplet formation along and away from the walls of a section of airway due to rapid transit of air will be demonstrated.

## Computational methods

A comprehensive discussion of these computational methods and the modeling assumptions that lead to them is given in [Sinnott et al. \(2021\)](#).

### SPH for fluids and foods

SPH (Smoothed Particle Hydrodynamics) is a Lagrangian mesh-free method that can automatically predict complex free surface behavior including fragmentation and splashing. It uses virtual particles to represent specific volumes of material. This gives specific advantages in tracking history dependence such as for material type, stress and strain history, species concentrations, and solidification state. The classical SPH method was introduced for incompressible fluid flow by [Monaghan \(1994\)](#). General reviews of SPH, method components, and some applications are given in [Monaghan \(2005, 2012\)](#) and [Cleary et al. \(2007, 2021\)](#).

The SPH continuity equation, from [Monaghan \(1992\)](#), is

$$\frac{d\rho_a}{dt} = \sum_b m_b (\mathbf{v}_a - \mathbf{v}_b) \cdot \nabla W_{ab} \quad (17.1)$$

with  $\mathbf{r}_{ab} = \mathbf{r}_a - \mathbf{r}_b$  being the position vector from particle  $b$  to particle  $a$ , and  $W_{ab} = W(\mathbf{r}_{ab}, h)$  being the interpolation kernel with smoothing length  $h$  evaluated for the relative particle separation  $|\mathbf{r}_{ab}|$ .

The momentum equation gives the acceleration of each SPH particle:

$$\frac{d\mathbf{v}_a}{dt} = - \sum_b m_b \left[ \left( \frac{P_b}{\rho_b^2} + \frac{P_a}{\rho_a^2} \right) - \frac{\xi}{\rho_a \rho_b} \frac{4\mu_a \mu_b}{(\mu_a + \mu_b)} \frac{\mathbf{v}_{ab} \cdot \mathbf{r}_{ab}}{\mathbf{r}_{ab}^2 + \eta^2} \right] \nabla_a W_{ab} + \mathbf{g} \quad (17.2)$$

where  $P_a$  and  $\mu_a$  are pressure and viscosity of particle  $a$ , and  $V_{ab} = V_a - V_b$ .  $\eta$  is a small parameter used to smooth out the singularity at  $\mathbf{r}_{ab} = 0$  and  $\mathbf{g}$  is gravity. This form is valid for single phase flows, for multiple material flows and ones where any density variation is small, continuous, and differentiable.

In the classical SPH method a weakly compressible (WC) assumption is made so that the pressure is explicitly given from the density using an equation of state. The form from [Batchelor \(1973\)](#) is used:

$$P = P_0 \left[ \left( \frac{\rho}{\rho_0} \right)^\gamma - 1 \right] \quad (17.3)$$

where  $P_0$  is the magnitude of the reference pressure and  $\rho_0$  is the reference density. The pressure scale is set based on  $c$  which is the numerical speed of sound according to

$$\frac{\gamma P_0}{\rho_0} = 100V^2 = c^2 \quad (17.4)$$

where the prefactor 100 means that the maximum particle speed corresponds to Mach 0.1 based on this choice of numerical sound speed.  $V$  is a characteristic maximum physical velocity for the flow. This means that density variations are at most 1% giving weakly compressible fluid flow behavior. For fluids such water or aqueous solutions,  $\gamma = 7$  is used.

The boundary surfaces of the human body with which the SPH discretized materials interact are represented by typically a single layer of boundary particles. Each exerts both a normal repulsive force and a shear viscous force on any nearby fluid particles. This approach is explained in detail in Cummins et al. (2012) and Cleary et al. (2021). This is a powerful and very flexible boundary treatment that allows extremely complex solid boundaries, both stationary and moving, to be modeled (Cleary et al., 2007). It also allows deforming boundaries to be modeled (Cohen et al., 2012; Sinnott et al., 2012). Geometry preparation (mesh clean-up and the construction of surface normals) is performed using preprocessing workflows built on Workspace (which is a workflow platform for building and configuring re-useable software (see Workspace (n.d.) and Cleary et al. (2020) for details).

The equations of motion for the particles (3) and (4) and any secondary physics or chemistry equations are integrated using an explicit second order predictor-corrector (see Monaghan, 1994 and Cummins et al., 2012 for details). The limit for stable explicit integration is given by the Courant condition modified for viscosity (see Monaghan, 1994).

The SPH heat equation is based on the internal energy equation developed in Cleary and Monaghan (1999), but modified to use an enthalpy formulation for solidifying metals (Cleary, 1998):

$$\frac{dH_a}{dt} = \sum_b \frac{4m_b}{\rho_a \rho_b} \frac{k_a k_b}{k_a + k_b} T_{ab} \frac{\mathbf{r}_{ab} \cdot \nabla_a W_{ab}}{\mathbf{r}_{ab}^2 + \eta^2} \quad (17.5)$$

where the summation is the heat conduction term. The enthalpy per unit mass is defined by

$$H = \int_0^T c_p(\theta) d\theta + L[1 - f_s(T)] \quad (17.6)$$

where  $\theta$  is a temperature variable,  $c_p$  is the temperature-dependent specific heat,  $L$  is the latent heat, and  $f_s(T)$  is the volume fraction of material that is solid at temperature  $T$ ,  $k_b$  is the conductivity, and  $T_{ab} = T_a - T_b$ .

Eq. (17.5) has an explicit conductivity which can be temperature dependent and ensures that heat flux is automatically continuous across material interfaces

(including discontinuous distributions). This allows heat conduction with and between multiple materials with substantially different conductivities and specific heats to be accurately simulated.

Following Cleary (2010), who introduced an approach for predicting phase changes in SPH, when a fluid particle has its temperature increase above the solidus temperature of the material, then the particle ceases to be part of the rigid body and its governing equation is changed to be the Navier–Stokes equations. The particle changes from a frozen state into a mobile state and is able to move in accordance with the fluid dynamic forces it experiences. The forms of the viscosity and enthalpy variations are chosen to be the same as those used in Cleary et al. (2010) but with magnitudes scaled by the measured liquid phase values.

Species diffusion is modeled in a similar way using Fick's diffusion law which in SPH discretized form gives the change in concentration of a species  $C^i$  for an SPH particle  $a$  as

$$\frac{dC_a^i}{dt} = \xi \sum_b \frac{m_b}{\rho_b} \frac{4\mathcal{D}_a \mathcal{D}_b}{\mathcal{D}_a + \mathcal{D}_b} (C_a^i - C_b^i) \frac{\mathbf{r}_{ab} \cdot \nabla_a W_{ab}}{\mathbf{r}_{ab}^2 + \eta^2} \quad (17.7)$$

where  $\mathcal{D}_q$  is the diffusivity of particle  $a$  for species  $i$ . Creation and destruction rate terms can be added as needed and different species can be coupled together if required.

## DEM for motion and collisions of particles

DEM (Discrete Element Method) was introduced by Cundall and Strack (1979) and is now a well-accepted numerical method for simulating the flow of granular materials. It tracks individual particles and predicts their collisional interactions.

A contact force law is used to relate the contact forces to the instantaneous positions, orientations, velocities, and spins of the particles colliding. A linear spring-dashpot is used since it is simplest and most robust contact model and is able to well reproduce oblique collisions with surfaces (Thornton et al., 2013). Defining the amount of overlap as  $\Delta x$ , and the normal  $v_n$  and tangential  $v_t$  relative velocities, the normal force is

$$F_n = -k_n \Delta x + C_n v_n \quad (17.8)$$

The linear spring provides a repulsive force while the dashpot dissipates a material-dependent relative fraction of the kinetic energy.  $F_n$  is restricted to be positive to prevent unphysical attractive forces at the end of collisions. The normal damping coefficient  $C_n$  is calculated from the coefficient of restitution. The maximum overlap between particles is determined by the stiffness  $k_n$  of the spring in the normal direction.

The tangential force is given by

$$F_t = \min \left\{ \kappa F_n, \sum k_t v_t \Delta t + C_t v_t \right\} \quad (17.9)$$

where the vector force  $\mathbf{F}_t$  and velocity  $\mathbf{v}_t$  are defined in the plane tangent to the surface at the contact point and  $\Delta t$  is the timestep. The summation is an incremental spring that represents the elastic tangential deformation of the contacting surfaces, while the dashpot with coefficient  $C_t$  dissipates energy from the tangential motion and represents the inelastic parts of the tangential deformation. The Coulomb frictional limit  $\kappa F_n$  limits the tangential force  $\mathbf{F}_t$ , due to sliding at the contact. Here  $\kappa$  is the dynamic friction coefficient for the pair of materials interacting. We also set  $k_t = 0.5k_n$ .

The DEM particles are nonspherical in shape and are represented as superquadric (SQ) level set surfaces, which are defined in a canonical Cartesian frame by

$$\left(\frac{x}{a}\right)^m + \left(\frac{y}{b}\right)^m + \left(\frac{z}{c}\right)^m = 1 \quad (17.10)$$

This shape approach is described and used in Cleary (2004, 2009). Here the power  $m$  is the blockiness which controls how sharp the corners and edges of the particle are. The semimajor axes, in the principal directions are  $a$ ,  $b$ , and  $c$ , respectively. The particle aspect ratios are  $A_{xy} = b/a$  and  $A_{xz} = c/a$ . This description of nonspherical particle shape is flexible and continuous and allows a broad range of particle shapes to be.

## Collisions and rigid body dynamics in SPH

SPH has predominantly been used to model fluids and deforming materials. Often these are in contact with solid boundaries which provide the boundary conditions for these flows. But sometimes these bodies can be dynamic and need to move in response to the dynamic forces applied by the other parts of the system, particularly, in response to collisions. In such cases we use contact mechanics (Eqs. 17.8 and 17.9), as described above for the DEM method but applied to these geometrically complex bodies that are discretized (here by the SPH method). This is then a hybrid DEM-SPH representation with the

1. contact detection and computational geometry performed using SPH search and distance calculations methods (as opposed to using an idealized shape representation as in equation 17.10),
2. contact forces resolved using a DEM like contact model (Eqs. 17.8 and 17.9) but calculated for pairwise interactions between discretized nodes on each body, and
3. then solving for the rigid body motion of the body (as occurs in DEM) based on the net force and torque applied to the body by its environment (noting that some of these forces can be DEM contact forces and some can be fluid dynamic forces).

Examples of such hybrid methods are given in Cummins and Cleary (2011) and Vyas et al. (2021, 2022) and used for simulating the powder in applications such as 3D printing when laser melting of the grains occurs (Cummins et al., 2021).

## DEM-SPH coupling for slurry simulation

The phase coupling between the DEM and SPH components of a slurry flow is performed using a continuum representation of the DEM particles. This is produced by local averaging of the instantaneous DEM particle configuration to give continuous solid fraction and velocity fields. Details are given in Cleary et al. (2006), Cleary (2015), and Cleary et al. (2017). These are used in a multiphase formulation of the SPH equations.

The coupling force on the SPH particles from the continuum representation of the granular particles is given by the Darcy drag law:

$$F_{darcy} = \varepsilon_{DEM}^2 \mu_a \frac{(v_a - v_{DEM})}{\rho_a K_{DEM}} = \vartheta_a u_a \quad \text{for } a = 1, \dots, N \quad (17.11)$$

where  $\varepsilon_{DEM}$  is the porosity (void fraction) of the continuum granular material at the location of SPH particle  $a$ . Here  $v_{DEM}$  is the local average solid phase velocity at that point (as also obtained by averaging the DEM particles), and  $\mathbf{u}_a = \mathbf{v}_a - \mathbf{v}_{DEM}$  is the superficial fluid velocity of SPH fluid particle  $a$  relative to the DEM solid phase. Following Cleary et al. (2006), the permeability of the continuum granular phase at each point can be estimated using the Kozeny–Carman equation:

$$K_{DEM} = \frac{\varepsilon^3}{L Z (1 - \varepsilon)^2 B^2} \quad (17.12)$$

where  $K_{DEM}$  is the permeability of the granular medium,  $(1-\varepsilon)$  is the solid fraction of the charge,  $L$  is the shape factor (typically 2–3),  $Z$  is the tortuosity of the fluid pathways through the charge, and  $B$  is the ratio of surface area to particle volume (from the DEM particles).

The SPH momentum equation is modified by inclusion of porosity for the DEM medium from which the Darcy drag force (18) is subtracted. The total acceleration on an SPH particle in the multiphase formulation (as given in Cleary et al., 2021) is

$$\frac{d\mathbf{v}_a}{dt} = -\varepsilon_a \sum_b m_b \left[ \left( \frac{P_b}{\rho_b^2} + \frac{P_a}{\rho_a^2} \right) - \frac{\xi}{\rho_a \rho_b} \frac{4\mu_a \mu_b}{(\mu_a + \mu_b)} \frac{\mathbf{v}_{ab} \cdot \mathbf{r}_{ab}}{\mathbf{r}_{ab}^2 + \eta^2} \right] \nabla_a W_{ab} - \vartheta_a \mathbf{u}_a + \mathbf{g} \quad (17.13)$$

For a full summary of the DEM and SPH methods as used here, and their coupling see Cleary et al. (2017).

## Flexible and deformable surfaces

For internal flows within the GI and respiratory tract, the body surfaces with which the fluids and solids interact are predominantly deformable. They change shape either

1. in response to skeletal movements or muscular contractions or
2. respond compliantly to applied loads reaching a dynamic equilibrium that controls the time-varying structure.

The first class of body surface deformation is included in the model as kinematically controlled or preprogrammed surface movements, while the second class is modeled by explicit inclusion of dynamic visco-elastic forces between boundary particles.

Kinematic motions are constructed using animation software such as Maya (Autodesk, USA). Surface mesh models of anatomical structures are rigged to virtual skeletons that represent skeletal or muscular constraints. Movements are prescribed by changes to joint angles of the virtual skeletons. Linear blend skin rigging ([Kavan, Collins, Žára, & O'Sullivan, 2008](#)) is used to calculate the displacement of individual nodes of the surface mesh models from the movements of the virtual skeletons. Sequences of joint angles are produced to replicate the desired surface deformations for each of the anatomical structures during physiological processes.

Dynamically deforming body surfaces are discretized to form regular arrays of SPH boundary particles one or more layers deep. Each pair of adjacent nodes is connected by a linear spring that allows for elastic deformation of the lumen and a dashpot that generates viscous damping. This network permits the boundary to flex in response to internal forces such as intraluminal pressures and contractions generated by passing peristaltic waves. Muscular forces that cause contraction and relaxation of the body surfaces (such as in the intestine) are generated by shortening or lengthening the natural lengths of elastic elements in an affected region which mimics the real nature of muscular activity. This is a powerful and effective model for an active boundary arising from the tightening or relaxing of muscle in the GI and respiratory surfaces. Gut wall motor patterns are then represented as traveling muscular waves (such as intestinal peristaltic waves). These are generated in the wall using a traveling cosine function so that the maximum contraction and expansion occur at the center of each affected region and decreases to zero at the edges. The magnitude of the contraction/expansion varies in time with the wave development described by a sine function over time with the period being the period of the waves.

## Specialized intestinal models

Simulating the entire digestive tract from mouth to anus or even multiple compartment subsystems within that length pose significant challenges in terms of the size of the computational domain and the residence time for food to be fully processed. The physical timescale for enzymatic digestion and microbial fermentation in the lower gut can be up to tens of hours, whereas 3D transient fluid dynamics of digesta motility and mixing have timescales of order seconds to minutes. This makes high fidelity 3D modeling computationally impractical for studying the long-term evolution of food breakdown along the intestines.

### ***Genome-scale metabolic models***

A huge challenge for modeling is coupling statistical models from genomics data to deterministic modeling of host/environment/microbiome interactions. Genome-

scale metabolic models (GSMMs) have been developed over the last 20 years and are an increasingly common tool to study system microbiomes (Lamichhane et al., 2018). Networks of all possible metabolic pathways are reconstructed for a given bacterial species using metabolomic sequencing of fecal samples. GSMMs can range in complexity from simple (flux balance) to dynamic/complex (agent-based models). Iterative solution of the matrix of all possible metabolic reactions in the system of interest is computationally expensive and restricts their application to very small domains and small numbers of species. Therefore, GSMMs alone are not well suited to studying large-scale host and environment dynamics. There is plenty of scope to develop more realistic models of the intestinal microbial environment that incorporate statistical genomic data into deterministic models of digesta flow. Such models may generate valuable insights as to how diet and spatiotemporal variation in microbial population structure influence microbiome metabolic function, colonization/decolonization, ecosystem stability/dysbiosis, inflammatory conditions, gut health, and the final stages of digestion. Taking advantage of the spatial localization implicit in the SPH type of 3D computational model one can then use only those specific microbial and chemical species present in each spatial region of the system. This allows for solution of a reduced set of metabolic reactions in the volume represented by each SPH particle which gives a large coupled but soluble transient system in the form of coupled Partial Differential Equations (PDEs). One such reduced reaction set is introduced in the next section.

### ***0D model of microbial fermentation***

For static flow systems such as in vitro test tube microbial cultures, a 0D model is sufficient for studying bulk microbial growth and metabolism. Rosendale et al. (2017) developed a concise mathematical formulation for microbial fermentation chemistry of a plant polysaccharide (kiwifruit) into Short-Chain Fatty Acids (SCFAs). These metabolic reactions are represented as a coupled sequence of PDEs (Eqs. 17.14-17.19). Their study used in vitro culturing of fecal samples from a small cohort of volunteers and tracked microbial growth/decay and SCFA metabolites. Fermentation rate parameters were calculated by fitting patient data using an empirical Bayesian approach (Markov Chain Monte Carlo). Model complexity (and the multitude of metabolic network pathways) was greatly reduced by functionally grouping the huge range of gut microbial species into just seven categories. The experiments kept the cultured microbes in an excess carbohydrate environment (which is not consistent with typical lower intestinal conditions) and did not consider the more relevant case of how SCFA production (and colonic pH) alters when carbohydrate fuel is depleted.

The rates of SCFA production are given by

$$\frac{dF}{dt} = \alpha(\theta_{cf2}M_2 + \theta_{cf3}M_3 + \theta_{cf6}M_6 + \theta_{cf7}M_7 - \delta_{f3}M_3F) \quad (17.14)$$

$$\frac{dS}{dt} = \alpha(\theta_{cs1}M_1 + \theta_{cs2}M_2 - \theta_{sp1}M_1S) \quad (17.15)$$

$$\frac{dB}{dt} = \alpha(\theta_{cb7}M_7 + \theta_{ab7}M_7A) \quad (17.16)$$

$$\frac{dA}{dt} = \alpha \left( \sum_{N=1}^6 \theta_{caN}M_N + \theta_{la6}M_6L - \theta_{ab7}M_7A \right) \quad (17.17)$$

$$\frac{dL}{dt} = \alpha \left( \sum_{N=2, N \neq 5}^7 \theta_{clN}M_N - \theta_{la6}M_6L - \theta_{lp5}M_5L \right) \quad (17.18)$$

$$\frac{dP}{dt} = \alpha(\theta_{sp1}M_1S + \theta_{lp5}M_5L) \quad (17.19)$$

where SCFA concentrations are  $F$  (Formate),  $S$  (Succinate),  $B$  (Butyrate),  $A$  (Acetate),  $L$  (Lactate), and  $P$  (Propionate); specific fermentation rates per microbe group are given by the parameters  $\theta_{xyn}$  and  $\delta_{xn}$  where  $x$  = source (carbohydrate (c) fuel or SCFA being consumed);  $y$  = SCFA produced; and  $M_n$  for ( $n = 1-7$ ) are the microbial numbers per group.

### **Reduced 1D models**

One approach to reducing the computation size is to reduce the system dimensionality and solve for 1D advection–reaction equations (Moxon et al., 2016) or 2D cross-sectional flow (Ishikawa et al., 2011; Karthikeyan et al., 2021) using Finite Difference or Finite Element methods. The value of such models is then in the coupling of complex chemistry and/or large microbial metabolic pathways, and in studying digesta flow between compartments such as gastric-duodenum flow (Trusov et al., 2016). However, in performing this dimensional reduction there is significant loss of mechanistic information on reactions, transport, and mixing. The challenge is to reduce the computational cost to make the problem amenable while still including the key processes arising at these smaller length and time scales.

### ***A potentially powerful multiscale approach: hierarchical 3D-1D-0D model***

The inherent multiple scales of the digestive process may also be combined into a set of coupled hierarchical multiscale models where each model is used to represent the appropriate physics at the appropriate scale treated by that model. Our prototype multiscale intestinal model consists of

- 3D SPH model simulating detailed flow and mixing of digesta in small domains over relatively short time periods arising from critical prescribed motor patterns. This transient flow can, in principle, then be averaged to inform bulk axial mass transport rates that are representative of different wall contraction and system conditions;
- 1D Finite Difference model of longer duration, simplified axial flow extrapolated over the full length of intestinal section being studied (e.g., colon). Sequences of different motor patterns can then be scheduled in any order over the digestive timescale with the corresponding mass transport relationships applied using data from the detailed 3D models; and

- 0D model of carbohydrate fermentation reactions and microbial growth using models such those proposed by Rosendale (Eqs. 17.14-17.19). The PDEs for the SCFA production and conversion reactions are solved at each axial point along the 1D model based on prescribed axial distributions of microbial colonies. SCFA concentrations are tracked as these metabolites are advected by the 1D digesta transport.

This type of model is likely to be particularly useful for simulating microbial fermentation and predicting SCFA abundances and total acidity in the colon over hours of digestion due to different dietary, microbial ecosystem, and motility conditions.

---

## Ingestion and oral digestion

### Background

Food digestion begins in the mouth and many processes that are critical to good health occur during oral digestion. The primary functions of the oral phase of digestion are to

1. Reduce the size of ingested solid food so that it is suitable for delivery to the stomach and for gastric processing, i.e., from whole foods with scales from 0.1 to 30 cm (e.g., from crumb to plate sized) to food fragments of maximum swallowable size of 2 cm or smaller.
2. Reduce the hardness of solid food so that it can be safely and easily transported through the GI tract. This is achieved via the mechanical actions of chewing (crushing, cutting, etc.), saliva ingress, melting, or emulsification.
3. Lubricate dry food particles for ease of transport through the GI tract via mixing with saliva and ingested liquids or melted solids.
4. Introduce digestion chemicals and enzymes, such as amylase, into the bolus and mix these throughout its volume to increase the contact area between them and the food particles so as to facilitate component breakdown.
5. Support sensory perception of the food including facilitating assessment of food safety and enjoyment (which links to motivation for future consumption and food type selection and satiety). This sensory perception is a combination of visual appearance, odor, texture, taste, and aroma; it is strongly influenced by learnt experience; and varies between different population and age groups.
6. Transport the masticated food to the esophagus for transport to the stomach during the swallowing process.

Experimental measurement of these processes is difficult to perform, and it is even harder to create controlled perturbations of individual variables to determine their specific effects on system outcomes. As a result, there is much to still learn

about how people process and sense food differently in the mouth. Measurements have been performed for a nonexhaustive range of foods for

- Jaw movements (Hiiemae & Palmer, 2003; Palmer et al., 1997)
- Tongue movements (Hiiemae & Palmer, 2003; Palmer et al., 1997)
- Food particle size (Harrison, Eyres, et al., 2014; Hoebler et al., 2000; Jalabert-Malbos et al., 2007; van Der Glas 1987)
- Tastant diffusion rates (Fischer et al., 1994; Koliandris et al., 2008)
- Sensory experience (Amerine et al., 1965; Labbe et al., 2009)

To date the application of physical measurement alone has not quantitatively elucidated the details of neurological control, physical processes, or sensory experience to the degree that predictions can be made for a new food structure or a proposed reformulation of existing food products. Virtual experimentation using dynamic three-dimensional computational simulation provides benefits including better and independent control over individual input variables, the ability to record data at all spatial locations and at all-time instances, and potentially lower per-experiment costs. Such models must however comprise representations of all required phenomena and be proven to provide sufficiently accurate predictions.

Simulation of each of the six oral digestion processes simultaneously requires the coupling of a large range of mechanical and chemical submodels. The modeling framework must be able to handle large changes to the shape and connectivity of ingested matter as well as state (solid, liquid, or gas including mixtures such as pastes, slurries, and emulsions) and material behavior (viscous, elastic, plastic, or brittle). The movements of the simulated anatomical structures (jaw, teeth, gums, tongue, palates) must be realistic and suited to both the nature of the content, i.e., liquid versus solid or dry and hard versus wetted and soft, and the time spent chewing it. Interactions between food and anatomical structures need to be predicted with sufficient spatiotemporal accuracy. Rates of saliva generation and its chemical constituents need to adapt to the content properties and the proximity to the timing of intended swallowing (Neyraud et al., 2009).

*In silico* modeling of mastication has recently become effective at predicting the spatiotemporal breakdown of food, tastant release, and mixing of food fragments with saliva. Early work comprised system level, one-dimensional, representations of key phenomena (Hoebler et al., 2000; Lucas et al., 1983; van Der Bilt et al., 1992). 3D simulations have tended to focus on finite element (FE) simulations of one chewing cycle, but these typically are limited by the lack of simulated food fragmentation, in-mouth chemical and temperature effects, and differences in jaw and tongue movements between individuals and for different foods (Amemiya et al., 2002; Commissio et al., 2015; Dejak et al., 2003).

Food breakdown simulations have been demonstrated using fracture model components for multiple chewing cycles (Harrison & Cleary, 2014; Harrison et al., 2014a&b; Cleary & Harrison, 2019) using an SPH-based computational model coupled with biomechanical models (BSPH). Breakdown over one chewing cycle has also been considered using Finite Element Analysis (FEA) by Skamniotis

et al. (2019). Saliva ingress and resulting softening of hard foods, coupled fluid–solid dynamics, amylase-starch reactions and melting have recently been incorporated into predictive models to enhance applicability to research questions for improved food design and health (Cleary et al., 2015; Cleary and Harrison 2016, 2019; Harrison, Cleary, et al., 2014).

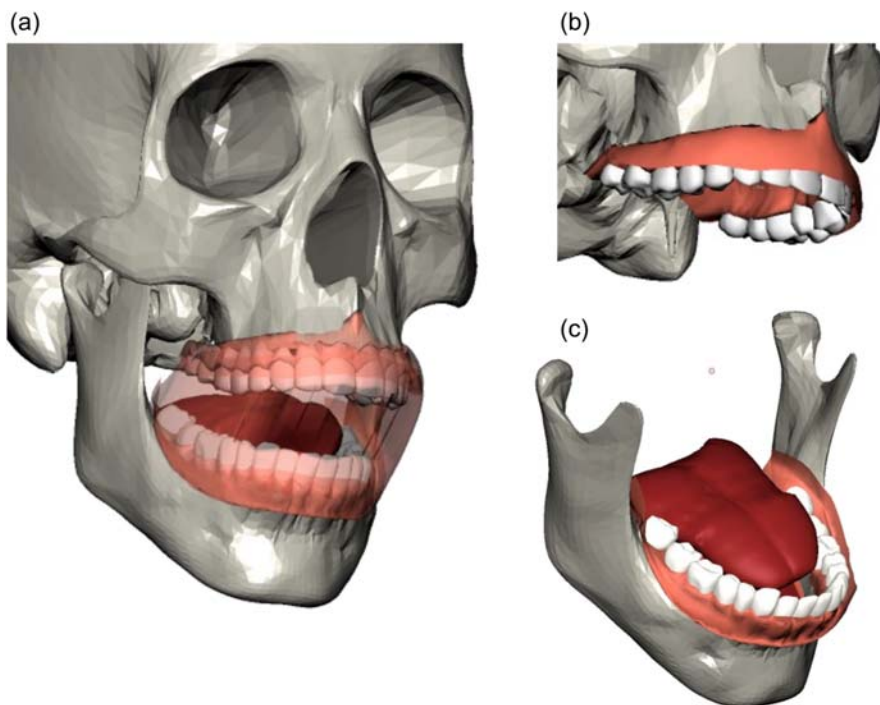
### Example simulation scenario: melting of chocolate on the tongue

Here we present an example simulation of BSPH oral digestive model extended to include heat transfer, phase change, and fluid–structure interaction of chocolate when it is placed on the tongue and allowed to melt. Many foods such as chocolate, ice, and yogurt are significantly affected by temperature when exposed to the 38°C oral environment. These temperature-induced outcomes affect the amount of mastication required to swallow, the release and transport of flavor compounds (both taste and aroma), the rheology of the bolus and potentially induce a sense of cooling in the mouth. This example shows how such models provide a path to understand the critical link between food structure and consumer perception of the eating experience as well as information on the nature of the bolus passed to the stomach.

The anatomical surfaces of the mouth are represented as moving and deformed surface meshes. Fig. 17.1 shows the configuration of the mesh models and shows a visualization of the prescribed anatomical movements. The mean node spacing of each of the meshes is 0.5 mm and the number of nodes in each mesh is listed in Table 17.1. The jaw and the lower gums and teeth are moved together as a rigid body and the movements are based on measurements of chewing of hard foods (Anderson et al., 2002; Palmer et al., 1997). The cheek mesh deforms as the jaw moves using the linear blend method (Kavan, Collins, Žára, & O’Sullivan, 2008). The tongue is also deformed using the linear blend method and its movements are based on published data (Palmer et al., 1997) but have been refined by trial and error to reposition large food fragments between the top and bottom rows of teeth prior to the preceding occlusion.

The chocolate food model is shown in Fig. 17.2. It is represented by 60,000 SPH particles that have an initial spacing of 0.3 mm. The material parameters used are listed in Table 17.2. The form of the temperature-dependent viscosity variation is the same as given in Cleary et al. (2010) but with the magnitude scaled to the free flow viscosity of liquid chocolate (Table 17.2).

The chocolate is initially at a temperature of 15°C while the anatomical structures (tongue, teeth, gums) are set at 38°C. The chocolate changes temperature by conduction of heat from the tongue on which it rests (and other anatomical structures if contact were to be made). The thermal boundary condition used for the tongue is isothermal since the blood flow within the tongue maintains its temperature at very close to its initial temperature. For colder foods such as ice cream, the temperature change within the surface layers of the tongue could not be reasonably neglected and the tongue would need to be discretized and included in the heat conduction solution.

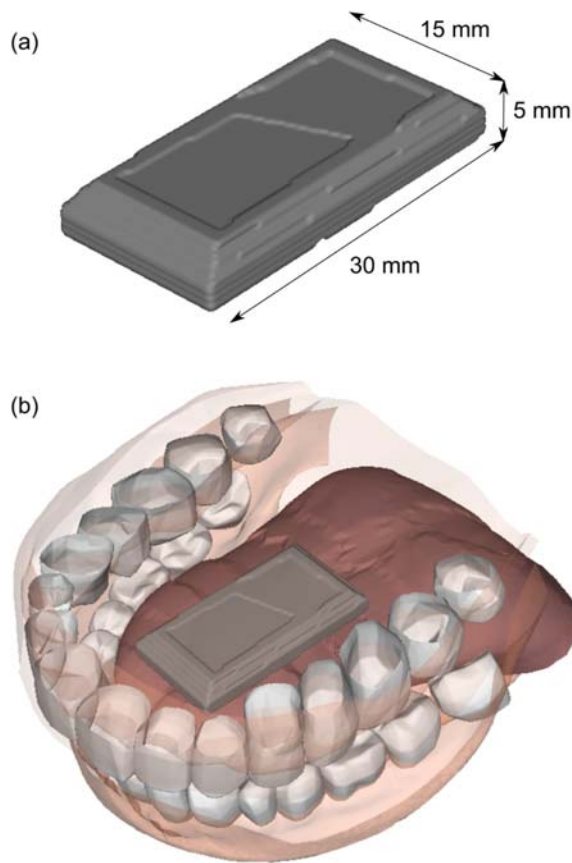
**FIGURE 17.1**

Virtual anatomical model of the mouth: (A) full model, (B) upper teeth and gums, and (C) lower teeth and gums and tongue.

**Table 17.1** Number of nodes in the surface meshes used to represent anatomical structures in the virtual mouth model.

Anatomical structure	Number of nodes
Upper teeth	55,515
Lower teeth	44,729
Tongue	43,760
Cheeks and gums	208,526

The solidus melting point (where it starts to become partially liquid) of this chocolate is 27°C while its liquidus temperature (where it is fully liquid) is 34°C, meaning that there is 4°C of superheat available for melting (meaning that the heat supply is 4°C above the liquidus melting point). Heat transfer is simulated by conduction between neighboring particles according to Eq. (17.5). Convection is naturally modeled by the flow of fluid particles (Cleary, 1998) but is negligible for the

**FIGURE 17.2**

(A) 3D model of the chocolate with external dimensions and (B) its position in the mouth model (skull and jaw omitted for clarity) at the start of the simulation.

temperature and spatial scales of the melted chocolate. Radiative heat is ignored as it is not insignificant at these temperatures.

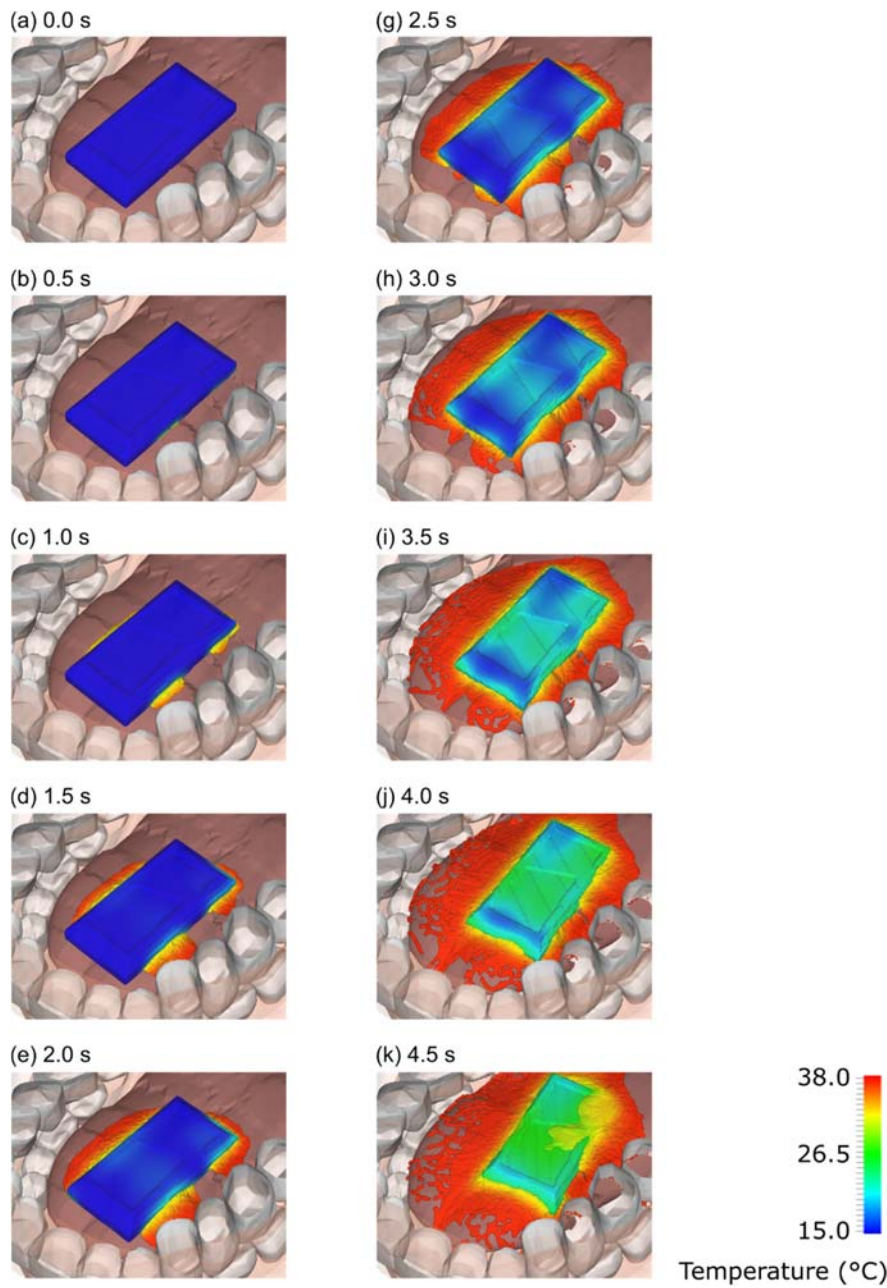
The flow of liquid chocolate and the coupled motion of the solid chocolate are simulated using the equations detailed in Section 2. Any contiguous particles representing the chocolate that are solid (below the solidus melting temperature) act as a rigid object. Collisional forces on this body are calculated using a linear spring dashpot contact model (as used in DEM) but calculated pairwise between SPH particles making up the body and those representing the anatomical surfaces. The spring stiffness used is 1.0 N/m and the coefficient of restitution is 0.2 (due to the strong compliance of the tongue). The motion of this body is calculated by solving Newton's equations and matching rotational ones based on the net external force and torque exerted on the body by the interactions between the chocolate and anatomical

**Table 17.2** Material model type and parameters used for the chocolate food model.

Type	Value [units]
Density	1000 [kg/m <sup>3</sup> ]
Conductivity	1.3 [W/m K]
Specific heat	1600 [J/kg K]
Latent heat	25,000 [J/kg]
Coefficient of thermal expansion	0.001
Viscosity (fully liquid phase)	0.05 Pa s

structures. Initially, the only interaction between the chocolate body and the tongue is collisional. But as the temperature of the surface SPH particles rises above the melting temperature they convert to fluid (as described in Section 2) and are no longer part of the solid body. The interaction between the chocolate and the tongue therefore rapidly transitions from solid–solid to solid–thin film liquid–solid. The stable resolution of the thin fluid film and the transition between two very different types of interaction physics can present challenges to computational models but for SPH the transition is very natural, and the solution is very stable and well behaved. This is an important advantage of using a particle method like SPH for this type of melting problem.

Fig. 17.3 shows a visualization of the chocolate melting simulation for a period of 4.5 s. The surface of the chocolate is colored by its local temperature. Initially the chocolate is entirely at 15°C (Fig. 17.3A). Between 0.0 and 1.0 s (Fig. 17.3A–C) three regions of the base of the chocolate that are in direct contact with the tongue warm up. The chocolate around these points starts to melt and to flow. The early heating of the base of the chocolate can be seen at 0.5 s (Fig. 17.3B). By 1.0 s (Fig. 17.3C) the bottom of the chocolate has started to melt around these contact points. A critical aspect of the physics of this application is that this thin layer of fluid then is weight bearing and has to support the weight of the chocolate above. This strongly compresses the fluid layer, generating high fluid pressure which forces the fluid to move laterally outward. The early forced flow of this liquid chocolate can be seen in Fig. 17.3C. The thickness of the liquid layer is then a dynamic balance between the rate of melting (which replenishes the liquid layer) and the rate of lateral ejection of the fluid (which is controlled by the liquid viscosity and the layer depth). The thickness of the fluid layer also controls the rate of heat conduction from tongue to the solid chocolate. These rapidly come into thermal-hydrodynamic equilibrium. If the fluid layer becomes too thick then the rate of melting decreases and the resistance to lateral flow decreases leading to a loss of liquid volume under the chocolate which reduces the fluid layer thickness. In contrast, if the liquid layer is too thin then the rate of melting increases while the lateral flow rate of liquid decreases allowing the layer thickness to build up.

**FIGURE 17.3**

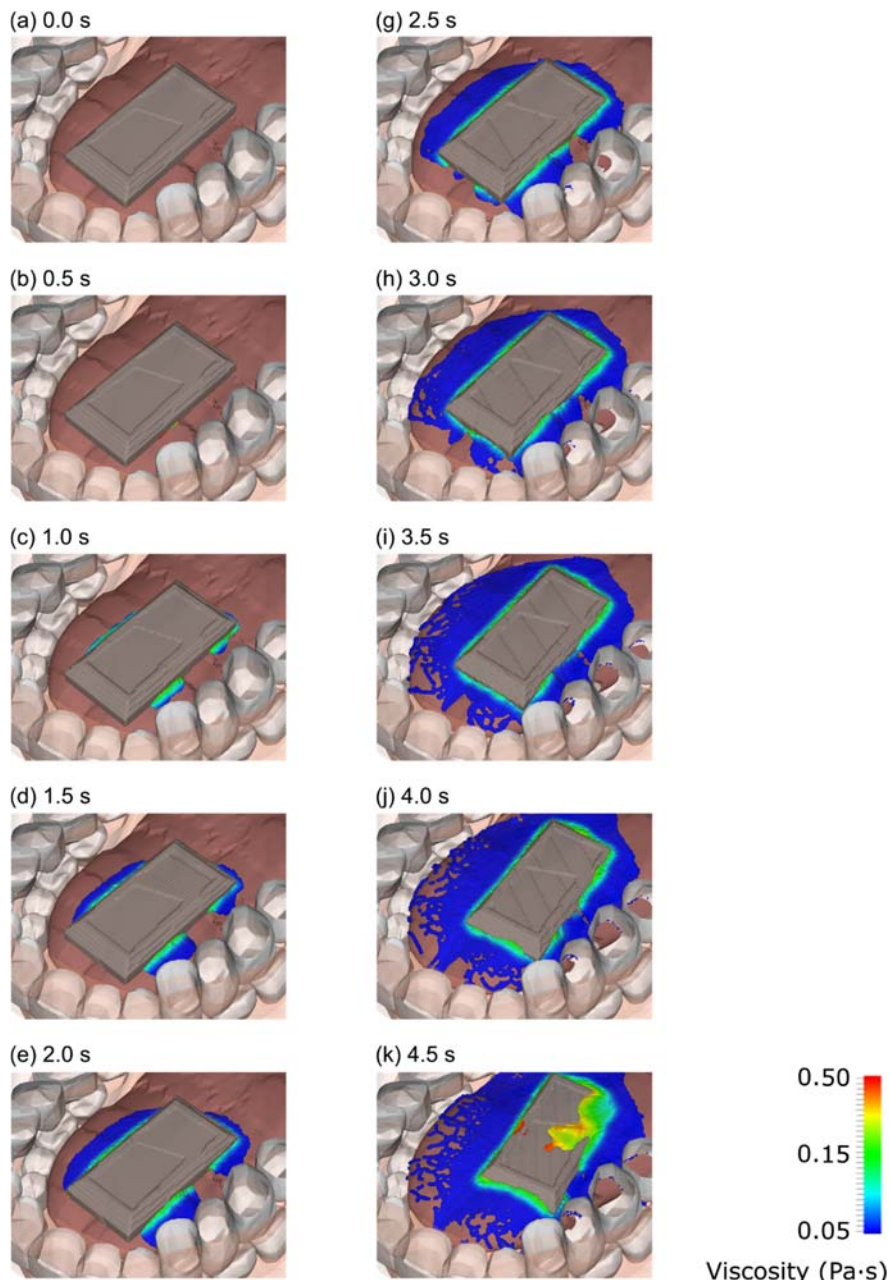
(A–K) Visualization of the SPH model of melting chocolate during 4.5 s of simulated time. The chocolate is colored by temperature per the color bar shown on the right.

The liquid warms from 15°C (blue) to 38°C (red) at the edges of the fluid phase. Regions of the chocolate that are not in direct contact slowly warm from 15°C (blue) to 21°C (cyan) as the heat is conducted through the solid material. The solid chocolate moves vertically downward as the melted material flows away from beneath. This lateral flow of liquid is well established by 1.5 s (Fig. 17.3D) with three fronts of flow established (one from each of the initial contact regions). As the chocolate melts its lower surface shape evolves so that it increasingly conforms to the current shape of the tongue. This means that the contact area increases leading to an increase in the heat transfer rate to the solid chocolate which accelerates the overall rate of melting. By 2.5 s (Fig. 17.3G) full contact between tongue and sculpted chocolate base has been established.

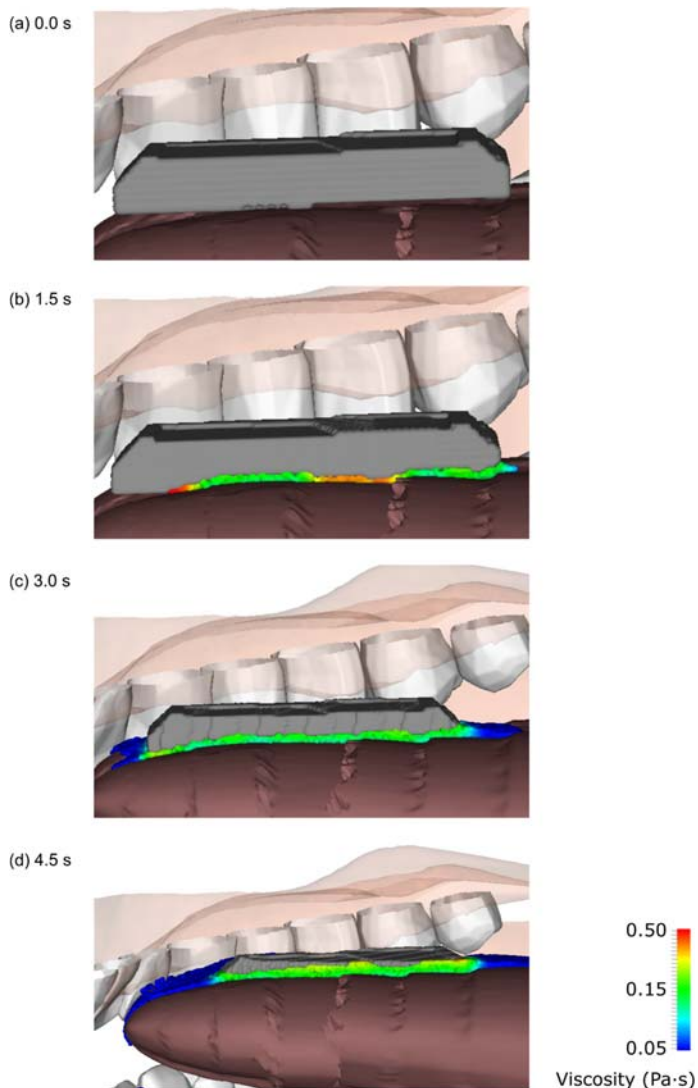
By 2.0 s (Fig. 17.3E) meaningful temperature variation can be seen on the top of the solid chocolate as the heat from below conducts upward. Between 2.5 and 4.0 s (Fig. 17.3G–J) the entire base of the chocolate is in contact with the tongue and the melting rate has reached a peak with fluid flowing strongly in three directions. Flow in the direction of the tip of the tongue is slower with such flow only being well established by 3.0 s. The majority of the top of the solid chocolate warms to 27°C during this period. At 3.0 s (Fig. 17.3) the fluid starts to flow off the tongue, accelerating under gravity due to the tongue curvature. By 4.0 s liquid chocolate is starting to pool against the lower jaw teeth and gums (which would usually trigger swallowing, but which is not included in the current simulation).

As the solid chocolate thins, its weight decreases. The decreasing inertia means that the solid is increasingly subject to the fluid dynamic forces. Since the tongue surface is uneven flow is not symmetric and so the solid chocolate starts to drift. This effect is small at first, but meaningful displacement can be seen by 4.0 s (Fig. 17.3J). The solid chocolate then moves more quickly toward the rear the mouth and rotates counterclockwise due to the dynamic flow of liquid chocolate between it and the tongue. By 4.5 s (Fig. 17.3K) the melting basal surface has reached the top of the solid chocolate meaning that it is now completely melted in the back right corner and along much of the front edge. Some breakthroughs of the melting can also be seen near the middle of the chocolate. By this stage the remainder of the solid is very thin and is now very mobile on the melted layer. The complexity of the melting pattern confirms the ability of the SPH method to predict challenging melting behavior with strongly coupled thermal and hydrodynamic effects.

Fig. 17.4 and Fig. 17.5 show the chocolate liquid colored by local viscosity from the top and side, respectively. Viscosity is displayed using a logarithmic color bar with blue correlating to 0.05 Pa s, green 0.15 Pa s, and red 0.5 Pa s. The solid chocolate is colored gray and the tongue is brown. Initially the chocolate is wholly below its solidus melting temperature (Fig. 17.4A) and only contacts the tongue in a few discrete regions (Fig. 17.5A) in its middle and rear. Between 0.0 and 1.5 s (Fig. 17.4A–D, Fig. 17.5A–B) the parts of the solid chocolate in contact with the tongue begin to melt. The viscosity is between 0.15 and 0.50 Pa•s close to the solid chocolate (partially melted and mushy), where the temperature is lowest (Fig. 17.3A–D), and decreases to 0.05 Pa s for the fully melted liquid that has

**FIGURE 17.4**

(A–K) Visualization of the SPH model of melting chocolate with the liquid phase colored by viscosity per the color bar shown on the right.

**FIGURE 17.5**

Side cross-section visualization of the melting chocolate simulation with the liquid phase colored by viscosity per the color bar shown on the right.

been warming for longer times and which has flowed beyond the immediate vicinity of the solid mass (Fig. 17.4D). Between 1.5 and 3.0 s a large amount of material melts and flows away from solid mass causing it to thin substantially (Fig. 17.4D–H, Fig. 17.5B–C). At 3.0 s enough of the chocolate has melted so that its entire base is thermally connected to the tongue surface via the thin layer of melted chocolate

(Fig. 17.5C). At 4.5 s (Fig. 17.4K, Fig. 17.5D) liquid has melted through the top of the solid mass (Fig. 17.3K), with higher local viscosity of 0.27 Pa s (yellow) to 0.37 Pa s (orange) visible indicating that these parts of the solid are now partially melted. Note that the melted layer of liquid chocolate is relatively constant in thickness over time (Fig. 17.5B–D) due to the balance between the fluid outflow and the weight of the solid chocolate remaining.

These results show that complex phenomena such as heat transfer and spatially varying material properties can be predicted in a transient simulation of oral digestion. This has included melt physics, a melting temperature range (between solidus and liquidus), and realistic temperature/enthalpy variation. Interesting melt-driven fluid mechanics are observed with liquid from basal melting forced tangentially outward by weight of remaining solid. Solid motion is then controlled by a combination of fluid mechanics and tongue deformation. The melting rate is not constant over time reflecting changes in contact area and in the depth of liquid under the remaining solid chocolate. The complexity of the melting pattern confirms the ability of the SPH method to predict challenging melting behavior with strongly coupled thermal and hydrodynamic effects.

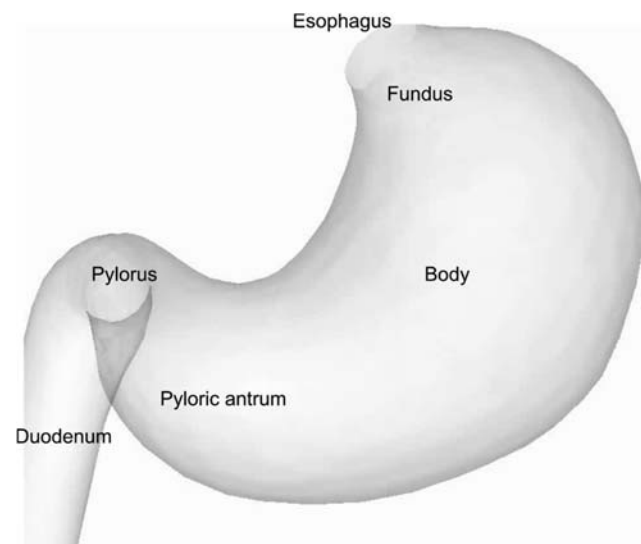
---

## Stomach

The stomach receives masticated food from the esophagus and is responsible for reducing the particle size and hardness of food fragments by mechanical and chemical breakdown. It is classified anatomically into four regions: the fundus, body, pyloric antrum, and pylorus (see Fig. 17.6). The fundus is the top of the stomach, the body is the middle, and the pyloric antrum is the lowest region. Food enters at the proximal sphincter, at the transition between the esophagus and fundus, and exits at the pylorus to the duodenum. Muscular contractions of the stomach wall occur in complex spatial and temporal patterns to control

- (1) the rate of emptying via relaxation of the pyloric sphincter, volumetric contraction of the whole stomach, and antral contraction waves (ACWs)
- (2) the rate of mixing of solid and liquid food and gastric juices
- (3) direct pressure imposed onto content from the gastric wall tissue to facilitate mechanical breakdown.

The pyloric sphincter can allow water-only content to pass through the stomach into the duodenum but if nutrients are sensed in the duodenum, then the pylorus is actively closed for large periods of time. This occurs so that the content can be broken down by mechanical forces and digested and diluted by gastric juices before being released into the duodenum. Experimental studies have shown that the stomach selectively passes smaller and softer solid food fragments while continuing to degrade and comminute larger and harder food fragments. As a result gastric emptying is fastest for liquid only content and slowest for solid only content (Camilleri et al., 1985). Liquid and solid mixtures (such as soup) empty at an intermediate

**FIGURE 17.6**

Anatomical classification of the stomach.

rate. This highly complex system is not yet well understood but virtual experimentation by numerical simulation can provide an important avenue for building this understanding.

Computational simulation has been used to investigate some aspects of gastric mixing and emptying but there remain many gaps in understanding of the physical and chemical processes that need to be represented in such models. Most studies consider fluid-only content (Ferrua and Singh 2010, 2011; Harrison et al., 2018; Imai et al., 2013; Miyagawa et al., 2016; Pal et al., 2004; Singh & Singh, 2011). Treatments of solid food fragments are typically based on continuum methods (Li et al., 2021; Xue et al., 2012) which have limited applicability due to the poorness of representing large discrete bodies as a continuum. Only one modeling study has considered the generation and mixing of gastric juices (Li et al., 2021). Additionally, most studies have used only a single set of kinematically prescribed wall deformations from Pal et al. (2004) (Ferrua and Singh 2010, 2011; Harrison et al., 2018; Singh & Singh, 2011) and do not consider the large range of contraction waves that are known to occur, such as large-scale tonic contraction, migratory motor complexes, and gastric dysrhythmia (Brandstaeter et al., 2019). No studies to date have fully considered the fluid–structure interaction that occurs during realistic muscle contractions.

Many challenges remain in simulating the entire gastric digestion process, including characterizations of

- gastric wall morphology and mechanical properties,
- the spatiotemporal variations in muscle contraction timing,

- gastric juice secretion rates,
- effect of constituent properties and proportions on rheology,
- the mechanical and chemical breakdown paths of foods for a large range of content types, and
- control mechanisms and strategies used by the body to regulate stomach content and the nature of the chyme passed onto the small intestine.

Mathematical representations of many of these processes have not yet been developed or shown to be effective at reproducing *in vivo* behavior.

Here we present a next stage in the modeling of gastric flow. It uses a coupled B-SPH-DEM method (as described in Section 2). A moderately dilute mixture of solid food fragments in liquid (20% solids by volume) is positioned in the pyloric antrum. The stomach anatomical model is the same as used in [Harrison et al. \(2018\)](#) and is constructed with the pylorus open. Liquid is Newtonian with density  $1000 \text{ kg/m}^3$  and viscosity  $0.01 \text{ Pa s}$  and is discretized into SPH particles with a resolution of 3 mm representing 340 mL. Solid food bodies are represented by super quadric DEM particles with a size range of 0.7–7 mm diameter, with moderately elongated and moderately blocky shapes (with aspect ratios of 1.0 and shape parameters  $m$  from 2.6 to 5.0). There are around 24,000 solid grains initially in the stomach content which have a density 10% higher than the fluid. The inner surfaces of the esophagus, stomach, and duodenum are represented by triangular surface meshes with a mean nodal spacing of 2.5 mm. The stomach in this case is passive (no ACW contractions) so we can focus on the nature of just the multiphase flow arising from the initial setup without ongoing perturbation. Model results are visualized from two viewing angles as shown in [Fig. 17.7](#).

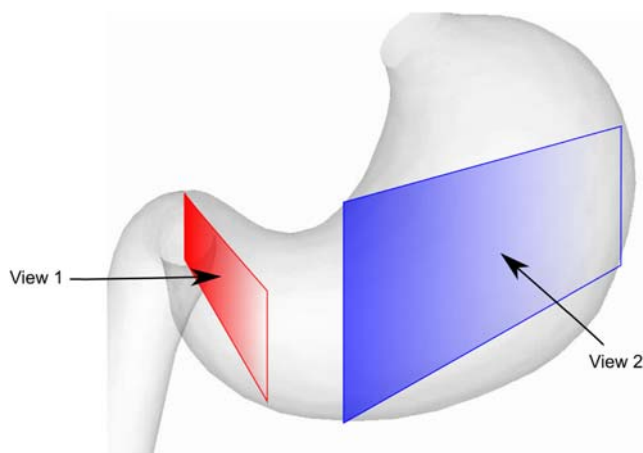


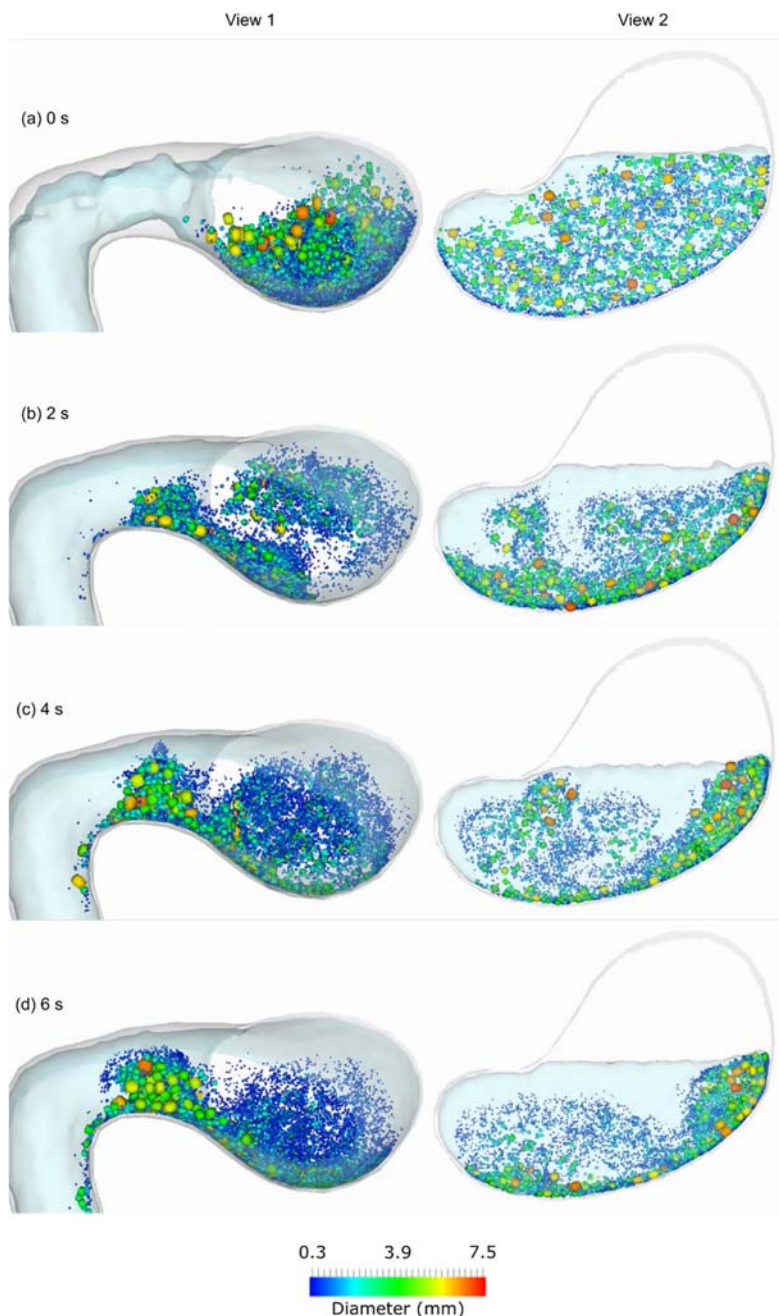
**FIGURE 17.7**

The two visualization view angles used to show results in Figures 8 and 9.

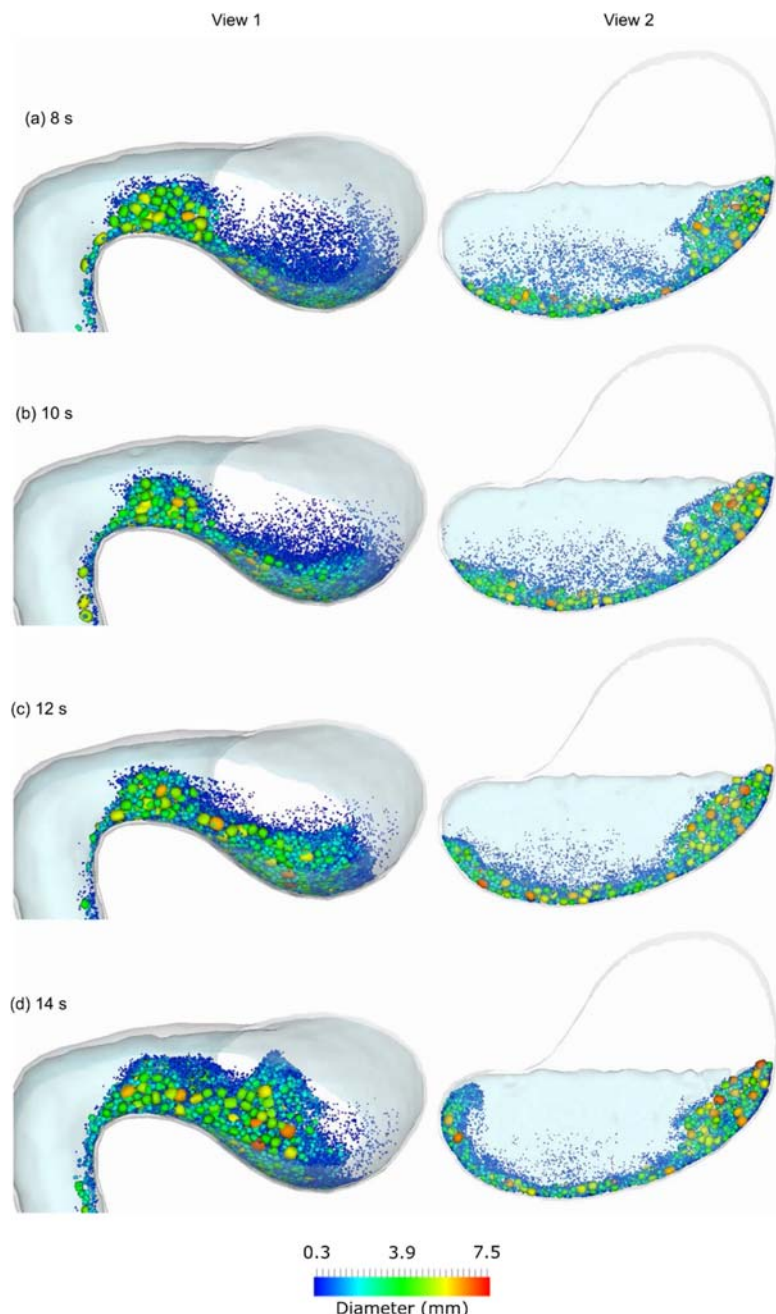
[Fig. 17.8](#) and [Fig. 17.9](#) show a visualization of fluid and particulate flow from these two viewing angles during 14 s of simulated gastric content motion without gastric wall movements. Particles are colored by size using the longest axis as a measure. Liquid is colored transparent blue. At 0 s ([Fig. 17.8A](#)) the particles are randomly positioned in the fluid and the pylorus (left side of the View 1 image) contains only fluid. After 2 s ([Fig. 17.8B](#)), fluid has flowed through to the duodenum and the fluid level (visible in View 2) has decreased. A reasonable fraction of the particles has settled downward under gravity. However, the coherent motion of these particles induces motion in the fluid which manifests as gravity currents. These currents entrain smaller particles and transport them both upwards and laterally. The resulting circulatory motions of a reasonable amount of the finer material is visible from 2 to 6 s ([Fig. 17.8B–D](#)). Since the fluid is mildly viscous and there is no ongoing energy input, these currents progressively dissipate between 4 and 14 s ([Figs 17.8C–D, and 17.9A–D](#)). The steady settling of these particles in the middle sections of the stomach forces fluid and particles to either side leading to a moderate strength wave of particles being forced up along the side walls of the stomach (to the left in View 1 and to the right in View 2). On the right, these particles lead to a recirculatory flow in the region immediately below the free surface. On the left, the dense jet of particles reaches the top of the stomach and is directed back to the right while part of this stream is pushed into the open pylorus with a moderate discharge stream observed leaving the stomach and passing into the duodenum (View 1 of [Figs 17.8B–D](#) and [17.9A–D](#)). It is also clear that there is significant particle size segregation with coarse particles settling quickly leading to dense coarse layers against the stomach wall which are then overlayed by thick layers of fine material. So any assumptions made in modeling about uniformly distributed content or content being well mixed are unjustified.

Despite this model only focusing on one aspect of the complex gastric environment the results are significantly dynamic. It shows that discrete particles and density variations can strongly affect gastric mixing substantially. In particular, it allows us to identify the mechanical drivers of particle flow, which are

- Movements of the food fragments result from a balance of buoyancy and drag on the particles which is controlled by the fluid flow, which is in turn controlled by the stomach wall contraction when present.
- Each of the forces operates on a different time scale controlled by different system parameters. These are summarized in [Table 17.3](#).  
The balance of controlling scales means that
  - In the absence of stomach wall excitation, the hindered settling period (a balance of buoyancy and drag) is of the order 0.5–50 s
  - Particle-rich parts of the fluid behave as a higher density fluid and so the distribution of the particles means that there are strong variations in mixture density which lead to gravity waves (1–2 s)
  - Wall contractions will drive fluid flow and gravity waves on a 5–10 s time scale
  - While the longest time scale is driven by the ACW, which is order 60 s

**FIGURE 17.8**

Visualization of fluid and particulate flow during 6 s of flow in a static stomach. Particles are colored by size per the color bar shown.

**FIGURE 17.9**

Visualization of fluid and particulate flow in a static stomach from 8 to 14 s of simulated time. Particles are colored by size per the color bar shown.

**Table 17.3** Mechanical drivers of multiphase flow in the stomach and their controlling factors and characteristic scales.

Driver	Controlling factor	Characteristic scales
Buoyancy	Density ratio to fluid	0%–10% of fluid density
Drag	Particle size and shape and fluid viscosity	0.1–10 mm $\mu = 0.001\text{--}1.0 \text{ Pa s}$
Stomach contraction	ACW speed, degree of occlusion	Speed = 1–10 mm/s

- There is a lot of overlap between these time scales, which will lead to complex interactions between the resulting flow from each of the driving timescales.

## Small intestine

Mixing, absorption, and transport of fine multiphase slurry take place in the small intestine. Traveling intestinal waves with both contractile and expansionary components lead to mixing on a range of scales as well as further fragment breakdown and nutrient transport to the intestine walls. This together with spatial variation in composition (and therefore material properties) of the digesta along the small intestine control the rate of absorption of nutrients and the nature of material transported to the large intestine.

The small intestine is coiled inside the abdominal cavity and divided into duodenum, jejunum, and ileum. Most chemical digestion occurs in the duodenum, a short 25 cm tubular section where food fragments (of 1–2 mm maximum size) are combined with secretions of pancreatic enzymes and bile that neutralize gastric acidity. This mixing occurs via bursts of short peristaltic activity. The duodenum is differentiated from the downstream intestinal sections in that its submucosa is lined with Brunner's glands which secrete alkaline mucus to protect the intestinal lining from gastric acid. The jejunum comprises the next 40% of the small intestine length ( $\sim 2.5 \text{ m}$ ) and is where the majority of absorption of sugars, amino acids, and fatty acids takes place. The walls comprise circular folds ("valves of Kerckring"), villi, and microvilli that increase the surface area available for absorption to around  $250 \text{ m}^2$  for the entire small intestine. The ileum (at about 3.5 m) is the last and longest section of the small intestine. It has thinner musculature and slightly reduced lumen diameter compared to the duodenum and jejunum; reduced permeability; and its contractile activity is weaker and less frequent than in earlier sections. It is also where absorption of Vitamin B12 and bile salts occurs.

Microbial populations increase in abundance from stomach to duodenum to jejunum (at around 10,  $10^3$ , and  $10^4$  bacteria/gram, respectively) and become more established in the terminal ileum with  $10^7$  bacteria/gram of digesta (Sekirov et al., 2010). The ileum

plays an important role in the immune system of the digestive tract. Due to the increased bacterial load, its walls have evolved embedded sections of aggregated lymphoid nodules (Peyer's patches) which monitor and respond to harmful bacteria. Abnormal motility in the ileum can cause "Small Intestinal Bacterial Overgrowth" (SIBO) leading to dysbiosis and local inflammation and can contribute to particular "Intestinal Bowel Disease" (IBD).

Direct measurement of motility and the intestinal environment is very challenging. The lower gut is largely inaccessible aside from surgery and our knowledge relies on MRI imaging, scintigraphy, and smart pills. Manometry is commonly used for studying colonic movements (Arkwright et al., 2013; Li et al., 2019), but there is little information on gastroduodenal movements except for Dent et al. (2020).

### Solute/nutrient diffusion and absorption

Nutrient uptake depends on both advection and diffusion of molecular-scale chemical species that are liberated from food fragments. It also depends on transfer from the luminal slurry content to the outside of the gut mucosa, and then through the mucus layer finally enabling absorption by the epithelial cells on the surface of the intestine wall. The interplay between the timescales of these different modes of transport has not been adequately studied for intestinal digesta subject to complex intestinal wall movements. Coordinated muscular contraction and relaxation of the wall generates strong vortical flow:

- 1) in advance of nonoccluding, moving contractions during peristalsis (Lentle & Janssen, 2008; Sinnott et al., 2012); and
- 2) both in front and behind of near-stationary contractions during segmentation.

This flow provides the rapid, large-scale radial advection required to agitate and mix content, as well as transport nutrients to the mucosa. Comparatively, diffusion is much slower and directed along concentration gradients. Nutrient release from real food fragments depends on complex transit across multiple layers of different materials each with their own diffusivities which also control release and diffusion of their own constituent molecules. Food fragmentation during digestive breakdown greatly increases the surface area available for nutrient release. Digesta rheology also influences advection. The presence of soluble and insoluble plant fiber increases viscosity which reduces the intensity of the vortical flow (Hardacre et al., 2015; Sinnott et al., 2012). Similarly, the presence of other solids will also affect digesta rheology. These not only influence gastric emptying in the stomach promoting satiety (Marciani et al., 2001; Moxon et al., 2017) but also have consequences for nutrient absorption in the small intestine.

Segmentative mixing of a spatially homogeneous viscous Newtonian fluid digesta is simulated, using SPH, in a 50 cm section of flexible-walled jejunum of diameter 2.5 cm. Periodic boundary conditions are applied at each end. Prescribed waves of alternating side-by-side stationary nonoccluding wall contractions and relaxations are applied with a frequency of 12 waves/minute. The wall shape is a

model prediction and is a function of the balance between muscle tensions in the wall and the digesta fluid pressures (with these components of the numerical scheme outlined in Section 2.). Two different digesta viscosities 0.01 and 0.1 Pa s are simulated. The digesta is initially seeded with a small cylindrical plug region of high concentration solute. We choose aspirin which has a diffusivity of  $1.7 \times 10^{-4} \text{ cm}^2/\text{s}$  (Anditi et al., 2013) as our model “nutrient” because it undergoes passive absorption at the intestinal wall, simplifying the requirements for the absorption model. We set a larger diffusivity ( $10^{-3} \text{ cm}^2/\text{s}$ ) for the wall material so that the absorption can be considered almost instantaneous. The wall is maintained at a zero nutrient concentration (so that it acts as a sink) to create a simple model of nutrient absorption.

Fig. 17.10 shows the effect of viscosity on dispersion of the nutrient-rich (red) plug into the surrounding digesta due to the segmentation induced flow. The lower viscosity case (Fig. 17.10A) has strong vertical flow fast enough to severely deform and disrupt the inner part of the nutrient plug before the next wave occurs. This greatly increases the interfacial area between the high concentration nutrient plug and the much lower concentrations in the surrounding digesta. This generates high spatial concentration gradients which drive rapid diffusion into the surrounding digesta and to the wall for absorption. This leads to rapid depletion of nutrients.

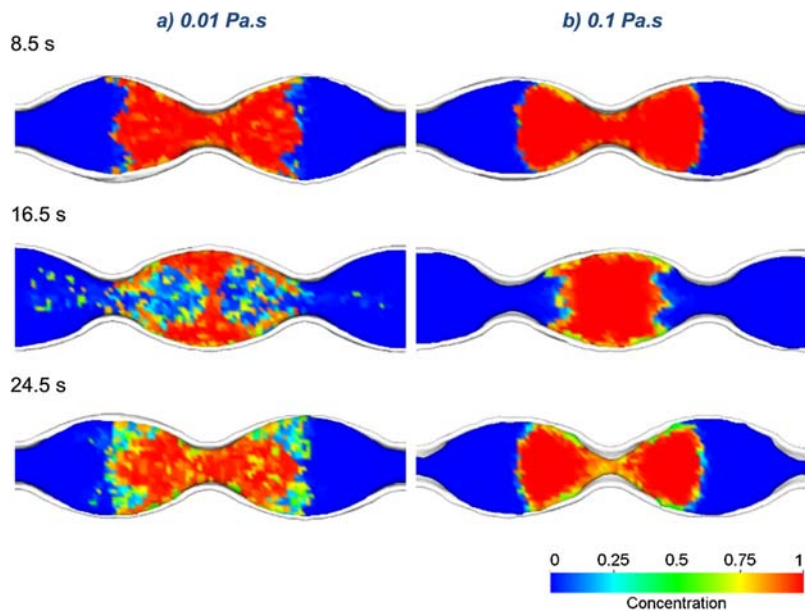


**FIGURE 17.10**

Effect of viscosity on digesta flow and nutrient absorption during segmentative mixing in the small intestine shown at three times. A high concentration plug of (red) generic nutrient is agitated by applied muscular wall contractions for (A) low viscosity content; and (B) high viscosity content.

For the high viscosity case (Fig. 17.10B) the rate of advection is greatly reduced and thus the alternating segmental contractions occur too quickly to allow time for sufficient deformation of the high concentration region resulting in smaller interfacial area for diffusion. Consequently, diffusive transport is only localized to a narrow, depleted region around the periphery of the plug and the core remains nutrient-rich for much longer times. The rate of nutrient uptake will therefore be slower and more regular for higher viscosity digesta. This helps explain why dietary fiber which increases content viscosity (Mackie et al., 2016) helps regulate glycemic response.

### Spatially varying multiphase digesta rheology

Multiphase digesta further complicate nutrient uptake with spatially varying rheology due to heterogeneous distributions of different food fragments which remain discrete in nature. Consequently, this can create spatially (both axially and radially) varying convection and diffusion along the intestine. “Sieving” is the separation of solids and liquid phases for selective emptying of liquids out of the gastrointestinal compartment being studied. This is frequently discussed for gravitational settling environments (stomach and ascending colon) but is often ignored in the small intestine. Hebden et al. (1998) showed that depending on meal composition some retention of solids occurs in the ileum causing preferential early delivery of a liquid “head” into the colon. This creates some axial gradation of viscosity along the length of the distal colon and subsequent spatial variation in mass transport. Similarly, differences in digesta composition radially out to the wall further influence transport and nutrient uptake. Lentle et al. (2005) identified different mechanisms that can establish a peripheral layer of lowered viscosity along the wall. Regular longitudinal contractions (in the absence of peristalsis) can induce

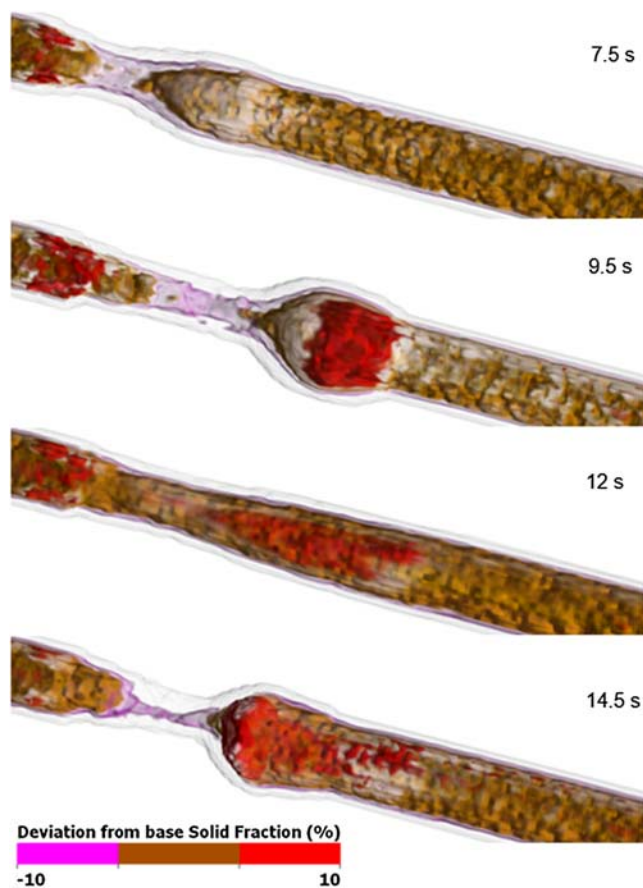
- shear thinning of the outer digesta layer;
- continual shear due to ongoing contractile activity which will force migration of larger particles from high shear rate regions near the wall to lower shear rate regions close to the center of the tube; and
- dilation of the tube in advance of the contractions which may draw fluid preferentially forwards into the bolus region.

The peripheral lubrication layer provides more mobility of digesta (and slip) at the wall, weakening the vortical flow and promoting plug flow of the central core of the digesta. The effect of this on spatial localization of enzymatic digestion, agitation of mucus layers (and resident microbial colonies), and nutrient transport across the mucus layer to the wall are unknown but can be explored using computational models of the type used here.

Here we extend the DEM/SPH multiphase digesta slurry model given by Sintott et al. (2017). This is a model of peristaltic transport of a slurry with high solids loading (40% by volume). A flexible walled intestinal segment with a

diameter of 2.5 cm and a length of 25 cm with closed ends is fully filled with multiphase slurry. Solid particulates are represented as neutrally buoyant, rigid, monodisperse 1 mm diameter DEM spheres. The slurry phase is modeled as a Newtonian SPH fluid with viscosity 0.01 Pa s. The coupled simulation solves for the drag forces between solids and liquid phases as well as collisions between the solids (and between the solids and the intestinal walls). Collectively, these components enable prediction of spatially varying effective viscosities due to the dynamically changing solids distribution. Short nonoccluding peristaltic bursts traveling at 2 cm/s are applied to the intestinal tube at a rate of 10 waves/minute. Again, the shape of the walls is a dynamic balance between the muscle forces and the internal fluid dynamical forces (as described in Section 2.5). To more easily visualize and interpret changes in the slurry composition, we collect solid fraction information on a data collection grid and generate iso-surfaces for 30%, 40%, and 50% solids to illustrate regions that increase or decrease their solids density over time. Based on Mueller et al. (2010), these local solids loadings equate to effective slurry viscosities of 0.034, 0.068, and 0.19 Pa s, respectively.

Fig. 17.11 shows such isosurfaces of digesta solids fraction at different times during the passage of multiple peristaltic waves. At 7.5 s the second peristaltic wave has commenced and there is a small increase (red) in solids density in the wake of the contraction with some apparent sieving of fluid (pink) through the partially open contracted region. By 9.5 s, there are substantial collisions between solid particles (and with the walls) that result in phase separation where the fluid phase is propelled forward and the slowing of the solids due to collisions produces increased solids density in particular locations (red) especially inside the leading edge of the dilated bulging wall. Between the second and third waves (at 12 s) there is a clear heterogenous distribution of solids with persistent much denser (red) regions remaining after the contractile wave has passed. This means the digesta effectively retains memory of compositional changes between successive waves. So digesta with high solids loading can exhibit history dependence and is often considered to be a pseudoplastic fluid (Hardacre et al., 2018). By 14.5 s, the dense region compacts further against the advancing contraction of the third wave. Intuitively, we might expect that given enough time multiple waves might agitate and mix the digesta slurry leading to spatial homogeneity. However, the model demonstrates that demixing and increasing spatial composition variation will naturally occur for multiphase digesta in the small intestine. The details of this will depend on the nature of the contractile behavior and the induced flow field. As digestion progresses further along the small intestine, real digesta will transition from slurry suspensions of particulates to multiple blended soft and sticky continuum materials. This will complicate the rheology and nutrient transport further and create huge challenges for modeling the structural complexity of such digesta.

**FIGURE 17.11**

Potential effect of repeated peristaltic contractions on phase separation in multiphase digesta resulting in local densification due to collisions between solids in the vortical flow region in advance of the contracting wall.

## Large intestine

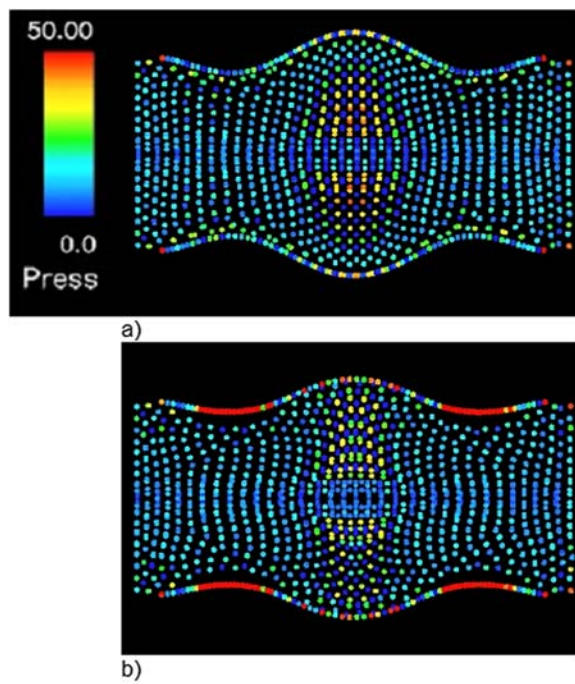
Digesta transfers from the ileum through the ileocecal valve into the large intestine which has a larger tube diameter of about 5–6 cm for most of its length. Collectively referred to as the colon this consists of the wider cecum (9 cm diameter), ascending colon, transverse colon, descending colon, and sigmoid colon. Contractile activity and subsequent movement of digesta greatly slow in the colon producing massive increases in microbial density to order  $10^{12}$  bacteria/gram. This shifts the digestion process to being primarily microbial fermentation of soluble and insoluble plant fiber. The other functions of the colon include absorption of water and electrolytes and

the final stages of chemical digestion. The remaining 10%–20% of water not absorbed in the small intestine is reclaimed in the colon progressively dehydrating the digesta as it moves toward the rectum to form solid stool.

Based on the reduced flow in the colon, models of the colonic environment typically focus on the gut microbiota interactions and metabolic chemistry with simplified mass transport of digesta. These treat the gut as a 1D bioreactor tube (Muñoz-Tamayo et al., 2010; Moorthy et al., 2015; Cremer et al., 2017) ignoring much of the fluid dynamics and transport. Labarthe et al. (2019) developed a comprehensive 2D PDE model to study microbial spatial structure incorporating simplified digesta flow, peristalsis, microbial population dynamics, microbe motility, mucus and SCFA production. Schutt et al. (2020) developed an SPH fluid dynamics model of partially and fully filled proximal colon segments with flexible-walls, high amplitude applied peristaltic waves, and multiphase gas/digesta to study drug delivery. This model has been extended to study drug release from solid tablets in the ascending colon (Schutt et al., 2021).

The musculature in the colon wall differs from that of the small intestine in that the longitudinal muscle is not uniformly distributed around the wall and is instead separated into three discrete bands of longitudinal muscle (termed taenia coli) that extend along the full length of the colon. Coordinated contractions and relaxations of both circular muscle and the taenia coli create bulging pouches (haustra). These are dynamic structures that change their position (hastral progression) very slowly over time as traveling waves. Much less frequent peristalsis may also occur which propels digesta downstream to pack into the rectum in preparation for evacuation. The innervation of the circular and longitudinal muscle may be such that their contractility is not spatially synchronized (Grider, 2003) at least during peristalsis. Local reciprocal activity of these muscle groups manages wall tensions during contractility. This is demonstrated in Fig. 17.12 by the SPH model of a single fluid filled haustra with prescribed contractions and relaxations of circular and longitudinal muscle. The viscoelasticity of the walls is directly represented here so that the transient changes in wall shape are a model prediction not prescribed kinematics. The resulting shape is a balance between muscle forces in the wall and fluid dynamical forces applied by the content to the walls. Contraction of longitudinal muscle thickens the wall. This tension creates resistance to any radial contraction of the circular muscle at the same location. Where the activity of the muscle groups is exactly reciprocal (Fig. 17.12A), a local longitudinal relaxation provides more stretch in the wall to accommodate the radial contraction. Stresses in the wall are uniform within the contracted and dilated regions and the haustra forms more easily in response to intraluminal pressures. Synchronous activity (Fig. 17.12B) results in much greater wall stress inside the contraction causing reduced occlusion, weaker vortical flow field and subsequently a smaller haustral bulge. So, this model is directly able to predict haustral pouch geometry and its time variation and the two-way coupling to the flow of digesta within.

Next, we extend this model to a more geometrically realistic representation of the colon. We use a 15 cm long, 5 cm diameter segment of transverse colon. This

**FIGURE 17.12**

Effect of coordination of circular and longitudinal muscle layers on haustral formation based on (A) out-of-phase (reciprocal innervation); (B) in-phase (synchronized innervation).

includes discrete musculature and contractility suitable for representing taenia coli, semilunar folds, and multiple hastra (where each is 3 cm long). For more details, see [Cleary et al. \(2021\)](#). This is filled with a fluid digesta with viscosity 0.01 Pa s. A haustral progression wave of 7.2 mm/s and contraction/relaxation amplitude of 40% muscle shortening/lengthening is applied to the colon wall.

[Fig. 17.13](#) shows the flow field due to the steady haustral progression wave. This is given in a thin vertical slice along the colon axis to show the internal flow details. Much of the digesta within each dilated haustral bulge have parallel flow lines. This indicates that there is very little capacity for mixing of digesta within each hastra. The flow is directed axially and is traveling at about half the speed of the applied wave. The lagging digesta flow is due to the contractions between hastra being only partially occluding allowing digesta to pass back through the contracted region (in the retrograde direction). The haustral bulges extend out between the contracted longitudinal muscle strips so that in an axial cross section they appear as three “lobes” distributed around the tube circumference. The lower of these three lobes is shown at the bottom of the colonic slice in [Fig. 17.13](#). At the top of the slice the upper wall contains a taenia coli band that bounds the flow and maintains axially

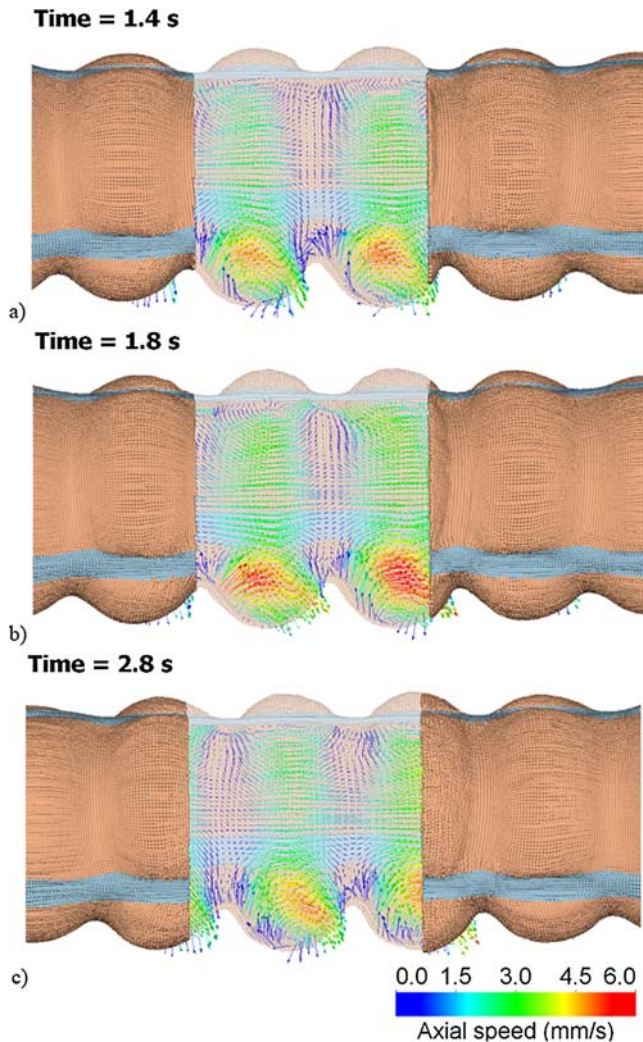


**FIGURE 17.13**

Haustral progression in a segment of the transverse colon. Mixing of content is driven by the flow field. Strong recirculation is visible inside each haustral bulge (brown) which extends outward between the taenia coli (light blue).

directed flow parallel to this band for the upper 60% of the tube diameter. Below this there is strong vortical flow in the lower 40% of the tube diameter inside the bulging dilated wall region. This demonstrates a key consequence of the spatially heterogeneous musculature and its effect on haustral geometry which is to create strong radial transport and mixing localized within the bulging haustral regions. This is expected to be an important transport mechanism for transport of water/nutrients/SCFAs

to the mucosa for absorption. The vortical flow will also create time-varying shear stresses applied to the mucus layers and microbial colonies in the mucosa which may influence aspects of colonization, and dynamic growth/reduction of microbial colonies. Introducing microbial structure and chemistry into the model, we have explored two approaches of coupling a 0D microbial fermentation model, such as the Rosendale formulation (Section 2.6.2), with digesta transport. The first approach is a 3D-0D coupled approach using the same 3D SPH colon segment model from [Fig. 17.13](#) with different species (such as carbohydrate fuel and SCFA reaction products; as well as microbial species numbers) represented as concentrations on the SPH particles each with their own diffusivity. This is similar to the advection/diffusion small intestine model in Section 5.1. Diffusion and reaction equations are solved for each SPH particle based on which species are present. This allows study of the effects of high advective transport and short timescale mixing on the fermentation chemistry. To simplify this model, we assume microbial species:

- (M1-M7) are fixed in space with M4 and M6 isolated in the first third of the colon;
- M3 and M7 are in the middle third; and
- M2 and M1 are in the latter third, while
- M5 is distributed throughout.

Diffusivities of  $10^{-9} \text{ m}^2/\text{s}$  were used for the SCFAs, and the carbohydrate fuel was assumed to be an infinite source (in line with the original *in vitro* experiments). A single prescribed “mass movement” peristaltic wave was applied to the colon segment with speed 7 mm/s and high amplitude (80% of circular muscle shortening during the active contraction).

[Fig. 17.14](#) shows the production and passage of a single SCFA product (Butyrate) due to the passage of multiple peristaltic waves. The colon is generally a much slower flow environment than the small intestine with incremental haustral progression occurring over minutes. This model represents a “wash out” (diarrhea conditions) that transports high concentrations of Butyrate inside the dilated bolus region over a very large axial distance with strong radial transport to enable rapid uptake of this nutrient at the wall.

The second proposed approach is the hierarchical 3D-1D-0D model proposed in Section 2.6.4. This is suited to much slower haustral progression movements with short bursts of peristalsis antegrade and retrograde with the model predictions being made for much longer timescales of multiple hours. 3D SPH simulations using the model in [Fig. 17.13](#) were performed, one for each of four different motor patterns. Two types of motor patterns (in antegrade and retrograde directions) were identified for premeal activity by [Dinning et al. \(2014\)](#) based on manometry. These consist of two types:

- Cyclic propagating waves. These rapid waves likely correspond to the ripples observed along the colon wall occur throughout the colon and have a mean speed of 7.2 mm/s, a period of 11 s and occur at a rate of 0.02 Hz; and

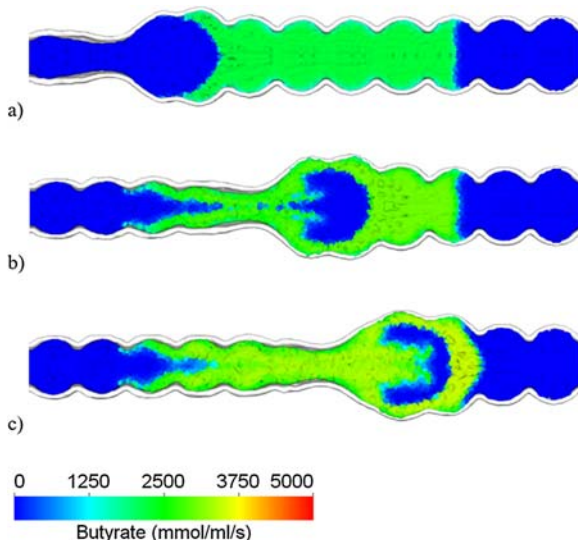


**FIGURE 17.14**

Microbial fermentation of dietary fiber to SCFA (butyrate) where butyrate producing microbes are located here in the central third of the colonic segment. A peristaltic propagating contractile wave is applied across the stationary haustral compartments. Fluid is colored by butyrate concentration.

- Short single propagating waves which we attribute to bursts of brief peristaltic activity. These occur predominantly in the proximal colon and have a mean speed of 6 mm/s, a period of 14 s and occur at a rate of 0.013 Hz.

Here we adopt the cyclic propagating wave parameters for haustral progression waves. The real haustral progressions are an order of magnitude slower in reality, but we have increased the speed of these here by a factor of 10 to reduce simulation duration. This is sufficient to demonstrate the operation of the coupled model. Following Dinning et al. (2014) we assume that 60% of the wall deformation activity is cyclic propagating haustra and 40% is short propagating peristalsis. For each SPH simulation, radially averaged axial velocity distributions are calculated and used as input to the 1D colon model (Section 2.6.4). The breadth of contractile propagating activity over the digestive timescale of hours may then be represented in the 1D model by choosing the frequencies of each of the different motility event types and the distribution of these in time. At each timestep, the 0D Rosendale microbial fermentation PDEs are solved to update metabolite concentrations at each axial coordinate of the 1D colon model based on the microbial population densities and at each location. The 1D flow solution is then solved for the applied motility event and the metabolite products are advected according to that flow. The 1D-0D coupled model therefore predicts the changing SCFA concentrations along the axial length

of the colon. As outlined in the 3D-0D SPH model, again we assume that the microbial species are stationary and located in specific parts of the proximal colon.

Fig. 17.15A shows model predictions of the axial distribution of SCFA concentration after 4 hours of fermentation. The locations of the microbial populations are

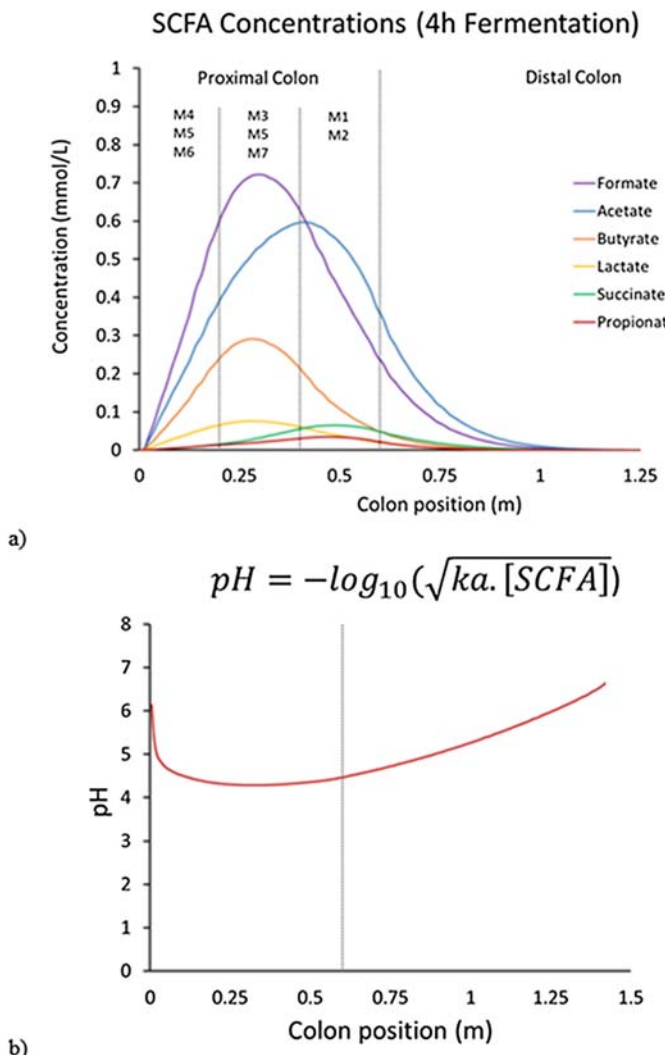


**FIGURE 17.15**

3D-1D-0D hierarchical model prediction of SCFA production from microbial fermentation of kiwifruit with (A) production rates along the proximal colon; (B) the corresponding gut acidity.

superimposed. The digesta flow advects the acids downstream once they are created. The individual concentration profiles then depend on

- when and where each SCFA is produced (based on the microbial species present),
- advection due to the digesta flow contribution for each motility event, and
- additional pathways where some of these SCFAs are consumed by specific microbial metabolic reactions which act as a sink for these species and convert them to other SCFAs (Section 2.6.2).

Gut acidity is defined in the model as

$$pH = -\log_{10} \sqrt{K_a \cdot [SCFA]} \quad (17.20)$$

where the acid dissociation constant ( $K_a$ ) is roughly independent of SCFA type. Therefore, the acid concentrations for each SCFA can be combined to give  $[SCFA]$ , the total concentration of SCFAs at any point in the gut. The spatial profile of pH along the full length of colon is shown in Fig. 17.15B. Gut acidity can be seen to decrease with distance along the colon as the SCFAs are absorbed at the mucosa. The majority of fermentation is known to occur in the proximal colon. This is consistent with depletion of carbohydrate fuel for fermentation (which will affect microbial colony distributions along the colon). A limitation of the current 0D model is that it assumes infinite carbohydrate source (which is based on the types of *in vitro* experimental conditions used to build this model). Gut acidity (and SCFA concentrations) decline with axial distance along the colon simply because the microbial locations are constrained in the proximal colon. In reality, this decline will be due to both reducing carbohydrate fuel as well as the distributions of microbial colonies in the mucosa.

---

## Liquid transport and droplet formation in the respiratory tract

Transmission of respiratory disease is often via virus or bacteria laden droplets of liquid (mucus) that are generated by the passage of air over the mucous layers within the respiratory system and which are then exhaled as aerosols. The mechanisms for generating these droplets are often not considered but are important for controlling their size distribution and infection load. Both of these factors affect the ability of droplets to be transferred between humans and the amount of virus or bacteria transferred to someone inhaling them. Other respiratory issues can relate to transport into, blockage of, and/or absorption by the lungs such as dysphagic ingestions of solids and liquids (Sura et al., 2012) and drug delivery (Heyder, 2004).

Structurally the lungs are made up of two major parts (Lust, 2007). The upper and middle parts consist of cartilaginous pipes that start with the trachea, subdividing iteratively into bronchi of decreasing size which divide to form bronchioles

whose smallest constituents are called terminal bronchioles. The resulting fractal like subdividing pipe network then transitions into the membranous gas exchange part of the lung. This consists at first of respiratory bronchioles and ends with alveolar sacs which are responsible for the dominant fraction of the gas exchange. The main bronchi range in diameter from 8.4 to 21.3 mm, with the right main bronchus typically wider, shorter in length, and more upright than the left. There is also a gender difference with bronchial diameters typically around 10% larger in men than women (Hampton et al., 2000). The smaller bronchioles that follow vary from 3.5 mm down to 0.6 mm (Lust, 2007). The bronchi and upper bronchiole structure comprise cartilaginous rings and plates connected by fibrous layers, making them flexible. They also contain a layer of circular smooth muscle controlled by the parasympathetic nervous system which provides for controlled expansion and contraction of the lung tissue. The innermost layer of the bronchi is a mucous membrane that is lined with ciliated epithelial cells. Mucus-secreting bronchial glands are connected to the surface through ducts. This creates a mucous film that coats the inside of the bronchi forming both a protection layer and providing a mechanism to collect, trap, and transport contaminants back out of the airways. Mucus transport is driven by the action of the cilia motion which pushes mucus upward but is also subject to fluid dynamic forces particularly when they are thicker. These mucous glands are densest in the medium-sized bronchi and decrease in number and size with depth into the lungs disappearing entirely when the airway structure transitions from the cartilaginous to the membranous bronchioles. This can be understood in terms of the roles of the different parts of the airways with the upper and middle section responsible for cleaning and warming air and providing distribution into the lower sections while these lower sections perform the gas exchange function. The presence of a mucous layer in the lower sections would obviously significantly impede the primary function of gas exchange so the decrease and then cessation of mucous glands with depth down into the lungs can be easily interpreted functionally.

The distribution of mucus within the lungs is a function of the spatially varying generation rates as well as its transport mechanisms. In a normal healthy person, the mucous layers are of moderate size and could be expected to be broadly distributed in accordance with the distribution of the mucous glands, allowing proper operation of the lungs. This mucous layer then plays multiple roles including to protect these surfaces and to provide a mechanism for the capture and transport of contaminants back out of the lungs. However, a broad range of medical conditions ranging from asthma to viral and bacterial infection can change this by increasing the rate of mucus generation and/or inhibiting the normal upward transport mechanism. This can lead to fluid build-up in the mucous layers until the point of congestion, which is then detrimental to oxygen transfer to the body. Severe acute respiratory syndrome coronavirus 2 (SARS-CoV-2) is a well-documented recent illness leading to significant fluid build-up in the lungs (Wiersinga et al., 2020; Xu et al., 2020). Transport of excess levels of mucus within the lungs is therefore useful to understand.

Droplet generation from the respiratory tract is poorly understood and there is little relevant modeling or measurement to inform about disease transmissibility. Instead, the majority of studies have concentrated on the transport of already existing droplets (April Si et al., 2021; Guo et al., 2020; Pourhashem et al., 2020; Wei et al., 2020), or mucus film migration up the airways (Ren et al., 2018, 2020). Airborne infection transmission is via droplets or aerosols expelled by an infected person. The risk of transmission is a function of the volume of droplets exhaled, their size distribution, and the infection load in each (Mao et al., 2020; Wells, 1955). The size distribution affects the distance that the droplets can move while remaining in the air. Large droplets fall and contact surfaces quickly (on the scale of up to a few meters), while fine aerosols can remain airborne for long times and distances. Some have attempted to estimate droplet sizes during different physiological processes, e.g., talking and coughing (Morawska et al., 2009), and for changes in mucus material properties (Anwarul Hasan et al., 2010; King et al., 1985). But there appears to be little understanding of the basic mechanisms that are responsible for such droplet formation or where in the respiratory system they are generated. Some mechanisms of generation have been proposed but not validated for *in vivo* conditions. For instance, Vadivukkarasan et al. (2020) discussed hydrodynamic processes that could lead to droplet generation, via three instability mechanisms, but did not consider how these processes originate from the physiological conditions of the respiratory tract. Wei and Li (2016) summarized possible mechanistic concepts for droplets as

- WL1. Shear-induced surface wave instability (only expected to occur at very high gas speeds such as during coughing and sneezing)
- WL2. Oral cavity mode (responsible for large droplets)
- WL3. Bronchiolar film rupture which relates to “reopening of collapsed terminal airways at the beginning of inspiration” and is thought to be responsible for very small droplets. However, since mucus is not generated in these regions of the lungs the mucus volumes available for droplet formation cannot be large.

Zhou and Zou (2021) presented a similar list of droplet formation mechanisms. During normal breathing, none of these mechanisms can create droplets from the main bronchi and bronchioles where the mucus is predominantly generated.

The location and processes for droplet generation will be heavily influenced by the mucus distribution within the airways and the thickness of the mucous films in each area (Guo et al., 2020). Since infections are also spatially concentrated within the body (not uniform), the viral/bacterial load in droplets will also reflect infection loads locally where droplets are being generated. So, it is useful to understand how these droplet generation mechanisms vary throughout the respiratory tract and how they vary with the scale (diameter) of the airway at each point.

Here we present an idealized SPH-based multiphase model of the interaction of mucous layers with internal gas flow and use this to demonstrate some key flow behaviors that influence droplet formation.

The surface topography of the mucous layer is also not well characterized, being highly time varying and of fine spatial scale which makes MRI or other tomography problematic. Since the surface is an interface between two fluids of differing density

and viscosity, one would expect this to be subject to Kelvin–Helmholtz instabilities ([Vadivukkarasan et al., 2020](#)), which would tend to cause the surface to become progressively more uneven as eddies are generated in the mucous layer as a result of the shear stress applied by the passing gas. This is the mechanism identified by [Wei and Li \(2016\)](#) as WP1. However, the thinness of the film and its surface tension can both be expected to limit or perhaps even inhibit the growth of such structures leading to at most moderately undulatory free surface shapes rather than the fully developed eddies that would develop based on density variation alone. The relatively high viscosity of the mucus will also limit the growth rates and amplitudes of these structures. But once formed these surface undulations can be driven along the respiratory pipes by the gas flow when it is sufficiently fast and could potentially provide opportunities for droplet shedding by the surface. [Wei and Li \(2016\)](#) report that this behavior is only possible at very high gas speeds.

A key physical structure in the respiratory system that could be expected to contribute to droplet formation is the branching structure. Air enters the lungs through the first level of bronchi from the trachea. The primary bronchi branch into smaller, but still substantive pipes (secondary and tertiary bronchi) which in turn branch to form bronchioles which in turn branch to form alveolar. So, a generic unit configuration that is representative of the lungs is an inverted Y-shaped junction where the lower branches are narrow, and the upper merged branch is larger in diameter. This is an idealized functional “unit” that is reproduced throughout the lungs with just the characteristic scale varying according to the depth into the lungs.

Here we demonstrate the SPH multiphase model operating in such a unit for one such scale. It is however representative of the basic behaviors that lead to droplet formation at all the length scales in the lungs and the model can be separately applied to each level. Since droplet formation is maximal at high gas flow rates, we further simplify the model by omitting the transient variation in the gas flow rates arising from the basal breathing pattern and strong perturbations relating to talking, singing, or most importantly coughing.

Human breathing has a typical at rest frequency for an adult of 12–20 Hz ([Rowden, 2021](#)) so the range of periods for a breath is around 3–5 s. Peak gas speeds for exhalation are measured as being of order 5–22 m/s ([Zhu et al., 2006](#)). Continuity of the gas flow means then that the peak speeds of gas flow in much of the respiratory system will be of similar order. For the current model we assume a comparable maximum gas inflow speed of 5 m/s. Assuming a sinusoidal time variation for the speed variation during a breath then the gas flow spends approximately ¼ of the breath period near the peak speed. So, this means that in terms of idealizing the flow we can neglect the time variation of the inflow speed and consider a period of order 0.75–1.25 s with the gas moving at this peak of 5 m/s. Gas speeds can be expected to be much higher for coughing, singing, and loud speaking so this can be considered a conservative modeling scenario.

Data on the thickness of the mucous layer within the human respiratory system is difficult to obtain. Some measurement in the trachea of rats ([Sims & Horne, 1997](#)) gave an indicative range from 0.2 to 50 microns. [Tilley et al. \(2015\)](#) report that cilia

length is typically in the range of 4–7 microns. One can therefore expect that the minimum layer thickness will be a small multiple of this length (so perhaps 10–20 microns). [Karamaoun et al. \(2018\)](#) also report trachea mucus thicknesses in the range 10–30 microns. [Ren et al. \(2020\)](#) indicate a representative mucous layer thickness for a healthy human is of order 30 microns and also report that for people with respiratory illness this can be up to 300 microns. [Wei and Li \(2016\)](#) quote a range of mucus thickness of 5–100 microns. Considering these indicative ranges for humans and taking consideration of the higher mucus generation rates in the middle bronchioles (compared to the trachea), a plausible estimate for the upper limit of mucus thickness for a healthy person may be of order 50–100 microns. Since the focus here is for infection transmission from persons with heavily congested lungs then mucous layer thicknesses up to 200 microns will be considered.

Air has a dynamic viscosity of  $1.8 \times 10^{-5}$  Pa s and a density of 1 kg/m<sup>3</sup>. For the mucus, which is a gel composed almost entirely of water ([Nicas et al., 2005](#)) we will assume that it has a Newtonian rheology with the properties of water at the flow conditions considered (see [Lai et al., 2009](#) for a detailed review of mucus rheology). The dynamic viscosity used for the mucus is  $10^{-3}$  Pa s and the density is 1000 kg/m<sup>3</sup>.

Large density differences between fluids present strong challenges for numerical methods. See [Cleary et al. \(2021\)](#) for an explanation of these issues for SPH. So the density used for water in the numerical model is reduced by one order to 100 kg/m<sup>3</sup> to improve numerical stability. The key consequence of this model change is that it makes the simulation slightly pseudo-transient, with inertial effects decreased by one order of magnitude relative to the viscous. Practically speaking this means that the mucus reacts to the fluid forces applied with accelerations that are 10 times larger, so the fluid accelerates more quickly. If the system was linear, then the main effect would be to scale the time variable used (so 1 ms in the model would be equivalent to 10 ms for the real-world version). This does not necessarily affect the speeds observed but does affect the rate at which these speeds are achieved. In practice the flow patterns do not seem to be particularly sensitive to the air to mucus density ratio used. The simulations considered here are performed over 20 ms (which is sufficient to remove much of a 200 micron thick mucus layer) which would then be equivalent to 200 ms for the full density ratio. This time is still small compared to the time period over which the air flow is near its peak speed during the peak of the breathing cycle, which is at least 750 ms. So, the idealized model with reduced density ratio is valid for its entire duration.

In this model we ignore the effect of the cilia beating to provide upward transport of mucus near the bronchi walls, since the speeds associated with this component of motion is very small compared to the gas and gas-induced mucus speeds. Gravity which is also relatively weak on this timescale compared to the other forces is also neglected. We also note that the upward cilia transport and downward gravity force are opposite and to some extent will cancel.

The variant of the SPH method used here is the one given in [Cleary et al. \(2021\)](#) for multidensity flows. The speed of sound used for both materials is 100 m/s based

on a maximum characteristic speed of 10 m/s (which corresponds to the highest speeds observed in the flow).

Two geometry configurations of the model are used here.

1. A straight section of pipe with width 2 mm (representing a midsize bronchiole where mucus generation is maximal) which is 6 mm long.
2. An inverted Y junction with outgoing pipe width of 2 mm and incoming pipe widths of 1.4 mm each (representing a typical midsize bronchiole junction again where mucus generation is maximal).

An SPH inflow boundary condition is applied to each of the incoming pipes. The Reynolds number ( $Re$ ) for these flows (with peak speed of 5 m/s, kinematic viscosity  $1.8 \times 10^{-5}$ , and pipe width of 1.4–2 mm) will be at most 250–500. This means that these flows will be laminar, and the inflow velocity profile will therefore be parabolic. The exit boundary condition at the tops of the pipes is a zero pressure Neumann condition. All the walls are initially covered by a uniform layer of mucus (water) of thickness  $\delta$  except in the immediate vicinity of the gas inflows at the bottoms of the tubes. As discussed earlier, the values used for  $\delta$  will be between 100 and 200 microns. All the cases shown here are for breath exhalation so that the flow is from the bottom of the pipe(s) to the top. It should be noted that fluid transport can also occur in the opposite direction during inhalation. These cases, while contributing to the generation of congestion in the lungs though, are not relevant to droplet generation for infection transmission prediction.

The straight pipe model used is fully three dimensional. It uses an SPH particle size of 25 micron and has 1.58 million particles in the model. The SPH formulation is constructed to ensure that the viscous stress is continuous across interfaces between materials with orders of magnitude difference in properties. The resolution used here is sufficient to well resolve the fluid film and its interaction with the fluid.

[Fig. 17.16](#) shows a cross section through the middle of the straight pipe section for a viscous layer thickness  $\delta = 100$  microns. [Fig. 17.16A](#) shows the initial state with the air-colored green, the viscous film fluid on the sides is colored violet, the inflow at the bottom where new air enters is colored red. [Fig. 17.16B](#) shows the system at 3.1 ms with both air and fluid colored fluid speed according to the color bar below. The viscous fluid starts higher having been forced upward by the air and has thickened at the base. It is colored dark blue since its speed is very low compared to that of the air. The air speed is highest in the center and decreases toward the side in accordance with the expected parabolic profile. Note that this profile extends the full width of the channel near the bottom and then narrows reflecting the nearly stationary fluid on the sides. The maximum speed of the gas along the centerline increases accordingly from 5.0 to 5.44 m/s. [Fig. 17.16C](#) shows the two materials at 9.0 ms. The air is colored almost entirely blue, meaning that all the initial air has flowed out the top of the straight pipe section and been replaced by new air from below. The fluid layer (violet) has been dragged around 1 mm higher from where it was at the start in 9 ms (so average fluid speed is around 0.11 m/s compared to peak gas flow of over 5 m/s). The end regions of the fluid have adopted a curved profile

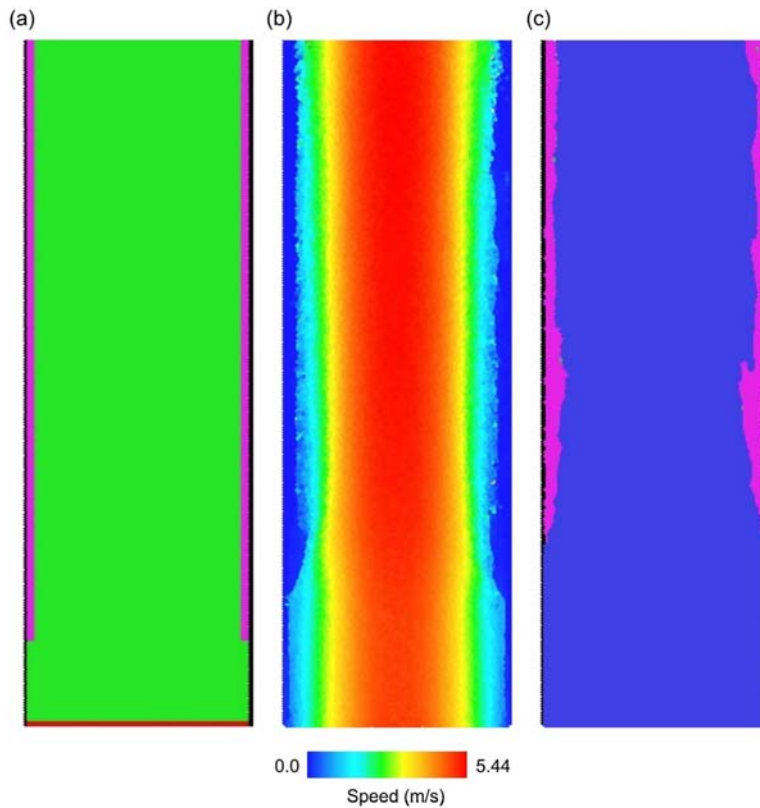


FIGURE 17.16

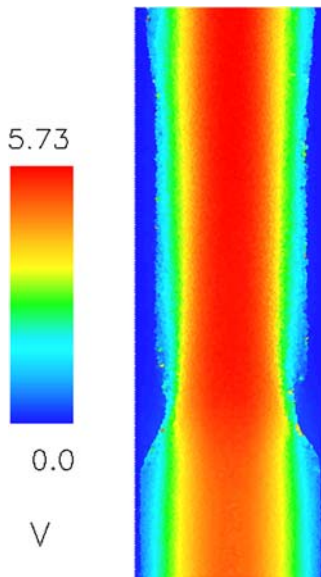
Cross section through the middle of the straight pipe section for a viscous layer thickness 100  $\mu\text{m}$ , (A) initial state with the air colored green, the viscous film fluid on the sides is colored violet, the inflow at the bottom where new air enters colored red, (B) state at 3.1 ms with both air and fluid colored fluid speed according to the color bar below, and (C) state at 9.0 ms with the air colored blue (reflecting that it is air that entered the domain since the start of the simulation in contrast to the air initially present in the pipe which was green) and the fluid is violet.

to a maximum layer thickness of around 250 microns around 1 mm higher than the lowest point of the layers. The layer on the left is stable but the lower bulge on the right has extended sufficiently far into the flow and that some very weak entrainment of fluid into the air beyond is observed, but the effect is weak. Above these end structures, the fluid layer maintains its thickness fairly evenly, developing only weak undulations in the free surface profile. There is no sign of shear induced or Kelvin–Helmholtz instability confirming that for these gas speeds (order 5 m/s) this type of mechanism is not active for generating droplets from the surface. The average layer thickness away from the bottom end at latter times is similar to that

of the original layer. So, an initial viscous layer of 100 micron is not particularly dynamic and does not show strong signs of fragmentation or of droplet creation. The flow in viscous fluid layer is very slow compared to that of the gas but the cumulative displacements are significant in terms of proportion of tube length over which the fluid is transported.

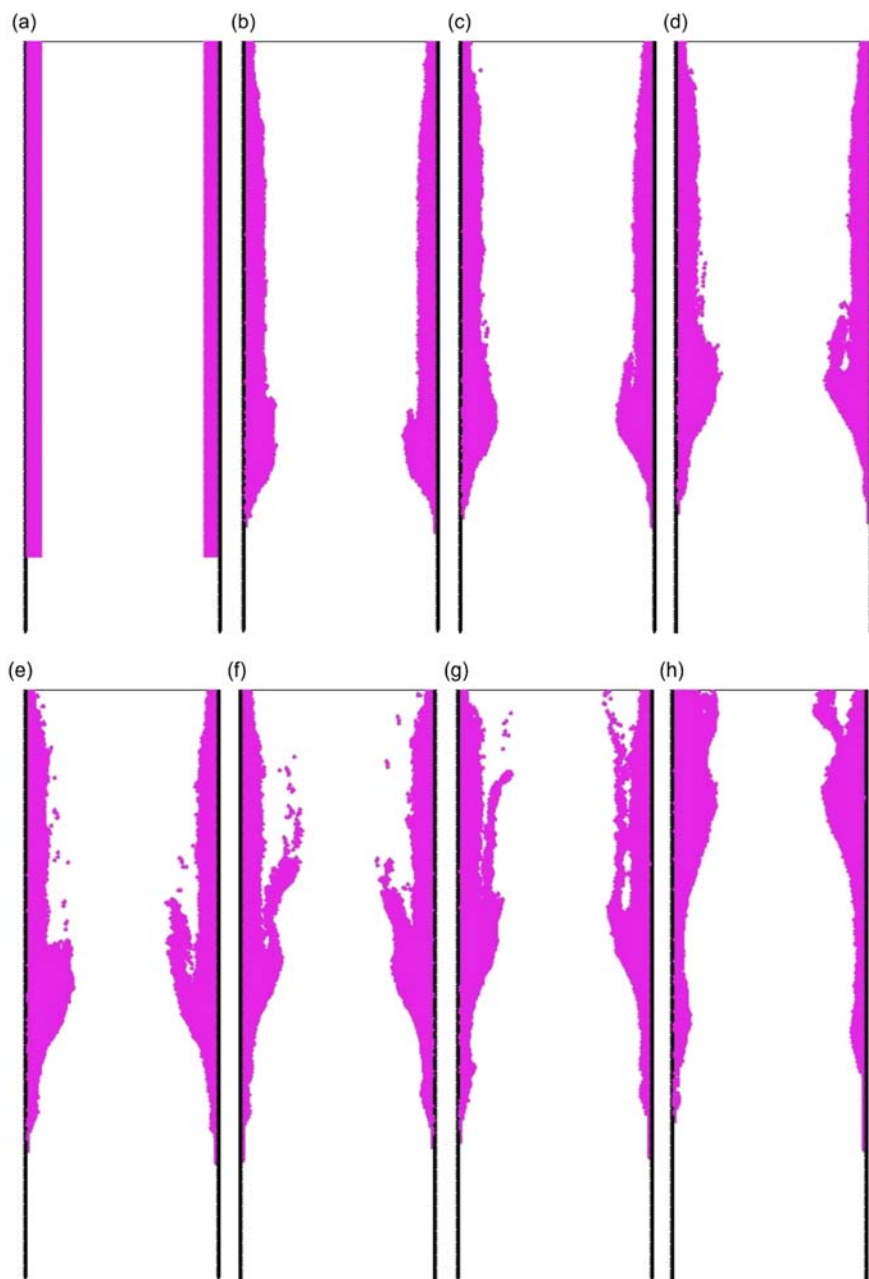
[Fig. 17.17](#) shows the speed distribution in a central cross section of the straight pipe with a larger viscous layer of thickness  $\delta = 150$  microns. The trailing ends of the viscous layer develop reasonably significant bulges but above this the layer remains quite uniform. The viscous fluid speed is again significantly lower than that of the gas, so the fluid is colored dark blue. The peak central speed has increased to 5.73 m/s (compared to the previous case) due to the small decrease in open area available for the gas to flow through.

[Fig. 17.18](#) shows the flow of just the viscous fluid (colored violet) in a central cross section for the straight pipe for an initial layer thickness of  $\delta = 150$  micron. In this case the air is not shown to improve the visual clarity of the fluid surface and its behavior. The initial fluid layer is uniform and extends to almost the bottom of the pipe as shown in [Fig. 17.18A](#). [Fig. 17.18B](#) shows the layer structure at 3 ms. There are three distinct zones of different behavior. There is a thinning of the layer near the top which is a consequence of the outflow boundary condition used and this should be ignored. The broad middle sections of the layer remain relatively uniform



**FIGURE 17.17**

Speed distribution in a central cross section of the straight pipe for a viscous layer of thickness  $150 \mu\text{m}$ . The fluid is colored by speed (in m/s) according to the color bar shown.

**FIGURE 17.18**

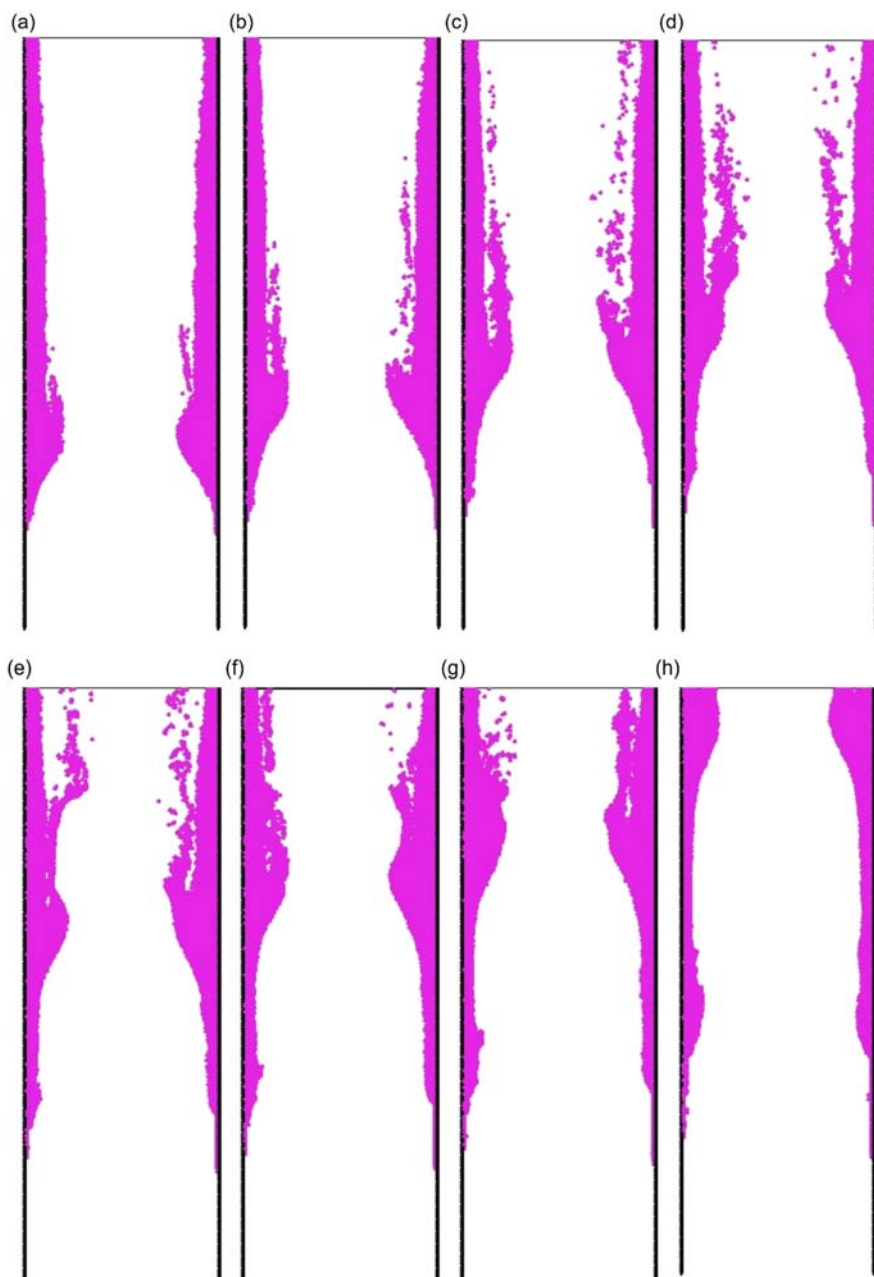
Flow of the viscous fluid (violet) in a central cross section for the straight pipe for an initial layer thickness of 150  $\mu\text{m}$ . The air is not shown. Images correspond to times, (A) 0 ms, (B) 3 ms, (C) 4 ms, (D) 5 ms, (E) 6 ms, (F) 7 ms, (G) 8 ms, and (H) 12 ms.

and simply flow upward along the walls and show no predisposition to become unstable or to break-up.

The lower zone around the end of the layer behaves very differently. This structure is representative of situations where there is an abrupt or fairly sharp change (increase) in the viscous layer thickness. The end of the fluid layer presents a surface to the gas flow that obstructs it. The gas is forced inward and around the end of fluid. Since the gas flow speed is so high, this imposes a strong shear stress on this fluid surface dragging it radially inward. The pressing of the gas against the fluid leads to elevated pressures in the fluid immediately above its end which also contributes to fluid being forced inward. Once fluid is located sufficiently inward, then it is unsupported in the axial direction and can also be pushed along the tube. This rapidly rounds the end of the fluid layer creating a bulge as fluid is directed obliquely inward by both the shear from the gas and the high pressure in the fluid. The bulge structure observed in Fig. 17.18B forms because of this process. This behavior was also observed for the 100 micron case, but the effect was quite weak. The effect is reasonably strong for the thicker fluid layer. This flow structure is self-reinforcing, in that as the structure becomes bigger, then the gas flow is more diverted around it and so entrainment into the flow increases. The distance that the bulge protrudes into the flow controls the magnitude of the high pressure generated in the fluid. Both of these effects force more fluid radially inward. So, while the layer is stable when it is of uniform thickness, when there are sharp changes in thickness, then its behavior becomes unstable. This is the first mechanism for droplet generation that we can identify for the bronchi and bronchioles.

Fig. 17.18C–F shows the ongoing evolution of this bulge structure which increases in thickness until it reaches around three times the initial layer thickness. Once this bulge is large enough for it to protrude meaningfully into the shear flow of gas then fragmentation of the fluid is observed with both small drop like structures being shed and larger elongated masses of fluid being sheared to the bulge in the viscous layer. By 10 ms, significant volumes of fluid have been shed from the fluid layer. Capillary instability will cause such elongated fluid fragments to break up into streams of droplets of varying sizes. So, a broad range of droplets will be generated from regions where there is a sharp change in viscous layer thickness. Note that bulge structure propagates along the tube more quickly than the fluid immediately adjacent to the walls. By 12 ms (Fig. 17.18H), the bulge has passed into the upper half of the tube while there is still a significant fluid layer below. The thickness of this residual stable viscous fluid layer is around 50–75 microns which confirms the previous observation of fluid layer stability when it is less than 100 microns thick.

Fig. 17.19 shows flow behavior in a straight pipe for a larger viscous layer thickness of  $\delta = 200$  micron. This is qualitatively similar to what was observed for a 150 micron layer but with faster growth rates and more intensive shedding of fluid with a much stronger tendency for these to be droplets rather than elongated fluid filaments. A layer of this thickness is sufficient to provide the fluid with greater mobility and opportunity to develop nonuniform structures. As the layer thickness increases the

**FIGURE 17.19**

Flow of the viscous fluid (violet) in a central cross section for the straight pipe for an initial layer thickness of 200  $\mu\text{m}$ . The air is not shown. Images correspond to times, (A) 3 ms, (B) 4 ms, (C) 5 ms, (D) 6 ms, (E) 7 ms, (F) 8 ms, (G) 9 ms, and (H) 12 ms.

stabilizing influence of the solid (no-slip) walls becomes more distant and the opportunity to develop transverse fluid motion increases. These drive faster and larger bulge structure formation which leads to increased fluid shedding. Note that the residual viscous fluid layer remaining after the passage of the bulge structure is similar (50–75 microns) to that found for the 150 micron case. This demonstrates that fluid layers of less than 100 microns appear to be stable and that excess fluid above this level can be quickly stripped away generating significant streams of droplets and a stable much thinner residual fluid layer. Viscous layers that are thicker than this appear to be stable if their thickness is fairly uniform but sharp changes in layer thickness trigger significant fluid fragmentation (mechanism 1) leading to reduced thickness and stable residual layer behavior.

Finally, we consider flow in the inverted Y shape junction of bronchioles with a 200 micron thickness fluid layer over most of the internal surface. This model is Cartesian with a periodic boundary condition in the depth direction allowing a thin slice of the problem to be simulated with high resolution. The number of particles spanning the depth direction is 10. The SPH particle size is again 25 microns so there are 80 particles across the 2.0 mm outflow pipe and 56 across the 1.4 mm wide inflow pipes. The material properties are the same as used previously.

**Fig. 17.20** shows the fluid and gas transport with color indicating speed. Gas enters from the ends of the two lower pipes. These have a parabolic velocity profile with a maximum speed of 5 m/s. The flow speed increases once the gas reaches the fluid-coated parts of the pipes. The outer dark blue areas correspond to the fluid layer. The gas streams merge immediately above the junction leading to a higher speed gas flow in the upper exit branch of the model with a maximum speed of 9.87 m/s.

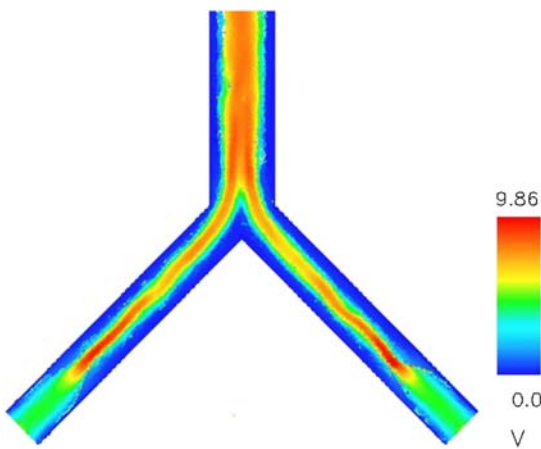


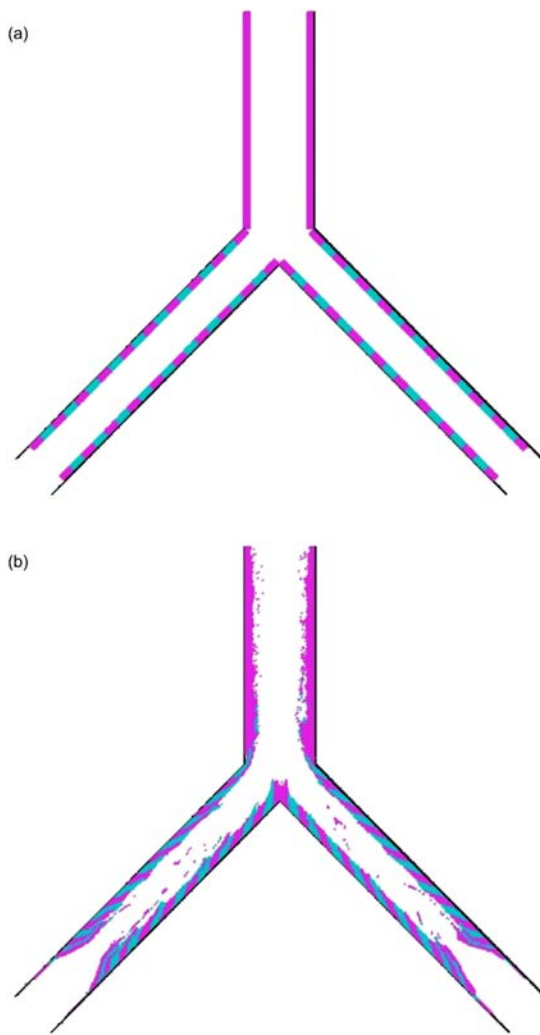
**FIGURE 17.20**

Fluid and gas transport in an inverted Y shape junction of bronchioles. These are colored by their speed (in m/s) with colors given in the color bar.

Gas flow through the Y branch leads to momentum transfer to the mucus layer providing it a generally upward motion that is maximal at the free surface, and which decreases with depth toward the walls. The behaviors identified earlier for the straight pipe occur in both the inflow branches of this configuration. This includes the unstable behavior that leads to fluid shedding for areas where there is a sharp change in viscous layer thickness (mechanism 1) and the relative stability of the layer surfaces where the thickness is fairly uniform (no surface wave instability manifested). This case demonstrates two additional mechanisms (mechanisms 2 and 3) for the shedding of fluid droplets arising from the convergence of the inflow pipes that have not previously been identified in the literature. These are made possible by the merging of airway branches at the inverted Y junctions. Fluid that is driven up along surfaces that end at the apex of the junction can no longer be just transported along the walls (because the walls end at the apex of the inverted Y) but must pool there forming increasing large volumes of trapped fluid that expands out into the gas flow. These fluid structures, once large enough, are then stretched predominantly in the streamwise direction until they split and detach. This is much the same as what occurs in a dripping tap (albeit in the opposite direction and driven by the gas flow rather than gravity). This pooling of fluid at and beyond the apex leading to the shedding of fluid structures and droplets on a wide range of scales will be identified as mechanism 2.

[Fig. 17.21](#) shows just the fluid transport in an inverted Y shape junction of bronchioles. The fluid layer is colored violet above the junction and with alternating blocks of light blue and violet below. The shape and location of these blocks allows the bulk transport and local deformation of the fluid to be visualized. In [Fig. 17.21B](#), these blocks have been stretched significantly in the flow direction demonstrating the strong cumulative deformation that the fluid layer is subject to. As the flow progresses the angle of these blocks increases, and they become increasingly aligned to the flow direction and then extremely elongated.

At 2.2 ms, one can see ([Fig. 17.21B](#)) that the same bulges have developed in the lower end regions of the fluid layers as were found for the straight pipe cases. As seen earlier, these are very effective at generating streams of droplets and fluid fragments which can be seen distributed along much of the length of the lower pipes. We can also see significant droplet generation in the upper pipe distributed along and above the fluid free surface. These arise from the fluid bulge that is created at the bottom of the upper pipe due to flow separation from the sharp corner on the upper walls. The gas flow separates from the corner and drags adjacent fluid radially inward in the region just above. The upper parts of the fluid bulge are subjected to significant shear by the high-speed gas flow which then rips fragments of fluid from the structure, carrying this upstream as stream of droplets. This is the third mechanism that the simulations identify for generating droplets (which we will term mechanism 3). The gas flow both drives fluid into this bulge and then removes it so the bulge maintains a fairly steady size and shape. In a more realistic anatomical geometry one may expect that such junctions will be somewhat rounded which would moderate or perhaps limit such flow separation driven droplet generation.

**FIGURE 17.21**

Fluid transport in an inverted Y shape junction of bronchioles. The gas is not shown. The fluid layer is colored violet above the junction and with alternating blocks of light blue and violet below. The shape and location of these blocks allows the bulk transport and local deformation of the fluid to be visualised, (A) at start and (B) at 2.2 ms.

Fig. 17.22 shows a close-up of the flow around and above the bronchiole junction. The gas flow drives upward migration of the viscous fluid. For the outer pipe walls the fluid simply transitions from the inflow pipe to the outflow, perhaps with some shedding due to the gas flow separation (mechanism 3). For the inner walls of the inflow pipes which meet at an apex near the middle of the Y there is no surface above and so

the fluid begins to pool (Fig. 17.22A). By 4 ms (Fig. 17.22B) this volume of fluid has been stretched vertically well into the gas flow. The strong converging gas flow on either side lifts and stretches this fluid. Over the next several ms, the volume of connected fluid attached to the apex becomes significant and due to its high relative viscosity, it has significant resilience and can be stretched very significantly with only occasional breaks. By 6 ms (Fig. 17.22D) the viscous main filament has stretched more than 3 mm and has reached above the halfway point of the upper pipe.

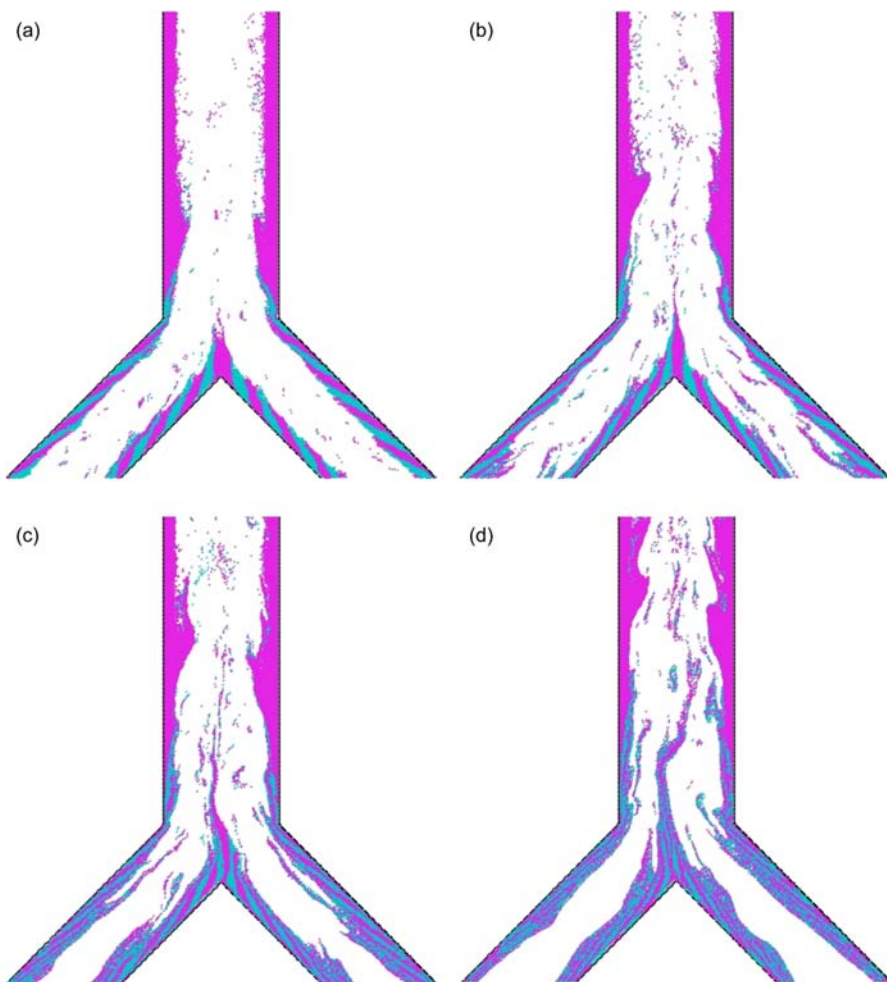


**FIGURE 17.22**

Close-up of the fluid transport in an inverted Y shape junction of bronchioles focusing on the flow from the apex of the junction of the lower pipes. The gas is not shown. Images are at: (A) 3 ms, (B) 4 ms, (C) 5 ms, (D) 6 ms, (E) 7 ms, (F) 8 ms, (G) 12 ms, and (H) 18 ms.

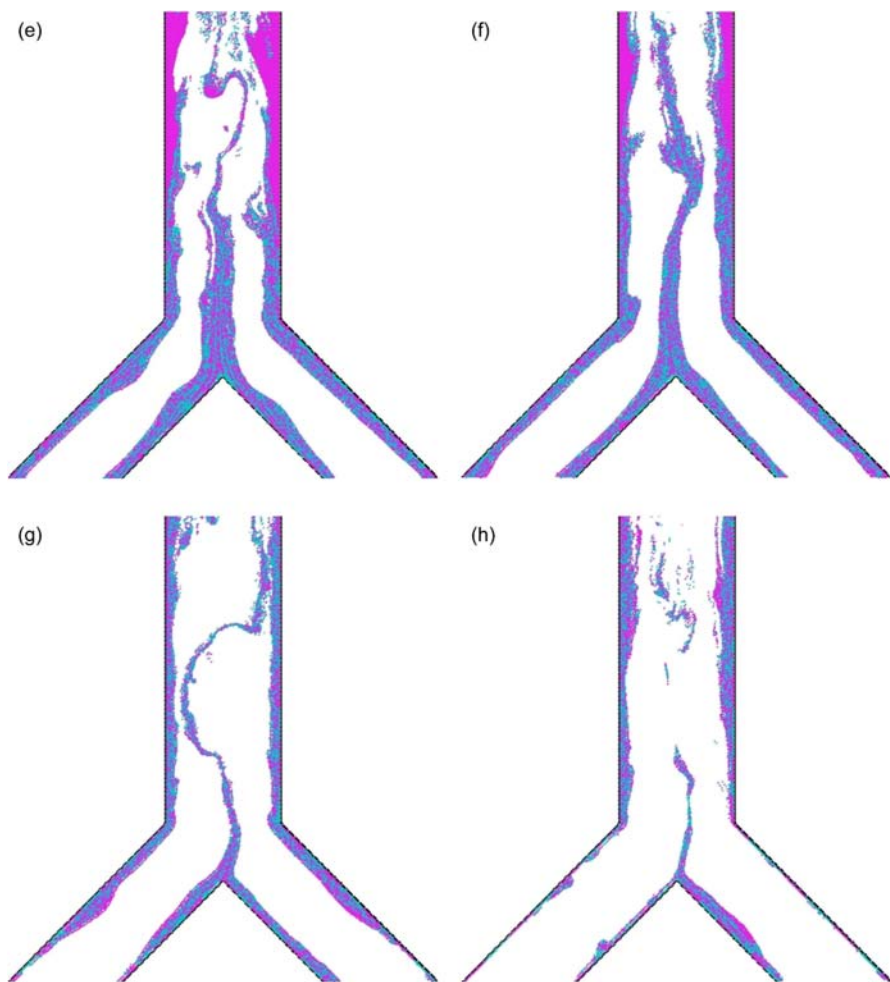


FIGURE 17.22 cont'd.

Significant fragment shedding has occurred from its end (demonstrating mechanism 2 and that it is highly effective at generating droplets and filaments of fluid). The presence of this filamentary structure maintains separation between the gas streams on either side. This generates strong lateral motions in the fluid separated, fluid filament leading to complex convolutions in its structure (see Fig. 17.22E). By 8 ms (Fig. 17.22F) the entrained filamentary structure has thickened to be of order 200 microns wide and has extended for more than 5 mm in length. Capillary instabilities in these elongated fluid masses (which are not included in this model) will in due course cause these to break up into streams of droplets.

By 12 ms (Fig. 17.22G) the amount of free fluid remaining on the walls has decreased to around 100 microns in many locations and the surface behavior has

become quite smooth. This is consistent with previous observations that fluid layers of this thickness or below are increasingly stable and well behaved (and that we do not observe surface wave instability). Such stability does not inhibit the migration of fluid from the apex into the long waving filament extending from it. This continues to drain fluid for several more ms. By 18 ms (Fig. 17.22H) the filament, which is becoming much thinner as the available supply of fluid decreases, has finally shortened significantly with a large range of fragments and droplets created by the rupture being expelled from the top pipe. In terms of volume of fluid entering into the gas flow, mechanism 2 is highly effective and is responsible for a much larger fraction of the fluid entrainment than both mechanisms 1 and 3.

Viscous fluid layers thinner than 100 microns can be expected to show even less variation than does the 100 micron case used for the base case simulation here and appears likely to become increasingly well behaved with decreasing transport and little predisposition to develop any nonuniformity.

For thicker fluid layers,

- These remain stable with only weak perturbations in the thickness along the pipe if the initial thickness variations along the pipe are small (little evidence of shear induced instability at the fluid free surface). There is a consistent observation across all cases that initially uniform films remain quite uniform and show little predisposition to droplet formation.
- If there is a sharp change in layer thickness, then strong shear from the gas that is forced around this structure and compression of the fluid behind it together force fluid radially inward. This leads to the unstable growth of bulge structures that can become significantly larger than the initial layer thickness. These can then shed significant streams of both droplets and extended fragments of fluid which will then break-up into streams of droplets. This is mechanism 1 and the first such identified using this model.

Two other new droplet generation mechanisms have been identified from this modeling that relate to the nature of flow in more complex network geometry. These are:

- Mechanism 2: The inner apex where two pipes merge has no wall structure for fluid to migrate along. So, fluid driven along the walls below has flow build up around the apex, creating large volumes of fluid available to enter the flow. This is typically in the form of long resilient filamentary structures that can extend significant distances from the junction apex and which eventually break up leading to significant volumes of droplets and free fluid. The scale of such entrained fluid structures increases strongly with the initial fluid layer thickness (the volume of fluid below the joint that is dragged up to these apexes).
- Mechanism 3: Flow separation occurs from the outer walls of junctions due to sharp angle changes that lead to the creation of fluid bulges just upstream of the junctions. These fluid masses are then subject to strong forces from the gas that rip fluid from them leading to significant shedding of droplets as the high-speed gas flow passes over the accumulations of fluid.

From such a model, droplet sizes and viral/bacterial load in each droplet can be calculated. This can provide useful information for understanding the distributions of those exhaled. It should be noted that the collisions of droplets with the walls of the higher up respiratory tract will mean that some fractions of each size will become reattached to the mucus layer so it cannot be assumed that all droplets formed at each level will be exhaled. This means that a complete solution to this problem is inherently multiscale and that different models are likely to be necessary for the generation and transport phases of the droplet production process.

These novel observations may have implications for how respiratory illness is understood and treated. Build-up of mucus due to illness can lead to significant droplet formation once mucus thickness is greater than 100 microns. The strongest of the three newly identified mechanisms (mechanism 2) only happens in one direction, during exhaling, and therefore is likely to be critical for the removal of excess mucus in the respiratory tract. Interperson variations in respiratory anatomy may help or hinder this mechanism and point to differences in intensity of ill-effects from infections. Importantly, the multiphase modeling approach used here, which allows for natural prediction of liquid breakup, is required to realistically represent the processes observed. It is not clear why these mechanisms have not been previously reported, but the lack to date of use of such methods and the difficulties in experimental measurement within the lungs may be contributing factors.

This exploration of the basic mechanisms of droplet formation provides useful foundation for understanding this problem but several extensions of the model will in future will be needed. These include

1. Using a density ratio of air to mucus of 1000 (increased from the present 100).
2. Inclusion of a yield stress in the mucus rheology model which should increase the minimum layer thicknesses that can result in flow.
3. Consideration of a range of higher viscosities for the mucus.
4. Use of less idealized anatomical geometry and performing simulations on sequences of branches (rather than the single branch considered here).
5. Inclusion of information on infection load at each location and how this is transferred to the local mucus.

---

## Conclusions

In this chapter, we present a detailed framework and a range of examples for using physics-based modeling approaches to understand flow processes occurring within the body but still external to the body's epithelial layer (gastrointestinal and respiratory tracts). The framework couples:

- A Smoothed Particle Hydrodynamics (SPH) representation of 3D continua, which is capable of simulating dynamics interactions between solids, liquids,

and gases; fracturing and large deformations; interactions with moving and deforming boundaries; heat transfer; and phase changes.

- A Discrete Element Model (DEM) representation of particulates, which includes particle–particle and particle boundary interactions; and two-way coupling with fluids using SPH for the fluid phase.
- Flexible and deformable surfaces that can represent intestinal structures; including contraction and expansion due to muscular activity; and stretching due to pressures from constrained fluids. This enables the shape of such wall structures to be directly predicted from the force balance between fluid dynamics and wall muscle activity.
- Specialist intestinal models that include Genome-Scale Metabolic Models (GSMMs), 0D kinetic models and coupled 3D/1D/0D models that can incorporate the biology of microbes in the aforementioned regions of the body coupled with the flow simulations.

This novel framework is applied to a range of in-body examples including

1. Heat transfer, melting, and solid–liquid interactions for a chocolate on the tongue during mastication.
2. Liquid-particulate flow in the stomach, including complex gravity currents that are generated by relatively small differences in density for the gastric content.
3. Segmentation-induced advection and diffusive transport of nutrients in the small intestine for uptake at the wall, and effect of contractile waves on multiphase digesta to produce spatial changes in composition and rheology.
4. Microbial fermentation coupled to digesta flow in the colon using hierarchical models to predict SCFA production in the colon over timescales of hours.
5. Droplet generation in the respiratory tract in which three novel mechanisms for mucus droplets have been identified. These results may have strong implications for understanding respiratory disease spread and intensity of infection, such as for the SARS-CoV-2 pandemic that began in 2020.

Challenges remain in fully representing the flow processes in the body using computer simulation. Many aspects of the processes are undercharacterized *in vivo*, including mechanical characterization of soft tissue elastic properties, quantification of muscular contraction behavior during different types of digestive and respiratory movements, and chemical reaction rates. Additionally, the processes are multiscale in nature and there remain many challenges in accurately representing and then coupling the nano-, micro-, and mesoscale processes simultaneously within the constraints of current computational and algorithmic technologies. Validation of model outputs is also difficult and presents ethical issues since invasive methods are often needed to produce sufficiently detailed and accurate data for comparison. We expect that as these challenges are addressed over time the utility of the modeling framework will increase and improvements to health and body performance will result.

---

## Acknowledgments

The authors acknowledge Leif Lundin, Ingrid Appelqvist, Amy Logan, and Nich Archer for contributions of expertise in the food sciences.

---

## References

- Amemiya, K., Hisano, M., Ishida, T., & Soma, K. (2002). Relationship between the flow of bolus and occlusal condition during mastication – computer simulation based on the measurement of characteristics of the bolus. *Journal of Oral Rehabilitation*, 29, 245–256.
- Amerine, M. A., Pangborn, R. M., & Roessler, E. B. (1965). *Principles of sensory evaluation of food*. Academic Press.
- Anderson, K., Throckmorton, G. S., Buschang, P. H., & Hayasaki, H. (2002). The effects of bolus hardness on masticatory kinematics. *Journal of Oral Rehabilitation*, 29, 689–696.
- Anditi, C., Okoth, M., Muthoka, T. M., Irina, J., & Kipkosegi, M. (2013). An investigative study of diffusion of commercial aspirin (acetylsalicylic acid) in sodium. *African Journal of Education, Science and Technology*, 1(2), 185–192.
- Anwarul Hasan, M. D., Lange, C. F., & King, M. L. (2010). Effect of artificial mucus properties on the characteristics of airborne bioaerosol droplets generated during simulated coughing. *Journal of Non-newtonian Fluid Mechanics*, 165, 1431–1441.
- April Si, X., Talaat, M., & Xi, J. (2021). SARS COV-2 virus-laden droplets coughed from deep lungs: Numerical quantification in a single-path whole respiratory tract geometry. *Physics of Fluids*, 33(2), 023306.
- Arkwright, J. W., Dickson, A., Maunder, S. A., Blenman, N. G., Lim, J., O'Grady, G., Archer, R., Costa, M., Spencer, N. J., Brookes, S., & Pullan, A. (2013). The effect of luminal content and rate of occlusion on the interpretation of colonic manometry. *Neurogastroenterology and Motility*, 25(1), e52–e59.
- Batchelor, G. K. (1973). *An introduction to fluid dynamics*. Cambridge University Press.
- Brandstaeter, S., Fuchs, S. L., Aydin, R. C., & Cyron, C. J. (2019). Mechanics of the stomach: A review of an emerging field of biomechanics. *GAMM-mitteilungen*, 42, e201900001.
- Camilleri, M., Malagelada, J. R., Brown, M. L., Becker, G., & Zinsmeister, A. R. (1985). Relation between antral motility and gastric emptying of solids and liquids in humans. *American Journal of Physiology-Gastrointestinal and Liver Physiology*, 249, G580–G585.
- Cleary, P. W. (1998). Modelling confined multi-material heat and mass flows using SPH. *Applied Mathematical Modelling*, 22, 981–993.
- Cleary, P. W. (2004). Large scale industrial DEM modelling. *Engineering Computations*, 21, 169–204.
- Cleary, P. W. (2009). Industrial particle flow modelling using discrete element method. *Engineering Computations*, 26, 698–743.
- Cleary, P. W. (2010). Extension of SPH to predict feeding, freezing and defect creation in low pressure die casting. *Applied Mathematical Modelling*, 34, 3189–3201.
- Cleary, P. W. (2015). Prediction of coupled particle and fluid flows using DEM and SPH. *Minerals Engineering*, 73, 85–99.
- Cleary, P. W., Ha, J., Prakash, M., & Nguyen, T. (2010). Short shots and industrial cases studies: Understanding fluid flow and solidification in high pressure die casting. *Applied Mathematical Modelling*, 34, 2018–2033.

- Cleary, P. W., & Harrison, S. (2016). Modeling food digestion in the oral cavity. In *Reference Module in food science*. Elsevier. <https://doi.org/10.1016/B978-0-08-100596-5.03238-8>
- Cleary, P. W., & Harrison, S. M. (2019). Extension of Virtual Mouth model for prediction of oral digestion to include material property variation from moisture absorption, enzymic breakdown and melting. *Food Structures, Digestion and Health (FSDH2019) International Conference*. Rotorua NZ, 30 Sept – 3 Oct.
- Cleary, P. W., Harrison, S. M., Sinnott, M. D., Pereira, G. G., Prakash, M., Cohen, R. C. Z., Rudman, M., & Stokes, N. (2021). Application of SPH to single and multiphase geophysical, biophysical and industrial fluid flows. *International Journal of Computational Fluid Dynamics*, 35, 22–78.
- Cleary, P. W., Hilton, J. E., & Sinnott, M. D. (2017). Modelling of industrial particle and multiphase flows. *Powder Technology*, 314, 232–252.
- Cleary, P. W., & Monaghan, J. J. (1999). Conduction modelling using smoothed particle hydrodynamics. *Journal of Computational Physics*, 148, 227–264.
- Cleary, P. W., Prakash, M., Ha, J., Stokes, N., & Scott, C. (2007). Smooth particle hydrodynamics: Status and future potential. *Progress in Computational Fluid Dynamics, An International Journal*, 7, 70.
- Cleary, P. W., Sinnott, M. D., Hari, B., Bakalis, S., & Harrison, S. M. (2015). 10 - modelling food digestion. In *Modeling food processing operations, Woodhead publishing series in food science, technology and nutrition* (pp. 255–305). Woodhead Publishing.
- Cleary, P. W., Sinnott, M., & Morrison, R. (2006). Prediction of slurry transport in SAG mills using SPH fluid flow in a dynamic DEM based porous media. *Minerals Engineering*, 19, 1517–1527.
- Cleary, P. W., Thomas, D., Hetherton, L., Bolger, M., Hilton, J. E., & Watkins, D. (2020). Workspace: A workflow platform for supporting development and deployment of modeling and simulation. *Mathematics and Computers in Simulation*, 175, 25–61.
- Cohen, R. C. Z., Cleary, P. W., & Mason, B. R. (2012). Simulations of dolphin kick swimming using smoothed particle hydrodynamics. *Human Movement Science*, 31, 604–619.
- Commisso, M. S., Martínez-Reina, J., Ojeda, J., & Mayo, J. (2015). Finite element analysis of the human mastication cycle. *Journal of the Mechanical Behavior of Biomedical Materials*, 41, 23–35.
- Cremer, J., Arnoldini, M., & Hwa, T. (2017). Effect of water flow and chemical environment on microbiota growth and composition in the human colon. *Proceedings of the National Academy of Sciences*, 114, 6438–6443.
- Cummins, S., & Cleary, P. W. (2011). Using distributed contacts in DEM. *Applied Mathematical Modelling*, 35, 1904–1914.
- Cummins, S., Cleary, P. W., Delaney, G., Phua, A., Sinnott, M., Gunasegaram, D., & Davies, C. (2021). A coupled DEM/SPH computational model to simulate Microstructure evolution in Ti-6Al-4V laser powder bed Fusion processes. *Metals*, 11, 858.
- Cummins, S. J., Silvester, T. B., & Cleary, P. W. (2012). Three-dimensional wave impact on a rigid structure using smoothed particle hydrodynamics. *International Journal for Numerical Methods in Fluids*, 68, 1471–1496.
- Cundall, P. A., & Strack, O. D. (1979). A discrete numerical model for granular assemblies. *Geotechnique*, 29(1), 47–65.
- Dejak, B., Młotkowski, A., & Romanowicz, M. (2003). Finite element analysis of stresses in molars during clenching and mastication. *The Journal of Prosthetic Dentistry*, 90, 591–597.

- Dent, J., Deloose, E., Dinning, P., Corsetti, M., Rommel, N., Tack, J., Wiklendt, L., Papageorgiou, A. W., & Arkwright, J. W. (2020). Manometric demonstration of duodenal/jejunal motor function consistent with the duodenal brake mechanism. *Neurogastroenterology and Motility*, 32(10), e13835.
- Dinning, P. G., Wiklendt, L., Maslen, L., Gibbins, I., Patton, V., Arkwright, J. W., Lubowski, D. Z., O'Grady, G., Bampton, P. A., Brookes, S. J., & Costa, M. (2014). Quantification of in vivo colonic motor patterns in healthy humans before and after a meal revealed by high-resolution fiber-optic manometry. *Neurogastroenterology and Motility*, 26(10), 1443–1457.
- Ferrua, M. J., & Singh, R. P. (2010). Modeling the fluid dynamics in a human stomach to Gain insight of food digestion. *Journal of Food Science*, 75, R151–R162.
- Ferrua, M. J., & Singh, R. P. (2011). Understanding the fluid dynamics of gastric digestion using computational modeling. *Procedia Food Science*, 11th International Congress on Engineering and Food (ICEF11), 1, 1465–1472.
- Fischer, U., Boulton, R. B., & Noble, A. C. (1994). Physiological factors contributing to the variability of sensory assessments: Relationship between salivary flow rate and temporal perception of gustatory stimuli. *Food Quality and Preference, Special Issue: Advances in Sensory Food Science – Rose Marie Pangborn Memorial Symposium*.
- Grider, J. R. (2003). Reciprocal activity of longitudinal and circular muscle during intestinal peristaltic reflex. *American Journal of Physiology-Gastrointestinal and Liver Physiology*, 284(5), G768–G775, 5, 55–64.
- Guo, Y., Wei, J., Ou, C., Liu, L., Sadrizadeh, S., Jin, T., Tang, L., Zhang, Y., & Li, Y. (2020). Deposition of droplets from the trachea or bronchus in the respiratory tract during exhalation: A steady-state numerical investigation. *Aerosol Science and Technology*, 54, 869–879.
- Hampton, T., Armstrong, S., & Russell, W. J. (2000). Estimating the diameter of the left main bronchus. *Anaesthesia and Intensive Care*, 28(5), 540–542.
- Hardacre, A. K., Lente, R. G., Yap, S. Y., & Monro, J. A. (2018). Predicting the viscosity of digesta from the physical characteristics of particle suspensions using existing rheological models. *Journal of The Royal Society Interface*, 15, 20180092.
- Hardacre, A. K., Yap, S. Y., Lente, R. G., & Monro, J. A. (2015). The effect of fibre and gelatinised starch type on amylolysis and apparent viscosity during in vitro digestion at a physiological shear rate. *Carbohydrate Polymers*, 123, 80–88.
- Harrison, S. M., & Cleary, P. W. (2014). Towards modelling of fluid flow and food breakage by the teeth in the oral cavity using smoothed particle hydrodynamics (SPH). *The Journal of European Food and Research Technology*, 238, 185–215.
- Harrison, S. M., Cleary, P. W., Eyres, G., Sinnott, M. D., & Lundin, L. (2014). Challenges in computational modelling of food breakdown and flavour release. *Food and Function*, 5(11), 2792–2805.
- Harrison, S. M., Cleary, P. W., & Sinnott, M. D. (2018). Investigating mixing and emptying for aqueous liquid content from the stomach using a coupled biomechanical-SPH model. *Food and Function*, 9(6), 3202–3219.
- Harrison, S. M., Eyres, G., Cleary, P. W., Sinnott, M. D., Delahunty, C., & Lundin, L. (2014). Computational modelling of food oral breakdown using smoothed particle hydrodynamics. *Journal of Texture Studies*, 45, 97–109.
- Hebden, J. M., Blackshaw, P. E., Perkins, A. C., D'Amato, M., & Spiller, R. C. (1998). Small bowel transit of a bran meal residue in humans: Sieving of solids from liquids and response to feeding. *Gut*, 42(5), 685–689.

- Heyder, J. (2004). Deposition of inhaled particles in the human respiratory tract and consequences for regional Targeting in respiratory drug delivery. *Proceedings of the American Thoracoc Society*, 1, 315–320.
- Hiiemae, K. M., & Palmer, J. B. (2003). Tongue movements in feeding and speech. *Critical Reviews in Oral Biology & Medicine*, 14, 413–429.
- Hoebler, C., Devaux, M. F., Karinthi, A., Belleville, C., & Barry, J. L. (2000). Particle size of solid food after human mastication and in vitro simulation of oral breakdown. *International Journal of Food Sciences and Nutrition*, 51, 353–366.
- Imai, Y., Kobayashi, I., Ishida, S., Ishikawa, T., Buist, M., & Yamaguchi, T. (2013). Antral recirculation in the stomach during gastric mixing. *American Journal of Physiology-Gastrointestinal and Liver Physiology*, 304, G536–G542.
- Ishikawa, T., Sato, T., Mohit, G., Imai, Y., & Yamaguchi, T. (2011). Transport phenomena of microbial flora in the small intestine with peristalsis. *Journal of Theoretical Biology*, 279(1), 63–73.
- Jalabert-Malbos, M. L., Mishellany-Dutour, A., Woda, A., & Peyron, M. A. (2007). Particle size distribution in the food bolus after mastication of natural foods. *Food Quality and Preference*, 18, 803–812.
- Karamaoun, C., Sobac, B., Mauroy, B., Van Muylem, A., & Haut, B. (2018). New insights into the mechanisms controlling the bronchial mucus balance. *PloS One*, 13(6), e0199319.
- Karthikeyan, J. S., Salvi, D., & Karwe, M. V. (2021). Modeling of fluid flow, carbohydrate digestion, and glucose absorption in human small intestine. *Journal of Food Engineering*, 292, 110339.
- Kavan, L., Collins, S., Žára, J., & O'Sullivan, C. (2008). Geometric skinning with approximate dual quaternion blending. *ACM Transactions on Graphics (TOG)*, 27(4), 1–23.
- Kavan, L., Collins, S., Zara, J., & O'Sullivan, C. (2008). Geometric skinning with approximate dual quaternion blending. *ACM T Graphic*, 27, 1–23. Article 105.
- King, M., Brock, G., & Lundell, C. (1985). Clearance of mucus by simulated cough. *Journal of Applied Physiology*, 58, 1776–1782.
- Koliandris, A., Lee, A., Ferry, A. L., Hill, S., & Mitchell, J. (2008). Relationship between structure of hydrocolloid gels and solutions and flavour release. *Food Hydrocolloids*, 22, 623–630.
- Labarthe, S., Polizzi, B., Phan, T., Goudon, T., Ribot, M., & Laroche, B. (2019). A mathematical model to investigate the key drivers of the biogeography of the colon microbiota. *Journal of Theoretical Biology*, 462, 552–581.
- Labbe, D., Schlich, P., Pineau, N., Gilbert, F., & Martin, N. (2009). Temporal dominance of sensations and sensory profiling: A comparative study. *Food Quality and Preference*, 20, 216–221.
- Lai, S. K., Wang, Y. Y., Wirtz, D., & Hanes, J. (2009). Micro- and macrorheology of mucus. *Advanced Drug Delivery Reviews*, 61, 86–100.
- Lamichhane, S., Sen, P., Dickens, A. M., Hyötyläinen, T., & Orešić, M. (2018). An overview of metabolomics data analysis: Current tools and future perspectives. *Comprehensive Analytical Chemistry*, 82, 387–413.
- Lentle, R. G., Hemar, Y., Hall, C. E., & Stafford, K. J. (2005). Periodic fluid extrusion and models of digesta mixing in the intestine of a herbivore, the common brushtail possum (*Trichosurus vulpecula*). *Journal of Comparative Physiology B*, 175(5), 337–347.
- Lentle, R. G., & Janssen, P. W. M. (2008). Physical characteristics of digesta and their influence on flow and mixing in the mammalian intestine: A review. *Journal of Comparative Physiology B*, 178(6), 673–690.

- Li, C., Xiao, J., Chen, X. D., & Jin, Y. (2021). Mixing and emptying of gastric contents in human-stomach: A numerical study. *Journal of Biomechanics*, 118, 110293.
- Li, Y. W., Yu, Y. J., Fei, F., Zheng, M. Y., & Zhang, S. W. (2019). High-resolution colonic manometry and its clinical application in patients with colonic dysmotility: A review. *World Journal of Clinical Cases*, 7(18), 2675.
- Lucas, P. W., & Luke, D. A. (1983). Computer simulation of the breakdown of carrot particles during human mastication. *Archives of Oral Biology*, 28, 821–826.
- Lust, R. M. (2007). In S. J. Enna, & D. B. Bylund (Eds.), *The pulmonary system, xPharm: The Comprehensive Pharmacology Reference* (pp. 1–6).
- Mackie, A., Bajka, B., & Rigby, N. (2016). Roles for dietary fibre in the upper GI tract: The importance of viscosity. *Food Research International*, 88, 234–238.
- Mao, N., An, C. K., Guo, L. Y., Wang, M., Guo, L., Guo, S. R., & Long, E. S. (2020). Transmission risk of infectious droplets in physical spreading process at different times: A review. *Building and Environment*, 185, 107307.
- Marciani, L., Gowland, P. A., Spiller, R. C., Manoj, P., Moore, R. J., Young, P., & Fillery-Travis, A. J. (2001). Effect of meal viscosity and nutrients on satiety, intragastric dilution, and emptying assessed by MRI. *American Journal of Physiology-Gastrointestinal and Liver Physiology*, 280(6), G1227–G1233.
- Miyagawa, T., Imai, Y., Ishida, S., & Ishikawa, T. (2016). Relationship between gastric motility and liquid mixing in the stomach. *American Journal of Physiology-Gastrointestinal and Liver Physiology*, 311, G1114–G1121.
- Monaghan, J. J. (1992). Smoothed particle hydrodynamics. *Annual Review of Astronomy and Astrophysics*, 30, 543–574.
- Monaghan, J. J. (1994). Simulating free surface flows with SPH. *Journal of Computational Physics*, 110, 399–406.
- Monaghan, J. J. (2005). Smoothed particle hydrodynamics. *Reports on Progress in Physics*, 68, 1703.
- Monaghan, J. J. (2012). Smoothed particle hydrodynamics and its diverse applications. *Annual Review of Fluid Mechanics*, 44, 323–346.
- Moorthy, A. S., Brooks, S. P., Kalmokoff, M., & Eberl, H. J. (2015). A spatially continuous model of carbohydrate digestion and transport processes in the colon. *PloS One*, 10, e0145309.
- Morawska, L. J., Johnson, G. R., Ristovski, Z. D., Hargreaves, M., Mengersen, K., Corbett, S., Chao, C. Y. H., Li, Y., & Katoshevski, D. (2009). Size distribution and sites of origin of droplets expelled from the human respiratory tract during expiratory activities. *Journal of Aerosol Science*, 40(3), 256–269.
- Moxon, T. E., Gouseti, O., & Bakalis, S. (2016). In silico modelling of mass transfer & absorption in the human gut. *Journal of Food Engineering*, 176, 110–120.
- Moxon, T. E., Nimmegeers, P., Telen, D., Fryer, P. J., Van Impe, J., & Bakalis, S. (2017). Effect of chyme viscosity and nutrient feedback mechanism on gastric emptying. *Chemical Engineering Science*, 171, 318–330.
- Mueller, S., Llewellyn, E. W., & Mader, H. M. (2010). The rheology of suspensions of solid particles. *Proceedings of the Royal Society A: Mathematical, Physical and Engineering Sciences*, 466, 1201–1228.
- Muñoz-Tamayo, R., Laroche, B., Walter, E., Doré, J., & Leclerc, M. (2010). Mathematical modelling of carbohydrate degradation by human colonic microbiota. *Journal of Theoretical Biology*, 266, 189–201.
- Neyraud, E., Heinzerling, C. I., Bult, J. H. F., Mesmin, C., & Dransfield, E. (2009). Effects of different tastants on Parotid saliva flow and composition. *Chemosensory Perception*, 2, 108–116.

- Nicas, M., Nazaroff, W. W., & Hubbard, A. (2005). Toward understanding the risk of secondary airborne infection: Emission of respirable pathogens. *Journal of Occupational and Environmental Hygiene*, 2(3), 143–154.
- Pal, A., Indreshkumar, K., Schwizer, W., Abrahamsson, B., Fried, M., & Brasseur, J. G. (2004). Gastric flow and mixing studied using computer simulation. *Proceedings of the Royal Society of London. Series B: Biological Sciences*, 271, 2587–2594.
- Palmer, J. B., Hiiemae, K. M., & Liu, J. (1997). Tongue-jaw linkages in human feeding: A preliminary videofluorographic study. *Archives of Oral Biology*, 42, 429–441.
- Pourhashem, H., Owen, M. P., Castro, N. D., & Rostami, A. A. (2020). Eulerian modeling of aerosol transport and deposition in respiratory tract under thermodynamic equilibrium condition. *Journal of Aerosol Science*, 141, 105501.
- Ren, S., Li, W., Wang, L., Shi, Y., Cai, M., Hao, L., Luo, Z., Niu, J., Xu, W., & Luo, Z. (2020). Numerical analysis of airway mucus clearance effectiveness using assisted coughing techniques. *Scientific Reports*, 10, 2030.
- Ren, S., Shi, Y., Cai, M., Zhoa, H., Zhang, Z., & Zhang, X. D. (2018). ANSYS-MATLAB co-simulation of mucus flow distribution and clearance effectiveness of a new simulated cough device. *Numerical Methods in Biomedical Engineering*, 34, e2978.
- Rosendale, D. I., Vetharaniam, I., Kelly, W. J., Upsdell, M., Cookson, A. L., & Roy, N. (2017). A case study: Using microbial abundance data to mathematically calculate organic acid production by human faecal microbiota within an in vitro batch fermentation. *Bioactive Carbohydrates and Dietary Fibre*, 9, 28–38.
- Rowden, A. (2021). What is a normal respiratory rate based on your age?. *Medical News Today*. <https://www.medicalnewstoday.com/articles/324409#summary-table>.
- Schütt, M., Stamatopoulos, K., Batchelor, H. K., Simmons, M. J., & Alexiadis, A. (2021). Modelling and simulation of the drug release from a solid dosage form in the human ascending colon: The influence of different motility patterns and fluid viscosities. *Pharmaceutics*, 13, 859.
- Schütt, M., Stamatopoulos, K., Simmons, M. J. H., Batchelor, H. K., & Alexiadis, A. (2020). Modelling and simulation of the hydrodynamics and mixing profiles in the human proximal colon using discrete multiphysics. *Computers in Biology and Medicine*, 121, 103819.
- Sekirov, I., Russell, S. L., Antunes, L. C., & Finlay, B. B. (2010). Gut microbiota in health and disease. *Physiological Reviews*, 90, 859–904.
- Sims, D. E., & Horne, M. M. (1997). Heterogeneity of the composition and thickness of tracheal mucus in rats. *Am. J. Physiol.*, 273, L1036–L1041.
- Singh, S., & Singh, R. P. (2011). Gastric digestion of foods: Mathematical modeling of flow field in a human stomach. In J. M. Aguilera, R. Simpson, J. Welti-Chanes, D. Bermudez-Aguirre, & G. Barbosa-Canovas (Eds.), *Food interfaces, food engineering series* (pp. 99–117). Springer.
- Sinnott, M. D., Cleary, P. W., Arkwright, J. W., & Dinning, P. G. (2012). Investigating the relationships between peristaltic contraction and fluid transport in the human colon using smoothed particle hydrodynamics. *Computers in Biology and Medicine*, 42, 492–503.
- Sinnott, M. D., Cleary, P. W., & Harrison, S. M. (2017). Peristaltic transport of a particulate suspension in the small intestine. *Applied Mathematical Modelling*, 44, 143–159.
- Sinnott, M. D., Harrison, S. M., & Cleary, P. W. (2021). A particle-based modelling approach to food processing operations. *Food and Bioproducts Processing*, 127, 14–57.
- Skamniotis, C. G., Elliott, M., & Charalambides, M. N. (2019). Computer simulations of food oral processing to engineer teeth cleaning. *Nature Communications*, 10(1), 1–12.

- Sura, L., Madhavan, A., Carnaby, G., & Crary, M. A. (2012). Dysphagia in the elderly: Management and nutritional considerations. *Clinical Interventions in Aging*, 7, 287–298.
- Thornton, C., Cummins, S. J., & Cleary, P. W. (2013). An investigation of the comparative behaviour of alternative contact force models during inelastic collisions. *Powder Technology*, 233, 30–46.
- Tilley, A. E., Walters, M. S., Shaykhiev, R., & Crystal, R. G. (2015). Cilia dysfunction in lung disease. *Annual Review of Physiology*, 77, 379–406.
- Trusov, P. V., Zaitseva, N. V., & Kamaltdinov, M. R. (2016). A multiphase flow in the antro-duodenal portion of the gastrointestinal tract: A mathematical model. *Computational and Mathematical Methods in Medicine*, 2016, Article ID 5164029.
- Vadivukkarasan, M., Dhivyaraja, K., & Panchagnula, M. V. (2020). Breakup morphology of expelled respiratory liquid: From the perspective of hydrodynamic instabilities. *Physics of Fluids*, 32(9), 094101.
- Van Der Bilt, A., Van Der Glas, H. W., & Bosman, F. (1992). A computer simulation of the influence of selection and breakage of food on the chewing efficiency of human mastication. *Journal of Dental Research*, 71, 458–465.
- Van Der Glas, H. W., Van Der Bilt, A., Olthoff, L. W., & Bosman, F. (1987). Measurement of selection chances and breakage functions during chewing in man. *Journal of Dental Research*, 66, 1547–1550.
- Vyas, D. R., Cummins, S. C., Delaney, G. W., Rudman, M., Cleary, P. W., & Khakhar, D. V. (2022). Elastoplastic frictional collisions with Collisional-SPH. *Tribology International*, 168, 107438.
- Vyas, D. R., Cummins, S. C., Rudman, M., Cleary, P. W., Delaney, G., & Khakhar, D. V. (2021). Collisional SPH: A method to model frictional collisions with SPH. *Applied Mathematical Modelling*, 94, 13–35.
- Wei, J., Guo, Y., Lei, H., Wang, L., Jin, T., & Tang, L. (2020). Numerical simulation of viral droplet sources in the respiratory tract. *Chinese Science Bulletin*, 66, 486–492.
- Wei, J., & Li, Y. (2016). Airborne spread of infectious agents in the indoor environment. *American Journal of Infection Control*, 44(9), S102–S108.
- Wells, W. F. (1955). *Airborne contagion and air hygiene. An ecological study of droplet infections*. Harvard University press (for the Commonwealth Fund), Geoffrey Cumberlege, Oxford University Press.
- Wiersinga, W. J., Rhodes, A., Cheng, A. C., Peacock, S. J., & Prescott, H. C. (2020). Pathophysiology, transmission, diagnosis, and treatment of coronavirus disease 2019 (COVID-19): A review. *JAMA*, 324, 782–793.
- Workspace. <https://research.csiro.au/workspace/>. (n.d.).
- Xue, Z., Ferrua, M. J., & Singh, P. (2012). Computational fluid dynamics modeling of granular flow in human stomach. *Alimentos Hoy*, 21, 3–14.
- Xu, Z., Shi, L., Wang, Y., Zhang, J., Huang, L., Zhang, C., Liu, S., Zhao, P., Liu, H., Zhu, L., Tai, Y., Bai, C., Gao, T., Song, J., Xia, P., Dong, J., Zhao, J., & Wang, F. S. (2020). Pathological findings of COVID-19 associated with acute respiratory distress syndrome. *The Lancet Respiratory Medicine*, 8, 420–422.
- Zhou, M., & Zou, J. (2021). A dynamical overview of droplets in the transmission of respiratory infectious diseases. *Physics of Fluids*, 33, 031301.
- Zhu, S., Kato, S., & Yang, J. H. (2006). Study on transport characteristics of saliva droplets produced by coughing in a calm indoor environment. *Building and Environment*, 41, 1691–1702.

# Digital modeling of the jaws for the evaluation of mandibular reconstruction techniques

# 18

Raymond Chung Wen Wong<sup>1,2</sup>, Somasundaram Prasad<sup>1</sup>, Timothy Jie Han Sng<sup>1</sup>,  
Vaishnavi Ratheesh<sup>1,3,4</sup>

<sup>1</sup>Discipline of Oral and Maxillofacial Surgery, Faculty of Dentistry, National University of Singapore, Singapore, Singapore; <sup>2</sup>National University of Singapore, Oral and Maxillofacial Surgery, Faculty of Dentistry, Oral and Maxillofacial Surgery, National University Centre for Oral Health, Singapore, Singapore; <sup>3</sup>National University Centre for Oral Health, Singapore, Singapore;  
<sup>4</sup>Faculty of Dentistry, Singapore, Singapore

## Chapter outline

Introduction.....	425
Anatomy and biomechanics of the mandible .....	427
The finite element method .....	429
Performing finite element analysis of the mandible.....	429
Alloplastic mandibular reconstruction methods: evaluating the implant design using finite element analysis .....	430
Computer-aided design of mandibular models.....	432
Design and plan of endoprostheses.....	432
Stress and magnitude of displacement of stem and wing design in unilateral loading conditions .....	433
Conclusion .....	437
References .....	438

## Introduction

Mandible defects can occur due to trauma, oncological ablation, or infection causing severe bone loss. A defect that affects the entire thickness of the mandible is called a segmental defect (Chanchareonsook, Tideman, et al., 2014). An unrepaired mandibular defect can lead to:

1. contraction of the remaining soft tissues leading to a poor occlusion caused by muscle pull,
2. dental arch collapse leading to difficulties in chewing and asymmetry,

3. poor esthetics commonly referred to as the Andy Gump defect, and
4. problems with swallowing and speech, affecting quality of life (Wong et al., 2010).

A segmental defect of the mandible comes with its attendant problem of consideration of the biomechanics acting on the mandible, which if not taken into account, causes failure of the reconstruction (Wong, Tideman, et al., 2011).

Various methods for mandibular reconstruction have been tried, many unsuccessful due to many factors but a prime reason is not respecting the biomechanics involved. Among these methods have been

1. using soft tissue flaps only;
2. autogenous free bone grafts;
3. reconstruction/bridging plate only;
4. cancellous bone contained in titanium mesh;
5. vascularized free bone flaps;
6. bone transport distraction osteogenesis; and
7. newer methods like the endoprosthesis or alloplastic replacement in the form of a customized prosthesis which may be combined with tissue engineered bone scaffold for complete regeneration (Wong et al., 2012b) and (Wong et al., 2012a).

Despite the advances in technology, mandibular reconstruction is still challenging. The current gold standard is to use a vascularized bone flap (Wong, Lee, et al., 2011). This requires borrowing bone and accompanying soft tissues from a separate site of the body, harvesting it with its own blood supply and comes with significant morbidity and extension of operating time (Prasad et al., 2020). As a result, fully alloplastic (synthetic) mandibular reconstruction has been investigated in an effort to reduce the morbidity. This method is lending itself to being able to be customized, is economical, and there is no need for prolonged rehabilitation (Prasad et al., 2020). Tissue-engineered scaffolds using cell-based and non-cell-based therapies have been shown to be able to regenerate bone but the ability to withstand the complex forces acting on the mandible for a segmental defect is still unproven. Many studies have combined the use of tissue-engineered scaffolds with some form of mandibular plate or a prosthesis in order to get around the poor material strength of the scaffold (Puleo & Nanci, 1999).

By understanding the stress and strains of different methods of reconstruction, we can then predict how it will perform. This method of looking at the mechanics first would then allow us to design and overengineer any implants in the form of osteosynthesis plates or a customized prosthesis before its use in humans (Vollmer et al., 2000). The study of the stress and strains in different parts of the mandible is easiest done using computational modeling of the mandible in the form of a finite element analysis. In order to be able to perform finite element analysis for this purpose, we first have to understand

1. the anatomy and biomechanics of the mandible;
2. finite element analysis—what is it and the steps needed and we will then consider some studies that have been done evaluating several alloplastic designs.

---

## Anatomy and biomechanics of the mandible

The human skeleton can be divided into the appendicular and axial skeleton. Appendicular bones comprises the bones of the upper and lower limbs and includes the shoulder and pelvic girdles. Axial bones are the bones that make up the central support (long axis of the body) like the vertebral bones and the mandible falls into this category ([Schubert et al., 1997](#)).

The mandible is the only load-bearing moveable bone of the skull, has a U-shape, and is connected at the temporomandibular joints at both ends to the skull ([Walker & MacLeod, 2017](#)). It consists of a body, the symphysis connecting the right and left in the midline, the alveolar process with bone supporting the dentition, proximal to the skull the ramus process with a turn in the direction at the angles and ends in the condylar and coronoid processes ([Hylander, 2006](#)), ([Flanagan & Metzger, 2011](#)), and ([Reagle & Rhue, 2011](#)).

The muscles that move the mandible are mainly the muscles of mastication, namely the lateral and medial pterygoids, masseter and temporalis muscles; there are accessory muscles of mastication which has some effect in moving the mandible in conjunction with swallowing and mouth opening, namely the suprathyroid muscles (mylohyoid, geniohyoid, hyoglossus, digastric muscles) ([Wong, Tideman, et al., 2011](#)), ([Hylander, 2006](#)) and ([Van Eijden, 2000](#)). The connection to the skull is at the temporomandibular joints ([Werner et al., 1991](#)). The temporomandibular joint is a ginglymo-arthrodial joint (of which there is only one other joint in the body that is similar, i.e., the sterno-clavicular joint) and is made up of two joint spaces, namely the superior and inferior joint spaces ([Werner et al., 1991](#)), ([Silveira et al., 2021](#)) and ([Domenyuk et al., 2020](#)). These spaces are surrounded by a joint capsule and are separated by a fibrocartilage termed the articular cartilage. The joint action is made up of two separate movements:

- (a) Phase I, which is a hinge rotation for the first 20 mm followed by
- (b) Phase 2, a translational forward movement caused by the pull of the lateral pterygoid muscle, pulling the condylar neck out of the glenoid fossa ([Alomar et al., 2007](#)) and ([Behzadi et al., 2020](#)). Thus, this means that the joint has a hinge and a rotational component and most of the forces are borne by the teeth, which is then transmitted to the bone and minimal forces are borne by the actual joint itself ([Domenyuk et al., 2020](#)).

The mandible, functioning as a Class III lever, experiences tension on the upper part of the alveolar bone and compressive forces on the lower border during function. Further back, at the region of the ramus/condyle, compressive forces act at the posterior border of the condyle with corresponding tension in the anterior ramus.

In the midline, the mandibular symphysis connects both ends of the mandible and due to the effects of the muscle pull, goes through three distinct types of deformation:

1. corporal rotation (relative outward rotation of the right and left halves of the mandible);
2. medial convergence (narrowing and widening of the mandible on function); and
3. dorsoventral shear (both mandibular halves moving in the vertical plane relative to each other) (Wong et al., 2010).

During function, the mandible undergoes deformation. It experiences differences in the magnitude of deformation between the outer and inner surfaces, caused by the U-shaped. Bending occurs in the lateral and transverse plane with the maximum bending happens around the symphysis. This bending produces compressive and tensile stresses at the buccal and lingual cortices, respectively (Panagiotopoulou et al., 2020) and (Shu et al., 2021).

How then do we utilize this information about the mandibular biomechanics? In the application of osteosynthesis for mandibular reconstruction, the forces and dimensional changes need to be accounted. In trauma, there is the ideal line of internal fixation of Champy, for the application of load sharing fixation plates. Placement of plates in the area between tension and compression will allow for cross buttressing of the bone fragments to help stabilize the mobile segments (Beltrán-Fernández et al., 2021) and (Saito & Murr, 2008), Fig. 18.1.

In instances of bone comminution or with a segmental defect where there is no longer the ability for cross buttressing and the mandible moves independently on each side depending on the muscle pull, we are then needed to use load-bearing plates and are dependent on the material strength and bulk of the plate to neutralize

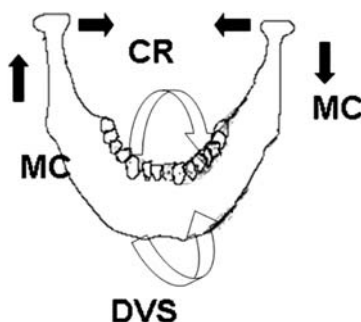


**FIGURE 18.1**

Forces acting about the midline of the mandible. CR, Corporal Rotation; MC, Medial Convergence; DVS, Dorsoventral Shear.

Modified from Wong, R. C. W., Tideman, H., Kin, L., & Merkx, M. A. W. (2010). Biomechanics of mandibular reconstruction: a review. *International Journal of Oral and Maxillofacial Surgery*, 39(4), 313e319. <https://doi.org/10.1016/j.ijom.2009.11.003>.

the forces to hold the mandible in one single piece. The forces acting around the symphysis may lead to fracture of the plate should one apply a plate that is not thick enough or cause loosening of the screw from the plate, leading to the development and use of locking screws and plates to neutralize the forces (Arya et al., 2020) and (Pandey & Kumar, 2021).

---

## The finite element method

Finite element analysis is a mathematical method to look at the stress and strain distribution in a rigid body undergoing deformation. It consists of dividing an object into smaller elements, which are connected at the boundaries, loads applied to it, and the forces mathematically solved. With the advent of computers, the calculations are easier to solve and models can be created for complex shapes (Hughes, 2012).

A very accurate model replicating the real-life complexities of the actual mandible is difficult to create and would need the computing power equal to several supercomputers to solve the calculations needed to account for all variables. Assumptions are commonly made to simplify the model in order to reduce the computing power needed. The key is to ensure that the assumptions made to simplify calculations are valid and that the models created are accurate.

Accurate models have, however, been created by previous authors, each incorporating different levels of complexity (Hughes, 2012).

## Performing finite element analysis of the mandible

There are several steps involved in creating a finite element model for a mandible. The first step is to obtain the 3D mesh of the mandible. Information is needed about the complex geometry of the mandible, and it can be obtained by (1) drawing a digital representation of the mandible; (2) converting digitized slices of a mandible into a whole 3D structure and the most commonly used method is to obtain the information from three-dimensional scans from Computer Tomographic (CT) or Cone Beam CT scans. The information will need to be converted from DICOM format (Digitised Communication in Medicine) into a 3D structure in STL (Standard Tessellation Language). This information can then be changed into a mesh using many available software programs (Caragiuli et al., 2021) and (Talarico, 2020). The 3D mesh is further subdivided into a number of discrete, finite elements which are simpler smaller shapes within the overall 3D shape. These elements are joined at the nodes. Most software with finite element function has to automatically generate relatively dense meshes that can be refined further (Jung et al., 2020), (Liu et al., 2017) and (Liu et al., 2018).

The material properties of the elements then need to be defined for the software. These values are generally available in the literature. Although the mandible consists of both cortical and cancellous bone, with the dentition connected with periodontal

ligaments to the alveolar bone, assumptions have to be made to simplify the calculations and reduce the computing power needed. These assumptions are as follows: (1) although the mandible is known to be anisotropic (material properties differ in differing dimensions), the mandible is assumed to be solely cortical bone and (2) the teeth are assumed to be perfectly bonded to the bone with no movement possible (i.e., ankylosed). Many previous studies have been done showing that models created with such assumptions are accurate enough to study the forces acting on the mandible (Caragiuli et al., 2021; Talarico, 2020; Jung et al., 2020).

The many individual elements or units are bound together at the nodes using boundary conditions so that the model can have loads placed at defined points and undergo deformation as a single rigid structure, allowing computations to be performed. These boundary conditions are divided into (1) essential boundary conditions meaning displacement constraints used to anchor the model, and (2) non-essential boundary conditions, which are defined as the loading force used on the model. The insertion, direction, and forces for each muscle of mastication need to be put in and this information is widely available in the literature. Again, for the purposes of simplification, only the major muscles of mastication are commonly taken into account.

Using available computer software and with input of the previous information, the model can then be mathematically calculated to obtain the displacements and the resulting stress and strain distribution. As the loading force is usually known, the information sought for such biomechanical models are often that of the stresses and strains. The last, most important step is to validate the created model to ensure the precision and accuracy. Precision can be gauged with a convergence test by creating meshes of different refinements and comparing the stress/strains at specific locations. Many studies have been published using precision as a measure to validate the created model.

---

### Alloplastic mandibular reconstruction methods: evaluating the implant design using finite element analysis

Several alloplastic designs have been studied for segmental mandibular reconstruction. The mandibular modular endoprosthesis was studied by Tideman et al. (Lee et al., 2008) in 2008 as a possible paradigm shift in mandibular reconstruction in moving away from using natural tissues like bone and soft tissues. This was inspired by the tremendous success seen in the field of musculoskeletal surgery where endoprostheses in stock, modular form is used to reduce the overall costs of fabrication, leading to cheaper surgical replacements (Lee et al., 2008) and (Malawer & Sugarbaker, 2001). The mandibular modular endoprosthesis went through several generations in design. There were two separate areas studied: (1) segmental mandibular defects and (2) defects including the ramus/condyle on one side. No attempts were made to make designs crossing the mandibular symphysis due to the already

well-known difficulties encountered for such defects and the unsolved solution to navigating the curvature of the mandible. Segmental defects and that involving the ramus/condyle tended to be in a straighter part of the mandible (Madsen & Haug, 2006).

Studies performed in pigs and macaque monkeys revealed numerous problems associated with loosening of the module connection for the segmental defects and no problems were seen for replacement of the ramus/condyles. This was consistent with the success encountered clinically with temporomandibular joint prostheses. It was postulated that the stresses could be dissipated in a defect ending in a joint, whereas these stresses would lead to eventual loosening of any module connection (Goh, Lee, Tideman, & Stoelinga, 2009; Goh, Lee, Tideman, Jansen, & Stoelinga, 2009; Lee, Goh, Lai, et al., 2009; Lee, Goh, Tideman, et al., 2009).

In the research, the structure and design of the endoprosthesis were adjusted and researched further utilizing finite element component and mechanical testing. Different variations were made to the stem of the endoprosthesis and deformity length to work with the assessment of changes in applied loads. As indicated by the outcomes, an expansion in deformity length caused an inclination for twisting at the stem and the module association. Moreover, a decline in stem length prompted insignificant contrasts barring a slight increase in magnitude. The endoprosthesis with stems fixed tightly to the mandibular stumps had been created up to the clinical preliminary stage (Lee, Goh, Tideman, et al., 2009).

Materials supported for alloplastic mandible reproduction are nonresorbable titanium compounds (TiAl6V4), possibly encouraging resorbable platform material, for example, polycaprolactone (PCL) alone or in mix with different materials (Chanchareonsook, Tideman, et al., 2014), (Chanchareonsook, Junker, et al., 2014) and magnesium (Mg) and its combinations (Prasad et al., 2019). Titanium and its combinations appear to have the longest history of utilization, especially as a solitary remaking plate crossing over a deformity, which, nonetheless, presents the best extent of issues as loosened up plates and screws (Wong et al., 2012a). Chanchareonsook et al. (Chanchareonsook, Junker, et al., 2014) had explored PCL beforehand in a mandibular endoprosthesis in blend with development factors, for example, recombinant human bone morphogenetic protein and beta fibroblastic development factor in a transporter. What's more, PCL has been applied either alone or in blend with different materials; be that as it may, it is yet to be applied clinically in segmental mandibular imperfections because of its strength concerns. Albeit the use of Mg and its combinations is promising, their utilization has been limited to a great extent to the research space.

Various plans have been upheld for and are applied presently for segmental mandibular deformities. The plans could be isolated into endoprosthetic (interior association) and extra prosthetic as a plate with “wings” or an enormous bone plate (Prasad et al., 2020). As of now, in clinical settings, the plate with wing configuration has been received by organizations for patient-explicit plans dependent on titanium composite, with the chance of adding cancellous bone or development factors whenever required.

The plans of reconstructive equipment assume a significant part in the life span of an endoprosthesis since stress focuses can create in basic regions prompting possible disappointment. It stays hazy which configuration better disperses such pressure. The point of the current examination was to research two distinct plans presently being utilized for mandibular segmental recreation utilizing limited component investigation as a device for inspecting the pressure fixations all through the reproduction, and construing the potential for progress and disappointment dependent on the greatest pressure focuses versus the properties of two materials right now being utilized including titanium composite and PCL. The aftereffects of the current investigation would control the determination of the ideal plans in future examinations and in the improvement of novel materials for in vivo and clinical use.

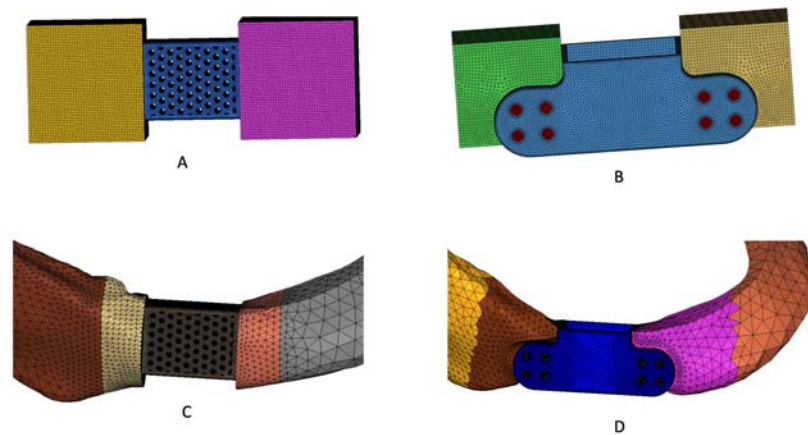
### Computer-aided design of mandibular models

The mandible morphology should be set up utilizing processed tomography pictures of a patient who was anonymized. The stereolithography picture designs needed to be gotten from the Advanced Imaging and Correspondences in Medication design. The anomalies and sharp components render the models inadmissible for limited component examination. Hence, the models should recoincede with 3-mati (V8.0) (Emerge, Leuven, Belgium) to make them more normal. To legitimize the computational assets, direct tetrahedrons (C3D4-four hub tetrahedral components) should be utilized to work the mandible to make it satisfactorily thick for limited component investigation. Since the primary request tetrahedral cross section effectively makes the design more unbending, it is smarter to address the test utilizing the specific decrease strategy with hub pivot during examination.

---

### Design and plan of endoprostheses

The endoprosthesis can be planned with a rectangular diagram. There are various designs of endoprosthesis. The most common are the stem and the wing designs. Prasad et al. ([Prasad et al., 2020](#)) designed titanium stem and the wing configuration and analyzed the stress distribution and magnitude of displacement for both the designs by applying the materials properties of titanium and polycaprolactone (PCL). The stem design was 20 mm length mesiodistally, 16 mm stature, and 1 mm divider thickness. The length and width of the stem estimated 18 and 4 mm distance across, separately. The inward pieces of the groups of the frameworks were made empty and the association spaces of the multitude of joints were made smooth with no sharp intersections. The elements of the wing body configuration were 20 mm length and 16 mm height. The thickness of the dividers of the body was 1 mm. All things considered, of a stem, an 18 mm long and 10 mm wide wing was demonstrated buccolingually with a 1 mm thick divider. The inward part between the wings was left open so it could hold the mandible from the base

**FIGURE 18.2**

(A) Stem design fixed in bone block, (B) Wing design fixed in bone block, (C) Stem design attached to mandible, (D) Wing design attached to mandible.

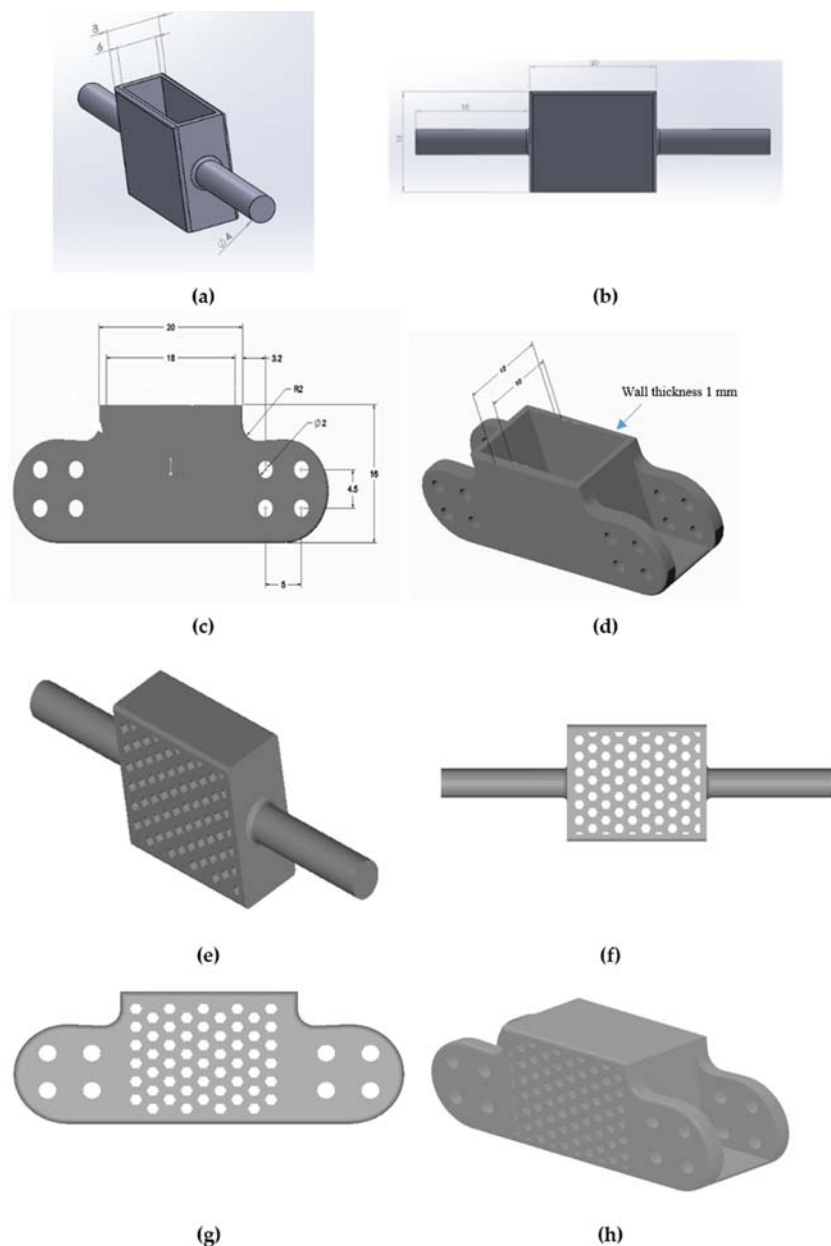
as a crate. Four screw openings every 2 mm in width were planned on every one of the wings for future adjustment of the wings to the mandible, Fig. 18.2.

The results showed that the mandible had a slight descending curve at first and afterward angled upwards on the two sides under stacking conditions. Stresses were dispersed all through the endoprostheses for both the stem and wing. For the stem, the stress estems were in the 557–803 MPa range reaching a maximum of 800 MPa. The wing displayed a lot of lower pressure estems in the 20–68 MPa range with a maximum of 68 MPa. The stem had a displacement of 0.781 mm while the wing had a displacement of 0.889 mm, Figs. 18.3 and 18.4.

---

### Stress and magnitude of displacement of stem and wing design in unilateral loading conditions

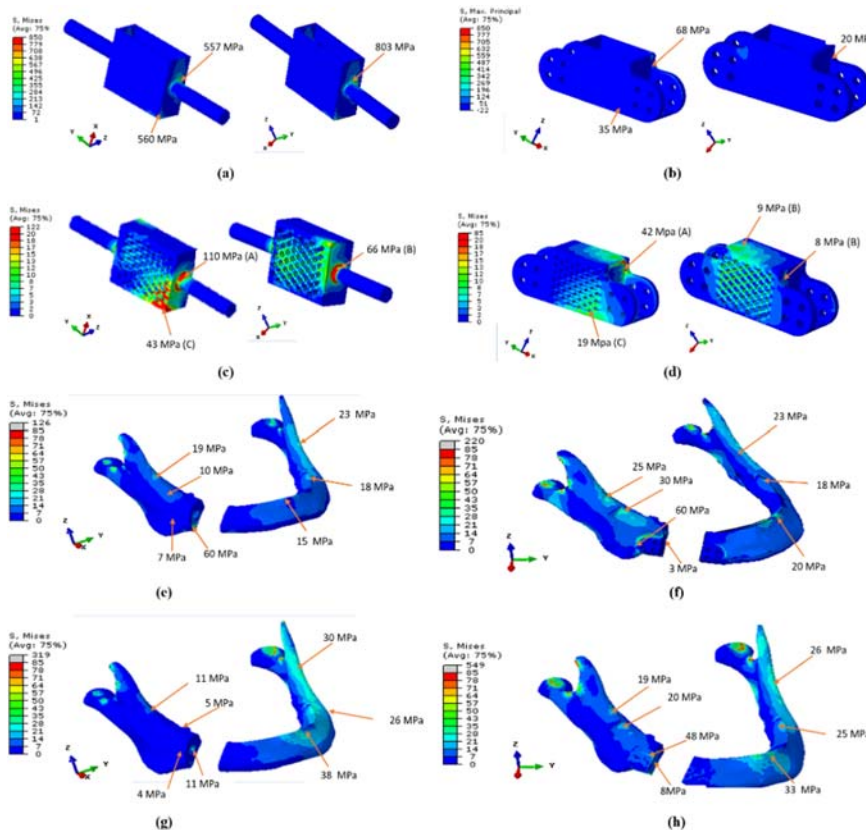
Previous methods used for mandibular reconstruction seemed to have integrated the biomechanical aspect of the reconstruction as an afterthought. The design of the fixation used influences the longevity of the reconstruction. Loading conditions and applied load play a major role in the stress concentrations and outcome of the prosthesis. An average adult with full dentition can apply a maximum force on their teeth ranging from 244 to 2143 N, with an average of 720 N (Van Eijden, 2000) and (Flanagan et al., 2008). In cases of malignancies, most patients tend to be edentulous with a maximum bite force ranging from 28 to 190 N and a chewing force ranging from 8.8 to 49.9 N (Wedel et al., 1994). An average bite force of 100–300 N can be selected for study application of segmental mandibular defects. This is because

**FIGURE 18.3**

Endoprosthesis design. (A, B) Titanium stem, (C, D) Titanium wing, (E, F) Polycaprolactone stem, (G) (H) Polycaprolactone wing.

*From Prasad, S., Suresh, S., Hong, K. L., Bhargav, A., Rosa, V., & Wong, R. C. W. (2020). Biomechanics of alloplastic mandible reconstruction using biomaterials: The effect of implant design on stress concentration influences choice of material. Journal of the Mechanical Behavior of Biomedical Materials, 103.*

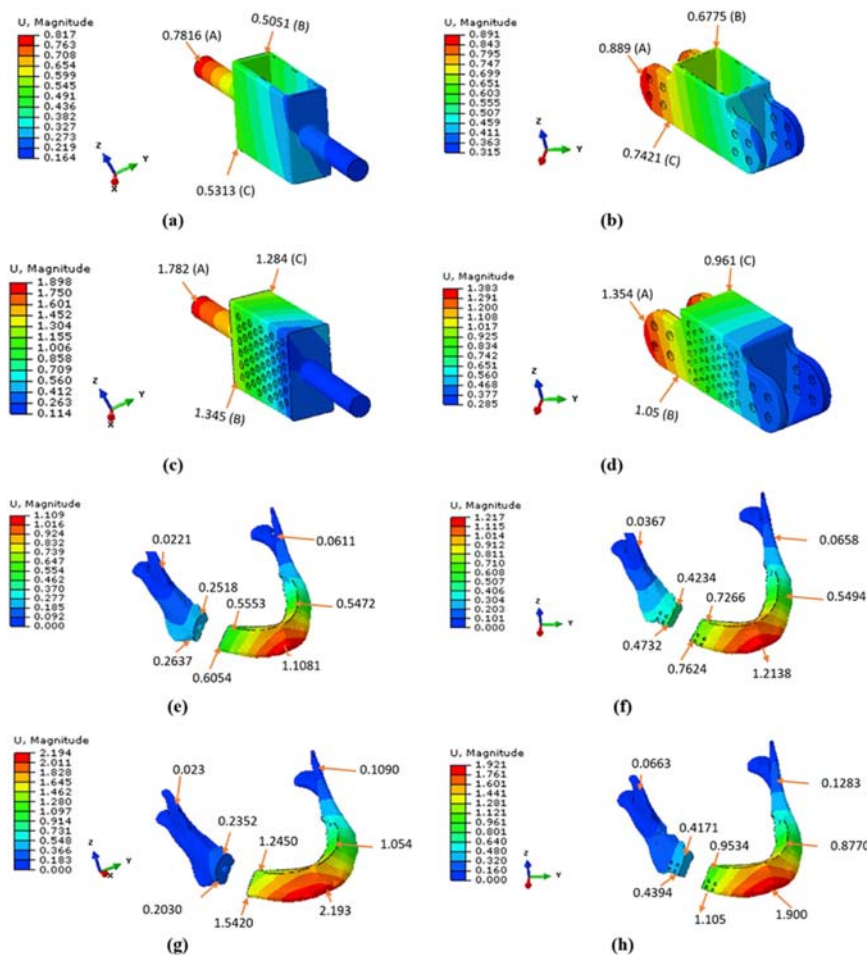
<https://doi.org/10.1016/j.jmbbm.2019.103548>.

**FIGURE 18.4**

Von Mises Stress Values (MPa). (A) Titanium Stem, (B) Titanium Wing, (C) Polycaprolactone Stem, (D) Polycaprolactone Wing, (E) Mandible-Titanium stem, (F) Mandible-Titanium Wing, (G) Mandible-Polycaprolactone Stem, (H) Mandible-Polycaprolactone Wing.

From Prasadh, S., Suresh, S., Hong, K. L., Bhargav, A., Rosa, V., & Wong, R. C. W. (2020). Biomechanics of alloplastic mandible reconstruction using biomaterials: The effect of implant design on stress concentration influences choice of material. Journal of the Mechanical Behavior of Biomedical Materials, 103. <https://doi.org/10.1016/j.jmbbm.2019.103548>.

studies have shown that some patients with mandibular reconstruction are able to achieve 100–300 N as a maximum force in the molar region (Van Eijden, 2000, Flanagan et al., 2008, Wedel et al., 1994). With this consideration, a short pilot study was done to evaluate the stress and displacement of the two common designs (Stem and Wing) by applying a force of 150 N. Since forces can be acting at any point of the prosthesis while mastication, a unilateral application of load was selected into considerations. The endoprosthesis assembly was set and the boundary

**FIGURE 18.5**

Magnitude of Displacement (mm). (A) Titanium Stem, (B) Titanium Wing, (C) Polycaprolactone Stem, (D) Polycaprolactone Wing, (E) Mandible-Titanium stem, (F) Mandible-Titanium Wing, (G) Mandible-Polycaprolactone Stem, (H) Mandible-Polycaprolactone Wing.

From Prasad, S., Suresh, S., Hong, K. L., Bhargav, A., Rosa, V., & Wong, R. C. W. (2020). Biomechanics of alloplastic mandible reconstruction using biomaterials: The effect of implant design on stress concentration influences choice of material. Journal of the Mechanical Behavior of Biomedical Materials, 103. <https://doi.org/10.1016/j.jmbbm.2019.103548>.

conditions were fixed, Figs. 18.5 and 18.6. The material properties of polycaprolactone were incorporated and unilateral load of 150 N was applied to the bone block and the stresses were evaluated. The results showed that maximum stress were at the junction of stem and the body. For stem design, the maximum von Mises stresses

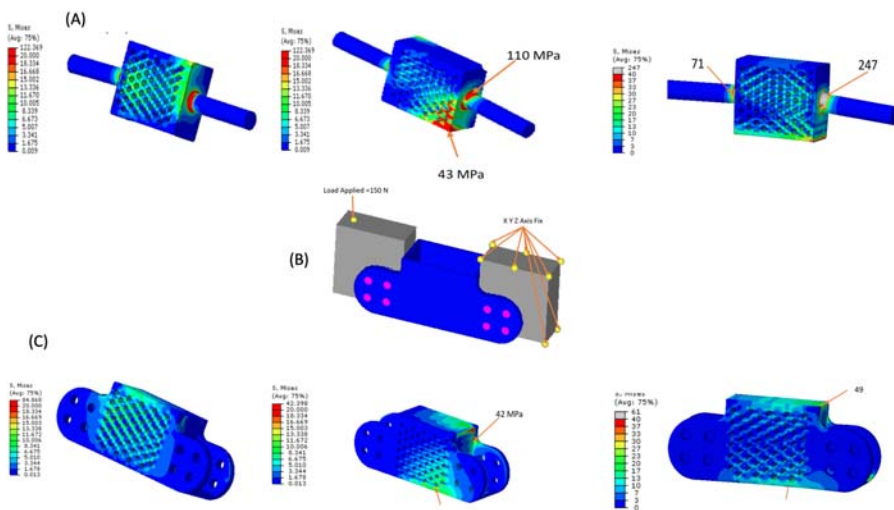


**FIGURE 18.6**

Endoprosthesis design. (A) Stress in stem design, (B) Loading and boundary conditions, (C) Stress in Wing design.

were from 122 to 247 MPa, whereas the stresses on the wing design showed values from 49 to 60 MPa. The magnitude of displacement of the prosthesis showed 2–3 mm of displacement for stem design, whereas 1 mm for the wing design.

Stress concentration is a leading cause of failure in any used endoprosthesis hardware. Stress beyond the limits of the strength of material would result in a fracture. This is deleterious to the longevity of a reconstruction. This is to be expected due to the sharp corners of the stem design of the endoprosthesis. The maximum stresses were concentrated at the junction of the stem and the body. Overall, the tray with wings design decreased stress and magnitude of displacement which could be attributed to the tray with wings design being able to distribute the stresses acting on the prosthesis.

## Conclusion

Digital analysis does not produce a solution in the form of a formula, nor does it solve a set of problems. This approach is used to arrive at a numerical solution to a problem. Digital modeling is a precise method for determining stress distribution, but it can only be used with a specific set of values. It varies from person to person, depending on the circumstance and biomechanical factors the understanding of living structure properties varies. As a result, prior to any decision-making process in experimental or clinical dentistry, the apparent flaws should be held in mind. The

studies can be repeated with no ethical concerns, and the study designs can be changed as required. There are certain drawbacks to FEA and digital modeling. Digital modeling research is still conducted while keeping in mind its limitations.

## References

- Alomar, X., Medrano, J., Cabratosa, J., Clavero, J. A., Lorente, M., Serra, I., Monill, J. M., & Salvador, A. (2007). Anatomy of the temporomandibular joint. *Seminars in Ultrasound, CT and MRI*, 28(3), 170–183. <https://doi.org/10.1053/j.sult.2007.02.002>
- Arya, S., Bhatt, K., Bhutia, O., & Roychoudhury, A. (2020). Efficacy of bioresorbable plates in the osteosynthesis of linear mandibular fractures. *National Journal of Maxillofacial Surgery*, 98. [https://doi.org/10.4103/njms.njms\\_54\\_19](https://doi.org/10.4103/njms.njms_54_19)
- Behzadi, F., Mandell, J. C., Smith, S. E., & Guenette, J. P. (2020). Temporomandibular joint imaging: Current clinical applications, biochemical comparison with the intervertebral disc and knee meniscus, and opportunities for advancement. *Skeletal Radiology*, 49(8), 1183–1193. <https://doi.org/10.1007/s00256-020-03412-0>
- Beltrán-Fernández, J. A., Gallardo-Ayala, H., Chagoya-López, M., Trujillo-Perez, C. A., González-Rebattú y González, M., Maturano-García, M. A., Hermida-Ochoa, J. C., Hernández-Gómez, L. H., Cuevas-Andrade, J. L., González-Peña, A. D., & Moreno-Garibaldi, P. (2021). Biomechanical evaluation of sharpened fractures in human jaws using plates articulated by the Champy method. In, Vol 146. *Advanced structured materials* (pp. 69–118). Springer Science and Business Media Deutschland GmbH. [https://doi.org/10.1007/978-3-030-65983-7\\_3](https://doi.org/10.1007/978-3-030-65983-7_3)
- Caragiuli, M., Mandolini, M., Landi, D., Bruno, G., De Stefani, A., Gracco, A., & Toniolo, I. (2021). A finite element analysis for evaluating mandibular advancement devices. *Journal of Biomechanics*, 119, 110298. <https://doi.org/10.1016/j.jbiomech.2021.110298>
- Chanchareonsook, N., Junker, R., Jongpaiboonkit, L., & Jansen, J. A. (2014). Tissue-engineered mandibular bone reconstruction for continuity defects: A systematic approach to the literature. *Tissue Engineering - Part B: Reviews*, 20(2), 147–162. <https://doi.org/10.1089/ten.teb.2013.0131>
- Chanchareonsook, N., Tideman, H., Feinberg, S. E., Jongpaiboonkit, L., Lee, S., Flanagan, C., Krishnaswamy, G., & Jansen, J. (2014). Segmental mandibular bone reconstruction with a carbonate-substituted hydroxyapatite-coated modular endoprosthetic poly( $\epsilon$ -caprolactone) scaffold in Macaca fascicularis. *Journal of Biomedical Materials Research - Part B Applied Biomaterials*, 102(5), 962–976. <https://doi.org/10.1002/jbm.b.33077>
- Domenyuk, D., Dmitrienko, S., Domenyuk, S., & Harutyunyan, Y. (2020). Structural arrangement of the temporomandibular joint in view of the constitutional anatomy. *Archiv EuroMedica*, 10(1), 126–136.
- Flanagan, D., Ilies, H., McCullough, P., & McQuoid, S. (2008). Measurement of the fatigue life of mini dental implants: A pilot study. *Journal of Oral Implantology*, 34(1), 7–11. [https://doi.org/10.1563/1548-1336\(2008\)34\[7:motflo\]2.0.co](https://doi.org/10.1563/1548-1336(2008)34[7:motflo]2.0.co)
- Flanagin, A. J., & Metzger, M. J. (2011). From Encyclopaedia Britannica to Wikipedia: Generational differences in the perceived credibility of online encyclopedia information. *Information Communication and Society*, 14(3), 355–374. <https://doi.org/10.1080/1369118X.2010.542823>
- Goh, B. T., Lee, S., Tideman, H., Jansen, J. A., & Stoelinga, P. J. W. (2009). Replacement of the condyle and ascending ramus by a modular endoprosthesis in Macaca fascicularis-Part

- 2: Microcomputed tomographic and histologic evaluation of the ramus and stem. *Journal of Oral and Maxillofacial Surgery*, 67(12), 2617–2626. <https://doi.org/10.1016/j.joms.2009.04.073>
- Goh, B. T., Lee, S., Tideman, H., & Stoelinga, P. J. W. (2009). Replacement of the condyle and ascending ramus by a modular endoprosthesis in Macaca fascicularis- Part 1: A clinical and radiographic study. *Journal of Oral and Maxillofacial Surgery*, 67(7), 1392–1400. <https://doi.org/10.1016/j.joms.2008.11.018>
- Hughes, T. J. (2012). The finite element method: Linear static and dynamic finite element analysis. *Courier Corporation*.
- Hylander, W. L. (2006). *Functional anatomy and biomechanics of the masticatory apparatus, temporomandibular disorders: An evidenced approach to diagnosis and treatment*.
- Jung, B. T., Kim, W. H., Park, B., Lee, J. H., Kim, B., & Lee, J. H. (2020). Biomechanical evaluation of unilateral subcondylar fracture of the mandible on the varying materials: A finite element analysis. *PLoS One*, 15(10). <https://doi.org/10.1371/journal.pone.0240352>
- Lee, S., Goh, B. T., Lai, S. H., Tideman, H., Stoelinga, P. J. W., & Jansen, J. A. (2009). Peri-implant and systemic release of metallic elements following insertion of a mandibular modular endoprosthesis in Macaca fascicularis. *Acta Biomaterialia*, 5(9), 3640–3646. <https://doi.org/10.1016/j.actbio.2009.05.028>
- Lee, S., Goh, B. T., Tideman, H., & Stoelinga, P. J. W. (2008). Modular endoprosthesis for mandibular reconstruction: A preliminary animal study. *International Journal of Oral and Maxillofacial Surgery*, 37(10), 935–942. <https://doi.org/10.1016/j.ijom.2008.07.021>
- Lee, S., Goh, B. T., Tideman, H., Stoelinga, P. J. W., & Jansen, J. A. (2009). Modular endoprosthesis for mandibular body reconstruction: A clinical, micro-CT and histologic evaluation in eight Macaca fascicularis. *International Journal of Oral and Maxillofacial Surgery*, 38(1), 40–47. <https://doi.org/10.1016/j.ijom.2008.11.020>
- Liu, Y. F., Fan, Y. Y., Jiang, X. F., & Baur, D. A. (2017). A customized fixation plate with novel structure designed by topological optimization for mandibular angle fracture based on finite element analysis. *Biomedical Engineering Online*, 16(1), 1–17. <https://doi.org/10.1186/s12938-017-0422-z>
- Liu, Y.F., Wang, R., Baur, D. A., & Jiang, X.f. (2018). A finite element analysis of the stress distribution to the mandible from impact forces with various orientations of third molars. *Journal of Zhejiang University: Science B*, 19(1), 38–48. <https://doi.org/10.1631/jzus.B1600552>
- Madsen, M. J., & Haug, R. H. (2006). A biomechanical comparison of 2 techniques for reconstructing atrophic edentulous mandible fractures. *Journal of Oral and Maxillofacial Surgery*, 64(3), 457–465. <https://doi.org/10.1016/j.joms.2005.11.018>
- Malawer, M. M., & Sugarbaker, P. H. (2001). *Musculoskeletal cancer surgery: Treatment of sarcomas and allied diseases*.
- Panagiotopoulou, O., Iriarte-Diaz, J., Mehari Abraha, H., Taylor, A. B., Wilshin, S., Dechow, P. C., & Ross, C. F. (2020). Biomechanics of the mandible of Macaca mulatta during the power stroke of mastication: Loading, deformation, and strain regimes and the impact of food type. *Journal of Human Evolution*, 147. <https://doi.org/10.1016/j.jhevol.2020.102865>
- Pandey, A., & Kumar, J. A. (2021). *Principles of osteosynthesis* (pp. 31–59). Springer Science and Business Media LLC. [https://doi.org/10.1007/978-981-33-6338-0\\_4](https://doi.org/10.1007/978-981-33-6338-0_4)
- Prasad, S., Manakari, V., Parande, G., Srivatsan, T. S., Wong, R., & Gupta, M. (2019). Bioresorbable nano-hydroxyapatite reinforced magnesium alloplastic bone substitute for

- biomedical applications: A study. In *Minerals, metals and materials series* (pp. 71–82). Springer. [https://doi.org/10.1007/978-3-030-35790-0\\_6](https://doi.org/10.1007/978-3-030-35790-0_6)
- Prasad, S., Suresh, S., Hong, K. L., Bhargav, A., Rosa, V., & Wong, R. C. W. (2020). Biomechanics of alloplastic mandible reconstruction using biomaterials: The effect of implant design on stress concentration influences choice of material. *Journal of the Mechanical Behavior of Biomedical Materials*, 103. <https://doi.org/10.1016/j.jmbbm.2019.103548>
- Puleo, D. A., & Nanci, A. (1999). Understanding and controlling the bone-implant interface. *Biomaterials*, 20(23–24), 2311–2321. [https://doi.org/10.1016/S0142-9612\(99\)00160-X](https://doi.org/10.1016/S0142-9612(99)00160-X)
- Reagle, J., & Rhue, L. (2011). *Gender bias in Wikipedia and Britannica* (Vol 5).
- Saito, D. M., & Murr, A. H. (2008). Internal fixation of mandibular angle fractures with the Champy technique. *Operative Techniques in Otolaryngology - Head and Neck Surgery*, 19(2), 123–127. <https://doi.org/10.1016/j.otot.2008.04.006>
- Schubert, W., Kobienia, B. J., & Pollock, R. A. (1997). Cross-sectional area of the mandible. *Journal of Oral and Maxillofacial Surgery*, 55(7), 689–692. [https://doi.org/10.1016/S0278-2391\(97\)90577-2](https://doi.org/10.1016/S0278-2391(97)90577-2)
- Shu, J., Xiong, X., Chong, D. Y. R., Liu, Y., & Liu, Z. (2021). The relations between the stress in temporomandibular joints and the deviated distances for mandibular asymmetric patients. *Proceedings of the Institution of Mechanical Engineers, Part H: Journal of Engineering in Medicine*, 235(1), 109–116. <https://doi.org/10.1177/0954411920962392>
- Silveira, C. R. da, Dias, P. E., Oenning, A. C., Junior, R. B. de B., Turssi, C. P., & Oliveira, L. B. (2021). Digital anatomy table in teaching-learning process of the temporomandibular joint anatomy. *European Journal of Dental Education*.
- Talarico, M. (2020). *Finite element analysis to evaluate mandible stress levels considering different malocclusions and impact conditions*.
- Van Eijden, T. M. G. J. (2000). Biomechanics of the mandible. *Critical Reviews in Oral Biology and Medicine*, 11(1), 123–136. <https://doi.org/10.1177/104544110001100101>
- Vollmer, D., Meyer, U., Joos, U., Végh, A., & Piffkò, J. (2000). Experimental and finite element study of a human mandible. *Journal of Cranio-Maxillofacial Surgery*, 28(2), 91–96. <https://doi.org/10.1054/jcms.2000.0125>
- Walker, C. J., & MacLeod, S. P. R. (2017). Anatomy and biomechanics of condylar fractures. *Atlas of the Oral and Maxillofacial Surgery Clinics of North America*, 25(1), 11–16. <https://doi.org/10.1016/j.cxom.2016.10.002>
- Wedel, A., Yontchev, E., Carlsson, G. E., & Ow, R. (1994). Masticatory function in patients with congenital and acquired maxillofacial defects. *The Journal of Prosthetic Dentistry*, 72(3), 303–308. [https://doi.org/10.1016/0022-3913\(94\)90344-1](https://doi.org/10.1016/0022-3913(94)90344-1)
- Werner, J. A., Tillmann, B., & Schleicher, A. (1991). Functional anatomy of the temporomandibular joint. *Anatomy and Embryology*, 183(1). <https://doi.org/10.1007/bf00185839>
- Wong, R. C. W., Lee, S., Tideman, H., Merkx, M. A. W., Jansen, J., & Liao, K. (2011). Effect of replacement of mandibular defects with a modular endoprosthesis on bone mineral density in a monkey model. *International Journal of Oral and Maxillofacial Surgery*, 40(6), 633–639. <https://doi.org/10.1016/j.ijom.2010.10.028>
- Wong, R. C. W., Tideman, H., Kin, L., & Merkx, M. A. W. (2010). Biomechanics of mandibular reconstruction: A review. *International Journal of Oral and Maxillofacial Surgery*, 39(4), 313–319. <https://doi.org/10.1016/j.ijom.2009.11.003>
- Wong, R. C., Tideman, H., Merkx, M. A. W., Jansen, J., & Goh, S. M. (2012a). The modular endoprosthesis for mandibular body replacement. Part 2: Finite element analysis of endoprosthesis reconstruction of the mandible. *Journal of Cranio-Maxillofacial Surgery*, 40(8), e487–e497.

- Wong, R. C. W., Tideman, H., Merkx, M. A. W., Jansen, J., & Goh, S. M. (2012b). The modular endoprosthesis for mandibular body replacement. Part 1: Mechanical testing of the reconstruction. *Journal of Cranio-Maxillofacial Surgery*, 40(8), e479–e486. <https://doi.org/10.1016/j.jcms.2012.03.009>
- Wong, R. C. W., Tideman, H., Merkx, M. A. W., Jansen, J., Goh, S. M., & Liao, K. (2011). Review of biomechanical models used in studying the biomechanics of reconstructed mandibles. *International Journal of Oral and Maxillofacial Surgery*, 40(4), 393–400. <https://doi.org/10.1016/j.ijom.2010.11.023>

This page intentionally left blank

# Cornea digital twins for studying the critical role of mechanics in physiology, pathology and surgical repair

# 19

**Ali Vahdati**

*Department of Engineering, College of Engineering and Technology, East Carolina University,  
Greenville, NC, United States*

## **Chapter outline**

<b>Introduction</b> .....	443
<b>Corneal biomechanics</b> .....	445
<b>In silico biomechanical models of cornea</b> .....	447
Toward accurate models of corneal collagen fibrils .....	449
Multiphasic and multiphysics computational models of cornea .....	452
Simulation-based subject-specific surgical planning .....	454
<b>Concluding remarks</b> .....	457
<b>References</b> .....	458

## **Introduction**

The human cornea is a highly organized connective tissue composed of collagen fibers, proteoglycans, interstitial fluid, and specialized cells, with unique mechanical properties that enable refraction of light while withstanding the intraocular pressure (IOP). The mechanical properties of cornea can be altered and disrupted in disease such as keratoconus and following surgical interventions including laser-assisted in situ keratomileusis (LASIK) and photorefractive keratectomy (PRK). In silico modeling and simulation offers great potential to advance our knowledge of corneal biomechanics in healthy and disease states by providing a cost- and time-effective approach through virtual experiments. Recent progress in computational modeling of corneal mechanics has enabled the preoperative screening of cornea for refractive surgery and provided the promise for prevention and early diagnosis of multiple corneal pathologies. In this chapter, after a brief introduction to corneal anatomy, physiology, and biomechanics, we will review the recent advances in computational

modeling of corneal mechanics and potential applications of cornea digital twins in disease prevention, diagnosis, management, and prediction of surgical outcomes.

The cornea is responsible for two-thirds of the eye's refractive power. While at first sight, the cornea may look like a simple, transparent tissue, it is in fact one of the most complex and organized connective tissues in the human body. The cornea performs a unique combination of optical and mechanical functions in the eye, and as a result, it exhibits a remarkable and highly organized multilayer structure. It consists primarily of three layers: epithelium, stroma, and endothelium. The outermost layer of the cornea, providing the first line of defense against pathogens and infections and simultaneously a smooth surface for clear light refraction, is the epithelium. The nonkeratinizing squamous epithelium of the cornea is covered by the tear film and is approximately 50 µm in thickness. The four to six layers of cells making up the epithelium have an average lifespan of 7–10 days; hence this layer is being constantly replaced by new cells. Below the epithelium, the approximately 15 µm thick Bowman's membrane is found which forms the most anterior surface of the stroma (DelMonte & Kim, 2011).

Stroma is the thickest and most structurally stable layer of cornea accounting for approximately 85% of corneal thickness. It is the depth-dependent intricate organization of collagen fibers and lamellae and other extracellular matrix (ECM) proteins including proteoglycans (PGs) that give stroma its remarkable mechanical properties and transparency. Stromal ECM is primarily composed of collagen type I and V fibrils, interacting closely with PGs to regulate hydration, swelling, and tension in the tissue. While corneal fibers form approximately 250 parallel lamellae, the lamellae are highly interconnected through transverse fibers. In the central cornea, the highest density of transverse fibers is found in the anterior stroma, which may be due to the important role of this region in maintaining the shape of the cornea and preventing fiber slippage (Winkler et al., 2013). Using wide-angle X-ray scattering (WAXS), Abass et al. (Abass et al., 2015) measured the transverse depth-dependent changes in corneal collagen lamellar orientation and distribution and showed that collagen fiber inclination angles are higher in the peripheral deeper stroma compared to the anterior stroma (Fig. 19.1). The highly organized ECM of the cornea is generated and maintained by flat-shaped corneal keratocytes. Furthermore, corneal keratocytes are responsible for repair and regeneration of the ECM as a result of corneal wounds. The thin Descemet membrane connects the stroma to its innermost layer, the endothelium. Lying at the interface of the cornea and the aqueous humor, the single layer of endothelial cells, arranged in hexagonal arrays, ensures the stroma remains in a dehydrated state by pumping fluid out of the stroma and into the aqueous humor. The net flux of ions out of the stroma by the action of endothelial pumps generates an osmotic gradient between the stroma and the aqueous humor, which drives fluid flow out of the stroma in this delicate pump-leak mechanism (DelMonte & Kim, 2011). Equipped with the knowledge of corneal anatomy and physiology, in the next section, we review the current state of scientific knowledge in regard to corneal biomechanics.

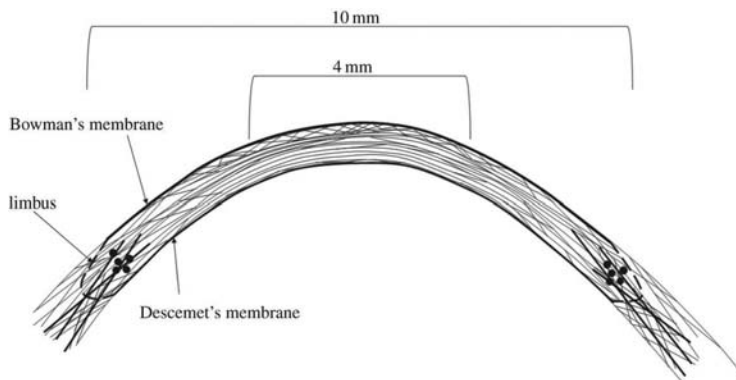


**FIGURE 19.1 Arrangement of collagen lamella in a cross section of the corneal stroma**

Schematic showing the proposed arrangement of collagen lamella in a cross section of the corneal stroma using WAXS. In the central region of the cornea, the angled or transverse fibers had the highest density in the anterior region. In the peripheral cornea and near the limbus region, a higher density of angled fibers was seen in the posterior cornea compared to the anterior stroma. Reprinted under the terms of the Creative Commons Attribution License <http://creativecommons.org/licenses/by/4>.

From Abass, A., Hayes, S., White, N., Sorensen, T., & Meek, K. M. (2015). Transverse depth-dependent changes in corneal collagen lamellar orientation and distribution. *Journal of the Royal Society Interface*, 12(104). <https://doi.org/10.1098/rsif.2014.0717>.

## Corneal biomechanics

Due to the nonlinear, viscoelastic, inhomogeneous, and anisotropic mechanical behavior and properties of the human cornea, comprehensive characterization of corneal mechanical properties is no trivial task. The interaction between internal and external forces and the structure of cornea determines the biomechanical behavior of the tissue. Lamellar tension, interlamellar cohesive forces, IOP, and swelling pressure all contribute to the overall mechanical response of the human cornea to loading. Disruption of central corneal lamellae which occurs in several refractive surgery techniques can result in transmission of centripetal forces to the underlying lamellae and at the same time may cause reduced lamellar tension and subsequently excessive swelling of the peripheral stroma as proposed by Duppss and Wilson (2006). For the past several decades, researchers have attempted to test and characterize the mechanical behavior of cornea in healthy and disease states using various methods including tensile, indentation, and inflation testing (Woo, Kobayashi, Schlegel, & Lawrence, 1972). As discussed in the previous section, collagen fibers and lamellae play a critical role in mechanical behavior of the cornea and as a result many researchers have attempted to characterize the anisotropic tensile behavior of the cornea. Below, we will review several different experimental studies on mechanical behavior of the cornea. This section is not meant to be a

comprehensive review of all mechanical testing studies of the human cornea. Rather, the section aims to introduce the readers to different approaches utilized by researchers to understand the mechanical behavior of cornea by reviewing some of the important studies in this research area. Readers interested in experimental corneal biomechanics in healthy, disease, and injury states can refer to several published comprehensive reviews on corneal biomechanics (Blackburn et al., 2019; Kling & Hafezi, 2017; Ruberti et al., 2011).

In one of the earliest studies on corneal biomechanics, Andreassen et al. (1980) performed uniaxial tensile tests on both healthy and keratoconic excised cornea specimens. While the study was conducted for a single loading rate and a single orientation of corneal strips, the results showed that keratoconic cornea may have a lower stiffness in tension compared to the healthy tissue samples. In a different approach, Jue and Maurice (1986) utilized inflation testing for intact whole human and rabbit corneas and isolated stroma and Descemet membrane specimens. Based on the nonlinear pressure-strain behavior observed in the experiments, the authors proposed and formulated a fiber-straightening hypothesis relating the waviness and uncrimping of collagen fibers to the strain-stiffening behavior of the tissue (Jue & Maurice, 1986). More controlled inflation experiments accounting for normal hydration and swelling of cornea in experiments were later performed by Hjortdal (1995) and again showed a highly nonlinear stress-strain behavior with higher strains observed on the posterior surface versus the anterior surface of cornea.

The distinct region-specific anisotropy of cornea was later shown by measuring interlamellar cohesive strength in the vertical and horizontal meridians of the human cornea (Smolek, 1993; Smolek & McCarey, 1990). Later on, a study published by Elsheikh and Anderson (2005) compared the strip extensometry and trephine inflation techniques by testing 10 pairs of porcine corneas. By comparing the two approaches, the authors presented a mathematical procedure to correct for several errors associated with strip extensometry of the cornea due to its aspheric shape and varying thickness. The authors were able to reasonably reconcile the strip extensometry and inflation test results using the developed mathematical procedure to accurately determine the nonlinear stress-strain behavior of cornea (Elsheikh & Anderson, 2005). In a subsequent study, Elsheikh et al. (2008) compared the mechanical response of human and porcine cornea subjected to inflation, creep, and stress relaxation using corneal strips in different orientations to determine the nonlinear, viscoelastic, and anisotropic behavior of the tissue. The study was able to demonstrate distinct differences in stress-strain behavior of human versus porcine corneas with the porcine cornea being significantly less stiff versus the human cornea under increased loading.

The viscoelastic behavior of the cornea has also been extensively studied not only by inflation testing and creep, for example, in the early study of Schwartz et al. (1966), but also more recently through unconfined compression testing (Hatami-Marbini & Etebu, 2013). More recently, the multiscale hierarchical mechanical behavior of cornea was investigated by combining small and wide-angle X-ray scattering (SAXS/WAXS) and digital image correlation (DIC) techniques

(Bell et al., 2018). The study quantified the hierarchical response of cornea to loading including the minor contribution of the lamellar residual crimp to mechanical response at low strain, the more significant straightening of molecular helical tilt relative to the fibril axis at strains below 2.8%, and the significant fibrillar uncrimping and lamellar and fibrillar reorientation at above strain of 2.8% Fig. 19.2 (Bell et al., 2018).

Other researchers studied the mechanical properties of corneal wounds particularly in LASIK procedures. For example, Schmack et al. (2005) measured the force required to separate the LASIK wound from the rest of the stroma in 13 donor corneas. The results showed that the central and paracentral scar left behind by LASIK procedure in the human corneal stroma heals very little over time as demonstrated by a minimal change in stiffness over time. However, the LASIK flap would show better healing response and regained 28% of its stiffness compared to the healthy cornea, still demonstrating incomplete healing of the stroma. Finally, in a more recent study, the temporal changes in corneal biomechanics during wound healing were characterized in rabbits by atomic force microscopy (Raghunathan et al., 2017). It was shown that after phototherapeutic keratectomy (PTK), the stroma is dynamically remodeled between days 10–42 after wounding with the elastic modulus having the highest value 7 days post-PTK (Raghunathan et al., 2017). Mechanical testing studies of cornea including the ones reviewed above laid the foundation for developing more accurate and validated computer models of corneal biomechanics in health, disease, and postsurgery states, reviewed in the next sections.

---

## In silico biomechanical models of cornea

With the advent of modern computers and the exponential increase in the available computing power over the past few decades, in silico biomechanical models of cornea have evolved in complexity over time. Some of the earliest computational models of corneal mechanics based on axisymmetric finite element (FE) analysis were developed by Woo and colleagues who assumed a trilinear exponential stress–strain relationship for the stroma and sclera, as determined from experimental data (Kobayashi et al., 1971; Woo, Kobayashi, Lawrence, & Schlegel, 1972; Woo, Kobayashi, Schlegel, & Lawrence, 1972). Later, other researchers developed thick membrane shell FE models of cornea incorporating orthotropic linear elastic material properties to represent both the fibrils and ECM of the stroma (Pinsky & Datye, 1991, 1992) and compared nonlinear elastic, transversely isotropic elastic, and hyperelastic models (Bryant & McDonnell, 1996) to better capture the material nonlinearity associated with tissue mechanical behavior. These early in silico models demonstrated the potential of FE analysis to better understand corneal biomechanics and were a step forward in creating more geometrically and materially accurate biomechanical models of cornea compared to the previously developed analytical models (Schwartz et al., 1966). Since then, many advances have been made in computational modeling of cornea including three-dimensional and

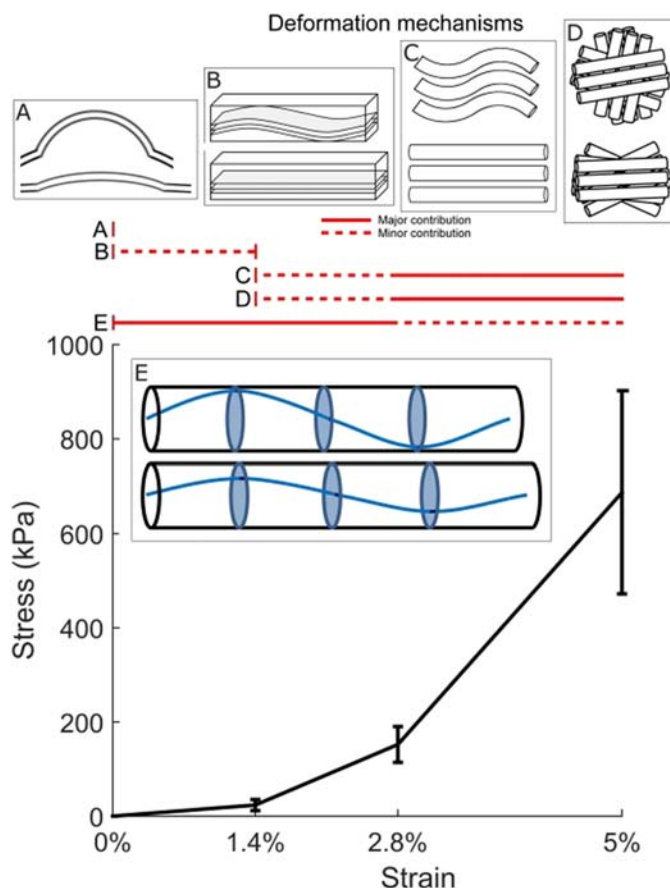


**FIGURE 19.2** The hierarchical response of the cornea to mechanical loading

The hierarchical response of the cornea to loading for different regions of the stress–strain curve. (A) in response to tare load, specimen curvature straightens at millimeter scale, (B) Lamellar residual crimp at makes a minor contribution to mechanical response at low strain (spatial scale of few hundred micrometers), (C) fibrillar uncrimping significantly changes (spatial scale of few hundred nanometers) at 2.8% strain, combined with (D) lamellar and fibrillar reorientation (spatial scale of few hundred nanometers), (E) more significant straightening of molecular helical tilt relative to the fibril axis at strains below 2.8% (spatial scale Angstrom). Reprinted under the terms of the Creative Commons Attribution License <http://creativecommons.org/licenses/by/4>.

From Bell, J. S., Hayes, S., Whitford, C., Sanchez-Weatherby, J., Shebanova, O., Vergari, C., Winlove, C. P., Terrill, N., Sorensen, T., Elsheikh, A., & Meek, K. M. (2018). The hierarchical response of human corneal collagen to load. *Acta Biomaterialia*, 65, 216–225. <https://doi.org/10.1016/j.actbio.2017.11.015>.

subject-specific geometric modeling, hyperviscoelastic, multiphasic, anisotropic, and microstructurally inspired constitutive material models.

### Toward accurate models of corneal collagen fibrils

One of the first fully three-dimensional FE models of cornea attached to a whole-eye model, accounting for the experimentally determined topography of the cornea, and asymmetry of its geometry was developed by Anderson et al. (2004). The model was meshed using shell elements in a commercial FE software and used an isotropic Ogden hyperelastic material model. A simplified case of keratoconus was simulated by modeling 75% tissue loss affecting either the central cornea or an area half-way between the center and the edge of the model. Furthermore, static tonometry was modeled by bringing the corneal model in contact with a rigid flat indenter and dynamic tonometry was simulated by incorporating fluid elements inside the whole-eye model. The simulations showed good agreement with several experimentally observed phenomena concerning corneal deformation behavior in tonometry (Anderson et al., 2004). However, the isotropic material model neglected the anisotropic collagen distribution of the cornea. Another attempt at modeling keratoconic corneas was made by Gefen et al. (2009) who investigated the effect of biomechanical factors contributing to corneal shape changes during the course of the disease. However, the material model employed in the study was a transversely orthotropic elastic model and hence only allowed for accurate simulation of small strains. Keratoconus was simulated either through regional manual thinning of the corneal geometry at the beginning of the simulation or alternatively via reducing the regional elastic modulus or shear modulus of the cornea.

A novel approach for incorporating the X-ray scattering data (Aghamohammadzadeh et al., 2004) in a biomechanical FE model of cornea using angular probability density of collagen fibril orientations was proposed by Pinsky et al. (2005). The proposed strain energy density function had two parts: the first part describing the isotropic ground matrix and the second part defining the anisotropic contribution of the collagen fibrils and their dispersion. The model was used to simulate the mechanical response of the cornea to a tunnel incision. In another anisotropic modeling approach, building on the earlier nearly incompressible anisotropic hyperelastic model of Pandolfi and Manganiello for healthy and keratoconic cornea (Pandolfi & Manganiello, 2006), Pandolfi and Holzapfel (2008) developed a full 3D (as opposed to axisymmetric and shell models) cornea model based on the idea of the generalized structural tensor (Gasser et al., 2006). Furthermore, the study incorporated a novel inverse approach to determine the unloaded or undeformed configuration of the cornea. Imaging techniques and experimental measurements of cornea *in vivo* always produce the deformed geometry of the tissue subjected to IOP. To obtain the undeformed geometry of the cornea, Pandolfi and Holzapfel (2008) implemented an iterative approach, in which the initial spatial configuration ( $X_0$ ) was assumed to be the sum of the unknown stress-free configuration ( $X$ ) of the

cornea geometry and the displacement ( $u$ ) following application of the IOP to the unknown configuration:

$$X_0 = X + u \quad (19.1)$$

The procedure for obtaining the undeformed configuration started out with setting the reference configuration  $X_1$  as  $X_0$ . The reference configuration ( $X_1$ ) was then subjected to a physiological IOP loading and its corresponding nodal displacements,  $u_1$  were computed. The displacements computed from the FE model were then used for updating the spatial configuration of the model for the next iteration such that

$$e^1 = ||X_1 + u_1 - X_0|| |X_2 = X_0 - u_1 \quad (19.2)$$

This process was repeated for number of iterations where the error and the updated spatial configuration of the model were obtained as

$$e^k = ||X_k + u_k - X_0|| |X_{k+1} = X_0 - u_k \quad (19.3)$$

The process stopped when the error was below the tolerance level of  $10^{-8}$  dmax with dmax representing the cornea's maximum diameter (Pandolfi & Holzapfel, 2008). Elsheikh et al. (2013) later performed a sensitivity analysis on the proposed approach in Pandolfi and Holzapfel (2008) to determine the undeformed configuration and found that three to four iterations are usually sufficient to find the undeformed configuration with reasonable accuracy. Pandolfi and Holzapfel (2008) further used their model to determine the refractive power of the cornea. While the model produced reasonable corneal deformations and refractive power for IOP of below 30 mmHg (which is well above the physiological range), the resulting mechanical response for IOP values of above 30 mmHg was unrealistic (Pandolfi & Holzapfel, 2008).

A microstructurally inspired constitutive model of stroma was proposed by Grytz and Meschke (2009), in which they assumed collagen fibrils in a crimped state can be simplified as a cylindrical helix. The authors adopted a Newtonian iterative solution approach to solve for the stretch in the geometrically nonlinear extensible helical spring. The mathematical model of the microscale helical spring model was based on the classical Kirchhoff–Love rod theory. The small number of parameters needed to calibrate the model was an important advantage of the proposed formulation. Following model calibration, good agreement with previously published strip extensometry data was obtained. This incompressible anisotropic model did not account for the time-dependent response of cornea to mechanical loading (Grytz & Meschke, 2009). The model was later applied to predict collagen fiber network remodeling in a corneo-scleral shell model in response to mechanical loading. The microstructurally motivated remodeling algorithm was able to produce an annulus of collagen fibrils encircling the limbus, thus qualitatively agreeing with experimental data (Grytz & Meschke, 2010).

Studer et al. (2010) developed another microstructurally inspired FE model of the cornea by incorporating the uncrimping of collagen fibers, their crosslinking

(by assuming a 90-degree angle between fibers of two adjacent layers) and distribution based on X-ray scattering data. The model was calibrated to reproduce both tensile and inflation test data of cornea in different age groups (Elsheikh et al., 2007, 2008). The fiber distribution function was adapted from the earlier work of Pinsky et al. (2005) and a polynomial Ogden law defined the anisotropic strain energy density function of the collagen fiber as proposed by Markert et al. (2005). The material model was later used to predict the patient-specific post-cataract surgery corneal mechanical behavior and was able to show on average good agreement with the topography measurements using clinical measurement devices for radii smaller than 3 mm (relative to the center of cornea). The FE predictions outside the 3 mm radius were less accurate compared to the in vivo measurements performed by the topography device. It should be noted that only the geometry of the computational model was patient-specific, while the material properties and collagen fibril distributions were assumed to be similar for all subjects. This lack of patient-specific material properties is a common limitation of many existing geometrically subject-specific FE models of cornea since measuring the individualized stiffness and anisotropy of the cornea in vivo and in clinical settings is a challenging task.

In another study by Nguyen and Boyce (2011), inflation experiments were combined with digital image correlation (DIC) to calculate the displacement field of the bovine anterior cornea and to determine the anisotropic hyperelastic material parameters by considering fiber dispersion. The inflation test simulations showed that the degree of collagen anisotropy in the limbus can have a large impact on the overall displacement of the cornea, while the degree of anisotropy in the central cornea had a negligible impact on the inflation response. However, some of the limitations of the model included neglecting viscoelasticity of the tissue and fitting an analytical ellipsoid the corneal surface which did not provide a good fit in the limbus region (Nguyen & Boyce, 2011). To account for the inclined lamellae and their depth-dependent distribution, Petsche and Pinsky (2013) incorporated the spatially varying 3-D collagen orientation based on X-ray diffraction data in an FE model of cornea. Thus, the model expanded the concept of angular integration, where stromal stress and stiffness is calculated by a weighted average of individual lamella properties to the case of inclined out-of-plane fibers. Unlike the model developed by Studer et al. (2010), the proposed model in Petsche and Pinsky (2013) did not account for the interlamellar interactions. However, the model was calibrated using both in vitro torsional shear and in vivo indentation test data and then was reasonably validated against in vitro inflation data. Nonetheless, the model neglected the time-dependent behavior of the cornea.

More recently, fitting both inflation and shear test data, Whitford et al. (2018) created a microstructural FE model of cornea accounting for the tissue viscoelasticity, regional variation of collagen density, and anisotropy and the contribution of interlamellar cohesion (ILC) to the mechanical response of the tissue to loading. The contribution of fibers to the strain density function of the cornea was given by

$$\bar{\psi}_f[\bar{C}, A, B] = \zeta \frac{1}{\pi} \int_0^\pi \chi(\bar{\psi}_{f,\text{lamellae}}[\bar{C}, A] + \bar{\psi}_{f,\text{ILC}}[\bar{C}, B]) d\theta_L \quad (19.4)$$

where  $\bar{\psi}_f$  is the contribution of fibrils to the total strain energy density,  $\bar{C}$  is distortional component of the right Cauchy–Green deformation tensor,  $A$  and  $B$  are anisotropic tensors defining the two predominant directions of anisotropy at each point,  $\zeta$  and  $\chi$  are angular distribution density functions showing the global and local distributions of collagen fibrils, respectively.  $\bar{\psi}_{f,\text{lamellae}}$  represents the lamellae fibril contribution and  $\bar{\psi}_{f,\text{ILC}}$  shows the interlamellar cohesion contribution of fibrils to the fibril strain energy density potential (Whitford et al., 2018).

To account for the subject-specific regional variation of collagen fibril density and arrangement, Zhou et al. (2019) developed a 3D ocular globe model and incorporated the collagen fibril orientation and density based on X-ray scattering measurements. Zernike polynomials were used for fitting the fibril map of a healthy eye specimen. The model neglected the through-thickness variations in fibril distribution. Also, due to the lack of experimental data on out-of-plane orientation interlamella fibrils, the same angular density distribution as lamella fibrils was assumed along with a constant fibril out-of-plane angle of 15 degrees. Inverse analysis was used to determine the model parameters based on inflation test data for tissue from subjects aged 50, 60, 70, 80, and 90 years (Zhou et al., 2019). In yet another recent study, Pandolfi et al. (2019) developed a two-fibril family anisotropic hyperelastic model of corneal stroma that included two different types of natural cross-links representing the transverse bonds within a single fibril family and across the two families. It was shown that damage and weakening of the transverse bonds could lead to localized thinning of the cornea and reproduce keratoconus-like anterior bulging in the simulations.

### Multiphasic and multiphysics computational models of cornea

Corneal stroma exhibits a highly time-dependent response to mechanical loading and, therefore, viscoelasticity is a main feature of corneal biomechanics. Also, while many hyperelastic and anisotropic models of collagen fibrils and fibers of the cornea have been developed, only more recently researchers have incorporated the detailed constitutive models of PGs and the interaction of the interstitial fluid with the solid matrix of the stroma. Nguyen et al. (2008) developed a nonlinear viscoelastic and anisotropic constitutive model of cornea calibrated to model the intrinsic viscoelasticity of the corneal tissue using tensile test data from corneal strips and incorporating in-plane fiber distributions based on available X-ray scattering data. The model assumed that the viscous stretching of the lamellae is the main mechanism for the nonlinear viscoelastic behavior of the stroma. While the model provided a good fit to cyclic tensile and creep data, the authors acknowledged the need for further calibration and validation using bulge experiments (Nguyen et al., 2008).

One of the earliest multiphasic constitutive models of the cornea was developed by Bryant and McDonnell (1998) in which they used the triphasic theory in a simplistic, one-dimensional domain to describe the interaction of stromal ECM, interstitial fluid, and osmotic pressure. More comprehensive and detailed models of corneal PGs were later developed by other researchers. For example, in order to better understand the role of stromal PGs and their sidechains of negatively charged glycosaminoglycans (GAGs) in the generation of restoring force mechanisms maintaining the organized lattice arrangement of the collagen fibrils, Cheng and Pinsky (2013) developed a mathematical model for the interaction of the swelling pressure and lattice restoring forces. Both electrostatic free energy and entropic elastic free energy were considered in the model and the interactions between the GAG fixed charges and mobile ions was described using the Poisson–Boltzmann mean-field theory. At normal corneal hydration, the equations were solved using molecular dynamics technique and the results showed that electrostatic restoring forces were able to reproduce the radial distribution function of the fibrils in the cornea while the entropic elastic restoring forces resulting from duplexed GAG structures made a minimal contribution to the restoring forces (Cheng & Pinsky, 2013). However, incorporating the subject-specific distribution of corneal PGs in the stroma remains a challenging task. Other researchers have proposed a Donnan approximation of the swelling pressure, which may provide a computationally efficient approach for the simulation of corneal swelling (Vahdati & Dupps, 2015).

In a subsequent study, Cheng et al. (2015) combined their previously developed models for the depth-dependent 3D organization of in-plane and inclined collagen fibers and PG-induced swelling pressure to develop a more comprehensive computational model of corneal mechanics. The model utilized a mean-field approximation of a binary electrolyte gel in thermodynamic equilibrium, hence using an energy approach to derive the homogenized energy-equivalent value of osmotic pressure in contrast to the pointwise approximation of the triphasic theory. In this detailed in silico model, osmotic pressure and hydration were modulated by endothelial ionic transport and the model was applied to the simulation of Fuchs' corneal dystrophy where fluid builds up in the stroma due to deterioration endothelial cells (Cheng et al., 2015). The model was also used for simulation of LASIK by creating a flap geometry and ablation profile in the FE model. The results showed the generation of modest negative osmotic pressure in the upper region of residual stroma as a result of removing the inclined lamellae. The authors concluded that accounting for the lamellae inclination is critical to the stability of the anterior surface of the cornea (Cheng et al., 2015). Cheng and Pinsky later extended the binary electrolyte gel model in Cheng et al. (2015) to account for cornea metabolism and metabolic transport in addition to coupling between osmotic pressure and mechanical swelling, and active endothelial transport (Cheng & Pinsky, 2017). This multiphysics model of cornea incorporated the aerobic respiration and anaerobic fermentation reactions of cellular metabolism in a diffusion–reaction mathematical framework. The model was applied to simulate the metabolically induced changes in tissue solute concentrations caused by a contact lens and an intrastromal inlay. Model validation

simulations provided good agreement with ex vivo osmotic pressure and in vivo measured corneal swelling (represented by thickness change) and oxygen transmissibility factors (Cheng & Pinsky, 2017).

It should be noted that the viscoelastic behavior of corneal stroma can be mainly attributed to two different mechanisms: (1) the intrinsic solid matrix (extracellular matrix) viscoelasticity stemming from the time-dependent mechanical behavior of collagen fibrils and PGs, and (2) interstitial fluid-induced viscoelasticity stemming from fluid flow in the permeable and porous stroma. Hatami-Marbini and Maulik (2016) proposed a biphasic transversely isotropic poroviscoelastic constitutive model of the stroma to account for both viscoelasticity mechanisms. While the assumption of transverse isotropy for cornea is an oversimplification of the complex organization of stromal collagen fibers, the poroviscoelastic aspect of the material model was the strength of this approach and allowed for reproducing unconfined compression results. Finally, detailed fluid–solid interaction (FSI) models of cornea biomechanics were developed to represent the complex interplay of the posterior corneal surface and the moving aqueous humor of the anterior chamber (Maklad et al., 2020; Montanino et al., 2018, 2019). For example, one such FSI modeling approach was used to simulate air puff tests on a 3D geometric model of the cornea and was able to produce a good agreement with the experimental data (Montanino et al., 2019). However, due to the potentially increased computational cost of fluid–solid interaction modeling compared to purely structural models, whether the additional numerical cost and added complexity of including the detailed fluid–solid interface load transfer is needed depends on the proposed application of the model and this added complexity should be well-justified by the modeler. The fluid–solid interaction modeling approach for investigation of corneal biomechanics will be explained in more detail in the next chapter.

### Simulation-based subject-specific surgical planning

Many of the sophisticated *in silico* biomechanical models of the cornea were developed to address a pressing need to understand the mechanical response of the tissue to surgery, including keratotomy, LASIK, PRK, corneal ring implant placement, and cross-linking treatment. Dupps (2005) highlighted the limitations of spherical shell models of cornea mechanics and emphasized the need for computer models that can capture the viscoelastic, shear, and interlamellar behavior and the structural nonuniformity of the tissue in order to simulate corneal ectasia realistically. Focusing on the refractive outcomes post-LASIK, Roy and Dupps (2010) developed a subject-specific geometric model of the cornea-sclera using Scheimpflug anterior and posterior corneal elevation maps. The authors used Zernike polynomials to interpolate the elevation maps of the corneal surfaces. The FE simulation results showed good agreement with in vivo measurements of curvature maps and spherical aberrations. However, the material model utilized was a simplistic polynomial hyperelastic model, which did not account for the anisotropy or viscoelasticity of the cornea (Roy & Dupps, 2010). While the spatial variation of elastic modulus was

incorporated in the model, the important role of collagen fibril anisotropy was again neglected. The model was later used in an inverse FE approach to determine the *in vivo* corneal elastic modulus change after collagen cross-linking for keratoconus ([Sinha Roy et al., 2013](#)). In spite of the isotropic material model used, corneal property changes post—cross-linking calculated from inverse FE provided good geometric agreement with the clinical topographical measurements. Additionally, the limitation of lack of anisotropy in the model was later addressed in a subsequent study by Seven et al. ([2014](#)) who used the anisotropic model developed in [Pandolfi and Holzapfel \(2008\)](#) and demonstrated novel corneal cross-linking spatial patterns can cause clinically significant reductions in astigmatism, depending on the subject-specific geometry, treatment orientation, and stiffening pattern.

FE models of corneal biomechanics can provide a powerful tool for preoperative screening and prediction of surgical outcomes. As an example, Vahdati et al. developed a computational approach for biomechanical risk analysis in LASIK and applied this technique to a case of unilateral post-LASIK ectasia ([Vahdati et al., 2016](#)). The 30-year-old male patient, in this case, had undergone LASIK surgery in both eyes, but only one eye developed progressive steepening and ectasia 18 months postoperatively ([Dupps et al., 2015](#)). The researchers developed a microstructurally inspired constitutive model of stroma by accounting for the crimping behavior of collagen fibrils based on the model of Freed et al. ([2005](#)). Anisotropic distribution of collagen fibers was based on the angular integration of the analytical function proposed by Pinsky et al. ([2005](#)). A smooth transition of the material properties between cornea, limbus, and sclera was modeled and the shear modulus of the ECM varied with depth in the stroma. This first application of FE simulations for analysis of post-LASIK ectasia combining patient-specific geometry and physiologic IOP loading provided new insights into case-specific risk factors. Preoperative FE simulations of both eyes showed higher maximum stress and strain values and more irregular distributions of these mechanical variables in the eye affected later by ectasia. Furthermore, virtual preoperative experiments were performed by increasing the IOP in both eyes. Interestingly, the largest preoperative steepening emerged in the eye that later developed ectasia, in a location where postoperative steepening eventually manifested clinically ([Vahdati et al., 2016](#)). On the contrary, the eye that did not develop ectasia postoperatively exhibited a flattening response when subjected to increased IOP in the preoperative simulations. These results represent an important progress toward patient-specific refractive surgery risk assessment using high-fidelity FE models. The constitutive and geometric modeling approach of [Vahdati et al. \(2016\)](#) was further used to assess the predictive accuracy of preoperative simulation-based LASIK outcomes for myopia correction in 20 eyes of 12 patients 3-month postoperatively ([Seven, Vahdati, De Stefano et al., 2016](#)). The FE simulation of changes in mean tangential curvature of the central 3 mm of cornea could account for 97% of the variance in corneal vertex—corrected changes of spherical-equivalent manifest refraction postoperatively ([Seven, Vahdati, & Dupps, 2016](#)).

The geometric patient-specific modeling approach and the automated workflow used in Vahdati et al. (2016) was also utilized to compare the biomechanical impact of flapless versus flap-based LASIK procedures (Seven et al., 2017). In contrast to flap-based LASIK, flapless LASIK or small incision lenticule extraction (SMILE) allows for pulling out the intrastromal lenticule cut by femtosecond laser through a small incision. Subject-specific simulations were performed for 10 eyes of 5 patients who underwent SMILE in one eye and flap-based femtosecond lenticule extraction in the other eye for correction of myopic astigmatism (Ibrahim Seven et al., 2015). The FE simulation and inverse analysis results showed that the flap-based procedure generated a 49% more reduction in stromal collagen fiber stiffness in the flap region compared to the contralateral SMILE cases. While on average SMILE cases showed lower stromal bed displacements and stresses compared to flap-based cases in the same subject, the results varied widely among the patients and this highlighted the need for more individualized simulation-based surgical risk assessment (Seven et al., 2017).

Additionally, FE simulations have also been used to study the effect of intrastromal corneal ring segments (ICRS) on corneal biomechanics. ICRS are small stromal implants that are used for refractive correction when laser refractive correction is not possible. Example applications of ICRS include treatment of keratoconus, post-LASIK ectasia, and marginal pellucid degenerations. In one *in silico* study, Lago et al. (2015) developed hyperelastic geometrically subject-specific FE models of corneas for seven keratoconus patients. The placement of ICRS in the stroma was simulated and the FE outcomes were compared to the actual postsurgical results. The simulation results of ICRS placement and postoperative clinical results showed general agreement. In another study (Flecha-Lescún et al., 2018), a novel template-based semiautomatic technique for modeling and simulation of ICRS in the stroma was developed. This 3D model also neglected the stromal anisotropy similar to several previously developed isotropic hyperelastic models of cornea used in ICRS placement simulations (Khan & Shiakolas, 2016; Kling & Marcos, 2013; Lago et al., 2015). However, the model of Flecha-Lescún et al. (2018) better lent itself to optimization procedures and parametric studies due to its reliance on previously generated templates corresponding to a discrete set of surgical scenarios. More recently, to better understand the effect of ICRS design and surgical parameters on the optical and biomechanical outcomes of the surgery, Ariza-Garcia et al. (2020) simulated the postsurgical optomechanical behavior of the cornea. The results showed that ICRS placement did not stiffen the cornea globally but resulted in localized mechanical deformations and higher stress in the surrounding of the implant only. However, to reduce the computational cost of the simulations, the model utilized an axisymmetric geometry and neglected the role of collagen fiber anisotropy in the stroma, which can limit its predictive accuracy in the simulation of corneal biomechanics. Hence, there is a need for implementing more accurate yet computationally efficient constitutive models of stroma in ICRS surgery simulation studies.

Another surgical technique that was simulated using *in silico* biomechanical models is endothelial keratoplasty, which is a type of corneal transplantation for

endothelial disorders. The graft attachment to the donor cornea facilitated by an air bubble was simulated in an FE model including a penalty-based node-to-surface contact algorithm (Mohamed et al., 2019). It was shown that the graft's material and geometric properties can have a considerable impact on the biomechanics of cornea in the surgical procedure. More compliant and thinner grafts caused higher deformation in the cornea during contact simulations. The constitutive model implemented in the simulation was a nearly incompressible Neo-Hookean hyperelastic model, thus neglecting both anisotropy and viscoelasticity of the cornea (Mohamed et al., 2019). Contact algorithms in FE simulations tend to come at high computational cost; therefore, combining a sophisticated anisotropic and viscoelastic material model of the cornea in surgical techniques involving contact such as in endothelial keratoplasty simulations can be computationally expensive.

One more application of FE models in predicting corneal mechanics is the simulation of intrastromal arcuate keratotomy for correction of astigmatism. Personalized biomechanical FE simulations were recently used to optimize the incision parameters and reduce overcorrection in large cohort of patients undergoing arcuate keratotomy (Truffer et al., 2019). Retrospective data from 28 patients was used to evaluate the FE model's accuracy followed by patient-specific simulation of arcuate interventions in another 621 corneal topographies to compare different planning strategies. The results showed that patient-specific biomechanical simulations can provide a valuable tool for increasing the safety and accuracy of the procedure, thus complementing the existing nomograms (Truffer et al., 2019). The FE model used was based on the work in Studer et al. (2010) and did not account for viscoelasticity of the cornea. The same constitutive model was previously also used for simulation of a single case of femtosecond keyhole endokeratophakia in which a donor lenticule extracted by SMILE procedure was inserted into a lamellar pocket of the cornea of another patient with hyperopia (Studer et al., 2015).

---

## Concluding remarks

In silico modeling of corneal biomechanics is a growing field of research that offers many opportunities for better understanding and predicting the mechanical implications of various pathologies and surgical techniques. Detailed constitutive models of cornea have been developed by different researchers incorporating the spatial distribution and orientation of collagen fibers, the effect of proteoglycans on swelling, and the viscoelastic behavior of the tissue. Additionally, many studies have focused on the simulation of surgical techniques with the aim of providing the surgeons with a biomechanical simulation-based decision support system. Despite all this progress, there is a need to better link the biomechanical digital twins to corneal biology. To this end, a recent computer model of corneal cells embedded in the ECM and biomechanical simulation of stress and strain distribution in the pericellular matrix of corneal cells (Pant et al., 2020) is a step toward the integration of corneal mechanics and biology. There is also a pressing need to develop novel experimental methods for

measuring the subject-specific mechanical properties of the cornea *in vivo*. Optical coherence tomography (Stefano et al., 2020) and Brillouin microscopy (Scarcelli et al., 2012) are two promising imaging methods that need further development to provide the necessary data for calibration and validation of sophisticated constitutive models with multiple parameters.

As the biomechanical digital twins of cornea grow in complexity, so does the computational cost of such models. Thus, research is needed into more computationally efficient and automated *in silico* modeling techniques and workflows to make these models accessible to a wider range of users, including clinicians. Furthermore, validation of computational models using data from large patient cohorts as performed in Truffer et al. (2019) will increase confidence in model predictions and will help with wider acceptance of *in silico* predictions among clinicians. Finally, more systematic reporting of FE model parameters and decision-making in the modeling process, standardized and extensive verification, validation, and uncertainty quantification of *in silico* biomechanical models of the cornea will make these valuable computational models more credible and reproducible (Erdemir et al., 2012) and can eventually lead to the widespread application of cornea digital twins in the evaluation of surgical techniques and medical devices.

---

## References

- Abass, A., Hayes, S., White, N., Sorensen, T., & Meek, K. M. (2015). Transverse depth-dependent changes in corneal collagen lamellar orientation and distribution. *Journal of the Royal Society Interface*, 12(104). <https://doi.org/10.1098/rsif.2014.0717>
- Aghamohammadzadeh, H., Newton, R. H., & Meek, K. M. (2004). X-ray scattering used to map the preferred collagen orientation in the human cornea and limbus. *Structure*, 12(2), 249–256. <https://doi.org/10.1016/j.str.2004.01.002>
- Anderson, K., El-Sheikh, A., & Newson, T. (2004). Application of structural analysis to the mechanical behaviour of the cornea. *Journal of the Royal Society Interface*, 1(1), 3–15. <https://doi.org/10.1098/rsif.2004.0002>
- Andreassen, T. T., Hjorth Simonsen, A., & Oxlund, H. (1980). Biomechanical properties of keratoconus and normal corneas. *Experimental Eye Research*, 31(4), 435–441. [https://doi.org/10.1016/S0014-4835\(80\)80027-3](https://doi.org/10.1016/S0014-4835(80)80027-3)
- Ariza-Gracia, M.Á., Flecha-Lescún, J., Büchler, P., & Calvo, B. (2020). Corneal biomechanics after intrastromal ring surgery: Optomechanical *in silico* assessment. *Translational Vision Science and Technology*, 9(11), 1–16. <https://doi.org/10.1167/tvst.9.11.26>
- Bell, J. S., Hayes, S., Whitford, C., Sanchez-Weatherby, J., Shebanova, O., Vergari, C., Winlove, C. P., Terrill, N., Sorensen, T., Elsheikh, A., & Meek, K. M. (2018). The hierarchical response of human corneal collagen to load. *Acta Biomaterialia*, 65, 216–225. <https://doi.org/10.1016/j.actbio.2017.11.015>
- Blackburn, B. J., Jenkins, M. W., Rollins, A. M., & Dupps, W. J. (2019). A review of structural and biomechanical changes in the cornea in aging, disease, and photochemical crosslinking. *Frontiers in Bioengineering and Biotechnology*, 7. <https://doi.org/10.3389/fbioe.2019.00066>

- Bryant, M. R., & McDonnell, P. J. (1996). Constitutive laws for biomechanical modeling of refractive surgery. *Journal of Biomechanical Engineering*, 118(4), 473–481. <https://doi.org/10.1115/1.2796033>
- Bryant, M. R., & McDonnell, P. J. (1998). A triphasic analysis of corneal swelling and hydration control. *Journal of Biomechanical Engineering*, 120(3), 370–381. <https://doi.org/10.1115/1.2798004>
- Cheng, X., Petsche, S. J., & Pinsky, P. M. (2015). A structural model for the in vivo human cornea including collagen-swelling interaction. *Journal of the Royal Society Interface*, 12(109). <https://doi.org/10.1098/rsif.2015.0241>
- Cheng, X., & Pinsky, P. M. (2013). Mechanisms of self-organization for the collagen fibril lattice in the human cornea. *Journal of the Royal Society Interface*, 10(87). <https://doi.org/10.1098/rsif.2013.0512>
- Cheng, X., & Pinsky, P. M. (2017). A numerical model for metabolism, metabolite transport and edema in the human cornea. *Computer Methods in Applied Mechanics and Engineering*, 314, 323–344. <https://doi.org/10.1016/j.cma.2016.09.014>
- Freed., A. D., & Doehring., T. C. (2005). Elastic model for crimped collagen fibrils. *Journal of Biomechanical Engineering*, 587–593. <https://doi.org/10.1115/1.1934145>
- DelMonte, D. W., & Kim, T. (2011). Anatomy and physiology of the cornea. *Journal of Cataract and Refractive Surgery*, 37(3), 588–598. <https://doi.org/10.1016/j.jcrs.2010.12.037>
- Duppss, W. J. (2005). Biomechanical modeling of corneal ectasia. *Journal of Refractive Surgery*, 21(2), 186–190. <https://doi.org/10.3928/1081-597x-20050301-15>
- Duppss, W. J., Vahdati, A., Mysore, N., Seven, I., Krueger, R. R., & Randleman, J. B. (2015). Computational modeling of unilateral ectasia after LASIK and PRK. *Investigative Ophthalmology & Visual Science*, 56(7), 1111–1111.
- Duppss, W. J., & Wilson, S. E. (2006). Biomechanics and wound healing in the cornea. *Experimental Eye Research*, 83(4), 709–720. <https://doi.org/10.1016/j.exer.2006.03.015>
- Elsheikh, A., Alhasso, D., & Rama, P. (2008). Biomechanical properties of human and porcine corneas. *Experimental Eye Research*, 86(5), 783–790. <https://doi.org/10.1016/j.exer.2008.02.006>
- Elsheikh, A., & Anderson, K. (2005). Comparative study of corneal strip extensometry and inflation tests. *Journal of the Royal Society Interface*, 2(3), 177–185. <https://doi.org/10.1098/rsif.2005.0034>
- Elsheikh, A., Wang, D., Brown, M., Rama, P., Campanelli, M., & Pye, D. (2007). Assessment of corneal biomechanical properties and their variation with age. *Current Eye Research*, 32(1), 11–19. <https://doi.org/10.1080/02713680601077145>
- Elsheikh, A., Whitford, C., Hamarashid, R., Kassem, W., Joda, A., & Büchler, P. (2013). Stress free configuration of the human eye. *Medical Engineering and Physics*, 35(2), 211–216. <https://doi.org/10.1016/j.medengphy.2012.09.006>
- Erdemir, A., Guess, T. M., Halloran, J., Tadepalli, S. C., & Morrison, T. M. (2012). Considerations for reporting finite element analysis studies in biomechanics. *Journal of Biomechanics*, 45(4), 625–633. <https://doi.org/10.1016/j.jbiomech.2011.11.038>
- Flecha-Lescún, J., Calvo, B., Zurita, J., & Ariza-Gracia, M.Á. (2018). Template-based methodology for the simulation of intracorneal segment ring implantation in human corneas. *Biomechanics and Modeling in Mechanobiology*, 17(4), 923–938. <https://doi.org/10.1007/s10237-018-1013-z>
- Gasser, T. C., Ogden, R. W., & Holzapfel, G. A. (2006). Hyperelastic modelling of arterial layers with distributed collagen fibre orientations. *Journal of The Royal Society Interface*, 3(6), 15–35. <https://doi.org/10.1098/rsif.2005.0073>

- Gefen, A., Shalom, R., Elad, D., & Mandel, Y. (2009). Biomechanical analysis of the keratoconic cornea. *Journal of the Mechanical Behavior of Biomedical Materials*, 2(3), 224–236. <https://doi.org/10.1016/j.jmbbm.2008.07.002>
- Grytz, R., & Meschke, G. (2009). Constitutive modeling of crimped collagen fibrils in soft tissues. *Journal of the Mechanical Behavior of Biomedical Materials*, 2(5), 522–533. <https://doi.org/10.1016/j.jmbbm.2008.12.009>
- Grytz, R., & Meschke, G. (2010). A computational remodeling approach to predict the physiological architecture of the collagen fibril network in corneo-scleral shells. *Biomechanics and Modeling in Mechanobiology*, 9(2), 225–235. <https://doi.org/10.1007/s10237-009-0173-2>
- Hatami-Marbini, H., & Etebu, E. (2013). A new method to determine rate-dependent material parameters of corneal extracellular matrix. *Annals of Biomedical Engineering*, 41(11), 2399–2408. <https://doi.org/10.1007/s10439-013-0842-2>
- Hatami-Marbini, H., & Maulik, R. (2016). A biphasic transversely isotropic poroviscoelastic model for the unconfined compression of hydrated soft tissue. *J Biomech Eng*, 138.
- Jue, B., & Maurice, D. M. (1986). The mechanical properties of the rabbit and human cornea. *Journal of Biomechanics*, 19(10), 847–853. [https://doi.org/10.1016/0021-9290\(86\)90135-1](https://doi.org/10.1016/0021-9290(86)90135-1)
- Khan, S., & Shiakolas, P. S. (2016). To study the effects of intrastromal corneal ring geometry and surgical conditions on the postsurgical outcomes through finite element analysis. *J Mech Med Biol*, 16.
- Kling, S., & Hafezi, F. (2017). Corneal biomechanics—a review. *Ophthalmic and Physiological Optics*, 37(3), 240–252. <https://doi.org/10.1111/opo.12345>
- Kling, S., & Marcos, S. (2013). Finite-element modeling of intrastromal ring segment implantation into a hyperelastic cornea. *Investigative Ophthalmology and Visual Science*, 54(1), 881–889. <https://doi.org/10.1167/iovs.12-10852>
- Kobayashi, A. S., Woo, S. L. Y., Lawrence, C., & Schlegel, W. A. (1971). Analysis of the corneo-scleral shell by the method of direct stiffness. *Journal of Biomechanics*, 4(5). [https://doi.org/10.1016/0021-9290\(71\)90053-4](https://doi.org/10.1016/0021-9290(71)90053-4). 323-IN1.
- Lago, M. A., Rupérez, M. J., Monserrat, C., Martínez-Martínez, F., Martínez-Sanchis, S., Larra, E., Díez-Ajenjo, M. A., & Peris-Martínez, C. (2015). Patient-specific simulation of the intrastromal ring segment implantation in corneas with keratoconus. *Journal of the Mechanical Behavior of Biomedical Materials*, 51, 260–268. <https://doi.org/10.1016/j.jmbbm.2015.07.023>
- Markert, B., Ehlers, W., & Karajan, N. (2005). A general polyconvex strain-energy function for fiber-reinforced materials. In *PAMM: Proceedings in Applied Mathematics and Mechanics* (Vol. 5, No. 1, pp. 245–246). Berlin: WILEY-VCH Verlag.
- Maklad, O., Eliasy, A., Chen, K. J., Wang, J. J., Abass, A., Lopes, B. T., Theofilis, V., & Elsheikh, A. (2020). Fluid-structure interaction based algorithms for IOP and corneal material behavior. *Frontiers in Bioengineering and Biotechnology*, 8. <https://doi.org/10.3389/fbioe.2020.00970>
- Mohamed, S., Coccarelli, A., Mauro, A., Massarotti, N., Romano, M. R., Romano, V., & Nithiarasu, P. (2019). A novel numerical modelling approach for keratoplasty eye procedure. *Biomechanics and Modeling in Mechanobiology*, 18(5), 1429–1442. <https://doi.org/10.1007/s10237-019-01156-y>
- Montanino, A., Angelillo, M., & Pandolfi, A. (2018). Modelling with a meshfree approach the cornea-aqueous humor interaction during the air puff test. *Journal of the Mechanical*

- Behavior of Biomedical Materials*, 77, 205–216. <https://doi.org/10.1016/j.jmbbm.2017.05.042>
- Montanino, A., Angelillo, M., & Pandolfi, A. (2019). A 3D fluid-solid interaction model of the air puff test in the human cornea. *Journal of the Mechanical Behavior of Biomedical Materials*, 94, 22–31. <https://doi.org/10.1016/j.jmbbm.2019.02.030>
- Nguyen, T. D., & Boyce, B. L. (2011). An inverse finite element method for determining the anisotropic properties of the cornea. *Biomechanics and Modeling in Mechanobiology*, 10(3), 323–337. <https://doi.org/10.1007/s10237-010-0237-3>
- Nguyen, T., Jones, R., & Boyce, B. L. (2008). A nonlinear anisotropic viscoelastic model for the tensile behavior of the corneal stroma. *J Biomech Eng*, 130.
- Hjortdal, J. O. (1995). Extensibility of the normo-hydrated human cornea. *Acta Ophthalmologica Scandinavica*, 73(1), 12–17. <https://doi.org/10.1111/j.1600-0420.1995.tb00005.x>
- Pandolfi, A., Gizzi, A., & Vasta, M. (2019). A microstructural model of cross-link interaction between collagen fibrils in the human cornea. *Philosophical Transactions of the Royal Society A: Mathematical, Physical and Engineering Sciences*, 377(2144). <https://doi.org/10.1098/rsta.2018.0079>
- Pandolfi, A., & Holzapfel, G. A. (2008). Three-dimensional modeling and computational analysis of the human cornea considering distributed collagen fibril orientations. *Journal of Biomechanical Engineering*, 130(6). <https://doi.org/10.1115/1.2982251>
- Pandolfi, A., & Manganiello, F. (2006). A model for the human cornea: Constitutive formulation and numerical analysis. *Biomechanics and Modeling in Mechanobiology*, 5(4), 237–246. <https://doi.org/10.1007/s10237-005-0014-x>
- Pant, A., Paul, E., & Vahdati, A. (2020). Developing a multiscale in silico cornea for understanding the role of cell mechanics in corneal pathologies. *Biocybernetics and Biomedical Engineering*, 40(4), 1369–1377. <https://doi.org/10.1016/j.bbe.2020.08.003>
- Petsche, S. J., & Pinsky, P. M. (2013). The role of 3-D collagen organization in stromal elasticity: A model based on X-ray diffraction data and second harmonic-generated images. *Biomechanics and Modeling in Mechanobiology*, 12(6), 1101–1113. <https://doi.org/10.1007/s10237-012-0466-8>
- Pinsky, P. M., & Datye, D. V. (1991). A microstructurally-based finite element model of the incised human cornea. *Journal of Biomechanics*, 24(10), 907–922. [https://doi.org/10.1016/0021-9290\(91\)90169-N](https://doi.org/10.1016/0021-9290(91)90169-N)
- Pinsky, P. M., & Datye, D. V. (1992). Numerical modeling of radial, astigmatic, and hexagonal keratotomy. *Refractive and Corneal Surgery*, 8(2), 164–172.
- Pinsky, P. M., Van Der Heide, D., & Chernyak, D. (2005). Computational modeling of mechanical anisotropy in the cornea and sclera. *Journal of Cataract and Refractive Surgery*, 31(1), 136–145. <https://doi.org/10.1016/j.jcrs.2004.10.048>
- Raghunathan, V. K., Thomasy, S. M., Strøm, P., Yañez-Soto, B., Garland, S. P., Sermenio, J., Reilly, C. M., & Murphy, C. J. (2017). Tissue and cellular biomechanics during corneal wound injury and repair. *Acta Biomaterialia*, 58, 291–301. <https://doi.org/10.1016/j.actbio.2017.05.051>
- Roy, A. S., & Dupps, W. J. (2010). Patient-specific modeling of corneal refractive surgery outcomes and inverse estimation of elastic property changes. *Journal of Biomechanical Engineering*, 133(1). <https://doi.org/10.1115/1.4002934>
- Ruberti, J. W., Sinha Roy, A., & Roberts, C. J. (2011). Corneal biomechanics and biomaterials. *Annual Review of Biomedical Engineering*, 13, 269–295. <https://doi.org/10.1146/annurev-bioeng-070909-105243>

- Scarcelli, G., Pineda, R., & Yun, S. H. (2012). Brillouin optical microscopy for corneal biomechanics. *Investigative Ophthalmology and Visual Science*, 53(1), 185–190. <https://doi.org/10.1167/iovs.11-8281>
- Schmack, I., Dawson, D. G., McCarey, B. E., Waring, G. O., Grossniklaus, H. E., & Edelhauser, H. F. (2005). Cohesive tensile strength of human LASIK wounds with histologic, ultrastructural, and clinical correlations. *Journal of Refractive Surgery*, 21(5), 433–445. <https://doi.org/10.3928/1081-597X-20050901-04>
- Schwartz, N. J., Mackay, R. S., & Sackman, J. L. (1966). A theoretical and experimental study of the mechanical behavior of the cornea with application to the measurement of intraocular pressure. *The Bulletin of Mathematical Biophysics*, 28(4), 585–643. <https://doi.org/10.1007/BF02476865>
- Seven, I., Roy, A. S., & Dupps, W. J. (2014). Patterned corneal collagen crosslinking for astigmatism: Computational modeling study. *Journal of Cataract and Refractive Surgery*, 40(6), 943–953. <https://doi.org/10.1016/j.jcrs.2014.03.019>
- Seven, I., Vahdati, A., De Stefano, V. S., Krueger, R. R., & Dupps, W. J. (2016). Comparison of patient-specific computational modeling predictions and clinical outcomes of lasik for myopia. *Investigative Ophthalmology and Visual Science*, 57(14), 6287–6297. <https://doi.org/10.1167/iovs.16-19948>
- Seven, I., Vahdati, A., & Dupps, W. J. (2016). Patient-specific computational analysis of laser in situ keratomileusis: A clinical validation study. *Investigative Ophthalmology & Visual Science*, 57(12), 2376–2376.
- Seven, I., Vahdati, A., Pedersen, I. B., Vestergaard, A., Hjortdal, J., Roberts, C. J., & Dupps, W. J. (2017). Contralateral eye comparison of SMILE and flap-based corneal refractive surgery: Computational analysis of biomechanical impact. *Journal of Refractive Surgery*, 33(7), 444–453. <https://doi.org/10.3928/1081597X-20170504-01>
- Seven, Ibrahim, Vahdati, A., Roberts, C. J., Pedersen, I. B., Hjortdal, J., & Dupps, W. J. (2015). Biomechanical comparison of contralateral flap-based and No-flap femtosecond lenticule extraction procedures using inverse finite element analysis. *Investigative Ophthalmology & Visual Science*, 56, 1110–1110.
- Sinha Roy, A., Rocha, K. M., Randleman, J. B., Stulting, R. D., & Dupps, W. J. (2013). Inverse computational analysis of invivo corneal elastic modulus change after collagen crosslinking for keratoconus. *Experimental Eye Research*, 113, 92–104. <https://doi.org/10.1016/j.exer.2013.04.010>
- Smolek, M. K. (1993). Interlamellar cohesive strength in the vertical meridian of human eye bank corneas. *Investigative Ophthalmology and Visual Science*, 34(10), 2962–2969.
- Smolek, M. K., & McCarey, B. E. (1990). Interlamellar adhesive strength in human eyebank corneas. *Investigative Ophthalmology and Visual Science*, 31(6), 1087–1095.
- Stefano, D. S. V., Ford, M. R., Ibrahim, S., & Dupps, W. J. (2020). Depth-dependent corneal biomechanical properties in normal and keratoconic subjects by optical coherence elastography. *Translational Vision Science & Technology*, 4. <https://doi.org/10.1167/tvst.9.7.4>
- Studer, H., Larrea, X., Riedwyl, H., & Büchler, P. (2010). Biomechanical model of human cornea based on stromal microstructure. *Journal of Biomechanics*, 43(5), 836–842. <https://doi.org/10.1016/j.jbiomech.2009.11.021>
- Studer, H. P., Pradhan, K. R., Reinstein, D. Z., Businaro, E., Archer, T. J., Gobbe, M., & Roberts, C. J. (2015). Biomechanical modeling of femtosecond laser keyhole endokeratophakia surgery. *Journal of Refractive Surgery*, 31(7), 480–486. <https://doi.org/10.3928/1081597X-20150623-07>

- Truffer, O., Abler, D., Pajic, B., Grabner, G., Kraker, H., & Büchler, P. (2019). Optimization of surgical parameters based on patient-specific models: Application to arcuate keratotomy. *Journal of Cataract and Refractive Surgery*, 45(8), 1084–1091. <https://doi.org/10.1016/j.jcrs.2019.02.022>
- Vahdati, A., & Dupps, W. J. (2015). A fiber-reinforced porohyperelastic swelling model for mechanical behavior of cornea: Application to prediction of keratoconus initiation. *Investigative Ophthalmology & Visual Science*, 56.
- Vahdati, A., Seven, I., Mysore, N., Randleman, J. B., & Dupps, W. J. (2016). Computational biomechanical analysis of asymmetric ectasia risk in unilateral post-LASIK ectasia. *Journal of Refractive Surgery*, 32(12), 811–820. <https://doi.org/10.3928/1081597X-20160929-01>
- Whitford, C., Movchan, N. V., Studer, H., & Elsheikh, A. (2018). A viscoelastic anisotropic hyperelastic constitutive model of the human cornea. *Biomechanics and Modeling in Mechanobiology*, 17(1), 19–29. <https://doi.org/10.1007/s10237-017-0942-2>
- Winkler, M., Shoa, G., Xie, Y., Petsche, S. J., Pinsky, P. M., Juhasz, T., Brown, D. J., & Jester, J. V. (2013). Three-dimensional distribution of transverse collagen fibers in the anterior human corneal stroma. *Investigative Ophthalmology and Visual Science*, 54(12), 7293–7301. <https://doi.org/10.1167/iovs.13-13150>
- Woo, S. L. Y., Kobayashi, A. S., Lawrence, C., & Schlegel, W. A. (1972). Mathematical model of the corneo-scleral shell as applied to intraocular pressure-volume relations and applanon tonometry. *Annals of Biomedical Engineering*, 1(1), 87–98. <https://doi.org/10.1007/BF02363420>
- Woo, S. L. Y., Kobayashi, A. S., Schlegel, W. A., & Lawrence, C. (1972). Nonlinear material properties of intact cornea and sclera. *Experimental Eye Research*, 14(1), 29–39. [https://doi.org/10.1016/0014-4835\(72\)90139-X](https://doi.org/10.1016/0014-4835(72)90139-X)
- Zhou, D., Abass, A., Eliasy, A., Studer, H. P., Movchan, A., Movchan, N., & Elsheikh, A. (2019). Microstructure-based numerical simulation of the mechanical behaviour of ocular tissue. *Journal of the Royal Society Interface*, 16(154). <https://doi.org/10.1098/rsif.2018.0685>

This page intentionally left blank

# Influence of fluid–structure interaction on human corneal biomechanics under air puff non-contact tonometry

# 20

**Osama M. Maklad**

*University of Liverpool, School of Engineering, Liverpool, United Kingdom; University of Greenwich, School of Engineering, Kent, United Kingdom*

## Chapter outline

<b>Introduction.....</b>	465
Corneal biomechanics.....	467
<i>In vivo nondestructive testing.....</i>	468
<i>Ex vivo destructive testing .....</i>	468
Glaucoma .....	469
Aeroelasticity .....	470
Classification of fluid–structure interaction problems .....	471
<b>Numerical methods .....</b>	472
Three-dimensional eye model .....	473
Three-dimensional CFD turbulence model of the air puff.....	475
<b>Air puff traverses and pressure on cornea .....</b>	476
<b>Parametric study statistics .....</b>	476
Clinical dataset .....	479
<b>Intraocular pressure algorithm (fIOP) .....</b>	481
<b>Corneal material stress–strain index (fSSI) .....</b>	483
<b>Conclusions.....</b>	485
<b>References.....</b>	486

## Introduction

The ocular globe is the most valuable sense organ in the human body. It helps in providing three-dimensional, colored, and moving images. The human eye can differentiate between 10 million different colors and even can detect a single photon

(Tinsley et al., 2016). It contains a viscoelastic fluid called vitreous humor which has a pressure that gives the eye its spherical shape called Intraocular pressure (IOP). The IOP is crucial in eye biomechanical analysis and important to understand in terms of how it is controlled and accurately measured. There are many ocular diseases connected directly or indirectly to IOP if it deviates from its normal values. Glaucoma, Ocular Hypertension, and Retinal Detachment are examples of these diseases. Glaucoma, for instance, is considered the second cause of blindness in the world (Elsheikh et al., 2011), and it develops when the eye internal fluid cannot drain properly and the intraocular pressure builds up. This can damage the optic nerve and nerve fibers from the retina (the light-sensitive nerve tissue that lines the back of the eye), Fig. 20.1.

These diseases can be treated with eye drops, laser treatment, or surgery, but early diagnosis is highly desired, as any damage to the eye cannot be reversed. Several comprehensive tests can be carried out to perform this diagnosis and it is

Structures of the Eye

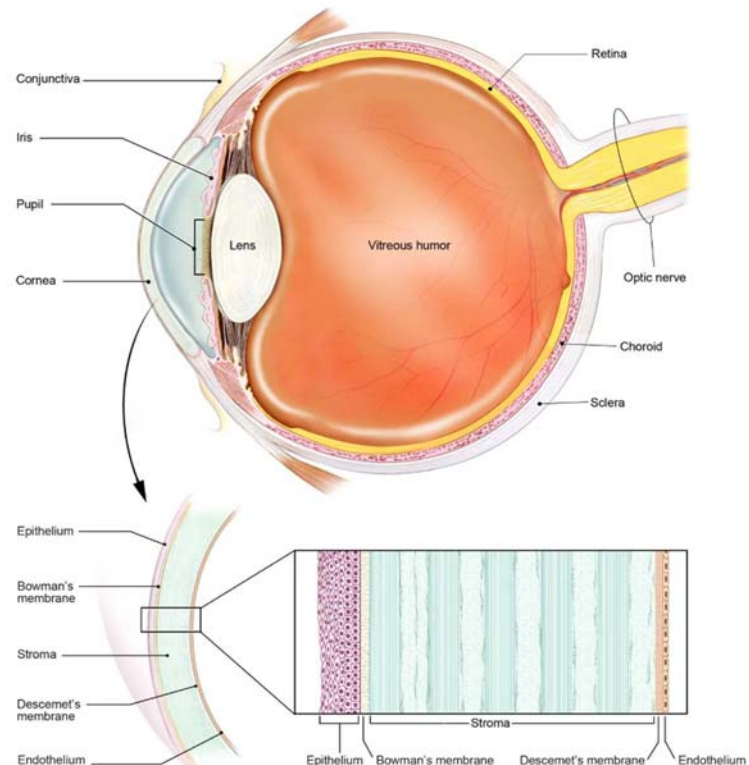


**FIGURE 20.1** The human eye and corneal structure.

From The National Eye Institute (NEI). (2016). (licensed under CC BY 2.0) <https://nei.nih.gov/photo/anatomy-of-eye>

vital to do it as early and accurately as possible. The technique used to measure the IOP is called Tonometry, which can be a contact or noncontact method. Goldmann applanation tonometer (GAT) is one of the contact tonometers and it is considered the gold standard of IOP measurements (Elsheikh et al., 2011; Goldmann & Schmidt, 1957; Moses, 1958). It depends on applying contact force to flatten the front part of the cornea and relate between the applied force and intraocular pressure. This technique was found to be affected by corneal material stiffness, the central thickness of the cornea, and corneal curvature, which are different between patients (Elsheikh, Geraghty, Alhasso, et al., 2010; Elsheikh, Geraghty, Rama, et al., 2010).

The air puff test is one of the noncontact tonometry techniques which uses a rapid jet of air to deform the cornea to estimate the value of intraocular pressure and measure the mechanical response of corneal material. The air puff test is commonly used nowadays since it's easy to use and noninvasive. Studying the dynamic deformation following an air puff has recently been proposed in different biomedical areas (skin (Boyer et al., 2012), bacteria (Fleury et al., 2010), cornea (Kling & Marcos, 2013), soft tissue tumors (Wang et al., 2012)), to noninvasively assess biomechanical properties. In most cases, the degree of deformation of the sample is empirically related to mechanical parameters. A major limitation with the air puff tonometry technique is the lack of consideration of the fluid—structure interaction effect between air puff and the cornea. These changes are not likely to be uniform due to the viscoelastic properties of the cornea and intraocular fluid. In ophthalmology, ocular biomechanics is essential for basic research, clinical evaluation, prognosis, and treatment (Fung, 1993; Kling et al., 2014). The demand for measuring biomechanical properties of biological tissue *in vivo* and noninvasively is high because tissue biomechanics play a key role in a wide range of diseases' diagnoses as a health indicator. Biomechanical properties are also indicative of muscle function and the effects of a disease, wound healing, aging, or cosmetics (Kling et al., 2014).

## Corneal biomechanics

Cornea is the dome-shaped clear surface that covers the front of the eye with a typical diameter of 11.5 mm. It allows the light to enter to back of the eye through the transparent liquid, called vitreous humor, and through the intraocular lens. The cornea plays a vital role in the focusing power of the eye as it contributes 65%–75% of the refractive power (Forrester et al., 2015). The cornea consists of five different layers, Epithelium, Bowman's membrane, Stroma Layer, Descemet's membrane, and Endothelium layer (Krachmer et al., 2005; The National Eye Institute (NEI), 2016) as shown in Fig. 20.1. The functional response of the cornea and ocular vision is greatly influenced by biomechanics of the cornea. The viscoelastic properties of the cornea are given by its physical composition, which has a mixture between the behavior of soft elastic material and high viscous fluids. This mixed behavior gives the cornea the so-called hysteresis effect, which is a history effect or a time delay that the cornea experiences when regaining the original shape after stress

unloading. Therefore, the structural integrity of the cornea can be affected by any corneal disease or after refractive surgeries if the collagen fiber network is disrupted, which will lead to vision distortion (Taylor, 2000). Corneal ectasia and Keratoconus are examples of these pathologies and early detection of corneas at risk is an important decision before any surgery which is done through eye tests and cornea imaging. Keratoconus is a progressive disease associated with irregularities in the fiber network and conical protrusion causing astigmatism and high myopia. The techniques which were developed to measure mechanical properties of the cornea are classified to be *in vivo* nondestructive testing and *ex vivo* destructive testing.

### ***In vivo nondestructive testing***

There are several techniques and methods that are used to measure the corneal biomechanical properties *in vivo* and the application of these techniques is different from one device to another. *In vivo* methods have the advantage of avoiding the error of removing the ocular tissue from its working environment, but on the other hand, they have a lot of limitations on the tools that can be used and the scope of investigation (David et al., 2008; Dolores et al., 2007; Luce, 2005). The Ocular Response Analyser (ORA; Reichert, Inc., Buffalo, NY) (Elsheikh et al., 2009; Luce, 2005a, 2005b) and the CorVis-ST (Oculus Optikgeräte GmbH, Wetzlar, Germany) (Renato et al., 2013) are the most common devices to give a direct analysis of biomechanical properties of the cornea. They are under further research and development to give a better understanding of corneal behavior, which will assist in diagnosing many diseases such as Glaucoma, corneal Ectasia or Keratoconus, and help in ocular surgical planning. They depend on a puff of air to deform the cornea and at the same time, an infrared beam or Scheimpflug imaging monitors shape of the cornea at forward and backward to record the applanation moments when the cornea is flat. A lot of valuable information can be obtained from analysis of the waveform signal generated by the infrared beam in the case of ORA or the Scheimpflug imaging in the case of CorVis-ST. The difference between pressure forces applied by the air puff at applanation times is the value of corneal hysteresis (CH) (Elsheikh et al., 2009; Luce, 2005).

### ***Ex vivo destructive testing***

Many experimental studies were performed on *ex vivo* preserved ocular tissues for donated eyes (Elsheikh, Geraghty, Alhasso, et al., 2010; Elsheikh, Geraghty, Rama, et al., 2010; Gloster et al., 1957; Hoeltzel et al., 1992; Nash et al., 1982; Seiler et al., 1992). This technique provides more flexibility in performing parametric studies and reduces tool limitations, but sacrificing some of the accuracy since the tissue is outside the human body using experimental setups that try to mimic the *in vivo* conditions. The information obtained from *ex vivo* testing including material properties, loading, geometry, and boundary conditions will feed into numerical simulations of these particular tissues. Some studies used uniaxial testing on parts of the cornea or sclera and some used inflation testing for the whole eye globe (Elsheikh, Geraghty, Alhasso, et al., 2010; Elsheikh, Geraghty, Rama, et al., 2010) to measure the tissue

deformation in response to tension or eye inflation. For validation purposes, the same devices that were applied to the eye *in vivo* can be used on the *ex vivo* eyes.

## Glaucoma

Glaucoma is a common visual disorder that can lead to complete vision loss if the optic nerve is severely affected due to the build-up of pressure inside the ocular globe (Sommer, 1989; Sullivan-Mee, 2008). Accurate measurement of IOP is essential in the management of glaucoma and diagnosis of other diseases. The two most common types of glaucoma are Open Angle Glaucoma (OAG) and Angle Closure Glaucoma (ACG). In 2010, more than 44.7 million patients, worldwide, were diagnosed with OAG and 15.7 million patients with ACG. The numbers in 2020 reached 80 million and are expected to increase to over 111 million by 2040 (Quigley, 1996; Sommer, 1989; Sullivan-Mee, 2008). Moreover, a large number of patients can have normal IOP values but have the condition and they are subject to optic nerve damage and gradual sight loss, which is known as normal-tension glaucoma (NTG) (Group, C. N. T. G. S., 1998; Symes & Mikelberg, 2017). Some recent studies looked at the effect of age on stiffness of the cornea and on IOP measurement as a result (Elsheikh, Geraghty, Rama, et al., 2010; Elsheikh et al., 2007; Kotecha et al., 2006). Statistical studies using clinical datasets were carried out to improve the IOP measurement accuracy (Sullivan-Mee, 2008). Measurement errors can be misleading and recommend false treatments. There are multiple reasons that can lead to increased pressure level inside the eye, which can be considered the same causes of glaucoma (Group, C. N. T. G. S., 1998; Symes & Mikelberg, 2017). Some of these reasons are listed below:

- The aqueous humor is a renewable fluid produced by the ciliary body located behind the iris. It flows via the pupil to fill the anterior chamber. The trabecular meshwork and Schlemm's canal are the drainage pathways for aqueous liquid located at the anterior chamber periphery, Fig. 20.2. If any blockage occurred at this meshwork, for whatever clinical reason, it will lead to excessive production of the aqueous humor over the drainage rate causing build-up of pressure inside the eye (The National Eye Institute (NEI), 2016; Sullivan-Mee, 2008).
- Some medications can have an influence on the production or drainage rate of aqueous from the eye as a side effect to treating another condition, for instance, steroid drops after LASIK surgery can increase eye pressure and patients are advised to monitor their IOP level for some time after surgery.
- Any injury or accident can cause blockage to the drainage pathways, leading to increased eye pressure levels even after months or years after the trauma.

The normal value of intraocular pressure is different between people and ethnic groups, but it ranges between 10 and 20 mmHg. If IOP increases above this range, the patient might be at risk of glaucoma (Caprioli & Coleman, 2008; Hong et al., 2007). In the current numerical simulations, despite there are multiple components inside the eye including ocular lens, iris, aqueous and vitreous, the human eye is

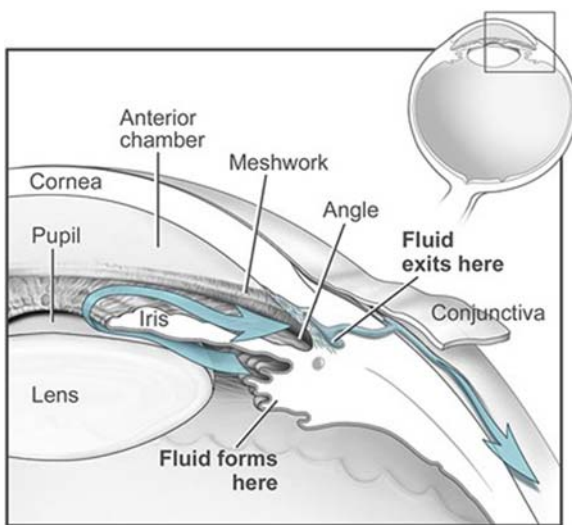


**FIGURE 20.2 Flow of the aqueous fluid inside the eye.**

From The National Eye Institute (NEI). (2016). (licensed under CC BY 2.0).

dealt with as a deformable pressure vessel that has internal pressure equal to IOP applied using a fluid cavity taking into account the change in pressure with change in volume.

### Aeroelasticity

Aeroelasticity deals with the combined features of fluid mechanics and solid mechanics. There are many applications based on this part of science including; air-crafts wing design, turbo-machinery, bridges and skyscrapers design, electric transmission lines, artificial heart valves, and the air puff test, moreover, it is considered the foundation of modern biomechanics (Dimitriadis, 2017; Hedges & Pierce, 2011; Hedges et al., 2003; Wang, 2008). In most of aeroelasticity applications, it is normally assumed that the external loading acting on a structure is, in general, independent of the deformation of that structure and this was the assumption made in the literature when simulating the air puff test, but actually, deformations of the cornea are in the same order of magnitude of air velocity compared to the eye and cornea size which will have an effect on the applied aerodynamic force by the air jet if it is ignored (Jaroslav & Stefan, 2006, pp. 146–170; Wang, 2008).

The main aim of this chapter is to produce estimation algorithms of intraocular pressure measurement and corneal material behavior by noncontact air puff method taking into account, fluid–structure interaction effects between the air puff and cornea via a parametric study with different eye geometries, material parameters, and pressure loadings. The specific objectives are to study the fluid–structure interaction effect on corneal deformation profiles and air puff pressure distribution, to

conduct a parametric study to understand the association of different eye parameters on IOP measurement and corneal biomechanical behavior, to produce an estimation algorithm of intraocular pressure with no association with eye biomechanical parameters, and to develop a biomechanical material behavior algorithm to represent the hyperelastic nonlinear nature of the cornea.

## Classification of fluid–structure interaction problems

In fluid mechanics, solids are considered as boundary conditions only and not in terms of what they are made of. For instance, in a flow around a cylinder, the cylinder deviates the uniform flow and prevents the fluid from penetrating the body of the cylinder. On the other hand, in solid mechanics, problems are solved for deformations of the solid under loading. Some of these loadings can be due to the presence of a fluid such as a deformation of a submarine under external pressure or inflation of a balloon under internal pressure or a building or a bridge subject to the wind (Abaqus, 2014; Jaroslav & Stefan, 2006, pp. 146–170; Wang, 2008). Usually, the fluid is considered a cause of loading at the boundary. The two approaches can work separately in many applications with acceptable results, but in other applications, separate solutions are not accurate enough and consideration of fluid–structure interaction becomes necessary. These interactions are mostly driven by practical and industrial applications such as biomechanics, aerospace, nuclear and civil engineering.

The reduced velocity ( $U_R = T_{\text{Solid}}/T_{\text{Fluid}}$ ) is a vital dimensionless number to be quantified. Fig. 20.3A explains the broad range of the reduced velocity and influence of this dimensionless number on classification of the problem and method of solution. For a small reduced velocity close to zero, the time scale of the fluid domain is much larger than the time scale of the solid domain. In other words, velocity of the fluid can be compensated in the structural model without the need to consider a separate fluid model. Simulating a boat oscillating in still water or offshore designs are examples of such problems. This assumption of neglecting

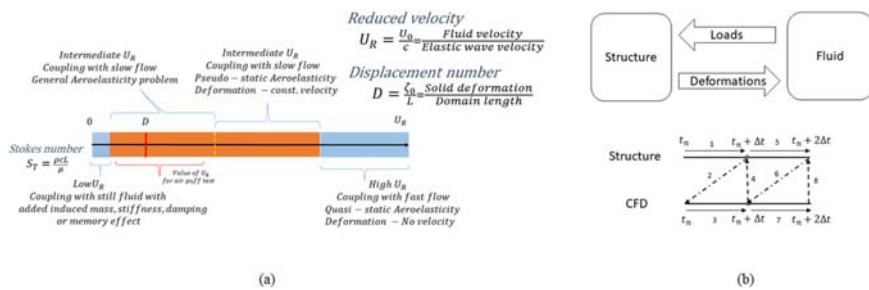


**FIGURE 20.3 Classification of fluid–structure interaction problems based on the value of the reduced velocity  $U_R$ .**

(A) Classification of fluid–structure interaction problems based on the value of the reduced velocity  $U_R$ , (B) Components of fluid–structure interaction (FSI) analysis and flow of the solution at each time step.

the fluid velocity simplifies the general equations allowing the two domains to be solved separately. The effect of the fluid on the solid will be in a form of fluid-induced stiffness to the oscillator equation, and based on the value of Stokes number ( $S T = RE/UR$ ), fluid-induced damping (viscous effect) (Low  $S T$ ), fluid-induced mass (inertia effect) (high  $S T$ ), or memory effect (intermediate  $S T$ ) is added to the solid equation, such as coupling between a solid tank and sloshing water (De Langre et al., 2016; Jaroslav & Stefan, 2006, pp. 146–170; Wang, 2008).

For high reduced velocities in the order of magnitude of 100, the solid deformations are coupled with a fast flow, when the timescale of the fluid is much smaller than the timescale of the solid. In aerospace engineering, this concept is called aeroelasticity approximation or quasi-static aeroelasticity, which neglects the velocity of the solid structure and considers the solid domain deformation is frozen in time. However, these deformations have to be calculated at different time intervals, and this is done separately as there is a separation between the two timescales. The effect of the fluid on the solid domain will be in a form of an added stiffness that depends totally, in terms of sign and magnitude, on the fluid velocity.

For intermediate reduced velocities in the order of magnitude close to the displacement number, the problems become more complicated as the two timescales are in the same order of magnitude and there is no model that is dominant over the other, so both models have to be solved simultaneously, which is known as coupling with a slow flow. The most general case will be when the interface has deformation, velocity, and acceleration, which is the case in the air puff test. In the case of pseudo-static aeroelasticity, acceleration of the interface is neglected and the velocity is considered constant with time as this can be simpler and computationally more economic. The reduced velocity of the air puff test ranges between 0 and 10 at the maximum velocity. The displacement number of the eye model is in order of magnitude of  $10^{-2}$ . So any approximation or selection to another method, rather than the full coupling between the two models, will have a major impact on accuracy of the solution (De Langre et al., 2016; Jaroslav & Stefan, 2006, pp. 146–170; Wang, 2008).

---

## Numerical methods

The interaction between the air puff and the eye includes the exchange of data and information between two different models with different governing equations; one is a structural model analyzed using finite element method to calculate deformations and stresses in ocular tissue material, and a computational fluid dynamics (CFD) model to simulate the air puff and calculate the pressure acting on the eye globe. As shown in Fig. 20.3B, the structural model calculates the deformations (line 1) and sends them to the fluid model (line 2) which in turn calculates the pressure loads (line 3) and returns them back to the structural model (line 4). This process takes place at each time step ( $\Delta t$ ) of the computation time and is repeated through the analysis. The finite element model of the whole eye, created by bespoke software, was

used as the structural model (Elsheikh, Geraghty, Alhasso, et al., 2010; Elsheikh et al., 2008, 2009, 2013), in which the hyper-elastic and viscoelastic properties of the ocular vessel are defined. In previous attempts made on that eye model to simulate the tonometry test, the air puff pressure was applied as an external static pressure load with a fixed spatial and temporal distribution as provided by Oculus, which didn't take into account the effect of fluid–structure interaction (Elsheikh et al., 2009; Joda et al., 2015; Luce, 2005). The presented results in this chapter depended on using ABAQUS/Explicit, ABAQUS/CFD (Version 6.14, Dassault Systemes Simulia Inc., USA) (Abaqus, 2014; Jaroslav & Stefan, 2006, pp. 146–170; Wang, 2008), and the cosimulation engine (CSE) available in ABAQUS. This cosimulation capability enables two-way coupling between the structure and the fluid models. This coupling mechanism was tried, tested, and validated against clinical data.

### Three-dimensional eye model

The eye model consisted of 10,000 fifteen-nodded continuum elements (C3D15H), a general-purpose element with nine integration points, arranged over two layers, distributed along 15 rings in the cornea and 35 rings in the sclera. The corneal topography was based on the Pentacam measurements of topography and thickness profile. For sclera, we do not have information on the accurate dimensions specific to each patient. Hence, we used idealized geometry for the sclera based on average clinical dimensions; however, depending on age of the patient, the scleral material stiffness was adjusted. Therefore, by patient-specific eye models, we mean the material of the whole eye globe is specific to the patient and adjusted based on age. However, the geometry of sclera is not specific to the patient and relies on idealized average values (Eliasy et al., 2019; Elsheikh, Geraghty, Rama, et al., 2010). The model also incorporated attributes to represent *in vivo* conditions including the nonuniform thickness of cornea and sclera, weak interlamellar adhesion in corneal stroma, and asphericity of the cornea's anterior and posterior surfaces (Elsheikh et al., 2013). The eye model included five different material definitions for cornea, limbus, anterior, equatorial and posterior sclera behaving hyperelastically, and their stiffness increases gradually under loading following an S-shaped stress–strain path, as reported previously in experimental studies (Elsheikh, Geraghty, Alhasso, et al., 2010; Elsheikh et al., 2010a, 2010b; Elsheikh et al., 2008, 2009). With these important features, the model can select which stress–strain path (under loading or unloading) that each element would follow based on its strain history. The hyperelastic materials have a rubber-like material behavior and the strain energy potential function ( $\Pi$ ) is different from elastic materials and it takes multiple forms. The following Ogden form was the one applied in the finite element model of the human eye (Abaqus, 2014; Jaroslav & Stefan, 2006, pp. 146–170; Wang, 2008):

$$\Pi = \sum_{i=1}^N \frac{2\mu_i}{\alpha_i^2} (\bar{\lambda}_1^{\alpha_i} + \bar{\lambda}_2^{\alpha_i} + \bar{\lambda}_3^{\alpha_i} - 3) + \sum_{i=1}^N \frac{1}{D_i} (J^{el} - 1)^{2i} \quad (20.1)$$

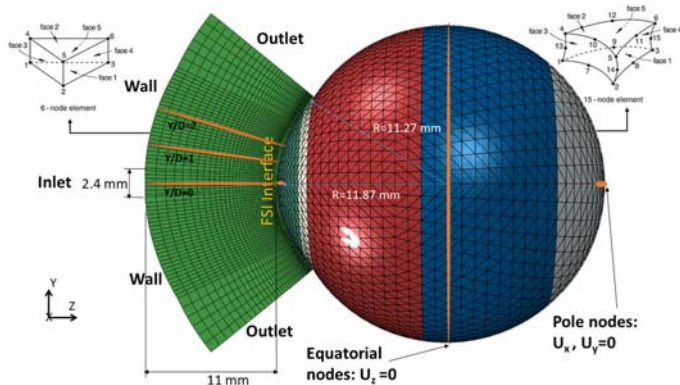


**FIGURE 20.4** Geometry definition of the air puff and eye domains showing key dimensions, element types, and boundary conditions.  $U_x$ ,  $U_y$ , and  $U_z$  are the deformations in the three dimensions.

where  $\bar{\lambda}_i$  are the deviatoric principal stretches which are related to the deformations at constant volume as outcome of shear stresses (Abaqus, 2014; Elsheikh et al., 2013);  $N$  defines the order of the Ogden model with maximum of sixth order ( $N = 6$ );  $\mu$  and  $\alpha$  are material parameters;  $J^{el}$  is the elastic volume ratio related to thermal expansion and  $D_i$  defines the material compressibility.

Finite element model of the eye was prevented from rigid body motion in the Z-direction (anterior–posterior) at the equatorial nodes. In addition, the posterior and anterior pole nodes were restricted in X and Y directions, to prevent rotation, but were free to move in the Z-direction (anterior–posterior) (see Fig. 20.4). The rest of the nodes in the model were free to move in all directions. Before analysis, the stress-free geometry of the eye was estimated. It is important to calculate the undeformed configuration of the eye before applying the IOP, since deformed geometry of the eye will not be suitable for applying different values of IOP when performing the parametric study. An iterative approach was used to gradually move the mesh nodes to reach the stress-free (relaxed) configuration of the ocular tissue (Elsheikh et al., 2013; Pandolfi & Holzapfel, 2008). An initial numerical model was generated based on a measured value of IOP and corneal patient-specific geometry of the ocular tissue. The calculated deformations were then subtracted using inverse calculations from the stressed geometry to get the relaxed (stress-free) geometry.

To represent intraocular pressure inside the eye, the fluid cavity technique was used. This technique was mainly used to simulate fluid-filled structures such as pressure vessels, hydraulic or pneumatic actuators, and automotive airbags. The fluid cavity behavior governs the relationship between cavity pressure, structure deformation, and volume (Abaqus, 2014; Jaroslav & Stefan, 2006, pp. 146–170; Wang, 2008). The fluid cavity calculates the change in IOP and internal volume during application of the air puff and corneal deformations. The fluid cavity was filled with a fluid with a density of  $1000 \text{ kg/m}^3$  and a bulk modulus of  $2.2 \times 10^3$ .

### Three-dimensional CFD turbulence model of the air puff

Model of the air puff consisted of 103,680 six-noded 3-D fluid continuum elements (FC3D6) and used Spalart–Allmaras turbulent eddy viscosity model (Maklad et al., 2018a; NASA, 2011; Versteeg & Malalasekera, 2007) to simulate the turbulence in the air jet. The air model domain and mesh were created over the cornea and a 4 mm ring of the sclera by projecting coordinates of the anterior surface nodes to a distance of 11 mm from the cornea apex, as shown in Fig. 20.4. The projection principle was based on the concept of similar triangles to calculate new coordinates of the air domain as projected from the eye coordinates. It was important to generate a MATLAB code that is applicable for all eye geometries, idealized and corneal patient-specific, healthy or with certain pathological conditions. Material properties of air were defined in terms of density  $1.204 \text{ kg/m}^3$  and dynamic viscosity  $1.83 \times 10^{-5}$ .

For the cosimulation step to run successfully, the interaction surfaces in the eye and air models should be exactly the same with the same node numbering. The air puff test is a transient problem, and Abaqus/CFD used an advanced second-order projection method to create an arbitrary deforming mesh (Shirokoff & Rosales, 2011). It used node-centered finite-element discretization for the pressure and a cell-centered finite volume discretization of all other transported variables (such as velocity, temperature, turbulence, etc.) (Abaqus, 2014; Jaroslav & Stefan, 2006, pp. 146–170; Wang, 2008). This hybrid meshing approach removed the need for any artificial dissipation while preserving the traditional conservation properties associated with the finite volume method. The parallel preconditioned Krylov solvers (DSGMRES–ILUFGMRES) (Drkošová et al., 1995; Kelley, 1995; Pueyo & Zingg, 1991) were the main solution methods for transport equations including momentum and turbulence with prescribed iteration limit and convergence criteria (Maklad, Eliasy, Chen, Theofilis, & Elsheikh, 2020). The pressure and distance function equations were solved with one of the Krylov solvers (diagonally scaled FGMRES, built-in Abaqus), and a strong multigrid algebraic preconditioner (Kincaid et al., 1982; Shirokoff & Rosales, 2011; Su et al., 2004). The time was integrated using second-order accuracy and all other diffusive and advective terms were integrated using the Crank–Nicolson method (Crank & Nicolson, 1947). The CFL (Courant–Friedrichs–Lewy) stability condition was also satisfied by continually adjusting the time increment size. The maximum value for CFL number was kept at 0.45. The CFL condition was necessary for partial differential equations' solution convergence (Courant et al., 1928; De moura, 2013). It must be less than one for explicit solvers to converge since the full numerical domain of dependence must contain the physical domain of dependence such as Laney's definition (Laney, 1998).

To prevent distortion of the fluid mesh in the air puff model, the adaptive Arbitrary Lagrangian–Eulerian (ALE) deforming mesh was used. In FSI applications, where there are large solid deformations, the adaptive mesh is important for stability of the solution (Donea et al., 2017, pp. 1–23; Hron & Turek, 2006; Kcharik et al., 2006). This method has the following characteristics: the mesh motion is constrained only at the free boundaries but everywhere else the material and mesh motion are

independent. Moreover, it incorporates two main tasks: creating a new mesh and remapping the solution variables, through a process named advection, from the old mesh to the new mesh (Donea et al., 2017, pp. 1–23; Hron & Turek, 2006; Kcharik et al., 2006; Souli & Zolesio, 2001). The meshing was created at a prespecified frequency accompanied by a combination of mesh smoothing methods (Abaqus, 2014; Jaroslav & Stefan, 2006, pp. 146–170; Wang, 2008). Then, the solution variables were remapped to the new mesh with second-order accuracy and conserving mass and momentum.

---

### Air puff traverses and pressure on cornea

The air puff was analyzed to see the change of velocity, pressure, and mesh deformation during the test. Fig. 20.5 shows two velocity components of the air puff, the axial velocity ( $V_3$ ) normal to the cornea and velocity component ( $V_1$ ) parallel to the cornea at three normal traverses ( $Y/D = 0$ ,  $Y/D = 1$ ,  $Y/D = 2$ ), shown in Fig. 20.4, and at four time steps  $T = 5, 8, 10$ , and  $16$  ms (Maklad et al., 2018b). By the time, the puff gets stronger to reach its maximum strength at  $T = 16$  ms and as the distance from the puff orifice increases, the normal velocity decreases until it reaches zero at the stagnation point on the corneal surface. By changing the path or the axial traverse further away from the corneal center, the puff gets weaker and is noticed at ( $Y/D = 1$  and  $2$ ), there are some negative values for the normal velocity indicating reflection of the air from the corneal surface in the opposite direction to the flow. The jet accelerates parallel to the cornea forming a radial wall jet, developing with time and going further from the corneal center axis. This explains why there is a negative pressure observed at this location of the cornea.

Fluid–structure interaction was found to have an effect on the pressure distribution on the cornea during time of the air puff test. Fig. 20.6A shows the pressure distribution change with time and the region where there is negative pressure and also indicates the difference between taking the FSI effect into account and ignoring it, if the cornea was considered as a rigid, nondeformable, surface (Maklad, Eliasy, Chen, Wang, et al., 2020). Two different simulations of the turbulent jet were performed; one impinging on a rigid corneal surface with no moving boundaries and the other using FSI coupling at the interface between air and eye models to consider corneal deformations. Additionally, Fig. 20.6B shows how the temporal pressure profile changes from one model to another due to changes in the corneal biomechanical parameters. The means of these differences were 3.4% at  $T = 8$  ms and increased to 8.4% at time =  $16$  ms.

---

### Parametric study statistics

A parametric study was carried out to gauge the influence of cornea biomechanical parameters on its response to the air puff since this provides valuable information on

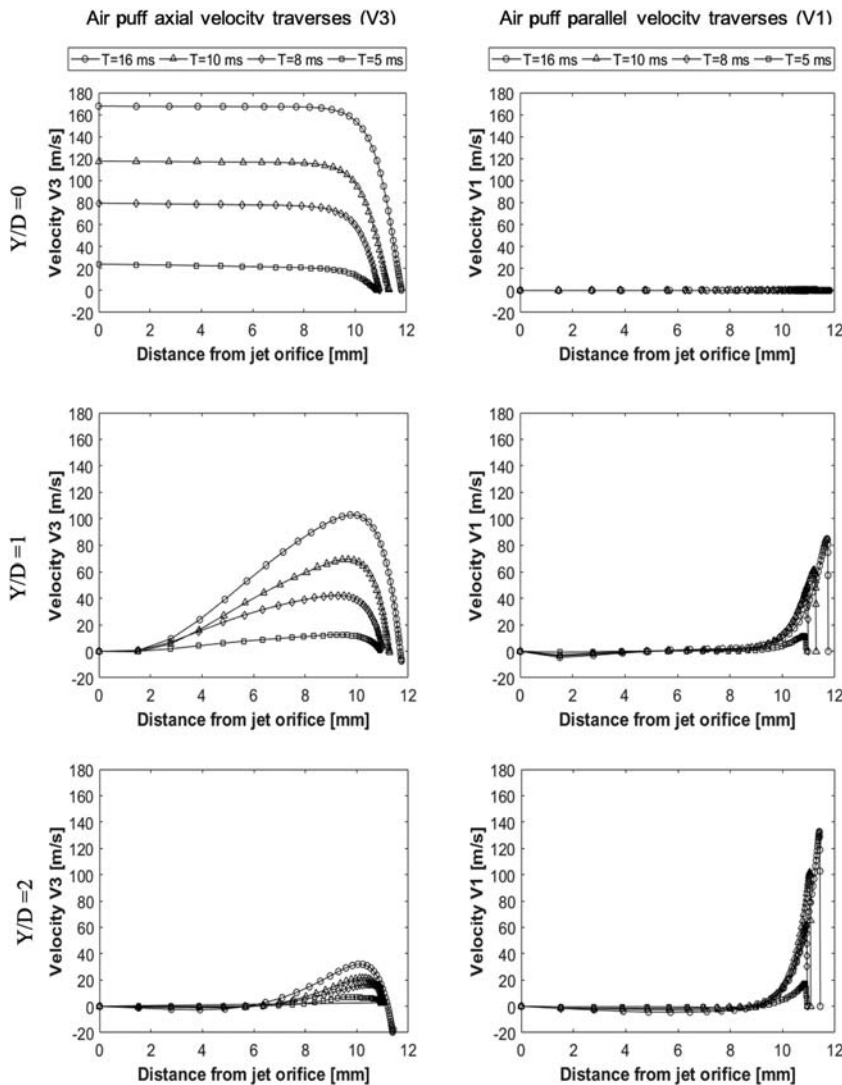


**FIGURE 20.5** Air puff velocity components (V3 and V1) at axial traverses  $Y/D = 0$ ,  $Y/D = 1$ ,  $Y/D = 2$ , and at four time steps at  $T = 5, 8, 10$ , and  $16$  ms.

how healthy the cornea is and to quantify the correlations and significance of relationships between parametric study's input and output parameters, to choose which response parameters were influenced more by changing IOP and corneal stiffness. This will help in correcting the effect of biomechanics on IOP measurement and corneal material behavior estimation. The eye parameters that were varied in the parametric study were central corneal thickness (CCT), between 445 and 645  $\mu\text{m}$ ,

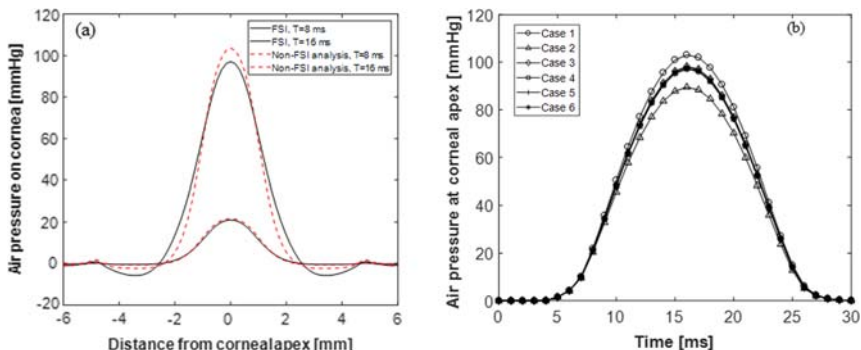


**FIGURE 20.6 (A)** Predicted pressure distribution on the cornea with and without FSI analysis, **(B)** Temporal pressure profiles for six different models.

intraocular pressure (IOP), between 10 and 25 mmHg, corneal curvature radius ( $R$ ), between 7.4 and 8.4 mm, and corneal material stiffness coefficient ( $\mu$ ), between 0.0422 and 0.1082. A bivariate correlation analysis using SPSS statistics (version 24, IBM Corp., Armonk, NY, USA) was performed to obtain Pearson's correlation coefficient ( $r$ ) and two-tailed significance t-test to know the significance level of correlations ( $P$ -value). Descriptive statistics of the parametric study are shown in Table 20.1, providing mean, standard deviation, minimum and maximum of input and output parameters for 110 different eye models.

**Table 20.1** Descriptive statistics of 110 models of the parametric study

Variable	Mean	Std. deviation	Minimum	Maximum
IOP (mmHg)	18.36	6.25	10	25
CCT ( $\mu\text{m}$ )	550.45	73.99	445	645
$\mu$	0.0712	0.0236	0.0422	0.1082
$R$ (mm)	7.82	0.33	7.4	8.4
A1 time (ms)	9.66	0.97	7.81	12.47
A1 length (mm)	2.15	0.19	1.91	2.62
A1 velocity (mm/s)	0.13	0.04	0.06	0.21
HC time (ms)	16.21	0.36	15.3	16.9
Peak distance (mm)	4.58	0.95	2.46	6.62
A1 Def. Amp. (mm)	0.23	0.05	0.17	0.39
HC Def. Amp. (mm)	0.84	0.3	0.42	1.77
AP1(mmHg)	42.09	12.09	18.82	75.24
SP-HC	34.69	21.92	5	109.59

Descriptive statistics of 110 models of the parametric study the first four parameters are the input parameters and the rest are output parameters.

Values of Pearson's correlation coefficient ( $r$ ) between input and output response parameters are shown in [Table 20.2](#). The highest correlated deformation parameters to IOP change were first applanation pressure (AP1), and the highest concavity radius ( $R_{HC}$ ) were the highest correlated parameters to IOP ( $r = 0.736$  and  $0.624$ , respectively, and  $P < .001$ ). For this reason, AP1 and  $R_{HC}$ , along with CCT, R and age were included in the fIOP equation. On the other hand, the stiffness parameter at highest concavity (SP-HC) was the most associated response parameters to corneal material change ( $r = 0.442$ ,  $P < .01$ ), and was therefore included with CCT and fIOP in the corneal material estimation algorithm ([Maklad, Eliasy, Chen, Wang, et al., 2020](#)).

### Clinical dataset

The Corvis data of right and left eyes of 476 healthy participants from the Vincieye Clinic in Milan, Italy, and Rio de Janeiro Corneal Tomography and Biomechanics Study Group, Brazil, were reviewed and used to validate the numerical model and the estimation algorithms. The participants had an age range between 10 and 87 years, CCT between 455 and 630  $\mu\text{m}$ , and IOP between 9 and 25 mmHg, [Table 20.3](#). The data included the maximum deformation, first applanation pressure, first applanation time, highest concavity radius, spatial and temporal corneal deformation. The Institutional review board of the University of Liverpool ruled that approval was not obligatory for this record review study. However, the ethical standards set out in the 1964 Declaration of Helsinki and their revision in 2013 were observed and all patients provided informed written consent before using their deidentified data in research. All participants provided informed consent before using their data in the study. All participants had a complete ophthalmic examination, including the CorVis ST (SW version 1.2r1307) and Pentacam (OCULUS Optikgeräte GmbH; Wetzlar, Germany). The inclusion criteria of healthy subjects were a Belin/Ambrósio Enhanced Ectasia total deviation index (BAD-D) of less than 1.6 the standard deviation (SD) from normative values in both eyes, no previous ocular surgery, and systematic conditions including diabetes, myopia less than 10D and no concurrent or previous glaucoma or hypotonic therapies ([Villavicencio et al., 2014](#)). Moreover, to confirm the diagnosis, all exams of each clinic were blindly reevaluated by a corneal expert at the other clinic. Corneal patient-specific numerical eye models were produced using an in-house MATLAB code to perform a parametric study with a wide range of CCT, IOP, and corneal material properties starting from the stress-free geometry for validation purposes. The data was also used to assess whether, as expected, fIOP was independent of CCT, age, and R. Similarly, independence of the corneal material stiffness parameter of CCT and IOP, and correlation with age.

**Table 20.2** Correlation and relationship significance analysis between input and output parameters of the parametric study.

Variable		A1 time (ms)	A1 length (mm)	A1 velocity (mm/s)	HC time (ms)	Peak Dist. (mm)	A1 deformation Amp. (mm)	HC deformation Amp. (mm)	AP1 (mmHg)	SP-HC stiffness parameter
IOP (mmHg)	Pearson correlation (r)	0.725**	-0.455**	-0.731**	-0.255**	-0.616**	-0.403**	-0.635**	0.736**	0.442**
	Sig. (two-tailed)	0	0	0	0.007	0	0	0	0	0
CCT (μm)	Pearson correlation (r)	0.382**	0.637**	-0.206*	-0.122	-0.500**	0.673**	-0.493**	0.385**	0.468**
	Sig. (two-tailed)	0	0	0.031	0.204	0	0	0	0	0
μ	Pearson correlation (r)	0.338**	0.471**	-0.367**	-0.280**	-0.407**	0.432**	-0.377**	0.355**	0.434**
	Sig. (two-tailed)	0	0	0	0.003	0	0	0	0	0
R (mm)	Pearson correlation (r)	-0.007	-0.056	-0.067	0.032	0.088	-0.253**	-0.052	0.007	-0.088
	Sig. (two-tailed)	0.946	0.564	0.486	0.741	0.362	0.008	0.592	0.945	0.362

\*: Correlation is significant at the 0.05 level. \*\*: Correlation is significant at the 0.01 level. A1 is the first applanation; AP1, first applanation pressure; CCTs, central corneal thickness; HC, highest concavity; IOP, intraocular pressure; μ, corneal material stiffness coefficient; R, corneal curvature radius; SP-HC, stiffness parameter at highest concavity.

**Table 20.3** The clinical dataset used in validation of the numerical model of the air puff test

CCT is the central corneal thickness and CVS-IOP is the CorVis-ST IOP measurement.

Datasets	Participants	Age (years)	CCT ( $\mu\text{m}$ )	CVS-IOP (mmHg)
Dataset 1 (Milan)	225	$38 \pm 17.2$ (7–91)	$543 \pm 31.5$ (458–635)	$15.7 \pm 2.35$ (11–25)
Dataset 2 (Rio)	251	$43 \pm 16.5$ (8–87)	$539 \pm 33.2$ (454–629)	$14.8 \pm 3.06$ (6–34)

### Intraocular pressure algorithm (fIOP)

The numerical models had IOP, CCT, R, and age as input parameters, and the output was corneal deformation profiles that resulted in response parameters including, most notably, peak distance, first applanation deformation amplitude, first applanation length, highest concavity deformation amplitude, and highest concavity radius, as shown by Fig. 20.7. Analysis of the input and output parameters allowed the development of fIOP as a function of CCT, R, age, the first applanation pressure (AP1), and the highest concavity radius (RHC) which were the highest correlated parameters to IOP ( $r = 0.736$  and  $0.624$ , respectively, and  $P < .001$ ).

For each of the parameters for which significant correlation was confirmed, an exercise was conducted to determine the lowest possible polynomial order that should be adopted in the fIOP equation based on the lowest route mean square error (RMSE). The objective function adopted took the form

$$\min \text{RMS} = \min \sqrt{\frac{1}{N} \sum_{i=1}^N (\text{fIOP}_i - \text{IOP}_{\text{true},i})^2} \quad (20.2)$$

where RMS is the root mean square of the error,  $N$  is the number of eye models, and  $\text{IOP}_{\text{true}}$  is the value set in the numerical models. Following using this objective function of the least-squares method, the fIOP equation took the form

$$\text{fIOP} = C_{\text{AP1}} \times C_{\text{CCT-age}} \times C_R \times C_{\text{RHC}} + C \quad (20.3)$$

where

$$\begin{aligned} C_{\text{AP1}} &= (-0.005 \times \text{AP1} + 0.19)C_{\text{CCT-age}} \\ &= (0.011 \times \text{CCT}^3 \mu^3 - 0.002 \times \text{CCT}^3 \mu^2 + 9.17 \times \text{CCT}^3 \mu + 8.34 \times \text{CCT}^3 \\ &\quad - 6.3 \times \text{CCT}^2 \mu^3 + 1.16 \times \text{CCT}^2 \mu^2 - 0.05 \times \text{CCT}^2 \mu \\ &\quad - 0.003 \times \text{CCT}^2 + 0.76 \times \text{CCT} \mu^3 + 5.67 \times \text{CCT} \mu^2 \\ &\quad - 4.87 \times \text{CCT} \mu + 1.73 \times \text{CCT} - 0.55 \times \mu^3 + 0.76 \times \mu^2 + 1.82 \times \mu + 4.09) \end{aligned} \quad (20.4)$$

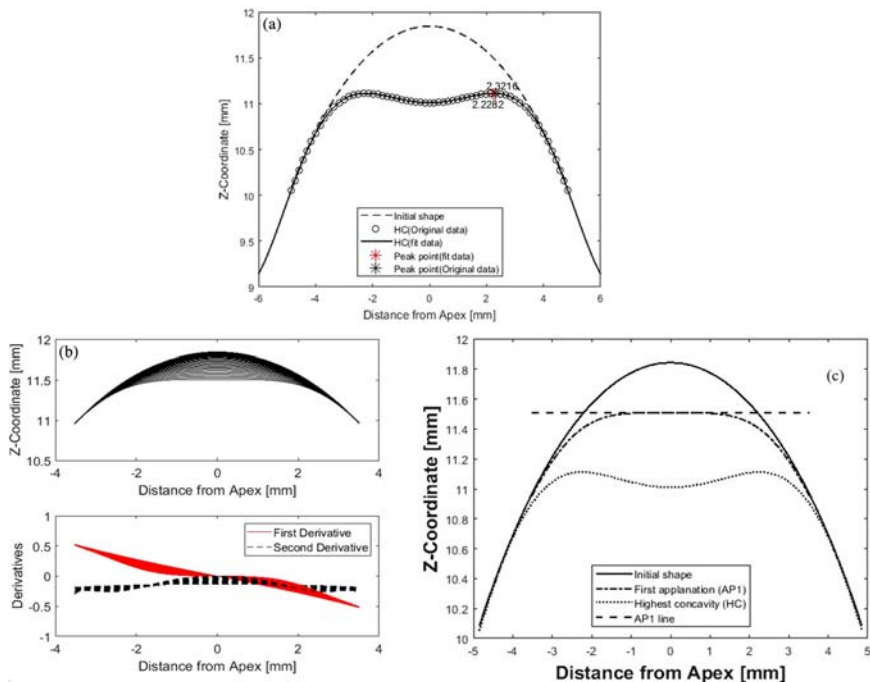


**FIGURE 20.7 Example results of a typical analysis showing corneal deformation parameters from the numerical model**

Example results of a typical analysis showing corneal deformation parameters from the numerical model including (A) peak point location at highest corneal concavity to calculate peak distance, which is the distance between the two corneal peaks, (B) first applanation moment determined by using first and second derivatives of corneal profiles over the 7 mm diameter central zone, and (C) applanation length by calculating the difference between Apex Z-coordinate and its neighboring points until a tolerance of 0.01 is broken.

$$\mu = 0.076e^{0.536age} \quad (20.5)$$

$$C_R = (0.045 \times R - 0.213 \times 10^{-3}) \quad (20.6)$$

$$C_{R_{HC}} = (-0.0008 \times R_{HC} - 0.68)C = 9.36 \quad (20.7)$$

In this equation, fIOP and AP1 were in mmHg, CCT in microns,  $R$  and  $R_{HC}$  in mm, and age in years. With this equation form, the RMS error was 4.5%. Fig. 20.8 presents an analysis of the association of fIOP, the previously developed bIOP (Eliasy et al., 2018), and the uncorrected Corvis IOP readings (CVS-IOP) with CCT, age, and corneal curvature. The results show a similar performance of fIOP with that of bIOP in reducing the association CVS-IOP with CCT. The figure

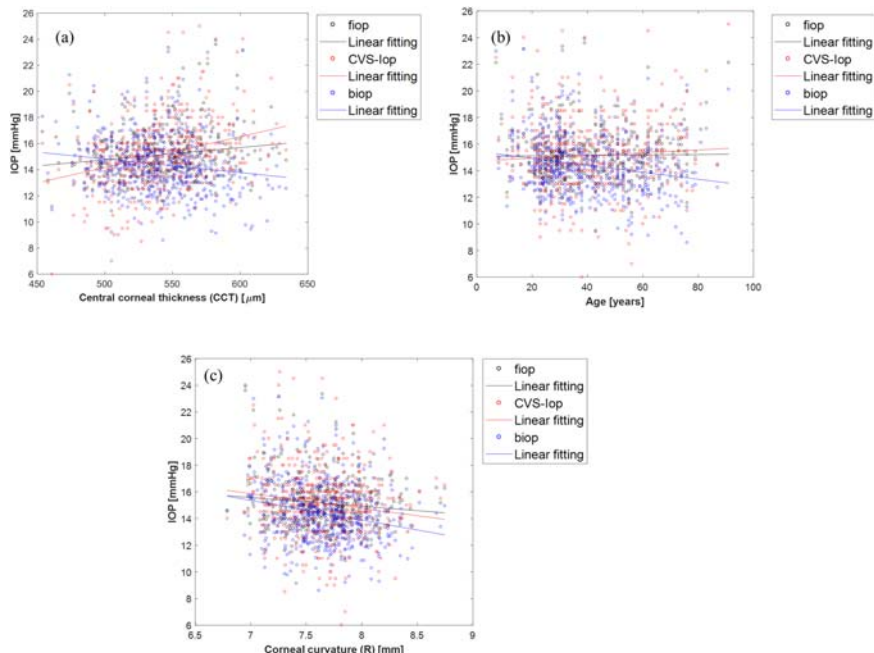


**FIGURE 20.8** Association of fIOP, CorVis, and bIOP values with (A) central corneal thickness, (B) age, and (C) corneal apical.

also demonstrates better performance with fIOP than with bIOP in reducing the association of CVS-IOP with both age and  $R$ .

### Corneal material stress–strain index (fSSI)

The development of the corneal material stiffness index, fSSI followed a similar route that was taken for fIOP and the objective function took the form:

$$\min \text{ RMS} = \min \sqrt{\frac{1}{N} \sum_{i=1}^N (\text{fSSI}_i - \text{SSI}_i)^2} \quad (20.8)$$

where RMS is the root mean square of the error,  $N$  is the number of eye models, and SSI is the value set in the numerical models. The analysis of the input and output parameters from the parametric study resulted in fSSI being a function of CCT, fIOP, and the stiffness parameter at highest concavity (SP-HC) which was the most associated response parameter to corneal material change ( $r = 0.442$ ,  $P < .01$ ). Using the least-squares method, the fSSI algorithm took the following form:

$$fSSI = \begin{cases} 0.5, & \text{for } \ln(SP - HC) = 0.026 + 1.83 \times (\text{fIOP}/20) + 2.26 \times (\text{CCT}/545) \\ 1.0, & \text{for } \ln(SP - HC) = 0.68 + 1.44 \times (\text{fIOP}/20) + 2.36 \times (\text{CCT}/545) \\ 1.5, & \text{for } \ln(SP - HC) = 0.85 + 1.49 \times (\text{fIOP}/20) + 2.35 \times (\text{CCT}/545) \\ 2.0, & \text{for } \ln(SP - HC) = 1.11 + 1.02 \times (\text{fIOP}/20) + 2.55 \times (\text{CCT}/545) \\ 3.0, & \text{for } \ln(SP - HC) = 1.33 + 1.05 \times (\text{fIOP}/20) + 2.54 \times (\text{CCT}/545) \end{cases} \quad (20.9)$$

where fIOP is in mmHg and CCT is in microns. For intermediate values of  $\ln(SP - HC)$ , interpolation between the values of fSSI could be performed. With this equation form, the RMS error was 8.83%. As additional validation of fSSI, its correlation with CCT, age and fIOP was assessed. Weak correlation with CCT and fIOP would be a sign of success along with positive correlation with age (where earlier evidence pointed at tissue stiffening with aging (Elsheikh, Geraghty, Alhasso, et al., 2010; Elsheikh, Geraghty, Rama, et al., 2010)). The results shown in Fig. 20.9 present better performance than SSI in maintaining weak correlation with CCT and IOP. Meanwhile, the correlation of fSSI with age was stronger than for SSI ( $r^2 = 0.415$  vs. 0.191) (Maklad et al., 2020).

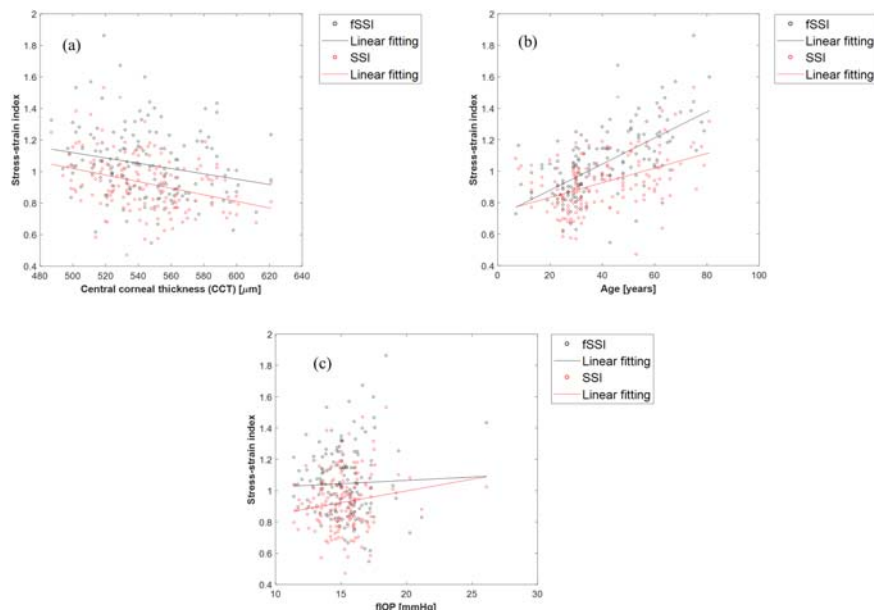


**FIGURE 20.9** Association of the corneal material parameter fSSI with (A) CCT, (B) age, and (C) fIOP.

## Conclusions

The intraocular pressure IOP is interlinked with corneal material stiffness in a complex loop as the measurement of IOP in tonometry is commonly influenced by corneal stiffness, while the tangent modulus (a measure of stiffness) is known to increase with the level of IOP (Eliasy et al., 2019; Kirstein et al., 2011, pp. 88–89). The challenge to provide estimations of IOP and corneal stiffness that are independent of each other was dealt with in the present study using numerical modeling and employing the results to build algorithms to estimate fIOP and corneal material index fSSI. These algorithms included a number of Corvis deformation parameters, namely the first applanation pressure (AP1) and the highest concavity radius ( $R_{HC}$ ) in the fIOP equation, and the stiffness parameter (SP-HC) in the fSSI equation. This study aimed to use more representative numerical modeling that considered the fluid–structure interaction between the air puff and the cornea via employing the arbitrary Lagrangian–Eulerian deforming mesh, changes could be observed in the temporal and spatial pressure distribution profiles on the cornea, and these changes were dependent on the eye's geometric features and material stiffness. The FSI effect was more evident when the cornea's deformation was high as in cases with small CCT or low IOP.

Consideration of these pressure distribution profiles in the development of an algorithm to estimate fIOP resulted in better performance compared to the bIOP in reducing the association of IOP measurements with both age and R but maintained a similar low correlation with CCT. Consideration of the pressure distribution profiles in developing the fSSI algorithm resulted in similar improvements compared with the SSI with slightly weaker dependence on CCT and fIOP while maintaining a similar correlation with age. The development of these algorithms could benefit clinical practice in providing biomechanically corrected IOP measurements to improve glaucoma diagnosis and management. They can also help in keratoconus detection by increasing the effectiveness of existing biomechanical indices such as the Tomography and Biomechanical Index (TBI) (Ambrósio et al., 2017) and the Corvis Biomechanical Index (CBI) (Vinciguerra et al., 2016), especially that the FSI effect is more evident in soft corneas such as those with keratoconus (Andreassen et al., 1980; Vinciguerra et al., 2016; Ye et al., 2015).

There were some limitations in the current study, which are important to note. The eye model employed in the study did not include soft tissue filling the orbital space and surrounding the eye which gives the eye freedom to move backward. Moreover, clinically, the air puff shooting direction can be sometimes at an angle from the eye axis and a modification for the mesh was done to apply the air puff at an angle, but the problem is that it's not known how the air puff will hit the cornea in order to make a global correction which fits with all patients. Finally, the current study concentrated on developing the numerical model and the algorithms for healthy eyes and the next step is to extend the study for keratoconic eyes before and after cross-linking.

---

## References

- Abaqus. (2014). *ABAQUS/Standard analysis user's manual v14.2*. SIMULIA. <http://130.149.89.49:2080/v6.14/books/usb/default.htm>.
- Ambrósio, R., Lopes, B. T., Faria-Correia, F., Salomão, M. Q., Bühren, J., Roberts, C. J., Elsheikh, A., Vinciguerra, R., & Vinciguerra, P. (2017). Integration of scheimpflug-based corneal tomography and biomechanical assessments for enhancing ectasia detection. *Journal of Refractive Surgery*, 33(7), 434–443. <https://doi.org/10.3928/1081597X-20170426-02>
- Andreassen, T. T., Hjorth Simonsen, A., & Oxlund, H. (1980). Biomechanical properties of keratoconus and normal corneas. *Experimental Eye Research*, 31(4), 435–441. [https://doi.org/10.1016/S0014-4835\(80\)80027-3](https://doi.org/10.1016/S0014-4835(80)80027-3)
- Boyer, G., Paillet Mattei, C., Molimard, J., Pericoi, M., Laquieze, S., & Zahouani, H. (2012). Non contact method for in vivo assessment of skin mechanical properties for assessing effect of ageing. *Medical Engineering and Physics*, 34(2), 172–178. <https://doi.org/10.1016/j.medengphy.2011.07.007>
- Caprioli, J., & Coleman, A. L. (2008). Intraocular pressure fluctuation. A risk factor for visual field progression at low intraocular pressures in the advanced glaucoma intervention study. *Ophthalmology*, 115(7), 1123–e3. <https://doi.org/10.1016/j.ophtha.2007.10.031>
- Courant, R., Friedrichs, K., & Lewy, H. (1928). Über die partiellen Differenzengleichungen der mathematischen Physik. *Mathematische Annalen*, 100(1), 32–74. <https://doi.org/10.1007/BF01448839>
- Crank, J., & Nicolson, P. (1947). A practical method for numerical evaluation of solutions of partial differential equations of the heat-conduction type. *Mathematical Proceedings of the Cambridge Philosophical Society*, 43(1), 50–67. <https://doi.org/10.1017/S0305004100023197>
- David, T., Cynthia, R., Julien, K., Caroline, G., Sylvie, M.-T., Elodie, S., & Joseph, C. (2008). Correlations between corneal hysteresis, intraocular pressure, and corneal central pachymetry. *Journal of Cataract and Refractive Surgery*, 34(4), 616–622. <https://doi.org/10.1016/j.jcrs.2007.11.051>
- De Langre, E., Amandolese, X., & Doaré, O. (2016). Fundamentals of fluid-solid interactions. *École Polytechnique*. <https://www.coursera.org/learn/fluid-solid-interaction>.
- De Moura, C. B. (2013). *The Courant–Friedrichs–Lewy (CFL) condition*. Birkhäuser.
- Hodges, D. H., Pierce, G. A., & Cutchins, M. A. (2003). Introduction to structural dynamics and aeroelasticity. *Applied Mechanics Reviews*, B35. <https://doi.org/10.1115/1.1566393>
- Dimitriadis, G. (2017). Introduction to nonlinear aeroelasticity. In *Introduction to nonlinear aeroelasticity*. Wiley. <https://doi.org/10.1002/9781118756478>
- Dolores, O., David, P., & Francisco, A.-M. (2007). Corneal biomechanical properties in normal, post-laser in situ keratomileusis, and keratoconic eyes. *Journal of Cataract and Refractive Surgery*, 33(8), 1371–1375. <https://doi.org/10.1016/j.jcrs.2007.04.021>
- Donea, J., Huerta, A., Ponthot, J.-P., & Rodríguez-Ferran, A. (2017). Arbitrary Lagrangian Eulerian methods. *n-Encyclopedia of computational mechanics* (2nd ed.).
- Drkošová, J., Greenbaum, A., Rozložník, M., & Strakoš, Z. (1995). Numerical stability of GMRES. *BIT Numerical Mathematics*, 35(3), 309–330. <https://doi.org/10.1007/BF01732607>
- Eliasy, A., Chen, K. J., Vinciguerra, R., Lopes, B. T., Abass, A., Vinciguerra, P., Ambrósio, R., Roberts, C. J., & Elsheikh, A. (May 2019). Determination of corneal biomechanical

- behavior in-vivo for healthy eyes using CorVis ST tonometry: Stress-strain index. *Frontiers in Bioengineering and Biotechnology*, 7. <https://doi.org/10.3389/fbioe.2019.105>
- Eliasy, A., Chen, K. J., Vinciguerra, R., Maklad, O., Vinciguerra, P., Ambrósio, R., Roberts, C. J., & Elsheikh, A. (2018). Ex-vivo experimental validation of biomechanically-corrected intraocular pressure measurements on human eyes using the CorVis ST. *Experimental Eye Research*, 175, 98–102. <https://doi.org/10.1016/j.exer.2018.06.013>
- Elsheikh, A., Alhasso, D., Gunvant, P., & Garway-Heath, D. (2011). Multiparameter correction equation for Goldmann applanation tonometry. *Optometry and Vision Science*, 88(1), E102–E112. <https://doi.org/10.1097/OPX.0b013e3181fc3453>
- Elsheikh, A., Geraghty, B., Alhasso, D., Knappett, J., Campanelli, M., & Rama, P. (2010). Regional variation in the biomechanical properties of the human sclera. *Experimental Eye Research*, 90(5), 624–633. <https://doi.org/10.1016/j.exer.2010.02.010>
- Elsheikh, A., Geraghty, B., Rama, P., Campanelli, M., & Meek, K. M. (2010). Characterization of age-related variation in corneal biomechanical properties. *Journal of the Royal Society Interface*, 7(51), 1475–1485. <https://doi.org/10.1098/rsif.2010.0108>
- Elsheikh, A., Ross, S., Alhasso, D., & Rama, P. (2009). Numerical study of the effect of corneal layered structure on ocular biomechanics. *Current Eye Research*, 26–35. <https://doi.org/10.1080/02713680802535263>
- Elsheikh, A., Wang, D., Brown, M., Rama, P., Campanelli, M., & Pye, D. (2007). Assessment of corneal biomechanical properties and their variation with age. *Current Eye Research*, 32(1), 11–19. <https://doi.org/10.1080/02713680601077145>
- Elsheikh, A., Wang, D., Rama, P., Campanelli, M., & Garway-Heath, D. (2008). Experimental assessment of human corneal hysteresis. *Current Eye Research*, 33(3), 205–213. <https://doi.org/10.1080/02713680701882519>
- Elsheikh, A., Whitford, C., Hamarashid, R., Kassem, W., Joda, A., & Büchler, P. (2013). Stress free configuration of the human eye. *Medical Engineering and Physics*, 35(2), 211–216. <https://doi.org/10.1016/j.medengphy.2012.09.006>
- Fleury, V., Al-Kilani, A., Boryskina, O. P., Cornelissen, A. J. M., Nguyen, T. H., Unbekandt, M., Leroy, L., Baffet, G., Le Noble, F., Sire, O., Lahaye, E., & Burgaud, V. (2010). Introducing the scanning air puff tonometer for biological studies. *Physical Review E—Statistical, Nonlinear, and Soft Matter Physics*, 81(2). <https://doi.org/10.1103/PhysRevE.81.021920>
- Forrester, J. V., Dick, A. D., McMenamin, P. G., Roberts, F., & Eric Pearlman, B. S. (2015). *The eye: Basic sciences in practice*. Elsevier Health Sciences. <https://books.google.co.uk/books?id=yOd1BwAAQBAJ>
- Fung, Y.-C. (1993). *Biomechanics*. Springer Nature. <https://doi.org/10.1007/978-1-4757-2257-4>
- Goldmann, H., & Schmidt, T. (1957). Über applanationstonometrie. *Ophthalmologica*, 134(4), 221–242. <https://doi.org/10.1159/000303213>
- Group, C. N. T. G. S. (1998). The effectiveness of intraocular pressure reduction in the treatment of normal-tension glaucoma. *American Journal of Ophthalmology*, 126(4), 498–505. [https://doi.org/10.1016/S0002-9394\(98\)00272-4](https://doi.org/10.1016/S0002-9394(98)00272-4)
- Hodges, D. H., & Pierce, G. A. (2011). Introduction to structural dynamics and aeroelasticity, second edition. In , Vol 9780521195904. *Introduction to structural dynamics and aeroelasticity* (pp. 1–247). Cambridge University Press. <https://doi.org/10.1017/CBO9780511997112>

- Hoeltzel, D. A., Altman, P., Buzard, K., & Choe, K. I. (1992). Strip extensiometry for comparison of the mechanical response of bovine, rabbit, and human corneas. *Journal of Biomechanical Engineering*, 114(2), 202–215. <https://doi.org/10.1115/1.2891373>
- Hong, S., Gong, J. S., & Young, J. H. (2007). Long-term intraocular pressure fluctuation and progressive visual field deterioration in patients with glaucoma and low intraocular pressures after a triple procedure. *Archives of Ophthalmology*, 125(8), 1010–1013. <https://doi.org/10.1001/archopht.125.8.1010>
- Hron, J., & Turek, S. (2006). A monolithic FEM/Multigrid solver for an ALE formulation of fluid–structure interaction with applications in biomechanics. *Lecture Notes in Computational Science and Engineering*, 53, 146–170. [https://doi.org/10.1007/3-540-34596-5\\_7](https://doi.org/10.1007/3-540-34596-5_7)
- Jaroslav, H., & Stefan, T. (2006). *A monolithic FEM/multigrid solver for an ALE formulation of fluid–structure interaction with applications in biomechanics*. Springer Science and Business Media LLC. [https://doi.org/10.1007/3-540-34596-5\\_7](https://doi.org/10.1007/3-540-34596-5_7)
- Joda, A. A., Shervin, M. M. S., Kook, D., & Elsheikh, A. (2015). Development and validation of a correction equation for Corvis tonometry. *Computer Methods in Biomechanics and Biomedical Engineering*, 19(9), 943–953. <https://doi.org/10.1080/10255842.2015.1077515>
- Gloster, J., Perkins, E. S., & Pommier, M. L. (1957). Extensibility of strips of sclera and cornea. *British Journal of Ophthalmology*, 103–110. <https://doi.org/10.1136/bjo.41.2.103>
- Kcharik, M., Liska, R., Vachal, P., & Shashkov, M. (2006). Arbitrary Lagrangian-Eulerian (ALE) methods in compressible fluid dynamics. *Programs and Algorithms of Numerical Mathematics*, 13, 178–183. <https://eudml.org/doc/271298>.
- Kelley, C. T. (1995). Iterative methods for linear and nonlinear equations. *Society for Industrial and Applied Mathematics*, 16, 33–61. <https://doi.org/10.1137/1.9781611970944>
- Kincaid, D. R., Respess, J. R., Young, D. M., & Grimes, R. R. (1982). Algorithm 586: Itpack 2C: A FORTRAN package for solving large sparse linear systems by adaptive accelerated iterative methods. *ACM Transactions on Mathematical Software (TOMS)*, 8(3), 302–322. <https://doi.org/10.1145/356004.356009>
- Kirstein, E. M., Elsheikh, A., & Gunvant. (2011). *Tonometry—past, present and future*.
- Kling, S., Bekesi, N., Dorronsoro, C., Pascual, D., & Marcos, S. (2014). Corneal viscoelastic properties from finite-element analysis of in vivo air-puff deformation. *PLoS ONE*, 9(8). <https://doi.org/10.1371/journal.pone.0104904>
- Kling, S., & Marcos, S. (2013). Finite-element modeling of intrastromal ring segment implantation into a hyperelastic cornea. *Investigative Ophthalmology and Visual Science*, 54(1), 881–889. <https://doi.org/10.1167/iovs.12-10852>
- Kotecha, A., Elsheikh, A., Roberts, C. R., Zhu, H., & Garway-Heath, D. F. (2006). Corneal thickness- and age-related biomechanical properties of the cornea measured with the ocular response analyzer. *Investigative Ophthalmology and Visual Science*, 47(12), 5337–5347. <https://doi.org/10.1167/iovs.06-0557>
- Krachmer, J. H., Mannis, M. J., & Holland, E. J. (2005). *Cornea*. Elsevier/Mosby. <https://books.google.co.uk/books?id=fImuzQEACAAJ>
- Laney, C. B. (1998). *Computational gasdynamics*. Cambridge University Press.
- Luce, D. (2005). Air–jet temporal and spatial pressure properties of the reichert ocular response analyzer (ORA). *Investigative Ophthalmology & Visual Science*, 46(13), 5009.
- Luce, D. A. (2005). Determining in vivo biomechanical properties of the cornea with an ocular response analyzer. *Journal of Cataract and Refractive Surgery*, 31(1), 156–162. <https://doi.org/10.1016/j.jcrs.2004.10.044>

- Maklad, O., Eliasy, A., Chen, K. J., Theofilis, V., & Elsheikh, A. (2020). Simulation of air puff tonometry test using arbitrary Lagrangian–Eulerian (ALE) deforming mesh for corneal material characterisation. *International Journal of Environmental Research and Public Health*, 17(1). <https://doi.org/10.3390/ijerph17010054>
- Maklad, O., Eliasy, A., Chen, K. J., Wang, J. J., Abass, A., Lopes, B. T., Theofilis, V., & Elsheikh, A. (2020). Fluid-structure interaction based algorithms for IOP and corneal material behavior. *Frontiers in Bioengineering and Biotechnology*, 8. <https://doi.org/10.3389/fbioe.2020.00970>
- Maklad, O., Theofilis, V., & Elsheikh, A. (2018a). Fluid structure interaction (FSI) simulation of the human eye under the air puff tonometry using computational fluid dynamics (CFD). *10th international conference on computational fluid dynamics, ICCFD 2018—proceedings. International conference on computational fluid dynamics 2018*. <https://iccfd.org/iccfd10/papers/ICCFD10-017-Paper.pdf>.
- Maklad, O., Theofilis, V., & Elsheikh, A. (2018b). *Role of impinging jets in the biomechanical correction of the intraocular pressure (IOP) measurement*.
- Moses, R. A. (1958). The Goldmann applanation tonometer. *American Journal of Ophthalmology*, 46(6), 865–869. [https://doi.org/10.1016/0002-9394\(58\)90998-X](https://doi.org/10.1016/0002-9394(58)90998-X)
- NASA. (2011). *Turbulence modeling resource: The spalart-allmaras turbulence*. Recherche. <https://turbmodels.larc.nasa.gov/>.
- Nash, I. S., Greene, P. R., & Foster, C. S. (1982). Comparison of mechanical properties of keratoconus and normal corneas. *Experimental Eye Research*, 35(5), 413–424. [https://doi.org/10.1016/0014-4835\(82\)90040-9](https://doi.org/10.1016/0014-4835(82)90040-9)
- Pandolfi, A., & Holzapfel, G. A. (2008). Three-dimensional modeling and computational analysis of the human cornea considering distributed collagen fibril orientations. *Journal of Biomechanical Engineering*, 130(6). <https://doi.org/10.1115/1.2982251>
- Pueyo, A., & Zingg, D. W. (1991). Efficient Newton-Krylov solver for aerodynamic computations. *AIAA Journal*, 36.
- Quigley, H. A. (1996). Number of people with glaucoma worldwide. *British Journal of Ophthalmology*, 80(5), 389–393. <https://doi.org/10.1136/bjo.80.5.389>
- Renato, A. J., Isaac, R., Allan, L., Correa, F. F., Andreas, S., Matthias, K., & Jane, R. C. (2013). Dynamic ultra high speed Scheimpflug imaging for assessing corneal biomechanical properties. *Revista Brasileira de Oftalmologia*, 99–102. <https://doi.org/10.1590/S0034-72802013000200005>
- Seiler, T., Matallana, M., Sendler, S., & Bende, T. (1992). Does Bowman's layer determine the biomechanical properties of the cornea? *Refractive and Corneal Surgery*, 8(2), 139–142.
- Shirokoff, D., & Rosales, R. R. (2011). An efficient method for the incompressible Navier-Stokes equations on irregular domains with no-slip boundary conditions, high order up to the boundary. *Journal of Computational Physics*, 230(23), 8619–8646. <https://doi.org/10.1016/j.jcp.2011.08.011>
- Sommer, A. (1989). Intraocular pressure and glaucoma. *American Journal of Ophthalmology*, 107(2), 186–188. [https://doi.org/10.1016/0002-9394\(89\)90221-3](https://doi.org/10.1016/0002-9394(89)90221-3)
- Souli, M., & Zolesio, J. P. (2001). Arbitrary Lagrangian-Eulerian and free surface methods in fluid mechanics. *Computer Methods in Applied Mechanics and Engineering*, 191(3–5), 451–466. [https://doi.org/10.1016/S0045-7825\(01\)00313-9](https://doi.org/10.1016/S0045-7825(01)00313-9)
- Su, G. W., Geller, J. T., Hunt, J. R., & Pruess, K. (2004). Small-scale features of gravity-driven flow in unsaturated fractures. *Vadose Zone Journal*, 3(2), 592–601. <https://doi.org/10.2113/3.2.592>

- Sullivan-Mee, M. (2008). The role of ocular biomechanics in glaucoma management: Understanding the role of ocular biomechanical properties may be key in the future of glaucoma management. Here's why. *Review of Optometry*, 145(10), 49–53.
- Symes, R. J., & Mikelberg, F. S. (2017). Normal tension glaucoma management: A survey of contemporary practice. *Canadian Journal of Ophthalmology*, 52(4), 361–365. <https://doi.org/10.1016/j.jcjo.2016.12.008>
- Taylor, H. R. (2000). Refractive errors: Magnitude of the need. *Journal of Community Eye Health*, 13(33), 1–2.
- The National Eye Institute (NEI). (2016). *Facts about the cornea and corneal disease*. <https://nei.nih.gov/photo/anatomy-of-eye>.
- Tinsley, J. N., Molodtsov, M. I., Prevedel, R., Wartmann, D., Espigulé-Pons, J., Lauwers, M., & Vaziri, A. (2016). Direct detection of a single photon by humans. *Nature Communications*, 7. <https://doi.org/10.1038/ncomms12172>
- Versteeg, H. K., & Malalasekera, W. (2007). *An introduction to computational fluid dynamics: The finite volume method*.
- Villavicencio, F. O., Gilani, F., Henriquez, M. A., Izquierdo, L., & Ambrósio, R. R. (2014). Independent population validation of the Belin/Ambrósio enhanced ectasia display: Implications for keratoconus studies and screening. *International Journal of Keratoconus and Ectatic Corneal Diseases*, 3(1), 1–8. <https://doi.org/10.5005/jp-journals-10025-1069>
- Vinciguerra, R., Ambrósio, R., Elsheikh, A., Roberts, C. J., Lopes, B., Morenghi, E., Azzolini, C., & Vinciguerra, P. (2016). Detection of keratoconus with a new biomechanical index. *Journal of Refractive Surgery*, 32(12), 803–810. <https://doi.org/10.3928/1081597X-20160629-01>
- Wang, X. (2008). Fundamentals of fluid-solid interactions: Analytical and computational approaches. In *Fundamentals of fluid-solid Interactions*. Elsevier.
- Wang, S., Li, J., Manapuram, R. K., Menodiado, F. M., Ingram, D. R., Twa, M. D., Lazar, A. J., Lev, D. C., Pollock, R. E., & Larin, K. V. (2012). Noncontact measurement of elasticity for the detection of soft-tissue tumors using phase-sensitive optical coherence tomography combined with a focused air-puff system. *Optics Letters*, 37(24), 5184–5186. <https://doi.org/10.1364/OL.37.005184>
- Ye, C., Yu, M., Lai, G., & Jhanji, V. (2015). Variability of corneal deformation response in normal and keratoconic eyes. *Optometry and Vision Science*, 92(7), e149–e153. <https://doi.org/10.1097/OPX.0000000000000628>

**SECTION**

Biomedicine

**4**

This page intentionally left blank

# Digital twins for understanding the mechanical adaptation of bone in disease and postsurgery

# 21

Elizabeth Dimbath<sup>1</sup>, Anup Pant<sup>2</sup>, Ali Vahdati<sup>2</sup>

<sup>1</sup>Department of Biomedical Engineering, Pratt School of Engineering, Duke University, Durham, NC, United States; <sup>2</sup>Department of Engineering, College of Engineering and Technology, East Carolina University, Greenville, NC, United States

## Chapter outline

Introduction—the basics of bone remodeling.....	493
Computational models of bone remodeling in response to mechanical stimuli .....	496
Strain energy density as a mechanical stimulus for bone remodeling.....	496
Incorporation of stress, strain, and damage as remodeling stimuli.....	500
Fluid flow as a mechanical stimulus for bone remodeling .....	502
Effects of implants and pharmaceuticals on bone remodeling .....	503
Alternative or complementary numerical approaches to FE for in silico bone remodeling .....	505
Conclusion .....	506
References .....	507

## Introduction—the basics of bone remodeling

Throughout life, human bones constantly undergo remodeling in response to physical and chemical cues as a result of daily loading and systemic regulation. The remodeling process is carried out by the concerted work of osteoclasts and osteoblasts with the removal of old mineralized bone and the deposition of new bone that is later mineralized (Hadjidakis & Androulakis, 2006). These cellular actions take place in synchrony for proper bone remodeling to occur. When cellular activities become imbalanced, it can lead to a multitude of pathologies including osteoporosis (Feng & McDonald, 2011). Current research has uncovered many aspects of bone remodeling, but continued research is needed to further elucidate the mechanical and chemical processes involved in this concerted process. As such, digital

twins of bone remodeling process can be coupled with in vivo and in vitro studies to explore these complex mechanobiological phenomena.

The hierarchical structure of bone is composed of solid tissue as well as the fluids such as blood, interstitial fluid, and bone marrow. These fluids, along with cells, are believed to contribute to bone's response to mechanical stimuli by means of the mechanosensory system (Klein-Nulend et al., 2003). Under mechanical loading, osteocytes in bone can act as strain and microdamage sensors transmitting stimuli to osteoblasts and osteoclasts. Osteocytes are simply osteoblasts that have become entrapped in mineralized bone matrix during the formation of new bone. Through cell protrusions in the canaliculi of the bone, osteocytes are able to interact with one another as well as other bone cells and induce remodeling in response to different stimuli. Through various pathways, bone cells orchestrate bone remodeling that is controlled by chemical and mechanical cues from the environment (Seyed Jamaleddin Mousavi et al., 2015; S.J. Mousavi, Doweidar, & Doblaré, 2014) (Santos et al., 2009).

Bone remodeling processes differ between different types of bone (Eriksen, 2010). Trabecular, or spongy bone, is located in the vicinity of bone marrow where osteoprogenitor cells reside, thus progenitor cells can easily reach the remodeling sites. Remodeling of the surface of trabeculae starts with resorption by osteoclasts which erode the resorption lacuna (Howship's lacuna) for about 48 days (Eriksen et al., 1984). Resorption is followed by formation of new bone by osteoblasts and mineralization of bone matrix that fills the resorption lacunae. The formation period lasts about 145 days (Eriksen et al., 1984). Bone distal to the marrow, more specifically cortical bone, is not as accessible to progenitor cells which must travel through the vasculature to reach the remodeling sites (Burkhardt et al., 1984). When remodeling occurs in cortical bone, "cutting cones" of osteoclasts create canals through the bone as resorption is carried out. Following the cutting cone are osteoblasts forming new bone matrix. In cortical bone, the average resorption and formation periods are about 27 and 89 days, respectively (Agerbæk et al., 1991).

As remodeling occurs in the trabecular and cortical bone, alterations occur in the internal and external structure of the tissue. With internal remodeling, there are changes in bone density and other properties like porosity, mineral content, and trabecular architecture. External remodeling causes changes in shape of the bone. The stimuli influencing bone remodeling can also be categorized as external or internal while arising from mechanical, chemical, or a combination of the two. Mechanical loading of bone by way of physiological loading, nonphysiological loading, or medical implants induces deformation and strain through the tissue, hence stimulating the remodeling process (Belinha et al., 2013). The remodeling response of bone to mechanical stimuli has been typically described by two theories, Wolff's law and the Mechanostat theory. Providing the foundational theory for many bone remodeling algorithms, Wolff's law states that bones will remodel their internal structure in a directional manner in response to an applied stress (Boyle & Kim, 2011; Ecker et al., 2019; Eser et al., 2010; Tsubota et al., 2009; A. W. L. Turner et al., 2005; Wolff et al., 1892, 1892). The Mechanostat theory is a mathematical description of bone remodeling postulating that bone porosity, and therefore the

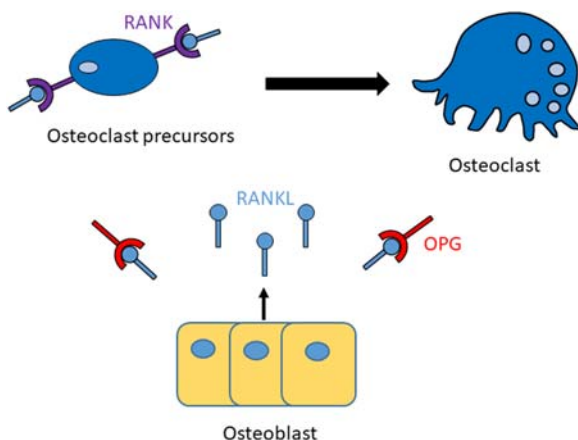


**FIGURE 21.1**

RANK- RANKL-OPG pathway showing the coupling effect of osteoblasts and osteoclast. RANKL expressed on osteoblasts bind to RANK expressed on osteoclast precursors and mature osteoclasts resulting in osteoclasts activation. OPG acts as a decoy receptor for RANKL hence preventing excessive bone resorption.

apparent density, changes as a result of bone remodeling when mechanical loading no longer falls within the normal physiological range (Frost, 1987).

To ensure balanced remodeling, bone cells communicate through chemical stimuli in response to mechanical loads. Osteoblasts and osteoclasts are tightly coupled through the receptor activator of nuclear factor kappa-B (RANK), RANK-Ligand (RANKL), Osteoprotegerin (OPG) system, and the action of transforming growth factor-beta (TGF- $\beta$ ) on bone cells. The RANKL protein binds to the osteoblastic membrane, while the receptor for RANKL, RANK, is expressed on osteoclast precursor cells and mature osteoclasts. Binding and subsequent RANKL/RANK signaling induces osteoclast precursor (OCP) differentiation. The cytokine receptor OPG prevents excessive bone resorption by acting as a decoy receptor and binding RANKL, preventing it from binding to RANK (Boyce & Xing, 2008) (Fig. 21.1). Recent studies have found RANK-RANKL signaling to play an important role in not only osteoclastogenesis but osteoblastogenesis as well (Cao, 2018; Ikebuchi et al., 2018). Forward RANK-RANKL signaling seems to inhibit osteogenic differentiation, whereas the reverse signaling seems to promote osteoblastic differentiation for bone formation (Ikebuchi et al., 2018). Bone morphogenetic proteins (BMPs), a family of the TGF- $\beta$  cytokines, also play a critical role in the differentiation of mesenchymal cells into osteoblasts (Katagiri & Takahashi, 2002).

As the processes involved in bone cells sensing mechanical stimuli are dependent on multiple factors, consideration in placement of implants is imperative as they can impact the apparent stress and strain sensed by the bone and the local remodeling

process. Also, since bone remodeling is also determined by cellular signaling pathways, chemicals introduced into the bone environment, by way of pharmaceutical drugs or other therapeutics, can affect the bone remodeling process (Hambli et al., 2016). Understanding bone remodeling from a mechanistic point of view can aid in thoughtful design of implants and therapeutics in treating bone damage and pathologies to minimize disruption of the essential mechanosensory mechanisms and mechanotransduction pathways.

To gain further insight into remodeling mechanisms and the effect of various stimuli on these processes, many *in silico* models have been developed. Computational bone remodeling algorithms take a noninvasive approach to studying the physiological processes that govern bone remodeling and can provide new insight into mechano-adaptive responses of bone (Seyed Jamaleddin Mousavi, Doweidar, & Doblaré, 2014; URDEITX et al., 2020). Such models use mathematical equations to simulate and visualize the bone remodeling process while also allowing for prediction of long-term stability and response to external factors in relation to orthopedic and orthodontic implants and drug therapies. As computational power increases and scientific knowledge of bone biology continues to advance, computer models have become more sophisticated, accounting for more variables and accommodating medical imaging for patient-specific simulations. Computational modeling approaches lay the foundation for development of digital twins of bone remodeling with potential for improved diagnosis of bone pathologies and long-term success of implants.

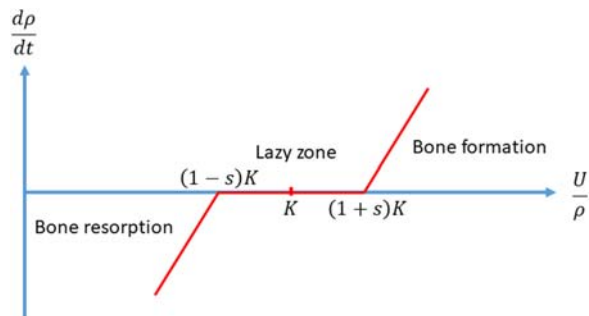
---

## Computational models of bone remodeling in response to mechanical stimuli

### Strain energy density as a mechanical stimulus for bone remodeling

Strain energy density (SED) is used as the mechanical stimulus in many bone remodeling algorithms based on a mechano-adaptive bone remodeling theory developed by Huiskes and colleagues (Huiskes et al., 2000; Rouhi et al., 2015a, 2015b; Vahdati et al., 2008; Lenthe et al., 1997; Weinans et al., 1992). In this approach, the rate of change in the bone density depends upon the strain energy density per element, the reference SED, a constant quantifying either bone loss or bone formation, and the width of the lazy zone. The lazy zone is the range of remodeling stimulus where it is assumed bone remodeling does not lead to net loss or formation of bone (Fig. 21.2).

Carter (Carter, 1984) also suggested the presence of a lazy zone in bone remodeling based on experimental studies and subsequently this concept was implemented in computational models by Huiskes et al. (Huiskes et al., 1987). However, the lazy zone concept has been disputed by some researchers. For instance, in a study of bone

**FIGURE 21.2**

Change in apparent bone density under different stimulus ranges. Different stimuli ranges determine whether bone formation, bone resorption, or no bone remodeling takes place.

remodeling in healthy postmenopausal women, Christen et al. (Christen et al., 2014) found that bone remodeling followed a linear relationship with loading with no lazy zone present. Other computational models for bone remodeling exclude the lazy zone for simplicity or described bone resorption and deposition as two separate stochastic processes that do not include an explicit lazy zone but still explain replicate realistic bone architecture (Dunlop et al., 2009; Li et al., 2007). Regardless, many bone remodeling algorithms continue to account for a lazy zone by using a trilinear model (Fig. 21.2), where stimuli below a lower threshold result in bone resorption while stimuli above a higher threshold result in bone formation, and stimuli between the two threshold values results in no change of bone density (Xinghua et al., 2002). The optimal width of the lazy zone can be determined through varying the model parameters and comparing computational results to clinical and experimental data (A. W. L. Turner et al., 2005; Weinans et al., 1992).

The SED-adaptive bone remodeling theories can also be extended with addition of an overload resorption zone. This extension includes bone resorption that occurs when strain energy density is above a maximum bone formation threshold (Behrens et al., 2009). Behren et al. (Behrens et al., 2009) modified the bone adaptation theory proposed by Huiskes et al. (Huiskes & Rietbergen, 1995) to account for bone loss due to necrosis of bone structure with severe loading of the femur after total hip arthroplasty (THA). Others have incorporated overloading into models focused on maxillary bone remodeling around dental implants with addition of an overload resorption variable into the SED-based remodeling rate equation (Wang et al., 2016), in line with the studies of Lin et al. (Lin et al., 2010). Wang et al. (Wang et al., 2016) also took their model beyond the traditional assumption of isotropy in bone tissue and included anisotropic bone remodeling in their algorithm (Jacobs et al., 1997). Another approach for modeling overload resorption around dental implants added a quadratic term to the density rate change equation allowing for negative rate of change when the stimulus becomes large (Li et al., 2007). Extension of

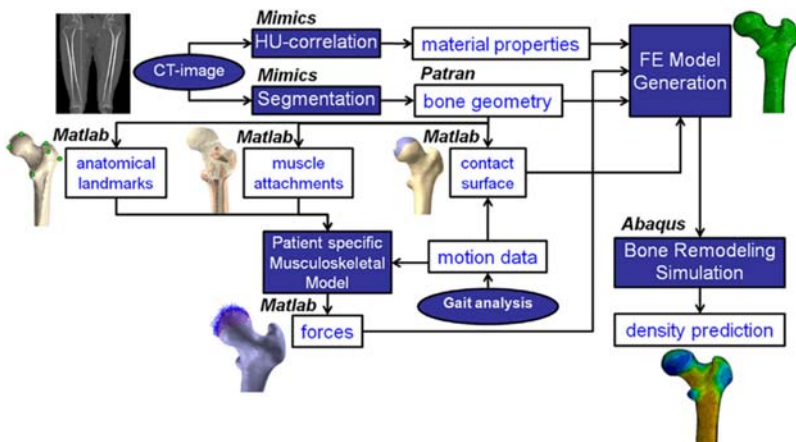
this work included a lazy zone and the results showed that for optimal dental implant design, overload-induced resorption must be considered along with realistic initial bone density (Huiskes et al., 1987; Nutu, 2018).

Since many of the developed algorithms only incorporated the magnitude of the loading, but not the loading frequency, Ostadi Moghaddam et al. (Ostadi Moghaddam et al., 2018) developed a bone remodeling algorithm that took into account the effects of bone vibrational behavior. They extended Weinans et al.'s (Weinans et al., 1992) approach and incorporated the bone vibration response through the effect of loading frequency and the vibrational characteristics of the bone since these factors were proposed to influence bone formation. To do so, they introduced a new frequency response coefficient in the SED term of the bone remodeling equations. The bone formation rate and the location was found to be dependent upon the loading frequency and correlated reasonably with experimentally observed bone vibrational behavior (Ostadi Moghaddam et al., 2018).

Accounting for differences in internal and external bone remodeling processes has been tackled by researchers in multiple ways. By separating the bone remodeling process into external and internal bone remodeling, Wang et al. (Wang et al., 2014) employed an algorithm in which an external remodeling algorithm predicted tooth movement and position, while the change in apparent bone density was a function of internal remodeling. For the external bone remodeling, the tooth movement velocity was determined considering strain as the factor driving the remodeling process. Other studies focused on unified theories of bone remodeling, such as the one developed by Beaupré et al. (Beaupré et al., 1990) which accounted for remodeling of endosteal, periosteal, Haversian, and cancellous bone. In this time-dependent approach, bone responded to daily loading and the model subsequently unified the internal and external remodeling processes assuming that the difference between the appropriate level and the actual imposed level of daily mechanical stimulation drove the remodeling process (Beaupré et al., 1990). The local net rate of bone apposition or resorption was controlled by tissue level difference in mechanical stimulus. This model was later applied to the anisotropic case (Doblaré & García, 2002) and also was used to include the role of subject-specific geometry and loading in bone remodeling (Vahdati et al., 2014) (Fig. 21.3).

As previously discussed, experimental evidence has shown that osteocytes are involved in sensing mechanical loads and orchestrating subsequent remodeling processes (Bonewald, 2011; Bonewald & Johnson, 2008). To better accommodate the role of bone cells in the SED-dependent remodeling algorithms, researchers have included sensors, representing mechanosensitive osteocytes, into computational models. Inclusion of these cellular sensors allows for performing sensitivity analysis for different parameters of the algorithm such as the effect of cell density and distribution throughout the bone.

An early computational model by Mullender et al. (Mullender et al., 1994) hypothesized that osteocytes regulate bone mass through sensing of mechanical loads. Based on this theory of local control of bone mass by cellular sensors, they developed a model that contained a large number of cell sensors distributed through

**FIGURE 21.3**

A subject-specific bone remodeling simulation pipeline. Example of schematic flowchart used in bone remodeling algorithms. This flowchart depicts process used for predicting bone density distribution due to subject-specific mechanical loading and geometry.

From Vahdati, A., Walscharts, S., Jonkers, I., Garcia-Aznar, J. M., Vander-Sloten, J., & van Lenthe, G. H. (2014). Role of subject-specific musculoskeletal loading on the prediction of bone density distribution in the proximal femur. *Journal of the Mechanical Behavior of Biomedical Materials*, 244–252. <https://doi.org/10.1016/j.jmbbm.2013.11.015>.

the bone. This approach improved upon previous techniques while also allowing for study of effects of sensory cell density on trabecular bone morphology (Mullender et al., 1994). The proposed model has since been extended to account for nonlinear effects of density change rate (Lian et al., 2010; Xinghua et al., 2002). A computational model presented by Huiskes et al. (Huiskes et al., 2000) accounted for metabolic processes in bone that allow for coupling of cells in bone remodeling processes. They postulated that the mechanical stimulus, the SED, stimulates osteocytes to provide signals to osteoclasts for resorption and the activation of osteoclasts was regulated by either the presence of microcracks or disuse of bone. Numerical algorithms were developed that accounted for SED rate at location of each osteocyte, mechanosensitivity of each osteocyte, effect of distance of osteocyte from bone surface, and number of osteocytes (Huiskes et al., 2000). Vahdati et al. (Vahdati & Rouhi, 2009) improved this model by addition of the cellular accommodation effect as well as incorporating effects of both SED and microdamage. Cellular accommodation recapitulates the principle that sensor cells will gradually adapt to new strain threshold in response to changes in mechanical loading as hypothesized by Turner et al. (C. H. Turner, 1999) and supported later by experimental findings (Jaasma et al., 2007; C. H. Turner, 1999). This modified bone remodeling theory allowed for better control over microdamage-stimulated remodeling parameters and may be better equipped to simulate disease states of bone (Vahdati & Rouhi, 2009).

Focusing on trabecular bone remodeling, Spingarn et al. (Spingarn et al., 2017) developed a multiscale approach to simulate the bone remodeling. They presented a remodeling algorithm based on a boundary detection technique in which the elastic deformation energy directly influenced bone biology in the developed SED function-based model. The biological stimulus at any point and at any time in the geometry was calculated using the strain energy, the mechanosensitivity of the osteocyte, and the osteocyte influence distance. Depending upon the stimulus level, bone synthesis, or bone resorption took place, which was reflected by the rate of change in bone density. To enable the localization of the bone cell activation on the trabecular surface, they presented an algorithm to detect the trabeculae boundary elements (Spingarn et al., 2017). Later, Cheong et al. (Cheong et al., 2018) introduced the concept of osteoconnectivity into the abovementioned bone remodeling algorithm. The osteoconnectivity method modeled the additive nature of bone formation where the new bone was sequentially laid down next to existing bone. In this model, they implemented osteoconnectivity as a map of neighboring elements that only permitted elements adjacent to bone stock or elements remodeled in previous time steps to remodel. They integrated the concept of osteoconnectivity with strain energy-based bone remodeling algorithms to control the extra cortical bone formation in the area of interest. The researchers found that bone formation around an implanted femur prosthesis predicted with the inclusion of the osteoconnectivity concept showed better agreement with radiographs than algorithms without osteoconnectivity (Cheong et al., 2018). Furthermore, others have accounted for the role of cells in bone remodeling through the inclusion of bone multicellular units (BMUs) (Field et al., 2010; Wang et al., 2011). For example, Wang et al.'s (Wang et al., 2011) algorithm assumed that BMU activation depends on state of damaged tissue. Remodeling was determined by the stimulus due to SED and the stimulus received from other osteocytes at each location (Wang et al., 2011).

### Incorporation of stress, strain, and damage as remodeling stimuli

Besides using SED as the mechanical stimulus, researchers have also implemented bone remodeling algorithms using both SED and damage level (Rouhi et al., 2015a, 2015b; Vahdati & Rouhi, 2009; Wang et al., 2011, 2014) (Fig. 21.4). To incorporate damage in bone remodeling, Idhammad et al. (Idhammad et al., 2013) presented a mathematical model taking into consideration the elastic damage and the SED mechanical stimulus in which damage caused the elastic modulus of the element to degrade gradually as it progressed. Marzban et al. (Marzban et al., 2015) used a different approach and based the bone remodeling process on the Von Mises stress. Using a 3D model of the femur, they calculated the stress due to hip contact and muscular forces to determine if remodeling occurred. Other models also used stress as the driving force for trabecular surface remodeling but focused instead on nonuniformity of local stress (Adachi et al., 2001; Tsubota et al., 2009).

While SED incorporates the combined effect of stress and strain, some bone remodeling algorithms are based on strain alone. To study the effects of fixed partial

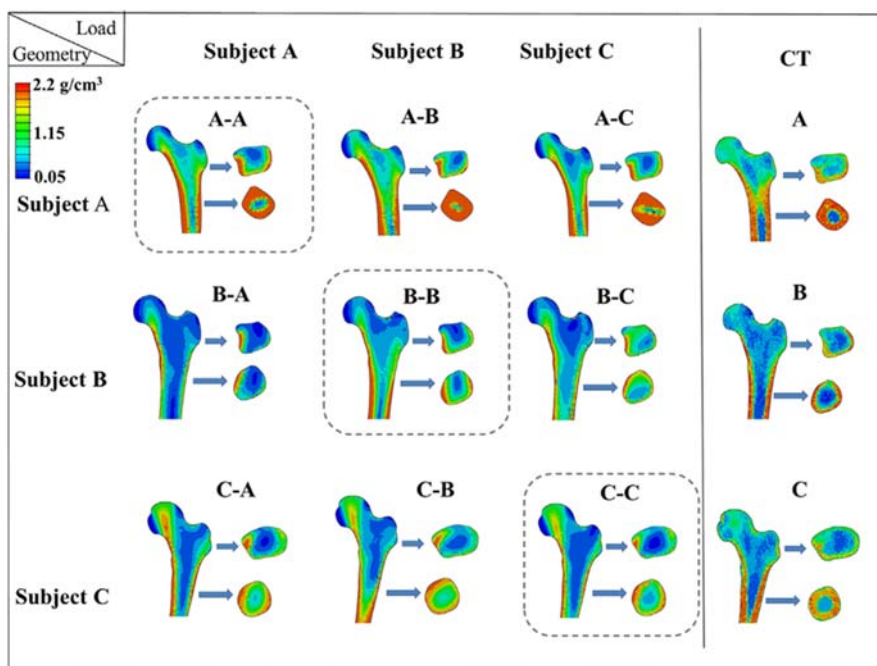


**FIGURE 21.4**

Use of subject-specific geometries and loading patterns to predict bone density using bone remodeling algorithm: Algorithm predictions are compared with density obtained from CT scans. Comparison was made through pairing of geometries with gait loading from different subject's with dotted boxes depicting case of gait loading applied to geometry of same subject.

From Vahdati, A., Walscharts, S., Jonkers, I., Garcia-Aznar, J. M., Vander-Sloten, J., & van Lenthe, G. H. (2014). Role of subject-specific musculoskeletal loading on the prediction of bone density distribution in the proximal femur. *Journal of the Mechanical Behavior of Biomedical Materials*, 244–252. <https://doi.org/10.1016/j.jmbbm.2013.11.015>

dentures on bone adaptation, Field et al. (Field et al., 2010) directly related the mechanical stimulus to the change in Hounsfield unit (HU) value in terms of surface area density. The mechanical stimulus used was the equivalent strain, with effective strain before implant being used as the reference strain. The HU values were updated based on the magnitude of the equivalent strain using the surface area density, effective strain, and strain threshold where the threshold values determined if bone resorption, apposition, or no remodeling took place. Equivalent strain was also used to predict stability of short-stem implants over time using a previously validated strain adaptive remodeling theory (D et al., 2010; A. W. L. Turner et al., 2005). Additionally, other models have incorporated the effect of strain and damage into the bone remodeling stimulus (Mulvihill & Prendergast, 2010; Prendergast

et al., 2011). Mulvihill et al. (Mulvihill & Prendergast, 2010) developed a mechano-biological algorithm that linked the strain and damage-based stimulus with the activation of osteoclasts and osteoblasts. The damage level in bone determined if a strain-mediated response occurred. When damage was below a critical level, there was strain-mediated response but if the damage exceeded the critical level, bone resorption only due to damage occurred. This model was applied to study the effects of changes in mechanosensitivity and elastic modulus on bone mass (Prendergast et al., 2011).

### Fluid flow as a mechanical stimulus for bone remodeling

While it is well accepted that mechanical stimuli activate osteocytes to orchestrate the actions of osteoclasts and osteoblasts in bone remodeling, less is known about how the induced stresses and strains are sensed by the cells and what allows osteoclasts and osteoblasts to be so well synchronized in remodeling (Burger et al., 2003). Fluid flow is expected to play a role in these mechanisms (Burger et al., 2003). Computational models of fluid flow in bone have used poroelastic approaches (Pereira & Shefelbine, 2014; Villette & Phillips, 2016) to account for the flow through trabeculae in bone. Also, bone marrow fills the porous structure of trabecular bone and may have a contributing role in mechanosensitivity of bone as it is home to multiple progenitor cell types (Birmingham et al., 2015; Metzger et al., 2015).

Fluid flow within bone can stimulate mechano-adaptation (Burger et al., 2003; Pereira & Shefelbine, 2014). While not directly studying bone remodeling, Pereira and Shefelbine (Pereira & Shefelbine, 2014) used a 3D poroelastic FE model to assess effects of permeability, frequency of loading, and rest time between loading cycles on mechanical cues, specifically fluid flow within cortical bone. They were able to quantify the motion of fluid and the rest time between loading cycles needed to maximize flow and restore mechanosensitivity (Pereira & Shefelbine, 2014). Kameo and Adachi (Kameo & Adachi, 2014) took a similar approach with considering interstitial fluid flow in a poroelastic model to study bone remodeling in trabecular bone. The fluid flow within the canaliculi was considered the mechanical stimulus for osteocyte regulated remodeling (Kameo & Adachi, 2014). Osteocytes were assumed to sense the shear stress induced by fluid flow, of which the magnitude was proportional to the level of stimulus. Through considering the microscale stimulus on osteocytes due to shear stress and surrounding osteocytes, they determined the macroscale response through changes in bone architecture based on application of different loads. Results showed progressive alignment of trabeculae parallel to direction of loading with a locally uniform state of stress in agreement with experimental studies and previous simulations of bone remodeling. Another poroelastic model of trabecular bone used a mechanistic iterative adaptation algorithm based on fluid velocity through pores of bone matrix to study remodeling effects (Villette & Phillips, 2016). The shear stress and strain applied on the cell membrane due to fluid velocity was the stimulus for bone apposition or resorption with a target

velocity range that determined the thresholds for mechanosensitivity. Bone remodeling was achieved by updating the position of surface points based on the state of apposition or resorption (Villette & Phillips, 2016).

Mechanical stimuli in the form of SED, stress, strain, damage, and fluid flow are often used in computational modeling of bone remodeling. However, bone remodeling is not solely governed by mechanical stimuli. While standalone mechanical stimuli-based approaches may provide new insights into different mechano-adaptive responses of the bone as well as aid in implant design, they have limitations with regard to their predictive capability for treatment of bone remodeling disorders. Mechanical stimuli-based models do not always consider the complex chemical signaling pathways that occur in the bone remodeling process. Therefore, other models have been developed that incorporate the cellular signaling pathways responding to mechanical stimuli (Avval et al., 2016; Scheiner et al., 2014; Scheiner, Pivonka, Hellmich, & Smith, 2012; Scheiner, Pivonka, Smith, & Dunstan, 2012). To learn more about recent advances, challenges, and opportunities in integration of mechanics and biology in bone remodeling, the readers are referred to a recent paper by Pant et al. (Pant et al., 2021).

## Effects of implants and pharmaceuticals on bone remodeling

Different pathologies can influence the bone remodeling process. Computational models are an invaluable tool for better understanding disease progression and long-term effects of medical interventions on bone remodeling. For example, in silico models have been applied to study osteoporotic and age-related effects on bone remodeling. These effects were incorporated using the Simulated Bone Atrophy (SIBA) algorithm and by varying the activation frequency of osteoblast and osteoclast activity (Müller, 2005). Other bone pathologies were also investigated through use of in silico models, such as osteoarthritis, that can impact multiple tissue types including bone and cartilage (Stender et al., 2016).

The effect of medical implants on bone remodeling is also widely studied with in silico modeling. Orthodontic and orthopedic pathologies are often treated with implants that disturb loading patterns in the tissue, leading to bone remodeling around the site of implantation. Orthopedic implants in the knee, hip, and shoulder have been examined for their stress shielding effects on bone morphology and duration of remodeling after implantation (Huiskes & Rietbergen, 1995; Prendergast et al., 2011; Weinans et al., 2000). Use of computer modeling allows for understanding effects that are difficult to view through in vitro and in vivo studies alone. Computational models can compare multiple types of prostheses of different geometries and materials for long-term stability and integration (Boyle & Kim, 2011). Using a mechano-biochemical thermodynamic-based model, Avval et al. (Avval et al., 2016) quantified the long-term changes of femoral density following hip implantation and plating. Sayyidmousavi et al. (Sayyidmousavi & Bougherara, 2012) also used the above-mentioned thermodynamic-based model to investigate stress

shielding around two different implants following total hip arthroplasty (THA) by predicting the bone density around the two different implant designs. In another approach that has been adopted in different studies, particularly in understanding bone remodeling following THA, the ratio of the SED per unit mass in the periprosthetic femur to the SED per mass in the physiologically intact bone was used as the bone remodeling stimulus (Huiskes & Rietbergen, 1995; Weinans et al., 2000). However, bone formation is usually restricted to an upper limit, because beyond a certain threshold of bone formation (considered as the severe overloading zone), necrosis may occur (Behrens et al., 2009; Huiskes & Rietbergen, 1995; Weinans et al., 2000). Additionally, in silico models have been extended to orthodontic implants. Such models are used to study effects of dentures and tooth implants on remodeling of the jawbone and help predict success of different implant designs (Field et al., 2010; Lian et al., 2010; Wang et al., 2014). Furthermore, bone remodeling algorithms can be used in conjunction with subject-specific geometries and loading patterns to inform surgeons about the impacts of such parameters in bone remodeling process prior to surgery, see Fig. 21.4 (Vahdati et al., 2014). For example, the study of Vahdati et al. (Vahdati et al., 2014) showed that combining the subject-specific geometry and gait loading patterns can result in improved bone density predictions using SED and damage-based bone remodeling theories.

Moreover, computer models often incorporate pharmacokinetics to investigate the effects of drugs on bone remodeling (Javier & Peter, 2019; Madge et al., 2020; Oumghar et al., 2020; Scheiner et al., 2014; Scheiner, Pivonka, Smith, & Dunstan, 2012; Trichilo & Pivonka, 2018). Specifically, pharmacokinetics models have been developed to study drug effects on cellular pathways involved in bone remodeling (Hambl et al., 2016). In one study, Hambl et al. (Hambl et al., 2016) combined a pharmacokinetic (PK) model with FE modeling to simulate the effects of denosumab, a drug used to inhibit RANKL receptor for the purpose of increasing bone mineral density. The reaserchers used the cell dynamics model developed by Komarova et al. (Komarova et al., 2003) to predict populations of bone cells. The PK model described the absorption of denosumab in the blood and was linked to the mechanobiological FE model by autocrine factors. Similarly, Bahia et al.'s model (Bahia et al., 2020) incorporated the SED evaluated at the microscale and the pharmacological effect of antiresorptive drugs on bone cell population dynamics. In the updated physiologically based pharmacokinetic model (PBPK) model, the dynamics of the preosteoblasts, active osteoblasts and osteoclasts, and amount of drug bound to the bone matrix changed depending on the drug concentration in the matrix and plasma. The effect of the drug in the PBPK model was simulated by modifying the RANK expression, increasing osteoclast apoptosis, and changing the preosteoblast differentiation rate. This bone remodeling algorithm was implemented in a proximal femur model, and the model was able to simulate the expected behavior in response to mechanical and pharmacological stimuli (Bahia et al., 2020).

Likewise, coupling both the mechano-biochemical pathways along with the effect of various drugs, Kameo et al. (Kameo et al., 2020) presented a

comprehensive mechano-biochemical bone remodeling algorithm. The multiscale approach connected cellular interactions at the microscale to the bone adaptation at the macroscale allowing for investigation of both spatial and temporal bone remodeling. The mechanical signal that influenced bone remodeling at the bone surface was computed considering neighboring osteocytes' contributions. Signaling molecules such as sclerostin, RANKL, OPG, and Sema3A were included in the model as well. Probability of genesis and apoptosis of osteoclasts and osteoblasts was based on concentrations of these signaling molecules. Through combination of this mechano-biological model with FE analysis, Kameo et al. ([Kameo et al., 2020](#)) were able to simulate disease states of osteoporosis and osteopetrosis as well as effects of drugs such as bisphosphonate, antisclerostin, and Sema3A on osteoporosis treatment.

Thus, use of computational models to study bone remodeling allows for not only deeper understanding of the underlying processes that drive remodeling, but also for deeper understanding of medical interventions that alter these processes.

---

### **Alternative or complementary numerical approaches to FE for in silico bone remodeling**

Aside from the FE-based techniques, other numerical approaches have also gained traction in bone remodeling simulations. For example, [Boyle and Kim \(2011\)](#) used the design space optimization (DSO) method that minimized the SED by distributing a finite amount of material to the regions with the highest loads, resulting in enhanced stiffness of bone. The optimization method first added a zero density element along the trabecular boundary, then after FE analysis, the material was added to the areas with high load and removed from the areas with low load depending upon the strain energy ([Boyle & Kim, 2011](#)).

[Hamblin et al. \(2011\)](#) utilized both FE analysis and neural networks to simulate bone remodeling in the femoral head at multiple length scales. They used FE analysis for the bone remodeling process at the macroscale and the neural networks at the mesoscale. The mesoscale model utilized the neural network to simulate the local behavior and compute the bone mechanical property changes and subsequently update the macroscopic model. The combined approach was faster compared to the standalone FE approach and provided the opportunity to integrate imaging data in the model. The use of neural networks along with FE in bone remodeling could also take into consideration the response of the bone at nanostructure considering the presence of collagen, the number of cross-links, and mineral volume fraction ([Barkaoui et al., 2014](#)). Another recent approach used an evolutionary game theory-based trabecular bone remodeling algorithm ([Ryser & Murgas, 2017](#)). The model considered the role of quiescent bone and embedded osteocytes and partitioned the trabecular zone into regions of bone resorption, bone formation, and a quiescent bone zone.

Other investigators have used meshless methods to study bone remodeling (Moreira et al., 2014). Peyroteo et al. (2019) combined biological bone remodeling algorithms with FE method as well as with two meshless techniques: radial point interpolation method (RPIM) and natural neighbor radial point interpolation method (NNRPIM). Unlike the FE approach, which discretized the problem domain into a finite number of elements, the RPIM and the NNRPIM performed discretization only at the nodes, thus, no elements and mesh were constructed. The use of nodal distribution alone to discretize the problem made the methods suitable for solving problems with a highly irregular domain. Both meshless methods used the concept of an influence region to determine nodal connectivity. The RPIM method used a radial search to find the nearest nodes to the desired integration point, whereas the NNRPIM used a Voronoi diagram. Despite being more computationally expensive than the FE method, these meshless methods can generate good results, in terms of quality of the spatial distribution of the bone density obtained compared to that of the clinical images (Peyroteo et al., 2019). Another technique used for studying bone remodeling, as mentioned by Javed et al. (2017), is the Lattice Boltzmann method (LBM). With the ability to be used with complex boundaries, LBM can be used effectively to study fluid flow in bone.

---

## Conclusion

As discussed in this chapter, bone remodeling algorithms have evolved from simple mechanical stimuli-based models to complex mechano-chemical approaches. However, the introduction of more complexity in such models may require the inclusion of additional parameters in the model. Thus, such models may require additional experimental and simulation studies for calibration, verification, validation, and sensitivity analysis to be considered credible. Furthermore, emerging numerical methods and tools such as neural networks and LBM provide opportunities to study bone remodeling at multiple temporal and spatial scales. Furthermore, meshless methods can help in studying bone remodeling in complex structures as well as provide clinical image grade outputs.

While much progress has been made toward developing digital twins for studying bone remodeling, there are still limitations to the applicability of computational models for mechanical adaptation of bone. The evidence and understanding around bone remodeling processes are constantly evolving, leading to revisions in model algorithms. While the evolution in the knowledge of bone remodeling does not devalue the previously developed bone remodeling algorithms, it does place additional emphasis on the need to validate these models against recent experimental data. Even though computational bone remodeling algorithms may not capture all relevant information and factors influencing the mechano-adaptive process, they can still provide important and new insights into this delicately balanced biological process by producing virtual hypothesis-testing platforms. Readers interested in challenges and opportunities for improved integration of bone biology and

computational remodeling algorithms may refer to a recent paper by Pant et al. on this subject (Pant et al., 2021).

Combination of different modeling approaches could open doors to understanding bone remodeling with incorporation of multiscale and complex mechanical and chemical events of the process along with emerging advanced numerical and big data analytics techniques (Maria-Ioana et al., 2018; Michele et al., 2014; R. et al., 2018) (Mora-Macías et al., 2020). In silico models of bone remodeling can be used as platforms to test new therapeutic drug products and design of orthopedic and orthodontic implants. Additionally, patient-specific bone remodeling simulations have the potential for translation into the clinic as digital twins, to inform healthcare decisions and to be integrated into standard of care. Proper validation of such models would enable creating digital twins for assessing patient-specific success of medical treatments prior to any invasive procedures or drug administration.

---

## References

- Adachi, T., Tsubota, K. I., Tomita, Y., & Scott, J. H. (2001). Trabecular surface remodeling simulation for cancellous bone using microstructural voxel finite element models. *Journal of Biomechanical Engineering*, 123(5), 403–409. <https://doi.org/10.1115/1.1392315>
- Agerbæk, M. O., Eriksen, E. F., Kragstrup, J., Mosekilde, L., & Melsen, F. (1991). A reconstruction of the remodelling cycle in normal human cortical iliac bone. *Bone and Mineral*, 12(2), 101–112. [https://doi.org/10.1016/0169-6009\(91\)90039-3](https://doi.org/10.1016/0169-6009(91)90039-3)
- Avval, P. T., Samiezdadeh, S., & Bougherara, H. (2016). Long-term response of femoral density to hip implant and bone fracture plate: Computational study using a mechano-biochemical model. *Medical Engineering and Physics*, 38(2), 171–180. <https://doi.org/10.1016/j.medengphy.2015.11.013>
- Bahia, M. T., Hecke, M. B., Mercuri, E. G. F., & Pinheiro, M. M. (2020). A bone remodeling model governed by cellular micromechanics and physiologically based pharmacokinetics. *Journal of the Mechanical Behavior of Biomedical Materials*, 104, 103657.
- Barkaoui, A., Chamekh, A., Merzouki, T., Hamblin, R., & Mkaddem, A. (2014). Multiscale approach including microfibril scale to assess elastic constants of cortical bone based on neural network computation and homogenization method. *International Journal for Numerical Methods in Biomedical Engineering*, 30(3), 318–338.
- Beaupré, G. S., Orr, T. E., & Carter, D. R. (1990). An approach for time-dependent bone modeling and remodeling—theoretical development. *Journal of Orthopaedic Research*, 8(5), 651–661. <https://doi.org/10.1002/jor.1100080506>
- Behrens, B. A., Nolte, I., Wefstaedt, P., Stukenborg-Colsman, C., & Bouguecha, A. (2009). *Biomedical Engineering Online*, 8, 1–9.
- Belinha, J., Jorge, R. M. N., & Dinis, L. M. J. S. (2013). A meshless microscale bone tissue trabecular remodelling analysis considering a new anisotropic bone tissue material law. *Computer Methods in Biomechanics and Biomedical Engineering*, 16(11), 1170–1184. <https://doi.org/10.1080/10255842.2012.654783>
- Birmingham, E., Kreipke, T. C., Dolan, E. B., Coughlin, T. R., Owens, P., McNamara, L. M., Niebur, G. L., & McHugh, P. E. (2015). Mechanical stimulation of bone marrow in situ

- induces bone formation in trabecular explants. *Annals of Biomedical Engineering*, 43(4), 1036–1050. <https://doi.org/10.1007/s10439-014-1135-0>
- Bonewald, L. F. (2011). Osteocyte mechanosensation and transduction. In , Vol9784431897576. *Mechanosensing biology* (pp. 141–155). Springer Japan. [https://doi.org/10.1007/978-4-431-89757-6\\_10](https://doi.org/10.1007/978-4-431-89757-6_10)
- Bonewald, L. F., & Johnson, M. L. (2008). Osteocytes, mechanosensing and Wnt signaling. *Bone*, 42(4), 606–615. <https://doi.org/10.1016/j.bone.2007.12.224>
- Boyce, B. F., & Xing, L. (2008). Functions of RANKL/RANK/OPG in bone modeling and remodeling. *Archives of Biochemistry and Biophysics*, 473(2), 139–146. <https://doi.org/10.1016/j.abb.2008.03.018>
- Boyle, C., & Kim, I. Y. (2011). Three-dimensional micro-level computational study of Wolff's law via trabecular bone remodeling in the human proximal femur using design space topology optimization. *Journal of Biomechanics*, 44(5), 935–942. <https://doi.org/10.1016/j.jbiomech.2010.11.029>
- Burger, E. H., Klein-Nulend, J., & Smit, T. H. (2003). Strain-derived canalicular fluid flow regulates osteoclast activity in a remodelling osteon - a proposal. *Journal of Biomechanics*, 36(10), 1453–1459. [https://doi.org/10.1016/S0021-9290\(03\)00126-X](https://doi.org/10.1016/S0021-9290(03)00126-X)
- Burkhardt, R., Bartl, R., Frisch, B., Jäger, K., Mahl, G., Hill, W., & Kettner, G. (1984). The structural relationship of bone forming and endothelial cells of the bone marrow. In Bone circulation (pp. 2–14). Baltimore: Williams and Wilkins.
- Cao, X. (2018). Inheriting the excellence to innovate medical research in China. *National Medical Journal of China*, 98(1), 1–2. <https://doi.org/10.3760/cma.j.issn.0376-2491.2018.01.001>
- Carter, D. R. (1984). *Calcified tissue international mechanical loading histories and cortical bone remodeling*.
- Cheong, V. S., Blunn, G. W., Coathup, M. J., & Fromme, P. (2018). A novel adaptive algorithm for 3D finite element analysis to model extracortical bone growth. *Computer Methods in Biomechanics and Biomedical Engineering*, 21(2), 129–138. <https://doi.org/10.1080/10255842.2018.1425997>
- Christen, P., Ito, K., Ellouz, R., Boutroy, S., Sornay-Rendu, E., Chapurlat, R. D., & Rietbergen, B. V. (2014). *Nat. Commun.*, 5.
- Dabirrahmani, D., Hogg, M., Kohan, L., & Gillies, M. (2010). Primary and long-term stability of a short-stem hip implant. *Proceedings of the Institution of Mechanical Engineers, Part H: Journal of Engineering in Medicine*, 214(11), 1109–1119. <https://doi.org/10.1243/09544119jeim704>
- Doñalaré, M., & García, J. M. (2002). Anisotropic bone remodelling model based on a continuum damage-repair theory. *Journal of Biomechanics*, 35(1), 1–17. [https://doi.org/10.1016/S0021-9290\(01\)00178-6](https://doi.org/10.1016/S0021-9290(01)00178-6)
- Dunlop, J. W. C., Hartmann, M. A., Bréchet, Y. J., Fratzl, P., & Weinkamer, R. (2009). New suggestions for the mechanical control of bone remodeling. *Calcified Tissue International*, 85(1), 45–54. <https://doi.org/10.1007/s00223-009-9242-x>
- Ecker, G., Yuan, D., Koster, A. M. C. A., & Schmeink, A. (2019). Accurate optimization models for interference constrained bandwidth allocation in cellular networks. *Computers and Operations Research*, 101, 1–12. <https://doi.org/10.1016/j.cor.2018.08.011>
- Eriksen, E. F. (2010). Cellular mechanisms of bone remodeling. *Reviews in Endocrine and Metabolic Disorders*, 11(4), 219–227. <https://doi.org/10.1007/s11154-010-9153-1>

- Eriksen, E. F., Melsen, F., & Mosekilde, L. (1984). Reconstruction of the resorptive site in iliac trabecular bone: A kinetic model for bone resorption in 20 normal individuals. *Metabolic Bone Disease and Related Research*, 5(5), 235–242. [https://doi.org/10.1016/0221-8747\(84\)90065-1](https://doi.org/10.1016/0221-8747(84)90065-1)
- Eser, A., Tonuk, E., Akca, K., & Cehreli, M. C. (2010). Predicting time-dependent remodeling of bone around immediately loaded dental implants with different designs. *Medical Engineering and Physics*, 32(1), 22–31. <https://doi.org/10.1016/j.medengphy.2009.10.004>
- Feng, X., & McDonald, J. M. (2011). Disorders of bone remodeling. *Annual Review of Pathology: Mechanisms of Disease*, 6, 121–145. <https://doi.org/10.1146/annurev-pathol-011110-130203>
- Field, C., Li, Q., Li, W., Thompson, M., & Swain, M. (2010). Prediction of mandibular bone remodelling induced by fixed partial dentures. *Journal of Biomechanics*, 43(9), 1771–1779. <https://doi.org/10.1016/j.jbiomech.2010.02.016>
- Frost, H. M. (1987). Bone “mass” and the “mechanostat”: A proposal. *The Anatomical Record*, 219(1), 1–9. <https://doi.org/10.1002/ar.1092190104>
- Hadjidakis, D. J., & Androulakis, I. I. (2006). Bone remodeling. In , Vol1092. *Annals of the New York academy of sciences* (pp. 385–396). Blackwell Publishing Inc. <https://doi.org/10.1196/annals.1365.035>
- Hamblin, R., Boughattas, M. H., Daniel, J. L., & Kourta, A. (2016). Prediction of denosumab effects on bone remodeling: A combined pharmacokinetics and finite element modeling. *Journal of the Mechanical Behavior of Biomedical Materials*, 60, 492–504. <https://doi.org/10.1016/j.jmbbm.2016.03.010>
- Hamblin, R., Katerchi, H., & Benhamou, C. L. (2011). Multiscale methodology for bone remodelling simulation using coupled finite element and neural network computation. *Biomechanics and Modeling in Mechanobiology*, 10(1), 133–145.
- Huiskes, R., & Rietbergen, B. van (1995). Preclinical testing of total hip stems. *Clinical Orthopaedics and Related Research*, 319, 64–76.
- Huiskes, R., Rulmerman, R., Van Lenthe, G. H., & Janssen, J. D. (2000). Effects of mechanical forces on maintenance and adaptation of form in trabecular bone. *Nature*, 405(6787), 704–706. <https://doi.org/10.1038/35015116>
- Huiskes, R., Weinans, H., Grootenhuis, H. J., Dalstra, M., Fudala, B., & Slooff, T. J. (1987). Adaptive bone-remodeling theory applied to prosthetic-design analysis. *Journal of Biomechanics*, 20(11–12), 1135–1150. [https://doi.org/10.1016/0021-9290\(87\)90030-3](https://doi.org/10.1016/0021-9290(87)90030-3)
- Idhammad, A., Abdali, A., & Alaa, N. (2013). Computational simulation of the bone remodeling using the finite element method: an elastic-damage theory for small displacements. *Theoretical Biology and Medical Modelling*, 10(1), 1–11.
- Ikeuchi, Y., Aoki, S., Honma, M., Hayashi, M., Sugamori, Y., Khan, M., Kariya, Y., Kato, G., Tabata, Y., Penninger, J. M., Udagawa, N., Aoki, K., & Suzuki, H. (2018). Coupling of bone resorption and formation by RANKL reverse signalling. *Nature*, 561(7722), 195–200. <https://doi.org/10.1038/s41586-018-0482-7>
- Jaasma, M. J., Jackson, W. M., Tang, R. Y., & Keaveny, T. M. (2007). Adaptation of cellular mechanical behavior to mechanical loading for osteoblastic cells. *Journal of Biomechanics*, 40(9), 1938–1945. <https://doi.org/10.1016/j.jbiomech.2006.09.010>
- Jacobs, C. R., Simo, J. C., Beaupré, G. S., & Carter, D. R. (1997). Adaptive bone remodeling incorporating simultaneous density and anisotropy considerations. *Journal of Biomechanics*, 30(6), 603–613. [https://doi.org/10.1016/S0021-9290\(96\)00189-3](https://doi.org/10.1016/S0021-9290(96)00189-3)

- Javed, S., Sohail, A., Maqbool, K., Butt, S. I., & Chaudhry, Q. A. (2017). The Lattice Boltzmann method and computational analysis of bone dynamics-I. *Complex Adaptive Systems Modeling*, 5(1), 1–14.
- Javier, M.-R., & Peter, P. (2019). Effects of long-term treatment of denosumab on bone mineral density: Insights from an in-silico model of bone mineralization. *Bone*, 87–95. <https://doi.org/10.1016/j.bone.2019.04.022>
- Kameo, Y., & Adachi, T. (2014). Interstitial fluid flow in canaliculi as a mechanical stimulus for cancellous bone remodeling: In silico validation. *Biomechanics and Modeling in Mechanobiology*, 13(4), 851–860. <https://doi.org/10.1007/s10237-013-0539-3>
- Kameo, Y., Miya, Y., Hayashi, M., Nakashima, T., & Adachi, T. (2020). In silico experiments of bone remodeling explore metabolic diseases and their drug treatment. *Science Advances*, 6(10), eaax0938.
- Katagiri, T., & Takahashi, N. (2002). Regulatory mechanisms of osteoblast and osteoclast differentiation. *Oral Diseases*, 8(3), 147–159. <https://doi.org/10.1034/j.1601-0825.2002.01829.x>
- Klein-Nulend, J., Nijweide, P. J., & Burger, E. H. (2003). Osteocyte and bone structure. *Current Osteoporosis Reports*, 1(1), 5–10. <https://doi.org/10.1007/s11914-003-0002-y>
- Komarova, S. V., Smith, R. J., Dixon, S. J., Sims, S. M., & Wahl, L. M. (2003). Mathematical model predicts a critical role for osteoclast autocrine regulation in the control of bone remodeling. *Bone*, 33(2), 206–215. [https://doi.org/10.1016/S8756-3282\(03\)00157-1](https://doi.org/10.1016/S8756-3282(03)00157-1)
- van Lenthe, G. H., de Waal Malefijt, M. C., & Huiskes, R. (1997). Stress shielding after total knee replacement may cause bone resorption in the distal femur. *The Journal of Bone and Joint Surgery*, 79(1), 117–122.
- Li, J., Li, H., Shi, L., Fok, A. S. L., Ucer, C., Devlin, H., Horner, K., & Silikas, N. (2007). A mathematical model for simulating the bone remodeling process under mechanical stimulus. *Dental Materials*, 23(9), 1073–1078. <https://doi.org/10.1016/j.dental.2006.10.004>
- Lian, Z., Guan, H., Ivanovski, S., Loo, Y. C., Johnson, N. W., & Zhang, H. (2010). Effect of bone to implant contact percentage on bone remodelling surrounding a dental implant. *International Journal of Oral and Maxillofacial Surgery*, 39(7), 690–698. <https://doi.org/10.1016/j.ijom.2010.03.020>
- Lin, C. L., Lin, Y. H., & Chang, S. H. (2010). Multi-factorial analysis of variables influencing the bone loss of an implant placed in the maxilla: Prediction using FEA and SED bone remodeling algorithm. *Journal of Biomechanics*, 43(4), 644–651. <https://doi.org/10.1016/j.jbiomech.2009.10.030>
- Madge, M., Vittorio, S., & Peter, P. (2020). *Development of a computational modelling platform for patient-specific treatment of osteoporosis* (pp. 85–107). Springer Science and Business Media LLC. [https://doi.org/10.1007/978-3-030-42428-2\\_6](https://doi.org/10.1007/978-3-030-42428-2_6)
- Maria-Ioana, P., Stefan, S., Peter, P., & Christian, H. (2018). A mathematical multiscale model of bone remodeling, accounting for pore space-specific mechanosensation. *Bone*, 208–221. <https://doi.org/10.1016/j.bone.2017.11.009>
- Marzban, A., Nayeb-Hashemi, H., & Vaziri, A. (2015). Numerical simulation of load-induced bone structural remodelling using stress-limit criterion. *Computer Methods in Biomechanics and Biomedical Engineering*, 18(3), 259–268. <https://doi.org/10.1080/10255842.2013.792915>
- Metzger, T. A., Schwaner, S. A., LaNeve, A. J., Kreipke, T. C., & Niebur, G. L. (2015). Pressure and shear stress in trabecular bone marrow during whole bone loading. *Journal of biomechanics*, 48(12), 3035–3043. <https://doi.org/10.1016/j.jbone.2014.03.050>

- Michele, C., Romane, B., Christian, H., Keita, I., & Bert, van R. (2014). A multiscale analytical approach for bone remodeling simulations: Linking scales from collagen to trabeculae. *Bone*, 303–313. <https://doi.org/10.1016/j.bone.2014.03.050>
- Mora-Macías, J., Ayensa-Jiménez, J., Reina-Romo, E., Doweidar, M. H., Domínguez, J., Doblaré, M., & Sanz-Herrera, J. A. (2020). A multiscale data-driven approach for bone tissue biomechanics. *Computer Methods in Applied Mechanics and Engineering*, 368. <https://doi.org/10.1016/j.cma.2020.113136>
- Moreira, S. F., Belinha, J., Dinis, L. M. J. S., & Jorge, R. N. (2014). A global numerical analysis of the “central incisor/local maxillary bone” system using a meshless method. *Molecular & Cellular Biomechanics*, 11(3), 151.
- Mousavi, Seyed Jamaleddin, Doblaré, M., & Doweidar, M. H. (2014). Computational modeling of multi-cell migration in a multi-signalling substrate. *Physical Biology*, 11(2), 026002. <https://doi.org/10.1088/1478-3975/11/2/026002>
- Mousavi, S. J., Doweidar, M. H., & Doblaré, M. (2014). Computational modelling and analysis of mechanical conditions on cell locomotion and cell-cell interaction. *Computer Methods in Biomechanics and Biomedical Engineering*, 17(6), 678–693. <https://doi.org/10.1080/10255842.2012.710841>
- Mousavi, Seyed Jamaleddin, Hamdy Doweidar, M., & Aegeuter, C. M. (2015). Role of mechanical cues in cell differentiation and proliferation: A 3D numerical model. *PLOS ONE*, 10(5), e0124529. <https://doi.org/10.1371/journal.pone.0124529>
- Mullender, M. G., Huiskes, R., & Weinans, H. (1994). A physiological approach to the simulation of bone remodeling as a self-organizational control process. *Journal of Biomechanics*, 27(11), 1389–1394. [https://doi.org/10.1016/0021-9290\(94\)90049-3](https://doi.org/10.1016/0021-9290(94)90049-3)
- Müller, R. (2005). Long-term prediction of three-dimensional bone architecture in simulations of pre-, peri-and post-menopausal microstructural bone remodeling. *Osteoporosis International*, 16(2), S25–S35.
- Mulvihill, B. M., & Prendergast, P. J. (2010). Mechanobiological regulation of the remodeling cycle in trabecular bone and possible biomechanical pathways for osteoporosis. *Clinical Biomechanics*, 25(5), 491–498. <https://doi.org/10.1016/j.clinbiomech.2010.01.006>
- Nutu, E. (2018). Role of initial density distribution in simulations of bone remodeling around dental implants. *Acta of Bioengineering and Biomechanics*, 20(4), 23–31. <https://doi.org/10.5277/ABB-01195-2018-02>
- Ostadi Moghaddam, A., Mahjoob, M. J., & Nazarian, A. (2018). Bone remodeling under vibration: A computational model of bone remodeling incorporating the modal behavior of bone. *Journal of Biomechanical Engineering*, 140(12).
- Oumghar, A., Imane, A., Barkaoui, P., & Chabrand. (2020). Towards a mathematical modeling of diseases’ impact on bone remodeling: Technical review. *Frontiers in Bioengineering and Biotechnology*, 8.
- Pant, A., Paul, E., Niebur, G. L., & Vahdati, A. (2021). Integration of mechanics and biology in computer simulation of bone remodeling. *Progress in Biophysics and Molecular Biology*, 164, 33–45. <https://doi.org/10.1016/j.pbiomolbio.2021.05.001>
- Pereira, A. F., & Shefelbine, S. J. (2014). The influence of load repetition in bone mechanotransduction using poroelastic finite-element models: The impact of permeability. *Biomechanics and Modeling in Mechanobiology*, 13(1), 215–225. <https://doi.org/10.1007/s10237-013-0498-8>
- Peyroteo, M. M. A., Belinha, J., Vinga, S., Dinis, L. M. J. S., & Jorge, R. N. (2019). Mechanical bone remodelling: Comparative study of distinct numerical approaches. *Engineering Analysis with Boundary Elements*, 100, 125–139.

- Prendergast, P. J., Galibarov, P. E., Lowery, C., & Lennon, A. B. (2011). Computer simulating a clinical trial of a load-bearing implant: An example of an intramedullary prosthesis. *Journal of the Mechanical Behavior of Biomedical Materials*, 4(8), 1880–1887. <https://doi.org/10.1016/j.jmbbm.2011.06.005>
- R., P. G., Angad, M., & Ralph, M. (2018). Mechanical stimuli in the local in vivo environment in bone: Computational approaches linking organ-scale loads to cellular signals. *Current Osteoporosis Reports*, 395–403. <https://doi.org/10.1007/s11914-018-0448-6>
- Rouhi, G., Vahdati, A., Li, X., & Sudak, L. (2015a). A three-dimensional computer model to simulate spongy bone remodeling under overload using a semi-mechanistic bone remodeling theory. *Journal of Mechanics in Medicine and Biology*, 15(04), 1550061.
- Rouhi, G., Vahdati, A., Li, X., & Sudak, L. J. (2015b). An investigation into the effects of osteocytes density and mechanosensitivity on trabecular bone loss in aging and osteoporotic individuals. *Biomedical Engineering Letters*, 5(4), 302–310. <https://doi.org/10.1007/s13534-015-0206-y>
- Ryser, M. D., & Murgas, K. A. (2017). Bone remodeling as a spatial evolutionary game. *Journal of Theoretical Biology*, 418, 16–26.
- Santos, A., Bakker, A. D., & Klein-Nulend, J. (2009). The role of osteocytes in bone mechanotransduction. *Osteoporosis International*, 20(6), 1027–1031. <https://doi.org/10.1007/s00198-009-0858-5>
- Sayyidmousavi, A., & Bougherara, H. (2012). Investigation of stress shielding around the Stryker Omnifit and Exeter periprosthetic hip implants using an irreversible thermodynamic-based model. *Journal of Biomedical Materials Research - Part B Applied Biomaterials*, 100(5), 1416–1424. <https://doi.org/10.1002/jbm.b.32500>
- Scheiner, S., Pivonka, P., Hellmich, C., & Smith, D. W. (2012). A mathematical model of bone remodeling considering mechanoregulatory mechanisms: Theoretical model development and numerical studies. *Blucher Mechanical Engineering Proceedings*, 1(1), 175–188.
- Scheiner, S., Pivonka, P., Smith, D. W., & Dunstan, C. R. (2012). Computer simulation-based modeling of the pharmaceutical intervention of postmenopausal osteoporosis by denosumab. In , Vol4. ASME 2012 11th Biennial Conference on Engineering systems design and analysis (pp. 285–289). ESDA. <https://doi.org/10.1115/ESDA2012-82990>, 2012.
- Scheiner, S., Pivonka, P., Smith, D. W., Dunstan, C. R., & Hellmich, C. (2014). Mathematical modeling of postmenopausal osteoporosis and its treatment by the anti-catabolic drug denosumab. *International Journal for Numerical Methods in Biomedical Engineering*, 30(1), 1–27. <https://doi.org/10.1002/cnm.2584>
- Spingarn, C., Wagner, D., Rémond, Y., & George, D. (2017). Multiphysics of bone remodeling: a 2D mesoscale activation simulation. *Biomedical Materials and Engineering*, 28(s1), S153–S158.
- Stender, M. E., Carpenter, R. D., Regueiro, R. A., & Ferguson, V. L. (2016). An evolutionary model of osteoarthritis including articular cartilage damage, and bone remodeling in a computational study. *Journal of Biomechanics*, 49(14), 3502–3508. <https://doi.org/10.1016/j.jbiomech.2016.09.024>
- Trichilo, S., & Pivonka, P. (2018). Application of disease system analysis to osteoporosis: From temporal to spatio-temporal assessment of disease progression and intervention. In , Vol578. CISM International Centre for mechanical sciences, Courses and Lectures (pp. 61–121). Springer International Publishing. [https://doi.org/10.1007/978-3-319-58845-2\\_2](https://doi.org/10.1007/978-3-319-58845-2_2)
- Tsubota, K.i., Suzuki, Y., Yamada, T., Hojo, M., Makinouchi, A., & Adachi, T. (2009). Computer simulation of trabecular remodeling in human proximal femur using large-scale

- voxel FE models: Approach to understanding Wolff's law. *Journal of Biomechanics*, 42(8), 1088–1094. <https://doi.org/10.1016/j.jbiomech.2009.02.030>
- Turner, C. H. (1999). Toward a mathematical description of bone biology: The principle of cellular accommodation. *Calcified Tissue International*, 65(6), 466–471. <https://doi.org/10.1007/s002239900734>
- Turner, A. W. L., Gillies, R. M., Sekel, R., Morris, P., Bruce, W., & Walsh, W. R. (2005). Computational bone remodelling simulations and comparisons with DEXA results. *Journal of Orthopaedic Research*, 23(4), 705–712. <https://doi.org/10.1016/j.orthres.2005.02.002>
- Urdeitz, P., Farzaneh, S., Mousavi, S. J., & Doweidar, M. H. (2020). Role of oxygen concentration in the osteoblasts behavior: A finite element model. *Journal of Mechanics in Medicine and Biology*, 20(01), 1950064. <https://doi.org/10.1142/s0219519419500647>
- Vahdati, A., & Rouhi, G. (2009). A model for mechanical adaptation of trabecular bone incorporating cellular accommodation and effects of microdamage and disuse. *Mechanics Research Communications*, 36(3), 284–293. <https://doi.org/10.1016/j.mechrescom.2008.10.004>
- Vahdati, A., Rouhi, G., Ghalichi, F., & Tahani, M. (2008). Mechanically induced trabecular bone remodeling including cellular accommodation effect: A computer simulation. *Transactions of the Canadian Society for Mechanical Engineering*, 32(3-4), 371–382.
- Vahdati, A., Walscharts, S., Jonkers, I., Garcia-Aznar, J. M., Vander-Sloten, J., & van Lenthe, G. H. (2014). Role of subject-specific musculoskeletal loading on the prediction of bone density distribution in the proximal femur. *Journal of the Mechanical Behavior of Biomedical Materials*, 244–252. <https://doi.org/10.1016/j.jmbbm.2013.11.015>
- Villette, C. C., & Phillips, A. T. M. (2016). Informing phenomenological structural bone remodelling with a mechanistic poroelastic model. *Biomechanics and Modeling in Mechanobiology*, 15(1), 69–82. <https://doi.org/10.1007/s10237-015-0735-4>
- Wang, C., Wang, L., Liu, X., & Fan, Y. (2014). Numerical simulation of the remodelling process of trabecular architecture around dental implants. *Computer Methods in Biomechanics and Biomedical Engineering*, 17(3), 286–295. <https://doi.org/10.1080/10255842.2012.681646>
- Wang, C., Zhang, W., Ajmera, D. H., Zhang, Y., Fan, Y., & Ji, P. (2016). Simulated bone remodeling around tilted dental implants in the anterior maxilla. *Biomechanics and Modeling in Mechanobiology*, 15(3), 701–712. <https://doi.org/10.1007/s10237-015-0718-5>
- Wang, C., Zhang, C., Han, J., Wu, H., & Fan, Y. (2011). Simulated evolution of the vertebral body based on basic multicellular unit activities. *Journal of Bone and Mineral Metabolism*, 29(4), 466–476. <https://doi.org/10.1007/s00774-010-0244-6>
- Weinans, H., Huiskes, R., & Grootenhuis, H. J. (1992). The behavior of adaptive bone-remodeling simulation models. *Journal of Biomechanics*, 25(12), 1425–1441. [https://doi.org/10.1016/0021-9290\(92\)90056-7](https://doi.org/10.1016/0021-9290(92)90056-7)
- Weinans, H., Sumner, D. R., Iglesia, R., & Natarajan, R. N. (2000). Sensitivity of periprosthetic stress-shielding to load and the bone density-modulus relationship in subject-specific finite element models. *Journal of Biomechanics*, 33(7), 809–817. [https://doi.org/10.1016/S0021-9290\(00\)00036-1](https://doi.org/10.1016/S0021-9290(00)00036-1)
- Wolff, J. (2000). Das Gesetz der Transformation der Knochen. In A. Hirschwald, Berlin (Ed.), *Translated as: the law of bone remodeling* (1986). Berlin: Springer-Verlag.
- Xinghua, Z., He, G., Dong, Z., & Bingzhao, G. (2002). A study of the effect of non-linearities in the equation of bone remodeling. *Journal of Biomechanics*, 35(7), 951–960. [https://doi.org/10.1016/S0021-9290\(02\)00028-3](https://doi.org/10.1016/S0021-9290(02)00028-3)

This page intentionally left blank

# Bone strength, bone remodeling, and biomechanics of fracture

# 22

Vee San Cheong<sup>1,2</sup>, Marco Palanca<sup>1,3</sup>, Enrico Dall'Ara<sup>1,3</sup>

<sup>1</sup>INSIGNEO Institute for In Silico Medicine, University of Sheffield, Sheffield, United Kingdom;

<sup>2</sup>Department of Automatic Control and Systems Engineering, University of Sheffield, Sheffield, United Kingdom; <sup>3</sup>Department of Oncology and Metabolism, University of Sheffield, Sheffield, United Kingdom

## Chapter outline

<b>Bone physiology .....</b>	516
<b>Bone cells .....</b>	517
<b>Bone modeling and remodeling .....</b>	520
<b>Bone mechanical properties and fracture .....</b>	521
Bone elasticity .....	523
Bone post-elastic behavior .....	523
Bone time-dependent properties .....	524
<b>Predictions of bone strength with finite element models .....</b>	525
DXA-based models.....	525
CT-based FE models.....	526
HR-pQCT-based FE models .....	527
MicroCT-based FE models.....	527
<b>Model validation .....</b>	528
Standard mechanical tests .....	528
Local deformation with strain gauges .....	528
Full field tests DIC and DVC .....	530
Examples of validation studies for FE models.....	531
<b>Predictions of bone remodeling .....</b>	531
Mechanoregulation .....	531
Bone adaptation algorithm and implementation in FE framework .....	532
Validation for murine studies.....	533
Morphometric and densitometric analysis .....	534
Spatial analysis and biomarkers for bone formation .....	536
<b>References .....</b>	537

## Bone physiology

The musculoskeletal system is made of bones, muscles, ligaments, tendons, and cartilage. Bone is a connective tissue that supports the body and enables the movement induced by the forces generated by the muscles. Bone has also a protective function for the vital organs and acts as a storage of minerals, mainly calcium and phosphorus.

Bone is a composite material with a complex hierarchical structure (Fig. 22.1).

The main constituents of bone are mineral (mainly impure hydroxyapatite  $\text{Ca}_{10}(\text{PO}_4)_6(\text{OH})_2$  crystals), organic matrix (90% collagen Type I and 10% noncollagenous proteins), and water (Cowin, 2001). The mineral constitutes 65% of bone mass. Variations in the proportions of mineral, organic matrix, and water result in a wide range of material properties (elastic modulus, strength, toughness) of bone across different species and anatomical sites (from the very hard and stiff hypermineralized rostrum of the whale Mesoplodon to the tough but compliant fish bones (Zioupos et al., 2000)). Nevertheless, the mechanical properties of bone are also driven by the arrangement of the components of the bone in the form of structural units at each dimensional scale, to optimize its resistance to fracture. Thanks to this hierarchical arrangement and a proportion of mineral and organic matrix, bone is hard, stiff yet ductile enough to resist external loads and fracture propagation (Cowin, 2001).

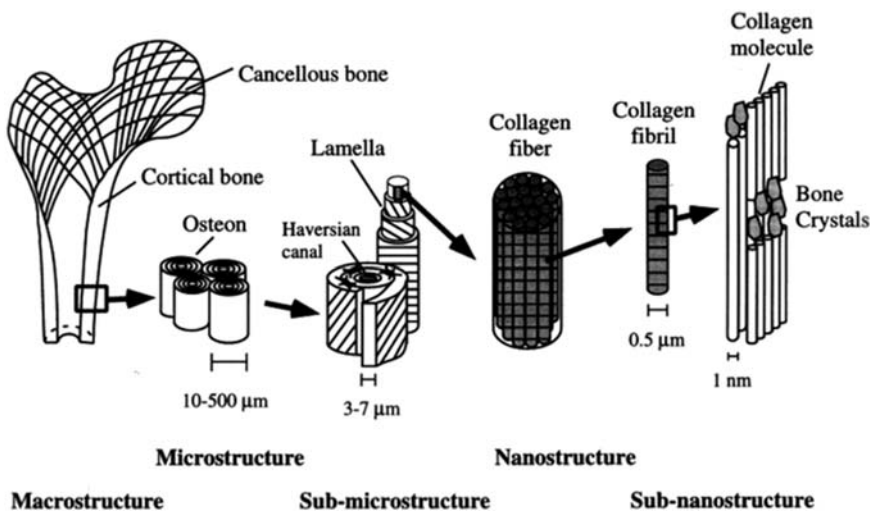


FIGURE 22.1 Hierarchical structure of bone.

Reprinted with permission from Rho, J.Y., Kuhn-Spearing, L., & Zioupos, P. (1998). Mechanical properties and the hierarchical structure of bone. Medical Engineering & Physics, 20, 92–102.

Bone comprises mainly two types of microstructures: trabecular bone (also referred to as spongeous bone or cancellous bone), located in the epiphysis of the long bones and in the central core of flat, short and irregular bones; and cortical bone (also referred to as compact bone or cortex) that constitutes the diaphysis of long bones and the external shell of short, flat, and irregular bones. Trabecular bone is more porous than cortical bone, with an organized matrix of interconnected rod-like or plate-like structures called trabeculae, between 100 and 640  $\mu\text{m}$  in thickness (Cowin, 2001). The denser cortical bone is formed of osteons—cylindrical substructures where circular rings of bone lamellae surround a longitudinal (Haversian canals) or transverse (Volkmann's canals) vascular channel—that are embedded in the remnant of old osteons, which are known as interstitial tissue (Cowin, 2001). Haversian and Volkmann systems are typically 100–300  $\mu\text{m}$  in diameter, and they can be up to a few millimeters long.

Trabeculae, osteons, and interstitial bone are formed by parallel or cylindrical packages of lamellae, 3–7  $\mu\text{m}$  in thickness, arranged in different microstructures to form the bone structure units.

Lamellae are made of packages of collagen fibers, each formed by collagen fibrils, which are composed by collagen molecules intercalated with mineral crystals.

A bone's hierarchical structure creates an intricate network of pores within the extracellular matrix. These pores, which span different dimensional levels and host the bone cells, blood vessels, bone marrow, or nerves, affect the tissue micro-architecture and the bone mechanical properties. Bone marrow fills the pores between trabeculae in the trabecular bone. The Haversian and Volkmann's canals (approximately 50  $\mu\text{m}$  in diameter) contain blood capillaries and nerve fibers. At lower dimensional scale, ellipsoidal micropores called lacunae (5–15  $\mu\text{m}$  in size) host osteocytes (Peyrin et al., 2014). These cells are embedded in the bone matrix and are thought to be mechanosensors and orchestrate bone remodeling. The osteocyte lacunae are connected to each other with a fine network of canals called canaliculari (average diameter 100–600 nm) (Yu et al., 2020). The lacuno-canalicular network (LCN) consists of several thousands of lacunae per  $\text{mm}^3$  and hundreds of thousands of canaliculari per  $\text{mm}^3$  (Peyrin et al., 2014; Van Tol et al., 2020).

The complex geometry, heterogeneous microstructure, and orientation of the bone structural units and porosities lead to heterogeneous, anisotropic, and nonlinear mechanical properties. Moreover, bone is a living tissue, continuously remodeled by the activity of bone cells (more details in Section [Bone cells](#)), to maintain the bone tissue, by repairing microdamage and microcracks.

## Bone cells

Bone has four main types of bone cells that are present in its biological milieu.

Osteoclasts (Fig. 22.2) are large multinucleated cells derived from mononuclear cells of the monocyte–macrophage lineage (Teitelbaum, 2000). Their precursor cells attach to the bone matrix, and differentiate to form osteoclasts in response to

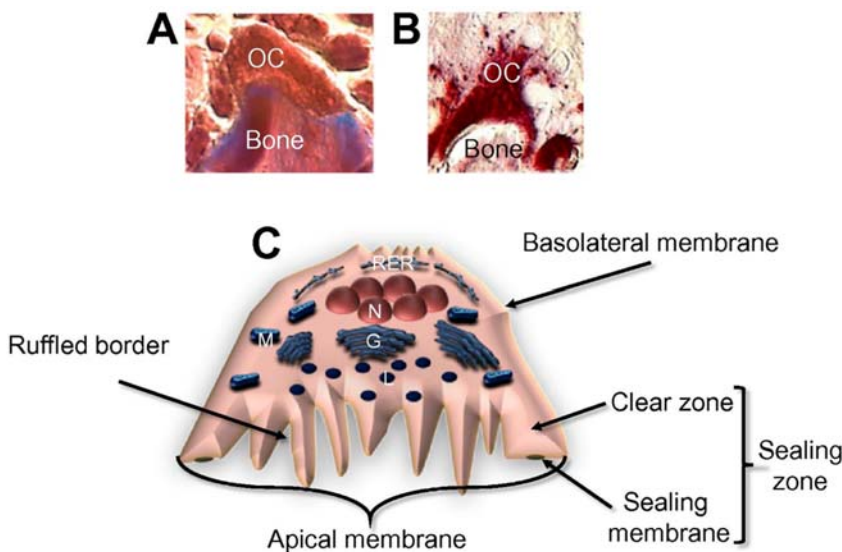


**FIGURE 22.2** Bone cells.

(A) Masson stain of a resorbing osteoclast in a mouse tibia. (B) Tartrate-resistant acid phosphatase (TRAcP) staining of an osteoclast (C) Illustration of the structure of an osteoclast. Reprinted with permission from Cappariello, A., Maurizi, A., Veeriah, V., & Teti, A. (2014). Reprint of: The Great Beauty of the osteoclast. Archives of Biochemistry and Biophysics, 561, 13–21.

macrophage colony-stimulating factor (M-CSF) and receptor activator of nuclear factor kappa-B ligand (RANK-L) proteins. Osteoclasts release acidified vesicles bearing H<sup>+</sup>-adenosine triphosphatase (H<sup>+</sup>-ATPase) into the resorptive compartment (Blair et al., 1989; Teitelbaum, 2000). The acid releases calcium from the bone matrix to form HCO<sub>3</sub><sup>-</sup>, which are transported out of the resorptive compartment in exchange for Cl<sup>-</sup>, forming HCl which further degrades the organic matrix of bone (Schlesinger et al., 1997).

**Osteoblasts** (Fig. 22.3) are derived mesenchymal stem cells that form bones by secreting a matrix termed osteoid, which comprises mainly of type I collagen (Ducy et al., 2000). They also produce the enzyme alkaline phosphatase (ALP) and proteins osteocalcin, osteonectin and osteopontin, which are used as markers for bone formation (Capulli et al., 2014). ALP is involved in the mineralization of osteoid, which begins 10–15 days after its formation and it is during this process that bone rapidly accumulates about 70% of its final mineral content; the remaining 30% is acquired over several months (Sommerfeldt & Rubin, 2001).

**Osteocytes** are postproliferative cells formed from the differentiation of osteoblasts that become encased within their own osteoid and mineralized bone matrix (Bonewald, 2011). They are the most populous cells in bone (90%–95%) and form an extensive three-dimensional network in the canaliculi with other osteocytes

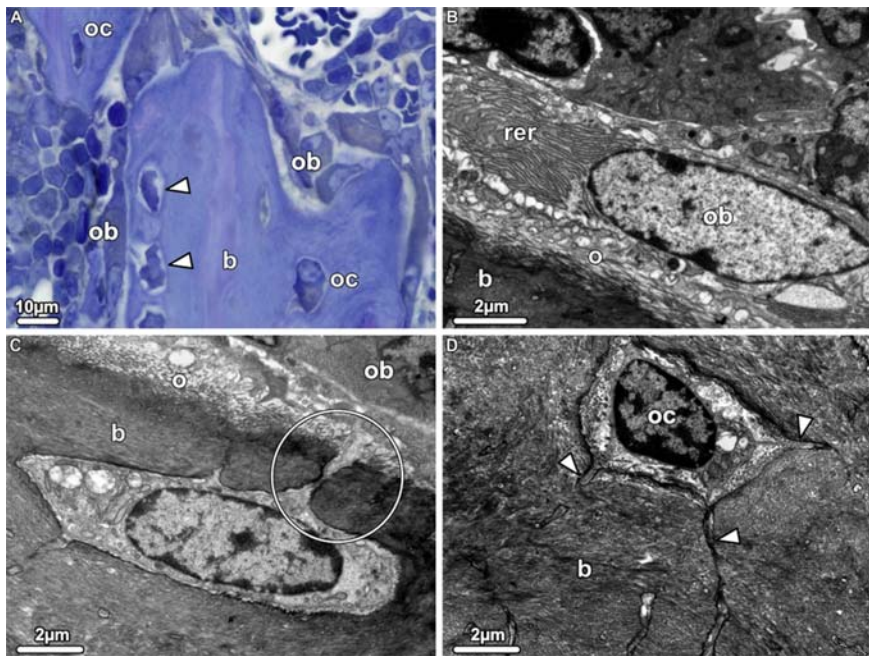


**FIGURE 22.3 Bone remodeling unit.**

Toluidine blue stains (A) and Transmission Electron Microscopy images (B-D) of the bone remodeling unit in demineralized bone of a four-week-old mouse. (A) Osteoblasts (ob) differentiating to preosteocytes (indicated by arrowheads), which will eventually form bone (b). (B) Endoplasmic reticulum (rer) of osteoblasts, which synthesizes type-I collagen fibrils or osteoid (o) (C) Preosteocytes have small amount of endoplasmic reticulum. The circled region shows a connection between the preosteocytes and osteoblast. (D) Long cytoplasmic processes (indicated by arrowheads) of an osteocyte embedded in woven bone. Source: Blumer, M.J. (2021). *Bone tissue and histological and molecular events during development of the long bones*. Annals of Anatomy, 235, 151704.

and bone lining cells via cytoplasmastic extensions (Sommerfeldt & Rubin, 2001). Osteocytes are mechanosensing cells that regulate bone formation and resorption by producing sclerostin and insulin-like growth factor-I (IGF-I) in response to mechanical loads. Apoptosis of osteocytes increases the expression of RANK-L which stimulates osteoclast formation and function (Capulli et al., 2014).

**Bone lining cells** are flat-shaped osteoblasts covering the external and internal surfaces of bone (i.e., periosteum and endosteum) that are not being remodeled (in quiescent state). However, one difference between the two cells is that bone lining cells do not express osteocalcin (Everts et al., 2002). Bone lining cells are closely associated with the function of osteoclasts as they secrete RANK-L to guide osteoclasts to the resorption site, and they remove demineralized collagen prior and following osteoclastic action (Everts et al., 2002).

---

## Bone modeling and remodeling

Frost (1963) identified two separate mechanisms which determine whole bone strength and anatomy: bone modeling and remodeling.

**Bone modeling** is the process whereby bone is formed without being preceded by resorption (Kobayashi et al., 2003). Modeling is most active from birth till skeletal maturity and it is characterized by formation and resorption drifts. In long bones, during the increase of bone length, the metaphysis is modeled to a diaphyseal shape by periosteal resorption and endosteal apposition in a process known as metaphyseal shaping (Sommerfeldt & Rubin, 2001). In the transverse section, osteoblasts add new circumferential lamellae to the periosteal surface, while osteoclasts resorb the endosteal surface, resulting in the cortical “drift” (Ruff & Hayes, 1982). Bone modeling is also responsible for changes in morphology after skeletal maturity as a response to mechanical load (Paiva & Granjeiro, 2017), such as in the dominant arm of the tennis player where the bone mass and cortical area are higher than in the contralateral limb (Kontulainen et al., 2002).

**Bone remodeling** is the dominant process of bone repair and renewal throughout the adult life to improve the quality of mineralized tissue and fracture toughness (Zimmermann et al., 2015). The removal of old and/or damaged bone and the laying of new bone is typically ascribed to the coupling of the osteoclasts and osteoblasts in local teams of basic multicellular units (BMUs). Bone remodeling is initiated by the apoptosis of osteocytes, which is the start of the activation–resorption–reversal–formation (ARRF) sequence (Sommerfeldt & Rubin, 2001). In the resorption phase, bone lining cells prepare the bone surface for resorption by removing the collagenous layer and triggering chemotactic factors to guide osteoclastic resorption. Osteoclasts leave behind demineralized collagen which are removed by bone lining cells, which are replaced by cement lines and a thin layer of fibrillar collagen (Everts et al., 2002). In the reversal phase, mesenchymal stem cells migrate to the resorption pit and differentiate to osteoblasts. Finally, osteoblasts lay down osteoid, which is mineralized with calcium and phosphate in the formation phase. In addition to the replacement of damaged and dead tissues, bone remodeling is responsible for bone adaptation due to changes in loading, for example in the aseptic loosening of orthopedic implants due to stress shielding (Cheong et al., 2018), and is affected by changes in nutrition and metabolism (Bain & Rubin, 1990).

In healthy adults under physiological conditions, the RANK/RANK-L/OPG system plays a crucial role to ensure that osteoclastic bone resorption is matched by osteoblastic activities, so that a balanced homeostatic amount of bone is maintained. RANK-L are produced by osteocytes and bone lining cells, which bind to RANK receptors on osteoclasts precursors and mesenchymal stem cells to drive the differentiation of osteoclasts and the inhibition of osteoblast differentiation, respectively (X. Chen et al., 2018). As osteoclasts mature, they secrete vesicular RANK which binds to osteoblastic RANKL and promote the differentiation of osteoblasts (Ikeuchi et al., 2018). Expression of RANK reduces as osteoblasts mature, which regulates further differentiation of mesenchymal stem cells to osteoblasts (X. Chen

et al., 2018). Other amino acids, cytokines, and hormone that play an important role in the regulation of homeostasis include the osteoprotegerin (OPG) ligand, which regulates osteoclastgenesis, transforming growth factor (TGF)- $\beta$ , which are secreted during bone resorption, to initiate local bone formation (Rahman et al., 2015), vitamin D<sub>3</sub>, parathyroid hormone (PTH), and estrogen (Robling & Turner, 2009).

Bone homeostasis is also responsible for regulating the ionic composition of blood and interstitial fluids in the body. Bone is the largest reservoir of calcium and is regulated by the parathyroid hormone (PTH). PTH promotes osteoclastgenesis which increases blood calcium and phosphate levels. Vitamin D or calcitriol (1,25-(OH)<sub>2</sub>D<sub>3</sub>) enhances the absorption of calcium and phosphate but promotes resorption through the stimulation of osteoclastgenesis at supraphysiological levels (Lee & Lorenzo, 1999). The release of PTH is inhibited by rising calcium levels.

Disruption to physiological bone remodeling results in bone pathologies that affect the bone mass or quality of bone formed. In diseases characterized by net bone loss, two possible pathways have been suggested: (1) imbalance of remodeling, where the matrix secreted by the osteoblast are insufficient to replace the resorbed bone; (2) decoupling/delayed coupling of osteoblast formation during and following bone resorption (Baron et al., 1983).

**Osteoporosis** is characterized by a decrease in bone mass and a deterioration of the trabecular architecture, leading to increased fracture risk (Fig. 22.4). Osteoporosis can be classified into primary or secondary osteoporosis. Secondary osteoporosis is caused by other medical conditions such as leukemia, hyperthyroidism, or hyperparathyroidism (Feng & McDonald, 2011). Primary osteoporosis is due to the reduction of osteoclast apoptosis increasing the lifespan of osteoclasts, caused by deficiencies in estrogen (type I primary), vitamin D, and/or calcium (type II primary) (Nakamura et al., 2007). Disruptions to the differentiation of mesenchymal stem cells to osteoblasts can also result in early onset osteoporosis and osteogenesis imperfecta, caused by mutations in the WNT1 gene (Laine et al., 2013).

**Osteoarthritis** (OA) is a degenerative joint disease affecting all tissues in the joint, leading to pain, joint stiffness, and dysfunction. Although the loss and degeneration of the articular cartilage is recognized as the primary cause of OA, results from several studies have shown that subchondral bone remodeling affects the progression of OA (Hayami et al., 2004). Although the exact pathological mechanism is still a topic of research, studies have shown an elevated level of transforming growth factor- $\beta$  (TGF- $\beta$ ) at the onset of OA, which increases angiogenesis and elevated bone and osteophyte formation (Hayami et al., 2004). This modifies the stress distribution in the subchondral bone and the articular cartilage, exacerbating their degeneration (Zhu et al., 2021).

## Bone mechanical properties and fracture

The mechanical properties of the bone are driven by its geometrical, microstructural, and material properties. The external loads at the whole organ level induce a

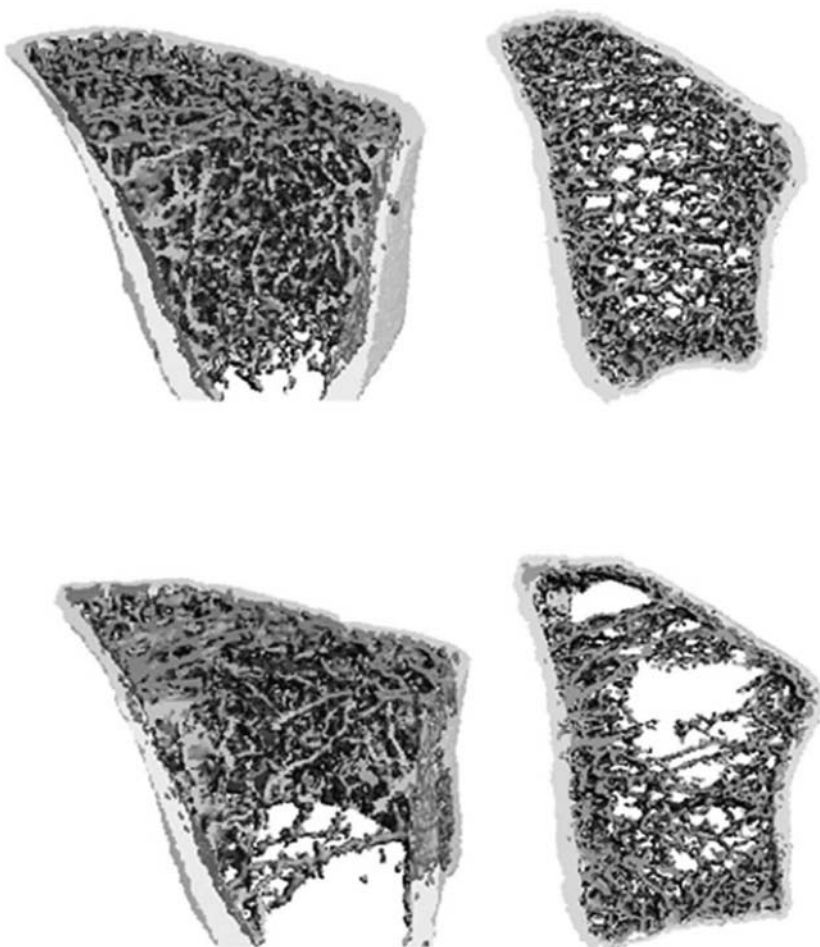


**FIGURE 22.4 Microstructure of the distal radius.**

Microstructure of the distal radius in a patient who suffered from an Osteoporotic fracture (bottom) and from a healthy patient (top). Adapted from Zhu, T.Y., Hung, V.W., Cheung, W.H., Cheng, J.C., Qin, L., & Leung, K.S. (2016). Value of measuring bone microarchitecture in fracture discrimination in older women with recent hip fracture: A case-control study with HR-pQCT. *Scientific Reports*, 6, 34185.

complex state of strains and stresses throughout the bone and the weakest regions will fail or fracture when the local strains and stresses at the tissue level are beyond the material limits of bone, which are functions of its local physical properties. The strain is the deformation of the tissue normalized by its original length. Stress is calculated as the internal force normalized by the area.

The bone microstructure plays a critical role in resisting fracture. Cortical and trabecular bone shows a complex heterogeneous structure, optimized through the cellular activities driven by external biomechanical and biochemical stimuli. Cortical bone is stiffer and less ductile than trabecular bone. This is mainly due to the higher bone density and lower porosity of the cortical bone tissue. The complex structure of trabecular bone gives rise to its highly heterogeneous and anisotropic mechanical properties. Bone strength and elastic properties are driven mainly by the bone density, its architecture, and the orientation of the trabeculae (Matsuura et al., 2008; Öhman et al., 2007). The morphometric parameters of trabecular bone specimens can be quantified with ex vivo micro computed tomography (microCT) that can be used to acquire high resolution 3D images with a resolution of approximately 5–20  $\mu\text{m}$ . Morphometric properties can also be assessed in the peripheral sites of small rodents with in vivo microCT (resolution of approximately 8–10  $\mu\text{m}$ ) or in the distal tibia and radius of humans by using high-resolution peripheral quantitative CT (HR-pQCT, resolution of approximately 40–80  $\mu\text{m}$ ) (Fig. 22.4). Typical morphometric parameters estimated from microCT images are bone volume (BV), total volume (TV), bone volume fraction (BV/TV), trabecular thickness (Tb.Th), trabecular number (Tb.N), and trabecular spacing (Tb.Sp), and degree of anisotropy (DA).

## Bone elasticity

Under low loads bone deforms elastically, which means that when the load is removed the bone recovers to its original geometry in the unloaded state. The relationship between stress and strain in the elastic load regime is linear for cortical and trabecular bone. In uniaxial testing, the proportionality coefficient between stress and strain is called elastic modulus (or Young's modulus) and is similar for tensile and compressive loads (Fig. 22.5) (Mercer et al., 2006). In three dimensions (3D) the stress (S) and the strain (E) second-order tensors, which have six independent components each, are related to each other through Hooke's elasticity law via symmetric positive definite fourth-order tensors called the stiffness tensor and the compliance tensor. For a generic material, these tensors have 21 independent material constants, which define the constitutive behavior of the material. After the comprehensive experimental characterization of the mechanical behavior of the bone tissue (Rincón-Kohli & Zysset, 2009), it is accepted that bone is orthotropic. This means that we can identify three planes of elastic symmetry, and the stiffness and compliance tensors can be defined with nine independent constants, that are a function of the local density and orientation of the porosities or building structures (Cowin, 2001; Zysset, 2003; Zysset & Curnier, 1995).

## Bone post-elastic behavior

When bone tissue is loaded beyond the yield state, the relationship between stress and strain is no more linear and bone is subjected to permanent deformation when unloaded. If bone is loaded beyond yield, it may reach the point of failure,

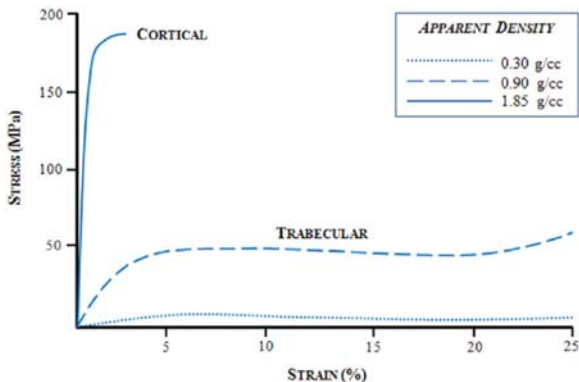


**FIGURE 22.5 Stress–Strain curves.**

Stress–Strain curves from compressive tests performed on Cortical and trabecular bone specimens.

Source: Hart, N.H., Nimphius, S., Rantalainen, T., Ireland, A., Siafarikas, A., & Newton, R.U. (2017 Sep). Mechanical basis of bone strength: influence of bone material, bone structure and muscle action. *Journal of Musculoskeletal and Neuronal Interactions*, 17(3), 114–139.

which is the state in the stress–strain relationship identified by a peak in stress (Fig. 22.5), beyond which a fracture will occur. The nonlinear relationship between stress and strain after yield is driven by the accumulation of cracks or diffuse damage in the tissue, which reduces its material properties and decreases the bone’s resistance to fracture.

Beyond the elastic region, bone failure behavior depends on the local bone density and orientation of the substructures. Anisotropic yield surfaces for trabecular bone have been modeled based on different criteria, and the most commonly used ones are Tsai-Wu (Wolfram et al., 2012), piecewise Hill (Garcia et al., 2009), and modified superellipsoidal (Bayraktar et al., 2004). The description of the complex constitutive laws for postelastic behavior of bone is not the main goal of this chapter but the interested reader can refer to Ref. (Schwiedrzik & Zysset, 2013) for more details.

### Bone time-dependent properties

Depending on the anatomical site, fractures can be very fast (e.g., fractures of the femur) or relatively slow (e.g., some fractures of the vertebral body) events. It should be noted that bone is a viscoelastic material and that its mechanical behavior depends on the loading rate. In particular, bone exhibits higher stiffness at higher loading rate and lower stiffness at lower loading rate.

The viscoelastic properties of bone can affect the ability of predicting the stiffness of bone and its failure mechanism. For this reason, more complex constitutive laws are needed to account for the effects of viscoelasticity and viscoplasticity on the bone elastic and postyield mechanics. The description of these constitutive laws is not the aim of this chapter, but the interested reader can refer to Ref (Xie et al., 2017) and Ref (Manda et al., 2017) for more details.

## Predictions of bone strength with finite element models

Bone fracture occurs when the external load is higher than the failure load that the bone can withstand. As explained in Section [Bone mechanical properties and fracture](#), bone strength is directly related to bone density.

Dual-energy X-ray Absorptiometry (DXA) is a diagnostic tool that is used to evaluate the patient's areal bone mineral density (aBMD) and to classify if patients are osteoporotic and therefore have a high risk of fracture. A patient is osteoporotic if the aBMD in the proximal femur or in the spine is 2.5 standard deviations below the average aBMD for a healthy young population. Subjects with aBMD higher than 1 standard deviation below the value for a young healthy population are considered healthy. Subjects with aBMD between  $-1$  and  $-2.5$  standard deviations below the reference value are considered to be osteopenic and have moderate risks of fracture. However, it has been observed that many fractures occur in patients who have not been identified as osteopenic or osteoporotic ([Siris et al., 2001](#)). Therefore, more reliable methods that better identify patients at high risk of fracture are needed.

In previous decades, much effort has been invested in the development and validation of computational models to predict patient-specific bone strength and their risk of fracture. These models utilize medical images to estimate the mechanical properties of bone tissue, and predict the effects of treatments and external stimuli on the bone properties at different dimensional levels, over time. Expanded from classical continuum mechanics, finite element (FE) analysis of bones reconstructed from medical images has become a popular and accurate tool to predict bone mechanical properties in patients. In the following paragraphs, FE models based on different medical images at different dimensional scales are described, followed by a section about typical experimental techniques to measure bone mechanical properties and validate the outputs of the models. The process of validation is fundamental to provide the credibility to the models needed to use these tools in clinical practice ([Musuamba et al., 2021](#)).

### DXA-based models

DXA images have been used to generate 2D or 3D FE models and predict the mechanical properties of the human femur ([Grassi et al., 2017](#); [L. Yang et al., 2014](#)). These models use 2D DXA images to estimate the bone geometry and assign the material properties based on the distribution of aBMD within the proximal femur ([Fig. 22.6](#)). Nevertheless, a 3D model can be generated using a statistical shape approach, registered to the original 2D DXA image ([Grassi et al., 2017](#)). The main advantage of these models is that they are subject-specific for the estimation of the biomechanical properties of the patients' femur from DXA, a widely available image modality that is used routinely to diagnose osteoporosis. Different studies have shown that DXA-based FE models ([Fig. 22.6](#)) can predict femoral strength reasonably well (at least under certain loading scenarios) ([Dall'Ara et al., 2016](#)) but they have limited ability to predict fracture risk compared to standard aBMD measurements or FRAX ([S. Yang et al., 2018](#)).

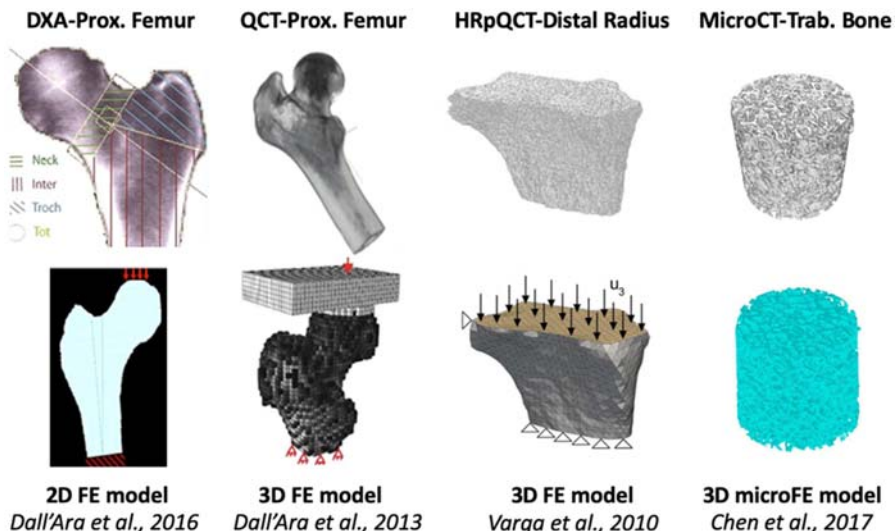


**FIGURE 22.6** Computational models based on biomedical images of bone.

Different types of computational models based on biomedical images. DXA can be used to create 2D FE models of the proximal femur (Source: Dall'Ara, E., Eastell, R., Viceconti, M., Pahr, D., & Yang, L. (2016). *Experimental validation of DXA-based finite element models for prediction of femoral strength*. Journal of the Mechanical Behavior of Biomedical Materials, 63, 17–25. <https://doi.org/10.1016/j.jmbbm.2016.06.004>); QCT images can be used to create 3D FE models of the proximal femur (Source: Dall'Ara, E., Luisier, B., Schmidt, R., Kainberger, F., Zysset, P., & Pahr, D. (2013). *A nonlinear QCT-based finite element model validation study for the human femur tested in two configurations in vitro*. Bone, 52(1), 27–38. <https://doi.org/10.1016/j.bone.2012.09.006>); HR-pQCT images can be used to create homogenized FE or microFE of the distal radius (adapted from Varga, P., Pahr, D. H., Baumbach, S., & Zysset, P. K. (2010 Nov). *HR-pQCT based FE analysis of the most distal radius section provides an improved prediction of Colles' fracture load in vitro*. Bone, 47(5), 982–988); microCT images can be used to create microFE models of trabecular bone at the biopsy level (Source: Chen, Y., Dall'Ara, E., Sales, E., Manda, K., Wallace, R., Pankaj, P., & Viceconti, M. (2017). *Micro-CT based finite element models of cancellous bone predict accurately displacement once the boundary condition is well replicated: Validation study*. Journal of the Mechanical Behavior of Biomedical Materials, 65, 644–651. <https://doi.org/10.1016/j.jmbbm.2016.09.014>).

### CT-based FE models

The main limitation of DXA-based FE models is that the geometry and the material properties are estimated from 2D projected images. To overcome this limitation Quantitative Computed Tomography (QCT) images calibrated with densitometric phantoms can be used to acquire the 3D geometry of the bone at higher resolution. QCT images can easily reach a spatial image resolution of approximately 1 mm, which allows for the characterization of the heterogeneous BMD of the bone and the identification of cortical and trabecular compartments in patients (Fig. 22.6). QCT-based FE models (Fig. 22.6) are created with automatic or semiautomatic pipelines that involve image segmentation, meshing, assignment of material properties based on the BMD

distribution and phenomenological laws, and the application of boundary conditions (external loading). Bone tissues have been modeled with different degrees of complexity, from simple linear elastic isotropic heterogeneous models (Schileo et al., 2008) to very complex heterogeneous and anisotropic materials with nonlinearities to account for plasticity and damage (Dall'Ara et al., 2013; Larsson et al., 2014; Zysset et al., 2013). Regardless of the way bone tissue is modeled, QCT-based FE models have generally been shown to predict bone strength better than clinical tools (aBMD or volumetric BMD) or DXA-based FE models (Dall'Ara et al., 2016), when compared to experimental measurements. Moreover, these models were applied to medical images collected in clinical trials to predict femoral strength (Keaveny et al., 2012), the risk of osteoporotic femoral fractures (Qasim et al., 2016), and the biomechanical properties of vertebrae with bone metastases (M.C Costa et al., 2017).

### HR-pQCT-based FE models

High-resolution peripheral QCT images (HR-pQCT, image resolution of approximately 60–80 µm) has been developed to evaluate the bone microstructure in the distal tibia and radius (Varga et al., 2011). The application of HR-pQCT in clinical research has allowed bioengineers to develop a new FE modeling approach to evaluate the biomechanical properties of bone while also accounting for the bone microstructure, which is clearly visible in HR-pQCT images (Fig. 22.6). In these models, usually referred to as “MicroFE,” bone geometry is acquired by segmenting trabecular and cortical structure from the HR-pQCT images. To reduce the radiation dose and the probability of movement artifacts during the scan, HR-pQCT images usually only include a short section of the proximal radius or distal tibia (9 or 18 mm in size). Each bone voxel is converted into a hexahedral element and at this dimensional scale bone is usually considered homogenous (Varga et al., 2011). Nevertheless, heterogeneous models based on local values of tissue mineral density (TMD) can be assigned, especially when the goal is to model bones from patients with diseases that are known to affect the local mineralization. This approach has been used to evaluate the effect of diseases such as Diabetes and Osteogenesis Imperfecta and their related interventions on the mechanical properties (stiffness and strength) of bone (Varga et al., 2020). The predictions of the mechanical properties of the distal radius and distal tibia have been extensively validated against experimental measurements (Varga et al., 2011).

### MicroCT-based FE models

MicroFE models can also be generated from high-resolution microCT images of bone biopsies extracted from the iliac crest or other anatomical sites (Y. Chen et al., 2017). The pipeline to generate these models is similar to the one described for HR-pQCT-based models. These high-resolution images (usually 10–20 µm) allow for a clear and easy identification of the bone regions and an accurate assessment of the local microstructure. The models can be used to predict in a nondestructive way the mechanical properties (stiffness, strength) of small trabecular bone specimens before processing for histological analyses (Wolfram et al., 2010) (Fig. 22.6). Moreover, microFE models can also provide a comprehensive

assessment of the strain distribution in different regions of the bone, to identify the weakest regions likely to accumulate damage under complex loading conditions. These types of models have been validated against standard mechanical testing ([Wolfram et al., 2010](#)) and advanced in situ mechanical testing and Digital Volume Correlation (DVC) approaches ([Y. Chen et al., 2017](#)) (see Section [Model validation](#)).

---

## Model validation

FE models enable the testing of the same specimen/bone at different loading conditions, using different constitutive laws to assign the proper material properties and account for heterogeneity, anisotropy, and nonlinearities for the tested applications. The ability to computationally model bone under different loading conditions is an enormous advantage compared to standard destructive experimental tests in which a single loading condition has to be chosen. However, before the outcomes obtained by FE models are considered reliable for exploiting their potential for clinical and preclinical applications, a validation process to assess their accuracy in predicting the bone mechanical properties is required. The validation process consists in the comparison of the measured mechanical properties during the physical events with the model outputs ([Anderson et al., 2005](#)). The following paragraph describes the experimental approaches most frequently used to assess the mechanical properties of the bone and to validate the outputs of FE models.

## Standard mechanical tests

Different mechanical tests could be performed to study the apparent mechanical properties of bone, at the organ (e.g., the femur, one vertebra) or at the tissue level (cortical or trabecular specimens). To reliably measure the mechanical properties of bones during the tests, particular care should be given to sample preparation (e.g., keeping or removing the soft tissues), specimen fixation in the machine (e.g., fully constrained or free to move in some directions), specimen conditions (e.g., hydrated or dehydrated), and the loading direction (e.g., compression, torsion, etc). However, despite the number of parameters involved in designing experimental tests that can provide the most accurate measurements of bone mechanical properties, common general aspects are that the specimen is loaded in a standard or custom made testing machine, and that the applied load and the resulting displacement are measured with internal sensors (load cells, Linear Variable Differential Transformer displacement sensors, LVDTs), or external sensors applied in a specific region of the bone (e.g., extensometer) ([Fig. 22.7](#)). Load–displacement curves obtained from these mechanical tests can be used to calculate the apparent properties of the whole tested bone, such as the stiffness, the strength, the failure load, or the energy absorbed up to fracture ([Fig. 22.7](#)).

## Local deformation with strain gauges

Local measurements cannot be obtained from standard mechanical testing alone. Hence, strain gauges are glued on the surface of cortical bone to measure local strain with great accuracy and precision during mechanical loading. Strain gauges are

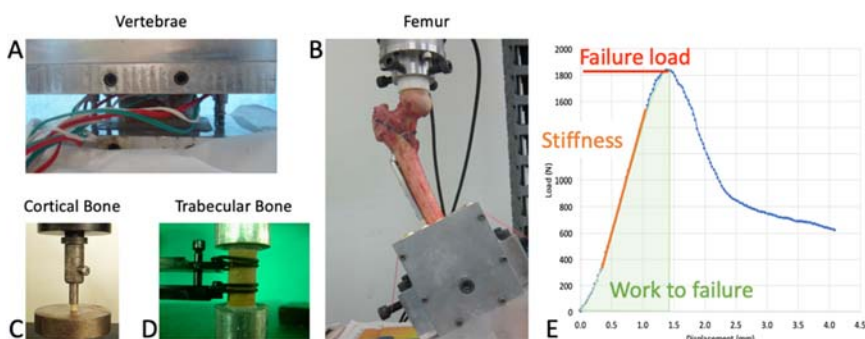


**FIGURE 22.7 Mechanical testing for bone.**

Examples of mechanical testing for characterizing the properties of bone at the organ and tissue levels; (A) Human vertebral body tested in flexion; (B) Human proximal femur with fixation screws tested in single leg stance configuration (Source: Wu, H. F., Chang, C. H., Wang, G. J., Lai, K. A., & Chen, C. H. (2019). Biomechanical investigation of dynamic hip screw and wire fixation on an unstable intertrochanteric fracture. BioMedical Engineering OnLine, 18, 49); (C) Rabbit cortical bone tested under compressive load (Source: Song, Y., Zheng, J., Yan, M., Ding, W., Xu, K., Fan, Q., & Li, Z. (2015). The Effect of irreversible electroporation on the Femur: Experimental study in a rabbit model. Scientific Reports, 5, 18187); (D) Trabecular bone cores tested under compressive load (Adapted with permission from: Perilli, E., Baleani, M., Ohman, C., Fognani, R., Baruffaldi, F., & Viceconti, M. (2008). Dependence of mechanical compressive strength on local variations in microarchitecture in cancellous bone of proximal human femur. Journal of Biomechanics, 41(2), 438–446). (E) Example of load–displacement curve from a destructive test of a human vertebral body. The blue dots represent the load and displacement values acquired by the sensors of the loading machine. The maximum load represents the failure load of the bone. The region below the curve up to the failure load represents the work to failure. The stiffness is the resistance to deflection and is calculated as the slope of the linear portion of the load–displacement curve.

small electrical conductors that change their electrical resistance when subjected to compressive or tensile strain (Freddi et al., 2015). If strategically positioned, strain gauges enable the evaluation of a point wise strain distribution within the external surface of the bone (Cristofolini, Angeli, et al., 2013), and thus the characterization of the bone behavior during the mechanical tests (Fig. 22.8). Strain gauges are available in different sizes, types, and construction, to fit different applications. However, they provide only point-wise measurements. Due to the effort involved in placing the sensors and acquiring the signals during mechanical tests, usually only a few strain gauges are attached to a bone. For example, local deformation has been measured in instrumented human tibiae with 28 triaxial rosettes (84 strain gauges) (Cristofolini, Angeli, et al., 2013) and in human vertebrae with 8 triaxial rosettes (24 strain gauges) (Cristofolini, Angeli, et al., 2013).

Therefore, the complex behavior of bone and possible strain concentrations in critical regions can only be partially detected and explained using these sensors. Moreover, strain gauges cannot be used to evaluate the strain in soft tissues or very porous tissues such as trabecular bone or, in general, specimens loaded to cause large deformations.

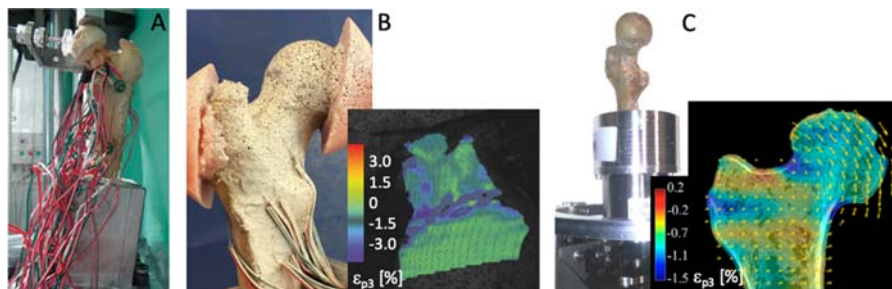


**FIGURE 22.8** Strain analyses in the human proximal femur.

Examples of strain analyses in the human proximal femur with strain gauges (A) (adapted with permission from Schileo et al., 2014); with a random speckle pattern for DIC measurements (B) (adapted with permission from Palanca, M., De Donno, G., Dall'Ara, E., & Blank, R. D. (2021). A novel approach to evaluate the effects of artificial bone focal lesion on the three-dimensional strain distributions within the vertebral body. PLOS ONE, 16(6), e0251873. <https://doi.org/10.1371/journal.pone.0251873>); with Digital Volume Correlation after time lapsed imaging with Synchrotron microCT scanning (C) (adapted with permission from Martelli, S., & Perilli, E. (2018). Time-elapsed synchrotron-light microstructural imaging of femoral neck fracture. Journal of the Mechanical Behavior of Biomedical Materials, 84, 265–272 and from Martelli, S., Giorgi, M., Dall'Ara, E., & Perilli, E. (2021). Damage tolerance and toughness of elderly human femora. Acta Biomaterialia, 123, 167–177. <https://doi.org/10.1016/j.actbio.2021.01.011>.

### Full field tests DIC and DVC

To overcome the limitations of point wise measurements, digital full-field optical measurement techniques (i.e., Digital Image Correlation (DIC) and Digital Volume Correlation (DVC)) have been used. These techniques have deeply changed our understanding of complex deformations within the bone tissue and have allowed us to better characterize its mechanical behavior (Grassi & Isaksson, 2015).

In particular, DIC enables the measurement of the displacements and strain fields on the external surface of the bone (Palanca et al., 2015). The specimen surface must have a random speckle pattern (natural or artificial) in order to make each region on the surface univocal. A set of images of the specimen surface in the undeformed and deformed states are acquired with one (two-dimensional) or more (stereo three-dimensional) cameras. The images are divided into smaller subimages (facets) and an image correlation algorithm is used to match the facets between the undeformed and deformed states. The displacements and strain fields are then computed (Fig. 22.8). DIC has been applied to correlate bone strength with bone strain pattern, identify the onset and fracture location on vertebral bodies (Palanca et al., 2018), and the mechanical response of femurs up to fracture in single leg stance (Grassi et al., 2014) and sideways fall (Palanca et al., 2021).

Complementary to the superficial measurements of DIC, the DVC approach (Roberts et al., 2014) enables the measurement of the displacements and strain fields within the bone structure. In this case, microCT images (or other three-dimensional image modalities) of the specimen are acquired during time-lapsed mechanical tests. The displacements and strains are computed using full three-dimensional image correlation algorithms, similar to DIC measurements at the surface. The DVC approach has been used to show the failure mechanism in the human proximal femur (Martelli et al., 2021) (Fig. 22.8) and the heterogeneous local deformation that occurs in a

large portion of the bone due to osteoarthritis (Ryan et al., 2020), metastasis (Palanca et al., 2021), or injections of bone cement (Danesi et al., 2016).

DIC and DVC have enabled the collection of an unprecedented amount of data compared to strain gauges. However, both measurement techniques still require deep optimization to reduce measurement uncertainty related with the imaging of specimens (Dall'Ara et al., 2017).

### Examples of validation studies for FE models

The data obtained from mechanical testing enable the experimental characterization of the bone's mechanical properties and the validation of computational models. For example, data obtained from load/displacement curves has been used to validate the predictions of failure load and stiffness of different anatomical sites (Zysset et al., 2013). The strain measurements obtained by strain gauges were used to validate the local predictions of cortical bone strain in the human femur (Schileo et al., 2008), identifying the best material modeling approach.

Despite the great results obtained with these applications, the prediction of the superficial or internal mechanical behavior of complex structures remained challenging to validate with experiments. For this reason, full-field superficial measurements of displacements and strains with DIC have been employed to validate the predictions of FE models for the vertebrae (Gustafson et al., 2017) and the femur (Katz & Yosibash, 2020). More recently, the predictions of internal displacements under complex loading conditions have been validated for different bone structures with DVC measurements (Costa et al., 2019; Kusins et al., 2020; Oliviero et al., 2018; Palanca et al., 2022).

---

## Predictions of bone remodeling

### Mechanoregulation

Bone adapts to meet the mechanical demands through the coupling actions of osteoclasts, osteoblasts, osteocytes, and bone lining cells (Section [Bone cells](#)). At the tissue scale, the recognition that strain is a stimulus of bone adaptation came after the first accurate assessment of bone strain *in vivo* using strain gauges ([Model validation](#)) (Lanyon & Smith, 1970). Several studies followed in the next decade that quantified peak strain, strain rates, and strains under physiological loading (Fritton & Rubin, 2001). In animals, walking produced strains of 200–1000  $\mu\epsilon$  depending on the location of the strain gauges (De Souza et al., 2005; Lanyon, 1973). Strains induced by higher impact activities ranged from 2000–3200  $\mu\epsilon$ , and as high as 5000  $\mu\epsilon$  in horses during galloping. Strains of 500–2000  $\mu\epsilon$  have been recorded in humans during walking and higher impact exercise (Lanyon et al., 1975). These 1–3Hz low frequency events contrast muscle contraction (<5 $\mu\epsilon$ , 10–50Hz) on the bone to maintain posture (Fritton et al., 2000). All values are subject-specific and are regulated by genetic, biochemical, and pharmacological factors (Skerry, 2006).

Human exercise studies and a preclinical skeletal loading model using a controlled load have been used since the 1960s to understand the mechanoregulation of bone adaptation. In exercise models, loads are applied to the skeleton. However, these loads are harder to characterize due to the systemic effect on bone adaptation which exercises induce, in contrast to controlled loading models where an external load is applied to the target limb to elucidate the response of bone to the external stimulus (Main et al., 2020). Preclinical models have also shown that apart from the strain magnitude (De Souza et al., 2005; Robling, Burr, & Turner, 2001), other parameters that determine bone adaptation include the strain rate (Mosley & Lanyon, 1998), the number of loading cycles (Robling et al., 2002), the frequency of loading cycles (Robling et al., 2002), the recovery time between loading cycles (Robling, Burr, & Turner, 2001), the amount of dynamic and static loading (Robling et al., 2001), and the strain distribution within the bone architecture (Skerry, 2006).

The transformation and transmission of strain changes to bone cells is known as mechanotransduction and it is generally assumed that tissue deformation of the bone matrix (Ehrlich & Lanyon, 2002) or interstitial flow in the lacunar–canalicular system (Weinbaum et al., 2003) produces local mechanical signals, which are detected by osteocytes to initiate mechanoadaptation. Several studies have shown that vibratory loading of the murine femur at tissue strains that are too low to induce an osteogenic response altered the intramedullary pressure and interstitial fluid in the limb (Stevens et al., 2006), suggesting that osteocytes are more mechanosensitive to fluid flow (Santos et al., 2009). However, the exact mechanisms and mechanoreceptors for the detection of mechanical signals in osteocytes remain a topic of research, and likewise the frequency, magnitude, and waveform of the fluid flow required to induce an osteogenic response (Willie et al., 2020). It is for these reasons that most predictions of bone adaptation have focused on changes at the tissue level.

### Bone adaptation algorithm and implementation in FE framework

The first complete mathematical model of bone adaptation by Ref (Cowin & Hegedus, 1976) led to the field of computational bone remodeling to model bone response to mechanical stimuli. Several categories of bone remodeling algorithms have been proposed since then, laying the foundation for current understanding of mechanoregulation. The first type is a phenomenological model which predicts the long-term adaptation of bone in response to physiological or pathological mechanical stimuli. There are different classes of phenomenological models, broadly categorized to:

- (i) Models based on achieving a homeostatic state of stress, strain, or strain energy density by using mechanical stimulus to model changes in bone density (V. S. Cheong, Blunn, et al., 2018; Huiskes et al., 2000). These models have been successfully applied to study the remodeling behavior of bone in the femur (Weinans et al., 1992) and around implants with good verification and validation with X-ray and DEXA scan results (Cheong et al., 2018, 2020). As changes in bone microarchitecture and shape can also occur during bone

adaptation, the fabric tensor (as a quantitative stereological measure of the trabecular structure) has also been included in recent anisotropic models (Martínez-Reina et al., 2009).

- (ii) Models based on a global optimality criterion, which premises that the topology of bone is optimized over time (Hollister et al., 1994; Villette & Phillips, 2016).
- (iii) Models based on damage repair, where the rate and direction of remodeling is dependent on the location and accumulation of microdamage (McNamara & Prendergast, 2007; Prendergast & Taylor, 1994).

The second category are mechanistic models which incorporate some biological processes in addition to the use of mechanical stimulus as the driver of bone adaptation (V. S. Cheong, Campos Marin et al., 2020; García-Aznar et al., 2005; Pereira et al., 2015). Finally, the third category of models explicitly incorporate cell dynamics and the metabolic pathways (e.g., RANK/RANKL/OPG pathway, cell proliferation to apoptosis) responsible for bone adaptation through the development of mechanochemical models to determine the mechanical response of the bone (Lerebours et al., 2016; Pivonka et al., 2013).

### Validation for murine studies

Animal models enable the control of experimental variables to understand the cellular, tissue and structural factors responsible for the regulation of bone adaptation. In the last 20 years, rodents have been the animals of choice due to their low cost, quick bone turnover, and similarity to the human genome. Moreover, genetic mouse models may be engineered to study specific disease and cellular pathways. This section will cover the validation of mechanoregulation algorithms in the murine tibial loading and the caudal vertebra model. The former is the most commonly used model today as unlike invasive models, it does not produce a local inflammatory reaction which may confound with loading-induced adaptation. Moreover, the tibial loading model enables the whole bone to be studied, the comparison of external loads to physiological strains, and it is better aligned with 3Rs (refinement, reduction and replacement of animals in research) principles (Meakin et al., 2014).

The tibial loading model involves placing the tibia/fibular between two custom-built fixtures which are attached to the actuator arm of a material testing machine and a load cell. Compressive load applied between the knee and ankle joints engenders, a highly repeatable compressive and tensile strain on the anterior-lateral and posterior-medial aspects of the tibia, respectively, due to the natural curvature of the tibia proximal to the tibiofibular joint. FE modeling enables the simulation of the loading conditions applied during the experiments to understand the effect of the applied load on bone adaptation, and also to compare the changes in structural properties and strain distribution after the adaptive response is completed. Validation of the local strain measurements is typically done through strain gauges, DIC (Carriero et al., 2018) or DVC (Giorgi & Dall'Ara, 2018). Although strain

gauges are used most commonly, measurements are limited to the attachment sites, and for small mouse bones this may cause local stiffening of the measurements. DIC overcomes the discrete nature of strain gauges but information is limited to the external surface, while DVC provides spatially rich information within trabecular structure of bone (Giorgi & Dall'Ara, 2018).

Validation of mechanoregulation algorithms in murine studies typically uses a combination of the following approaches by comparing the predicted pseudo-microCT images with the experimental dataset: morphometric analysis, densitometric analysis, spatial analysis, and/or biomarkers of bone formation. The first three analyses are obtained from image analysis after the acquired images (typically microCT) are segmented by applying a threshold to obtain binarized stacks. Although the predicted shape and density of the loaded limb is traditionally simulated using the contralateral control limb as input, it assumes that the control leg has not undergone any (re)modeling changes since the start of the experiments, but studies in the rat ulna have shown systemic effects of loading that benefitted the contralateral limb (Sample et al., 2010). Although systemic effects have not been reported in the murine loading model, the recommended guideline is to confirm that the contralateral limb is equivalent to the limbs of non-loaded animals, and to normalize morphometric and densitometric parameters against the contralateral limb (Main et al., 2020). Studies are increasingly turning to combined *in vivo* longitudinal imaging and dynamic 3D assessments to monitor changes before, during and after the withdrawal of loading, as it reduces the intersubject variation and the number of animals required in the experiments (V. Cheong et al., n.d.; Viceconti & Dall'Ara, 2019).

### Morphometric and densitometric analysis

A 1 mm region of interest (ROI) is defined in the trabecular region, 0.3 mm distal to the proximal growth plate (Bouxsein et al., 2010; van 't Hof & Dall'Ara, 2019). The cortical 1 mm ROI is centered at the middiaphysis (Bouxsein et al., 2010; Lu et al., 2016). 3D bone parameters can be computed using specialized software packages: trabecular bone volume fraction (Tb.BV/TV), trabecular thickness (Tb.Th), trabecular separation (Tb.Sp), trabecular number (Tb.N), cortical total cross-sectional area (Tt.Ar), cortical bone area (Ct.Ar), cortical area fraction (Ct.Ar/Tt.Ar), and cortical thickness (Ct.Th). In the cortical ROI, minimum ( $I_{\min}$ ) and maximum ( $I_{\max}$ ) principal moments of inertia, polar moment of inertia (J), and eccentricity (Ecc) are commonly computed in addition to the cortical parameters described above. A thorough description of the parameters are described in Ref (Bouxsein et al., 2010). Standard morphometric analysis has also been extended to analysis in the whole bone for Tb.N, Tb.Th, and bone surface–volume ratio (BS/BV) to compare between experimental data and predicted results in the murine caudal vertebrae (Levchuck et al., 2014), and  $I_{\min}$  and  $I_{\max}$  for the murine loading model (Carriero et al.,

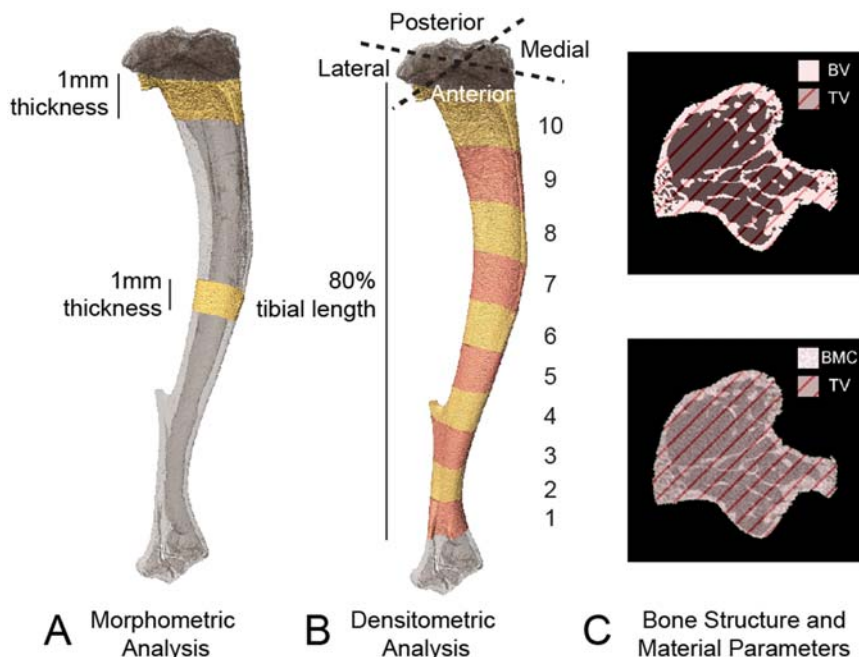


**FIGURE 22.9 Morphometric and densitometric analysis in the mouse tibia.**

Comparison between morphometric and densitometric analysis. (A) Morphometric analysis is performed in two 1 mm thick regions of interest below the growth plate and in the middiaphysis. (B) Densitometric parameters are computed in the whole bone, with further subanalysis in 40 compartments. (C) Calculations of bone volume (BV), bone volume fraction (BV/TV), bone mineral content (BMC), and bone mineral density (BMD) are similar for both morphometric and densitometric analyses.

2018; Pereira et al., 2015). Three-dimensional dynamic bone morphometry has also been developed, such as bone formation rate (BFR), bone resorption rate (BRR), mineral apposition rate (MAR), and mineral resorption rate (MRR) per day. These parameters have been applied to analyze experimental data in the mouse tibia (Birkhold et al., 2017), and so far have only been used for validation in the mouse tail model (Levchuk et al., 2014). Densitometric analyses are conducted across the whole bone as a minimum, with subanalysis across the tibial compartment (anterior, medial, lateral, posterior) and length (Lu et al., 2016) (Fig. 22.9). From the binarized images, BV is computed as the sum of the volumes identified as bone, while TV is the total enclosed volume of the periosteal surface. Information on the material properties of the bone is first evaluated from the local TMD, obtained in each voxel from the densitometric calibration of the gray levels in the microCT images. BMC is the product of the TMD and the volume of the voxel, and bone mineral density is defined as the ratio between BMC and TV.

### Spatial analysis and biomarkers for bone formation

Two metrics based on superimposing the predicted and experimentally obtained images and assessing the differences have been developed: 1) spatial match, defined as the amount of bone changes that has the same state change (apposition, resorption, quiescent) on the surface of the two datasets, normalized by the total number of voxels with the specified state change in the predicted dataset (V. S. Cheong, Campos Marin et al., 2020; Schulte et al., 2013) and 2) prediction accuracy, which was defined as the number of voxels with the same state change on the experimental and simulated surfaces, normalized by total number of voxels with the state change in the experimental dataset (V. S. Cheong, Campos Marin et al., 2020; V. S. Cheong, Roberts, et al., 2020) (Fig. 22.10). Other approaches that have been used include the overlap ratio, which is based on the Jaccard index and defined as the intersection of the binarised predicted and the experimental images, normalized by the union of the area occupied by the two datasets (V. S. Cheong, Campos Marin et al., 2020). The normalized change in cortical thickness across the image slices have also been used, with the thickness computed for every azimuthal range of 15 degrees (Pereira et al., 2015).

To conduct histomorphometry, mice will receive intraperitoneal injection of alizarin red and/or calcein at two time points prior to euthanasia. A histocutter, combining a rotary microtome, microscope, fluorescent filters, and light source, is then used to section and image the embedded tibia (Carriero et al., 2018; Javaheri et al., 2020). The locations of the fluorescent labels is used to compare the regions of bone adaptation, and distance between the inner and outer labels, normalized by the number of days between the injections, is used to compute the MAR, for comparison with the simulated results.

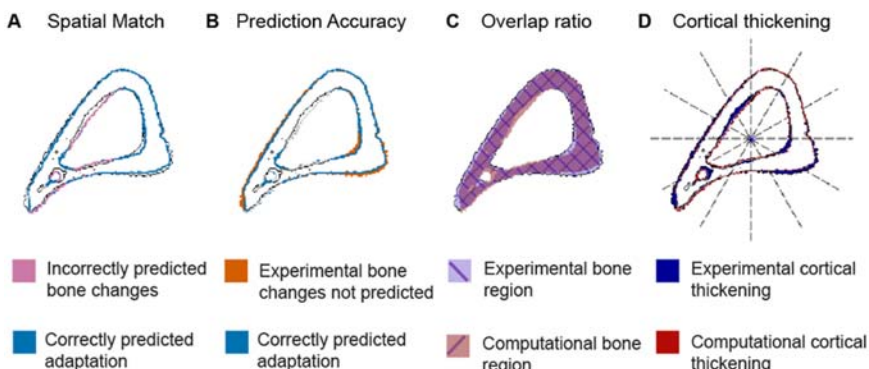


**FIGURE 22.10 Metrics for bone remodeling.**

Commonly used metrics for determining the accuracy of mechanoregulation models in predicting bone remodeling. (A) Spatial match. (B) Prediction accuracy. (C) Overlap ratio. (D) Cortical thickening.

---

## References

- Anderson, A. E., Peters, C. L., Tuttle, B. D., & Weiss, J. A. (2005). Subject-specific finite element model of the pelvis: Development, validation and sensitivity studies. *Journal of Biomechanical Engineering*, 127(3), 364–373. <https://doi.org/10.1115/1.1894148>
- Bain, S. D., & Rubin, C. T. (1990). Metabolic modulation of disuse osteopenia: Endocrine-dependent site specificity of bone remodeling. *Journal of Bone and Mineral Research*, 5(10), 1069–1075. <https://doi.org/10.1002/jbmr.5650051011>
- Baron, R. S., Magee, S., Silverglate, A., Broadus, A., & Lang, R. (1983). Estimation of trabecular bone resorption by histomorphometry: evidence for a prolonged reversal phase with normal resorption in postmenopausal osteoporosis and coupled increase in primary hyperparathyroidism. *Clinical Disorders of Bone and Mineral Metabolism* (4th edn., pp. 191–195). Amsterdam: Excerpta Medica.
- Bayraktar, H. H., Gupta, A., Kwon, R. Y., Papadopoulos, P., & Keaveny, T. M. (2004). The modified super-ellipsoid yield criterion for human trabecular bone. *Journal of Biomechanical Engineering*, 126(6), 677–684. <https://doi.org/10.1115/1.1763177>
- Birkhold, A. I., Razi, H., Duda, G. N., Checa, S., & Willie, B. M. (2017). Tomography-based Quantification of regional differences in cortical bone surface remodeling and mechano-response. *Calcified Tissue International*, 100(3), 255–270. <https://doi.org/10.1007/s00223-016-0217-4>
- Blair, H. C., Teitelbaum, S. L., Ghiselli, R., & Gluck, S. (1989). Osteoclastic bone resorption by a polarized vacuolar proton pump. *Science*, 245(4920), 855–857. <https://doi.org/10.1126/science.2528207>
- Blumer, M. J. (2021). Bone tissue and histological and molecular events during development of the long bones. *Annals of Anatomy*, 235, 151704.
- Bonewald, L. F. (2011). The amazing osteocyte. *Journal of Bone and Mineral Research*, 26(2), 229–238. <https://doi.org/10.1002/jbmr.320>
- Bouxsein, M. L., Boyd, S. K., Christiansen, B. A., Guldberg, R. E., Jepsen, K. J., & Müller, R. (2010). Guidelines for assessment of bone microstructure in rodents using micro-computed tomography. *Journal of Bone and Mineral Research*, 25(7), 1468–1486. <https://doi.org/10.1002/jbmr.141>
- Cappariello, A., Maurizi, A., Veeriah, V., & Teti, A. (2014). Reprint of: The Great Beauty of the osteoclast. *Archives of Biochemistry and Biophysics*, 561, 13–21.
- Capulli, M., Paone, R., & Rucci, N. (2014). Osteoblast and osteocyte: Games without frontiers. *Archives of Biochemistry and Biophysics*, 561, 3–12. <https://doi.org/10.1016/j.abb.2014.05.003>
- Carriero, A., Pereira, A. F., Wilson, A. J., Castagno, S., Javaheri, B., Pitsillides, A. A., Marenzana, M., & Shefelbine, S. J. (2018). Spatial relationship between bone formation and mechanical stimulus within cortical bone: Combining 3D fluorochrome mapping and poroelastic finite element modelling. *Bone Reports*, 8, 72–80. <https://doi.org/10.1016/j.bonr.2018.02.003>
- Chen, Y., Dall'Ara, E., Sales, E., Manda, K., Wallace, R., Pankaj, P., & Viceconti, M. (2017). Micro-CT based finite element models of cancellous bone predict accurately displacement once the boundary condition is well replicated: A validation study. *Journal of the Mechanical Behavior of Biomedical Materials*, 65, 644–651. <https://doi.org/10.1016/j.jmbbm.2016.09.014>
- Chen, X., Zhi, X., Wang, J., & Su, J. (2018). RANKL signaling in bone marrow mesenchymal stem cells negatively regulates osteoblastic bone formation. *Bone Research*, 6(1). <https://doi.org/10.1038/s41413-018-0035-6>

- Cheong, V. S., Blunn, G. W., Coathup, M. J., & Fromme, P. (2018). A novel adaptive algorithm for 3D finite element analysis to model extracortical bone growth. *Computer Methods in Biomechanics and Biomedical Engineering*, 21(2), 129–138. <https://doi.org/10.1080/10255842.2018.1425997>
- Cheong, V. S., Campos Marin, A., Lacroix, D., & Dall'Ara, E. (2020). A novel algorithm to predict bone changes in the mouse tibia properties under physiological conditions. *Biomechanics and Modeling in Mechanobiology*, 19(3), 985–1001. <https://doi.org/10.1007/s10237-019-01266-7>
- Cheong, V. S., Fromme, P., Mumith, A., Coathup, M. J., & Blunn, G. W. (2018). Novel adaptive finite element algorithms to predict bone ingrowth in additive manufactured porous implants. *Journal of the Mechanical Behavior of Biomedical Materials*, 87, 230–239. <https://doi.org/10.1016/j.jmbbm.2018.07.019>
- Cheong, V., Roberts, B., & Kadirkamanathan, V. (2021). Positive interactions of mechanical loading and PTH treatments on spatio-temporal bone remodelling. *Acta Biomaterialia*, 21, 623–1.
- Cheong, V. S., Roberts, B. C., Kadirkamanathan, V., & Dall'Ara, E. (2020). Bone remodelling in the mouse tibia is spatio-temporally modulated by oestrogen deficiency and external mechanical loading: A combined in vivo/in silico study. *Acta Biomaterialia*, 116, 302–317. <https://doi.org/10.1016/j.actbio.2020.09.011>
- Costa, M. C., Eltes, P., Lazary, A., Varga, P. P., Viceconti, M., & Dall'Ara, E. (2019). Biomechanical assessment of vertebrae with lytic metastases with subject-specific finite element models. *Journal of the Mechanical Behavior of Biomedical Materials*, 98, 268–290. <https://doi.org/10.1016/j.jmbbm.2019.06.027>
- Costa, M. C., Tozzi, G., Cristofolini, L., Danesi, V., Viceconti, M., & Dall'Ara, E. (2017). Micro Finite Element models of the vertebral body: Validation of local displacement predictions. *PLOS ONE*, 12(7), e0180151. <https://doi.org/10.1371/journal.pone.0180151>
- Cowin, S. C. (2001). *Bone mechanics handbook*. CRC Press. <https://doi.org/10.1201/b14263>
- Cowin, S. C., & Hegedus, D. H. (1976). Bone remodeling I: Theory of adaptive elasticity. *Journal of Elasticity*, 6(3), 313–326. <https://doi.org/10.1007/BF00041724>
- Cristofolini, L., Angeli, E., Juszczak, J. M., & Juszczak, M. M. (2013). Shape and function of the diaphysis of the human tibia. *Journal of Biomechanics*, 46(11), 1882–1892. <https://doi.org/10.1016/j.jbiomech.2013.04.026>
- Cristofolini, L., Brandolini, N., Danesi, V., Juszczak, M. M., Erani, P., & Viceconti, M. (2013). Strain distribution in the lumbar vertebrae under different loading configurations. *Spine Journal*, 13(10), 1281–1292. <https://doi.org/10.1016/j.spinee.2013.06.014>
- Dall'Ara, E., Eastell, R., Viceconti, M., Pahr, D., & Yang, L. (2016). Experimental validation of DXA-based finite element models for prediction of femoral strength. *Journal of the Mechanical Behavior of Biomedical Materials*, 63, 17–25. <https://doi.org/10.1016/j.jmbbm.2016.06.004>
- Dall'Ara, E., Luisier, B., Schmidt, R., Kainberger, F., Zysset, P., & Pahr, D. (2013). A nonlinear QCT-based finite element model validation study for the human femur tested in two configurations in vitro. *Bone*, 52(1), 27–38. <https://doi.org/10.1016/j.bone.2012.09.006>
- Dall'Ara, E., Peña-Fernández, M., Palanca, M., Giorgi, M., Cristofolini, L., & Tozzi, G. (2017). Precision of digital volume correlation approaches for strain analysis in bone imaged with micro-computed tomography at different dimensional levels. *Frontiers in Materials*, 4. <https://doi.org/10.3389/fmats.2017.00031>

- Danesi, V., Tozzi, G., & Cristofolini, L. (2016). Application of digital volume correlation to study the efficacy of prophylactic vertebral augmentation. *Clinical Biomechanics*, 39, 14–24. <https://doi.org/10.1016/j.clinbiomech.2016.07.010>
- De Souza, R. L., Matsuura, M., Eckstein, F., Rawlinson, S. C. F., Lanyon, L. E., & Pitsillides, A. A. (2005). Non-invasive axial loading of mouse tibiae increases cortical bone formation and modifies trabecular organization: A new model to study cortical and cancellous compartments in a single loaded element. *Bone*, 37(6), 810–818. <https://doi.org/10.1016/j.bone.2005.07.022>
- Ducy, P., Schinke, T., & Karsenty, G. (2000). The osteoblast: A sophisticated fibroblast under central surveillance. *Science*, 289(5484), 1501–1504. <https://doi.org/10.1126/science.289.5484.1501>
- Ehrlich, P. J., & Lanyon, L. E. (2002). Mechanical strain and bone cell function: A review. *Osteoporosis International*, 13(9), 688–700. <https://doi.org/10.1007/s001980200095>
- Everts, V., Delaissié, J. M., Korper, W., Jansen, D. C., Tigchelaar-Gutter, W., Saftig, P., & Beertsen, W. (2002). The bone lining cell: Its role in cleaning Howship's lacunae and initiating bone formation. *Journal of Bone and Mineral Research*, 17(1), 77–90. <https://doi.org/10.1359/jbmr.2002.17.1.77>
- Feng, X., & McDonald, J. M. (2011). Disorders of bone remodeling. *Annual Review of Pathology: Mechanisms of Disease*, 6, 121–145. <https://doi.org/10.1146/annurev-pathol-011110-130203>
- Freddi, Olmi, G., & Cristofolini, L. (2015). *Experimental stress analysis for materials and structures*. Springer.
- Fritton, S. P., McLeod, J. K., & Rubin, C. T. (2000). Quantifying the strain history of bone: Spatial uniformity and self-similarity of low-magnitude strains. *Journal of Biomechanics*, 33(3), 317–325. [https://doi.org/10.1016/S0021-9290\(99\)00210-9](https://doi.org/10.1016/S0021-9290(99)00210-9)
- Fritton, S. P., & Rubin, C. T. (2001). In vivo measurement of bone deformations using strain gauges. In *Bone mechanics handbook* (second Edition, p. 8). CRC Press, 8–42.
- Frost, H. M. (1963). *Bone remodeling dynamics*. Springfield, Illinois: Charles C Thomas.
- García-Aznar, J. M., Rueberg, T., & Doblaré, M. (2005). A bone remodelling model coupling microdamage growth and repair by 3D BMU-activity. *Biomechanics and Modeling in Mechanobiology*, 4(2–3), 147–167. <https://doi.org/10.1007/s10237-005-0067-x>
- Garcia, D., Zysset, P. K., Charlebois, M., & Curnier, A. (2009). A three-dimensional elastic plastic damage constitutive law for bone tissue. *Biomechanics and Modeling in Mechanobiology*, 8(2), 149–165. <https://doi.org/10.1007/s10237-008-0125-2>
- Giorgi, M., & Dall'Ara, E. (2018). Variability in strain distribution in the mice tibia loading model: A preliminary study using digital volume correlation. *Medical Engineering and Physics*, 62, 7–16. <https://doi.org/10.1016/j.medengphy.2018.09.001>
- Grassi, L., & Isaksson, H. (2015). Extracting accurate strain measurements in bone mechanics: A critical review of current methods. *Journal of the Mechanical Behavior of Biomedical Materials*, 50, 43–54. <https://doi.org/10.1016/j.jmbbm.2015.06.006>
- Grassi, L., Väänänen, S. P., Ristinmaa, M., Jurvelin, J. S., & Isaksson, H. (2017). Prediction of femoral strength using 3D finite element models reconstructed from DXA images: Validation against experiments. *Biomechanics and Modeling in Mechanobiology*, 16(3), 989–1000. <https://doi.org/10.1007/s10237-016-0866-2>
- Grassi, L., Väänänen, S. P., Yavari, S. A., Jurvelin, J. S., Weinans, H., Ristinmaa, M., Zadpoor, A. A., & Isaksson, H. (2014). Full-field strain measurement during mechanical testing of the human femur at physiologically relevant strain rates. *Journal of Biomechanical Engineering*, 136(11). <https://doi.org/10.1115/1.4028415>

- Gustafson, H. M., Cripton, P. A., Ferguson, S. J., & Helgason, B. (2017). Comparison of specimen-specific vertebral body finite element models with experimental digital image correlation measurements. *Journal of the Mechanical Behavior of Biomedical Materials*, 65, 801–807. <https://doi.org/10.1016/j.jmbbm.2016.10.002>
- Hart, N. H., Nimphius, S., Rantalainen, T., Ireland, A., Siafarikas, A., & Newton, R. U. (2017 Sep). Mechanical basis of bone strength: influence of bone material, bone structure and muscle action. *Journal of Musculoskeletal and Neuronal Interactions*, 17(3), 114–139.
- Hayami, T., Pickarski, M., Wesolowski, G. A., McLane, J., Bone, A., Destefano, J., Rodan, G. A., & Duong, L. T. (2004). The role of subchondral bone remodeling in osteoarthritis: Reduction of cartilage degeneration and prevention of osteophyte formation by alendronate in the rat anterior cruciate ligament transection model. *Arthritis and Rheumatism*, 50(4), 1193–1206. <https://doi.org/10.1002/art.20124>
- van 't Hof, R. J., & Dall'Ara, E. (2019). Analysis of bone architecture in rodents using micro-computed tomography. In , Vol 1914. *Methods in molecular biology* (pp. 507–531). Humana Press Inc. [https://doi.org/10.1007/978-1-4939-8997-3\\_28](https://doi.org/10.1007/978-1-4939-8997-3_28)
- Hollister, S. J., Brennan, J. M., & Kikuchi, N. (1994). A homogenization sampling procedure for calculating trabecular bone effective stiffness and tissue level stress. *Journal of Biomechanics*, 27(4), 433–444. [https://doi.org/10.1016/0021-9290\(94\)90019-1](https://doi.org/10.1016/0021-9290(94)90019-1)
- Huiskes, R., Ruimerman, R., van Lenthe, G. H., & Janssen, J. D. (2000). Effects of mechanical forces on maintenance and adaptation of form in trabecular bone. *Nature*, 405(6787), 704–706. <https://doi.org/10.1038/35015116>
- Ikebuchi, Y., Aoki, S., Honma, M., Hayashi, M., Sugamori, Y., Khan, M., Kariya, Y., Kato, G., Tabata, Y., Penninger, J. M., Udagawa, N., Aoki, K., & Suzuki, H. (2018). Coupling of bone resorption and formation by RANKL reverse signalling. *Nature*, 561(7722), 195–200. <https://doi.org/10.1038/s41586-018-0482-7>
- Javaheri, B., Razi, H., Gohin, S., Wylie, S., Chang, Y. M., Salmon, P., Lee, P. D., & Pitsillides, A. A. (2020). Lasting organ-level bone mechanoadaptation is unrelated to local strain. *Science Advances*, 6(10). <https://doi.org/10.1126/sciadv.aax8301>
- Katz, Y., & Yosibash, Z. (2020). New insights on the proximal femur biomechanics using Digital Image Correlation. *Journal of Biomechanics*, 101, 109599. <https://doi.org/10.1016/j.jbiomech.2020.109599>
- Keaveny, T. M., McClung, M. R., Wan, X., Kopperdahl, D. L., Mitlak, B. H., & Krohn, K. (2012). Femoral strength in osteoporotic women treated with teriparatide or alendronate. *Bone*, 50(1), 165–170. <https://doi.org/10.1016/j.bone.2011.10.002>
- Kobayashi, S., Takahashi, H. E., Ito, A., Saito, N., Nawata, M., Horiuchi, H., Ohta, H., Iorio, R., Yamamoto, N., & Takaoka, K. (2003). Trabecular minimodeling in human iliac bone. *Bone*, 32(2), 163–169. [https://doi.org/10.1016/S8756-3282\(02\)00947-X](https://doi.org/10.1016/S8756-3282(02)00947-X)
- Kontulainen, S., Sievänen, H., Kannus, P., Pasanen, M., & Vuori, I. (2002). Effect of long-term impact-loading on mass, size, and estimated strength of humerus and radius of female racquet-sports players: A peripheral quantitative computed tomography study between young and old starters and controls. *Journal of Bone and Mineral Research*, 17(12), 2281–2289. <https://doi.org/10.1359/jbmr.2002.17.12.2281>
- Kusins, J., Knowles, N., Ryan, M., Dall'Ara, E., & Ferreira, L. (2020). Full-field comparisons between strains predicted by QCT-derived finite element models of the scapula and experimental strains measured by digital volume correlation. *Journal of Biomechanics*, 113, 110101. <https://doi.org/10.1016/j.jbiomech.2020.110101>
- Laine, C. M., Joeng, K. S., Campeau, P. M., Kiviranta, R., Tarkkonen, K., Grover, M., Lu, J. T., Pekkinen, M., Wessman, M., Heino, T. J., Nieminen-Pihala, V., Aronen, M., Laine, T.,

- Kröger, H., Cole, W. G., Lehesjoki, A. E., Nevarez, L., Krakow, D., Curry, C. J. R., ... Mäkitie, O. (2013). WNT1 mutations in early-onset osteoporosis and osteogenesis imperfecta. *New England Journal of Medicine*, 368(19), 1809–1816. <https://doi.org/10.1056/NEJMoa1215458>
- Lanyon, L. E. (1973). Analysis of surface bone strain in the calcaneus of sheep during normal locomotion. *Journal of Biomechanics*, 6(1), 41–49. [https://doi.org/10.1016/0021-9290\(73\)90036-5](https://doi.org/10.1016/0021-9290(73)90036-5)
- Lanyon, L. E., Hampson, W. G. J., Goodship, A. E., & Shah, J. S. (1975). Bone deformation recorded in vivo from strain gauges attached to the human tibial shaft. *Acta Orthopaedica*, 46(2), 256–268. <https://doi.org/10.3109/17453677508989216>
- Lanyon, L. E., & Smith, R. N. (1970). Bone strain in the tibia during normal quadrupedal locomotion. *Acta Orthopaedica*, 41(3), 238–248. <https://doi.org/10.3109/17453677008991511>
- Larsson, D., Luisier, B., Kersh, M. E., Dall'Ara, E., Zysset, P. K., Pandy, M. G., & Pahr, D. H. (2014). Assessment of transverse Isotropy in clinical-level CT images of trabecular bone using the gradient structure tensor. *Annals of Biomedical Engineering*, 42(5), 950–959. <https://doi.org/10.1007/s10439-014-0983-y>
- Lee, S. K., & Lorenzo, J. A. (1999). Parathyroid hormone stimulates TRANCE and inhibits osteoprotegerin messenger ribonucleic acid expression in murine bone marrow cultures: Correlation with osteoclast-like cell formation. *Endocrinology*, 140(8), 3552–3561. <https://doi.org/10.1210/endo.140.8.6887>
- Lerebours, C., Buezli, P. R., Scheiner, S., & Pivonka, P. (2016). A multiscale mechanobiological model of bone remodelling predicts site-specific bone loss in the femur during osteoporosis and mechanical disuse. *Biomechanics and Modeling in Mechanobiology*, 15(1), 43–67. <https://doi.org/10.1007/s10237-015-0705-x>
- Levchuk, A., Zwahlen, A., Weigt, C., Lambers, F. M., Badilatti, S. D., Schulte, F. A., Kuhn, G., & Müller, R. (2014). The Clinical Biomechanics Award 2012 - presented by the European Society of Biomechanics: Large scale simulations of trabecular bone adaptation to loading and treatment. *Clinical Biomechanics*, 29(4), 355–362. <https://doi.org/10.1016/j.clinbiomech.2013.12.019>
- Lu, Y., Boudiffa, M., Dall'Ara, E., Bellantuono, I., & Viceconti, M. (2016). Development of a protocol to quantify local bone adaptation over space and time: Quantification of reproducibility. *Journal of Biomechanics*, 49(10), 2095–2099. <https://doi.org/10.1016/j.jbiomech.2016.05.022>
- Main, R. P., Shefelbine, S. J., Meakin, L. B., Silva, M. J., van der Meulen, M. C. H., & Willie, B. M. (2020). Murine axial compression tibial loading model to study bone Mechanobiology: Implementing the model and reporting results. *Journal of Orthopaedic Research*, 38(2), 233–252. <https://doi.org/10.1002/jor.24466>
- Manda, K., Wallace, R. J., Xie, S., Levrero-Florencio, F., & Pankaj, P. (2017). Nonlinear viscoelastic characterization of bovine trabecular bone. *Environmental Economics and Policy Studies*, 16(1), 173–189. <https://doi.org/10.1007/s10237-016-0809-y>
- Martelli, S., Giorgi, M., Dall'Ara, E., & Perilli, E. (2021). Damage tolerance and toughness of elderly human femora. *Acta Biomaterialia*, 123, 167–177. <https://doi.org/10.1016/j.actbio.2021.01.011>
- Martelli, S., & Perilli, E. (2018). Time-elapsed synchrotron-light microstructural imaging of femoral neck fracture. *Journal of the Mechanical Behavior of Biomedical Materials*, 84, 265–272.

- Martínez-Reina, J., García-Aznar, J. M., Domínguez, J., & Doblaré, M. (2009). A bone remodelling model including the directional activity of BMUs. *Biomechanics and Modeling in Mechanobiology*, 8(2), 111–127. <https://doi.org/10.1007/s10237-008-0122-5>
- Matsuura, M., Eckstein, F., Lochmüller, E. M., & Zysset, P. K. (2008). The role of fabric in the quasi-static compressive mechanical properties of human trabecular bone from various anatomical locations. *Biomechanics and Modeling in Mechanobiology*, 7(1), 27–42. <https://doi.org/10.1007/s10237-006-0073-7>
- McNamara, L. M., & Prendergast, P. J. (2007). Bone remodelling algorithms incorporating both strain and microdamage stimuli. *Journal of Biomechanics*, 40(6), 1381–1391. <https://doi.org/10.1016/j.jbiomech.2006.05.007>
- Meakin, L. B., Price, J. S., & Lanyon, L. E. (2014). The contribution of experimental in vivo models to understanding the mechanisms of adaptation to mechanical loading in bone. *Frontiers in Endocrinology*, 5. <https://doi.org/10.3389/fendo.2014.00154>
- Mercer, C., He, M. Y., Wang, R., & Evans, A. G. (2006). Mechanisms governing the inelastic deformation of cortical bone and application to trabecular bone. *Acta Biomaterialia*, 2(1), 59–68. <https://doi.org/10.1016/j.actbio.2005.08.004>
- Mosley, J. R., & Lanyon, L. E. (1998). Strain rate as a controlling influence on adaptive modeling in response to dynamic loading of the ulna in growing male rats. *Bone*, 23(4), 313–318. [https://doi.org/10.1016/S8756-3282\(98\)00113-6](https://doi.org/10.1016/S8756-3282(98)00113-6)
- Musuamba, F. T., Skottheim Rusten, I., Lesage, R., Russo, G., Bursi, R., Emili, L., Wangorsch, G., Manolis, E., Karlsson, K. E., Kulesza, A., Courcelles, E., Boissel, J. P., Rousseau, C. F., Voisin, E. M., Alessandrello, R., Curado, N., Dall'ara, E., Rodriguez, B., Pappalardo, F., & Geris, L. (2021). Scientific and regulatory evaluation of mechanistic *in silico* drug and disease models in drug development: Building model credibility. *CPT: Pharmacometrics and Systems Pharmacology*, 10(8), 804–825. <https://doi.org/10.1002/psp4.12669>
- Nakamura, T., Imai, Y., Matsumoto, T., Sato, S., Takeuchi, K., Igarashi, K., Harada, Y., Azuma, Y., Krust, A., Yamamoto, Y., Nishina, H., Takeda, S., Takayanagi, H., Metzger, D., Kanno, J., Takaoka, K., Martin, T. J., Chambon, P., & Kato, S. (2007). Estrogen Prevents bone loss via Estrogen receptor  $\alpha$  and Induction of Fas ligand in osteoclasts. *Cell*, 130(5), 811–823. <https://doi.org/10.1016/j.cell.2007.07.025>
- Öhman, C., Baleani, M., Perilli, E., Dall'Ara, E., Tassani, S., Baruffaldi, F., & Viceconti, M. (2007). Mechanical testing of cancellous bone from the femoral head: Experimental errors due to off-axis measurements. *Journal of Biomechanics*, 40(11), 2426–2433. <https://doi.org/10.1016/j.jbiomech.2006.11.020>
- Oliviero, S., Giorgi, M., & Dall'Ara, E. (2018). Validation of finite element models of the mouse tibia using digital volume correlation. *Journal of the Mechanical Behavior of Biomedical Materials*, 86, 172–184. <https://doi.org/10.1016/j.jmbbm.2018.06.022>
- Paiva, K. B. S., & Granjeiro, J. M. (2017). Matrix Metalloproteinases in bone resorption, remodeling, and repair. In, Vol 148. *Progress in molecular Biology and Translational science* (pp. 203–303). Elsevier B.V. <https://doi.org/10.1016/bs.pmbts.2017.05.001>
- Palanca, M., Barbanti-Bròdano, G., & Cristofolini, L. (2018). The size of simulated lytic metastases affects the strain distribution on the anterior surface of the vertebra. *Journal of Biomechanical Engineering*, 140(11). <https://doi.org/10.1115/1.4040587>
- Palanca, M., De Donno, G., Dall'Ara, E., & Blank, R. D. (2021). A novel approach to evaluate the effects of artificial bone focal lesion on the three-dimensional strain distributions within the vertebral body. *PLOS ONE*, 16(6), e0251873. <https://doi.org/10.1371/journal.pone.0251873>

- Palanca, M., Oliviero, S., & Dall'Ara, E. (2022). MicroFE models of porcine vertebrae with induced bone focal lesions: Validation of predicted displacements with digital volume correlation. *Journal of the Mechanical Behavior of Biomedical Materials*, 125, 104872. <https://doi.org/10.1016/j.jmbbm.2021.104872>
- Palanca, M., Tozzi, G., & Cristofolini, L. (2015). The use of digital image correlation in the biomechanical area: a review. *International Biomechanics*, 3(1), 1–20.
- Pereira, A. F., Javaheri, B., Pitsillides, A. A., & Shefelbine, S. J. (2015). Predicting cortical bone adaptation to axial loading in the mouse tibia. *Journal of the Royal Society Interface*, 12(110). <https://doi.org/10.1098/rsif.2015.0590>
- Perilli, E., Baleani, M., Ohman, C., Fognani, R., Baruffaldi, F., & Viceconti, M. (2008). Dependence of mechanical compressive strength on local variations in microarchitecture in cancellous bone of proximal human femur. *Journal of Biomechanics*, 41(2), 438–446.
- Peyrin, F., Dong, P., Pacureanu, A., & Langer, M. (2014). Micro- and nano-CT for the study of bone ultrastructure. *Current Osteoporosis Reports*, 12(4), 465–474. <https://doi.org/10.1007/s11914-014-0233-0>
- Pivonka, P., Buenzli, P. R., Scheiner, S., Hellmich, C., & Dunstan, C. R. (2013). The influence of bone surface availability in bone remodelling—A mathematical model including coupled geometrical and biomechanical regulations of bone cells. *Engineering Structures*, 47, 134–147. <https://doi.org/10.1016/j.engstruct.2012.09.006>
- Prendergast, P. J., & Taylor, D. (1994). Prediction of bone adaptation using damage accumulation. *Journal of Biomechanics*, 27(8), 1067–1076. [https://doi.org/10.1016/0021-9290\(94\)90223-2](https://doi.org/10.1016/0021-9290(94)90223-2)
- Qasim, M., Farinella, G., Zhang, J., Li, X., Yang, L., Eastell, R., & Viceconti, M. (2016). Patient-specific finite element estimated femur strength as a predictor of the risk of hip fracture: The effect of methodological determinants. *Osteoporosis International*, 27(9), 2815–2822. <https://doi.org/10.1007/s00198-016-3597-4>
- Rahman, M. S., Akhtar, N., Jamil, H. M., Banik, R. S., & Asaduzzaman, S. M. (2015). TGF- $\beta$ /BMP signaling and other molecular events: Regulation of osteoblastogenesis and bone formation. *Bone Research*, 3. <https://doi.org/10.1038/boneres.2015.5>
- Rho, J. Y., Kuhn-Spearing, L., & Ziopoulos, P. (1998). Mechanical properties and the hierarchical structure of bone. *Medical Engineering & Physics*, 20, 92–102.
- Rincón-Kohli, L., & Zyssset, P. K. (2009). Multi-axial mechanical properties of human trabecular bone. *Biomechanics and Modeling in Mechanobiology*, 8(3), 195–208. <https://doi.org/10.1007/s10237-008-0128-z>
- Roberts, B. C., Perilli, E., & Reynolds, K. J. (2014). Application of the digital volume correlation technique for the measurement of displacement and strain fields in bone: A literature review. *Journal of Biomechanics*, 47(5), 923–934. <https://doi.org/10.1016/j.jbiomech.2014.01.001>
- Robling, A. G., Burr, D. B., & Turner, C. H. (2001). Recovery periods restore mechanosensitivity to dynamically loaded bone. *Journal of Experimental Biology*, 204(19), 3389–3399.
- Robling, A. G., Duijvelaar, K. M., Geevers, J. V., Ohashi, N., & Turner, C. H. (2001). Modulation of appositional and longitudinal bone growth in the rat ulna by applied static and dynamic force. *Bone*, 29(2), 105–113. [https://doi.org/10.1016/S8756-3282\(01\)00488-4](https://doi.org/10.1016/S8756-3282(01)00488-4)
- Robling, A. G., Hinant, F. M., Burr, D. B., & Turner, C. H. (2002). Improved bone structure and strength after long-term mechanical loading is greatest if loading is separated into short bouts. *Journal of Bone and Mineral Research*, 17(8), 1545–1554. <https://doi.org/10.1359/jbmr.2002.17.8.1545>

- Robling, A. G., & Turner, C. H. (2009). Mechanical signaling for bone modeling and remodeling. *Critical Reviews in Eukaryotic Gene Expression*, 19(4), 319–338. <https://doi.org/10.1615/CritRevEukarGeneExpr.v19.i4.50>
- Ruff, C. B., & Hayes, W. C. (1982). Subperiosteal expansion and cortical remodeling of the human femur and tibia with aging. *Science*, 217(4563), 945–948. <https://doi.org/10.1126/science.7112107>
- Ryan, M. K., Oliviero, S., Costa, M. C., Wilkinson, J. M., & Dall'Ara, E. (2020). Heterogeneous strain distribution in the subchondral bone of human osteoarthritic femoral Heads, measured with digital volume correlation. *Materials*, 13(20), 4619. <https://doi.org/10.3390/ma13204619>
- Sample, S. J., Collins, R. J., Wilson, A. P., Racette, M. A., Behan, M., Markel, M. D., Kalscheur, V. L., Hao, Z., & Muir, P. (2010). Systemic effects of ulna loading in male rats during functional adaptation. *Journal of Bone and Mineral Research*, 25(9), 2016–2028. <https://doi.org/10.1002/jbmr.101>
- Santos, A., Bakker, A. D., & Klein-Nulend, J. (2009). The role of osteocytes in bone mechanotransduction. *Osteoporosis International*, 20(6), 1027–1031. <https://doi.org/10.1007/s00198-009-0858-5>
- Schileo, E., Dall'Ara, E., Taddei, F., Malandrino, A., Schotkamp, T., Baleani, M., & Viceconti, M. (2008). An accurate estimation of bone density improves the accuracy of subject-specific finite element models. *Journal of Biomechanics*, 41(11), 2483–2491. <https://doi.org/10.1016/j.jbiomech.2008.05.017>
- Schlesinger, P. H., Blair, H. C., Teitelbaum, S. L., & Edwards, J. C. (1997). Characterization of the osteoclast ruffled border chloride channel and its role in bone resorption. *Journal of Biological Chemistry*, 272(30), 18636–18643. <https://doi.org/10.1074/jbc.272.30.18636>
- Schulte, F. A., Zwahlen, A., Lambers, F. M., Kuhn, G., Ruffoni, D., Betts, D., Webster, D. J., & Müller, R. (2013). Strain-adaptive in silico modeling of bone adaptation - a computer simulation validated by in vivo micro-computed tomography data. *Bone*, 52(1), 485–492. <https://doi.org/10.1016/j.bone.2012.09.008>
- Schwiedrzik, J. J., & Zysset, P. K. (2013). An anisotropic elastic-viscoplastic damage model for bone tissue. *Biomechanics and Modeling in Mechanobiology*, 12(2), 201–213. <https://doi.org/10.1007/s10237-012-0392-9>
- Siris, E. S., Miller, P. D., Barrett-Connor, E., Faulkner, K. G., Wehren, L. E., Abbott, T. A., Berger, M. L., Santora, A. C., & Sherwood, L. M. (2001). Identification and fracture outcomes of undiagnosed low bone mineral density in postmenopausal women: Results from the National Osteoporosis Risk Assessment. *Journal of the American Medical Association*, 286(22), 2815–2822. <https://doi.org/10.1001/jama.286.22.2815>
- Skerry, T. M. (2006). One mechanostat or many? Modifications of the site-specific response of bone to mechanical loading by nature and nurture. *Journal of Musculoskeletal Neuronal Interactions*, 6(2), 122–127.
- Sommerfeldt, D., & Rubin, C. (2001). Biology of bone and how it orchestrates the form and function of the skeleton. *European Spine Journal*, 10(2), S86–S95. <https://doi.org/10.1007/s005860100283>
- Song, Y., Zheng, J., Yan, M., Ding, W., Xu, K., Fan, Q., & Li, Z. (2015). The Effect of irreversible electroporation on the Femur: Experimental study in a rabbit model. *Scientific Reports*, 5, 18187.
- Stevens, H. Y., Meays, D. R., & Frangos, J. A. (2006). Pressure gradients and transport in the murine femur upon hindlimb suspension. *Bone*, 39(3), 565–572. <https://doi.org/10.1016/j.bone.2006.03.007>

- Teitelbaum, S. L. (2000). Bone resorption by osteoclasts. *Science*, 289(5484), 1504–1508. <https://doi.org/10.1126/science.289.5484.1504>
- Van Tol, A. F., Schemenz, V., Wagermaier, W., Roschger, A., Razi, H., Vitienes, I., Fratzl, P., Willie, B. M., & Weinkamer, R. (2020). The mechanoresponse of bone is closely related to the osteocyte lacunocanicular network architecture. *Proceedings of the National Academy of Sciences of the United States of America*, 117(51), 32251–32259. <https://doi.org/10.1073/pnas.2011504117>
- Varga, P., Dall'Ara, E., Pahr, D. H., Pretterklober, M., & Zysset, P. K. (2011). Validation of an HR-pQCT-based homogenized finite element approach using mechanical testing of ultra-distal radius sections. *Biomechanics and Modeling in Mechanobiology*, 10(4), 431–444. <https://doi.org/10.1007/s10237-010-0245-3>
- Varga, P., Pahr, D. H., Baumbach, S., & Zysset, P. K. (2010 Nov). HR-pQCT based FE analysis of the most distal radius section provides an improved prediction of Colles' fracture load in vitro. *Bone*, 47(5), 982–988.
- Varga, P., Willie, B. M., Stephan, C., Kozloff, K. M., & Zysset, P. K. (2020). Finite element analysis of bone strength in osteogenesis imperfecta. *Bone*, 133. <https://doi.org/10.1016/j.bone.2020.115250>
- Viceconti, M., & Dall'Ara, E. (2019). From bed to bench: How in silico medicine can help ageing research. *Mechanisms of Ageing and Development*, 177, 103–108. <https://doi.org/10.1016/j.mad.2018.07.001>
- Villette, C. C., & Phillips, A. T. M. (2016). Informing phenomenological structural bone remodelling with a mechanistic poroelastic model. *Biomechanics and Modeling in Mechanobiology*, 15(1), 69–82. <https://doi.org/10.1007/s10237-015-0735-4>
- Weinans, H., Huiskes, R., & Grootenhuis, H. J. (1992). The behavior of adaptive bone-remodeling simulation models. *Journal of Biomechanics*, 25(12), 1425–1441. [https://doi.org/10.1016/0021-9290\(92\)90056-7](https://doi.org/10.1016/0021-9290(92)90056-7)
- Weinbaum, S., Zhang, X., Han, Y., Vink, H., & Cowin, S. C. (2003). Mechanotransduction and flow across the endothelial glycocalyx. *Proceedings of the National Academy of Sciences of the United States of America*, 100(13), 7988–7995. <https://doi.org/10.1073/pnas.1332808100>
- Willie, B. M., Zimmermann, E. A., Vitienes, I., Main, R. P., & Komarova, S. V. (2020). Bone adaptation: Safety factors and load predictability in shaping skeletal form. *Bone*, 131. <https://doi.org/10.1016/j.bone.2019.115114>
- Wolfram, U., Gross, T., Pahr, D. H., Schwiedrzik, J., Wilke, H. J., & Zysset, P. K. (2012). Fabric-based Tsai-Wu yield criteria for vertebral trabecular bone in stress and strain space. *Journal of the Mechanical Behavior of Biomedical Materials*, 15, 218–228. <https://doi.org/10.1016/j.jmbbm.2012.07.005>
- Wolfram, U., Wilke, H. J., & Zysset, P. K. (2010). Valid  $\mu$  finite element models of vertebral trabecular bone can be obtained using tissue properties measured with nanoindentation under wet conditions. *Journal of Biomechanics*, 43(9), 1731–1737. <https://doi.org/10.1016/j.jbiomech.2010.02.026>
- Wu, H. F., Chang, C. H., Wang, G. J., Lai, K. A., & Chen, C. H. (2019). Biomechanical investigation of dynamic hip screw and wire fixation on an unstable intertrochanteric fracture. *BioMedical Engineering OnLine*, 18, 49.
- Xie, S., Manda, K., Wallace, R. J., Levrero-Florencio, F., Simpson, A. H. R. W., & Pankaj, P. (2017). Time dependent behaviour of trabecular bone at Multiple load levels. *Annals of Biomedical Engineering*, 45(5), 1219–1226. <https://doi.org/10.1007/s10439-017-1800-1>

- Yang, S., Luo, Y., Yang, L., Dall'Ara, E., Eastell, R., Goertzen, A. L., McCloskey, E. V., Leslie, W. D., & Lix, L. M. (2018). Comparison of femoral strength and fracture risk index derived from DXA-based finite element analysis for stratifying hip fracture risk: A cross-sectional study. *Bone*, 110, 386–391. <https://doi.org/10.1016/j.bone.2018.03.005>
- Yang, L., Palermo, L., Black, D. M., & Eastell, R. (2014). Prediction of incident hip fracture with the estimated femoral strength by finite element analysis of DXA scans in the study of osteoporotic fractures. *Journal of Bone and Mineral Research*, 29(12), 2594–2600. <https://doi.org/10.1002/jbmr.2291>
- Yu, B., Pacureanu, A., Olivier, C., Cloetens, P., & Peyrin, F. (2020). Assessment of the human bone lacuno-canalicular network at the nanoscale and impact of spatial resolution. *Scientific Reports*, 10(1). <https://doi.org/10.1038/s41598-020-61269-8>
- Zhu, X., Chan, Y. T., Yung, P. S. H., Tuan, R. S., & Jiang, Y. (2021). Subchondral bone remodelling: A Therapeutic target for osteoarthritis. *Frontiers in Cell and Developmental Biology*, 8. <https://doi.org/10.3389/fcell.2020.607764>
- Zhu, T. Y., Hung, V. W., Cheung, W. H., Cheng, J. C., Qin, L., & Leung, K. S. (2016). Value of measuring bone microarchitecture in fracture discrimination in older women with recent hip fracture: A case-control study with HR-pQCT. *Scientific Reports*, 6, 34185.
- Zimmermann, E. A., Busse, B., & Ritchie, R. O. (2015). The fracture mechanics of human bone: Influence of disease and treatment. *BoneKEy Reports*, 4. <https://doi.org/10.1038/bonekey.2015.112>
- Zioupos, P., Currey, J. D., & Casinos, A. (2000). Exploring the effects of hypermineralisation in bone tissue by using an extreme biological example. *Connective Tissue Research*, 41(3), 229–248. <https://doi.org/10.3109/03008200009005292>
- Zysset, P. K. (2003). A review of morphology-elasticity relationships in human trabecular bone: Theories and experiments. *Journal of Biomechanics*, 36(10), 1469–1485. [https://doi.org/10.1016/S0021-9290\(03\)00128-3](https://doi.org/10.1016/S0021-9290(03)00128-3)
- Zysset, P. K., & Curnier, A. (1995). An alternative model for anisotropic elasticity based on fabric tensors. *Mechanics of Materials*, 21(4), 243–250. [https://doi.org/10.1016/0167-6636\(95\)00018-6](https://doi.org/10.1016/0167-6636(95)00018-6)
- Zysset, P. K., Dall'Ara, E., Varga, P., & Pahr, D. H. (2013). Finite element analysis for prediction of bone strength. *BoneKEy Reports*, 2. <https://doi.org/10.1038/bonekey.2013.120>

# Single-cell based models for cell–cell and cell– extracellular matrix interactions

# 23

Pau Urdeix<sup>1,2,3</sup>, Mohamed H. Doweidar<sup>1,2,3</sup>

<sup>1</sup>Mechanical Engineering Department, School of Engineering and Architecture (EINA), University of Zaragoza Zaragoza, Spain; <sup>2</sup>Aragon Institute of Engineering Research (I3A), University of Zaragoza Zaragoza, Spain; <sup>3</sup>Centro de Investigación Biomédica en Red en Bioingeniería, Biomateriales y Nanomedicina (CIBERBBN), Madrid, Spain

## Chapter outline

<b>Introduction</b> .....	548
<b>Methodology</b> .....	550
Cell motility .....	552
Cell mechanotaxis .....	553
Cell electrotaxis.....	555
Drag force.....	556
Cell–cell interaction.....	557
Cell–cell contact.....	558
Cell–cell adhesion .....	558
Cell fate decision .....	559
Cell maturation .....	560
Cell differentiation.....	560
Cell proliferation .....	561
Model parameters and experiment setup .....	562
ECM discretization .....	562
Boundary conditions .....	562
Assumptions .....	562
<b>Numerical implementation and applications</b> .....	564
Cell–cell contact forces .....	565
Cell differentiation modulated by ECM stiffness .....	566
Cell adhesions modulated by ECM stiffness .....	569
Mechanically stimulated ECMS .....	570
Electrically stimulated ECM .....	574
Advanced materials for mechanoelectrical stimulation coupling.....	576
<b>Conclusions</b> .....	578

Acknowledgments .....	580
References .....	581

---

## Introduction

Cardiovascular diseases are the leading cause of death in the developed world. Due to the low regenerative capacity of the heart tissue, damage caused after infarction is not recoverable, which may complicate the problem. Currently, the only effective treatment goes through organ transplantation, with its associated complexity and risks (Fischer & Glas, 2013). In the last decades, novel and promising cell therapies have been developed with the aim of establishing new methods to combat cardiac dysfunctions (Di Meglio et al., 2017; Shadrin et al., 2017). These therapies benefit from the extraordinary regenerative capacities of stem cells, which include a high rate of proliferation along with the ability to differentiate into resident tissue cell subtypes. The adequation of the integration of stem cells into the tissue, as well as the induction of tissue regeneration, has been observed to depend on the active interaction of the cells with the extracellular matrix (ECM), as well as the stimuli in their surroundings. In this sense, it has been shown that different stimuli such as mechanical, chemical, electrical, and thermal stimuli play a key role in the regulation of the main cellular processes such as migration, proliferation, maturation, and apoptosis (Lee et al., 2011; Rodriguez et al., 2014; Stoppel et al., 2016). For instance, mesenchymal stem cells (MSCs) differentiation has been shown to be regulated, among others, by the ECM stiffness (Kelly & Prendergast, 2005; Li et al., 2012; Maul et al., 2011; Young & Engler, 2011). Thus, cells are capable of recognizing the ECM stiffness, which is representative of the resident tissue, and differentiate into the tissue's own cells. Engler et al., 2006 studied the specification of the cell lineage of MSCs, concluding that the stiffness of the ECM is a relevant factor in inducing cell differentiation (Discher et al., 2005; Engler et al., 2006). Other studies deepened this concept, observing that it is possible to obtain spontaneous differentiation in certain cell lines due to the stiffness of the ECM (Huebsch et al., 2010; Li et al., 2012; Yang et al., 2017). Furthermore, the different stimuli of the ECM, as well as their coordination, are essential to control tissue regeneration (Pullar, 2016; Robinson & Messerli, 2003), embryonic development (Levin, 2014; Meng et al., 2013), and the adoption of a specific cellular architecture (Bissell et al., 2003; Costa et al., 2003; Kim et al., 2010). It has also been shown that there is a close relationship between the functionality and the cellular architecture of many tissues (Ferrari, 2002; Mycielska & Djamgoz, 2004; Walker & Spinale, 1999). In particular, cardiac tissue has a clear anisotropy both in structure and properties. Thus, cardiac tissue structure is determined by the orientation and morphology of cardiomyocytes (CMs), which are oriented in the direction of stress development. So, the relationship between the different stimuli and the cellular processes that they regulate is essential for the correct development of heart tissues.

Recently, different authors have presented novel methodologies to develop cardiac tissues in-vitro (Bhana et al., 2010; Heller et al., 2000; Madden et al., 2015; Stedman et al., 1991). However, the contractile properties of the developed tissues are, in general, lower than those developed in adult tissues (Stoppel et al., 2016). Some authors attribute this deficiency to the lack of maturity and innervation of the obtained tissues (Rao et al., 2018; Stoppel et al., 2016). In turn, the maturation of cardiac tissue is closely related to the mechanical and electrical stimulation of cells during their development (Stoppel et al., 2016). Defining and controlling all the in-vitro cellular stimuli involved in cell maturation is a great technological challenge with a high economic cost (Salvador-Clavell et al., 2020). In addition, developing numerous experimental assays, varying the ECM conditions, involves a very high time cost. In this sense, different computational models have been proposed to support experimental studies, providing new perspectives and enriching the initial experimental information (Gavagnin & Yates, 2018; Rodriguez et al., 2013; Setty, 2014; Wendt et al., 2009). Whereas the computational models can perform multiple experiments, varying the ECM conditions in a wide range, with relatively reduced economic and temporary cost. The obtained results can be useful to define the best conditions to develop in-vitro experiments, reducing the number of experimental assays (Galbusera et al., 2008; Mogilner, 2009; Mogilner & Oster, 1996; Te Boekhorst et al., 2016).

Computational models can be classified into two large groups (Rodriguez et al., 2013). Continuous models, where large cell populations are studied, and discrete models, which focus on the study of each individual cell's conditions (Bissell et al., 2003; Costa et al., 2003; Kim et al., 2010). Continuous models are widely used to study nutrient concentration and oxygen consumption (Ayensa-Jiménez et al., 2020; Cioffi et al., 2008), as well as cell distributions of different cell species under different ECM conditions (Carlier et al., 2016; Kang et al., 2011), with a relatively low computational cost. However, with these models, it is very difficult to study cell–cell and cell–ECM interactions, which are essential to define the cellular architecture of the tissues. For instance, Manzano et al. (2015) developed a model with which they described cell–cell and cell–ECM interaction through continuous models, considering the contraction of a cell population (Manzano et al., 2015). However, this model did not consider individual cell behavior or cell adhesion during the contraction forces transmission, which is relevant in cell migration mechanics. For their part, discrete models can consider the decisions made by each individual cell due to the particular conditions of its cellular environment, including cell–cell and cell–ECM interactions during cell migration. In this way, it is possible to study tissue growth as a consequence of the cell–cell and cell–ECM interactions, as well as individual cell processes, such as differentiation, proliferation, and apoptosis (Doweidar, 2019; Mousavi et al., 2013a, 2013b; Mousavi & Doweidar, 2019).

To study cell mechanics, discrete models are highly recommended. DiMilla et al. (1991), presented a new mathematical model to describe the mechanics of cell migration (DiMilla et al., 1991). In their model, cell migration was presented

considering, on one hand, the equilibrium of cell adhesion forces, and on the other hand, a viscoelastic model to represent cell mechanics. This interesting idea has been developed in subsequent computational models. For instance, Zaman et al., 2005 presented a computational model of cell migration in which variables such as ECM stiffness, cell ligand density, and differences between 2D and 3D culture conditions were considered (Zaman et al., 2005). However, this model was applied to study one single cell, and cell migration is only described by the cell ligand density, but no other external stimuli have been considered. Subsequently, new models were presented in which electrical, chemical, and thermal stimuli were considered in the study of protrusion generation (Marzban & Yuan, 2017; Stéphanou et al., 2008), cell migration in 3D environments (Mousavi, Doblaré et al., 2014; Mousavi et al., 2013a, 2013b; Urdeix & Doweidar, 2020a, 2020b), cell morphology (Mousavi & Doweidar, 2014), and cell differentiation (Mousavi et al., 2015a; Mousavi & Doweidar, 2016). S. Mousavi et al. presented a computational model for multicell migration in a multisignaling ECM, where multiple cells migration is studied under electrical, chemical, thermal, and mechanical stimulation (Mousavi, Doblaré et al., 2014). Recently, M. Krim et al. have developed a computational model for cell migration in 3D matrices where cell–ECM interactions, through focal adhesions, can be precisely described (Kim et al., 2018). This model can be useful to study cell morphology and cell–ECM transmission forces, but the number of cells that can be studied is limited due to the required computational cost. In any case, single-cell models are highly helpful in deepening the knowledge of cell mechanics. However, in the last decade, these models have helped to get important advances in defining cell behavior, as well as the influence of different stimuli of the ECM on the cell (Maul et al., 2011; Te Boekhorst et al., 2016).

In this chapter, we will introduce a short review of some interesting results and conclusions that have recently been obtained with single-cell models applied to cardiac cells (Urdeix & Doweidar, 2020a; 2020b, 2021). The employment of these models helps us to study cardiac cell–cell and cell–ECM interactions, which are particularly relevant during tissue growth for the formation of anisotropic tissue structures. Besides, these models allow us to analyze, with an acceptable level of detail, the forces generated by the cells. Moreover, they can predict and evaluate the contractile capacities of the tissue based on the individual contributions of the cells. Additionally, we will show the latest advances in this direction supported by examples, results, and conclusions. These models have been used to study the conformation of cardiac tissues in its early stages of the tissue development, as well as the influence of different factors, such as ECM stiffness, mechanical and electrical stimuli (Urdeix & Doweidar, 2020a; 2020b, 2021).

---

## Methodology

In recent decades, there is an increased interest in understanding cell mechanics as well as the cells' response to different mechanical stimuli, which has led to the

appearance of a new field of research called cell mechanobiology (Camelliti et al., 2005; Kresh & Chopra, 2011; Mathur et al., 2001; Wang & Thampatty, 2006). This new multidisciplinary branch of knowledge combines the efforts of biologists, geneticists, and engineers, among others, to deepen the understanding of different cellular processes such as migration, differentiation, proliferation, and apoptosis. These cellular processes are essential for defining the characteristics of the regenerated tissues based on cells' individual behavior. For example, cardiac tissue tends to form cellular structures composed of highly ordered and alienated myofibrils in the main direction of stress generation (Camelliti et al., 2005). This allows, among others, a high level of specialization and capacity to exert contractile forces that, ultimately, define the stresses to generate the heartbeat (Rodriguez et al., 2013). All of these processes are highly sensitive to the mechanical conditions of the cellular environment and are highly dependent on cells' internal mechanical processes including generation of cellular forces, remodeling of the cell cytoskeleton, and cell–ECM interaction. This last one includes ECM remodeling, cell–ECM anchors, and ECM degradation and deposition, among others (De Pascalis & Etienne-Manneville, 2017; Kresh & Chopra, 2011; Mogilner, 2009). However, there is constant and reciprocal interaction between the cell and the ECM (Imanaka-Yoshida et al., 2004; Van Helvert et al., 2018). Cells are able to perceive their environment and modulate their behavior in response to the conditions of the ECM. In turn, it reshapes the conditions of the ECM, for example, by ECM degradation and deposition, altering its environment and the cellular response in its environment. Understanding these processes entails a big deal of analysis of different individual cell processes, including factors that regulate them, and the effects they produce on their environment.

Taking these considerations into account, a model that simply describes different cell processes, and allows evaluating the effects on the cellular environment, including the cell–cell and cell–ECM interaction, is needed. From an engineering point of view, it seeks to establish the physical principles behind the different cellular processes in a similar way to any other physical event. In this sense, the cell is described as a mechanical element capable of interacting with its environment through stress generation. These stresses are generated internally by the activity of the different cell components, and externally by the activity of nearby cells in the ECM, the stiffness of the ECM, and the presence of external mechanical stimuli. For instance, the cell migration process can be described by means of a balance of the forces that act on the cell, including the traction forces, due to the internal contraction of the Actin–Myosin machinery, the protrusion forces, due to the random generation of protrusions in the cell membrane, and the drag forces due to the viscous effects of the ECM (Mousavi et al., 2015b; Urdeix et al., 2020). The complexity of performing this type of analysis lies in the ability of cells to actively interact with their environment, affecting the behavior of a cell to all those in its environment, and the presence of multiple coupled regulatory factors of cells' behavior.

## Cell motility

Cell migration can be described as a balance between internal and external forces of the cell, as well as the generation and release of focal adhesions within the ECM (De Pascalis & Etienne-Manneville, 2017; Deshpande et al., 2008). During migration, the cell generates a migration front, where new cell adhesions are generated. At the same time, at the back of the cell, existing focal adhesions are released, allowing the cell to propel itself to a new location (Mogilner & Oster, 1996). The forces necessary to propel the cell toward the new location are generated by the contraction of the Actin–Myosin (AM) filaments (Gardel et al., 2008). AM, through the hydrolysis of ATP (Adenosine Triphosphate) molecule, generates the mechanical energy necessary for the contraction of the cell. This allows the cell to reorient and reshape the cytoskeleton during migration processes (Fig. 23.1). The generated contraction, along with the imbalance of focal adhesions between the front and back of the cell, propels the cell forward. Thus, the direction of migration is determined by the direction of cell polarization, which determines the front and the back direction of the cell. This direction of polarization is determined by different mechanical, thermal, electrical, and chemical factors received by the cell from the ECM. The determination of which of these factors defines the direction of cell polarization can be of vital importance to define, for example, the potential for metastasis in cancer (Lintz et al., 2017).

It has been observed that the presence of a stiffness or chemical gradient within the ECM contributes to the definition of cell polarization. Thus, different studies have shown that cells can be guided by the stiffness of the ECM, among other factors, which can be very helpful to control different processes such as migration, differentiation, and proliferation (Ng et al., 2012). Other stimuli, such as thermal or

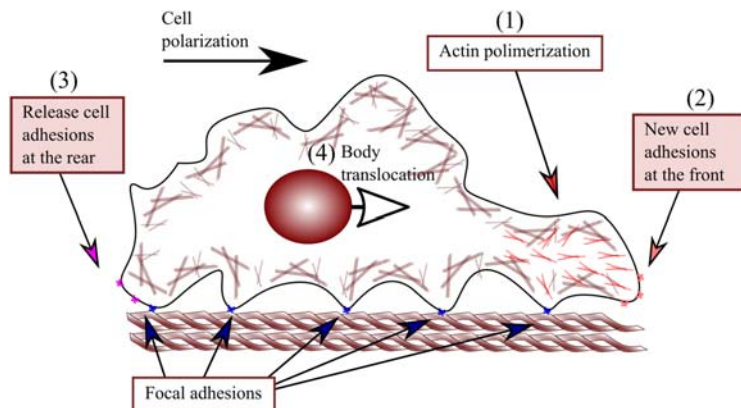


**FIGURE 23.1 Cell translocation.**

Cell translocation is produced by four simultaneous cell processes. (1) Cell polarization and actin polymerization. (2) Generation of new cell adhesions at the front of the cell. (3) Release of cell adhesions at the rear of the cell. (4) Body translocation due to the differences in cell adhesions between the front and the rear parts of the cell.

electrical gradients can also favor cell polarization in a certain direction. However, there is also a random factor associated with the polymerization of actin filaments and the generation of protrusions, which contribute to the cell trajectory and generates a random migration pattern. Thus, the first step to define cell motility is to establish the forces involved, which take into account all these concepts. These forces can be classified according to their nature and characteristics. Among them, the mechanical forces, associated with the contraction of the AM filaments and the deformation of the cell-ECM set, the electrical forces, due to external electrical stimulus and the concentration of ionic species in the ECM, and the viscous forces, due to the drag associated with the viscosity and composition of the ECM.

## Cell mechanotaxis

Cell mechanotaxis represents the mechanism by which cells are able to detect the mechanical conditions of the ECM, interacting mechanically with the ECM through the focal adhesions, and allowing the cell to move to a new favorable position. For instance, cells such as fibroblasts have been observed to move to more rigid positions where they feel more comfortable (Reig et al., 2014). The elements involved in the process of mechanotaxis include AM filaments, cytoskeleton, and cell membrane, as well as focal adhesions located in the cell membrane. The AM filaments generate an internal contraction transmitted in the form of stresses by the cytoskeleton to the cell membrane. These contractions do double functions. First, they serve as a cellular mechanism to predict the mechanical conditions of its near environment, including stiffness, availability of new anchors, and the presence of other cells (Chen et al., 2004; Trubelja & Bao, 2018). Second, they serve as a cellular propellant motor, generating forces capable of remodeling or reorienting the cytoskeleton, propelling the cell body toward a new location.

To determine these stresses, a cell mechanical model is defined (DiMilla et al., 1991). This model associates the different internal components of the cell with the active or the passive structural elements. The passive elements, such as the cell membrane or the cytoskeleton, oppose the deformation of the cell, while the active elements, in this case, the AM machinery, are responsible for the cell deformations (Fig. 23.2A). Thus, through this mechanical model, cell properties can be established and migration efforts formulated, establishing a balance among the different components.

The main factor that triggers the cell to propel itself is related to the internal stresses generated by the contraction of the AM filaments. This internal stress is considered to be proportional to the internal deformation of the cell. Thus, a model is proposed to calculate cell internal stresses,  $\sigma_i$ , from the cell internal deformations,  $\varepsilon_i$ , where the active and passive contributions are considered as (Mousavi et al., 2015b):

$$\sigma_i = \begin{cases} K_{pas}\varepsilon_i & \varepsilon_i < \varepsilon_{min} \text{ or } \varepsilon_i > \varepsilon_{max}, \\ \frac{K_{act} \sigma_{max} (\varepsilon_{min} - \varepsilon_i)}{K_{act} \varepsilon_{min} - \sigma_{max}} + K_{pas}\varepsilon_i & \varepsilon_{min} \leq \varepsilon_i \leq \tilde{\varepsilon}, \\ \frac{K_{act} \sigma_{max} (\varepsilon_{max} - \varepsilon_i)}{K_{act} \varepsilon_{max} - \sigma_{max}} + K_{pas}\varepsilon_i & \varepsilon_{max} \geq \varepsilon_i \geq \tilde{\varepsilon}, \end{cases} \quad (23.1)$$

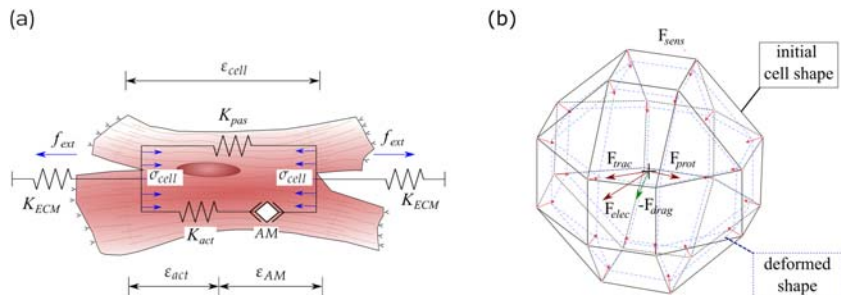


**FIGURE 23.2 Mechanical model of the cell.**

(A) A cell equivalent mechanical model has been established considering active (Actin–myosin filaments) and passive elements (cell membrane and cytoskeleton). AM exerts cell internal deformations that generate cell internal stresses. The internal deformation of the cell is considered as a balance between the internal and external (ECM) stresses. (B) The cell is discretized as a quasi-spherical finite element composed of 24 nodes in the cell membrane. Cell–ECM interaction forces are considered in the membrane nodes of the cell, while migration forces are considered from the cell centroid.

where  $K_{act}$  and  $K_{pas}$  are the stiffness of the active and passive elements, respectively.  $\sigma_{max}$  is the maximum cell internal stress generated by the AM.  $\epsilon_{min}$  and  $\epsilon_{max}$  correspond to the minimum and maximum cell internal deformations for which the AM is able to generate active stresses.  $\tilde{\epsilon}$  is the result of establishing a linear approximation between the minimum and maximum cell internal deformations, defined as

$$\tilde{\epsilon} = \sigma_{max} / K_{act}.$$

Cell internal deformations are transmitted to the ECM through the multiple focal adhesions as nodal traction forces evaluated at each node in which the cell is discretized. Thus, each nodal traction force,  $\mathbf{F}_{trac}^i$ , at each cell node,  $i$  th (see Fig. 23.2B), is proportional to the internal stress and the cell adhesions as:

$$\mathbf{F}_{trac}^i = \sigma_i S k n_r \psi \mathbf{e}_i, \quad (23.2)$$

where  $k$  is the binding constant,  $n_r$  is the number of available receptors, and  $\psi$  is the ligand density.  $\mathbf{e}_i$  is the direction unit vector of the membrane node toward the cell centroid, and  $S$  is the cell surface. The resultant traction force,  $\mathbf{F}_{trac}$ , is obtained as a sum of the contributions of all nodal traction forces of the cell as:

$$\mathbf{F}_{trac} = \sum_{i=1}^n \mathbf{F}_{trac}^i, \quad (23.3)$$

where  $n$  is the number of nodes in which the cell is discretized.

Cell traction forces act in conjunction with the protrusion forces,  $\mathbf{F}_{prot}$ , which are generated by the random polymerization of actin filaments in the cell membrane. Actin polymerization generates protrusions in the cell membrane which increase the penetration capacity of the cell in the direction in which they are generated. The protrusions act as an element capable of altering the migration direction without altering the magnitude of the total cell force. Besides, the magnitude of the protrusion force is proportional to the traction force, since the motor force is equally defined by cell contraction and internal stresses. In this way, the protrusion force can be considered as a random factor, which can be defined as:

$$\mathbf{F}_{prot} = \kappa \parallel \mathbf{F}_{trac} \parallel \mathbf{e}_{rnd}, \quad (23.4)$$

where  $\kappa$  and  $\mathbf{e}_{rnd}$  are random parameters to define the magnitude and the direction of the protrusion force, respectively.

## Cell electrotaxis

Cells can be guided by different ECM stimuli such as chemical, thermal, and electric fields (EF). Chemical and thermal stimuli promote the polymerization of actin filaments and the generation of protrusions in a certain direction, altering the directionality of migration without altering the cell speed (Mousavi & Doweidar, 2019; Vanegas-Acosta et al., 2012). However, electrical stimuli affect both the speed and the directionality of migration. Although cell processes behind cell electrotaxis are still unclear, some studies point to a relationship between  $Ca^{2+}$  and cell hyperpolarization and depolarization. In the cell face close to the anodal zone, cell membrane tends to hyperpolarize, due to the increase of the ionic species, and the cell face in the cathodic zone tends to depolarize by the influx of the  $Ca^{2+}$ . These effects produce an increase in the cell polarization which is proportional to the electric gradient potential. In this sense, different studies have observed a linear relationship between the cell migration and the electric field gradients (Banks et al., 2015; Chen et al., 2019; Radisic et al., 2004). Frederich et al., 2017 observed proportional effects in cardiac cell migration for different direct current EF (dcEF) showing an increase in cell migration in both directionality and velocity of the cell migration (Frederich et al., 2017). Thus, an electric force,  $\mathbf{F}_{EF}$ , proportional to the electric field,  $\mathbf{E}$ , can be defined as (Mousavi, Doweidar et al., 2014; Mousavi & Doweidar, 2019):

$$\mathbf{F}_{EF} = \begin{cases} -\mathbf{E} \Omega S \mathbf{e}_{EF} & \mathbf{E} \leq \mathbf{E}_{sat}, \\ -\mathbf{E}_{sat} \Omega S \mathbf{e}_{EF} & \mathbf{E} \geq \mathbf{E}_{sat}, \end{cases} \quad (23.5)$$

where  $\Omega$  corresponds to the cell surface charge density, which can be calculated through the Gouy–Chapman membrane charge equations, by considering the cell surface potential (Crommelin, 1984; Kinraide & Wang, 2010; Rostovtseva et al., 1998).  $S$  is the cell surface and,  $\mathbf{e}_{EF}$ , is a unit vector that defines the direction

of the EF.  $E_{sat}$  is the saturation electric field, which is the EF for where the cell velocity is maintained even with the increase of the EF (Zhao et al., 2011).

The electric forces between cells due to the cell surface charge,  $\mathbf{F}_{EF}^{ij}$ , are proportional to the distance between the evaluated cells,  $\mathbf{e}_{ij}$ , and the cell charge,  $\Omega$ , and can be defined as:

$$\mathbf{F}_{EF}^{ij} = \frac{k_e}{\epsilon_r} \frac{\Omega_i S_i \Omega_j S_j}{r_{ij}^2} \mathbf{e}_{ij}, \quad (23.6)$$

where  $\Omega_i$  and  $\Omega_j$  are the surface charge of the  $i$  th and  $j$  th cells, respectively.  $k_e$  is the coulomb constant, and  $\epsilon_r$  is the ECM relative electric permittivity.

The total electric force over the cell,  $\mathbf{F}_{elec}$ , can be defined by the contribution of the EF force,  $\mathbf{F}_{EF}$ , and the electric forces between cells,  $\mathbf{F}_{EF}^{ij}$ , as (Mousavi & Doweidar, 2019)

$$\mathbf{F}_{elec} = \mathbf{F}_{EF} + \sum_{j=1}^{n-1} \mathbf{F}_{EF}^{ij}. \quad (23.7)$$

## Drag force

Drag forces should be considered due to the cellular translocation within its viscous ECM. In such a case, the drag force is considered as the main force that opposes the cell movement. It is proportional to the cell velocity and the cell geometry. Thus, for a single cell moving on a viscous ECM, an equilibrium of the acting forces of the cell can be established by (Mousavi & Doweidar, 2019):

$$\mathbf{F}_{trac} + \mathbf{F}_{elec} + \mathbf{F}_{prot} = \mathbf{F}_{drag}. \quad (23.8)$$

Besides, the drag force,  $\mathbf{F}_{drag}$ , can be defined though the Stokes' law, by considering the cell as a geometry moving at velocity,  $\mathbf{v}$ , in an ECM with,  $\eta$ , viscosity as:

$$\mathbf{F}_{drag} = f_{sh} \eta \mathbf{v}, \quad (23.9)$$

where  $f_{sh}$  is the shape factor of the cell. For a single cell with a constant spherical shape, it can be simplified by the radius,  $r$ , as (Mousavi & Doweidar, 2014):

$$f_{sh} = 6\pi r \quad (23.10)$$

Through these equations, the collective cell migration of groups of cells attached together can be described considering that each cell contributes to the group motility with its individual cell force. Thus, the acting forces in the group can be defined as:

$$\mathbf{F}_{drag}^{grp} = \sum_{k=1}^n \mathbf{F}_{trac}^k + \mathbf{F}_{elec}^k + \mathbf{F}_{prot}^k, \quad (23.11)$$

where  $\mathbf{F}_{drag}^{grp}$  is the drag force of the group of attached cells.  $\mathbf{F}_{trac}^k$ ,  $\mathbf{F}_{elec}^k$ , and  $\mathbf{F}_{prot}^k$  are the traction forces, electric forces, and protrusion forces of the  $k$ th cell in the group, respectively.

Besides, in such a case,  $f_{sh}$  can be calculated by defining the equivalent group radius,  $r_{grp}$ , which is the mean section radius perpendicular to the moving direction, and a correction factor dependent on the group geometry as (Mousavi et al., 2015b):

$$f_{sh} = \left[ \frac{l_{max}l_{med}}{l_{min}^2} \right]^{0.09} 6\pi r_{grp}, \quad (23.12)$$

where  $l_{max}$ ,  $l_{med}$ , and  $l_{min}$  are the maximum, medium, and minimum dimensions of the group defined in an orthogonal local system, respectively.

## Cell–cell interaction

Cell–cell interactions play a key role in main cell processes such as cell migration (Carey et al., 2012; Van Helvert et al., 2018), proliferation (Aragona et al., 2013; Low et al., 2014; McClatchey & Yap, 2012), and apoptosis (Elmore, 2007), as well as in tissue-level processes (Kresh & Chopra, 2011; Loeffler & Roeder, 2002). Besides, cells regulate different cell processes through cell–cell molecular intercommunication. For instance, molecular intercommunication is essential during collective cell migration where cells are observed to play different roles in the group (De Pascalis & Etienne-Manneville, 2017; Lintz et al., 2017). Cell-cell interactions in cardiac tissues are particularly relevant, where the coordinated contraction of the tissue is due to the propagation of an electrical stimulus through ion channels in cell–cell interconnections (Fearnley et al., 2011; Walker & Spinale, 1999). Hence, the cardiac tissue functionality depends on cell–cell interaction, which requires adequate cell architecture and cell–cell orientations (Jackman et al., 2016, 2018; Papas et al., 2007; Stinstra et al., 2005). Single-cell models let us define cell–cell interactions to study the effects of different stimuli during tissue architecture conformations. Thus, cell’s contact and cell adhesion conditions have been defined by considering cell–cell distance and cell orientation (Fig. 23.3).

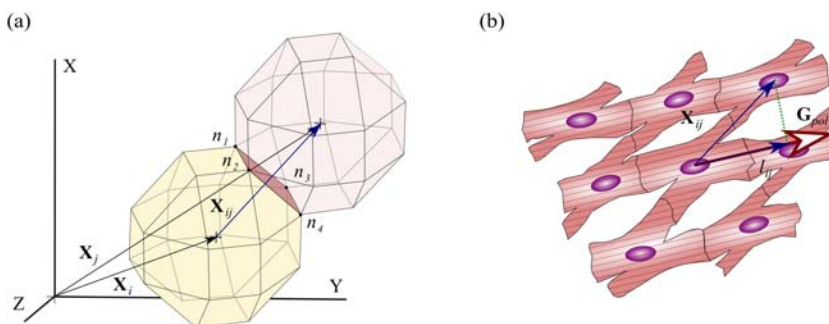


**FIGURE 23.3 Cell interaction.**

(A) Cell–cell contact is defined by the position vectors of the cells. (B) Cardiac cell adhesions are considered for cells adequately oriented with respect to the global polarization direction.

## Cell–cell contact

Cell–cell contacts are defined through the noninterpenetration criteria. Being  $\mathbf{X}_i$  and  $\mathbf{X}_j$  the coordinates of the  $i$ th and the  $j$ th cells, respectively. Taking into account the constant spherical shape of the cells, the distance between the cells,  $\mathbf{X}_{ij}$ , can be defined as (see Fig. 23.3A):

$$\mathbf{X}_{ij} = \mathbf{X}_i - \mathbf{X}_j. \quad (23.13)$$

Any pair of cells must fulfill  $|\mathbf{X}_{ij}| \geq 2r$  at any time to avoid cell superposition. Besides, it is considered that any two cells are in contact when  $|\mathbf{X}_{ij}| = 2r$ . In this particular case, if cells are considered adherent cells, as is the case of cardiac cells, cell–cell adhesion can be considered depending on the cell orientation and cell–cell contact directionality. For this purpose, cell–cell contact direction,  $\mathbf{e}_i$ , can be defined as

$$\mathbf{e}_{ij} = \frac{\mathbf{X}_{ij}}{\|\mathbf{X}_{ij}\|}. \quad (23.14)$$

## Cell–cell adhesion

Cell adhesion considers that cells, which are in contact, are collaborating to maintain a collective behavior. To define cell–cell adhesion, it is necessary that two or more cells are considered in contact with  $|\mathbf{X}_{ij}| = 2r$ . Moreover, the considered cell phenotype should be able to attach to other cells by establishing stable cell–cell adhesions or Cell Junctions (CJ) (see Fig. 23.3B). In this sense, cardiac cells are considered to establish stable CJs defining a highly ordered myofibrils structure during tissue development (Ahuja et al., 2007; Ghafar-Zadeh et al., 2011; Lee et al., 2008; Nunes et al., 2013). Cells’ orientation is highly correlated with the direction of the tissue contraction. For instance, Tahara et al., 2016 observed how cardiac precursors become interconnected to form coherent epithelia in bilateral cardiac precursor population (Tahara et al., 2016). Besides, Planat-Bénard et al., 2004 were able to obtain myotubule-like structures after 14 days of cell culture during cardiac cell differentiation studies (Planat-Bénard et al., 2004).

Cell orientation depends, among other factors, on the present stimuli in the ECM (Camelliti et al., 2005; Heidi Au et al., 2009; Ikonen et al., 2013). Thus, considering mechanical and electrical effects, the cell polarization direction,  $\mathbf{e}_{pol}$ , can be defined as (Urdeix & Doweidar, 2020a, 2020b, 2021):

$$\mathbf{e}_{pol}^i = \frac{\mathbf{e}_{mech}^i + \mathbf{e}_{elec}^i}{\|\mathbf{e}_{mech}^i + \mathbf{e}_{elec}^i\|}, \quad (23.15)$$

being  $\mathbf{e}_{mech}^i$  and  $\mathbf{e}_{elec}^i$  the directions of the mechanical and electrical stimuli, respectively, which are defined as:

$$\mathbf{e}_{mech}^i = \frac{\mathbf{F}_{trac}}{\|\mathbf{F}_{trac}\|}, \quad (23.16)$$

and:

$$\mathbf{e}_{elec}^i = \frac{\mathbf{F}_{elec}^i}{\|\mathbf{F}_{elec}^i\|}. \quad (23.17)$$

To define the tissue direction (Fig. 23.3), which indicates the direction of cell–cell adhesion, the global polarization,  $\mathbf{G}_{pol}$ , is defined through the direction of each individual cell polarization,  $\mathbf{e}_{pol}^i$ , as (Urdeitx & Doweidar, 2020a, 2020b, 2021):

$$\mathbf{G}_{pol} = \frac{\mathbf{R}_{pol}}{\|\mathbf{R}_{pol}\|}, \quad (23.18)$$

with

$$\mathbf{R}_{pol} = \sum_{i=1}^n \frac{\mathbf{e}_{pol}^i}{\|\mathbf{e}_{pol}^i\|}. \quad (23.19)$$

$\mathbf{G}_{pol}$  defines the direction of the orientation of the tissue fibers. To establish a stable CJs between two or more cells, it is necessary that both cells are in contact, and the orientation of the cell–cell contact,  $\mathbf{e}_i$ , is coherent with the direction of the global polarization,  $\mathbf{G}_{pol}$ . Thus, to compare both direction vectors, the contact projection,  $l_{ij}$ , can be defined as (Urdeitx & Doweidar, 2020a, 2020b, 2021):

$$l_{ij} = \frac{Proj(\mathbf{e}_{ij}, \mathbf{G}_{pol})}{\|\mathbf{G}_{pol}\|}, \quad (23.20)$$

where  $0 < l_{ij} \leq 1$ , being  $l_{ij} = 0$  if the direction is perpendicular, and  $l_{ij} = 1$  if both vectors have the same direction. Finally, cell–cell adhesion is considered when  $l_{ij} \geq l_{adh}$ , which is an established value that considers the cell geometry limitations of the model for the different experimental cases (Camelliti et al., 2005; Chen et al., 2008; Sassoli et al., 2011). Cells that are considered attached and form stable CJ, tend to form groups of cells that migrate collectively (Holtzman et al., 2007; Kresh & Choppa, 2011).

## Cell fate decision

Mechanical conditions of the ECM are shown to play a key role in different cellular processes such as differentiation (Discher et al., 2005; Engler et al., 2006), maturation (Bhana et al., 2010; Jackman et al., 2018), and apoptosis (Elmore, 2007; Kearney et al., 2008). For instance, a determined ECM stiffness, or certain mechanical stimulation, can stimulate MSCs to differentiate to a determinate cell phenotype (Engler et al., 2004; Delaine-Smith & Reilly, 2012; Li et al., 2012; Shake et al., 2002). MSCs are able to identify the mechanical characteristics of different tissues, triggering cell differentiation into a typical cellular phenotype of the resident tissue. Some studies have suggested that deformations in the cell nucleus, due to the cell internal deformations, can trigger specific pathways which induce the synthesis of different factors involved in cell differentiation (Buxboim et al., 2010; Trubelja &

Bao, 2018). It has also been shown how excessive cell deformations, or long times with cyclic deformations, can undergo cell apoptosis (Cheng et al., 2009; Gladman et al., 2010). For instance, cells evaluate the mechanical conditions over time, and different cell processes are triggered depending on the specific cell conditions. In this sense, it is necessary to define the cell maturation time, which is the time at which the cell is interacting with the ECM, as well as the dependency of the different cellular processes and the mechanical stimuli.

### Cell maturation

Cell processes, such as cell differentiation, proliferation, and apoptosis, require a certain time to be triggered, which is related to the cell cycle time. The time necessary to complete a cell-cycle process is defined as the time of maturation,  $t_{mat}$ , which depends, among others, on the cell type and the mechanical stimulus perceived by the cell (Delaine-Smith & Reilly, 2012; Ulrich et al., 2009; Wu & Chen, 2000). It is defined for each cell at each step time as (Mousavi et al., 2015a; 2015b):

$$t_{mat}(\gamma_c, t) = t_{min} + t_p \gamma_c(t), \quad (23.21)$$

where  $t_{min}$  is the minimum time needed to complete a cell-cycle, and  $t_p$  is a time proportional to the mechanical stimulus,  $\gamma_c$ , to which the cell is subjected at time  $t$ . The mechanical stimulus,  $\gamma_c(t)$ , is evaluated at each time considering the cell internal deformations as (Mousavi & Doweidar, 2016):

$$\gamma_c(t) = \frac{1}{n} \sum_{i=1}^n \mathbf{e}_i : \boldsymbol{\varepsilon}_i : \mathbf{e}_i^T, \quad (23.22)$$

where  $\mathbf{e}_i$  is the director vector of the  $i$ th node membrane toward the cell centroid, and  $\boldsymbol{\varepsilon}_i$  is the strain tensor at the  $i$ th node of the cell membrane.

The maturation state of the cell is defined by the Maturation Index (MI), which can be calculated as (Urdeix & Doweidar, 2020a):

$$MI = \begin{cases} \frac{t}{t_{mat}} & t < t_{mat}, \\ 1 & t \geq t_{mat}. \end{cases} \quad (23.23)$$

Thus, as the MI represents the cell cycle progress, the different cell processes are triggered when  $MI = 1$ .

### Cell differentiation

MSCs can be mechanically stimulated to promote cell differentiation into certain cell lineages (Delaine-Smith & Reilly, 2012; Kang et al., 2011; Kelly & Prendergast, 2005). For instance, mechanical stimulus derived from an ECM whose stiffness is similar to that found in cardiac tissues is able to stimulate MSCs differentiation into CMs (Li et al., 2012). Thus, when maturity is reached, MSCs differentiation

can be considered depending on the mechanical stimulus,  $\gamma_c$ , perceived by the cell as:

$$\text{Cell state} = \begin{cases} \text{CM} & \gamma_{\min} < \gamma_c \leq \gamma_{\max} \& \text{MI} = 1, \\ \text{apoptosis} & \gamma_{\text{apop}} < \gamma_c, \\ \text{no differentiation} & \text{otherwise,} \end{cases} \quad (23.24)$$

where  $\gamma_{\min}$  and  $\gamma_{\max}$  are the minimum and maximum mechanical stimulus which triggers MSC differentiation into cardiac cell lineages, respectively.  $\gamma_{\text{apop}}$  corresponds to an excessive mechanical stimulus in the cell, which triggers cell apoptosis.

## Cell proliferation

Cell proliferation plays a key role in tissue regeneration, by replicating cells to renew the damaged tissue. Cell proliferation capacity seems to be closely related to the level of cell differentiation, being lower the proliferation for more specialized cell phenotypes (Hatzistergos et al., 2010). In fact, cardiac cells have shown a reduced proliferation capacity, which is related to cell cycle arrest (Ahuja et al., 2007; Roveimiab et al., 2019; Asumda, 2013). Besides, cell-cell contacts can inhibit cell proliferation through contact proliferation inhibition (Cheng et al., 2006; McClatchey & Yap, 2012). In any case, cells go through a complete cell-cycle to be able to proliferate, which requires the fulfilment of  $\text{MI} = 1$ . Thus, cell proliferation can be defined as (Urdeix & Doweidar, 2020a):

$$\text{Cell proliferation} = \begin{cases} 1 \text{ mother} \rightarrow 2 \text{ daughters} & CJ_i < CJ_{\max} \& \text{MI} = 1, \\ \text{no proliferation} & \text{otherwise,} \end{cases} \quad (23.25)$$

where  $CJ_i$  is the number of cell-cell contacts for the  $i$ th cell, and  $CJ_{\max}$  is the maximum number of cell-cell contacts, which triggers contact proliferation inhibition. In this case, it is considered that the cell triggers proliferation inhibition when at least 50% of the cell surface is covered, which, due to cell discretization, corresponds to  $CJ_{\max} = 4$ .

Once a cell proliferates, two cells are generated from the mother cell, which share the cell phenotype with the mother cell. One of these cells is located in the position of the mother cell, and the second is located in a random position, in contact with the mother cell as (Mousavi et al., 2015a):

$$\mathbf{x}_{\text{daut}}^{(1)} = \mathbf{x}_{\text{moth}}, \mathbf{x}_{\text{daut}}^{(2)} = \mathbf{x}_{\text{moth}} + 2r \mathbf{e}_{\text{rand}}, \quad (23.26)$$

where  $\mathbf{x}_{\text{daut}}^{(1)}$  and  $\mathbf{x}_{\text{daut}}^{(2)}$  are the coordinates position of the (1) st and (2) nd daughter cells, and  $\mathbf{x}_{\text{moth}}$  are the coordinates of the mother cell.  $\mathbf{e}_{\text{rand}}$  is a random unit vector, and  $r$  is the radius of the cell.

## Model parameters and experiment setup

The presented model has been implemented as a Finite Element Model (FEM) in the commercial software ABAQUS through the implementation of different user subroutines (UEL, UELMAT). Through these subroutines, the cell element has been defined as a quasi-spherical element established by 24 nodes in the cell membrane ([Fig. 23.2B](#)). The cell interacts with the ECM through the membrane nodes applying sensing forces. Consequently, a stress–strain equilibrium is established in the cell–ECM interface (cell membrane). The cell internal deformations are calculated through the membrane node deformations, repeating the stress–strain equilibrium at each time step.

All the model parameters are listed in [Table 23.1](#), and the model algorithm has been illustrated in [Fig. 23.4](#).

## ECM discretization

The ECM has been modeled as a continuous elastic material. Its material is considered as a hydrogel with enough porous to enable cells migration. Although live tissues and hydrogels are considered to have viscoelastic properties, due to the scale of the problem (nano-deformations), it has been considered as an elastic material to reduce computational cost and implementation complexity. The ECM has total dimensions of  $400 \times 400 \times 800 \mu\text{m}$ , and it has been discretized by 128.000 trilinear hexahedrons. Each calculation time step corresponds to 0.8 h of cell–ECM interaction.

## Boundary conditions

ECM external faces are considered to be free of restrictions. To ensure calculation stability, a central point at each external face has been restricted in its plane (see [Fig. 23.5](#)). Mechanical stimulation, when applied, has been applied in the longitudinal direction, as a traction force on the external faces of the ECM. The applied traction force has been previously calculated to generate the required effective longitudinal deformation, in the range of 5%–35%. The electric field, when considered, was applied in the longitudinal direction as a constant charge on the outer faces of the ECM. Coupling of the electric and mechanical stimuli can be applied through the consideration of a central fiber with piezoelectric properties.

## Assumptions

Some assumptions have been taken into account during the implementation of the model. These assumptions are necessary to ensure computational stability and an easy understanding of the model. Thus, ECM has been considered as a homogeneous elastic material, equivalent to hydrogel with tunable stiffness, where cells can move without any restriction ([Enrica, 2009](#)). In this sense, ECM degradation and remodeling have not been considered. It has also been considered that the ECM conditions

**Table 23.1** Model parameters.

Parameter	Description	Value	Ref.
$K_{pas}$	Cell passive elements stiffness	2.8 kPa	Darling et al., 2008; Schäfer & Radmacher, 2005
$K_{act}$	Actin–myosin machinery stiffness	7.0 kPa	Schäfer & Radmacher, 2005; Discher et al., 2005
$\varepsilon_{max}$	Maximum actin–myosin active deformation	0.09	Mousavi et al., 2015b; Ramtani, 2004
$\varepsilon_{min}$	Minimum actin–myosin active deformation	-0.09	Mousavi et al., 2015b; Ramtani, 2004
$\sigma_{max}$	Maximum stress exerted by the actin–myosin machinery	0.25 kPa	Gardel et al., 2008; Rodriguez et al., 2013
$\nu$	ECM Poisson ratio	0.4	Bhana et al., 2010; Mathur et al., 2001
$\eta$	ECM viscosity	1000 Pa·s	Ulrich et al., 2009; Zaman et al., 2005
$k$	Binding constant	$10^8$ mol <sup>-1</sup>	Mousavi & Doweidar, 2019; Zaman et al., 2005
$n_r$	Number of available receptors of the cell	$1.5 \times 10^5$	Mousavi & Doweidar, 2019; Zaman et al., 2005
$E_{sat}$	Saturation value of the electric field	$1200 \text{ V} \cdot \text{m}^{-1}$	Frederich et al., 2017
$\Omega_{sat}$	Cell surface charge saturation point	$5^{-2} \text{ C} \cdot \text{m}^{-2}$	Huang et al., 2011; Fearnley et al., 2011
$\psi$	Ligand concentration	$10^{-5}$ mol	Zaman et al., 2005; Mousavi & Doweidar, 2019
$I_{adh}$	Minimum projection value for cell-cell attachment	0.50	Costa et al., 2003
$t_{min}$	Minimum time for cell maturation	6 days	Planat-Bénard et al., 2004; Asumda, 2013
$t_p$	Time proportionality	200 days	Kang et al., 2011; Schäfer & Radmacher, 2005
$\gamma_{min}$	Minimum mechanical stimulation for CM differentiation	-0.04	Li et al., 2012; Stoppel et al., 2016
$\gamma_{max}$	Maximum mechanical stimulation for CM differentiation	-0.01	Li et al., 2012; Stoppel et al., 2016
$\gamma_{apop}$	Maximum mechanical stimulation for cell apoptosis	0.6	Chen et al., 2008; Kang et al., 2011

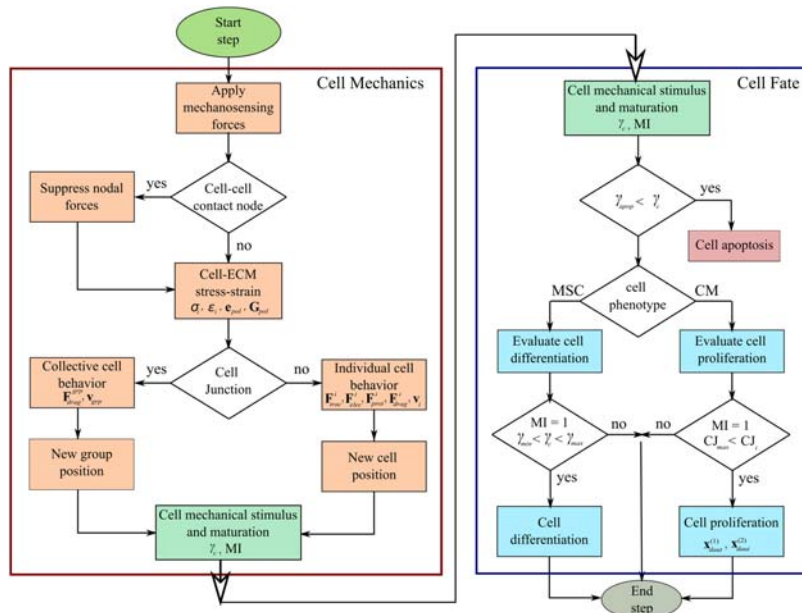


FIGURE 23.4 Algorithm. Model algorithm.

are able to ensure cell survival. Besides, neither nutrient nor oxygen consumption has been considered. The considered cell phenotypes have been simplified to determinate cell mechanical properties, i.e., cell stiffness, maximum cell strains, etc. These properties need to be calibrated for new simulations. In addition, cell morphology has been considered as a constant quasi-spherical cell defined by a constant cell radius.

## Numerical implementation and applications

Single-cell models, which are based on individual cells, are very helpful to understand cell behavior, as well as its evolution over time. In fact, processes such as cell maturation and differentiation, which depend on the active interaction of cells with their environment, must be considered as a continuous evolution during cell development. In addition, these models can study specific positions of cells during the formation of tissues. This makes it possible to evaluate cell–cell interactions and the establishment of stable cell adhesions, being very useful to define the cellular architecture of tissues (Urdeix & Doweidar, 2020a, 2020b, 2021).

On the other hand, using single-cell models, it is possible to evaluate the stresses and strains to which the cell is subjected. In this sense, different studies have highlighted the importance of mechanical stimulation during the development of cardiac

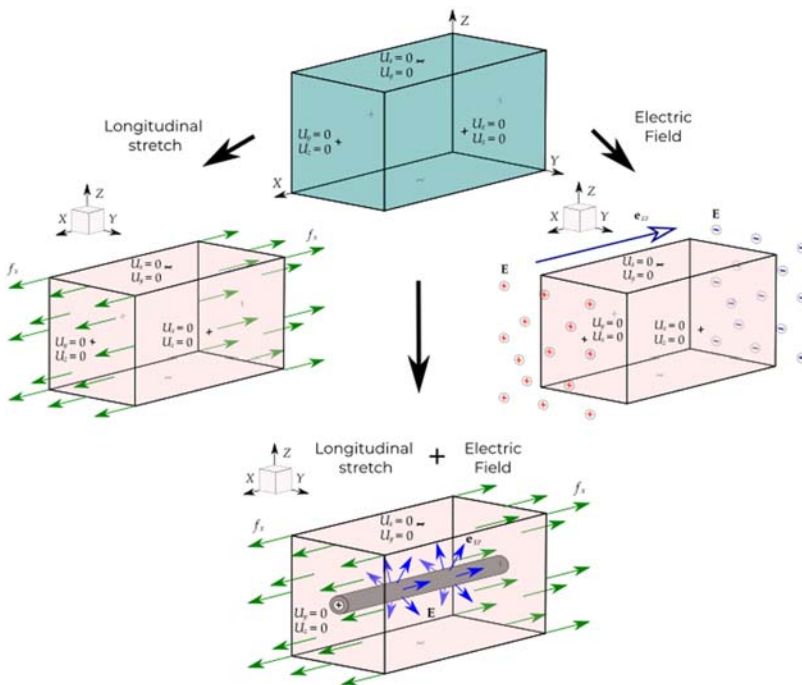


**FIGURE 23.5 Boundary conditions.**

Boundary conditions applied to the ECM. A central point on the ECM external faces are restricted in the plain direction. Longitudinal stretch is applied by applying longitudinal forces on the external faces of the ECM. EFs are applied through the consideration of differential electric charges on the external faces of the ECM in the longitudinal direction. Coupling of the electric and mechanical stimuli can be applied through the stretch of a central fiber with piezoelectric properties.

tissues. Hence, mechanical stimulation may be beneficial for the growth and reorientation of the contractile apparatus of cells (Stoppel et al., 2016). Next, a series of experiments are presented where some of the most relevant aspects of cell mechanics are evaluated under different stimulation conditions. These experiments make it possible to qualitatively predict the behavior of cells with adherent characteristics such as MSCs and CMs.

## Cell–cell contact forces

Cells have an innate ability to recognize and respond to the different stimuli in their environment (mechanical, chemical, thermal, etc.). This aspect, from the biological point of view, establishes the survival capacity of cells by adapting themselves to their environment. Furthermore, it provides a feasible explanation for the integration of diverse cellular phenotypes in complex microenvironments within the organism.

For example, the bone matrix, made up of osteocytes, osteoblasts, and osteoclasts, is capable of remodeling itself locally in the direction and density of the fibers depending on the mechanical stresses (direction and magnitude) to which it is subjected (Roesler, 1987). On the other hand, the specific processes of mechanotransduction in specific biological responses are multiple and still should be studied in depth (De et al., 2008; Saez et al., 2005). Some studies point to the deformations in the cell nucleus membrane (Buxboim et al., 2010), or to changes in proteins in the environment of the cell nucleus (Trubelja & Bao, 2018).

Moreover, the presence of other cells in the environment is another important aspect to be considered in evaluating the mechanical stimulus. This will generate cell–cell and cell–ECM interaction, which produces complex interactions between strain and stresses in the ECM (see Fig. 23.6). Cell contractions generate an increase in the ECM stiffness in its closest surrounding, which is able to alter the deformations of neighboring cells. For instance, when analyzing a specific case, such as that of two cells in contact (see Fig. 23.6), it is possible to realize that strains in the direction of the cell radius (according to Eq. 23.19) should be zero. However, the stresses, which are essential to maintain cell–cell adhesion, are not zero (Fig. 23.6) (Shrivastava et al., 2012). This illustrates that strain-based migration can be representative of cell behavior.

### Cell differentiation modulated by ECM stiffness

ECM stiffness, among others, is capable of modulating the behavior of cells. In fact, different studies have shown that cell differentiation can be guided spontaneously by the ECM stiffness (Bhana et al., 2010; Engler et al., 2006; Schmelter et al., 2006).

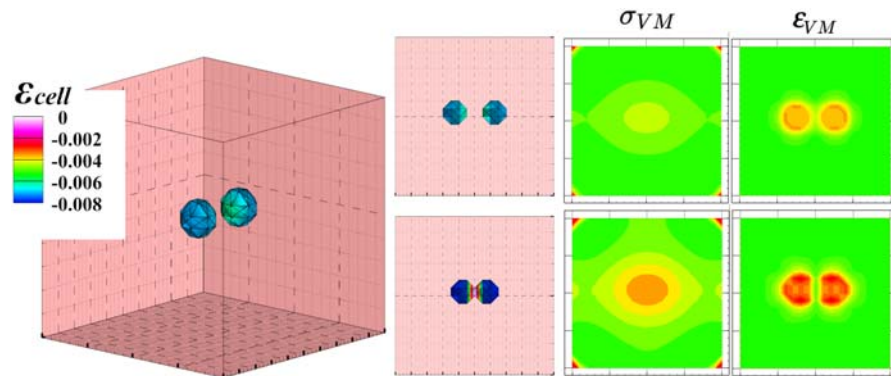


**FIGURE 23.6 Cell–cell contact forces.**

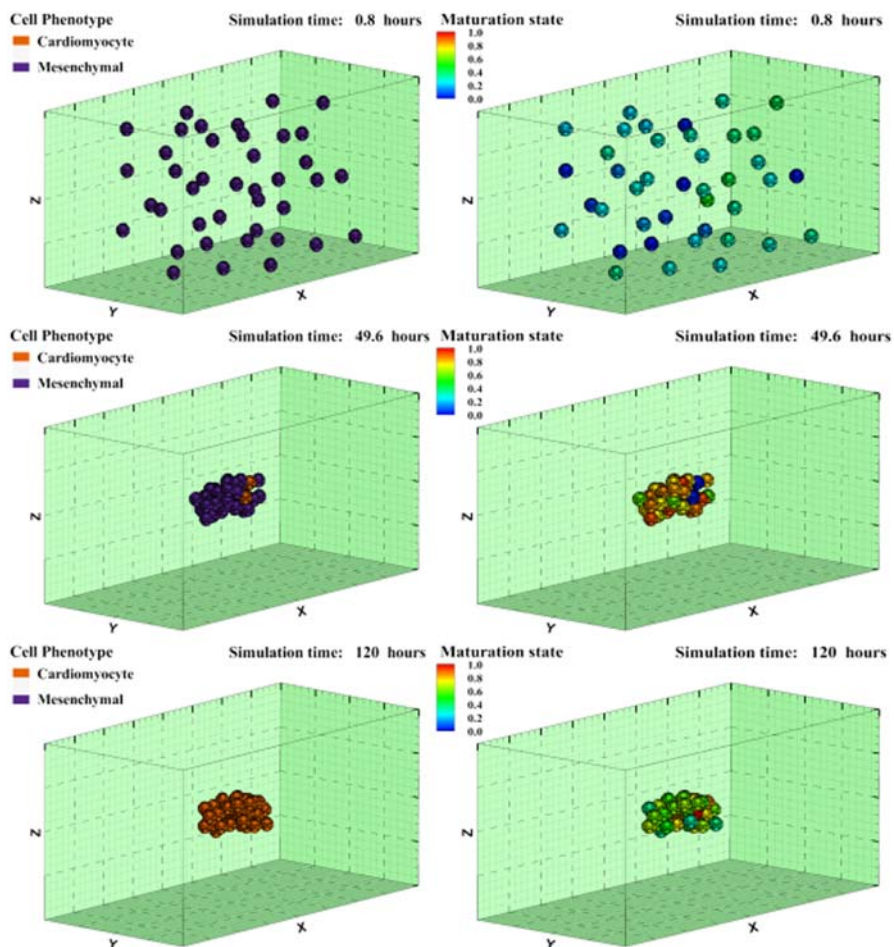
Cells are able to detect surrounding cells due to the effect of the cell–ECM interaction. Thus, cell internal deformations are less pronounced in faces close to other cells. Cell–cell interactions, due to the active cell sensing forces, produce zero deformations in cell–cell contact faces where the cell stresses are not equal to zero.

Engler et al. studied the differentiation of MSCs in hydrogels of different stiffness. In their study, they concluded that the use of matrices whose stiffness mimics a determined living tissue could guide cell differentiation into imitated tissue phenotypes (Engler et al., 2006). Later, Li et al. studied the effects of stiffness on the differentiation of MSCs into cardiac cells, obtaining better results for stiffnesses comparable to those of healthy cardiac tissues (Li et al., 2012). Similarly, Young et al. observed the differentiation of CMs in matrices of 1, 11, and 34 kPa, with better results for greater stiffness (Young et al., 2014). However, for stiffness of 34 kPa, equivalent to the stiffness of fibrotic niches, cell maturation was more affected by higher stiffnesses. Stoppel et al., in their interesting review, pointed out that the use of matrices with stiffness higher than that of cardiac tissue could impair or even inhibit cell maturation (Stoppel et al., 2016). In this way, it is observed that the complexity of the mechanical environment of the cells, as well as their temporal evolution, is of high relevance in the development of cardiac tissues. The evaluation of optimal conditions can be studied using independent cell-based computational models.

In the following example, the spontaneous differentiation of MSCs into CMs has been evaluated within ECMs with stiffnesses in the range of 8–20 kPa (see Fig. 23.5). In this example, the evolution of the differentiation of 40 MSCs, initially randomly distributed within a free surface ECM, during a period of 5 days is presented. When MSCs are cultured within an ECM of a rigidity that is comparable to the rigidity of cardiac tissue, they evaluate the rigidity of their environment and, progressively, initiate differentiation.

Cells, initially distributed on the ECM, are guided by the ECM stiffness and migrate toward the center of the ECM, which, due to the boundary conditions, is the stiffest part of the ECM. As the cells migrate, their internal deformation is proportional to the ECM stiffness, which defines the mechanical stimulus perceived by the cell. As the ECM stiffness is in the range of the cardiac tissue, cell mechanical stimulus is in the range to promote cardiac differentiation. Later, as more cells migrate toward the central zone, cell internal deformations are reduced due to the presence of surrounding cells. Once cells reach the central zone, they interact with other cells and remain close to the central zone. After 30 h of interaction, MSCs start to trigger differentiation, and some CMs can be seen in the simulation (Fig. 23.7). Different MI can be observed for different cells, due to the specific mechanical conditions of each cell. The maturation of the cells is faster in stiffer ECMs, and faster differentiation can be observed with stiffer ECM (Fig. 23.8). For instance, in ECM with 8.0 kPa, cells initiate the differentiation after 48 h, and after 92 h all the cells have been differentiated. On the stiffer ECM, with 20.0 kPa, cells start differentiation after 30 h, and after 60 h all the cells have been differentiated.

As it is exposed in the model formulation, cell forces are proportional to the internal cell deformations, being the mean traction forces higher in stiffer ECM (Fig. 23.8). As cells differentiate, cells are considered to acquire specialization in stress generation. An increase in the traction force can be observed during cell differentiation into CMs. In Fig. 23.8, two transitions can be observed in the mean cell

**FIGURE 23.7 Cell differentiation;**

Cell phenotype (left) and cell Maturation Index (right) for cells distributed into a ECM with 15 kPa stiffness. Cells start differentiation after 49 h of cell–ECM interaction. After 120 h, all the cells are properly differentiated into CMs phenotype.

traction forces. The first increase in the cell traction forces is related to the migration of the cell toward the central zone, which is the stiffest zone of the ECM and where cell internal deformations are reduced. The second transition corresponds to cell differentiation, where cell internal stresses are considered to be higher due to phenotype specialization. Finally, traction forces are stabilized due to the end of cell differentiation and the reduced cell motility. As the ECM stiffness increases, this can be clearly observed.

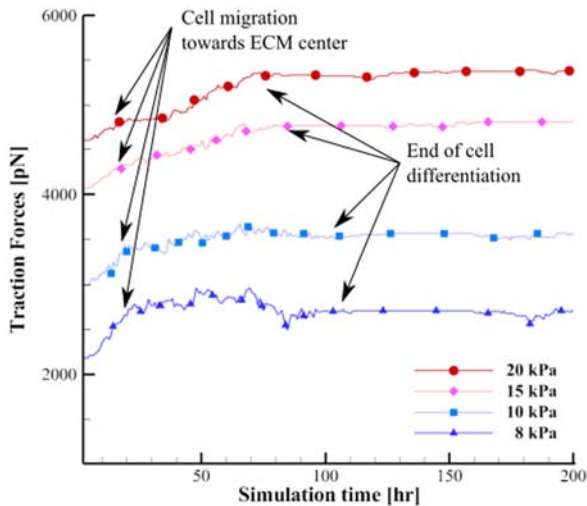


**FIGURE 23.8 Mean cell traction forces.**

Cell traction forces depend on the cell phenotype and the cell internal deformations. As cells migrate toward the central zone of the ECM, cell internal deformation is reduced, which increases mean cell traction forces. Cell differentiation times depend on the ECM stiffness being faster on stiffer ECMs.

### Cell adhesions modulated by ECM stiffness

Cardiac cells have the ability to establish special cell–cell stable adhesions, which define cardiac cell architectures. In this sense, cell architectures adopted by CMs would be different from those adopted by other cell phenotypes. Thus, the architectures adopted by CMs due to their interaction with ECMs of 8, 10, 15, and 20 kPa stiffness have been compared with fibroblasts seeded in ECMs with 35 kPa stiffness. The first group of stiffnesses corresponds to the healthy cardiac tissues, while the last one corresponds to fibrotic niches (Mousavi et al., 2013a, 2013b; Young et al., 2014). In both cases, 40 cells are randomly seeded in the ECM during 15 days of cell–cell and cell–ECM interactions. In this case, cells are considered previously differentiated, so CMs and fibroblasts are considered throughout the simulation.

The results show, in all the cases, cells migration toward the central zone of the ECM, with faster migration for stiffer ECM (Fig. 23.9). While CMs are migrating toward the central zone, they are interacting and forming some groups with stable cell adhesions. Initially, these groups are formed by a few cells, and more cells tend to be incorporated as cell–cell contact increases. Cells that lack stable adhesion have the ability to proliferate. However, when considerable groups of cells are formed, cells in the interior zones exhibit cell proliferation inhibition due to the stable contact with other cells. This is not the case for fibroblasts, where cell contact inhibition is not considered. Thus, the final total number of cells is higher in fibroblasts simulation. Moreover, as cell maturation is faster in rigid ECMs, at the end of

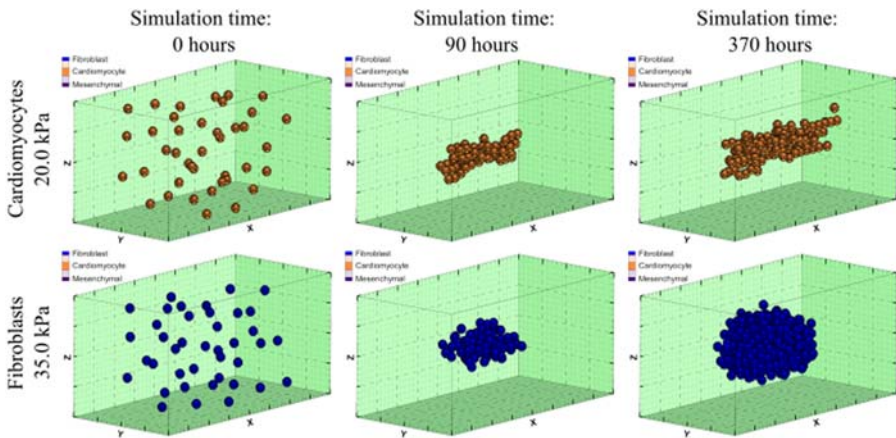


**FIGURE 23.9 Cell–cell adhesions.**

Cell–cell interaction has been compared for CMs and fibroblasts. In the case of CMs, an elongated group of cells is formed after 90 h of simulation. In contrast, fibroblasts are grouped into a spherical aggregation. After 370 h, the total number of fibroblasts is much higher than CMs, where contact inhibition of proliferation has been considered.

the experiments, the total number of CMs is higher in stiffer ECMs than in softer ECMs (Fig. 23.10A).

The rate of group formation seems to be different for the different ECMs stiffnesses. This is due to the increase of the motility of the cells in stiffer ECMs (Fig. 23.10B). As cells migrate faster in stiffer ECMs, groups of cells tend to be formed faster in the center of the ECM. In contrast, in soft ECMs, the major groups of cells are formed by pairs of cells. Besides, they are formed in the outer parts of the ECMs, then migrate collectively toward the central zone. Once these groups join each other, more elongated groups are formed. Later, the increasing number of CMs, due to cell proliferation, increases the groups' population. Both the number of cells in the main chain and the chain longitude are shown to be higher in stiffer ECMs (Fig. 23.10). At the end of the simulation, CMs form one main elongated aggregation, while fibroblasts form a spherical aggregation in the center of the ECMs.

### Mechanically stimulated ECMs

Cardiac cells have shown some alterations in their maturation when they are mechanically stimulated (Stoppel et al., 2016). Some studies have shown that mechanical stimulation can be beneficial for the development of the cardiac cell–cell junctions, as well as for the contractile apparatus orientation and development (Camelliti et al., 2005; Chen et al., 2008; Costa et al., 2003; Formigli et al., 2009; Heidi Au et al., 2009). For instance, during tissue development in embryonic stages, a combination of the mechanical and chemical cues promotes cell alignment in muscle tissues which improves muscle tissue functionality (Reig et al., 2014; Stoppel

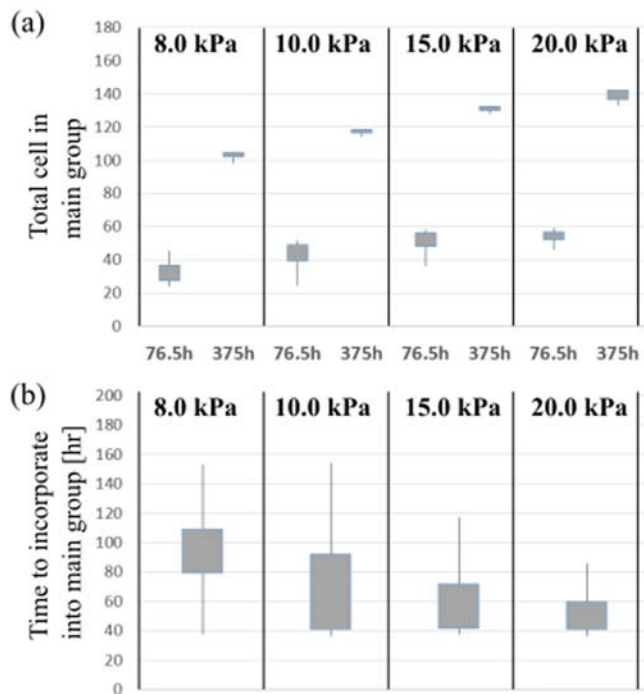


**FIGURE 23.10 Cell response to the ECM stiffness.**

ECMs stiffness increases cell maturation rates and cell motility. (A) The number of cells in the main group is higher as the ECM stiffness is increased. (B) Cell motility is increased in stiffer ECMs, which reduced time is necessary to form one main group of cells (at least 50% of the cells).

et al., 2016). However, an excessive strain on the cell membrane, due to excessive external mechanical stimulation, can increase cell apoptosis (Elmore, 2007; Kearney et al., 2008). In this sense, it is necessary to adequately evaluate the mechanical conditions applied for cell stimulation to avoid cell damage, but increasing cell maturation and correctly orientated cell architectures. In the last decades, different strategies have been studied to promote cell alignment in the development of cardiac tissues, which improves tissue functionality (Rangarajan et al., 2014; Stoppel et al., 2016; Zhang et al., 2013). Although the generated contractile forces by in-vitro cardiac tissues have been improved, they are still not comparable to those developed by healthy adult tissues (Jackman et al., 2016; Planat-Bénard et al., 2004; Rodriguez et al., 2014; Asumda, 2013). Thus, computational single-cell models, which are able to focus on the study of cell–cell and cell–ECM interaction under mechanical stimulation, can be a useful tool to define the optimal conditions for cell mechanical stimulation.

In the next example (Fig. 23.11), CMs are randomly seeded in different ECMs stiffnesses which have been mechanically stimulated by imposing a longitudinal deformation between 5% and 35% (see Fig. 23.5). Cell deformation due to the passive ECM deformation is not considered, as cells are able to adapt themselves quickly (compared to the simulation time scale) to these deformations. However, the ECM presents residual internal stresses proportional to the applied deformation in the longitudinal axis. These internal stresses reduce cell deformations in this direction, inducing cell polarization in the longitudinal direction. Like the other examples, 40 CMs are initially randomly seeded in predeformed ECMs with stiffnesses in the range of 8–50 kPa. Cell–cell interaction and groups formations have been studied for 15 days.

Results for the different cases have been compared via the Aspect Ratio (AR) of the formed groups. This parameter compares group's length with their width. It can be defined as:

$$AR = \left[ \frac{l_x^2}{l_y l_z} \right]^{0.5} \quad (23.27)$$

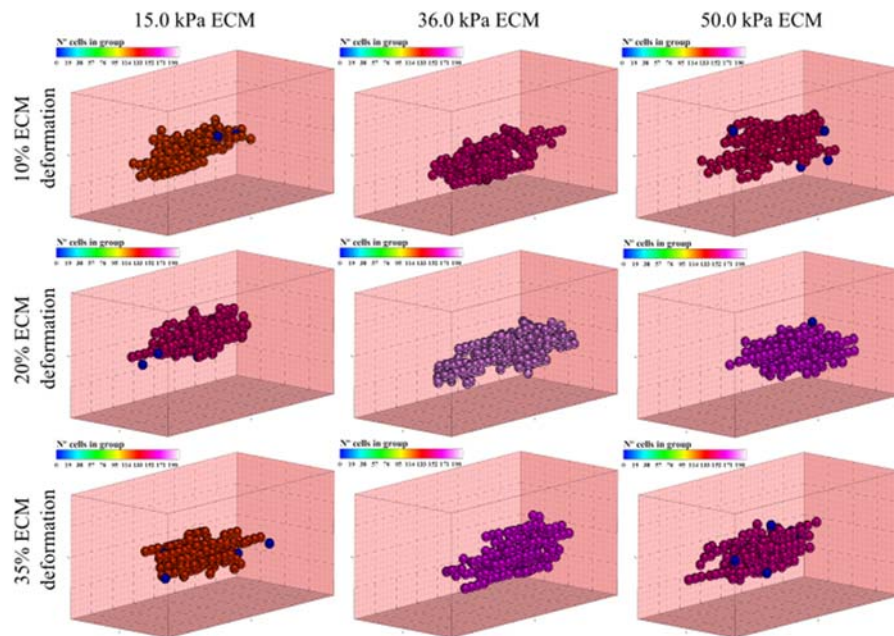


**FIGURE 23.11** Group's formation under mechanical stimulation.

CMs are seeded in ECMs with 15, 36, and 50 kPa stiffness, and mechanically stimulated by 10%, 20%, and 35% of ECM deformation. An increase in cell number is observed, and better group's orientation are obtained for intermediate ECM stiffness (36 kPa) with intermediate ECM deformations (20%). An excessive ECM stiffness (50 kPa), or excessive ECM deformation (35%), is unfavorable for cells interaction, proliferation, and groups formation.

being  $l_x$ ,  $l_y$ , and  $l_z$ , the dimensions of the groups in  $X$ ,  $Y$ , and  $Z$  direction, respectively.

Compared to nonstimulated cases, an increase in cell alignment can be observed in all the cases (Fig. 23.11). The residual forces of the ECM reduce the cell's internal deformation, which translates into faster maturation and an increase in cell proliferation. For the same ECM stiffness, an increase in the total number of cells is observed (Fig. 23.12A). However, in higher ECM deformations a decrease in the number of cells is observed, which shows a worsening in the mechanical conditions. Thus, better results are obtained for medium ECM deformations (20%–25%). Moreover, as in the previous example, an increase in the ECM stiffness is translated to an increase of the cell proliferation for stiffnesses up to 40 kPa. At this point, any increase in the stiffness reduces the total number of cells at the end of the simulation. These two cases illustrate how excessive mechanical stimulation, out of the working range of the healthy tissue, can produce negative effects in CMs maturation and, consequently, cardiac tissue formation (Fig. 23.12). Besides, an excessive rigid condition, both for elevated stiffness and/or elevated residual stresses, can reduce cell penetration during cell migration and even cell apoptosis can be triggered. This can also be observed for the AR values, where intermediate ECM stiffness shows better results (Fig. 23.12B). In this sense, only a slight increase in AR can be observable. However, considering the increase of the cell number in groups, even if the increase in the AR is not highly pronounced, the visual aspect of the cell groups is clearly more elongated for the intermediate cases (see Fig. 23.11). This observable difference can be attributed to the growth of the groups, which inherently entails a thickening of the groups. Slight increases in AR, while progressively increasing the number of cells in the group, will lead to large groups of cells with an architecture properly oriented in the longitudinal direction. In this way, it is possible to observe

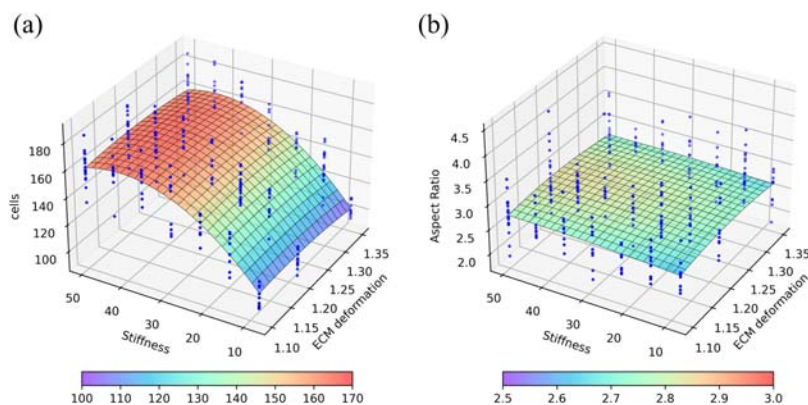


**FIGURE 23.12 Group's formation under mechanically stimulated ECM.**

(A) The increase in the ECM stiffness increases cell proliferation. (B) The AR is higher for ECM deformations in the range of the 1.2–1.3.

that the effect of the residual forces is maintained throughout the simulation and contributes to the reposition of the new cells generated in the proliferation.

### Electrically stimulated ECM

Electrical stimulation has been shown to be relevant for CMs maturation. As well, it has benefits in the cell–cell ion channels, which promote the coordination of cell contractility due to the increase of AM spontaneous contractility. For such stimulation, pulsative low-frequency currents are usually applied. For instance, Radisic et al., 2004 studied CMs electric stimulation under monophasic EF. They observed an increase in the cell alignment, which promotes the formation of aligned myofibers in the direction of the applied stimulus (Stoppel et al., 2016). In this sense, in-vitro experiments have been developed where physiological dcEFs are applied (Baumgartner et al., 2015; Pietronave et al., 2014; Radisic et al., 2004). These experiments have shown that the application of dcEFs improves the formation of GAP junctions and cell contractility. Moreover, Pietronave et al., 2014 have studied Cardiac Progenitor cells (CPCs) under electric stimulation (monophasic and biphasic EFs), they observe an increase in the expression of the cardiac markers and in the cell alignment (Pietronave et al., 2014). Due to the observed relevance of the electric stimulation in CMs maturation and tissue functionality, it could be interesting to evaluate the optimum specific cell conditions for controlled cell response. Thus, some examples are prepared for different electric stimulation conditions, where individual cell response and groups' formation can be evaluated.

In these examples, 40 CMs are studied under the effect of different EFs in the range of 50–350 V/m, in ECMs with stiffness in the range of 10–40 kPa (see Fig. 23.5). The EF conditions have also been varied by stimulating the cells with unidirectional continuous and pulsative EFs, and bidirectional alternating EFs (Fig. 23.13). In such cases, cells are guided by the ECM mechanical stiffness as well as the applied direction of the electric stimulation, which is applied in the longitudinal direction for all the cases. The ECM stiffness guides the cells toward the central zone of the ECM, which is the stiffer part of the ECM, where the EF guides the cells to migrate longitudinally. For low ECM stiffnesses, the EF stimulus tends to be higher, which pulls the cells out of the central zones. On the contrary, at high ECM stiffness, with low EF, cells tend to migrate toward the central zone. The adequate equilibrium of the mechanical and electrical stimuli seems to be the key clue to reproduce appropriate cell orientation, as well as to improve cell–cell contact and tissue maturation.

Cells studied under unidirectional continuous EF show a tendency to migrate in the direction of the EF, depending on the ECM stiffness and the EF intensity. As the stiffness increases, this migratory tendency is reduced. At 40 kPa ECM stiffness, cells remain in the center of the ECM. In high EF stimulation, with low ECM stiffness, groups formation seems to be reduced due to the excessive drag produced by the EF. Increasing the ECM stiffness, the drag effect of the EF is reduced while the effect of the cell directionality is maintained. In this sense, better results are obtained

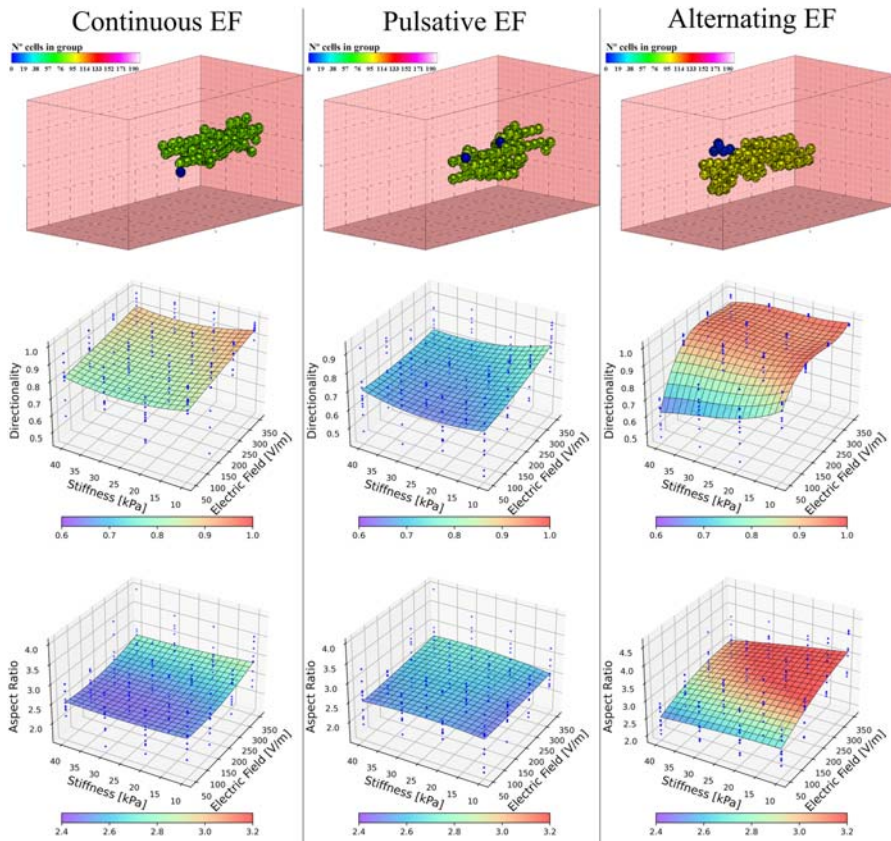


**FIGURE 23.13 CMs electrically stimulated.**

CMs are electrically stimulated under continuous, pulsatile, and alternative EFs. The directionality of the cells is clearly increased with the increase of the EF intensity. Continuous EFs generate an excessive drag of the cells toward the external face of the ECM. Pulsatile EFs reduce this drag effect, which reduces cells directionality and groups AR. Alternative EFs maintain cells directionality without the undesired drag effect, which turns into high directionality of the cells, and highly elongated groups. Maximum directionality is obtained for 150 V/m EF, where a saturation effect of the directionality is being observed.

when the electric and mechanical stimuli are equilibrated. The excessive drag produced by the continuous EF can be reduced by applying a discontinuous EF. In this case, cells are oriented by the EF during the active phase, while cells are guided toward the central zone when the EF is deactivated. This equilibrium improves groups formation by reducing the CMs migration toward the direction of the EF. At the end of the simulation, even for high EF and low ECM stiffness, cells remain close to the central zone. However, the reduction of the effective electric stimulation, due to the

deactivation of the EFs, reduces both the directionality of the cells and the AR of the formed groups (Fig. 23.13). Alternating EF can also be applied to reduce cells migration toward the outer faces of the ECM. In this case, cells are oriented in the longitudinal direction, but the migration direction is reversed as the EF changes its directionality. This effect reduces the effective cell migration along the longitudinal direction while the cells remain migrating toward the central zone of the ECM. Cell's directionality is maintained even with the change of the direction of the EF, which stimulates the formation of elongated groups morphology (Fig. 23.13). In this sense, AR is highly increased. It can also be observed that a saturation in the directionality is obtained for EFs above 150 V/m, while the AR seems to increase linearly with the increase of the EF intensity. As cell–cell contact is established, the high directionality of the cells establishes a well-oriented CJ. When more cells are incorporated into the groups, high elongated groups are formed. Low EF intensities reduce the migration due to the EF effect, and cells migrate faster toward the central zone but maintaining a well-oriented directionality. This produces elongated groups in the central zone of the ECM. On the contrary, high EF reduces the effective migration of the cells toward the central zone, which stimulates the cells to proliferate while they are approaching the ECM center. This effect delays the formation of the groups, but when formed, the elongated shape is increased compared with low EFs. In the case of the alternating EF, the effect of the key role of the ECM stiffness seems to be reduced. In all the cases, cells migrate toward the central zone, and the effective cell translocation is mainly controlled by the EF intensity.

### Advanced materials for mechanoelectrical stimulation coupling

Advanced materials can be a valuable tool to mimic biological tissues, which usually present complex properties (Chen et al., 2008; Tibbitt & Anseth, 2009; Yim et al., 2010). For instance, Young et al., 2011 presented time-dependent stiffness hydrogels which promote cardiac cell differentiation. These hydrogels mimic the mechanical properties in cardiac tissues which show an increase in stiffness as cells mature. Moreover, other characteristics can be mimicked with advanced materials, for example, to induce electric and mechanical stimulation on the cells (Banks et al., 2015; Ribeiro et al., 2015). In this sense, piezoelectric collagen fibers can be a good alternative with which mechanical and electrical stimuli can be coupled (Banks et al., 2015). Thus, it may be possible to stimulate a tissue by external electric fields to induce an internal mechanical stimulation in the tissue, or to stimulate mechanically (by applying ECM deformations) to induce an internal electric field (Urdeitx & Doweidar, 2021). This can be useful to stimulate cardiac cells by coupling mechanical and electric stimuli to improve cell alignment, maturation, and tissue formation.

In the next example, a single-cell model has been applied to study cardiac cell maturation and cell–cell interaction in an electric and mechanically stimulated ECM. The ECM includes an internal piezoelectric (PZE) material, which can produce an EF due to mechanical stimulation (see Fig. 23.5). The PZE fiber, located longitudinally in the center of the ECM, has been considered as a rigid body where

cells cannot migrate. The longitudinal deformation in the ECM, translated into an electric field around the PZE fiber, is considered to be proportional to the ECM deformation, which guides cells to migrate toward the central fiber. In this case, 60 pre-differentiated CMs were placed randomly in the ECM. The ECM has 20 kPa stiffness with a PZE fiber which has 25 kPa stiffness. Cells are stimulated by applying different considerations to compare the PZE effect on the cells. In the first step, cells are located into the ECM without any external deformations, and with this, no EF stimuli exist. In the second step, the effect of the ECM deformation has been studied without considering PZE effect (no EFs were applied). For this purpose, it has been applied a longitudinal deformation of 0.25, which is in the range of cardiac deformation. Finally, to modulate the electric field generated by the PZE fiber, different thicknesses of the central PZE are considered in the range of 2–18  $\mu\text{m}$ . These configurations, considering an external deformation of the ECM of 0.25, generate EF in the range of 50–200 V/m, being higher the EF as the thickness of the PZE fiber increases. In this last step, the mechanical and electrical stimuli are coupled and can be controlled easily by controlling the ECM deformations as well as the PZE thickness. For all the cases, cell–cell and cell–ECM interactions are simulated for 250 h ([Fig. 23.14](#)).

Cells without either electrical or mechanical stimulation tend to migrate toward the central zone of the ECM, forming groups in the central zone ([Fig. 23.14](#)). As the ECM longitudinal deformation is applied, cells increase the tendency to spread over the central fiber, due to the increase of the stiffness in the longitudinal direction. When PZE effect is considered, the mechanical stimulus in the longitudinal direction is coupled with the EF toward the central fiber. These two effects increase the velocity with which the cells migrate toward the central fiber, which highly increases the AR of the groups. In this last case, as the cells migrate faster toward the central fiber, which corresponds to the stiffer part of the ECM due to the stiffening effect of the stiffer PZE fiber, cell maturation is faster and cell proliferation increases.

As the PZE fiber thickness is increased, the generated EF is higher, which increases cell electrotaxis and cell migration toward the central fiber. This implies faster cell migrations due to the higher EF stimulations, as was observed in other cases. Thus, as PZE thickness increases, the longitudinal orientation of the groups is increased, which is represented by the AR parameter ([Fig. 23.14](#)). In this sense, PZE fiber can be useful to promote determined cell architectures during tissue formation by guiding cell orientation, while tissue maturation is improved due to the coupling of the mechanical and electrical stimuli. These two effects can play a key role in developing high functional tissues, with well-oriented sarcomeres and synchronous tissue contractions.

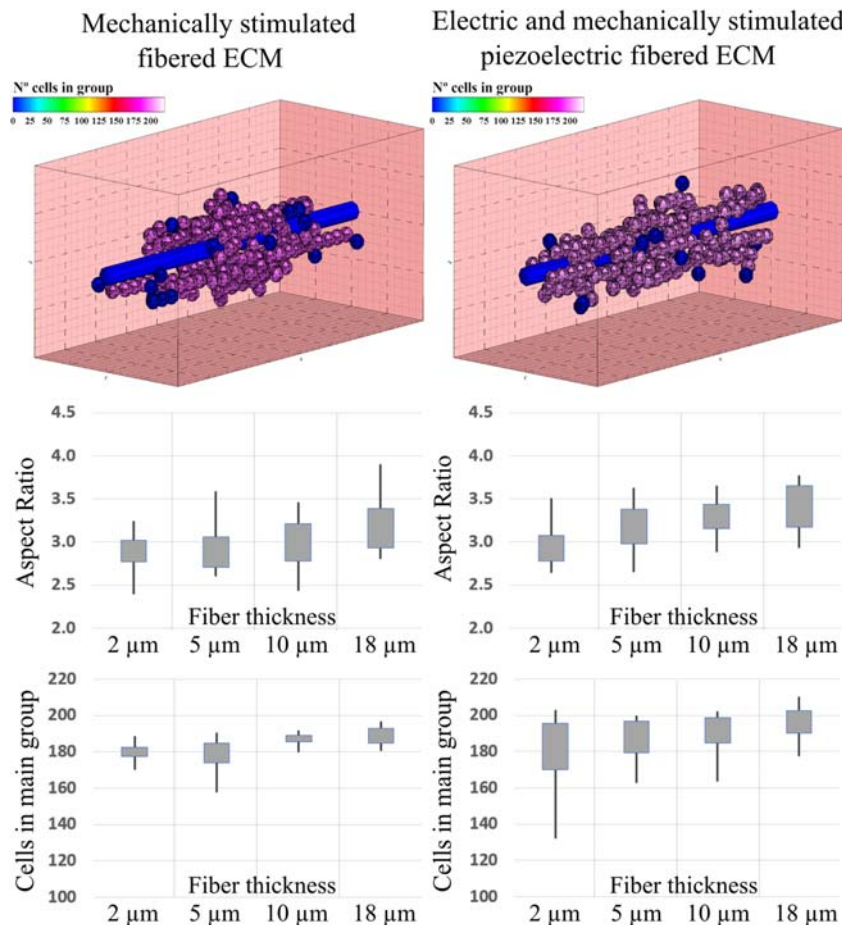


FIGURE 23.14 CMs seeded on a fibered ECM.

Cells interact with a PZE fibered electromechanically stimulated ECM. AR of the groups is strongly related to the fiber thickness, due to the stiffening effect of the central fiber. Cell proliferation is also increased with an increase in fiber thickness. As long as we consider PZE effect generated by the central fiber, which is proportional to the fiber thickness, cell migration toward the central zone increases. Besides, cell proliferation (cell number) and AR of the groups are increased.

## Conclusions

Electric and mechanical stimulation have been observed to play a key role in cardiac cell maturation and tissue formation, being relevant during the formation of cell architectures and tissue anisotropy. In fact, the generated cardiac tissue stresses

depend on the cell architecture, including the formation of well-organized sarcomeres, and cell–cell ion-channel intercommunications (Formigli et al., 2009; Li et al., 2012). Single-cell models can offer new perspectives to study cell–cell and cell–ECM interactions being able to define cell–cell organization during tissue formation under the effects of different stimuli (Mousavi, Doblaré et al., 2014; Urdeix & Doweidar, 2021). In this sense, the presented model establishes the bases to define and simulate different cell key role processes including cell migration, differentiation, proliferation, and apoptosis, as well as the consideration collective cell behavior by the formation of stable groups. All these processes are studied in 3D environments with multiple stimuli, including ECM stiffness, and mechanical and electrical active stimulation. Due to the simplicity of the model, several cell–cell interactions can be studied in complex multisignalling ECMs. The parametrization of different cell properties allows us to define multiple cell conditions, and differences in cell properties, to establish parametric studies which can be helpful for in-vitro studies.

The presented model has been employed to study cardiac tissue formation from a single-cell perspective, giving high interest to the formation of cell group architectures in cardiac tissues due to the anisotropic ECM conditions. In the first step, cardiac cell differentiation has been considered from MSCs, due to the ECM stiffness. Then, different mechanical and electrical conditions have been considered to stimulate differentiated CMs. When both mechanical and electrical stimuli are applied, their values in all the cases are in the range of those that can be found in biological tissues. Taking into account the assumptions of the presented model, it can be observed that the obtained results are qualitatively consistent with the corresponding bibliography (Baumgartner et al., 2015; Chen et al., 2019; Pietronave et al., 2014; Radisic et al., 2004; Sauer et al., 1999).

The ECM stiffness increases the mechanical stimulus of the cells, which increases cell maturation and cell proliferation. Besides, longitudinal ECM deformations can promote the formation of elongated cell group architectures depending on the applied deformation. However, for ECM deformations out of the range of cardiac tissues, worse results can be observed, which indicates suboptimum conditions for cell development. Moreover, electric stimulation plays a key role in the directionality of the cell polarization, being this proportional to the intensity of the applied EFs. So, it is necessary to take into account that an excessive EF can drag cells toward the outer face of the ECM rapidly, which impede adequate cell–cell interactions. The electric stimulus is proportional to the EF intensity and inversely proportional to the ECM stiffness. Thus, stiff ECMs are able to retain cells at the center of the ECM even for high EFs stimulation, due to the increase of the mechanical stimulus. However, for low stiffness ECMs, the electric stimulus is more intense. The excess drag effect of the EFs can be avoided by changing the mode of application of the EFs (Hiemer et al., 2018; Urdeix & Doweidar, 2020a). With discontinuous EFs, although the effect of the electric stimulus is reduced, cells, and groups retain the migratory tendency toward the cathodic face of the ECM. By applying alternating EFs, cells' effective motility in the longitudinal direction is dramatically

reduced, and cells are retained in the center of the ECM. In this case, high EFs can be applied to induce cell polarization in the longitudinal direction, and well-oriented cell group architectures can be obtained. Finally, the electric and mechanical stimulation can be coupled by using advanced materials where an electric response can be generated due to their mechanical deformation as in the case of the PZE materials. PZE fibers generate an electric field proportional to the applied strain, by exchanging strain energy with electrical energy, which can be a useful tool to mimic complex mechanoelectric environments in cardiac tissues (Chen et al., 2008). Thus, PZE fiber has been considered to apply electric stimulation due to the longitudinal deformation of the ECM, coupling in this way the mechanical and electrical stimuli. The coupling of these effects highly increases the cell group longitudinal formation. In this case, the EF guides cells to migrate toward the central fiber, being the cell motility proportional to the electric field generated by the PZE fiber. Once the cells reach the central fiber, they tend to remain close to it, where elongated groups of cells are formed. In this case, the topographic stimulus can also be considered for cells in contact with the PZE fiber due to the differences between the ECM and fiber stiffness. In consequence, groups with higher AR can be obtained by the consideration of the PZE fiber with the maximum EF in comparison with those obtained without mechanical and electrical stimulation. The consideration of PZE fibers into the ECM can be a helpful tool for the coupling of the mechanical and electrical stimuli. Moreover, the PZE properties make it possible to control internal mechanical deformations on the ECM by applying an external EF, and vice versa.

Despite the model limitations, which have been defined in the Assumptions section, the presented single-cell model can be considered a valuable tool to predict cardiac cell behavior under complex mechanical and/or electrical conditions. With this model, the coupling of electrical and mechanical stimuli can be evaluated, which has been observed to be relevant in cardiac tissue formation. The EFs mode of application, such as external EFs or by the consideration of the PZE effects, can significantly change cell–cell interaction and the adopted cell architectures. This gives support to the idea of establishing preliminary studies with computational models, to define the appropriate boundary conditions for in-vitro cell cultures. Thus, some parametric studies can be developed with computational models, with reduced time and economic cost, to dramatically reduce the number of in-vitro and in-vivo experiments needed to validate the proposed hypothesis.

---

## Acknowledgments

The authors gratefully acknowledge the financial support through the project PID2019-106099RB-C44, funded by MCIN/AEI/10.13039/501100011033, the Government of Aragon (DGA-T24\_20R), and the Biomedical Research Networking Center in Bioengineering, Biomaterials and Nanomedicine (CIBER-BBN). CIBER-BBN is financed by the Instituto de Salud Carlos III with assistance from the European Regional Development Fund.

---

## References

- Ahuja, P., Sdek, P., & MacLellan, W. R. (2007). Cardiac myocyte cell cycle control in development, disease, and regeneration. *Physiological Reviews*, 87(2), 521–544. <https://doi.org/10.1152/physrev.00032.2006>
- Asumda, F. Z. (2013). Towards the development of a reliable protocol for mesenchymal stem cell cardiomyogenesis. *Stem Cell Discovery*, 13–21. <https://doi.org/10.4236/scd.2013.31003>
- Aragona, M., Panciera, T., Manfrin, A., Giulitti, S., Michielin, F., Elvassore, N., Dupont, S., & Piccolo, S. (2013). A mechanical checkpoint controls multicellular growth through YAP/TAZ regulation by actin-processing factors. *Cell*, 154(5), 1047–1059. <https://doi.org/10.1016/j.cell.2013.07.042>
- Ayensa-Jiménez, J., Pérez-Aliacar, M., Randelovic, T., Oliván, S., Fernández, L., Sanz-Herrera, J. A., Ochoa, I., Doweidar, M. H., & Doblaré, M. (2020). Mathematical formulation and parametric analysis of in vitro cell models in microfluidic devices: Application to different stages of glioblastoma evolution. *Scientific Reports*, 10(1). <https://doi.org/10.1038/s41598-020-78215-3>
- Banks, T. A., Luckman, P. S. B., Frith, J. E., & Cooper-White, J. J. (2015). Effects of electric fields on human mesenchymal stem cell behaviour and morphology using a novel multi-channel device. *Integrative Biology (United Kingdom)*, 7(6), 693–712. <https://doi.org/10.1039/c4ib00297k>
- Baumgartner, S., Halbach, M., Krausgrill, B., Maass, M., Srinivasan, S. P., Sahito, R. G. A., Peinkofer, G., Nguemo, F., Müller-Ehmsen, J., & Hescheler, J. (2015). Electrophysiological and morphological maturation of murine fetal cardiomyocytes during electrical stimulation in vitro. *Journal of Cardiovascular Pharmacology and Therapeutics*, 20(1), 104–112. <https://doi.org/10.1177/1074248414536273>
- Bhana, B., Iyer, R. K., Chen, W. L. K., Zhao, R., Sider, K. L., Likhitpanichkul, M., Simmons, C. A., & Radisic, M. (2010). Influence of substrate stiffness on the phenotype of heart cells. *Biotechnology and Bioengineering*, 105(6), 1148–1160. <https://doi.org/10.1002/bit.22647>
- Bissell, M. J., Rizki, A., & Mian, I. S. (2003). Tissue architecture: The ultimate regulator of breast epithelial function. *Current Opinion in Cell Biology*, 15(6), 753–762. <https://doi.org/10.1016/j.ceb.2003.10.016>
- Buxboim, A., Ivanovska, I. L., & Discher, D. E. (2010). Matrix elasticity, cytoskeletal forces and physics of the nucleus: How deeply do cells “feel” outside and in? *Journal of Cell Science*, 123(3), 297–308. <https://doi.org/10.1242/jcs.041186>
- Camelliti, P., McCulloch, A. D., & Kohl, P. (2005). Microstructured cocultures of cardiac myocytes and fibroblasts: A two-dimensional in vitro model of cardiac tissue. *Microscopy and Microanalysis*, 11(3), 249–259. <https://doi.org/10.1017/S1431927605050506>
- Carey, S. P., D’Alfonso, T. M., Shin, S. J., & Reinhart-King, C. A. (2012). Mechanobiology of tumor invasion: Engineering meets oncology. *Critical Reviews in Oncology/Hematology*, 83(2), 170–183. <https://doi.org/10.1016/j.critrevonc.2011.11.005>
- Carlier, A., Skvortsov, G. A., Hafezi, F., Ferraris, E., Patterson, J., Koc, B., & Van Oosterwyck, H. (2016). Computational model-informed design and bioprinting of cell-patterned constructs for bone tissue engineering. *Biofabrication*, 8(2). <https://doi.org/10.1088/1758-5090/8/2/025009>

- Chen, C., Bai, X., Ding, Y., & Lee, I. S. (2019). Electrical stimulation as a novel tool for regulating cell behavior in tissue engineering. *Biomaterials Research*, 23(1). <https://doi.org/10.1186/s40824-019-0176-8>
- Cheng, G., Tse, J., Jain, R. K., & Munn, L. L. (2009). Micro-environmental mechanical stress controls tumor spheroid size and morphology by suppressing proliferation and inducing apoptosis in cancer cells. *PLoS One*, 4(2). <https://doi.org/10.1371/journal.pone.0004632>
- Cheng, G., Youssef, B. B., Markenscoff, P., & Zygourakis, K. (2006). Cell population dynamics modulate the rates of tissue growth processes. *Biophysical Journal*, 90(3), 713–724. <https://doi.org/10.1529/biophysj.105.063701>
- Chen, Q. Z., Harding, S. E., Ali, N. N., Lyon, A. R., & Boccaccini, A. R. (2008). Biomaterials in cardiac tissue engineering: Ten years of research survey. *Materials Science and Engineering R: Reports*, 59(1–6), 1–37. <https://doi.org/10.1016/j.mser.2007.08.001>
- Chen, C. S., Tan, J., & Tien, J. (2004). Mechanotransduction at cell-matrix and cell-cell contacts. *Annual Review of Biomedical Engineering*, 6, 275–302. <https://doi.org/10.1146/annurev.bioeng.6.040803.140040>
- Cioffi, M., Küffer, J., Ströbel, S., Dubini, G., Martin, I., & Wendt, D. (2008). Computational evaluation of oxygen and shear stress distributions in 3D perfusion culture systems: Macro-scale and micro-structured models. *Journal of Biomechanics*, 41(14), 2918–2925. <https://doi.org/10.1016/j.jbiomech.2008.07.023>
- Costa, K. D., Lee, E. J., & Holmes, J. W. (2003). Creating alignment and anisotropy in engineered heart tissue: Role of boundary conditions in a model three-dimensional culture system. *Tissue Engineering*, 9(4), 567–577. <https://doi.org/10.1089/107632703768247278>
- Crommelin, D. J. A. (1984). Influence of lipid composition and ionic strength on the physical stability of liposomes. *Journal of Pharmaceutical Sciences*, 73(11), 1559–1563. <https://doi.org/10.1002/jps.2600731118>
- Darling, E. M., Topel, M., Zauscher, S., Vail, T. P., & Guilak, F. (2008). Viscoelastic properties of human mesenchymally-derived stem cells and primary osteoblasts, chondrocytes, and adipocytes. *Journal of Biomechanics*, 41(2), 454–464. <https://doi.org/10.1016/j.jbiomech.2007.06.019>
- De Pascalis, C., & Etienne-Manneville, S. (2017). Single and collective cell migration: The mechanics of adhesions. *Molecular Biology of the Cell*, 28(14), 1833–1846. <https://doi.org/10.1091/mbc.E17-03-0134>
- Delaine-Smith, R. M., & Reilly, G. C. (2012). Mesenchymal stem cell responses to mechanical stimuli. *Muscles, Ligaments and Tendons Journal*, 2(3), 169–180. <http://www.mltj.org/common/php/portiere.php?ID=b765655317669983b11ec156f3cbf7f5>.
- Deshpande, V. S., Mrksich, M., McMeeking, R. M., & Evans, A. G. (2008). A bio-mechanical model for coupling cell contractility with focal adhesion formation. *Journal of the Mechanics and Physics of Solids*, 56(4), 1484–1510. <https://doi.org/10.1016/j.jmps.2007.08.006>
- De, R., Zemel, A., & Safran, S. A. (2008). Do cells sense stress or strain? Measurement of cellular orientation can provide a clue. *Biophysical Journal*, 94(5), L29–L31. <https://doi.org/10.1529/biophysj.107.126060>
- Di Meglio, F., Nurzynska, D., Romano, V., Miraglia, R., Belviso, I., Sacco, A. M., Barbato, V., Di Gennaro, M., Granato, G., Maiello, C., Montagnani, S., & Castaldo, C. (2017). Optimization of human myocardium decellularization method for the construction of implantable patches. *Tissue Engineering - Part C: Methods*, 23(9), 525–539. <https://doi.org/10.1089/ten.tec.2017.0267>

- DiMilla, P. A., Barbee, K., & Lauffenburger, D. A. (1991). Mathematical model for the effects of adhesion and mechanics on cell migration speed. *Biophysical Journal*, 60(1), 15–37. [https://doi.org/10.1016/S0006-3495\(91\)82027-6](https://doi.org/10.1016/S0006-3495(91)82027-6)
- Discher, D. E., Janmey, P., & Wang, Y. L. (2005). Tissue cells feel and respond to the stiffness of their substrate. *Science*, 310(5751), 1139–1143. <https://doi.org/10.1126/science.1116995>
- Doweidar, M. H. (Ed.). (2019). *Advances in biomechanics and tissue regeneration*. Elsevier. <https://doi.org/10.1016/C2018-0-00433-8>
- Elmore, S. (2007). Apoptosis: A review of programmed cell death. *Toxicologic Pathology*, 35(4), 495–516. <https://doi.org/10.1080/01926230701320337>
- Engler, A. J., Griffin, M. A., Sen, S., Bönnemann, C. G., Sweeney, H. L., & Discher, D. E. (2004). Myotubes differentiate optimally on substrates with tissue-like stiffness. *Journal of Cell Biology*, 166(6), 877–887. <https://doi.org/10.1083/jcb.200405004>
- Engler, A. J., Sen, S., Sweeney, H. L., & Discher, D. E. (2006). Matrix elasticity directs stem cell lineage specification. *Cell*, 126(4), 677–689. <https://doi.org/10.1016/j.cell.2006.06.044>
- Enrica, T. (2009). *Hydrogels: Biological properties and applications*.
- Fearnley, C. J., Roderick, H. L., & Bootman, M. D. (2011). Calcium signaling in cardiac myocytes. *Cold Spring Harbor Perspectives in Biology*, 3(11). [https://doi.org/10.1101/cshperspect.a004242-a004242](https://doi.org/10.1101/cshperspect.a004242)
- Ferrari, R. (2002). Healthy versus sick myocytes: Metabolism, structure and function. *European Heart Journal*, 4(Supplement), G1–G12. [https://doi.org/10.1016/S1520-765X\(02\)90084-2](https://doi.org/10.1016/S1520-765X(02)90084-2)
- Fischer, S., & Glas, K. E. (2013). A Review of cardiac transplantation. *Anesthesiology Clinics*, 31(2), 383–403. <https://doi.org/10.1016/j.anclin.2013.01.003>
- Formigli, L., Francini, F., Nistri, S., Margheri, M., Luciani, G., Naro, F., Silvertown, J. D., Orlandini, S. Z., Meacci, E., & Bani, D. (2009). Skeletal myoblasts overexpressing relaxin improve differentiation and communication of primary murine cardiomyocyte cell cultures. *Journal of Molecular and Cellular Cardiology*, 47(2), 335–345. <https://doi.org/10.1016/j.yjmcc.2009.05.008>
- Frederich, B. J., Timofeyev, V., Thai, P. N., Haddad, M. J., Poe, A. J., Lau, V. C., Moshref, M., Knowlton, A. A., Sirish, P., & Chiamvimonvat, N. (2017). Electrotaxis of cardiac progenitor cells, cardiac fibroblasts, and induced pluripotent stem cell-derived cardiac progenitor cells requires serum and is directed via PI3'K pathways. *Heart Rhythm*, 14(11), 1685–1692. <https://doi.org/10.1016/j.hrthm.2017.06.038>
- Galbusera, F., Cioffi, M., & Raimondi, M. T. (2008). An in silico bioreactor for simulating laboratory experiments in tissue engineering. *Biomedical Microdevices*, 10(4), 547–554. <https://doi.org/10.1007/s10544-008-9164-9>
- Gardel, M. L., Sabass, B., Ji, L., Danuser, G., Schwarz, U. S., & Waterman, C. M. (2008). Traction stress in focal adhesions correlates biphasically with actin retrograde flow speed. *Journal of Cell Biology*, 183(6), 999–1005. <https://doi.org/10.1083/jcb.200810060>
- Gavagnin, E., & Yates, C. A. (2018). Stochastic and deterministic modeling of cell migration. In , Vol 39. *Handbook of statistics* (pp. 37–91). Elsevier B.V. <https://doi.org/10.1016/bs.host.2018.06.002>
- Ghafar-Zadeh, E., Waldeisen, J. R., & Lee, L. P. (2011). Engineered approaches to the stem cell microenvironment for cardiac tissue regeneration. *Lab on a Chip*, 11(18), 3031–3048. <https://doi.org/10.1039/c1lc20284g>

- Gladman, S. J., Ward, R. E., Michael-Titus, A. T., Knight, M. M., & Priestley, J. V. (2010). The effect of mechanical strain or hypoxia on cell death in subpopulations of rat dorsal root ganglion neurons in vitro. *Neuroscience*, 171(2), 577–587. <https://doi.org/10.1016/j.neuroscience.2010.07.009>
- Hatzistergos, K. E., Quevedo, H., Oskouei, B. N., Hu, Q., Feigenbaum, G. S., Margitich, I. S., Mazhari, R., Boyle, A. J., Zambrano, J. P., Rodriguez, J. E., Dulce, R., Pattany, P. M., Valdes, D., Revilla, C., Heldman, A. W., McNiece, I., & Hare, J. M. (2010). Bone marrow mesenchymal stem cells stimulate cardiac stem cell proliferation and differentiation. *Circulation Research*, 107(7), 913–922. <https://doi.org/10.1161/CIRCRESAHA.110.222703>
- Heidi Au, H. T., Cui, B., Chu, Z. E., Veres, T., & Radisic, M. (2009). Cell culture chips for simultaneous application of topographical and electrical cues enhance phenotype of cardiomyocytes. *Lab on a Chip*, 9(4), 564–575. <https://doi.org/10.1039/b810034a>
- Heller, L. J., Mohrman, D. E., & Prohaska, J. R. (2000). Decreased passive stiffness of cardiac myocytes and cardiac tissue from copper-deficient rat hearts. *American Journal of Physiology - Heart and Circulatory Physiology*, 278(6), H1840–H1847. <https://doi.org/10.1152/ajpheart.2000.278.6.h1840>
- Hiemer, B., Krogull, M., Bender, T., Ziebart, J., Krueger, S., Bader, R., & Jonitz-Heincke, A. (2018). Effect of electric stimulation on human chondrocytes and mesenchymal stem cells under normoxia and hypoxia. *Molecular Medicine Reports*, 18(2), 2133–2141. <https://doi.org/10.3892/mmr.2018.9174>
- Holtzman, N. G., Schoenebeck, J. J., Tsai, H.-J., & Yelon, D. (2007). Endocardium is necessary for cardiomyocyte movement during heart tube assembly. *Development*, 134(12), 2379–2386. <https://doi.org/10.1242/dev.02857>
- Huang, Y.-X., Zheng, X.-J., Kang, L.-L., Chen, X.-Y., Liu, W.-J., Huang, B.-T., & Wu, Z.-J. (2011). Quantum dots as a sensor for quantitative visualization of surface charges on single living cells with nano-scale resolution. *Biosensors and Bioelectronics*, 26(5), 2114–2118. <https://doi.org/10.1016/j.bios.2010.09.016>.
- Huebsch, N., Arany, P. R., Mao, A. S., Shvartsman, D., Ali, O. A., Bencherif, S. A., Riverafeliciano, J., & Mooney, D. J. (2010). Harnessing traction-mediated manipulation of the cell/matrix interface to control stem-cell fate. *Nature Materials*, 9(6), 518–526. <https://doi.org/10.1038/nmat2732>
- Ikonen, L., Kerkelä, E., Metselaar, G., Stuart, M. C. A., De Jong, M. R., & Aalto-Setälä, K. (2013). 2D and 3D self-assembling nanofiber hydrogels for cardiomyocyte culture. *Bio-Med Research International*. <https://doi.org/10.1155/2013/285678>
- Imanaka-Yoshida, K., Hiroe, M., & Yoshida, T. (2004). Interaction between cell and extracellular matrix in heart disease: Multiple roles of tenascin-C in tissue remodeling. *Histology and Histopathology*, 19(2), 517–525.
- Jackman, C. P., Carlson, A. L., & Bursac, N. (2016). Dynamic culture yields engineered myocardium with near-adult functional output. *Biomaterials*, 111, 66–79. <https://doi.org/10.1016/j.biomaterials.2016.09.024>
- Jackman, C. P., Ganapathi, A. M., Asfour, H., Qian, Y., Allen, B. W., Li, Y., & Bursac, N. (2018). Engineered cardiac tissue patch maintains structural and electrical properties after epicardial implantation. *Biomaterials*, 159, 48–58. <https://doi.org/10.1016/j.biomaterials.2018.01.002>
- Kang, K. T., Park, J. H., Kim, H. J., Lee, H. M., Lee, K. I., Jung, H. H., Lee, H. Y., Shim, Y. B., & Jang, J. W. (2011). Study on differentiation of mesenchymal stem cells by mechanical stimuli and an algorithm for bone fracture healing. *Tissue Engineering and Regenerative Medicine*, 8(4), 359–370.

- Kearney, E. M., Prendergast, P. J., & Campbell, V. A. (2008). Mechanisms of strain-mediated mesenchymal stem cell apoptosis. *Journal of Biomechanical Engineering*, 130(6). <https://doi.org/10.1115/1.2979870>
- Kelly, D. J., & Prendergast, P. J. (2005). Mechano-regulation of stem cell differentiation and tissue regeneration in osteochondral defects. *Journal of Biomechanics*, 38(7), 1413–1422. <https://doi.org/10.1016/j.jbiomech.2004.06.026>
- Kim, D. H., Lipke, E. A., Kim, P., Cheong, R., Thompson, S., Delannoy, M., Suh, K. Y., Tung, L., & Levchenko, A. (2010). Nanoscale cues regulate the structure and function of macroscopic cardiac tissue constructs. *Proceedings of the National Academy of Sciences of the United States of America*, 107(2), 565–570. <https://doi.org/10.1073/pnas.0906504107>
- Kim, M. C., Silberberg, Y. R., Abeyaratne, R., Kamm, R. D., & Asada, H. H. (2018). Computational modeling of three-dimensional ECMrigidity sensing to guide directed cell migration. *Proceedings of the National Academy of Sciences of the United States of America*, 115(3), E390–E399. <https://doi.org/10.1073/pnas.1717230115>
- Kinraide, T. B., & Wang, P. (2010). The surface charge density of plant cell membranes ( $\sigma$ ): An attempt to resolve conflicting values for intrinsic  $\sigma$ . *Journal of Experimental Botany*, 61(9), 2507–2518. <https://doi.org/10.1093/jxb/erq082>
- Kresh, J. Y., & Chopra, A. (2011). Intercellular and extracellular mechanotransduction in cardiac myocytes. *Pflugers Archiv European Journal of Physiology*, 462(1), 75–87. <https://doi.org/10.1007/s00424-011-0954-1>
- Lee, E. J., Holmes, J. W., & Costa, K. D. (2008). Remodeling of engineered tissue anisotropy in response to altered loading conditions. *Annals of Biomedical Engineering*, 36(8), 1322–1334. <https://doi.org/10.1007/s10439-008-9509-9>
- Lee, D. A., Knight, M. M., Campbell, J. J., & Bader, D. L. (2011). Stem cell mechanobiology. *Journal of Cellular Biochemistry*, 112(1), 1–9. <https://doi.org/10.1002/jcb.22758>
- Levin, M. (2014). Molecular bioelectricity: How endogenous voltage potentials control cell behavior and instruct pattern regulation in vivo. *Molecular Biology of the Cell*, 25(24), 3835–3850. <https://doi.org/10.1091/mbc.E13-12-0708>
- Li, Z., Guo, X., Palmer, A. F., Das, H., & Guan, J. (2012). High-efficiency matrix modulus-induced cardiac differentiation of human mesenchymal stem cells inside a thermosensitive hydrogel. *Acta Biomaterialia*, 8(10), 3586–3595. <https://doi.org/10.1016/j.actbio.2012.06.024>
- Lintz, M., Muñoz, A., & Reinhart-King, C. A. (2017). The mechanics of single cell and collective migration of tumor cells. *Journal of Biomechanical Engineering*, 139(2). <https://doi.org/10.1115/1.4035121>
- Loeffler, M., & Roeder, I. (2002). Tissue stem cells: Definition, plasticity, heterogeneity, self-organization and models - a conceptual approach. *Cells Tissues Organs*, 171(1), 8–26. <https://doi.org/10.1159/000057688>
- Low, B. C., Pan, C. Q., Shivashankar, G. V., Bershadsky, A., Sudol, M., & Sheetz, M. (2014). YAP/TAZ as mechanosensors and mechanotransducers in regulating organ size and tumor growth. *FEBS Letters*, 588(16), 2663–2670. <https://doi.org/10.1016/j.febslet.2014.04.012>
- Madden, L., Juhas, M., Kraus, W. E., Truskey, G. A., & Bursac, N. (2015). Bioengineered human myobundles mimic clinical responses of skeletal muscle to drugs. *eLife*, 2015(4). <https://doi.org/10.7554/eLife.04885>
- Manzano, S., Moreno-Loshuertos, R., Doblaré, M., Ochoa, I., & Hamdy Doweidar, M. (2015). Structural biology response of a collagen hydrogel synthetic extracellular matrix with embedded human fibroblast: Computational and experimental analysis. *Medical and*

- Biological Engineering and Computing*, 53(8), 721–735. <https://doi.org/10.1007/s11517-015-1277-8>
- Marzban, B., & Yuan, H. (2017). The effect of thermal fluctuation on the receptor-mediated adhesion of a cell membrane to an elastic substrate. *Membranes*, 7(2). <https://doi.org/10.3390/membranes7020024>
- Mathur, A. B., Collinsworth, A. M., Reichert, W. M., Kraus, W. E., & Truskey, G. A. (2001). Endothelial, cardiac muscle and skeletal muscle exhibit different viscous and elastic properties as determined by atomic force microscopy. *Journal of Biomechanics*, 34(12), 1545–1553. [https://doi.org/10.1016/S0021-9290\(01\)00149-X](https://doi.org/10.1016/S0021-9290(01)00149-X)
- Maul, T. M., Chew, D. W., Nieponice, A., & Vorp, D. A. (2011). Mechanical stimuli differentially control stem cell behavior: Morphology, proliferation, and differentiation. *Biomechanics and Modeling in Mechanobiology*, 10(6), 939–953. <https://doi.org/10.1007/s10237-010-0285-8>
- McClatchey, A. I., & Yap, A. S. (2012). Contact inhibition (of proliferation) redux. *Current Opinion in Cell Biology*, 24(5), 685–694. <https://doi.org/10.1016/j.ceb.2012.06.009>
- Meng, S., Rouabchia, M., & Zhang, Z. (2013). Electrical stimulation modulates osteoblast proliferation and bone protein production through heparin-bioactivated conductive scaffolds. *Bioelectromagnetics*, 34(3), 189–199. <https://doi.org/10.1002/bem.21766>
- Mogilner, A. (2009). Mathematics of cell motility: Have we got its number? *Journal of Mathematical Biology*, 58(1–2), 105–134. <https://doi.org/10.1007/s00285-008-0182-2>
- Mogilner, A., & Oster, G. (1996). Cell motility driven by actin polymerization. *Biophysical Journal*, 71(6), 3030–3045. [https://doi.org/10.1016/S0006-3495\(96\)79496-1](https://doi.org/10.1016/S0006-3495(96)79496-1)
- Mousavi, S. J., Doblaré, M., & Doweidar, M. H. (2014). Computational modelling of multi-cell migration in a multi-signalling substrate. *Physical Biology*, 11(2). <https://doi.org/10.1088/1478-3975/11/2/026002>
- Mousavi, S. J., & Doweidar, M. H. (2014). A novel mechanotactic 3D modeling of cell morphology. *Physical Biology*, 11(4). <https://doi.org/10.1088/1478-3975/11/4/046005>
- Mousavi, S. J., & Doweidar, M. H. (2016). Numerical modeling of cell differentiation and proliferation in force-induced substrates via encapsulated magnetic nanoparticles. *Computer Methods and Programs in Biomedicine*, 130, 106–117. <https://doi.org/10.1016/j.cmpb.2016.03.019>
- Mousavi, S. J., & Doweidar, M. H. (2019). Encapsulated piezoelectric nanoparticle–hydrogel smart material to remotely regulate cell differentiation and proliferation: A finite element model. *Computational Mechanics*, 63(3), 471–489. <https://doi.org/10.1007/s00466-018-1604-7>
- Mousavi, S. J., & Doweidar, M. H. (2019). Computational simulation of cell behavior for tissue regeneration. In M. H. Doweidar (Ed.), *Advances in biomechanics and tissue regeneration*. Elsevier. <https://doi.org/10.1016/B978-0-12-816390-0.00015-7>
- Mousavi, S. J., Doweidar, M. H., & Doblaré, M. (2013a). Cell migration and cell-cell interaction in the presence of mechano-chemo-thermotaxis. *Molecular & Cellular Biomechanics : MCB*, 10(1), 1–25.
- Mousavi, S. J., Doweidar, M. H., & Doblaré, M. (2013b). 3D computational modelling of cell migration: A mechano-chemo-thermo-electrotaxis approach. *Journal of Theoretical Biology*, 329, 64–73. <https://doi.org/10.1016/j.jtbi.2013.03.021>
- Mousavi, S. J., Doweidar, M. H., & Doblaré, M. (2014). Computational modelling and analysis of mechanical conditions on cell locomotion and cell-cell interaction. *Computer Methods in Biomechanics and Biomedical Engineering*, 17(6), 678–693. <https://doi.org/10.1080/10255842.2012.710841>

- Mousavi, S. J., Hamdy Doweidar, M., & Aegeerter, C. M. (2015a). Role of mechanical cues in cell differentiation and proliferation: A 3D numerical model. *PLOS ONE*, 10(5), e0124529. <https://doi.org/10.1371/journal.pone.0124529>
- Mousavi, S. J., Hamdy Doweidar, M., & Aegeerter, C. M. (2015b). Three-Dimensional numerical model of cell morphology during migration in multi-signaling substrates. *PLOS ONE*, 10(3), e0122094. <https://doi.org/10.1371/journal.pone.0122094>
- Mycielska, M. E., & Djamgoz, M. B. A. (2004). Cellular mechanisms of direct-current electric field effects: Galvanotaxis and metastatic disease. *Journal of Cell Science*, 117(9), 1631–1639. <https://doi.org/10.1242/jcs.01125>
- Ng, M. R., Besser, A., Danuser, G., & Brugge, J. S. (2012). Substrate stiffness regulates cadherin-dependent collective migration through myosin-II contractility. *Journal of Cell Biology*, 199(3), 545–563. <https://doi.org/10.1083/jcb.201207148>
- Nunes, S. S., Miklas, J. W., Liu, J., Aschar-Sobbi, R., Xiao, Y., Zhang, B., Jiang, J., Massé, S., Gagliardi, M., Hsieh, A., Thavandiran, N., Laflamme, M. A., Nanthakumar, K., Gross, G. J., Backx, P. H., Keller, G., & Radisic, M. (2013). Biowire: A platform for maturation of human pluripotent stem cell-derived cardiomyocytes. *Nature Methods*, 10(8), 781–787. <https://doi.org/10.1038/nmeth.2524>
- Papas, K. K., Pisania, A., Wu, H., Weir, G. C., & Colton, C. K. (2007). A stirred microchamber for oxygen consumption rate measurements with pancreatic islets. *Biotechnology and Bioengineering*, 98(5), 1071–1082. <https://doi.org/10.1002/bit.21486>
- Pietronave, S., Zamperone, A., Oltolina, F., Colangelo, D., Follenzi, A., Novelli, E., Diena, M., Pavesi, A., Consolo, F., Fiore, G. B., Soncini, M., & Prat, M. (2014). Monophasic and biphasic electrical stimulation induces a precardiac differentiation in progenitor cells isolated from human heart. *Stem Cells and Development*, 23(8), 888–898. <https://doi.org/10.1089/scd.2013.0375>
- Planat-Bénard, V., Menard, C., André, M., Puceat, M., Perez, A., Garcia-Verdugo, J. M., Pénicaud, L., & Casteilla, L. (2004). Spontaneous cardiomyocyte differentiation from adipose tissue stroma cells. *Circulation Research*, 94(2), 223–229. <https://doi.org/10.1161/01.RES.0000109792.43271.47>
- Pullar, C. E. (2016). The physiology of bioelectricity in development. *Tissue Regeneration and Cancer*. <https://doi.org/10.1201/b10799>
- Radisic, M., Park, H., Shing, H., Consi, T., Schoen, F. J., Langer, R., Freed, L. E., & Vunjak-Novakovic, G. (2004). Functional assembly of engineered myocardium by electrical stimulation of cardiac myocytes cultured on scaffolds. *Proceedings of the National Academy of Sciences of the United States of America*, 101(52), 18129–18134. <https://doi.org/10.1073/pnas.0407817101>
- Ramtani, S. (2004). Mechanical modelling of cell/ECM and cell/cell interactions during the contraction of a fibroblast-populated collagen microsphere: Theory and model simulation. *Journal of Biomechanics*, 37(11), 1709–1718. <https://doi.org/10.1016/j.jbiomech.2004.01.028>.
- Rangarajan, S., Madden, L., & Bursac, N. (2014). Use of flow, electrical, and mechanical stimulation to promote engineering of striated muscles. *Annals of Biomedical Engineering*, 42(7), 1391–1405. <https://doi.org/10.1007/s10439-013-0966-4>
- Rao, L., Qian, Y., Khodabukus, A., Ribar, T., & Bursac, N. (2018). Engineering human pluripotent stem cells into a functional skeletal muscle tissue. *Nature Communications*, 9(1). <https://doi.org/10.1038/s41467-017-02636-4>
- Reig, G., Pulgar, E., & Concha, M. L. (2014). Cell migration: From tissue culture to embryos. *Development*, 141(10), 1999–2013. <https://doi.org/10.1242/dev.101451>

- Ribeiro, C., Sencadas, V., Correia, D. M., & Lanceros-Méndez, S. (2015). Piezoelectric polymers as biomaterials for tissue engineering applications. *Colloids and Surfaces B: Biointerfaces*, 136, 46–55. <https://doi.org/10.1016/j.colsurfb.2015.08.043>
- Robinson, K. R., & Messerli, M. A. (2003). Left/right, up/down: The role of endogenous electrical fields as directional signals in development, repair and invasion. *BioEssays*, 25(8), 759–766. <https://doi.org/10.1002/bies.10307>
- Rodriguez, M. L., Graham, B. T., Pabon, L. M., Han, S. J., Murry, C. E., & Sniadecki, N. J. (2014). Measuring the contractile forces of human induced pluripotent stem cell-derived cardiomyocytes with arrays of microposts. *Journal of Biomechanical Engineering*, 136(5). <https://doi.org/10.1115/1.4027145>
- Rodriguez, M. L., McGarry, P. J., & Sniadecki, N. J. (2013). Review on cell mechanics: Experimental and modeling approaches. *Applied Mechanics Reviews*, 65(6). <https://doi.org/10.1115/1.4025355>
- Roesler, H. (1987). The history of some fundamental concepts in bone biomechanics. *Journal of Biomechanics*, 20. <https://doi.org/10.1016/0021-9290>, 90020–0.
- Rostovtseva, T. K., Aguilella, V. M., Vodyanoy, I., Bezrukov, S. M., & Parsegian, V. A. (1998). Membrane surface-charge titration probed by gramicidin A channel conductance. *Biophysical Journal*, 75(4), 1783–1792. [https://doi.org/10.1016/S0006-3495\(98\)77620-9](https://doi.org/10.1016/S0006-3495(98)77620-9)
- Roveimiab, Z., Lin, F., & Anderson, J. E. (2019). Emerging development of microfluidics-based approaches to improve studies of muscle cell migration. *Tissue Engineering - Part B: Reviews*, 25(1), 30–45. <https://doi.org/10.1089/ten.teb.2018.0181>
- Saez, A., Buguin, A., Silberzan, P., & Ladoux, B. (2005). Is the mechanical activity of epithelial cells controlled by deformations or forces? *Biophysical Journal*, 89(6), L52–L54. <https://doi.org/10.1529/biophysj.105.071217>
- Salvador-Clavell, R., Rodríguez-Fortún, J.-M., López, I., Martín de Llano, J. J., Orús, J., Sancho-Tello, M., Carda, C., & Doweidar, M. H. (2020). Design and experimental validation of a magnetic device for stem cell culture. *The Review of Scientific Instruments*, 91(12), 124103. <https://doi.org/10.1063/5.0016374>
- Sassoli, C., Pini, A., Mazzanti, B., Quercioli, F., Nistri, S., Saccardi, R., Orlandini, S. Z., Bani, D., & Formigli, L. (2011). Mesenchymal stromal cells affect cardiomyocyte growth through juxtacrine Notch-1/Jagged-1 signaling and paracrine mechanisms: Clues for cardiac regeneration. *Journal of Molecular and Cellular Cardiology*, 51(3), 399–408. <https://doi.org/10.1016/j.yjmcc.2011.06.004>
- Sauer, H., Rahimi, G., Hescheler, J., & Wartenberg, M. (1999). Effects of electrical fields on cardiomyocyte differentiation of embryonic stem cells. *Journal of Cellular Biochemistry*, 75(4), 710–723. [https://doi.org/10.1002/\(SICI\)1097-4644\(19991215\)75:4<710::AID-JCB16>3.0.CO;2-Z](https://doi.org/10.1002/(SICI)1097-4644(19991215)75:4<710::AID-JCB16>3.0.CO;2-Z)
- Schäfer, A., & Radmacher, M. (2005). Influence of myosin II activity on stiffness of fibroblast cells. *Acta Biomaterialia*, 1(3), 273–280. <https://doi.org/10.1016/j.actbio.2005.02.004>.
- Schmelter, M., Ateghang, B., Helmig, S., Wartenberg, M., Sauer, H., Schmelter, M., Ateghang, B., Helmig, S., Wartenberg, M., & Sauer, H. (2006). Embryonic stem cells utilize reactive oxygen species as transducers of mechanical strain-induced cardiovascular differentiation. *The FASEB Journal*, 20(8), 1182–1184. <https://doi.org/10.1096/fj.05-4723fje>
- Setty, Y. (2014). In-silico models of stem cell and developmental systems. *Theoretical Biology and Medical Modelling*, 11(1). <https://doi.org/10.1186/1742-4682-11-1>
- Shadrin, I. Y., Allen, B. W., Qian, Y., Jackman, C. P., Carlson, A. L., Juhas, M. E., & Bursac, N. (2017). Cardiopatch platform enables maturation and scale-up of human

- pluripotent stem cell-derived engineered heart tissues. *Nature Communications*, 8(1). <https://doi.org/10.1038/s41467-017-01946-x>
- Shake, J. G., Gruber, P. J., Baumgartner, W. A., Senechal, G., Meyers, J., Redmond, J. M., Pittenger, M. F., & Martin, B. J. (2002). Mesenchymal stem cell implantation in a swine myocardial infarct model: Engraftment and functional effects. *Annals of Thoracic Surgery*, 73(6), 1919–1926. [https://doi.org/10.1016/S0003-4975\(02\)03517-8](https://doi.org/10.1016/S0003-4975(02)03517-8)
- Shrivastava, S., Ghosh, C., & Jonas, J. J. (2012). A comparison of the von Mises and Hencky equivalent strains for use in simple shear experiments. *Philosophical Magazine*, 92(7), 779–786. <https://doi.org/10.1080/14786435.2011.634848>
- Stedman, H. H., Sweeney, H. L., Shrager, J. B., Maguire, H. C., Panettieri, R. A., Petrof, B., Narusawa, M., Leferovich, J. M., Sladky, J. T., & Kelly, A. M. (1991). The mdx mouse diaphragm reproduces the degenerative changes of Duchenne muscular dystrophy. *Nature*, 352(6335), 536–539. <https://doi.org/10.1038/352536a0>
- Stéphanou, A., Mylona, E., Chaplain, M., & Tracqui, P. (2008). A computational model of cell migration coupling the growth of focal adhesions with oscillatory cell protrusions. *Journal of Theoretical Biology*, 253(4), 701–716. <https://doi.org/10.1016/j.jtbi.2008.04.035>
- Stinstra, J. G., Hoppenfeld, B., & MacLeod, R. S. (2005). On the passive cardiac conductivity. *Annals of Biomedical Engineering*, 33(12), 1743–1751. <https://doi.org/10.1007/s10439-005-7257-7>
- Stoppel, W. L., Kaplan, D. L., & Black, L. D. (2016). Electrical and mechanical stimulation of cardiac cells and tissue constructs. *Advanced Drug Delivery Reviews*, 96, 135–155. <https://doi.org/10.1016/j.addr.2015.07.009>
- Tahara, N., Brush, M., & Kawakami, Y. (2016). Cell migration during heart regeneration in zebrafish. *Developmental Dynamics*, 245(7), 774–787. <https://doi.org/10.1002/dvdy.24411>
- Te Boekhorst, V., Preziosi, L., & Friedl, P. (2016). Plasticity of cell migration in vivo and in silico. *Annual Review of Cell and Developmental Biology*, 32, 491–526. <https://doi.org/10.1146/annurev-cellbio-111315-125201>
- Tibbitt, M. W., & Anseth, K. S. (2009). Hydrogels as extracellular matrix mimics for 3D cell culture. *Biotechnology and Bioengineering*, 103(4), 655–663. <https://doi.org/10.1002/bit.22361>
- Trubelja, A., & Bao, G. (2018). Molecular mechanisms of mechanosensing and mechano-transduction in living cells. *Extreme Mechanics Letters*, 20, 91–98. <https://doi.org/10.1016/j.eml.2018.01.011>
- Ulrich, T. A., De Juan Pardo, E. M., & Kumar, S. (2009). The mechanical rigidity of the extracellular matrix regulates the structure, motility, and proliferation of glioma cells. *Cancer Research*, 69(10), 4167–4174. <https://doi.org/10.1158/0008-5472.CAN-08-4859>
- Urdeitx, P., & Doweidar, M. H. (2020a). A computational model for cardiomyocytes mechano-electric stimulation to enhance cardiac tissue regeneration. *Mathematics*, 8(11), 1–23. <https://doi.org/10.3390/math8111875>
- Urdeitx, P., & Doweidar, M. H. (2020b). Mechanical stimulation of cell microenvironment for cardiac muscle tissue regeneration: A 3D in-silico model. *Computational Mechanics*, 66(4), 1003–1023. <https://doi.org/10.1007/s00466-020-01882-6>
- Urdeitx, P., & Doweidar, M. H. (2021). Enhanced piezoelectric fibered extracellular matrix to promote cardiomyocyte maturation and tissue formation: A 3d computational model. *Biology*, 10(2), 1–27. <https://doi.org/10.3390/biology10020135>

- Urdeitx, P., Farzaneh, S., Mousavi, S. J., & Doweidar, M. H. (2020). ROLE of oxygen concentration in the osteoblasts behavior: A finite element model. *Journal of Mechanics in Medicine and Biology*, 20(1). <https://doi.org/10.1142/S0219519419500647>
- Van Helvert, S., Storm, C., & Friedl, P. (2018). Mechanoreciprocity in cell migration. *Nature Cell Biology*, 20(1), 8–20. <https://doi.org/10.1038/s41556-017-0012-0>
- Vanegas-Acosta, J. C., Garzón-Alvarado, D. A., & Zwamborn, A. P. M. (2012). Mathematical model of electrotaxis in osteoblastic cells. *Bioelectrochemistry*, 88, 134–143. <https://doi.org/10.1016/j.bioelechem.2012.08.002>
- Walker, C. A., & Spinale, F. G. (1999). The structure and function of the cardiac myocyte: A review of fundamental concepts. *Journal of Thoracic and Cardiovascular Surgery*, 118(2), 375–382. [https://doi.org/10.1016/S0022-5223\(99\)70233-3](https://doi.org/10.1016/S0022-5223(99)70233-3)
- Wang, J. H. C., & Thampatty, B. P. (2006). An introductory review of cell mechanobiology. *Biomechanics and Modeling in Mechanobiology*, 5(1), 1–16. <https://doi.org/10.1007/s10237-005-0012-z>
- Wendt, D., Riboldi, S. A., Cioffi, M., & Martin, I. (2009). Potential and bottlenecks of bioreactors in 3D cell culture and tissue manufacturing. *Advanced Materials*, 21(32–33), 3352–3367. <https://doi.org/10.1002/adma.200802748>
- Wu, Q. Q., & Chen, Q. (2000). Mechanoregulation of chondrocyte proliferation, maturation, and hypertrophy: Ion-channel dependent transduction of matrix deformation signals. *Experimental Cell Research*, 256(2), 383–391. <https://doi.org/10.1006/excr.2000.4847>
- Yang, G., Xiao, Z., Ren, X., Long, H., Ma, K., Qian, H., & Guo, Y. (2017). Obtaining spontaneously beating cardiomyocyte-like cells from adipose-derived stromal vascular fractions cultured on enzyme-crosslinked gelatin hydrogels. *Scientific Reports*, 7. <https://doi.org/10.1038/srep41781>
- Yim, E. K. F., Darling, E. M., Kulangara, K., Guilak, F., & Leong, K. W. (2010). Nanotopography-induced changes in focal adhesions, cytoskeletal organization, and mechanical properties of human mesenchymal stem cells. *Biomaterials*, 31(6), 1299–1306. <https://doi.org/10.1016/j.biomaterials.2009.10.037>
- Young, J. L., & Engler, A. J. (2011). Hydrogels with time-dependent material properties enhance cardiomyocyte differentiation in vitro. *Biomaterials*, 32(4), 1002–1009. <https://doi.org/10.1016/j.biomaterials.2010.10.020>
- Young, J. L., Kretchmer, K., Ondeck, M. G., Zambon, A. C., & Engler, A. J. (2014). Mechanosensitive kinases regulate stiffness-induced cardiomyocyte maturation. *Scientific Reports*, 4. <https://doi.org/10.1038/srep06425>
- Zaman, M. H., Kamm, R. D., Matsudaira, P., & Lauffenburger, D. A. (2005). Computational model for cell migration in three-dimensional matrices. *Biophysical Journal*, 89(2), 1389–1397. <https://doi.org/10.1529/biophysj.105.060723>
- Zhang, D., Shadrin, I. Y., Lam, J., Xian, H. Q., Snodgrass, H. R., & Bursac, N. (2013). Tissue-engineered cardiac patch for advanced functional maturation of human ESC-derived cardiomyocytes. *Biomaterials*, 34(23), 5813–5820. <https://doi.org/10.1016/j.biomaterials.2013.04.026>
- Zhao, Z., Watt, C., Karystinou, A., Roelofs, A., McCaig, C., Gibson, I., & De Bari, C. (2011). Directed migration of human bone marrow mesenchymal stem cells in a physiological direct current electric field. *European Cells and Materials*, 22, 344–358. <https://doi.org/10.22203/eCM.v022a26>

# Flow and remodeling processes occurring within the body proper

# 24

Matthew D. Sinnott, Paul W. Cleary, Simon M. Harrison

CSIRO Data61, Clayton, VIC, Australia

## Chapter outline

<b>Introduction.....</b>	592
<b>Computational methods .....</b>	593
SPH method for fluids and solids .....	593
Continuity equation .....	593
Momentum equation for fluid (Navier–Stokes) .....	593
Momentum equation for solid deformation.....	594
Pressure solution.....	595
Solid boundary conditions .....	595
Soft bodies with flexible surfaces (such as cell membranes) .....	596
Species concentration and diffusion.....	597
Integration of the SPH ordinary differential equations.....	597
<b>Models for biological processes .....</b>	598
Adhesion modeling for cells.....	598
<i>Elastic regime</i> .....	599
<i>Viscous regime</i> .....	601
Simple model for thrombin-controlled coagulation.....	602
SPH solid evolution for remodeling processes .....	603
<b>Hemodynamics of vascular disease.....</b>	603
Explicit modeling of cell mechanics at capillary scale.....	605
White blood cell rolling adhesion .....	611
Arterial scale flow.....	614
<b>Blood coagulation and clot formation modeling .....</b>	620
Background .....	620
Simple SPH coagulation model and predictions .....	622
<b>Plaque rupture in an artery .....</b>	630
Background .....	630
SPH model for plaque rupture .....	632
<b>Bone remodeling.....</b>	641

Conclusions .....	644
Acknowledgments .....	646
References .....	646

---

## Introduction

This chapter focuses on processes that occur within the internal volume of the human body. Processes within the digestive and respiratory systems, which are readily accessible to the external environment, have been considered in another chapter titled “Flow processes occurring within the body but still external to the body’s epithelial layer (gastrointestinal and respiratory tracts).”

Physics-based computational models have been applied to a range of in-body processes, especially blood flow (Fatahian et al., 2018). Such models have been used to investigate fundamental process behavior, causes of illness, and dysfunction, and to evaluate surgical interventions including medical devices. In-body processes present many challenges for traditional Computational Fluid Dynamics (CFD) methods, which rely on grids or meshes to represent flow regions, and which were originally designed for flow around or within static rigid objects. Challenges include

- The multiphase and heterogenous nature of the flowing materials, such as blood, which can comprise a liquid (plasma) and entrained viscoelastic bodies such as red and white blood cells and fats in both liquid and solid form.
- The geometrically complex and deforming shapes of the bounding surfaces, such as arterial walls, which can apply significantly different boundary conditions on the flowing material depending on body movements, their compliance, and transient blood pressure.
- Dynamic changes to material properties and behaviors of the fluids and boundaries due to biological processes such as modeling and remodeling.

In contrast, particle methods, being meshfree and Lagrangian, have specific advantages to modeling biological flow and material evolution involving large flow deformation, deforming surfaces and where the material behavior is history dependent (Fernandez et al., 2010, 2013; Sinnott et al., 2015; Sinnott & Cleary, 2010).

The use of particle methods to simulate intra-body processes and their advantages are discussed via a series of examples. These include

1. Blood flow ranging from the scale of individual red or white blood cells in capillaries to full artery scale in the carotid artery.
2. Blood coagulation/clot formation using a simple thrombin-controlled phase change model that allows clot rheology to be coupled to blood flow.
3. Plaque rupture in an artery, where a liquid-filled, deformable plaque mass located on an artery wall deforms and ruptures. This is predicted from the stresses generated by the adjacent blood flow.

4. Bone remodeling, where bone structure changes are due to competing bone growth and loss mechanisms whose activity is controlled by the stress loading of the bone.

## Computational methods

A comprehensive discussion of these computational methods and the modeling assumptions that lead to them is given in [Sinnott et al. \(2021\)](#).

### SPH method for fluids and solids

Smoothed Particle Hydrodynamics (SPH) is a Lagrangian meshfree method that is well suited to simulating complex multiphysics applications, particularly when there are fluids coupled to deforming solids and to particulates. It also provides strong advantages in tracking material composition, material and flow history dependence, stress and strain history dependence, species concentrations, and phase state. The method uses virtual “particles” to represent specific volumes of material that move in response to the applied forces, and which calculate gradients directly on the SPH particles without use of structures such as grids or meshes. Since the equations are solved on the “particles” with these acting as discretization points for the governing partial differential equations the method is Lagrangian—which avoids difficulties relating to advection of material.

The classical SPH method is introduced for incompressible fluid flow by [Monaghan \(1994\)](#). General reviews of SPH, method components, and some applications are given in [Monaghan \(2005, 2012\)](#), [Cleary et al. \(2007, 2021\)](#) and [Cleary, Harrison, et al. \(2020\)](#).

### Continuity equation

For the SPH continuity equation, we use the differential form from [Monaghan \(1992\)](#) to solve for the particle density  $\rho$  using

$$\frac{d\rho_a}{dt} = \sum_b m_b (\mathbf{v}_a - \mathbf{v}_b) \cdot \nabla W_{ab}. \quad (24.1)$$

with  $\mathbf{r}_{ab} = \mathbf{r}_a - \mathbf{r}_b$  being the position vector from particle  $b$  to particle  $a$  and  $W_{ab} = W(\mathbf{r}_{ab}, h)$  being the interpolation kernel with smoothing length  $h$  evaluated for the relative particle separation  $|\mathbf{r}_{ab}|$ . This form is suitable for both solids and liquids.

### Momentum equation for fluid (Navier–Stokes)

The momentum equation converted to SPH form gives the acceleration of each SPH particle:

$$\frac{d\mathbf{v}_a}{dt} = - \sum_b m_b \left[ \left( \frac{P_b}{\rho_b^2} + \frac{P_a}{\rho_a^2} \right) - \frac{\xi}{\rho_a \rho_b} \frac{4\mu_a \mu_b}{(\mu_a + \mu_b)} \frac{\mathbf{v}_{ab} \cdot \mathbf{r}_{ab}}{\mathbf{r}_{ab}^2 + \eta^2} \right] \nabla_a W_{ab} + \mathbf{g}. \quad (24.2)$$

where  $P_a$  and  $\mu_a$  are pressure and viscosity of particle  $a$  and  $\mathbf{v}_{ab} = \mathbf{v}_a - \mathbf{v}_b$ .  $\eta$  is a small parameter used to smooth out the singularity at  $\mathbf{r}_{ab} = 0$ ,  $\xi$  is a kernel-related normalization constant (see [Cleary, 1998](#)) and  $\mathbf{g}$  is gravity. This form is valid for single phase flows, for multiple material flows and ones where any density variation is small, continuous, and differentiable.

### Momentum equation for solid deformation

SPH can also be used to predict solid deformation including elastoplastic behavior ([Cleary & Das, 2008](#); [Gray et al., 2001](#)). Its Lagrangian nature gives specific advantages in tracking history dependence such as for material type, stress and strain history, yield stress change, and plastic strain.

The stress tensor  $\boldsymbol{\sigma}$  is partitioned into a volumetric (pressure),  $P$ , and deviatoric component,  $\mathbf{S}$ . A linear elastic (Hookean) constitutive model is assumed for the stress  $\boldsymbol{\sigma}$  versus strain  $\boldsymbol{\epsilon}$  relationship. This gives an evolution equation for  $\mathbf{S}$  which in component form ([Liberky & Petschek, 1990](#)) is

$$\frac{dS^{ij}}{dt} = 2G\left(\dot{\epsilon}^{ij} - \frac{1}{3}\delta^{ij}\dot{\epsilon}^{kk}\right) + S^{ik}\Omega^{jk} + \Omega^{ik}S^{kj} \quad (24.3)$$

where the superscripts refer to coordinate directions with summation implied on repeated indices.  $G$  is the shear modulus of the material and  $\delta$  is the Kronecker delta (or identity matrix). The strain rate tensor is calculated in component form (from [Gray et al., 2001](#)) and summed on each particle (see [Harrison et al., 2014](#)):

$$\dot{\epsilon}_a = \frac{1}{2} \sum_b \frac{m_b}{\rho_b} [(\mathbf{v}_{ab} \nabla_a W_{ab})^T + \mathbf{v}_{ab} \nabla_a W_{ab}]. \quad (24.4)$$

The rotation tensor is summed on each particle by

$$\Omega_a = \frac{1}{2} \sum_b \frac{m_b}{\rho_b} [(\mathbf{v}_{ab} \nabla_a W_{ab})^T - \mathbf{v}_{ab} \nabla_a W_{ab}]. \quad (24.5)$$

The SPH discretization of the momentum equation for solids (from [Gray et al., 2001](#)) is

$$\frac{d\mathbf{v}_a}{dt} = \sum_b m_b \left( \frac{\boldsymbol{\sigma}_a}{\rho_a^2} + \frac{\boldsymbol{\sigma}_b}{\rho_b^2} + \Pi_{ab} \mathbf{I} \right) \cdot \nabla_a W_{ab} + \mathbf{g} \quad (24.6)$$

where  $\boldsymbol{\sigma}_a$  and  $\boldsymbol{\sigma}_b$  are the stress tensors of particles  $a$  and  $b$  and  $I$  is the identity matrix. The artificial viscosity,  $\Pi_{ab}$ , proposed by [Monaghan & Gingold, 1983](#), provides numerical stabilization. The tensile instability correction of Monaghan (described by [Das and Cleary \(2015\)](#)) is also used with coefficient 0.3. Detailed verification of transient and long-term stresses under uniaxial loading conditions was performed by [Das and Cleary \(2015\)](#), demonstrating that SPH solutions are comparably accurate to FEM solutions.

## Pressure solution

In classical SPH for fluids, a weakly compressible assumption is made so that the pressure is explicitly given from the density using an equation of state.

The form [Batchelor \(1974\)](#) is suitable for the purposes here:

$$P = P_0 \left[ \left( \frac{\rho}{\rho_0} \right)^\gamma - 1 \right]. \quad (24.7)$$

The pressure scale  $P_0$  is given by the magnitude of the pressure. Also,  $\rho_0$  is the reference density. For fluids such water or aqueous solutions,  $\gamma = 7$  is used.

The pressure scale is set based on  $c$ , which is the numerical speed of sound, according to

$$\frac{\gamma P_0}{\rho_0} = 100V^2 = c^2, \quad (24.8)$$

where the prefactor 100 means that the maximum particle speed corresponds to Mach 0.1 based on this choice of numerical sound speed.  $V$  is a characteristic maximum physical velocity for the flow. This means that density variations are at most 1% giving weakly compressible fluid flow behavior.

For solid deformation, the equation of state in the solid material is

$$P = c^2 (\rho - \rho_0). \quad (24.9)$$

The sound speed  $c$  is calculated from the material bulk modulus  $\kappa$  using

$$c = \sqrt{\frac{\kappa}{\rho_0}}. \quad (24.10)$$

## Solid boundary conditions

The boundary surfaces of the human body with which the SPH discretized materials interact are typically represented by a single layer of either moving or stationary boundary particles. Each exerts both a normal repulsive force and a shear viscous force on any nearby fluid particles. This approach is explained in detail in [Cummins et al. \(2012\)](#) and [Cleary et al. \(2021\)](#). This is a powerful and very flexible boundary treatment that allows extremely complex solid boundaries, both stationary and moving, to be modeled ([Cleary et al., 2007](#)).

This boundary force method also allows deforming boundaries to be modeled, such as the sports and human modeling in [Cohen et al. \(2012, 2020\)](#), [Harrison et al. \(2018, 2019, 2022\)](#), and [Sinnott et al. \(2012, 2017\)](#).

Geometry preparation (mesh clean-up and the construction of surface normals) is performed using preprocessing workflows built on Workspace (which is a workflow platform for building and configuring reusable software (see [Workspace \(n.d.\)](#) and [Cleary, Thomas, et al. \(2020\)](#) for details).

### Soft bodies with flexible surfaces (such as cell membranes)

The internal body surfaces with which the fluids and solids interact are often changing shape compliantly in response to applied loads and usually reaching dynamic equilibrium with the flow in a way that controls the time varying shape of the surface.

Dynamically deforming body surfaces are discretized in as regular a way as is possible considering the geometry of the body. This is typically much easier for two-dimensional models. These SPH boundary particles, which are then one or more layers deep, form elastic walls or membranes for soft deformable fluid filled bodies, which are a very good representation for mechanical behavior of biological cells. These can be used both within an external fluid (such as for blood flow) or as free surface bodies, in which case the surface force behaves functionally like a form of surface tension constraining the internal fluid but independent of the curvature. The resolution of the SPH spatial discretization of the membranes needs to take account for the anticipated maximum extension of the viscoelastic bonds to ensure that they remain smaller than the SPH interpolation length  $h$ .

Each pair of adjacent membrane nodes is connected by a linear spring that allows for elastic deformation of the surface and a dashpot that generates viscous damping. This viscoelastic network permits the boundary to flex in response to internal and external forces such as circulatory pressures, shear, and collisions. This is a powerful and effective model for including compliant surfaces and being able to predict their dynamic response. This approach was proposed in [Cleary and Slinnott \(2006\)](#). These particles are also included in the usual SPH continuity, momentum, and pressure equations [\(24.1\)](#), [\(24.2\)](#) and [\(24.7\)](#) which enables combination of the membrane surface forces and the internal and external fluid dynamic forces. Collision between such soft bodies is automatically handled via the continuity/pressure equations. In this implementation, this means that the surfaces of the soft bodies also have a non-slip boundary condition for fluid flow. Note that there is no frictional component for the surface contacts, which is appropriate for the cellular systems of interest here.

The deformability of the soft body is dependent both on the

- viscosity of enclosed fluid, which controls the timescale for the internal rearrangement of the fluid in response to changes of shape of the body, and
- elasticity of the membrane which controls its tangential extensibility.

With these two physical components, bodies can exhibit behavior ranging from mild deformation at contact points up to total flattening of the body with transverse flattening with aspect ratios of 10:1 or more.

[Fig. 24.1](#) shows the motion and collision of three such soft bodies with a horizontal surface and with each other. The elastic to viscous force ratio is chosen to give a moderate level of deformation for the bodies. The bodies fall from above and collide with the ground or the previously dropped bodies producing both complex motion and significant deformations.

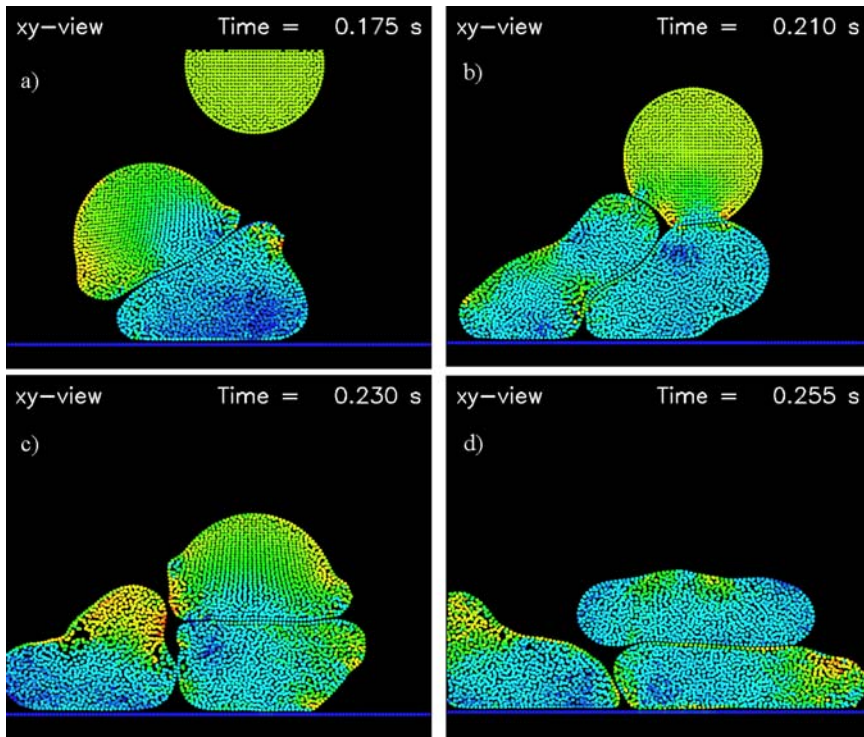


**FIGURE 24.1**

Multiple soft bodies represented as fluid-filled viscoelastic membranes. The bodies fall from above and collide with the ground or with previously dropped soft bodies. Very high deformations are observed.

### Species concentration and diffusion

Species diffusion is modeled using Fick's diffusion law which in SPH discretized form (following Cleary & Monaghan, 1999) gives the change in concentration of a species  $C^i$  for an SPH particle  $a$  as

$$\frac{dC_a^i}{dt} = \xi \sum_b \frac{m_b}{\rho_b} \frac{4\mathcal{D}_a \mathcal{D}_b}{\mathcal{D}_a + \mathcal{D}_b} (C_a^i - C_b^i) \frac{\mathbf{r}_{ab} \cdot \nabla_a W_{ab}}{\mathbf{r}_{ab}^2 + \eta^2}, \quad (24.11)$$

where  $\mathcal{D}_a$  is the diffusivity of particle  $a$ , for species  $i$ . Creation and destruction rate terms can be added as needed and different species can be coupled together. This will be used in the modeling of blood clotting.

### Integration of the SPH ordinary differential equations

The equations of motion of the particles and for the rates of change of their properties (Eqs. 24.1–24.11) are integrated using an explicit second-order predictor-

corrector (see Monaghan (1994) and Cummins et al. (2012) for details). The limit for stable explicit integration is given by the Courant condition modified for viscosity (see Monaghan, 1994).

---

## Models for biological processes

### Adhesion modeling for cells

The free energy,  $H$ , of a molecular bond may be derived from the force as

$$H = \int f(x)dx, \quad (24.12)$$

where  $x$  is a scalar length in the direction of the bond, and  $f$  represents the force loaded onto the bond. The kinetic rates of bond association/disassociation are related according to the following form (Dembo et al., 1988):

$$\frac{k_+}{k_-} = \exp\left(\frac{-H}{k_B T}\right), \quad (24.13)$$

where  $k_+$  is the on (bond association) rate,  $k_-$  is the off (bond disassociation) rate,  $k_B$  is Boltzmann's constant, and  $T$  is the temperature. From Eqs. (24.12) and (24.13) the kinetic rates may be derived from one another, as long as the force is a known function.

The first formulation of the kinetic rates was given by Bell (1978) as

$$k_- = k_-^0 \exp\left(\gamma_0 f/k_B T\right), \quad (24.14)$$

where  $k_-^0$  is the disassociation rate in the absence of applied force (Tees & Goetz, 2003) and  $\gamma_0$  is the reactive compliance (Bhatia et al., 2003).

If the force is assumed to be a linear spring, such that

$$f(x) = \alpha(x - \beta), \quad (24.15)$$

where  $\alpha$  is the spring constant and  $\beta$  the equilibrium spring length, then the off rate is given by substituting Eq. (24.13) into Eq. (24.14) such that

$$k_- = k_-^0 \exp\left(\gamma_0 \alpha(x - \beta)/k_B T\right) \quad (24.16)$$

From Eq. (24.15), free energy is given as

$$H = \int \alpha(x - \beta)dx = \frac{1}{2} \alpha(x - \beta)^2 + H_0. \quad (24.17)$$

Noting that  $H_0$  is a constant, Eq. (24.13) becomes

$$\frac{k_+}{k_-} = \frac{k_+^0}{k_-^0} \exp\left(-\alpha(x - \beta)^2/2k_B T\right), \quad (24.18)$$

where  $k_+^0$  is the association rate in the absence of applied force.

From Eqs. (24.16) and (24.18) the on rate for the Bell model may be derived as

$$k_+ = k_+^0 \exp\left(2\gamma_0\alpha(x - \beta) - \alpha(x - \beta)^2/2k_B T\right). \quad (24.19)$$

An alternative formulation using the Hookean spring model for the kinetic rates was developed for which the free energy was again given as  $H = \frac{1}{2} \alpha(x - \beta)^2 + H_0$ . The Hookean spring bond model was developed according to the following assumptions (Dembo et al., 1988):

- The energy of an unattached adhesion molecule is constant,
- The free energy of the transition state (where the bonding molecules are yet to establish a bond with one another) has the same form as that of the general free energy (i.e., Hookean), and
- While the base energy, spring constant, and equilibrium length will be different from the bound state, these differences can be approximated by a change in spring constant.

From the above, the following expression for the on rate is derived:

$$k_+ = k_+^0 \exp\left(-\alpha_{ts}(x - \beta)^2/2k_B T\right), \quad (24.20)$$

where  $\alpha_{ts}$  is the transition state bond constant.

From Eqs. (24.13), (24.16) and (24.20) the off rate for the Hookean spring model is given as

$$k_- = k_-^0 \exp\left((\alpha - \alpha_{ts})(x - \beta)^2/2k_B T\right). \quad (24.21)$$

It is of interest to note that if  $\alpha_{ts} > \alpha$ , then the off rate of a more stretched bond will be less than the off rate of a less stretched bond. This means that the more the bond is stretched the more strongly locked in place it becomes. Such a bond is termed a “catch” bond, as opposed to a slip bond, for which  $\alpha_{ts} < \alpha$  (Dembo, 1994). Similarly, if  $\alpha_{ts} = \alpha$ , then the bonds break at the same frequency regardless of the force that is loaded onto them.

Evans et al. (2005) showed that the loading of force onto a P-selectin: PSGL-1 bond is a two-phase process. In the first phase, the bond behaves as an elastic spring causing the cell membrane of the endothelial cells to stretch. Beyond some critical force value, the cell membrane separates from the cytoskeleton, causing the microvillus to stretch into a tether. In this stage the bond behaves in a more viscous fashion with increases in force loading. At any point in this process the bond may rupture according to the off rate of the current regime.

### Elastic regime

In the first phase, the bond may be modeled as a spring, as described above, such that  $f(x) = \alpha(x - \beta)$ . The Bell model was chosen over the Hookean spring model as a means of deriving the kinetic rates as it allows for

- (i) a continuous transition in moving to the viscous regime, and
- (ii) greater consistency with existing models of integrin adhesion, which also apply the Bell model.

This decision was made despite the fact that the Hookean spring model was designed to better handle the concept of cell adhesion than the Bell model, since it is based on the concept of kinetic rates, whereas the Bell model is based on equilibrium (N'Dri et al., 2003). The kinetic rates are thus given by Eqs. (24.16) and (24.19). The constants for this model are given in Table 24.1.

For the in vitro results obtained by Evans et al. (2005) the exact value of  $\alpha$  was found to partly depend on the speed at which attached cells were pulled apart. This behavior is not accounted for in the above model, and perhaps is not significant as the in vitro tests were performed on white blood cells attached to microspheres mounted upon red blood cells, which may be more prone to elastic extension than the endothelium.

The probability  $Q$  that a receptor–ligand bond will either form or break in a time  $\Delta t$  is given by Shyy et al. (2001) as

$$\frac{dQ}{dt} = k(1 - Q), \quad (24.22)$$

where  $k$  can be either the reverse ( $k_r$ ) or forward ( $k_f$ ) reaction rate, depending on whether the bond is due to form or break. Integrating Eq. (24.22) gives the following probability that a receptor–ligand complex will bind,  $Q_b$  (Jadhav et al., 2005):

$$Q_b = 1 - \exp(-k_{on} \Delta t), \quad (24.23)$$

where  $\Delta t$  is the simulation time step and  $k_{on}$  is defined as

$$k_{on} = k_+ A(n_L - n_B), \quad (24.24)$$

where  $A$  is the ligand-coated surface area (i.e., the area on the end of the microvillus).  $n_L$  is the total density of ligands and  $n_B$  is the density of bound ligands each on the end of the microvillus.

Similarly, the probability of bond rupture  $Q_r$  is given as

$$Q_r = 1 - \exp(-k_r \Delta t), \quad (24.25)$$

**Table 24.1** Parameters for the elastic regime of the bond model.

Parameter	Value	References
$\gamma_0$	0.39 A	Smith et al. (1999)
$\alpha$	0.25 pN/nm	King et al. (2005)
$\alpha$	43 pN/ $\mu$ m	Zhao et al. (2001)
$\beta$	80 nm	King et al. (2005)
$k^0$	2.4 s	(Smith et al., 1999)
$k_+^0$	84 s	Bhatia et al. (2003) (not experimentally verified)

The rate constant by which the membrane is found to detach from the cytoskeleton (from Evans et al., 2005),  $k_m$ , is defined as

$$k_m = \frac{1}{t_0} \exp\left(\frac{x_\xi f}{k_B T}\right), \quad (24.26)$$

where  $1/t_0$  is in the range 0.7–1.7 [1/s] and where the force required to lower the free energy barrier by one unit of thermal energy is given by  $k_B T/x_\xi \approx 17$  [pN] where  $x_\xi$  is a fixed length in the direction of this force. The probability of membrane detachment,  $Q_m$ , is

$$Q_m = 1 - \exp(-k_m \Delta t). \quad (24.27)$$

### Viscous regime

For a bond which has formed a tether, the force from Heinrich et al. (2005) is

$$f(t) = f_\infty - (f_\infty - f_1) \exp\left(-(t - t_1)/\tau\right), \quad (24.28)$$

where  $f_\infty$  represents the maximum force of the tethered bond toward which the force plateaus and is a function of the speed at which the tether is pulled,  $v$  [ $\mu\text{m}/\text{s}$ ], given as  $f_\infty = 60v^{1/4}$  [pN] and  $\tau = 0.3v^{-0.75}$ .  $f_1 = f(t_1)$  represents the force at which the membrane detaches from the cytoskeleton to initiate the tether regime, and  $t_1$  the time at which detachment occurs.

The off rate for a tethered bond is given by substituting Eq. (24.28) into the Bell relation for the off rate, Eq. (24.26). The probability of bond rupture during the viscous regime is derived from the same relation as for the elastic regime, Eq. (24.27), by substituting the new relation for the off rate. It is important to note that no “on rate” for the viscous tether regime (or an associated probability of binding) since it is assumed that no bonds will be formed that are initially in the tether phase.

The adhesion model used to calculate the total bond force was implemented separately to the main SPH neighbor list since the length scales over which a bond could realistically stretch were far greater than those permitted by the SPH neighbor list for the chosen resolution.

The algorithm for resolving the adhesive bonding forces and associated events was as follows:

- (1) Determine bonding events for membrane/boundary particle pairs passed into the SPH solver from the neighbor list. If a bond was found to have formed, add it to the bonding list.
- (2) Traverse the bonding list invoking each of the following procedures upon each membrane/boundary particle pair in the bonding list:
  - Reset the displacement vector between bonding particles according to the periodic boundary conditions of the tube if required.

- If the bond is elastic, then determine whether it has formed into a tether.
- Calculate the force load for the given particle pair, depending on their bonding regime.
- Determine whether the bond has detached, and if so, then remove it from the bonding list.
- Increment both membrane and boundary particle forces by those determined from the bonding model.

The inclusion of method components to accommodate short-range particle-particle adhesion bond kinetics as well as long-range tether forces (without the requirement to spatially resolve the fine tethers themselves) provides a powerful physiologically realistic treatment for white blood cell rolling adhesion.

### Simple model for thrombin-controlled coagulation

The simple model for blood coagulation (clotting) that will be used here is based around the transport of the protein thrombin and the gelation that this causes in the blood. Thrombin, when introduced to blood, causes the conversion of liquid phase fibrinogen into a fibrin gel that becomes increasingly stiff. The biological processes related to clotting will be reviewed in Section [Blood coagulation and clot formation modelling](#). Here we describe the components of the simple SPH model that will be used to demonstrate usage of this method in developing computational models of clotting.

The key elements of this model are

1. Track thrombin transport through the flowing blood phase.
2. Represent the effect of increasing cross-linked fibrin gel on the blood as an increasing viscosity with a yield stress limit, after which the clot can be regarded as having become solid and leading to zero blood flow in that location.

This model is very simplified, omitting for example the role of platelets and related chemicals. The intent of this simple model is to demonstrate that a particle method allows for the easy inclusion of clot rheology and importantly the effect of the flow on the thrombin transport where the viscosity of the gel is taken into account from a flow perspective. It also shows that all the required model components can be made available within an SPH framework.

Thrombin transport is the result of a combination of diffusion within the fluid parts of the gel and advection by the free-flowing blood. This can be modeled as a molecular diffusion ([Eq. 24.11](#)) with a diffusivity that depends on the degree of gelation. The SPH method being Lagrangian automatically accounts for the advection of chemical species such as thrombin. The gelation is modeled as a solidification process following [Cleary \(2010a\)](#) with chemical species concentration now playing the role that temperature played in the thermodynamic-driven solidification. This method has been successfully used for solidification prediction for both low-pressure die casting ([Cleary et al., 2010](#)) and in powder bed laser additive manufacturing ([Cummins et al., 2021](#)).

In this approach, the fraction of solid in the liquid is related to the control property (here thrombin concentration and previously temperature). The viscosity of the fluid is then a function of this solid fraction. When the solid fraction reaches a level that is able to inhibit flow then the governing equation of that SPH particle is changed from being the Navier–Stokes equations (here Eqs. 24.1, 24.2 and 24.7) to either elastic solid deformation equations (given by Eqs. 24.1, 24.6 and 24.9) or more simply freezing that particle in place. Such solidification is only able to occur if some of the neighbors of the particle are already frozen. This is simple to implement in a meshless method such as SPH because the solid fraction and freezing state relate to each specific volume of material which is automatically advected with each volume of material (as represented by each SPH particle) in such a Lagrangian method.

### SPH solid evolution for remodeling processes

Biological processes in the human body often lead to remodeling of tissue in response to the conditions and loads that they experience. Muscle mass gain (or loss) in response to exercise (or lack of) is a well-known example. The SPH method is well suited to problems that involve the selective addition or removal of mass from the modeled solid tissues. In this chapter, we consider the remodeling on bone in response to cyclic load applied to the bone.

The underlying theory is given by Prendergast and Taylor (1994) and McNamara and Prendergast (2007). This involves the identification of a threshold equilibrium strain which represents conditions where no bone remodeling occurs. Smaller strains lead to a reduction in bone density while larger strains lead to enhanced bone density. The methodology for such prediction was established by Fernandez et al. (2010, 2013).

This is implemented in the SPH method by changing reference density  $\rho_0$ . Its rate of change from remodeling is proportional to the strain stimulus,  $\epsilon$ ; and is given by

$$\frac{\partial \rho_0}{\partial t} = \Theta \epsilon, \quad (24.29)$$

where  $\Theta$  is the proportionality constant. The resultant change in density then changes the Young's modulus such that the addition of new bone increases bone stiffness, while loss of bone makes it less stiff. This variation of Young's modulus is related exponentially to density. The new Young's modulus at timestep  $j + 1$  is given by

$$Y^{j+1} = \zeta \rho_0^\chi \quad (24.30)$$

after  $\rho_0$  has been updated by integrating Eq. (24.29). This model was determined experimentally by Currey (1988). Here  $\zeta$  and  $\chi$  are the elastic fitting constants.

---

### Hemodynamics of vascular disease

The vascular circulation is an essential transit system within the body that bridges the scales of entire body down to microscale for delivery of oxygen and nutrients

to cells and removal of cell metabolism waste products, such as carbon dioxide (Rowell, 1974). This multiscale branched flow network (Safaei et al., 2016) has evolved in step with the overall physiology to create an efficient balance between:

- delivering the required blood volume and flow rate required to supply all tissue cells across the entire body with necessary nutrients at a rate sufficient to maintain life at a cellular level, while
- keeping arterial diameters narrow enough to minimize turbulence within the body (Horsfield & Woldenberg, 1989).

Essential parts of the body's immune and wound healing subsystems take advantage of this network to allow cellular agents (e.g., white blood cells, platelets, etc.) to traverse the entire body and take part in monitoring, identifying, and triggering responses to pathogens, abnormal (e.g., cancerous) tissue, inflammation, and direct damage to tissue lining (Friedl & Weigelin, 2008; Muller, 2013).

The vast extent of the circulatory network therefore makes it our most vulnerable system-wide physiological component for disease development and propagation. When functioning correctly, the circulation supports very effective supply and defense mechanisms. However, when dysfunction occurs, transport within this network can also exacerbate local complications that then extend to widespread or downstream disease conditions. This includes

- Diseases that involve red blood cells (RBCs) due to inherited genetic defects (such as sickle-cell), invasive parasites or bacteria (e.g., malaria, babesia, and Lyme disease) that result in RBC damage (McCullough, 2014), or conditions that lead to lowered iron levels resulting in anemia. Since RBCs contain no cellular replication machinery, they are not direct targets for viral infection but may be used for transport since some viruses can bind to RBC receptors (e.g., influenza A). Engineered RBCs may therefore be a promising viral trap therapy for the human immunodeficiency virus (HIV) and the severe acute respiratory syndrome coronavirus 2 (SARS-CoV-2) (Hoffmann et al., 2021).
- Viral illnesses that target and damage white blood cells (WBCs) lowering immunity (Bhardwaj et al., 2020) such as HIV and SARS-CoV-2.
- Impaired platelet function and secretion, or lowered platelet counts which can cause excessive bleeding or thrombocytopenia. This is often an observed patient outcome from clinical application of ECMO (Extra-Corporeal Membrane Oxygenation) machines, but the cause is not yet fully understood (Jiritano et al., 2020).
- Atherosclerosis, where large-scale rupture of plaque on the vascular wall results in thrombosis that can block smaller blood vessels downstream resulting in significant organ damage, heart attack, and stroke (Sakakura et al., 2013), and
- Spread of cancer cells throughout the body once they enter the bloodstream, and potential for triggering prothrombotic activity in blood vessels (Mitrugno et al., 2016).

Health complications may also be associated with the development of patient-specific vascular complications in particular blood vessels based on extrinsic risk

factors such as diet, demographic, genetics, and lifestyle (Roth et al., 2020). To improve patient risk assessment and develop better intervention strategies requires greater understanding of the onset and development stages of vascular disease. That is, the hemodynamics of “at-risk” parts of the network due to abnormal flow, plaque deposition/growth/rupture and potential thrombus formation leading to ischemic stroke in the brain or embolism in the lungs. Computer simulations of patient-specific geometry and flow conditions are promising diagnostic approaches that are still largely underutilized.

### Explicit modeling of cell mechanics at capillary scale

The arterial network branches into arterioles ( $<100\text{ }\mu\text{m}$  diameter). These connect to the venous system via a fine network of capillaries that proliferate in tissue throughout the body. These capillaries have diameters ranging from around 3–40  $\mu\text{m}$  and cumulatively together with the arterioles and venules are referred to as the microcirculation. Regulated oxygen and glucose transport to tissue cells and removal of the waste products of cellular metabolism (e.g., carbon dioxide) are performed by RBCs. Supporting the large metabolic demands of the human body relies on effective, continual migration of RBCs through the microcirculation. Mature RBCs are deformable biconcave discs, 7–8  $\mu\text{m}$  in diameter, with no nucleus or mitochondria. Oxygen binds effectively to the 280 million molecules of hemoglobin protein stored in each RBC and is released when and where in the body it is needed based on environmental conditions. The oxygen-binding affinity of hemoglobin is modulated by temperature, pH, and local partial pressures of oxygen and carbon dioxide. For example, metabolic activity in muscle tissue postexercise leads to conditions of increased temperature, increased carbon dioxide in the bloodstream, and lowered pH which trigger hemoglobin to release its stored oxygen. In the smallest capillaries (3–5  $\mu\text{m}$ ), RBCs squeeze through one at a time. Oxygen diffuses out through the RBC membrane into the blood plasma, then across the single layer of flattened endothelial cells that form the capillary wall and finally into the oxygen depleted tissue cells where it is used. Carbon dioxide is removed from the microcirculation in three ways (Doyle & Cooper, 2018):

1. dissolved in the plasma,
2. bound to hemoglobin within RBCs, but
3. predominantly it is carried out in bicarbonate form.

RBCs complete their journey back to the lungs via the venous system where they are reoxygenated and where carbon dioxide is collected and expelled from the body.

At the capillary scale, viscoelastic cell bodies occupy much of the blood volume and the flow dynamics are dominated by contact mechanics interactions between the cells and with the walls. Flow into the capillary network is regulated by the nervous system and hormone control in response to the body’s metabolic demands. Exercise and postprandial digestion can both influence whether blood flows into the capillary networks or is redirected via vasodilation or vasoconstriction of smooth muscle in the

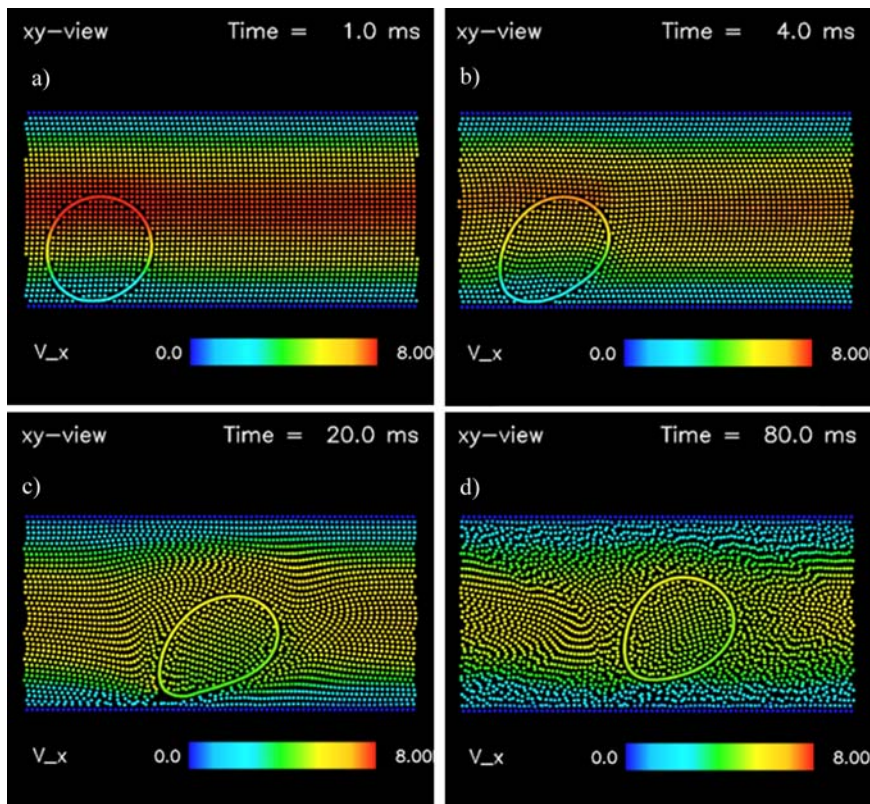
arteriole walls (precapillary sphincters), which are able to short-circuit the capillary beds and redirect flow directly to the venous system. At any one time, only about 7% of total blood volume is present in the arterioles and capillaries (Wolff et al., 2016).

Within the microcirculation, the viscosity of whole blood reduces with vessel diameter down to a capillary size of 40  $\mu\text{m}$ , but then sharply increases for smaller capillary sizes below this. This effect was first observed experimentally *ex vivo* by Fahraeus and Lindqvist (1931) and is often referred to as the Fahraeus–Lindqvist effect. This is a consequence of the multiphase nature of blood in these small vessels. RBCs occupy a significant fraction of the vascular space in such capillaries so that the fluid dynamics is dominated by cell–cell and cell–wall interactions. The effect of viscosity reduction is caused by RBC migration away from the walls. A satisfactory explanation for the hydrodynamic mechanism responsible has not yet been determined (Ascolese et al., 2019; Secomb, 2017). Below 40  $\mu\text{m}$  diameter, the increase in viscosity is due to multi-cell crowding in narrow channels that increase cell collisions with the walls. This behavior continues down to capillaries that are sufficiently small that only individual cells can squeeze along single file.

To explore the dynamics of a single deformable cell in the shear flow of a capillary, we consider an SPH model of an 8  $\mu\text{m}$  deformable RBC in a 15  $\mu\text{m}$  capillary tube. For simplicity this is demonstrated in two dimensions with a domain that is periodic in the flow direction. For the plasma flow, a parabolic profile with peak speed of 0.6 mm/s traveling from left to right along the tube is specified. The RBC is modeled as a fluid-filled soft body with a flexible membrane surface as proposed in Section [Soft bodies with flexible surfaces \(such as cell membranes\)](#). All materials have a density of 1000 kg/m<sup>3</sup>. The plasma is assumed to have a viscosity of 1 mPa s, while the viscosity of the interior of the cell is double this. The membrane stiffness is 200 N/m. To reduce the computation time required, this was run as a pseudo-transient simulation.

[Fig. 24.2](#) shows the RBC inside the capillary tube with a starting position touching the bottom wall. The SPH particle color shows the particle speed in units of 100  $\mu\text{m}/\text{s}$ . The RBC is a significant obstacle to the flow of the plasma and strongly perturbs the flow. It both modifies the flow field of the plasma outside the cell and deforms the cell based on changes in stress in the membrane arising from both the fluid flow within and exterior to the cell. Overall, the cell obstructs fluid flow leading to a more uniform distribution, particularly near the cell, with a lower peak speed.

The presence of the cell rapidly modifies the parabolic profile reducing the peak speeds at the center of the tube and forcing the fluid to flow more as a plug in the region near the cell. The shear flow creates spatially varying stress along the surface of the cell membrane with the peak stress felt toward the top of the cell. The cell shape then changes in response to the balance of elastic force in the cell membrane and the differential force across the cell from the shear flow. The top of the cell at 4 ms and shown in [Fig. 24.2B](#) elongates in the flow direction and begins to rotate clockwise. By 20 ms, the flow has a more constant plug profile across the central half of the tube in response to the cell body obstacle. The cell continues to rotate.

**FIGURE 24.2**

RBC in a capillary flow demonstrating migration away from the wall due to the uplift force. The particle color shows the particle speed in  $100 \mu\text{m/s}$ . The cell shape changes over time in response to the balance of elastic force in the cell membrane and the differential force across the cell from the shear flow. This also generates a lift force away from the wall. The cell motion is shown at: (A) 1 ms, (B) 4 ms, (C) 20 ms, and (D) 80 ms.

Since the cell is neutrally buoyant (with no other forces such as adhesion binding it to the wall), it tumbles forward rotating about its center of mass so that its elongated tail is pulled away from the wall. Plasma flows downward to the base of the cell (with flow speed shown yellow) and under it as the cell moves upward away from the wall. By 80 ms (Fig. 24.2D), the cell has moved upward to the center of the tube and adopts a more symmetrical shape in response to the more uniform flow profile in the center of the channel.

The cell shape deforms in a shear flow because there are different fluid velocities acting on different parts of the membrane. This leads to acceleration and deceleration of different parts of the cell membrane relative to the cell center, which differentially stretches and bends the membrane and leads to shape changes. The cell and

external flow quickly equilibrate. The requirement for equilibrium is that all the fluid within the cell is moving at the same velocity. The membrane shape and tension variations balance the velocity differentials applied by the external crossflow at different transverse locations across the capillary. In doing so the membrane toward the center of capillary moves more rapidly than does the membrane near the wall. This manifests as a rotation of the cell which is largest at around 15–20 rad/s when the cell is near the wall and declines to zero when the cell is centrally located within the capillary (as shown in Fig. 24.3A). In the streamwise direction the cell moves at the same speed as the average speed of the fluid on either streamwise side.

The interaction of the cell with the shear flow generates an uplift force that pushes the cell away from the wall moving it toward the channel center channel. This SPH-soft body model is naturally able to capture this phenomenon without the need to include any artificial representation of this uplift force. The transverse

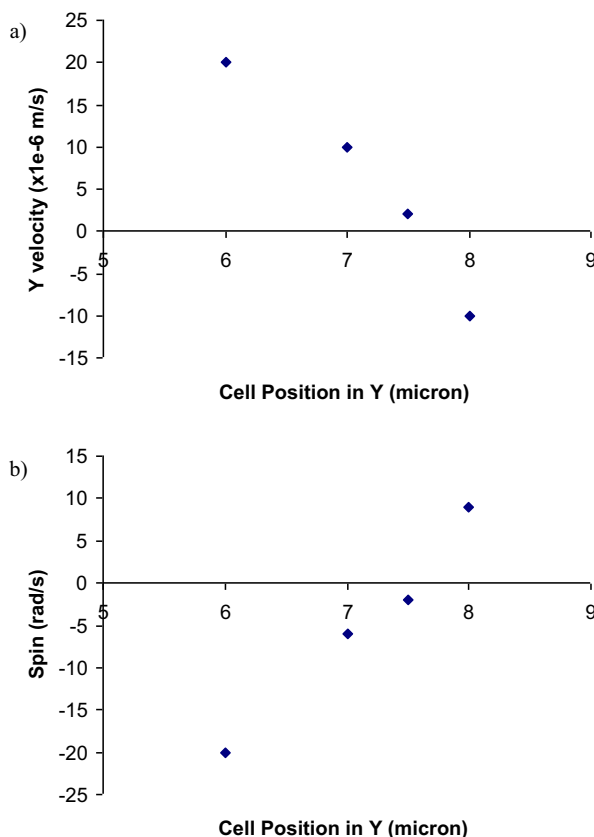


**FIGURE 24.3**

Average motion of an RBC at different transverse locations  $Y$  across a 15- $\mu\text{m}$  capillary, (A) transverse velocity, and (B) spin.

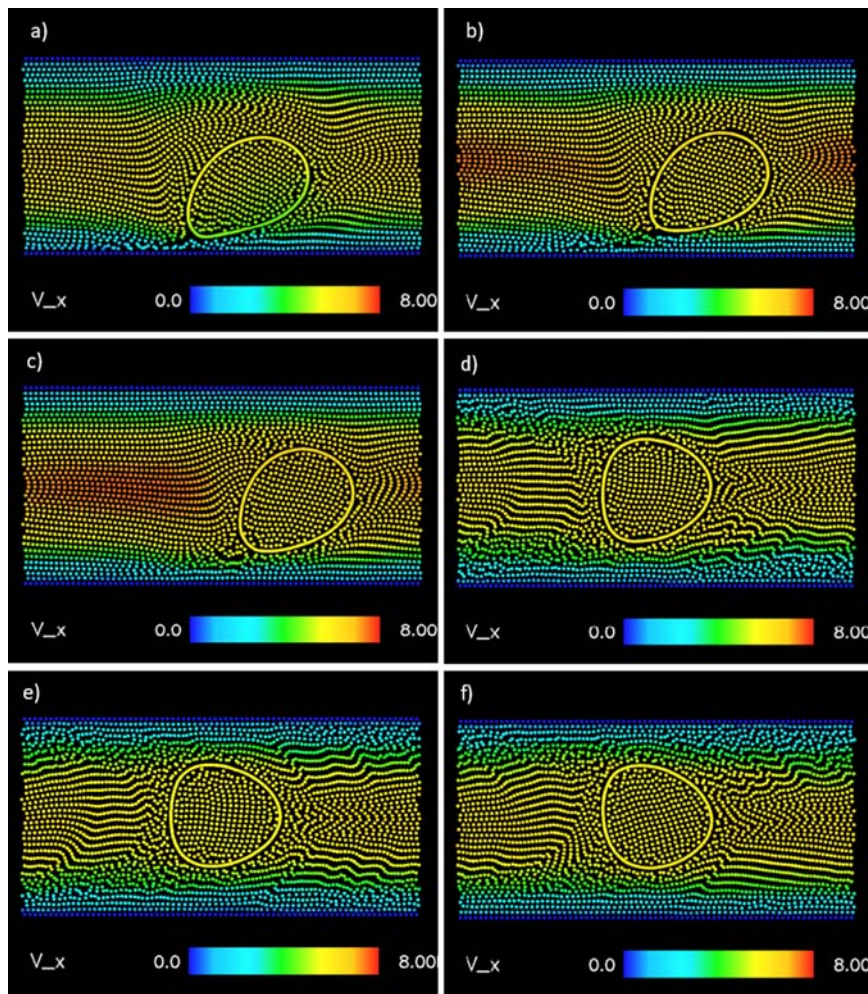
velocity for the cell in this simulation is observed to vary linearly on the distance from the capillary centreline (as shown in Fig. 24.3B). It is well known that rotation of solid bodies in a fluid flow generates a lift force. So, a natural explanation for the observed lift force occurring for these deformable cells is that it arises as a classical lift force from the cell rotation. This in turn arises from the membrane motion that is required to balance the external shear forces so as to create uniform interior motion of the cell contents in the streamwise direction.

This uplift force can also be mechanistically related to a transverse force imbalance between the leading and trailing sides of the cell. The fluid upon reaching the left (trailing) side of the cell is predominantly forced inward at a reasonable speed by the inclined cell surface. This generates a shear force on the membrane dragging it toward the center of the capillary (inwards and to the right). On the (leading) right side of the cell, the flow is directed down toward the lower wall. This also generates a shear force (this time directed outward). However, this transverse force is weaker because the vertical flow on the right of the cell is weaker than that on the left. This causes a force imbalance on the particle with a stronger inward force on the trailing side and a weaker outward force on the leading side. The difference between these is the inward directed lift force. This force couple also creates a torque on the cell which is what causes it to rotate. It also causes the higher deformation of the cell on the upper left side (closer to the center of the capillary) than for the similar locations on the right.

Fig. 24.4 shows the equilibrium shape for the RBC at different positions in the shear flow. The distance of the center vertically from the bottom wall is (a) 4.4  $\mu\text{m}$ ; (b) 5.0  $\mu\text{m}$ ; (c) 6.0  $\mu\text{m}$ ; (d) 7.0  $\mu\text{m}$ ; (e) 7.5  $\mu\text{m}$ ; and (f) 8.0  $\mu\text{m}$ . The particles are colored by speed in the same manner as Fig. 24.2. Near the wall (Fig. 24.4A and B), the cell is heavily asymmetric and elongated in response to the strong shear in that part of the flow. The elongation in the strong part of the shear generates higher cell rotation and lift force away from the wall. The cell shape transitions to a more symmetrical “parachute-like” shape (Fig. 24.4D and E) when it is near the centerline of the flow where the stresses are more uniform across the cell and the cell has ceased rotating. If the cell is located in the upper-half of the channel, then its shape is the mirror image of the shape at the matching distance below the centerline, so Fig. 24.4F is reflectively symmetric to Fig. 24.4D with its elongation being now at the top and rotating in the opposite (anticlockwise) direction.

The uplift mechanism is dynamically very important for blood flow as it causes RBCs to be preferentially located toward the center of the flow in blood vessels. Their traveling centrally has important physiological benefits:

- Their transport rate and therefore the transport rate of oxygen is maximized.
- Generation of the observed RBC-depleted annular region at the wall (Ascolese et al., 2019) which reduces crowding effects for other cells that prefer or need to be located near the walls. WBCs are found in higher concentrations near the walls to which they adhere. Being able to do this with limited interference from RBCs is important for enabling their immune response actions. Less deformable

**FIGURE 24.4**

Equilibrium shape of an RBC in a 15- $\mu\text{m}$  wide capillary for different positions in the shear flow. The distance of the center vertically from the bottom wall is: (A) 4.4  $\mu\text{m}$ , (B) 5.0  $\mu\text{m}$ , (C) 6.0  $\mu\text{m}$ , (D) 7.0  $\mu\text{m}$ , (E) 7.5  $\mu\text{m}$ , and (F) 8.0  $\mu\text{m}$ . The particles are colored by speed as shown in the color bar with red corresponding to 0.8 mm/s.

inactivated platelets also remain closer to the walls which facilitates their entry into and migration through the tissue and endothelial tissue repair, respectively. This RBC depleted region also occurs in much larger blood vessels ([Secomb, 2017](#)) and RBC crowding in arterial flows helps push other cells (WBCs and platelets) toward the wall. Conversely, there is some evidence that increasing RBC rigidity negatively impacts WBC adhesions to the vessel wall ([Gutierrez](#)

et al., 2018) which is consistent with the origins of the uplift force identified using this model.

- Fewer interactions between RBCs and the wall, which results in a lower apparent viscosity of whole blood. This depends on the diameter of the blood vessel and hematocrit level (Secomb & Pries, 2013). Viscosity controls pressure drop across the vascular system and therefore the load on the heart, so the systemic reductions in viscosity arising from this central concentration of RBCs is important for operation of the circulatory system and human health.
- In the center of the tube, the obstructed “plug-like” flow profile and symmetrical cell shape together greatly reduce hemodynamic stresses onto the RBC membrane, which can be expected to lead to less wear and tear on them contributing to the average 120 days of RBC lifespan in the circulatory system.

### White blood cell rolling adhesion

As an integral part of our immune system, white blood cells (WBCs) or “leukocytes” are produced in bone marrow and traverse great distances throughout the body via the circulatory system. Adhesion of WBCs to the endothelium of blood vessels is important for migration of these cells to sites of inflammation and proceeds via a complex multistage process:

- WBCs move toward the endothelium under hydrodynamic shear stress until close enough to anchor to the wall. This occurs by means of P-selectin glycoprotein ligand-1 (PSGL-1) molecules, which are distributed on the ends of the microvilli. These are structures that protrude from the cell membrane, typically extending a distance 0.2–0.4 μm (Park et al., 2002). The 0.1 μm thick microvilli (Zhao et al., 2001) probe the glycocalyx (a porous media approximately 0.5 μm thick that lines the endothelium, see Kamm, 2002), forming bonds with the P-selectin molecules on the endothelium underneath.
- The initial loading of these bonds follows an elastic regime, over which the force loaded onto each bond grows linearly with distance, reflecting membrane stretching (Evans et al., 2005). However, after a bond has been loaded with a certain critical force, or pulled with sufficient speed, it may cause the microvillus to rupture from the cytoskeleton. This forms a “tether” (or membrane nanotube) which extends reasonably freely to prolong the life of the bond. The tether elongation follows a viscous regime with a logarithmic relationship between loaded force and distance stretched (Heinrich et al., 2005). These tethers cause the microvilli to stretch to as long as 40 μm but have an average length of 10 μm (Kamm, 2002). Experiments have shown that tethers have an elastic constant of 0.25 pN/μm (King et al., 2005), with a force of 60–120 pN required to pull a single tether, depending on the pulling speed (Evans et al., 2005).
- The hydrodynamic flow within the blood vessel applies a strong shear rate across the WBC which deforms the cell into a teardrop shape increasing its contact area with the endothelium. New bonds continually form at the leading edge of

the cell and others break as the trailing edge peels away from the endothelium. This leads to a staggered unsteady rolling motion along the endothelium at a rate  $10\times$  slower than the surrounding hydrodynamic flow. This process is also selectin mediated (Tees and Goetz, 2003), and occurs at an unsteady rate, as the bonds break somewhat randomly.

- The final stage involves the firm adhesion of the WBC to the endothelium, which occurs via  $\beta_2$  integrin distributed along the WBC membrane surface between the microvilli. These bond to integrin cell adhesion molecule (ICAM-1) ligands in the endothelium. The adhesions are made more robust by the growth of focal contacts that traverse the WBC membrane to attach directly with the cytoskeleton. These focal adhesions help facilitate WBC migration through the endothelium (Irvine et al., 2002).

Most current selectin-mediated adhesion models are based on the kinetics concept, by which rates of bond association and disassociation are determined from the potential or existent bonding forces. These kinetic rates are based on either the Bell (1978) or Hookean spring (Dembo et al., 1988) models. These rates are then either used as inputs into differential equations for the bond density (N'Dri et al., 2003; Dong & Lei, 2000) or into probabilistic equations (Bhatia et al., 2003; Jadhav et al., 2005) to determine the number of formed or ruptured bonds. Alternative probabilistic methods have also been developed (Zhu, 2000). The force information from the bonds is then fed back up to the fluid dynamics solver to determine the position of the cell relative to the vessel wall at the next iterative time step. This process is then repeated for the duration of the simulation.

All of the reviewed models employ Eulerian methods for solving the governing fluid equations at the nodes of a static grid. Such an approach has some advantages in that it allows for an easy application of multiscale methods to accurately resolve the bonding forces, which are present at lengths far smaller than that of the cell itself. Such a method simply involves breaking up the domain into a larger number of smaller sized cells in the contact region (N'Dri et al., 2003). However, it is difficult to resolve the shape of the cell as it moves through the fluid with an Eulerian approach, since the cell membrane usually does not align with the nodes of the grid.

Different techniques are used to resolve the shape of the cell in the presence of a hydrodynamic force in the context of a Eulerian grid. The immersed boundary technique is employed by several authors to determine the position of discrete nodes along the cell with respect to the neighboring nodes of the Eulerian grid (N'Dri et al., 2003; Jadhav et al., 2005) but this can lead to numerical diffusion and inaccuracy of gradients near the cell wall. Others employ the method of adhesive dynamics, which assumes the cell to be perfectly spherical and undeformable (Bhatia et al., 2003; Krasik & Hammer, 2004) which is problematic since the cells clearly change shape according to the balance between hydrodynamic and cell wall forces. Additionally, Dong et al. (1999) assumed that only specific regions of the cell are capable of peeling and adhering (with the rest of the cell-substrate contact region remaining flat) to derive a governing equation for the curvature of the cell.

Models of integrin-mediated adhesion also exist, but these only consider static interfaces for constant separation distance (Irvine et al., 2002; Palacek et al., 1999; Schwarz et al., 2002). As such they do not feature in any of the models reviewed here of leukocyte–endothelium adhesion, since dynamic forces are integral to the adhesion process and the separation between cell membrane and vessel wall varies considerably.

There are only a small number of Lagrangian models that have attempted to model aspects of WBCs. Cleary and Sinnott (2006) identified the opportunity to use SPH models of flow and explicit representations of the cells as elastic fluid filled membranes. Gholami et al. (2014, 2015) developed multiscale SPH simulations of WBC deposition and adhesion in the context of larger scale blood vessel flows. These did not attempt to resolve the shape and deformability of individual cells, nor did they seek to predict the rolling adhesion behavior of WBCs at the wall. Tan and Xu (2020) also developed large-scale hydrodynamic flow models with RBCs, WBCs, and platelets represented. They used a coupled SPH/Immersed Boundary Method (IBM) approach with IBM used to model the interactions between fluid and cells, but also did not represent the full WBC deformation and rolling adhesion.

To demonstrate the utility of a meshfree method for this type of coupled adhesive elastic cell and fluid hydrodynamics system, we introduce here an SPH model of rolling adhesion behavior for a single WBC experiencing shear flow inside a small capillary with 15  $\mu\text{m}$  diameter. This is a model of the type introduced by Cleary and Sinnott (2006) but with more realistic adhesion modeling. To enable simpler visualization in the demonstration it is modeled in two dimensions. Similar usage in three dimensions is straightforward. The resolution of the SPH fluid and boundaries (cell and capillaries) is 0.4  $\mu\text{m}$ . The viscosity of the fluid outside the cell is 0.001 Pa s. To increase computational speed, the simulations were run pseudo-transient with a scaled-up density of  $1.06 \times 10^5 \text{ kg/m}^3$  (which is a scale factor of 100). This recognizes the dominance of the viscous scales and that the cell shape quickly equilibrates to the current fluid flow structure which changes much more slowly. This approach is valid as long as the fluid dynamic timescale remains longer than the timescale for cell shape changes. A parabolic flow profile is used since the flow is laminar (with Reynolds number of approximately 1). The peak speed for the fluid was 1 mm/s with flow directed from left to right along the capillary.

The 8  $\mu\text{m}$  diameter cell consists of a viscoelastic membrane boundary enclosing a cytoplasm with viscosity 3 mPa s and density the same as the fluid outside the cell. This viscosity for the cellular contents is lower than for the physical system and is chosen to keep the simulation time step modest. To compensate for this low cell viscosity, the membrane particles are given a relatively high spring stiffness of 50 N/m to maintain cell shape during adhesion and rolling. The membrane is colored in alternating blue/white bands to help visually track the rotation of the cell.

It is of interest to note that the length of an average microvillus roughly equals that of the chosen SPH resolution for this simulation. From Zhao et al. (2001), there are approximately 26 microvilli for a given 2D WBC cross section. An average

microvillus has approximately 50 PSGL-1 molecules on its tip (Moore et al., 1995), so each membrane particle is assumed to have on average 50 possible bonding sites. A more physically exact model might assume that each fifth membrane particle possessed 50 bonding sites, as opposed to averaging these over all the membrane particles, however, the choice of 10 sites per particle was made in order to obtain a more consistent rolling motion. With a less consistent distribution of bonding sites, some initialized simulations might never allow for a rolling cell, due to the absence of bonding sites in the membrane-boundary contact region. Therefore, the more consistent distribution was chosen in order to capture the required macro-scale dynamics within the limited time available. In a similar fashion, the number of receptors per boundary particle was determined by taking the product of the average selectin density in one dimension and the boundary particle diameter (which was the same as for all other SPH particles in the simulation).

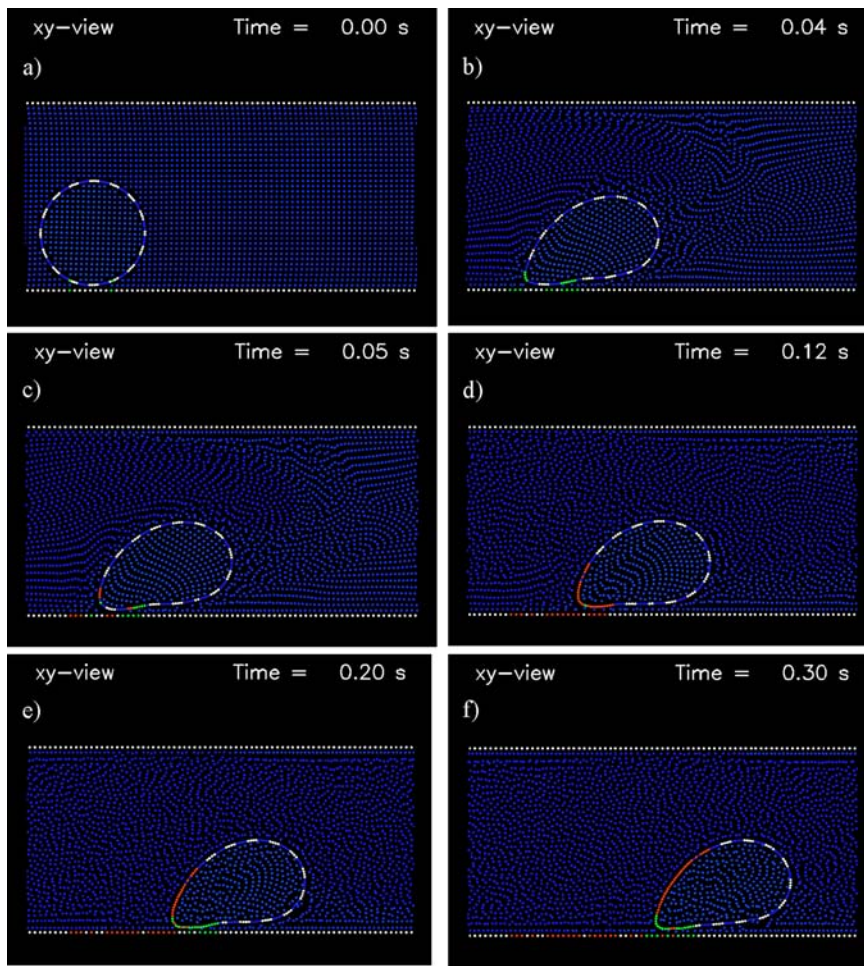
**Fig. 24.5** shows the rolling adhesion progression of the WBC along the channel. Initially, the cell is undeformed by the flow and has a circular cross section. The membrane is colored with alternating blue/white bands so as to more easily visually track the rotation of the cell. By 0.04 s, the cell has formed adhesive bonds with the capillary wall and the spatially varying shear across the cell height due to the parabolic flow profile deforms the cell into the characteristic teardrop shape of experimentally observed WBCs. Matching pairs of green points on the membrane and wall indicate that tethers have formed between these points although the tether structures are not shown. At 0.05 s, some of these tethers at the tail end have broken (represented by the points changing to a red color), the tail begins to peel from the underlying surface contact and the WBC begins rolling.

By 0.12 s, almost all the previous tethers have broken, and the WBC lurches forward a short distance before being arrested by the formation of new tethers by 0.02 s. This highlights that WBC rolling motion is not continuous but rather a series of stick-slip interactions with the wall that cumulatively result in a slower rate of motion than the surrounding plasma. It also demonstrates that such an SPH-elastic cell model is able to capture both the characteristic shape and this irregular surging motion. From 0.2 to 0.3 s, there is a steady phase of tail peeling with tethers rupturing and new tethers forming at roughly a similar rate.

The average observed speed of the WBC was 500  $\mu\text{m}/\text{s}$  which is 1/20 of the peak speed of the plasma in the absence of the WBC. The elongated length of the fully deformed cell is 1.3 times that of the diameter of the undeformed cell, consistent with observation (Firrell & Lipowsky, 1989). The 2D particle-based model predictions capture many realistic elements of WBC rolling adhesion behavior such as the stochastic stick-slip adhesions resulting in greatly reduced transport rates as well as the characteristic deformed teardrop shape for the rolling cell.

### Arterial scale flow

At the scale of large arteries, there are a number of physical differences from the microcirculation which influence the flow fields and wall stresses, and consequently

**FIGURE 24.5**

WBC rolling adhesion model at different times during its motion along the capillary wall. Bond formation between membrane and wall are shown in green. When a tether breaks, the corresponding wall and membrane nodes change to red. The tethers themselves are not explicitly shown. The cell motion is shown at: (A) initially, (B) 40 ms, (C) 50 ms, (D) 120 ms, (E) 200 ms, and (F) 300 ms.

the disease incidence and progression within particular arteries. These add significant complexity to the development of computational models:

- Much higher Reynolds number flows due to much higher flow rates and larger length scales so there is opportunity for turbulent instabilities in accelerated flow after constrictions.

- Flow is strongly pulsatile driven by regular cardiac pumping from upstream. This can result in recirculatory flow structures as well as different high, low, and oscillatory flow regions.
- Vessel geometries are much more complex in shape.
- The walls of the arteries are viscoelastic and provide transient elastic storage such that the stretch of the walls under load can modify the pulsatile flow profile. Elastic regions are able to distend in order to relieve intravascular pressure. Around rigid atherosclerotic plaques this may lead to large strain at the interface between the two materials which may alter plaque morphology resulting in greater risk of plaque rupture and thrombosis.
- Blood is typically treated as a single phase, non-Newtonian fluid rather than a multiphase large ensemble of discrete cells suspended in plasma since it is too computationally intensive to resolve the individual cells. However, the multiphase nature of whole blood is responsible for the complex rheology observed under different flow conditions and the single-phase models may not adequately represent aspects of the system such as leukocyte migration to sites of plaque formation ([Jung & Hassanein, 2008](#)).

Since the late 1990s, CFD models of arterial blood flow in patient-specific arterial geometries sourced directly from medical imaging (CT, MRI) have become common. These primarily focus on disturbed flow and wall stresses in the carotid artery ([Birchall et al., 2006](#); [Cibis et al., 2016](#); [Gharahi et al., 2016](#); [Long et al., 2000](#); [Lopes et al., 2020](#); [Sinnott et al., 2015](#)) to understand the development of atherosclerotic plaques and as a major risk factor for cerebral stroke. More recently, modeling has been applied to other arterial branches throughout the body:

- Coronary ([Malve et al., 2012](#); [Wu et al., 2015](#); [Zhang et al., 2014](#)),
- Aortic arch ([Numata et al., 2016](#); [Pirola et al., 2017](#)),
- Thoracic arch ([Perinajova et al., 2021](#)),
- Pulmonary ([Kheyfets et al., 2015](#)),
- Cerebral ([Berg et al., 2014](#); [Sekhane, 2016](#); [Thirugnanachandran et al., 2021](#)), and
- Liver ([Taebi et al., 2020](#)).

CFD models have also been used for studying hemodynamics within aneurysms ([Liang et al., 2019](#); [Tse et al., 2011](#); [Xiang et al., 2014](#)) and to understand the effect of surgical intervention with stents ([Conti et al., 2016](#); [Midulla et al., 2012](#)) or for clot retrieval ([Phan et al., 2020](#)). The influence of cardiac cycle pulsatility ([Marshall et al., 2004](#)), non-Newtonian blood rheology ([Arzani, 2018](#); [Fatahian et al., 2018](#)), downstream network back pressures ([Pirola et al., 2017](#); [Sinnott et al., 2015](#)), and wall elasticity ([Lopes et al., 2019](#); [Nowak et al., 2019](#)) on flow have also been investigated.

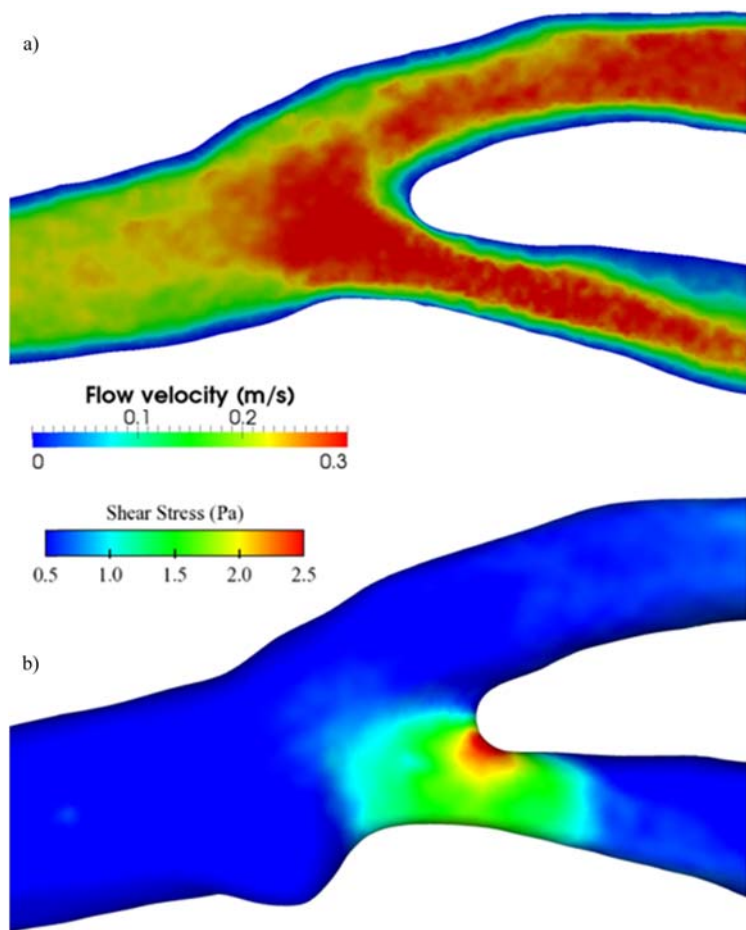
Here, we present an SPH model of 3D arterial flow through a carotid bifurcation. This physiological geometry has previously been used in [Sinnott et al. \(2015\)](#) to study the influence of branch angle and downstream pressures on the flow field and wall shear stress within the bifurcation.

The artery bifurcates into the external carotid artery (ECA) that supplies the face and neck with blood, and the internal carotid artery (ICA) that supplies the brain. The ECA is typically narrower with side branches and has much higher flow resistance than the ICA which reduce flow rate within this branch. Conversely, in normal patients the ICA is generally slightly larger than the ECA and has much less flow resistance, so flow rate is much higher. Higher wall stresses and rate of lipid deposition tends to favor intimal thickening and/or plaque formation in the higher flow branch. This can lead to narrowing (stenosis) of the ICA and produce elevated velocities, potentially turbulent conditions downstream and significant stresses onto the plaque which make it particularly vulnerable to rupturing. Since the ICA directly supplies the cerebral vasculature, the high risk for initiating cerebral stroke in patients with vascular disease make this a common anatomical region to study for assessing dangerous flow and wall stress conditions. The ICA in the patient geometry being considered here is mildly stenosed. Here, we use the same type of model as used in [Sinnott et al. \(2015\)](#) to highlight specific sites where high flow velocity and high wall shear stress may promote further wall thickening, plaque morphology change, and increase the risks for plaque rupture and ischemic stroke.

A sinusoidal pulsatile flow profile (following [Sinnott et al., 2006](#)) was applied at the inlet of the Common Carotid Artery. Blood rhythmically pumps from the left cardiac ventricle into the aorta during the systolic (high arterial pressure) phase and then ceases during the diastolic (low arterial pressure) phase as the heart chambers refill. The duration of the systolic phase in our model was chosen to be 0.125 s with a peak velocity of 0.5 m/s. The duration of the quiescent diastolic tail was assumed to be much longer with a total cardiac cycle period of 0.5 s (equivalent to 120 bpm of rapid heartbeat) and a peak flow velocity of 0.1 m/s. An SPH resolution of 0.2 mm was used for the fluid and the wall boundary. The arterial model includes a clinical patient geometry segmented from CT scan that has been used previously ([Sinnott et al., 2006, 2015](#)).

[Fig. 24.6A](#) shows the flow velocity field throughout the carotid bifurcation at a time corresponding to the arrival of the peak of the systolic pulse. Just prior to the bifurcation and throughout both ECA and ICA branches there are elevated high velocities exceeding 0.3 m/s. The lower ICA branch contains a (red) high speed jet extending through the stenosis and angled downward into the ICA. At the top of the ICA branch is a (blue) region of low flow. The combination of these is a potential risk for slow circulatory flow and lipid deposition that may promote plaque growth in this region.

[Fig. 24.6B](#) shows a prediction of wall shear stress at the same time. A peak stress of 2.5 Pa occurs in a small region at the top of the ICA exactly corresponding to the point of maximum stenosis. These typically are sites of plaque formation and wall thickening responsible for the flow constriction. Therefore, high wall stress in the vicinity of brittle plaques can cause rupture and clotting. Moderate stresses of 1.5 Pa are also observed inside the carotid sinus prior to the stenosed region as well as immediately downstream.

**FIGURE 24.6**

3D arterial flow in a clinical carotid artery with fluid colored by: (A) flow speed; and (B) wall shear stress.

*Reprinted with permission from Sinnott, M. D., Cleary, P. W., Arkwright, J. W., & Dinning, P. G. (2012). Investigating the relationships between peristaltic contraction and fluid transport in the human colon using smoothed particle hydrodynamics. Computers in Biology and Medicine, 42, 492–503.*

Principle aims of such modeling of arterial flow are as a diagnostic for predicting risk and as a means of assessing outcomes from surgical intervention. Fig. 24.7 takes the same artery with the aforementioned low flow region at the top of the ICA and poses the question: what if we could modify the artery branch angle so that the jet through the stenosis is redirected to remove or minimize the low flow region? Fig. 24.7A shows the artery prior to modification and Fig. 24.7B shows a prediction of the modified flow after performing this “virtual surgery” to bend the ICA branch

downward. Consequently, the flow in the center of the ICA becomes much more uniform. Note: that since the slice plane showing the flow field has been angled downward to focus on the ICA branch, it is no longer in a consistent position for comparing flow velocities through the stenosis or ECA so these should be ignored. The outcome of the hypothetical virtual surgery highlights the value of such models for assisting surgeons—whether through modifying parts of the arterial network, optimizing stent designs, or assessing outcomes postsurgery.

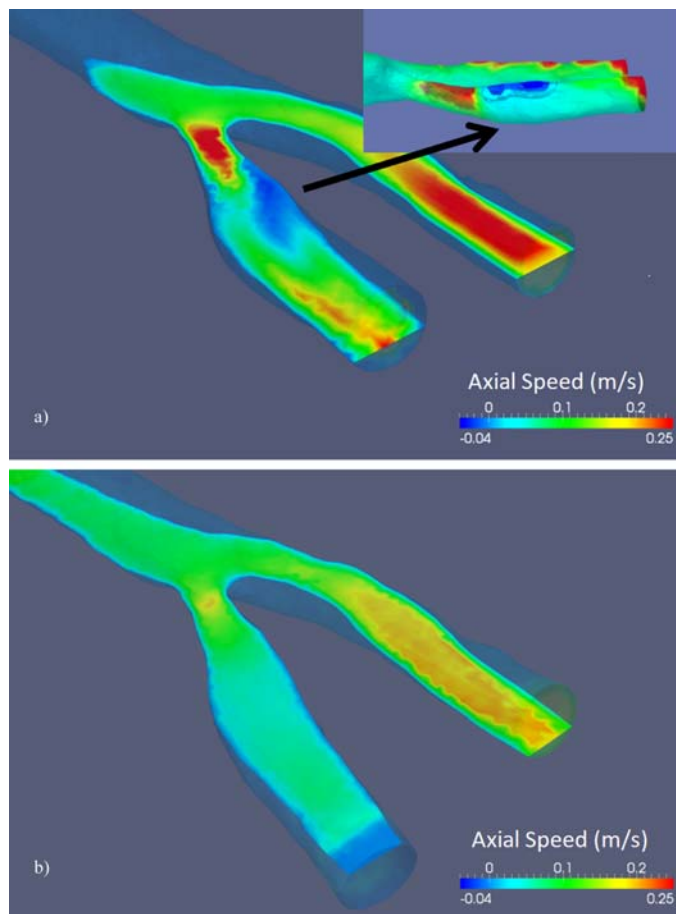


**FIGURE 24.7**

Virtual surgery: trialling the effect of adjusting ICA angle on arterial flow within the ICA for:  
(A) original patient geometry; (B) artificially modified geometry.

---

## Blood coagulation and clot formation modeling

### Background

Blood clotting is an essential fundamental maintenance process in the body to preserve the integrity of the vascular network and prevent significant blood loss from the circulation. When the clotting process is well regulated so that the clot remains small and local to the vascular wall, this is referred to as hemostasis. When regulation mechanisms become compromised such that the clot grows larger and forms within the blood vessel, then this is referred to as thrombosis and the clot is termed a thrombus. Thrombus morphology, structural stability, and adherence to the blood vessel wall vary with location in the body since thrombus development is sensitive to aspects of the local fluid dynamics (flow shear rate and blood pressure), blood composition (relative amounts of RBCs and platelets), and wall properties. For example, arterial thrombi are platelet dominated (Freedman, 2005), whereas venous thrombi are WBC dominated (Chandrashekhar et al., 2018).

Specific anatomical region complications can occur when regulation of the clotting process is impaired and the thrombus (or smaller fragments called emboli that break off from this) become large enough to block or impede flow in a blood vessel. This causes a rapid and significant rise in upstream blood pressure and wall stress (producing pain in the surrounding tissue), and greatly reduced downstream pressure and loss of oxygen transport that can result in rapid cell death. Deep vein thrombosis (DVT) refers to clots that specifically occur in the low flow venous system but in many cases may also associate with arterial thrombosis risk (Prandoni, 2009). A pulmonary embolism is often the result of emboli initiated by DVT that travel to and create a blockage in the lung vasculature. Coronary thrombosis involves blood clots within cardiac blood vessels. Ischemic stroke is cerebral vascular blockage due to a clot. This may be a consequence of thrombosis in upstream vulnerable regions of disturbed arterial flow (see Section [Arterial scale flow](#)), typically in the aortic arch and carotid bifurcation where atherosclerotic lesions can develop and rupture. It is extremely difficult to identify and construct therapies to specifically target thrombi formation. Anticoagulant pharmaceutical approaches (e.g., aspirin) also target normal hemostatic clotting and so there is elevated risk of death due to excessive bleeding for “at-risk” patients.

Clot formation is very complex involving many different prothrombotic and antithrombotic factors, as well as platelet recruitment/adhesion/activation and coagulation mechanisms. A comprehensive discussion of the different processes involved in thrombogenesis and review of existing multiscale models for these can be found in Xu et al. (2012). Briefly, the stages of the process are

- Injury: Trauma to the blood vessel wall disrupts the endothelial cell barrier exposing subendothelial extra cellular matrix and collagen to the blood.  
Inflammation at the site of injury triggers chemical signaling to recruit platelets for tissue repair.
- Hemodynamic response: Smooth muscle in the vessel walls constrict in response to the trauma to reduce blood flow rate.

- Platelet recruitment, adhesion, and activation: Platelets normally exist in the blood stream in their resting state as 2–3  $\mu\text{m}$  sized, disc-shaped, anucleated cells. Low affinity binding of platelets with the wall occurs via a glycoprotein (von Willebrand Factor) released by the exposed extracellular matrix. This weak adherence initiates platelet rolling adhesion along the vessel wall in a similar manner to that of WBCs discussed in Section [White blood cell \(WBC\)](#) [rolling adhesion](#). At the injury site, platelets develop stronger adhesions via fibrinogen and integrin that slow and then fix them in place ([Ruggeri & Mendolicchio, 2007](#)). Platelet activation mediated via thrombin or Adenosine Diphosphate (ADP) initiates complex intracellular signaling that enhances integrin adhesions and modifies platelet morphology necessary for clot development. [Sorrentino et al. \(2015\)](#) provides a detailed discussion of the relationships between platelet structural mechanics and function. When activated, they experience fragmentation and reorganization of their cortical actin cytoskeleton just below the membrane. This initiates a change in cell elasticity and shape so that they spread out and become more spherical. The changes in actin filament structure create filopodia (long “finger-like” actin-rich membrane protrusions) which greatly increase surface contact area and likelihood of collisions with other platelets, RBCs, and the vascular wall. When a platelet adheres to a substrate and flattens out, lamellipodia (plate-like protrusions) develop which control platelet motility so they are also able to actively migrate around sites of inflammation ([Bordon, 2018](#)), including against the direction of blood flow. The rate of migration is too slow to influence thrombus growth but may play an important immune system role by trapping and clearing bacteria in and around the thrombus site. Lamellipodia formation does not appear to be a requirement for stable, strong thrombus generation ([Schurr et al., 2019](#)).
- Platelet microplug formation: Platelet adhesion, activation, and aggregation at the exposed substrate forms a thin microplug single cell layer that temporarily seals the site of injury and acts as a scaffold for the fibrin clot development. This quickly inhibits further interaction between subendothelium matrix proteins and the plasma entering the wound.
- Coagulation: The coagulation process transforms liquid blood plasma into a fibrous gel. Interaction between an enzyme factor in the hemorrhaging blood with tissue factor (a transmembrane receptor on the exposed subendothelial cells) initiates a cascade of coagulation reactions involving multiple different enzymes, receptors, and cofactors (mostly proteins) to produce the enzyme, thrombin. Clotting dysfunction can occur if any of these cofactors fall outside their normal ranges. Thrombin acts on the soluble protein fibrinogen present in blood converting it to fibrin which then readily undergoes auto-polymerization to form a complex fibrin matrix. This matrix solidifies around the loose platelet aggregates providing structural strength and stabilizing the developing clot and preventing platelet detachment due to hemodynamic stresses. Fibrin branch sizes and network structure are predominantly responsible for the mechanical strength and stability of the clot ([Chandrashekhar et al., 2018](#)). It can be a

challenge for continuum clot models to accurately represent this network structure and strength based on fibrin concentration (Pancaldi et al., 2022).

- Fibrin clot formation: Continuing platelet aggregation, thrombin generation, and coagulation progressively grow the clot to a sufficient size to close over the vascular wall damage and withstand the stresses from normal hemodynamic conditions once vasoconstriction of the blood vessel ceases. Platelet activation releases internal stores of ADP which activate and recruit free-flowing platelets to the clot structure. Platelet aggregation occurs via fibrinogen bonding of new platelets to the clot which forms new prothrombotic surface and stimulates further thrombin generation at the surface and coagulation. Thrombus growth therefore depends on continual platelet activation and deposition. Anticoagulant factors in the blood and thrombus porosity eventually limit the size of a clot (Brass et al., 2011).

Models to represent the different stages of clot formation typically involve representing the essential chemical pathways as a series of coagulation reactions using ODEs coupled with continuum CFD transport models to predict coagulation spread and platelet recruitment and aggregation from the surrounding flow. A broad review of clot models is given in Yesudasan and Averett (2019). Fogelson (1984) proposed an early treatment of platelet adhesion and aggregation in a shear flow. Kuharsky and Fogelson (2001) developed the first comprehensive treatment of coagulation biochemistry with platelet deposition and flow in a small reaction zone around the site of injury. The model provided the cause of thrombin inhibition associated with hemophilia and thrombocytopenia and hypothesized the role of the platelet microplug in sealing off subendothelium enzymes. The Lagrangian nature of the platelets was eventually included via Immersed Boundary Method (Fogelson & Guy, 2008). The original Kuharsky–Fogelson model was extended by Leiderman and Fogelson (2011) to fully couple the effect of the vascular fluid dynamics and the growing platelet mass. This predicted the entry and exit of fluid into the thrombus and predicted thrombus porosity as a model outcome. The effect of reduced coagulation (via fibrinogen deficiency) on clot growth has been studied by Tosenberger et al. (2016) using a coupled Partial Differential Equation (PDE)-Dissipative Particle Dynamics (DPD) model. Shear-induced platelet activation has been modeled by Han et al. (2022) using DPD. Platelets that experience high levels of shear stress can also activate in the absence of chemically mediated activation pathways and cause clotting dysfunction and excessive platelet consumption, but the mechanism is still not understood.

### Simple SPH coagulation model and predictions

A simple coagulation (clotting) prediction capability based on thrombin diffusion and the fibrin gel creation is shown here. The proposed model represents the clotting blood by a thrombin concentration dependent viscosity with a phase change representing when the matrix is sufficiently stiff that deformations become unimportant.

It is therefore able to include deformation effects for the clot shape resulting from the stresses from the adjacent shear flow.

This model is highly simplified in order to demonstrate the value in using a Lagrangian method which naturally includes gel deformation. It considers only the diffusion of thrombin from damaged parts of capillary walls and the resulting growth of a fibrin gel. We assume here that the source fibrinogen concentration is sufficient that fibrin growth is not restricted by fibrinogen diffusion into the forming clot. For this model the platelets are also not included. The SPH method allows the variable rheological behavior of the developing fibrin matrix to be easily included and coupled to the fluid flow. This model also neglects the consumption of thrombin in the fibrin polymerization process. These effects can be added to the model later. The intent here is to show how a particle-based method can be used to include fibrin matrix rheology in the model.

Idealized forms for the rheological and polymerization processes are also assumed. A log-linear variation of viscosity with fibrin concentration (which is assumed proportional to thrombin concentration) reflects the increasing flow resistance of the fibrin gel as it progressively polymerizes. When the fibrin density reaches a sufficient level then that part of the structure becomes essentially rigid (nondeformable). Then, as described in Section [Simple model for thrombin-controlled coagulation](#), the SPH particles representing this part of the material are frozen in place. This is important as high viscosity fluid continues to creep and does not well represent structures that should be rigid. That is, high viscosity does not well represent the emergence of a yield stress in a solid material. This method therefore simulates both the deformation of the densifying fibrin, its effective “phase change” to being a solid as well as its effect on the blood flow in the now partially blocked blood vessel. Thrombin diffusivity in the blood plasma has an assumed exponential form so that diffusion is high in free blood (when the fibrin has a low solid fraction) but decreases by up to an order of magnitude as the fibrin becomes dense and restricts plasma flow through its matrix.

Clot formation is then a balance between outward thrombin diffusion (including any reaction losses from fibrin polymerization) and advective removal of lower concentrations of thrombin from the periphery of the clot. As the fibrin matrix becomes denser this adversely affects molecular diffusion rates of these species into and through the forming clot as well as limiting advective transport of plasma through the matrix ultimately leading to an asymptotic state that defines the final clot size and shape.

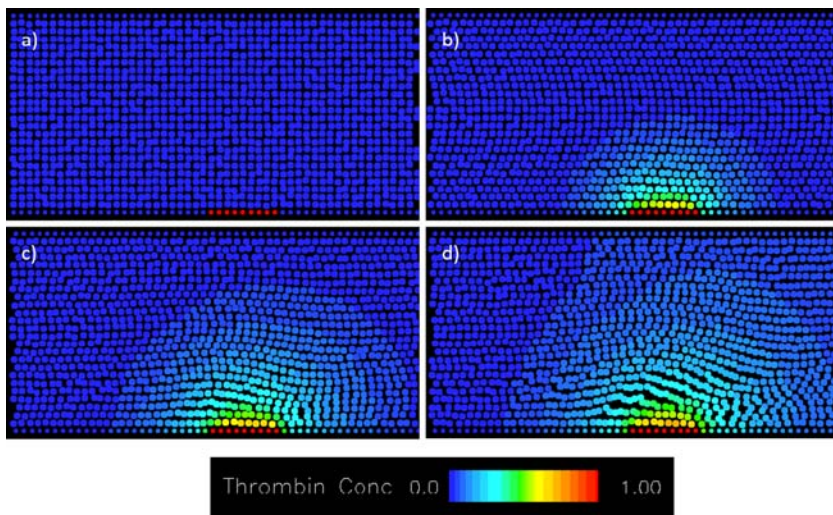
The diffusion rates are such that they lead to clot thickening at rates of 1  $\mu\text{m}$  per minute. This makes the problem computationally stiff and expensive. A pseudo-transient approach could be adopted, but for the purposes of this demonstration, the diffusion rates are scaled up by two orders of magnitude to reduce the computational expense. This is reasonable because of the weak dependence of structure on the fluid advection.

For this demonstration of the use of SPH for clot prediction, an 80- $\mu\text{m}$  length of uniform capillary of width 20  $\mu\text{m}$  is used. The domain is chosen as periodic with an

applied pressure drop implemented as a streamwise body force. This gives a steady-state parabolic profile with a peak speed that is controlled by the applied pressure gradient and the degree of blockage of the tube. An SPH resolution of  $0.8 \mu\text{m}$  is used meaning that there are 25 particles across the capillary and 100 along its length. The walls are assumed rigid. The viscosity of the fluid (blood) in the absence of any fibrin is  $1 \text{ mPa s}$ . The maximum viscosity at the solid fraction where the transition to rigid behavior of the clot occurs is  $100 \text{ mPa s}$  so this means that the viscosity of the blood as it is coagulating varies over two orders of magnitude. The density of the fluid is  $1 \text{ g/cm}^3$ . For ease of demonstration the model is built in two dimensions but implementation in three dimensions is straightforward. The diffusivity of the fluid to thrombin is highest for blood with zero fibrin concentration. This decreases exponentially with fibrin/thrombin concentration until it is an order of magnitude lower in any solid part of the clot. The specific values and forms of dependence assumed do not materially impact on the demonstration or its key observations but for clinical use of such a model more physically based data would be needed.

In the first example a small  $8\text{-}\mu\text{m}$  long section of wall on the left side of the bottom wall is considered damaged and emits thrombin. The diffusion boundary condition at these locations is assumed to be isoconcentration (constant concentration of thrombin). Fig. 24.8 shows the transport of thrombin from the damaged section of lower capillary wall. The fluid is moving from the left to the right driven by the applied pressure gradient. The color shows thrombin concentration arising from the combination of diffusion and fluid advection. The initial situation is shown in Fig. 24.8A. The red particles are the damaged part of the capillary wall. Fig. 24.8B shows the early diffusion from the wall. By 4 ms (Fig. 24.8C), the trace amounts of thrombin (light blue) at the periphery have diffused out to the center of the channel with high concentrations present immediately adjacent to the damaged section of wall. This pattern continues at later times (Fig. 24.8C and D) with the concentrations increasing. The shape of the region containing thrombin is affected by the external flow which advects thrombin in the streamwise direction producing the asymmetry in the isoconcentration surfaces. The effect of the upscaling of the diffusivity to change the timescale is that the ms timescale observed here is equivalent to the second timescale in the real physical system.

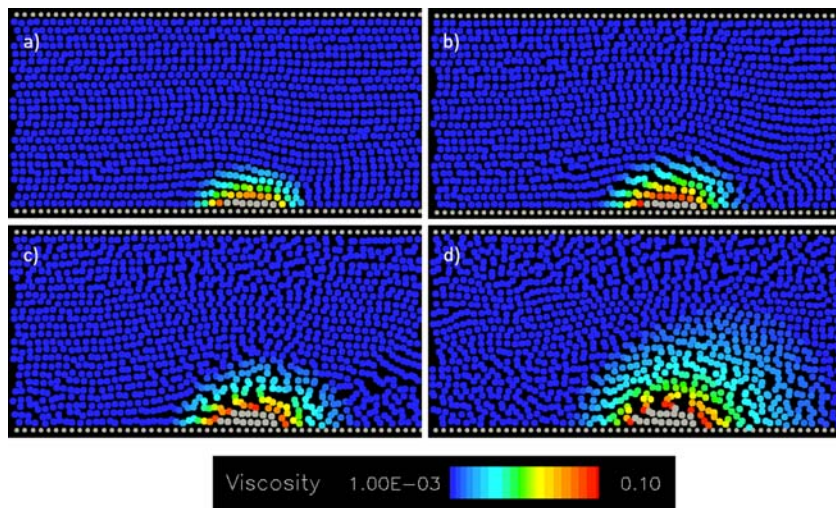
Fig. 24.9 shows the resulting growth of the simple model clot represented as a solidifying gel arising from damage to the wall of a capillary and the transport of thrombin from these locations. The particles are colored by their viscosity which increases exponentially with fibrin concentration, so we use a logarithmic color map (meaning green in the color bar corresponds to a viscosity of  $10 \text{ mPa s}$ ). When the fibrin level is sufficient that the clot particles behave effectively as being rigid then they are shaded gray. The clot at 10 ms (Fig. 24.9A) already has one solidified layer of particles with a second layer of viscous gel like fluid surrounding this. Beyond this the thrombin concentrations are low, and the viscosity variation is low. By 20 ms (Fig. 24.9B), the concentration of thrombin in the second layer has increased and its viscosity has increased sharply and is now red). At 40 ms (Fig. 24.9C), a second layer of particles has solidified with a thin (1–2 particles) layer surrounding

**FIGURE 24.8**

Transport of thrombin from a short (8- $\mu\text{m}$  length), damaged section of lower capillary wall (where the capillary is 20- $\mu\text{m}$  wide). The fluid is moving from the left to the right. Only the left half of the domain is shown here. The color shows thrombin concentration arising from the combination of diffusion and fluid advection as indicated in the color bar, (A) initial time of damage, (B) 4 ms, (C) 10 ms, and (D) 20 ms.

this. By 80 ms (Fig. 24.9D), the clot has reached a nearly asymptotic size and shape with only a small increase in the thickness of the surrounding deformable gel layer. This reflects the effect of the sharply reduced diffusivity in the solidified part of the clot which sharply reduces the diffusion of thrombin through the clot to the gel layer, strongly limiting its growth. Low concentrations of thrombin continue to diffuse further out from the clot and are substantially advected streamwise (to the right), but the viscosity increases due to these low levels (light blue shading of the particles) is only weak.

Fig. 24.10 shows the streamwise velocity distribution of the blood flow along a capillary as the blood clot forms from damage to a small section of the lower wall of a capillary. The particles are colored by the streamwise flow speed. The fluid is stationary (dark blue) within the denser parts of the fibrin gel which have solidified. As the clot grows the flow is increasingly obstructed leading to relatively faster flow through the narrowed section above the clot. By 120 ms (Fig. 24.10C) the clot and flow field are changing little, and the system is almost steady. As the degree of obstruction of the flow increases the resulting flow rate in the capillary declines which is controlled by the increasing resistance to flow and the constant streamwise pressure gradient driving the flow. The peak flow velocity is initially 9 mm/s, decreases to 8 mm/s at 40 ms, steadily declining to 4.8 mm/s by 120 ms. This shows both the decrease in flow speed with the obstruction generated by the formation of the clot as well as the structure of the clot and the resulting flow field.

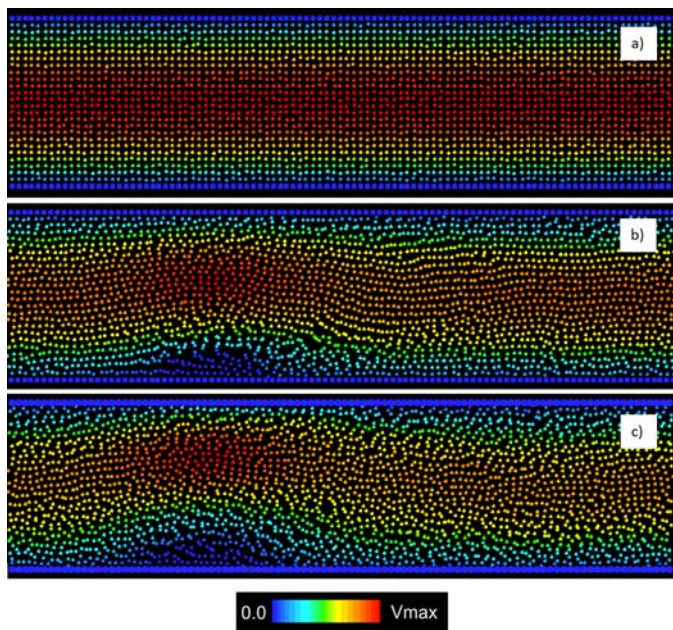
**FIGURE 24.9**

Growth of a simple model clot represented as a solidifying gel arising from damage to the wall of a capillary. The particles are colored by viscosity which increases exponentially with fibrin concentration. The viscosity range is given in the color bar. Only the left half of the domain is shown here. When the fibrin level is sufficient that the clot particles behave effectively as being rigid then they are shaded gray. The clot is shown at: (A) 10 ms, (B) 20 ms, (C) 40 ms, and (D) 80 ms.

If the weak gel beyond the immediate vicinity of the viscous part of the clot can span the capillary, then the flow slows much more strongly. This in turn changes the thrombin transport balance with the advection declining strongly while the diffusion declines more slowly. This means that the clot will be able to continue to grow across the capillary albeit increasingly slowly until it is fully blocked by firstly the viscous gel layer and finally by solidified parts of the clot. Non-blockage of the capillary therefore appears to be dependent on maintaining sufficient advective flow above the clot. This in turn will also be dependent on the rate of consumption of thrombin, which has been omitted from this initial model.

[Fig. 24.11](#) compares the clot and flow structure at 60 ms, for the base case conditions, and when thrombin diffusivity in the blood is halved. The top row shows the particles colored by viscosity which indicates that the solid part of the clot is modestly smaller with a similar mild reduction in the surrounding viscous gel layer. The most visible changes are the extent of the low concentrations in the middle distance from the clot. The bottom row shows the resulting change in the flow structure arising from the modestly smaller clot. The reduction in clot size is relatively quite a bit smaller than the size of the reduction in the diffusion.

[Fig. 24.12](#) shows the model prediction for clot formation from a much longer damaged section. The damaged region emitting thrombin is 32  $\mu\text{m}$  long. At

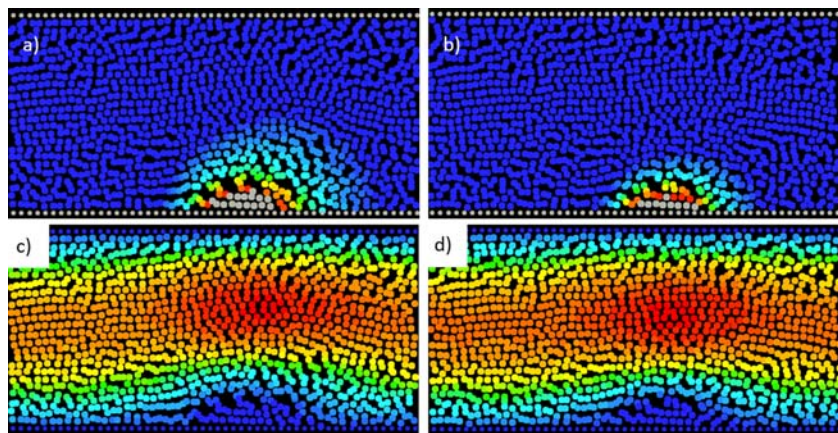


**FIGURE 24.10**

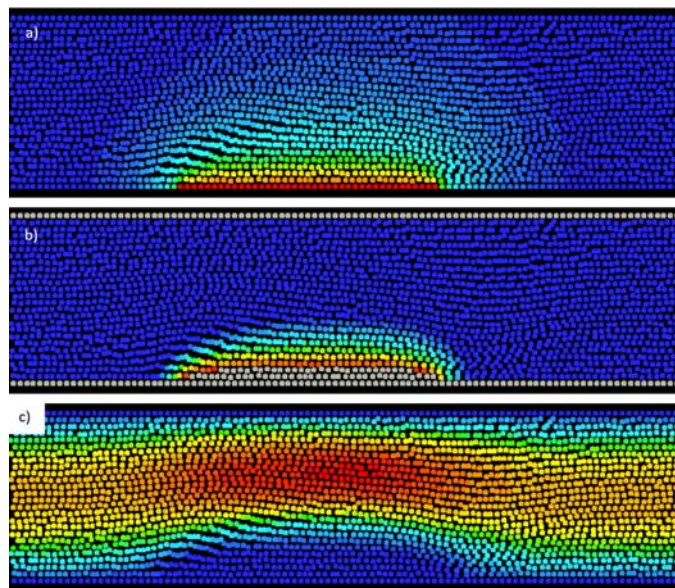
Blood flow along a capillary as a clot forms from damage to a small section of the lower wall of a capillary. The full length of the computational domain is shown. The particles are colored by the streamwise flow speed. Blood flow is stationary (*dark blue*) within the denser parts of the fibrin gel. As the clot grows the flow is increasingly obstructed leading to faster flow through the narrowed section above the clot. As the degree of obstruction increases the flow rate in the capillary declines. The blood flow is shown at: (A) initially ( $V_{\text{max}} = 9 \text{ mm/s}$ ), (B) 40 ms ( $V_{\text{max}} = 8 \text{ mm/s}$ ), and (C) 120 ms ( $V_{\text{max}} = 4.8 \text{ mm/s}$ ).

20 ms, thrombin has diffused extensively into the capillary (Fig. 24.12A). The total amount of thrombin entering the system is four times higher due to the four times increase in the length of the source (the damaged section of wall). The asymmetry in the thrombin concentration due to the advection from left to right is clearly visible. The resulting viscosity distribution in the blood is shown in Fig. 24.12B. Two layers of SPH particles have solidified forming an extended clot along the full length of the damaged wall. Beyond this is the viscous gel layer which extends around 20% of the capillary width into the flow. There is a modest asymmetry reflecting the effect of the advection pushing thrombin to the right leading to moderately higher concentrations at the end of the clot than at the start causing the clot to thicken slightly along its length. Fig. 24.12C shows the resulting flow field with an extended relatively high speed concentrated above the clot.

Fig. 24.13 shows a comparison of clot formed by 60 ms for a long (30  $\mu\text{m}$ ) damaged section for the base case streamwise flow speed and one with double the flow speed. This increase in flow speed doubles the contribution of the advection

**FIGURE 24.11**

Clot and flow structure at 60 ms, for (*left*) base case conditions, and (*right*) when thrombin diffusivity in the blood is halved. The top row shows the particles colored by viscosity (with the same scheme as used in Fig. 24.8). The bottom row shows the particles colored by streamwise flow speed (with the same color scheme as used in Fig. 24.9).

**FIGURE 24.12**

Clot formation predicted at 20 ms by the simple model arising from a long section of damage (32  $\mu\text{m}$ ) for a 20- $\mu\text{m}$  wide capillary, colored by: (A) thrombin concentration, (B) blood/fibrin gel viscosity, and (C) streamwise flow speed. The color bars for each case are as given in previous figures.

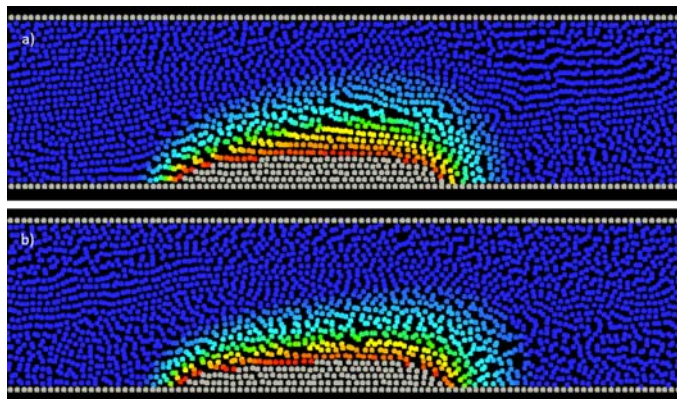


FIGURE 24.13

Comparison of clot formed by 60 ms for a long ( $30 \mu\text{m}$ ) damaged section of a  $20-\mu\text{m}$  capillary for: (A) base case streamwise flow speed, and (B) double streamwise pressure gradient (which doubles the flow rates).

to the thrombin transport and therefore to the distribution of fibrin. The clot is observably more asymmetric with it being relatively thicker downstream than upstream. The rate of growth of the clot thickness is also slightly reduced. The scale of these changes though is much weaker than the doubling of the flow speed, so the effects of flow speed have a much weaker than linear dependence. This occurs because of the dominance of the nonlinearity in both the diffusivity and viscosity variations on thrombin concentration.

The model used here has been able to predict clotting up to and including blockage of the blood vessel. This leads to sharply reduced blood flow rates while parts of the clot are still viscous and flow cessation if the solid part of the clot has grown to span the capillary. The extent of clot growth is a balance between diffusion of thrombin within the clot and the advection in the adjacent shear flow of blood with the diffusion rate decreasing with degree of clot solidification, which is a key limiting factor on clot growth.

There are many aspects of the full coagulation process missing from this model, but it is sufficient to demonstrate that a Lagrangian method can provide additional capability in prediction of this system. However, there are many aspects enumerated in the earlier background (Section [Background](#)) that can also be included for increasing realism. One aspect that should be particularly amenable to particle methods is the treatment of platelets in clotting. Platelets in capillaries are not microscopically small compared to the vessel diameter so homogenization approaches leading to continuum representations (that are conventionally used for including these effects) become increasingly unrepresentative. The use of a Lagrangian method for the fluid and clot structure is easily able to be coupled to a discrete particle method (as shown in [Cleary, 2015](#)) for the platelets. This approach would allow explicit inclusion of the platelets and would allow more

realistic representation of clot structure and prediction of its permeability. The release of ADP and its effect on platelet activity would be easily included in such a method.

---

## Plaque rupture in an artery

### Background

Atherosclerosis is a vascular disease characterized by the development of vulnerable plaques over timescales of tens of years which can potentially rupture triggering thrombosis and cause downstream cerebral or coronary damage in the form of stroke and heart attack, respectively. The disease involves progressive structural adaptation and hardening of arterial walls in response to hemodynamic stresses (Pries et al., 2005) and deposition of low-density lipoprotein (LDL) at sites of low wall shear stress (WSS) and reduced blood flow, e.g., arterial branches and regions of high curvature. The initiation and progression of the disease involves multiple complex inflammatory and pathological immunological responses, and proceeds as follows:

- The arterial wall suffers damage, due to stresses or chemical irritants, resulting in endothelial barrier dysfunction, enabling LDL molecules in the blood stream to leak through tiny perforations in the wall and accumulate within the intimal layer of the wall.
- Oxidation of the LDL in vascular cells causes it to release its bound cholesterol and the process creates atherogenic inflammatory responses which stimulate innate and adaptive immune responses. These trigger the defenses of the endothelial cells which release chemoattractants and adhesion molecules to recruit WBCs and other immune cells such as T-cells and B-cells to the endothelium and then into the wall.
- The WBCs differentiate into macrophages and dendritic cells and engulf and clear the modified LDL. In the process they convert to foam cells which serve as lipid deposits and form the characteristic yellow fatty streaks called xanthomas which are associated with early atherogenesis. If these lipid pools remain small and isolated and do not disrupt the structure of the vascular wall, then such lesions are considered to contribute to pathological intimal thickening of the wall.
- Plaque formation occurs once there is sufficient lipid-rich accumulation to induce further macrophage invasion. Apoptosis of foam cells, macrophages and smooth muscle cells form a necrotic lipid core. This also causes degradation of extracellular matrix and large-scale irreversible disruption of the intimal layer structure once smooth muscle cells are recruited into the plaque. The inclusion of smooth muscle cells changes the fatty streak to a fibrous fatty lesion.
- Further entry and oxidation of LDL promotes collagen production by smooth muscle cells which help increase the lesion size and also formation of the fibrous plaque cap.

Advanced plaques can create significant modification of both vascular geometry and material properties: high arterial occlusion, spatially varying stiffness due to microcalcifications in the wall, variable thickness of the fibrous cap, and changes in plaque morphology and composition. Hemodynamic responses to the changes in vasculature can lead to abnormal flow structures, such as high-speed turbulent jets and recirculation regions, which in turn modify the stresses imparted to the walls and the plaque formed. There is strong indication that high WSS correlates with high-risk plaque features. It has been shown to modify endothelial function in ways that increase both inflammation and growth of necrotic lipid core (Eshtehardi et al., 2017).

Plaque rupture in an artery has multiple paths to damaging the circulatory system. In some cases, a hardened cap is pulled from the accumulated substrate of the plaque exposing the rich necrotic lipid core. The rupture damages the epithelial layers and the subsequent exposure of the lipid core to the blood creates strong pro-thrombotic conditions in and around the damage site leading to thrombus formation extending out into the flow (as discussed in Section [Blood coagulation and clot formation modelling](#)). Fragments of the plaque cap or the thrombus itself can break off in the flow and be carried downstream to block smaller arteries and initiate a stroke or coronary blockage. If the lesion occurs within the cerebral vasculature, thrombus formation in these small arteries can quickly directly block them.

A major clinical focus for surgical intervention is to identify which plaques are at risk of rupturing. Plaques with cap thicknesses  $<65\text{ }\mu\text{m}$  and lipid cores comprising more than half the plaque volume are referred to as Thin Cap Fibroatheroma (TCFA) (Moreno, 2009) and comprise what we refer to as vulnerable plaques. The dynamics of plaque rupture are not understood due to the unpredictable timing and short period of the rupture events. This may describe a single catastrophic breakup of a TCFA plaque resulting in thrombosis. For some lesions, progressive stenosis of arteries via vascular remodeling involves multiple stages of partial rupture and healing (Bentzon et al., 2014).

There are a small number of suitably advanced models in the literature that attempt to simulate aspects of plaque development and its effect on hemodynamic flow. Kock et al. (2008) developed a coupled Finite Element/CFD model for Fluid Structure Interaction (FSI) that treats the deformation of the plaque and lipid core based on mechanical stress predictions from hemodynamics and plaque morphology. Teng et al. (2010) calculated plaque wall stress (PWS) and flow shear stress (FSS) in ruptured and unruptured plaques of patient-specific geometries derived from MRI imaging. They developed a multicomponent FSI model using the Arbitrary Lagrangian–Eulerian (ALE) approach. They showed that FSS was unable to reliably determine the site of rupture and in fact, the peak FSS occurs downstream of the peak PWS. More favorably, the 3D critical plaque wall stress (CPWS) was found to better differentiate between ruptured plaques and advanced nonruptured plaques than existing clinical stenosis severity plaque assessment measures. Corti et al. (2020) developed a multiscale model combining CFD for the hemodynamic flow and agent-based modeling for the cross-endothelium transfer of chemical species. They used this to successfully predict plaque formation (including

morphological and compositional changes) at sites of disturbed flow. Their arterial stenosis profile prediction is qualitatively consistent with histological data but awaits more thorough clinical validation in a future study. The development of fissures in the plaque once the cap ruptures has been studied with solid mechanics models of fatigue analysis and crack propagation in plaques with lipid cores (Pei et al., 2013; Rezvani-Sharif et al., 2017) but in such models the hemodynamic stresses are assumed to be steady. None of these models attempt to simulate the full dynamic plaque rupture event itself which is largely unexplored and not well understood.

### SPH model for plaque rupture

To demonstrate SPH method capabilities in relation to plaque rupture and to explore the dynamics of the plaque rupture process, we again choose a very idealized representation of the geometry of a stenosed region of artery and show this in two dimensions. The straightened artery section is 5.5 mm in diameter and 40 mm long. Periodic boundary conditions are used in the streamwise direction with a streamwise pressure gradient applied to the fluid. This is chosen to give a realistic arterial flow speed of between 0.3 and 0.4 m/s. Note that arterial blood flow is strongly pulsatile. However, since plaque failure can be expected to occur when stresses are largest this should typically correspond to periods when the blood flow is at its systolic peak. This will lead to maximal shear stress being applied to the surface of the plaque (the cap). So, for modeling plaque rupture it is sufficient to consider the blood flow speed only at its peak value.

The stenosis is generated by an elongated plaque deposit on the bottom wall of the artery. The plaque deposit is assumed to have a cosine shape with length of 16 mm long and height 3.53 mm which gives a degree of arterial blockage of 70% (which is a medically important level of stenosis that is representative of many clinical cases). More realistic arterial geometries such as those used in Section [Arterial scale flow](#) can be used but these aspects do not add to the demonstration of capability or the general observations that follow from the model. All materials have a density of 1 g/cm<sup>3</sup>.

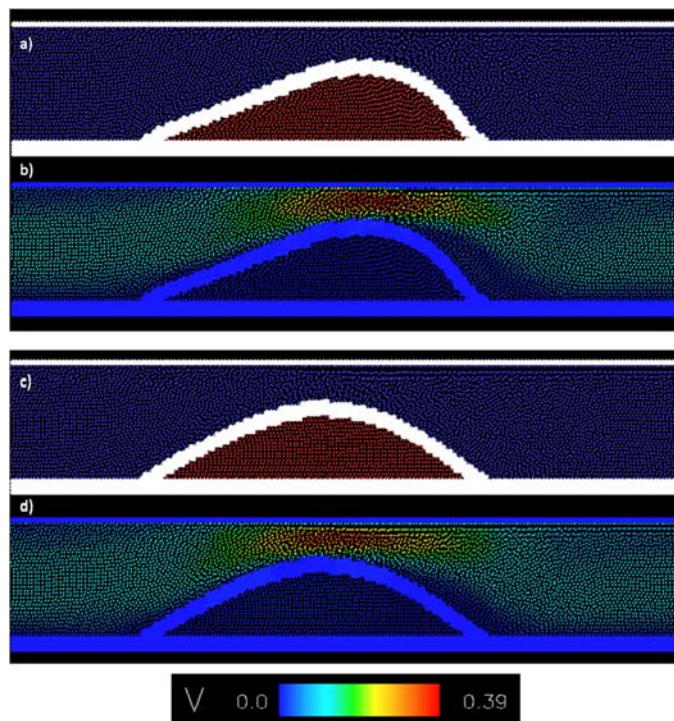
Plaque usually consists of a fibrous cap that is effectively rigid in comparison to the artery walls and an underlying soft core that is often necrotic and formed from lipids. This material is rheologically ambiguous and could be represented either as a viscous liquid or as a very soft solid. In this case we choose to represent it as a high viscosity liquid. The physical viscosity of 4 mPa s is used for the arterial blood. A somewhat arbitrary viscosity of 100 mPa s is chosen for the core of the plaque. This is sufficiently more viscous than the blood that its precise value is not critical for the observed behavior. There are no specific limitations in this model on the material parameter choices. The cap of the plaque is uniform along the length of the plaque deposit. For the base case it is chosen to be 0.67 mm thick based on the median value for maximum cap thickness measured for Type A plaques by Felton et al. (1997). For such plaques, the cap thickness can in clinical cases vary widely from 10 μm to 1.5 mm. The effect of cap thickness will be explored later in this section. Its

elastic properties can vary widely and are often heterogenous due to the presence of microcalcification inclusions that cause local increases in stiffness. The cap is modeled here as an elastic material, but plastic and brittle rheological attributes (Cleary & Das, 2008) can be readily included depending on the nature of specific plaque caps. The bulk modulus of the solid used is varied from 100 kPa to 2 MPa while the shear modulus is half this value. Typical clinical values for the Young's modulus of the hard plaque cap are estimated from strain measurements to be around 150 kPa (Ohayon et al., 2014). The lipid core occupies more than half of the plaque volume, so this example is representative of a vulnerable plaque of the type more likely to produce adverse outcomes.

Since the fluid and elastic equations are solved in a fully coupled manner in the SPH method, the stress between phases is automatically transferred, and no internal boundary conditions are required. This makes the method robust and very well suited to this type of rheologically complex fluid structure interaction application with very high deformations.

The SPH resolution used in most of the simulations reported here is 0.167 mm which means that there are 32 SPH particles across the full artery width. Higher resolutions are used for cases with thinner caps. This model involves a combination of rigid and elastic walls, a low viscosity fluid (blood) and a high viscosity fluid (lipid core) all fully coupled together. Details of the SPH equations for both fluid flow and solid deformation are given in Section [Computational method](#). The failure of the plaque will be initiated by the removal of a small number of particles from the left side of the cap. The effect of different locations and different shapes for the damage to the cap will be explored.

[Fig. 24.14](#) shows the steady-state configuration of this model system when the plaque remains stable for two values of the bulk modulus. [Fig. 24.14A](#) and [B](#) show the equilibrium state for a cap with bulk modulus  $10^5$  Pa colored by material type and streamwise flow velocity, respectively. The equilibrated plaque shape is heavily skewed to the right as a result of the strong force applied by the flow of the fluid from the left onto the left side of the plaque structure. This includes a strong pressure force as well as shear stress applied by the fluid as it is forced along and over the plaque. Minor flow separation occurs at the start of the plaque and a reasonable size region of quiescent fluid is located on the leeway side of the plaque structure. High fluid velocity occurs in the narrow space between the top of the plaque and the upper wall of the artery since this is where the flow channel is narrowest. The peak flow speed is 0.39 m/s. [Fig. 24.14C](#) and [D](#) show the corresponding situation for a cap with a larger bulk modulus of  $10^6$  Pa. This order of magnitude increase in cap stiffness sharply reduces its flexibility leading to a much more symmetric shape for the plaque and a smaller quiescent region on its leeward side. The plaque shape is the result of a dynamic balance between the forces applied to the cap by the fluid above and below, and the internal pressure and deviatoric stress that is generated in the elastic cap material by the extension and bending deformation. From a computational perspective, the stability of elastic sheet when resolved by only four particles across is high. An advantage in using the SPH method to represent

**FIGURE 24.14**

Stenosed arterial blood flow over and coupled to a stable 16 mm long fluid-filled plaque deposit which restricts flow to the upper 30% of the 5.5 mm wide artery. Equilibrium configuration for: (A) cap with bulk modulus  $10^5$  Pa colored by material type, (B) cap with bulk modulus  $10^5$  Pa colored by streamwise flow velocity, (C) cap with bulk modulus  $10^6$  Pa colored by material type, and (D) cap with bulk modulus  $10^6$  Pa colored by streamwise flow velocity. In frames A and C, particles are colored by their material type with *blue* being blood, *red* being viscous liquid initially inside the plaque, and *white* are the elastic cap of the plaque and the walls of the artery. The elastic particles (making up the bottom wall of the artery and the cap of the plaque) are rendered larger so that this material appears solid allowing it to be differentiated from the fluid. In frames B and D, particles are colored by streamwise flow velocity with range given in color bar.

biological tissues is that it is very robust and stable for this type of high deformation fluid-structure calculation. This observed numerical stability is consistent with the very high stability identified by [Cleary \(2010b\)](#) for thin-walled elastic and elasto-plastic impact problems.

This model allows us to explore the stability of this plaque structure to different types of damage. If the damage is in the form of a small split in the cap, then its location and orientation can affect the subsequent evolution of the plaque structure. If the split is vertical (as is shown in [Fig. 24.15A and B](#)), then the pressure from the

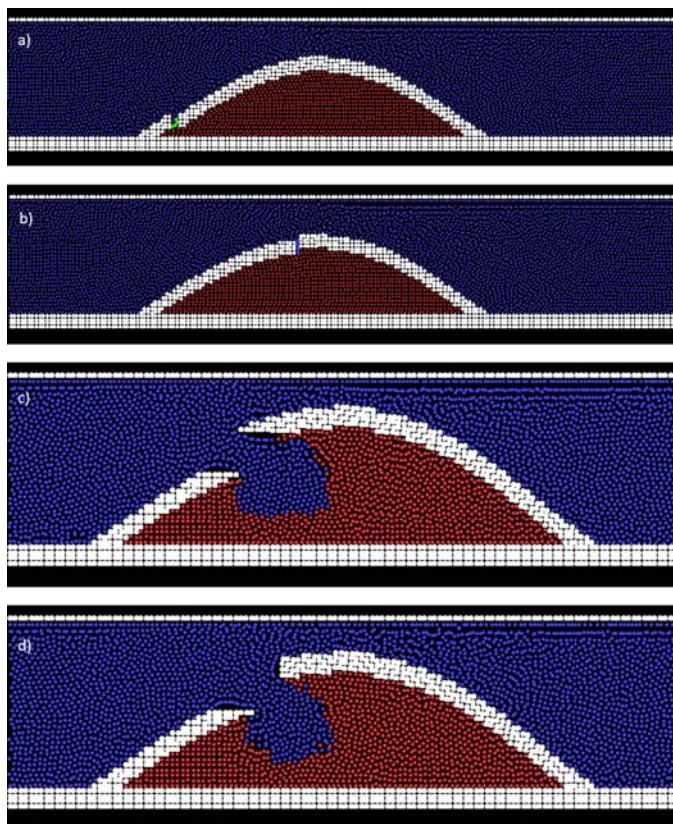


**FIGURE 24.15**

Postrupture behavior for plaque with a 0.67 mm thick cap for different shapes and locations for the damage to the cap, (A) vertical cut near start of plaque, (B) vertical cut near the peak of the plaque, (C) horizontal cut in the upper part of the leading face of the plaque, and (D) a wedge in the upper part of the leading face of the plaque. Frames A and B are shown from the same view as previous figures. Frames C and D are shown in closer view so that the details of the fluid entry to the plaque are visually larger. Particles are colored by their material type with *blue* being blood, *red* being viscous liquid initially inside the plaque, and *white* are the elastic cap of the plaque and the walls of the artery.

crossflow tends to close the split in the cap preventing flow into or out of the plaque core. So, the cut is resealed as the result of the blood flow and the plaque remains stable. In contrast, if the cut in the cap is parallel to the flow, then this allows blood from outside to flow into the plaque core increasing the fluid pressure within the plaque and forcing the cap upward. Consequently,

- The plaque mass increases sharply in volume,
- The degree of stenosis becomes larger, and

- More seriously, with reduced open artery cross-sectional area remaining for the blood to flow through above the plaque there is a sharply reduced rate of blood flow.

Such cases are shown in Fig. 24.15C and D for a horizontal and a wedge cut. In both cases a significant amount of blood (shown as blue) has been able to enter the opening in the plaque and has sharply increased its size. Both expanded plaque configurations are stable, with increased pressure force applied by the fluid balanced by larger deviatoric stress in the cap which limits the degree of deformation. In the dynamical approach to this steady state, there is an overshoot with the maximum plaque size being somewhat larger. However, the increased degree of stenosis reduces the overall blood flow rate in the artery (which is controlled by the applied pressure gradient) which then reduces the supply of blood into the inflated plaque wall “balloon.” This limits the degree of plaque inflation. Typically, this also leads to a somewhat reduced pressure outside which results in partial elastic unloading of the cap deformation and a return of the upper part of the cap wall to an intermediate position (as shown in Fig. 24.15C and D). This combination leads to some reverse flow out from the plaque structure that reduces the degree of its expansion after which it reaches a steady state structure (as shown in Fig. 24.15C and D). In these cases, the cap is too stiff to allow further filling with more blood through the opening. This partial rupture scenario can be expected to be clinically negative as it increases the degree of stenosis and sharply reduces the blood flow rate. This configuration is also obviously then quite vulnerable to further damage to the cap. The two different damage shapes used in Fig. 24.15C and D do not substantively influence the dynamic expansion behavior. As long as the cut is oriented in a way that promotes flow into the plaque volume the subsequent expansion behavior is broadly consistent. This inflationary mechanism has been identified using this SPH model.

Significant shape change in the cap is required for large-scale collapse of the plaque structure (rupturing). The model suggests that there are two main scenarios where this can occur. These are if the cap:

1. Is very flexible (either because it has low moduli or because it is thin) then it can deform significantly and the free end of the cap can be dragged downstream by the crossflow, or
2. Has an elastic brittle rheology so that when the deformations observed are sufficiently large then they can generate macroscopic cracking across its downstream side, enabling complete fracture and the removal of the cap by the crossflow as one or more fragments.

If the cap does not separate from the rest of the plaque, then the influx of additional fluid inflates the plaque increasing its volume sharply, potentially leading to complete blockage of the artery (which would obviously be a poor clinical outcome).

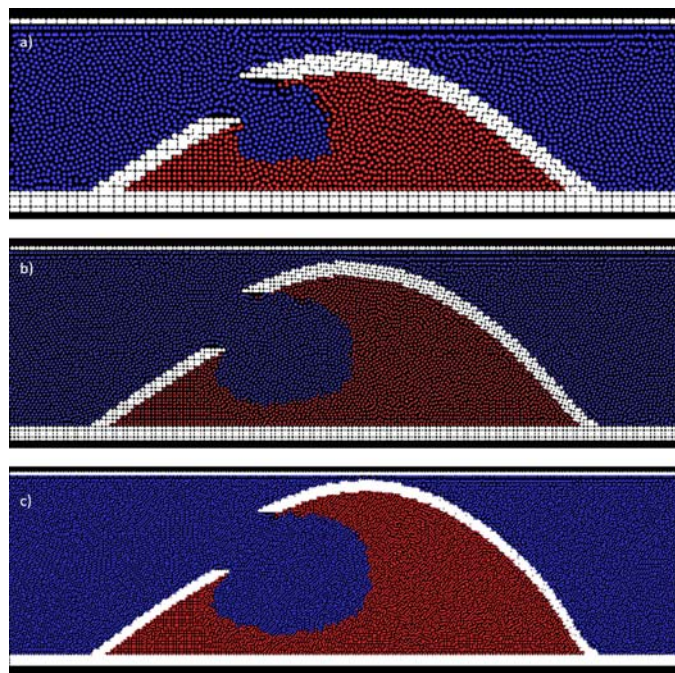
Although this “inflationary mechanism” is predicted using a fluid-filled plaque, the rheology of the core does not control the inflation process. It does, however, strongly influence the distribution of the blood that has entered the core. If the plaque

core is sufficiently fluid-like, then the blood entering spreads radially and isotropically forming a “bubble” within the previous plaque core material. If the core is rheologically a soft brittle solid, then it will be subject to transverse tension which will lead to radial (from the opening in the cap) fracture with cracks radiating from this location. These fractures will then fill with blood, become pressurized which will drive further crack growth. This behavior can be clearly linked to the intraplaque hemorrhage behavior that has previously been identified in pathology samples (Daemen et al., 2016). That postrupture plaque in such cases has been found with fissures and cracks which supports the inflation mechanism hypothesis identified.

Bentzon et al. (2014) found that large stenosis of arteries can be caused by vascular remodeling involving multiple stages of partial rupture and healing. This is consistent with the stability observed for the plaque post rupture (Fig. 24.15A and B) and the inflation mechanism (Fig. 24.15C and D). Many small ruptures would appear to be dynamically stable based on the behavior of this model, so healing/sealing should reasonably be expected in these scenarios. If a stable inflation process occurs to a plaque (Fig. 24.15C and D) then sealing across the opening (by clotting) will occur. What this suggests is that large scale plaque formation could proceed more as a sequence of minor rupture events involving abrupt volume increases due to this inflation mechanism rather than by slow, steady accretive growth via continual lipid deposition and inflammation response mechanisms. Being able to generate large plaque formation in several abrupt steps would sharply reduce the expected timescales for the development of serious blockage.

Fig. 24.16 explores the effect of cap thickness on the rupture dynamics for cap thicknesses varying from 0.67  $\mu\text{m}$  (as in Fig. 24.15) down to 0.33  $\mu\text{m}$ . In all three cases, the cap is constructed to be four particles thick so that it has consistent accuracy and stability enabling comparison. This means that the SPH resolution needs to decrease with particle sizes of 0.167, 0.113, and 0.083  $\mu\text{m}$  respectively, being used. Particles are again colored by their material type. The three cases behave qualitatively similarly but with a trend of increasing degree of inflation as the cap becomes thinner and therefore more flexible. This means that the degree of blockage/stenosis resulting after the expansion is strongly dependent on the stiffness of the plaque cap. The blood flow rate decreases sharply with the decreasing space between the top of the cap and the upper wall of the artery. The volume of blood able to enter the plaque structure at equilibrium increases faster than the decrease in stiffness arising from the thinning of the cap.

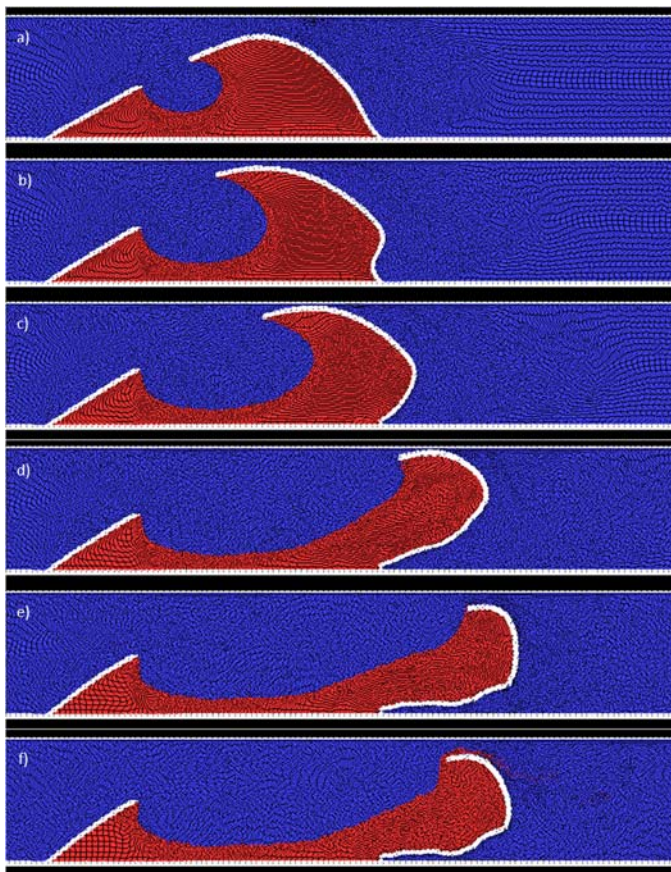
For a cap thickness of 0.22  $\mu\text{m}$ , which is at the lower end of clinically observed plaque structures, the system behavior is quite different with full rupture of the plaque occurring. This case uses an SPH resolution of 0.056  $\mu\text{m}$  giving a nontrivial model size of around 80,000 particles. The evolution of the plaque is shown in Fig. 24.17. The early stages of the plaque expansion are similar to what is observed for the thicker cap cases (Fig. 24.16). Fig. 24.17A shows the state at 40 ms (Fig. 24.17A). For the thicker caps, the lower part right hand side of the plaque near the lower artery wall remains inclined to the left. But for this 0.22  $\mu\text{m}$  case, the cap is now sufficiently flexible that its upper sections are able to be displaced

**FIGURE 24.16**

Comparison of stable equilibrium ruptured plaque for a cap of thickness, (A) 0.67  $\mu\text{m}$ , (B) 0.44  $\mu\text{m}$ , (C) 0.33  $\mu\text{m}$ . The cap is four particles thick in each case with the resolution used being 0.167, 0.113, and 0.083  $\mu\text{m}$ , respectively. Particles are colored by their material type with *blue* being blood, *red* being viscous liquid initially inside the plaque, and *white* are the elastic cap of the plaque and the walls of the artery.

downstream sufficiently for the lower part of the cap wall to become vertical (which occurs at 50 ms). The wall is then subject to a snap through buckling instability. Fig. 24.17B shows the structure at 60 ms, where the lower right side of the cap has an S-shape. With this shape the cap has lost most of its ability to resist the shear flow. The decrease in resistance from the right side of the cap leads to a rapid influx of blood into the space formerly occupied by the plaque and the right wall and much of the lipid core are rapidly pushed to the right.

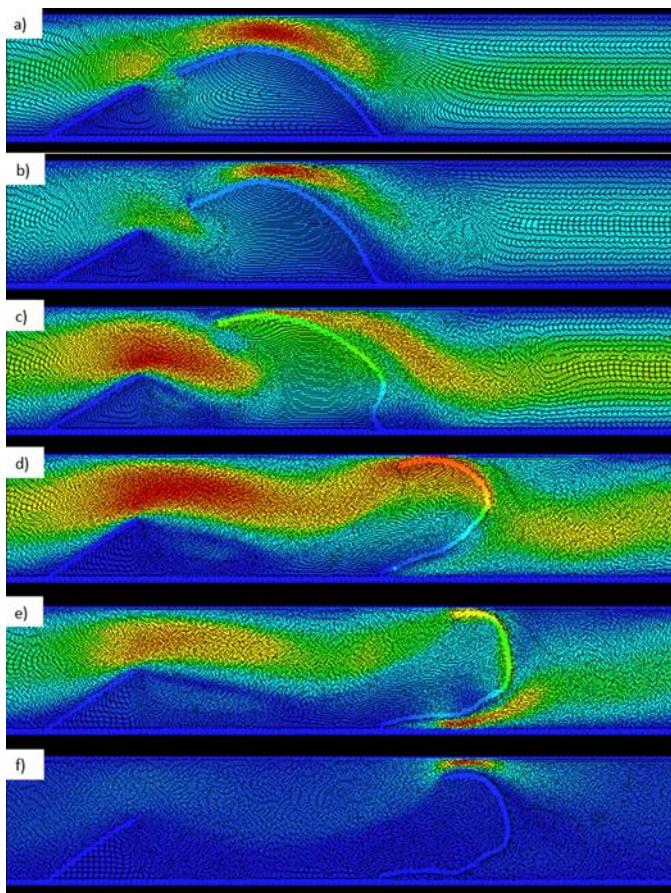
By 80 ms (Fig. 24.17C) the angle of the cap with the artery wall now has the opposite sign and the cap is fully directed to the right. Over the next 90 ms (Fig. 24.17D and E) the cap is rolled out to the right and the lipid core (red) is advected strongly to the right. Note that the cap structure remains an elastic body with memory of its original shape so is able to maintain some curvature in its upper section which constrains the viscous liquid (lipid core) which is held back behind the cap. The extension of the cap to the right is maximal at 150 ms (Fig. 24.17E). After this the overall blood flow rate declines in response to the nearly complete blockage

**FIGURE 24.17**

Progress of full rupture of a plaque structure with cap of thickness 0.22  $\mu\text{m}$  using an SPH resolution of 0.056  $\mu\text{m}$  with particles colored by their material type with *blue* being blood, *red* being viscous liquid initially inside the plaque, and *white* are the elastic cap of the plaque and the walls of the artery. Frames are at: (A) 40 ms, (B) 60 ms, (C) 80 ms, (D) 120 ms, (E) 150 ms, and (F) 340 ms.

of the artery which lessens the fluid pressure on the cap which then partially elastically unloads returning modestly to the left. Fig. 24.17F shows the behavior much later (340 ms) when the cap and flow is in equilibrium. The flow of blood into the upper part of the plaque structure is now visibly eroding the lipid core material (red) which is being entrained into the blood flow forming a distinct plume from the top surface of the plaque. This continues until this liquid has been substantially removed being deposited progressively into the blood stream.

Fig. 24.18 shows frames from the same complete rupture scenario as for Fig. 24.17 but with the fluid colored by its streamwise relative velocity. At early

**FIGURE 24.18**

Progress of full rupture of a plaque structure with cap of thickness  $0.22 \mu\text{m}$  using an SPH resolution of  $0.056 \mu\text{m}$  with particles colored by their streamwise flow velocity using the same relative color bar as shown in previous velocity figures. Frames are shown at: (A) 20 ms, (B) 40 ms, (C) 60 ms, (D) 120 ms, (E) 140 ms, and (F) 340 ms.

times (Fig. 24.18A) the flow is dominated by the flow of blood over the top of the plaque. Some flow through the expanding opening in the cap on the left is visible. The flow into the plaque structure increases strongly over the next 80 ms (Fig. 24.18B–D) with the flow over top of the cap weakening as the cap is forced up toward the top wall of the artery, essentially cutting off this part of the flow. Once the buckling instability has occurred (Fig. 24.18C) all the parts of the cap on the right can be seen to be traveling at the same speed as that of the surrounding fluid. The buckling instability has almost entirely removed the mechanical strength of the cap which is transported rapidly downstream with the fluid. Fig. 24.18F shows

the final equilibrium flow pattern. The cap is now almost stationary, and the fluid trapped to the left of the right part of the cap and protected below the left part of the cap is very quiescent. Fast fluid flow is observed over the top of the cap through the small open space between this and the upper artery wall. The blood flow from the left is slowly migrating core lipid fluid from the protected region below into the jet that passes above the cap. Liberated core fragments or droplets (which are made of materials rich in prothrombotic factors) will act as nucleation sites for coagulation forming free stream thrombi surrounding these that are then transported through the circulation.

This type of rupture scenario, where there is incomplete separation of the cap from the artery wall, leads to nearly complete blockage of the artery (to an extent that is much worse than that of the original stenosis) and which will obviously be clinically adverse. If the cap has some brittle behavior, then it will likely fracture into one or more fragments which will be transported away from the plaque site. This will lead to significantly reduced stenosis (which is positive) but the exposed artery wall below the necrotic core is subject to strong clotting (see Section [Blood coagulation and clot formation modeling](#)) which can then lead to partial or complete reblockage with newly clotted blood. The fate of cap fragments and lipid core material that are transported from the ruptured plaque into the circulatory system and the consequences can be very varied, although none are positive.

Overall gross deformation of the cap is likely to be insensitive to minor variations in the elastic properties. It is average elastic moduli that controls the degree of plaque inflation and the degree of increased stenosis in the partial rupture cases. For caps which are brittle and subject to cracking, these will be much more dependent on the spatial distribution of the mechanical properties.

The SPH fluid–structure model for plaque rupture has proved to be stable and robust. It has enabled an exploration of the effects of damage location, shape, cap stiffness and thickness on plaque rupture. Both stable partial rupture and full rupture scenarios were able to be predicted, dependent on the plaque cap thickness. In all cases, if the cap does not explicitly fracture then the expansion and/or unrolling of the cap structure leads to nearly complete blockage of the artery (to an extent that is much worse than the original stenosis).

The model can easily be extended to clinical geometries in three dimensions and more complex rheology, both for the cap and the core, can be readily included.

---

## Bone remodeling

Bone remodeling is a process in the body where bone structure changes as a result of the balance of bone growth and bone loss and is induced by the stress loading that the bone experiences. Osteoporotic fracture which arises from age-related bone loss is an important cause of elderly morbidity. Such bone loss occurs due to an imbalance in the remodeling process. These osteoporotic fractures have been estimated to cost billions in additional health care ([Fazzalari, 2008](#)) and significantly adversely impact

on quality of life for the elderly. Between 10% and 20% of those experiencing hip fractures die in the first year after fracture with order half suffering lifelong impacts. With the aging of many populations this is expected to become a progressively more important problem for society.

Bone readily adapts to the loads to which it is subjected. Mechanosensitive bone cells, called osteocytes, are believed to respond to mechanical stimulus and generate cellular changes in the bone ([Boneworld, 2002](#)). This involves signaling both the

- absorbance of existing bone cells, by osteoclasts, in regions of low strain, and
- generation of new bone, by osteoblasts, in regions of high strain.

Bone also changes according to cellular damage. It is useful to develop computational models of the bone remodeling process in order to assist in understanding these fundamental mechanisms and to assist in clinical decision-making.

Models of bone remodeling have included those using damage models ([Prendergast & Taylor, 1994](#)), strain energy density in finite element analysis ([Huiskes et al., 2000](#)), and strain coupled with damage ([McNamara & Prendergast, 2007](#)). All these methods were limited to describing aggregate bone loss over time without considering local variations in the strain field due to the osteon arrangement (vascular channels in the outer cortical bone known as Haversian canals). [Fernandez et al. \(2010, 2013\)](#) proposed the use of SPH to capture bone remodeling features efficiently. Key findings were that:

- Bone remodeling due to strain at the osteon level generates pore merging, which increases with age.
- SPH is a suitable approach for representing the conversion between bone and marrow and for predicting the intricate pore shapes that consequently evolve over time.

[Fernandez et al. \(2010, 2013\)](#) used strain stimulus levels adapted from [Prendergast and Taylor \(1994\)](#) so that when stress was below 2 MPa bone was converted to marrow and when stress was above 1.8 GPa additional bone was created. The implementation of this model in SPH is described earlier in Section [SPH solid evolution for remodeling processes](#). They generated pore geometries from segmentation of micro-CT scans that were sufficient to resolve osteons for samples at a range of ages.

[Fig. 24.19](#) shows the pore shapes in the bone during the remodeling process reproduced from [Fernandez et al. \(2010\)](#) for three ages each based on segmented micro-CT data for samples. The von Mises stress predicted by the SPH method is shown in row a. The osteons are smaller and more uniform at young age and the resultant stresses are low. The osteons grow in size with age and the stress becomes more spatially concentrated with high stresses (red) occurring for the oldest sample. Row b shows the initial state of the bone (distribution of bone and narrow), while row c shows the predicted state after 3 months. For the youngest sample, the net bone loss was predicted to be 0.3% with a fairly stable pore arrangement. The intermediate old subject showed three regions where pores demonstrated a predisposition to merging that were correlated areas predicted by the SPH model to have low strain

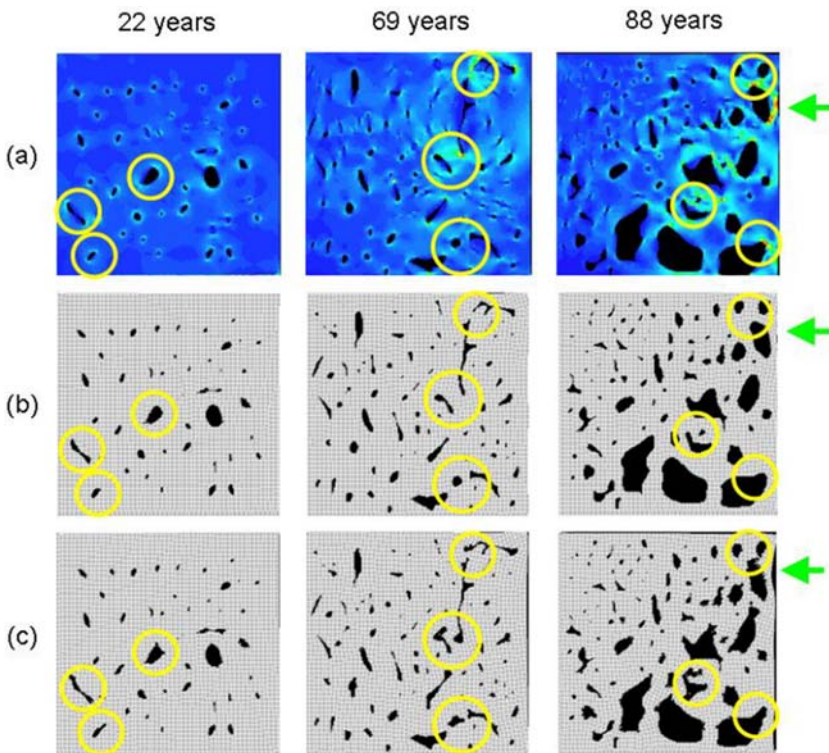


**FIGURE 24.19**

Bone remodeling simulation predictions for patients of different ages (column 1: 22; column 2: 69; column 3: 88). The circles highlight specific remodeling sites. SPH model predictions are shown in each row for: (A) compression induced initial Von Mises strain; (B) initial geometric distributions of bone (gray) and marrow (black); (C) and changes in bone/marrow distributions due to 30 months of bone remodeling.

*Reprinted with permission from Fernandez, J. W., Das, R., Thomas, C. D. L., Cleary, P. W., Sinnott, M. D., & Clement, J. (2010). Strain reduction between cortical pore structures leads to bone weakening and fracture susceptibility: An investigation using smooth particle hydrodynamics. In IFMBE proceedings series. Proceedings of 6th world congress of biomechanics. Singapore: Springer.*

and having a net bone loss of 1.8%. [Fernandez et al. \(2010\)](#) found that the oldest sample “showed very clear shape change in three regions and complete pore merging in two regions” with a predicted net bone loss of around 4%. “Fine crack-like structures were also observed as part of the bone evolution” in the older samples.

The study of [Fernandez et al. \(2010\)](#) demonstrated that “the cortical pore structure gave rise to a strongly non-uniform strain pattern with distinct region of low Von Mises strain between and around the pores. The strain pattern when coupled with remodeling rules leads to merging of the pores as age increases.” This and the subsequent study by [Fernandez et al. \(2013\)](#) showed that SPH was “a suitable method

for the purpose of bone remodeling with specific advantages” including its ability to capture behavior of the bone at the individual SPH particle level with creation and destruction of bone and the ability to capture complex emergent bone structures. These capabilities would also provide specific advantages in predicting remodeling of other tissues within the human body.

---

## Conclusions

In this chapter we present a detailed physics-based computational framework, based upon the SPH method and extensions for compliant walls and soft bodies, to understand flow and some remodeling processes occurring within the body proper. This framework comprises:

- An SPH representation of continua (in 2D or 3D), which is capable of simulating dynamics interactions between solids, liquids, and gases; fracturing and large deformations; interactions with moving and deforming boundaries; and bone modeling and remodeling.
- Flexible and deformable surfaces that can represent cell walls or membranes and soft bodies, including stretching due to pressures from constrained internal and external fluids or direct boundary contact. This enables the shape of such wall structures to be directly predicted from the force balance between fluid dynamics and wall elastic stresses.
- Specialized models of cell adhesion which represent tethering between cells and arterial walls, coagulation, and bone remodeling.

The use of this framework has been demonstrated for flow and remodeling processes within the body with the following example applications:

1. A model of a deformable RBC subjected to shear flow inside a capillary has enabled explanation of the hydrodynamic mechanism responsible for the Fahraeus–Lindqvist effect. The cell-depleted layer at the wall is due to cell migration away from the wall caused by an uplift force on the RBC. Flow around the cell body creates differences in shear force acting across the cell. This produces a stronger inward force on the trailing side of the cell and a weaker outward force on the leading side which generates a transverse force imbalance that manifests as an inward lift force. This also creates significant torque generating rotational motion and asymmetric deformation of the cell. The lift force can also be related back to the rotation of the cell. The lift force, cell shape, and angular speed all depend on radial position of the cell in the channel. As the cell is located more toward the center of the channel, it becomes increasingly symmetrical and the lift force, transverse velocity and rotation rate all decline toward zero at the center of the channel
2. Prediction of rolling adhesion along a capillary wall for a deformable white blood cell model which incorporates bond kinetics, tether formation, and

rupture have been made. The influence of a shear flow in the microcirculation applies stresses to the cell membrane which deform the cell, increase its contact area, and push it forward. The large contact area between the cell and wall promotes significant adhesion due to P-selectin mediated bonds and tether formation which together restrict the free motion of the cell. The combination of dynamic tether formation and rupture and the applied shear flow cumulatively produce realistic discontinuous slip/stick rolling motion that reduces the cell migration rate to 1/20 that of the plasma. The model also successfully predicts a realistic degree of elongation of the cell for a physiologically reasonable capillary flow rate.

3. A model of arterial flow within a mildly stenosed patient-specific ICA geometry has been used to predict regions of peak wall shear stress and high flow velocity that can be expected to correlate with risk sites for further vascular remodeling of the wall. The model has been used to highlight the potential use of such models to test the efficacy of particular surgical interventions and their likely outcomes.
4. A simple coagulation prediction capability based on thrombin diffusion and fibrin gel creation has been demonstrated. The model represents the coagulating material by a thrombin concentration dependent viscosity with a phase change representing when the matrix is sufficiently stiff that deformations become unimportant. This model is therefore able to include deformation effects on the clot shape resulting from the stresses from the adjacent shear flow. The model was shown to be able to predict clotting up to and including blockage of the blood vessel which leads to sharply reduced blood flow rates while it is still viscous and flow cessation if the solid part of the clot is able to grow to span the capillary. The extent of clot growth is a balance between diffusion of thrombin within the clot and the advection in the adjacent shear flow of blood with the diffusion rate decreasing with degree of clot solidification, which is a key limiting factor on clot growth.
5. A coupled fluid–structure SPH model of vulnerable plaque in an artery shows that the nature of the damage to the cap is important for determining if rupture will occur or if the plaque will remain stable. Damage that is oriented orthogonal to the fluid flow is stable and often sealed by deformation of the cap in response to the fluid force. If the damage is oriented with the flow, then it can promote direct flow of blood into the plaque structure which then expands with the cap rising to the opposite wall of the artery leading to near complete blockage. Such structures are stable if the cap is not sufficiently deformable. This inflation mechanism can be linked to observations of intraplaque hemorrhage. Sequences of partial ruptures with inflationary events can lead to nonlinear growth of plaque at a rate that can be much faster than by the usual absorption and remodeling processes. The thickness of the cap and its stiffness play a critical role in determining the extent of plaque rupture. For a reasonable physiological stiffness, plaque with a cap between 0.33 and 0.67  $\mu\text{m}$  undergoing inflationary expansion, is then stable and nearly fully blocks the artery.

However, a 0.22- $\mu\text{m}$  thick cap has sufficient flexibility that it undergoes a snap through buckling instability allowing the cap, still anchored at its leeward end, to be advected downstream releasing the viscous core fluid into the arterial flow. Although plaque inflation has been identified as a mechanism using a fluid lipid core model the same dynamics apply for soft brittle elastic solid cores but with different final distributions of the captured blood.

6. Remodeling of bone at the Haversian scale showing that heterogeneity of cortical pore structures causes strongly nonuniform strain patterns that lead to merging of the pores as age increases and eventually to weakening of the bone. This example shows that such particle methods are very well suited to predicting body remodeling processes because of their flexibility in enabling complex surface deformations and evolution.

Numerous challenges remain in accurately modeling in-body flow processes and understanding how to use model predictions to gain knowledge and/or guide clinical decision-making. The practical and ethical difficulties in performing physical measurement limit the availability of physical data that could be used to develop hypotheses of function, or to calibrate and validate models. Many aspects of the processes are undercharacterized *in vivo*, including mechanical characterization of fluid rheology and soft tissue elastic properties, and how these vary with biological changes. Computational and algorithmic improvements are required to account for the multiscale nature of these processes, which can include important nano-, micro-, and meso-scale features. Systematic resolution of these challenges will increase the utility of such modeling frameworks for understanding and improving health.

---

## Acknowledgments

The authors kindly acknowledge the significant contributions of Mr. David Lee in helping develop the white blood cell model through the CSIRO Vacation Student program; and our collaborators Drs. Thanh Phan and Richard Beare at Monash Medical Centre for access to the clinical patient geometry used in the arterial flow model.

---

## References

- Arzani, A. (2018). Accounting for residence-time in blood rheology models: Do we really need non-Newtonian blood flow modelling in large arteries? *Journal of The Royal Society Interface*, 15(146), 20180486.
- Ascolese, M., Farina, A., & Fasano, A. (2019). The Fåhræus-Lindqvist effect in small blood vessels: How does it help the heart? *Journal of Biological Physics*, 45(4), 379–394.
- Batchelor, G. K. (1974). *An Introduction to Fluid Mechanics*. Cambridge: Cambridge University Press.
- Bell, G. I. (1978). Models for the specific adhesion of cells to cells. *Science*, 200, 618–627.
- Bentzon, J. F., Otsuka, F., Virmani, R., & Falk, E. (2014). Mechanisms of plaque formation and rupture. *Circulation Research*, 114, 1852–1866.

- Berg, P., Stucht, D., Janiga, G., Beuing, O., Speck, O., & Thévenin, D. (2014). Cerebral blood flow in a healthy circle of Willis and two intracranial aneurysms: Computational fluid dynamics versus four-dimensional phase-contrast magnetic resonance imaging. *Journal of Biomechanical Engineering*, 136(4), 041003.
- Bhardwaj, S., Almaeen, A., Wani, F. A., & Thirunavukkarasu, A. (2020). Hematologic derangements in HIV/AIDS patients and their relationship with the CD4 counts: A cross-sectional study. *International Journal of Clinical and Experimental Pathology*, 13(4), 756.
- Bhatia, S. K., King, M. R., & Hammer, D. A. (2003). The state diagram for cell adhesion mediated by two receptors. *Biophysical Journal*, 84, 2671–2690.
- Birchall, D., Zaman, A., Hacker, J., Davies, G., & Mendelow, D. (2006). Analysis of haemodynamic disturbance in the atherosclerotic carotid artery using computational fluid dynamics. *European Radiology*, 16(5), 1074–1083.
- Bonewold, L. F. (2002). Osteocytes: A proposed multifunctional bone cell. *Journal of Musculoskeletal and Neuronal Interaction*, 2, 239–241.
- Bordon, Y. (2018). Platelets on the prowl. *Nature Reviews Immunology*, 18(1), 3–3.
- Brass, L. F., Wannemacher, K. M., Ma, P., & Stalker, T. J. (2011). Regulating thrombus growth and stability to achieve an optimal response to injury. *Journal of Thrombosis and Haemostasis*, 9, 66–75.
- Chandrashekhar, A., Singh, G., Garry, J., Sikallas, N., & Labropoulos, N. (2018). Mechanical and biochemical role of fibrin within a venous thrombus. *European Journal of Vascular and Endovascular Surgery*, 55(3), 417–424.
- Cibis, M., Potters, W. V., Selwaness, M., Gijsen, F. J., Franco, O. H., Lorza, A. M. A., de Brujne, M., Hofman, A., van der Lugt, A., Nederveen, A. J., & Wentzel, J. J. (2016). Relation between wall shear stress and carotid artery wall thickening MRI versus CFD. *Journal of Biomechanics*, 49(5), 735–741.
- Cleary, P. W. (1998). Modelling confined multi-material heat and mass flows using SPH. *Applied Mathematical Modelling*, 22, 981–993.
- Cleary, P. W. (2010a). Extension of SPH to predict feeding, freezing and defect creation in low pressure die casting. *Applied Mathematical Modelling*, 34, 3189–3201.
- Cleary, P. W. (2010b). Elastoplastic deformation during projectile-wall collision. *Applied Mathematical Modelling*, 34, 266–283.
- Cleary, P. W. (2015). Prediction of coupled particle and fluid flows using DEM and SPH. *Minerals Engineering*, 73, 85–99.
- Cleary, P. W., & Das, R. (2008). The potential for SPH modelling of solid deformation and fracture. In D. Reddy (Ed.), *IUTAM proceedings book series volume “theoretical, modeling and computational aspects of inelastic Medi”* (pp. 287–296). Springer-Verlag.
- Cleary, P. W., Ha, J., Prakash, M., & Nguyen, T. (2010). Short shots and industrial cases studies: Understanding fluid flow and solidification in high pressure die casting. *Applied Mathematical Modelling*, 34, 2018–2033.
- Cleary, P. W., Harrison, S. M., Sinnott, M. D., Pereira, G. G., Prakash, M., Cohen, R. C. Z., Rudman, M., & Stokes, N. (2020). Application of SPH to single and multiphase geophysical, biophysical and industrial fluid flows. *International Journal of Computational Fluid Dynamics*, 1–57.
- Cleary, P. W., Harrison, S. M., Sinnott, M. D., Pereira, G. G., Prakash, M., Cohen, R. C. Z., Rudman, M., & Stokes, N. (2021). Application of SPH to single and multiphase geophysical, biophysical and industrial fluid flows. *International Journal of Computational Fluid Dynamics*, 35, 22–78.
- Cleary, P. W., & Monaghan, J. J. (1999). Conduction modelling using smoothed particle hydrodynamics. *Journal of Computational Physics*, 148, 227–264.

- Cleary, P. W., Prakash, M., Ha, J., Stokes, N., & Scott, C. (2007). Smooth particle hydrodynamics: Status and future potential. *Progress in Computational Fluid Dynamics*, 7, 70.
- Cleary, P. W., & Sinnott, M. S. (2006). A micromechanical model for cell deformation in shearing flows using smoothed particle hydrodynamics. *Journal of Biomechanics*, 39, S639.
- Cleary, P. W., Thomas, D., Hetherton, L., Bolger, M., Hilton, J. E., & Watkins, D. (2020b). Workspace: A workflow platform for supporting development and deployment of modeling and simulation. *Mathematics and Computers in Simulation*, 175, 25–61.
- Cohen, R. C. Z., Cleary, P. W., & Mason, B. R. (2012). Simulations of dolphin kick swimming using smoothed particle hydrodynamics. *Human Movement Science*, 31, 604–619.
- Cohen, R. C. Z., Cleary, P. W., Mason, B. R., & Pease, D. L. (2020). Studying the effects of asymmetry on freestyle swimming using smoothed particle hydrodynamics. *Computer Methods in Biomechanics and Biomedical Engineering*, 23, 271–284.
- Conti, M., Long, C., Marconi, M., Berchiolli, R., Bazilevs, Y., & Reali, A. (2016). Carotid artery hemodynamics before and after stenting: A patient specific CFD study. *Computers and Fluids*, 141, 62–74.
- Corti, A., Chiastra, C., Colombo, M., Garbey, M., Migliavacca, F., & Casarin, S. (2020). A fully coupled computational fluid dynamics–agent-based model of atherosclerotic plaque development: Multiscale modeling framework and parameter sensitivity analysis. *Computers in Biology and Medicine*, 118, 103623.
- Cummins, S., Cleary, P. W., Delaney, G., Phua, A., Sinnott, M., Gunasegaram, D., & Davies, C. (2021). A coupled DEM/SPH computational model to simulate microstructure evolution in Ti-6Al-4V laser powder bed fusion processes. *Metals*, 11, 858.
- Cummins, S. J., Silvester, T. B., & Cleary, P. W. (2012). Three-dimensional wave impact on a rigid structure using smoothed particle hydrodynamics. *International Journal for Numerical Methods in Fluids*, 68, 1471–1496.
- Currey, J. D. (1988). The effect of porosity and mineral-content on the Youngs modulus of elasticity of compact-bone. *Journal of Biomechanics*, 21(2), 131–139.
- Daemen, M. J., Ferguson, M. S., Gijsen, F. J., Hippe, D. S., Kooi, M. E., Demarco, K., van der Wal, A. C., Yuan, C., & Hatsukami, T. S. (2016). Carotid plaque fissure: An underestimated source of intraplaque hemorrhage. *Atherosclerosis*, 254, 102–108.
- Das, R., & Cleary, P. W. (2015). Evaluation of the accuracy and stability of the classical SPH method under uniaxial compression. *Journal of Scientific Computing*, 64, 858–897.
- Dembo, M. (1994). On peeling an adherent cell from a surface. *Lectures on Mathematics in the Life Sciences, Some Mathematical Problems in Biology*, 24, 51–77.
- Dembo, M., Torney, D. C., Saxman, K., & Hammer, D. (1988). The Reaction-limited kinetics of membrane-to-surface adhesion and detachment. *Proceedings of the Royal Society of London, Series B*, 234, 55–83.
- Dong, C., Cao, J., Struble, E. J., & Lipowsky, H. H. (1999). Mechanics of leukocyte deformation and adhesion to endothelium in shear flow. *Annals of Biomedical Engineering*, 27(3), 298–312.
- Dong, C., & Lei, X. X. (2000). Biomechanics of cell rolling: Shear flow, cell-surface adhesion, and cell deformability. *Journal of Biomechanics*, 33(1), 35–43.
- Doyle, J., & Cooper, J. S. (2018). Physiology, carbon dioxide transport. In *StatPearls*. Treasure Island (FL): StatPearls Publishing.
- Eshtehardi, P., Brown, A. J., Bhargava, A., Costopoulos, C., Hung, O. Y., Corban, M. T., Hosseini, H., Gogas, B. D., Giddens, D. P., & Samady, H. (2017). High wall shear stress

- and high-risk plaque: An emerging concept. *International Journal of Cardiovascular Imaging*, 33(7), 1089–1099.
- Evans, E., Heinrich, V., Leung, A., & Kinoshita, K. (2005). Nano-to-Micro dynamics of P-selectin detachment from leukocyte interfaces. I. Membrane separation from the cytoskeleton. *Biophysical Journal*, 88, 2288–2298.
- Fahraeus, R., & Lindqvist, T. (1931). The viscosity of the blood in narrow capillary tubes. *American Journal of Physiology-Legacy Content*, 96(3), 562–568.
- Fatahian, E., Kordani, N., & Fatahian, H. (2018). The application of computational fluid dynamics (CFD) method and several rheological models of blood flow: A review. *Gazi University Journal of Science*, 31(4), 1213–1227.
- Fazzalari, N. L. (2008). Bone remodeling: A review of the bone micro-environment perspective for fragility fracture (osteoporosis) of the hip. *Seminars in Cell and Developmental Biology*, 19, 467–472.
- Felton, C. V., Crook, D., Davies, M. J., & Oliver, M. F. (1997). Relation of plaque lipid composition and morphology to the stability of human aortic plaques. *Arteriosclerosis, Thrombosis, and Vascular Biology*, 17(7), 1337–1345.
- Fernandez, J. W., Das, R., Cleary, P. W., Hunter, P. J., Thomas, C. D. L., & Clement, J. G. (2013). Using smooth particle hydrodynamics to investigate femoral cortical bone remodelling at the Haversian level. *International Journal of Numerical Methods in Biomedical Engineering*, 29, 129–143.
- Fernandez, J. W., Das, R., Thomas, C. D. L., Cleary, P. W., Sinnott, M. D., & Clement, J. (2010). Strain reduction between cortical pore structures leads to bone weakening and fracture susceptibility: An investigation using smooth particle hydrodynamics. In *IFMBE proceedings series, Springer, proceedings of 6th world congress of biomechanics, Singapore*.
- Firrell, J. C., & Lipowsky, H. H. (1989). Leukocyte margination and deformation in mesenteric venules of rat. *American Journal of Physiology-Heart and Circulatory Physiology*, 256(6), H1667–H1674.
- Fogelson, A. L. (1984). A mathematical model and numerical method for studying platelet adhesion and aggregation during blood clotting. *Journal of Computational Physics*, 56(1), 111–134.
- Fogelson, A. L., & Guy, R. D. (2008). Immersed-boundary-type models of intravascular platelet aggregation. *Computer Methods in Applied Mechanics and Engineering*, 197(25-28), 2087–2104.
- Freedman, J. E. (2005). Molecular regulation of platelet-dependent thrombosis. *Circulation*, 112(17), 2725–2734.
- Friedl, P., & Weigelin, B. (2008). Interstitial leukocyte migration and immune function. *Nature Immunology*, 9(9), 960–969.
- Gharabi, H., Zambrano, B. A., Zhu, D. C., DeMarco, J. K., & Baek, S. (2016). Computational fluid dynamic simulation of human carotid artery bifurcation based on anatomy and volumetric blood flow rate measured with magnetic resonance imaging. *International Journal of Advances in Engineering Sciences and Applied Mathematics*, 8(1), 46–60.
- Gholami, B., Comerford, A., & Ellero, M. (2014). A multiscale SPH particle model of the near-wall dynamics of leukocytes in flow. *International Journal for Numerical Methods in Biomedical Engineering*, 30(1), 83–102.
- Gholami, B., Comerford, A., & Ellero, M. (2015). SPH simulations of WBC adhesion to the endothelium: The role of haemodynamics and endothelial binding kinetics. *Biomechanics and Modeling in Mechanobiology*, 14(6), 1317–1333.

- Gray, J. P., Monaghan, J. J., & Swift, R. P. (2001). SPH elastic dynamics. *Computer Methods in Applied Mechanics and Engineering*, 190, 6641–6662.
- Gutierrez, M., Fish, M. B., Golinski, A. W., & Eniola-Adefeso, O. (2018). Presence of rigid red blood cells in blood flow interferes with the vascular wall adhesion of leukocytes. *Langmuir*, 34(6), 2363–2372.
- Han, D., Zhang, J., Griffith, B. P., & Wu, Z. J. (2022). Models of shear-induced platelet activation and numerical implementation with computational fluid dynamics approaches. *Journal of Biomechanical Engineering*, 144(4).
- Harrison, S. M., Cleary, P. W., & Cohen, R. C. Z. (2019). Dynamic simulation of flat water kayaking using a coupled biomechanical-smoothed particle hydrodynamics model. *Human Movement Science*, 64, 252–273.
- Harrison, S. M., Cleary, P. W., & Sinnott, M. D. (2018). Investigating mixing and emptying for aqueous liquid content from the stomach using a coupled biomechanical-SPH model. *Food and Function*, 9, 3202–3219.
- Harrison, S. M., Cohen, R. C. Z., Cleary, P. W., Mason, B. R., & Pease, D. L. (2014). Torque and power about the joints of the arm during the freestyle stroke. In B. R. Mason (Ed.), *XIIth international symposium for biomechanics and medicine in swimming* (pp. 349–355).
- Harrison, S. M., Whitton, R. C., Stover, S. M., Symons, J. E., & Cleary, P. W. (2022). A coupled biomechanical-smoothed particle hydrodynamics model for Horse racing tracks. *Frontiers in Bioengineering and Biotechnology*, 10, 766748.
- Heinrich, V., Leung, A., & Evans, E. (2005). Nano-to-micro scale dynamics of P-selectin detachment from leukocyte interfaces. II. Tether flow terminated by P-selectin dissociation from PGSL-1. *Biophysical Journal*, 88, 2299–2308.
- Hoffmann, M. A., Kieffer, C., & Bjorkman, P. J. (2021). In vitro characterization of engineered red blood cells as viral traps against HIV-1 and SARS-CoV-2. *Molecular Therapy-Methods and Clinical Development*, 21, 161–170.
- Horsfield, K., & Woldenberg, M. J. (1989). Diameters and cross-sectional areas of branches in the human pulmonary arterial tree. *The Anatomical Record*, 223, 245–251.
- Huiskes, R., Ruimerman, R., Van Lenthe, G. H., & Janssen, J. D. (2000). Effects of mechanical forces on maintenance and adaptation of form in trabecular bone. *Nature*, 405(6787), 704–706.
- Irvine, D. J., Hue, K., Mayes, A. M., & Griffith, L. G. (2002). Simulations of cell-surface integrin binding to nanoscale-clustered adhesion ligands. *Biophysical Journal*, 82, 120–132.
- Jadhav, S., Eggleton, C. D., & Konstantopoulos, K. (2005). A 3-D computational model predicts that cell deformation affects selectin-mediated leukocyte rolling. *Biophysical Journal*, 88, 96–104.
- Jiritano, F., Serraino, G. F., Ten Cate, H., Fina, D., Matteucci, M., Mastroroberto, P., & Lorusso, R. (2020). Platelets and extra-corporeal membrane oxygenation in adult patients: A systematic review and meta-analysis. *Intensive Care Medicine*, 46(6), 1154–1169.
- Jung, J., & Hassanein, A. (2008). Three-phase CFD analytical modeling of blood flow. *Medical Engineering and Physics*, 30(1), 91–103.
- Kamm, R. D. (2002). Cellular fluid mechanics. *Annual Review of Fluid Mechanics*, 34(1), 211–232.
- Kheyfets, V. O., Rios, L., Smith, T., Schroeder, T., Mueller, J., Murali, S., Lasorda, D., Zikos, A., Spotti, J., Reilly, J. J., Jr., & Finol, E. A. (2015). Patient-specific computational

- modeling of blood flow in the pulmonary arterial circulation. *Computer Methods and Programs in Biomedicine*, 120(2), 88–101.
- King, M. R., Heinrich, V., Evans, E., & Hammer, D. A. (2005). Nano-to-micro scale dynamics of P-selectin detachment from leukocyte interfaces. III. Numerical simulation of tethering under flow. *Biophysical Journal*, 88, 1676–1683.
- Kock, S. A., Nygaard, J. V., Eldrup, N., Fründ, E. T., Klærke, A., Paaske, W. P., Falk, E., & Kim, W. Y. (2008). Mechanical stresses in carotid plaques using MRI-based fluid–structure interaction models. *Journal of Biomechanics*, 41(8), 1651–1658, 1.
- Krasik, E. F., & Hammer, D. A. (2004). A semianalytic model of leukocyte rolling. *Biophysical Journal*, 87, 2919–2930.
- Kuharsky, A. L., & Fogelson, A. L. (2001). Surface-mediated control of blood coagulation: The role of binding site densities and platelet deposition. *Biophysical Journal*, 80(3), 1050–1074.
- Leiderman, K., & Fogelson, A. L. (2011). Grow with the flow: A spatial–temporal model of platelet deposition and blood coagulation under flow. *Mathematical Medicine and Biology*, 28(1), 47–84.
- Liang, L., Steinman, D. A., Brina, O., Chnafa, C., Cancelliere, N. M., & Pereira, V. M. (2019). Towards the clinical utility of CFD for assessment of intracranial aneurysm rupture—a systematic review and novel parameter-ranking tool. *Journal of Neurointerventional Surgery*, 11(2), 153–158.
- Liberky, L. D., & Petschek, A. G. (1990). Smooth particle hydrodynamics with strength of materials. In Trease, & Crowley (Eds.), *Advances in the free-Lagrange method*. Berlin: Springer.
- Long, Q., Xu, X. Y., Ariff, B., Thom, S. A., Hughes, A. D., & Stanton, A. V. (2000). Reconstruction of blood flow patterns in a human carotid bifurcation: A combined CFD and MRI study. *Journal of Magnetic Resonance Imaging*, 11(3), 299–311.
- Lopes, D., Puga, H., Teixeira, J., & Lima, R. (2020). Blood flow simulations in patient-specific geometries of the carotid artery: A systematic review. *Journal of Biomechanics*, 111, 110019.
- Lopes, D., Puga, H., Teixeira, J. C., & Teixeira, S. F. (2019). Influence of arterial mechanical properties on carotid blood flow: Comparison of CFD and FSI studies. *International Journal of Mechanical Sciences*, 160, 209–218.
- Malvè, M., García, A., Ohayon, J., & Martínez, M. A. (2012). Unsteady blood flow and mass transfer of a human left coronary artery bifurcation: FSI vs. CFD. *International Communications in Heat and Mass Transfer*, 39(6), 745–751.
- Marshall, I., Zhao, S., Papathanasopoulou, P., Hoskins, P., & Xu, X. Y. (2004). MRI and CFD studies of pulsatile flow in healthy and stenosed carotid bifurcation models. *Journal of Biomechanics*, 37(5), 679–687.
- McCullough, J. (2014). RBCs as targets of infection. *Hematology 2014, the American Society of Hematology Education Program Book*, 2014(1), 404–409.
- McNamara, L., & Prendergast, P. (2007). Bone remodelling algorithms incorporating both strain and micro damage stimuli. *Journal of Biomechanics*, 40, 1381–1391.
- Midulla, M., Moreno, R., Baali, A., Chau, M., Negre-Salvayre, A., Nicoud, F., Pruvost, J. P., Haulon, S., & Rousseau, H. (2012). Haemodynamic imaging of thoracic stent-grafts by computational fluid dynamics (CFD): Presentation of a patient-specific method combining magnetic resonance imaging and numerical simulations. *European Radiology*, 22(10), 2094–2102.

- Mitrugno, A., Tormoen, G. W., Kuhn, P., & McCarty, O. J. (2016). The prothrombotic activity of cancer cells in the circulation. *Blood Reviews*, 30(1), 11–19.
- Monaghan, J. J. (1992). Smoothed particle hydrodynamics. *Annual Rev. Astron. Astrophys.*, 30, 543–574.
- Monaghan, J. J. (1994). Simulating free surface flows with SPH. *Journal of Computational Physics*, 110, 399–406.
- Monaghan, J. J. (2005). Smoothed particle hydrodynamics. *Reports on Progress in Physics*, 68, 1703.
- Monaghan, J. J. (2012). Smoothed particle hydrodynamics and its diverse applications. *Annual Review of Fluid Mechanics*, 44, 323–346.
- Monaghan, J. J., & Gingold, R. A. (1983). Shock simulation by the particle method SPH. *Journal of Computational Physics*, 52(2), 374–389.
- Moore, K. L., Patel, K. D., Bruehl, R. E., Li, F., Johnson, D. A., Lichenstein, H. S., Cummings, R. D., Bainton, D. F., & McEver, R. P. (1995). P-selectin glycoprotein ligand-1 mediates rolling of human neutrophils on P-selectin. *Journal of Cell Biology*, 128, 661–671.
- Moreno, P. R. (2009). The high-risk thin-cap fibroatheroma: A new kid on the block. *Circulation: Cardiovascular Interventions*, 2(6), 500–502.
- Muller, W. A. (2013). Getting leukocytes to the site of inflammation. *Veterinary Pathology*, 50(1), 7–22.
- N'Dri, N. A., Shyy, W., & Tran-Son-Tay, R. (2003). Computational modelling of cell adhesion and movement using a continuum-kinetics approach. *Biophysical Journal*, 85, 2273–2286.
- Nowak, M., Melka, B., Rojczyk, M., Gracka, M., Nowak, A. J., Golda, A., Adamczyk, W. P., Isaac, B., Bialecki, R. A., & Ostrowski, Z. (2019). The protocol for using elastic wall model in modeling blood flow within human artery. *European Journal of Mechanics-B/Fluids*, 77, 273–280.
- Numata, S., Itatani, K., Kanda, K., Doi, K., Yamazaki, S., Morimoto, K., Manabe, K., Ikemoto, K., & Yaku, H. (2016). Blood flow analysis of the aortic arch using computational fluid dynamics. *European Journal of Cardio-Thoracic Surgery*, 49(6), 1578–1585.
- Ohayon, J., Finet, G., Floc'h, L., Cloutier, G., Gharib, A. M., Heroux, J., & Pettigrew, R. I. (2014). Biomechanics of atherosclerotic coronary plaque: Site, stability and in vivo elasticity modeling. *Annals of Biomedical Engineering*, 42(2), 269–279.
- Palacek, S. P., Horwitz, A. F., & Lauffenburger, D. A. (1999). Kinetic model for integrin-mediated adhesion release during cell migration. *Annals of Biomedical Engineering*, 27, 219–235.
- Pancaldi, F., Kim, O. V., Weisel, J. W., Alber, M., & Xu, Z. (2022). Computational biomechanical modeling of fibrin networks and platelet-fiber network interactions. *Current Opinion in Biomedical Engineering*, 100369.
- Park, E. Y. H., Smith, M. J., Stropp, E. S., Snapp, K. R., DiVietro, J. A., Walker, W. F., Schmidtke, D. W., Diamond, S. L., & Lawrence, M. B. (2002). Comparison of PSGL-1 micorobead and neutrophil rolling: Microvillus elongation stabilizes P-selectin bond clusters. *Biophysical Journal*, 82, 1835–1847.
- Pei, X., Wu, B., & Li, Z. Y. (2013). Fatigue crack propagation analysis of plaque rupture. *Journal of Biomechanical Engineering*, 135(10), 101003.
- Perinajová, R., Juffermans, J. F., Westenberg, J. J., van der Palen, R. L., van den Boogaard, P. J., Lamb, H. J., & Kenjereš, S. (2021). Geometrically induced wall shear

- stress variability in CFD-MRI coupled simulations of blood flow in the thoracic aortas. *Computers in Biology and Medicine*, 133, 104385.
- Phan, T. G., Ma, H., Goyal, M., Hilton, J., Sinnott, M., Srikanth, V., & Beare, R. (2020). Computer modeling of clot retrieval—circle of Willis. *Frontiers in Neurology*, 11, 773.
- Pirola, S., Cheng, Z., Jarrai, O. A., O'Regan, D. P., Pepper, J. R., Athanasiou, T., & Xu, X. Y. (2017). On the choice of outlet boundary conditions for patient-specific analysis of aortic flow using computational fluid dynamics. *Journal of Biomechanics*, 60, 15–21.
- Prandoni, P. (2009). Venous and arterial thrombosis: Two aspects of the same disease? *Clinical Epidemiology*, 1, 1–6.
- Prendergast, P., & Taylor, D. (1994). Prediction of bone adaptation using damage accumulation. *Journal of Biomechanics*, 27, 1067–1076.
- Pries, A. R., Reglin, B., & Secomb, T. W. (2005). Remodeling of blood vessels: Responses of diameter and wall thickness to hemodynamic and metabolic stimuli. *Hypertension*, 46(4), 725–731.
- Rezvani-Sharif, A., Tafazzoli-Shadpour, M., Kazemi-Saleh, D., & Sotoudeh-Anvari, M. (2017). Stress analysis of fracture of atherosclerotic plaques: Crack propagation modeling. *Medical and Biological Engineering and Computing*, 55(8), 1389–1400.
- Roth, G. A., Mensah, G. A., Johnson, C. O., Addolorato, G., Ammirati, E., Baddour, L. M., Barengo, N. C., Beaton, A. Z., Benjamin, E. J., Benziger, C. P., & Bonney, A. (2020). Global burden of cardiovascular diseases and risk factors, 1990–2019: Update from the GBD 2019 study. *Journal of the American College of Cardiology*, 76(25), 2982–3021.
- Rowell, L. B. (1974). Human cardiovascular adjustments to exercise and thermal stress. *Physiological Reviews*, 54, 75–159.
- Ruggeri, Z. M., & Mendolicchio, G. L. (2007). Adhesion mechanisms in platelet function. *Circulation Research*, 100(12), 1673–1685.
- Safaei, S., Bradley, C. P., Suresh, V., Mithraratne, K., Muller, A., Ho, H., Ladd, D., Hellevik, L. R., Omholt, S. W., Chase, J. G., Müller, L. O., Watanabe, S. M., Blanco, P. J., de Bono, B., & Hunter, P. J. (2016). Roadmap for cardiovascular circulation model. *Journal of Physiology*, 594, 6909–6928.
- Sakakura, K., Nakano, M., Otsuka, F., Ladich, E., Kolodgie, F. D., & Virmani, R. (2013). Pathophysiology of atherosclerosis plaque progression. *Heart, Lung and Circulation*, 22(6), 399–411.
- Schurr, Y., Sperr, A., Volz, J., Beck, S., Reil, L., Kusch, C., Eiring, P., Bryson, S., Sauer, M., Nieswandt, B., Machesky, L., & Bender, M. (2019). Platelet lamellipodium formation is not required for thrombus formation and stability. *Blood*, 134(25), 2318–2329.
- Schwarz, U. S., Balaban, N. Q., Bershadsky, A., Geiger, B., & Safran, S. A. (2002). Calculation of forces at focal adhesions from elastic substrate data: The effect of localized force and the need for regularization. *Biophysical Journal*, 83, 1380–1394.
- Secomb, T. W. (2017). Blood flow in the microcirculation. *Annual Review of Fluid Mechanics*, 49, 443–461.
- Secomb, T. W., & Pries, A. R. (2013). Blood viscosity in microvessels: Experiment and theory. *Comptes Rendus Physique*, 14(6), 470–478.
- Sekhane, D. (2016). Image-based Computational fluid dynamics (CFD) Modeling cerebral blood flow in the circle of Willis. *Journal of Advanced Research in Physics*, 6(2).
- Shyy, W., Francois, M., Udaykumar, H. S., N'Dri, N., & Tran-Son-Tay, R. (2001). Moving boundaries in micro-scale biofluid dynamics. *Applied Mechanics Review*, 54, 405–453.
- Sinnott, M. D., & Cleary, P. W. (2010). Effect of rotor blade angle and clearance on blood flow through a non-pulsatile, axial, heart pump. *Progress in Computational Fluid Dynamics*, 10(5-6), 300–306.

- Sinnott, M. D., Cleary, P. W., Arkwright, J. W., & Dinning, P. G. (2012). Investigating the relationships between peristaltic contraction and fluid transport in the human colon using smoothed particle hydrodynamics. *Computers in Biology and Medicine*, 42, 492–503.
- Sinnott, M. D., Cleary, P. W., & Harrison, S. M. (2017). Peristaltic transport of a particulate suspension in the small intestine. *Applied Mathematical Modelling*, 44, 143–159.
- Sinnott, M. D., Cleary, P. W., Harrison, S. M., Cummins, S. J., Beare, R., Srikanth, V., & Phan, T. G. (2015). How arterial pressures affect the consideration of internal carotid artery angle as a risk factor for carotid atherosclerotic disease. *Progress in Computational Fluid Dynamics*, 15(2), 87–101.
- Sinnott, M., Cleary, P. W., & Prakash, M. (2006). An investigation of pulsatile blood flow in a bifurcation artery using a grid-free method. In *Proceedings of fifth international conference on CFD in the process industries* (pp. 1–6).
- Sinnott, M. D., Harrison, S. M., & Cleary, P. W. (2021). A particle-based modelling approach to food processing operations. *Food and Bioproducts Processing*, 127, 14–57.
- Smith, M. J., Berg, E. L., & Lawrence, M. B. (1999). A direct comparison of selectin-mediated transient, adhesive events using high temporal resolution. *Biophysical Journal*, 77(6), 3371–3383.
- Sorrentino, S., Studt, J. D., Medalia, O., & Sapra, K. T. (2015). Roll, adhere, spread and contract: Structural mechanics of platelet function. *European Journal of Cell Biology*, 94(3–4), 129–138.
- Taebi, A., Pillai, R. M., S Roudsari, B., Vu, C. T., & Roncali, E. (2020). Computational modeling of the liver arterial blood flow for microsphere therapy: Effect of boundary conditions. *Bioengineering*, 7(3), 64.
- Tan, S., & Xu, M. (2020). Smoothed particle hydrodynamics simulations of whole blood in three-dimensional shear flow. *International Journal of Computational Methods*, 17(10), 2050009.
- Tees, D. F. J., & Goetz, D. J. (2003). Leukocyte adhesion: An exquisite balance of hydrodynamic and molecular forces. *News in Physiological Sciences*, 18, 186–190.
- Teng, Z., Canton, G., Yuan, C., Ferguson, M., Yang, C., Huang, X., Zheng, J., Woodard, P., & Tang, D. (2010). 3D critical plaque wall stress is a better predictor of carotid plaque rupture sites than flow shear stress: An *in vivo* MRI-based 3D FSI study. *Journal of Biomechanical Engineering*, 132, 031007.
- Thirugnanachandran, T., Beare, R., Mitchell, M., Wong, C., Vuong, J., Singhal, S., Slater, L. A., Hilton, J., Sinnott, M., Srikanth, V., Ma, H., & Phan, T. (2021). Anterior cerebral artery stroke: Role of collateral systems on infarct topography. *Stroke*, 52(9), 2930–2938.
- Tosenberger, A., Ataullakhonov, F., Bessonov, N., Panteleev, M., Tokarev, A., & Volpert, V. (2016). Modelling of platelet–fibrin clot formation in flow with a DPD–PDE method. *Journal of Mathematical Biology*, 72(3), 649–681.
- Tse, K. M., Chiu, P., Lee, H. P., & Ho, P. (2011). Investigation of hemodynamics in the development of dissecting aneurysm within patient-specific dissecting aneurismal aortas using computational fluid dynamics (CFD) simulations. *Journal of Biomechanics*, 44(5), 827–836.
- Wolff, C. B., Collier, D. J., Shah, M., Saxena, M., Brier, T. J., Kapil, V., Green, D., & Lobo, M. (2016). A discussion on the regulation of blood flow and pressure. In *Oxygen transport to tissue XXXVII* (pp. 129–135). New York, NY: Springer.
- Workspace, (n. d.), <https://research.csiro.au/workspace/>.

- Wu, J., Liu, G., Huang, W., Ghista, D. N., & Wong, K. K. (2015). Transient blood flow in elastic coronary arteries with varying degrees of stenosis and dilatations: CFD modelling and parametric study. *Computer Methods in Biomechanics and Biomedical Engineering*, 18(16), 1835–1845.
- Xiang, J., Tutino, V. M., Snyder, K. V., & Meng, H. (2014). CFD: Computational fluid dynamics or confounding factor dissemination? The role of hemodynamics in intracranial aneurysm rupture risk assessment. *American Journal of Neuroradiology*, 35(10), 1849–1857.
- Xu, Z., Christley, S., Lioi, J., Kim, O., Harvey, C., Sun, W., Rosen, E. D., & Alber, M. (2012). Multiscale model of fibrin accumulation on the blood clot surface and platelet dynamics. In *Methods in cell biology* (Vol 110, pp. 367–388). Academic Press.
- Yesudasan, S., & Averett, R. D. (2019). Recent advances in computational modeling of fibrin clot formation: A review. *Computational Biology and Chemistry*, 83, 107148.
- Zhang, J. M., Zhong, L., Su, B., Wan, M., Yap, J. S., Tham, J. P., Chua, L. P., Ghista, D. N., & Tan, R. S. (2014). Perspective on CFD studies of coronary artery disease lesions and hemodynamics: A review. *International Journal for Numerical Methods in Biomedical Engineering*, 30(6), 659–680.
- Zhao, Y., Chien, S., & Weinbaum, S. (2001). Dynamic contact forces on leukocyte microvilli and their penetration of the endothelial glycocalyx. *Biophysical Journal*, 80, 1124–1140.
- Zhu, C. (2000). Kinetics and mechanics of cell adhesion. *Journal of Biomechanics*, 33(1), 23–33.

This page intentionally left blank

**SECTION**

Medical devices

5

This page intentionally left blank

# Digital co-creation: an early-stage product individualization framework to bridge the customer–designer void

# 25

**Roatchanamat Anattasakul, Timothy James Slama, H. Onan Demirel**

*Oregon State University, Corvallis, OR, United States*

## Chapter outline

<b>Introduction</b> .....	659
<b>Background</b> .....	661
The transition from mass customization to mass individualization.....	661
The lack of customer participation in conventional product development.....	662
<b>Methodology</b> .....	663
Theoretical bases of the co-creation framework .....	663
Stages of the co-creation framework.....	665
<i>Ideation</i> .....	665
<i>Modeling</i> .....	665
<i>Analysis</i> .....	667
<i>Visualization</i> .....	667
<b>Case study</b> .....	668
Step 1: ideation and configure.....	668
Step 2: modeling and modify.....	669
Step 3: analysis and revise.....	672
Step 4: visualization and experience .....	673
<b>Discussion and conclusions</b> .....	674
<b>References</b> .....	675

## Introduction

The early design phase of product development involves multidisciplinary design teams focusing on a broad set of activities, including market research to identify customer requirements, conceptual modeling to generate variants, and embodiment to build prototypes (Demirel, 2015; Otto & Wood, 2001). Most of these activities concentrate on innovating solutions that answer a market opportunity. Overall, the

entire process requires an orchestrated effort to fulfill customer needs within feasible engineering requirements or technical possibilities while meeting business objectives (Demirel, 2020; Griffin & Hauser, 1993). Typically, during the early stages of the design, mechanical engineers and industrial designers collaborate with product innovation teams to develop strategies that capture customer needs and inject them into the product's final design (Demirel, 2015; Otto & Wood, 2001). With today's fast-moving marketplace, the need for agile and creative design methodologies that capture customer needs is at an all-time high (Smith & Reinertsen, 1998). This is especially prominent for design companies that deal with human-centered products and services. For example, design activities within biomedical and healthcare domains heavily focus on customization due to users' unique physiological and cognitive attributes. Products such as orthotics and prostheses require digital design and production systems to capture user needs and develop personalized solutions. Thus, product development strategies that reduce the overall design costs and time-to-market while capturing actual customer needs are critical ingredients for market success (Bayus, 1994). However, many conventional product design and development roadmaps have limitations in capturing and delivering customer needs (Euiyoung et al., 2018).

Among many production strategies introduced in the past couple of decades, perhaps, mass customization is regarded as the leading strategy that brings product customization flexibility based on highly variant products at mass production cost (Gilmore & Pine, 1997). Current mass customization techniques use knowledge-based or model-based configurations to generate product variants that aim to provide extended amounts of options to represent customer preferences (Blecker & Abdelkafi, 2006; Piller & Tseng, 2009). However, often they only partially capture the customer needs and fail to keep the customers in the loop during the design process due to a lack of direct-to-customer design and logistics systems (Zipkin, 2001). Although the mass customization strategy aims to integrate customers into the production process by building a customer–company interaction (Jost & Süsser, 2020), it often fails to establish a substantial level of partnership—customer—designer collaboration. Thus, mass customization does not always allow the customer's voice to be heard by the design teams directly. The above is especially true for medical and healthcare products since the design solutions concentrating on medical needs and services require fine-tuning the products and processes based on customers' unique physiological and cognitive needs. Therefore, there is a need for flexible direct-to-customer design methodologies that tailor products around customers' specific needs and preferences while keeping the customer's voice and input in the loop throughout the early design process.

Based on the pressing limitations discussed above, this chapter proposes a customer-centric design framework as an alternative strategy to capture customer needs and preferences early in design via the co-creation approach. The framework aims to present a computational design methodology that bridges the void between the customers and designers, primarily focusing on the medical market, such as orthotics and prostheses. It focuses on alleviating the challenges of mass customization

through product individualization. One of the critical aspects of this methodology is enabling designers to create individualized products at a comparable cost to mass customization and shortening time-to-market compared to traditional bespoke product development strategies. The process calls for collaborative design with digital technologies and tools enabling products tailored to customer needs and preferences, aligning with the goals and objectives discussed within the “Digital Patient” concept.

---

## Background

### The transition from mass customization to mass individualization

Mass customization is an economic model that combines the low unit cost of manufacturing during mass manufacturing with the unique customer-product fit that customization provides (Fogliatto et al., 2012). It has been implemented to varying degrees in several successful business models and has been a popular approach for many product design companies. For example, Gillette’s Razor Maker program allows users to choose from over 100 different razor handle designs and customize the choices related to grip, blade type, and the addition of text or logos. The razor handles are then printed on a stereolithography (SLA) printer and promptly shipped to the user (Formlabs, 2018). Likewise, the Nike By You (formerly NIKEiD) customization plan is another well-known example wherein users pay a small premium to make the color, material, and text choices to personalize existing Nike products (Forbes, 2015). Mass customization applications such as custom mouth guards, hearing aids, and implants provide better fit and usability within the medical and healthcare sector by capturing users’ unique physiological and anthropometric attributes. For example, end-users utilize three-dimensional (3D) scanning technologies at local doctor’s clinics to enable the creation of digital molds that provide better-fitting products (Dawood et al., 2015).

However, with the ever-increasing trends and market need to support product customization, several barriers have slowed down the effective implementation of mass customization approaches. A significant issue in mass customization product development models is the lack of direct customer input throughout the early design process (Wang et al., 2017). The early design methodologies used in mass customization often fail in collaborative product development—the process of including the end-user early into the design process (Lagrosen, 2005). While mass customization enables design teams to address broader customer needs, it has limitations in bringing customers into the product development process. Moreover, mass customization methodologies still lean heavily toward derivatives of mass manufacturing techniques with additional modularization and increased variability. Manufacturers provide a wider variety of options in the form of predefined selections, packages, or configurations to address a broad spectrum of customer needs. However, this approach often makes customers waive their priorities or relax their requirements

(Koomsap, 2013). Therefore, there is significant room for improvement, especially in developing mass personalization methodologies that promote customer–designer collaboration.

The technological advancements in computer-aided engineering (CAE) and intelligent manufacturing (e.g., Ergonomics 4.0) have promoted a paradigm shift by enabling cost-effective and rapid product personalization methodologies that bring customer–designer collaboration opportunities. Many researchers note that this shift has created a transition from mass customization to mass individualization, which requires a new set of product design methodologies that promote co-creation (Tseng et al., 2010; Wang et al., 2017). For example, Koomsap (2013) introduced a Design by Customer framework, which proposed passive (including customer's voice) and active (including modification on actual design process) customer involvement in improving customer satisfaction (Koomsap, 2013). Similarly, Zheng et al. (2017) introduced a model-based framework for conducting a user experience study to support mass personalization (Zheng et al., 2017). Overall, the general trend in recent years endorses the potential growth of next-generation open hardware and software systems, user-friendly design interfaces, and modular platforms connected via intelligent applications that enable customers to collaborate with design teams (Koren et al., 2015).

### **The lack of customer participation in conventional product development**

A plethora of design methodologies, with design flowcharts or data flow diagrams summarizing what design activities occur at which stage of the product development, have been proposed in the past to describe the product development process. Each design methodology has a slightly different overview of the design activities that occur depending on the phases of the design process (Demirel, 2015; Ullman, 1992). Commonly, during the early stages of product development, the typical phases cover design activities where design teams explore and refine ideas through brainstorming and ideation and evaluate concept models based on a combination of rough physical and computational prototyping techniques. Typically, these activities involve various customer needs gathering studies (e.g., surveys and user studies) to identify engineering targets by bridging customer requirements and engineering requirements via product planning methods such as the house of quality (HoQ) (Hauser & Clausing, 1988). The initial customer needs gathering activities are known to have wide-ranging effects. Incorrect findings, misleading assumptions, or deceptive feedback at this stage could set the design team down a path to failure.

Based on the engineering targets identified, designers use a combination of creative (e.g., brainstorming, C-sketches) and technical activities (e.g., Pugh charts, TRIZ) to generate concept models (Otto & Wood, 2001). At this stage, designers utilize manual and digital ideation techniques ranging from industrial design sketches to 3D computer-aided design (CAD) models and virtual reality (VR) models to express the rough concepts generated during ideation visually (Ahmed, Irshad,

Gawand, & Demirel, 2021). These computer models are used for running simulations to ensure the product meets engineering targets. Possible studies include digital human modeling (DHM) simulations that incorporate computational fluid dynamics (CFD) to examine fluid interactions, biomechanics to check fatigue and ergonomics-related concerns, and finite element analysis (FEA) to verify structural integrity (Demirel et al., 2021). These digital simulations allow for early product analysis and error detection. A significant amount of time and money can be saved by detecting errors while the product is still a computer model (Ahmed, Irshad, & Demirel, 2021; Camburn et al., 2017).

After the infeasible ideas are eliminated via computer simulations, the improved concepts are turned into functional prototypes. Prototyping is a resource-intensive stage as it involves the physical manufacturing of initial products to verify that the early assumptions are confirmed. At this stage, physical prototypes are built through additive or subtractive manufacturing techniques. This stage also focuses on determining whether the product functions as intended and includes human subject evaluations. The knowledge gained from these assessments informs the design team about the shortcomings related to the form, function, and user needs, which often results in the costly rework as the design teams typically revise product variables and attributes (Irshad et al., 2019). As seen in the above description, concept designs go through changes that shape the final product as the product progresses through the product development stages. It is critical to note that the customer only comes into contact with the product after the beta prototype becomes available or the final product is launched. During the beta prototype evaluations, only a few customers have a proxy interaction with the product development process via representation in focus groups and human subject studies, which are not entirely reflective of all end consumers' specific needs and preferences. This limited scope of interaction between a customer and product during the early design phase can often result in an ill product-market fit and expensive product failures (Henard & Szymanski, 2001). Any issues discovered during focus group studies, through mock-ups or functional full-scale prototypes, require design rework and retrofitting, which are costly and time-consuming (Irshad et al., 2019). In summary, product development methodologies based on the conventional approach lack continuous user–product interaction, specifically in the early design phase, consisting of long periods of design, engineering, and refinement, where customers are left isolated before the product enters the market.

---

## Methodology

### Theoretical bases of the co-creation framework

The proposed design framework, Digital Co-Creation, aims to address some of the shortcomings of the conventional product development methods described in the previous sections. These shortcomings include the lack of customer integration

into the early design process, expensive late-stage rework resulting from poor focus group feedback, and ill-defined final product-market fit. The Digital Co-Creation approach supports a partnered design of products alongside customers to create an improved end-product market fit. The proposed approach aims to create a method that allows user feedback to be promptly integrated back into the product for rapid iterations that lead to improvements. This methodology alleviates mass customization challenges by capturing customer needs and preferences early in design via a dual-way customer–designer feedback mechanism.

Because of the current limitations of manufacturing techniques (e.g., high initial setup cost of injection molding) and demand for low unit cost, many products fall into the category of mass production, which typically results in a lower price point for the product due to economies of scale. In contrast, due to the intense customization labor and craftsmanship required in the custom production market, which eventually reduces the total unit sales, bespoke products are sold at a premium, limiting the market size. The proposed methodology aims to create a product design approach that leverages the benefits of both ends of the spectrum illustrated in Fig. 25.1 to deliver custom personalized products to end consumers.

Types of products that emerge from the proposed framework focus on “mass individualization,” which lies somewhere on the spectrum between bespoke products and mass customization (Fig. 25.1). On the far left of the spectrum, mass-produced products take full advantage of economies of scale by producing large quantities of identical parts (Duguay et al., 1997). To the right of the spectrum, one can see the mass personalization and mass customization sector, which allows for changes to the existing components to create custom scalable products (Hu, 2013). The far right of the spectrum contains bespoke or custom production where the end product is built from the ground up exclusively for the customer (Campbell et al., 2003). The proposed methodology would create a product between mass customization and bespoke production by utilizing common functional product bases and modular feature integration with a large variety of add-ons via a digitized interface. Thus, the “mass individualization” approach enables customers to be directly involved in final product design instead of solely relying on limited options (Koren et al., 2015).

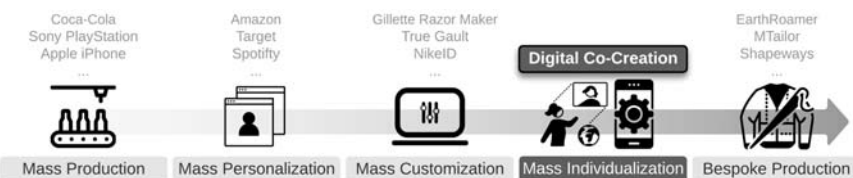


**FIGURE 25.1**

The Digital Co-Creation framework described in this chapter falls between mass customization and bespoke production. The methodology utilizes common functional product bases, modular add-ons, and digital tools, enabling customers to participate in the product design directly.

This approach enables designers to conduct needs gathering activities via establishing direct communication with customers through a digitized platform. Thus, keeping the customers in the loop throughout the product development ensures that products meet the customers' actual needs and preferences. The proposed methodology leverages state-of-the-art computational technologies such as DHM ([Demi-rel et al., 2022](#)) and augmented reality (AR) to bridge the user–designer gap ([Ahmed et al., 2019](#)). A theoretical illustration of the proposed methodology is provided in [Fig. 25.2](#), which outlines the customer–designer interactions as the product moves through the product development process.

Before discussing each stage in detail, it is essential to note that the framework is based on an interactive application (a configurator “app”) that enables direct communication between the customer and designer. The interactive configurator contains a user-friendly graphic user interface (GUI) and enables a dual-way exchange of ideas (text, 2D, or 3D multimedia) via a mobile/tablet application (or “app”).

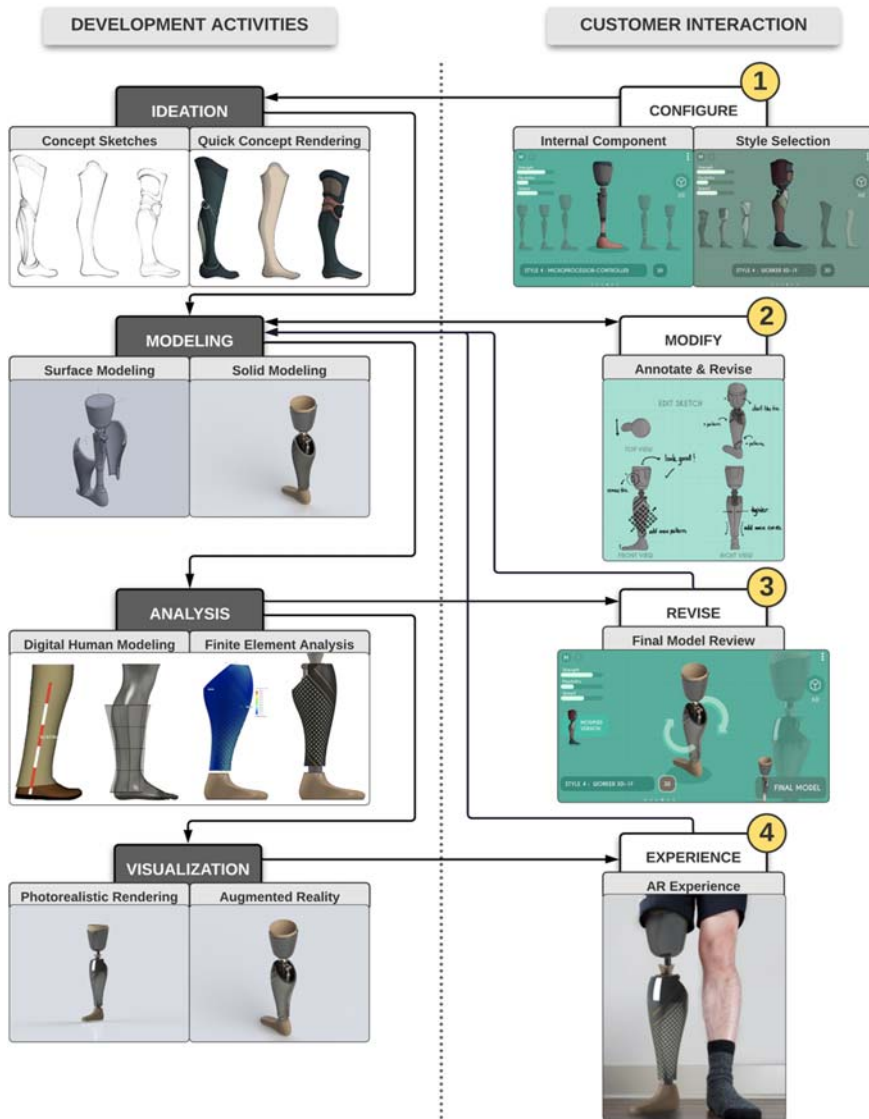
## Stages of the co-creation framework

### *Ideation*

The proposed methodology starts with the Ideation stage. Ideation begins when a customer makes a product inquiry by describing the desired product and or needs over the app (configurator) that supports product selections and configurations. Customers' needs and preferences are collected through a set of application-based surveys, user entry forms, and product configurations. After the primary collection of information has occurred, the software app renders a rough concept design. If needed, customers can further personalize their products by providing text and graphics media that describe features and preferences via activating a mood board within the app. After personalized design elements and specifications are gathered, the design team performs initial digital sketches and shares them with the consumer, allowing customers to mark sketches up with a digital stylus, mouse, or keyboard. At this stage, the customer can point out the unique aspects of the initial digital sketches that are not available within the configuration selection. The digital markup provides immediate feedback to the design team and allows for effective early-stage communication. Upon receiving the marked-up copy, the design team addresses the feedback and implements necessary changes. The iterative loops implemented throughout the Ideation stage enable customers to provide feedback on designs with simple annotation and markup features found in the app. After the customer is happy with the end sketch, the process moves forward into the Modeling stage.

### *Modeling*

The next stage in the proposed methodology is Modeling. In this stage, 3D digital surface and parametric modeling construction begin based on the digital sketches (established at the Ideation stage). This direct sketch-to-model integration allows for a reduction of rework because changes to either the digital model or sketches

**FIGURE 25.2**

The flowchart illustrates the proposed design process, including customer interactions with the product design activities (on the right) and internal design and engineering development activities (on the left).

will carry through. The ability to easily tweak and make changes at a low cost is one of the driving factors behind the widespread adoption of the computer-aided engineering (CAE) platform. With the introduction of digital modeling within CAD

platforms, digital sketches can be constructed using simple digital sculpts or surfaces using universal point-and-line manipulation techniques such as NURBS and S-splines. Next, the designer uses photorealistic rendering techniques to generate high-fidelity still images and animations. Thus, based on the customer preferences, a batch of final photorealistic renderings including varying material, texture, and color options reflects the customer's intended use conditions (e.g., outdoors vs. indoors) shared with customers via the software application. At this stage, users can navigate in 3D space, visualize what the product looks like, scribble notes, or use callout functions to provide additional information via annotations. Customers then send the annotated documents back to the designer, and the additional customer preferences and needs are integrated into the digital product model. This step provides another crucial customer touch-point early in the product design. This cycle proceeds until both parties are happy with the result. While the Modeling phase might be slower and more costly than the traditional product design methodology, it is faster than bespoke design and ensures a better customer needs gathering process.

### ***Analysis***

After the 3D modeling is completed, the product moves out of the customer's eyes as internal engineering analyses and simulations ensure no functional issues arise with the product specifications. For these studies to be conducted, it is essential to know the product's extreme use-case scenarios: this can be determined based on user weight, height, and planned intent. With each attribute in mind, the engineer can create scenarios that inform the designed product's functionality and failure modes. During this stage, some of the specific user information such as anthropometry is gathered (e.g., Kinect, 3D scanning tools), and a representative human manikin is constructed via DHM. The versatility of using DHM to create accurate customer models based on limited inputs allows for faster design and validation times. Overall, structural and human factors simulations allow engineers to conduct further performance tests (e.g., add structural reinforcements, modify materials) to further refine and develop a concept product that fits customer product use scenarios.

### ***Visualization***

Next, the product moves forward into the penultimate customer-to-product interaction phase, virtual and augmented reality try-on. This phase provides a unique opportunity to the customer in visualizing digital product concepts. The vast majority of mobile communication devices such as smartphones and tablets have access to ARCore (Android) or ARKit (Apple) platforms. AR is becoming a user-friendly, affordable, and high-fidelity method to visualize conceptual ideas in the physical space surrounding them. The AR environment allows users to see the size, scale, and materials in "real-world" settings. This approach is similar to how the user can try various clothing to visualize how it matches or fits via AR-enabled intelligent systems.

---

## Case study

The medical product domain proposes a niche market opportunity to create individualized products tailored for specific users. Research and market trends indicate that there is currently a pressing need for the individualization of various medical devices, and prostheses are among the top that can take advantage of the Digital Co-Creation methodology described in this chapter. The case study aims to present the intricacies of the methodology proposed in this chapter through the design and digital evaluation of a lower-limb prosthetic casing. This study defines prosthetic casing as the exterior packaging unit or the frame covering the internal electromechanical components. Lower-limb prosthetic casing possesses an intimate relationship with the customer. It adds functionality (e.g., structural support, providing protection) while making the device more aesthetically pleasing and user-friendly (e.g., fit for environmental conditions, easy to change). These product attributes are aligned with customers who have different daily routines and needs (e.g., marathon runner vs. avid motorcyclist). The product development process in this case study involves two hypothetical customers with different anthropometric backgrounds, lifestyles, and usability needs. The first customer is RK, a 60-year-old female (173 cm height and 53 kg weight) from Japan and working as a professor. RK's main physical activity consists of commuting via train daily, delivering long lectures, and occasionally hiking. The second customer is CG, a 32-year-old American male (180 cm in height and 70 kg in weight) who works as a software engineer. He is future-focused in his approach to life and product purchases, and he enjoys his daily commute to work with his motorcycle.

In this case study, to keep the storytelling compact, customer–designer collaboration activities associated only with CG's lower-limb prosthetic casing design journey are summarized in detail. We include images from the conceptual prototype app interface (configurator framework) to demonstrate design changes and iterations for both hypothetical customers—RK and CG.

### Step 1: ideation and configure

The typical product design starts first with customers selecting the base component architecture that fits their needs. This stage is very similar to what is currently available in existing mass customization interfaces, where customers select the desired components from a list of product variants or configurations. For instance, an active person may choose a dynamic microprocessor-controlled knee configuration with varying tuned-mass dampers and shock-absorbing mechanisms. In contrast, another customer who might only need a prosthetic limb for minimum mobility can proceed with static architecture without electromechanical arrangement. In either case, only product variants coming from off-the-shelf model configurations are provided to customers in this stage.

In this case study, RK was interested in a budget option and did not require in-depth individualization. She went through the selection categories and made

selections regarding materials, finish, and colors. However, she did not like the final casing concept presented on the app screen and sent a message to the design team to note that it is essential for her to the final casing design to “capture the natural beauty of the material.” In contrast, CG selected his prosthetic casing to have a smooth metal finish with a minimalistic look. However, he wanted to follow up with the design team to inject more individualization. CG answered a few survey questions and filled up a mood board with thematic images representing his lifestyle by navigating through the app’s interface. Finally, he also left a short video message reflecting his design language—maintaining a futuristic casing design while preserving the traditional form (Figs. 25.3 and 25.4).

After reviewing RK’s and CG’s configurations, surveys, and special requests, the design team started working on preliminary design ideas by sharing initial rapid industrial design sketches with customers. The app interface allows designers to draw on multiple layers and use digital sketching tools such as predictive stroke to smooth lines or create parametric point or line sketches, enabling rapid changes based on the predefined casing models stored in libraries. For example, sketches in Fig. 25.5 include the design team’s initial rough ideation and customers’ feedback with annotations and drawings.

## Step 2: modeling and modify

The next major step in the proposed methodology is Modeling. 2D and 3D CAD models were developed via surface and solid modeling techniques in this case study. Also, anthropometric libraries were used to capture users’ different physical attributes and construct digital human models representing RK and CG. In both cases, the lower-limb dimensions were generated based on the customers’ anthropometric information—population database, height, and weight data. For instance, Siemens Jack software was used to build a custom female and male manikin based on the Japanese (International Organization for Standardization reports—ISO7250-1 and ISO/TR 7250-2) and US anthropometric databases (ANSUR—Anthropometric survey of



**FIGURE 25.3**

Screenshots from the prototype app showing the configuration interface—internal mechanism selection options.

**FIGURE 25.4**

Screenshots from the prototype app showing the configuration interface—style selection menus and options.

**FIGURE 25.5**

Preliminary design sketches shared with the customer and customer accents features to be added (or removed) via annotation tools provided within the app interface.

US army personnel) that represent RK and CG, respectively (Fig. 25.6). Typically, the app would allow other data collection methods, including importing point cloud data via motion capture, 3D scanning systems, and mesh models from online libraries.

In both cases, having access to the representative DMH models allowed the prosthetic casing model to have a reference geometry. This proved helpful in preserving some symmetry of the human leg and delivering the preservation of form that was established in the Ideation stage. After the initial surfaces were created by taking the DHM surface geometry (exported as .stl or .iges/step mesh models) as a reference, the design team used a combination of surface modeling and digital sculpting tools to generate a conceptual model based on the desired target anthropometric dimensions. At this stage, each of the surface regions can be broken down into smaller grid surfaces or meshes that can be individually transformed to alter the shape of the surface. After the surface models are converted into solid bodies, the final model was prepared for photo-realistic rendering by including a specific material, color,



**FIGURE 25.6**

The manikins represent the hypothetical customers used in the case study. The anthropometric measurements were used in scaling the prosthetics casing model used in building the preliminary surface and solid models.

lighting, and texture attributes. After the photo-realistic renderings were completed, the designer shared the rendering outputs with the customers, which helped visualize the changes being made in the modeling stage with different material options (Fig. 25.7).

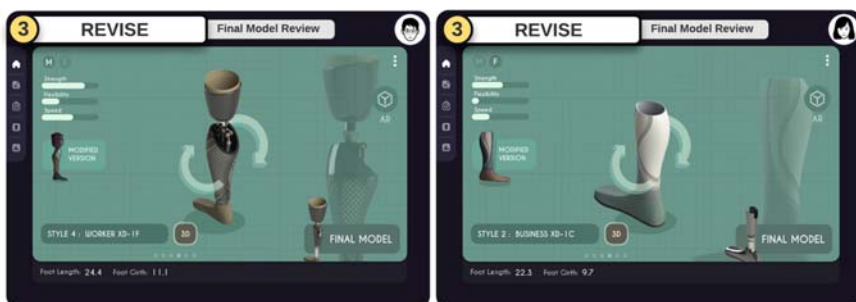


**FIGURE 25.7**

The final photorealistic rendering of the 3D CAD model.

In the Modify phase, the high-fidelity renders (in the form of still images or animations) can be sent to the customer as an image embedded into a PDF to capture further customer feedback. The solid model can also be sent as a Wavefront Technologies (.obj) format file, which is a common 3D data exchange standard, especially with standard 3D viewers in modern operating systems. Later, customer feedback was taken into consideration during the modeling process; thus, suggestions were integrated into the current 3D model.

### Step 3: analysis and revise

The next stage of the design process was to simulate and validate design alternatives. During this stage, the customer was not directly involved with the simulation activities; however, the needs and preferences collected in the previous stages (Configure and Modify) were integrated into the functional simulation model. In this phase, the objective was to ensure that the design was feasible and functional with the given design parameters. Depending on the use case and product being designed, various multiphysical simulations can be conducted as necessary. In this study, using the combined information of FEA and DHM, a maximum load scenario on the prosthetic casing was executed to measure the casing's structural integrity. The computational simulation was also run for several material properties, which yielded results about the center of mass, the estimated overall weight, and the moment of inertia (Fig. 25.8).

Negative attributes of the current design were found during these simulation studies, corrective measures (updates on the design parameters) were made, and simulations were reperformed. In this study, after conducting numerous simulations, it was discovered that the wall thickness defined early in the design for CG's casing model needed to change. Even after changing the casing wall thickness, the overall assembly was still heavy; therefore, a material swap from stainless steel to titanium was proposed to CG. This decision, bringing the customer into the loop, is an

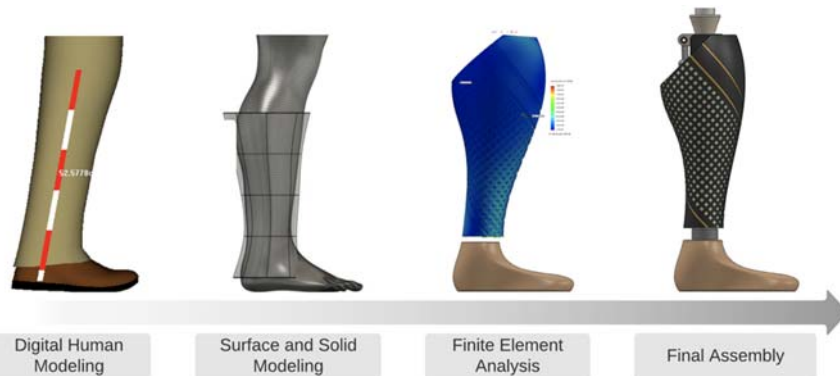


**FIGURE 25.8**

A series of thumbnails showing development activities—from DHM surface modeling to final assembly.

example of how this methodology helps to tune products precisely for the end-user and their needs. The titanium came at a premium price (i.e., it was three times higher for the raw material than stainless steel), but the weight savings were a priority for the customer, and CG agreed to make the swap.

### Step 4: visualization and experience

In this study, by using the AR interface, first, CG started the AR experience by importing the final 3D concept prosthetics leg model to the application. Then, with the help of the live tracking capabilities, CG spun the tracking image and, in real-time, visualized the final design that was blended with the use environment. Similarly, CG could change some of the design attributes using the same application, such as the color and material. CG could also see alternate versions of the prosthetic leg casing designs with varying image targets.

In this phase, the data flow starts with exporting the CAD file as stereolithography (.stl) file and converting file types to a Unity-compatible model. We used the Autodesk Maya platform, an animation and graphics software, to convert the data into the Autodesk (.fbx) format and mapped a basic cylindrical UV Map. This workflow enabled projecting a 2D image onto a 3D model to create a texture mapping. The UV map was then used to render different materials based on the material textures finalized by the customer. Therefore, CG could make changes to the material and quickly visualize the prosthetic leg concept with other materials. To further read about data exchange models, readers should consult DHM Data Exchange Protocols in DHM and Posturography ([Peters et al., 2019](#)).

To display the 3D model with tracking and projection, we used the Vuforia platform (Augmented reality software by PTC) to track and project data onto various shapes and sizes found in the actual product use environment. We used the Vuforia development portal to create an image target, which takes an uploaded image and processes it into a version that the camera will identify. When selecting an image, it needs to have a large amount of detail and contrast, which helps Vuforia's built-in image processing software quickly recognize the target in various environments. We also utilized a QR Code wrapped around a cylinder prompt to enable better AR mapping, tracking, and projection. For graphics and interaction with the on-screen model, we used Unity (Augmented reality platform by Unity Technologies). We placed the cylindrical image into the Unity environment and aligned it with the CAD model, which was imported into Unity as an .obj file.

The final step was to run the application and point it at the cylindrical image target to view the prosthetic limb within the use environment. At this point, CG could interact with the limb model through the app screen. For CG, this was an excellent opportunity to experiment with seeing different material finishes. Additionally, if CG had determined that the material selection was not aesthetically pleasing, he could examine and explore different materials within the AR setting ([Fig. 25.9](#)). Similarly, RK visualized different wood finishes and explored how they would impact the final design esthetics.



FIGURE 25.9

Screenshots from the interface showing the final AR model blended with the use environment.

## Discussion and conclusions

The Digital Co-Creation methodology discussed in this chapter synthesizes computational design research (e.g., digital human modeling) and emerging technologies (e.g., augmented reality) to capture and represent customer needs and preferences in early design phases via a continuous feedback cycle. The notion of product individualization via co-creation was demonstrated as an alternative method to alleviate challenges associated with mass customization. The case study presented how the Digital Co-Creation methodology functions, including data flow from sketching to visualization via AR. Through conceptual case study, we demonstrated how the methodology enables designers to create a personalized lower-limb prosthetic casting for two hypothetical customers with contrasting needs and preferences.

Overall, this chapter aims to provide evidence to designers interested in alternative methodologies to inject customer needs and preferences early in the design process. As technology continues to drive economic commoditization, the proposed framework serves as a significant value-added service in various industries. With the increasing accessibility of digital visualization tools (such as digital sketching, CAD, and AR), there are fewer barriers to long-distance communication between customers and designers. This chapter demonstrates room for the future of product design to become personalized (customizable, individualized, and interactive). By doing so, companies can create additional value through the design process.

A further benefit comes from quickly making changes to the digital sketching and CAD models, which reduces resource allocation (time and money) associated with traditional physical prototyping. Moreover, another significant positive outcome of this methodology is visualizing the prosthetic limb casing design within the actual use conditions. The integrated use of CAD models and AR technology through smartphones or handheld devices generates new product evaluation capabilities such as visualizing, interacting, and navigating via digital models. However, integrating CAD to AR and creating a fluid GUI with high-fidelity feedback is still challenging for many applications. This process is arduous and involves numerous

modeling, file conversions, and coding, which may not be immediately suitable for many small-sized companies without a solid technology infrastructure or expertise. For the AR model to be accessible to the consumer, building the app and exporting it from the Unity platform is necessary.

The lack of human data leaves room for improvements that could be addressed in future work. For example, a human subject data collection study consisting of testing the case study illustrated in this paper could be conducted with actual users who use lower-limb prostheses. Such a study could reveal intricacies about how users co-designed improved prostheses through the co-creation methodology. Other future work should include mobile app development and deployment, allowing designers to communicate and collaborate with actual users virtually. Although the case study discussed in this chapter explores the design process and illustrates the potential benefits of Digital Co-Creation, this chapter only provides a proof-of-concept for the design framework. The prototype framework is currently not yet ready to be deployed at scale. Due to the daily commute and travel restrictions that many elderly with mobility-related limitations face amid COVID-19, the study also motivates us to explore whether remote customer data gathering techniques described in this framework enable higher customer satisfaction. Another area to explore is how the entire framework might take advantage of artificial intelligence and generative design methods to provide cognitive assistance to designers.

Another intriguing limitation that creates opportunities to conduct future studies is how the customer's input impacts the final results—product innovation, integrity, and usability. Since users would have direct shaping power over the end product, some of them (e.g., expert users) may bring specific skill sets or abilities that will make the design process more accessible or challenging to perform. Likewise, another challenge with the proposed methodology is incorporating nontechnical users into technical products. Moreover, an adjacent topic to study is whether keeping customers in the loop throughout the early design impacts design teams' quality of ideation and conceptualization. Future studies should also look into how designing with customers (customer–designer collaboration) affects a design team's design fixation.

---

## References

- Ahmed, S., Irshad, L., & Demirel, H. O. (2021). Prototyping human-centered products in the age of industry 4.0. *Journal of Mechanical Design*, 143(7). <https://doi.org/10.1115/1.4050736>
- Ahmed, S., Irshad, L., Demirel, H. O., & Tumer, I. Y. (2019). A comparison between virtual reality and digital human modeling for proactive ergonomic design. Digital human modeling and applications in health, safety, ergonomics and risk management. Human body and motion. *HCII 2019. Lecture Notes in Computer Science*, 11581, 3–21. [https://doi.org/10.1007/978-3-030-22216-1\\_1](https://doi.org/10.1007/978-3-030-22216-1_1)

- Ahmed, S., Irshad, L., Gawand, M., & Demirel, H. O. (2021). Integrating human factors early in the design process using digital human modelling and surrogate modelling. *Journal of Engineering Design*, 32(4), 165–186. <https://doi.org/10.1080/09544828.2020.1869704>
- Bayus, B. (1994). Are product life cycles really getting shorter? *Journal of Product Innovation Management*, 11(4), 300–308. [https://doi.org/10.1016/0737-6782\(94\)90085-X](https://doi.org/10.1016/0737-6782(94)90085-X)
- Blecker, T., & Abdelkafi, N. (2006). *Mass customization: State-of-the-art and challenges* (pp. 1–18). Springer.
- Camburn, B., Viswanathan, V., Linsey, J., Anderson, D., Jensen, D., Crawford, R., Otto, K., & Wood, K. (2017). Design prototyping methods: State of the art in strategies, techniques, and guidelines. *Design Science*, 3, 1–33.
- Campbell, R., Hague, R., Sener, B., & Wormald, P. (2003). The potential for the bespoke industrial designer. *The Design Journal*, 6(3), 24–34. <https://doi.org/10.2752/146069203789355273>
- Dawood, A., Marti, B., Sauret-Jackson, V., & Darwood, A. (2015). 3D printing in dentistry. *British Dental Journal*, 219(11), 521–529.
- Demirel, H. O. (2015). Modular human-in-the-loop design framework based on human factors. *Purdue University*.
- Demirel, H. O. (2020). Digital human-in-the-loop framework. In V. Duffy (Ed.), *Vol 12198. Digital human modeling and applications in health, safety, ergonomics and risk management. Posture, motion and health: 11th international conference, DHM 2020, held as part of the 22nd HCI international conference, HCII 2020, Copenhagen, Denmark, July 19–24, 2020, Proceedings, Part I* (pp. 18–32). Cham: Springer. [https://doi.org/10.1007/978-3-030-49904-4\\_2](https://doi.org/10.1007/978-3-030-49904-4_2)
- Demirel, H. O., Ahmed, S., & Duffy, V. (2022). Digital human modeling: A review and reappraisal of origins, present, and expected future methods for representing humans computationally. *International Journal of Human–Computer Interaction*, 1–41. <https://doi.org/10.1080/10447318.2021.1976507>
- Demirel, H. O., Irshad, L., Ahmed, S., & Tumer, I. Y. (2021). Digital twin-driven human-centered design frameworks for meeting sustainability objectives. *Journal of Computing and Information Science in Engineering*, 21(3). <https://doi.org/10.1115/1.4050684>
- Duguay, C., Landry, S., & Pasin, F. (1997). From mass production to flexible/agile production. *International Journal of Operations & Production Management*, 17(12), 1183–1195. <https://doi.org/10.1108/01443579710182936>
- Euiyoung, K., Beckman, S. L., & Agogino, A. (2018). Design roadmapping in an uncertain world: Implementing a customer-experience-focused strategy. *California Management Review*, 61(1), 43–70. <https://doi.org/10.1177/0008125618796489>
- Fogliatto, F. S., Da Silveira, G. J., & Borenstein, D. (2012). The mass customization decade: An updated review of the literature. *International Journal of Production Economics*, 138(1), 14–25.
- Forbes. (2015). *How NIKEiD is helping Nike's push for greater profits*. Forbes [www.forbes.com/sites/greatspeculations/2015/07/09/how-nikeid-is-helping-nikes-push-for-greater-profits/?sh=19bdda7f4e65](http://www.forbes.com/sites/greatspeculations/2015/07/09/how-nikeid-is-helping-nikes-push-for-greater-profits/?sh=19bdda7f4e65).
- Formlabs. (2018). Gillette stays ahead of the competition by using 3D printing to unlock consumer personalization. Formlabs Blog <https://formlabs.com/blog/gillette-uses-3d-printing-to-unlock-consumer-personalization/>.
- Gilmore, J., & Pine, J. (1997). *The Four Faces of Mass Customization*, 75(Issue 1), 91–102.
- Griffin, A., & Hauser, J. (1993). The voice of the customer. *Marketing Science*, 12(1), 1–27. <https://doi.org/10.1287/mksc.12.1.1>

- Hauser, J., & Clausing, D. (1988). The house of quality. *Harvard Business Review*, 63–73.
- Henard, D., & Szymanski, D. (2001). Why some new products are more successful than others. *Journal of Marketing Research*, 38(3), 362–375. <https://doi.org/10.1509/jmkr.38.3.362.18861>
- Hu, J. (2013). Evolving paradigms of manufacturing: From mass production to mass customization and personalization. *Procedia CIRP*, 7, 3–8. <https://doi.org/10.1016/j.procir.2013.05.002>
- Irshad, L., Ahmed, S., Demirel, H. O., & Tumer, I. (2019). Computational functional failure analysis to identify human errors during early design stages. *Journal of Computing and Information Science in Engineering*, 19(3). <https://doi.org/10.1115/1.4042697>
- Jost, P. J., & Süsser, T. (2020). Company-customer interaction in mass customization. *International Journal of Production Economics*, 220. <https://doi.org/10.1016/j.ijpe.2019.07.027>
- Koomsap, P. (2013). Design by customer: Concept and applications. *Journal of Intelligent Manufacturing*, 24(2), 295–311.
- Koren, Y., Shpitalni, M., Gu, P., & Hu, S. (2015). Product design for mass-individualization. *Procedia Cirp*, 36, 64–71. <https://doi.org/10.1016/j.procir.2015.03.050>
- Lagrosten, S. (2005). Customer involvement in new product development: A relationship marketing perspective. *European Journal of Innovation Management*, 8(4), 424–436.
- Otto, K., & Wood, K. (2001). *Product design: Techniques in reverse engineering and new product development*. Pearson.
- Peters, M., Wischniewski, S., & Paul, G. (2019). DHM data exchange protocols. In S. Scataglini, & G. Paul (Eds.), *DHM and posturography*. Academic Press. <https://doi.org/10.1016/C2018-0-00529-0>
- Piller, F., & Tseng, M. (2009). *Handbook of research in mass customization and personalization*. World Scientific Publishing Company.
- Smith, P. G., & Reinertsen, D. G. (1998). Faster to market. *Mechanical Engineering*, 120(12), 68–70. <https://doi.org/10.1115/1.1998-DEC-5>
- Tseng, M., Jiao, R., & Wang, C. (2010). Design for mass personalization. *CIRP Annals*, 59(1), 175–178.
- Ullman, D. (1992). *The mechanical design process* (Vol 2). New York: McGraw-Hill.
- Wang, Y., Ma, H.-S., Yang, J.-H., & Wang, K.-S. (2017). Industry 4.0: A way from mass customization to mass personalization production. *Advances in Manufacturing*, 5(4), 311–320.
- Zheng, P., Shiqiang, Y., Wang, Y., Zhong, R., & Xu, X. (2017). User-experience based product development for mass personalization: A case study. In , Vol 63. *Procedia CIRP* (pp. 2–7).
- Zipkin, P. (2001). The limits of mass customization. *MIT Sloan Management Review*, 42(3), 81–87.

This page intentionally left blank

# Implant design on virtual digital human skull models for the creation of customized patient-specific regenerative implants: biomechanical consideration

# 26

Jing Lim<sup>1</sup>, Timothy Jie Han Sng<sup>2</sup>, Raymond Chung Wen Wong<sup>2</sup>

<sup>1</sup>Osteopore International Pte Ltd, Singapore, Singapore; <sup>2</sup>Discipline of Oral and Maxillofacial Surgery, Faculty of Dentistry, National University of Singapore, Singapore, Singapore

## Chapter outline

Introduction .....	679
Regenerative craniofacial surgery—current state of the art .....	681
Customized implant design—design considerations .....	683
Customized implant design—biomechanics .....	684
Commercialization considerations—a balancing act between design and regulation through in vivo tissue engineering .....	687
Future outlook .....	688
References .....	688

## Introduction

Additive Manufacturing (AM), or 3D Printing as it is commonly known nowadays, is a manufacturing process where sequential layers of materials are built-up to eventually obtain a three-dimensional object. The 1950s and 1970s saw the conceptualization of AM, first by Raymond F. Jones in “Tools of the Trade” (Jones, 1950) and then by Johannes F. Gottwald and David E. H. Jones in separate publications (Patent, n.d.) and (*The Inventions of Daedalus: A compendium of plausible schemes*, 1982). The 1980s saw the equipment and materials for AM being developed, while a reasonable acceptance of AM particularly in the metal industry gained traction in the 1990s. It was at this time where powder bed AM (the original form of the

term 3D printing), fused deposition modeling (FDM), inkjet printing, and selective laser melting were commercialized one after another.

In 1985, bioengineer Y. C. Fung first proposed the combination of “tissue” and “engineering” to the National Science Foundation ([A proposal to the national science foundation for an engineering research center at UCSD, Center for the Engineering of Living Tissues, n.d.](#)). Through this process, the concept of tissue engineering was successfully created. Robert Langer and Joseph Vacanti, now household names for the tissue engineering community, popularized this term in an article in *Science* in 1993 ([Langer & Vacanti, 1993](#)). According to the concept of tissue engineering (TE), cells, scaffolds, and tissue-inducing factors and any combination of the three, are possible ways to engineer tissue. With the concurrent development of AM technology in the 1990s, AM and TE have become increasingly combined to great effect. The impact created by this combined technology is long lasting until today, and continues to subject of innovation and application in clinics.

A search conducted in PubMed database relating to the topic of regenerative craniofacial surgery demonstrated that since 2014, the interest in this area has been consistent and growing ([Fig. 26.1](#)).

However, for the purpose of applying TE in the clinic, medical device regulations and policies limit the extent of which can be possible. More specifically, current regulatory requirements from the FDA and European Commission are relatively arduous if a pure TE solution is to be used to treat patients. Obviously, such decisions are driven from a risk-mitigation perspective, as cutting-edge laboratory research embarks on the path to quality assured, reproducible outcomes before such therapies may actually be made available for use in patients.

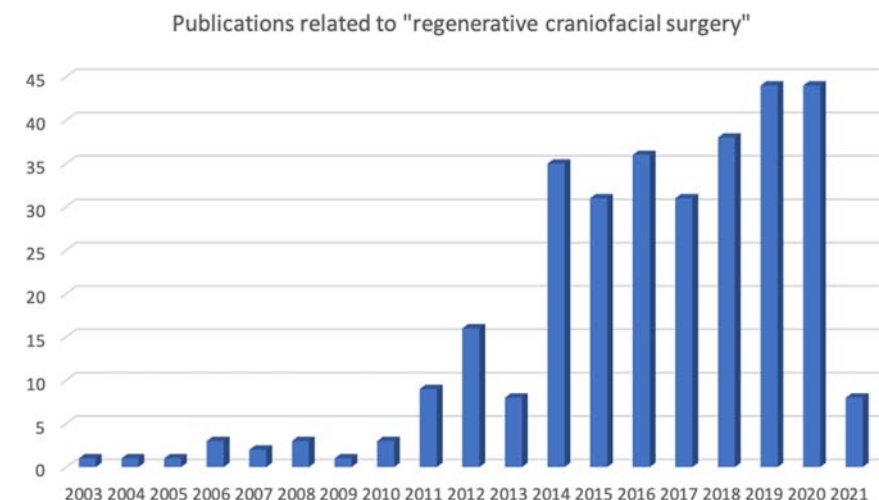


**FIGURE 26.1**

Consistent and growing trend in regenerative craniofacial surgery since 2014.

In December of 2016, the Food and Drug Administration (FDA) approved Maci as a product that combines autologous chondrocytes grown on a collagen membrane ex vivo, which is then implanted into the cartilage defect site for natural regeneration—this is the first tissue engineered product approved for use ([FDA, 2016](#)).

The above advances as well as recent and continuous advances in many fronts related to manufacturing, communications, informatics, technology, engineering, healthcare, artificial intelligence among many sectors have been termed the 4th Industrial Revolution (4IR) by The World Economic Forum in 2016. The subsectors of advanced materials and 3D printing form an important pillar for the 4th IR in healthcare.

---

## Regenerative craniofacial surgery—current state of the art

Craniofacial reconstruction can be challenging to perform due to significant complexities in the musculoskeletal anatomy, as well as consideration on esthetic outcomes. The “gold standard” of bone reconstruction may be the use of autologous tissue, but it is not always the easiest material to work with. In addition, significant surgical time is required due to a second surgical site, and shaping/modification to harvested bone. In June 2012, Abidi and colleagues presented their findings on the cost analysis of autologous bone grafting at the AOFAS meeting ([Abidi et al., 2012](#)). They developed an interactive budgetary impact model in accordance with the International Society for Pharmacoeconomics and Outcomes Research (ISPOR) principles, which included data from 10 US-based AOFAS/AOOS surgeons in academic and private practice, multicenter RCT, primary survey with end-users representing 15 Canadian hospitals, and review of literature related to bone graft harvest in foot and ankle procedures. Their findings indicated that bone grafting carries notable incremental costs relating to OR time, length of stay, complications, and short- and long-term patient experience with donor site issues. Importantly, a statement that orthobiologic bone graft substitute, despite having comparatively higher up-front acquisition cost, can overcome disadvantages relating to bone grafting to yield annualized cost savings.

Bone graft substitutes, sometimes referred to as alloplastics, have been used for a variety of craniofacial bone reconstruction procedures. They can be broadly categorized into permanent and bioresorbable. Recently, with the uptake in interest of AM in medical device manufacturing and treatment, 3D printed implants form the third category of alloplastics; these 3D implants may be constructed with permanent or bioresorbable materials. For example, customized PEEK has been shown to be a viable implant option for cranioplasty ([Wolff et al., 2018](#)), while customized Titanium implants have been used in mandible reconstruction ([Park et al., 2020](#)). The pursuit of improved patient care, however, pushes stakeholders to continue the search and development of therapies that continue to refine clinical outcomes.

With regard to the biomechanics of the skull, with the exception of the mandible, the rest of the skull does not move and does not need to withstand much functional

forces. Thus, alloplastics can be placed without much need for consideration of the forces. So long as the alloplastics are not exposed to the cavities of the skull (paranasal sinuses, oral and nasal cavity), the main differences are those of the length of time bone takes to form, quality, and quantity of bone formed, ease of use, and cost. As the only movable, load-bearing bone of the skull, the mandible is commonly regarded as 2 Class III levers joined at the midline, with the bilateral condyles as fulcrums (Wong et al., 2016). With insertion of depressor and elevator muscles, different zones of the mandible are subjected to varying types and magnitude of forces during function. Also, the mandible is merely separated from the oral cavity by relatively thin mucoperiosteum. While being vulnerable to opportunistic infection from the oral microbes directly or indirectly via dental caries or periodontal diseases, the mandibular graft must still provide mechanical support for masticatory loads and functional movements. Ideally, it should also restore the lower facial contours and provide sufficient bone stock for dental prosthesis in replacement of missing teeth. Among the craniofacial bones, reconstruction of the mandible thus appears to be uniquely challenging.

The 3D implant category, subcategorized into permanent and bioresorbable materials, is mostly understood to be customized or patient-matched. However, there is another facet to 3D implants that allows clinicians to improve patient care in small bone defects: standard sized implants that have a three-dimensional scaffold structure. 3D printed polycaprolactone scaffolds have been applied in such a scenario with published long-term outcomes (Young et al., 2017; Seen et al., 2018; Yang et al., 2020). Revisiting TE concepts, the basis of a successful TE strategy is the combination of three-dimensional scaffold (customized or not), biologics (cells, growth factors), and biomimetic environment. The purpose of a three-dimensional scaffold is naturally to allow incorporation of biologics, facilitate ingrowth of vessels and surrounding tissue such that tissue regeneration occurs.

Due to restrictions in regulations, the method by which clinicians can create the most-immediate impact in the continuum of patient care is therefore to combine a three-dimensional bioresorbable scaffold with autologous biologics. Fortunately, the industry is laced with a myriad of options for autologous biologics (Table 26.1).

Three-dimensional scaffolds, on the other hand, remain few and far between in availability, especially for craniofacial applications. Notable scaffolds that are bone

**Table 26.1** Summary of commonly found solutions for cells, growth factors.

Cells (source)	Growth factors (source or supplier)
Bone marrow progenitor cells (autologous bone marrow aspirate)	PDGF, TGF- $\beta$ , VEGF, EGF, IGF, FGF (platelet-rich plasma)
Adipose progenitor cells (lipoaspirate)	PDGF, TGF- $\beta$ 1, VEGF, IGF-1 (platelet-rich fibrin) rhBMP-2

**Table 26.2** Summary of structural and nonstructural scaffolds.

Structural scaffold	Nonstructural scaffold
Polycaprolactone (Osteomesh, Osteopore® International)	Collagen (multiple suppliers including Geitslich, Zimmer)

fillers and are already on the market can be categorized into structural and nonstructural **Table 26.2**.

Structural refers to having a well-defined matrix that has potential for weight-bearing. Collagen is a well-studied biomaterial and scaffold that does not require further introduction. It is highly porous and contains ECM that is relevant to bone regeneration, and has been used in many dental applications (Urban et al., 2016; Hong et al., 2019). Since it is mostly provided as a sponge, it is thus incapable of significant load-bearing. Its degradation time (usually not more than 3 months) is also not long enough to support tissue regeneration in very large defects, which may require more time for bone to regenerate as opposed to smaller, noncritical size defects. A significant amount of research done in this area has indicated that the scaffold degradation period should outlast bone regeneration rate so that continued structural support may be provided throughout the healing period (Woodruff et al., 2012).

## Customized implant design—design considerations

Customized or patient matched devices have taken over the clinical world by storm with the adoption of 3D printing as a manufacturing technique, due to the ability to print unique and intricate structures that are incorporated into an implant that matches the defect area intimately. Customized cranioplasty implants (Koller, 2020), mandibular implants, and various facial implants (Chepurnyi et al., 2020) have progressively increased in usage.

Based on what has been made available in the market thus far, customized design can be broadly categorized into functional- or regeneration-focus design. In functional-focused designs, the basic requirement is typically related to almost-immediate restoration of function. This is normally achieved with the use of strong materials such as PEEK, Titanium, and PEKK. Park et al. recently published a case report where an SLM 3D printed Titanium implant was combined with conventional dental implant fixtures to achieve occlusal rehabilitation (Park et al., 2020). Instead of the tested-and-proven approach of autologous bone grafting, the surgical team opted for an innovative approach with a functional-focused design. As described in **Table 26.3**, functional-focused designs do not have strict requirements on microstructure, which was consistent with this clinical case report—a part of the 3D printed Titanium implant was made hollow to decrease the overall weight of the implant.

**Table 26.3** Key features of functional- or regeneration-focused designs.

	<b>Functional-focus</b>	<b>Regeneration-focus</b>
Basic requirement	Should allow almost-immediate restoration of function	Should gradually restore function and lead to tissue regrowth
Design	Microstructure design is not as important as structural stability	Microstructure design is as important as structural stability
Material selection	Material selected can be nonbioresorbable	Material selected is bioresorbable
Surgical technique	Does not require additional biologics to achieve intended purpose	Requires additional biologics to achieve intended purpose OR already includes biologics necessary to achieve intended purpose
Extent of TE concept application	Limited if nonbioresorbable material is chosen	Applies TE concept fully
Examples	PEEK, Titanium, PMMA, PEKK	Polycaprolactone, polycaprolactone-tricalcium phosphate, polycaprolactone-hydroxyapatite

In different example by Schukert et al. (Schuckert et al., 2009), an FDM 3D printed polycaprolactone implant was incorporated with an interconnected honeycomb microstructure, and combined with growth factors (BMP and PRP) to reconstruct bone loss due to peri-implantitis across two dental implants. 6 months on, sufficient bone regeneration allowed for the placement of two new dental implants and subsequently, a dental bridge. This example shows the regeneration-focused design: emphasis on microstructure design, use of bioresorbable material, and addition of biologics.

Polycaprolactone by itself is not sufficiently strong enough by itself to take functional masticatory loads, especially in segmental mandibular defects. Thus, it needs to be buttressed by additional forms of fixation (in the form of a metal plate usually), combined with other materials or modified to help optimize the mechanical properties and yet still capitalize on the bioresorbable and osteoconductive features of PCL implants.

### Customized implant design—biomechanics

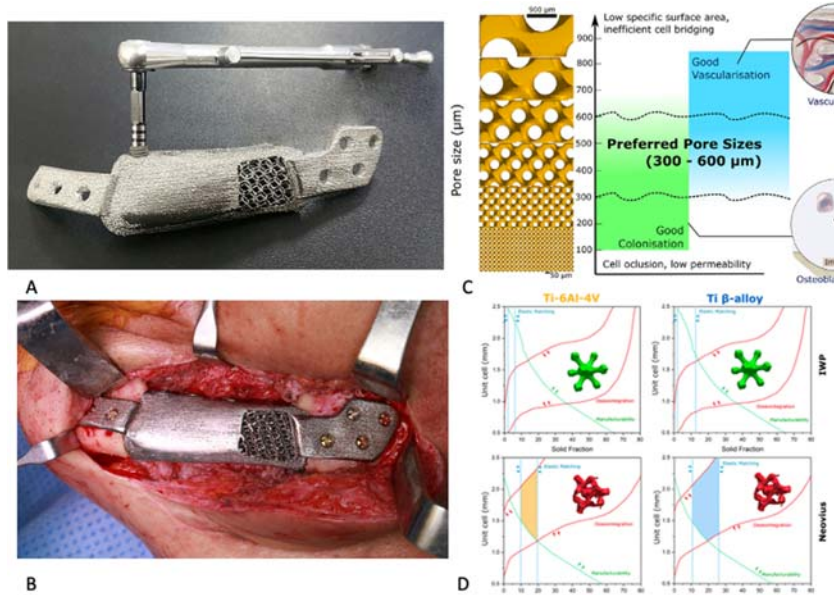
Consideration of biomechanics becomes more significant as we proceed down from head to chin: in the cranium, the main biomechanical considerations become more apparent only in large cranial reconstruction; in the orbital floor, bending stiffness, and strength is critical to ensure correct position of the orbit; in the mandible, a

complex interaction of compression, tensile, torsional, and bending forces exist (Wong et al., 2010). This has significant implications in implant design particularly in the mandible due to the complex interplay of forces between hard and soft tissue. We have earlier conducted FEM studies comparing PCL and Titanium material for consideration in an endoprosthesis design (Prasad et al., 2020). Based on the results of that study, PCL was unable to withstand mandible forces even with stress-reduced designs. This brings into question material selection, and importantly, microstructural design considerations if a regeneration-focused approach is desired.

Microstructural designs, or lattice designs, have been the subject of research and innovation over the past decade. Gyroid structures, for example, were shown to improve strength to weight ratio when the angle of the struts relative to the axial direction was less than 35 degrees (Yáñez et al., 2016). Strut-based lattice designs are commonly found in commercially available products, such as Osteomesh (Osteopore International), due to their excellent manufacturability and consistency (Zein et al., 2002). The clinical success of such strut-based lattice designs (Wiggenhauser et al., 2019; Teo et al., 2015; Ahn et al., 2020) may have potential for further improvement as surface-based lattices have demonstrated improved osseointegration (Van Bael et al., 2012). Barba et al. (2019) recently published an in-depth study that captures geometry and how it relates to manufacturability, mechanical properties, and osseointegration. By combining published data and their findings, they propose that depending on the choice of material, the “design space” may vary Fig. 26.2. From a materials science standpoint, there are ways to improve the strength, stiffness, and crack-resistance. To this end, composite materials tend to have the potential to combine desired properties of each material to achieve a different mechanical property. An extensive publication has earlier been reported (Liu et al., 2013).

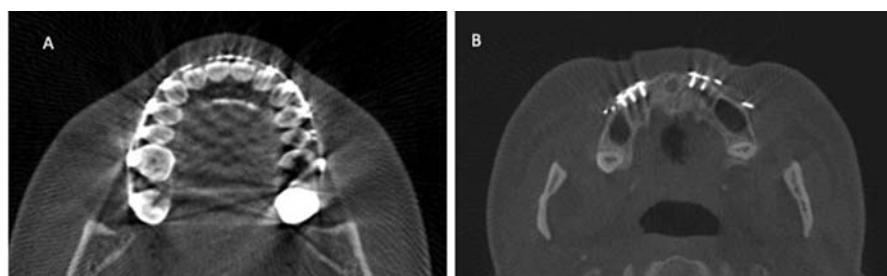
Naturally, biomechanical considerations, lattice choice, material selection become critical components in any virtual planning for reconstruction. The starting point of a customized patient matched design is usually the CT scan. It is important to take note that during the CT scan process, any existing metal-based implants may lead to significant artifacts that may distort Hounsfield units (HU) and hence, inaccuracy during segmentation Fig. 26.3.

There are ways to mitigate the artifact distortion through application of CT scan protocols that attenuate the impact of artifacts, including projection-based metal artifact reduction (MAR) and dual energy CT (DECT) (Katsura et al., 2018). Removing or reducing metal artifacts may also aid in the subsequent segmentation of cancellous bone from cortical bone, which may then drive the development of cancellous bone–based biomechanical analysis via FEM, to derive customized patient matched devices (Nassef, 2012). Due to partial volume effect, a common concept in cross-section imaging, the features of the trabeculae structure may not appear accurately. There are of course ways to mitigate or improve the resolution, which include using refined voxel sizes and longer RF pulses. Research into this area has been conducted in order to improve the accuracy of such segmentations (Augat et al., 1998; Rajon et al., 2006; Liu et al., 2020), although a fixed

**FIGURE 26.2**

(A) SLM Titanium mandible implant with traditional dental fixtures. (B) Placement of SLM Titanium mandible implant in situ. (C) Mapping of pore size to bone integration and vascularization. (D) Optimized design spaces comparing various TPMS lattice designs. Picture (A) and (B) from Park et al., (C) and (D) from Barba et al.

*From Park, J.-H., Odkhuu, M., Cho, S., Li, J., Park, B.-Y., & Kim, J.-W. (2020). 3D-printed titanium implant with pre-mounted dental implants for mandible reconstruction: a case report. Maxillofacial Plastic and Reconstructive Surgery. <https://doi.org/10.1186/s40902-020-00272-5>.*

**FIGURE 26.3**

Two different views of CT or Cone Beam CT scans of the skulls frequently will have scatter if metallic implants or orthodontic brackets/wires are present. A lot of time is needed to clean these images to ensure accuracy of placement for designed implants.

methodology has not yet been agreed. Cone beam CT (CBCT) is a more commonly used imaging modality in oral maxillofacial surgery. Due to the principle of operation of CBCT, there may be some level of linear measurement deviations. A simple way of overcoming this would be to increase the number of projections in order to reduce degradation of image acquisition quality. However, based on a study by Ref (Brown et al., 2009), these deviations may not be significant (mean difference range from 0.56 to 3.3 mm), depending on the fiducial landmark. That being said, due to the relatively smaller dimensions of the mandibular bone, 3 mm of linear deviation may affect implant design especially when screw placement needs to be factored in.

Once the 3D information of the bone has been obtained, it is converted digitally to enable visualization and planning of any 3D printed scaffold. Fixation points can then be designed, the scaffold printed, sterilized, and implanted (Fig. 26.4).

---

### Commercialization considerations—a balancing act between design and regulation through *in vivo* tissue engineering

The likelihood of a patient being treated with state-of-the-art technology is dependent on its commercial availability, which is in turn controlled by regulations.

Fig. 26.5 maps the interactions between regulatory barrier and tissue engineering implementation. Combining commercially available scaffolds and biologics have the most-immediate impact to enhanced patient care with high-level implementation of TE concepts. Recently Kobbe et al. published their findings on using a customized patient matched device made from polycaprolactone-tricalcium phosphate (three-dimensional bioresorbable scaffold), combined with RIA and BMP-2 (collectively biologics) in a femur diaphyseal reconstruction case (Kobbe et al., 2020). The patient had previously undergone previous surgeries to achieve bone healing without success. This combination of three-dimensional scaffold with biologics acquired in the same surgery corresponds to the most-immediate impact to patient care, that



**FIGURE 26.4**

Two different views for design and modeling of the regenerative implant scaffold to graft a defect in the anterior mandible on a digital model of the patient. Lattices and screw holes for fixation are incorporated taking into account unique anatomical traits of the patient.

		Regulatory Barrier to Implementation	
		Lower	Higher
Extent of Tissue Engineering Implementation	Higher	<b>Most-immediate impact to patient care</b> <ul style="list-style-type: none"> <li>▪ 3-dimensional bioresorbable scaffold + autologous cells and/or biologics (acquired in the same surgery)</li> </ul>	<b>High potential but limited availability</b> <ul style="list-style-type: none"> <li>▪ Autologous stem cells + scaffold cultured <i>ex vivo</i></li> <li>▪ Osteoinductive biologics</li> </ul>
	Lower	<b>Like-for-like replacement</b> <ul style="list-style-type: none"> <li>▪ Customized patient matched devices made from non-bioresorbable material</li> <li>▪ Implants made from non-bioresorbable material</li> </ul>	<b>Good potential</b> <ul style="list-style-type: none"> <li>▪ 2-dimensional bioresorbable implants</li> <li>▪ Customized patient matched devices made from bioresorbable material</li> </ul>

**FIGURE 26.5**

Comparison matrix between the extent of clinical implementation of tissue engineering and regulatory barriers.

can be provided by the clinician in order to resolve a clinical need (boxed top left of comparison matrix Fig. 26.5).

In fact, the aforementioned example is an application of *in vivo* TE, which is a subcategory of tissue engineering. While the industry continues to work with regulatory agencies to put on the market quality assured products, *in vivo* TE has provided clinicians with the opportunity to treat patients with a regenerative concept. In this method, the components of TE are chosen by the clinician based on clinical needs, and implanted at the site of reconstruction. There are a number of advantages associated with *in vivo* TE: wider availability of solutions in the market; actual *in vivo* biochemical, biomechanical, and three-dimensional microenvironment; earlier adoption of methods that lead to tissue regeneration.

## Future outlook

The future of osseo-integrating implants for craniomaxillofacial reconstruction is exciting. Significant developments in lattice design, materials science, biomechanics, and 3D printing technology along with a growing understanding on their interrelationships pave the way for better designs that meet the needs of the patient.

## References

A proposal to the national science foundation for an engineering research center at UCSD, Center for the Engineering of Living Tissues. (n.d.).

- Abidi, N. A., Carlson, A. M., & Harris, E. M. (2012). An analysis of cost of autologous bone graft. San Diego: Summer AOFAS.
- Ahn, T. H., Heo, C. Y., & Ahn, K. C. (2020). A compound osteocartilaginous graft with polycaprolactone (PCL) mesh in Asian rhinoplasty. *Journal of Plastic, Reconstructive and Aesthetic Surgery*, 73(9), e6–e7. <https://doi.org/10.1016/j.bjps.2020.05.098>
- Augat, P., Gordon, C. L., Lang, T. F., Iida, H., & Genant, H. K. (1998). Accuracy of cortical and trabecular bone measurements with peripheral quantitative computed tomography (pQCT). *Physics in Medicine and Biology*, 43(10), 2873–2883. <https://doi.org/10.1088/0031-9155/43/10/015>
- Barba, D., Alabot, E., & Reed, R. C. (2019). Synthetic bone: Design by additive manufacturing. *Acta Biomaterialia*, 97, 637–656. <https://doi.org/10.1016/j.actbio.2019.07.049>
- Brown, A. A., Scarfe, W. C., Scheetz, J. P., Silveira, A. M., & Farman, A. G. (2009). Linear accuracy of cone beam CT derived 3D images. *Angle Orthodontist*, 79(1), 150–157. <https://doi.org/10.2319/122407-599.1>
- Chepurnyi, Y., Chernogorskyi, D., Kopchak, A., & Petrenko, O. (2020). Clinical efficacy of peek patient-specific implants in orbital reconstruction. *Journal of Oral Biology and Craniofacial Research*, 10(2), 49–53. <https://doi.org/10.1016/j.jobcr.2020.01.006>
- FDA. (2016). [www.fda.gov/news-events/press-announcements/fda-approves-first-autologous-cellularized-scaffold-repair-cartilage-defects-knee](http://www.fda.gov/news-events/press-announcements/fda-approves-first-autologous-cellularized-scaffold-repair-cartilage-defects-knee).
- Hong, H. R., Chen, C. Y., Kim, D. M., & Machtei, E. E. (2019). Ridge preservation procedures revisited: A randomized controlled trial to evaluate dimensional changes with two different surgical protocols. *Journal of Periodontology*, 90(4), 331–338. <https://doi.org/10.1002/JPER.18-0041>
- Jones, R. F. (1950). Tools of the trade. Astounding Science Fiction.
- Katsura, M., Sato, J., Akahane, M., Kunimatsu, A., & Abe, O. (2018). Current and novel techniques for metal artifact reduction at CT: Practical guide for radiologists. *Radiographics*, 38(2), 450–461. <https://doi.org/10.1148/rg.2018170102>
- Kobbe, P., Laubach, M., Hutmacher, D. W., Alabdulrahman, H., Sellei, R. M., & Hildebrand, F. (2020). Convergence of scaffold-guided bone regeneration and RIA bone grafting for the treatment of a critical-sized bone defect of the femoral shaft. *European Journal of Medical Research*, 25(1). <https://doi.org/10.1186/s40001-020-00471-w>
- Koller, M. (2020). A retrospective descriptive study of cranioplasty failure rates and contributing factors in novel 3D printed calcium phosphate implants compared to traditional materials. *3D Print. Med.*, 6, 1–10.
- Langer, R., & Vacanti, J. (1993). Tissue engineering. *Science*, 920–926. <https://doi.org/10.1126/science.8493529>
- Liu, Y., Lim, J., & Teoh, S. H. (2013). Review: Development of clinically relevant scaffolds for vascularised bone tissue engineering. *Biotechnology Advances*, 31(5), 688–705. <https://doi.org/10.1016/j.biotechadv.2012.10.003>
- Liu, Y., Wang, L., Su, Y., Brown, K., Yang, R., Zhang, Y., Duanmu, Y., Guo, Z., Zhang, W., Yan, C., Yan, D., & Cheng, X. (2020). CTXA hip: The effect of partial volume correction on volumetric bone mineral density data for cortical and trabecular bone. *Archives of Osteoporosis*, 15(1). <https://doi.org/10.1007/s11657-020-00721-8>
- Nassef, T. M. (2012). New segmentation approach to extract human mandible bones based on actual computed tomography data. *American Journal of Biomedical Engineering*, 2, 197–201.
- Patent, J. F. G. (n.d.). Liquid metal recording (Vol. Vol 3596285).

- Park, J.-H., Odkhuu, M., Cho, S., Li, J., Park, B.-Y., & Kim, J.-W. (2020). 3D-printed titanium implant with pre-mounted dental implants for mandible reconstruction: A case report. *Maxillofacial Plastic and Reconstructive Surgery*. <https://doi.org/10.1186/s40902-020-00272-5>
- Prasad, S., Suresh, S., Hong, K. L., Bhargav, A., Rosa, V., & Wong, R. C. W. (2020). Biomechanics of alloplastic mandible reconstruction using biomaterials: The effect of implant design on stress concentration influences choice of material. *Journal of the Mechanical Behavior of Biomedical Materials*, 103, 103548. <https://doi.org/10.1016/j.jmbbm.2019.103548>
- Rajon, D. A., Pichardo, J. C., Brindle, J. M., Kielar, K. N., Jokisch, D. W., Patton, P. W., & Bolch, W. E. (2006). Image segmentation of trabecular spongiosa by visual inspection of the gradient magnitude. *Physics in Medicine and Biology*, 51(18), 4447–4467. <https://doi.org/10.1088/0031-9155/51/18/002>
- Schuckert, K. H., Jopp, S., & Teoh, S. H. (2009). Mandibular defect reconstruction using three-dimensional polycaprolactone scaffold in combination with platelet-rich plasma and recombinant human bone morphogenetic protein-2: De novo synthesis of bone in a single case. *Tissue Engineering - Part A*, 15(3), 493–499. <https://doi.org/10.1089/ten.tea.2008.0033>
- Seen, S., Young, S. M., Teo, S. J., Lang, S. S., Amrith, S., Lim, T. C., & Sundar, G. (2018). Permanent versus bioresorbable implants in orbital floor blowout fractures. *Ophthalmic Plastic and Reconstructive Surgery*, 34(6), 536–543. <https://doi.org/10.1097/IOP.0000000000001077>
- Teo, L., Teoh, S. H., Liu, Y., Lim, L., Tan, B., Schantz, J. T., & Seah, L. L. (2015). A novel bioresorbable implant for repair of orbital floor fractures. *Orbit*, 34(4), 192–200. <https://doi.org/10.3109/01676830.2015.1015263>
- The inventions of Daedalus: A compendium of plausible schemes. (1982).
- Urban, I. A., Lozada, J. L., Wessing, B., del Amo, F. S. L., & Wang, H. L. (2016). Vertical bone grafting and periosteal vertical mattress suture for the fixation of resorbable membranes and stabilization of particulate grafts in horizontal guided bone regeneration to achieve more predictable results: A technical report. *International Journal of Periodontics and Restorative Dentistry*, 36(2), 153–159. <https://doi.org/10.11607/prd.2627>
- Van Bael, S., Chai, Y. C., Truscello, S., Moesen, M., Kerckhofs, G., Van Oosterwyck, H., Kruth, J. P., & Schrooten, J. (2012). The effect of pore geometry on the in vitro biological behavior of human periosteum-derived cells seeded on selective laser-melted Ti6Al4V bone scaffolds. *Acta Biomaterialia*, 8(7), 2824–2834. <https://doi.org/10.1016/j.actbio.2012.04.001>
- Wiggenhauser, P. S., Balmayor, E. R., Rotter, N., & Schantz, J. T. (2019). In vivo evaluation of a regenerative approach to nasal dorsum augmentation with a polycaprolactone-based implant. *European Journal of Medical Research*, 24(1). <https://doi.org/10.1186/s40001-019-0364-y>
- Wolff, A., Santiago, G. F., Belzberg, M., Huggins, C., Lim, M., Weingart, J., Anderson, W., Coon, A., Huang, J., Brem, H., & Gordon, C. (2018). Adult cranioplasty reconstruction with customized cranial implants: Preferred technique, timing, and biomaterials. *Journal of Craniofacial Surgery*, 29(4), 887–894. <https://doi.org/10.1097/SCS.0000000000004385>
- Wong, R., Loh, J., & Islam, I. (2016). The role of finite element analysis in studying potential failure of mandibular reconstruction methods.
- Wong, R. C. W., Tideman, H., Kin, L., & Merkx, M. A. W. (2010). Biomechanics of mandibular reconstruction: A review. *International Journal of Oral and Maxillofacial Surgery*, 39(4), 313–319. <https://doi.org/10.1016/j.ijom.2009.11.003>

- Woodruff, M. A., Lange, C., Reichert, J., Berner, A., Chen, F., Fratzl, P., Schantz, J. T., & Hutmacher, D. W. (2012). Bone tissue engineering: From bench to bedside. *Materials Today*, 15(10), 430–435. [https://doi.org/10.1016/S1369-7021\(12\)70194-3](https://doi.org/10.1016/S1369-7021(12)70194-3)
- Yáñez, A., Herrera, A., Martel, O., Monopoli, D., & Afonso, H. (2016). Compressive behaviour of gyroid lattice structures for human cancellous bone implant applications. *Materials Science and Engineering C*, 68, 445–448. <https://doi.org/10.1016/j.msec.2016.06.016>
- Yang, M., Ng, H. J. H., Nga, V. D. W., Chou, N., & Yeo, T. T. (2020). Cranial reconstruction using a polycaprolactone implant after burr hole trephination. *Journal of 3D printing in medicine*, 4, 9–16.
- Young, S. M., Sundar, G., Lim, T. C., Lang, S. S., Thomas, G., & Amirth, S. (2017). Use of bioresorbable implants for orbital fracture reconstruction. *British Journal of Ophthalmology*, 101(8), 1080–1085. <https://doi.org/10.1136/bjophthalmol-2016-309330>
- Zein, I., Hutmacher, D. W., Tan, K. C., & Teoh, S. H. (2002). Fused deposition modeling of novel scaffold architectures for tissue engineering applications. *Biomaterials*, 23(4), 1169–1185. [https://doi.org/10.1016/S0142-9612\(01\)00232-0](https://doi.org/10.1016/S0142-9612(01)00232-0)

This page intentionally left blank

# Virtual reality—assisted treatment planning, patient management, and educational approaches in dentistry

# 27

Poornima Ramamurthy<sup>1</sup>, Dileep Sharma<sup>2</sup>

<sup>1</sup>College of Medicine & Dentistry, James Cook University, Smithfield, QLD, Australia;

<sup>2</sup>School of Health Sciences, College of Health, Medicine and Wellbeing, The University of Newcastle, NSW, Australia

## Chapter outline

Introduction .....	693
Implant treatment planning .....	695
Digital workflow in dental implantology .....	696
Software-guided implant surgery .....	696
Digital smile design .....	697
Virtual reality and dental anxiety .....	699
Virtual reality and dental education .....	700
Future directions .....	701
References .....	702
Further reading .....	706

## Introduction

Good oral health and a complete set of dentition is considered vital for overall health and well-being (Australian Institute of Health and Welfare, 2020). Oral diseases incorporate conditions that affect teeth, gingiva, alveolar bone supporting the teeth, and the surrounding hard or soft tissues around the oral cavity. A range of inflammatory and infectious diseases are known to affect the oral tissues leading to significant morbidities (Scannapieco & Cantos, 2016). Particularly, polymicrobial dental plaque induced diseases can lead to partial or complete loss of hard tissues in the oral cavity, including dental caries affecting mainly the exposed part of the teeth itself and periodontal diseases that affect the hard and soft tissue surrounding and connecting the teeth to the jawbone (“periodontium”) (Fejerskov, 1997; Kinane, 2001).

Independent of cause, a clinical situation involving loss of single or multiple teeth is called partial or complete edentulism, respectively. Edentulism is known to significantly affect ability to masticate, speak, and experience social comfort leading to restricted involvement at workplace, home, or other social settings and thus compromising the general quality of life (Niesten et al., 2012). Currently, management of edentulism involves the use of removable and fixed partial or full dentures, depending on clinical indications (Mazurat, 1992). Although a removable denture is the most economical approach to manage both partial and complete edentulism, they are generally least preferred by the patients due to their inherent lack of stability, “removability” and the social stigma around dentures (Shaha et al., 2021).

The advent of titanium and its alloys as a dental implant material has ushered a new treatment modality for replacement of missing teeth using implant supported dentures prosthesis (Nicholson, 2020; Özcan & Hämerle, 2012). Dental implants have consequently become the mainstay in management of edentulism in the last few decades. Furthermore, a discipline termed *dental implantology* has become one of the most dynamic and researched fields within dentistry.

Dental implant is a “screw” that is surgically placed into the bone to serve as an anchor and support an individual crown to replace a missing (extracted or otherwise) tooth structurally and functionally (Fig. 27.1). In situations wherein more than a single tooth needs to be replaced, multiple implants are placed with or without intervening connectors to restore the partial or complete arch of the dentition. This approach has been widely accepted as a method to restore edentulous areas to achieve optimal form, function, and esthetics (Fillion et al., 2013). Materials used to fabricate dental implants have evolved over time with newer and more favourable materials being introduced ever so often. In addition to titanium alloys, zirconia

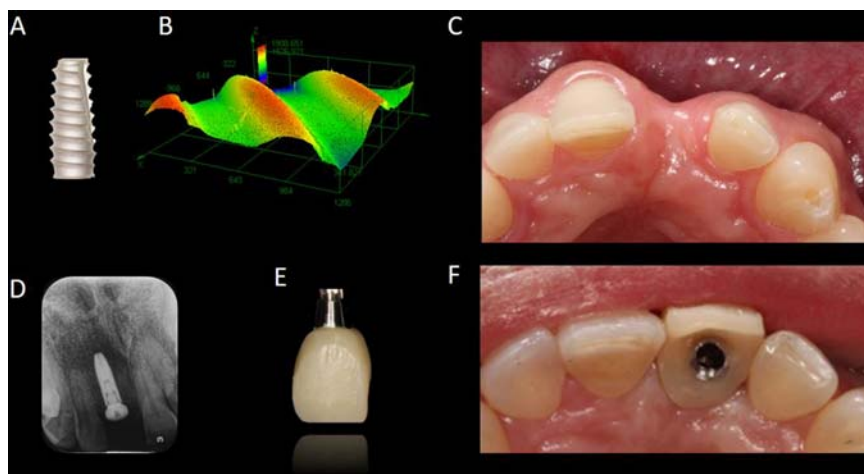


**FIGURE 27.1**

Implant supported prosthesis. A—Dental implant, B—Surface topography of dental implant, C—Missing maxillary anterior tooth, D—Dental implant placed in the anterior maxilla, E—Ceramic crown for restoring tooth, F—Prosthetic crown placed on the implant.

dental implants have been gaining popularity due to their biocompatibility and tooth-colored appearance (Grech & Antunes, 2019; Munro et al., 2020).

## Implant treatment planning

An accurate assessment of jawbone dimensions and location of anatomical structures in the vicinity of planned implant site is a vital step in implant treatment planning. Traditionally, dental implant therapy involves extensive assessment beginning with clinical examination, diagnostic dental models, and a range of two-dimensional radiographic imaging including panoramic views and intra-oral radiographs. In recent years, addition of three-dimensional radiographic imaging to the repertoire of diagnostic tools has further enhanced the clinician's ability to provide optimal and customized implant therapy.

Based on the high-resolution data obtained from modern 3D imaging systems including computed tomography (CT) and dental specific-cone beam CT (CBCT), digital human modeling-assisted implant planning software systems have essentially revolutionized implant treatment planning. Data recorded by 3D-imaging systems and generally stored within the Digital Imaging and Communication in Medicine (DICOM-format) can support simulation and analysis using a range of commercially available implant planning software, as exemplified in Fig. 27.2.

Computer-aided design (CAD) and computer-aided manufacturing (CAM) technology utilizes 3D-imaging (DICOM) data at various stages of implant therapy ranging from implant size selection, optimal positioning of an implant into the edentulous jawbone through fabrication of an implant drill guide, to the provisional and



**FIGURE 27.2**

Digital dental implant treatment planning using radiographic imaging (DICOM file format) and 3D-reconstruction software.

final implant-supported prosthesis (Schnutenhaus et al., 2018). However, data in DICOM files do have limitations, specifically in the case of patients with metallic restorations or fixed partial dentures with metal framework that leads to a “streaks” artifact limiting the diagnostic detail around the implant site (Nagarajappa et al., 2015; Schulze et al., 2011). Therefore, in addition to radiological scans, a “virtual model” of the remaining dentition recorded using an intraoral optical scanner or dental impression scanner are used as overlay to enable comprehensive treatment planning (Jones, 2013).

---

## Digital workflow in dental implantology

The introduction of three-dimensional dental software in the late 1980s capable of converting the standard axial slices sourced from computerized tomography into diagnostic quality cross-sectional images of the alveolar ridges ushered a new era in implant therapy (D’Haese et al., 2017). Subsequently, software-assisted guided implant surgery protocols based on the combination of various imaging sources have been quite successful in ensuring optimal implant positioning and function for long-term stability of the implant supporting hard and soft tissues.

### Software-guided implant surgery

Traditionally, two types of software-guided surgery approaches have been utilized in implant therapy; static and dynamic, differing mainly in the flexibility they offer while the dental implant is being surgically placed. A static approach involves use of a custom-made surgical template or drill guide that is CAD-designed using computerized tomographic images overlayed on a planned surgical site with the virtual implant positioning software (Fig. 27.2). The drill guide is subsequently CAM-fabricated using milling, 3D-printed or molded using polymerization of liquid resins (Buser et al. 2009, 2011). The main limitation of static drill guides is that they do not offer any flexibility in final positioning of the implant, and the need for multiple guides to accommodate for the increasing diameter of drills used in the various stages of implant surgery, including the placement of the implant (termed fully guided protocol) (Vercruyssen et al., 2015). A partially guided protocol utilizes guides only for osteotomy drills and not for the final stage, i.e., placement of the implant into the osteotomy site. Furthermore, these surgical guides need to be fabricated so as to be supported by the remaining teeth (i.e., tooth-supported), mucosa alone (i.e., mucosa-supported), bone (bone supported) or (mini) implant or pin supported, of which the mini-implant or pin supported drill guides are considered the most accurate (D’Haese et al., 2017; Tahmaseb et al., 2009). It is worth noting that the static approach is still the most widely used approach due to their cost-effectiveness and uncomplicated handling (D’Haese et al., 2017).

Newer dynamic systems utilize real-time motion tracking of the implant surgical drills and allow for modification of implant position intraoperatively. Historically,

dynamic systems have been limited by high costs associated with the real-time tracking systems that need tomography. However, with the advent of smaller CBCT units and advances in augmented reality, the dynamic systems are gaining ground as they become less expensive, less fragile, and easier to use in routine practice.

A major advantage of guided surgical approaches has been their precision, specifically in situations where the implant site is in the vicinity of anatomical structures such as the mandibular nerve or mental nerve in the mandible. However, accuracy in the static approach is purely dependent on the stability of the drill guide. Any movement of the drill guides can be minimized by using large grit sandblasting and acid-etching of the drill guides' tissue fitting surface (Di Giacomo et al., 2005). Alternatively, use of mini-implants or pins to act as support guides for the fabrication and use of a surgical template enhances accuracy in implant positioning (Tahmaseb et al., 2009) (Fig. 27.3).

### Digital smile design

A smile is often considered to reflect a person's mood, psychological state of mind, and is invariably dependent on their emotions and personality. Appearance of front (anterior) teeth is often the area of focus and critical for the redesigning of smile due to the need for balance between the patient expectations and the preexisting biological, physiological, and skeletal physiognomy of the face. Traditionally, designing smile in a dental practice has been a multistep process involving an ongoing dialogue, generally through lab forms, between the dentist (and patient) within the clinic and the dental laboratory staff working off-site, to achieve optimal dental esthetics through fabrication of dental crowns and veneers to enhance overall esthetics. Based on the recommendations from the clinician, the lab technician redesigns the smile through manipulation of a patient's dental cast followed by a "wax up" to

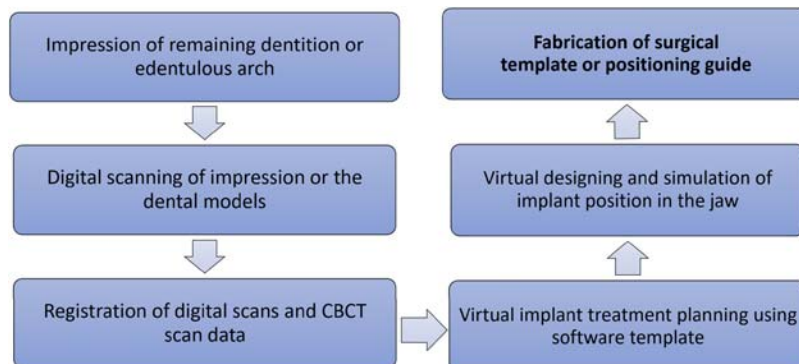


**FIGURE 27.3**

Flow diagram of digitally guided implant surgery protocol—static approach using 3D-imaging techniques.

reflect the redesigned smile for the patient. Generally, these waxed up cast models are returned to the clinic to ensure that the esthetics and functional expectations of the patient and the dentist are met on these waxed try-ins before the final prostheses are fabricated in the laboratory (Fig. 27.4).

Over the last 2 decades, the process of smile design has evolved drastically from the use of analogue photographs and drawings to the scanning of dentition and/or models to transform a 2D image into a virtual 3D model. With the advent of digital impressions and image scanning software tools, the field of virtual smile designing has grown leaps and bounds in the last decade or so. Currently, a range of subscription-based software packages are available to utilize a combination of data sources including CBCT files, digital impressions, and digital images to create a virtual model for treatment planning (Bini, 2015; Galibour & Brenes, 2019; Lin et al., 2018; McLaren et al., 2013) (Fig. 27.5). Multiple clinical researcher groups have published protocols around the use of generic imaging software such as Adobe Photoshop with predesigned templates created based on the “golden proportion” and customized to be used in a variety of facial forms, including rectangular, square, ovoid, or triangular (McLaren et al., 2013; Sundar & Chelliah, 2018). With the ever-evolving mobile phones and tablet cameras, commercial software packages are now available to simulate smile in a matter of minutes on a hand-held device (SmileFly, Inc USA).

A virtual smile designing procedure has the additional advantage of assisting patients in visualizing the expected treatment outcomes for various irreversible surgical and nonsurgical steps of the planned treatment. This is an invaluable advantage in setting patient expectations and obtaining a valid informed consent for the procedure that is often expensive and rarely covered by health insurance due the elective nature of these esthetic procedures (Iliev, 2016; Zanardi et al., 2016). Virtual smile modeling is particularly useful in discussing and visualizing dental crown

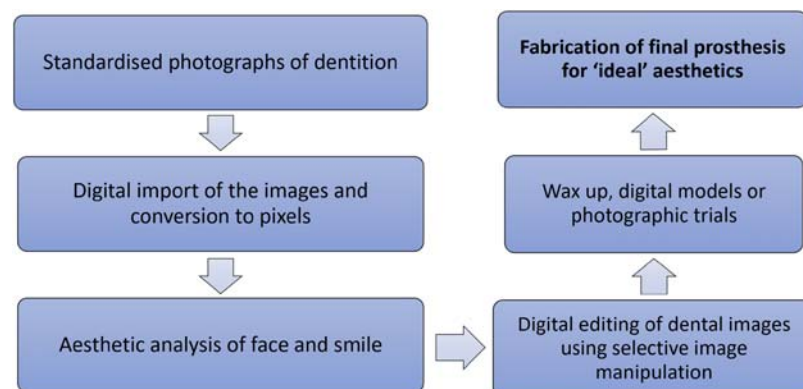


**FIGURE 27.4**

Flow diagram of digital smile design protocol—approach using images and software.

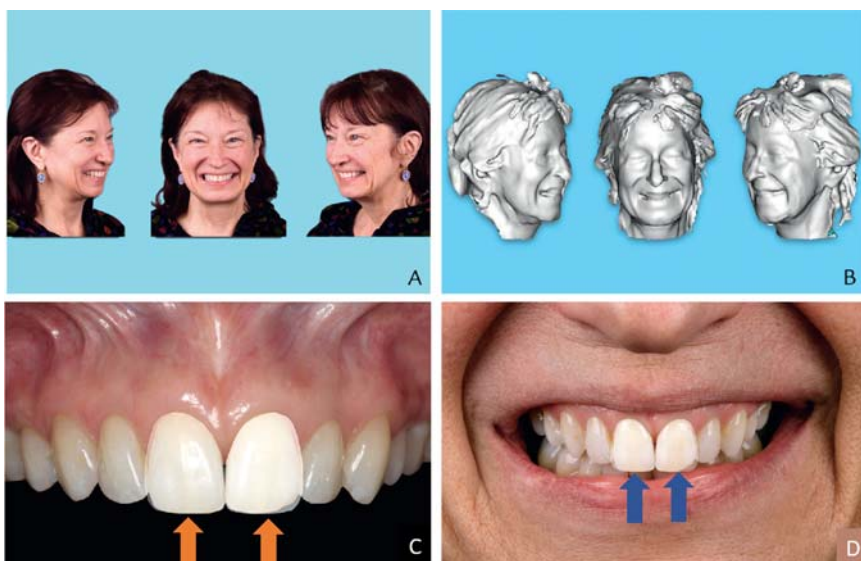


**FIGURE 27.5**

Extraoral pretreatment condition at full smile position from mid-facial, right and left 45-degree views. A. Digital extraoral photographs. B. Digital extraoral facial scan with customized 2D virtual smile design and digitally superimposed central incisors (*arrows*). C. Intraoperative view. D. Extraoperative view.

*Reproduced with permission from Lin, W. S., Harris, B. T., Phasuk, K., Llop, D. R., & Morton, D. (2018). Integrating a facial scan, virtual smile design, and 3d virtual patient for treatment with cad-cam ceramic veneers: A clinical report. Journal of Prosthetic Dentistry, 119(2), 200–205.*

lengthening, which is a surgical procedure often used in conjunction with reshaping of supporting alveolar bone (Coachman et al., 2022; Lo Giudice et al., 2020).

### Virtual reality and dental anxiety

A visit to a dental office and dental treatments are often associated with anxiety attacks in both children (up to 43%) and adults (10%–20%) (Shim et al., 2015a). In fact, dental anxiety is one of the most significant barriers to the patients' presentation for periodic check-ups that are essential for long-term prevention of chronic oral diseases (Newton et al., 2012). Although dental anxiety can affect any gender, females are more likely to experience anxiety (Shim et al., 2015a). Dental phobia is the specific term used to describe a severe form of dental anxiety. Generally, dental anxiety is either associated with the fear of local anesthesia injections or the treatment that follows anesthesia administration (López-Valverde et al., 2020). Needles, syringes, the rotary instrument noise, and other sharp instruments used in dental treatment can induce fear or anxiety in adults, but children are generally more fearful of dental practices.

Various approaches have been used to alleviate dental anxiety, including pharmacological and non-pharmacological modalities. Use of pharmacological agents for anxiety management is indicated in dental-phobics and patients with special needs due to mental illness or retardation, autism, or traumatic brain injury and is generally achieved through the use of either sedation or general anesthesia (Newton et al., 2003). Non-pharmacological modalities include a range of strategies such as relaxation, distraction, and cognitive behavior therapy for severe dental phobia (Berggren et al., 2000). Relaxation through the use of music and essential oil aromatherapy has been employed in various clinical studies with variable success rates as reported by a recent systematic review with meta-analysis wherein aromatherapy was noted to significantly reduce levels of dental anxiety experience in patients (Purohit et al., 2021; Venkataramana et al., 2016).

The American Academy of Paediatric Dentistry (AAPD) defines distraction, as “technique of diverting the patient’s attention from what may be perceived as an unpleasant procedure” (Clinical Affairs Committee, 2015). Various forms of distractors, classed as either non-digital distractors or digital distractors, such as virtual reality, television, handheld devices such as tablets and smartphones, have been utilized to manage dental anxiety through Cognitive Behavioral Therapy (Gates et al., 2020). Recently, the use of virtual reality–based distraction techniques also called Virtual Reality Exposure Therapy (VRET) has been researched in different age groups with significant success. VRET offers an immersive virtual experience effectively blocking out stimuli that may initiate a negative emotion or fear (Gujjar et al., 2019). VRET devices have been effective in both children and adults to manage pain perception and anxiety during the administration of local anesthesia as well as treatment procedures such as dental fillings and periodontal treatments (Bagattoni et al., 2018; Felemban et al., 2021; Gujjar et al., 2019; Nuvvula et al., 2015). A range of content including virtual nature (costal) walk to distract and relax the patient or in contrast, exposure to the different situations that the patient would be generally exposed to, within the dental settings have been used to effectively desensitize patients to the common external triggers for dental anxiety (Gujjar et al., 2019; Tanja-Dijkstra et al., 2018).

### **Virtual reality and dental education**

Simulated clinical sessions are an integral part of dental education and primarily performed on dental manikins and models of dentition wherein the training for preparation of teeth including fillings, root canal therapy, crowns, restoration of cavities, removal of dental calculus, and application of local anesthesia are completed in a preclinical or simulation laboratory. These sessions ensure that the students are competent and safe in performing the procedures, prior to their clinical sessions wherein they are expected to perform treatment on patients, under supervision. Advances in technology have led to an increasing use of VR-based simulators in dental education within dental training institutions. They have proven to be very effective in training and assessing the fine motor skills and hand–eye coordination in the

early, preclinical learners and have replaced some of the lab-based activities within the dentistry course. Additionally, they offer an opportunity to train and assess the level of proficiency even in the absence of the simulation instructors. Student profiles that can be created on such systems can effectively be used to track the progress of students and their skill levels remotely and asynchronously. An unintended yet positive outcome with the advent of VR-based dental simulation systems includes student-centric and student-led learning that facilitates better utilization of a limited skilled work force within the educational and training institutions. Generally, these systems offer virtual 3D models and an option to perform a range of procedures such as different grasps used in dental procedures, a selection of appropriate dental burs and the process of drilling teeth, to simulation of dental caries removal. Haptic (sense of touch) capability of various systems has further value-added to the use of VR systems in learning environments (Fig. 27.6).

Various VR-based approaches have been developed commercially to train students and enhance the students' learning experience, satisfaction, and engagement levels with the subject content (Mansoory et al., 2022). In addition to the possibility of unlimited repetition of the task, self and peer assessment, the approach provides ongoing feedback on skill improvement and identifies areas that need further improvement without posing risk for patients (Moussa et al., 2022). Further advances in VR technology have also expanded the scope of their application to other aspects of dental training including the use of virtual patients and immersive VR for local anesthesia delivery, treatment planning for complex orthognathic cases and maxillofacial fractures, virtual implant placement, dental radiography training, and calculus removal (Moussa et al., 2022).

The use of Augmented Reality (AR) through specialized glasses and an integrated screen is a new trend in medicine. AR technology allows for the visualization, in real-time, of patient information such as radiographs, a previously planned 3D reconstruction or may offer an interactive screen (Badiali et al., 2014). In dentistry, AR has recently been used along with the Microsoft Hololens to visualize diagnostic data such as CBCTs, face scans, or oral scans without a need for the clinician to move their field of vision to look at a monitor while interacting with the system through voice commands or gestures (Pellegrino et al., 2019; Zhu et al., 2017). The AR-based approach can significantly enhance overall treatment outcomes and patient satisfaction.

---

## Future directions

The introduction of digital human modeling and virtual reality-based systems has significantly improved the treatment options of dental practitioners and the acceptance of a range of treatment modalities by patients. Advancements in material science and the uptake of digital human modeling and virtual reality-based treatment planning software tools have significantly enhanced the treatment outcomes and quality of life for the patients undergoing a range of dental treatments including

**FIGURE 27.6**

Simodont dental trainer with haptic technology. (A) Simulator unit, (B) Panel PC, (C) Stereo Projection, (D) Spacemouse (Joystick), (E) Handpiece, (F) Handrest, (G) Foot Pedal, (H) Mirror Stick, (I) 3D Glasses.

*Reproduced with permission from Roy, E., Bakr, M. M., & George, R. (2017). The need for virtual reality simulators in dental education: A review. Saudi Dental Journal, 29(2), 41–47.*

implant therapy. A range of limitations with the currently available digital human modeling and VR-based systems in treatment planning and student training systems include the initial cost of hardware (scanning) installation and the ongoing software licensing or subscription requirement. Additionally, the requirement for training of end users i.e., dental practitioners or dental students can be a significant barrier in the uptake of state-of-the-art systems. With the cost of dental implants and indirect restorations on gradual decline, more patients will be able to afford implant supported prostheses and esthetic restorations in the near future.

## References

- Australian Institute of Health and Welfare. (2020). *National oral health plan 2015–2024: Performance monitoring report*. Canberra Available from [\(https://www.aihw.gov.au/reports/dental-oral-health/national-oral-health-plan-2015-2024/contents/summary\)](https://www.aihw.gov.au/reports/dental-oral-health/national-oral-health-plan-2015-2024/contents/summary). (Accessed 20 July 2022).
- Badiali, G., Ferrari, V., Cutolo, F., Freschi, C., Caramella, D., Bianchi, A., & Marchetti, C. (2014). Augmented reality as an aid in maxillofacial surgery: Validation of a wearable

- system allowing maxillary repositioning. *Journal of Cranio-Maxillofacial Surgery*, 42(8), 1970–1976.
- Bagattoni, S., D'Alessandro, G., Sadotti, A., Alkhamis, N., & Piana, G. (2018). Effects of audiovisual distraction in children with special healthcare needs during dental restorations: A randomized crossover clinical trial. *International Journal of Paediatric Dentistry*, 28(1), 111–120.
- Berggren, U., Hakeberg, M., & Carlsson, S. G. (2000). Relaxation vs. Cognitively oriented therapies for dental fear. *Journal of Dental Research*, 79(9), 1645–1651.
- Bini, V. (2015). Aesthetic digital smile design: Software-aided aesthetic. *Dental Tribune International*, 2. Available from <https://www.dental-tribune.com/news/aesthetic-digital-smile-design-software-aided-aesthetic-dentistry-part-ii/>. (Accessed 20 July 2022).
- Buser, D., Halbritter, S., Hart, C., Bornstein, M. M., Grüter, L., Chappuis, V., & Belser, U. C. (2009). Early implant placement with simultaneous guided bone regeneration following single-tooth extraction in the esthetic zone: 12-month results of a prospective study with 20 consecutive patients. *Journal of Periodontology*, 80(1), 152–162.
- Buser, D., Wittneben, J., Bornstein, M. M., Grüter, L., Chappuis, V., & Belser, U. C. (2011). Stability of contour augmentation and esthetic outcomes of implant-supported single crowns in the esthetic zone: 3-year results of a prospective study with early implant placement postextraction. *Journal of Periodontology*, 82(3), 342–349.
- Clinical Affairs Committee-Behavior Management Subcommittee, American Academy of Pediatric Dentistry. (2015). Guideline on behavior guidance for the pediatric dental patient. *Pediatric Dentistry*, 37(5), 57–70.
- Coachman, C., Valavanis, K., Silveira, F. C., Kahn, S., Tavares, A. D., Mahn, E., Parize, H., & Saliba, F. M. P. (2022). The crown lengthening double guide and the digital perio analysis. *Journal of Esthetic and Restorative Dentistry*. <https://doi.org/10.1111/jerd.12920> (Online ahead of print).
- D'Haese, J., Ackhurst, J., Wismeijer, D., De Bruyn, H., & Tahmaseb, A. (2017). Current state of the art of computer-guided implant surgery. *Periodontology*, 73(1), 121–133, 2000.
- Di Giacomo, G. A., Cury, P. R., de Araujo, N. S., Sendyk, W. R., & Sendyk, C. L. (2005). Clinical application of stereolithographic surgical guides for implant placement: Preliminary results. *Journal of Periodontology*, 76(4), 503–507.
- Fejerskov, O. (1997). Concepts of dental caries and their consequences for understanding the disease. *Community Dentistry and Oral Epidemiology*, 25(1), 5–12.
- Felemban, O. M., Alshamrani, R. M., Aljeddawi, D. H., & Bagher, S. M. (2021). Effect of virtual reality distraction on pain and anxiety during infiltration anesthesia in pediatric patients: A randomized clinical trial. *BMC Oral Health*, 21(1), 321.
- Fillion, M., Aubazac, D., Bessadet, M., Allègre, M., & Nicolas, E. (2013). The impact of implant treatment on oral health related quality of life in a private dental practice: A prospective cohort study. *Health and Quality of Life Outcomes*, 11(1), 197.
- Galibourg, A., & Brenes, C. (2019). Virtual smile design tip: From 2d to 3d design with free software. *Journal of Prosthetic Dentistry*, 121(5), 863–864.
- Gates, M., Hartling, L., Shulhan-Kilroy, J., MacGregor, T., Guitard, S., Wingert, A., Featherstone, R., Vandermeer, B., Poonai, N., Kircher, J., et al. (2020). Digital technology distraction for acute pain in children: A meta-analysis. *Pediatrics*, 145(2), e20191139.
- Grech, J., & Antunes, E. (2019). Zirconia in dental prosthetics: A literature review. *Journal of Materials Research and Technology*, 8(5), 4956–4964.

- Gujar, K. R., van Wijk, A., Kumar, R., & de Jongh, A. (2019). Efficacy of virtual reality exposure therapy for the treatment of dental phobia in adults: A randomized controlled trial. *Journal of Anxiety Disorders*, 62, 100–108.
- Iliev, G. V. (2016). Personalized digital smile design for predictable aesthetic results. *Balkan Journal of Dental Medicine*, 20, 172–177.
- Jones, P. E. (2013). Accurate implant placement. Digital scanning and use of tooth-guided, tooth-supported surgical guides. *Dentistry Today*, 32(11), 124, 126, 128.
- Kinane, D. F. (2001). Causation and pathogenesis of periodontal disease. *Periodontology*, 25, 8–20, 2000.
- Lin, W. S., Harris, B. T., Phasuk, K., Llop, D. R., & Morton, D. (2018). Integrating a facial scan, virtual smile design, and 3d virtual patient for treatment with cad-cam ceramic veneers: A clinical report. *Journal of Prosthetic Dentistry*, 119(2), 200–205.
- Lo Giudice, A., Ortensi, L., Farronato, M., Lucchese, A., Lo Castro, E., & Isola, G. (2020). The step further smile virtual planning: Milled versus prototyped mock-ups for the evaluation of the designed smile characteristics. *BMC Oral Health*, 20(1), 165–165.
- López-Valverde, N., Muriel-Fernández, J., López-Valverde, A., Valero-Juan, L. F., Ramírez, J. M., Flores-Fraile, J., Herrero-Payo, J., Blanco-Antona, L. A., Macedo-de-Sousa, B., & Bravo, M. (2020). Use of virtual reality for the management of anxiety and pain in dental treatments: Systematic review and meta-analysis. *Journal of Clinical Medicine*, 9(10).
- Mansoori, M. S., Azizi, S. M., Mirhosseini, F., Yousefi, D., & Moradpoor, H. (2022). A study to investigate the effectiveness of the application of virtual reality technology in dental education. *BMC Medical Education*, 22(1), 457.
- Mazurat, R. D. (1992). Longevity of partial, complete and fixed prostheses: A literature review. *Journal of the Canadian Dental Association*, 58(6), 500–504.
- McLaren, E. A., Garber, D. A., & Figueira, J. (2013). The photoshop smile design technique (part 1): Digital dental photography. *Compendium of Continuing Education in Dentistry*, 34(10), 772, 774, 776 passim.
- Moussa, R., Alghazaly, A., Althagafi, N., Eshky, R., & Borzangy, S. (2022). Effectiveness of virtual reality and interactive simulators on dental education outcomes: Systematic review. *European Journal of Dentistry*, 16(1), 14–31.
- Munro, T., Miller, C., Antunes, E., & Sharma, C. G. D. (2020). Interactions of osteoprogenitor cells with a novel zirconia implant surface. *Journal of Functional Biomaterials*, 11, 50.
- Nagarajappa, A. K., Dwivedi, N., & Tiwari, R. (2015). Artifacts: The downturn of cbct image. *Journal of International Society of Preventive and Community Dentistry*, 5(6), 440–445.
- Newton, T., Asimakopoulou, K., Daly, B., Scambler, S., & Scott, S. (2012). The management of dental anxiety: Time for a sense of proportion? *British Dental Journal*, 213(6), 271–274.
- Newton, J. T., Naidu, R., & Sturmy, P. (2003). The acceptability of the use of sedation in the management of dental anxiety in children: Views of dental students. *Eur J Dent Educ*, 7(2), 72–76.
- Nicholson, J. (2020). Titanium alloys for dental implants: A review. *Prosthesis*, 2, 100–116.
- Niesten, D., van Mourik, K., & van der Sanden, W. (2012). The impact of having natural teeth on the qol of frail dentulous older people. A qualitative study. *BMC Public Health*, 12(1), 839.
- Nuvvula, S., Alahari, S., Kamatham, R., & Challa, R. (2015). Effect of audiovisual distraction with 3d video glasses on dental anxiety of children experiencing administration of local

- analgesia: A randomised clinical trial. *European Archives of Paediatric Dentistry*, 16(1), 43–50.
- Özcan, M., & Hämmерle, C. (2012). Titanium as a reconstruction and implant material in dentistry: Advantages and pitfalls. *Materials (Basel)*, 5(9), 1528–1545.
- Pellegrino, G., Mangano, C., Mangano, R., Ferri, A., Taraschi, V., & Marchetti, C. (2019). Augmented reality for dental implantology: A pilot clinical report of two cases. *BMC Oral Health*, 19(1), 158.
- Purohit, A., Singh, A., Purohit, B., Shakti, P., & Shah, N. (2021). Is aromatherapy associated with patient's dental anxiety levels? A systematic review and meta-analysis. *Journal of Dental Anesthesia and Pain Medicine*, 21(4), 311–319.
- Roy, E., Bakr, M. M., & George, R. (2017). The need for virtual reality simulators in dental education: A review. *Saudi Dental Journal*, 29(2), 41–47.
- Scannapieco, F. A., & Cantos, A. (2016). Oral inflammation and infection, and chronic medical diseases: Implications for the elderly. *Periodontology*, 72(1), 153–175, 2000.
- Schnuttenhaus, S., Edelmann, C., Rudolph, H., Dreyhaupt, J., & Luthardt, R. G. (2018). 3d accuracy of implant positions in template-guided implant placement as a function of the remaining teeth and the surgical procedure: A retrospective study. *Clinical Oral Investigations*, 22(6), 2363–2372.
- Schulze, R., Heil, U., Gross, D., Bruellmann, D. D., Dranischnikow, E., Schwanecke, U., & Schoemer, E. (2011). Artefacts in cbct: A review. *Dentomaxillofacial Radiology*, 40(5), 265–273.
- Shaha, M., Varghese, R., & Atassi, M. (2021). Understanding the impact of removable partial dentures on patients' lives and their attitudes to oral care. *British Dental Journal*. Epub ahead of print. <https://doi.org/10.1038/s41415-021-2949-4>.
- Shim, Y.-S., Kim, A.-H., Jeon, E.-Y., & An, S.-Y. (2015a). Dental fear & anxiety and dental pain in children and adolescents; a systemic review. *Journal of Dental Anesthesia and Pain Medicine*, 15(2), 53–61.
- Sundar, M. K., & Chelliah, V. (2018). Ten steps to create virtual smile design templates with adobe photoshop(r) cs6. *Compendium Continuing Education Dentistry*, 39(3), e4–e8.
- Tahmaseb, A., De Clerck, R., & Wismeijer, D. (2009). Computer-guided implant placement: 3d planning software, fixed intraoral reference points, and cad/cam technology. A case report. *The International Journal of Oral & Maxillofacial Implants*, 24(3), 541–546.
- Tanja-Dijkstra, K., Pahl, S., White, M. P., Auvray, M., Stone, R. J., Andrade, J., May, J., Mills, I., & Moles, D. R. (2018). The soothing sea: A virtual coastal walk can reduce experienced and recollected pain. *Environment and Behavior*, 50(6), 599–625.
- Venkataratnam, M., Pratap, K. V. N. R., Padma, M., Kalyan, S., Reddy, A., & Sandhya, P. (2016). Effect of aromatherapy on dental patient anxiety: A randomized controlled trial. *Journal of Indian Association of Public Health Dentistry*, 14(2), 131–134.
- Vercruyssen, M., Coucke, W., Naert, I., Jacobs, R., Teughels, W., & Quirynen, M. (2015). Depth and lateral deviations in guided implant surgery: An rct comparing guided surgery with mental navigation or the use of a pilot-drill template. *Clinical Oral Implants Research*, 26(11), 1315–1320.
- Zanardi, P. R., Laia Rocha Zanardi, R., Chaib Stegun, R., Sesma, N., Costa, B. N., & Cruz Laganá, D. (2016). The use of the digital smile design concept as an auxiliary tool in aesthetic rehabilitation: A case report. *Open Dentistry Journal*, 10, 28–34.
- Zhu, M., Liu, F., Chai, G., Pan, J. J., Jiang, T., Lin, L., Xin, Y., Zhang, Y., & Li, Q. (2017). A novel augmented reality system for displaying inferior alveolar nerve bundles in maxillofacial surgery. *Scientific Reports*, 7(1), 1–11.

### **Further reading**

AI smile simulation—Smilefy, Inc. Available from <https://smilefy.com/ai-smile-simulation-sp/files/39/ai-smile-simulation-sp.html> Last accessed on 15 July 2022.

Exocad GmbH. Smile creator photo protocol. Available from: [https://wiki.exocad.com/wiki/index.php/Smile\\_Creator\\_Photo\\_Protocol%E2%80%8B\\_%E2%80%8B](https://wiki.exocad.com/wiki/index.php/Smile_Creator_Photo_Protocol%E2%80%8B_%E2%80%8B) Last accessed 20 July 2022.

SECTION

Medical application

6

This page intentionally left blank

# Whole-body movement modeling in realistic environments for understanding performance and injury

# 28

**Simon M. Harrison, Raymond C.Z. Cohen, Paul W. Cleary**

*CSIRO Data61, Clayton South, VIC, Australia*

## Chapter outline

<b>Introduction</b> .....	710
<b>Markerless motion capture for digital human model construction</b> .....	712
Background .....	712
Overview of MMC pipeline .....	714
<i>Two-dimensional pose estimation models</i> .....	715
<i>Three-dimensional pose reconstruction</i> .....	716
<i>Joint angles from inverse kinematics</i> .....	717
Benefits and future applications .....	718
<b>Computational methods</b> .....	719
Biomechanical methods .....	719
<i>Introduction</i> .....	719
<i>Kinematic definitions and theory</i> .....	720
<i>Kinetics</i> .....	724
<i>Dynamics</i> .....	725
SPH method for simulating the external environment .....	726
<i>SPH method for fluids</i> .....	726
<i>SPH method for elastic and elastoplastic solids</i> .....	727
<i>SPH boundary modeling</i> .....	729
<i>Integration of SPH equations</i> .....	729
<b>Using digital twins to understand performance and injury: sports examples</b> .....	729
Swimming .....	729
Diving .....	736
Snow skiing .....	742
<b>Realtime digital human applications: workplace injury example</b> .....	749
<b>Creating software products based on human digital twins</b> .....	755

Conclusions .....	756
Acknowledgments .....	759
References .....	759

---

## Introduction

The nature of the mechanical interactions between the body and its environment determine how we move; during work, play, or rest; and if our body is damaged by the forces that result. For instance, an elite springboard diver can perform a near splash-less entry into the pool water by using specific arm, leg, and torso movements to control their in-air and in-water motion trajectories. Alternatively, with only small differences to the body movements, the diver could impact the water sub-optimally, creating a large splash (which will result in a poorer competitive outcome) and imparting higher forces on the body (which could lead to injury, see (Harrison et al., 2016)). However, measurement of body movements is typically limited to biomechanics laboratories where the quantification of external body forces can only be measured for a small number of very simple scenarios, such as ground reaction forces (GRF) during walking. This strongly restricts scientific investigation and evidence-based development of technique.

Modeling of the human body during such movement can lead to significantly better understanding that can contribute strongly to

- informed performance improvement, and
- identification of the causes of both short-term acute injuries and longer-term chronic injuries.

Activities that can benefit from such models, often called digital twins, include sports, workplace safety, falls for the elderly and infirm, and rehabilitation. A large number of studies (see, for instance, reviews by Moissenet et al. (2017), Smith et al. (2021)) employ a combination of marker-based motion capture, GRF measurement, muscle electrical activation via electromyography, and dynamics software such as OpenSim (Delp et al., 2007) to understand and improve health outcomes. However, these studies are typically limited to the confines of a laboratory and by small sample sizes, both in number of participants and number of repetitions of movements. This is primarily due to the restrictions of the measurement methods and equipment. Additionally, broad usage of such methods is limited by the lack of user-friendly software tools (Smith et al., 2021).

Use of digital twin models has advantages over physical experimentation alone, but they need to contain sufficient detail and be shown to be sufficiently accurate for their intended uses. They can also produce data that cannot be directly measured, such as internal forces and stresses (Anderson & Pandy, 2001; Dorn et al., 2012; Harrison, Chris Whitton et al., 2014; Harrison et al., 2010; Kersh et al., 2013; Schache et al., 2010). Individual variables are more easily controlled than for physical experiments, which enables more controlled and more complex investigations. The methods applied need to include

- whole-body dynamics to predict the human pose and body shape dynamically throughout the activity,
- sufficient internal biomechanical structure so as to enable prediction of muscle and joint loads, and
- realistic models of the external world whose interactions drive the human body's responses.

Models can also be personalized by including individual specific representations of anatomy, physiological attributes (such as strength, flexibility, and pathologies), and movements (or technique). Movement data, with high spatiotemporal resolution, is needed for real environments and realistic activities. It is suboptimal to substitute the real activity for a laboratory-based measurement of the scenario because the participants move artificially and the body–environment interactions will be different (Riley et al., 2008). There is also value in being able to make such models accessible to the end users (athletes, coaches, sports scientists, physiotherapists, and medical professionals) in interactive and intuitive software, so that the maximum benefit can be realized.

This chapter describes the construction and usage of such digital twins in circumstances where the digital twin is interacting with a complex external environment. These digital twins have three key components:

1. A biomechanical model of the body that can be personalized for individuals and which captures their relevant physical attributes,
2. Kinematic data that describes the time-dependent motion of the human during activities, and
3. A numerical method for predicting the two-way coupled effects of the environment on the human model and the human-model on the environment. The SPH (Smoothed Particle Hydrodynamics) method is used here for this purpose because of its natural abilities to predict complex free surface fluid flows and large solid deformations.

A Markerless Motion Capture (MMC) method based on a combination of traditional deep learning (computer vision) approaches, biomechanical models of the human body, and optimization methods is used to perform digitization of human motion from video. This can provide superior twinning of the digital and real-world human motions than can be achieved using computer vision alone. Techniques for predicting muscle and joint loads and peak force acute injury risk using these methods will be described.

The capabilities of such digital twins will be demonstrated in a series of advanced case studies covering:

1. Sporting activities (swimming, diving, and snow skiing).
2. Back injury risk from lifting in workplace Health and Safety scenarios.
3. Intuitive software design using digital twins.

---

## Markerless motion capture for digital human model construction

### Background

Motion capture of human activities is the process of generating a digital representation of the human body undertaking a particular task. The kinematic outputs of this are typically human body joint time series in world coordinates (positions and speeds) or in body coordinates (joint angles and angular speeds). This data can then be used in the construction of digital human models or digital twins.

Optical-based automated motion capture systems have cameras and processing which enables them to complete this task with minimal effort. Fixed cameras can be arranged around a working area where humans will undertake an activity. The cameras need to be calibrated to determine the intrinsic and extrinsic parameters for each camera in a common global coordinate system. Calibration processes make use of relationships between automatically detected image features in 2D (camera) coordinates, their 3D (world) coordinates and known relationships between features in 3D. These input datasets can be obtained by taking multiple pictures of planar boards with patterns like checkerboards ([Zhang, 2000](#)) or using wand-based approaches ([Mitchelson, 2003](#)). After calibration is completed, a particular feature of interest identified in multiple two-dimensional camera views can then be triangulated to determine its three-dimensional location. Repeating this process for multiple features at different times can produce a digital representation of full body kinematics.

Marker-based motion capture has been the industry standard in biomechanics research for the past few decades ([Baker, 2006](#); [Griffiths, 2006](#); [Nagymáte & Kiss, 2018](#); [Richards, 1999](#)). A human subject is covered in dozens of reflective markers and then filmed performing an activity using infrared cameras. Automated computer vision algorithms have been established for detecting these markers. Such methods are robust under controlled good quality lighting conditions inside laboratories. Unfortunately, this is not the case outdoors or in larger or more dynamic environments where varying lighting, glare, and reflections can make marker detection challenging. After manually labeling the recorded marker trajectories, inverse kinematics algorithms can then be used to determine the human body joint angles throughout the activity. This type of approach has seen large-scale adoption in the movie industry with 70% of top grossing films in 2016 using optical motion capture ([Frankton, 2018](#)), in sports with 57 studies identified from 2013 to 2016 using these systems ([Pueo & Jimenez-Olmedo, 2017](#)) and in a large range of biomedical applications primarily to assess movement disorders ([Cimolin & Galli, 2014](#); [Valevicius et al., 2018](#)) or rehabilitation outcomes ([Baker, 2006](#)).

Markerless motion capture (MMC) systems are ones that use the full human subject as recorded by video without the use of specific high visibility markers being attached to the body. MMC is technically more challenging to perform robustly,

but not being dependent on markers creates several advantages. Use of markers takes time and can be uncomfortable and restrictive because of the glue or tape required to hold them in place. Some environments, particularly aquatic ones (e.g., swimming and diving), are challenging for keeping markers attached because of the high fluid and impact forces applied to them. Conventional camera systems can be used (either inside or outside) to record activities.

In a sequence of swimming modeling studies and in the absence of a functioning marker-based motion capture system, the authors developed a manual markerless motion capture process that used orthogonal video footage of the swimmer (Cohen et al., 2014). The process involved animating a rigged biomechanical model of the athletes (based on laser scans) to match the footage from multiple angles. While this produced visually matching kinematics, it was

- labor-intensive and tedious,
- heavily dependent on the skill of the person performing the digitization,
- is not necessarily repeatable, and
- can have a degree of subjectivity.

Ultimately, this bottleneck limits the volume of trials that can be digitized and studied. The authors also used such digitization for platform and springboard diving studies (Cohen, Harrison, & Cleary, 2020; Harrison et al., 2016). This utilized footage from five fixed cameras situated around a diving pool. Camera calibration used visible landmarks around the pool (with known world coordinates) and was refined using landmarks on the athlete simultaneously visible in multiple views. The motion capture used a similar process to the swimming digitization but was assisted by a dynamics engine which could realistically predict rotation and translation of the athletes through their dives. This partial automation enabled almost 60 dives to be digitized. However, this semiautomated approach still remains too labor-intensive for high volume usage.

Computer vision–based human motion capture has been under development for several decades (Moeslund & Granum, 2001). With the broad adoption of Deep Learning–based image processing in recent years, robust automated human pose estimation (identification of body joints and segments) within images are now possible in real time (Cao et al., 2021). Each joint that is automatically identified in at least two camera views can then be triangulated to determine the three-dimensional joint positions. Also, the type of digitization can be undertaken *in situ* (e.g., outside on a sporting field or in a swimming pool) or even during competition. Motion capture for swimming presents additional challenges of water splashing, reflection, refraction, and occlusion that are discussed in *Swimming*. van der Kruk and Reijne (van der Kruk & Reijne, 2018) compared 17 different motion capture systems for sports and concluded that there still remains a gap in measuring systems for high accuracy digitization in large volume spaces for sports like swimming, speed skating, rowing, and track and field. This presents an opportunity for emerging markerless motion capture technologies.

### Overview of MMC pipeline

The steps involved in a general MMC pipeline are shown in Fig. 28.1, which highlights the dependency graph for equipment, activities, and data flow throughout the process. A multicamera system is typically set up and the cameras are calibrated to

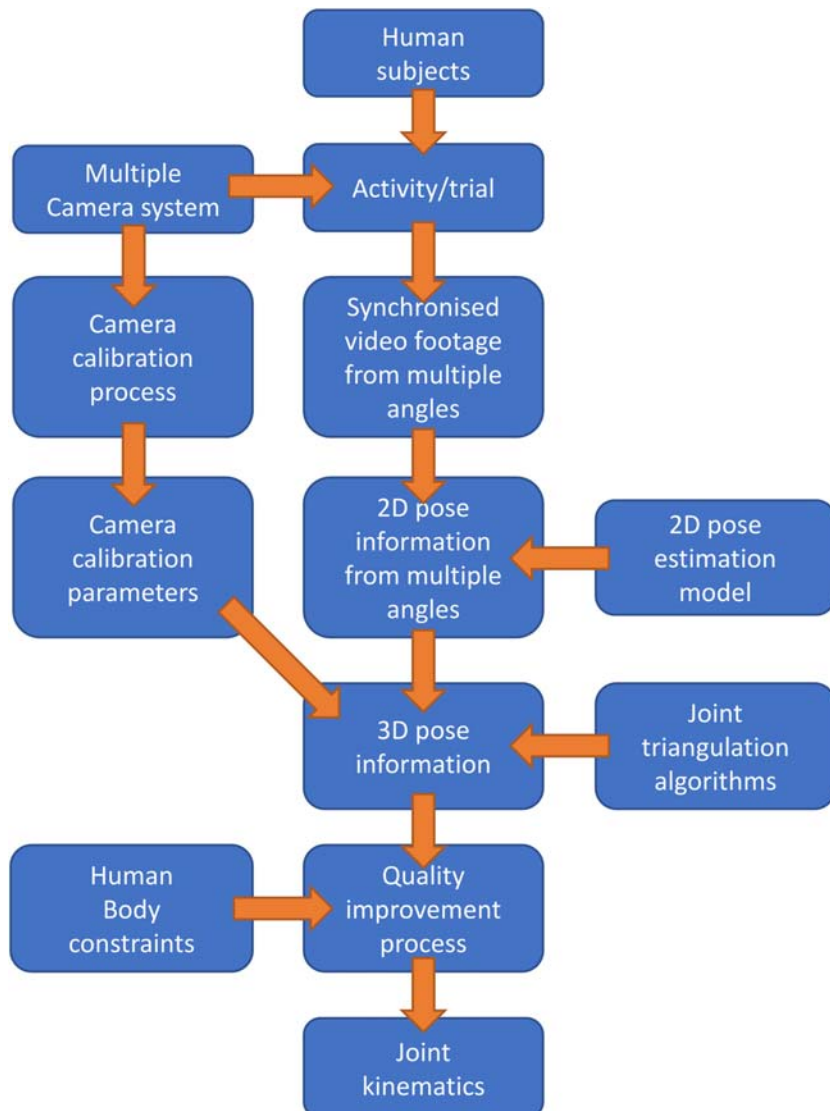


**FIGURE 28.1**

Flow chart of an operational markerless motion capture system for capturing human kinematics for creating human digital twins.

produce the intrinsic and extrinsic camera parameters. Human subjects then undertake activities or trials which are recorded by the multicamera system to produce synchronized video footage from multiple angles. Each frame of footage is then fed through a 2D pose estimation model which identifies image coordinates ( $u, v$ ) of each visible joint. These 2D joint coordinates and the camera calibration parameters are then inputted into joint triangulation algorithms to determine the 3D coordinates ( $x, y, z$ ) of the joints. This data then feeds through an inverse kinematics process (Lu & O'Connor, 1999), which ensures the body pose satisfies the human body constraints (segment lengths, joint flexibility limits, speed limits) and smoothness. Finally, the timeseries of joint angles are outputted from this process for each human considered. The following subsections detail each of the major components of this MMC pipeline.

### ***Two-dimensional pose estimation models***

There are currently several openly available GPU accelerated Deep Learning models for identifying human pose in two dimensions from optical images as shown in Table 28.1. OpenPose (Cao et al., 2021) is capable of real-time multi-person pose estimation, enabling it to detect 25 key points of a simplified human skeleton. It comes pretrained but has licensing restrictions for commercial use. Nakano et al. (2020), reported OpenPose's accuracy (mean absolute error when compared to manual digitization) within 30 mm for 80% of joints in a study with walking, jumping, and ball throwing. DeepLabCut (Mathis et al., 2018) is a flexible feature tracking model (not limited to detecting human body key points) that is useful for research applications but requires training

**Table 28.1** List of publicly available 2D pose estimation models.

Name	Description	Training	Licensing	Detection
OpenPose (Cao et al., 2021)	Real-time multiperson pose estimation	Pretrained	Free for research use, licensing fees for commercial use LGPL	20 key point body and 5 key point face
DeepLabCut (Mathis et al., 2018)	Easy to train models for any object tracking task including human pose estimation	Requires training		User specified
Detectron2 (Wu et al., 2019)	Facebook's pose estimator for PyTorch	Pretrained	Apache 2.0	14 key point body and 5 key point face
BlazePose/ ML kit (Bazarevsky et al., 2020)	Google's pose estimator for iOS and android	Pretrained	Apache 2.0	23 key point body and 9 key point face

for human pose detection. Also, it is unclear how much training effort is required to make this model as robust in different environments as other models like OpenPose. Detectron2 (Wu et al., 2019) is a pose estimator that comes pretrained (for a similar set of key points and simplified skeleton as OpenPose) but is not as suitable for real-time applications because of its slower computation times (processing only a small number of frames per second). However, it runs on desktop machines and its licensing is permissible for deployment in commercial applications. Finally, BlazePose (Bazarevsky et al., 2020) is a fast real-time pose estimator that comes pretrained but is restricted for use on mobile device hardware. The needs of the work described in this chapter were best met by using OpenPose and Detectron2 in the MMC pipeline. The range and capability of the models available highlight that 2D pose estimation functionality is becoming a commodity capability in computer vision.

### ***Three-dimensional pose reconstruction***

The Deep Learning pose estimation models from the previous section identify 2D human poses from still images (Fig. 28.2A, B) that are in different image planes orthogonal to the principal ray direction of each camera. The detected human joints have 2D coordinates ( $u, v$ ) that denote their location within each image. The process of reconstructing a 3D pose (Fig. 28.2C) from two or more 2D poses involves a triangulation step to determine each 3D joint coordinate which is most consistent with the corresponding set of 2D joint coordinates from each camera view. A common optimization approach used is to find the 3D joint coordinate which minimizes the sum of the pixel reprojection error. This error is defined as the distance between the original 2D image coordinates and the reprojection of the 3D coordinate back into each 2D camera view.

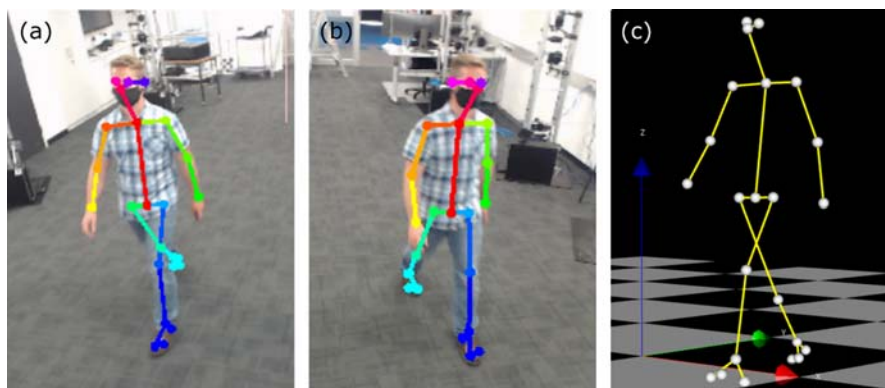


**FIGURE 28.2**

Example of three-dimensional pose reconstruction. Images (A) and (B) show two simultaneous views of a subject walking with the 2D pose identified and overlaid, while image (C) shows the 3D reconstruction of the body pose.

For each joint  $i$ , the pixel reprojection error ( $E$ ) may be expressed as

$$E(x_i, y_i, z_i) = \sum_c w_{i,c} |T_c(x_i, y_i, z_i) - (u_{i,c}, v_{i,c})|^2 \quad (28.1)$$

where  $(x_i, y_i, z_i)$  are the 3D coordinates of the joint  $i$ ,  $(u_{i,c}, v_{i,c})$  are the image coordinates of joint  $i$  in camera  $c$  (detected by the Deep Learning model),  $T_c$  is the projection function for camera  $c$  from world coordinates to 2D image coordinates and  $w_{i,c}$  is the confidence weighting of joint  $i$  in camera  $c$ . Standard iterative nonlinear optimization library algorithms from Dlib (King, 2012) are used to determine the 3D coordinate which minimizes the reprojection error  $E$ . The weighting parameter ( $w_{i,c}$ ) allows for the 2D joint coordinates for a camera to be weighted more or less depending on the confidence in the joint detection by the Deep Learning model (e.g., obscured joints should have lower confidence). Some pose estimation models (e.g., Detectron2) provide joint confidence values as outputs which may be used to specify these weight parameter values.

The optimization to minimize the pixel reprojection error requires an initial guess. A good choice for this is an approximate solution that can be evaluated quickly. Using the calibration parameters for each camera, 2D image coordinates  $(u, v)$  can be transformed into a corresponding ray that originates at the camera,  $R(k)$ . This ray may be expressed as

$$R(k) = (c_x, c_y, c_z) + k F(u, v) = (c_x, c_y, c_z) + k(d_x, d_y, d_z), \quad (k \geq 0) \quad (28.2)$$

where  $F$  is the transformation function,  $(c_x, c_y, c_z)$  are the camera coordinates,  $(d_x, d_y, d_z)$  is the ray direction, and  $k$  is the length of the ray. For each 2D joint coordinate of the cameras, the corresponding rays will pass through the joint in 3D world coordinates. This will not be exact due to camera calibration errors and errors in the pose detection model. However, finding a 3D joint coordinate that minimizes the distance to these rays can be calculated explicitly and only involves a single matrix solution. Therefore, this is a suitable way to provide nonlinear optimization with a reasonable starting guess. Robust convergence of the optimization is affected by the accuracy of camera calibrations, 2D pose estimations, and the number of cameras viewing the joint (using more than two cameras could have multiple locally optimal solutions).

### **Joint angles from inverse kinematics**

To convert the kinematics from 3D joint locations into body joint angles (which define a 3D pose for a human digital twin) requires the use of inverse kinematics. This requires a digital model of each human consisting of a rigid linked skeletal structure, with suitable segment lengths and joint constraints (degrees of freedom and angle limitations). Each of these model parameters and constraints can be determined by the MMC system for an individual by using a specific motion recording procedure. An example of the 3D joint locations for an individual is shown in Fig. 28.2C.

Essentially, the inverse kinematics algorithm tries to determine the  $n$  coordinates (joint angles and center of mass translations) given by  $(\theta_1, \theta_2, \dots, \theta_n)$  that describe the pose, and which minimize the total joint distance error ( $E$ ) between the previously determined 3D joint coordinates  $(x_i, y_i, z_i)$  and the human model joint coordinates  $(X_i, Y_i, Z_i)$ . This error is expressed as

$$\begin{aligned} E(\theta_1, \theta_2, \dots, \theta_n) &= \sum_i w_i |T_i(\theta_1, \theta_2, \dots, \theta_n) - (x_i, y_i, z_i)|^2 \\ &= \sum_i w_i |(X_i, Y_i, Z_i) - (x_i, y_i, z_i)|^2 \end{aligned} \quad (28.3)$$

where  $T_i$  maps the  $n$  joint angles to the 3D coordinates of joint  $i$ , and  $w_i$  is the weighting factor for that particular joint. Standard nonlinear optimization algorithms (King, 2012) are used to find the coordinates  $(\theta_1, \theta_2, \dots, \theta_n)$  which minimize this error function for a given pose. This can be repeated for the entire timeseries, using the joint angles from the previous video frame as the initial guess for the following timestep.

This basic approach, considering each frame in isolation, can result in jittery and unsmooth kinematics. If left untreated, these results can be unphysical and their use can lead to highly erroneous calculations of external and internal body forces. There are a few methods of obtaining physically realistic constrained movements from this type of noisy data. First, the high frequency component can be considered to be system noise and removed by low-pass filtering (e.g. (Sinclair et al., 2013)). Second, and ideally, the closest set of dynamically consistent kinematics to the recorded set can be calculated by optimization approaches such as the direct collocation method (Ackermann & van den Bogert, 2010). This cleansed kinematics data can then be used as input for detailed dynamics models and is then suitable for investigating the external and internal loading of the body and to evaluate effects of movement choices on health and performance.

## Benefits and future applications

The principal benefits of MMC are

- The small amount of setup time that is required. Marker-based systems require lengthy calibration procedures and marker preparation and application processes. Markerless systems are much more quickly calibrated and require no invasive procedures.
- The subjects have no markers on their body that can constrain them or interfere with their natural motions.
- It is potentially more robust than marker-based systems because it cannot suffer from markers falling off during activity. Results are also not dependent on skin movement, which can lead to time-varying offset errors between joints and markers.
- It is not constrained to a biomechanics laboratory because it does not have the strict lighting requirements of a marker-based system. The subjects can perform their activity in the natural environment (or “in the wild”), thereby removing any artificiality of reconstructing the performance in a laboratory.

- It can also be performed using any video data source, including broadcast television.

Since the MMC method detects joints directly from images, its accuracy could be better than approaches which use markers attached to the skin because markers can move relative to the parent body segment throughout an activity and produce substantial measurement errors (Akbarshahi et al., 2010). In sports, huge volumes of previously unquantified video data from competition, in large environments, with varied lighting conditions and in further challenging environments (e.g., during swimming and diving) can be digitized by use of an MMC approach.

---

## Computational methods

A digital twin consists of two types of numerical methods which are then coupled together. The Biomechanics method will be introduced first. The numerical method preferred for the external environment is the Smoothed Particle Hydrodynamics (SPH) method, which will be explained next. The acronym used for the fully coupled Biomechanical-SPH method is B-SPH. Kinematics data determined from motion capture (either manual or MMC) is then used to control the motions of the digital twin with the biomechanics model providing internal information such as joint forces and torques while the SPH component predicts the interaction with the environment (such as water in swimming or diving or snow in skiing).

## Biomechanical methods

### *Introduction*

The structure of the whole-body human model and its anatomical definitions are shown in Fig. 28.3. The model comprises 19 joints and 19 body segments between these joints which is of suitable complexity for each of the applications shown later in the chapter. Each body segment has the prescribed properties:

- center of mass (CoM)
- mass
- moments of inertia
- length

which are determined from data including the motion capture (MMC) data, the mass of the person, and regression equations for body segment inertial properties (Dumas et al., 2007).

The method for simulating the dynamics of the body segments is based on the methods of Legnani et al. (1996a, 1996b). The following kinematics, kinetics, and dynamics algorithms are implemented in C++ code using the CSIRO Workspace platform (Cleary, Thomas, et al., 2020; Workspace, n.d.), and accessed as a plugin to Workspace called Bio-Mechanic (Harrison & Cohen, 2019).

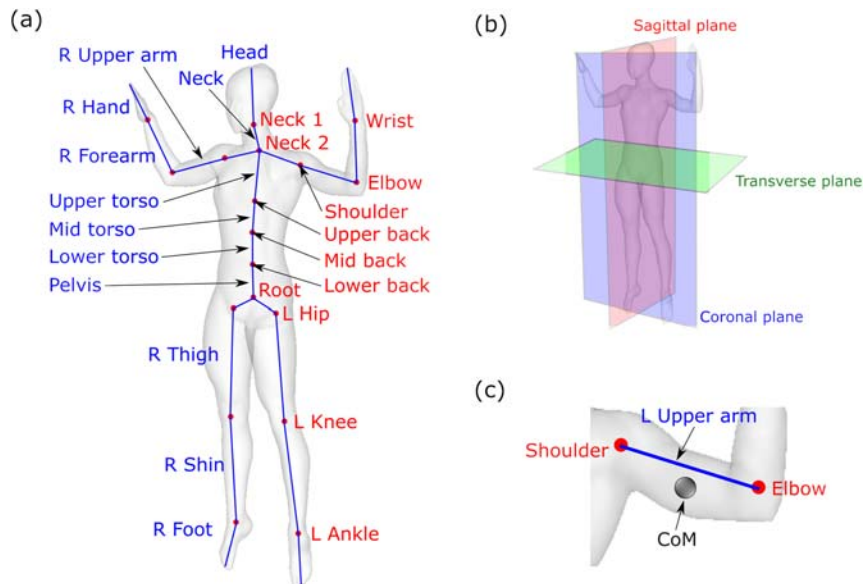


FIGURE 28.3

Biomechanical model of the skeletal system. The entire model is shown in (A). The joints are shown as solid red circles and their names are given in red text. Only the *left-side joints* (from the digital twin's perspective) of the arms and legs are labeled. The *right-side joints* are identified similarly with an "R" prefix. The body segments are shown as blue lines and labeled with blue text. Only the *right-side* (again from the digital twin's perspective) body segments of the arms and legs are labeled. The *left-side* body segments are identified similarly with an "L" prefix. The anatomical planes are shown in (B). The coronal plane is normal to the *front-rear direction*, the sagittal plane is normal to the *left-right direction* and the transverse plane is normal to the *up-down direction*. A typical body segment is shown in (C). Each has a center of mass (CoMs) which is offset from its joints.

### Kinematic definitions and theory

Consider a linkage of rigid body segments, connected by joints (Fig. 28.4). The segment closest to the root joint is called the parent body segment. The one furthest from the root is the child body segment. The parent body segment is proximal to the child body segment, and the child is distal to the parent.

The position and orientation of a body segment can be represented in 3D space using a  $4 \times 4$  matrix,  $T$ :

$$T = \begin{bmatrix} \mathbf{R} & \mathbf{u} \\ 0 & 1 \end{bmatrix} \quad (28.4)$$

where  $R$  is the  $3 \times 3$  rotation matrix defining the orientation of the body segment and  $u$  is a  $3 \times 1$  vector specifying the translation of the body segment from the origin of the world coordinate frame (WC).

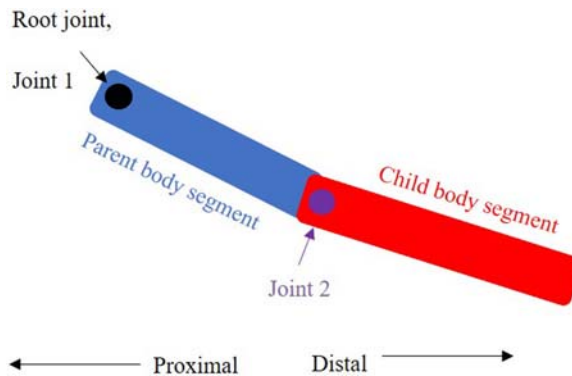


**FIGURE 28.4**

Example arrangement of joints and body segments in the human body model. The model starts with a root joint, which is a point in 3D space. It can have 0–6 degrees of freedom, DoF (either or both rotational and translational DoF). A body segment attaches to this root joint and, like all body segments, has properties of mass, moments of inertia, and center of mass. This body segment has a distal joint, called joint 2 in this example. This joint can have 0–6 DoFs, but typically only has rotational DoF for most applications. A second body segment is attached to joint 2. Body 1 is defined as the parent body of body 2, and body 2 is the child body of body 1.

Each joint  $i$  in the human structural model has between 0 and 6 degrees of freedom (DoF). The total number of DoF for the whole body is  $N$ . The value of each DoF at any time instance is stored in a single vector,  $q$ , for the whole body.

$$\mathbf{q} = \begin{bmatrix} q_1 \\ \dots \\ q_N \end{bmatrix} \quad (28.5)$$

These DoFs are either rotational or translational, and the direction of the movement is determined by an axis and an origin that are defined in the local frame of the body segment. For instance, the knees and elbows are often treated as a one DoF joint in which the DoF is the flexion angle. The shoulders and hips are treated as three DoF joints that can rotate about all three axes. The root joint can rotate and translate relative to the origin and so this interaction is treated as a six DoF joint.

The position and orientation of the  $i$ th body segment relative to its parent body ( $k$ th body segment) in the  $j$ th coordinate frame is expressed as a  $4 \times 4$  matrix,  $T_{i,k}(j)$ , which is dependent only on the degrees of freedom:

$$\mathbf{T}_{i,k(j)} = \begin{bmatrix} \mathbf{R}(\mathbf{q}) & \mathbf{u}(\mathbf{q}) \\ 0 & 1 \end{bmatrix} \quad (28.6)$$

The position of the  $i$ th body segment in WC (0th frame) can be calculated recursively using the relative transforms from each body segment from the root joint to the  $i$ th segment:

$$\mathbf{T}_{i,0(0)} = \prod_{j=1}^i \begin{bmatrix} \mathbf{R}(\mathbf{q}) & \mathbf{u}(\mathbf{q}) \\ 0 & 1 \end{bmatrix} \quad (28.7)$$

Similarly, the velocity of the  $i$ th body segment relative to its parent ( $k$ th body segment), in its local frame ( $i$ ), is prescribed by the rate of change of  $\mathbf{q}$ :

$$\mathbf{V}_{i,k(i)} = \begin{bmatrix} \Omega(\dot{\mathbf{q}}) & \mathbf{v}(\dot{\mathbf{q}}) \\ 0 & 0 \end{bmatrix} \quad (28.8)$$

where  $\Omega$  and  $\mathbf{v}$  are spin and translational velocity terms for the current body segment:

$$\Omega = \begin{bmatrix} 0 & -\omega_z & \omega_y \\ \omega_z & 0 & -\omega_x \\ -\omega_y & \omega_x & 0 \end{bmatrix} \quad (28.9)$$

and

$$\mathbf{v} = \begin{bmatrix} v_x \\ v_y \\ v_z \end{bmatrix}. \quad (28.10)$$

The velocity components,  $v_x$ ,  $v_y$ ,  $v_z$ , and  $\omega_x$ ,  $\omega_y$ ,  $\omega_z$ , are functions of  $\dot{\mathbf{q}}$  and are most often equal to the time derivative of the corresponding DoF,  $\dot{q}_i$ , for the translational and rotational DoF of each axis respectively.

This velocity matrix,  $V$ , can be transformed from the  $i$ th frame to the frame of another body segment, such as the origin (0) using the transform  $T$ :

$$\mathbf{V}_{i,k(0)} = \mathbf{T}_{i,0(0)} \mathbf{V}_{i,k(i)} \mathbf{T}_{i,0(0)}^{-1} \quad (28.11)$$

The velocity of the body segment relative to the origin (the 0th coordinate frame)  $\mathbf{V}_i$  is called the absolute velocity matrix, and this can be calculated from the absolute velocity matrix of the parent's body  $\mathbf{V}_{A_k}$  and the relative velocity between the body segments in the WC frame (0),  $V_{i,k}(0)$ :

$$\mathbf{V}_i^A = \mathbf{V}_k^A + \mathbf{V}_{i,k(0)} \quad (28.12)$$

The acceleration of the current body segment, relative to its parent, in its local frame is prescribed by the matrix  $H$ :

$$\mathbf{H}_{i,k(i)} = \begin{bmatrix} \mathbf{G}(\ddot{\mathbf{q}}, \dot{\mathbf{q}}) & \mathbf{a}(\ddot{\mathbf{q}}) \\ 0 & 0 \end{bmatrix} \quad (28.13)$$

where  $G$  and  $a$  are spin and translational acceleration terms on the current body segment:

$$\mathbf{G} = \dot{\Omega} + \Omega^2, \quad (28.14)$$

$\dot{\Omega}$  is a function of the rotational accelerations,  $\alpha_x$ ,  $\alpha_y$ , and  $\alpha_z$  of the current joint:

$$\dot{\Omega} = \begin{bmatrix} 0 & -\alpha_z & \alpha_y \\ \alpha_z & 0 & -\alpha_x \\ -\alpha_y & \alpha_x & 0 \end{bmatrix}, \quad (28.15)$$

$$\mathbf{a} = \begin{bmatrix} a_x \\ a_y \\ a_z \end{bmatrix}. \quad (28.16)$$

and  $a$  is a vector of linear accelerations  $a_x$ ,  $a_y$ , and  $a_z$  of the current joint:

The acceleration components,  $a_x$ ,  $a_y$ ,  $a_z$  and  $\alpha_x$ ,  $\alpha_y$ ,  $\alpha_z$ , are functions of  $\ddot{\mathbf{q}}$  and are most often equal to the second time derivative of the corresponding DoF,  $\ddot{q}_i$ , for the translational and rotational DoF of each axis, respectively.

The relative acceleration matrix  $H_{i,k}$  can be transformed to another frame, such as the WC frame (0) using the transform  $T$ , in the same way as for the velocity in Eq. (28.11):

$$\mathbf{H}_{i,k(0)} = \mathbf{T}_{i,0(0)} \mathbf{H}_{i,k(i)} \mathbf{T}_{i,0(0)}^{-1} \quad (28.17)$$

The acceleration matrix relative to the WC frame is called the absolute acceleration matrix, and it can be calculated from the absolute acceleration HA and absolute velocity VA matrices of its parent body segment. Note that the velocity terms correspond to centripetal and Coriolis accelerations, which are the diagonal and nondiagonal terms in the  $\mathbf{V}_k^A \mathbf{V}_{i,k(0)}$  terms:

$$\mathbf{H}_i^A = \mathbf{H}_k^A + \mathbf{H}_{i,k(0)} + \mathbf{V}_k^A \mathbf{V}_{i,k(0)} \quad (28.18)$$

The instantaneous screw axis (ISA),  $L$ , is useful for understanding how speeds, accelerations, and forces can be mapped to an individual DoF ( $q_i$ ). For instance, one may wish to calculate the magnitude of the joint torque about the instantaneous flexion–extension axis of the knee from the full torque vector in the WC frame. It can be defined for any infinitesimal time period as the axis about which that coordinate acts.  $L$  is calculated from the velocity matrix:

$$\mathbf{L}_{(j)}^i = \frac{\mathbf{V}(\hat{\mathbf{q}}^i)_{j,k(j)}}{\dot{q}_i}, \quad (28.19)$$

where  $\hat{\mathbf{q}}^i$  is a vector of length  $N$  (equal to the length of  $q$ ) in which  $\hat{q}_i^i = q_i$ , but all other components are zero.

When  $q_i$  specifies a linear motion for body segment  $i$ , then

$$\mathbf{L}_{(j)}^i = \frac{\begin{bmatrix} 0 & v(\hat{\mathbf{q}}^i) \\ 0 & 0 \end{bmatrix}}{\dot{q}_i} \quad (28.20)$$

And when  $q_i$  specifies a rotational motion for body segment  $i$ , then

$$\mathbf{L}_{(j)}^i = \frac{\begin{bmatrix} \Omega(\hat{\mathbf{q}}^i) & 0 \\ 0 & 0 \end{bmatrix}}{\dot{q}_i}. \quad (28.21)$$

As with the other kinematic variables,  $L$  is transformed from the local body segment frame to the WC frame using  $T$ :

$$\mathbf{L}_{(0)}^i = \mathbf{T}_{i,0(0)} \mathbf{L}_{(j)}^i \mathbf{T}_{i,0(0)}^{-1} \quad (28.22)$$

### Kinetics

The mathematical treatment of forces in the field of Biomechanics is termed “Kinetics.” Here, we define the matrices that quantify external, inertia, and gravity forces, which are used in the next section to relate kinematics to kinetics.

The external forces (and muscle or spring forces, if present) applied to a body are prescribed as an action matrix  $\Phi$ :

$$\Phi_{i(i)} = \begin{bmatrix} 0 & -t_z & t_y & f_x \\ t_z & 0 & -t_x & f_y \\ -t_y & t_x & 0 & f_z \\ -f_x & -f_y & -f_z & 0 \end{bmatrix} \quad (28.23)$$

where  $t_x, t_y, t_z$  are the torques and  $f_x, f_y, f_z$  are the linear forces about the axes on the  $i$ th body segment in its local frame.

The inertia matrix for each body segment is given by  $J$

$$\mathbf{J}_{i(i)} = \begin{bmatrix} I_{xx} & I_{xy} & I_{xz} & p_x \\ I_{yx} & I_{yy} & I_{yz} & p_y \\ I_{zx} & I_{zy} & I_{zz} & p_z \\ -p_x & -p_y & -p_z & m \end{bmatrix} \quad (28.24)$$

where  $m$  is the mass of the body segment, vector  $P$  is defined by

$$\mathbf{p} = [p_x \ p_y \ p_z] = m[r_x \ r_y \ r_z] \quad (28.25)$$

and  $r_x, r_y, r_z$  are the coordinates of the center of mass of the body segment in its own frame.

The acceleration due to gravity,  $G$  (which acts in the world frame and is then inherited by all the child segments in the body structure), is simply

$$\mathbf{G}_{(0)} = \begin{bmatrix} 0 & 0 & 0 & g_x \\ 0 & 0 & 0 & g_y \\ 0 & 0 & 0 & g_z \\ 0 & 0 & 0 & 0 \end{bmatrix} \quad (28.26)$$

where  $g_x, g_y, g_z$  are the components of gravity in the world frame.

The net force,  $\Psi$ , on the  $k$ th joint is obtained by summing its action matrix ( $\Phi_{k(0)}$ ) with the actions of joints distal to it (joints  $k + 1$  to  $P$ ), as well as their inertia and gravity actions:

$$\Psi_{k(0)} = \sum_{i=k}^P [-\text{skew}(\mathbf{H}_{i,0(0)} \mathbf{J}_{i(0)}) + \text{skew}(\mathbf{G}_{i(0)} \mathbf{J}_{i(0)}) + \Phi_{i(0)}], \quad (28.27)$$

where the operator “skew” is defined as

$$\text{skew}(\mathbf{AB}) = \mathbf{AB} - \mathbf{BA}^T \quad (28.28)$$

### Dynamics

Newton–Euler or Lagrangian methods can be used to relate kinematic and kinetic terms above for each of the joints and body segments. Lengani et al. (1996a, 1996b) showed that the dynamics of the system can be represented using the following equations:

$$\mathbf{M}\ddot{\mathbf{q}} = \mathbf{D}(\mathbf{q}, \dot{\mathbf{q}}) + \mathbf{F}, \quad (28.29)$$

where  $D$  and  $F$  are column vectors of length  $N$  and  $M$  is an  $N \times N$  mass matrix, and it should be recalled that  $q$  is a vector with all DoF for the entire body.

The operator  $\otimes$  is defined as (Legnani et al., 1996a, 1996b)

$$\mathbf{A} \otimes \mathbf{B} = \mathbf{A}_{2,1} \mathbf{B}_{2,1} + \mathbf{A}_{1,3} \mathbf{B}_{1,3} + \mathbf{A}_{3,2} \mathbf{B}_{3,2} + \mathbf{A}_{1,4} \mathbf{B}_{1,4} + \mathbf{A}_{2,4} \mathbf{B}_{2,4} + \mathbf{A}_{3,4} \mathbf{B}_{3,4}. \quad (28.30)$$

$F$  is the action on the  $i$ th joint about the ISA of the  $j$ th DoF.

$$\mathbf{F} = \sum_{m=j}^P (\Phi_{m(0)} \otimes \mathbf{L}_{(0)}^j) \quad (28.31)$$

Here actions are summed from the  $i$ th joint to the  $P$ th joint, which is the most distal joint to the  $i$ th joint.

The components of the mass matrix,  $M$ , are given by

$$\mathbf{M}_{ij} = \text{trace} \left( \mathbf{L}_{(0)}^j \left\{ \sum_{k=\max(i,j)}^P \mathbf{J}_{k(0)} \right\} \mathbf{L}_{(0)}^{j \ T} \right). \quad (28.32)$$

Inertia and gravity terms are lumped into a matrix  $D$  which represents the dynamic effects:

$$\mathbf{D}_j = \text{trace} \left[ \sum_{m=j}^P \left( (\mathbf{C}_{m,0(0)} - \mathbf{G}_{(0)}) \mathbf{J}_{m(0)} \mathbf{L}_{(0)}^{j \ T} \right) \right] \quad (28.33)$$

Here  $\mathbf{C}_{i,0(0)}$  are the acceleration terms with the  $\ddot{q}$  contributions removed, leaving only the Coriolis ( $V_i \times V_j$ ) and centrifugal ( $V_i^2/2$ ) terms:

$$\mathbf{C}_{i,0(0)} = \sum_{m=1}^i (\mathbf{V}_{m-1,0(0)} \mathbf{V}_{m,m-1(0)} - \mathbf{V}_{m,m-1(0)} \mathbf{V}_{m-1,0(0)}) + \mathbf{V}_{i,i-1(0)}^2 \quad (28.34)$$

The second derivative of  $q$  can then be calculated by rearranging Eq. (28.29):

$$\ddot{\mathbf{q}} = \mathbf{M}^{-1} [\mathbf{D} + \mathbf{F}] \quad (28.35)$$

Critically, the acceleration vector  $\ddot{\mathbf{q}}$  depends on the inertia, muscle, gravity, and external forces from only the joints distal to the current joint (hence the sums from  $j$  to  $P$  in the  $F$ ,  $M$  and  $D$  terms). If individual  $q$  terms are known (i.e., are not dynamically predicted), then the corresponding components of  $D$  and  $F$  can be calculated from Eq. (28.29).

Values of  $q$  can be calculated from Eq. (28.35) using numerical integration. We use the semiimplicit Euler method:

$$\dot{\mathbf{q}}_{n+1} = \dot{\mathbf{q}}_n + \Delta t \mathbf{M}^{-1} [\mathbf{D} + \mathbf{F}] \quad (28.36)$$

$$\mathbf{q}_{n+1} = \mathbf{q}_n + \Delta t \dot{\mathbf{q}}_{n+1} \quad (28.37)$$

## SPH method for simulating the external environment

### SPH method for fluids

The Smoothed Particle Hydrodynamics (SPH) method is a Lagrangian mesh-free CFD (Computational Fluid Dynamics) method that can automatically predict complex free surface behavior, including waves and splashing. It uses virtual particles to represent specific volumes of material. The classical SPH method was introduced for incompressible fluid flow by Monaghan (1994) and has been broadly adopted over the last 2 decades. General reviews of SPH, method components and some applications are given by Monaghan (2005, 2012) and Cleary et al. (2007), Cleary, Harrison, et al. (2020).

The SPH continuity equation, from Monaghan (1992), is

$$\frac{d\rho_a}{dt} = \sum_b m_b (\mathbf{v}_a - \mathbf{v}_b) \cdot \nabla W_{ab}. \quad (28.38)$$

with  $\mathbf{r}_{ab} = \mathbf{r}_a - \mathbf{r}_b$  being the position vector from particle b to particle a and  $W_{ab} = W(\mathbf{r}_{ab}, h)$  being the interpolation kernel with smoothing length h evaluated for the relative particle separation  $|\mathbf{r}_{ab}|$ .

The momentum equation gives the acceleration of each SPH particle:

$$\frac{d\mathbf{v}_a}{dt} = \mathbf{g} - \sum_b m_b \left[ \left( \frac{P_b}{\rho_b^2} + \frac{P_a}{\rho_a^2} \right) - \frac{\xi}{\rho_a \rho_b} \frac{4\mu_a \mu_b}{(\mu_a + \mu_b)} \frac{\mathbf{v}_{ab} \mathbf{r}_{ab}}{\mathbf{r}_{ab}^2} \right] \nabla_a W_{ab} \quad (28.39)$$

where  $P_a$  and  $\mu_a$  are the pressure and viscosity of particle  $a$ ,  $\mathbf{v}_{ab} = \mathbf{v}_a - \mathbf{v}_b$ ,  $\eta$  is a small parameter used to smooth out the singularity at  $r_{ab} = 0$ , and  $\mathbf{g}$  is gravity. This form is suitable for all the fluid modeling applications presented in this chapter.

In the classical SPH method, a weakly compressible (WC) assumption is made so that the pressure is explicitly given from the density using an equation of state. The form from Batchelor (1973) is used:

$$P = P_0 \left[ \left( \frac{\rho}{\rho_0} \right)^\gamma - 1 \right] \quad (28.40)$$

where  $P_0$  is the magnitude of the pressure and  $\rho_0$  is the reference density. The pressure scale is set based on  $c$  which is the numerical speed of sound according to

$$\frac{\gamma P_0}{\rho_0} = 100 V^2 = c^2, \quad (28.41)$$

where the pre-factor 100 means that the maximum particle speed corresponds to Mach 0.1 based on this choice of numerical sound speed.  $V$  is a characteristic maximum physical velocity for the flow. This means that density variations are at most 1%, giving weakly compressible fluid flow behavior. For fluids such as water or aqueous solutions,  $\gamma = 7$  is used.

### **SPH method for elastic and elastoplastic solids**

SPH can also be used to predict solid deformation including elastoplastic behavior (Cleary & Das, 2008; Gray et al., 2001). Its Lagrangian nature gives specific advantages in tracking history dependence such as for material type, stress and strain history, yield stress change, and plastic strain.

The stress tensor  $s$  is partitioned into a volumetric (pressure)  $P$  and deviatoric component  $S$ . A linear elastic (Hookean) constitutive model is assumed for the stress versus strain relationship. This gives an evolution equation for  $S$  which in component form (Liberky & Petschek, 1990) is

$$\frac{dS^{ij}}{dt} = 2G \left( \dot{\epsilon}^{ij} - \frac{1}{3} \delta^{ij} \dot{\epsilon}^{kk} \right) + S^{ik} \Omega^{jk} + \Omega^{ik} S^{kj} \quad (28.42)$$

where the superscripts refer to coordinate directions with summation implied on repeated indices and  $G$  is the shear modulus of the material. The strain rate tensor

is calculated in component form (Gray et al., 2001) and summed on each particle (Harrison & Cleary, 2014):

$$\dot{\varepsilon}_a = \frac{1}{2} \sum_b \frac{m_b}{\rho_b} [(\mathbf{v}_{ab} \nabla_a W_{ab})^T + \mathbf{v}_{ab} \nabla_a W_{ab}]. \quad (28.43)$$

The rotation tensor is summed on each particle by

$$\Omega_a = \frac{1}{2} \sum_b \frac{m_b}{\rho_b} [(\mathbf{v}_{ab} \nabla_a W_{ab})^T - \mathbf{v}_{ab} \nabla_a W_{ab}]. \quad (28.44)$$

The SPH discretization of the momentum equation for solids (from Gray et al., 2001) is

$$\frac{d\mathbf{v}_a}{dt} = \sum_b m_b \left( \frac{\boldsymbol{\sigma}_a}{\rho_a^2} + \frac{\boldsymbol{\sigma}_b}{\rho_b^2} + \Pi_{ab} \mathbf{I} \right) \cdot \nabla_a W_{ab} + \mathbf{g} \quad (28.45)$$

where  $\boldsymbol{\sigma}_a$  and  $\boldsymbol{\sigma}_b$  are the stress tensors of particles  $a$  and  $b$ . The artificial viscosity  $\Pi_{ab}$  proposed by Monaghan and Gingold (Monaghan & Gingold, 1983) provides numerical stabilization. The tensile instability correction of Monaghan is also used with coefficient 0.3 (Das & Cleary, 2015a).

The SPH form of the continuity equation for solid deformation is the same as for fluids and is given in Eq. (28.38). The equation of state used for solids is

$$P = c^2 (\rho - \rho_0) \quad (28.46)$$

where  $\rho_0$  is the reference density,  $\rho$  is the current density, and  $c$  is the speed of sound in the solid material. The sound speed  $c$  is calculated from the material bulk modulus  $K$  using

$$c = \sqrt{\frac{K}{\rho_0}}. \quad (28.47)$$

The Poisson ratio,  $\nu$ , is

$$\nu = \frac{\left(\frac{3K}{G} - 2\right)}{2\left(\frac{3K}{G} + 1\right)} \quad (28.48)$$

Detailed verification of transient and long-term stresses under uniaxial loading conditions has been performed (Das & Cleary, 2015a), demonstrating that SPH solutions are comparably accurate to FEM solutions.

The radial return plasticity model of Wilkins (1964) is used to model elastoplastic deformation. This is sometimes known as the von Mises plasticity model. A trial deviatoric stress  $S_{tr}$  is calculated assuming an initial elastic response. The increment of plastic strain is

$$\Delta \varepsilon^p = \frac{\sigma_{vm} - \sigma_y}{3G + H} \quad (28.49)$$

where  $\sigma_{vm}$  is the von Mises stress,  $\sigma_y$  is the current yield stress, and  $H$  is the hardening modulus of the material. The plastic strain is then incremented:

$$\epsilon^p = \epsilon^p + \Delta\epsilon^p \quad (28.50)$$

The yield stress increment  $\Delta\sigma_y$  at each time step is calculated as

$$\Delta\sigma_y = H\Delta\epsilon^p \quad (28.51)$$

The deviatoric stress at the end of a time step is given by

$$\mathbf{S} = r_s \mathbf{S}_{tr} \quad (28.52)$$

where  $r_s$  is the radial scale factor given by

$$r_s = \sigma_y / \sigma_{vm} \quad (28.53)$$

The SPH implementation of this model is described in Cleary and Das (2008), and applications of this method to elastoplastic solid deformation are given in Cleary (2010), Das and Cleary (2015b), (2015c), Cleary et al. (2012), and Prakash and Cleary (2015).

### **SPH boundary modeling**

The boundary surfaces of the human body and the environment (such as the pool for swimming or the skis in ski jumping) with which the SPH discretized fluids and solids interact are represented by typically a single layer of boundary particles. Each particle exerts both a normal repulsive force and a shear viscous force on any nearby fluid particles. This approach is explained in detail in Cummins et al. (2012), and Cleary, Harrison, et al. (2020). This is a powerful and very flexible boundary treatment that allows extremely complex solid boundaries, both stationary and moving, to be modeled (Cleary et al., 2007). It also allows deforming boundaries to be modeled (Cohen et al., 2012; Sinnott et al., 2012).

Geometry preparation (mesh clean-up and the construction of surface normals) is performed using preprocessing workflows built on Workspace (which is a workflow platform for building and configuring reusable software (see Workspace (n.d.) and Cleary, Thomas, et al. (2020), for details).

### **Integration of SPH equations**

The equations of motion for the particles (28.38) and (28.39), and any secondary physics or chemistry equations, are integrated using an explicit second-order predictor–corrector (see Monaghan (1994), and Cummins et al. (2012), for details). The limit for stable explicit integration is given by the Courant condition modified for viscosity (see Monaghan (1994)).

## **Using digital twins to understand performance and injury: sports examples**

### **Swimming**

SPH modeling of elite level swimming is a tool for investigating athlete performance that aims to complement pool-based experimentation, testing, and training. Such

modeling is subject-specific, using anthropometry and technique from each individual athlete. It produces extensive data that is otherwise unavailable including time-series of bulk speeds, accelerations, and forces; whole body and part-body forces; and flow structure visualizations. When coupled with biomechanical modeling, additional data can be predicted, including joint torques, joint powers, and muscle forces. Aside from providing insightful data, modeling also allows the researcher to experiment with each aspect of technique in isolation to consider their impacts. A series of SPH swimming modeling studies have been published by the authors (Cleary et al., 2013; Cleary, Harrison, et al., 2020; Cohen et al., 2012, 2015, 2018; Cohen, Cleary, et al., 2020; Harrison, Cohen, et al., 2014). Human swimming modeling is challenging because it requires very detailed motion capture of individual athletes and computationally intensive fluid dynamics modeling. Both of these key aspects are expanded upon in this section.

The motion capture accuracy requirements for swimming are very high because the whole-body surface interacts with the water to propel the swimmer, and this is critical to any CFD modeling. Traditional industry standard marker-based motion capture systems (e.g., Vicon Motion Capture System, Vicon, USA) are impractical in swimming because the bulky markers cannot withstand the rigors of the water, and the infra-red capture system does not work well in a water environment. Optical-based markerless systems are still challenging because of the effects of water surface refraction and reflection, splashing, and bubbles, which occlude varying fractions of the swimmer throughout each stroke. These problems can be overcome by redundancy, using many cameras both above and below the water surface. Manual MMC was used in the early SPH studies using the process outlined in Cohen et al. (2014), but automated markerless motion capture using deep learning and computer vision may soon become a time- and labor-saving alternative (see section titled “Markerless Motion Capture”). Manual MMC was also used by von Loebbecke et al. (2009), for CFD simulations of full body swimming.

Human swimming presents a unique combination of challenges to computational fluid dynamics (CFD) modeling. The water free surface, splashing, and the rapidly deforming swimmer geometry are difficult to model using mesh-based CFD approaches, however the mesh-less Lagrangian SPH method is very well suited to these requirements (Cleary, Harrison, et al., 2020). To date, the SPH method has been used with a single uniform spatial resolution. This necessitates a large number of particles to be used in the discretization of the computational domain to adequately resolve the small-scale flow features such as a boundary layer adjacent to the dynamically deforming swimmer and the wake regions. Adaptive variable resolution is available as a part of the method but has so far not been used to reduce computation times. Additionally, SPH does not employ an explicit physical turbulence model for the subgrid scales and instead relies on numerical dissipation to absorb energy transferred from the large to small scales (Cleary et al., 2007; Cleary, Harrison, et al., 2020). In spite of these challenges, SPH has been shown to produce realistic simulation results with swimming speeds consistent with those observed in real swimmers (Cohen et al., 2018).

In this section, a case study of a swimmer completing a freestyle turn is considered. Most competitive swimming is conducted in 50 m long pools with races exceeding this distance requiring multiple laps to be completed. Transitioning from one lap to another necessitates the swimmer to execute a turn, whereby they rotate their body and push off the wall using their legs and feet. Optimizing this maneuver is critical to the success of the swimmer, because significant time can be gained or lost on their competitors. The typical performance metric for the turn is the “total turning time” (Morais et al., 2019), which is defined as how long it takes a swimmer to travel from the 5 m point before the wall on approach (before the turn) to the 15 m point from the wall (after the turn). This single parameter encapsulates many key aspects of the technique including:

1. How fast they surface free-swim on approach.
2. How quickly they somersault (tumble) to reverse their body orientation.
3. How crouched their legs get when in contact with the wall, to facilitate bigger push-off.
4. How fast they leave the wall from the push off (leg extension).
5. How well they glide under water.
6. How well they perform dolphin kick under water.
7. How well they surface and transition to surface-swimming.

It is well known that swimming at least 0.7 m below the water surface is effective for maintaining the high speeds achieved after wall push-off because it reduces wave drag (Vennell et al., 2006). This is such an advantage that international racing rules mandate that swimmers must surface before the 15 m point of each lap.

In this study, video footage was taken from multiple cameras (some stationary and some moving above and below the water surface) of a swimmer completing a freestyle turn (Fig. 28.5). A laser body scan of the athlete was rigged to a skeletal structure using the commercial animation package Maya (Autodesk Inc., San

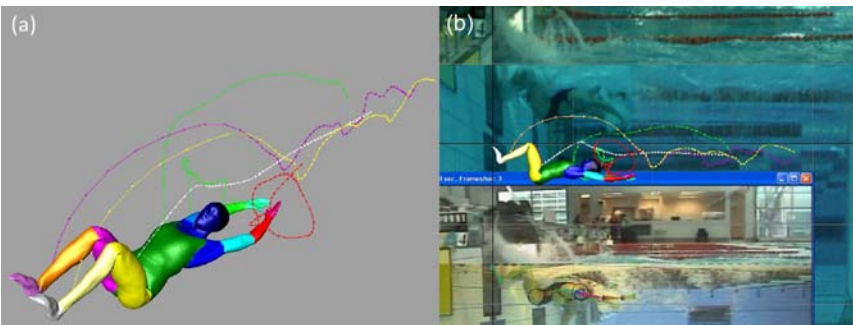


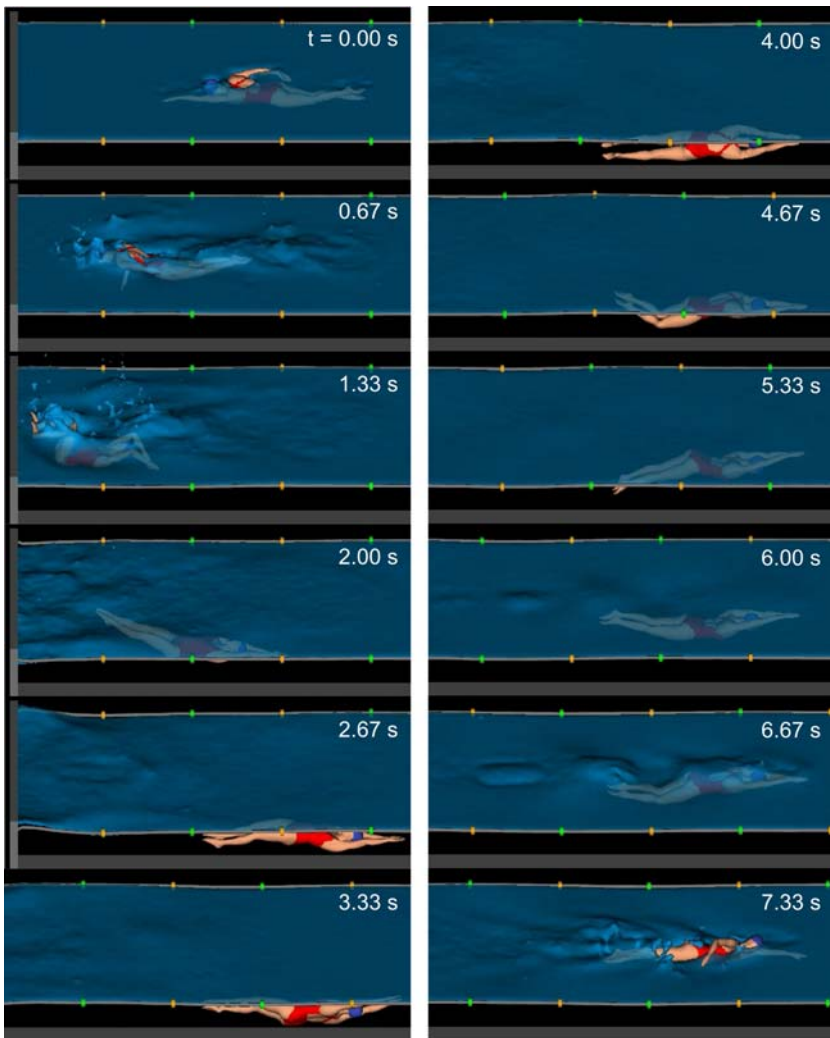
**FIGURE 28.5**

Screenshots of the manual motion capture process showing the biomechanical model (multicolored) from the same perspective at the video footage, skeletal structure, and joint motion trails. (A) Oblique view, and (B) side-on view.

Rafael, CA) using the process outlined in Cohen et al. (2014). The previously described manual MMC process was then performed to obtain the full technique and motion of the swimmer (Fig. 28.5), however it was done in a stationary (pool)-based reference frame which also generated the center of mass translations of the swimmer. For each time frame, the pose of the swimmer was simultaneously matched to the footage from each video perspective. This process produced the full three-dimensional kinematics of the swimmer for use by the biomechanical model that interacts with the SPH model of the fluid.

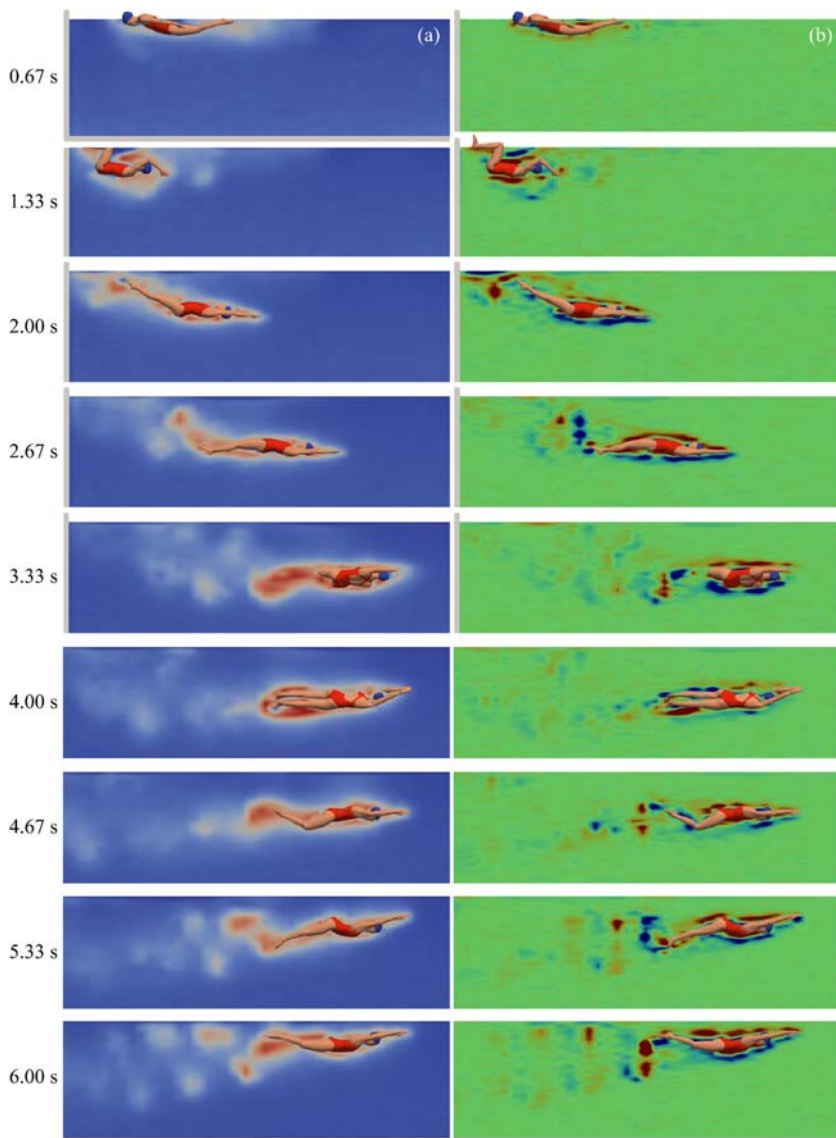
The biomechanical model of the swimmer completing a freestyle turn was then placed within a 15 m long tank of fluid simulated using the SPH method. The swimmer digital twin was then allowed to swim through the fluid and execute the turn maneuver as shown in Fig. 28.6. At time 0.0 the swimmer is located on the surface and is just completing the right arm recovery part of the stroke. The water surface appears undisturbed because this is the start (initial condition) of the fluid simulation. At time 0.66 s (from the start of the simulation), the swimmer is approaching the wall, and both a bow wave and wake are visible on the free surface. The right arm has almost completed its pull phase after causing a splash on arm entry while the left arm has completed its pull phase and is about to exit the water. The higher frequency kicking legs have caused visible surface waves behind the swimmer. At time 1.33 s, the swimmer is in contact with the wall in a crouched position, after having completed a forward somersault in the water. The swimmer then pushes off the wall and commences a high-speed underwater glide while rolling from the supine orientation that is produced by the somersault to the prone orientation needed to resume the freestyle stroke (2.00–4.00 s). By time 4.67 s the swimmer has commenced dolphin kicking while they move higher in the water approaching the free surface. As the depth of water above the swimmer decreases (as the swimmer rises toward the surface) the water activated by the swimmer's kicking starts to reach and interact with the surface. The kicking strokes visibly affect the water surface by time 6.00 s, which is well before the swimmer breaks the surface at time 7.33 s and recommences freestyle swimming. These qualitative aspects of the free surface behavior are consistent with the video footage and provide confidence in the modeling of the swimmer–water interaction.

By coloring a sagittal plane slice of the fluid by speed and spanwise vorticity (Fig. 28.7), the behavior of the water around the swimmer during the turn maneuver can also be analyzed. The swimmer speed slices (Fig. 28.7A) displays the entrained fluid around the swimmer due to the no slip boundary condition. This is a visual representation of the added water mass that the swimmer has to accelerate with them during the turn maneuver, which has been experimentally shown to be about one quarter of a swimmer's effective mass during glides (Caspersen et al., 2010). After push-off ( $t \geq 2.00$  s) the alternating dolphin kick produces high speed fluid which remains visible in the wake as the swimmer moves along the pool. Stable vortex rings are shed by the legs and feet (Fig. 28.7B). This is consistent with the flow structures observed in an earlier dolphin kick study (Cohen et al., 2012). By considering the spanwise vorticity (b), one can observe that the alternating spanwise vorticity

**FIGURE 28.6**

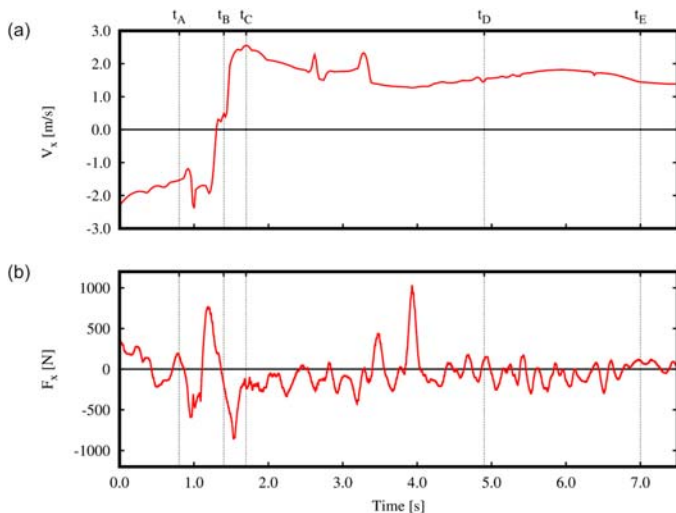
Side-on free surface visualization of the digital twin swimmer model completing the freestyle turn during the SPH simulation.

generated by the legs is strongest (in this particular plane) when the swimmer is supine ( $t = 2.67$  s) and prone ( $t \geq 4.67$  s) since the vortex structures are orientated differently during the roll. The entrained fluid near the body is observed to be a shear (boundary) layer that has opposite signs of spanwise vorticity on the top and bottom surfaces of the body. The longer this boundary layer can stay attached along the body before separating, the more the pressure can recover (increase toward the rear) and reduce the resulting pressure drag (created by the pressure difference between the

**FIGURE 28.7**

Side-on views of the fluid in the sagittal plane colored by (A) fluid speed (*blue* is 0.0 m/s and *red* is 1.5 m/s) and (B) fluid spanwise vorticity (*red* is 10 m<sup>2</sup>/s, *green* is 0.0 m<sup>2</sup>/s and *blue* is -10 m<sup>2</sup>/s).

high-pressure fluid at the front of the swimmer and the low pressure fluid in the wake) experienced by the swimmer. Managing such deferral of flow separation while simultaneously maximizing propulsion is a delicate balance that swimmers and coaches are challenged by.

**FIGURE 28.8**

Time history of the (A) digital twin swimmer velocity and (B) net fluid force on the digital swimmer. The labeled times are the tumble turn start ( $t_A$ ), wall touch start ( $t_B$ ), wall touch end ( $t_C$ ), swimmer completed rotating from supine to prone orientations ( $t_D$ ), and swimmer surfacing ( $t_E$ ).

Finally, the motion of the swimmer can also be scrutinized by considering the time histories of the (fully prescribed) swimmer speed and net fluid forces (Fig. 28.8). As the swimmer approaches the wall their velocity is negative (approximately  $-2.0$  m/s) and changes to a high positive velocity (approximately  $2.5$  m/s) after tumbling and pushing off the wall (at  $t_C$ ). This speed gradually reduces to about  $1.5$  m/s (at  $t_D$ ) after gliding and rolling. This velocity slightly increases then decreases before the swimmer breaks the water surface (at  $t_E$ ). The corresponding streamwise fluid forces (calculated from the SPH simulation) on the swimmer show positive and negative values throughout each stroke. This is to be expected in predominantly free swimming. During the somersault (tumble turn) and before the wall touch there is a large peak in force which slows down the swimmer. This should be expected as the somersault position is not at all streamlined and presents a large cross-sectional area in the streamwise direction leading to strong drag. The contact forces from the swimmer pushing off the wall are not represented in this fluid force plot shown. Once the swimmer is moving away from the wall at high speed ( $t > t_C$ ), there is a period of mainly negative force (drag) which slows down the swimmer slightly until they achieve a speed where there is a balance between propulsion and drag at about  $t = 4.0$  s. After this there are regular positive and negative fluctuations throughout the stroke.

Further investigation into technique variations can be carried out using this type of model to determine how the swimmer can improve their baseline turn technique.

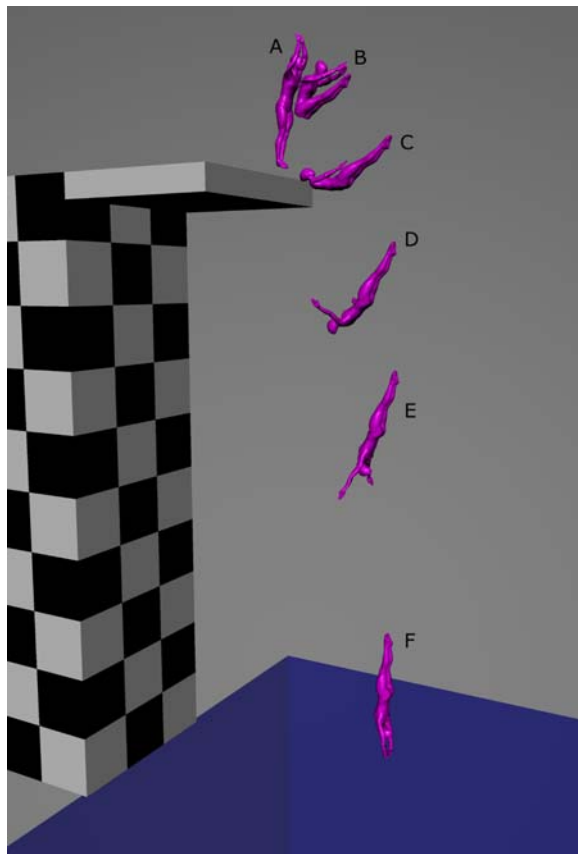
## Diving

Platform and springboard diving are sports that combine strength, explosive power, and precise technique to produce somersaults and twists in the air before entering the water with a vertical body orientation and minimal splash. Small changes to in-flight movements can result in large changes to body alignment at water entry. The high approach speed between the body and water (especially for the 10 m platform dive) imparts large forces on the arms, head, neck, and torso. These forces are implicated in injuries to the shoulders, back, and upper arms (Rubin, 1999). Efforts to improve performance come with the challenges associated with the effects of small changes to technique on performance outcomes and increased injury risk. Physical experimentation such as marker-based motion capture, electromyography (EMG), or pressure measurements are impossible due to the long travel of the athlete through the air and the high forces that occur at water impact. Computational modeling has been successfully used to experiment with and refine in-flight technique (Cohen, Harrison, & Cleary, 2020) and calculate forces at water entry (Harrison et al., 2016) to enable injury risk evaluation.

Here we demonstrate a use of a digital twin to compare two entry techniques used by an athlete for the same dive. The surface of the athlete's body is modeled using a surface mesh derived from a laser scan and deformed using a virtual skeleton and linear blend skin rigging (Harrison et al., 2016). The technique was digitized using a combination of video footage from five synchronized cameras and a markerless motion capture method that matches the deformed surface mesh shape with projections into each camera view (Cohen et al., 2014; Harrison et al., 2016).

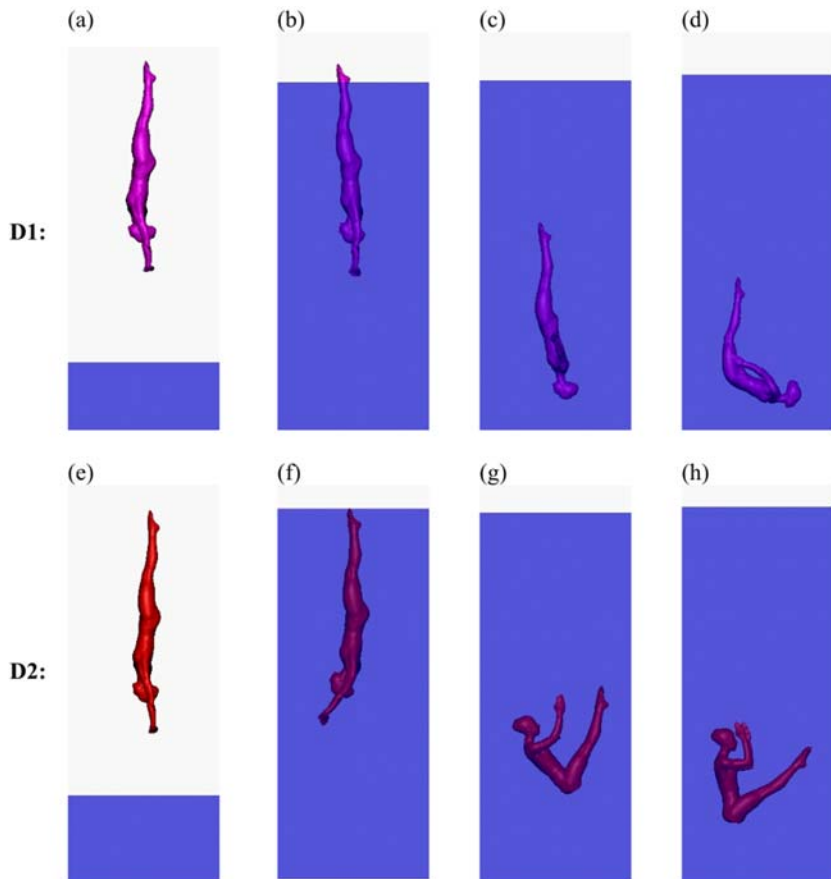
Figs. 28.9 and 28.10 show the digitized technique for two separate variants of a reverse pike dive, termed D1 and D2, that were performed by one athlete from the 10 m platform. The variants differ predominantly in their underwater stages. The times are shown relative to the timing of water entry in both figures. The aerial technique for D1 is shown in Fig. 28.9. The athlete starts by facing the pool and leaping forward. They raise their feet to their hands as they start to slowly somersault backward. The athlete then extends their body and continues to rotate backward so that they enter the water approximately perpendicular to the water surface. The aerial technique for D2 is almost identical to D1 and is not shown. Fig. 28.10 shows the water entry technique for both D1 and D2 repetitions. In D1 the athlete rotates forward underwater, while in D2 they somersault in the reverse direction. It is desirable to understand better the consequences of the different underwater motion choices.

The dynamics of the athlete are simulated using the biomechanical modeling method described in [Biomechanical methods](#). A section of pool water 5 m deep, 2 m wide, and 4 m long is represented by 13.3 million SPH particles with an initial spacing of 15 mm and as a Newtonian fluid with a density of  $1000 \text{ kg/m}^3$  and viscosity of  $0.001 \text{ Pa s}$ . The interaction between the mesh model of the athlete and the SPH model of the water is calculated as per the method in the section titled “SPH boundary modeling.”

**FIGURE 28.9**

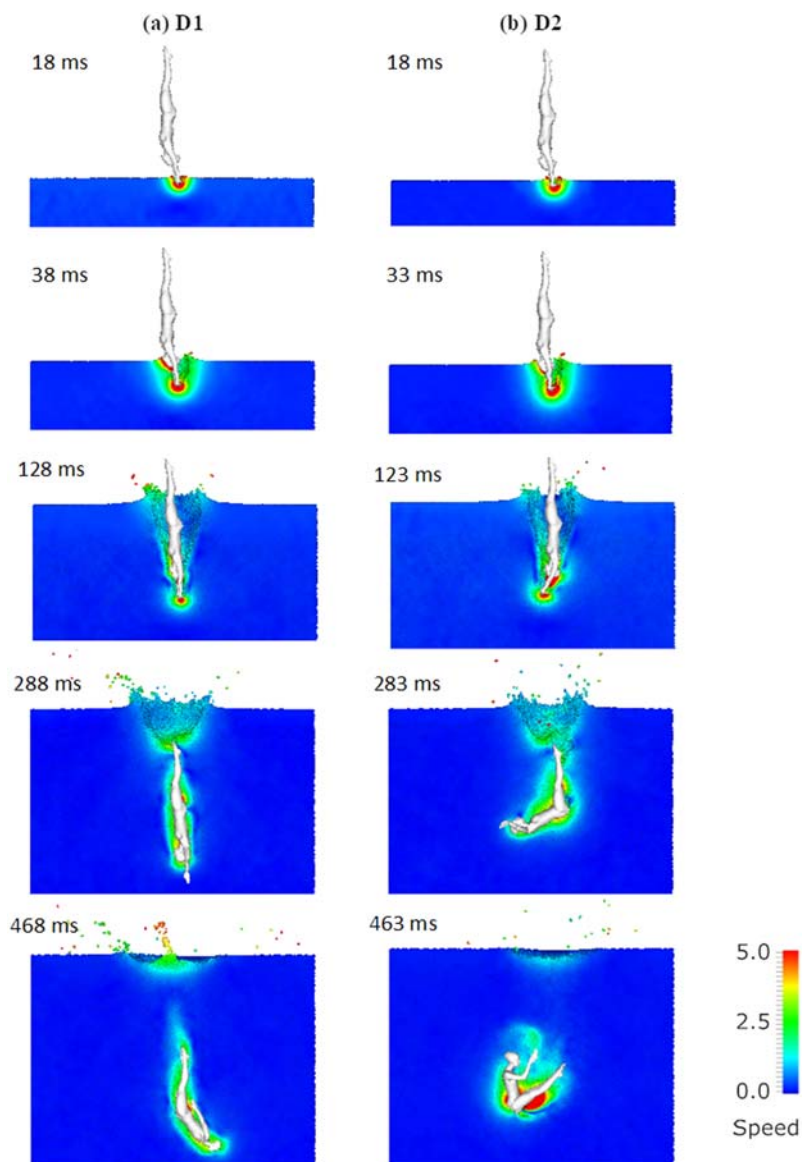
Aerial technique for the D1 reverse pike dive as performed by the digital twin based on MMC digitized kinematics. The aerial technique for the D2 repetition is almost identical. The digital twin of the athlete starts by facing the pool at the edge of the 10 m platform (A). They then leap forward and start to somersault backward (B). Simultaneously, they flex their body and rotate their arms downward and legs upward until they touch (B). They next extend the body straight again (C). Subsequently, the athlete rotates backward (D–E) at a speed that results in a vertical orientation of their body at the time of water entry (F).

*Fig. 28.11* shows a visualization of the two simulated dive variants (D1 and D2) from the time of water entry onward. The water is sectioned at the position of the center of mass of the athlete and is colored by speed from 0 to 5 m/s. The hands make contact with the water at 10 ms, and high speeds are induced in the water as a cavity begins to form around them. At 30 ms the body has moved downward enough for the head to contact the water. High fluid speeds are generated near to the hands and head as momentum is transferred from the body and the water. The water cavity expands as the hands move downward. After 120 ms the differences

**FIGURE 28.10**

Water entry technique of the digital twin diver for the two digitized reverse pike dives for the same athlete. Prior to water impact, the athlete is approximately vertically aligned (A) and (E). After water entry, the athlete remains vertically aligned for D1 (B) and bends forward for D2 (F). For D1 the diver slowly extends the back and lower limbs to rotate in a counter-clockwise direction (C, D). For D2 the athlete somersaults in the clockwise direction (G, H).

in technique between repetitions D1 and D2 become visibly apparent. For D1 the body remains vertical, with the arms having shifted to the sides to form a “T” shape pose. For D2 the arms move to the front of the body and the neck starts to flex forward. All of the body except the lower legs is now below the water level. The water cavity has grown sufficiently that only the hands and head remain in contact with the water. The highest fluid speeds continue to be induced near the regions of contact with the head and hands.

**FIGURE 28.11**

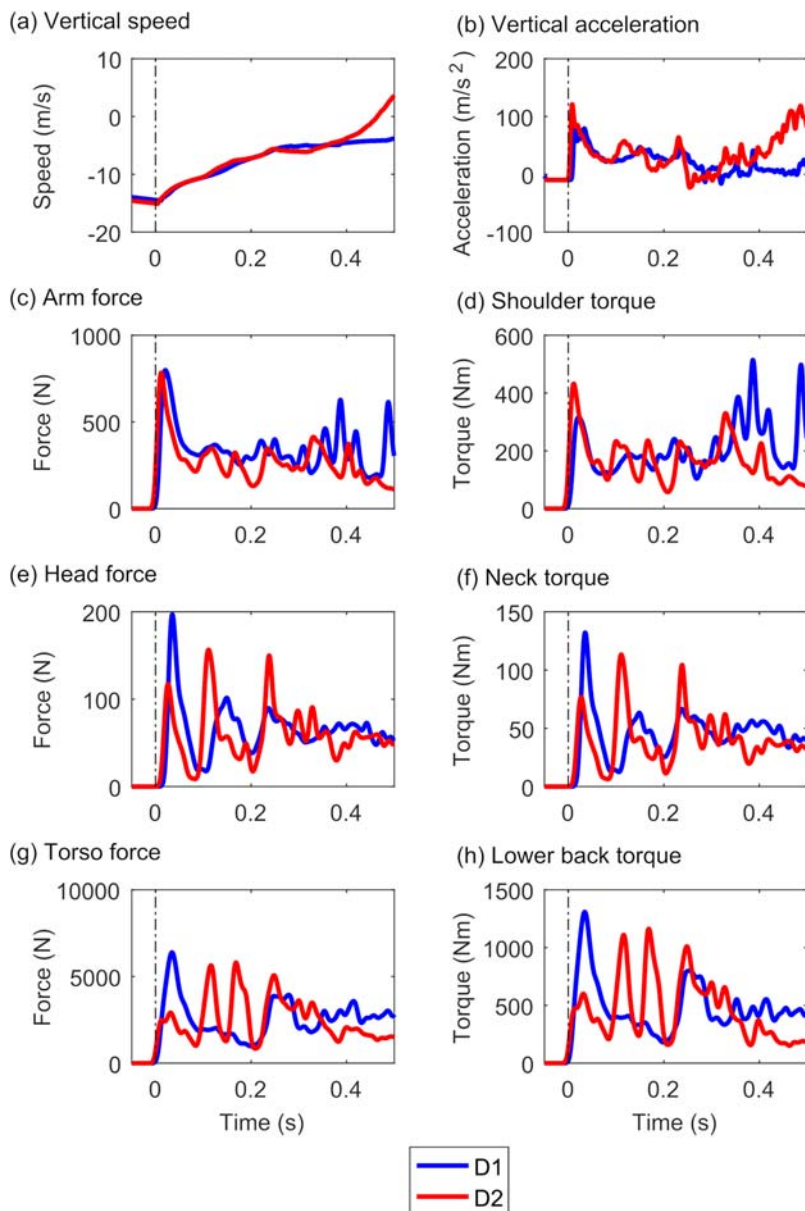
Visualization of simulated diving performance for dives (A) D1 and (B) D2. The time for each image is indicated in ms and is relative the timing of initial contact between the hands and the water. Fluid is colored by speed as indicated in the color bar.

Between 120 and 460 ms the cavity collapses and the body rotates: forward for D1 and backward for D2 (Fig. 28.11). At 280 ms the fluid surface near the body is at the height of the feet and so the entire body is now in contact with the fluid. Medium to high fluid speeds are induced across the full body—fluid contact area due to the drag forces created by this contact. The diver's body is still vertically aligned for the D1 case, but the upper body is horizontally aligned for the D2 case. At 460 ms the body has rotated further than before for each technique. In both cases the cavity has collapsed completely, and substantial splashing has occurred. The splash is smaller for the D2 case than the D1 case. The complex shape changes of the free surface from initial cavity generation to its collapse, with waves and splashing, is particularly suited to the capabilities of the meshless Lagrangian SPH method. The fluid speeds are higher for the D2 than for D1 due to the quick flexion of the legs and arms for the D2 case which changes the cross-sectional area of the body in the direction of motion and therefore the magnitude of drag forces (and the resulting fluid accelerations).

Fig. 28.12 shows plots of the velocity and acceleration of the body CoM, the forces on the hands, head, and torso and the torque about the shoulders, neck, and lower back. The CoM speed (Fig. 28.12A) is approximately 15 m/s for both D1 and D2 at 0.0 s. After water contact (0.0 s) the diver speed quickly reduces, at a rate that is similar for both cases. After 100 ms the vertical acceleration (Fig. 28.12B) for D1 and D2 diverges due to the differing movements first of the arms and then of the entire body (Fig. 28.11). After 280 ms the upper body is vertical for D1 (Fig. 28.11A), but horizontal for D2 (Fig. 28.11B). The pressure drag force for D2 is much higher than D1 because the projected area of the body in the horizontal plane is much larger. As a result, the vertical acceleration is higher for D2 than D1 after 280 ms, which results in the athlete completing the dive much deeper to a substantially higher vertical speed for D2 than D1 in the latter stages of the underwater movements.

Initially, the forces on the hands, head, and torso are similar for D1 and D2 (Fig. 28.12C, E and G) because the early movements are very similar (Fig. 28.11). After 30 ms the arms separate for D1 and move quickly toward the sides of the body. However, for D2 the hands stay together longer and move in front of the body. As a result of this difference the force on the head and torso is temporarily higher for D1 than D2 between 30 and 100 ms. However, after 100 ms the body rotates substantially for D2 while it remains vertical for D1, which causes the force on the head and torso to be higher for D2 than D1. After 280 ms the legs are moving ahead of the rest of the body for D2 and reduce the drag forces on the upper body. As a result, the force on the arms, head, and torso are smaller for D2 than D1 between 280 and 460 ms.

High magnitudes of joint torque are better indicators of injury risk than high levels of external force alone. This is because large joint torques occur when muscle forces, which are not measurable by noninvasive means, are also high. These combine to produce large joint, bone, and tendon forces. We observe the following results for the major joints:

**FIGURE 28.12**

CoM (A) speed and (B) acceleration and joint torque about the (C) shoulders, (D) hips, (E) wrists, (F) ankles, (G) neck, and (H) lower back. Results for virtual dives D1 and D2 are shown as *blue and red*, respectively.

- The torque about the shoulders (Fig. 28.12D) is different between D1 and D2 despite the peak force on the hands being similar (Fig. 28.12C), because of differences in arm position. For D2 there is a peak in shoulder torque of 320 Nm at 20 ms, while for D1 the peak is 430 Nm at 10 ms. After 300 ms the arm forces increase for D1 (but not D2) as the arms move from above the head to beside the body in a swimming stroke movement. Shoulder torque increases substantially during this motion and peaks at 513 Nm. These results show that despite the drag forces being similar in magnitude (Fig. 28.12C) the injury risk to the shoulder is likely higher for D1 than D2 due to the associated arm movements at the end of the underwater movement.
- Neck torque peaks for D1 at 132 Nm when the head initially makes contact with the water (at 30 ms). For D2 it peaks at 113 Nm when the arms and head start to tilt forward.
- Lower back torque peaks for D1 at 1.28 kNm soon after water entry (30 ms) and for D2 at a very high level of 1.16 kNm when the body rotates, and the entire torso is in contact with the fluid (around 170 ms).

These results show that joint torque can be calculated using a B-SPH model and correlated to body movement and body–fluid interaction behavior.

Here we have demonstrated the use of a combination of MMC kinematic digitization and B-SPH simulation to investigate human performance and injury during platform diving. Using two digitizations of different dive techniques, we are able to predict body motion, fluid behavior, and body loading. The same framework can be used to investigate proposed changes to technique, to compare the injury risk of different dive types (Cleary, Harrison, et al., 2020) and to understand the injury risk associated with performance errors in technique (Harrison et al., 2016). Such simulation is distinctly attractive because it is safer, more ethical, and more easily controllable than physical experimentation.

## Snow skiing

Success in sports such as snow skiing, kayaking, snowboarding, water skiing, and surfing requires both elite athleticism and optimal equipment design (Harrison et al., 2019). The athlete must have precise technique, endurance, and strength to move their body and their equipment in response to the external environment (e.g., snow slope, lake, ocean wave) in a manner that maximizes speed and results in visually impressive performances when a qualitative scoring of technique is used (e.g., snowboard halfpipe and surfing). Currently, technique and equipment can only be improved using trial and error approaches, in which the control of variables is highly limited. Digital twins of the type described in this chapter can be used instead and provide precise control over model parameters, creating greater potential for the optimization of both technique and equipment design. Modelers are faced with substantial challenges though, including characterization of technique and environment properties (such as snow topology and material behavior) and the

ability of the modeling technique to replicate the complex fluid or solid deformation that occurs during the activity.

The measurement of technique in the snow is challenging as outdoor lighting conditions limit the accuracy of marker-based systems, and the athlete covers a large distance during activity. Video motion capture has previously been used to assess center of mass (CoM) movement, distance of travel, and body kinematics (Federolf, 2012; Krosshaug et al., 2007; Krüger & Edelmann-Nusser, 2010). Wearable sensors (accelerometers, gyroscopes, magnetometers, GPS devices, and electromyography) have also been used to evaluate technique and performance (Brodie et al., 2008; Krüger & Edelmann-Nusser, 2010; Rosso et al., 2017). Additionally, external forces have been measured using in-boot sensors (Komi & Virmavirta, 2000). However, the variables in these experiments are too numerous and difficult to control for the purpose of developing quantitative decision tools for improving skiing performance. If sufficiently detailed and accurate, then computational modeling may fill this need.

Computational simulation of skiing performance has to-date used simplified representations of the athlete, skis, and snow interaction. Simple 1D and 2D models have been used to estimate the speed, downhill trajectory, and flex in the skis (Casolo & Lorenzi, 2001; Federolf, 2012; Hirano & Tada, 1996; Kaps et al., 2001). While extremely quick to predict ski movements, this simple interaction model does not account for changes in body movement, ground topology or large deformations of snow which can substantially change ski motions. FEM models of the internal stresses in the skis have been used to estimate their deformation during simplified representations of downhill movement in which the interaction with the snow has not been resolved in 3D, and large deformations of the snow were not included (Federolf, Lüthi, et al., 2010; Federolf, Roos, et al., 2010). The authors are not aware of any published models that incorporate predictions of body dynamics, large deformation snow behavior and suitable 3D interactions between the skis and snow during realistic skiing movement.

Here we present a dynamic digital twin model of snow ski jumping for two variants of ski equipment design. Fig. 28.13 shows the model configurations. In one case the skier is using a set of long skis that are 2.44 m in length. The skis each have a rounded square profile which is 39 mm thick throughout, 76 mm wide at the ends, and 58 mm wide in the middle. They have an upturned front section 220 mm long which is 54 mm from the base at its highest point. The front and rear sections are also rounded in the horizontal plane. The second set of skis were created by scaling the long skis by a factor of 0.75 in the lengthwise direction only, resulting in a length of 1.83 m.

A run up, jump, and landing area are all represented in the simulation (see Fig. 28.13). The run up consists of a hill with a 45-degree down slope which is covered with snow. The snow in the run up section has a rectangular cross section with a width of 1.2 m and a depth of 100 mm. Approximately 10 m downhill there is an increase in gradient that represents the ski jump section. The jump has a maximum height of 450 mm. Below this is a gap in snow that is 1.5 m in length.

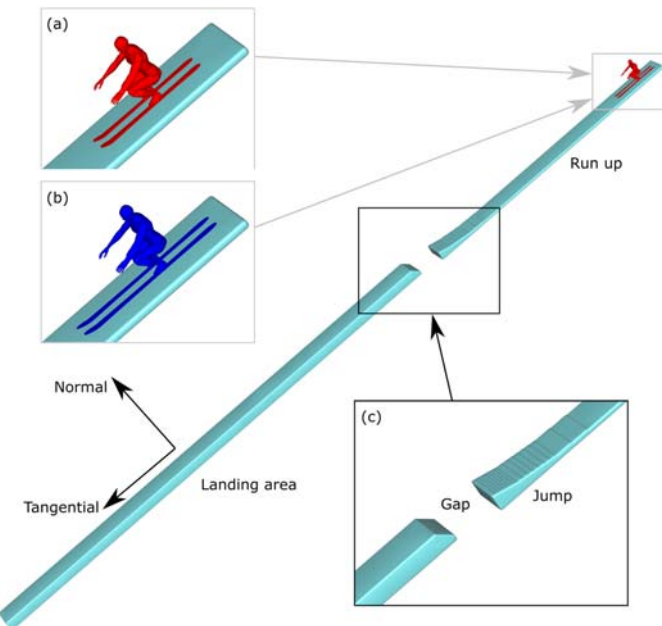


**FIGURE 28.13**

Model configuration for the snow ski simulations of a digital twin skier. The snow (shown as *light blue regions*) has a rectangular cross section and four distinct sections as labeled in the figure (Run-up, Jump, Gap, and Landing area). The run-up section is the highest part of the slope. 10 m down from the top of the slope there is a rise in gradient to simulate a ski jump. Beyond the jump is a gap that is approximately 1 m long. The landing area is further downhill from the gap. The initial location of the athlete is shown in the run-up area. The (A) short ski and (B) long ski models are shown in the insets. Inset (C) shows a close-up view of the jump and gap sections. The normal and tangential directions are defined in the figure.

Further along the slope is the landing area which is represented by snow with a cross section 25 m long, 1.2 m wide, and 500 mm depth.

The athlete is posed in a static position with the hips extended and the knees flexed. The skis are rigidly connected to the athlete's feet. No deformations or movements of the athlete or skis are considered in this demonstration of the model. The mass of the skier and skis together is 82 kg. All six degrees of freedom of the combined athlete and skis are predicted during the simulation.

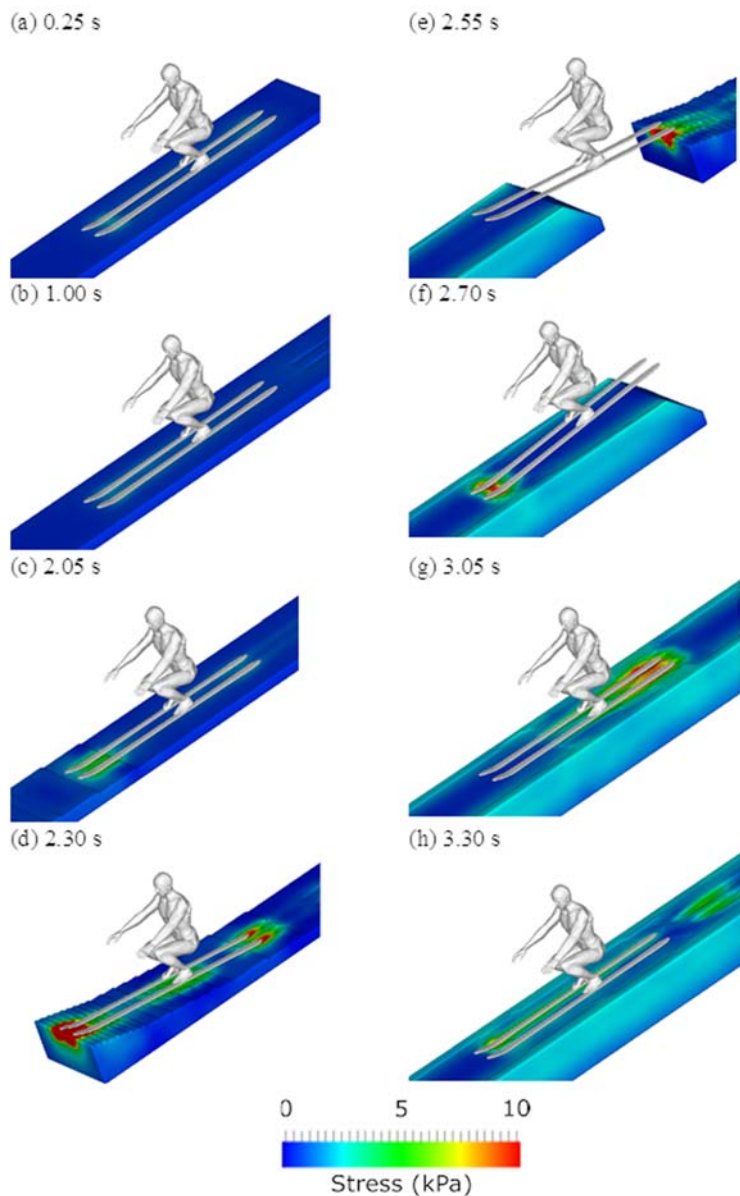
The snow is commonly represented as an elastoplastic material, and it is known that its mechanical properties vary substantially depending on factors such as temperature, age, and liquid water content (Stomakhin et al., 2013). Here we use an elastoplastic model (as detailed in the section titled “SPH method for elastic and elastoplastic solids”) and assume the following material parameters which produce realistic simulation results: a bulk modulus of 500 kPa, a shear modulus of 100 kPa,

a yield strength of 1 kPa, and a hardening modulus of 100 kPa. The spatial discretization of the snow, which is simulated using the SPH method, has a resolution of 20 mm which gives a model size of around two million particles. The skier and skis are represented by a surface mesh with 60,000 nodes with an average spacing of 10 mm.

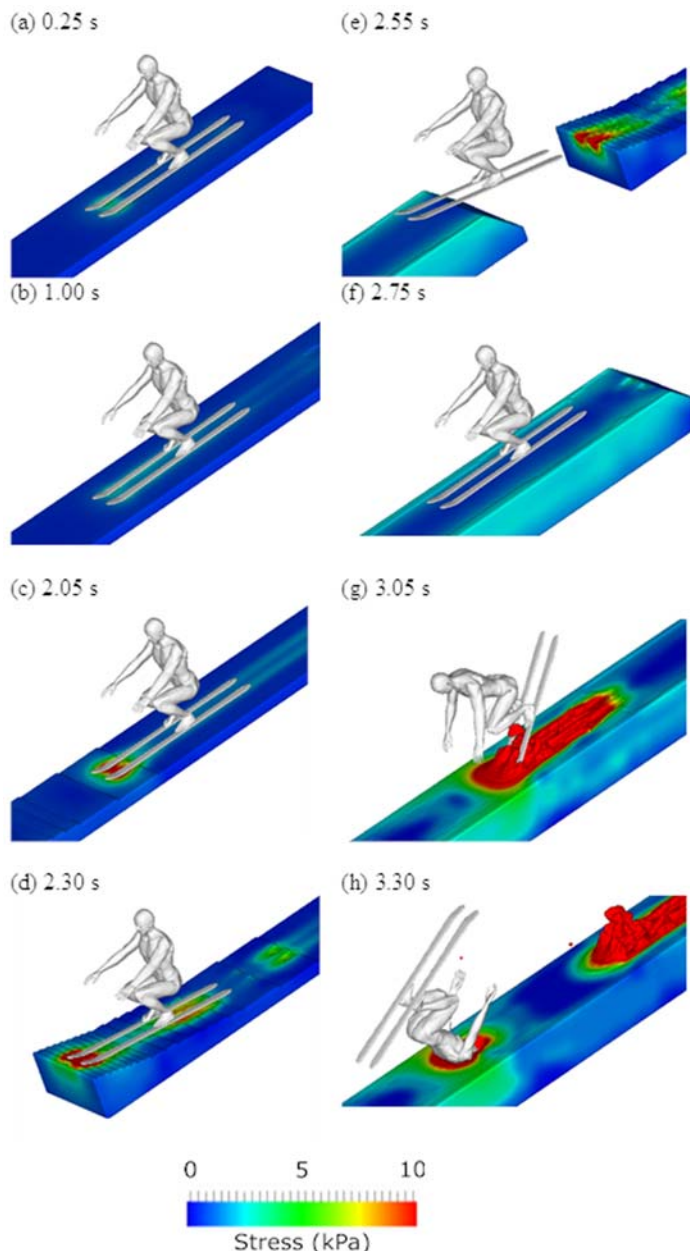
[Fig. 28.14](#) shows a visualization of the skier with the long ski equipment design. Between 0.25 s ([Fig. 28.14A](#)) and 1.00 s ([Fig. 28.14B](#)) the athlete gains speed down the hill. The weight of the athlete and skis causes plastic deformation of the snow which is visible as an indented trail behind the athlete in [Fig. 28.14B](#). At 2.05 s ([Fig. 28.14C](#)) the athlete reaches the jump, and the skis push deeper into the snow surface as the resulting ground reaction force starts to pitch the athlete backward. At 2.30 s ([Fig. 28.14D](#)) the fronts of the skis have reached the end of the jump. Large stresses are induced in the snow at the front of the skis where the maximum force is being applied. Behind the skis there is a large deformation visible in the snow at the start of the jump, from when the front of the skis initially made contact and the backward rotation of the skier was initiated. At 2.55 s ([Fig. 28.14E](#)) the athlete is mid-air after having left the jump with an upward and forward trajectory. However, before completely clearing the jump, the rear section of the skis make contact with it and additional torque is imparted onto the skis and skier. Large deformations of the snow are visible at the end of the jump which have resulted from this interaction. At 2.70 s ([Fig. 28.14F](#)) the athlete has consequently pitched forward, and the fronts of the skis have contacted the snow. Large stresses and plastic deformations are induced in the snow by the landing impact. Between 3.05 s ([Fig. 28.14H](#)) and 3.30 s ([Fig. 28.14I](#)) the skis rebound off and then fall back onto the snow surface and the athlete successfully rides out of the jump.

[Fig. 28.15](#) shows a visualization of the skier with the short ski equipment design. The lead up to the jump ([Fig. 28.15A–D](#)) is visibly similar to that of the large ski design ([Fig. 28.14A–D](#)). However, unlike for the long ski case, there is no extra contact between the rear section of the skis and the jump ([Fig. 28.15E](#)) and therefore, in contrast, the athlete does not pitch forward as they do when using the long skis ([Fig. 28.14E](#)). Instead, the short skis contact the start of the landing area and this causes the athlete to start pitching forward at high speed ([Fig. 28.15F](#)). At 3.05 s ([Fig. 28.15G](#)) the fronts of the skis have dug into the snow causing the athlete to pitch sharply forward—much more quickly than earlier. The skier completes a half somersault and lands headfirst into the snow at 3.30 s ([Fig. 28.15H](#)), which is obviously a disastrous outcome for the skier. Very deep deformations and large movements of the snow are visible from where the skis and upper body have impacted with high force. The ability to predict such large-scale deformations and such high plastic strains is a consequence of the meshfree nature of the SPH which enables complex free surface solid deformation to be predicted with complex human driven loading conditions. This type of model allows detailed investigation of such ski jumping and can help guide both technique and equipment design choices.

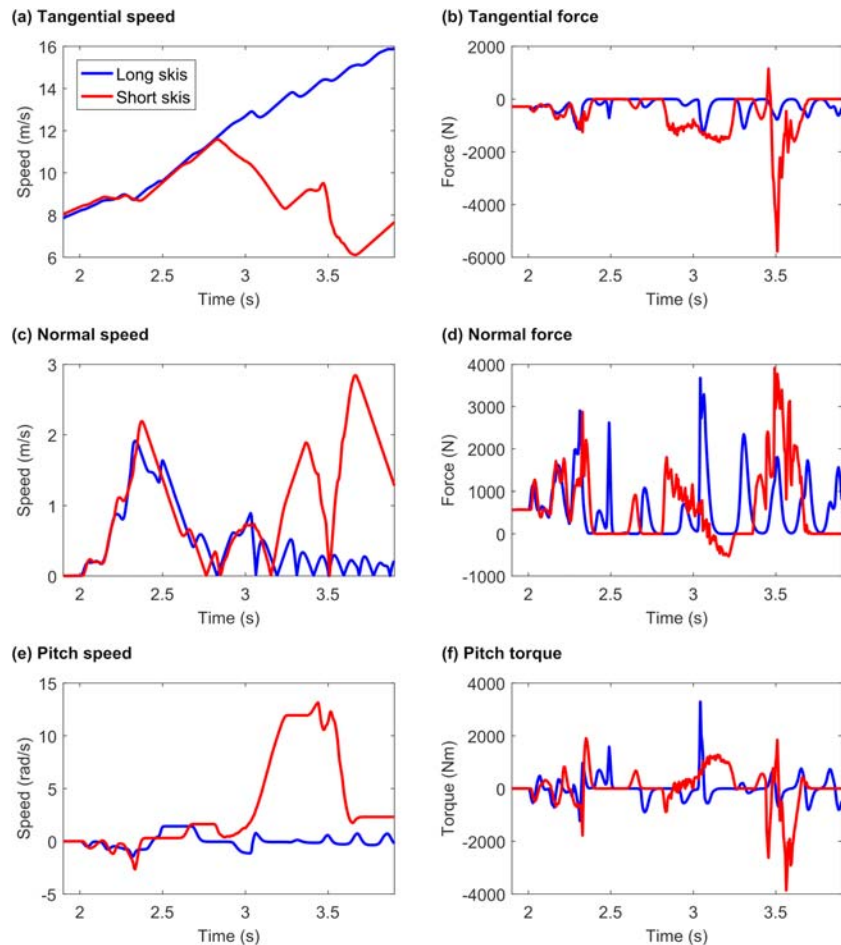
[Fig. 28.16](#) shows the speeds and forces in the normal, tangential direction and pitch angular speed and torque for the two ski designs. Prior to 2.0 s the skier is

**FIGURE 28.14**

Visualization of digital twin skiing for the case with long skis. The snow is colored by its von Mises stress, which measures the local stress field anisotropy (which then controls the resulting snow deformation).

**FIGURE 28.15**

Visualization of digital twin skiing for the case with short skis. The snow is again colored by von Mises stress.

**FIGURE 28.16**

Variation of tangential (A) speed and (B) force, normal (C) speed and (D) force, and pitch (E) speed and (F) torque for the digital skier performing skiing in the two scenarios considered, that is with long ski and short ski designs. The normal and pitch directions are defined in Fig. 28.13.

traveling at approximately 8 m/s for both cases (Fig. 28.16A) with the speed increasing due to the component of gravity in the slope direction. Immediately after 2.0 s the skis contact the jump and the normal force (Fig. 28.16D) increases to a peak of 1.26 kN for the short skis and 1.15 kN for the long skis. The tangential force (Fig. 28.16B) also increases at this time as the front of the skis compress the top of the snow jump. The pitch rotation rate (Fig. 28.16E) increases in the negative direction as the forces on the front of the skis create torque about the pitch axis (Fig. 28.16F). The skis and skier oscillate vertically against the snow surface

(with small amplitude) due to its elastic behavior. This causes the oscillations observed in speed, force, and torque between 2.10 and 2.40 s (Fig. 28.16). At 2.40 s the short ski case shows zero normal and tangential force as the athlete and skis have cleanly left the jump. The pitch speed remains small (0.30 rad/s) and constant for the short ski case between 2.39 and 2.64 s. For the long ski case there is a large peak of force and torque at 2.49 s when the rear ends of the skis re-contact the jump. This increases the pitch rotation rate to 1.37 rad/s. The difference in pitch behavior between the two cases at the end of the jump interaction is the primary cause of the substantially different landing behavior shown in Figs. 28.14 and 28.15. For the short skis the athlete has not rotated sufficiently to miss the first section of the snow in the landing area. The rear of each ski contacts the snow at 2.65 s, inducing a peak normal force of 916 N and a peak torque of 655 Nm. The pitch rotation rate increases to 1.63 rad/s. The skis then re-contact with the snow at 2.81 s and a torque of -886 Nm is imparted onto the skis, which partially counteracts the forward rotation. However, the fronts of the skis embed in the snow producing a dangerous and unacceptable landing.

In this section, we have demonstrated how a model that couples the athlete, the equipment, and the physical environment can predict differences in performance outcomes. There are many extensions that can be made to the model to improve its utility for such applications. First, the athlete is not changing their pose in this example and changes to technique could be easily implemented using the framework outlined in the section titled “Biomechanical modeling.” Second, it could be desirable to include the dynamics of the joints and muscles, for instance, to understand how the musculoskeletal system actively and passively absorbs energy from the ski–snow interactions and controls the whole-body movement and balance. Third, specific jump geometries can also be simulated, for instance, the shape of a ski jump at an upcoming major competition. Fourth, the snow constitutive model can be expanded to account for temperature effects, and heterogeneity of constituents, and should be validated against experimental results. Future applications of this model could include investigations into

- The relationship between changes to ski design and technique with performance and injury risk outcomes.
- Different snow-based sports, such as snowboarding, cross-country skiing.
- Ski resort design and maintenance for improved safety and enjoyment.

---

## Realtime digital human applications: workplace injury example

Movement-related injury in the workplace is linked to lost worker income, business losses, poor mental health, decreased physical health from inactivity, and, in the worse cases, death (Nelson & Hughes, 2009). Arguably, the biggest challenge in prevention is the difficulty in identifying exact causes of injury so that they can be

reliably mitigated. Many, such as overuse strain-type injuries, occur due to slow accumulation of damage in the musculoskeletal system and are therefore very difficult to predict (Keyserling, 2000). Cause identification is severely limited by the inability to adequately quantify the activity that proceeded the injury. The digital twin approach presented in this chapter, especially using the MMC method, is prospective for yielding new insights into injury causes and for predicting and preventing injuries in the future. Specifically, the system could be used to:

- measure movement and external loading on the body,
- predict acute injury risk from instantaneous body loading using known risk indicators,
- predict the accumulation of damage for chronic injury using known risk indicators,
- develop new risk indicators based upon injuries that occur during recordings,
- generate synthetic data for the training of machine learning engines to predict injury.

Since the digital twin approach is noninvasive and highly scalable, the system can be deployed at large scale (including covering many workers across multiple shifts performing a broad range of manual handling activities). The resulting dataset would be highly valuable for reducing injury rates and the negative consequences that result.

Manual materials handling (MMH) has long been indicated as a cause of workplace injury, especially for the lower back (Nelson & Hughes, 2009). Marras et al. (1995), identified the range of key kinematic and kinetic measures during MMH across industries and correlated these measures against recorded injury rates. Activities with a large angle between the torso and the vertical direction, fast rates of joint movement, and/or high levels of lower back joint torque were found to be well correlated with increased back injury risk. However, while these correlations are useful for developing general guidelines, they are not sufficiently specific to enable the prediction of injury for a particular individual or movement technique. The risk for the individual is dependent on the shape, strength, and flexibility of their body, their emotional state, the amount of sleep that they have had, and environmental factors such as lighting and noise. Some workers can lift using what is considered poor technique and never be injured throughout their career, while others can be injured using what is considered the correct technique. Personalized prediction of injury risk will require much more data to be collected and correlated with injury risk and the use of new real-time systems to track risk indicating variables. To date, such data collection has been limited by the restrictions arising from motion capture technologies. Plamondon et al. (2014) showed that marker-based motion capture can be used to adequately quantify kinematics and calculate torque. They observed differences in movement choices between expert and novice workers that could be used to guide training. These types of studies have been useful for developing a fundamental understanding of injury causation, but the use of marker-based motion capture systems limits measurement to lab-based idealizations of actual work activities and are

restricted in their utility. An MMC approach, as outlined in [Markerless motion capture for digital human model construction](#), does not have such limitations, and can be deployed at scale in real operational conditions (not just for testing but to provide ongoing decision support in health and safety).

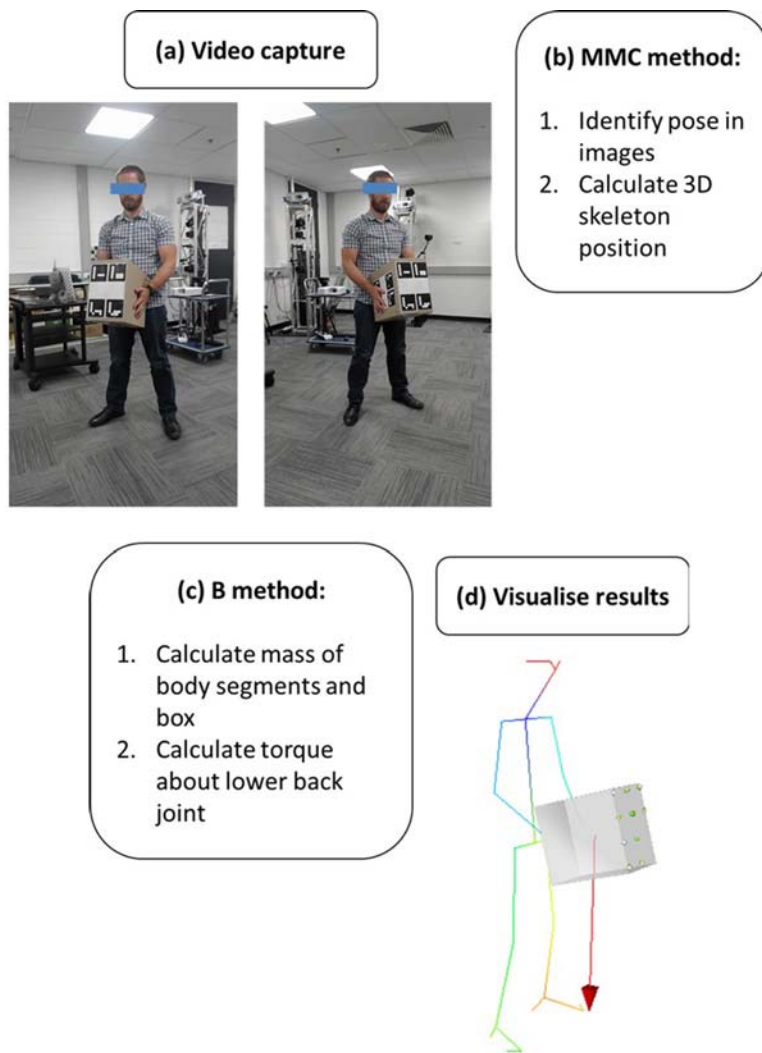
Here we present an example of a digital twin of a human worker that is suitable for evaluating the lifting of heavy, bulky bodies (such as a heavy box). Two different methods of lifting were considered:

1. L1—the worker bends their knees to keep the box close to their CoM;
2. L2—they bend over with straight legs (or stoop) to pick up the box and then hold it far from the body.

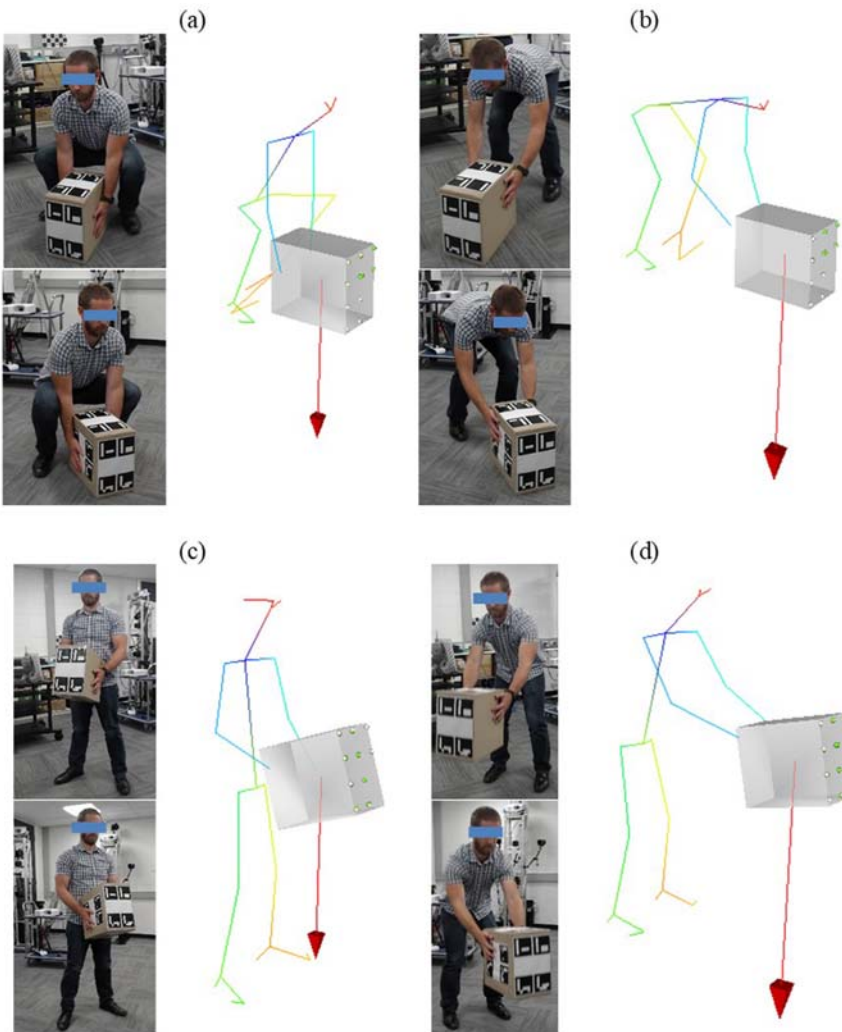
The two lifting motions were recorded and digitized using MMC (as explained in [Markerless motion capture for digital human model construction](#)). Two HD webcams were placed in positions with approximately orthogonal views of the body. The extrinsic and intrinsic properties of the camera arrangement were calibrated using a chessboard pattern with embedded ArUco markers ([Muñoz-Salinas & Garrido-Jurado, 2021](#)). The motions were recorded at five frames per second because of the slow movement associated with such lifting (but can be recorded much faster if required). The torque about the lower back was next calculated (over the duration of the lift process) for each lift type. These are compared and provide an example of a quantitative metric that can be measured in real time. This information can then be used in a range of ways, ranging from real-time intervention to inclusion in a database for offline study or for training of a deep learning model. Other potential injury risk metrics such as body pose and rate of joint movement can be easily calculated and compared in the same way. These metrics can be determined noninvasively for workers throughout the workday using the MMC system that supplies motion data to the biomechanical model for the torque estimation. Workers showing high levels of key metrics can be identified, and risks can then be mitigated. This system can be continuously improved by correlating available metrics against recorded injury events as they occur.

[Fig. 28.17](#) shows a schematic of the method used to calculate torque about the lower back. A reduced implementation of the biomechanical simulation method from the section titled “Biomechanical methods” is employed to reduce computational expense and enable real-time feedback. Velocity and acceleration terms are assumed to be insignificant (which is reasonable for most MMH applications), so the torque about the joints of the lower back is a function only of gravity and the external loads. The calculation of joint positions is also simplified as body segment length is not enforced, thus removing the need to perform costly inverse kinematics optimization routines. The load from the box is also assumed to be evenly distributed between the two hands. This assumption may not always be valid, and future applications of the method should include the ability for estimating the load sharing between the hands.

[Fig. 28.18](#) shows the system results for two lifting cases (L1 and L2) of manual lifting of the heavy box. Images from two of the raw video sources are shown for the

**FIGURE 28.17**

Real-time workplace injury pipeline. First, (A), video is collected of the activity from multiple angles. Second, (B), the 3D skeleton position is calculated using the MMC method (as described in [Markerless motion capture for digital human model construction](#)). Third, (C), the loading on the lower back is calculated using the B method (as described in the Biomechanical methods section, above). Fourth, (D) the results are visualized for ease of communication to the worker.

**FIGURE 28.18**

Visualizations of the (A, C) L1 and (B, D) L2 lift techniques captured using the MMC method. For the first position of each lift (A, B) the box has just been lifted off the ground. In the second position of each lift (C, D) the box is held in front of the body. Both of the captured video frames are shown at the left of each panel. On the right of each panel the digital twin is shown as a 3D stick figure with each body segment colored differently. The box is shown with transparent gray coloring. The torque about the joints of the lower back is shown as a red vector located at the center of the box.

start and end positions. Next to each pair of video images is the corresponding 3D reconstruction of the body and box. For each of the panels of Fig. 28.18 the 3D visualization of the skeleton corresponds well to the corresponding source images. The torque about the lower back joints, shown as a red arrow extending down from the center of the box, is clearly larger for L2 than for L1. This type of visualization provides clear and unambiguous information that can be used to communicate the differences between movement types to workers, such as during training sessions.

The magnitude of torque about the back is shown in Fig. 28.19. For L1 the torque peaks at 80 Nm at the start of the lift and then reduces to 58 Nm when the box is moved close to the body's CoM. For L2 the torque is initially over 241 Nm and reduces to 172 Nm at the top of the lift. The lower back muscles must counteract this torque, and the forces that they generate put additional load on the spine, in body shear and compression directions. These results show that the force in the spine is likely to be around four times higher for the poor L2 lift case than the ergonomically superior L1 lift case. This indicates that the risk of both acute and chronic (overuse) injury to the musculoskeletal system is significantly higher for L2 than L1. Correlations of such data with recorded injuries will enable quantitative risk assessments once these types of systems are sufficiently in use so that there is sufficient data to enable statistically meaningful correlations to be obtained.

This demonstration of a real-time digital human application shows how MMC and biomechanical modeling can be combined into an application that could be used for continuous risk monitoring in real-world environments. A number of improvements can be made to the modeling approach, including automatic identification of the weight and location of the body without large markers, automatic

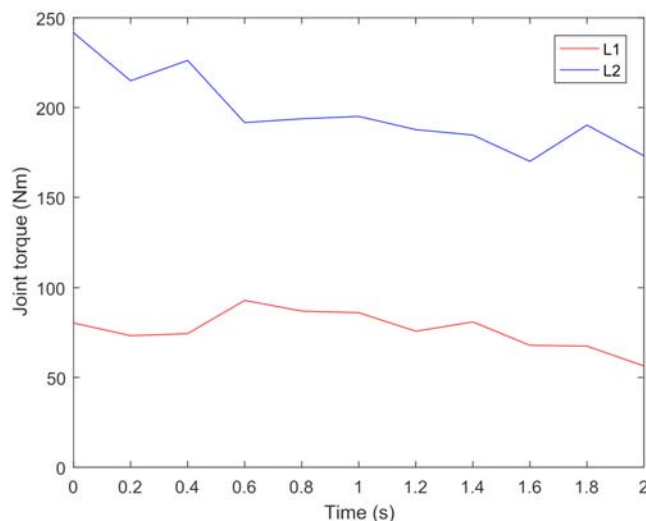


FIGURE 28.19

Time variation of torque about the lower back joints for the L1 and L2 lifting scenarios.

determination of which hands (if any are holding the box), and implementation of the whole biomechanical method from the section titled “Biomechanical methods.”

Many other industries could benefit from this type of real-time monitoring, such as

- elderly care,
- clinical practice, and
- sports.

The following section outlines how the methods described here can be implemented into deployable software that nontechnical experts can use, which is key to the uptake of such technologies into the wider community and industries.

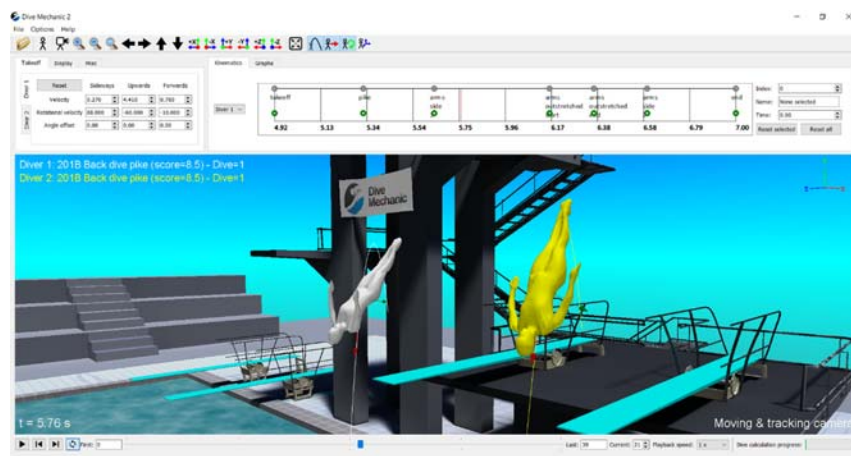
---

## Creating software products based on human digital twins

This chapter has highlighted the many benefits of using human digital twins to improve understanding of performance and injury risk. Historically, this technology has remained within the realm of academic research communities, inaccessible to less technical stakeholders and practitioners. Creating intuitive software products based on human digital twins that are tailored to the end user requirements (and their technical skill levels) can help liberate the intellectual property and broaden the total impact on the community. A recent example of this was the development of the Dive Mechanic software by [Cohen, Harrison and Cleary \(2020\)](#).

Dive Mechanic is a 3D software application for modeling elite level diving performance that was designed to be used by coaches, athletes, and sports biomechanists. It allows for the visualization and analysis of the aerial phase of both platform and springboard diving. It is athlete specific, with digital twin models of each athlete performing the same technique as the athlete at the pool. Critically, the software allows the user to change the base technique of the diver and to observe the resultant changes in their aerial motion. This rapid virtual experimental capability is useful for both exploring technique improvement (optimization) and for communication of concepts between coaches and athletes. The interface of the software ([Fig. 28.20](#)) consists of a 3D viewport of the diver within the arena, playback controls to move forward and backward in time through the dive, corresponding graphs of key performance metrics and widgets for adjusting key aspects of the diver technique.

The Dive Mechanic software was developed upon the Workspace workflow engine ([Cleary, Thomas, et al., 2020](#); [Workspace, n.d.](#)). This platform allowed for modular design, extensive reuse, and agile development. The biomechanics algorithms and data structures were developed in C++ in a generic and reusable manner as part of a Bio-Mechanic plugin for Workspace ([Harrison & Cohen, 2019](#)). The Dive Mechanic application was primarily designed within Workspace’s graphical workflow environment with a graphical user interface having widgets connected

**FIGURE 28.20**

Dive Mechanic software interface.

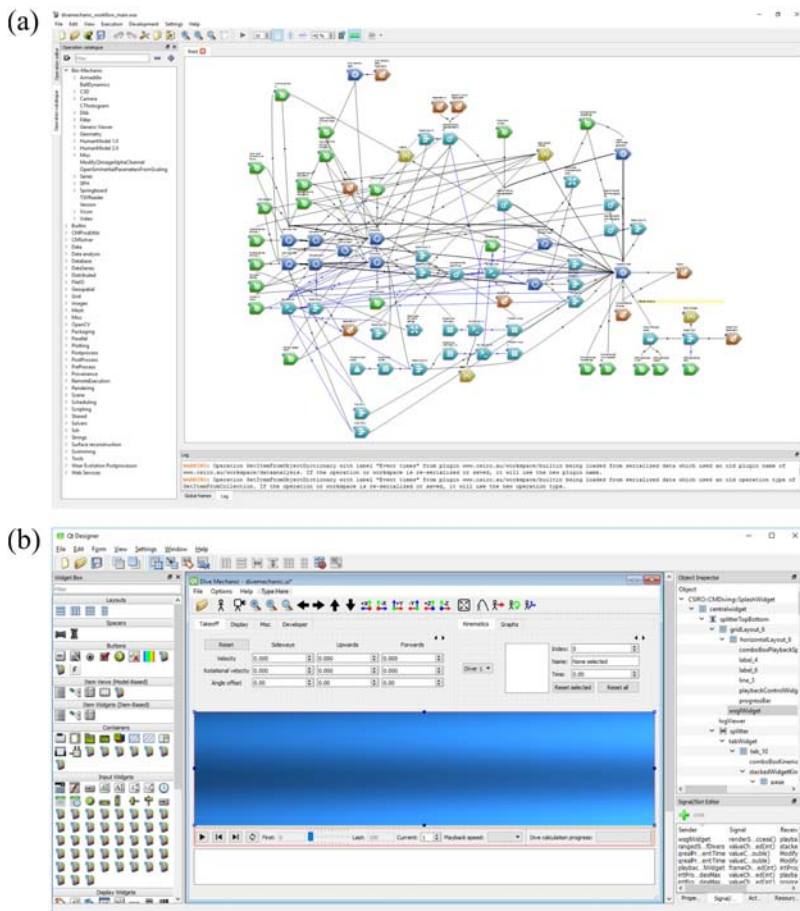
to data elements (inputs and outputs) within the complex workflow. These main components are shown in Fig. 28.21.

Software products for digital twin motion capture have also been developed in a similar manner using the Workspace workflow engine. Camera calibration algorithms and data structures were developed within a Computer Vision plugin. These were then composed into a workflow to drive a Multiple Fixed Camera Calibration Application (Fig. 28.22). Finally, a markerless motion capture application called Ergomechanic (elements of which were introduced in the section titled “Markerless motion capture for digital human model construction”) was developed using workflows and a Motion Capture plugin (Fig. 28.22B). This is a software implementation of the method described in the section titled “Biomechanical methods.” These examples further highlight the strong benefits of developing software within Workspace. Importantly this enables easy translation of digital twin technologies from bespoke research capability into software that can be supplied to and used by the domain experts and stakeholders.

## Conclusions

In this chapter, we present a detailed framework and a range of examples of using digital twinning to investigate how the body interacts with realistic environments for understanding performance and injury. The framework couples:

- A noninvasive markerless motion capture (MMC) method for personalizing the digital twin, both in static physical dimensions and dynamic movement

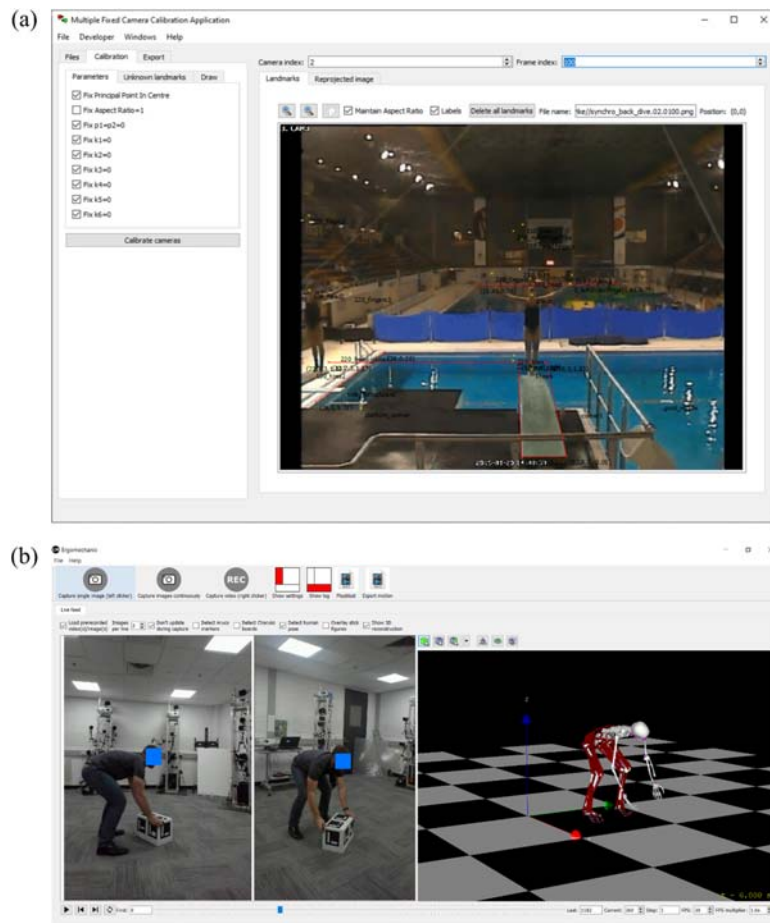


**FIGURE 28.21**

Dive Mechanic components included (A) Workspace workflow including operations from the C++ Bio-Mechanic Workspace plugin, and (B) graphical user interface (GUI) being developed in Qt Designer.

behavior in the natural environment (whether performing sport, work, or general daily activities).

- A comprehensive biomechanical (B) modeling method for the internal and external body which includes the dynamics of all major body segments and joints and deformations of the external surface.
- A physics-based solver that can predict numerically the behavior changes induced in the external environment by the action of the human. Here we choose this to be based on the Smoothed Particle Hydrodynamics (SPH) method where that environment could be a combination of water, air, or land. This method can

**FIGURE 28.22**

Software applications built using workspace: (A) multiple fixed camera calibration application, and (B) ergomechanic.

represent complex environment behavior such as splashing and fragmentation of water free-surfaces and large-scale plastic deformation of ground surfaces.

A Markerless Motion Capture (MMC) method has been proposed for robust non-laboratory kinematic digitization. A working implementation of the MMC pipeline has been described and demonstrated. It is based on a combination of

- deep learning (computer vision) approaches,
- biomechanical models of the human body, and
- optimization methods

This approach can provide superior twinning of the digital and real-world human motions than can be achieved using computer vision alone.

The strength and breadth of the MMC-B-SPH modeling system is demonstrated by application to

1. Sports (swimming, diving, and snow skiing).
2. Workplace Health and Safety scenarios (real time identification of workplace injury risk, specifically back injury risk from lifting heavy objects).

Such personalized digital twin modeling of the human body during activities can lead to significantly better understanding that can contribute strongly to

- improved performance with evidence-based guidance for training, event or activity selection, strength and endurance training, and talent identification
- identification of the causes of both short-term acute injuries and longer-term chronic injuries.

Finally, the translation of such methods and software to user-friendly customer-centric software tools is supported by the development of the modeling and MMC pipelines being built using the Workspace workflow platform.

Many challenges remain in improving the bio-fidelity of the approaches and the ease and range of use for industry and the community. Substantially, more data must be collected by MMC and internal imaging approaches to understand how movement is correlated with performance and injury risk. More detailed biomechanical modeling methods such as simulation of 3D stresses and the biophysical responses in bones and soft tissue can be included in the framework to improve output measures. Machine learning approaches may also be used to map numerical modeling outputs to quantitative metrics for decision-making. The speed of the framework processes needs to be increased by use of improved computer hardware and faster algorithms. It is anticipated that as these challenges are addressed, the digital human approach will have greater uptake and an increasing impact on the community as a whole.

---

## Acknowledgments

The authors gratefully acknowledge contributions of expertise and data from Bruce Mason and Dave Pease from the Australian Institute of Sport; Graeme Rose, Valerie Beddoe and David Bell from Diving Australia; Kay Crossley, Kane Middleton, and Jodie McClelland from La Trobe University; and the Workspace team in CSIRO Data61.

---

## References

- Ackermann, M., & van den Bogert, A. J. (2010). Optimality principles for model-based prediction of human gait. *Journal of Biomechanics*, 43(6), 1055–1060. <https://doi.org/10.1016/j.jbiomech.2009.12.012>

- Akbarshahi, M., Schache, A. G., Fernandez, J. W., Baker, R., Banks, S., & Pandy, M. G. (2010). Non-invasive assessment of soft-tissue artifact and its effect on knee joint kinematics during functional activity. *Journal of Biomechanics*, 43(7), 1292–1301. <https://doi.org/10.1016/j.jbiomech.2010.01.002>
- Anderson, F. C., & Pandy, M. G. (2001). Dynamic optimization of human walking. *Journal of Biomechanical Engineering*, 123(5), 381–390. <https://doi.org/10.1115/1.1392310>
- Baker, R. (2006). Gait analysis methods in rehabilitation. *Journal of NeuroEngineering and Rehabilitation*, 3. <https://doi.org/10.1186/1743-0003-3-4>
- Batchelor, G. K. (1973). *An introduction to fluid dynamics*.
- Bazarevsky, V., Grishchenko, I., Raveendran, K., Zhu, T., Zhang, F., & Grundmann, M. (2020). BlazePose: On-device real-time body pose tracking. arXiv <https://arxiv.org>.
- Brodie, M., Walmsley, A., & Page, W. (2008). Fusion motion capture: A prototype system using inertial measurement units and GPS for the biomechanical analysis of ski racing. *Sports Technology*, 17–28. <https://doi.org/10.1002/jst.6>
- Cao, Z., Hidalgo, G., Simon, T., Wei, S.-E., & Sheikh, Y. (2021). OpenPose: Realtime multi-person 2D pose estimation using Part Affinity fields. *IEEE Transactions on Pattern Analysis and Machine Intelligence*, 43(1), 172–186. <https://doi.org/10.1109/tpami.2019.2929257>
- Casolo, F., & Lorenzi, V. (2001). Relevance of ski mechanical and geometrical properties in carving technique: A dynamic simulation. *Science and Skiing II : Second International Congress on Science and Skiing*, 165–179.
- Caspersen, C., Berthelsen, P. A., Eik, M., Pâkozdi, C., & Kjendlie, P. (2010). Added mass in human swimmers: Age and gender differences. *Journal of Biomechanics*, 43(12), 2369–2373. <https://doi.org/10.1016/j.jbiomech.2010.04.022>
- Cimolin, V., & Galli, M. (2014). Summary measures for clinical gait analysis: A literature review. *Gait and Posture*, 39(4), 1005–1010. <https://doi.org/10.1016/j.gaitpost.2014.02.001>
- Cleary, P. W. (2010). Elastoplastic deformation during projectile-wall collision. *Applied Mathematical Modelling*, 34(2), 266–283. <https://doi.org/10.1016/j.apm.2009.04.004>
- Cleary, P. W., Cohen, R. C. Z., Harrison, S. M., Sinnott, M. D., Prakash, M., & Mead, S. (2013). Prediction of industrial, biophysical and extreme geophysical flows using particle methods. *Engineering Computations (Swansea, Wales)*, 30(Issue 2), 157–196. <https://doi.org/10.1108/02644401311304845>
- Cleary, P. W., & Das, R. (2008). The potential for SPH modelling of solid deformation and fracture. In , 11. *IUTAM bookseries* (pp. 287–296). Springer Verlag. [https://doi.org/10.1007/978-1-4020-9090-5\\_26](https://doi.org/10.1007/978-1-4020-9090-5_26)
- Cleary, P. W., Harrison, S. M., Sinnott, M. D., Pereira, G. G., Prakash, M., Cohen, R. C. Z., Rudman, M., & Stokes, N. (2020). Application of SPH to single and multiphase geophysical, biophysical and industrial fluid flows. *International Journal of Computational Fluid Dynamics*. <https://doi.org/10.1080/10618562.2020.1841897>
- Cleary, P. W., Prakash, M., Das, R., & Ha, J. (2012). Modelling of metal forging using SPH. *Applied Mathematical Modelling*, 36(8), 3836–3855. <https://doi.org/10.1016/j.apm.2011.11.019>
- Cleary, Paul W., Prakash, M., Ha, J., Stokes, N., & Scott, C. (2007). Smooth particle hydrodynamics: Status and future potential. *Progress in Computational Fluid Dynamics, An International Journal*, 7(2–4), 70. <https://doi.org/10.1504/PCFD.2007.013000>
- Cleary, P. W., Thomas, D., Hetherton, L., Bolger, M., Hilton, J. E., & Watkins, D. (2020). Workspace: A workflow platform for supporting development and deployment of

- modelling and simulation. *Mathematics and Computers in Simulation*, 175, 25–61. <https://doi.org/10.1016/j.matcom.2019.11.011>
- Cohen, R. C. Z., Cleary, P. W., Harrison, S. M., Mason, B. R., & Pease, D. L. (2014). Pitching effects of buoyancy during four competitive swimming strokes. *Journal of Applied Biomechanics*, 30(5), 609–618. <https://doi.org/10.1123/JAB.2013-0260>
- Cohen, R. C. Z., Cleary, P. W., & Mason, B. R. (2012). Simulations of dolphin kick swimming using smoothed particle hydrodynamics. *Human Movement Science*, 31(3), 604–619. <https://doi.org/10.1016/j.humov.2011.06.008>
- Cohen, R. C. Z., Cleary, P. W., Mason, B. R., & Pease, D. L. (2015). The role of the hand during freestyle swimming. *Journal of Biomechanical Engineering*, 137(11).
- Cohen, R. C. Z., Cleary, P. W., Mason, B. R., & Pease, D. L. (2018). Forces during front crawl swimming at different stroke rates. *Sports Engineering*, 21(1), 63–73. <https://doi.org/10.1007/s12283-017-0246-x>
- Cohen, R. C. Z., Cleary, P. W., Mason, B. R., & Pease, D. L. (2020). Studying the effects of asymmetry on freestyle swimming using smoothed particle hydrodynamics. *Computer Methods in Biomechanics and Biomedical Engineering*, 23(7), 271–284. <https://doi.org/10.1080/10255842.2020.1718663>
- Cohen, R. C. Z., Harrison, S. M., & Cleary, P. W. (2020). Dive Mechanic: Bringing 3D virtual experimentation using biomechanical modelling to elite level diving with the Workspace workflow engine. *Mathematics and Computers in Simulation*, 175, 202–217. <https://doi.org/10.1016/j.matcom.2020.03.007>
- Cummins, S. J., Silvester, T. B., & Cleary, P. W. (2012). Three-dimensional wave impact on a rigid structure using smoothed particle hydrodynamics. *International Journal for Numerical Methods in Fluids*, 68(12), 1471–1496. <https://doi.org/10.1002/fld.2539>
- Das, R., & Cleary, P. W. (2015c). Application of a mesh-free method to modelling brittle fracture and fragmentation of a concrete column during projectile impact. *Computers and Concrete*, 933–961. <https://doi.org/10.12989/cac.2015.16.6.933>
- Das, R., & Cleary, P. W. (2015a). Evaluation of accuracy and stability of the classical SPH method under uniaxial compression. *Journal of Scientific Computing*, 64(3), 858–897. <https://doi.org/10.1007/s10915-014-9948-4>
- Das, R., & Cleary, P. W. (2015b). Novel application of the mesh-free SPH method for modeling thermo-mechanical responses in arc welding. *International Journal of Mechanics and Materials in Design*, 11(3), 337–355. <https://doi.org/10.1007/s10999-014-9279-5>
- Delp, S. L., Anderson, F. C., Arnold, A. S., Loan, P., Habib, A., John, C. T., Guendelman, E., & Thelen, D. G. (2007). OpenSim: Open-source software to create and analyze dynamic simulations of movement. *IEEE Transactions on Biomedical Engineering*, 54(11), 1940–1950. <https://doi.org/10.1109/TBME.2007.901024>
- Dorn, T. W., Schache, A. G., & Pandy, M. G. (2012). Muscular strategy shift in human running: Dependence of running speed on hip and ankle muscle performance. *Journal of Experimental Biology*, 215(11), 1944–1956. <https://doi.org/10.1242/jeb.064527>
- Dumas, R., Chèze, L., & Verriest, J. P. (2007). Adjustments to McConvile et al. and Young et al. body segment inertial parameters. *Journal of Biomechanics*, 40(3), 543–553. <https://doi.org/10.1016/j.jbiomech.2006.02.013>
- Federolf, P. A. (2012). Quantifying instantaneous performance in alpine ski racing. *Journal of Sports Sciences*, 30(10), 1063–1068. <https://doi.org/10.1080/02640414.2012.690073>
- Federolf, P., Lüthi, A., Roos, M., & Dual, J. (2010). Parameter study using a finite element simulation of a carving Alpine ski to investigate the turn radius and its dependence on

- edging angle, load, and snow properties. *Sports Engineering*, 12(3), 135–141. <https://doi.org/10.1007/s12283-010-0039-y>
- Federolf, P., Roos, M., Lüthi, A., & Dual, J. (2010). Finite element simulation of the ski-snow interaction of an alpine ski in a carved turn. *Sports Engineering*, 12(3), 123–133. <https://doi.org/10.1007/s12283-010-0038-z>
- Frankton, A. (2018). *Motion capture for live performance*.
- Gray, J. P., Monaghan, J. J., & Swift, R. P. (2001). SPH elastic dynamics. *Computer Methods in Applied Mechanics and Engineering*, 190(49–50), 6641–6662. [https://doi.org/10.1016/S0045-7825\(01\)00254-7](https://doi.org/10.1016/S0045-7825(01)00254-7)
- Griffiths, I. W. (2006). *Principles of biomechanics & motion analysis*.
- Harrison, S. M., Chris Whitton, R., Kawcak, C. E., Stover, S. M., & Pandy, M. G. (2014). Evaluation of a subject-specific finite-element model of the equine metacarpophalangeal joint under physiological load. *Journal of Biomechanics*, 47(1), 65–73. <https://doi.org/10.1016/j.jbiomech.2013.10.001>
- Harrison, S. M., & Cleary, P. W. (2014). Towards modelling of fluid flow and food breakage by the teeth in the oral cavity using smoothed particle hydrodynamics (SPH). *European Food Research and Technology*, 238(2), 185–215. <https://doi.org/10.1007/s00217-013-2077-8>
- Harrison, S. M., Cleary, P. W., & Cohen, R. C. Z. (2019). Dynamic simulation of flat water kayaking using a coupled biomechanical-smoothed particle hydrodynamics model. *Human Movement Science*, 64, 252–273. <https://doi.org/10.1016/j.humov.2019.02.003>
- Harrison, S. M., & Cohen, R. C. Z. (2019). The bio-mechanic workspace plugin: Enabling biomechanical measurement and simulation across workflows and software applications. In *23rd international congress on modelling and simulation—supporting evidence-based decision making: The role of modelling and simulation, MODSIM 2019* (pp. 442–448). Modelling and Simulation Society of Australia and New Zealand Inc. (MSSANZ).
- Harrison, S. M., Cohen, R. C. Z., Cleary, P. W., Barris, S., & Rose, G. (2016). A coupled biomechanical-Smoothed Particle Hydrodynamics model for predicting the loading on the body during elite platform diving. *Applied Mathematical Modelling*, 40(5–6), 3812–3831. <https://doi.org/10.1016/j.apm.2015.11.009>
- Harrison, S. M., Cohen, R. C. Z., Cleary, P. W., & Pease, D. L. (2014). Torque and power about the joints of the arm during the freestyle stroke. In *XIIth international symposium for biomechanics and medicine in swimming* (pp. 349–355).
- Harrison, S. M., Whitton, R. C., Kawcak, C. E., Stover, S. M., & Pandy, M. G. (2010). Relationship between muscle forces, joint loading and utilization of elastic strain energy in equine locomotion. *Journal of Experimental Biology*, 213(23), 3998–4009. <https://doi.org/10.1242/jeb.044545>
- Hirano, Y., & Tada, N. (1996). Numerical simulation of a turning alpine ski during recreational skiing. *Medicine and Science in Sports and Exercise*, 28(9), 1209–1213. <https://doi.org/10.1097/00005768-199609000-00020>
- Kaps, Mössner, M., Nachbauer, W., & Stenberg, R. (2001). Pressure distribution under a ski during carved turns. *Science and Skiing II: Second International Congress on Science and Skiing*, 180–202.
- Kersh, M. E., Pandy, M. G., Bui, Q. M., Jones, A. C., Arns, C. H., Knackstedt, M. A., Seeman, E., & Zebaze, R. M. D. (2013). The heterogeneity in femoral neck structure and strength. *Journal of Bone and Mineral Research*, 28(5), 1022–1028. <https://doi.org/10.1002/jbmr.1827>
- Keyserling, W. M. (2000). Workplace risk factors and occupational musculoskeletal disorders, part 2: A review of biomechanical and psychophysical research on risk factors associated

- with upper extremity disorders. *American Industrial Hygiene Association Journal*, 61(2), 231–243. [https://doi.org/10.1202/0002-8894\(2000\)061<0231:wraom>2.0.co](https://doi.org/10.1202/0002-8894(2000)061<0231:wraom>2.0.co)
- King, D. (2012). *Dlib C++ library*. <http://dlib.net>.
- Komi, P. V., & Virmavirta, M. (2000). Determinants of successful ski-jumping performance. *Biomechanics in Sport*, 60.
- Krosshaug, T., Slauterbeck, J. R., Engebretsen, L., & Bahr, R. (2007). Biomechanical analysis of anterior cruciate ligament injury mechanisms: Three-dimensional motion reconstruction from video sequences. *Scandinavian Journal of Medicine and Science in Sports*, 17(5), 508–519. <https://doi.org/10.1111/j.1600-0838.2006.00558.x>
- Krüger, A., & Edelmann-Nusser, J. (2010). Application of a full body inertial measurement system in alpine skiing: A comparison with an optical video based system. *Journal of Applied Biomechanics*, 26(4), 516–521. <https://doi.org/10.1123/jab.26.4.516>
- van der Kruk, E., & Reijne, M. M. (2018). Accuracy of human motion capture systems for sport applications; state-of-the-art review. *European Journal of Sport Science*, 18(6), 806–819. <https://doi.org/10.1080/17461391.2018.1463397>
- Legnani, G., Righettini, P., Zappa, B., & Casolo, F. (1996a). A homogeneous matrix approach to 3D kinematics and dynamics—I. Theory. *Mechanism and Machine Theory*, 31(5), 573–587. [https://doi.org/10.1016/0094-114X\(95\)00100-D](https://doi.org/10.1016/0094-114X(95)00100-D)
- Legnani, G., Righettini, P., Zappa, B., & Casolo, F. (1996b). A homogeneous matrix approach to 3D kinematics and dynamics—II. Applications to chains of rigid bodies and serial manipulators. *Mechanism and Machine Theory*, 31(5), 589–605. [https://doi.org/10.1016/0094-114X\(95\)00101-4](https://doi.org/10.1016/0094-114X(95)00101-4)
- Liberky, L. D., & Petschek, A. G. (1990). Smooth particle hydrodynamics with strength of materials. In *Advances in the free-Lagrange method*.
- Lu, T. W., & O'Connor, J. J. (1999). Bone position estimation from skin marker co-ordinates using global optimisation with joint constraints. *Journal of Biomechanics*, 32(2), 129–134. [https://doi.org/10.1016/S0021-9290\(98\)00158-4](https://doi.org/10.1016/S0021-9290(98)00158-4)
- Marras, W. S., Lavender, S. A., Leurgans, S. E., Fathallah, F. A., Ferguson, S. A., Allread, W. G., & Rajulu, S. L. (1995). Biomechanical risk factors for occupationally related low back disorders. *Ergonomics*, 38(2), 377–410. <https://doi.org/10.1080/00140139508925111>
- Mathis, A., Mamidanna, P., Cury, K. M., Abe, T., Murthy, V. N., Mathis, M. W., & Bethge, M. (2018). DeepLabCut: Markerless pose estimation of user-defined body parts with deep learning. *Nature Neuroscience*, 21(9), 1281–1289. <https://doi.org/10.1038/s41593-018-0209-y>
- Mitchelson, J. (2003). *Multiple-camera studio methods for automated measurement of human motion* [PhD Thesis] (University of Surrey).
- Moeslund, T. B., & Granum, E. (2001). A survey of computer vision-based human motion capture. *Computer Vision and Image Understanding*, 81(3), 231–268. <https://doi.org/10.1006/cviu.2000.0897>
- Moissenet, F., Modenese, L., & Dumas, R. (2017). Alterations of musculoskeletal models for a more accurate estimation of lower limb joint contact forces during normal gait: A systematic review. *Journal of Biomechanics*, 63, 8–20. <https://doi.org/10.1016/j.jbiomech.2017.08.025>
- Monaghan, J. J. (1992). Smoothed particle hydrodynamics. *Annual Review of Astronomy and Astrophysics*, 30(1), 543–574. <https://doi.org/10.1146/annurev.aa.30.090192.002551>
- Monaghan, J. J. (1994). Simulating free surface flows with SPH. *Journal of Computational Physics*, 399–406. <https://doi.org/10.1006/jcph.1994.1034>

- Monaghan, J. J. (2005). Smoothed particle hydrodynamics. *Reports on Progress in Physics*, 68(8), 1703–1759. <https://doi.org/10.1088/0034-4885/68/8/R01>
- Monaghan, J. J. (2012). Smoothed particle hydrodynamics and its diverse applications. *Annual Review of Fluid Mechanics*, 44, 323–346. <https://doi.org/10.1146/annurev-fluid-120710-101220>
- Monaghan, J. J., & Gingold, R. A. (1983). Shock simulation by the particle method SPH. *Journal of Computational Physics*, 374–389. [https://doi.org/10.1016/0021-9991\(83\)90036-0](https://doi.org/10.1016/0021-9991(83)90036-0)
- Morais, J. E., Marinho, D. A., Arellano, R., & Barbosa, T. M. (2019). Start and turn performances of elite sprinters at the 2016 European Championships in swimming. *Sports Biomechanics*, 18(1), 100–114. <https://doi.org/10.1080/14763141.2018.1435713>
- Muñoz-Salinas, R., & Garrido-Jurado, S. (2021). ArUco library. <http://sourceforge.net/projects/aruco/>.
- Nagymáté, G., & Kiss, R. (2018). Application of OptiTrack motion capture systems in human movement analysis: A systematic literature review. *Recent Innovations in Mechatronics*, 5(1), 1–9. <https://doi.org/10.17667/riim.2018.1/13>
- Nakano, N., Sakura, T., Ueda, K., Omura, L., Kimura, A., Iino, Y., Fukashiro, S., & Yoshioka, S. (2020). Evaluation of 3D markerless motion capture accuracy using Open-Pose with multiple video cameras. *Frontiers in Sports and Active Living*, 2, 1–9. <https://doi.org/10.3389/fspor.2020.00050>
- Nelson, N. A., & Hughes, R. E. (2009). Quantifying relationships between selected work-related risk factors and back pain: A systematic review of objective biomechanical measures and cost-related health outcomes. *International Journal of Industrial Ergonomics*, 39(1), 202–210. <https://doi.org/10.1016/j.ergon.2008.06.003>
- Plamondon, A., Delisle, A., Bellefeuille, S., Denis, D., Gagnon, D., & Larivière, C. (2014). Lifting strategies of expert and novice workers during a repetitive palletizing task. *Applied Ergonomics*, 45(3), 471–481. <https://doi.org/10.1016/j.apergo.2013.06.008>
- Prakash, M., & Cleary, P. W. (2015). Modelling highly deformable metal extrusion using SPH. *Computational Particle Mechanics*, 2(1), 19–38. <https://doi.org/10.1007/s40571-015-0032-0>
- Pueo, B., & Jimenez-Olmedo, J. M. (2017). Application of motion capture technology for sport performance analysis. *Retos*, 32, 241–247. <https://dialnet.unirioja.es/servlet/articulo?codigo=6352311>.
- Richards, J. G. (1999). The measurement of human motion: A comparison of commercially available systems. *Human Movement Science*, 18(5), 589–602. [https://doi.org/10.1016/S0167-9457\(99\)00023-8](https://doi.org/10.1016/S0167-9457(99)00023-8)
- Riley, P. O., Dicharry, J., Franz, J., Croce, U. D., Wilder, R. P., & Kerrigan, D. C. (2008). A kinematics and kinetic comparison of overground and treadmill running. *Medicine & Science in Sports & Exercise*, 40(6), 1093–1100. <https://doi.org/10.1249/mss.0b013e3181677530>
- Rosso, V., Gastaldi, L., Rapp, W., Lindinger, S., Vanlandewijck, Y., & Linnamo, V. (2017). Biomechanics of simulated versus natural cross-country sit skiing. *Journal of Electromyography and Kinesiology*, 32, 15–21. <https://doi.org/10.1016/j.jelekin.2016.11.002>
- Rubin, B. D. (1999). The basics of competitive diving and its injuries. *Clinics in Sports Medicine*, 18(2), 293–303. [https://doi.org/10.1016/S0278-5919\(05\)70145-9](https://doi.org/10.1016/S0278-5919(05)70145-9)
- Schache, A. G., Kim, H. J., Morgan, D. L., & Pandy, M. G. (2010). Hamstring muscle forces prior to and immediately following an acute sprinting-related muscle strain injury. *Gait and Posture*, 32(1), 136–140. <https://doi.org/10.1016/j.gaitpost.2010.03.006>

- Sinclair, J., John Taylor, P., & Jane Hobbs, S. (2013). Digital filtering of three-dimensional lower extremity kinematics: An assessment. *Journal of Human Kinetics*, 39(1), 25–36. <https://doi.org/10.2478/hukin-2013-0065>
- Sinnott, M. D., Cleary, P. W., Arkwright, J. W., & Dinning, P. G. (2012). Investigating the relationships between peristaltic contraction and fluid transport in the human colon using Smoothed Particle Hydrodynamics. *Computers in Biology and Medicine*, 42(4), 492–503. <https://doi.org/10.1016/j.combiomed.2012.01.002>
- Smith, S. H. L., Coppack, R. J., van den Bogert, A. J., Bennett, A. N., & Bull, A. M. J. (2021). Review of musculoskeletal modelling in a clinical setting: Current use in rehabilitation design, surgical decision making and healthcare interventions. *Clinical Biomechanics*, 83. <https://doi.org/10.1016/j.clinbiomech.2021.105292>
- Stomakhin, A., Schroeder, C., Chai, L., Teran, J., & Selle, A. (2013). A material point method for snow simulation. *ACM Transactions on Graphics*, 32(4), 1–10. <https://doi.org/10.1145/2461912.2461948>
- Valevicius, A. M., Jun, P. Y., Hebert, J. S., & Vette, A. H. (2018). Use of optical motion capture for the analysis of normative upper body kinematics during functional upper limb tasks: A systematic review. *Journal of Electromyography and Kinesiology*, 40, 1–15. <https://doi.org/10.1016/j.jelekin.2018.02.011>
- Vennell, R., Pease, D., & Wilson, B. (2006). Wave drag on human swimmers. *Journal of Biomechanics*, 39(4), 664–671. <https://doi.org/10.1016/j.biomech.2005.01.023>
- Von Loebbecke, A., Mittal, R., Mark, R., & Hahn, J. (2009). A computational method for analysis of underwater dolphin kick hydrodynamics in human swimming. *Sports Biomechanics*, 8(1), 60–77. <https://doi.org/10.1080/14763140802629982>
- Wilkins, J. L. (1964). Calculation of elastic-plastic flow. In *Methods of computational physics* (pp. 211–263).
- Workspace. (n.d.). <https://research.csiro.au/workspace/>.
- Wu, Y., Kirillov, A., Massa, F., Lo, W. Y., & Girshick, R. (2019). Detectron2. <https://github.com/facebookresearch/detectron2>.
- Zhang, Z. (2000). A flexible new technique for camera calibration. *IEEE Transactions on Pattern Analysis and Machine Intelligence*, 22(11), 1330–1334. <https://doi.org/10.1109/34.888718>

This page intentionally left blank

# Digital human modeling in cleft care

# 29

Hanyao Huang, Jingtao Li, Bing Shi

*State Key Laboratory of Oral Diseases and National Clinical Research Center for Oral Diseases and Department of Oral and Maxillofacial Surgery, West China Hospital of Stomatology, Sichuan University, Chengdu, Sichuan, China*

## Chapter outline

Introduction.....	767
Presurgical infant orthopedics .....	769
Cleft lip and cleft lip nasal deformity repair.....	771
Cleft palate repair.....	773
Alveolar bone cleft reconstruction .....	775
Orthognathic surgery in cleft care.....	776
Conclusion .....	778
References .....	778

## Introduction

Congenital craniomaxillofacial clefts are birth defects in humans (Worley et al., 2018). Cleft lip and palate and alveolar cleft are the most common (Fig. 29.1). Cleft lip and palate are the results of facial tissues not joining correctly during development. Cleft lip presents as openings in the upper lip that can affect the shape of the nose. The opening may be lateral, bilateral, or in the middle. Cleft palate is present at the palate where exists an opening into the nasal cavity. In China, newborns' incidence rate is as high as 1 in 700, forming a population of more than one million patients under a huge population (Fan et al., 2018). Cleft lip and palate affect almost all oral and maxillofacial physiological functions except vision, severely reducing the quality of life of patients and cause a heavy medical burden (Sitzman et al., 2016). Fortunately, under the complete multiexpert team treatment mode, cleft lip and palate have become the most promising congenital defects that can be repaired entirely to normal.

Given that cleft lip and palate deformity involves various types of soft and hard tissues defects, with ectopic positions in the orofacial regions, multiple treatments by team works are needed. Because of this, surgeons, orthodontists, and speech-language therapists form the core of the multidisciplinary treatment team for cleft lip and palate (Vig & Mercado, 2015). For the past decades, doctors and surgeons



**FIGURE 29.1 Cleft lip, cleft palate, and alveolar bone cleft.**

(A) Cleft lip. (B) Cleft Palate. (C) Alveolar bone cleft.

have tried to develop a better strategy for the treatment of cleft patients, and the therapeutic effect was indeed improved. However, all these improvements were based on experience, and the mechanisms were not clear. The representative questions are as follows: what biomechanics changes happen after modifying a surgical maneuver for cleft lip repair? How to decide whether the patients after cleft palate repair are velopharyngeal insufficiency? How alveolar bone grafting helps restore occlusion?

Digital human modeling is one best choice as a tool to reveal the biomechanics of the surgery and treatments and assist surgeons in improving surgical care for patients. As such a complex process of treatments, the primary goals should include clarification of surgical goals, rationalization of surgical methods, precision and personalization of surgical design and preparation, and improved convenience of doctor–patient communication. Digital human modeling can become an effective way to achieve these goals (Shi & Huang, 2020).

Digital technology is widely popularized and applied in the fields of dentistry and oral and maxillofacial surgery. Digital imaging data collection and long-distance transmission can reduce the number of patient visits; digital analysis methods help to understand the characteristics of maxillofacial deformities fully, formulate personalized treatment plans and simulate the treatment process and effects; digital design and 3D printing technology can effectively improve the accuracy and success rate of the treatment, and reduce the operation time. Thus, digital human modeling can form the connection between the principle and practice.

In cleft care, digital human modeling can assist in exploring the role of physical factors like measuring facial landmarks, which cannot be easily measured on photos or natural human faces. It can also predict the results, which can help modify the external conditions applied in practice. Digital human modeling has become an important tool for cleft care due to its high efficiency, low costs, and ability to analyze and simulate organs and tissues independently. Based on the above advantages, digital technology has been successfully applied in the multiple-team treatment for cleft lip and palate. It has achieved initial results in simplifying the diagnosis and treatment process, improving treatment efficiency, and reducing the medical burden of patients.

In this chapter, we would like to introduce the applications of digital human modeling and related computational simulation in cleft care and how these applications were carried out. We also summarized the advantages, latest findings, and application progress of various digital human modelling-related technologies used in clinic cleft care and research.

## Presurgical infant orthopedics

Primary surgical reconstruction is the basis of the entire team treatment, and the quality of its completion directly determines the complexity of the subsequent treatments and the final surgical outcomes. However, the skeletal structural dislocation existing in primary cleft lip and palate deformity cannot be corrected by primary cleft lip repair. The tissue gap caused by the bony deformity significantly limits the reconstruction of the nasolabial soft tissue morphology of primary operation.

McNeil first proposed Presurgical Infant Orthopedics before the primary surgical repair of cleft lip and palate assisted by orthodontic methods in 1950 (Mc, 1950). Latham introduced his technical experience of using a nail-retained palatal plate with a threaded distractor and an elastic rubber ring to actively adjust the position of the alveolar bone segment of the cleft lip and palate (Latham, 1980). After that, Grayson proposed in the 1990s to use the palatal plate to passively guide the changes in the position of the bone segment and to add a nasal support device to the palate to shape the nose at the same time, forming nasoalveolar molding (NAM) technology (Grayson et al., 1999). NAM technology is noninvasive and has been proven to effectively improve the long-term effect of nasolabial repair without affecting the average growth and development of children.

However, NAM treatment requires children to see a doctor early after birth, adjust the appliance every 1–2 weeks, and require about 10 frequent follow-up visits before the primary operation, which causes great inconvenience to children and their families in remote areas. It is especially noticeable when combined with systemic problems such as feeding and breathing. Taking our center as an example, the traditional NAM treatment process suggests that the child should be diagnosed within 4 weeks after birth to clarify the diagnosis and the necessity of preoperative orthopedics, obtain an intraoral impression, and make a palatal plate. This treatment process has high requirements for the compliance of the children's family, which significantly limits the popularization and application of NAM technology.

Suppose a mode similar to invisible orthodontic treatment can be introduced into NAM treatment. In that case, the aligner can be designed step by step with the help of digital technology. The design and production of all the corrective devices required for the entire treatment can be completed within a single visit, which will greatly improve the ease of use of NAM technology. In 2009, Lozko et al. first proposed to use digital technology to simulate the phase changes of the alveolar segment of cleft lip and palate during NAM treatment (Lozko et al., 2009). On this basis, the combination of computer-aided design (CAD) and manufacturing

(CAM) technology to develop a variety of digital NAM diagnosis and treatment processes became popular (Fig. 29.2).

The current NAM digitization process reported in the works of literature is mainly divided into two categories. The first type is called CAD-NAM, that is, after the digital simulation of the orthopedic process, a series of 3D dental models are printed out, and on this basis, NAMs for each treatment stage are made at one time (Gong et al., 2017; Gong & Yu, 2012; Shen et al., 2015; Yu et al., 2011, 2013). Although this method achieves the centralized production of multiple NAMs, it still requires manual power and time. The second category further digitizes the production process. After simulating the digital models at each stage of the correction, the palatal plates that match each model are manually designed, or the Freeform manual designed through parametric design, and the nasal support parts are manually added after 3D printing (Loeffelbein et al., 2015). This process is more digital, but the whole design process needs to judge the extension of the palatal plate according to the soft tissue area based on the physician's clinical experience. Fixed parametric design often fails to estimate highly individualized anatomical details. Freeform manual design is reliable but time-consuming. To this end, Bauer et al. introduced an automated method and proposed the RapidNAM process (Bauer, Schonberger, et al., 2017). In the design software, artificial intelligence algorithms are used to automatically identify the range of the alveolar bone and generate a palatal plate for physician review, which significantly improves the efficiency of NAM manufacturing.

Although studies have shown that the current digital process can achieve better treatment effects than traditional NAM, it still needs further improvement. In the staged model simulation, the growth of the occlusion and oral structure during the treatment process is an important variable that cannot be ignored. RapidNAM automated design estimates 18% growth. Generally, six pairs of NAMs are made, and 3% of the growth is evenly distributed among each pair. However, the fixed-parameter setting ignores the huge individualized differences in children's visit time and growth potential, partially explaining why the current NAMs manufactured by the RapidNAM process meet about 80% of the clinical requirements (Bauer, Gull, et al., 2017).



**FIGURE 29.2** Digital modeling—assisted presurgical infant orthopedics.

(A) Pretreatment cleft. (B) Computer-aided molding manufacturing. (C) Posttreatment cleft.

Besides, due to the risk of airway obstruction caused by material retention, the existing digital design is mainly based on the physical impression or plaster model's three-dimensional scanning. Limited case reports apply the intraoral 3D scanner to the NAM process. Still, it suggests that the existing device probe does not match newborns' oral environment with cleft lip and palate and cannot stably obtain the whole structure of the cleft and the morphology of the maxillary nodules (Krey et al., 2018). It is believed that the continuous improvement of artificial intelligence algorithms and the advancement of equipment will gradually solve the above problems. If the entire process from data acquisition to NAM production can be automated and digitized, this means that remote NAM treatment will become possible, significantly reducing the cost of treatment time for children and their families.

---

### Cleft lip and cleft lip nasal deformity repair

Cleft lip repair is the first surgical intervention for patients. The goals of cleft lip repair are to close the cleft of the skin, reconstruct the muscle of the lip, and close the nasal floor to restore the symmetry to the lip and nose. Although contemporary surgical repair could constantly achieve satisfactory lip morphology, the accompanying scar and nasal deformity persist.

To better understand the cleft and the related surgical intervention, a suitable evaluation method should be used. The biggest advantage of 2D evaluation for cleft patients is that it can be applied to most medical centers, requiring some practice to make the photograph standardized (Farkas et al., 2000; Xu et al., 2014). However, 3D evaluation should still be the most objective way to measure the face. The first attempt for the 3D evaluation of cleft patients was by using stereophotogrammetry (Ras et al., 1994). Since then, 3D evaluation has been applied to assess cleft-related facial asymmetry (Bugaighis et al., 2014; Djordjevic et al., 2014; Kuijpers et al., 2015; Meyer-Marcotty et al., 2011). The plaster model can also be used for 3D assessment (Xu et al., 2013).

Besides landmarks measurements, dividing the face into right and left halves and analyzing each side using a set of linear and angular measurements is also a standard method (Ferrario et al., 2001). Another method of assessing facial asymmetry is the mirror image technique, which is usually illustrated in a color map to demonstrate the differences between the right and left sides of the face (Verhoeven et al., 2016). Moreover, longitudinal evaluation of asymmetry to assess facial appearance can be a more precise method for cleft morphology evaluation (Al-Rudainy et al., 2019).

As for cleft lip nasal deformity, because of the displacement and hypoplasia of the cartilage framework in the cleft nose, cleft lip nasal deformity has some typical morphological characteristics, including the deviation of nasal tip and columella, displacement of nasal base, collapse of the alar dome, and discontinuity of the nasal sill. Various surgical maneuvers have been applied to restore both the upper lip's

shape and the anatomical nasal structure. Cleft lip and cleft lip nasal deformity remain the major challenges to surgeons and cleft management teams. The digital modeling of the cartilage is the key to the application of digital modeling in cleft lip nasal deformity.

Thus, advances in 3D imaging technology will promote digital modeling to cleft lip nasal deformity. MRI data has been used to reconstruct nasal cartilage. Patient-specific nasal cartilage structure can be reconstructed based on individual patient data. Our team proved that using MRI to scan the nasolabial part of ordinary people and patients with unilateral cleft lip and nose deformities can get acceptable imaging data for reconstructing their nose's cartilage structure and designed surgery based on their cartilage structure. However, the resolution should be as higher as possible in the future (Huang, Li, et al., 2018; Huang, Luo, Cheng, Zhang, et al., 2018).

After digital modeling of the nasal structure, we can study the surgical maneuver mechanism, which will help surgeons understand surgery better and modify the operation. Our team works on the finite element analyses of nasal cartilage of cleft lip rhinoplasty, which reconstructs nasal cartilage based on individual patient imaging data (Fig. 29.3). The clinical outcomes were also included in the study for more comprehensive analyses. Finite element analysis was first applied to study the pathological tethers on the nasal cartilages during the development of unilateral cleft lip nasal deformities, and we verified the pathological tethers with clinical observation

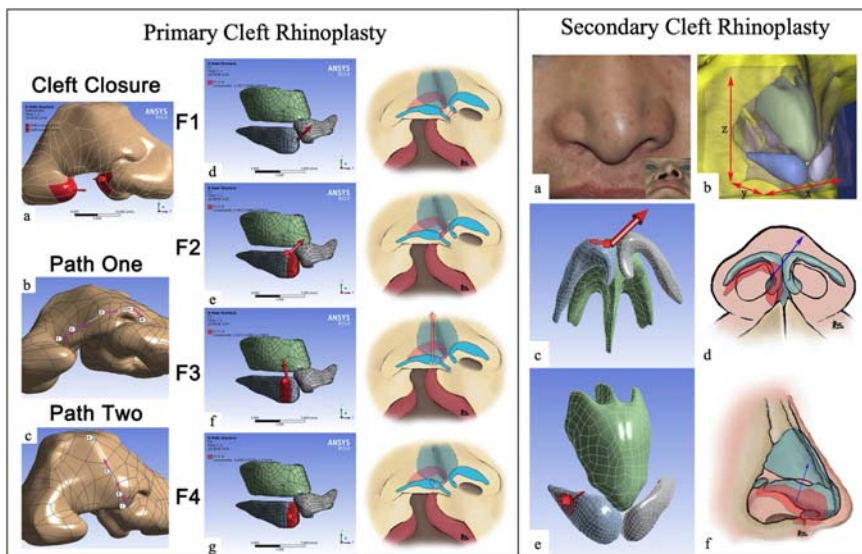


**FIGURE 29.3 Application of digital modeling in cleft lip nasal deformity.**

From Shi, B., & Huang, H. (2020). Computational technology for nasal cartilage-related clinical research and application. International Journal of Oral Science, 12(1), 21. <https://doi.org/10.1038/s41368-020-00089-y>  
 (Left) Analyses of primary cleft lip rhinoplasty. (Right) Analyses of secondary cleft lip rhinoplasty.

(Huang, Luo, Cheng, Zhang, et al., 2018). Then finite element method was used to assess the effect of several common-used alar cartilage suspension maneuvers during primary cleft lip rhinoplasty and demonstrated the characteristics of different maneuvers (Huang, Cheng, Luo, et al., 2019). We also studied the biomechanical force that should be included during cleft lip rhinoplasty (Huang, Luo, Cheng, Shi, et al., 2018). A secondary unilateral cleft lip nasal deformity model was also established, and two suturing maneuvers of secondary cleft lip rhinoplasty were simulated. Thus, the functional biomechanical characteristics of the nasal structure can be demonstrated clearly, which can be combined with clinical data to verify the finite element outcomes (Huang, Li, et al., 2018).

Digital modeling is also used in surgical education of cleft care. In 2002, Cutting et al. used 3D computational animation to teach cleft lip and palate surgery. These animations demonstrated the surgical process of cleft lip reconstruction. The animations made the medical students or surgeons understand the surgical process much more straightforward. This technology has been further developed recently, turning it into the digital simulation that realized human–computer interaction, enabling students to study each surgical step more carefully (Kantar et al., 2020). Now the student can learn the surgical process on their smartphone with the APP SmileTrain.

However, if we want to use digital modeling in clinical treatment for cleft lip noses, the problem that needs to be solved is the limitation of 3D imaging technology, as the resolution of ordinary MRI is low (Shi & Huang, 2020). However, it is believed that with the development of technology, these problems will be gradually solved, and virtual surgery planning will be well applied to cleft lip rhinoplasty.

---

## Cleft palate repair

The purpose of cleft palate repair is to reconstruct the velopharyngeal structure and restore speech ability. Unlike cleft lip repair, which is only the change of outlook, cleft palate repair changes the airway structure that cannot be easily observed. Thus, digital modeling can help solve the problem, as well model reconstruction is much easier than cartilage model reconstruction.

No model including all the muscle structures has been reconstructed for the cleft palate–related soft tissue reconstruction. Simplified models are jointly used. In 1999, the first finite element model of the soft palate was established (Berry et al., 1999). The finite element model of the velopharyngeal structure was used to investigate factors affecting velopharyngeal closure (Srodon et al., 2012). Digital modeling also helps demonstrate more details of the cleft uvular muscle (Landes et al., 2012). Then the correlation of the velopharyngeal structure and cleft palate repair was revealed (Inouye et al., 2015, 2016). Anyway, a more complex digital model should be reconstructed for a more comprehensive study in the future.

As for digital airway modeling, it is much easier because of the apparent boundary between the airway and tissues. A study investigated 3D differences of the pharynx in adult patients with unrepaired cleft palate versus normal adults using digital

modeling. Digital models can help demonstrate the specific structures of the airways: An enlarged nasopharynx in the sagittal plane and increased nasopharyngeal airway volume at the palatal plane in patients with unilateral cleft palate.

Airway structure influences the airflow dynamics through the airway. Thus, surgical intervention to the airway will change the air dynamics, which may affect patients' speech. The ventilation function of the airway is also critical. There are many methods for assessing ventilation function, such as peak nasal rhinomanometry (RM) and acoustic rhinometry (AR). Although these methods can help to understand the status of the ventilation function, it is still not clear about the characteristics of airflow. Therefore, digital modeling combined with computational fluid dynamics (CFD) can become an effective method for analyzing the characteristics of airway airflow. Visualizing and quantifying the fluid by CFD can significantly improve the understanding of the physiological functions of the airway.

For understanding the velopharyngeal function, CFD can be applied (Fig. 29.4). Different velopharyngeal functions have different airflow dynamic features, and CFD simulation is found as application potential in individualized velopharyngeal surgery planning (Huang, Cheng, Wang, et al., 2019). Different velopharyngeal closure patterns decide the airflow dynamics of the velopharynx and had different largest permitted orifice areas for getting the appropriate oral pressures for normal speech (Huang, Yin, et al., 2020). Posterior pharyngeal flap application will heavily change the airflow dynamics of the upper airway (Huang, Liao, et al., 2020).

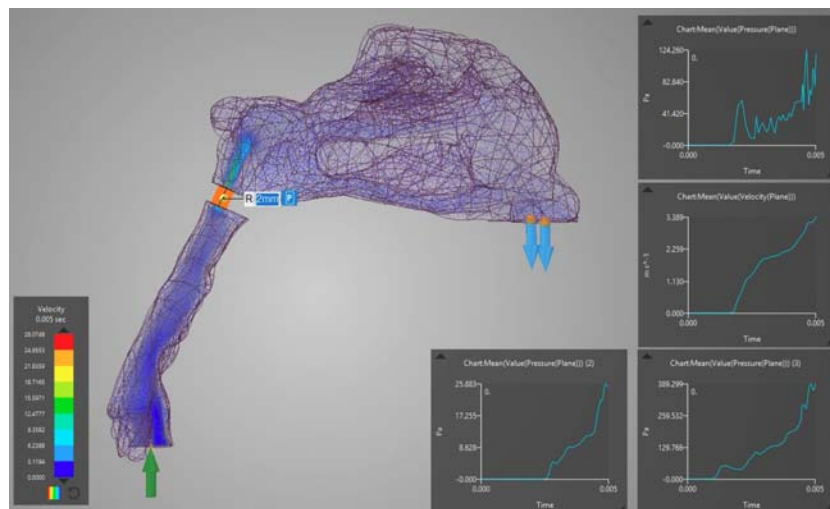


**FIGURE 29.4** Application of digital modeling in cleft palate.

## Alveolar bone cleft reconstruction

The congenital alveolar bone cleft is manifested as a defect in the front mandible bone from the base of the nose to the top of the alveolar ridge, causing the continuity of the dental arch to be interrupted and the stability of the mandible bone to be lost, which in turn leads to the subsequent collapse of the bony base of the dental arch and nasolabial area as well as related abnormal growth. Alveolar bone cleft reconstruction is the treatment that involves hard tissue reconstruction. It is of great significance to the restoration of nasolabial shape, the reconstruction of alveolar bone function, and the subsequent average growth and development of the maxillofacial structure. It is the key to the succession of the cleft lip and palate sequence treatment (Cho-Lee et al., 2013).

The shape of the alveolar bone cleft is generally a funnel-shaped hexahedron with a wide top and a narrow bottom. The digital analysis of CBCT images helps understand the positional relationship and coordinate with the surgeon to formulate an appropriate plan under the premise of clear risk, and at the same time to make a comprehensive measurement of the effect of the bone graft restoration (Kasaven et al., 2017; Kesztyüs et al., 2019). The volume of unilateral and bilateral alveolar cleft defects can be quantified by 3D-printed and virtual surgical simulation methods, which can serve as a reference for the planning and execution of alveolar bone graft surgery (Chou et al., 2019).

For excessively wide alveolar bone cleft, autogenous bone grafting is not effective, and using the orthodontic method alone cannot effectively reduce the distance between the bone segments on both sides of the cleft (Long et al., 1995). At this time, osteotomy of the alveolar bone and distraction osteogenesis techniques are needed to close the cleft (Liou et al., 2000).

Digital modeling can help effectively simulate the position of the osteotomy line, the direction of movement of the bone segment, the distance of the distraction, and the final shape of the dental arch. Orthodontists can intuitively compare the advantages and disadvantages of osteotomy options between different teeth and choose the most conducive design to restore normal dentition after surgery. For surgeons, digital modeling helps to select the appropriate osteotomy line position, evaluate the airway morphology after the bone being moved, and estimate the interference that may need to be removed. On this basis, with the help of computer-aided manufacturing and 3D printing technology, a physical model of the bone in the surgical area is obtained, and the personalized bending of the distractor is completed before the operation; the osteotomy guide can also be designed and manufactured to assist in the precise operation to avoid iatrogenicity injury.

As for bilateral cleft lip, the dental arch of patients is divided into three segments by the cleft. The premaxillary bone is connected to the septum structure only by the vomer. The bone segments are not synchronized in the process of growth and development. The premaxillary bone may overgrow in the sagittal and vertical directions, and the lateral mandible bone segments on both sides may rotate and narrow into the cleft. This type of deformity correction requires orthodontic arch expansion and

premaxillary bone osteotomy reduction (Almas et al., 2019). Therefore, digital modeling also contributes to the design and implementation of the treatment plan. The preoperative digital design helps to quantify the preoperative expansion distance, select the best reduction position, and determine the osteotomy position and range. On this basis, designing corresponding osteotomy guides and terminal occlusal guides can significantly improve the accuracy and success rate of surgical treatment, minimize the time loss of trial and error during surgery, and obtain effective bone segment retention after surgery.

Meanwhile, the three-dimensional finite element analysis based on the digital jaw bone model can simulate the patient's actual maxillofacial structure and deepen the understanding of the secondary deformity of cleft lip and palate from the perspective of biomechanics. For example, through digital modeling and finite element model construction of different types of cleft lip and palate bone defects, applying bite force along the long axis of the tooth can observe the stress distribution and offset the trend of various parts of the jaw under different deformities. The study found that when the alveolar bone cleft extends to the palate, the asymmetry of the deformation and the degree of the alveolar bone segment collapsing toward the cleft significantly increase; the deformation can be observed after the bite force is applied, but the degree is significantly reduced in the alveolar bone cleft. These results are highly consistent with clinical imaging observations, suggesting that the stability of the alveolar bone may be one of the related mechanisms of bony dysplasia (Fig. 29.5) (Luo et al., 2019).

---

### Orthognathic surgery in cleft care

Patients with cleft lip and palate often suffer from severe maxillary underdevelopment due to the primary deformity and iatrogenic growth interference caused during the treatment process. Compared with the orthodontic treatment of the general population, patients with cleft lip and palate are usually more severely deformed. The maxilla is insufficient in the sagittal, vertical, and horizontal directions, and the range of bone movement is more extensive; and patients with cleft lip and palate often have asymmetry of the bony structure; also, the cleft lip and palate has scars in the nasolabial and palatine pharynx, and the resistance of the bone movement is more significant. Thus, the risk of recurrence is higher (Jiang et al., 2020). These factors have significantly increased the complexity and the uncertainty of the effect of bony deformity restoration in patients with cleft lip and palate. Compared with traditional plaster model surgery, digital modeling and surgical design help doctors more accurately grasp the influence of the treatment plan on the structure of the maxillofacial soft and hard tissues. The preoperative design is often challenging to complete by only relying on the plaster model of the dentition, which highlights the advantages of digital modeling (Wang et al., 2020).

Another part of digital assisted treatment is the computer-aided production of occlusal guides and surgical guides (Fig. 29.6). The 3D printed digitally designed

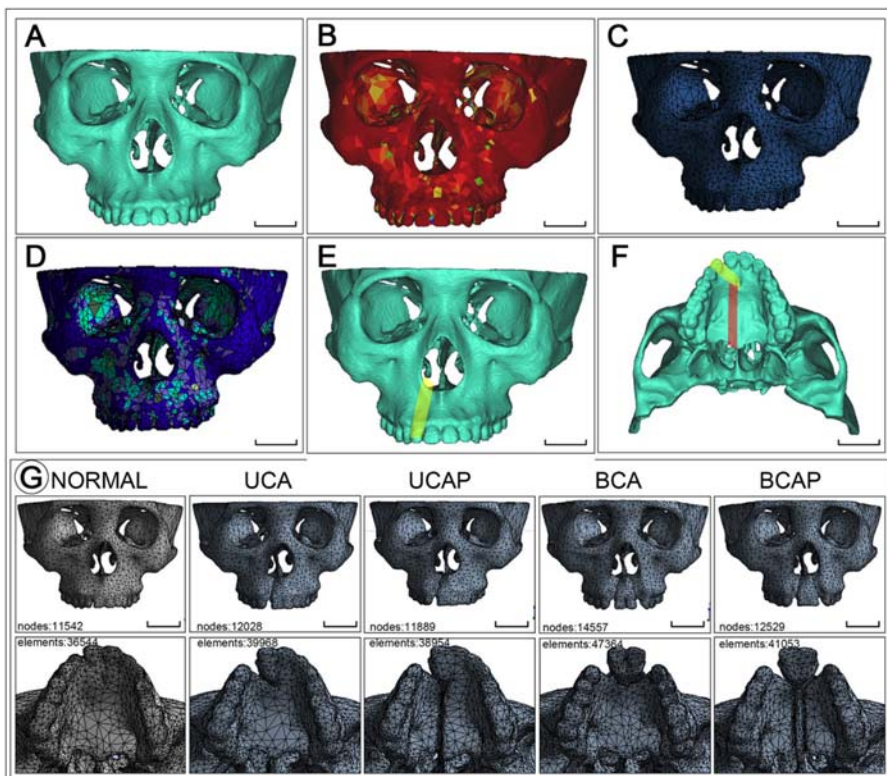


**FIGURE 29.5 Application of digital modeling in alveolar bone cleft.**

From Luo, X., Huang, H., Yin, X., Shi, B., & Li, J. (2019). Functional stability analyses of maxillofacial skeleton bearing cleft deformities. *Scientific Reports*, 9(1), 4261. <https://doi.org/10.1038/s41598-019-40478-w>  
Application of digital modeling in alveolar bone cleft.

occlusal guide is more convenient and quicker than the traditional handmade occlusal guide, but there is no significant difference in manufacturing accuracy. The advantages of the digital occlusal guide are more derived from the accuracy of the digital surgical plan design. The surgical guide theoretically helps to implement the designed osteotomy, advancement, and retention more accurately. However, based on our experience, in the treatment of bimaxillary orthodontics for type III patients, although the surgical guide can achieve more accurate bone movement immediately after the operation, its advantages are entirely reduced during the follow-up process. Covered by the relapse, it did not significantly improve the long-term accuracy after surgery (Xu et al., 2020). Therefore, the application value of digital surgical guides in maxillary advancement remains to be discussed, and more relevant studies are needed.

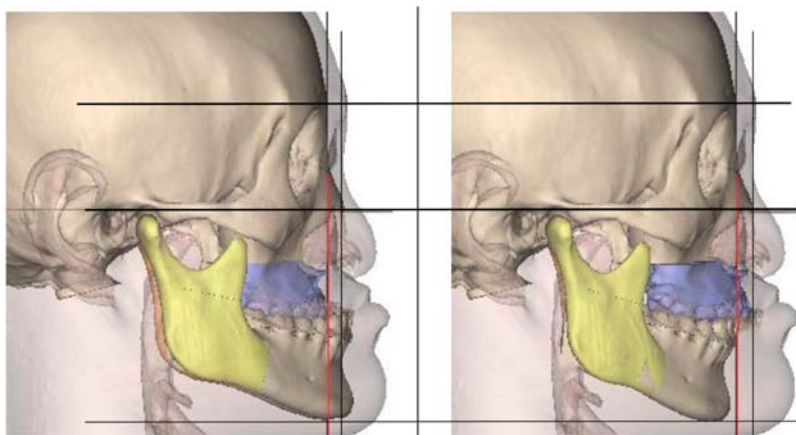


**FIGURE 29.6 Application of digital modeling in orthognathic surgery of cleft patients.**

## Conclusion

The requirements of the team treatment for cleft lip and palate provide a broad application stage for digital technology. Digital technology has demonstrated extensive application value in the analysis of the deformity characteristics of cleft lip and palate, the design of treatment plans, and the research of related mechanisms, providing new ideas and methods to simplify the treatment process, reduce the medical burden, and improve the therapeutic effect. Besides, the digitization of case data collection and diagnosis and treatment process helps promote the management of the biological information database of cleft lip and palate. Therefore, exploration of the application of digital modeling in the clinical and related research of cleft care is expected to improve cleft care.

## References

- Al-Rudainy, D., Ju, X., Mehendale, F. V., & Ayoub, A. (2019). Longitudinal 3D assessment of facial asymmetry in unilateral cleft lip and palate. *The Cleft Palate-Craniofacial Journal*, 56(4), 495–501. <https://doi.org/10.1177/1055665618780108>
- Almas, F., Cote, V., Ramly, E. P., Kantar, R. S., & Hamdan, U. (2019). Premaxillary setback with posterior vomerine osteotomy: Outcomes of single-stage repair of complete bilateral cleft lip with a severely protruding premaxilla. *The Cleft Palate-Craniofacial Journal*, 56(4), 471–478. <https://doi.org/10.1177/1055665618782806>
- Bauer, F. X., Gull, F. D., Roth, M., Ritschl, L. M., Rau, A., Gau, D., Gruber, M., Eblenkamp, M., Hilmer, B., Wolff, K. D., & Loeffelbein, D. J. (2017). A prospective longitudinal study of postnatal dentoalveolar and palatal growth: The anatomical basis for CAD/CAM-assisted production of cleft-lip-palate feeding plates. *Clinical Anatomy*, 30(7), 846–854. <https://doi.org/10.1002/ca.22892>

- Bauer, F. X., Schonberger, M., Gattinger, J., Eblenkamp, M., Wintermantel, E., Rau, A., Gull, F. D., Wolff, K. D., & Loeffelbein, D. J. (2017). RapidNAM: Generative manufacturing approach of nasoalveolar molding devices for presurgical cleft lip and palate treatment. *Biomedical Engineering (Berl)*, 62(4), 407–414. <https://doi.org/10.1515/bmt-2016-0035>
- Berry, D. A., Moon, J. B., & Kuehn, D. P. (1999). A finite element model of the soft palate. *The Cleft Palate-Craniofacial Journal*, 36(3), 217–223. [https://doi.org/10.1597/1545-1569\\_1999\\_036\\_0217\\_afemot\\_2.3.co\\_2](https://doi.org/10.1597/1545-1569_1999_036_0217_afemot_2.3.co_2)
- Bugaighis, I., Mattick, C. R., Tiddeman, B., & Hobson, R. (2014). 3D asymmetry of operated children with oral clefts. *Orthodontics & Craniofacial Research*, 17(1), 27–37. <https://doi.org/10.1111/ocr.12026>
- Cho-Lee, G. Y., Garcia-Diez, E. M., Nunes, R. A., Marti-Pages, C., Sieira-Gil, R., & Rivera-Baro, A. (2013). Review of secondary alveolar cleft repair. *Annals of Maxillofacial Surgery*, 3(1), 46–50. <https://doi.org/10.4103/2231-0746.110083>
- Chou, P.-Y., Denadai, R., Hallac, R. R., Dumrongwongsiri, S., Hsieh, W.-C., Pai, B. C., & Lo, L.-J. (2019). Comparative volume analysis of alveolar defects by 3D simulation. *Journal of Clinical Medicine*, 8(9), 1401. <https://doi.org/10.3390/jcm8091401>
- Djordjevic, J., Lewis, B. M., Donaghy, C. E., Zhurov, A. I., Knox, J., Hunter, L., & Richmond, S. (2014). Facial shape and asymmetry in 5-year-old children with repaired unilateral cleft lip and/or palate: An exploratory study using laser scanning. *European Journal of Orthodontics*, 36(5), 497–505. <https://doi.org/10.1093/ejo/cjs075>
- Fan, D., Wu, S., Liu, L., Xia, Q., Tian, G., Wang, W., Ye, S., Wang, L., Rao, J., Yang, X., Yu, Z., Xin, L., Li, S., Duan, Z., Zhang, T., Wu, S., Guo, X., & Liu, Z. (2018). Prevalence of non-syndromic orofacial clefts: Based on 15,094,978 Chinese perinatal infants. *Oncotarget*, 9(17), 13981–13990. <https://doi.org/10.18632/oncotarget.24238>
- Farkas, L. G., Forrest, C. R., & Phillips, J. H. (2000). Comparison of the morphology of the “cleft face” and the normal face: Defining the anthropometric differences. *Journal of Craniofacial Surgery*, 11(2), 76–82. <https://doi.org/10.1097/00001665-20001102-00003>
- Ferrario, V. F., Sforza, C., Ciusa, V., Dellavia, C., & Tartaglia, G. M. (2001). The effect of sex and age on facial asymmetry in healthy subjects: A cross-sectional study from adolescence to mid-adulthood. *Journal of Oral and Maxillofacial Surgery*, 59(4), 382–388. <https://doi.org/10.1053/joms.2001.21872>
- Gong, X., & Yu, Q. (2012). Correction of maxillary deformity in infants with bilateral cleft lip and palate using computer-assisted design. *Oral Surgery, Oral Medicine, Oral Pathology, and Oral Radiology*, 114(5 Suppl. 1), S74–S78. <https://doi.org/10.1016/j.tripleo.2011.08.031>
- Gong, X., Zhao, J., Zheng, J., & Yu, Q. (2017). A digital assessment of the maxillary deformity correction in infants with bilateral cleft lip and palate using computer-aided nasoalveolar molding. *Journal of Craniofacial Surgery*, 28(6), 1543–1548. <https://doi.org/10.1097/SCS.0000000000003812>
- Grayson, B. H., Santiago, P. E., Brecht, L. E., & Cutting, C. B. (1999). Presurgical nasoalveolar molding in infants with cleft lip and palate. *The Cleft Palate-Craniofacial Journal*, 36(6), 486–498. [https://doi.org/10.1597/1545-1569\\_1999\\_036\\_0486\\_pnmiiw\\_2.3.co\\_2](https://doi.org/10.1597/1545-1569_1999_036_0486_pnmiiw_2.3.co_2)
- Huang, H., Cheng, X., Luo, X., Shi, B., & Li, J. (2019). Biomechanical analyses of common suspension sutures in primary cleft lip rhinoplasty. *Head & Face Medicine*, 15(1), 20. <https://doi.org/10.1186/s13005-019-0203-y>

- Huang, H., Cheng, X., Wang, Y., Huang, D., Wei, Y., Yin, H., Shi, B., & Li, J. (2019). Analysis of velopharyngeal functions using computational fluid dynamics simulations. *Annals of Otology, Rhinology & Laryngology*, 128(8), 742–748. <https://doi.org/10.1177/0003489419842217>
- Huang, H., Liao, R., Yin, X., Chen, N., Huang, D., Yin, H., Deng, C., Zheng, Q., Shi, B., & Li, J. (2020). Airflow of the two-port velopharyngeal closure: Study using computational fluid dynamics. *Journal of Craniofacial Surgery*, 31(8), 2188–2192. <https://doi.org/10.1097/scs.0000000000006772>
- Huang, H., Li, Y., Luo, X., Cheng, X., Shi, B., & Li, J. (2018). Mechanical analyses of critical surgical maneuvers in the correction of cleft lip nasal deformity. *PLoS One*, 13(4), e0195583. <https://doi.org/10.1371/journal.pone.0195583>
- Huang, H., Luo, X., Cheng, X., Shi, B., & Li, J. (2018). Biomechanical simulation of correcting primary unilateral cleft lip nasal deformity. *PLoS One*, 13(6), e0199964. <https://doi.org/10.1371/journal.pone.0199964>
- Huang, H., Luo, X., Cheng, X., Zhang, Z., Ma, G., Shi, B., & Li, J. (2018). Recapitulation of unilateral cleft lip nasal deformity on normal nasal structure: A finite element model analysis. *Journal of Craniofacial Surgery*, 29(8), 2220–2225. <https://doi.org/10.1097/scs.0000000000005024>
- Huang, H., Yin, H., Wang, Y., Chen, N., Huang, D., Luo, X., Yin, X., Zheng, Q., Shi, B., & Li, J. (2020). Computational fluid dynamic analysis of different velopharyngeal closure patterns. *Annals of Otology, Rhinology & Laryngology*, 129(2), 157–163. <https://doi.org/10.1177/0003489419879176>
- Inouye, J. M., Lin, K. Y., Perry, J. L., & Blemker, S. S. (2016). Contributions of the musculus uvulae to velopharyngeal closure quantified with a 3-dimensional multimuscle computational model. *Annals of Plastic Surgery*, 77(Suppl. 1), S70–S75. <https://doi.org/10.1097/sap.0000000000000777>
- Inouye, J. M., Pelland, C. M., Lin, K. Y., Borowitz, K. C., & Blemker, S. S. (2015). A computational model of velopharyngeal closure for simulating cleft palate repair. *Journal of Craniofacial Surgery*, 26(3), 658–662. <https://doi.org/10.1097/scs.0000000000001441>
- Jiang, L., Zheng, Y., Li, N., Chen, X., Lu, Z., Tong, H., Yin, N., & Song, T. (2020). Relapse rate after surgical treatment of maxillary hypoplasia in non-growing cleft patients: A systematic review and meta-analysis. *International Journal of Oral and Maxillofacial Surgery*, 49(4), 421–431. <https://doi.org/10.1016/j.ijom.2019.08.012>
- Kantar, R. S., Alfonso, A. R., Ramly, E. P., Cohen, O., Rifkin, W. J., Maliha, S. G., Diaz-Siso, J. R., Eisemann, B. S., Saadeh, P. B., & Flores, R. L. (2020). Knowledge and skills acquisition by plastic surgery residents through digital simulation training: A prospective, randomized, blinded trial. *Plastic and Reconstructive Surgery*, 145(1), 184e–192e. <https://doi.org/10.1097/prs.0000000000006375>
- Kasaveni, C. P., McIntyre, G. T., & Mossey, P. A. (2017). Accuracy of both virtual and printed 3-dimensional models for volumetric measurement of alveolar clefts before grafting with alveolar bone compared with a validated algorithm: A preliminary investigation. *British Journal of Oral and Maxillofacial Surgery*, 55(1), 31–36. <https://doi.org/10.1016/j.bjoms.2016.08.016>
- Kesztyüs, A., Fábián, Z., Kádár, K., & Nagy, K. (2019). Alveolar defects repair in cleft patients using a pre-operatively planned and 3d printed surgical template. *International Journal of Oral and Maxillofacial Surgery*, 1(48), 15.

- Krey, K. F., Ratzmann, A., Metelmann, P. H., Hartmann, M., Ruge, S., & Kordass, B. (2018). Fully digital workflow for presurgical orthodontic plate in cleft lip and palate patients. *International Journal of Computerized Dentistry*, 21(3), 251–259. [www.ncbi.nlm.nih.gov/pubmed/30264054](http://www.ncbi.nlm.nih.gov/pubmed/30264054).

Kuijpers, M. A., Desmedt, D. J., Nada, R. M., Bergé, S. J., Fudalej, P. S., & Maal, T. J. (2015). Regional facial asymmetries in unilateral orofacial clefts. *European Journal of Orthodontics*, 37(6), 636–642. <https://doi.org/10.1093/ejo/cju104>

Landes, C. A., Weichert, F., Steinbauer, T., Schröder, A., Walczak, L., Fritsch, H., & Wagner, M. (2012). New details on the clefted uvular muscle: Analyzing its role at histological scale by model-based deformation analyses. *The Cleft Palate-Craniofacial Journal*, 49(1), 51–59. <https://doi.org/10.1597/11-034>

Latham, R. A. (1980). Orthopedic advancement of the cleft maxillary segment: A preliminary report. *Cleft Palate Journal*, 17(3), 227–233. [www.ncbi.nlm.nih.gov/pubmed/6994932](http://www.ncbi.nlm.nih.gov/pubmed/6994932).

Liou, E. J., Chen, P. K., Huang, C. S., & Chen, Y. R. (2000). Interdental distraction osteogenesis and rapid orthodontic tooth movement: A novel approach to approximate a wide alveolar cleft or bony defect. *Plastic and Reconstructive Surgery*, 105(4), 1262–1272. <https://doi.org/10.1097/00006534-200004040-00002>

Loeffelbein, D. J., Ritschl, L. M., Rau, A., Wolff, K. D., Barbarino, M., Pfeifer, S., Schonberger, M., & Wintermantel, E. (2015). Analysis of computer-aided techniques for virtual planning in nasoalveolar moulding. *British Journal of Oral and Maxillofacial Surgery*, 53(5), 455–460. <https://doi.org/10.1016/j.bjoms.2015.03.002>

Long, R. E., Jr., Spangler, B. E., & Yow, M. (1995). Cleft width and secondary alveolar bone graft success. *The Cleft Palate-Craniofacial Journal*, 32(5), 420–427. [https://doi.org/10.1597/1545-1569\\_1995\\_032\\_0420\\_cwasab\\_2.3.co\\_2](https://doi.org/10.1597/1545-1569_1995_032_0420_cwasab_2.3.co_2)

Lozko, V., Stoddard, P., Roscoe, B., & Gettens, R. (2009). Design of a nasal support for a cleft palate appliance. In *2009 IEEE 35th annual northeast bioengineering conference*. <https://doi.org/10.1109/NEBC.2009.49676701-2>

Luo, X., Huang, H., Yin, X., Shi, B., & Li, J. (2019). Functional stability analyses of maxillofacial skeleton bearing cleft deformities. *Scientific Reports*, 9(1), 4261. <https://doi.org/10.1038/s41598-019-40478-w>

Mc, N. C. (1950). Orthodontic procedures in the treatment of congenital cleft palate. *The Dental Record (London)*, 70(5), 126–132. [www.ncbi.nlm.nih.gov/pubmed/24537837](http://www.ncbi.nlm.nih.gov/pubmed/24537837).

Meyer-Marcotty, P., Kochel, J., Boehm, H., Linz, C., Klammert, U., & Stellzig-Eisenhauer, A. (2011). Face perception in patients with unilateral cleft lip and palate and patients with severe Class III malocclusion compared to controls. *Journal of Cranio-Maxillofacial Surgery*, 39(3), 158–163. <https://doi.org/10.1016/j.jcms.2010.05.001>

Ras, F., Habets, L. L., van Ginkel, F. C., & Prahl-Andersen, B. (1994). Three-dimensional evaluation of facial asymmetry in cleft lip and palate. *The Cleft Palate-Craniofacial Journal*, 31(2), 116–121. [https://doi.org/10.1597/1545-1569\\_1994\\_031\\_0116\\_tdeofa\\_2.3.co\\_2](https://doi.org/10.1597/1545-1569_1994_031_0116_tdeofa_2.3.co_2)

Shen, C., Yao, C. A., Magee, W., 3rd, Chai, G., & Zhang, Y. (2015). Presurgical nasoalveolar molding for cleft lip and palate: The application of digitally designed molds. *Plastic and Reconstructive Surgery*, 135(6), 1007e–1015e. <https://doi.org/10.1097/PRS.0000000000001286>

Shi, B., & Huang, H. (2020). Computational technology for nasal cartilage-related clinical research and application. *International Journal of Oral Science*, 12(1), 21. <https://doi.org/10.1038/s41368-020-00089-v>

- Sitzman, T. J., Coyne, S. M., & Britto, M. T. (2016). The burden of care for children with unilateral cleft lip: A systematic review of revision surgery. *The Cleft Palate-Craniofacial Journal*, 53(4), 84–94. <https://doi.org/10.1597/14-202>
- Srodon, P. D., Miquel, M. E., & Birch, M. J. (2012). Finite element analysis animated simulation of velopharyngeal closure. *The Cleft Palate-Craniofacial Journal*, 49(1), 44–50. <https://doi.org/10.1597/10-131>
- Verhoeven, T., Xi, T., Schreurs, R., Bergé, S., & Maal, T. (2016). Quantification of facial asymmetry: A comparative study of landmark-based and surface-based registrations. *Journal of Cranio-Maxillofacial Surgery*, 44(9), 1131–1136. <https://doi.org/10.1016/j.jcems.2016.07.017>
- Vig, K. W., & Mercado, A. M. (2015). Overview of orthodontic care for children with cleft lip and palate, 1915–2015. *American Journal of Orthodontics and Dentofacial Orthopedics*, 148(4), 543–556. <https://doi.org/10.1016/j.ajodo.2015.07.021>
- Wang, Y., Li, J., Xu, Y., Huang, N., Shi, B., & Li, J. (2020). Accuracy of virtual surgical planning-assisted management for maxillary hypoplasia in adult patients with cleft lip and palate. *Journal of Plastic, Reconstructive & Aesthetic Surgery*, 73(1), 134–140. <https://doi.org/10.1016/j.bjps.2019.07.003>
- Worley, M. L., Patel, K. G., & Kilpatrick, L. A. (2018). Cleft lip and palate. *Clinics in Perinatology*, 45(4), 661–678. <https://doi.org/10.1016/j.clp.2018.07.006>
- Xu, Y., Li, J., Zhao, S., Shi, B., Zheng, Q., Wang, Y., & Lo, L. J. (2013). Four-dimensional changes of nasolabial positions in unilateral cleft lip and palate. *Journal of Craniofacial Surgery*, 24(2), 473–478. <https://doi.org/10.1097/SCS.0b013e318275ee3b>
- Xu, Y., Yang, C., Schreuder, W. H., Shi, J., Shi, B., Zheng, Q., & Wang, Y. (2014). Cephalometric analysis of craniofacial morphology and growth in unrepaired isolated cleft palate patients. *Journal of Cranio-Maxillofacial Surgery*, 42(8), 1853–1860. <https://doi.org/10.1016/j.jcems.2014.07.003>
- Xu, R., Ye, N., Zhu, S., Shi, B., Li, J., & Lai, W. (2020). Comparison of the postoperative and follow-up accuracy of articulator model surgery and virtual surgical planning in skeletal class III patients. *British Journal of Oral and Maxillofacial Surgery*. <https://doi.org/10.1016/j.bjoms.2020.04.032>
- Yu, Q., Gong, X., & Shen, G. (2013). CAD presurgical nasoalveolar molding effects on the maxillary morphology in infants with UCLP. *Oral Surgery, Oral Medicine, Oral Pathology, and Oral Radiology*, 116(4), 418–426. <https://doi.org/10.1016/j.oooo.2013.06.032>
- Yu, Q., Gong, X., Wang, G. M., Yu, Z. Y., Qian, Y. F., & Shen, G. (2011). A novel technique for presurgical nasoalveolar molding using computer-aided reverse engineering and rapid prototyping. *Journal of Craniofacial Surgery*, 22(1), 142–146. <https://doi.org/10.1097/SCS.0b013e3181f6f9ae>

# The virtual patient model for correction of facial deformity and accuracy of simulation and surgical guide construction

# 30

**Raymond Chung Wen Wong<sup>1,2</sup>, Chee Weng Yong<sup>1</sup>, Matthias Wei Jin Chen<sup>1</sup>,  
Timothy Jie Han Sng<sup>1</sup>, Kian How Tan<sup>1</sup>, Roland Lim<sup>1</sup>**

<sup>1</sup>*Discipline of Oral and Maxillofacial Surgery, Faculty of Dentistry, National University of Singapore, Singapore, Singapore; <sup>2</sup>Oral and Maxillofacial Surgery, Faculty of Dentistry, National University Centre for Oral Health, National University of Singapore, Singapore, Singapore*

## Chapter outline

<b>Historical methods of planning .....</b>	784
Overview.....	784
Orthognathic surgery.....	785
Postablative reconstructive jaw surgery.....	785
Craniofacial surgery .....	786
Limitations of traditional planning .....	787
<b>3D imaging and biomechanical soft tissue simulation .....</b>	787
Introduction .....	787
Multislice computed tomography .....	788
Applications.....	788
Cone beam computed tomography .....	788
Dental records.....	789
Stereophotogrammetry .....	789
Biosimulations .....	789
<b>Virtual surgical planning, customized surgical guide, and fixation plates .....</b>	790
Introduction .....	790
VSP in orthognathic surgery.....	791
Integration of digital information.....	791
Virtual operating theater.....	791
Designing and printing of surgical aids, guides, or implants .....	792
VSP in reconstructive surgery of the jaw .....	794
VSP in craniofacial surgery .....	794
VSP in posttraumatic deformities.....	794

VSP in temporomandibular joint surgery .....	795
<b>Comparison between traditional and modern planning.....</b>	<b>797</b>
Traditional versus modern planning.....	797
Accuracy of surgical plan transfer .....	797
Cost and time .....	798
Surgical outcome/patient satisfaction.....	798
<b>References .....</b>	<b>799</b>

## Historical methods of planning

*Think thrice, measure twice, cut once.*

**Unknown**

### Overview

The goals of surgical correction of maxillofacial deformities involve restoration of form so as to attain optimal function and esthetics.

To adequately address such surgical problems, one must first derive the etiology and diagnosis via judicious history and record taking, clinical investigations, analysis. Armed with these information, surgeons can then proceed to plan and propose relevant surgical options to meet the treatment objectives. The planned surgical outcome is strongly desired as the face is the greatest representation of one's identity.

With the progress of technology, the mode of preoperative records and planning has undergone several transitions (Fig. 30.1).

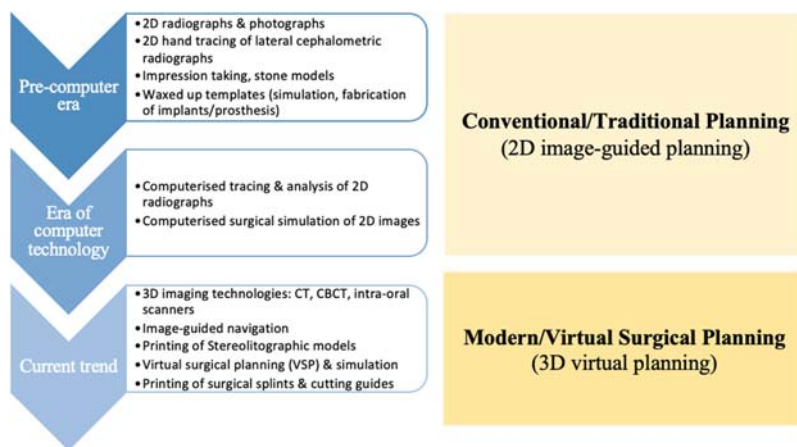


**FIGURE 30.1**

We classify “precomputer era” and “era of computer technology” as “conventional/traditional planning.” While “modern/virtual” planning involves the use of 3D imaging and virtual surgical planning (VSP) and printing. It is a slight misnomer to simply differentiate the two types of planning as “2D versus 3D” planning as the traditional way also involves 3D models (dental casts and facial moulages).

## Orthognathic surgery

In orthognathic surgery, conventional surgical planning involves collection of the following presurgical records:

- (1) Facial anthropometric measurements
- (2) Radiographic records and cephalometric tracing
- (3) Dental records
  - (a) Impressions of the maxillary and mandibular arch
  - (b) Bite registration in centric relation (CR)
  - (c) Facebow record of the relationship of the maxilla with the cranial base
- (4) Clinical photographs

The premise of model orthognathic surgery is to replicate the surgical movements of the maxilla and mandible with reference to the desired maxilla-mandibular relationship (MMR) or “final bite.” This final bite is determined by the patient’s preference and surgeon’s perception of facial esthetics and ideal occlusion guided by the various preoperative records.

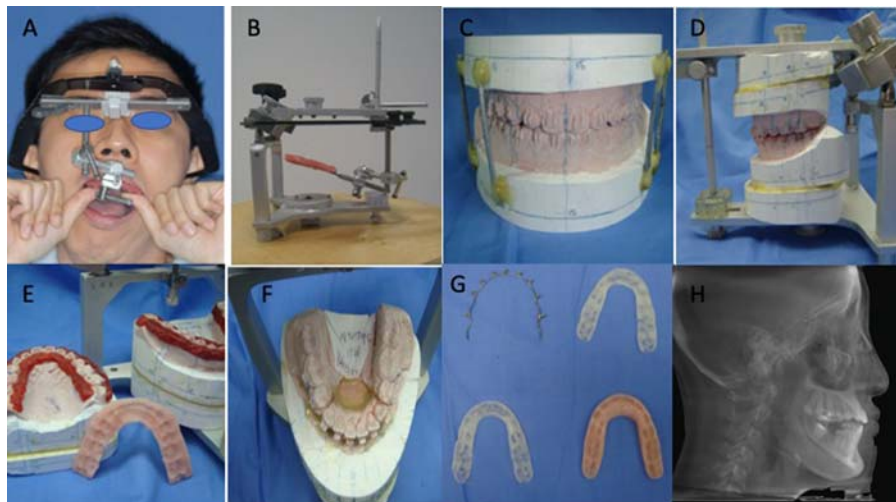
To do so, the maxillary model is first mounted on a dental articulator in accordance with the facebow recording ([Farhad & Naini, 2017](#); [Kademanli, 2015](#)).

Historically, the principle of cephalometric tracing in orthognathic surgery involves identification of landmarks on the radiograph, performing the tracings of the relevant hard and soft tissues over transparent acetate paper and measuring the relevant angles, projection, and distances. Next, cut-outs of tracing paper of the relevant dentoskeletal segments can be moved and pasted onto the desired position over the radiograph. This permits visualization of the proposed post-op dentoskeletal outcome and an estimation of the post-op soft tissue profile ([Farhad & Naini, 2017](#)). The use of tracings alone made it difficult to visualize the end results and surgeons moved on to use life-sized photographs with superimposed tracings to visualize how patients will look like ([Fig. 30.2](#)).

With the introduction of computer technology, 2D cephalometric tracing and simulation via software programs brought about greater convenience. Within seconds, relatively accurate identification of cephalometric landmarks, digital tracing, calculation of values, and cephalometric analysis can in fact be performed. In addition, 2D “osteotomies,” planned surgical movements, and the resulting soft tissue outcomes can be digitally simulated. To compare among different accompanying soft tissue changes, multiple alterations to the surgical movements can be easily and digitally made. This provides clearer illustrations for patients and better communication among clinicians. The advent of stereophotogrammetry (discussed later), CT, and cone beam CT scans plus improved computing power allowed close to real-life simulations to be made.

## Postablative reconstructive jaw surgery

Prior to the availability of CT/CBCT and stereolithographic models, the diagnostic imaging available for the planning of mandibular reconstructive surgery was

**FIGURE 30.2**

(A) Facebow records to replicate the angulation of the maxilla to the skull base. (B) Facebow is attached to an articulator and the maxillary plaster cast is mounted. (C) Mandibular cast is mounted, lines drawn, the models are sawn and put into ideal occlusion. (D) Movement of the whole occlusal complex made according to plan. (E) Wax placed around occlusal surface of teeth and acrylic placed to construct an occlusal wafer. (F) Segmental surgery planned. (G) Different occlusal wafers and custom arch bar are made following planned sequence. (H) Plain Lateral Cephalograms were used for planning.

*Courtesy of Raymond Wong (N.d.).*

likewise largely based on 2D radiographs. Traditionally, the neo-mandibular region is prepared via freehand segmental osteotomies of a fibula graft (Powcharoen et al., 2019). This is then followed by fixation with either a reconstructive plate bent by hand intraoperatively or based on precontoured 2D templates (Santis et al., 2019). Often, this resulted in less predictability as it is heavily dependent on individual surgical experience and skills. In addition, increased time in graft contouring and segmentation may be incurred intraoperatively, translating to extended duration of surgery.

### Craniofacial surgery

The facial moulage is a nondigital 3D record of the craniofacial deformity that has been useful for analysis, teaching, and fabrication of alloplastic implants and prostheses. It serves to mimic the dimensions of the unaffected side as determined by the preoperative fabrication of the wax template. This wax template is made by camouflaging the deformity via matching the unaffected side of facial moulage. It has been used as a guide in the selection of vascularized flap or fabrication of alloplastic

implants for reconstruction by ease of marking of necessary dimensions onto the donor site and appropriate debulking of the flap to match the varied thickness of the flap (Kadam et al., 2013).

However, some disadvantages of the facial moulage include (Germec-Cakan et al., 2010)

- (1) Patient's discomfort during the process of plaster cast impression over the face
- (2) Hassle of handling the impression material
- (3) Material warpage and 3D instability
- (4) Soft tissue deformation due to tension and weight of the impression resulting in inaccuracy of detail reproduction by facial moulage (reported 1–3 mm of soft tissue deformations with alginate impressions)
- (5) Problems associated with the casts:
  - (a) Difficulty in archiving due to physical storage space needed and potential "data loss" due to the fragility of the models
  - (b) Accessibility and availability of these casts for communication between clinicians may be difficult

### Limitations of traditional planning

While the above-mentioned traditional planning based on conventional record taking and 2D imaging has its merits, they are not without inherent limitations (Box 30.1).

#### Box 30.1 The various data sources use different coordinate systems

- The physical examination and clinical photographs are taken with the patient's head oriented to the natural head position (NHP)
- However, the cephalogram is oriented to the Frankfurt horizontal (FH) plane
- The articulated dental models are oriented to the axis-orbital plane
- On an average, these planes differ from each other by approximately 8 degrees
- This discrepancy alone can be responsible for a 15% difference in maxillary projection between planned and actual outcomes

## 3D imaging and biomechanical soft tissue simulation

### Introduction

With the development of various 3D imaging modalities together with software advancements, that allow the integration of digital information, the virtual patient model was made available as a useful surgical planning tool.

### Multislice computed tomography

Invented by Hounsfield in 1972, computer tomography has revolutionized diagnostic medicine and surgery (Hounsfield, 1973). It allowed highly accurate reconstruction of anatomical features without the need for excessively invasive surgery. In the production of MCT images, multiple narrow fan-shaped X-ray beams are first projected through the subject and captured by a 2D detector array on the opposite side. The captured 2D images are then processed, reconstructed into a 2D cross-sectional image. Finally, these slices are stacked together to produce a 3D reconstruction, allowing views from the axial, sagittal, and coronal planes. MCT today involves the rotation of multiple X-rays in a helical or spherical manner with multiple detectors, allowing for high quality images with faster acquisition times.

### Applications

MCT is an invaluable tool in the diagnosis of benign and malignant pathologies, infections, and trauma. In the management of craniofacial pathologies, MCTs used in conjunction with other clinical and imaging modalities allow for staging of tumors, planning for resection margins, identification of adjacent vital structures, screening of suitable graft harvest sites. MCTs are used to identify the size, location, and stage of craniofacial infections and can aid in surgical decision making and treatment planning. In craniofacial trauma, MCTs can identify and monitor traumatic brain injuries, bony injuries to the skull and facial bones, as well as to observe for spinal injuries. Intraoperative imaging allows surgeons to determine adequacy of reduction of facial fractures.

In orthognathic surgery, use of MCT has been limited due to cost, radiation dose concerns, and access.

### Cone beam computed tomography

The introduction of CBCT as an in-office imaging modality was a significant advancement in maxillofacial imaging and quickly became widely used in maxillofacial surgery and dentistry. In contrast with MCT, divergent cone or pyramidal shaped X-ray beams that capture the entire area of interest are projected toward an opposing detector array. In this manner, the entire area of interest is captured in a single rotation. The acquisition time for modern CBCTs is often equal to or less than that of a standard dental panoramic radiograph. Increased accessibility, low cost, and low radiation dosages has led to its popularization in the field of maxillofacial surgery.

Information from MCTs can be used as a base for the design and manufacture of patient specific models, surgical plates, and guides, and has been used in image-guided surgery as will be elaborated on later in this chapter.

## Dental records

The digitalization of dental records and occlusion can be done either via a direct or indirect workflow. The direct workflow uses intraoral scanners to capture a digital impression of the patient which can then be integrated with the patient's CBCT or MCT. The indirect workflow involves conventional impressions, model casting, and digitalization of analog casts using a desktop scanner.

The direct workflow has the advantage of being more comfortable for the patient in comparison to conventional impressions using alginate or elastomeric impression materials. Clinical workflow is also simplified and allows for immediate ease of communication with patient and technician. Although the accuracy of intraoral scanners remains an area for improvement, multiple studies have indicated that they are accurate enough for use in orthodontic and removal prosthodontics, and splint fabrication.

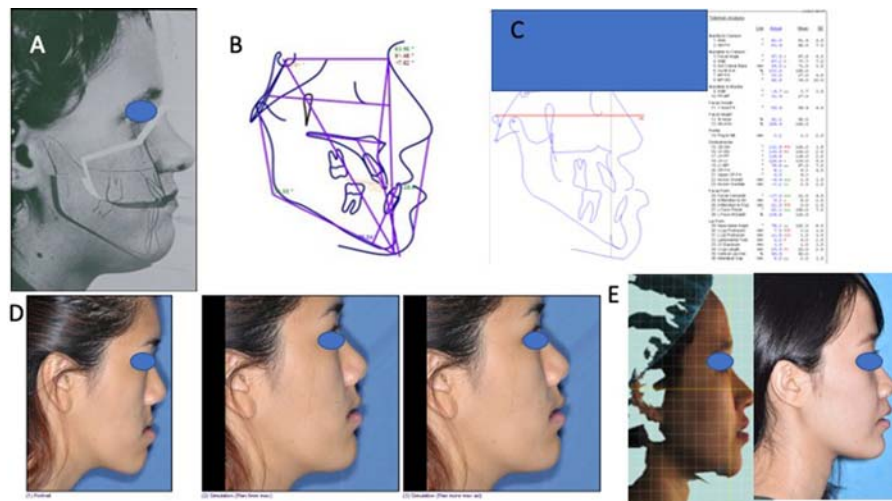
Challenges remain for integration of full digital systems into some aspects of maxillofacial surgery. A key objective of orthognathic surgery involves guiding the maxilla and mandible segments into a functionally stable occlusion. This step commonly involves the hand articulation of model casts to allow surgeons to judge the stability of the planned final occlusion. Doing so also allows the surgeon to determine interferences toward achieving a final occlusion and aids in determining and planning if occlusal adjustment intraoperatively is required. This is even more true in segmental orthognathic surgery where there are multiple tooth-bearing segments in a single arch, making virtual setting of the final occlusion challenging. One possible work-around is through 3D printing of casts taken via intraoral scanners. However, printed casts have been found to be less accurate when compared with analog casts. This adds a second degree of inaccuracy to the process.

## Stereophotogrammetry

Stereophotogrammetry is a method of 3D surface imaging. Stereophotogrammetry systems involve the use of multiple cameras from different viewpoints to record depth and surface geometry. The capture of textures and color data also allows recreation of realistic images of the subject in 3D. Stereophotogrammetry of the craniofacial region allows for objective evaluation of face with applications toward surgical planning and outcome analysis. Advantages of stereophotogrammetry are that it is minimally invasive, has quick capture times usually in milliseconds, and has been shown to be both reliable and accurate.

## Biosimulations

Integration of data allows for performance of virtual surgery to simulate outcomes. This is especially relevant in orthognathic surgery and correction of craniofacial deformities, where a key aim of surgery is to restore the patient to an acceptable facial form. Advancements in technology have allowed surgeons to simulate 3D soft tissue outcomes (Fig. 30.3). Across varying software platforms, different physical models are used to predict soft tissue displacement after movement of underlying bone.

**FIGURE 30.3**

Evolution of surgical simulation. (A) Life-sized photographs and paper tracings were superimposed and the relevant parts of the jaws were cut out and moved. (B) Hand tracings were laborious and the advent of digital tracings allowed faster measurements. (C) Measurements could be generated instantaneously after the points had been marked on the digital cephalogram. (D) Surgical simulation in flat 2D plane using rudimentary software. Soft tissues were highly inaccurate. (E) Stereophotogrammetry allowed photographs to be taken in three dimensions and the superimposition of the 3D photo onto the digital CT scans allowed close to real life surgical simulation. There are still some inaccuracies to the soft tissue position especially the lips.

Some of these are based on sparse models that require landmarking and rely on interpolation between points, others use dense volumetric models, including finite element models, mass tensor models, or mass spring models. These models are useful in both assessing potential outcomes, as well as patient education and discussions regarding surgery. The accuracy and reliability of soft tissue simulations are a subject of growing research interest. Some studies show various prediction programs have errors <2 mm which is considered clinically acceptable, while other studies have contradicted these findings.

## **Virtual surgical planning, customized surgical guide, and fixation plates**

### **Introduction**

As the result of accumulative progress in digital technology, we have reached the level where virtual surgical planning (VSP) is slowly becoming a cornerstone of

surgical planning. Besides improving the anatomical visualization and surgical planning process, VSP has the potential to produce superior operative outcomes via 3D printing. The applications of VSP in maxillofacial surgery include orthognathic surgery, oncologic reconstruction, cranio-facial surgery, correction of posttraumatic deformities and replacement of temporomandibular joint. In time to come, it is highly possible that traditional surgical planning will be replaced by VSP.

### VSP in orthognathic surgery

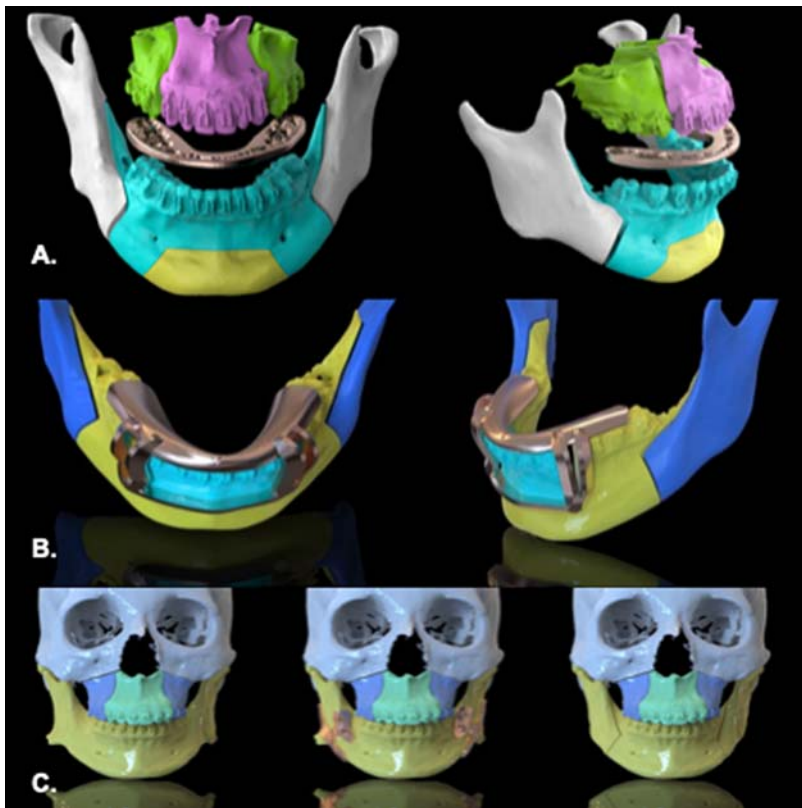
Patients with dentofacial or maxillofacial deformities present with discrepancies in the position, dimensions, or symmetry of the mandible, maxilla, or the zygoma. As a result, these patients present with malocclusion which may affect their speech, mastication, and facial esthetics. In patients with obstructive sleep apnoea secondary to a retruded jaw, there may be a need to bring forward the entire maxillomandibular complex to increase the airway space. The aim of the VSP is to improve the predictability in achieving the improvement in functions while either maintaining or improving the facial appearance of these patients (Gateno et al., 2007). The following entails the process of VSP, relevant to orthognathic surgery.

### Integration of digital information

The first step of VSP is to create a virtual patient by integrating the information collected. This includes the 3D imaging (CBCT or MCT), stereophotogrammetry, and scans of the patient's teeth (Kuroda et al., 1996; Ras et al., 1996; Syrek et al., 2010). The scans of the patient's teeth can be acquired either directly from intra-oral scans of the patient's dentition or indirectly by scanning the patient's stone models. It is preferable for the scans of the dentition to be superimposed with images of the teeth in the 3D imaging, as the latter is not sufficiently accurate for jaw and facial VSP (Kärcher, 1992; Nkenke et al., 2004; Plooij et al., 2011; Terai et al., 1999). At the same time, the stereophotogrammetry will be matched with the soft tissue render obtained from the 3D imaging. Vital or anatomical structures can be segmentalized or "marked out" such that they can be visualized clearly during the planning procedures. This typically includes the inferior alveolar nerves, infra-orbital nerves, and the roots of the dentition. Once the fusion of the information is complete, the surgeon can evaluate the anatomical structures of the skull in 3D (Okumura et al., 1999). This provides an opportunity to either reconfirm the findings from clinical examination or pick up information that was missed previously. A model of the skull, or parts of it, can also be printed out for better visualization (Bill et al., 1995).

### Virtual operating theater

The next part of VSP will be the surgical planning process itself. The planned surgical cuts can be simulated on the skull of the virtual patient (Fig. 30.4). Based on both the clinical examinations and the visual aid from the virtual patient, the cut

**FIGURE 30.4**

Application of CADCAM in Orthognathic Surgery; (A) Occlusal surgical splint; (B) Tooth-borne cutting guide for anterior mandibular subapical osteotomy; (C) Bilateral mandibular angle ostectomy cutting guides.

segments can be moved into the planned position (Polley & Figueroa, 2013; Marchetti et al., 2011; Moss et al., 1988; Swennen et al., 2009).

### Designing and printing of surgical aids, guides, or implants

A surgical splint or wafer can be designed and printed digitally (3D printed) in order to transfer the surgical plan to the surgery (Choi et al., 2009; Hernández-Alfaro & Guijarro-Martínez, 2013; Metzger et al., 2008). The shape, thickness, and width of the splint can be digitally modified prior to printing. As many duplicates of the splint can be printed according to the surgeon's needs. There are also many other appliances or devices which can be created to further improve the accuracy of the surgery. This includes cutting guides and positioning guides (Chen et al., 2021; Koyachi et al., 2020; Monteiro Carneiro et al., 2020; Wong et al., 2020).

Cutting guides are appliances which allow the osteotomies performed to be as per the virtual planning. As such, it not only replicates the morphology of the planned osteotomies but also the direction and angulation of the cuts. This is especially important in certain osteotomies where the risk of iatrogenic injury is higher. For example, the segmental subapical anterior mandibular osteotomy. Such osteotomies have a high risk of damaging the roots of the adjacent dentition and the mental nerve. Using a guide may help in reducing stress when performing these procedures (Yong et al., 2021). Instead of a “trim as you go” method until the segments fit as planned, another benefit of using a cutting guide would be that a precise amount of bone can be cut out. This is useful in segmental surgeries with set-back or posterior movements of the segment. Cutting guides are also useful when certain anatomical structures must be included within the cut segment, i.e., genial tubercle when planning genioplasty for an obstructive sleep apnoea patient.

Apart from the cutting guide, a positioning guide will help in further enhancing the accuracy of the surgeries. While the cutting guides allows the osteotomies to be done as planned, it does not offer any help in the positioning of the cut segments. A positioning guide helps to locate and hold the cut segments exactly to the planned positioning. With the guide as an interim fixation, the surgeons can then bend the fixation plates accordingly. With the use of VSP, fixation plates can also be digitally designed and printed (Fig. 30.5).

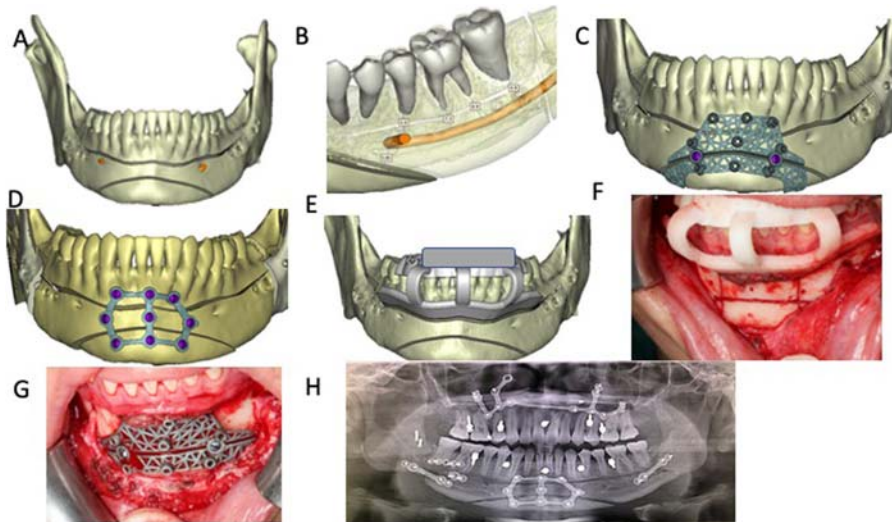


**FIGURE 30.5**

Titanium and SLA cutting guide for complex total subapical osteotomy, genioplasty and sagittal split osteotomy of mandible. (A) Cuts made virtually on model; (B) Very close proximity of vital structures; (C, D) Titanium cutting and fixation plate designed (Materialise, Belgium); (E) SLA cutting guide designed on virtual model; (F) SLA printed polyamide cutting guide in situ during surgery; (G) Titanium cutting guide in situ; (H) Postoperative radiograph showing no injury to the teeth roots or inferior alveolar nerve.

*Courtesy of Raymond Wong (N.d.).*

### VSP in reconstructive surgery of the jaw

Discontinuity or defects of the jaw bones may occur after a variety of etiologies which may be congenital, developmental, or acquired in nature. Acquired etiologies can include benign pathologies, malignancy pathologies, traumatic bone loss, congenital or developmental bone hypoplasia. While there is a range of possible reconstructive modalities available, free vascularized autogenous bone grafts are currently the gold standard in the reconstruction of large jaw bone defects (Niu et al., 2017; Shingaki et al., 2002). There are certain key considerations when planning for the use of vascularized bone flaps. For a larger area of resection/reconstruction, a longer duration is generally spent in reshaping the graft and inset it into the defect site. The delay in the inset procedure will extend the ischemic time of the harvested tissue. This has an effect on the success of the free flap. The purpose of VSP is to allow the surgeons to virtually plan the reshaping or reconfiguration of the harvested bone prior to the surgery itself (Han et al., 2017; Hirsch et al., 2009). By using the cutting guides, the bone can be shaped even before detachment from the main vascular supply on the donor site (Avraham et al., 2014; Tarsitano et al., 2016).

### VSP in craniofacial surgery

Another field of surgery which can benefit greatly from virtual simulation would be the treatment of patients with craniofacial deformities. The afflicted patient may present with deformities of the cranial vault, facial bones, or both. Surgical treatment of the cranial vault deformities typically involves altering the abnormal morphology of the existing cranial bones to a shape that better matches the patient's age group or in other words, toward a normal morphology (Chim et al., 2014; Mardini et al., 2014). With the use of VSP, the surgical plan can be trialled and tested virtually until a satisfactory outcome is achieved (Fig. 30.6). The surgical plan can then be transferred to the operation with the use of cutting and positioning guides. This allows for the exact shape of the osteotomies to be created, and also, for the separate pieces to come together at the planned position (Khechyan et al., 2014; Seruya et al., 2013).

### VSP in posttraumatic deformities

Deformities may occur as a result of traumatic injuries to the facial region. Upon impact of great magnitude, disruption of the facial skeletal framework may occur. Treatment will entail reduction of fractured bone edges back into their original position and subsequent fixation. However, in the presence of marked swelling, severely comminuted pieces or tissue loss, it may be difficult to regain the pretraumatic anatomical framework of the patient. VSP allows the surgeon to virtually piece the broken pieces together and plan ahead for the surgery (Tepper et al., 2011). The virtual plan can be transferred to the surgery through several methods. When the maxillary or mandibular regions are involved, occlusal surgical wafers, palatal plate, lingual plates or customized arch bars can be designed and printed.

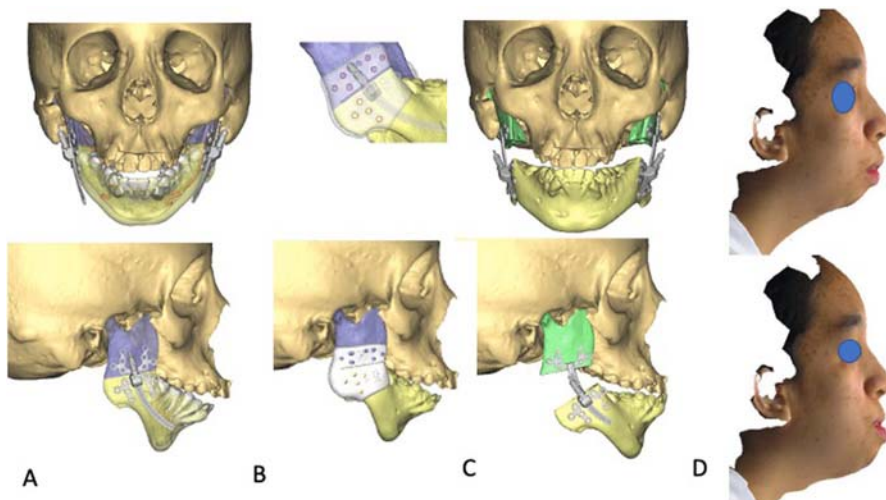


**FIGURE 30.6**

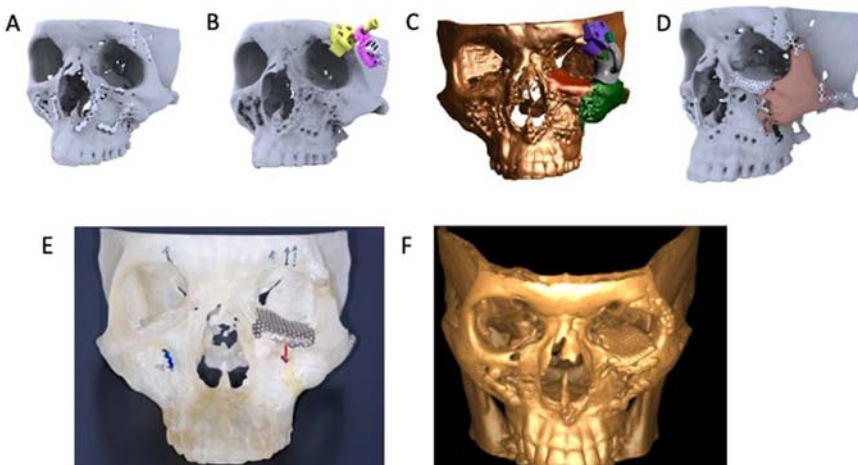
Mandibular advancement case in Treacher-Collins Syndrome patient. (A) Virtual skull model with virtual model of curvilinear distractor (DePuy Synthes, Johnson & Johnson, USA); (B) Cutting guides designed avoiding teeth and nerve (Materialise, Belgium); (C) Planned advancement of mandible can be seen virtually; (D) Stereophotogrammetry allows us to visualise the soft tissues. There was a deliberate overadvancement, in this case, to accommodate for future planned procedures.

*Courtesy of Raymond Wong (N.d.).*

Surgical guides can also be printed to act as reference for bone reduction or reconstruction (Fig. 30.7). This will guide the surgeon on the projection or contour that is required to be recreated. Similar to orthognathic surgery, implants for the fixation of the reduced bone or replacement of lost bone can be printed (Maloney & Rutner, 2019). This can include thick reconstructive plates spanning across the entire mandible, titanium mesh replacing portions of the cranial vault, or orbital plates that replace part of the orbital cavity.

### VSP in temporomandibular joint surgery

VSP can also be used to design and print customized prosthetic replacement of a joint system (Ackland et al., 2017, 2018; Pinto-Borges et al., 2021). Surgical removal and alloplastic replacement of the temporomandibular Joint (TMJ) may be indicated for severe inflammatory or degenerative diseases which are not responsive to nonsurgical treatment (Fig. 30.8). Contemporary TMJ replacement typically consists of the inferior “condylar” component and the superior “glenoid fossa” component. These components are designed to simulate the movement of a normal TMJ complex and thus, retain or even improve the masticatory function of the patient.

**FIGURE 30.7**

Post traumatic deformity of the left zygoma. (A) Virtual skull model with bone plates; (B) Bone plates digitally removed with custom central locator, to be placed into screw holes of old plates; (C) Symmetry creation by mirroring the right zygoma and orbit onto the left zygoma/orbit. A new orbital floor and rim is designed virtually. (D) Virtual representation of new zygoma position and fixation. (E) Physical 3D printed model (Polyjet) with custom formed titanium mesh orbital rim and floor and cutting guides; (F) Postoperative CT scan showing better symmetry.

*Courtesy of Raymond Wong (N.d.).*

**FIGURE 30.8**

Customized alloplastic replacement of the temporomandibular joint system. The alloplastic implant consists of a superior glenoid fossa component and an inferior condylar component.

Pinto-Borges, H., Carvalho, O., Henriques, B., Silva, F., Ramos, A., & Souza, J. (2021). *A preliminary analysis of the wear pathways of sliding contacts on temporomandibular joint total joint replacement prostheses*. *Metals*, 11, 685–698 <https://doi.org/10.3390/met11050685>.

---

## Comparison between traditional and modern planning

### Traditional versus modern planning

3D imaging, virtual surgical planning, and printing technologies have generally improved diagnosis and treatment planning capabilities, while creating new possibilities in orthognathic and craniofacial surgery.

Traditional surgical planning involves 2D cephalometric radiographs, dental casts mounted on articulators with facebow records and model surgery. The accuracy of the records and execution of surgical plan depends heavily on the accuracy of facebow record and transfer.

In theory, 3D imaging, planning technology, and CAD/CAM capabilities improve the surgeon's ability to diagnose, analyze, and execute the desired surgical plan. In particular, 3D imaging eliminates the risk of errors in traditional facebow record and transfer, allowing more accurate diagnosis and replication of the surgical plan. Furthermore, the identification of important landmarks and the ability to fabricate custom surgical guides aims to lower the rate of complications and duration of surgery.

Comparison of traditional facebow transfer against CBCT-based 3D virtual reconstruction ([Farhad & Naini, 2017](#)) found that dental casts were often mounted with steeper occlusal plane angles, and that the error of facebow transfer is more severe in the sagittal than in the transverse dimension. Transverse canting was shown to be underrepresented as often as overrepresented, both of which would still result in surgical inaccuracies.

### Accuracy of surgical plan transfer

In orthognathic surgical planning, Van Hemelen et al. ([n.d.](#)) recorded the mean differences in planned surgical landmarks and actual postoperative clinical results on pre- and postoperative imaging. For hard tissue landmarks, the mean differences when comparing planning using 2D versus 3D imaging were not statistically significant. When comparing soft tissue landmarks, there was a significantly smaller mean difference between planned and actual post-op results in planning with 3D imaging. Despite that, both planning methods were still considered to result in accurate surgical plan transfers.

3D imaging and planning software further enables technology such as patient-specific implants, 3D printed splints, and intraoperative navigation. Zinser et al. ([n.d.](#)) compared the precision of 3D printed surgical splints, intraoperative navigation, and traditional intermaxillary occlusal splints for surgical plan transfer. Similarly, pre- and postoperative imaging were used to compare planned and postoperative landmarks for hard and soft tissues. The highest accuracy was found in the 3D printed surgical splint group, followed by intraoperative navigation and traditional occlusal splints. In particular, 3D printed surgical splints allowed more precise replication of maxillary movements in all dimensions. However, there was

still soft tissue discrepancies for all three groups. Additionally, 3D printed and intraoperative imaging resulted in a longer surgery duration.

A randomized controlled trial (Kraeima et al., 2020) comparing the surgical accuracy of Le Fort I osteotomies when using patient-specific surgical guides and implants, versus conventional splint-based surgery and miniplate fixation. The authors found that patient-specific guides and implants resulted in improved accuracy over the conventional osteotomy and miniplate group, in antero-posterior translations of more than 3.67 mm. However, the patient-specific group showed no benefit in maxilla impaction, and surgeons generally considered it easier to remove interferences when performing conventional osteotomies.

In mandibular reconstruction using fibula free flaps, virtual surgical planning (VSP) suggested improved surgical accuracy (Barr et al., 2020; Tang et al., n.d.). This was despite the lack of large numbers of randomized controlled trials and nonuniform methods used among different authors to assess accuracy of VSP. Authors used parameters such as gonial angle, intergonial angle difference, gonion–gnathion distance, and comparison in fibula volume.

### Cost and time

Resnick et al. (n.d.) compared the cost of planning orthognathic surgery using VSP and 3D printing of surgical splints with that of traditional 2D radiographs, stone model surgery, and manual splint fabrication. They found that VSP required less time and money for all types of cases, and that the greatest time and cost differences were seen in patients with transverse asymmetries. On the other hand, Bengtsson et al. (2019) found no difference in time taken between 2D and 3D planning, and that the 2D planning technique was less costly.

With regard to the use of VSP in mandibular reconstruction with fibula free flaps, significant improvements in operative and ischemic time were displayed. Barr et al. also reported a mean trend toward shorter hospital admissions (Barr et al., 2020).

Such cost–benefit comparisons will likely vary among institutions, depending on planning protocol and surgeon experience in using 3D planning software.

Such improvements will also likely present in cost and resource savings for patient and healthcare facilities. However, this must be weighed against additional costs incurred when using VSP, which will vary among different institutions. Additionally, the systematic reviews found no significant difference in rate of operative complications between VSP and conventional fibula free flap reconstruction, which may be due to the small number of studies with significant heterogeneity in study design.

### Surgical outcome/patient satisfaction

Postoperative outcomes and patient satisfaction were compared in conventional versus virtual surgical planning for Le Fort I, bilateral sagittal split osteotomies in Class III patients (Wu et al., 2017).

Upon comparison of pre- and postoperative 2D cephalometric radiographs, improved outcomes were noted in the virtual surgical planning group for correction of midline deviation, ramus inclination asymmetry, occlusal plane canting, and chin deviation. Also, greater patient satisfaction, in surgical outcomes and facial esthetics, was reported in the virtual surgical planning group.

Bengtsson et al. (2017) also found improved prediction and surgical accuracy in the virtual surgical planning group when comparing conventional and virtual surgical planning methods, especially in correction of facial asymmetry.

While traditional planning still resulted in satisfactory treatment outcomes in both papers, virtual surgical planning with simulation provided obvious benefits in patient consultation and correction of facial asymmetry.

Hsu et al. (2020) studied outcomes of facial contour asymmetry in unilateral cleft lip and palate patients after conventional versus computer assisted 3D planning in cleft orthognathic surgery. In contrast to previously published studies, the main outcome measured was soft tissue asymmetry rather than hard tissue landmarks. 2D and 3D facial images were acquired pre- and postoperatively. The 3D facial contour asymmetry analysis found significantly improved root mean square deviation (RMSD) values for the 3D simulation group postoperatively, but not for the 2D imaging guided planning group. Additionally, the 3D simulation group had no significant difference in RMSD values postoperatively when compared to a normal group. In 2D facial contour asymmetry analysis, blinded raters consistently rated the 3D simulation group as more symmetrical than the 2D planning group. This study suggests that 3D planning results in superior outcomes when correcting facial asymmetry as compared to 2D planning-based surgery.

Postoperative skeletal stability of maxillary segments after Le Fort I osteotomy was also compared when using patient-specific implants versus mini-plate fixation (Kotaniemi et al., 2019). Postoperative lateral cephalograms were taken at 1 year and compared with immediate postop lateral cephalograms. The authors found no statistical significance in skeletal relapse between the two groups.

## References

- Ackland, D., Robinson, D., Lee, P. V. S., & Dimitroulis, G. (2018). Design and clinical outcome of a novel 3D-printed prosthetic joint replacement for the human temporomandibular joint. *Clinical Biomechanics*, 56, 52–60. <https://doi.org/10.1016/j.clinbiomech.2018.05.006>
- Ackland, D. C., Robinson, D., Redhead, M., Lee, P. V. S., Moskaljuk, A., & Dimitroulis, G. (2017). A personalized 3D-printed prosthetic joint replacement for the human temporomandibular joint: From implant design to implantation. *Journal of the Mechanical Behavior of Biomedical Materials*, 69, 404–411. <https://doi.org/10.1016/j.jmbbm.2017.01.048>
- Avraham, T., Franco, P., Brecht, L. E., Ceradini, D. J., Saadeh, P. B., Hirsch, D. L., & Levine, J. P. (2014). Functional outcomes of virtually planned free fibula flap reconstruction of the mandible. *Plastic and Reconstructive Surgery*, 134(4), 628–634. <https://doi.org/10.1097/PRS.0000000000000513>

- Barr, M. L., Haveles, C. S., Rezzadeh, K. S., Nolan, I. T., Castro, R., Lee, J. C., Steinbacher, D., & Pfaff, M. J. (2020). Virtual surgical planning for mandibular reconstruction with the fibula free flap: A systematic review and meta-analysis. *Annals of Plastic Surgery*, 84(1), 117–122. <https://doi.org/10.1097/SAP.0000000000002006>
- Bengtsson, M., Wall, G., Becktor, J. P., & Rasmusson, L. (2019). A comparison of cost-effectiveness of computer-assisted 2-and 3-dimensional planning techniques in orthognathic surgery. *British Journal of Oral and Maxillofacial Surgery*, 57(4), 352–358. <https://doi.org/10.1016/j.bjoms.2019.03.012>
- Bengtsson, M., Wall, G., Greiff, L., & Rasmusson, L. (2017). Treatment outcome in orthognathic surgery—a prospective randomized blinded case-controlled comparison of planning accuracy in computer-assisted two- and three-dimensional planning techniques (part II). *Journal of Cranio-Maxillofacial Surgery*, 45(9), 1419–1424. <https://doi.org/10.1016/j.jcms.2017.07.001>
- Bill, J. S., Reuther, J. F., Dittmann, W., Kübler, N., Meier, J. L., Pistner, H., & Wittenberg, G. (1995). Stereolithography in oral and maxillofacial operation planning. *International Journal of Oral and Maxillofacial Surgery*, 24(1), 98–103. [https://doi.org/10.1016/S0901-5027\(05\)80869-0](https://doi.org/10.1016/S0901-5027(05)80869-0)
- Chen, H., Bi, R., Hu, Z., Chen, J., Jiang, N., Wu, G., Li, Y., Luo, E., & Zhu, S. (2021). Comparison of three different types of splints and templates for maxilla repositioning in bimaxillary orthognathic surgery: A randomized controlled trial. *International Journal of Oral and Maxillofacial Surgery*, 50(5), 635–642. <https://doi.org/10.1016/j.ijom.2020.09.023>
- Chim, H., Wetjen, N., & Mardini, S. (2014). Virtual surgical planning in craniofacial surgery. *Seminars in Plastic Surgery*, 28(3), 150–158. <https://doi.org/10.1055/s-0034-1384811>
- Choi, J. Y., Song, K. G., & Baek, S. H. (2009). Virtual model surgery and wafer fabrication for orthognathic surgery. *International Journal of Oral and Maxillofacial Surgery*, 38(12), 1306–1310. <https://doi.org/10.1016/j.ijom.2009.06.009>
- Farhad, B., & Naini, D. S. G. (2017). *Orthognathic surgery: Principles, planning and practice*.
- Gateno, J., Xia, J. J., Teichgraeber, J. F., Christensen, A. M., Lemoine, J. J., Liebschner, M. A. K., Gliddon, M. J., & Briggs, M. E. (2007). Clinical feasibility of computer-aided surgical simulation (CASS) in the treatment of complex craniomaxillofacial deformities. *Journal of Oral and Maxillofacial Surgery*, 65(4), 728–734. <https://doi.org/10.1016/j.joms.2006.04.001>
- Germec-Cakan, D., Canter, H. I., Nur, B., & Arun, T. (2010). Comparison of facial soft tissue measurements on three-dimensional images and models obtained with different methods. *Journal of Craniofacial Surgery*, 21(5), 1393–1399. <https://doi.org/10.1097/SCS.0b013e3181ec6976>
- Han, H. H., Kim, H. Y., & Lee, J. Y. (2017). The pros and cons of computer-aided surgery for segmental mandibular reconstruction after oncological surgery. *Archives of Craniofacial Surgery*, 149–154. <https://doi.org/10.7181/acs.2017.18.3.149>
- Hemelen, V., Genechten, Renier, L., Desmedt, M., Verbruggen, E., & Nadimi, N. (n.d.). Three-dimensional virtual planning in orthognathic surgery enhances the accuracy of soft tissue prediction (pp. 1878–4119).
- Hernández-Alfaro, F., & Guijarro-Martínez, R. (2013). New protocol for three-dimensional surgical planning and CAD/CAM splint generation in orthognathic surgery: An in vitro and in vivo study. *International Journal of Oral and Maxillofacial Surgery*, 42(12), 1547–1556. <https://doi.org/10.1016/j.ijom.2013.03.025>
- Hirsch, D. L., Garfein, E. S., Christensen, A. M., Weimer, K. A., Saddeh, P. B., & Levine, J. P. (2009). Use of computer-aided design and computer-aided manufacturing to produce

- orthognathically ideal surgical outcomes: A paradigm shift in head and neck reconstruction. *Journal of Oral and Maxillofacial Surgery*, 67(10), 2115–2122. <https://doi.org/10.1016/j.joms.2009.02.007>
- Hounsfield, G. N. (1973). Computerized transverse axial scanning (tomography): I. Description of system. *British Journal of Radiology*, 46(552), 1016–1022. <https://doi.org/10.1259/0007-1285-46-552-1016>
- Hsu, P. J., Denadai, R., Pai, B. C. J., Lin, H. H., & Lo, L. J. (2020). Outcome of facial contour asymmetry after conventional two-dimensional versus computer-assisted three-dimensional planning in cleft orthognathic surgery. *Scientific Reports*, 10(1). <https://doi.org/10.1038/s41598-020-58682-4>
- Kadam, D., Pillai, V., Bhandary, S., Hukkeri, R., & Kadam, M. (2013). Facial contour deformity correction with microvascular flaps based on the 3-dimensional template and facial moulage. *Indian Journal of Plastic Surgery*, 46(3), 521. <https://doi.org/10.4103/0970-0358.122000>
- Kademani. (2015). *Atlas of oral & maxillofacial surgery*.
- Kärcher, H. (1992). Three-dimensional craniofacial surgery: Transfer from a three-dimensional model (endoplan) to clinical surgery: A new technique (graz). *Journal of Cranio-Maxillofacial Surgery*, 20(3), 125–131. [https://doi.org/10.1016/S1010-5182\(05\)80094-0](https://doi.org/10.1016/S1010-5182(05)80094-0)
- Khechyan, D. Y., Saber, N. R., Burge, J., Fattah, A., Drake, J., Forrest, C. R., & Phillips, J. H. (2014). Surgical outcomes in craniosynostosis reconstruction: The use of prefabricated templates in cranial vault remodelling. *Journal of Plastic, Reconstructive and Aesthetic Surgery*, 67(1), 9–16. <https://doi.org/10.1016/j.bjps.2013.09.009>
- Kotaniemi, K. V. M., Heliövaara, A., Kotaniemi, M., Stoor, P., Leikola, J., Palotie, T., & Suojanen, J. (2019). Comparison of postoperative skeletal stability of maxillary segments after Le Fort I osteotomy, using patient-specific implant versus mini-plate fixation. *Journal of Cranio-Maxillofacial Surgery*, 47(7), 1020–1030. <https://doi.org/10.1016/j.jcms.2019.04.003>
- Koyachi, M., Sugahara, K., Odaka, K., Matsunaga, S., Abe, S., Sugimoto, M., & Katakura, A. (2020). Accuracy of Le Fort I osteotomy with combined computer-aided design/computer-aided manufacturing technology and mixed reality. *International Journal of Oral and Maxillofacial Surgery*. <https://doi.org/10.1016/j.ijom.2020.09.026>
- Kraeima, J., Schepers, R. H., Spijkervet, F. K. L., Maal, T. J. J., Baan, F., Witjes, M. J. H., & Jansma, J. (2020). Splintless surgery using patient-specific osteosynthesis in Le Fort I osteotomies: A randomized controlled multi-centre trial. *International Journal of Oral and Maxillofacial Surgery*, 49(4), 454–460. <https://doi.org/10.1016/j.ijom.2019.08.005>
- Kuroda, T., Motohashi, N., Tominaga, R., & Iwata, K. (1996). Three-dimensional dental cast analyzing system using laser scanning. *American Journal of Orthodontics and Dentofacial Orthopedics : Official Publication of the American Association of Orthodontists, Its Constituent Societies, and the American Board of Orthodontics*, 110(4), 365–369. [https://doi.org/10.1016/S0889-5406\(96\)70036-7](https://doi.org/10.1016/S0889-5406(96)70036-7)
- Maloney, K., & Rutner, T. (2019). Virtual surgical planning and hardware fabrication prior to open reduction and internal fixation of atrophic edentulous mandible fractures. *Cranio-maxillofacial Trauma & Reconstruction*, 156–162. <https://doi.org/10.1055/s-0039-1677723>
- Marchetti, C., Bianchi, A., Muylldermans, L., Di Martino, M., Lancellotti, L., & Sarti, A. (2011). Validation of new soft tissue software in orthognathic surgery planning. *International Journal of Oral and Maxillofacial Surgery*, 40(1), 26–32. <https://doi.org/10.1016/j.ijom.2010.09.004>

- Mardini, S., Alsubaie, S., Cayci, C., Chim, H., & Wetjen, N. (2014). Three-dimensional pre-operative virtual planning and template use for surgical correction of craniosynostosis. *Journal of Plastic, Reconstructive and Aesthetic Surgery*, 67(3), 336–343. <https://doi.org/10.1016/j.bjps.2013.11.004>
- Metzger, M. C., Hohlweg-Majert, B., Schwarz, U., Teschner, M., Hammer, B., & Schmelzeisen, R. (2008). Manufacturing splints for orthognathic surgery using a three-dimensional printer. *Oral Surgery, Oral Medicine, Oral Pathology, Oral Radiology and Endodontology*, 105(2), e1–e7. <https://doi.org/10.1016/j.tripleo.2007.07.040>
- Monteiro Carneiro, N. C., Oliveira, D. V., Real, F. H., Karla da Silva Tabosa, A., & Carneiro Júnior, J. T. (2020). A new model of customized maxillary guide for orthognathic surgery: Precision analysis. *Journal of Craniomaxillofacial Surgery*, 48(12), 1119–1125. <https://doi.org/10.1016/j.jcms.2020.10.007>
- Moss, J. P., Grindrod, S. R., Linney, A. D., Arridge, S. R., & James, D. (1988). A computer system for the interactive planning and prediction of maxillofacial surgery. *American Journal of Orthodontics and Dentofacial Orthopedics*, 94(6), 469–475. [https://doi.org/10.1016/0889-5406\(88\)90004-2](https://doi.org/10.1016/0889-5406(88)90004-2)
- Niu, L. X., Feng, Z. E., Wang, D. C., Zhang, J. Y., Sun, Z. P., & Guo, C. B. (2017). Prognostic factors in mandibular gingival squamous cell carcinoma: A 10-year retrospective study. *International Journal of Oral and Maxillofacial Surgery*, 46(2), 137–143. <https://doi.org/10.1016/j.ijom.2016.09.014>
- Nkenke, E., Zachow, S., Benz, M., Maier, T., Veit, K., Kramer, M., Benz, S., Häusler, G., Neukam, F. W., & Lell, M. (2004). Fusion of computed tomography data and optical 3D images of the dentition for streak artefact correction in the simulation of orthognathic surgery. *Dentomaxillofacial Radiology*, 33(4), 226–232. <https://doi.org/10.1259/dmfr/27071199>
- Okumura, H., Chen, L. H., Tsutsumi, S., & Oka, M. (1999). Three-dimensional virtual imaging of facial skeleton and dental morphologic condition for treatment planning in orthognathic surgery. *American Journal of Orthodontics and Dentofacial Orthopedics: Official Publication of the American Association of Orthodontists, Its Constituent Societies, and the American Board of Orthodontics*, 116(2), 126–131. [https://doi.org/10.1016/S0889-5406\(99\)70208-8](https://doi.org/10.1016/S0889-5406(99)70208-8)
- Pinto-Borges, H., Carvalho, O., Henriques, B., Silva, F., Ramos, A., & Souza, J. (2021). A preliminary analysis of the wear pathways of sliding contacts on temporomandibular joint total joint replacement prostheses. *Metals*, 11, 685–698. <https://doi.org/10.3390/met11050685>
- Plooij, J. M., Maal, T. J. J., Haers, P., Borstlap, W. A., Kuijpers-Jagtman, A. M., & Bergé, S. J. (2011). Digital three-dimensional image fusion processes for planning and evaluating orthodontics and orthognathic surgery. A systematic review. *International Journal of Oral and Maxillofacial Surgery*, 40(4), 341–352. <https://doi.org/10.1016/j.ijom.2010.10.013>
- Polley, J. W., & Figueroa, A. A. (2013). Orthognathic positioning system: Intraoperative system to transfer virtual surgical plan to operating field during orthognathic surgery. *Journal of Oral and Maxillofacial Surgery*, 71(5), 911–920. <https://doi.org/10.1016/j.joms.2012.11.004>
- Powcharoen, W., Yang, W. F., Yan Li, K., Zhu, W., & Su, Y. X. (2019). Computer-assisted versus conventional freehand mandibular reconstruction with fibula free flap: A systematic review and meta-analysis. *Plastic and Reconstructive Surgery*, 144(6), 1417–1428. <https://doi.org/10.1097/PRS.0000000000006261>
- Ras, F., Habets, L. L. M. H., Van Ginkel, F. C., & Prahl-Andersen, B. (1996). Quantification of facial morphology using stereophotogrammetry—demonstration of a new concept. *Journal of Dentistry*, 24(5), 369–374. [https://doi.org/10.1016/0300-5712\(95\)00081-X](https://doi.org/10.1016/0300-5712(95)00081-X)

- Resnick, C. M., Inverso, G., Wrzosek, M., Padwa, B. L., Kaban, L. B., & Peacock, Z. S. (n.d.). Is there a difference in cost between standard and virtual surgical planning for orthognathic surgery? (pp. 1531–5053).
- Santis, G. D., C. P. G., & Chiarini, L. (2019). *Atlas of mandibular and maxillary reconstruction with the fibula flap-A step-by-step approach.*
- Seruya, M., Borsuk, D. E., Khalifian, S., Carson, B. S., Dalesio, N. M., & Dorafshar, A. H. (2013). Computer-aided design and manufacturing in craniosynostosis surgery. *Journal of Craniofacial Surgery, 24*(4), 1100–1105. <https://doi.org/10.1097/SCS.0b013e31828b7021>
- Shingaki, S., Nomura, T., Takada, M., Kobayashi, T., Suzuki, I., & Nakajima, T. (2002). Squamous cell carcinomas of the mandibular alveolus: Analysis of prognostic factors. *Oncology, 62*(1), 17–24. <https://doi.org/10.1159/000048242>
- Swennen, G. R. J., Mollemans, W., & Schutyser, F. (2009). Three-dimensional treatment planning of orthognathic surgery in the era of virtual imaging. *Journal of Oral and Maxillofacial Surgery, 67*(10), 2080–2092. <https://doi.org/10.1016/j.joms.2009.06.007>
- Syrek, A., Reich, G., Ranftl, D., Klein, C., Cerny, B., & Brodesser, J. (2010). Clinical evaluation of all-ceramic crowns fabricated from intraoral digital impressions based on the principle of active wavefront sampling. *Journal of Dentistry, 38*(7), 553–559. <https://doi.org/10.1016/j.jdent.2010.03.015>
- Tang, N. S. J., Ahmadi, I., & Ramakrishnan, A. (n.d.). Virtual surgical planning in fibula free flap head and neck reconstruction: A systematic review and meta-analysis (p. 1878).
- Tarsitano, A., Ciocca, L., Scotti, R., & Marchetti, C. (2016). Morphological results of customized microvascular mandibular reconstruction: A comparative study. *Journal of Cranio-Maxillofacial Surgery, 44*(6), 697–702. <https://doi.org/10.1016/j.jcms.2016.03.007>
- Tepper, O. M., Sorice, S., Hershman, G. N., Saadeh, P., Levine, J. P., & Hirsch, D. (2011). Use of virtual 3-dimensional surgery in post-traumatic craniomaxillofacial reconstruction. *Journal of Oral and Maxillofacial Surgery, 69*(3), 733–741. <https://doi.org/10.1016/j.joms.2010.11.028>
- Terai, H., Shimahara, M., Sakinaka, Y., & Tajima, S. (1999). Accuracy of integration of dental casts in three-dimensional models. *Journal of Oral and Maxillofacial Surgery, 57*(6), 662–665. [https://doi.org/10.1016/S0278-2391\(99\)90425-1](https://doi.org/10.1016/S0278-2391(99)90425-1)
- Wong, A., Goonewardene, M. S., Allan, B. P., Mian, A. S., & Rea, A. (2020). Accuracy of maxillary repositioning surgery using CAD/CAM customized surgical guides and fixation plates. *International Journal of Oral and Maxillofacial Surgery.* <https://doi.org/10.1016/j.ijom.2020.08.009>
- Wu, T. Y., Lin, H. H., Lo, L. J., & Ho, C. T. (2017). Postoperative outcomes of two- and three-dimensional planning in orthognathic surgery: A comparative study. *Journal of Plastic, Reconstructive and Aesthetic Surgery, 70*(8), 1101–1111. <https://doi.org/10.1016/j.bjps.2017.04.012>
- Yong, C. W., Tan, T. S., Lim, R. S. K., & Lim, A. A. T. (2021). Surgical cutting guide for orthognathic anterior segmental subapical surgery. *British Journal of Oral and Maxillofacial Surgery, 59*(1), 125–126. <https://doi.org/10.1016/j.bjoms.2020.08.003>
- Zinser, M. J., Ritter, Sailer HF Fau-, Braumann, Ritter L. Fau-, Braumann, B., Maegele, M. F., Maegele, M., Zöller, & Zöller, J. E. (n.d.). A paradigm shift in orthognathic surgery? A comparison of navigation, computer-aided designed/computer-aided manufactured splints, and \classic\ intermaxillary splints to surgical transfer of virtual orthognathic planning (pp. 1531–5053).

This page intentionally left blank

# 31

## Patient-specific modeling of pain progression: a use case on knee osteoarthritis patients using machine learning algorithms

S. Moustakidis<sup>1</sup>, C. Kokkotis<sup>2,3</sup>, D. Tsaopoulos<sup>2</sup>

<sup>1</sup>AIDEAS OU, Tallinn, Estonia; <sup>2</sup>Institute for Bio-Economy & Agri-Technology, Center for Research and Technology Hellas, Marousi, Greece; <sup>3</sup>TEFAA, Department of Physical Education and Sport Science, University of Thessaly Trikala, Greece

### Chapter outline

Introduction.....	805
Dataset description .....	808
Methods .....	810
Grouping/labeling .....	810
Data preprocessing.....	811
Feature selection.....	811
Machine learning.....	812
Validation .....	813
Results and discussion.....	813
Predictive capacity of the binary classifiers without pain-related variables .....	814
Predictive capacity of the binary classifiers with pain variables.....	814
Feature selection results .....	820
Data fusion results .....	823
Comparative analysis .....	823
Conclusions.....	826
References .....	826

### Introduction

Knee Osteoarthritis (KOA) is one of the most common forms of osteoarthritis. KOA is a multifactorial disease, that results from biological and mechanical factors (Silverwood et al., 2015; Toivanen et al., 2010). This complex interplay consists of genetic predisposition, joint integrity, mechanical forces, biochemical processes, and local inflammation. The KOA process begins before motion restriction and pain

symptoms are noticed. Furthermore, KOA shows a variation in intensity, symptom frequency, and patterns, whereas a high correlation of KOA has been observed with obesity, previous injuries due to daily activities or sports, and age (B. Antony et al., 2016; Jack Farr et al., 2013; Lespasio et al., 2017). Nowadays, most medical diagnostic practices for KOA lead to rough estimates of outcomes for a particular treatment plan based on the results of clinical trials. Being based on averages, these results cannot be applied directly to individual patients. Patient-specific modeling and artificial intelligence (AI) have recently emerged as key drivers that can synergistically lead to tailored treatments and optimized individuals' therapy, while at the same time, they can facilitate the development of diagnostic and predictive tools in the field of healthcare. According to the literature (Kokkotis, Moustakidis, Papa-georgiou, et al., 2020), there are plenty of predictive and diagnostic tools for KOA modeling, but the main challenge for the scientific community remains to develop robust personalized prediction models that will be capable to cope with the multifactorial causality of KOA (Antony et al., 2017; Moustakidis et al., 2019; Ntakolia et al., 2020; Tiulpin et al., 2018).

One of the main challenges in the research community is the development and optimization of prognostic KOA models that will be applicable not only to groups of the population or the entire population but also tailored for patient-specific application. An increasing trend of such AI-empowered patient-specific modeling approaches has been observed in the field of KOA research, mainly due to the existence of big datasets. Specifically, several approaches have been reported in the literature in which feature selection (FS) techniques and machine learning (ML) models were used to predict KOA progression (Jamshidi et al., 2019). Datasets with high dimensionality and heterogenous sources were considered, including nutrition questionnaires, symptoms (e.g., swelling, stiffness, and pain), behavioral questionnaires data, subject characteristics, medical imaging outcomes, and physical exams. Lazzarini et al. employed a guided iterative feature elimination algorithm and principal component analysis for the prediction of KOA incidence in overweight and obese women (Lazzarini et al., 2017). They used a small subset of the available information (only five selected variables) and they accurately predicted the incidence of KOA (with a 0.823 area under the curve (AUC)) utilizing random forests as the main learning technique.

Du et al. used magnetic resonance imaging (MRI) to predict the progression of Kellgren and Lawrence (KL), joint space narrowing in the medial compartment (JSM) and joint space narrowing in the lateral (JSL) compartment grades (Du et al., 2018). They used principal component analysis combined with 4 ML models that finally achieved an AUC of up to 0.785. It was concluded that the medial compartment had more informative locations than the lateral compartment. In another study, Halilaj et al. used radiographic assessments of joint space narrowing (JSN) and self-reported knee pain questionnaire data to predict long-term KOA progression (Halilaj et al., 2018). For this aim, they used LASSO regression models (AUC of 0.86). Pedoia et al. met the existing gap for early prediction of cartilage lesion progression in KOA by using multidimensional data analysis (Pedoia et al.,

2018). In this task, they achieved an AUC of 0.838 by combining topological data analysis and logistic regression as the ML model. Furthermore, Abedin et al. predicted KOA severity using elastic net regression (Abedin et al., 2019). An overall root-mean-square error of 0.97 was achieved in the quantification of the contribution of each variable. Tiulpin et al. built a multi-modal ML-based prediction model for KOA progression (Tiulpin et al., 2019). They used deep convolutional neural networks to calculate probabilities of KOA progression, which were combined with clinical data, baseline characteristics, and radiographic assessments to serve as inputs in the ML models. To handle the high dimensionality and heterogeneity of the dataset, they used a gradient boosting machine model (AUC of 0.79–0.82).

In the task of predicting KOA progression, Widera et al. used recursive feature elimination to select the best risk factors and cope with the problem of imbalanced longitudinal data (Widera et al., 2020). They employed five well-known ML classifiers (F1 scores ranging from 0.573 up to 0.689). Kokkotis et al. worked on the same task, proposing a robust hybrid FS approach for the identification of important risk factors (Kokkotis, Moustakidis, Giakas, & Tsaopoulos, 2020). They achieved a 74.07% accuracy using support vector machines trained at 55 selected risk factors. The same hybrid FS technique was employed by Alexos et al. to predict the progression of pain in KOA (Alexos et al., 2020). They achieved accuracies of up to 84.3% with only a small number of risk factors. Moreover, Wang et al. used longitudinal time series data (5-year clinical data) in a long short-term memory (LSTM) model to predict KOA progression (Wang et al., 2020). They achieved 90% accuracy in the task of KL grade prediction. In addition, Kokkotis et al. proposed an evolutionary genetic algorithm—based wrapper technique for the identification of robust risk factors in KOA progression (Kokkotis et al., 2021). This approach overcame two crucial problems: a) the high dimensionality and b) the heterogeneity of the dataset by increasing the generalization of the model. They achieved a mean accuracy of 71.25% at 35 risk factors.

Although there is a growing trend in the development of personalized prediction models for KOA progression, there is still a research need to develop robust techniques capable of identifying important risk factors from multidimensional and heterogeneous clinical data that could contribute to the development of patient-specific models. This chapter contributes to (i) the identification of different clusters of KOA pain progression, (ii) the selection of informative and robust parameters that are relevant to pain progression, and (iii) the development of AI-powered predictive models that could be used for patient-specific prediction of pain progression. To accomplish the aforementioned targets, we rely on an innovative evolutionary ML methodology capable of achieving state-of-the-art accuracy results. One of the novelties of the proposed methodology is that the prediction task has been decomposed into local binary classification problems. Each of the local problems is treated separately (with custom ML models trained on selected feature subsets) and the final prediction is derived by fusing the outputs of these local models. The nature of the selected risk factors is discussed, and the superiority of the proposed methodology over well-known ML algorithms is also demonstrated. The rest of this chapter is organized

as follows. Section “**Dataset description**” presents the main characteristics of the dataset employed in this study. Section “**Methods**” presents the proposed methodology along with detailed descriptions of its main processing steps. Results and discussion are given in the Section “**Results and discussion**”, whereas conclusions are drawn in the “**Conclusions**” section.

## Dataset description

Data were obtained for this study from the OAI database (available at <https://nda.nih.gov/oai/>). OAI is a multicenter, 10-year observational study of men and women with the ultimate objective of providing resources to enable a better understanding of the prevention and treatment of KOA. In this work, we considered only clinical data from the baseline study of OAI. OAI is a big pool of risk factors, which is characterized by heterogeneity and high dimensionality. In total, 649 features were considered as possible risk factors for the prediction of pain progression (Table 31.1). Specifically, we divided the available clinical data from the baseline visit into seven categories: (i) subject characteristics, including variable, e.g., BMI and height; (ii) symptoms, which are related to swelling, knee difficulty, stiffness, and pain; (iii) behavioral, including participants’ quality level of social status and daily routine; (iv) medical history, which includes variables regarding a participant’s medications

**Table 31.1** Characteristics of OAI’s risk factors

*Characteristics of OAI’s risk factors including the category they belong, a short description of the category and the number of features contained.*

Feature category	Description of categories	Number of features
Subject characteristics	Anthropometric parameters of participants, e.g., BMI and height	34
Symptoms	Symptoms related to stiffness, swelling, knee difficulty, and pain (only for experiment B)	122
Behavioral	Questionnaire results regarding participants’ social status and quality level of daily routine	39
Medical history	Questionnaire results regarding a participant’s medications and general health histories	138
Nutrition	Variables which derived from Block Food Frequency questionnaire	205
Physical activity	Questionnaire data regarding activities during a typical week or the last 7 days	41
Physical exam	Participants’ physical measurements and performance measures	70
Total number of features:		649

and general health histories; (v) nutrition, which includes variables from the Block Food Frequency questionnaire; (vi) physical activity, which consists of questionnaire results regarding activities during a typical week or the last 7 days; and (vii) physical exam, which are related to physical measurements of participants.

Pain prediction has been formulated as a three-class classification problem. Specifically, the participants of the study were divided into three groups: (1) participants who experienced a decline in pain intensity; (2) participants that had no significant change in pain intensity; and (3) participants who experienced an increase in pain intensity during the course of the study (Fig. 31.1). The main objective of the study is to build ML models that could discriminate between the three aforementioned groups and therefore be able to decide whether a participant sample will experience any pain progression in the future. A secondary objective is to identify which of the available risk factors contribute more to the classification output and, as a result, can be considered as contributing factors in the prediction of pain.

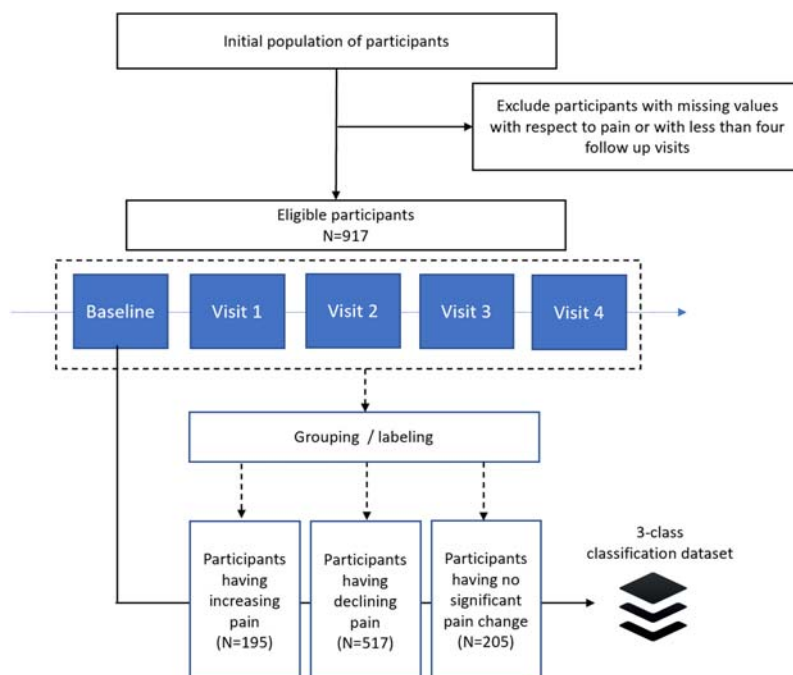


**FIGURE 31.1**

Stratification of patients in the current study.

## Methods

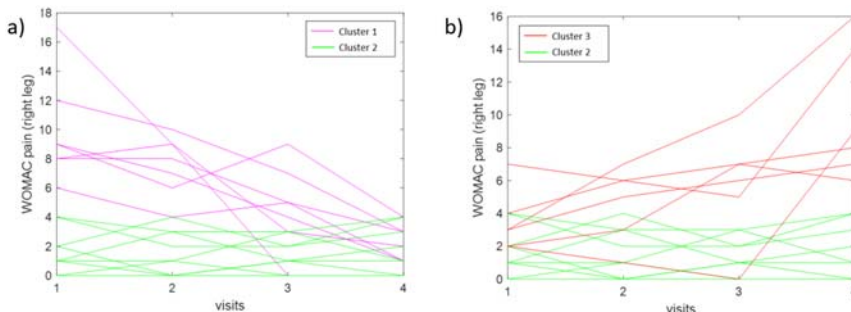
The proposed methodology comprises of the following components: (i) grouping/labeling of the available data employing a linear fitting technique to model the progression of pain, (ii) an evolutionary feature selection technique that selects robust predictive risk factors, (iii) ML for decision-making, and (iv) a well-known validation scheme.

### Grouping/labeling

For each patient in the OAI dataset, WOMAC pain variables (“[Western Ontario McMaster Arthritis Index \(WOMAC\)](#),” 2006) were collected from the four first visits. Specifically, the variables  $V_{xx}\text{WOMKPR}$  and  $V_{xx}\text{WOMKRL}$ ,  $xx = 0, \dots, 4$  where  $xx$  denotes the number of the visit, were collected for the right and left leg, respectively. Indicative pain progression data from each cluster is given in [Fig. 31.2](#). We only considered data from the first four visits given that a significant number of patients did not follow up after visit 4.

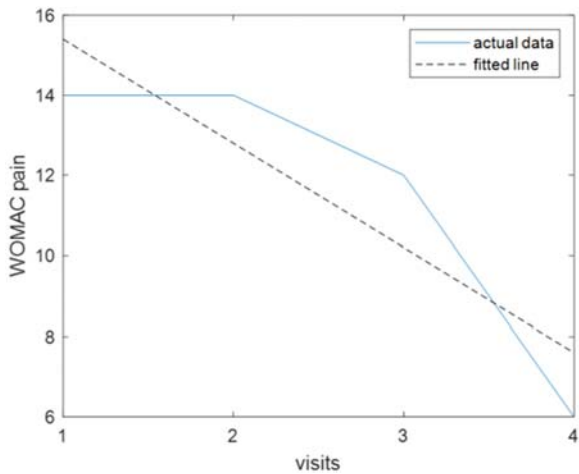
Linear fitting ([Alexos et al., 2020](#)) was then applied to the WOMAC pain progression data of each patient, as shown in [Fig. 31.3](#). Each leg was treated separately, and the slope of the fitted models was considered as the main criterion for grouping the patients. Thresholding was applied to the calculated slopes, leading to the generation of three clusters, each one representing a different pain progression condition:

1. Cluster 1: pain decline ( $slope < -0.3$ ),
2. Cluster 2: no significant pain change ( $-0.3 < slope < 0.3$ ), and
3. Cluster 3: pain increase ( $slope > 0.3$ ).



**FIGURE 31.2**

(A) Representative examples from pain progression clusters 1 (pain decline) and 2 (no significant pain change), (B) representative examples from pain progression clusters 2 (no significant pain change) and 3 (pain increase), [Alexos et al. \(2020\)](#).

**FIGURE 31.3**

Example of actual pain progression data and the associated fitted line [Alexos et al., 2020](#).

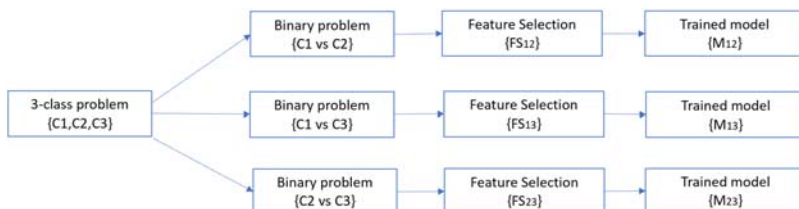
The thresholds were carefully selected to generate equally sized, well-represented, and nonoverlapping clusters.

## Data preprocessing

Data imputation was implemented to cope with the problem of missing points. Mode imputation ([Dodge & Commenges, 2006](#)) was applied to handle both numerical and non-numerical variables. To homogenize and bring variables into the same range, data was also standardized by subtracting the mean and by scaling the resulted values with respect to their variance ([Shanker et al., 1996](#)).

## Feature selection

A recently published FS technique, termed GenWrapper ([Kokkotis et al., 2021](#)), was employed to identify the most informative risk factors from the baseline visit that

**FIGURE 31.4**

The proposed FS methodology.

could be used to discriminate the three aforementioned clusters of pain progression (Fig. 31.4). The employed FS is an evolutionary genetic algorithm—based wrapper technique that selects features that consistently work well in any possible data sample and thus has increased generalization capacity with respect to KOA progression. GenWrapper also performs well on imbalanced datasets, and this is another reason why it was selected in the current study, where the number of samples per class varies considerably. The 3-class problem was formulated as a group of three binary classification problems, and GenWrapper was applied separately at each one. This leads to the creation of three selected feature subsets (FS12, FS13, and FS23) on which three local ML models were trained (M12, M13, and M23, respectively). Specifically:

- FS12 comprises selected risk factors that are sensitive to the discrimination of classes 1 (pain decline) and 2 (stable pain or no pain);
- FS13 comprises selected risk factors that can effectively discriminate classes 1 (pain decline) and 3 (pain increase); and
- FS23 comprises selected risk factors that can effectively discriminate classes 2 (stable pain or no pain) and 3 (pain increase).

## Machine learning

Decision-making was based on the combination of the outputs of the three trained models M12, M13, and M23 as shown in Fig. 31.5. Overall, the process of assigning a decision on a sample  $x_i$  can be described as follows:

- $x_i$  is provided as input into the three different ML pipelines.
- Three variants of  $x_i$  are created ( $x_i^{12}$ ,  $x_i^{13}$ , and  $x_i^{23}$ ), each one comprising features as they have been selected from the FS applied on the three binary problems.
- Three decisions  $d_i^{12}$ ,  $d_i^{13}$ , and  $d_i^{23}$  are produced from the trained models M12, M13, and M23 after supplying them with  $x_i^{12}$ ,  $x_i^{13}$ , and  $x_i^{23}$ , respectively.
- Decision fusion is performed and the decisions with the majority counts are considered as the final predicted outputs. For example, if  $d_i^{12} = 1$ ,  $d_i^{13} = 1$ , and

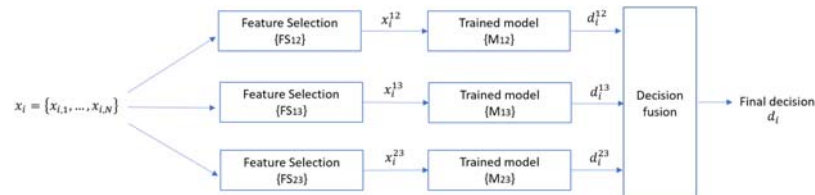


**FIGURE 31.5**

Decision-making as a combination of binary classifiers trained on selected feature subsets.

$d_i^{23} = 2$ , then the final predicted output of the model is class 1 as it has been produced by the majority of the models.

Various classification models were explored for their suitability in implementing the learning task. Given their effective application in previous KOA studies (Kokkotis et al., n.d.; Ntakolia et al., 2021), Support Vector Machines (SVMs) were finally selected because of their capacity to handle highdimensional feature spaces and their high generalization performance.

## Validation

10-fold cross validation (10FCV) was used to evaluate the predictive capacity of the proposed methodology (Moustakidis et al., 2019). The dataset was first shuffled randomly and then it was split into 10 groups. For each unique group, we took the group as a hold out or test data set and the remaining ones as our training set. The proposed ML methodology was applied to the training set and the performance metrics were calculated on the testing set. The procedure was repeated 10 times until all 10 groups were used for testing. The overall performance of the method was calculated by averaging the collected 10 evaluation scores.

The predictive performance of the competing ML models was evaluated with respect to a number of evaluation criteria that are extracted on the basis of the confusion matrix that is given below (Table 31.2).

- Precision is also referred to as positive predictive value (PPV) and is defined as TP/(TP + FP).
- Sensitivity is the proportion of true positives that are correctly identified by the model and is defined by TP/(TP + FN).
- Specificity is the proportion of the true negatives correctly identified by the model and is defined by TN/(TN + FP).
- Classification accuracy (ACC) is the percentage of correct predictions (either positive or negative) over the total number of samples.

---

## Results and discussion

This section presents the performance of the proposed predictive modeling methodology. The predictive capacity of each of the three binary classifiers is initially

**Table 31.2** Confusion matrix.

	Positive true value	Negative true value
Positive prediction	True positive (TP)	False positive (FP)
Negative prediction	False negative (FN)	True negative (TN)

demonstrated with respect to the number of selected risk factors. Two different approaches were investigated: (i) in the first one, all pain-related variables were omitted from the available feature set (refer to Section “[Predictive capacity of the binary classifiers without pain related variables](#)”) and (ii) in the second experimentation, the pain-related variables of the baseline were retained (refer to Section “[Predictive capacity of the binary classifiers with pain variables](#)”). The overall performance of the proposed methodology is finally presented in Sections “[Feature selection results](#)” and “[Data fusion results](#)”, and a comparative analysis with a number of competing approaches is given in the “[Comparative analysis](#)” section.

### **Predictive capacity of the binary classifiers without pain-related variables**

The experimentation in this subsection focuses on a subset of the initial feature space in which all the pain-related variables were excluded. The list of the excluded variables is given in the appendix ([Table 31.3](#)). [Fig. 31.6](#) shows the performance (10FCV) of the M12 classifier with respect to the number of features as they have been selected by the employed FS algorithm. As it is observed, the accuracy increases rapidly for the 15 first selected, whereas the inclusion of additional features only leads to a slight performance increase. The overall best performance (88.82%) was achieved at 32 risk factors that were finally selected to be included in the FS12 subset.

The 10FCV performance of the M23 classifier is depicted in [Fig. 31.7](#). Similar to M12, the predictive accuracy of M23 increases with respect to the number of features that are added in the training feature set and reaches a maximum of 80.36% at 42 selected features. A slight decrease in the accuracy is then observed with the addition of more features.

A larger number of features were selected to maximize the performance of the M13 classifier as shown in [Fig. 31.8](#). Specifically, the maximum 10FCV accuracy of 84.51% was achieved for 58 selected features. The necessity of including more features indicates that the discrimination between classes 1 (declining pain) and 3 (increasing pain) is a more difficult task compared to the tasks where class 2 (no significant pain change) is being discriminated from classes 1 and 3.

### **Predictive capacity of the binary classifiers with pain variables**

[Figs. 31.9, 31.10, and 31.11](#) show the performance of the three binary classifiers M12, M23, and M13 which are trained on risk factors selected from the full feature set available at the baseline visit (with the pain variables included).

The following remarks can be extracted from the figures above: (i) The maximum performance (90.46%) was achieved by the M12 classifier, the M13 classifier also gave a high accuracy (86.56%), whereas a 79.41% discrimination was accomplished by the M23 classifier; (ii) Concerning the number of selected features, 23, 27, and 57 risk factors are needed to maximize the predictive accuracy of M12,

**Table 31.3** Features that are related to pain from the OAI database.

Features	Description
P02KPN	Either knee pain, aching or stiffness: any, past 12 months
P01KPNREV	Right knee pain, aching or stiffness: ever had more than half the days of a month
P01KPNR12	Right knee pain, aching or stiffness: any, past 12 months
P01KPNLEV	Left knee pain, aching or stiffness: ever had more than half the days of a month
P01KPNL12	Left knee pain, aching or stiffness: any, past 12 months
P01KPACT30	Either knee, limit activities due to pain, aching or stiffness, past 30 days
P01HPNR12	Right hip pain, aching or stiffness: any, past 12 months (includes pain in groin and in front and sides of upper thigh)
P01HPNL12	Left hip pain, aching or stiffness: any, past 12 months (includes pain in groin and in front and sides of upper thigh)
P01BP30	Any back pain, past 30 days
P01TMJE6M	Jaw joint or in front of ear, experienced pain or aching, past 6 months
P01TMJF6M	Across face or cheek, experienced pain or aching, past 6 months
V00WPRKN1	Right knee pain: walking, last 7 days
V00WPRKN2	Right knee pain: stairs, last 7 days
V00WPRKN3	Right knee pain: in bed, last 7 days
V00WPRKN4	Right knee pain: sit or lie down, last 7 days
V00WPRKN5	Right knee pain: standing, last 7 days
V00KPRKN1	Right knee pain: twisting/pivoting on knee, last 7 days
V00KPRKN2	Right knee pain: straightening knee fully, last 7 days
V00KPRKN3	Right knee pain: bending knee fully, last 7 days
V00P7RKFR	Right knee pain: how often
V00WPLKN1	Left knee pain: walking, last 7 days
V00WPLKN2	Left knee pain: stairs, last 7 days
V00WPLKN3	Left knee pain: in bed, last 7 days
V00WPLKN4	Left knee pain: sit or lie down, last 7 days
V00WPLKN5	Left knee pain: standing, last 7 days
V00KPLKN1	Left knee pain: twisting/pivoting on knee, last 7 days
V00KPLKN2	Left knee pain: straightening knee fully, last 7 days
V00KPLKN3	Left knee pain: bending knee fully, last 7 days
V00P7LKFR	Left knee pain: how often
P02KPNRCV	Right knee pain, aching or stiffness: more than half the days of a month, past 12 months (calc, used for study eligibility)
P02KPNLCV	Left knee pain, aching or stiffness: more than half the days of a month, past 12 months (calc, used for study eligibility)
P01KPR30CV	Right knee pain, aching or stiffness: more than half the days, past 30 days
P01KPL30CV	Left knee pain, aching or stiffness: more than half the days, past 30 days

*continued*

**Table 31.3** Features that are related to pain from the OAI database.—*cont'd*

Features	Description
P01KPACTCV	Either knee, limits or avoids activities due to pain, aching or stiffness, past 30 days
P01HPR12CV	Right hip pain, aching or stiffness: more than half the days of a month, past 12 months
P01HPL12CV	Left hip pain, aching or stiffness: more than half the days of a month, past 12 months
P01BPTOT	Total days in bed and/or limited activity due to back pain, past 30 days
V00KOOSKPR	Right knee: KOOS Pain Score
V00KOOSKPL	Left knee: KOOS Pain Score
P01SXKOA	Baseline symptomatic knee OA status by person (calc, used for study elig (>0) and in OAI definition of cohort status)
P01KPR12CV	Right knee pain, aching or stiffness: more than half the days of a month, past 12 months
P01KPL12CV	Left knee pain, aching or stiffness: more than half the days of a month, past 12 months
P01KPA30CV	Either knee, avoid/reduce pain, aching or stiffness by changing or cutting back on normal activities, past 30 days
P01TJE30CV	Jaw joint or in front of ear, experienced pain or aching, past 30 days
P01TJF30CV	Across face or cheek, experienced pain or aching, past 30 days
P01TJE30WC	Jaw joint or in front of ear, how often worried or concerned about pain or aching, past 30 days
P01TJF30WC	Across face or cheek, how often worried or concerned about pain or aching, past 30 days
V00WOMTSL	Left knee: WOMAC Total Score
V00WOMTSR	Right knee: WOMAC Total Score
P01RKSX	Right knee baseline symptom status (combines past 30 days and 12 months, calc, used in OAI definition of symptomatic knee OA)
P01LKSX	Left knee baseline symptom status (combines past 30 days and 12 months, calc, used in OAI definition of symptomatic knee OA)
P01BPDAYCV	How many days limit activities due to back pain, past 30 days
P01BPBEDCV	How many days stay in bed due to back pain, past 30 days
P01KPACTCV	Limit activities due to back pain, past 30 days
P01KSX	Frequent knee pain status by person
P01BL12SXL	Left knee baseline frequent knee pain status (IEI, SV, both, or neither)
P01BL12SXR	Right knee baseline frequent knee pain status (IEI, SV, both, or neither)
P01KPACDCV	Either knee, how many days limit activities due to pain, aching or stiffness, past 30 days
P01LKP30CV	Left knee pain, aching or stiffness: any, past 30 days
P01RKP30CV	Right knee pain, aching or stiffness: any, past 30 days
P02KPMED	Either knee, used medication for pain, aching or stiffness, past 12 months
P02KINJ	Either knee, ever injured so badly difficult to walk for at least 1 week
P01KPMED	

**Table 31.3** Features that are related to pain from the OAI database.—*cont'd*

<b>Features</b>	<b>Description</b>
	Either knee, used medication for pain, aching or stiffness, past 12 months
V00TYLEN	Used Tylenol (Acetaminophen) for joint pain or arthritis more than half the days of the month, past 30 days
V00NSAIDS	Used nonprescription NSAIDS (e.g., Aspirin, Ibuprofen ...) for joint pain or arthritis more than half the days of the month, past 30 days
V00NSAIDRX	Used prescription NSAIDS (e.g., Ibuprofen, Diclofenac ...) for joint pain or arthritis more than half the days of the month, past 30 days
V00COXIBS	Used COXIBS (e.g., Bextra, Celebrex ...) for joint pain or arthritis more than half the days of the month, past 30 days
V00NARCOT	Used strong prescription pain medications (e.g., narcotics) for joint pain or arthritis more than half the days of the month, past 30 days
V00SAME	Used SAMe (S-adenosylmethionine) for joint pain or arthritis more than half the days of the month, past 30 days
V00MSM	Used MSM (methylsulfonylmethane) for joint pain or arthritis more than half the days of the month, past 30 days
V00DOXYCYC	Used Doxycycline (includes Vibra-Tabs, Doryx, Adoxa ...) for joint pain or arthritis more than half the days of the month, past 30 days
V00PNMEDT	Take any pain medication today (include both prescription and over-the-counter medications for any type of pain)
V00CHON	Used chondroitin sulfate for joint pain or arthritis, past 6 months
V00GLUC	Used glucosamine for joint pain or arthritis, past 6 months
V00CAM12	Seen someone other than medical doctor or nurse, such as chiropractor or acupuncturist, specifically for arthritis or joint pain, past 12 months
V00DIET12	Follow special food plan or diet, such as a vegetarian or low-fat diet, for arthritis or joint pain, past 12 months
V00VITM12	Use vitamins or minerals, such as selenium or vitamin C or D, for arthritis or joint pain, past 12 months
V00HERB12	Use herbs, such as echinacea, ginger or garlic, for arthritis or joint pain, past 12 months
V00RUBS12	Used rubs, lotions, liniments, creams or oils, such as tiger balm or horse liniment, for arthritis or joint pain, past 12 months
V00BRAC12	Worn copper bracelets or used magnets for arthritis or joint pain, past 12 months
V00YOGA12	Do any health or special movement activity, such as Tai Chi, Yoga, Chi Gong, or Pilates, for arthritis or joint pain, past 12 months
V00RELA12	Do relaxation or mind-body activities, such as meditation, deep breathing, or visualization, for arthritis or joint pain, past 12 months
V00SPIR12	Do spiritual activities (e.g., prayer, laying on of hands, healing circles, or faith healing) for arthritis or joint pain, past 12 months
P02KPMEDCV	Either knee, used medication for pain, aching or stiffness more than half the days of a month, past 12 months

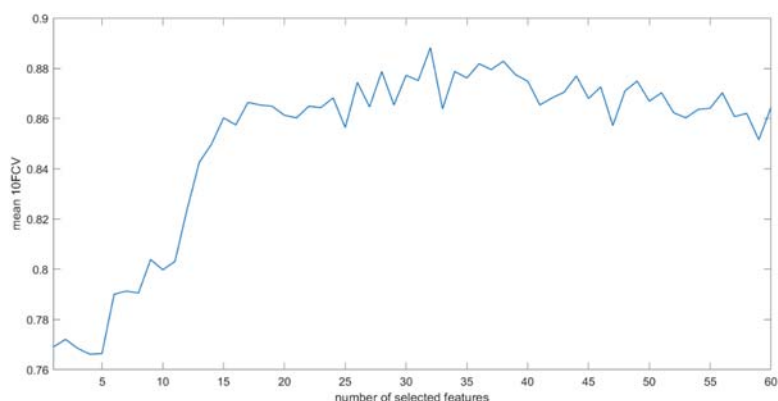
*continued*

**Table 31.3** Features that are related to pain from the OAI database.—*cont'd*

Features	Description
P01OAEGCV	Doctor said you had osteoarthritis/degenerative arthritis in knee
P01KPMEDCV	Either knee, used med for pain, aching or stiffness more than half the days of a month, past 12 months
V00ACUTCV	Seen acupuncture practitioner for arthritis or joint pain, past 12 months
V00ACUSCV	Seen acupressure practitioner for arthritis or joint pain, past 12 months
V00CHELCV	Seen chelation therapy practitioner for arthritis or joint pain, past 12 months
V00CHIRCV	Seen chiropractic care practitioner for arthritis or joint pain, past 12 months
V00FOLKCV	Seen folk medicine practitioner for arthritis or joint pain, past 12 months
V00HOMECV	Seen homeopathy/homeopathic treatment practitioner for arthritis or joint pain, past 12 months
V00MASSCV	Seen massage practitioner for arthritis or joint pain, past 12 months
V00DIETCV	Currently following special food plan or diet for arthritis or joint pain
V00VITMCV	Currently using vitamins/minerals for arthritis or joint pain
V00RUBCV	Currently using rubs, lotions, liniments, creams or oils for arthritis or joint pain
V00CAPSNCV	Currently using Capsaicin (pepper cream) for arthritis or joint pain
V00BRACCV	Currently wear copper bracelets or use magnets for arthritis or joint pain
V00YOGACV	Currently do any type of health or special movement activity for arthritis or joint pain
V00HERBCV	Currently using any herbs for arthritis or joint pain
V00RELACV	Currently do relaxation or mind-body activities for arthritis or joint pain
V00SPIRCV	Currently do any type of spiritual activities for arthritis or joint pain
V00OTHCAMC	Currently seeing ayurveda/biofeedback/energy healing/hypnosis/naturopathy practitioner for arthritis or joint pain
V00OTHCAM	Seen ayurveda/biofeedback/energy healing/hypnosis/naturopathy practitioner for arthritis or joint pain, past 12 months
V00REXPN	Isometric strength: right knee extension, any knee pain during test
V00RFXPN	Isometric strength: right knee flexion, any knee pain during test
V00LEXPN	Isometric strength: left knee extension, any knee pain during test
V00RKPATPN	Right knee exam: patellar quadriceps tendinitis, pain/tenderness at any four sites
V00LKPATPN	Left knee exam: patellar quadriceps tendinitis, pain/tenderness at any four sites
V00RKRFXPN	Right knee exam: knee flexion pain/tenderness present on exam
V00LKRFXPN	Left knee exam: knee flexion pain/tenderness present on exam
V00RKLTPPN	Right knee exam: lateral tibiofemoral pain/tenderness present on exam
V00RKMTTPN	Right knee exam: medial tibiofemoral pain/tenderness present on exam
V00RKABPN	Right knee exam: anserine bursa, pain/tenderness present on exam
V00LKLTPPN	Left knee exam: lateral tibiofemoral pain/tenderness present on exam
V00LKMTPPN	Left knee exam: medial tibiofemoral pain/tenderness present on exam

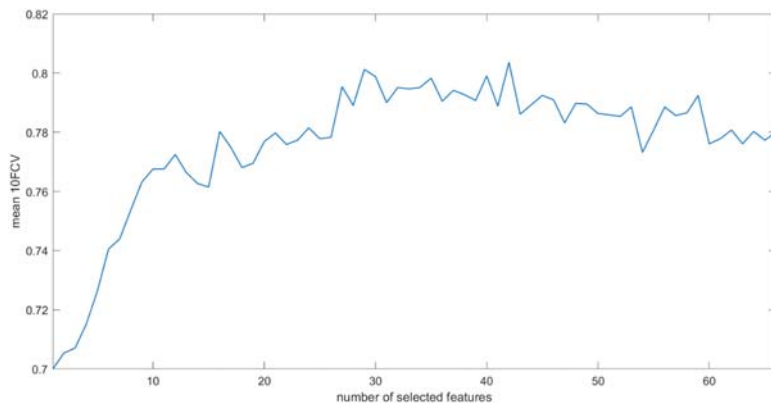
**Table 31.3** Features that are related to pain from the OAI database.—*cont'd*

Features	Description
V00LKABPN	Left knee exam: anserine bursa, pain/tenderness present on exam
V00RKPGDPN	Right knee exam: patellar grind, painful or tender behind knee cap
V00LKPGDPN	Left knee exam: patellar grind, painful or tender behind knee cap
V00REXP1CV	Isometric strength: right knee extension, severity of pain
V00REXP2CV	Isometric strength: right knee extension, knee pain prevent from pushing as hard as can
V00RFXP1CV	Isometric strength: right knee flexion, severity of pain
V00RFXP2CV	Isometric strength: right knee flexion, pain prevent from pulling as hard as can
V00LEXP1CV	Isometric strength: left knee extension, severity of pain
V00LEXP2CV	Isometric strength: left knee extension, pain prevent from pushing as hard as can
V00LFXP1CV	Isometric strength: left knee flexion, severity of pain
V00LFXP2CV	Isometric strength: left knee flexion, pain prevent from pulling as hard as can
P02IKPRISK	Either knee symptom status at IEI
V00WOMKPR	Right knee: WOMAC Pain Score
V00WOMKPL	Left knee: WOMAC Pain Score

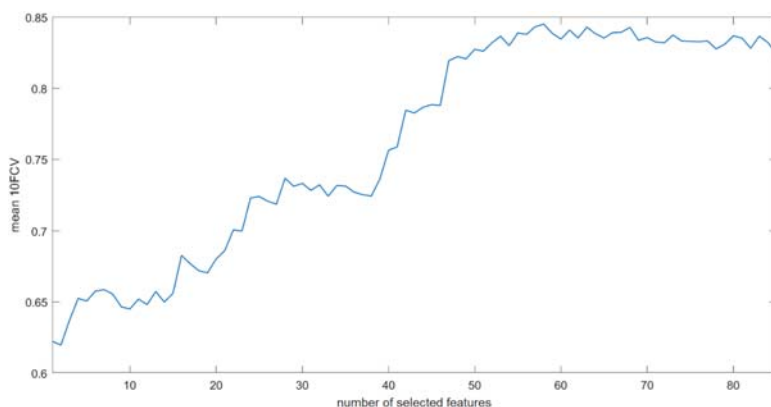
**FIGURE 31.6**

Performance of the binary classifier M12 (declining pain vs. no pain progression) with respect to the number of selected risk factors. Pain-related variables have been excluded from the feature set.

M23, and M13, respectively; (iii) Overall, it was concluded that the inclusion of pain-related variables leads to higher accuracy on less features compared to the experimentation of the previous subsection where the pain-related variables had been excluded.

**FIGURE 31.7**

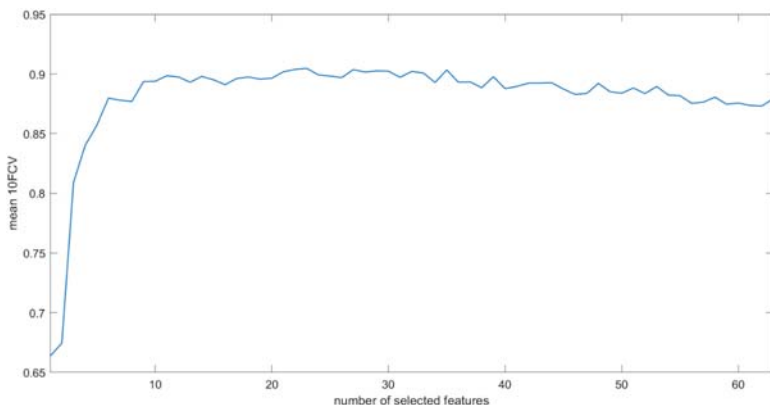
Performance of the binary classifier M23 (no pain progression vs. increasing pain) with respect to the number of selected risk factors. Pain-related variables have been excluded from the feature set.

**FIGURE 31.8**

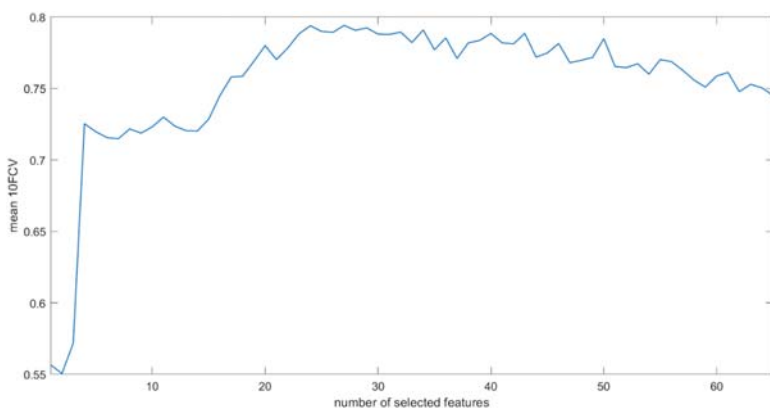
Performance of the binary classifier M13 (declining pain vs. increasing pain) with respect to the number of selected risk factors. Pain-related variables have been excluded from the feature set.

## Feature selection results

Table 31.4 cites the number of selected features for each one of the local binary models (with and without pain-related features). The following conclusions could be drawn from the analysis of Table 31.4 with respect to the first experimentation without pain-related risk factors: (i) Symptoms and nutrition seem to be the most informative feature categories. Specifically, 30 symptoms and 42 nutrition

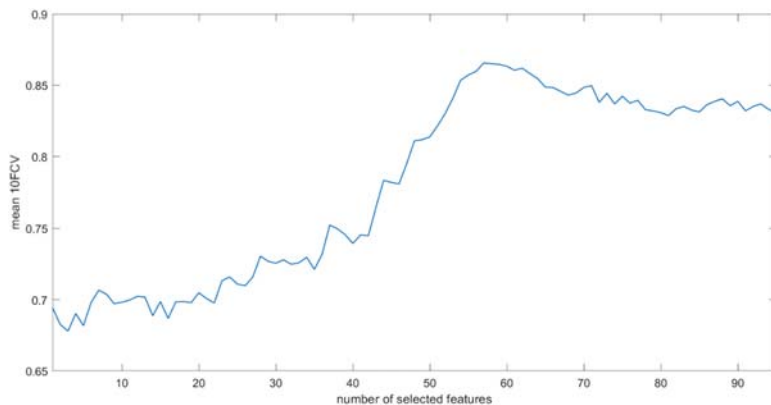
**FIGURE 31.9**

Performance of the binary classifier M12 (declining pain vs. no pain progression) with respect to the number of selected risk factors. Pain-related variables have been retained in the feature set.

**FIGURE 31.10**

Performance of the binary classifier M23 (no pain progression vs. increasing pain) with respect to the number of selected risk factors. Pain-related variables have been retained in the feature set.

parameters were selected in the experiment without pain variables, demonstrating that the contribution of these two categories to the prediction output is significant; (ii) Behavioral data, medical history, and physical exam variables were also selected by the proposed FS (13, 19, and 15, respectively), providing complementary valuable information to the ones mentioned above (symptoms and nutrition); (iii) Subject characteristics and physical activity had a smaller impact on the prediction output (with five features selected per category).

**FIGURE 31.11**

Performance of the binary classifier M13 (declining pain vs. increasing pain) with respect to the number of selected risk factors. Pain-related variables have been retained in the feature set.

**Table 31.4** Number of features selected per category in both experiments with and without pain-related features.

Feature category	Without pain-related features			With pain-related features		
	C1 vs C2	C2 vs C3	C1 vs C3	C1 vs C2	C2 vs C3	C1 vs C3
Subject characteristics	—	1	4	—	—	2
Symptoms	10	11	9	14	7	18
Behavioral	5	4	4	2	2	3
Medical history	4	5	10	2	9	9
Nutrition	9	15	18	1	6	15
Physical activity	—	2	3	—	1	4
Physical exam	4	4	7	4	2	6
Total number of features	32	42	58	23	27	57

Similar findings were observed in the experimentation with the whole feature set (including the pain-related variables). The main difference between the two experiments (with and without pain variables) was that the inclusion of pain variables led to the selection of less features in total (107 compared to 132). Moreover, the number of selected features for the symptoms' category was increased (39 in total). This could be attributed to the fact that the initial state of pain at baseline is obviously a

significant indicator of pain for future progression and therefore a significant number of pain variables and other similar risk factors from the baseline visit were selected by the proposed FS. Overall, it was concluded that a combination of heterogeneous features coming from almost all feature categories is needed to predict pain progression highlighting the necessity of adopting a multiparametric approach that could handle the complexity of the available data.

### Data fusion results

This section presents the final performance of the proposed predictive methodology after combining the outputs of the three binary classifiers. Table 31.5 cites the confusion matrixes along with a variety of complementary performance metrics (including precision, sensitivity, and specificity) for both approaches (with and without pain-related variables). Including pain variables in the training sets led to a small increase in the overall accuracy (0.76 with pain data compared to 0.74 without pain data) and this performance improvement was reflected in the majority of the rest of the performance metrics, especially for classes C1 and C2. A small decrease in precision, sensitivity, and specificity was observed for C3 compared to the associated results without pain variables.

### Comparative analysis

The proposed methodology was compared with well-known FS techniques. The same classifier (SVM) was used to perform the final class discrimination for all

**Table 31.5** Performance of the proposed pain prediction methodology with and without pain variables.

	Without pain-related variables			With pain-related variables		
C1	C1 147	C2 12	C3 36	C1 164	C2 7	C3 24
C2	57	388	72	35	398	84
C3	31	33	141	39	33	133
TP	147	388	141	164	398	133
FP	48	129	64	31	119	72
FN	88	45	108	74	40	108
TN	634	355	604	648	360	604
Precision	0.75	0.75	0.69	0.84	0.77	0.65
Sensitivity	0.63	0.90	0.57	0.69	0.91	0.55
Specificity	0.93	0.73	0.90	0.95	0.75	0.89
Accuracy	0.74			0.76		

the competing approaches, forming a fair basis for comparison. The main characteristics of the competing algorithms are given below.

- Least Absolute Shrinkage and Selection Operator (Lasso): This method applies a regularization process that penalizes the coefficients of the regression variables while setting the less relevant ones to zero to respect the constraint on the sum. FS is a consequence of this process when all the variables that still have non-zero coefficients are selected to be part of the model (Muthukrishnan & Rohini, 2016).
- Relief-F: An iterative, randomized, and supervised approach that estimates the quality of features according to how well their values differentiate data samples that are near to each other; it does not discriminate among redundant features, and performance decreases with few data (Liu & Motoda, 2007).
- Minimum Redundancy Maximum Relevance (mRMR): An FS algorithm that systematically performs variable selection, achieving a reasonable trade-off between relevance and redundancy (Peng et al., 2005).
- The entire feature set was also employed to form a basis for estimating the effectiveness of the proposed and remaining rest competing FS algorithms. In this case, the SVM classifier was trained on the initial high-dimensional feature set.

The same validation scheme (10FCV) was used to evaluate the performance of all the FS algorithms. For Lasso, Relief-F and mRMR, the optimal number of features was selected. This was achieved by progressively applying SVM on feature subsets of increasing dimensionality (up to 100 selected features based on the ranking that has been determined by each FS algorithm). The feature subset that maximizes the 10FCV performance was the one selected for this comparative analysis.

Table 31.6 cites the performance of the proposed methodology compared to the performance of the competing algorithms. The proposed methodology was proven to be 6% more accurate than mRMR, which was the second-best performer. The confusion matrix and the associated performance metrics verify the superiority of the proposed method, especially with regards to the minority classes (C1 and C3) that have considerably less samples compared to class C2.

One of the limitations of the approach is the relatively large number of selected risk factors (more than 100) that contribute to the development of the proposed methodology. This could be attributed to the multifactorial nature of the KOA, which results from a number of biological and mechanical factors. Moreover, all the tested ML models were treated as black boxes and therefore they are insufficient to provide explanations on how a certain output has been drawn and which is the impact of the selected features on it. The application of explainable AI tools or transparent ML models could be considered as future work toward the development of trustworthy and more reliable patient-specific predictive models.

**Table 31.6** Comparison between the proposed methodology and well-known state-of-the-art techniques.

Technique	Confusion matrix			Precision	Sensitivity	Specificity	Overall accuracy
Entire feature set + SVM	100	15	43	0.63	0.51	0.92	0.68
	54	463	101	0.75	0.89	0.61	
	41	39	61	0.43	0.30	0.89	
Lasso for FS (81) + SVM	90	27	58	0.51	0.46	0.88	0.65
	58	453	95	0.75	0.88	0.62	
	47	37	52	0.38	0.25	0.88	
Relief-F (41) + SVM	94	21	38	0.61	0.48	0.92	0.67
	50	462	108	0.75	0.89	0.60	
	51	34	59	0.41	0.29	0.88	
mRMR (40) + SVM	119	20	40	0.66	0.61	0.92	0.70
	48	455	99	0.76	0.88	0.63	
	28	42	66	0.49	0.32	0.90	
Proposed + SVM	164	7	24	0.84	0.69	0.95	0.76
	35	398	84	0.77	0.91	0.75	
	39	33	133	0.65	0.55	0.89	

---

## Conclusions

This chapter focuses on the development of patient-specific models of KOA prediction, with a special emphasis on pain progression. The presented method contributes to the identification of different clusters of KOA pain progression, the selection of informative and robust parameters that are relevant to pain progression, and the development of AI-powered predictive models that could be used for patient-specific prediction of pain progression. Unlike previous approaches, our approach decomposes the pain prediction problem into local binary subproblems that are dealt with separately, whereas the final outcomes are derived via decision fusion. The outcome of our predictive models offers a significant step forward as a source of decision support, enabling clinicians to be more effective in screening and detecting patients at risk of structural progressive OA. Further work, however, is needed to fully validate this method and implement it into clinical practice.

---

## References

- Abedin, J., Antony, J., McGuinness, K., Moran, K., O'Connor, N. E., Rebholz-Schuhmann, D., & Newell, J. (2019). Predicting knee osteoarthritis severity: Comparative modeling based on patient's data and plain X-ray images. *Scientific Reports*, 9(1). <https://doi.org/10.1038/s41598-019-42215-9>
- Alexos, A., Kokkotis, C., Moustakidis, S., Papageorgiou, E., & Tsaopoulos, D. (2020). Prediction of pain in knee osteoarthritis patients using machine learning: Data from osteoarthritis initiative. <https://doi.org/10.1109/IISA50023.2020.9284379>.
- Antony, B., Jones, G., Jin, X., & Ding, C. (2016). Do early life factors affect the development of knee osteoarthritis in later life: A narrative review. *Arthritis Research and Therapy*, 18(1). <https://doi.org/10.1186/s13075-016-1104-0>
- Antony, J., McGuinness, K., Moran, K., & O'Connor, N. E. (2017). Automatic detection of knee joints and quantification of knee osteoarthritis severity using convolutional neural networks. In *Lecture notes in computer science (including subseries lecture notes in artificial intelligence and lecture notes in bioinformatics)* (Vol 10358, pp. 376–390). Springer Verlag. [https://doi.org/10.1007/978-3-319-62416-7\\_27](https://doi.org/10.1007/978-3-319-62416-7_27)
- Dodge, Y., & Commenges, D. (2006). *The Oxford dictionary of statistical terms*.
- Du, Y., Almajalid, R., Shan, J., & Zhang, M. (2018). A novel method to predict knee osteoarthritis progression on MRI using machine learning methods. *IEEE Transactions on Nanobioscience*, 17(3), 228–236. <https://doi.org/10.1109/TNB.2018.2840082>
- Halilaj, E., Le, Y., Hicks, J. L., Hastie, T. J., & Delp, S. L. (2018). Modeling and predicting osteoarthritis progression: Data from the osteoarthritis initiative. *Osteoarthritis and Cartilage*, 26(12), 1643–1650. <https://doi.org/10.1016/j.joca.2018.08.003>
- Jack Farr, L., Miller, L. E., & Block, J. E. (2013). Quality of life in patients with knee osteoarthritis: A commentary on nonsurgical and surgical treatments. *The Open Orthopaedics Journal*, 7, 619–623. <https://doi.org/10.2174/1874325001307010619>
- Jamshidi, A., Pelletier, J. P., & Martel-Pelletier, J. (2019). Machine-learning-based patient-specific prediction models for knee osteoarthritis. *Nature Reviews Rheumatology*, 15(1), 49–60. <https://doi.org/10.1038/s41584-018-0130-5>

- Kokkotis, C., Moustakidis, S., Baltzopoulos, V., Giakas, G., & Tsaopoulos, D. (2021). Identifying robust risk factors for knee osteoarthritis progression: An evolutionary machine learning approach. *Healthcare (Basel, Switzerland)*, 9(3), 260. <https://doi.org/10.3390/healthcare9030260>
- Kokkotis, C., Moustakidis, S., Giakas, G., & Tsaopoulos, D. (2020). Identification of risk factors and machine learning-based prediction models for knee osteoarthritis patients. *Applied Sciences*, 10(19). <https://doi.org/10.3390/app10196797>
- Kokkotis, C., Moustakidis, S., Papageorgiou, E., Giakas, G., & Tsaopoulos, D. E. (2020). Machine learning in knee osteoarthritis: A review. *Osteoarthritis and Cartilage Open*, 2(3), 100069. <https://doi.org/10.1016/j.ocarto.2020.100069>
- Kokkotis, C., Moustakidis, S., Papageorgiou, E., Giakas, G., & Tsaopoulos, D. (n.d.). A Machine Learning workflow for Diagnosis of Knee Osteoarthritis with a focus on post-hoc explainability. In 2020 11th International Conference on Information, Intelligence, Systems and Applications (IISA) (pp. 1–7). <https://doi.org/10.1109/IISA50023.2020.9284354>.
- Lazzarini, N., Runhaar, J., Bay-Jensen, A. C., Thudium, C. S., Bierma-Zeinstra, S. M. A., Henrotin, Y., & Bacardit, J. (2017). A machine learning approach for the identification of new biomarkers for knee osteoarthritis development in overweight and obese women. *Osteoarthritis and Cartilage*, 25(12), 2014–2021. <https://doi.org/10.1016/j.joca.2017.09.001>
- Lespasio, M. J., Piuzzi, N. S., Husni, M. E., Muschler, G. F., Guarino, A., & Mont, M. A. (2017). Knee osteoarthritis: A primer. *The Permanente Journal*, 21, 16–183. <https://doi.org/10.7812/TPP/16-183>. PMID: 29035179; PMCID: PMC5638628.
- Liu, H., & Motoda, H. (2007). *Computational methods of feature selection*.
- Moustakidis, S., Christodoulou, E., Papageorgiou, E., Kokkotis, C., Papandrianos, N., & Tsaopoulos, D. (2019). Application of machine intelligence for osteoarthritis classification: A classical implementation and a quantum perspective. *Quantum Machine Intelligence*, 1, 1–14. <https://doi.org/10.1007/s42484-019-00008-3>
- Muthukrishnan, R., & Rohini, R. (2016). LASSO: A feature selection technique in predictive modeling for machine learning. In *2016 IEEE international conference on advances in computer applications (ICACA)*.
- Ntakolia, C., Kokkotis, C., Moustakidis, S., & Tsaopoulos, D. (2020). *A machine learning pipeline for predicting joint space narrowing in knee osteoarthritis patients* (pp. 934–941). <https://doi.org/10.1109/BIBE50027.2020.00158>
- Ntakolia, C., Kokkotis, C., Moustakidis, S., & Tsaopoulos, D. (2021). Prediction of joint space narrowing progression in knee osteoarthritis patients. *Diagnostics*, 11(2). <https://doi.org/10.3390/diagnostics11020285>
- Pedoia, V., Haefeli, J., Morioka, K., Teng, H. L., Nardo, L., Souza, R. B., Ferguson, A. R., & Majumdar, S. (2018). MRI and biomechanics multidimensional data analysis reveals R2-R1ρ as an early predictor of cartilage lesion progression in knee osteoarthritis. *Journal of Magnetic Resonance Imaging*, 47(1), 78–90. <https://doi.org/10.1002/jmri.25750>
- Peng, H., Long, F., & Ding, C. (2005). Feature selection based on mutual information: Criteria of max-dependency, max-relevance, and min-redundancy. *IEEE Transactions on Pattern Analysis and Machine Intelligence*, 27(8), 1226–1238. <https://doi.org/10.1109/TPAMI.2005.159>
- Shanker, M., Hu, M. Y., & Hung, M. S. (1996). Effect of data standardization on neural network training. *Omega*, 24(4), 385–397. [https://doi.org/10.1016/0305-0483\(96\)00010-2](https://doi.org/10.1016/0305-0483(96)00010-2)

- Silverwood, V., Blagojevic-Bucknall, M., Jinks, C., Jordan, J. L., Protheroe, J., & Jordan, K. P. (2015). Current evidence on risk factors for knee osteoarthritis in older adults: A systematic review and meta-analysis. *Osteoarthritis and Cartilage*, 23(4), 507–515. <https://doi.org/10.1016/j.joca.2014.11.019>
- Tiulpin, A., Klein, S., Bierma-Zeinstra, S., Thevenot, J., Rahtu, E., Meurs, J., Oei, E., & Saarakkala, S. (2019). Multimodal machine learning-based knee osteoarthritis progression prediction from plain radiographs and clinical data. *Scientific Reports*, 9. <https://doi.org/10.1038/s41598-019-56527-3>
- Tiulpin, A., Thevenot, J., Rahtu, E., Lehenkari, P., & Saarakkala, S. (2018). Automatic knee osteoarthritis diagnosis from plain radiographs: A deep learning-based approach. *Scientific Reports*, 8(1). <https://doi.org/10.1038/s41598-018-20132-7>
- Toivanen, A. T., Heliövaara, M., Impivaara, O., Arokoski, J. P. A., Knekt, P., Lauren, H., & Kröger, H. (2010). Obesity, physically demanding work and traumatic knee injury are major risk factors for knee osteoarthritis—a population-based study with a follow-up of 22 years. *Rheumatology*, 49(2), 308–314. <https://doi.org/10.1093/rheumatology/kep388>
- Wang, Y., You, L., Chyr, J., Lan, L., Zhao, W., Zhou, Y., Xu, H., Noble, P., & Zhou, X. (2020). Causal discovery in radiographic markers of knee osteoarthritis and prediction for knee osteoarthritis severity with attention-long short-term memory. *Frontiers in Public Health*, 8. <https://doi.org/10.3389/fpubh.2020.604654>
- Western Ontario McMaster Arthritis Index (WOMAC). (2006). *Journal of Orthopaedic Trauma*, 20(Supplement), S108. <https://doi.org/10.1097/00005131-200609001-00029>
- Widera, P., Welsing, P., Ladel, C., Loughlin, J., Lafeber, F., Dop, F., Larkin, J., Weinans, H., Mobasher, A., & Bacardit, J. (2020). Multi-classifier prediction of knee osteoarthritis progression from incomplete imbalanced longitudinal data. *Scientific Reports*, 10, 8427. <https://doi.org/10.1038/s41598-020-64643-8>

# A design procedure for the development of VR platforms for the rehabilitation of patients after stroke

# 32

**Daniel Lanzoni, Andrea Vitali, Daniele Regazzoni, Caterina Rizzi**

*Department of Management, Information and Production Engineering, University of Bergamo,  
Bergamo, Italy*

## **Chapter outline**

<b>Introduction .....</b>	829
<b>Scientific background .....</b>	831
<b>Methods and tools .....</b>	832
Definition of the rehabilitation exercise and related devices.....	833
Identification of ICT tools.....	833
Medical data management .....	834
<b>Use cases .....</b>	835
VR platform for the evaluation of the extra-personal neglect .....	835
VR platform for the recovery of severe memory loss .....	838
3D scanning acquisition.....	839
Development of the serious game .....	840
Motor-skills tele-rehabilitation of hands.....	840
<b>Evaluation .....</b>	842
<b>Conclusion .....</b>	845
<b>Acknowledgments .....</b>	846
<b>References .....</b>	846

## **Introduction**

In Europe, every year there are approximatively 500,000 new cases of people with cerebral stroke (Mozaffarian et al., 2016). Brain stroke is the third most likely cause of death after cancer and cardiovascular diseases (Mozaffarian et al., 2016; Roger et al., 2011). A stroke is usually an unexpected event resulting in severe impairments for the patients and causing a difficult situation for their relatives. The level of disability thereafter depends on the type, severity, and position of the stroke

occlusion: a rapid identification of the brain zone is important to rapidly intervene for reducing the brain damage and the level of disability. In general, a stroke causes cognitive and motor impairments. Cognitive disabilities include memory loss, everyday problem solving, and aphasia, while motor disabilities limit the actions of upper and lower limbs. Besides the direct impairments, stroke can also generate other kind of disorders, such as hemispatial negligence in the initial acute phase after the stroke. Hemispatial neglect affects two-thirds of patients and is a neuropsychological disorder in which a deficit in attention and awareness of one side of the field of vision are observed. It is defined by the inability of a person to process and perceive stimuli on one side of the body or environment, where that inability is not due to a lack of sensation (Cipresso et al., 2018).

Recovery after a stroke involves specific exercises which patients usually perform in a rehabilitation facility during the early stage and then at home according to the physiotherapists' and physicians' recommendations. For example, the recovery of mnemonic functions is attempted by showing the patient a set of pictures of a known environment, such as the patient's house. Executive functions can be recovered through a set of actions to be performed in an ordered way (e.g., making a dish by following a recipe). Motor skill rehabilitation requires specific exercises; for example, to recover the ability to grab thin objects with the fingers, a patient starts with grabbing voluminous objects (e.g., an apple or a bottle) and, when control of the hands improves, the patient grabs thinner objects, such as a pencil. As for neglect, a set of very simple tests evaluate the level of severity, such as the cancellation test and the reading test (Pizzamiglio et al., 1989; Halligan & Marshall, 1989).

The main aim of post-stroke rehabilitation is to help patients regain as much independence as possible. Traditional cognitive and motor rehabilitation processes usually require objective responses to specific events and are performed in a controlled environment of the rehabilitation center. During the last 2 decades, the advent of innovative technologies allowed the development of IT tools that permit to design realistic virtual environments. This allows the improvement of the ecological validity, which is the capability of a rehabilitation process to mimic daily real-life tasks (Dawson & Marcotte, 2017). In particular, Virtual Reality (VR) technologies have been exploited to develop platforms for the rehabilitation based on serious games. VR devices embed several types of sensors for recording data, which can be useful to assess the patient's performance in a more objective way.

Even if VR gives a valid support, the technological skills required by VR solutions discourage the medical personnel. Furthermore, they are usually oriented to a wide category of disorders with almost no specific customizations for the specific patient.

This chapter describes the development of VR solutions for poststroke rehabilitation to improve the ecological validity and the level of usability using low-cost and consumer technology.

First, this chapter introduces the scientific background about the use of VR for post-stroke rehabilitation; then, the methodology and its applications for three different case studies are described. The authors, who are experts in VR and motion

capture systems for medical rehabilitation, present experimentation outcomes and conclusions to complete this chapter.

## Scientific background

In the last two decades, the evolution of VR allowed the design of many tools useful for stroke rehabilitation. VR solutions are based on serious games and the main aim is the rehabilitation combined with the entertainment to increase patients' engagement. Nolin et al. (2019) presented a wide scientific review with more than 100 research works from 1989 to 2017 and several VR solutions. Many research studies emulate traditional rehabilitation exercises with serious games developed using dedicated virtual environments (Baheux et al., 2006; Kang et al., 2008; Rand et al., 2009). Traditional approaches have been compared with VR solutions to understand their real benefits. On one side, the research works highlighted that the use of VR can speed up patients' improvement since the exercises are more engaging than traditional ones. On the other hand, VR technologies and dedicated environments are expensive and time consuming for both the physicians and patients. Furthermore, in many cases the level of usability is not very high since the exploited technologies are complex to be used and replicated in the rehabilitation facilities. With the advent of more innovative Head Mounted Displays (HMDs) (e.g., the HTC Vive Pro and the Facebook Oculus Rift), interactive and immersive serious games can be developed using a normal laptop (Cameirão et al., 2016; Gamito et al., 2017; Nir-Hadad et al., 2017).

Smith et al. (2019) presented a scientific overview of more than 150 scientific papers on VR for episodic memory recovery, categorized according to the level of ecological validity. The results highlight how the use of VR has still to be highly customized for the specific patient to reach a higher ecological validity compared with the traditional approach.

The last generation of VR technologies allows an immersive interaction with the virtual environment avoiding cybersickness which may be caused by image latency. Moreover, motion capture systems, hand tracking and haptic devices combined with HMDs, can guarantee an interaction using hands. Kim et al. (2020) presented a scientific review about immersive VR for motor skill rehabilitation. Even though the researchers confirmed its potential, medical personnel and patients did not appreciate the level of usability because no specific technical guidelines were provided to facilitate the VR integration into the clinical practice and their use at home.

Usability plays a crucial role and Levac et al. (Glegg & Levac, 2018) conducted a review in which several strategies for the adoption of VR were discussed. The aim was to identify facilitators and interventions to increase the acceptance of physicians and patients about the use of VR as a tool for rehabilitation. The final discussion reported that few VR rehabilitation tools had been developed starting from the end-user needs or introducing specific demonstrations to support the medical personnel in their adoption of VR.

With the pandemic situation, the need to support rehabilitation processes at home has increased. Tele-rehabilitation is one of the most important challenges since the solutions provided should be based on low-cost and user-friendly devices. Nowadays, VR solutions based on consumer technologies are available (e.g., a smartphone can be used as a VR screen for a low-cost head mounted display), but the user guidance is mandatory to guarantee a high level of usability at home (Pedroli et al., 2020). Esparza et al. (Rybaczuk et al., 2019) report a usability study on a web-based platform for motor skill rehabilitation at home. The results highlighted a need for simple technologies to increase the adherence to rehabilitation therapy.

This chapter introduces a specific procedure to develop VR serious games driven by the needs of the end-users who can be medical personnel and post-stroke patients. Consumer technologies are used to guarantee a good level of usability and a higher ecological validity.

## Methods and tools

Fig. 32.1 shows the main steps adopted to design VR serious games for post-stroke rehabilitation: (i) medical requirement analysis, (ii) identification of ICT tools, and (iii) data management.

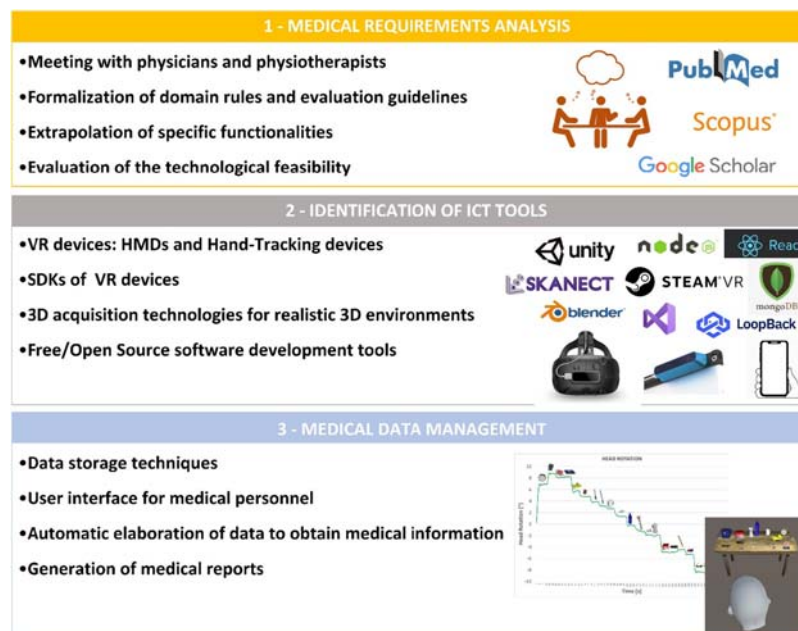


FIGURE 32.1

Main steps to design VR solutions for after stroke rehabilitation.

Particular attention has been applied to the customization of serious games for each patient. Consumer technology and inexpensive VR devices are evaluated according to usability criteria defined in collaboration with the medical staff. The easy navigation of the 3D virtual space and the intuitive interaction style are the two features of usability that are considered in the development of the Serious Games. The usability depends on the patient's condition. Usually, the deficits lead to other consequences for the patient, which may be different from each case. Furthermore, addressing usability has a positive impact on eventual cybersickness issues. For this reason, it is important to consider several user interface solutions and different level of difficulty to perform the test.

### **Definition of the rehabilitation exercise and related devices**

The first step provides for the acquisition of medical knowledge through meetings and scientific literature analysis. This defines the body of knowledge needed to design and perform rehabilitation exercises with the VR technology. Moreover, data acquired by the devices can be used to objectively assess parameters which help to understand if rehabilitation exercises are correctly performed. In particular, sensor raw data allows the computation of several measurable parameters (e.g., the time to perform a task, the position and the orientation of the patient's head, the velocity to perform an action with a hand), which are then used for the customization of a serious game and to adapt the level of difficulty according to a patient's skills.

When all medical requirements have been identified, a further meeting is held with the physicians to check that all medical aspects have been considered and to proceed with the evaluation of the feasibility. This includes the identification of consumer technologies (e.g., laptops, smartphones, and tablets) and VR devices (e.g., HMDs and marker-less motion capture systems).

The hardware device selection process is conceived to meet physicians' and physiotherapists' usability requirements and to receive feedback on their user experience which can be used for further improvement. Furthermore, the medical personnel evaluate and provide feedback about the patients' experience of the serious game interaction, and to understand if the proposed VR devices are adequate for the final purpose of the rehabilitation exercises.

### **Identification of ICT tools**

ICT tools have been selected to be economically affordable for both rehabilitation facilities and patients. Wi-fi and Bluetooth connections for data exchange and a standard graphic card for the rendering of serious games are needed. In after-stroke rehabilitation, head mounted displays and hand tracking devices can be used.

HMDs allow visualizing the 3D environment of a serious game with realistic depth sense. They are easily wearable and comfortable even when the patient has glasses. The most suitable HMDs are Oculus and HTC Vive since they make available a set of Software Development Kits (SDKs) to be easily integrated in serious games and interfaced with hand-tracking devices. Among these, the HTC Vive

Pro and the Leap Motion ([Leap Motion, 2022](#)) devices are the most recommended ([Aguilera-Rubio et al., 2022; Borrego et al., 2018](#)).

For hand motor-skill recovery, the VR experience has to be as immersive as possible. Hand tracking devices can be marker-less motion capture systems able to track the movements of hands, fingers, and palms during the interaction with a serious game. Tracked data are useful to understand how the patient performs each movement during the rehabilitation exercise. The motion data are analyzed with specific algorithms to measure if the patient is performing the exercise in the correct way or not. The Leap Motion controller has been chosen since it provides detailed and high-quality data (e.g., 3D positions and rotations of all phalanges).

Furthermore, 3D modeling tools can be employed to increase the level of ecological validity. In particular, the 3D acquisition of real environments makes the rehabilitation tasks for memory impairments more immersive and realistic. Economic 3D scanning systems, such as Structure Sensor and the 3D Sense scanner, can be used for the acquisition of familiar environments. Applications, such as Skanect ([Skanect, 2022](#)) and Blender ([Blender, 2022](#)), are used to model and refine the 3D interactive environment.

For software development, three main categories of tools have been identified: (i) for the development of the serious game, (ii) for the development of the interface between the environment and the VR devices, and (iii) for data exchange among medical personnel and patients. The choice was among available open-source or free development environments. Unity ([Unity, 2022](#)) has been selected for the development of serious games and Steam VR as SDK to interface the HTC Vive Pro with Unity. Also, the Leap Motion device has an SDK to easily embed the hand interaction style in Unity. Finally, the development of the software module for data exchange depends on the type of VR platform. If the application is standalone, a Bluetooth or a Wi-Fi connection can be used to route the data between the laptops of physicians and patients.

## Medical data management

Algorithms have been developed to translate raw data from the HMDs and Leap Motion devices into the parameters defined in the first step (see section [Definition of the rehabilitation exercise and related devices](#)). The data from the HMD provides the position and orientation of the head during the exploration of the virtual environment, while data tracked by the Leap Motion device adds the kinematics of hand motion.

After the automatic computation of parameters, which depend on any specific application as shown in the following paragraph, an ad-hoc user interface (monitor, head-mounted display, controllers, hands tracking) allows the medical personnel to visualize the outcome of patient performance. An objective overview of patient' performance permits variation of parameter settings for each patient. Finally, the user interface can provide any information in standard file formats such as Microsoft Excel and/or Adobe Acrobat PDF. These features require the development of further software modules to record, store and modify any data.

---

## Use cases

Three VR solutions have been developed that cover different tasks for the rehabilitation of post-stroke patients: (i) a platform for the cognitive rehabilitation of patients with severe memory loss, (ii) an application to test the level of extra-personal neglect, and (iii) a web platform for hand motor skill rehabilitation.

### VR platform for the evaluation of the extra-personal neglect

The aim for this VR solution is to objectively evaluate extra-personal neglect (Lanzoni et al., 2020). Several meetings with medical staff were held to identify medical needs and translate them into a VR platform specification.

The neglect disorder is classified according to the distance of neglected objects, starting from a patient's body to the surrounding environment (Cipresso et al., 2018). Therefore, neglect is classified as

- *Personal*: A patient is not conscious of their contralesional body side;
- *Peripersonal*: Reachable objects using hands on the neglected side are not considered;
- *Extrapersonal*: A patient is not aware of a hemi-space in the surrounding environment which is not within reaching distance (Kim et al., 2010).

Extra-personal neglect has a strong impact on the patient's daily life. Examples are the risk for a pedestrian crossing a street without considering the cars coming from one side, or a patient hitting a door frame because they do not consider half of the door.

At present, there are no standard tests to measure and evaluate the level of extra-personal neglect (Bowen et al., 2013; Azouvi, 2017). An objective test would help doctors performing a precise neuro-psychological assessment to establish the most suitable rehabilitation plan.

In the case study medical personnel requested a VR environment with a table on which 20 objects were placed covering the entire width from the right to the left. The aim of the serious game is to determine to which extent a patient considers the objects. Voice recognition is used to recognize objects when the patient calls their name. The greater the severity of the neglect, the greater will be the patient's limit in observing the objects in the contralesional side after the midline of the table. Thus, the test allows physicians to assess the initial level of extra-personal neglect and, therefore, to prescribe the most suitable rehabilitation process. The initial position of the table is 2 meters away in front of the patient, but it may be changed in the game settings according to the physician's prescription.

A therapist initializes the VR platform by entering the patient's personal data, choosing the distance from the virtual table and, finally, starting the application. The videogame must be simple and user-friendly, so that it may be used by people of all ages. No interaction is allowed between the physiotherapist and the patient to exclude events relative to the peripersonal component of neglect during the test.

Physicians and physiotherapists are interested in the way the patient rotates the head to recognize virtual objects. Thus, a replay of tests must be available for assessments and comparisons.

For a medical evaluation the following parameters have been identified:

- The name of the observed object and if the patient has truly seen the mentioned object. This feature permits to avoid that the patient says names of objects without observing them.
- The time required by the patient to recognize an object.
- The time to explore both the left and right side of the space to evaluate the speed of exploration. Patients with neglect perform the evaluation slower in the contralesional area.
- The movements of the head to replicate how the patient performed the test. In this way, medical personnel can analyze rotations and velocity when patients observe 3D objects in the contralesional side.

The serious game has been developed using Unity and HTC Vive Pro. Fig. 32.2 depicts the software architecture of the solution.

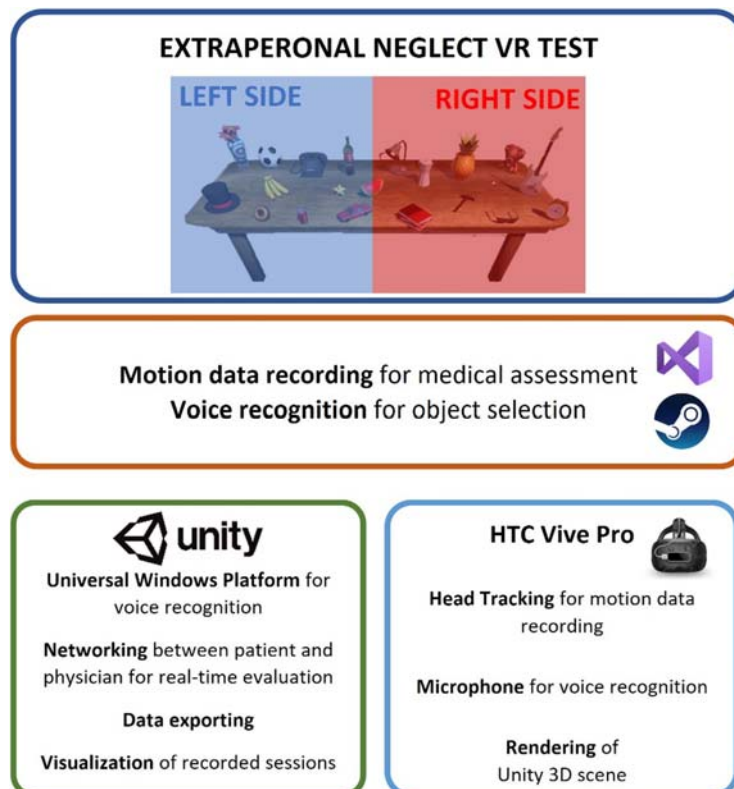


**FIGURE 32.2**

Software architecture for the extra-personal neglect serious game.

To ensure real-time monitoring of the test, the 3D scene is shared by the patient and the therapist. The serious game makes available an online gaming software interface, which allows the sharing of the 3D scene between two users over a Wi-Fi connection. The connection guarantees the data exchange between the doctor's laptop and the VR system used by the patient on another laptop ([Fig. 32.3](#)). The use of two systems allows carrying out the test in a comfortable way; the patient executes the test alone with no influence of external factors while the doctor can observe what is happening in the 3D environment. All data are sent from the client (i.e., patient's VR system) to the server (i.e., doctor's laptop) to save all information exclusively available for medical personnel. The patient can see a red dot on any 3D objects according to their head orientation, while the physician can see the patient's field of view.

HTC Vive includes a set of sensors to track head movements during the recognition of objects placed on the table. Furthermore, HTC Vive offers a microphone, which has been used for voice recognition. The implementation of the voice recognition feature is based on Unity's "Universal Windows Platform." Using this software module, a dictionary has been defined which composes the names of 3D objects used by Unity as voice commands to interact with a 3D virtual scene. In the 3D scene, when the patient says the correct name of an observed object, the recognized object disappears in the 3D scene seen by the physician.

All the recorded data are saved in two files. The first one contains the kinematic data related to the head's orientation along the recognition of any virtual objects on the table. A specific software module exploits the recorded data to replay tracked movements for future evaluation and monitoring. The second file is a report that contains a plotted graph of the head rotations and the time needed to locate each 3D object on the table.

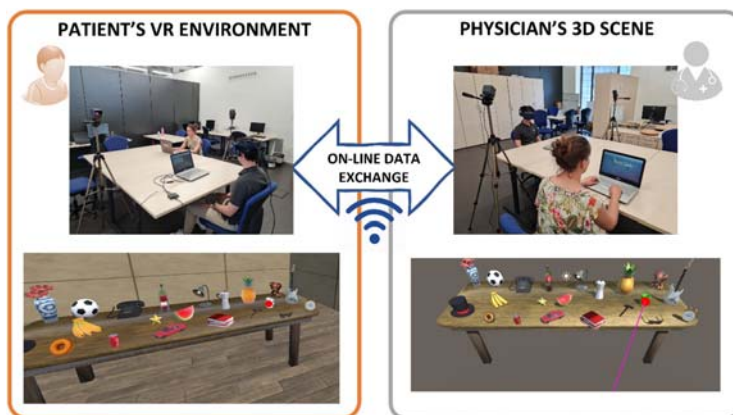


**FIGURE 32.3**

Use of the VR platform to perform the test.

### VR platform for the recovery of severe memory loss

Retrograde amnesia prevents a person from remembering events or information acquired before the stroke. For this kind of memory loss, the patient has complete lucidity for everything that happens after the brain trauma and has no difficulty memorizing new information (Ferguson et al., 2019; Parsons & Barnett, 2017).

The aim here is the introduction of VR technologies to increase the level of ecological validity of memory rehabilitation (Vitali et al., 2021). Initially, a set of guidelines has been defined in collaboration with a medical team composed by neuropsychologists and physiotherapists to get a clear overview of the medical needs during the rehabilitation process at the hospital and at home.

Nowadays, the recovery of serious memory loss begins from regaining awareness of familiar environments where patients live after the stroke, such as the hospital room during the early rehabilitation period or their home after hospital discharge. Physiotherapists use pictures of familiar environments which are shown to the patient to teach them awareness of their environment. Even if the approach is easily adopted by physiotherapists, the limited visual perception given by a single point of view does not allow memorizing of important details. Therefore, when the patient returns home, they do not recognize all areas and may be disoriented when attempting to find objects (e.g., the patient does not know which is the cutlery drawer) and thus, the traditional approach has a low ecological validity.

As proposed by medical staff, the exploration of a virtual environment stimulates a patient's interest, and therefore interactive task levels specifically designed for memory recovery have been added to the VR solutions.

The first task level "Explore" has been designed for patients with difficulties remembering their home environment. It allows the recovery of a patient's orientation and the possibility of practicing the serious game.

The second task level is called "Object by Object" It provides the possibility to put objects from an ordered list in their correct places inside a room. In this case, the user has to identify the name of the object, that is suggested by a user interface. To understand which object is to be searched for, further textual information is shown.

The last task level is the "Treasure Hunt" which is the most difficult. The user interface shows a text, which asks to search for an object in the virtual room and the patient must remember where the object is placed with no further helps. In this task, the sequence of objects is random.

The proposed tasks aim at training the memory so that when the patient is discharged from the rehabilitation facilities, they will be familiar with their home environment and know the location of everyday objects without external help.

The parameter considered to evaluate a patient's improvements and therapy outcome is the time to find each object in the 3D home environment.

To increase the ecological validity, VR devices and a 3D scanner are used. The identification of appropriate technologies is subdivided in three main steps (Fig. 32.4):

- Definition of the procedure for 3D acquisition of one or multiple rooms of a patient's house (Fig. 32.4A).

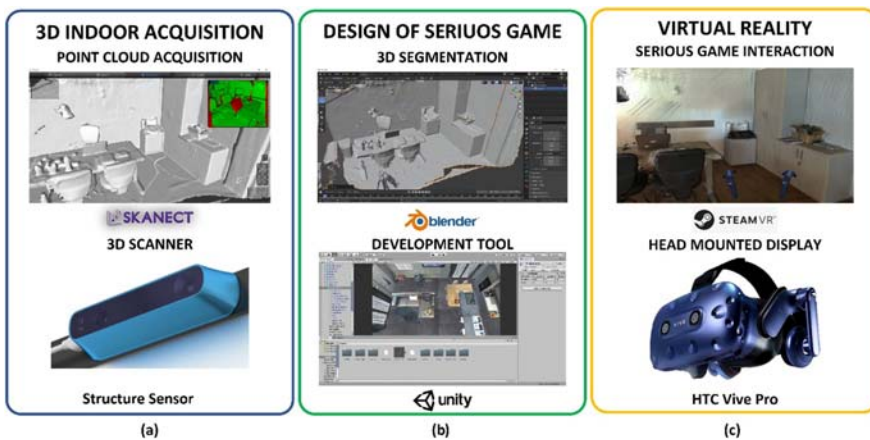


**FIGURE 32.4**

Identification of the technologies exploited to design the VR solution for the rehabilitation of strong memory loss.

- Development of a serious game with tasks to help the recovery of lost memory by means of a game-logic easily adaptable to each new 3D environment (Fig. 32.4B).
- Use of the serious game by means of a laptop or using an HMD to navigate in a more natural and intuitive way (Fig. 32.4C).

### ***3D scanning acquisition***

The acquisition of a 3D indoor environment allows for the generation of the 3D environment to be explored during the task for memory recovery. The scanning system is composed of a structure sensor and the commercial application Skanect. The structure sensor has been chosen due to the low-cost and ease of use. The sensor acquired polygonal mesh is modeled in order to segment the point cloud into a set of 3D models representing the objects of the virtual scene (e.g., table, kitchen sink, chairs, sofa) which the user can interact with. Each 3D object must have a detailed shape and colors to be easily recognized by the patient.

After the room acquisition, a set of 3D modeling operations is required to create the virtual objects ready to be used in the serious game:

- Replace walls and floor with flat surfaces in such a way as to reduce the size of the polygonal models. The flat surface has the same color as the real one.
- Replace standard objects, such as chairs and tables, with predefined 3D models.
- Increase the perceived quality of the virtual environment; for example, check the mesh for errors and fill out visible holes.
- Generate the final 3D model of the environment by assembling all the cleaned 3D models.

Blender is used to perform the operations previously described. The result of this step is the 3D model of a room ready to be used for the design of the interactive environment.

### ***Development of the serious game***

Unity is used to design and develop the serious game. The development requires two main steps: (i) the design of an interactive style and (ii) the implementation of the game-logic following medical guidelines for memory recovery.

The design of an interactive style consists of making the objects of a virtual room responsive to user interaction. For example, when a user clicks the mouse on a drawer, the drawer opens as in the real world. The interactive access to containers then allows placing simple 3D objects which the patient can search according to the memory tasks previously described.

The logic for memory-related issues is essentially the same for all patients with brain injury. Therefore, the game-logic is designed to be easily reused by only changing the 3D environment specifically acquired for the patient. Fig. 32.5 describes the Unity script component of the game logic for the “Treasure Hunt” task. The treasure hunt requires a list of the objects. Given the list of 3D objects, the script automatically creates the randomized sequence which the patient must follow to correctly complete the treasure hunt. The developer can use the same logic to develop a serious game for a new patient by only changing the 3D interactive scene. The serious games can be used either with a traditional approach based on monitor, mouse, and keyboard or using the HTC Vive Pro device.

Finally, the software module for data management allows reporting in both Adobe PDF and Microsoft Excel file format. The report contains the time taken to find each object.

### ***Motor-skills tele-rehabilitation of hands***

This use-case presents a web platform for motor skills rehabilitation of the hands. According to physicians’ prescription, the web platform is based on a serious game which allows a patient to interact with a task by moving the hands in order to improve finger control. The main aim is to perform small movements, such as pinch, grasp, and touch with fingertips. The serious game must be used at home and thus, consumer technologies and a low-cost hand-tracking device have



**FIGURE 32.5**

The Unity component of the game-logic for the treasure hunt task: four fruits must be found.

been proposed (Kim et al., 2010, 2020; Glegg & Levac, 2018; Pedroli et al., 2020; Rybarczyk et al., 2019; Leap Motion, 2022; Aguilera-Rubio et al., 2022; Borrego et al., 2018; Skanect, 2022; Lanzoni et al., 2020; Cipresso et al., 2018; Bowen et al., 2013; Azouvi, 2017; Ferguson et al., 2019; Parsons & Barnett, 2017; Vitali et al., 2021; Medina et al., 2019).

Post-stroke patients with hand motor-skills impairment may not be able to complete a pinch grip as fingertips don't touch. This condition prevents the grasping of small or thin objects, affecting everyday life quality. Therefore, the solution must be able to automatically recognize a partial gesture to evaluate the improvements during any consecutive sessions. In particular, the physiotherapist has the possibility to set a parameter to also classify partial gestures as acceptable. The more the patient improves, the more the value of the parameter is decreased to reach the performance of a complete gesture.

For example, the patient can grasp objects, such as a bottle or a cup, for which the pinch movement is intrinsically limited. A pinch movement can be detected and recognized even when incomplete to avoid a patient's disappointment. The game measures the distance between the tips of the forefinger and thumb to provide the doctors with an indicator of how the patient is performing in the rehabilitation session. The interaction with the game can be modified according to the patient's skill level.

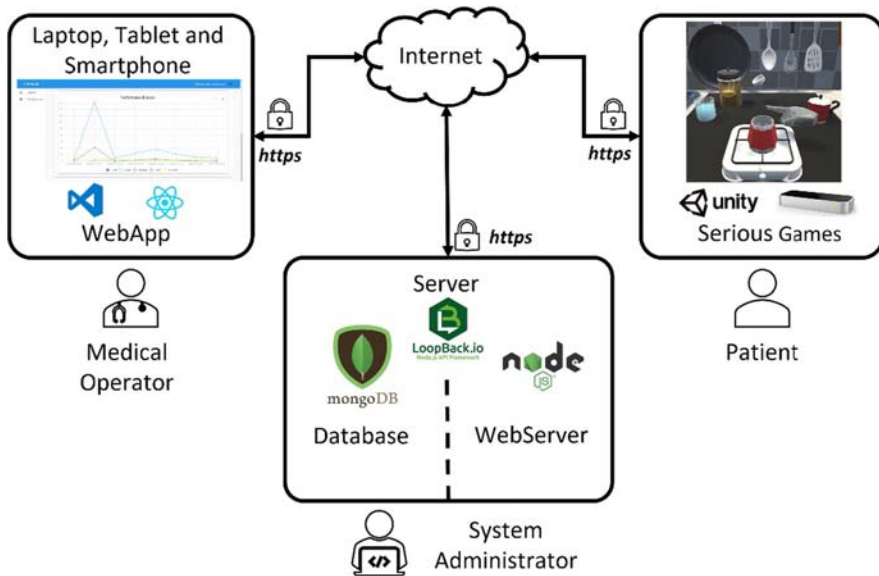
In addition, the game keeps records of partial and total times of any task or game performed.

All the described information must be easily readable: each session of interaction must be recorded, and the application must replay the patient performance and show the measured parameters and the graphs of all the relevant quantities. The medical staff must define a setting plan for the parameters relative to the measurements of the partial gestures for each patient. The parameter must be sent to the serious game, which automatically sets the interaction style of the patient.

[Fig. 32.6](#) depicts the software architecture of the web platform. The serious games have been developed with Unity and the hand tracking interaction style is based on the Leap motion device. The application for the medical personnel is a web tool available on laptops, smartphones, and tablets. The website has been developed using React ([React, 2022](#)). The back-end of the web platform is based on the web-server Node.js ([Node.js, 2022](#)). The data are stored on a MongoDB ([MongoDB, 2022](#)) database and the REST APIs have been developed using Loopback 4 ([Loopback 4, 2022](#)). The use of the HTTPS protocol guarantees the data cybersecurity.

This serious game concerns the coffee preparation with a Moka pot, and the interaction style allows the evaluation of two types of gestures: touching with the fingertip or grasping objects with a pinch action. The final goal is reached when a patient correctly picks the sequence of objects from their initial position and places them on the stove according to the following instructions:

1. Place the lower part of the Moka pot on the stove;
2. Fill the lower part with water;

**FIGURE 32.6**

The software architecture of the web platform.

3. Place the filter;
4. Fill the filter with ground coffee;
5. Position the upper part of the Moka pot.

During the interaction, all the movements of the hand and the time spent are recorded and sent to the server to be shown in the web application of the medical personnel.

The web application is composed of two main user interfaces. Fig. 32.7 presents the user interface for setting the parameters for gesture evaluation. In particular, physicians can set if the patient will interact with the fingertips or with a pinch action, in which case the physician can choose the minimum distance between thumb and index finger to consider if the gesture is correctly performed.

Finally, a physician can define the maximum time to perform the whole task. A second user interface reports the data recorded during each rehabilitation session. The web page includes a 3D viewer with which the physician can review a 3D virtual skeleton of the hand during the execution of each task. A set of graphs show the trend of the parameters to assess motor skills' recovery. Finally, a medical report can be exported and downloaded in Adobe PDF or Microsoft Excel file formats.

## Evaluation

The described applications have been experimented involving physicians and physiotherapists. Healthy testers have been enrolled to test the applications since the

**Game settings**

<b>Configuration Name</b>	<b>Max. Score</b>
<input type="text" value="Configuration #1"/>	<input type="text" value="20"/>
<b>Lifes</b>	<b>Level of Difficulty</b>
<input type="text" value="5"/>	<input type="text" value="3"/>
<b>Distance Thumb-Index [mm]</b>	
<input type="text" value="15"/>	
<b>Hand Interaction Style</b>	
<input checked="" type="checkbox"/> Thumb <input checked="" type="checkbox"/> Index <input type="checkbox"/> Middle <input type="checkbox"/> Ring <input type="checkbox"/> Pinky <input checked="" type="checkbox"/> Palm	
<a href="#" style="color: blue;">BACK</a> <a href="#" style="color: blue;">SAVE</a>	

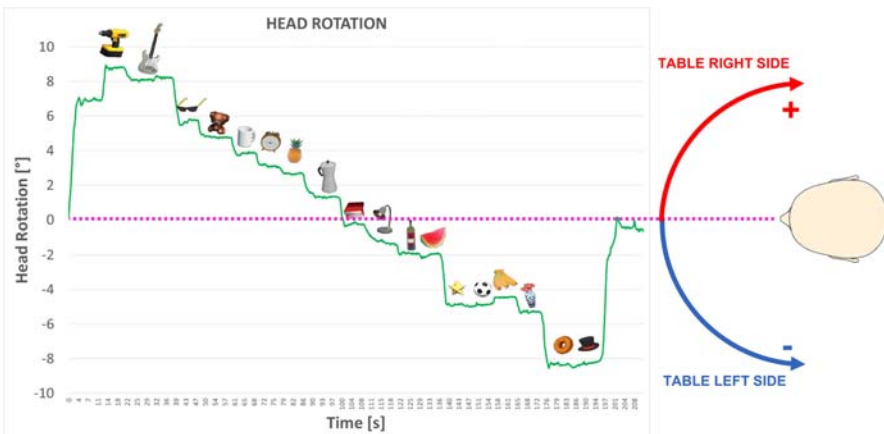
**FIGURE 32.7**

The web page for the game settings available for the physicians.

involvement of patients requires the approval of the hospital's ethical committee, which at the time of writing is still pending due to COVID-19 pandemic restrictions.

The VR test for extra-personal neglect has been evaluated through presentation to medical staff. In the first instance, a list of technical instructions to set up the VR devices were shown to the staff. Then, doctors executed the procedure and started to use the platform until a good level of confidence was reached.

Physicians and physiotherapists evaluated the solution as very simple to assemble and found no specific technological features that slowed down its use. The involved physicians were able to generate a report of the VR application as shown in Fig. 32.8, depicting a graph of head rotations required to see each 3D

**FIGURE 32.8**

Head rotations and time to recognize each 3d object.

object in the center of the patient's field of view and the time needed to evaluate and recognize each one of them. The data reported have been considered to be extremely useful for the fast evaluation of a patient's condition.

The replay mode is another function that has been tested. This function replicates rehabilitation sessions and we checked if the serious game may thus be used to monitor patient improvement. In particular, the replay mode has been considered very useful by medical staff to review a patient's last performance before every new medical examination. Medical staff evaluated the VR platform in its prototype stage.

The VR platform for severe memory loss has been evaluated with a focus on the ecological validity of rehabilitation tasks. Three familiar environments were acquired (Fig. 32.9): a hospital room, a kitchen, and a living room.

The virtual model of the hospital room has been generated from three acquisitions focused on the left and the right corners of the room and on the bed. Four 3D objects were chosen for each level of the game logic: a cup, a tea bag, a bottle of water, and a teapot. The kitchen required five acquisitions, one for each side of the room and one for the entrance. A 3D segmentation was performed in Blender to subdivide the interactive doors of all the cabinets. Table and chairs were replaced with predefined 3D objects since they were part of the standard models. The cooker and the armchair were acquired separately. Finally, the living room required six acquisitions. For both the kitchen and the living room, the sequence includes six 3D objects, which are an egg, a knife, a soup tureen, a glass, a salt-shaker, and a dish.

For all 3D environments, the most time-consuming task was the 3D modeling phase, which is not correlated to the size of a room. Indeed, the hospital room and the kitchen required similar time for 3D modeling. The Unity script of the customizable game-logic allowed the generation of the serious game in less than one hour for the three rooms; however, the 3D acquisition required an engineer with good skills in 3D scanning and modeling to work 3 h generating the data. Medical staff appreciated the high similarity of the virtual rooms with the real ones as well as the potential to improve the ecological validity of the rehabilitation process.

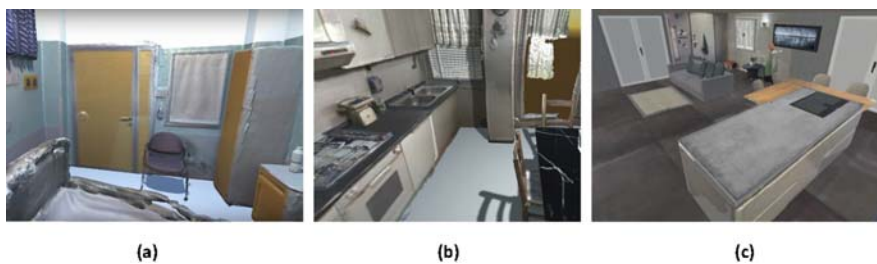


**FIGURE 32.9**

The 3D acquisition of a hospital room (A), a kitchen (B) and a living room (C).

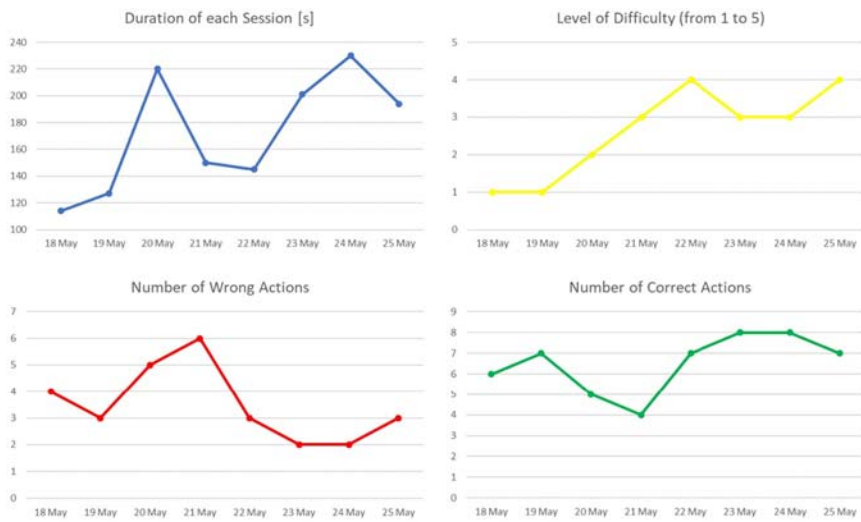


**FIGURE 32.10**

Parameters measured during rehabilitation sessions.

The evaluation of the web platform for motor-skills rehabilitation tested only technological aspects and relevant measured parameters with the involved medical staff. A physician was asked to trial the web application with two healthy subjects to simulate patients using the Leap motion device connected to their own laptop at home. The subjects interacted with the serious game by applying the forefinger tip and pinch grip actions. It was tested if several sessions of 3 minutes or less of recorded motion data were correctly uploaded to the server, together with the other parameters necessary to evaluate patient performance (Fig. 32.10). Every three sessions, the physician changed the parameters settings to modify either the interaction style or the level of difficulty to test data transmission. The data exchange worked as expected, guaranteeing the cybersecurity protocol. The VR-based tele-rehabilitation platform is now ready for testing with patients.

## Conclusion

This chapter presents a virtual reality platform–based method for the rehabilitation of post-stroke patients with the aim of improving the ecological validity of traditional rehabilitation exercises. Three different applications are implemented. Each VR solution has been developed in collaboration with medical experts to improve the quality of the rehabilitation process, such as informing a more objective assessment of rehabilitation outcomes. VR devices track movements to automatically generate parameters required for medical assessment. High fidelity virtual reality 3D scenes are generated from 3D scans.

For all applications, resulting evaluations of the method were considered to be satisfactory by the involved medical experts, providing sufficient justification for the development of new VR tasks to be applied in post-stroke rehabilitation.

---

## Acknowledgments

The authors would like to thank the physicians and physiotherapists of the Italian hospitals Papa Giovanni XXIII and Clinica Quarenghi, who supported the development of the described virtualized methods. A warm thank you goes to the engineering students who participated in the refinement and testing of the solutions.

---

## References

- Aguilera-Rubio, Á., Alguacil-Diego, I. M., Mallo-López, A., & Cuesta-Gómez, A. (2022). Use of the leap motion controller® system in the rehabilitation of the upper limb in stroke. A systematic review. *Journal of Stroke and Cerebrovascular Diseases*, 31, 106174. <https://doi.org/10.1016/J.JSTROKECEREBROVASDIS.2021.106174>
- Azouvi, P. (2017). The ecological assessment of unilateral neglect. *Annals of Physical and Rehabilitation Medicine*, 60(3), 186–190.
- Baheux, K., Yoshizawa, M., Seki, K., & Handa, Y. (2006). Virtual reality pencil and paper tests for neglect: A protocol. *CyberPsychology & Behavior*, 9(2), 192–195.
- Blender. <https://www.blender.org/>. Last accessed May 2022.
- Borrego, A., Latorre, J., Alcañiz, M., & Llorens, R. (2018). Comparison of Oculus Rift and HTC vive: Feasibility for virtual reality-based exploration, navigation, exergaming, and rehabilitation. *Games for Health Journal*, 7, 151–156. <https://doi.org/10.1089/G4H.2017.0114>
- Bowen, A., Hazelton, C., Pollock, A., & Lincoln, N. B. (2013). Cognitive rehabilitation for spatial neglect following stroke. *Cochrane Database of Systematic Reviews*, 2013(7).
- Cameirão, M. S., Faria, A. L., Paulino, T., Alves, J., & i Badia, S. B. (2016). The impact of positive, negative and neutral stimuli in a virtual reality cognitive-motor rehabilitation task: A pilot study with stroke patients. *Journal of Neuroengineering and Rehabilitation*, 13(1), 1–15.
- Cipresso, P., Pedroli, E., Serino, S., Semonella, M., Tuena, C., Colombo, D., ... Riva, G. (2018). Assessment of Unilateral Spatial Neglect using a free mobile application for Italian clinicians. *Frontiers in Psychology*, 9, 2241.
- Dawson, D. R., & Marcotte, T. D. (2017). Special issue on ecological validity and cognitive assessment. *Neuropsychological Rehabilitation*, 27, 599–602.
- Ferguson, M. A., Lim, C., Cooke, D., Darby, R. R., Wu, O., Rost, N. S., Corbetta, M., Grafman, J., & Fox, M. D. (2019). A human memory circuit derived from brain lesions causing amnesia. *Nature Communications*, 10(1), 1–9. <https://doi.org/10.1038/s41467-019-11353-z>
- Gamito, P., Oliveira, J., Coelho, C., Morais, D., Lopes, P., Pacheco, J., ... Barata, A. F. (2017). Cognitive training on stroke patients via virtual reality-based serious games. *Disability and Rehabilitation*, 39(4), 385–388.

- Glegg, S. M. N., & Levac, D. E. (2018). Barriers, facilitators and interventions to support virtual reality implementation in rehabilitation: A scoping review. *PM&R, 10*(11), 1237–1251.
- Halligan, P. W., & Marshall, J. C. (1989). Two techniques for the assessment of line bisection in visuo-spatial neglect: A single case study. *Journal of Neurology, Neurosurgery & Psychiatry, 52*, 1300–1302.
- Kang, Y. J., Ku, J., Han, K., Kim, S. I., Yu, T. W., Lee, J. H., & Park, C. I. (2008). Development and clinical trial of virtual reality-based cognitive assessment in people with stroke: Preliminary study. *CyberPsychology & Behavior, 11*(3), 329–339.
- Kim, W.-S., Cho, S., Ku, J., Kim, Y., Lee, K., Hwang, H.-J., & Paik, N.-J. (2020). Clinical application of virtual reality for upper limb motor rehabilitation in stroke: Review of technologies and clinical evidence. *Journal of Clinical Medicine, 9*(10), 3369. <https://doi.org/10.3390/jcm9103369>
- Kim, D. Y., Ku, J., Chang, W. H., Park, T. H., Lim, J. Y., Han, K., Kim, I. Y., & Kim, S. I. (2010). Assessment of post-stroke extrapersonal neglect using a three-dimensional immersive virtual street crossing program. *Acta Neurologica Scandinavica, 121*(3), 171–177.
- Lanzoni, D., Vitali, A., Regazzoni, D., & Rizzi, C. (August 2020). Medical assessment test of extrapersonal neglect using virtual reality: A preliminary study. In *International design engineering technical conferences and computers and information in engineering conference* (Vol. 83983). American Society of Mechanical Engineers, p. V009T09A064.
- Leap Motion. <https://www.ultraleap.com/>. Last accessed May 2022.
- Loopback 4. <https://loopback.io/index.html>. Last accessed May 2022.
- Medina, J. L. P., González, M., Pilco, H. M., Vargas, K. B. J., Acosta-Vargas, P., Sanchez-Gordon, S., ... Rybaczuk, Y. (2019). Usability study of a web-based platform for home motor rehabilitation. *IEEE Access, 7*, 7932–7947.
- MongoDB. <https://www.mongodb.com/>. Last accessed May 2022.
- Writing Group Members, Mozaffarian, D., Benjamin, E. J., et al. (2016). Executive summary: Heart disease and stroke statistics—2016 update: A report from the American heart Association. *Circulation, 133*(4), 447–454. <https://doi.org/10.1161/CIR.000000000000366>
- Nir-Hadad, S. Y., Weiss, P. L., Waizman, A., Schwartz, N., & Kizony, R. (2017). A virtual shopping task for the assessment of executive functions: Validity for people with stroke. *Neuropsychological Rehabilitation, 27*(5), 808–833.
- Node.js. <https://nodejs.org/it/>. Last accessed May 2022.
- Nolin, P., Besnard, J., Allain, P., & Banville, F. (2019). Assessment and rehabilitation using virtual reality after stroke: A literature review. *Virtual reality for psychological and neurocognitive interventions* (pp. 307–326).
- Parsons, T. D., & Barnett, M. (2017). Validity of a newly developed measure of memory: Feasibility study of the virtual environment grocery store. *Journal of Alzheimer's Disease, 59*(4), 1227–1235. <https://doi.org/10.3233/JAD-170295>
- Pedroli, E., Cipresso, P., Greci, L., Arlati, S., Mahroo, A., Mancuso, V., ... Gaggioli, A. (2020). A new application for the motor rehabilitation at home: Structure and usability of Bal-App. *IEEE Transactions on Emerging Topics in Computing, 9*, 1290–1300.
- Pizzamiglio, L., Judica, A., Razzano, C., & Zoccolotti, P. (1989). Toward a comprehensive diagnosis of visual-spatial disorders in unilateral brain damaged patients. *Evaluación Psicológica.*

- Rand, D., Weiss, P. L. T., & Katz, N. (2009). Training multitasking in a virtual supermarket: A novel intervention after stroke. *American Journal of Occupational Therapy*, 63(5), 535–542.
- React. <https://reactjs.org/>. Last accessed May 2022.
- Writing Group Members, Roger, V. L., Go, A. S., Lloyd-Jones, D. M., Adams, R. J., Berry, J. D., ... Turner, M. B. (2011). Executive summary: Heart disease and stroke statistics—2011 update: A report from the American Heart Association. *Circulation*, 123(4), 459–463.
- Rybarczyk, Y., Pérez Medina, J. L., Leconte, L., Jimenes, K., González, M., & Esparza, D. (2019). Implementation and assessment of an intelligent motor tele-rehabilitation platform. *Electronics*, 8(1), 58. <https://doi.org/10.3390/electronics8010058>
- Skanect. <https://skanect.occipital.com/>. Last accessed May 2022.
- Smith, S. A. (2019). Virtual reality in episodic memory research: A review. *Psychonomic Bulletin & Review*, 26(4), 1213–1237.
- Unity. <https://unity.com/>. Last accessed May 2022.
- Vitali, A., Regazzoni, D., Rizzi, C., & Spajani, A. (2021). VR serious games for neurocognitive rehabilitation of patients with severe memory loss. *Computer-Aided Design and Applications*, 18, 1233–1246.

# Personalization for surgical implants

# 33

**Naomi C. Paxton<sup>1</sup>, Kevin Tetsworth<sup>2</sup>, Maria A. Woodruff<sup>1</sup>**

<sup>1</sup>*Centre for Biomedical Technologies, Queensland University of Technology (QUT), Brisbane, QLD, Australia;* <sup>2</sup>*Department of Orthopaedic Surgery, Royal Brisbane & Women's Hospital, Herston, QLD, Australia*

## Chapter outline

<b>Introduction to personalization of surgical implants .....</b>	849
<b>Personalized medical device definitions.....</b>	851
<b>Adoption of personalization in surgery .....</b>	853
Orthopedic surgery .....	853
Craniomaxillofacial surgery.....	855
Spinal surgery .....	857
Vascular surgery .....	858
Urology surgery .....	860
<b>Regulation.....</b>	861
<b>Summary and future perspectives .....</b>	863
<b>References .....</b>	866

## Introduction to personalization of surgical implants

Personalization in surgical implant manufacturing is being leveraged by the adoption of digital human modeling (DHM) in routine clinical practice. With the development and translation of advanced software for rapid segmentation and 3D model generation using patient scan data, a new era in personalized medical device manufacturing is being realized in hospitals and healthcare settings globally (Fig. 33.1). This movement in medical device manufacturing is contributing to the substantial growth of the personalized medicine market, projected to be worth \$3.1 billion USD by 2025 (Grand View Research, 2019).

Computer-aided design (CAD) and manufacturing (CAM) are playing a crucial role in this new era of medical device manufacturing, bridging the divide between patient anatomy and medical device design specification to produce customized implants which more closely match patient anatomy (Paxton et al., 2016). CAD software, developed in the 1960s, was initially used for designing parts and tools for the automotive, aircraft, and industrial control industries (Hirz et al., 2017). CAD software has continued to increase in complexity and capability through the release of

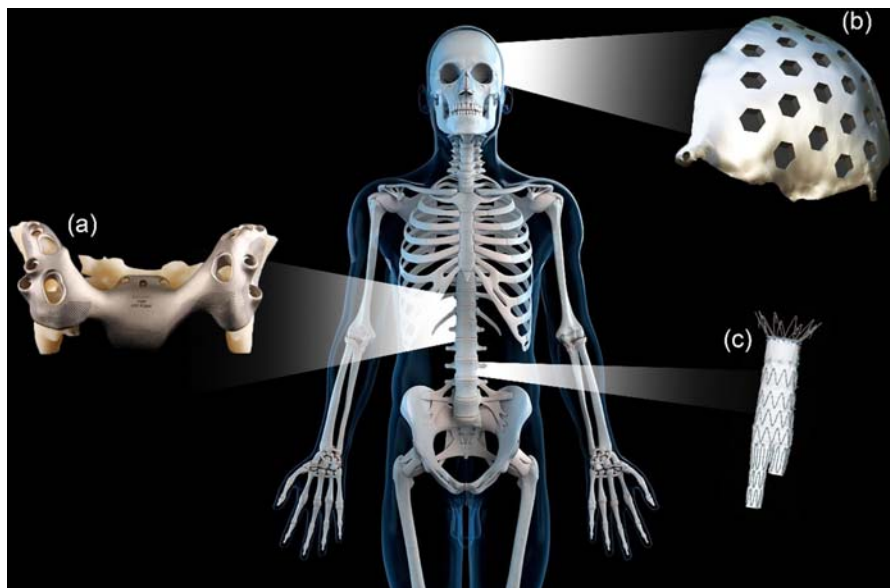


**FIGURE 33.1 Examples of personalized surgical implants**

(A) A patient-matched custom sacrum implant manufactured by 3D Systems Healthcare, (B) a titanium cranial implant, and (C) an endovascular bifurcated graft produced by Cook Medical.

*Figures reproduced with permission from (A) 3D Systems, USA (2021) <https://www.3dsystems.com/customer-stories/spine-solutions-expert-k2m-broadens-capabilities-strategic-3d-printing-partner>, (B) Dr. Vjekoslav Kopacić, University Hospital Osijek & Faculty of Medicine Osijek, Croatia, and (C) Courtesy of Cook Medical (2022) [https://www.cookmedical.com/products/ndo\\_aaamain\\_webds/](https://www.cookmedical.com/products/ndo_aaamain_webds/).*

industry-standard programs in the 1990s such as SolidWorks (Dassault Systèmes), AutoCAD (Autodesk), and CATIA (Dassault Systèmes) which are widely used today. However, these programs favor mechanical vector-based drawings and are not optimized for manipulating organic designs, such as anatomical models derived directly from patient scan data (Bibb et al., 2015). In parallel, imaging techniques have rapidly evolved to allow 3D model generation from stacked 2D slice images, such as those acquired from computed tomography (CT) or magnetic resonance imagining (MRI) modalities (Paxton et al., 2022). Only recently have specialized software packages been developed which can translate patient scan data into 3D models, with optimized functions for medical device design and to satisfy regulatory approval, such as Mimics Innovation Suite (Materialise, Leuven, Belgium) (Materialise, 2018).

With the implementation of DHM in the medical device design and manufacturing pathway, virtual surgical planning can be undertaken using the same digital data to plan surgical approaches and reduce the number of in-theatre decisions being made, increasing patient safety and reducing surgical time and costs

(Xia et al., 2006). While the potential benefits of this personalized DHM-based approach to surgical implant manufacturing are considerable, the adoption and uptake of personalization in medical devices in a range of surgical contexts is varied, where surgical implant markets must balance clinical need with commercial feasibility and regulatory burden. This chapter will initially discuss definitions for categories of personalized medical devices depending on their degree of customization, and provide examples of surgical implants in cardiovascular, orthopedic, craniomaxillofacial, and spinal surgery. Finally, this chapter will summarize current research and regulatory implications for the translation of novel personalized surgical implants.

---

## Personalized medical device definitions

With the growing demand and availability of medical devices designed, manufactured, or altered for individuals, terminology was inconsistently used among regulation authorities in various jurisdictions when trying to capture the novelty of medical devices manufactured for individual patients with varying degrees of customization (Horst et al., 2019). In the context of surgical implants, a variety of terms have been historically used in the literature for describing devices designed specifically based on the anatomical features or pathology of an individual patient which are typically manufactured in single units. Previously, no harmonized definition existed to differentiate between implants manufactured in single units, designed specifically to match the anatomical features of a patient, compared to those modified, adjusted, or shaped from existing batch-manufactured implants produced in standardized “off-the-shelf” shapes or sizes.

In orthopedic research, “patient-specific” or “customized” surgical implants have been reported as early as 2008 (Parthasarathy et al., 2008), primarily with the advent and adoption of titanium additive manufacturing to produce personalized joint replacement components and bone fixation devices (Du et al., 2020). In cardiovascular surgery, “custom-made” is the preferred term for vascular grafts and stents made to suit specific patient anatomy (Fernandez et al., 2016), which have been available from medical device companies such as Cook Medical, who pioneered the translation of personalized stents over 30 years ago (Hao & Harris, 2008). Most commonly, stents are customized in diameter, length, and branching to suit individual anatomy for endovascular aneurysm repair.

A global initiative was therefore launched to harmonize the lexicon surrounding medical devices manufactured for individuals. The International Medical Device Regulators Forum (IMDRF) launched an international working group to provide guidance and seek consultation from the international community to agree on definitions for terms such as “personalised,” “custom-made,” and “patient-specific,” which had previously been inconsistently adopted by regulation authorities. In 2018, the “Definitions for Personalised Medical Devices” was released, defining

several key terms summarized in Table 33.1 ([International Medical Device Regulators Forum, 2018](#)).

These definitions critically distinguish between devices which are produced in single units for a specific patient (custom-made) (e.g., [Aranda et al., 2015](#);

**Table 33.1** Definitions for personalized medical devices.

*Definitions for personalized medical devices, from the international medical device regulators forum (IMDRF) (2018).*

Term	Definition	Examples
<b>Personalized medical device</b>	A generic term to describe any of the types of medical devices that are intended for a particular individual, which could be either a <b>custom-made</b> , <b>patient-matched</b> , or <b>adaptable</b> medical device.	See below.
<b>Custom-made medical device</b>	A medical device that, at a minimum, meets the following requirements: it is intended for the sole use of a particular individual; and it is specifically made in accordance with a written request of an authorized healthcare professional, which gives, under their responsibility, specific design characteristics; and it is intended to address the specific anatomo-physiological features or pathological condition of the individual for whom it is intended.	<a href="#">Aranda et al. (2015)</a> , <a href="#">Anatomics Pty Ltd (2020)</a>
<b>Patient-specific or Patient-matched medical device</b>	A medical device produced by a manufacturer based on a standard device template model, or specified design envelope (e.g., minimum and maximum dimensions, mechanical performance limits, and other clinically relevant factors), that is matched to a patient's anatomy using techniques such as scaling of the device based on anatomic references, or by using the full anatomic features from patient imaging, and which is produced through a process that is capable of being validated.	<a href="#">Cook Medical (2021)</a> , <a href="#">Nunley et al. (2012)</a>
<b>Adaptable medical device</b>	A mass-produced medical device that must be adapted or assembled at the point of care, in accordance with the manufacturer's validated instructions, to suit an individual patient's specific anatomo-physiologic features prior to use.	<a href="#">Stryker (2017)</a>

(Anatomics Pty Ltd, 2020), compared to those produced in batches or mass manufactured with personalized design elements incorporated prior to manufacturing within a specific design envelope (patient-specific or patient-matched) (e.g., Cook Medical, 2021; Nunley et al., 2012), or following manufacturing and adjusted by a healthcare professional at the point of care (adaptable) (e.g., Stryker, 2017) which is readily undertaken by surgeons at their discretion (International Medical Device Regulators Forum, 2018). This also informs the designation of design and manufacturing responsibility, which is a critical consideration for medical device regulation, as discussed in detail below. The following section discusses the range of surgical implants commonly used in several surgical disciplines to examine the growing role of personalization, and how custom-made and patient-matched implants are being adopted for a range of treatments compared to standardized, “off-the-shelf,” or adaptable surgical implants.

---

## Adoption of personalization in surgery

### Orthopedic surgery

Orthopedic surgery has been a pioneering surgical discipline in the adoption of custom-made implants in clinical practice. Custom acetabular components for complex revision hip arthroplasty have been available for the past 25 years, but are now used much more frequently. This previously involved a design team that worked remotely from the surgeon, and was therefore generally only undertaken on a limited basis. However, recently some surgeons have taken the initiative to design their own patient-specific implants for these complex, demanding cases, and the resulting implants have now become more readily available (Schwartz et al., 2015; Tetsworth & Mettyas, 2016). Leveraging novel metal 3D printing technology, custom-made surgical implants can be rapidly designed from patient scan data, typically CT or MRI data, and used as a blueprint for the design of personalized plates, rods, joint replacements, screw guides, and bone fixation devices (Green et al., 2016). These devices have demonstrated wide-reaching impact in reducing surgical time and cost and improving patient outcomes through shorter recovery and lower risk of implant failure or other complications requiring further revision surgery (Culler et al., 2017; Dall'Ava et al., 2019; O'Connor & Blau, 2019).

In general, surgeons have a range of off-the-shelf implants at their disposal, many of which can be adapted and modified at the point of care and are suitable for most routine cases (e.g., Zimmer Biomet products). Titanium and polyether ether ketone (PEEK) are typically favored for their biocompatibility, mechanical strength, and durability (Haleem & Javaid, 2019). These materials can also be processed via advanced 3D printing technologies, such as electron beam melting (EBM) and selective laser melting (SLM) to layer-by-layer melt powered metals and polymers into complex and personalized 3D implants (Shahali et al., 2017). Off-the-shelf products remain predominantly suitable for routine total hip and knee arthroplasty where

standard sizes of implants are suitable for most patients (Ejnisman et al., 2021). However, complex reconstruction cases, for example from failed arthroplasties or tumor resections, often involve complex tissue architecture and unique defects for which off-the-shelf implants are unsuitable and more complex DHM is required (Durand-Hill et al., 2020; Fröschen et al., 2020; Stryker, USA, 2018; Yao et al., 2021). Case studies have reported the successful design, manufacture, and clinical use of custom-made titanium implants, including a talus (Hussain, 2021), calcaneus (Imanishi & Choong, 2015), sternum (Aranda et al., 2015), and fixation plates (Chen, 2018; Harith et al., 2016).

Given the prevalence and widespread clinical need for these custom-made and patient-matched implants, companies now offer services for designing and manufacturing personalized implants, such as joint replacement implants. For example, Conformis, a US-based medical device company, provides a service for surgeons to order patient-matched knee and hip replacement implants based on scan data (Steinert et al., 2017). Interestingly, while Conformis initially exclusively offered “patient-specific” implant manufacturing, the company is now offering off-the-shelf implants in standard sizes to complement their personalized manufacturing service, as a more cost effective and timely option (Conformis, 2021). Other examples include bespoke medical implant manufacturers such as 3D Systems (USA) and Peter Brehm GmbH (Germany), which offer manufacturing of custom-made implants with conformity to medical manufacturing standards including ISO 13485 (Fröschen et al., 2020; Stryker, 2021a). Other manufacturers such as Smith & Nephew (UK) and Stryker (USA) have also transitioned to the use of 3D printing to manufacture titanium acetabular cup implants for hip replacements (Fig. 33.2), however these products are yet to leverage the capability of patient-matched or custom-made manufacturing using 3D printing and are only available in standardized sizes (Sorokina, 2018).

Customized manufacturing using 3D printers has also dramatically expanded the potential reconstructive options following complex high-energy trauma. One particular strategy involves patient-specific custom 3D printed titanium truss constructs, or cages, to address the challenging problem of massive segmental bone loss



**FIGURE 33.2 Trident II Acetabular cups (Stryker, USA)**

Off-the-shelf titanium acetabular cups for total hip arthroplasty, manufactured using titanium.

From Stryker, USA. (2018). <https://www.stryker.com/us/en/about/news/2018/stryker-launches-next-generation-trident-ii-acetabular-system.html>.

(Tetsworth et al., 2017; Tetsworth et al., 2019). Highly mechanically robust, these 3D printed titanium truss cages have an inherent stability that allows immediate motion and early weight bearing, extremely important for preserving joint motion and limb function. These unique implants also act as a lattice for bone graft, and are often used in combination with the induced membrane technique whereby a PMMA spacer is initially implanted to induce the formation of a biologic membrane over a period of 4–8 weeks (Taylor et al., 2012). Following maturation, the spacer is removed and replaced with the final graft or implant material, using the membrane as a barrier to prevent resorption and promote vascularization and implant integration (Taylor et al., 2012). These 3D printed titanium truss cages are therefore designed in a virtual surgical procedure that provides a patient specific option for simultaneous deformity correction, restoring anatomy based on the uninvoluted contralateral limb. Although currently taking a period of weeks to design, manufacture, package, sterilize, and deliver the final implant, the staged approach plays a critical role in the success of the procedure, and the membrane that develops during the interim period has biologic properties that are favorable (Tetsworth et al., 2017; Tetsworth et al., 2019). However, as these technologies become more widely available and routinely employed, the transition period between stages should gradually diminish, and they may then become more frequently employed.

### Craniomaxillofacial surgery

Successful outcomes in craniomaxillofacial (CMF) surgery are strongly dominated by patient aesthetic outcomes, considering the obvious cosmetic implications of augmenting the underlying body structure of the face, jaw, and skull. Accordingly, surgical practice has rapidly integrated DHM and personalized surgical implants into clinical practice for cases where the benefits of readily available off-the-shelf implants do not outweigh the substantial benefits of full customization for bone-interfacing and soft tissue-reinforcing surgical implants.

Porous high-density polyethylene (pHDPE) implants remain some of the most common porous, biocompatible implants for facial reconstruction on the market since their inception in the 1980s (Maas et al., 1990). MEDPOR implants (Stryker) and equivalent products from other manufacturers (e.g., DePuy Synthes, Poriferous, Matrix Surgical USA, Anatomics) are available in a range of shapes and sizes for various CMF applications (Paxton et al., 2019). These adaptable implants come with manufacturer instructions to enable surgeons to heat, mold, and sculpt implants in theater to better conform with patient anatomy. More recently, however, several of these manufacturers have started to offer personalized implant manufacturing based on medical scan data (Anatomics Pty Ltd, 2020; Paxton et al., 2021; Stryker, 2018). Many of these personalized implants fit under the “patient-matched” definition (Table 33.1), where the same style of implant is manufactured to comply with one or more measurements from the patient anatomy within a design envelope.

Custom-made implants are often manufactured for difficult cranial reconstruction cases, where complex deformities resulting from birth abnormalities or trauma

require the design and manufacture of highly intricate and customized implants (Fig. 33.3) (Bonda et al., 2015). Common materials include titanium (Jardini et al., 2014), HDPE (Marlier et al., 2017), and PEEK (J&J Medical Devices, 2021; Stryker, 2022), offering suitable mechanical reinforcement, biocompatibility, and aesthetic outcomes.

While there is an expanding body of literature reporting single case studies and small cohort studies utilizing patient-matched or custom-made CMF implants, a systematic understanding of how personalized CMF implants influence the cost and efficacy of treatments is lacking. Since one of the key factors for surgical success is the patient's satisfaction with the aesthetic outcomes which is challenging to systematically measure, there have been few studies analyzing the overall success of routine personalized CMF treatments. Furthermore, the rapidly emergence of this technology means long-term follow-up data is not yet available.

Studies have presented hospital-based analyses of the time and costs involved in personalized treatments compared to the use of off-the-shelf products (Ciocca et al., 2012; Goodson et al., 2021). Personalized treatments were found to involve extended preoperative planning, implant design, and manufacturing time, the costs of which were offset by reduced surgical and patient recovery time (Goodson et al., 2021). A cost comparison was also undertaken to analyze the viability of establishing hospital-based design and manufacturing capability to reduce reliance on commercial providers (Tarsitano et al., 2016). These studies, however, only consider the use of personalized implants in specific clinical cases with CMF surgery, and highlight the lack of understanding by clinicians and other stakeholders in the impact of the adoption of personalization in routine clinical practice (Goodson et al., 2021). Further research is required to understand how the widespread adoption of hospital-based manufacturing of patient-matched CMF implants may affect health-care provision.

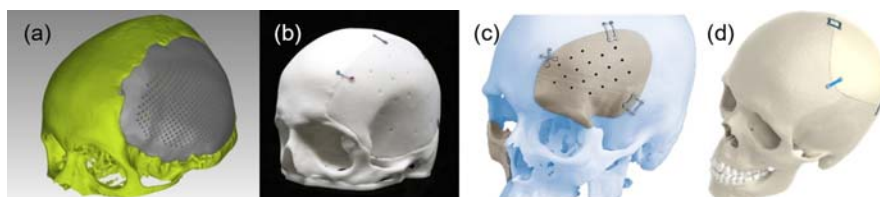


**FIGURE 33.3 Custom-made cranial implants**

Custom-made cranial implants manufactured from (a) titanium, (b) StarPore HDPE, and (c–d) PEEK.

Images reproduced with permission from (a) Elsevier, from Jardini, A. L., Larosa, M. A., Filho, R. M., Zavaglia, C. A. D. C., Bernardes, L. F., Lambert, C. S., Calderoni, D. R., & Kharmandayan, P. (2014). Cranial reconstruction: 3D biomodel and custom-built implant created using additive manufacturing. *Journal of Cranio-Maxillofacial Surgery*, 42(8), 1877–1884. <https://doi.org/10.1016/j.jcms.2014.07.006>. <https://www.sciencedirect.com/science/article/pii/S1010518214002303>, (b) Anatomics Pty Ltd, Australia (2022) <https://www.anatomics.com.au/applications/facial.html>, (c) DePuy Synthes, USA. All rights reserved. (2022) <https://www.jnjmedtech.com/en-US/product/patient-specific-implant-psi>, (d) Stryker, USA (2022) <https://cmf.stryker.com/products/peek-customized-implant>.

## Spinal surgery

In spinal surgery, implants are often used in treatments for lower back pain, which is a leading cause of disability worldwide (Ehrlich, 2003). There are many causes for back pain, including scoliosis, kyphosis, degenerative disc disease, and fracture. In severe cases, surgical intervention is required to correct deformities, restore stability, and reduce pain. Surgical implants used in these treatments are broadly categorized into fusion or nonfusion implants (Lan et al., 2017). The goal of many surgical interventions is to fuse together two or more vertebrae to restrict their movement and reduce pain. Fusion implants include inter-body cages which are porous blocks surgically implanted between vertebrae to encourage bone ingrowth between them, thereby facilitating fusion. Plates and rods are also used to stabilize the spine, screwed directly into the vertebrae. Nonfusion implants are used in alternative treatments where motion is preserved in the spine using nonrigid implants. Artificial disc replacements are used to replace injured or damaged intervertebral discs without fusing adjacent vertebrae to retain motion in the spine. Expandable rods can also be used to straighten the spine without vertebral fusion. These interventions are often more suitable for pediatric patients, since they can accommodate movement and growth to reduce the number of invasive surgeries required.

Routinely, spinal fusion procedures including anterior and posterior lumbar interbody fusion (ALIF and PLIF) require the use of titanium inter-body cages filled with bone grafts and growth factors to promote rapid bone growth to fuse the vertebrae. These devices are available in a range of off-the-shelf shapes and sizes and limited patient-specificity has been required. Plates and rods are also widely available in a range of sizes; however, there has been an increasing demand for personalized spinal plates to treat patients with complex conditions (Choy & Mobbs, 2019).

Recently, Willemse and colleagues reported their experience in partnering with engineers to design personalized spine-supporting implants, which were subsequently manufactured from medical grade titanium using 3D printing for two clinical cases (Fig. 33.4) (Willemse et al., 2019). The authors note that for routine surgeries, off-the-shelf products are suitable. However, personalized devices are required for some specialized cases where off-the-shelf products would lead to poorer outcomes (Willemse et al., 2019). Several other studies report the use of personalized titanium inter-body cages in clinical case studies (Girolami et al., 2018; Siu et al., 2018; Tartara et al., 2020), and favorably recommended the combined adoption of preoperative planning using 3D digital models of the patient anatomy, combined with surgical tools and personalized implants designed from the same data (Floyd et al., 2020; Putzier et al., 2017; Thayaparan et al., 2018).

Despite these reports of successful applications of personalized implants in a range of spinal surgeries (Choy et al., 2017), clinical research has yet to conclusively ascertain whether the routine use of personalized implants leads to better patient outcomes. Studies have indicated that the lack of long-term follow-up data, combined with a lack of consistency in reporting clinical, radiographic, and biomechanical results, compromises the ability to conclusively assess the efficacy of personalized

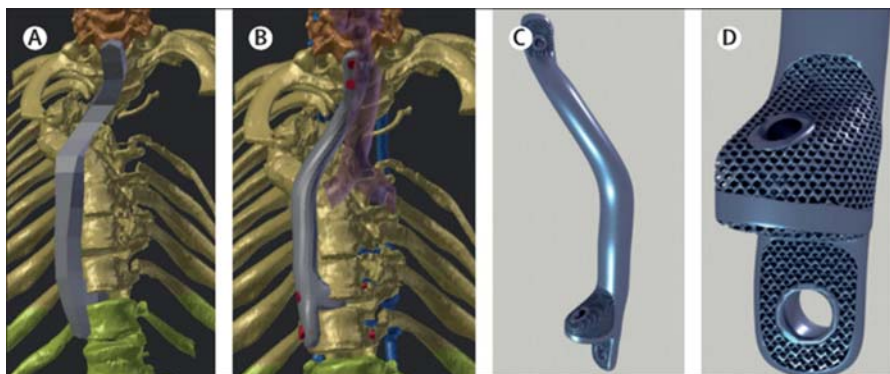


**FIGURE 33.4 Design process for a personalized, custom-made titanium spinal implant.**

(A) Skeleton form of the custom implant connecting stable vertebrae and bridging the defect area with (B) the addition of screw holes (red). (C, D) Design of the final implant, including porous mesh regions to enable bone integration and stabilization between vertebrae.

From Willemse, K., Nizak, R., Noordmans, H. J., Castelein, R. M., Weinans, H., & Kruyt, M. C. (2019). Challenges in the design and regulatory approval of 3D-printed surgical implants: A two-case series. *The Lancet Digital Health*, 1(4), e163–e171. [https://doi.org/10.1016/S2589-7500\(19\)30067-6](https://doi.org/10.1016/S2589-7500(19)30067-6). <https://www.sciencedirect.com/science/article/pii/S2589750019300676>.

implants compared to conventional methods (Burnard et al., 2020). As these approaches are increasingly adopted and longer-term data becomes available, greater certainty into the efficacy of personalization will be gained (Habib et al., 2022).

## Vascular surgery

Stents and grafts are widely used surgical implants in vascular surgery, the market for which is estimated to grow to \$13 billion USD by 2025 (Fortune Business Insights, 2019). In general terms, stents are used for structural support to reinforce the shape of a blood vessel, whereas grafts provide a conduit for blood flow. These two devices may be used in isolation or in conjunction in a stent-graft to both retain the outer morphology of a blood vessel while providing a lining to restore flow through blocked, damaged, or diseased vessels. Stents are typically manufactured from metals, including stainless steel (e.g., OrbusNeich, Medtronic), cobalt or platinum-chromium alloys (e.g., Abbott Vascular, Omega BMS), or nickel titanium (also known as nitinol, e.g., Norman Noble), often with a drug-eluting capacity (Leon & Greisler, 2003). Grafts, on the other hand, may be derived from biological or synthetic sources, including autogenous or donor vessels, or woven polymer textiles manufactured from polytetrafluoroethylene (PTFE, Gore-Tex), and polyethylene terephthalate (PET) (Dacron) (Leon & Greisler, 2003). With suitable size selection, the wide availability of stents and grafts in different sizes and materials from various manufacturers leads to acceptable patient outcomes (Kitahara et al.,

2017; Pantaleo et al., 2016). Personalized stents and grafts are also readily available, often manufactured by hand to accommodate complex anatomical features (Fig. 33.5) (Hu et al., 2019).

Interestingly in some areas of vascular surgery, progression has moved away from personalized stent grafts toward modular and adaptable off-the-shelf products. This is primarily due to the benefit of less delay due to manufacturing custom-made products, particularly in emergency cases where such delays critically impact patient safety (Bissada et al., 2013; Chuter et al., 2011). Historically, the complexity and variability of patient anatomy in endovascular aneurysm repair led to the production of “custom-made” (likely defined as “patient-matched” under the new definitions provided in Table 33.1) stent grafts which could feature the personalized positioning of branching and tapering to varying diameters. However, the invention of more readily adaptable kits is now circumventing the requirement for time-consuming design and manufacturing processes for customized stent grafts (Chuter et al., 2011). One study retrospectively analyzed the suitability of novel adaptable off-the-shelf implants in

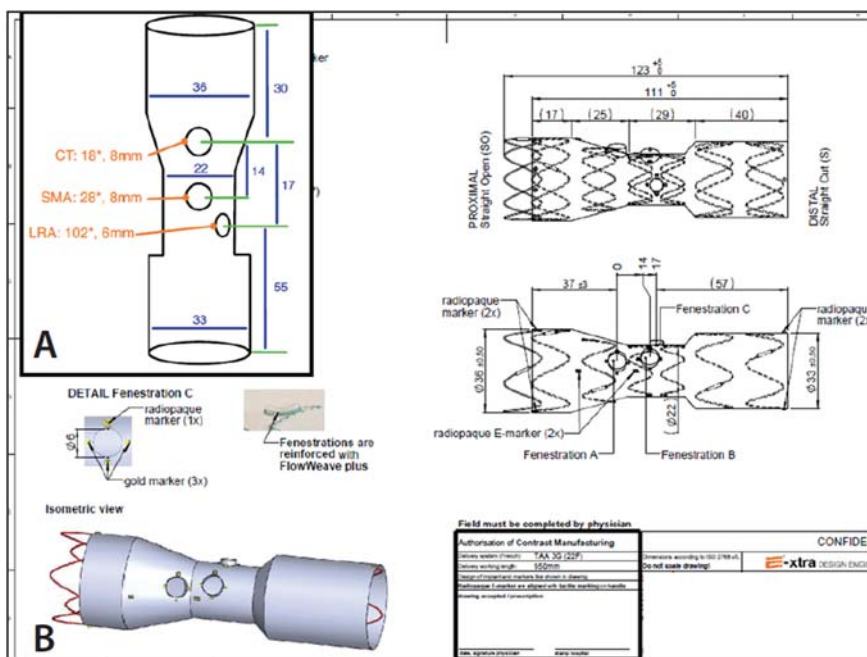


**FIGURE 33.5 Design of a customized fenestrated stent graft.**

(A) Customization design sketch and (B) technical drawings for a custom-made fenestrated stent graft with specific diameters, tapering and fenestrations for the celiac trunk, superior mesenteric artery (SMA), and left renal artery (LRA).

*From (2018). The advantages of customized vascular implants for challenging aortic anatomy. Endovascular Today, 6(7), 22–27. <https://evtoday.com/articles/2018-nov/the-advantages-of-customized-vascular-implants-for-challenging-aortic-anatomy>.*

patients who had been treated with custom-made multibranched endografts. The study found that up to 63% of patients were suitable candidates for off-the-shelf products, which could have reduced surgical delays (Bisdas et al., 2013).

For heart valve repair, surgical intervention may be required to reconstruct or replace a damaged or diseased heart valve. Current replacement treatment options involve off-the-shelf biological or mechanical valves which are available in sizes ranging from 19 to 33 mm in diameter, suitable for the majority of adult patients. With respect to anatomical compliance, off-the-shelf products are largely suitable for patients, however, there are several drawbacks in their function. Biological tissue valves, typically bovine in origin, may last 10–20 years and are typically recommended for patients over 70 years old due to their limited longevity which would otherwise require younger patients to undergo revision surgeries. Mechanical valves are therefore recommended for younger patients; however, they often have an audible clicking sound and require continuous blood thinning therapies to reduce the risk of clotting in the valve (Pibarot & Dumesnil, 2009). As an alternative, tissue engineered valves are now in clinical trials (Miyazaki et al., 2017), offering a fully restorative approach to heart valve replacement and offering a promising treatment avenue for pediatric patients where there are very few other treatment options available and surgical options are critically lacking (Henaine et al., 2012). Significant research efforts have focused on combining tissue engineering technology and personalization with promising preclinical data for heart valve replacements. However, such products have yet to be translated into clinical use (Fioretta et al., 2021; Saidy et al., 2019). Patient-matched aortic root supports have also been successfully manufactured and used to treat aortic root aneurysms in patients with Marfan's syndrome, as a means of preserving the aortic valve (Treasure et al., 2014).

With aspects of vascular surgery requiring immediate but adaptable off-the-shelf systems, personalization may only remain necessary when treating cases of complex or abnormal anatomy where adaptable systems cannot be used.

## Urology surgery

In urology surgical practice, routinely used surgical implants include prostheses, as well as stents and grafts with similarities to their vascular counterparts in terms of function and manufacturing method. Ureteric stents (JJ stents) are thin polymer tubes commonly used in the treatment of a variety of conditions, including kidney stones, ureteral strictures, or blockages (Al-Aown et al., 2010). These tubes temporarily or permanently facilitate unrestricted drainage between the kidneys and bladder and are typically manufactured from low-stiffness polymers such as silicone (Cook Medical), polyurethane (Rüsch, Teleflex), or metals (Cook Medical, Ni–Co–Cr–M alloy) with the aim of reducing irritation or discomfort as well as encrustation (Patel et al., 2017). The availability of adaptable off-the-shelf products has sufficiently met the clinical need to suit a range of patient anatomies (Vogt, 2020). Similarly, for prosthetic implants such as testicular prostheses, the range of available sizes for silicone-shell, liquid silicone-filled implants have been largely suitable

for both pediatric and adult patients (Dieckmann et al., 2015; Peycelon et al., 2016). However, reported concerns with mismatch between prostheses and native tissue stiffness have motivated research to produce more mechanically compliant alternatives (Skewes et al., 2021).

The translation of personalized surgical implants has yet to be realized for routine clinical practice (Mathews et al., 2020). Current research in biofabrication and tissue engineering promises the on-demand fabrication of personalized regenerative implants such as kidneys, testicles, and other reproductive tissues and organs (Atala, 2012; Kim et al., 2015). However, personalization has largely not been a clinical requirement for urological surgical implants, aside from the well-documented benefits of incorporating parallel DHM technologies enabling surgical planning and patient education with more accessible 3D visualizations of patient anatomy and treatment procedures (Cacciamani et al., 2019; Chen et al., 2020; Porpiglia et al., 2018).

---

## Regulation

Medical device regulation varies substantially between jurisdictions and is managed by regulatory authorities such as the Food and Drug Administration (FDA) in the USA, European Union Medical Device Regulation, or the Therapeutic Goods Administration (TGA) in Australia. Many authorities base their medical device regulation legislation around a risk management approach, categorizing the intended use of the device and degree of invasiveness, among other factors. A class-based scale distinguishes simple tools such as surgical instruments, tongue depressors, or dressings as to whether they perform a measurement function or those which must be supplied sterile (typically Class I). Class II devices often include minimally invasive products such as needles, sutures, and catheters, while Class III *high-risk* devices may include surgical implants and other devices, where in the case of breakage or failure, the risk to human life is high. Medical device manufacturing is also subject to specific regulatory oversight, often in the form of compliance with “essential principles” (Australia) or controls (USA), depending on jurisdiction and risk class, which describe the fundamental design and manufacturing requirements to demonstrate that a product is safe and will perform as intended. A large component of the regulatory process in the US is also demonstrating that the new product performs to the same standard as one or more predicate devices, thus justifying its approval compared to existing products on the market.

For personalized medical devices, where only single units are produced based on individual patient anatomy, exemption pathways have been established to allow clinicians to rapidly commission the manufacturing of bespoke implants without the burden of undertaking, adhering, and complying to the complex and time-consuming regulatory process for each individual product (Willemsen et al., 2019). Historically, this has been a suitable and seldom-used pathway for clinicians since manufacturing one-off personalized implants has historically been highly

time-consuming and costly. However, with the adoption of DHM, CAD/CAM, and additive manufacturing, elements of this process can now be more readily automated. Regulatory authorities have had to reconsider the exemption pathways for such personalized implants since they can now be rapidly produced and are readily accessible.

The current exemption pathways for personalized surgical implants still requires the manufacturers to conform to the essential principles or controls of the same class level devices, but does not require the manufacturer to perform an official assessment (Willemse et al., 2019). Furthermore, if the exemption pathway is being leveraged, a “sponsor” who assumes responsibility for the design and manufacturing of the product, is responsible for reporting any adverse events to the regulatory authority. Manufacturers are also still required to implement a quality management system (QMS) to ensure manufacturing is compliant with medical device standards (such as ISO 13485 or 21 CFR 820), and harmonized auditing programs have been established such that manufacturers can comply with the requirements in multiple jurisdictions through a common pathway.

After substantial stakeholder engagement, regulatory authorities are currently in the process of overhauling the regulation approach for personalized medical devices, aligned with the definitions established by the International Medical Device Regulators Forum (IMDRF). For example, in early 2021, the TGA introduced substantial changes for the regulation of custom-made and patient-matched medical devices to exclude an increasing number of personalized surgical implants leveraging regulatory exemptions (Therapeutic Goods Administration (TGA), 2020). These new changes fundamentally seek to recognize the growing number of patient-matched medical devices which are manufactured based on individual patient-anatomy but vary only slightly in dimension or geometry within specified limits, for example, the length of a vascular stent, or size of an orthopedic joint replacement implant which does not vary between patients outside of predefined limits. The majority of such personalized implants, now considered “patient-matched,” must be listed on the Australian Register of Therapeutic Goods (ARTG) as routinely undertaken for all mass-manufactured devices with, however, additional considerations for demonstrating safety and efficacy over the range of design feature limits, known as the “design envelope” (Therapeutic Goods Administration (TGA), 2020). This acknowledgment of this “design envelope,” in which patient-matched devices can be manufactured and regulated under routine medical device manufacturing regulatory pathways falls into line with other jurisdictions such as the FDA who have previously recognized personalization of medical devices within a design or performance envelope under the umbrella of existing regulatory pathways (US Food and Drug Administration (FDA), 2017). True custom-made devices may still be eligible for exemption in Australia, however new additional requirements have been established to increase reporting obligations and manufacturing transparency.

Adaptable surgical implants are not included in these new regulatory pathways since they can be considered under the routine class-based medical device regulation framework, typically categorized as Class III devices. Manufacturers supply

specifications and procedures for clinicians to modify the implants at the point of care. For example, MEDPOR implants are readily molded and trimmed to conform to patient anatomy, guided by supplied instructions for clinicians to perform these modifications in surgery (Paxton et al., 2019). Considering the substantial precedence and widespread adoption of this regulation pathway for surgical implants, personalized medical device manufacturers may remain committed to marketing their products as “adaptable” to leverage this established avenue. The FDA’s 510k pathway, for example, allows manufacturers to claim substantial equivalence for implant safety and efficacy compared to existing “predicate” products on the market. If suitable point-of-care modifications to the implants can be achieved using manual trimming, molding, or adjusting processes by the surgeons, this will remain a faster, lower risk, and cheaper translation pathway than offering custom-made implant manufacturing and navigating a new regulatory pathway.

---

## Summary and future perspectives

The future of surgical implant personalization will remain a delicate balancing act between meeting clinical need, commercial viability, and regulatory compliance. The next stages in personalized surgical implant translation through the new regulatory pathways will be critical for establishing precedence to allow novel surgical implant technologies to become clinically available.

Extensive research in tissue engineering, regenerative medicine, and the evolving multidisciplinary field of biofabrication has yet to be consolidated with these regulatory requirements and the reality of the competitive commercial landscape. The goal of these novel techniques is to completely regenerate injured or diseased tissue using regenerative and dissolvable biomaterial implants, coupled with cell delivery, bioactive ingredients, and drug delivery, to optimize the rapid regeneration of tissues (Groll et al., 2016). These high-risk strategies promise substantially improved patient outcomes, using a highly disruptive approach compared to the current strategy of surgical implants that augment or reinforce damaged tissues.

Personalized bone tissue engineering devices have been in development for over 40 years, with only a handful of products successfully translated into clinical use. Examples include Osteoplug, a 3D printed polycaprolactone scaffold developed by a Singapore-based medical device company, Osteopore, to fill burr holes during neurosurgery (Low et al., 2009). The highly porous scaffold provides mechanical support while enabling bone marrow and blood saturation to facilitate bone remodeling as it resorbs. Osteoplug achieved FDA approval in 2020 and is available in three sizes (FDA News, 2020). Osteopore has also been reported to be involved in manufacturing several custom-made polycaprolactone surgical implants for long bone and cranial reconstruction (Hutmacher & Wagels, 2021), however these have been supplied through the exemption pathway in conjunction with Australian-based surgeons and are not offered as a routine commercial service.

In vascular surgery, resorbable PLLA drug-eluting stents briefly made an appearance on the market as an alternative to metallic stents. This product, called Absorb, was developed by Abbott Vascular and initially approved in Europe in 2011, followed by the US FDA in 2016 (O'Riordan, 2019). However, within a year, concerns with increased risk of major cardiac events led to the FDA issuing several warnings, and the use of the device being heavily restricted. Eventually in September 2017, the product was discontinued and withdrawn from the market (O'Riordan, 2019). Several studies have also noted that the resorbable product did not achieve more favorable patient outcomes than the existing metallic stents on the market (Stuijfzand et al., 2019). Abbott Vascular has since launched a new clinical trial to investigate the efficacy of a new resorbable stent to treat critical limb ischemia in the lower leg (Abbott Medical Devices, 2020). Researchers continue to be heavily invested in exploring resorbable alternatives for vascular stents and grafts (Mostaed et al., 2018; Somszor et al., 2020; van Lith et al., 2016).

Biofabrication research is also heavily committed to investigating the combination of cell-based therapies in surgical implants to instigate rapid autologous cell infiltration and tissue regeneration (Levato et al., 2020). Cell seeded scaffolds and cell-laden hydrogels have been extensively investigated for their capacity to recapitulate native tissue architecture during in vitro tissue culture prior to implantation. Promising preclinical studies have demonstrated their efficacy in regenerating mature bone in critical-sized defects (Berner et al., 2015; Sparks et al., 2020), highly vascularized soft tissues (Cho et al., 2021), cartilage (Mancini et al., 2020), and vascular grafts (Akentjew et al., 2019) among many other tissue engineering applications for human tissue and organs (Melchels et al., 2012). The ultimate goal is to combine advances in tissue engineering and regenerative medicine with advanced biomaterial processing to enable patient-specific implant design and manufacturing (Kang et al., 2016; Paxton et al., 2020). There are several challenges in translating these complex, multicomponent tissue engineered systems. Aside from the inherent challenges of regulating personalized implants, these novel biofabrication approaches feature the combination of scaffold-based implant structures and human cell or tissue-based products, leading them to be classified as “combination products,” as they fit the definition of both medical devices with the inclusion of biological components which would routinely be regulated through pathways for “biologics.” The regulatory pathways for such combination products are complex and often involve compiling applications which encompass the requirements of all individual components of the product, such as medical device and biologics for a cell-laden scaffold system (Oberweis et al., 2020).

These case studies demonstrate the substantial hurdles faced by medical device companies to both validate the long-term efficacy of tissue engineering and biofabricated products, and the competing restrictions imposed by commercial demand and regulation which has, to date, substantially limited the feasibility of offering custom-made devices.

The more immediate step for the translation of tissue engineered products will likely not involve customization under the “custom-made” definition, despite the

promise of DHM and additive manufacturing. Currently, regulatory authorities are substantially better equipped to regulate resorbable and/or combination products which are not custom-made. The commercial feasibility of producing a range of off-the-shelf products which can be adapted by surgeons has been shown to be a more feasible model leading to faster commercialization, rather than offering entirely revolutionary custom-made implant design and manufacturing services which cannot yet be consolidated within a harmonized regulation policy between jurisdictions. This present challenge in regulation either leads to commercially impractical administrative overheads for multinational commercialization or limiting the commercial impact to just one jurisdiction.

An additional concern for the impending availability of routine custom-made surgical implant manufacturing is the cost. The steep costs associated with clinician involvement as well as customized and single-unit manufacturing which will remain a key requirement for custom-made surgical implants, inevitably increases the costs of such products compared to adaptable off-the-shelf alternatives. This is likely to restrict the availability of such implants to patients seeking treatment through private healthcare services, if government-funded healthcare providers do not cover the high costs of custom-made implants, especially when cheaper alternatives remain available with similar clinical outcomes. The onus will be on surgical implant manufacturers to demonstrate the significant improvements to patient outcomes using these personalized approaches to overcome this critical challenge. However, higher implant costs may be recovered through improved surgical practice and patient outcomes, leading to reduced costs for the initial treatment as well for follow up treatments, rehabilitation, and recovery. For some personalized implants, this has been demonstrated by surveying the costs for 4427 patients, where the 12-month costs for total knee arthroplasty using personalized implants designed from CT scans ( $n = 732$ ) was lower than for patients mass-produced implants ( $n = 3695$ ) ([O'Connor & Blau, 2019](#)). The economic impact in the adoption of personalized surgical implants requires further study to ensure the greatest impact to patient care can be realized.

With the rapid development of new technology, market growth, and strong engagement from regulatory authorities to improve translation pathways, personalized surgical implant manufacturing is evolving into a rapidly expanding commercial landscape. Underpinned by the more mainstream adoption of DHM and access to high quality 3D patient scan data, personalization can be readily incorporated into medical implant manufacturing. This chapter has explored the adoption of personalization in five surgical disciplines, identifying the varying adoption and clinical need for personalized surgical implants. In orthopedics, personalization of metallic implants has been applied for several decades, expanding toward routine use for several surgical procedures. In spinal surgery as well as craniomaxillofacial surgery where aesthetic outcomes are highly critical, personalization is meeting a growing clinical need for the treatment of specialized cases. By contrast, in vascular surgery, the urgency of treating conditions such as abdominal aortic aneurysms has motivated the trend toward adaptable, mass-produced endovascular graft implants to overcome

the lead time for manufacturing personalized implants. The development of combination products, such as tissue engineered regenerative implants utilizing cells and other bioactive ingredients within personalized implants, are in development as a fully regenerative approach for surgical interventions to replace injured or diseased tissues, leveraging the capacity of DHM to generate personalized treatment options for improved patient outcomes.

*The authors declare that they have no competing financial interests or personal relationships that could have appeared to influence the information reported in this chapter.*

---

## References

- Abbott Medical Devices. (2020). *LIFE-BTK Randomized Controlled trial*. <https://clinicaltrials.gov/ct2/show/NCT04227899>.
- Akentjew, T. L., Terraza, C., Suazo, C., Maksimecka, J., Wilkens, C. A., Vargas, F., Zavala, G., Ocaña, M., Enrione, J., García-Herrera, C. M., Valenzuela, L. M., Blaker, J. J., Khouri, M., & Acevedo, J. P. (2019). Author correction: Rapid fabrication of reinforced and cell-laden vascular grafts structurally inspired by human coronary arteries. *Nature Communications*, 10(1). <https://doi.org/10.1038/s41467-019-11446-9>
- Al-Aown, A., Kyriazis, I., Kallidonis, P., Kraniotis, P., Rigopoulos, C., Karnabatidis, D., Petsas, T., & Liatsikos, E. (2010). Ureteral stents: New ideas, new designs. *Therapeutic Advances in Urology*, 2(2), 85–92. <https://doi.org/10.1177/1756287210370699>
- Anatomics Pty Ltd. (2020). StarPore facial applications. <https://www.anatomics.com/au/applications/facial.html>.
- Aranda, J. L., Jiménez, M. F., Rodríguez, M., & Varela, G. (2015). Tridimensional titanium-printed custom-made prosthesis for sternocostal reconstruction. *European Journal of Cardio-Thoracic Surgery*, 48(4), e92–e94. <https://doi.org/10.1093/ejcts/ezv265>
- Atala, A. (2012). Tissue engineering of reproductive tissues and organs. *Fertility and Sterility*, 98(1), 21–29. <https://doi.org/10.1016/j.fertnstert.2012.05.038>
- Berner, A., Henkel, J., Woodruff, M. A., Steck, R., Nerlich, M., Schuetz, M. A., & Hutmacher, D. W. (2015). Delayed minimally invasive injection of allogenic bone marrow stromal cell sheets regenerates large bone defects in an ovine preclinical animal model. *Stem Cells Translational Medicine*, 4(5), 503–512. <https://doi.org/10.5966/sctm.2014-0244>
- Bibb, R., Eggbeer, D., & Paterson, A. (2015). Medical modelling: The application of advanced design and rapid prototyping techniques in medicine. In *Medical modelling: The application of advanced design and rapid prototyping techniques in medicine: Second edition* (2nd ed., pp. 1–500). Elsevier Inc. <https://doi.org/10.1016/C2014-0-01365-2>
- Bisdas, T., Donas, K. P., Bosiers, M., Torsello, G., & Austermann, M. (2013). Anatomical suitability of the T-branch stent-graft in patients with thoracoabdominal aortic aneurysms treated using custom-made multibranched endografts. *Journal of Endovascular Therapy*, 20(5), 672–677. <https://doi.org/10.1583/13-4400MR.1>
- Bonda, D. J., Manjila, S., Selman, W. R., & Dean, D. (2015). The recent revolution in the design and manufacture of cranial implants: Modern advancements and future directions. *Neurosurgery*, 77(5), 814–824. <https://doi.org/10.1227/NEU.0000000000000899>

- Burnard, J. L., Parr, W. C. H., Choy, W. J., Walsh, W. R., & Mobbs, R. J. (2020). 3D-printed spine surgery implants: A systematic review of the efficacy and clinical safety profile of patient-specific and off-the-shelf devices. *European Spine Journal*, 29(6), 1248–1260. <https://doi.org/10.1007/s00586-019-06236-2>
- Cacciamani, G. E., Okhunov, Z., Meneses, A. D., Rodriguez-Socarras, M. E., Rivas, J. G., Porpiglia, F., Liatsikos, E., & Veneziano, D. (2019). Impact of three-dimensional printing in urology: State of the Art and future perspectives. A systematic review by ESUT-YAUWP group. *European Urology*, 76(2), 209–221. <https://doi.org/10.1016/j.eururo.2019.04.044>
- Chen, X. (2018). Parametric design of patient-specific fixation plates for distal femur fractures. *Proceedings of the Institution of Mechanical Engineers, H: Journal of Engineering in Medicine*, 232(9), 901–911. <https://doi.org/10.1177/0954411918793668>
- Chen, M. Y., Skewes, J., Desselle, M., Wong, C., Woodruff, M. A., Dasgupta, P., & Rukin, N. J. (2020). Current applications of three-dimensional printing in urology. *BJU International*, 125(1), 17–27. <https://doi.org/10.1111/bju.14928>
- Cho, W., Kim, B. S., Ahn, M., Ryu, Y. H., Ha, D., Kong, J. S., Rhie, J., & Cho, D. (2021). Flexible adipose-vascular tissue assembly using combinational 3D printing for volume-stable soft tissue reconstruction. *Advanced Healthcare Materials*, 10(6), 2001693. <https://doi.org/10.1002/adhm.202001693>
- Choy, W. J., & Mobbs, R. J. (2019). Current state of 3D-printed custom-made spinal implants. *The Lancet Digital Health*, 1(4), e149–e150. [https://doi.org/10.1016/S2589-7500\(19\)30081-0](https://doi.org/10.1016/S2589-7500(19)30081-0)
- Choy, W. J., Mobbs, R. J., Wilcox, B., Phan, S., Phan, K., & Sutterlin, C. E. (2017). Reconstruction of thoracic spine using a personalized 3D-printed vertebral body in adolescent with T9 primary bone tumor. *World Neurosurgery*, 105, 1032–1032.e17. <https://doi.org/10.1016/j.wneu.2017.05.133>
- Chuter, T. A. M., Hiramoto, J. S., Park, K. H., & Reilly, L. M. (2011). The transition from custom-made to standardized multibranched thoracoabdominal aortic stent grafts. *Journal of Vascular Surgery*, 54(3), 660–668. <https://doi.org/10.1016/j.jvs.2011.03.005>
- Ciocca, L., Mazzoni, S., Fantini, M., Persiani, F., Marchetti, C., & Scotti, R. (2012). CAD/CAM guided secondary mandibular reconstruction of a discontinuity defect after ablative cancer surgery. *Journal of Crano-Maxillofacial Surgery*, 40(8), e511–e515. <https://doi.org/10.1016/j.jcms.2012.03.015>
- Conformis. (2021). *Knee replacement implants for knee joint replacement*. <https://www.conformis.com/patient-specific-knee-and-hip-implants/custom-made-knees/>.
- Cook Medical. (2021). *Zenith Flex AAA endovascular graft bifurcated main body graft*. Cook Medical.
- Culler, S. D., Martin, G. M., & Swearingen, A. (2017). Comparison of adverse events rates and hospital cost between customized individually made implants and standard off-the-shelf implants for total knee arthroplasty. *Arthroplasty Today*, 3(4), 257–263. <https://doi.org/10.1016/j.artd.2017.05.001>
- Dall'Ava, H., Laura, D., Henckel, & Hart. (2019). 3D printed acetabular cups for total hip arthroplasty: A review article. *Metals*, 9(7), 729. <https://doi.org/10.3390/met9070729>
- Dieckmann, K. P., Anheuser, P., Schmidt, S., Soyka-Hundt, B., Pichlmeier, U., Schriefer, P., Matthies, C., Hartmann, M., & Ruf, C. G. (2015). Testicular prostheses in patients with testicular cancer—acceptance rate and patient satisfaction Urological oncology. *BMC Urology*, 15(1). <https://doi.org/10.1186/s12894-015-0010-0>

- Durand-Hill, M., Henckel, J., Di Laura, A., & Hart, A. J. (2020). Can custom 3D printed implants successfully reconstruct massive acetabular defects? A 3D-CT assessment. *Journal of Orthopaedic Research*, 38(12), 2640–2648. <https://doi.org/10.1002/jor.24752>
- Du, R., Su, Y. X., Yan, Y., Choi, W. S., Yang, W. F., Zhang, C., Chen, X., Curtin, J. P., Ouyang, J., & Zhang, B. (2020). A systematic approach for making 3D-printed patient-specific implants for craniomaxillofacial reconstruction. *Engineering*, 6(11), 1291–1301. <https://doi.org/10.1016/j.eng.2020.02.019>
- Ehrlich, G. E. (2003). Lower back pain. *Bulletin of the World Health Organization*, 81, 671–676.
- Ejnisman, L., Gobbato, B., de França Camargo, A. F., & Zancul, E. (2021). Three-dimensional printing in orthopedics: From the basics to surgical applications. *Current Reviews in Musculoskeletal Medicine*, 14(1). <https://doi.org/10.1007/s12178-020-09691-3>
- FDA News. (2020). TGA approves osteopore's 3D-printed scaffolds for bone regeneration. <https://www.fdanews.com/articles/196738-tga-approves-osteopores-3d-printed-scaffolds-for-bone-regeneration>.
- Fernandez, C. C., Sobel, J. D., Gasper, W. J., Vartanian, S. M., Reilly, L. M., Chuter, T. A. M., & Hiramoto, J. S. (2016). Standard off-the-shelf versus custom-made multibranched thoracoabdominal aortic stent grafts. *Journal of Vascular Surgery*, 63(5), 1208–1215. <https://doi.org/10.1016/j.jvs.2015.11.035>
- Fioretta, E. S., Motta, S. E., Lintas, V., Loerakker, S., Parker, K. K., Baaijens, F. P. T., Falk, V., Hoerstrup, S. P., & Emmert, M. Y. (2021). Next-generation tissue-engineered heart valves with repair, remodelling and regeneration capacity. *Nature Reviews Cardiology*, 18(2), 92–116. <https://doi.org/10.1038/s41569-020-0422-8>
- Floyd, E., Cohn, P., Ferguson, J., & Kalantar, S. B. (2020). A review of preoperative planning technologies for spinal deformity correction. *Seminars in Spine Surgery*, 32(2). <https://doi.org/10.1016/j.semss.2020.100787>
- Fortune Business Insights. (2019). *Cardiovascular stents market size, value & growth report 2025*. <https://www.fortunebusinessinsights.com/industry-reports/cardiovascular-stents-market-100061>.
- Fröschen, F. S., Randau, T. M., Hischebeth, G. T. R., Gravius, N., Wirtz, D. C., Gravius, S., & Walter, S. G. (2020). Outcome of repeated multi-stage arthroplasty with custom-made acetabular implants in patients with severe acetabular bone loss: A case series. *HIP International*, 30(1), 64–71. <https://doi.org/10.1177/1120700020928247>
- Girolami, M., Boriani, S., Bandiera, S., Barbanti-Bródano, G., Ghermandi, R., Terzi, S., Tedesco, G., Evangelisti, G., Pipola, V., & Gasbarrini, A. (2018). Biomimetic 3D-printed custom-made prosthesis for anterior column reconstruction in the thoracolumbar spine: A tailored option following en bloc resection for spinal tumors: Preliminary results on a case-series of 13 patients. *European Spine Journal*, 27(12), 3073–3083. <https://doi.org/10.1007/s00586-018-5708-8>
- Goodson, A. M. C., Parmar, S., Ganesh, S., Zakai, D., Shafi, A., Wicks, C., O'Connor, R., Yeung, E., Khalid, F., Tahim, A., Gowrishankar, S., Hills, A., & Williams, E. M. (2021). Printed titanium implants in UK craniomaxillofacial surgery. Part II: Perceived performance (outcomes, logistics, and costs). *British Journal of Oral and Maxillofacial Surgery*, 59(3), 320–328. <https://doi.org/10.1016/j.bjoms.2020.08.088>
- Grand View Research. (2019). *Personalized medicine market size worth \$3.18 trillion by 2025*. <https://www.grandviewresearch.com/press-release/global-personalized-medicine-market>.

- Green, N., Glatt, V., Tetsworth, K., Wilson, L. J., & Grant, C. A. (2016). A practical guide to image processing in the creation of 3D models for orthopedics. *Techniques in Orthopaedics*, 31(3), 153–163. <https://doi.org/10.1097/BTO.0000000000000181>. Lip-pincott Williams and Wilkins.
- Groll, J., Boland, T., Blunk, T., Burdick, J. A., Cho, D.-W., Dalton, P. D., Derby, B., Forgacs, G., Li, Q., Mironov, V. A., Moroni, L., Nakamura, M., Shu, W., Takeuchi, S., Vozzi, G., Woodfield, T. B. F., Xu, T., Yoo, J. J., & Malda, J. (2016). Biofabrication: Reappraising the definition of an evolving field. *Biofabrication*, 8(1), 013001. <https://doi.org/10.1088/1758-5090/8/1/013001>
- Habib, A., Jovanovich, N., Muthiah, N., Alattar, A., Alan, N., Agarwal, N., Ozpinar, A., & Hamilton, D. K. (2022). 3D printing applications in spine surgery: an evidence-based assessment toward personalized patient care. *European Spine Journal*, 31, 1682–1690. <https://doi.org/10.1007/s00586-022-07250-7>
- Haleem, A., & Javaid, M. (2019). Polyether ether ketone (PEEK) and its 3D printed implants applications in medical field: An overview. *Clinical Epidemiology and Global Health*, 7(4), 571–577. <https://doi.org/10.1016/j.cegh.2019.01.003>
- Hao, L., & Harris, R. (2008). *Bio-materials and prototyping applications in medicine*. Springer US.
- Harith, H., Malekani, J., Schmutz, B., Schuetz, M., & Yarlagadda, P. K. D. V. (2016). A method for optimal fit of patient-specific fracture fixation plates. *Proceedings of the Institution of Mechanical Engineers, L: Journal of Materials: Design and Applications*, 230(1), 282–290. <https://doi.org/10.1177/1464420715569586>
- Henaine, R., Roubertie, F., Vergnat, M., & Ninet, J. (2012). Valve replacement in children: A challenge for a whole life. *Archives of Cardiovascular Diseases*, 105(10), 517–528. <https://doi.org/10.1016/j.acvd.2012.02.013>
- Hirz, M., Rossbacher, P., & Gulánová, J. (2017). Future trends in CAD—from the perspective of automotive industry. *Computer-Aided Design and Applications*, 14(6), 734–741. <https://doi.org/10.1080/16864360.2017.1287675>
- Horst, A., McDonald, F., & Hutmacher, D. W. (2019). A clarion call for understanding regulatory processes for additive manufacturing in the health sector. *Expert Review of Medical Devices*, 16(5), 405–412. <https://doi.org/10.1080/17434440.2019.1609353>
- Hussain, R. M. (2021). Metallic 3D printed total talus replacement: A case study. *Journal of Foot and Ankle Surgery*, 60(3), 634–641. <https://doi.org/10.1053/j.jfas.2020.10.005>
- Hutmacher, D., & Wagels, M. (2021). *Remarkable recovery of patient Reuben Lichter with our 3D-printed scaffold for tibial bone repair*.
- Hu, Y., Zhang, L., Seneci, C. A., Li, W., Abdelaziz, M. E. M. K., & Yang, G. Z. (2019). Design, fabrication, and testing a semiautomatic sewing device for personalized stent graft manufacturing. *IEEE/ASME Transactions on Mechatronics*, 24(2), 517–526. <https://doi.org/10.1109/TMECH.2019.2894722>
- Imanishi, J., & Choong, P. F. M. (2015). Three-dimensional printed calcaneal prosthesis following total calcanectomy. *International Journal of Surgery Case Reports*, 10, 83–87. <https://doi.org/10.1016/j.ijscr.2015.02.037>
- International Medical Device Regulators Forum. (2018). *Definitions for personalized medical devices*. <https://www.imdrf.org/consultations/definitions-personalized-medical-devices>.
- J&J Medical Devices. (2021). *Cranial implant | patient specific implant*.
- Jardini, A. L., Larosa, M. A., Filho, R. M., Zavaglia, C. A. D. C., Bernardes, L. F., Lambert, C. S., Calderoni, D. R., & Kharmandayan, P. (2014). Cranial reconstruction: 3D biomodel and custom-built implant created using additive manufacturing. *Journal*

- of *Cranio-Maxillofacial Surgery*, 42(8), 1877–1884. <https://doi.org/10.1016/j.jcms.2014.07.006>
- Kang, H. W., Lee, S. J., Ko, I. K., Kengla, C., Yoo, J. J., & Atala, A. (2016). A 3D bioprinting system to produce human-scale tissue constructs with structural integrity. *Nature Biotechnology*, 34(3), 312–319. <https://doi.org/10.1038/nbt.3413>
- Kim, I. H., Ko, I. K., Atala, A., & Yoo, J. J. (2015). Whole kidney engineering for clinical translation. *Current Opinion in Organ Transplantation*, 20(2), 165–170. <https://doi.org/10.1097/MOT.0000000000000173>
- Kitahara, H., Okada, K., Kimura, T., Yock, P. G., Lansky, A. J., Popma, J. J., Yeung, A. C., Fitzgerald, P. J., & Honda, Y. (2017). Impact of stent size selection on acute and long-term outcomes after drug-eluting stent implantation in de novo coronary lesions. *Circulation: Cardiovascular Interventions*, 10(10). <https://doi.org/10.1161/CIRCINTERVENTIONS.116.004795>
- Lan, T., Chen, Y., Hu, S. Y., Li, A. L., & Yang, X. J. (2017). Is fusion superior to non-fusion for the treatment of thoracolumbar burst fracture? A systematic review and meta-analysis. *Journal of Orthopaedic Science*, 22(5), 828–833. <https://doi.org/10.1016/j.jos.2017.05.014>
- Leon, L., & Greisler, H. P. (2003). Vascular grafts. *Expert Review of Cardiovascular Therapy*, 1(4), 581–594. <https://doi.org/10.1586/14779072.1.4.581>
- Levato, R., Jungst, T., Scheuring, R. G., Blunk, T., Groll, J., & Malda, J. (2020). From shape to function: The next step in bioprinting. *Advanced Materials*, 32(12). <https://doi.org/10.1002/adma.201906423>
- van Lith, R., Baker, E., Ware, H., Yang, J., Farsheed, A. C., Sun, C., & Ameer, G. (2016). 3D-printing strong high-resolution antioxidant bioresorbable vascular stents. *Advanced Materials Technologies*, 1(9). <https://doi.org/10.1002/admt.201600138>
- Low, S. W., Ng, Y. J., Yeo, T. T., & Chou, N. (2009). Use of Osteoplug polycaprolactone implants as novel burr-hole covers. *Singapore Medical Journal*, 50(8), 777–780. <http://smj.sma.org.sg/5008/5008a4.pdf>.
- Maas, C. S., Merwin, G. E., Wilson, J., Frey, M. D., & Maves, M. D. (1990). Comparison of biomaterials for facial bone augmentation. *Archives of Otolaryngology—Head and Neck Surgery*, 116(5), 551–556. <https://doi.org/10.1001/archotol.1990.01870050051005>
- Mancini, I. A. D., Schmidt, S., Brommer, H., Pouran, B., Schäfer, S., Tessmar, J., Mensinga, A., van Rijen, M. H. P., Groll, J., Blunk, T., Levato, R., Malda, J., & van Weeren, P. R. (2020). A composite hydrogel-3D printed thermoplast osteochondral anchor as example for a zonal approach to cartilage repair: In vivo performance in a long-term equine model. *Biofabrication*, 12(3), 035028. <https://doi.org/10.1088/1758-5090/ab94ce>
- Marlier, B., Kleiber, J. C., Bannwarth, M., Theret, E., Eap, C., & Litre, C. F. (2017). Reconstruction of cranioplasty using medpor porouspolyethylene implant. *Neurochirurgie*, 63(6), 468–472. <https://doi.org/10.1016/j.neuchi.2017.07.001>
- Materialise. (2018). *Materialise first company to receive FDA clearance for diagnostic 3D-printed anatomical models*. <https://www.materialise.com/en/press-releases/materialise-first-company-to-receive-fda-clearance-for-diagnostic-3d-printed-models>.
- Mathews, D. A. P., Baird, A., & Lucky, M. (2020). Innovation in urology: Three dimensional printing and its clinical application. *Frontiers in Surgery*, 7. <https://doi.org/10.3389/fsurg.2020.00029>
- Melchels, F. P. W., Domingos, M. A. N., Klein, T. J., Malda, J., Bartolo, P. J., & Hutmacher, D. W. (2012). Additive manufacturing of tissues and organs. *Progress in Polymer Science*, 37(8), 1079–1104. <https://doi.org/10.1016/j.progpolymsci.2011.11.007>

- Miyazaki, Y., Soliman, O. I., Abdelghani, M., Katsikis, A., Naz, C., Lopes, S., Warnack, B., Cox, M., Onuma, Y., & Serruys, P. W. (2017). Acute performance of a novel restorative transcatheter aortic valve: Preclinical results. *EuroIntervention*, 13(12), e1410–e1417. <https://doi.org/10.4244/EIJ-D-17-00554>
- Mostaed, E., Sikora-Jasinska, M., Drelich, J. W., & Vedani, M. (2018). Zinc-based alloys for degradable vascular stent applications. *Acta Biomaterialia*, 71, 1–23. <https://doi.org/10.1016/j.actbio.2018.03.005>
- Nunley, R. M., Ellison, B. S., Ruh, E. L., Williams, B. M., Foreman, K., Ford, A. D., & Barrack, R. L. (2012). Are patient-specific cutting blocks cost-effective for total knee arthroplasty? *Clinical Orthopaedics & Related Research*, 470(3), 889–894. <https://doi.org/10.1007/s11999-011-2221-3>
- Oberweis, C. V., Marchal, J. A., López-Ruiz, E., & Gálvez-Martín, P. (2020). A worldwide overview of regulatory frameworks for tissue-based products. *Tissue Engineering B: Reviews*, 26(2), 181–196. <https://doi.org/10.1089/ten.teb.2019.0315>
- O'Connor, M. I., & Blau, B. E. (2019). The economic value of customized versus off-the-shelf knee implants in medicare fee-for-service beneficiaries. *American Health and Drug Benefits*, 12(2), 66–73. [http://ahbonline.com/components/com\\_mams/dl.php?dlid=1793](http://ahbonline.com/components/com_mams/dl.php?dlid=1793).
- O'Riordan, M. (2019). *Three years on, absorb BVS still doesn't improve myocardial blood flow*. TCTMD, cardiovascular research foundation.
- Pantaleo, A., Jafrancesco, G., Buia, F., Leone, A., Lovato, L., Russo, V., Di Marco, L., Di Bartolomeo, R., & Pacini, D. (2016). Distal stent graft-induced new entry: An emerging complication of endovascular treatment in aortic dissection. *Annals of Thoracic Surgery*, 102(2), 527–532. <https://doi.org/10.1016/j.athoracsur.2016.02.001>
- Parthasarathy, J., Starly, B., & Raman, S. (2008). Design of patient specific porous titanium implants for craniofacial applications. *Technical Paper-Society of Manufacturing Engineers*, 116.
- Patel, C., Loughran, D., Jones, R., Abdulmajed, M., & Shergill, I. (2017). The resonance metallic ureteric stent in the treatment of chronic ureteric obstruction: A safety and efficacy analysis from a contemporary clinical series. *BMC Urology*, 17(1). <https://doi.org/10.1186/s12894-017-0204-8>
- Paxton, N. C., Allenby, M. C., Lewis, P. M., & Woodruff, M. A. (2019). Biomedical applications of polyethylene. *European Polymer Journal*, 118, 412–428. <https://doi.org/10.1016/j.eurpolymj.2019.05.037>
- Paxton, N. C., Dinoro, J., Ren, J., Ross, M. T., Daley, R., Zhou, R., Bazaka, K., Thompson, R. G., Yue, Z., Beirne, S., Harkin, D. G., Allenby, M. C., Wong, C. S., Wallace, G. G., & Woodruff, M. A. (2021). Additive manufacturing enables personalised porous high-density polyethylene surgical implant manufacturing with improved tissue and vascular ingrowth. *Applied Materials Today*, 22. <https://doi.org/10.1016/j.apmt.2021.100965>
- Paxton, N. C., Lanaro, M., Bo, A., Crooks, N., Ross, M. T., Green, N., Tetsworth, K., Allenby, M. C., Gu, Y., Wong, C. S., Powell, S. K., & Woodruff, M. A. (2020). Design tools for patient specific and highly controlled melt electrowritten scaffolds. *Journal of the Mechanical Behavior of Biomedical Materials*, 105, 103695. <https://doi.org/10.1016/j.jmbbm.2020.103695>
- Paxton, N. C., Nightingale, R. C., & Woodruff, M. A. (2022). Capturing patient anatomy for designing and manufacturing personalized prostheses. *Current Opinion in Biotechnology*, 73, 282–289. <https://doi.org/10.1016/j.copbio.2021.09.004>

- Paxton, N. C., Powell, S. K., & Woodruff, M. A. (2016). Biofabrication: The future of regenerative medicine. *Techniques in Orthopaedics*, 31(3), 190–203. <https://doi.org/10.1097/BTO.0000000000000184>. Lippincott Williams and Wilkins.
- Peycelon, M., Rossignol, G., Muller, C. O., Carricaburu, E., Philippe-Chomette, P., Paye-Jaouen, A., & El Ghoneimi, A. (2016). Testicular prostheses in children: Is earlier better? *Journal of Pediatric Urology*, 12(4), 237.e1–237.e6. <https://doi.org/10.1016/j.jpurol.2016.04.022>
- Pibarot, P., & Dumesnil, J. G. (2009). Prosthetic heart valves: Selection of the optimal prosthesis and long-term management. *Circulation*, 119(7), 1034–1048. <https://doi.org/10.1161/CIRCULATIONAHA.108.778886>
- Porpiglia, F., Amparore, D., Checcucci, E., Autorino, R., Manfredi, M., Iannizzi, G., & Fiori, C. (2018). Current use of three-dimensional model technology in urology: A road map for personalised surgical planning. *European Urology Focus*, 4(5), 652–656. <https://doi.org/10.1016/j.euf.2018.09.012>
- Putzier, M., Strube, P., Cecchinato, R., Lamartina, C., & Hoff, E. K. (2017). A new navigational tool for pedicle screw placement in patients with severe scoliosis. *Clinical Spine Surgery*, 30(4), E430–E439. <https://doi.org/10.1097/BSD.0000000000000220>
- Saidy, N. T., Wolf, F., Bas, O., Keijdener, H., Hutmacher, D. W., Mela, P., & De-Juan-Pardo, E. M. (2019). Biologically inspired scaffolds for heart valve tissue engineering via melt electrowriting. *Small*, 15(24). <https://doi.org/10.1002/smll.201900873>
- Schwartz, A., Money, K., Spangehl, M., Hattrup, S., Claridge, R. J., & Beauchamp, C. (2015). Office-based rapid prototyping in orthopedic surgery: A novel planning technique and review of the literature. *American Journal of Orthopedics (Belle Mead, N.J.)*, 44(1), 19–25.
- Shahali, H., Jaggesar, A., & Yarlagadda, P. K. D. V. (2017). Recent advances in manufacturing and surface modification of titanium orthopaedic applications. *Procedia Engineering*, 174, 1067–1076. <https://doi.org/10.1016/j.proeng.2017.01.259>. Elsevier Ltd.
- Siu, T. L., Rogers, J. M., Lin, K., Thompson, R., & Owbridge, M. (2018). Custom-made titanium 3-dimensional printed interbody cages for treatment of osteoporotic fracture-related spinal deformity. *World Neurosurgery*, 111, 1–5. <https://doi.org/10.1016/j.wneu.2017.11.160>
- Skewes, J., Chen, M. Y., Forrestal, D., Rukin, N. J., & Woodruff, M. A. (2021). 3D printing improved testicular prostheses: using lattice infill structure to modify mechanical properties. *Frontiers in Surgery*, 8. <https://doi.org/10.3389/FSURG.2021.626143>
- Somszor, K., Bas, O., Karimi, F., Shabab, T., Saidy, N. T., O'Connor, A. J., Ellis, A. V., Hutmacher, D., & Heath, D. E. (2020). Personalized, mechanically strong, and biodegradable coronary artery stents via melt electrowriting. *ACS Macro Letters*, 9(12), 1732–1739. <https://doi.org/10.1021/acsmacrolett.0c00644>
- Sorokina, Y. (2018). *Personalized hip and knee replacements: U.S. manufacturers battle for innovation spotlight* (Vol. 5). Orthopedic Design & Technology.
- Sparks, D. S., Saifzadeh, S., Savi, F. M., Dlaska, C. E., Berner, A., Henkel, J., Reichert, J. C., Wullschleger, M., Ren, J., Cipitria, A., McGovern, J. A., Steck, R., Wagels, M., Woodruff, M. A., Schuetz, M. A., & Hutmacher, D. W. (2020). A preclinical large-animal model for the assessment of critical-size load-bearing bone defect reconstruction. *Nature Protocols*, 15(3), 877–924. <https://doi.org/10.1038/s41596-019-0271-2>

- Steinert, A. F., Beckmann, J., Holzapfel, B. M., Rudert, M., & Arnholdt, J. (2017). Bicompartimental individualized knee replacement. *Operative Orthopädie und Traumatologie*, 29(1), 51–58. <https://doi.org/10.1007/s00064-017-0484-x>
- Stryker. (2017). MEDPOR Plastic surgery. [https://cmf.stryker.com/assets/files/50/cmf-br-94\\_rev-none\\_13909-medpor-plastics-brochure.pdf](https://cmf.stryker.com/assets/files/50/cmf-br-94_rev-none_13909-medpor-plastics-brochure.pdf).
- Stryker. (2018). iD Solutions. <https://www.stryker.com/us/en/craniomaxillofacial/systems/id-solutions.html>.
- Stryker, U. S. A. (2018). <https://www.stryker.com/us/en/about/news/2018/stryker-launches-next-generation-trident-ii-acetabular-system.html>.
- Stryker. (2021a). Stryker | 3D systems: Advancing personalized surgery, together. <https://cmf.stryker.com/products/3d-systems>.
- Stryker. (2021b). Stryker CMF customized implant PMMA. [https://cmf.stryker.com/assets/files/16/2021-29598\\_peek\\_customized\\_implant\\_brochure\\_update\\_2021.pdf](https://cmf.stryker.com/assets/files/16/2021-29598_peek_customized_implant_brochure_update_2021.pdf).
- Stryker. (2022). PEEK Customized Implant. <https://cmf.stryker.com/products/peek-customized-implant>.
- Stuijffzand, W. J., Schumacher, S. P., Driessen, R. S., Lammertsma, A. A., Bakker, A. L., Rijnierse, M. T., van Rossum, A. C., van de Ven, P. M., Nap, A., Appelman, Y., van Royen, N., van Leeuwen, M. A., Lemkes, J. S., Raijmakers, P. G., & Knaapen, P. (2019). Myocardial blood flow and coronary flow reserve during 3 years following bioresorbable vascular scaffold versus metallic drug-eluting stent implantation. *JACC: Cardiovascular Interventions*, 12(10), 967–979. <https://doi.org/10.1016/j.jcin.2019.03.004>
- Tarsitano, A., Battaglia, S., Crimi, S., Ciocca, L., Scotti, R., & Marchetti, C. (2016). Is a computer-assisted design and computer-assisted manufacturing method for mandibular reconstruction economically viable? *Journal of Cranio-Maxillofacial Surgery*, 44(7), 795–799. <https://doi.org/10.1016/j.jcms.2016.04.003>
- Tartara, F., Bongetta, D., Pilloni, G., Colombo, E. V., & Giombelli, E. (2020). Custom-made trabecular titanium implants for the treatment of lumbar degenerative discopathy via ALIF/XLIF techniques: Rationale for use and preliminary results. *European Spine Journal*, 29(2), 314–320. <https://doi.org/10.1007/s00586-019-06191-y>
- Taylor, B. C., French, B. G., Ty Fowler, T., Russell, J., & Poka, A. (2012). Induced membrane technique for reconstruction to manage bone loss. *Journal of the American Academy of Orthopaedic Surgeons*, 20(3), 142–150. <https://doi.org/10.5435/JAAOS-20-03-142>
- Tetsworth, K., Woloszyk, A., & Glatt, V. (2019). 3D printed titanium cages combined with the Masquelet technique for the reconstruction of segmental femoral defects. *OTA International: The Open Access Journal of Orthopaedic Trauma*, 2(1), e016. <https://doi.org/10.1097/otj.0000000000000016>
- Tetsworth, K., Block, S., & Glatt, V. (2017). Putting 3D modelling and 3D printing into practice: Virtual surgery and preoperative planning to reconstruct complex post-traumatic skeletal deformities and defects. *SICOT-J*, 3. <https://doi.org/10.1051/sicotj/2016043>
- Tetsworth, K. D., & Mettyas, T. (2016). Overview of emerging technology in orthopedic surgery: What is the value in 3d modeling and printing? *Techniques in Orthopaedics*, 31(3), 143–152. <https://doi.org/10.1097/BTO.0000000000000187>. Lippincott Williams and Wilkins.
- Thayaparan, G. K., Owbridge, M. G., Thompson, R. G., & D'Urso, P. S. (2018). Designing patient-specific 3D printed devices for posterior atlantoaxial transarticular fixation surgery. *Journal of Clinical Neuroscience*, 56, 192–198. <https://doi.org/10.1016/j.jocn.2018.06.038>

- Therapeutic Goods Administration (TGA). (2020). Personalised medical devices (including 3D-printed devices) Regulatory changes for custom-made medical devices. *Therapeutic Goods Administration (TGA)*. <https://www.tga.gov.au/resource/personalised-medical-devices-including-3d-printed-devices>.
- Treasure, T., Takkenberg, J. J. M., Golesworthy, T., Rega, F., Petrou, M., Rosendahl, U., Mohiaddin, R., Rubens, M., Thornton, W., Lees, B., & Pepper, J. (2014). Personalised external aortic root support (PEARS) in Marfan syndrome: Analysis of 1-9 year outcomes by intention-to-treat in a cohort of the first 30 consecutive patients to receive a novel tissue and valve-conserving procedure, compared with the published results of aortic root replacement. *Heart*, 100(12), 969–975. <https://doi.org/10.1136/heartjnl-2013-304913>
- US Food and Drug Administration (FDA). (2017). *Technical considerations for additive manufactured medical devices*. US Food and drug administration (FDA). <http://www.regulations.gov>.
- Vogt, B. (2020). A new customized ureteral stent with nonrefluxing silicone end-piece to alleviate stent-related symptoms in malignant diseases. *Urology*, 137, 45–49. <https://doi.org/10.1016/j.urology.2019.12.022>
- Willemse, K., Nizak, R., Noordmans, H. J., Castelein, R. M., Weinans, H., & Kruyt, M. C. (2019). Challenges in the design and regulatory approval of 3D-printed surgical implants: A two-case series. *The Lancet Digital Health*, 1(4), e163–e171. [https://doi.org/10.1016/S2589-7500\(19\)30067-6](https://doi.org/10.1016/S2589-7500(19)30067-6)
- Xia, J. J., Phillips, C. V., Gateno, J., Teichgraeber, J. F., Christensen, A. M., Gliddon, M. J., Lemoine, J. J., & Liebschner, M. A. K. (2006). Cost-effectiveness analysis for computer-aided surgical simulation in complex crano-maxillofacial surgery. *Journal of Oral and Maxillofacial Surgery*, 64(12), 1780–1784. <https://doi.org/10.1016/j.joms.2005.12.072>
- Yao, A., George, D. M., Ranawat, V., & Wilson, C. J. (2021). 3D printed acetabular components for complex revision arthroplasty. *Indian Journal of Orthopaedics*, 55(3), 786–792. <https://doi.org/10.1007/s43465-020-00317-x>

# Index

'Note: Page numbers followed by "f" indicate figures and "t" indicate tables.'

## A

Accurate models, 429

Acoustic Radiation Force Impulse (ARFI),  
312–313

Acoustic rhinometry (AR), 774

Actin–Myosin filaments (AM filaments),  
551–552

Activation–resorption–reversal–formation  
sequence (ARRF sequence), 520

Activities of Daily Living (ADL), 185

Adaptability, 332

Additive manufacturing (AM), 679–680

Adenosine Diphosphate (ADP), 598–602

Adenosine Triphosphate (ATP), 552

Adhesion modeling for cells, 598–602

elastic regime, 599–601

viscous regime, 601–602

Advanced materials for mechanoelectrical stimula-  
tion coupling, 576–577

Advection–reaction–diffusion equations, 40–41

Aeroelasticity, 470–471

approximation, 472

Aerosolized airborne bacteria and virus inhalation,  
276–277

materials and method, 278–280

computational model, 278

governing equations, 279–280

results, 280–283

Aerosolized drugs, 228

Aerosols, 282

delivery, 228

deposition efficiency, 283

diameter, 281

particles, 234

Agonistic muscles, 96–97

Air puff

test, 467, 475

three-dimensional CFD turbulence model of,  
475–476

tonometry technique, 467

traverses on cornea, 476

Airflow, 231–234, 256

patterns in healthy and stented airways, 235–239  
rate, 281

turbulent patterns in healthy and stented airways,  
239–240

Airways stenting technique, 230

Algebraic differential equations (DAEs), 22

Alkaline phosphatase (ALP), 518

Alloplastic mandibular reconstruction methods,  
430–432

computer-aided design of mandibular models,  
432

Alloplastics, 681–682

Alpha motor neurons (aMot), 173–175

Alveolar bone cleft reconstruction, 775–776

American Academy of Paediatric Dentistry  
(AAPD), 700

Amniotic fluid volumes measurement, 307–308

Amyotrophic lateral sclerosis, 190–191

Anatomical detail required for clinical  
applications, 343–345

Anatomical joints, 146

Anatomography, 6

Anatomy reconstruction, foot digital twin,  
337–338

Anatomy simplifications model, 335

Angle Closure Glaucoma (ACG), 469

Animal models, 533

Ankle CM&S not yet in clinic, 350–353

Ankle joint movements, 332

Ankle-related arthrodesis, 332–333

ANSYS, 280

Antagonistic muscles, 96–97

Anterior cruciate ligament (ACL), 87–88, 138

ACL-deficient joint stability, 98–99

Antisclerostin, 504–505

Antral contraction waves (ACWs), 381

AnyBody Managed Model Repository (AMMR),  
127

AnyBody Modeling System (AMS), 143

applications, 148–153

fundamental science applications, 148–149

industrial product design, 150

orthopedic applications, 149–150

sports, 151–152

workplace ergonomics, 153

digital human models and digital patient,

155–156

software design choices, 144–146

v.7.3.3, 127

AnyScript, 145

AnyScript Managed Model Repository (AMMR),

146

- Aortic arch behaviour  
methods, 291–294  
boundary conditions and numerical solution, 293–294  
geometry reconstruction and grid generation, 291  
governing equations, 292–293  
results, 294–297
- Aortic arch pressoreceptor, 290
- Aqueous humor, 469
- Arbitrary Lagrangian–Eulerian formulation (ALE formulation), 292–293, 475–476, 631–632
- Archimedean copulas, 35
- Area under curve (AUC), 806
- Areal bone mineral density (aBMD), 525
- Arms26 model, 172–173
- Arterial scale flow, 614–619
- Arteriovenous fistula (AV fistula), 206
- Artificial intelligence (AI), 8–12, 14, 64, 311–312, 805–806
- Artificial Neural Networks (ANN), 65, 69–71, 108–109
- Artificial neurons, 65
- Aspect Ratio (AR), 572
- Assclerostin, 504–505
- Atheroma plaque, 64–65  
3D parametric study, 66–68  
mathematical methods for regression, 68–77  
problem, 66–68  
source data, 68
- Atherosclerosis, 630
- Atherosclerosis disease, 64–65
- Atherosclerotic plaque, 66–67
- Atlas-based templates, 114–115
- Augmented reality (AR), 665, 701
- Australian Register of Therapeutic Goods (ARTG), 862
- B**
- Bacteria, 467
- Bacterial aerosols, 278
- Bacterial diseases, 285
- Baroreceptor activation therapy (BAT), 204–206
- Baroreceptors, 290
- Baseline model, 231
- Basic multicellular units (BMU), 520
- Belin/Ambrósio Enhanced Ectasia total deviation index (BAD-D), 479
- Bell model, 599
- Big data, 156
- Bilateral renal artery stenosis, 203
- Bio-digital twin, 166
- Bioaerosols, 277–278, 283–284
- Biological processes, 533, 603  
adhesion modeling for cells, 598–602  
models for, 598–603  
simple model for thrombin-controlled coagulation, 602–603
- SPH solid evolution for remodeling processes, 603
- Biomarkers for bone formation, 536
- Biomechanical methods, 372–373, 719–726  
dynamics, 725–726  
kinematic definitions and theory, 720–724  
kinetics, 724–725
- Biomechanical uterine prolapse simulation, 218
- Biomechanics, 684–687  
of fracture  
bone cells, 517–519  
bone mechanical properties and fracture, 521–524  
bone modeling and remodeling, 520–521  
bone physiology, 516–517  
model validation, 528–531  
predictions of bone remodeling, 531–536  
predictions of bone strength with finite element models, 525–528
- macro/biomechanics, 168
- meso/biomechanics, 168
- micro/biomechanics, 168
- Biomedical engineering, 20–21
- Biophysical profile measurement, 307–308
- Biosimulations, 789–790
- Biotechnology, 20–21
- Bisphosphonate, 504–505
- Blood, 494  
clotting, 620  
coagulation and clot formation modeling, 620–630  
background, 620–622  
simple SPH coagulation model and predictions, 622–630
- flow, 592  
simulation, 144
- Blood pressure (BP), 203, 290
- Body Fluids, 201
- Body Mass Index (BMI), 133
- Body models, 148
- “BodyParts3D”, 6
- Body’s epithelial layer  
collisions and rigid body dynamics in SPH, 366
- computational methods, 363–371

- DEM for motion and collisions of particles, 365–366
- DEM-SPH coupling for slurry simulation, 367
- ingestion and oral digestion, 371–381  
example simulation scenario, 373–381
- large intestine, 392–399
- liquid transport and droplet formation in respiratory tract, 399–416
- small intestine, 387–391
- stomach, 381–387
- Boltzmann constant, 259
- Bone formation rate (BFR), 534–535
- Bone morphogenetic proteins (BMP), 495
- Bone multicellular units (BMU), 500
- Bone resorption rate (BRR), 534–535
- Bone surface–volume ratio (BS/BV), 534–535
- Bone volume (BV), 523
- Bone volume fraction (BV/TV), 523
- Bones, 121, 521  
adaptation algorithm, 532–533  
cells, 517–519, 518f  
computational models of bone remodeling in response to mechanical stimuli, 496–503  
fluid flow as mechanical stimulus, 502–503  
incorporation of stress, strain, and damage, 500–502  
SED as mechanical stimulus, 496–500
- elasticity, 523  
stress–strain curves, 524f
- fracture, 525
- geometry, 527
- graft, 681
- homeostasis, 521
- lining cells, 519
- marrow, 494
- mechanical fracture, 521–524  
bone elasticity, 523  
bone post-elastic behavior, 523–524  
bone time-dependent properties, 524
- mechanical properties, 521–524  
bone elasticity, 523  
bone post-elastic behavior, 523–524  
bone time-dependent properties, 524
- mechanics, 144
- microstructure, 523
- model validation, 528–531
- modeling, 520–521
- modeling and remodeling, 520–521
- physiology, 516–517
- post-elastic behavior, 523–524
- predictions of bone remodeling, 531–536
- predictions of bone strength with finite element models, 525–528
- CT-based FE models, 526–527
- DXA-based models, 525
- HR-pQCT-based FE models, 527
- MicroCT-based FE models, 527–528
- remodeling, 520–521, 641–644  
basics of, 493–496
- bone adaptation algorithm and implementation in FE framework, 532–533
- mechanoregulation, 531–532
- morphometric and densitometric analysis, 534–535
- predictions of, 531–536
- process, 493–494
- spatial analysis and biomarkers for bone formation, 536
- unit, 519f
- validation for murine studies, 533–534
- time-dependent properties, 524
- tissues, 526–527
- Boundary condition method, 293–294
- Bowman’s membrane, 467–468
- Brain stroke, 829–830
- Brownian force, 259
- C**
- Cadaver template, 128
- Cadaver-based lower extremity model, 127–130  
scaling of template model to subject-specific data, 129–130
- Calibration processes, 712
- Canalicular, 517
- Cancer cells, 306
- Cardan angles, 124–125
- Cardiac cells, 567–568
- Cardiac output (CO), 203
- Cardiac Progenitor cells (CPCs), 574
- Cardiac sympathetic nerve activity, 205–206
- Cardiac tissue, 548–549, 560–561
- Cardinal ligament, 216
- Cardiomyocytes (CMs), 548
- Cardiovascular diseases, 548
- Cardiovascular surgery, 851
- Cardiovascular system, 290
- Cartesian formulation, 124–125
- Cartilage, 121
- Cauchy–Green deformation tensor, 451–452
- Cauchy–Green tensor, 219
- Cell junctions (CJ), 558
- Cells, 567, 574–576  
adhesions modulated by ECM stiffness, 569–570

- Cells (*Continued*)  
 cell-based therapies, 426  
 cell–cell adhesion, 558–559  
 cell–cell contact forces, 558, 565–566  
 cell–cell interaction, 549, 557  
 cell–ECM interaction, 549  
 contractions, 566  
 differentiation, 560–561  
     modulated by ECM stiffness, 566–568  
 electrotaxis, 555–556  
 fate decision, 559–560  
 internal deformations, 554–555  
 maturation, 560  
 mechanical model, 553  
 mechanics, 549–550  
 mechanobiology, 550–551  
 mechanotaxis, 553–555  
 membrane, 553  
 model, 169  
 motility, 552–553  
 proliferation, 561  
 traction forces, 555
- Cellular model, 167
- Center of mass (CoM), 743
- Central corneal lamellae, 445–446
- Central corneal thickness (CCT), 476–478
- Central motor programs, 188
- Central nervous system (CNS), 92
- Centric relation (CR), 785
- Chemical field, 555–556
- Chocolate, 373  
     food model, 373  
     melting on tongue, 373–381
- Chronic bronchitis and emphysema, 229
- Chronic obstructive pulmonary disease (COPD), 229, 253–255
- Cleft care, 768
- Cleft lip, 767  
     and nasal deformity repair, 771–773  
     digital modeling in cleft lip nasal deformity, 772f
- Cleft palate repair, 773–774  
     application of digital modeling in, 774f
- Clinical dataset, 479
- Clinical instability, 86–87
- Co-creation framework  
     analysis, 667  
     ideation, 665  
     modeling, 665–667  
     stages of, 665–667  
     visualization, 667
- Coactivity, role of, 95–96
- Cognitive Behavioral Therapy, 700
- Collagen, 285  
     fibers, 443–446  
         anisotropy, 456  
         network, 467–468  
     toward accurate models of collagen fibrils, 449–452
- Collisional forces, 375–376
- Color Doppler Ultrasound (CDU), 308–309
- Component models, 167
- Computational fluid dynamics (CFD), 228, 255, 290, 472–473, 592, 662–663, 726, 774  
     preprocessor software, 278  
     three-dimensional CFD turbulence model of air puff, 475–476
- Computational methods, 88–89, 276–277, 593–598  
     continuity equation, 593–598  
     integration of SPH ordinary differential equations, 597–598  
     momentum equation  
         for fluid, 593–594  
             for solid deformation, 594  
     pressure solution, 595  
     soft bodies with flexible surfaces, 596  
     solid boundary conditions, 595  
     species concentration and diffusion, 597  
     SPH method for fluids and solids, 593–598
- Computational modeling and simulation (CM&S), 332  
     potential of foot CM&S, 335–336
- Computational modeling of aerosol particle airflow patterns in healthy and stented airways, 235–239  
     airflow turbulent patterns in healthy and stented airways, 239–240  
     clinical background, 228–230  
     materials and methods, 231–235  
         geometries, 231  
         numerical model and boundary conditions, 231–235
- particle deposition and transport, 240  
     regional deposition fractions, 243–245  
     validation of numerical findings, 240–242  
         comparison between healthy and stented human upper airways, 242
- Computational models, 171, 218, 228, 278, 503, 549  
     biomechanical properties of soft tissues and mesh implant, 220  
     biomechanical uterine prolapse simulation, 218

- of bone remodeling in response to mechanical stimuli, 496–503  
 fluid flow as mechanical stimulus, 502–503  
 incorporation of stress, strain, and damage, 500–502  
 SED as mechanical stimulus, 496–500  
 of implant, 219–220  
 isotropic constitutive model, 218–219  
 mechanism of development of POP, 215–218  
 of pelvic cavity, 219  
 personalized models to repair uterine prolapse, 223  
 uterine prolapse simulation, 221  
 Computational single-cell models, 570–571  
 Computational technology, 143–144  
 Computed tomography (CT), 4, 308–309, 695, 788, 849–850  
 CT-based FE models, 526–527  
 CT-based upper airway model, 256–257  
 Computer and manufacturing technology (CAM technology), 769–770, 849–850  
 Computer graphics (CG), 668  
 Computer science, 63–64  
 Computer technology, 228, 785  
 Computer vision–based human motion, 713  
 Computer-aided design (CAD), 13, 349, 695–696, 769–770, 849–850  
 of mandibular models, 432  
 models, 662–663  
 Computer-aided engineering (CAE), 13, 144, 662, 665–667  
 Computer-aided manufacturing technology (CAM technology), 695–696  
 Computer-assisted therapy, 63–64  
 Cone beam computed tomography (CBCT), 429, 685–687, 788  
 Continuity equations, 279  
 Copulas, 20–21, 32–36  
 mathematical definition, 33–34  
 nonparametric copulas, 35–36  
 parametric models, 34–35  
 Sklar's theorem, 34  
 Cornea, 467  
 air puff traverses and pressure on, 476  
 distinct region-specific anisotropy of, 446  
 in silico biomechanical models of, 447–457  
 multiphasic and multiphysics computational models of cornea, 452–454  
 simulation-based subject-specific surgical planning, 454–457  
 toward accurate models of collagen fibrils, 449–452  
 viscoelastic behavior of, 446–447  
 Corneal biomechanics, 446, 455, 467–469  
 aeroelasticity, 470–471  
 air puff traverses and pressure on cornea, 476  
 classification of fluid–structure interaction problems, 471–472  
 ex vivo destructive testing, 468–469  
 fIOP, 481–483  
 fSSI, 483–484  
 glaucoma, 469–470  
 numerical methods, 472–476  
 three-dimensional CFD turbulence model of air puff, 475–476  
 three-dimensional eye model, 473–474  
 parametric study statistics, 476–479  
 in vivo nondestructive testing, 468  
 Corneal hysteresis (CH), 468  
 Corneal material stress–strain index (fSSI), 483–484  
 Cortical area fraction (Ct. Ar/Tt. Ar), 534–535  
 Cortical bone area (Ct. Ar), 534–535  
 Cortical thickness (Ct. Th), 534–535  
 Cortical total cross-sectional area (Tt. Ar), 534–535  
 Corticomotoneurons (CM), 179–180  
 Corvis Biomechanical Index (CBI), 485  
 Corvis IOP readings (CVS-IOP), 482–483  
 Cosimulation engine (CSE), 472–473  
 Coupling model, 472  
 Courant–Friedrichs–Lewy (CFL), 475  
 Craniofacial reconstruction, 681  
 Craniofacial surgery, 786–787  
 in VSP, 794  
 Craniomaxillofacial surgery (CMF surgery), 855–856  
 custom-made cranial implants, 856f  
 Critical plaque wall stress (CPWS), 631–632  
 Cross-sectional modeling of stroke severity and corticospinal residuum, 186–188  
 Cross-validation process, 71  
 Cumulative distribution function (CDF), 28, 31  
 Curvature analysis, 112–114  
 Cutting cones, 494  
 Cyber-Physical-Systems (CPS), 8–12  
 Cytoskeleton, 553
- D**
- Damage, incorporation of, 500–502  
 Darcy drag force, 367  
 Darcy drag law, 367  
 Data, 5, 362  
 generation, 42

- Data (*Continued*)  
 preprocessing, 811  
 uncertainty management, 28–30
- Decision support system works, 74–75
- Decision trees, 108–109
- Decision-making, 812–813
- Deep learning techniques, 108–109, 715–716
- Deep vein thrombosis (DVT), 620
- Degree of anisotropy (DA), 523
- Degrees of freedom (DoFs), 129, 177–178, 721
- Densitometric analysis, 534–535
- Dental anxiety, 699–700
- Dental implant, 694–695
- Dental records, 789
- Deposition efficiency, 281
- Deposition fraction (DF), 259, 263
- Descemet's membrane, 467–468
- Design of experiments (DOE), 31–32
- Design space optimization method (DSO method), 505
- Diabetes, 527
- Diabetic foot, 186
- Diabetic neuropathy, 186
- DiffusionTensor Imaging (DTI), 186–187
- Digital analysis methods, 768
- Digital co-creation framework  
 background, 661–663  
 lack of customer participation in conventional product development, 662–663  
 transition from mass customization to mass individualization, 661–662  
 case study, 668–673  
 analysis and revise, 672–673  
 ideation and configure, 668–669  
 modeling and modify, 669–672  
 visualization and experience, 673
- methodology, 663–667  
 stages of co-creation framework, 665–667  
 theoretical bases of the co-creation framework, 663–665
- Digital Human Modeling (DHM), 8–12, 662–663, 849  
 in cleft care  
 alveolar bone cleft reconstruction, 775–776  
 cleft lip and cleft lip nasal deformity repair, 771–773  
 cleft palate repair, 773–774  
 orthognathic surgery in cleft care, 776–777  
 presurgical infant orthopedics, 769–771
- Digital Human Models, 152, 155–156
- Digital image correlation (DIC), 446–447, 451, 530
- Digital Imaging and Communications in Medicine (DICOM), 291, 695
- Digital Patient, 152, 155–156, 660–661
- Digital sketching tools, 669
- Digital smile design, 696–697
- Digital technology, 768
- Digital transformation, 8–12
- Digital Twin (DT), 3–5, 8–15, 710. *See also* Foot digital twin  
 alternative or complementary numerical approaches to FEA for in silico bone remodeling, 505–506  
 anatomography, 6  
 basics of bone remodelling, 493–496  
 of bone remodeling process, 493–494  
 computational models of bone remodeling in response to mechanical stimuli, 496–503  
 effects of implants and pharmaceuticals, 503–505  
 performance and injury, 729–749  
 diving, 736–742  
 snow skiing, 742–749  
 swimming, 729–735
- VHP, 4–6
- VPH, 6–8
- Digital Volume Correlation approaches (DVC approaches), 527, 530
- Digital workflow in dental implantology, 696–701  
 digital smile design, 696–697  
 software-guided implant surgery, 696–697  
 virtual reality  
 and dental anxiety, 699–700  
 and dental education, 700–701
- Digitised Communication in Medicine (DICOM), 429
- Direct current EF (dcEF), 555–556
- Discrete Element Method (DEM), 365, 417  
 DEM-SPH coupling for slurry simulation, 367  
 0D model of microbial fermentation, 369–370  
 flexible and deformable surfaces, 367–368  
 genome-scale metabolic models, 368–369  
 potentially powerful multiscale approach, 370–371  
 reduced 1D models, 370  
 specialized intestinal models, 368–371  
 for motion and collisions of particles, 365–366
- Discrete Phase Model method (DPM method), 277–278
- Dissipative Particle Dynamics (DPD), 622

Dive Mechanic software, 755–756  
 Diving technique, 736–742  
 Doppler, modern placental imaging method, 308–310  
 Dorsal Root Ganglion (DRG), 173–175  
 Drag force, 556–557  
 Drugs, 504–505  
   aerosol therapy, 228  
   concentrations, 230  
   delivery, 263  
 Dual energy CT (DECT), 685–687  
 Dual-energy X-ray Absorptiometry (DXA), 525  
   DXA-based models, 525  
   images, 525  
 Dumon stent, 230–231  
 Dynamics-based tracking methods, 126

**E**

Early Diastole (ED), 294–295  
 Eccentricity (Ecc), 534–535  
 Elastic modulus, 523  
 Elastin, 285  
 Electric field (EF), 555–556  
 Electric forces, 556  
 Electrocardiography (ECG), 298–299  
 Electrodes, 163–164  
 Electrolytes, 201  
 Electromyography (EMG), 91–92, 126, 736  
 Electron beam melting (EBM), 853–854  
 Electrophysiological tools, 164–165  
 Electrotaxis, cell, 555–556  
 Empirical copulas, 36  
 Endoprostheses, design and plan of, 432–433  
 Endothelial cells, 295–296  
 Endothelial keratoplasty, 456–457  
 Endothelium layer, 467–468  
 Endurance sports, 151–152  
 Epithelium, 467–468  
 Equilibrium model of spine, 90–91  
 Equilibrium state, 89–90  
 Equivalent strain, 500–502  
 Estrogen, 520–521  
 Euler parameters, 125  
 Euler–Euler method (E-E method), 277–278  
 Euler–Lagrange method (E-L method), 277–280  
 Euler's equation, 124  
 European Virtual Physiological Human (VPH), 3–4  
 Ex vivo destructive testing, 468–469  
 Experimental model, 228  
 Experiments  
   design, 52–57  
   NEUROiD movement simulation platform, 169

External carotid artery (ECA), 617  
 External sensors, 528  
 Extra-Corporeal Membrane Oxygenation (ECMO), 604  
 Extra-personal neglect, VR platform for evaluation of, 835–837  
 Extracellular matrix (ECM), 285, 548  
   cell adhesions modulated by, 569–570  
   cell differentiation modulated by, 566–568  
   discretization, 562  
   electrically stimulated ECM, 574–576  
   mechanically stimulated ECMs, 570–574  
 Eye, 444, 474

**F**

Fast Fatigable muscle fibers (FF muscle fibers), 191–192  
 Feature selection techniques (FS techniques), 806, 811–812, 820–823  
 Feature space, 69–70  
 Fetal Doppler velocimetry measurement, 307–308  
 Fetal growth assessment, 307–308  
 Fetal Growth Restriction (FGR), 307–308  
 Fiber distribution function, 450–451  
 Fick's diffusion law, 365, 597  
 Finite element (FE), 372, 447–449, 457  
   examples of validation studies for, 531  
   implementation in FE framework, 532–533  
   method, 65, 429–430  
   performing finite element analysis of mandible, 429–430  
 Finite Element Analysis (FEA), 216, 372–373, 505, 525, 662–663  
   for *in silico* bone remodelling  
     alternative numerical approaches to, 505–506  
     complementary numerical approaches to, 505–506  
 Finite Element Model (FEM), 75–77, 92, 339, 346, 562, 773  
   predictions of bone strength with, 525–528  
     CT-based FE models, 526–527  
     DXA-based models, 525  
     HR-pQCT-based FE models, 527  
     MicroCT-based FE models, 527–528  
 Finite volume method, 280  
 Finite volume–based discretization techniques, 258  
 First applanation pressure (AP1), 481  
 Fixed cameras, 712

- Flow and remodeling processes  
 blood coagulation and clot formation modeling, 620–630  
 bone remodeling, 641–644  
 computational method, 593–598  
 hemodynamics of vascular disease, 603–619  
 models for biological processes, 598–603  
 plaque rupture in an artery, 630–641
- Flow jets, 277–278
- Flow shear stress (FSS), 631–632
- Fluids, 281, 494  
 coupling domain, 294  
 flow, 502  
 geometries, 291  
 layer, 411  
 as mechanical stimulus, 502–503  
 mechanics, 471
- Fluid–structure interaction method (FSI method), 277–278, 290, 454, 476, 631–632  
 classification of, 471–472
- 10-fold cross validation (10FCV), 813
- Food and Drug Administration (FDA), 214, 681, 861
- Foot and ankle complex, 332
- Foot and ankle surgeries, 334
- Foot biomechanics, 331–332
- Foot CM&S  
 in clinic, 350–353  
 for clinical applications, 345–347  
 for footwear industry, 348–350  
 linear elastic material models, 340  
 potential of, 335–336
- Foot digital twin, 331–336. *See also* Digital Twin (DT)  
 build foot digital twin, 336–342  
 anatomy reconstruction, 337–338  
 initiatives to improve model credibility in healthcare, 341–342  
 loading and boundary conditions, 338–339  
 tissue properties, 339–340  
 verification and validation, 341
- foot biomechanics, 331–332  
 future, 342–353  
 foot and ankle CM&S not yet in clinic, 350–353  
 foot CM&S for clinical applications, 345–347  
 foot CM&S for footwear industry, 348–350  
 level of anatomical detail required for clinical applications, 343–345  
 in silico trials, 342–343
- main foot pathologies by volume, 332–334  
 potential of foot CM&S, 335–336
- Foot finite element, 339
- Foot models, 334, 344
- Foot pathologies by volume, 332–334
- Foot-lower limb “walking” model, 344
- Foot-related arthrodesis, 332–333
- Footwear industry, foot CM&S for, 348–350
- Forward dynamics, 126
- Forward RANK-RANKL signalling, 495
- Foundational Model of Anatomy (FMA), 6
- 4th Industrial Revolution (4IR)Accuracy (ACC), 681, 813
- Frankfurt horizontal plane (FH plane), 787
- Freedom biomechanical model, 97
- Full cartesian method, 146
- Full field tests DIC and DVC, 530–531
- Full-body musculoskeletal model, 155
- Fused deposition modeling (FDM), 679–680
- G**
- Gadolinium-based contrast agents, 317–318
- Gait, 98  
 analysis of gait modifications, 136  
 model, 147–148
- Gas, 305
- Gasser, Ogden, and Holzapfel (GOH), 66–67
- Gastrointestinal tract (GI tract), 362
- Gaussian curvature, 112
- Gaussian random number, 259
- Genome-Scale Metabolic Models (GSMMs), 368–369, 417
- GenWrapper, 811–812
- Geometry reconstruction method, 291
- Ginglymo-arthrodistal joint, 427
- Glaucoma, 465–466, 469–470
- Glioblastoma (GBM), 39–40  
 evolution, 39–57  
 data generation, 42  
 experiments design, 52–57  
 mathematical model, 40–42  
 model adjustment, 43–45  
 model validation, 45–48  
 parameter estimation, 48–52
- Glottal, 277–278
- Glycosaminoglycans (GAGs), 453
- Goldmann applanation tonometer (GAT), 466–467
- Gouy–Chapman membrane charge equations, 555–556
- Governing equations, 279–280, 292–293
- Graphical User Interface (GUI), 144–145, 665  
 GUI-based system, 145

- Graphics media, 665  
 Grid generation method, 291  
 Grid independency analysis, 291  
 Grid parameters, 291  
 Ground reaction forces (GRF), 710
- H**
- $H^+$ -adenosine triphosphatase ( $H^+$ -ATPase), 517–518  
 Hand tracking devices, 834  
 Hardware device selection process, 833  
 Haversian canals, 517  
 Head Mounted Displays (HMDs), 831  
 Health data, 15  
 Healthcare, 13  
     initiatives to improve model credibility in, 341–342  
 Health–risk assessment, 255  
 Heat, 201  
 Heavy inhalations, 237–239  
 Hemodynamics  
     parameters, 291  
     of vascular disease, 603–619  
         arterial scale flow, 614–619  
         explicit modeling of cell mechanics at capillary scale, 605–611  
         white blood cell rolling adhesion, 611–614  
 Hexagonal arrays, 444  
 Hierarchical 3D-1D-0D model, 370–371  
 High-Definition Flow (HDF), 308–309  
 High-Performance Computing (HPC), 15  
 High-resolution peripheral QCT images (HR-pQCT), 527  
     HR-pQCT-based FE models, 527  
 Highest concavity radius (RHC), 481  
 Highest Density Regions (HDR), 38  
 Hooken constitutive model, 594, 727–728  
 Hooken spring model, 599  
 Hook's law, 123  
 Hormones, 201  
 Hounsfield unit value (HU value), 500–502  
 House of quality (HoQ), 662  
 Human body contains multiple bones, 122  
 Human cast model, 228  
 Human eye, 465–466  
 Human Factors and Ergonomics (HFE), 8–12  
 Human health, 319–320, 362  
 Human immunodeficiency virus (HIV), 604  
 Human knee joint, stability of, 97–99  
 Human MS systems, stability of, 91–93  
 Human musculoskeletal systems  
     methods, 88–93  
     criteria of structural stability, 88–91  
     stability of human MS systems, 91–93  
 stability  
     of human knee joint, 97–99  
     of human spine, 94–97  
 Human organs and diseases, 306  
 Human placenta models, 307  
 Human Placenta Project (HPP), 319  
 Human spine  
     role of coactivity, 95–96  
     role of load orientation and elevation, 94–95  
     role of posture and passive ligamentous stiffness, 94  
     stability of, 94–97  
     stability-based multicriteria simulations, 96–97  
 Human upper respiratory system, 278  
 HumMod, 200  
     model content, 201  
     for testing physiological concepts and hypotheses  
         in pathophysiology, 201–208  
             AV fistula, 206  
             BAT, 204–206  
             future of modelling, 206–208  
             salt sensitivity, 203–204  
 Hybrid methods, 366  
 Hyperparathyroidism, 521  
 Hyperthyroidism, 521
- I**
- ICT tools, identification of, 833–834  
 Idealized model, 228–229  
 Idealized Weibel models, 229  
 Image diagnosis, 64–65  
 Image-based models, 290–291  
 Imaging techniques, 214–215  
 Immersed Boundary Method (IBM), 613  
 Implants  
     computational model of implant synthetic, 219–220  
     design, 684–687  
     effects of, 503–505  
     treatment planning, 695–696  
 In silico  
     clinical trials, 343  
     cornea models  
         corneal biomechanics, 445–447  
         in silico biomechanical models of cornea, 447–457  
         medicine, 7–8  
         modeling of mastication, 372  
         trials, 342–343  
 In vivo nondestructive testing, 468

- In-Silico Clinical Trials of medical devices and drugs, 162
- Incremental cost-effectiveness ratio (ICER), 335–336, 352
- Inflationary mechanism, 636–637
- Injury, 749–750
- Instantaneous screw axis (ISA), 723
- Insulin-like growth factor-I (IGF-I), 518–519
- Integrative model development, NEUROiD, 171
- Integrin cell adhesion molecule (ICAM-1), 612
- Interlamellar cohesion (ILC), 451–452
- Intermediate model representation, 164–165
- Internal carotid artery (ICA), 617
- Internal energy equation, 258
- Internal sensors, 528
- International Medical Device Regulators Forum (IMDRF), 851–852, 862
- International Society for Pharmacoeconomics and Outcomes Research (ISPOR), 681
- Interstitial fluid, 443–444, 494
- Intestinal Bowel Disease (IBD), 387–388
- Intraocular pressure (IOP), 443–444, 465–466, 469–470, 476–478
- Intraocular pressure algorithm (fIOP), 481–483
- Intrastromal corneal ring segments (ICRS), 456
- Intravascular ultrasound (IVUS), 66
- Inverse dynamics, 126  
analysis, 134–135
- Inverse kinematics process, 714–715
- Ion channels, 168
- Isootropic constitutive model, 218–219
- J**
- Jaw surgery, postablative reconstructive, 785–786
- Joint angles, 368
- Joint equilibrium states, 92–93
- Joint space narrowing (JSN), 806–807
- Joint space narrowing on lateral (JSL), 806–807
- Joint space narrowing on medial compartment (JSM), 806–807
- K**
- k-epsilon turbulence model, 280
- K-fold cross-validation, 73
- Kellgren and Lawrence (KL), 806–807
- Kelvin–Helmholtz instabilities, 401–402
- Kendall’s tau matrix, 55–57
- Kendall’s  $\tau$  coefficient, 29–30
- Keratoconus, 449, 467–468
- Kernel distribution, 31
- Kernel estimation, 31
- Kernel Trick, 71
- Key performance indicators (KPIs), 352–353
- Kinematically overdeterminate system, 133
- Kinematically scaled model, 132
- Kinematics-driven MS models, 92
- Kinematics-driven optimization approach, 92
- Kirchhoff–Love rod theory, 450
- Knee joint model, 92
- Knee model, 147
- Knee osteoarthritis (KOA), 136, 805–806
- Knowledge-based techniques, 107–108, 111–116.  
*See also* Machine Learning Techniques (MLT)
- curvature analysis, 112–114
  - patient-specific templates, 115–116
  - shape analysis, 111–112
  - SSMs, 115
  - template-based approaches, 114–115
- Kozeny–Carman equation, 367
- L**
- Labor-intensive model, 335
- Lacuno-canicular network (LCN), 517
- Lagrangian discrete phase model, 259
- Lagrangian mesh-free method, 363
- Lagrangian meshfree method, 593
- Lagrangian methods, 725
- Lagrangian scheme techniques, 258
- Lamellae, 445–446
- Laminae boundaries, 167
- Landmarks  
detection of human tissue  
knowledge-based techniques, 111–116  
machine learning techniques, 108–110  
or regions of organs, 109
- Laser-assisted *in situ* keratomileusis (LASIK), 443–444
- Lattice Boltzmann method (LBM), 506
- Learning models, 110
- Least absolute shrinkage and selection operator (Lasso), 824  
regression models, 806–807
- Left lung (LL), 263–264
- Leukemia, 521
- Leukocytes, 611–612
- Levenberg–Marquardt algorithm, 22
- Ligaments, 121, 213–214  
thoracolumbar spine model, 92
- Light, 233–234, 237–239
- Limbs *in silico*  
design and characterization of, 172–179  
lower limb, 177–179  
upper limb, 172–175

- Linear geometric scaling law, 130–131  
 Linear Least Squares (LLS), 23  
 Linear material models, 335  
 Linear scaling  
     functions, 130–131  
     law, 130–131  
 Linear spinal rhythm, 129  
 Linear spring-dashpot, 365  
 Linear Variable Differential Transformer  
     displacement sensors, (LVDT), 528  
 Linearized system, 89–90  
 Linearly scaled model, 132  
 Lipid core, 67, 76  
 Liquid, 383  
     chocolate, 375–376  
     layer, 376  
     mixture, 381–382  
     transport and droplet formation in respiratory tract, 399–416  
 Load orientation and elevation, role of, 94–95  
 Load–displacement curves, 528  
 Loading and boundary conditions, foot digital twin, 338–339  
 Local Field Potential (LFP), 168  
 Long short-term memory model (LSTM model), 807  
 Longitudinal modeling of recovery and computational neurorehabilitation, 188–190  
 Low-density lipoprotein (LDL), 630  
 Lower extremity model, 129  
 Lower limb, 177–179  
     gait models, 332  
 Lower motor neuron (LMN), 190–191  
 Lung contamination, 282–283  
 Lung disease, 284–285  
 Lung injury, 229
- M**
- Machine learning (ML), 806, 812–813  
     models, 806  
     setup, 180–182  
 Machine learning algorithm, 180  
 Machine Learning Techniques (MLT), 63–64, 108–110, 152. *See also* Knowledge-based techniques  
     artificial neural networks, 108–109  
     decision trees, 109  
     support vector machines, 110  
 Macrophage colony-stimulating factor (M-CSF), 517–518  
 Magnesium (Mg), 431  
 Magnetic Resonance Elastography (MRE), 315  
 Magnetic resonance imaging (MRI), 4, 214–215, 306–307, 316–319, 806–807, 849–850  
 Malign tumors, 230  
 Mandible  
     anatomy and biomechanics of, 427–429  
     performing finite element analysis of, 429–430  
 Mandibular defect, 425–426  
 Mandibular modular endoprosthesis, 430–431  
 Mandibular reconstruction techniques  
     alloplastic mandibular reconstruction methods, 430–432  
     anatomy and biomechanics of mandible, 427–429  
     design and plan of endoprostheses, 432–433  
     finite element method, 429–430  
     stress and magnitude of displacement of stem and wing design in unilateral loading conditions, 433–437  
 Manual materials handling (MMH), 750–751  
 Markerless Motion Capture (MMC), 719–729, 773  
     for digital human model construction, 712–719  
         background, 712–713  
         benefits and future applications, 718–719  
         joint angles from inverse kinematics, 717–718  
         of MMC pipeline, 714–718  
         three-dimensional pose reconstruction, 716–717  
         two-dimensional pose estimation models, 715–716  
 Mass customization, 661  
     to mass individualization, transition from, 661–662  
 Mass function, 28  
 Mass individualization, 664  
     transition from mass customization to, 661–662  
 Mass-fat muscle strength scaling law, 133  
 Materials, 432  
 Maternal Doppler velocimetry measurement, 307–308  
 Maternal–fetal network, 306  
 Materno–fetal exchange, 306  
 Mathematical methods for regression, 68–77  
     artificial neural network, 69–71  
     assuring quality of machine, 71–74  
     finite element models, 75–77  
     support vector machine, 71  
     validation with real geometry, 74–75  
         decision support system works, 74–75  
 Mathematical models, 199–200  
     GBM, 40–42  
 Maturation Index (MI), 560

- Maxilla-mandibular relationship (MMR), 785  
 Maximum Likelihood Estimation (MLE), 36  
 Maximum likelihood method, 30–31  
 Maximum Maximal Principal Stress (MPS), 65–66  
 Mean curvature, 112  
 Measured marker-based multibody models, 345  
 Mechanical stimuli based—models, 503  
 Mechanics of materials, 143–144  
 Mechanostat theory, 494–495  
 Mechanotaxis, cell mechanotaxis, 553–555  
 Medical data management, 834  
 use cases, 835  
 Medicine, NEUROiD in, 182–192  
 Mesenchymal stem cells (MSCs), 548  
 Mesh implant, biomechanical properties of, 220  
 Metal artifact reduction (MAR), 685–687  
 Method of moments (MME), 36  
 Micro computed tomography (microCT), 523  
 microCT-based FE models, 527–528  
 techniques, 308–309  
 MicroFE, 527  
 Microfluidics, 20, 39–40  
 Microparticles, 253–255  
 Microprocessors, 143–144  
 Microsoft Word, 145  
 Microstructures, 517  
 Microvascular Flow Imaging (MFI), 309–310  
 Mimics software, 291  
 Mineral, 516  
 Mineral apposition rate (MAR), 534–535  
 Mineral resorption rate (MRR), 534–535  
 Minimum redundancy maximum relevance (mRMR), 824  
 Model adjustment, GBM, 43–45  
 Model complexity correlation, 40  
 Model content, HumMod, 201  
 Model integration type, 165–166  
 Model separability, 26  
 Model validation, 528–531  
 examples of validation studies for FE models, 531  
 full field tests DIC and DVC, 530–531  
 local deformation with strain gauges, 528–529  
 standard mechanical tests, 528  
 Model-Activity-Twinning (MAT), 184  
 Model-View-Controller, 144–145  
 Model–environment connection, 148  
 Modeling human physiology, 201–202  
 Modern placental imaging method  
 Doppler, 308–310  
 MRI, 316–319  
 placental elastography, 315–316  
 sonoelastography, 312–315  
 ultrasound, 307–308  
 volume rendering, 310–312  
 Modern planning, 797  
 comparison between traditional and modern planning, 797–799  
 Mononuclear cells of monocyte–macrophage lineage, 517–518  
 Morphometric analysis, 534–535  
 Morphometric parameters, 523  
 Motion capture–based model, 127–135  
 cadaver-based lower extremity model, 127–130  
 inverse dynamic analysis, 134–135  
 linear geometric scaling law, 130–131  
 mass and inertial properties, 132–133  
 mass-fat muscle strength scaling law, 133  
 overdeterminate kinematic analysis, 133–134  
 parameter identification, 131–132  
 Motoneuron model, 167  
 Motor neuron disease, 190–191  
 Motor unit structure, mechanisms and consequences of aging-induced changes in, 191–192  
 Motor-skills tele-rehabilitation of hands, 840–842  
 Mouth–throat (MT), 263–265  
 Mucous layers, 400  
 Mucus transport, 399–400  
 Multibody dynamics systems, 143–144  
 Multibody modelling, fundamentals of, 123–126  
 Multibody system, 122  
 formulation, 146  
 Multidiscipline platform, 163–166  
 Multifactorial disease, 805–806  
 Multifunction platform, 163–166  
 Multilayer perceptron (MLP), 65  
 Multiphase digesta rheology, 390–391  
 Multiphasic computational models of cornea, 452–454  
 Multiphysics computational models of cornea, 452–454  
 Multiple numerical algorithms, 111  
 Multiscale platform, 163–166  
 Multislice computed tomography (MCT), 788  
 Muscles, 91–92, 95–96, 121  
 cells, 162  
 Muscular forces, 368  
 Musculoskeletal joint, 166–167  
 Musculoskeletal modelling, 148–149, 162, 338  
 Musculoskeletal models, 122, 127–128, 136, 138, 151, 172, 339  
 Musculoskeletal subsystems, 162

Musculoskeletal systems (MS systems), 85–86, 121, 146, 516  
 analysis of gait modifications, 136  
 applications, 139  
 fundamentals of multibody modeling, 123–126  
 motion capture–based model, 127–135  
 Musculoskeletal twinning, 183

## N

Nanoparticles, 253–255  
 deposition, 256  
 transport, 256, 258  
 Narrow validations model, 335  
 Nasal cavity, 681–682  
 Nasal inhalation, 283  
 Nasal rhinomanometry, 774  
 Nasoalveolar molding technology (NAM technology), 769  
 Native tissue repairs, 214  
 Natural head position (NHP), 787  
 Natural neighbor radial point interpolation method (NNRPIM), 506  
 Navier–Stokes equations, 279, 603  
 Nervous system, 172, 200–201  
 Network  
   architecture, 69  
   of canals, 517  
   functional model, 69  
 Neural networks, 108, 505  
 NEUROmotor integration and Design platform (NEUROID platform), 163  
 choosing musculoskeletal model, 172  
 curation and definition, 167–169  
   definition across scale and discipline, 167–168  
   model specification to definition, 167  
   neuromusculoskeletal interface design, 168–169  
 design and characterization of limbs in silico, 172–179  
 design philosophy and architecture, 163–167  
   multiscale, multidiscipline, and multifunction platform, 163–166  
   workflow in NEUROID, 166–167  
 experiment and simulation, 169  
   experiment specification to definition, 169  
   parallelization, 169  
 integrative model development, 171  
 model definition, simulation, and visualization, 167–169  
 movement simulation platform, 163–172

movement training of virtual limbs, 179–182  
 NEUROID in medicine, 182–192  
   clinical triage for spasticity, 184–185  
   clinical trials and experimentation in silico with NEUROID, 184–192  
   cross-sectional modeling of stroke severity and corticospinal residuum, 186–188  
   design and test of prostheses, 185–186  
   diabetic neuropathy–induced diabetic foot, 186  
   limitations, 192  
   longitudinal modeling of recovery and computational neurorehabilitation, 188–190  
   mechanisms and consequences of aging–induced changes in motor unit structure, 191–192  
   medical education and training, 192  
   motor neuron disease, 190–191  
   NEUROID activities, 183  
   NEUROID models, 183  
   peripheral neuropathies, 191  
   spinal cord stimulation, 190  
   twinning in, 183  
   visualization, 169  
 Neuromusculoskeletal interface design, 168–169  
 Neuromusculoskeletal model, 173, 180  
 Neuromusculoskeletal system, 162  
 Neuronal cell models, 163–164  
 Neurons, 69  
 Neuroscience, 187  
 Newton–Euler equations, 124–126  
 Newton–Euler methods, 725  
 Newton’s first law of motion, 123  
 Newton’s laws, 123  
 Newton’s second law of motion, 123  
 Newton’s third law, 123  
 Nodal traction force, 554  
 Non–cell-based therapies, 426  
 Nonlinear analysis predicts, 88–89  
 Nonlinear hyperelastic models, 340  
 Nonparametric copulas, 35–36  
 Nonparametric methods, 31, 37  
 Nonuniform scaling law, 130–131  
 Normal-tension glaucoma (NTG), 469  
 Numerical model and boundary conditions, 231–235  
   continuous phase, 231–234  
   discrete phase, 234–235  
 Numerical solution method, 293–294  
 Nutrients, 305–306

**O**

Occupational injuries, 153  
 Ocular globe, 465–466  
 Ocular Hypertension, 465–466  
 Ocular Response Analyser (ORA), 468  
 Ogden constitutive model, 219  
 Ogden law, 450–451  
 1D models, 370  
 Open Angle Glaucoma (OAG), 469  
 OpenSim models, 172  
 Optical-based markerless systems, 730  
 Optimization-driven model, 97  
 Oral cavity, 681–682  
 Oral digestion  
     example simulation scenario, 373–381  
     ingestion and, 371–381  
 Oral health, 693  
 Ordinary differential equations (ODEs), 22  
 Organic matrix, 516  
 Organs, 107–108  
 Orthodontic methods, 769  
 Orthognathic surgery, 785  
     in cleft care, 776–777  
 Orthognathic surgical planning, 797  
 Orthopedics, 149–150, 338  
     surgery, 853–855  
 Osim\_muscle.xlsx, model, 178–179  
 Osteoarthritis (OA), 85–86, 503, 521  
 Osteoblasts, 518  
 Osteoclast precursor (OCP), 495  
 Osteoclasts, 517–518  
 Osteoconnectivity method, 500  
 Osteocytes, 494, 518–519  
     lacunae, 517  
 Osteogenesis Imperfecta, 527  
 Osteoporosis, 521  
 Osteoporotic fractures, 641–642  
 Osteoprotegerin (OPG), 520–521  
     ligand, 520–521  
     system, 495  
 Osteotomies, 785  
 Oxygen, 306  
 Oxygenated maternal blood, 306

**P**

P-selectin glycoprotein ligand-1 (PSGL-1), 611  
 Pain prediction, 809  
 Parameter estimation, 38–39, 48–52  
     GBM evolution, 39–57  
     general framework, 21–28  
         about experiments, 22–26  
         model separability, 26  
     including model uncertainty, 26–28  
     about modeling, 21–22  
 mathematical tools and concepts, 28–36  
     copulas, 32–36  
     design of experiments, 31–32  
     estimation of probabilistic models, 30–31  
     managing data uncertainty, 28–36  
     methodology, 36–39  
     model adjustment, 36–37  
     model analysis and applications, 37–39  
 Parametric models for copulas, 34–35  
 Parametric study statistics  
     clinical dataset, 479  
     corneal biomechanics, 476–479  
 Parathyroid hormone (PTH), 520–521  
 Partial differential equations (PDEs), 22, 368–369  
     , 622  
 Particle deposition  
     fraction, 263–267  
     and transport, 240  
 Particle Reynolds number, 258  
 Particle transport and deposition modelling,  
     234–235  
 Passive ligamentous stiffness, role of, 94  
 Pathophysiological states, 201  
 Pathophysiology, HumMod for testing physiolog-  
     ical concepts and hypotheses in, 201–208  
 Patient-specific human airways model, 228–229  
 Patient-specific implant manufacturing, 854  
 Patient-specific modelling, 216  
     dataset description, 808–809  
     methods, 810–813  
         data preprocessing, 811  
         feature selection, 811–812  
         grouping/labeling, 810–811  
         machine learning, 812–813  
         validation, 813  
     results, 813–824  
         comparative analysis, 823–824  
         data fusion results, 823  
         feature selection, 820–823  
         predictive capacity of binary classifiers with  
             pain variables, 814–819  
         predictive capacity of binary classifiers without  
             pain-related variables, 814  
 Patient-specific nasal cartilage, 772  
 Patient-specific templates, 115–116  
     spatial coherence, 115–116  
 Peak Systole (PS), 294–295  
 Pearson's correlation coefficient, 479  
 Pelvic biomechanics, 216  
 Pelvic cavity, computational model of, 219

- Pelvic floor dysfunction (PFD), 213–214  
 Pelvic floor muscles (PFMs), 213–214  
 Pelvic floor tissues, 217  
 Pelvic Organ Prolapse (POP), 213–214  
     mechanism of development of POP, 215–218  
 Per unit mass, 364  
 Periodontium, 693  
 Peripheral neuropathies, 191  
 Personalization  
     in surgery, 853–861  
         craniomaxillofacial surgery, 855–856  
         orthopedic surgery, 853–855  
         spinal surgery, 857–858  
         urology surgery, 860–861  
         vascular surgery, 858–860  
     for surgical implants, 849–851  
         adoption of personalization in surgery, 853–861  
     examples of, 850f  
     personalized medical device definitions, 851–853, 852t  
     regulation, 861–863  
 Personalized healthcare, 15  
 Personalized medical device, 851–853  
 Personalized medicine (PM), 223, 343  
 Personalized models, 335–336  
     to repair uterine prolapse, 223  
 Personalized patient model, 223  
 Pharmaceuticals, effects of, 503–505  
 Pharmacokinetic models (PK models), 504  
 Pharynx, 277–278  
 Phosphatidylglycerols (PGs), 285  
 Photorefractive keratectomy (PRK), 443–444  
 Phototherapeutic keratectomy (PTK), 447  
 Physics-based computational models, 592  
 Physics-based musculoskeletal models, 162  
 Physiological cross-sectional area (PCSA), 129, 172  
 Physiologically maternal blood, 306  
 Piezoelectric material (PZE material), 576–577  
 Placenta Imaging Project (PIP), 319  
 Placental development and disease, 307–308  
 Placental elastography, 315–316  
 Placental lakes, 307  
 Placental vascular network, 308–309  
 Plantar soft tissue, 340  
 Plaque morphology models, 67  
 Plaque rupture  
     n artery, 630–641  
     SPH model for plaque rupture, 632–641  
 Plaque vulnerability, 65–66  
 Plaque wall stress (PWS), 631–632  
 Plaster model, 771  
 Point Shear Wave Elastography (pSWE), 313–314  
 Poisson's ratio, 280  
 Polycaprolactone (PCL), 431–433, 684  
 Polyether ether ketone (PEEK), 853–854  
 Polyethylene terephthalate (PET), 858–859  
 Polytetrafluoroethylene (PTFE), 858–859  
 Porous high-density polyethylene implants  
     (pHDPE implants), 855  
 Positive predictive value (PPV), 813  
 Posttraumatic deformities in VSP, 794–795  
 Posture ligamentous stiffness, role of, 94  
 Power Doppler Ultrasound (PDU), 308–309  
 Pressoreceptors, 290, 297–298  
 Pressure on cornea, 476  
 Pressure variations, 261–262  
 Presurgical Infant Orthopedics, 769  
 Probabilistic models, 30–31  
     estimation of, 30–31  
     maximum likelihood method, 30–31  
     method of moments, 30  
 Probability, 31–33  
 Probability density function (pdf), 31  
 Prosthesis, 695–696  
 Proteoglycans (PGs), 443–444  
 Protrusion force, 555
- Q**  
 Qualisys Track Manager v.2.12 (QTM), 127  
 Quality managementsystem (QMS), 862  
 Quality-adjusted life-year gain (QALY), 335–336  
 Quantitative Circulatory Physiology (QCP), 199–200  
 Quantitative Computed Tomography images  
     (QCT images), 526–527  
 Quantitative finance and risk theory, 33  
 Quasi-static aeroelasticity, 472  
 Quasi-static simulations model, 335
- R**  
 Radial point interpolation method (RPIM), 506  
 Radiofrequency (RF), 316–317  
 Random variables, 28–29  
 Randomized Controlled Trials (RCT), 184, 223  
 RANK-Ligand (RANKL), 495, 504–505, 520–521  
 RANK-RANKL signaling, 495  
 Real-Time Locating Systems (RTLS), 14  
 Realistic model, 228–229  
 Reconstructive surgery of jaw in VSP, 794

- Red blood cells (RBCs), 604  
 Refinement, reduction and replacement of animals (3R of animals), 533  
 Region of interest (ROI), 534–535  
 Rehabilitation process, 830  
 Reinforcement learning, 180  
 Reliability-Based Design Optimization (RBDO), 33  
 Renin–angiotensin system, 203–204  
 Respiratory diseases, 284–285  
 Respiratory system, 277–278  
 Respiratory tract, liquid transport and droplet formation in, 399–416  
 Retinal Detachment, 465–466  
 Reynolds averaged Navier–Stokes (RANS), 234  
 Reynolds number (Re), 404  
 Right lung (RL), 263–264  
 Root mean square deviation (RMSD), 799  
 Rouché–Fröbenius–Capelli theorem, 26  
 Route mean square error (RMSE), 481–482
- S**  
 Sacrocolpopexy, 218  
 meshes, 214  
 Samples variability correlation, 40  
 Scalable bronchial airway model, 256–257  
 Scaling matrix, 131  
 Segmental defect, 425–426  
 Selective laser melting (SLM), 853–854  
 Sema3A, 504–505  
 Severe acute respiratory syndrome coronavirus 2 (SARS-CoV-2), 400, 604  
 Severe memory loss  
     3D scanning acquisition, 839  
     development of serious game, 840  
     VR platform for recovery of, 838–840  
 Shape analysis, 111–112  
     approximation to simple shapes, 111–112  
     shape analysis–based approaches, 111  
 Shear Wave Elastography (SWE), 312–313  
 Shear Wave Velocity (SWV), 313  
 Short-Chain Fatty Acids (SCFAs), 369  
 Signaling molecules, 504–505  
 Silico, limbs in, 172–179  
 Silico medicine, 15  
 Silico models, 228, 503  
 Simulated Bone Atrophy (SIBA), 503  
 Simulation, NEUROID movement simulation platform, 169  
 Simulation-based subject-specific surgical planning, 454–457  
 Single-cell–based models, 550, 564  
 methodology, 550–564  
     assumptions, 562–564  
     boundary conditions, 562  
     cell differentiation, 560–561  
     cell electrotaxis, 555–556  
     cell fate decision, 559–560  
     cell maturation, 560  
     cell mechanotaxis, 553–555  
     cell motility, 552–553  
     cell proliferation, 561  
     cell–cell adhesion, 558–559  
     cell–cell contact, 558  
     cell–cell interaction, 557  
     drag force, 556–557  
     ECM discretization, 562  
     model parameters and experiment setup, 562  
     numerical implementation and applications, 564–577  
         advanced materials for mechanoelectrical stimulation coupling, 576–577  
     cell adhesions modulated by ECM stiffness, 569–570  
     cell differentiation modulated by ECM stiffness, 566–568  
     cell–cell contact forces, 565–566  
     electrically stimulated ECM, 574–576  
     mechanically stimulated ECMs, 570–574  
 Six-nodded 3-D fluid continuum elements (FC3D6), 475  
 Skeletal muscle, 199–200  
 Skew-symmetric matrix, 125–126  
 Sklar’s theorem, 34  
 Slice boundaries, 278  
 Small incision lenticule extraction (SMILE), 456  
 Small Intestinal Bacterial Overgrowth (SIBO), 387–388  
 Small intestine, 387–391  
     solute/nutrient diffusion and absorption, 388–390  
     spatially varying multiphase digesta rheology, 390–391  
 Small microaerosols, 277–278  
 Small-angle X-ray scattering (SAXS), 446–447  
 Smart experiments, 27  
     divide and conquer, 25  
     general situation, 25–26  
     in one stroke, 23–24  
     process, 22–26  
 Smoothed Particle Hydrodynamics (SPH), 362–363, 416–417, 593, 711, 726  
 coagulation model and predictions, 622–630  
 collisions and rigid body dynamics in, 366

- DEM-SPH coupling for slurry simulation, 367
- momentum equation, 367
- for simulating external environment, 726–729
  - for elastic and elastoplastic solids, 727–729
  - for fluids, 726–727
  - integration of SPH equations, 729
  - SPH boundary modeling, 729
  - solid evolution for remodeling processes, 603
- Snow skiing technique, 742–749
- Soft constraint equations, 131–132
- Soft tissues
  - biomechanical properties of, 220
  - deformation, 144
  - tumors, 467
- Soft-Margin algorithm, 71
- Software design choices, 144–146
  - AnyScript, 145
  - multibody system formulation, 146
  - structuring principles, 146–148
- Software Development Kits (SDKs), 833–834
- Software-guided implant surgery, 696–697
- Solids, 471
  - chocolate, 378
  - coupling domain, 294
  - deformations, 472
  - domain, 293
  - equation, 471–472
  - food bodies, 383
  - geometries, 291
  - mixture, 381–382
  - motion, 378–381
- Solute/nutrient diffusion and absorption, 388–390
- Sonoelastography, 312–315
- Spalart–Allmaras turbulent eddy viscosity model, 475
- Spatial analysis, 534, 536
- Spearman’s  $\rho$  coefficient, 29–30
- Specialized cells, 443–444
- Spherical joint, 146
- Spinal circuitry, 162
- Spinal cord stimulation, 190
- Spinal reflex pathways, 168
- Spinal surgery, 857–858
- Spinal\_neurons.xlsx model, 175
- Spine, 95–96
- Sports, 151–152
- Stability, 86–87
  - dynamic criterion of, 89–90
  - of human knee joint, 97–99
  - of human MS systems, 91–93
  - of human spine, 94–97
  - stability-based multicriteria simulations, 96–97
- stability-driven model, 97
- Stable system, 89–90
- Stand-alone foot model, 343
- Standard deviation (SD), 29, 98, 479
- Standard Linear Solid (SLS), 284–285
- Standard Tessellation Language (STL), 429
- State-of-the-art models, 339
- Statistical approach, 111
- Statistical shape models (SSMs), 115
- Statistics, 32–33
- Stem cells, 548
- Stented airways
  - airflow patterns in, 235–239
  - airflow turbulent patterns in, 239–240
- Stented human upper airways, comparison between healthy and, 242
- Stereolithography (SLA), 432, 661, 673
- Stereophotogrammetry, 789
- Stiffness parameter at highest concavity (SP-HC), 479
- Stokes’ law, 556
- Stokes number, 280, 283–284
- Stomach, 381–387
- Strain, 523
  - incorporation of, 500–502
- Strain Elastography (SE), 312–313
- Strain energy density (SED), 496
  - as mechanical stimulus, 496–500
  - subject-specific bone remodeling simulation pipeline, 497f
  - trilinear bone remodeling model, 495f
- Strain energy function (SEF), 66–67
- Strain gauges, 528–529
  - local deformation with, 528–529
  - strain analyses in the human proximal femur, 530f
- Strain Rate Imaging (SRI), 312–313
- Stress, 523
  - concentration, 437
  - incorporation of, 500–502
  - stress–strain equilibrium, 562
- Stress urinary incontinence (SUI), 216
- Stroke
  - cross-sectional modeling of stroke severity and corticospinal residuum, 186–188
  - longitudinal modeling of recovery and computational neurorehabilitation, 188–190
- Stroma, 444
- Stroma, 450
- Stroma layer, 467–468
- Subject-specific model, 129–130
- Supercomputers, 3–4
- Superquadric (SQ), 366

- Support Vector Machine (SVM), 65, 71, 108, 110, 812–813
- Surgical maneuvers, 771–772
- Surgical replacements, 430–431
- Surrounding matrix, 285
- Swimmer digital twin, 732
- Swimming technique, 729–735
- System-level physiology models, 168
- T**
- Taba-Parto Shiraz radiology center, 291
- Tangential force, 365–366
- Tele-rehabilitation, 832
- Template model to subject-specific data, scaling of, 129–130
- Template-based approaches, 114–115  
atlas-based templates, 114–115
- Temporomandibular joint surgery (TMJ surgery) in VSP, 795
- Terminal bronchioles, 399–400
- Therapeutic Goods Administration (TGA), 861
- Thermal field, 555–556
- Thermal index (TI), 316
- The temporomandibular joint, 427
- Thin cap fibroatheroma (TCFA), 631
- Three-dimension (3D)  
bone parameters, 534–535  
CFD turbulence model of air puff, 475–476  
computational model, 368–369  
dynamic bone morphometry, 534–535  
eye model, 473–474  
foot–shoe model, 349–350  
image-based model of aortic arch, 290–291  
imaging and biomechanical soft tissue simulation, 787–790  
applications, 788  
biosimulations, 789–790  
cone beam computed tomography, 788  
dental records, 789  
multislice computed tomography, 788  
stereophotogrammetry, 789  
imaging technology, 773  
model, 278  
modeling system, 146  
modeling tools, 834  
parametric models, 76–77  
parametric study, 66–68  
placenta models, 306–307  
poroelastic FE model, 502–503  
printing, 679–680, 853  
visualization, 107  
volumes, 310–311
- Thrombin transport, 602
- Tidal volume (TV), 280–281
- Time-consuming model-building strategies, 335
- Tissue engineering (TE), 680
- Tissue mineral density (TMD), 527
- Tissues, 107–108  
properties, foot digital twin, 339–340  
tissue-engineered scaffolds, 426
- Titanium, 431–433  
implant, 683
- Tomography and Biomechanical Index (TBI), 485
- Tonometry, 466–467
- Total ankle replacement (TAR), 346–347
- Total deposition fractions, 242
- Total hip arthroplasty (THA), 497–498
- Total peripheral resistance (TPR), 203
- Total volume (TV), 523
- Toxic nanoparticles, 253–255
- Trabeculae, 517
- Trabecular bone, 517
- Trabecular bone volume fraction (Tb. BV/TV), 534–535
- Trabecular number (Tb. N), 523, 534–535
- Trabecular separation (Tb. Sp), 534–535
- Trabecular spacing (Tb. Sp), 523
- Trabecular thickness (Tb. Th), 523, 534–535
- Trachea (TR), 264–265
- Traditional EMG-assisted models, 97
- Traditional planning, 797  
comparison between traditional and modern planning, 797–799
- Training  
backpropagation for training technique, 65  
data, 71
- Transcranial Magnetic Stimulation (TMS), 186–187
- Transforming growth factor-beta (TGF- $\beta$ ), 495, 520–521
- Transient Elastography (TE), 313
- Tumor MicroEnvironment (TME), 39–40
- Tumors, 39–40
- Turbulence, 239  
flow, 239–240  
intensity, 299
- Turbulent aortic flow, 294–295
- Turbulent blood flow, 299
- Twinning  
model, 182–183  
in NEUROiD, 183
- Two-dimensional Shear Wave Elastography (2D-SWE), 313–314

**U**

Ultrafine particles, 253–255  
 transport to lower airways  
 escaped particles, 267–269  
 geometrical development, 256–257  
 numerical methods, 258–260  
 particle deposition fraction, 263–267  
 pressure variations, 261–262  
 result, 260  
 velocity functions, 260–261

Ultrasound, 306–308

elastography, 311–312  
 system, 313–314

Uniform nanoparticle distribution, 259

Uniform scaling law, 130–131

Unilateral loading conditions, stress and  
 magnitude of displacement of stem and  
 wing design in, 433–437

United States National Institute of Child Health  
 and Development (NICHD), 319

Upper airways, 255–256

Upper limb, 172–175

Upper motor neuron (UMN), 190–191

Urology surgery, 860–861

US National Library of Medicine's (NLM), 3–4

Uterine prolapse simulation, 221

Uterosacral ligament, 216

Uterosacral–cardinal ligaments, 216

**V**

Validation

examples of validation studies for FE models, 531  
 of mechanoregulation algorithms, 534  
 for murine studies, 533–534  
 process, 528

Valsalva maneuver, 218

Vascular surgery, 858–860

Velocity contours, 260

Velopharyngeal function, 774

Ventilation function, 774

Viral aerosols, 278

Viral respiratory diseases, 285

Virtual digital human skull models

biomechanics, 684–687  
 commercialization considerations, 687–688  
 customized implant design, 683–684  
 regenerative craniofacial surgery, 681–683

Virtual foot models, 334

Virtual limbs

machine learning setup, 180–182  
 movement training of, 179–182

Virtual models, 228–229, 695–696

Virtual Organ Computer-aided AnaLysis  
 (VOCAL), 310–311

Virtual patient model

comparison between traditional and modern  
 planning, 797–799  
 accuracy of surgical plan transfer, 797–798  
 cost and time, 798  
 surgical outcome/patient satisfaction, 798–799  
 traditional vs. modern planning, 797  
 historical methods of planning, 784–787  
 craniofacial surgery, 786–787  
 limitations of traditional planning, 787  
 orthognathic surgery, 785  
 postablative reconstructive jaw surgery,  
 785–786

3D imaging and biomechanical soft tissue  
 simulation, 787–790

virtual surgical planning, customized surgical  
 guide, and fixation plates, 790–795

Virtual Physiological Human (VPH), 6–8

*in silico* medicine, 9t–11t

up-to-date *in silico* relevant resources listed by  
 VPH, 12t

Virtual populations, HumMod, 206–208

Virtual reality (VR), 662–663

and dental education, 700–701

evaluation, 842–845

methods and tools, 832–834

definition of rehabilitation exercise and related  
 devices, 833

identification of ICT tools, 833–834

medical data management, 834

motor-skills tele-rehabilitation of hands,  
 840–842

VR platform for evaluation of extra-personal  
 neglect, 835–837

VR platform for recovery of severe memory  
 loss, 838–840

models, 662–663

scientific background, 831–832

Virtual Reality Exposure Therapy (VRET), 700

Virtual smile modeling, 698–699

Virtual surgery, 618–619

Virtual surgical planning (VSP), 785, 790–795

in craniofacial surgery, 794

designing and printing of surgical aids, guides, or  
 implants, 792–793

integration of digital information, 791

in orthognathic surgery, 791

in posttraumatic deformities, 794–795

in reconstructive surgery of jaw, 794

in temporomandibular joint surgery, 795

Virtual surgical planning (VSP) (*Continued*)  
 virtual operating theater, 791–792  
 Viscoelastic properties of bone, 524  
 Viscoelasticity, 452  
 Visible Human Project (VHP), 3–6, 165  
 Vitamin D3, 520–521  
 Vivo tissue engineering, 687–688  
 Volkmann’s canals, 517

**W**

Wall shear stress (WSS), 290, 630  
 Water, 516  
 Wavefront technologies, 672  
 Weakly compressible assumption  
 (WC assumption), 363–364, 727  
 Web-based teaching tool, 199–200  
 Weighting parameter, 717  
 Western Ontario McMaster Arthritis Index  
 (WOMAC), 810  
 White blood cells (WBCs), 604  
 rolling adhesion, 611–614  
 Whole-body movement model  
 computational methods, 719–729  
 biomechanical methods, 719–726  
 SPH method for simulating external  
 environment, 726–729  
 creating software products based on human  
 digital twins, 755–756  
 using digital twins to understand performance and  
 injury, 729–749  
 markerless motion capture for digital human  
 model construction, 712–719  
 realtime digital human applications, 749–755  
 Wi-fi connections, 833  
 Wide-angle X-ray scattering (WAXS), 444,  
 446–447

**X**

X-ray scattering data, 449–450  
 “XYZ” scaling law, 131

**Y**

Yeoh constitutive model, 219  
 Young’s modulus, 280, 314

**Z**

0D model of microbial fermentation, 369–370

# DIGITAL HUMAN MODELING AND MEDICINE

## THE DIGITAL TWIN

EDITED BY GUNTHER E. PAUL AND MOHAMED H. DOWEIDAR

*Digital Human Modeling and Medicine: The Digital Twin* explores the body of knowledge and state-of-the-art in Digital Human Modeling (DHM) and its applications in medicine. DHM is the science of representing humans with their physical properties, characteristics, and behaviors in computerized, virtual models. These models can be used as standalone or integrated with other computerized object design systems to both design and study designs of medical devices or medical device products and their relationship with humans. They serve as fast and cost-efficient computer-based tools for the assessment of human functional systems and human-system interaction.

This book provides an industry first introductory and practitioner-focused overview of human simulation tools, with detailed chapters describing body functional elements and organs, organ interactions, and fields of application. Thus, DHM tools and a specific scientific/practical problem—functional study of the human body—are linked in a coherent framework. Eventually, this book shows how DHM interfaces with common physical devices in medical practice, answering to a gap in literature and a common practitioner question. Case studies provide the applied knowledge for practitioners to make informed decisions.

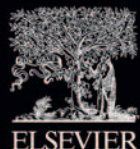
### KEY FEATURES

- Provides mathematical modeling approaches applied to biological systems comprising the digital twin
- Features biomedical and biomechanical system models enabling a holistic human digital twin
- Contains medically relevant DHM systems to inform trialing, procurement decisions, and initial application
- Includes user-level examples and case studies of digital twin applications in various medical fields
- Clearly structured and focused compendium of digital twin developments that is easy to access, read, and understand

### ABOUT THE EDITORS

**Gunther Paul** is an Ergonomist and James Cook University Principal Research Fellow for Occupational Health and Safety at the Australian Institute for Tropical Health and Medicine (AITHM). He holds a PhD in Ergonomics and MPhil in Control Engineering from Darmstadt University of Technology. His research focuses on complex work system-related issues, such as health systems, respiratory health, human-in-the-loop modeling, or musculoskeletal disorders. Gunther has been the Chief Investigator in 17 research projects. He has published over 100 journal articles, books, and book chapters and has been regularly presenting and chairing sessions at international conferences over the last 25 years. In his most recent previous employments, Gunther led the Health Safety Environment Discipline in the School of Public Health and Social Work at QUT, and before that he was the Director of Ergolab at UniSA. In his 10-year industrial career, he worked as a Project Manager for Ford, Daimler, and Faurecia.

**Mohamed H. Doweidar** has taught at various schools of engineering from 1994 until now. He received his doctorate in CFD (2005) along with a Diploma of Advanced Studies in CFM (2004) from the University of Zaragoza; Master in Mathematics for Engineers (2001) from Ain Shams University; Bachelor of Statistics and Informatics (1997) from the University of Mansoura; Industrial Engineering degree (1993) from BHIT. He is a member of the Applied Mechanics and Bioengineering Group (AMB); the CIBER-BBN; the I3A and the ESB. Dr. Doweidar has participated in 24 projects of national and international research. In addition, he is the author and co-author of 47 JCR articles and 12 books and book chapters. Besides, he has participated in 55 conferences. He is a member of the editorial board and reviewer for 35 JCR journals. He is also an evaluator of research projects for the ANEP. He has directed three doctoral theses, one of which won the special prize of the university and another one was a candidate. Now, there are two doctoral theses in progress. His research interests include Computational Biomechanics, Simulation of cellular behavior, hyperelastic materials, large deformation, FEM, NEM, CFM, Error Estimation and Adaptivity.



ACADEMIC PRESS

An imprint of Elsevier

[elsevier.com/books-and-journals](http://elsevier.com/books-and-journals)

ISBN 978-0-12-823913-1



9 780128 239131